TECTONICS, VOL. 18, NO. 6, PAGES 1275-1291 DECEMBER 1999

Flexural rift flank uplift at the Rio Grande rift, New Mexico

C. David Brown and Roger J. Phillips

Department of Earth and Planetary Sciences, Washington University, Saint Louis, Missouri

Abstract. Like other Cenozoic continental rifts, the Rio Grande rift in Colorado and New Mexico exhibits prominent flanking uplifts. Several driving stresses and thermal-mechanical processes have been proposed to explain the origin of rift flank relief, which can be modeled to infer lithospheric structure. Although we have identified multiple uplift styles at the Rio Grande rift, only one range—the Sacramento Mountains—is attributable to flexural upwarping of the lithosphere, the process most suitable for geodynamic modeling and interpretation. We demonstrate that two common assumptions in such modeling potentially introduce serious errors. First, presuming only one mechanism acts to uplift the flanks is inappropriate; various forces influence flank topography at different depths and wavelengths and no single one is dominant. Second, the end-member boundary conditions of complete mechanical continuity or discontinuity (broken plate) at the range-bounding normal fault are, in general, not applicable at rift flanks. We examine alternative analytic plate flexure solutions by comparing them to finite element models of footwall flexure at a normal fault in a two-dimensional elastic plate undergoing extension. These simulations indicate that broken plate fits to rift flanks underestimate the plate thickness unless the uplift is large (at least ~1 km), which promotes decoupling between the hanging wall and footwall. If denudation dominates the flank unloading, as may commonly be the case, the best-fit broken plate thickness error can be even greater. Our flexural analysis of the Sacramento Mountains suggests that the Pecos River Valley originated as a flexural downwarp adjacent to the rift flank. Sensitivity tests of least-squares fits to the Sacramento Mountains imply typical plate thickness errors of <20%, although in extreme cases the combined errors may be ~50%. The average effective elastic lithosphere thickness is ~23 km. We find that elastic–plastic models of rift flank flexure are unable to provide meaningful constraints on the thermal structure of continental lithosphere.

1. Introduction

The Rio Grande rift (RGR) is one of the most thoroughly studied Cenozoic continental rifts, but it is perhaps the most complicated because of its superposition on other Cordilleran structures of the western United States. The rift extends over 1000 km from Colorado through New Mexico to Chihuahua, Mexico (Figure 1), and it shows substantial changes in basin and flank physiography along strike [*Olsen et al.*, 1987; *Baldridge et al.*, 1995]. The RGR has been the focus of numerous geologic and geophysical investigations, including seismic refraction, seismic reflection, teleseismic tomography, gravity, basin stratigraphy, heat flow, magmatism, xenolith geothermobarometry, and apatite fission-track analyses. The large amount of data amassed on the RGR provides invaluable constraints on geodynamic models over a range of structural scales, from the upper crust to the entire lithosphere and upper asthenosphere.

In the present study we examine the lithosphere-scale flexural uplift of the rift flanks. Rift flank uplift has been attributed to a variety of mechanisms and driving forces. For instance, flank uplift has been explained with elastic, viscous, and elastic-viscous-plastic models of the lithosphere, and authors have invoked crustal thinning (i.e., basin formation) [*Weissel and Karner*, 1989], necking of the mechanical lithosphere [*Chéry et al.*, 1992], lateral heat conduction [*Alvarez et al.*, 1984], small-scale convection [*Buck*, 1986], erosion and denudation [*Gilchrist and Summerfield*, 1990], and dynamic flow stresses [*Zuber and Parmentier*, 1986] as responsible processes. Obviously, these mechanisms are not mutually exclusive; several are likely to contribute to flank uplift, and no one may dominate.

This paper is structured as follows. First, we discuss the flank uplifts at the Rio Grande rift and evaluate whether or not they originate by lithospheric flexure (section 2). We find that only one flanking range, the Sacramento Mountains in southeastern New Mexico, is convincingly flexural, and therefore only it can be modeled using flexural techniques. Second, we use the Sacramento Mountains to test existing flexural rift flank uplift models—specifically, whether common assumptions of a completely broken or continuous lithosphere are reasonable, and whether a basin load can fully account for the uplift (section 3). We employ finite element models to investigate the role of an explicit, range-bounding normal fault on the behavior of the lithosphere (section 4). With the results of these simulations, we determine the effective elastic thickness of the lithosphere at the Sacramento Mountains as well as the uncertainty in this value (section 5). We end with a discussion of the relevance of our results to flexural rift flank modeling and the tectonics of southeastern New Mexico (section 6).

All of our modeling assumes an elastic lithosphere. An eventual goal, to which this work contributes, is to determine if flexural methods can be used as probes of the thermal structure of rifted continental lithosphere (as has been done with oceanic lithosphere [*McNutt*, 1984; *Wessel*, 1992]), or, conversely, if independent information on the geotherm can be used to test the mechanical and rheological precepts of lithospheric deformation modeling.

2. Flank Uplifts at the Rio Grande Rift

2.1. Background

Extension at the Rio Grande rift was preceded by several key geologic events that significantly influenced the late-Cenozoic rifting phase, including the flank structures. Two orogenies modified the crust of the North American craton where the RGR later formed: the Ancestral Rocky Mountains in the late Paleozoic

Paper number 1999TC900031.
0278-7407/99/1999TC900031$12.00

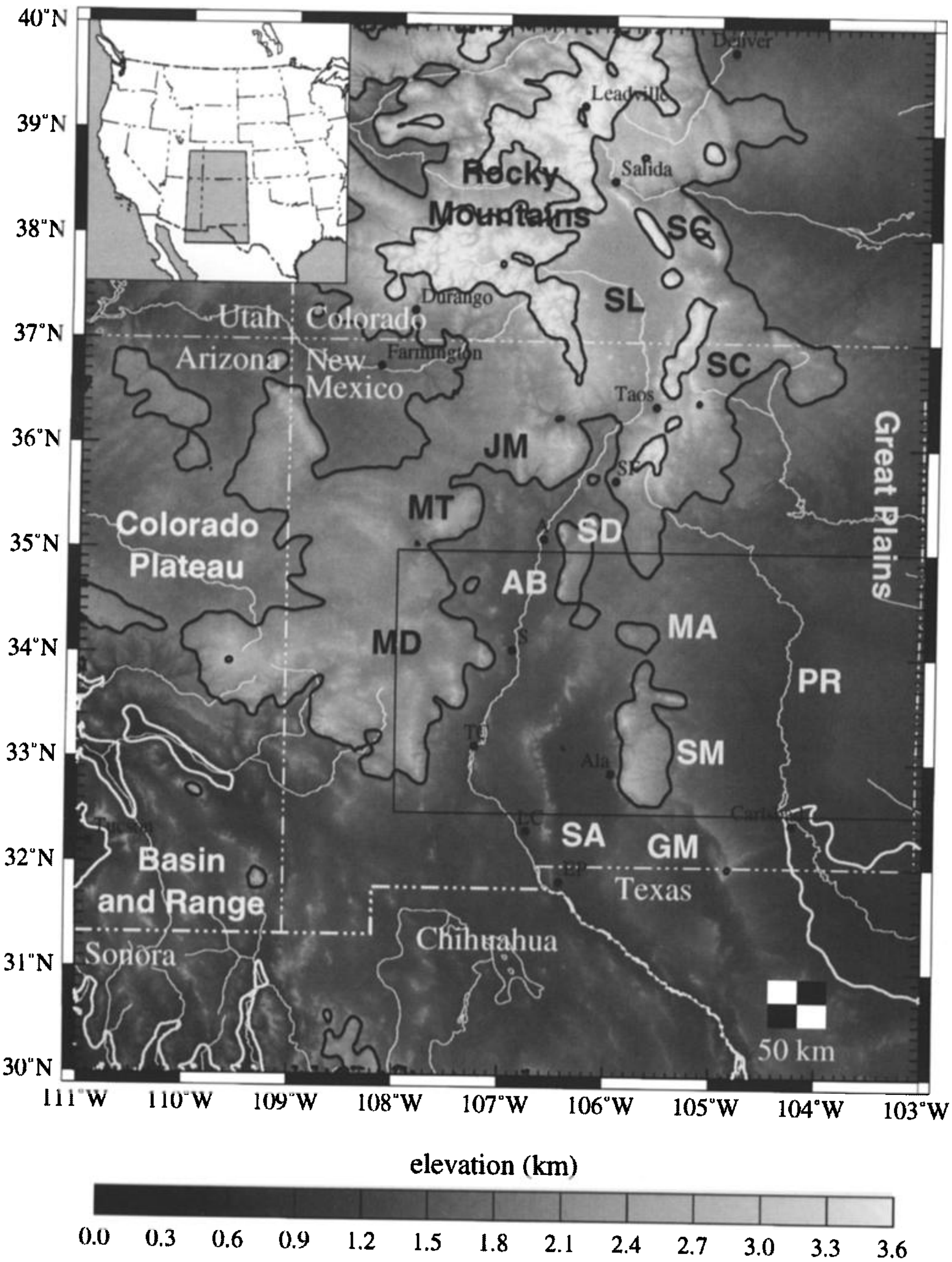

Figure 1. Topography and rivers of the Rio Grande rift region in Colorado, New Mexico, Texas, and northern Mexico. Long-wavelength topography is contoured at 1-km intervals (the white contour is 1-km elevation). Abbreviated major cities (north to south) are SF—Santa Fe, A—Albuquerque, S—Socorro, TC—Truth or Consequences, Ala—Alamosa, LC—Las Cruces, and EP—El Paso. Major features include SC—Sangre de Cristo Mountains, SL—San Luis Basin, JM—Jemez Mountains, MT—Mount Taylor, SD—Sandia Mountains, AB—Albuquerque Basin, MA—Mescalero arch, MD—Mogollon–Datil volcanic field, PR—Pecos River, SM—Sacramento Mountains, SA—San Andres Mountains, and GM—Guadalupe Mountains. Location of Figure 2a is outlined by box.

(~300 Ma) and the Laramide orogeny in the Late Cretaceous to early Tertiary (~80–40 Ma) [*Chapin and Seager*, 1975; *Burchfiel et al.*, 1992]. Topography was beveled during and following the Laramide, forming the low-relief Eocene erosion surface [*Epis and Chapin*, 1975; *Gregory and Chase*, 1994]. In the middle Tertiary (~40–20 Ma), voluminous intermediate–rhyolitic magmatism related to subduction of the Farallon plate emplaced large volcanic fields such as the Mogollon–Datil [e.g., *Keller et al.*, 1991; *Baldridge et al.*, 1995]. Initiation of extension in the late Oligocene (~29–27 Ma) is marked by a change in magmatic style to basaltic and bimodal, deposition of ash-flow tuffs, and development of early rift structures [*Ingersoll et al.*, 1990; *Brister and*

Gries, 1994; *Chapin and Cather*, 1994]. Two phases of extension and volcanism are commonly described for the rift [*Morgan et al.*, 1986]. The first was characterized by broad basins and low-angle normal faulting; it overlapped the end of the mid-Tertiary magmatic episode. The lithosphere is inferred to have been hot and weak; topographic relief generated during this phase was apparently modest. The second period of extension formed the primary features of the RGR we see today. High-angle normal faults accommodated strains of ~10–30%. Volcanism was less voluminous during this time.

2.2. Types of Flank Uplifts

The RGR is flanked by topographic highs along most of its length (Figure 1), but the nature and origin of these uplifts varies along rift strike. Flank topography is associated with Laramide basement-cored uplifts (which might have experienced additional, later uplift during rifting), volcanic structures, tilted fault blocks, and flexural uplifts. These features are all superimposed upon a regional, long-wavelength (>500-km) topographic upwarp [*Eaton*, 1987] that may have arisen from Laramide crustal thickening [*Chapin and Cather*, 1994], a remnant thermal anomaly from arc volcanism associated with subduction of the Farallon plate [*Davis*, 1991], prerift or synrift magmatic crustal thickening [*Morgan et al.*, 1986], or rift-driven asthenospheric upwelling [*Bridwell and Anderson*, 1980].

Several large volcanic fields along the western margin of the rift interfere with identification of possible tectonic uplift. Prominent examples include the Jemez Mountains (JM), the Mount Taylor volcanic shield (MT), and the Mogollon–Datil volcanic field (MD in Figure 1). The latter, though it is bordered by several rises on the east (Magdalena Mountains, San Mateo Mountains, and Black Ranges), has a deformation history dominated by volcanic processes, such as caldera formation and collapse [*Coney*, 1976]. It is difficult to distinguish tectonic uplift from these structures, making geodynamic modeling problematical.

2.3. Northern Rio Grande Rift

The northern and central RGR (north of Socorro, New Mexico, at 34°N) is narrow, and the rift is bounded to the west by the Colorado Plateau and to the east by the Great Plains (i.e., the North American craton). Rift basins are no more than 100 km wide. Here the flanks are delineated by prominent exposures of Proterozoic basement that stand out from the surrounding Phanerozoic sedimentary strata and Neogene rift-basin infill [*Woodward et al.*, 1975; *Baldridge et al.*, 1983]. Some of these ranges are continuous, ~100-km-long features (e.g., Sangre de Cristo Mountains (SC), Los Pinos–Manzano–Sandia Mountains (SD in Figure 1)) while others are isolated blocks bounded on two or three sides by normal faults (e.g., Lemitar Mountains, Ladron Peak [*May et al.*, 1994]). The southern Rocky Mountains were uplifted during the Laramide orogeny, but some ranges experienced further uplift during late Tertiary rifting [*Tweto*, 1975]. For example, the Sangre de Cristo Mountains in south-central Colorado comprise the eastern edge of a broader Laramide uplift, part of which was down-faulted as the San Luis Basin graben (SL in Figure 1). The Sangre de Cristo Mountains are now bordered on both the west and east by Neogene normal faults that express additional uplift during rifting [*Tweto*, 1979]. Similarly, the Los Pinos–Manzano uplift is a composite of Laramide and Rio Grande uplifts [*Kelley*, 1979].

Kelley and Duncan [1986] and *Kelley et al.* [1992] performed detailed apatite fission track (AFT) analyses of rocks from several northern and central RGR flanks. AFT dates reflect the time since the rock rose through the 100 ± 40°C isotherm, as fission tracks anneal at higher temperatures. However, hydrothermal processes and magmatism can mimic the effects of denudation-induced uplift and cooling. *Kelley et al.* [1992] found AFT ages indicative of Laramide deformation, late Eocene denudation, rift-related uplift, and volcanic and hydrothermal modification. The former two processes involved slow cooling rates (<5 K Myr^{-1}) and show AFT ages greater than 30 Ma. Uplifts attributed to rifting, but spared the effects of volcanism, have AFT ages of 10–25 Ma and include the northern Sangre de Cristo Mountains, Blanca Peak, the Sandia Mountains, and Ladron Peak. These rocks experienced relatively rapid cooling rates of >5 K Myr^{-1} and ascended at least 2–3 km.

The AFT results demonstrate that several flanks did form by uplift during rifting, including ranges that were first uplifted as Laramide basement-cored anticlines. There is a clear correlation between the locations of major rift-bounding normal faults and flanks exhibiting significant Neogene uplift [*May et al.*, 1994]. For instance, the Albuquerque Basin (AB in Figure 1) is the deepest half-graben of the rift (with over 7 km of synrift sediments [*Russell and Snelson*, 1994]); the adjacent Sandia Mountains have some of the highest Precambrian basement structural relief of the rift (over 3 km [*Woodward et al.*, 1975]), and among the fastest cooling rates (up to 12 K Myr^{-1} [*Kelley et al.*, 1992]). These observations imply that faulting and thinning of the crust drive rift flank uplift by unloading of the footwall.

2.4. Southern Rio Grande Rift

The southern RGR (south of Socorro) is distinct in character from the north: the rift widens and physiographically resembles the Basin and Range, into which it merges south of the Colorado Plateau (Figure 1). The flanks are dominated by ranges in the Mogollon–Datil volcanic field (MD) on the west and the Sacramento Mountains (SM) on the east. The interior is divided into several sub-basins (Palomas, Jornada del Muerto, and Tularosa) and structural highs such as the San Andres Mountains (SA in Figure 1). The flanks are composed of Tertiary volcanic and Paleozoic sedimentary rocks but not Precambrian basement [*Woodward et al.*, 1975; *Baldridge et al.*, 1983]. Like the central RGR, here the flanks are generally narrower and not as long as in the north. Southern basins are not as deep [*Lozinsky*, 1987; *Harrison*, 1994; *Adams and Keller*, 1994], but late-phase extension was apparently greater than in the north because the crust at the rift axis is thinner [*Cordell*, 1982; *Morgan et al.*, 1986].

AFT analyses indicate Miocene uplift ages for interior fault blocks of the southern rift, like the Caballo and San Andres Mountains [*Kelley and Chapin*, 1997]. There is essentially no Laramide AFT signature in the southern RGR, suggesting the net Laramide and late-Tertiary uplift is less compared to the north. AFT dating of two Proterozoic metasedimentary samples at the base of the western scarp of the Sacramento Mountains yielded ages of 35–41 Ma. Combined with age and apatite fission track length measurements of samples at higher elevations, these results reflect a fairly slow uplift synchronous with late rifting [*Kelley and Chapin*, 1997].

2.5. Implications for Modeling

From the preceding overview of Rio Grande rift flank uplifts we can begin to explore the likely tectonic uplift mechanisms and determine if any flanks involve flexure of the lithosphere. Flank topography north of Santa Fe is dominantly Laramide in origin. Eocene denudation and rift-related unloading have contributed to uplift, as demonstrated by AFT dating, but preexisting orogenic topography and structural complexity preclude any straightforward mechanical interpretation of RGR uplift. These ranges lack cross-sectional topographic asymmetry diagnostic of flexural flank uplift. Although several uplifts in the central rift (between Socorro and Santa Fe) are directly attributable to rifting by their more modest Laramide deformation, AFT ages, and association with late-Tertiary normal faults and deep half grabens, they, too, are quite structurally complicated.

For example, the Sandia Mountains appear to represent a "classic" rift flank uplift. This range comprises an eastward-tilted fault block on the eastern margin of the Albuquerque Basin. Uplift was accommodated by one or more west-dipping normal faults [*Kelley and Northrop*, 1975]; net structural relief across these range-bounding faults exceeds 10 km [*Chapin and Cather*, 1994]. Laramide faults are evident, and the Sandia Mountains may have been the site of a Laramide anticline. The ~20-km-long range is bordered to the south by a northeast-striking Laramide fault, and to the north by a northeast-striking normal fault. The back slope of the mountains is thoroughly cut by faults that have experienced both reverse and normal motions, some of which may have been concurrent with late Tertiary uplift [*Kelley and Northrop*, 1975]. Other flanking ranges similar in both scale and structure to the Sandia Mountains include Ladron Peak and the Sierra Lucero [*Lewis and Baldridge*, 1994]; these mountains all experienced late Tertiary uplift, are of the order of 10 km in planform scale, and are bounded on two or more sides by faults. Extensional unloading of these three fault blocks certainly was a cause of their uplift, but they lack structural continuity parallel to the rift strike and the crust lacks mechanical continuity due to pervasive faulting (perhaps relict Laramide deformation). The first factor makes a two-dimensional modeling approximation inappropriate, and any three-dimensional model would require inclusion of the multiple controlling faults. Furthermore, deformation of these fault blocks probably contains no information on the lithospheric thickness or geotherm. We do not pursue modeling of these uplifts.

2.6. Sacramento Mountains

Only one range at the RGR, the Sacramento Mountains (SM), is a compelling example of a flexural rift flank uplift. This ~60-km-long, ~1.5-km-high range defines the eastern boundary of the RGR with the Great Plains (Figures 1 and 2), and it is bordered to the west by the Tularosa Basin (TB) and to the east by the Pecos River Valley (PR). While not as well studied as many regions in the central and northern rift, some limited but thorough field work in the TB–SM area substantiates the interpretation of a flank uplift at the SM concurrent with rifting. *Pray* [1961] mapped the SM, focusing on the thick Paleozoic sedimentary section exposed in the dramatic west-facing escarpment. He observed that most structures in the area trend north and date to the Pennsylvanian–Permian (Ancestral Rocky Mountains) [*Bowsher*, 1991]. This was a period of uplift of what is called the Pedernal Mountains [e.g., *Kelley*, 1971]. The nearly complete absence of Mesozoic rocks in the area reflects substantial erosion at least into the early Cenozoic and the formation of the Sacramento Mountains peneplain [*Kelley*, 1971]. Structurally there is little evidence for significant Laramide deformation at the SM, and *Kelley and Chapin*'s [1997] AFT age measurements lack a strong signature of Laramide uplift. Minor Tertiary volcanism in the SM is expressed by sills and dikes crossing the range [*Pray*, 1961], although the more substantial Sierra Blanca igneous complex and Capitan pluton are situated to the north [*Moore et al.*, 1991].

The present form of the SM results from late Cenozoic uplift accommodated by slip on one or more major west-dipping normal faults at the eastern edge of the Tularosa Basin. These motions resulted in a north-trending topographically asymmetric mountain range with a steep west-facing escarpment and the gentle east-dipping Pecos slope [*Bartsch-Winkler*, 1995] (Figure 2b). The youth of the uplift is demonstrated by the truncation of the peneplain and volcanic intrusives by the escarpment [*Pray*, 1961], the ~40-Ma AFT ages from two Proterozoic samples near the base of the escarpment [*Kelley and Chapin*, 1997], the predominantly Neogene-aged sediments infilling the adjacent Tularosa Basin [*Lozinsky and Bauer*, 1991], and Quaternary and Holocene fault scarps along the TB margin [*Machette*, 1987]. Minimum stratigraphic offsets on the central segment of the uplift are 2000 m [*Pray*, 1961].

Unlike the broad Laramide ranges in the northern RGR, the Sacramento Mountains were dominantly uplifted in the late Tertiary and display an asymmetric profile. Erosion apparently beveled preexisting Paleozoic and any Laramide relief, leaving a relatively level surface prior to rifting. Also distinct from the small, narrow fault blocks of the central and southern rift, the SM are a major, continuous structure. They are bounded by faulting on only one edge and are not cut by late Tertiary faults on the back slope. Free air gravity is highly correlated with the SM topography, and a strong isostatic residual gravity anomaly over the SM [*Heywood*, 1992] is indicative of upward lithospheric flexure [*Kooi et al.*, 1992]. We interpret the above evidence to show that the SM represent a flexural deformation of the lithosphere in response to driving forces associated with opening of the RGR. The SM are therefore a suitable subject for flexural modeling.

2.7. Pecos River Valley

The development of the Pecos River Valley (PR) is intimately related to the uplift of the SM (Figure 1). The Pecos River did not exist before the late Pliocene; drainages from the Southern Rocky Mountains flowed southeast across the present Southern High Plains (Llano Estacado) for most of the Tertiary. This was a period of moist climate and active erosion. In the late Miocene, changes related to topographic uplift at the RGR and a transition to a more semiarid climate resulted in deposition of Ogallala Formation sands and gravels on the Great Plains [*Walker*, 1978; *Frye et al.*, 1982; *Gustavson et al.*, 1990]. The oldest dated Ogallala strata are ~11 Ma [*Winkler*, 1987; *Caran*, 1991].

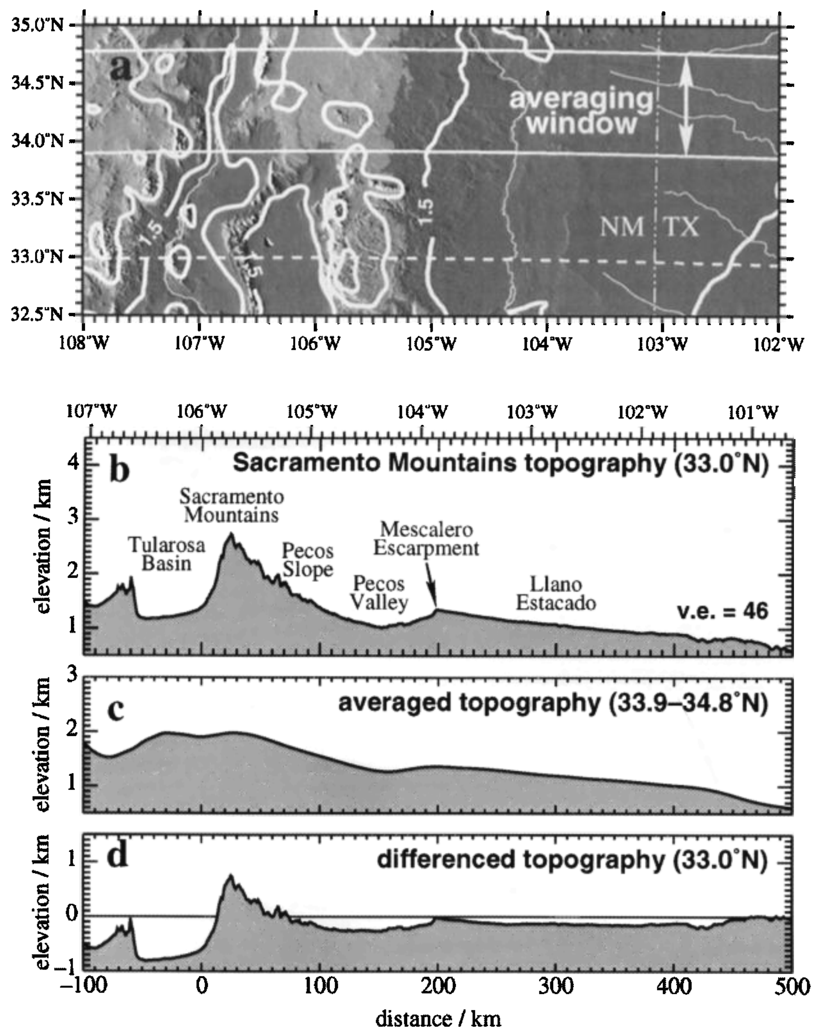

Figure 2. Separation of short- and long-wavelength topography at the Sacramento Mountains. (a) Elevations contoured in 500-m intervals over a shaded relief rendition of topography (cf. Figure 1). Areas with elevations above 1.8 km have a lighter shade, marking the broad north-trending eastern flank of the Rio Grande rift—the Mescalero arch and Sacramento Mountains. Window of averaged east–west profiles is indicated, as is the trace of the 33°N profile. (b) Original topography at 33°N. (c) Averaged and smoothed Mescalero arch east–west cross section. (d) Differenced topography: original elevations minus averaged cross section. Vertically exaggerated (v.e.) by a factor of 46.

Fluvial Ogallala deposits were mostly replaced by eolian materials at ~7 Ma [*Gustavson et al.*, 1990; *Caran*, 1991]. This change also reflects a drier climate, but it is primarily attributable to diversion of the southeast-flowing streams on the High Plains by the south-flowing Pecos River. An ancestral Pecos drainage in northwest Texas may have existed earlier in the Miocene, but Ogallala outcrops west of the present Pecos River as far south as 32°N [*Frye et al.*, 1982] seemingly preclude a major drainage in southeast New Mexico at that time. By the late Pliocene, the Pecos River existed east of the SM, and by the Pleistocene it had eroded headward to the Sangre de Cristo Mountains [*Bachman*, 1976]. Another view holds that the Pecos River developed to the south rather than by headward erosion [*Gustavson and Finley*, 1985].

The formation of the Pecos Valley probably postdated deposition of the fluvial Ogallala sediments, assuming that they were transported across a continuous, relatively planar surface from their source areas in the west [*Frye et al.*, 1982]. However, eolian deposition of the upper Ogallala would not have been impeded by the presence of the valley, which in fact was an important source for these sediments. Hence an incipient Pecos River Valley probably existed in the late Miocene. Development of this valley is commonly ascribed to two processes: fluvial erosion and collapse caused by groundwater dissolution of Permian evaporite beds [e.g., *Gustavson and Finley*, 1985; *McGookey et al.*, 1988]. A possible difficulty with salt dissolution is that salt beds are absent beneath the Pecos slope even though it has not subsided. If the Permian evaporites tapered out to the west at the current location of the Pecos Valley, dissolution would have been responsible for much less subsidence. We suggest that a third mechanism—flexural downwarping—caused Pecos River Valley subsidence, and may have nucleated aqueous processes. This argument is based on the spatial association of the valley peripheral and parallel to the SM and our flexural fits (section 5). There is also an inferred temporal association as the SM were a source for Ogallala clasts and must have had some relief by ~11 Ma. Initial uplift of the Guadalupe Mountains to the south (GM in Figure 1), which have a similar origin and geometry to the SM, has been dated at 11 Ma [*Polyak et al.*, 1998].

3. Broken and Continuous Elastic Plate Flexure

In this and the following sections we apply three types of two-dimensional lithospheric flexure models to the Sacramento Mountains with the purpose of determining the best approach to analyzing rift flank flexure. We begin with the simplest analytic elastic-plate models that have a specified line-load boundary condition. We follow with somewhat more sophisticated models that tie the mechanical response of the rifted lithosphere to the distributed loads at the surface and at depth. Next we compare analytic models to finite element models that explicitly include a fault within the plate (section 4). Finally, we derive an effective elastic thickness for the SM using the results of these comparisons (section 5).

3.1. Line-Load Models

The most direct approach to modeling flexure is to assume an entirely elastic plate and to specify (or solve for) boundary conditions at the origin [*Zandt and Owens*, 1980]. A plane-strain solution for the vertical displacements (w) as a function of distance (x) of a thin elastic plate in mechanical equilibrium with an applied line load is [*Turcotte and Schubert*, 1982, ch. 3]

$$w(x)=\left[A\sin\left(\frac{x}{\lambda}\right)+B\cos\left(\frac{x}{\lambda}\right)\right]\exp\left(-\frac{x}{\lambda}\right) \tag{1}$$

We label this the "general solution." The flexural wavelength (or parameter) is defined as

$$\lambda=\left(\frac{4D}{\rho g}\right)^{1/4} \tag{2}$$

and the flexural rigidity is

$$D=\frac{Eh_e^3}{12\left(1-v^2\right)} \tag{3}$$

The density ρ refers to the inviscid substrate beneath the plate; g is gravitational acceleration, E is Young's modulus, v is Poisson's ratio, and h_e is the elastic plate thickness.

The vertical shear force (per unit length) at the origin, equivalent to the applied line load (positive up) is given by

$$V_0=\frac{2D}{\lambda^3}(A+B) \tag{4}$$

For a broken plate the bending curvature, moment, and stress are zero at the origin (Figure 3a), giving A = 0. For a continuous plate the slope is zero at the origin (Figure 3b) which requires A = B. The flexural bulge of the hanging wall is implicitly downfaulted so that the net displacements result in a basin.

We define the origin for the SM modeling with a linear approximation to the surface trace of the bounding normal fault. The fault trace in the Tularosa Basin is sinuous, but it has an azimuth of N15°W as mapped by *Pray* [1961] and *Woodward et al.* [1975]. The lithospheric thickness and applied load inferred from matching flexural solutions to flank topography are sensitive to the location of this origin. We recognize a further uncertainty due to the dip of the fault; that is, it is unclear what depth along the fault plane should be used to define the horizontal origin. The accommodation of uplift on multiple faults introduces additional uncertainties. We use east-trending topographic cross sections for model fitting because the elevation contours on the Pecos Slope trend north (Figure 2a).

A least-squares fit of the broken plate model to the SM profile using the parameters of Table 1 gives a best-fit elastic plate thickness of 42 km. Alternatively, fitting the continuous plate model with the line load at the origin yields a 25-km elastic plate.

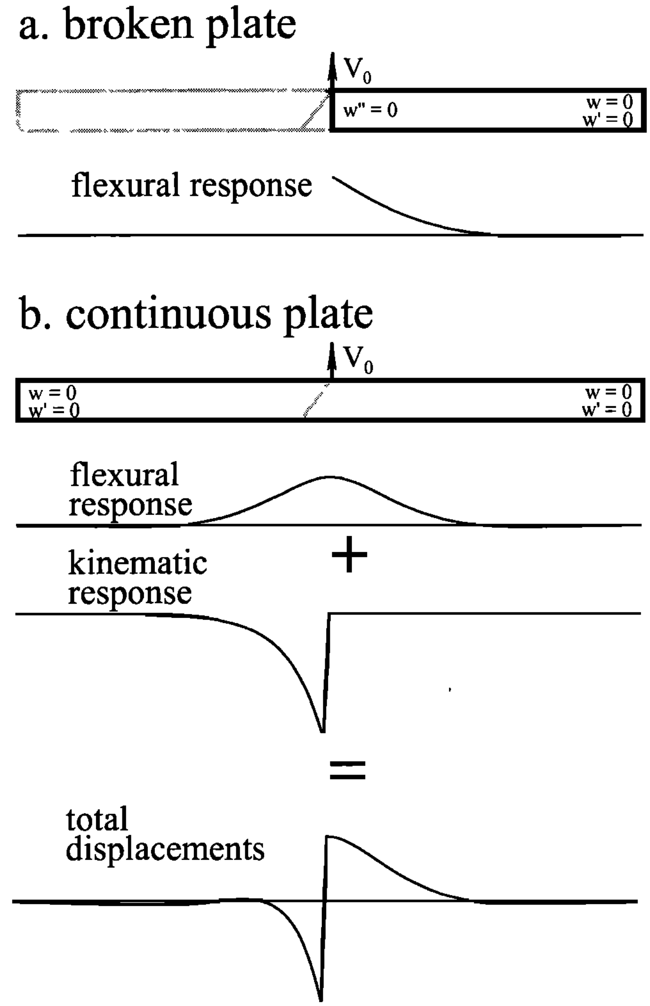

Figure 3. Broken and continuous elastic plate flexure. (a) For a broken plate, footwall uplift is assumed to be mechanically independent of the hanging wall. The boundary condition is zero bending curvature (moment) at the fault, and a vertical force (V_0) represents the unloading at this edge. (b) If the plate is continuous, the applied force or distributed stresses cause upwarping of the lithosphere. The superimposed effect of fault slip and basin subsidence results in an asymmetric flank–basin system.

Table 1. Physical Constants

Parameter	Definition	Value
E	Young's modulus	65 GPa
g	gravity at surface	9.80 m s^{-2}
ρ_s	sediment infill density	2100 kg m^{-3}
ρ_c	crustal density	2800 kg m^{-3}
ν	Poisson's ratio	0.25

A continuous plate might be dominantly loaded at the rift axis rather than at the flanks; shifting the origin to the west can give a 45-km-thick elastic plate. Therefore, changes in the type and location of the flank-uplift boundary condition can produce a range of elastic thickness estimates approaching a factor of 2. So far we have neglected to address many additional free parameters in the analysis and clearly the above flexural results are extremely nonunique. A possible solution to the boundary condition dilemma is to constrain the loads acting on the lithosphere from geologic information and not treat the load as a free parameter. Given independent information on the loading mechanisms, positions, and magnitudes (e.g., Tularosa Basin dimensions and infill density), we can limit our boundary condition choices and perhaps better determine the lithospheric thickness.

3.2. Residual Flank Topography

Before pursuing flexure models with prescribed distributed loads, we concern ourselves with the variety of processes responsible for topography at the SM. We wish to isolate the relief produced by shallow loads like basin infill and flank erosion that are compensated by lithospheric flexural rigidity. We note that a wide topographic rise, the Mescalero arch (distinct from the Mescalero escarpment), trends north of the SM along the eastern rift flank at ~105.5°W (MA in Figure 1, Figure 2a). This uplift is not bordered by major normal faults or basins [*Woodward et al.*, 1975], unlike the SM. It may have originated before rifting, perhaps during the Laramide orogeny [*Kelley*, 1971], or it may reflect a deep density anomaly of uplifted hot asthenosphere beneath the RGR [e.g., *Slack et al.*, 1996] related to lithospheric necking. This broad, deeply compensated uplift is of regional extent, and it probably also accounts for some of the SM relief. A long-wavelength topographic uplift that cannot be flexurally supported is also present in the Cordillera and Great Plains [*Eaton*, 1987]. We might simulate these components of the SM uplift by estimating the deep loads from seismic velocities and gravity (which reflect thermal and density anomalies) [*Parker et al.*, 1984] and applying them to our flexure models. However, there are substantial uncertainties involved in determining the magnitude and distribution of stresses from these data.

Instead, we separate the short-wavelength flexural topography attributed to shallow unloading (e.g., faulting, basins, and erosion) from the long-wavelength uplift associated with deep thermal and compositional buoyancy loads. We perform this separation by averaging 100 east–west topographic profiles over the unfaulted Mescalero arch (33.9–34.8°N), which we assume has no short-wavelength flexural component, and subtracting this averaged profile from the SM cross sections (Figure 2). This manipulation is strictly valid only if the deep-seated loads and the flexural rigidity are the same at the SM and the Mescalero arch, a reasonable supposition given the ~150-km north–south distance of these two features. The residual topography has a much smaller SM flank amplitude, less than 1 km (Figure 2d), which is presumably independent of all deep loads. We fit the succeeding models to these short-wavelength topographic profiles.

3.3. Distributed-Load Models

Several workers have taken the approach of applying a known or inferred distributed load to a continuous elastic plate in performing rift flank flexure modeling [e.g., *Weissel and Karner*, 1989; *Egan*, 1992]. One can designate a fault geometry (planar or listric, dip, and décollement depth), apply a heave to the hanging wall, and thereby calculate the horizontal distribution of upward-directed reduced overburden stress on the lithosphere (for a particular choice of infill, crust, and mantle densities). Other loads may be included in this analysis, such as replacement of crust by mantle due to pure shear thinning of the lower crust (a downward stress), reduction in density due to uplifted isotherms and thermal expansion (an upward stress), and erosion of positive topography (an upward stress). The net laterally distributed stresses are included in the forward solution of the flexure equation for a continuous elastic plate. The flexural displacements are superimposed on those arising from slip on the fault (Figure 3b); therefore, this approach assumes a kinematic description of the extension, and it treats separately the mechanical response of the lithosphere to this extension.

We implement a variation on this technique for the Sacramento Mountains. We solve the flexure equation for an elastic plate subject to a distributed load using a finite difference method [*Mueller and Phillips*, 1995]. The structure of the Tularosa Basin is complex, and it is not satisfactorily described by a normal fault only at the eastern edge [*Lozinsky and Bauer*, 1991; *Adams and Keller*, 1994]. The basin has also been down-dropped at the western edge, adjacent to the San Andres Mountains, and encloses a buried north-trending horst. To test the continuous plate, distributed-load model, we define a simplified polygonal basin designed to maximize the unloading stresses. The model basin is 60 km wide, 2 km deep, and bounded by 60° faults; the crustal density is 2800 kg m^{-3} and the infill density is 2100 kg m^{-3} (Figure 4a). (Measured densities of Santa Fe Group sediments in the San Luis basin are 1900–2600 kg m^{-3} [*Keller et al.*, 1984], with a depth-weighted mean of 2200 kg m^{-3}.) These parameter choices should maximize the vertical unloading stress, which attains 14 MPa (Figure 4a). For comparison, we show the contribution of pure shear (mantle uplift and thermal expansion) to buoyancy stresses assuming a sinusoidal variation in extension centered over the basin, with the net extension equal to the 2.3-km total heave on the faults. Parameter values are similar to those of *Weissel and Karner* [1989]. Pure shear contributes a negligible stress compared to the basin (dotted line, Figure 4a). The stress caused by thinning the crust and forming the basin, which integrates to a force of 8×10^{11} N m^{-1}, results in only a few hundred meters of flexural uplift, even for a thin lithosphere; the modeled flank relief is almost a factor of 10 smaller than the SM residual topography (Figure 4b). This result implies that we have left out important loads and/or that the continuous plate assumption is not applicable.

Another significant applied stress is produced by denudation of the footwall fault scarp. Eroded material is transferred into the

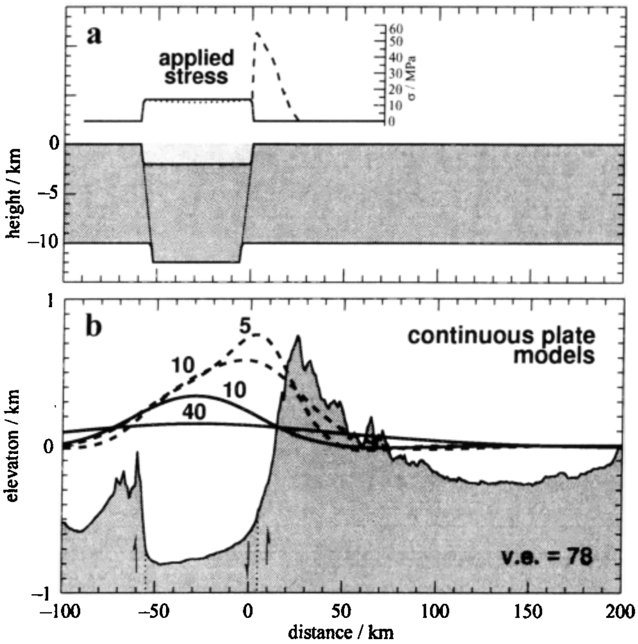

Figure 4. Continuous plate model of rift-flank flexure for a specified stress distribution. (a) Lower cross section shows assumed Tularosa Basin geometry. Applied stresses resulting from the replacement of crust by basin infill (solid line), the basin plus pure shear in the lithosphere (dotted line), and the basin plus erosion on the flank (dashed line) are plotted in the upper diagram. (b) Sacramento Mountains residual topography at 33°N. Solid curves are continuous plate flexural solutions for the basin infill load alone, with elastic plate thicknesses of 10 and 40 km. Dashed curves are continuous plate solutions for combined basin infill and erosional loads, with elastic plate thicknesses of 5 and 10 km. Normal faults are drawn at their mapped locations.

basin and the removed mass causes a substantial upward load. We estimate the stress distribution due to erosional unloading by calculating the cross-sectional area of missing rock between the fault and the crest of the SM. We assume a 60° dip to the master fault and extrapolate the Pecos slope to the west with a 2° dip. We assign a density of 2800 kg m^{-3} to the eroded crust. This stress distribution is plotted with the dashed line in Figure 4a. The horizontally integrated erosional force is 7×10^{11} N m^{-1}, comparable to the basin infill load. Varying the fault dip by ±15° causes a negligible (<3%) change in this force. Figure 4b shows continuous plate flexural deflection curves for 5- and 10-km elastic plates subject to the combined basin and erosion loads; these solutions are still unable to match either the amplitude or shape of the SM. The continuous plate condition forces the uplift to occur too far west; a thicker lithosphere distributes the uplift farther east, but then produces too small an amplitude. A lower datum (e.g., the base of the Pecos Valley) would produce even greater misfits.

Denudation of the Pecos slope may also have contributed to unloading of the SM. Late Tertiary erosion of this surface has undoubtedly occurred because the eastern flanks of the RGR were one source of the Ogallala Formation on the Great Plains. Examination of geologic cross sections published by *Bartsch-Winkler* [1995] and *McGookey et al.* [1988] suggests the degree of erosion is similar to that on the Mescalero arch; thus, to first order, the isostatic effects of such erosion have been removed from the residual topography (Figure 2). The continuous plate model will match the SM residual topography with an additional ~20-MPa peak stress that decreases linearly to the east across the Pecos slope. This load corresponds to an additional 700 m of denudation at the crest, exceeding plausible amounts of differential erosion between the SM and Mescalero arch as well as between the SM and Pecos River. We conclude that the continuous plate flexural model is not viable at the SM—provided that we have fully accounted for all loads, a caveat we return to in section 6.3. We must consider at least partial decoupling at the range-bounding fault.

4. Finite Element Models Including a Fault

Given the apparent shortcomings of the continuous plate model, we must also ask if the broken plate solution is an appropriate representation of footwall flexure. To address this question we take the approach of using finite element modeling (FEM) of flank uplift associated with normal faulting of an elastic lithosphere to test whether the broken plate equation fit to FEM solutions accurately determines the plate thickness. This approach is founded on two premises. First, we assume that observed lithospheric flexure, like that at the Sacramento Mountains, can be characterized by an effective elastic plate thickness (h_e). Therefore, we use a perfectly elastic plate model rather than perform simulations with a realistic but complex rheology. Second, we surmise that the finite element model including a fault is a closer approximation to reality than either the continuous or broken plate solutions. Hence, the error in h_e derived from an analytic equation fit to synthetic FEM "topography" (with a known elastic thickness) should be representative of errors in fits to real flexural topography.

4.1. Model Description

Our model of a lithosphere cut by a single master normal fault is similar in many respects to that of *Bott* [1996, 1997; also *Bott and Stern*, 1992]. We use the commercial finite element software MARC, version K6 (MARC Analysis Research Corporation, Palo Alto, California). MARC is a general-purpose engineering package applicable to structural, heat flow, and electromagnetic problems, which is readily adapted to geodynamic studies. In this paper we consider only an isotropic elastic plate cut by a throughgoing planar normal fault.

The two-dimensional, plane-strain finite element grid is comprised of four-node, isoparametric, quadrilateral elements and three-node, isoparametric, triangular elements near the fault (Figure 5). These elements use bilinear basis functions, meaning that strain is constant within each element. The grid is horizontally biased such that the mesh is finest near the fault, where the smallest elements have dimensions of 2 km. The physical properties of the plate are as given in Table 1; the plate density is ρ_c = 2800 kg m^{-3}.

The fault is defined by a series of "gap–friction" contact elements that connect structural nodes on either side of the 2-m-wide fault. Gaps are described by a closure distance, a gap direction (normal to the fault), a shear direction (parallel to the fault), gap and shear spring stiffnesses, and a coefficient of friction. The gap stiffness is infinite to prevent the hanging wall from passing through or separating from the footwall. The shear stiffness is

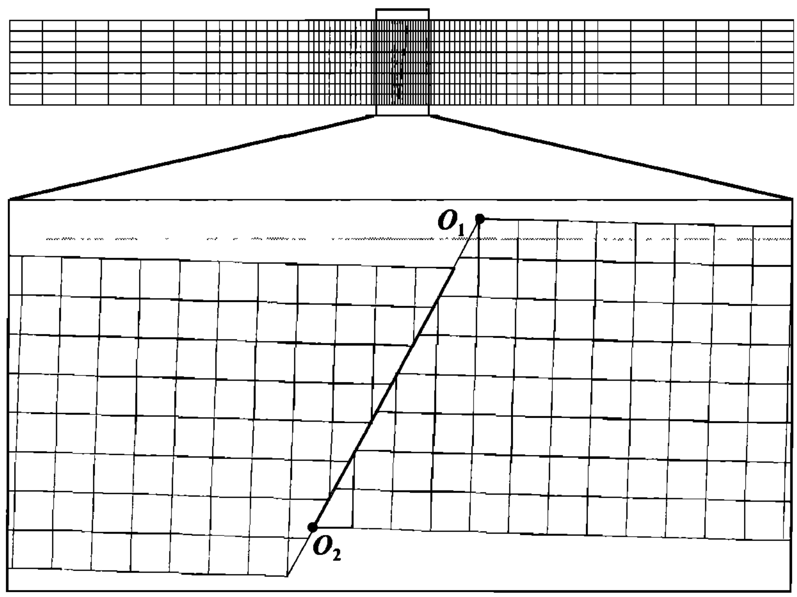

Figure 5. A complete 600-km-long, 16-km-thick finite element grid (vertically exaggerated by a factor of 4) is shown at top. Below it is a close-up of the region near the 63° fault after a heave of 1280 m, with no vertical exaggeration. (No basin infill or erosion loading applied.) Points O_1 and O_2 are alternative locations for the horizontal origin when performing analytic least-squares fits to the surface displacements.

zero for models with no friction. Mechanical problems with gap–friction elements are solved in MARC by imposing kinematic constraints and using a Lagrange multiplier method. This approach is similar to the "slippery-node" technique of *Melosh and Williams* [1989] and the "dual-node" technique of *Bott* [1997].

Restoring forces are applied by a frictionless elastic (Winkler) foundation at the base of the plate that has a stiffness $\rho_0 g$. *Bott and Stern* [1992] and *Bott* [1996, 1997] placed restoring forces only at density interfaces, such as the surface. However, restoring forces exist where the mechanical lithosphere, which can sustain deviatoric stresses, is displaced in a low-viscosity, hydrostatic asthenosphere which applies a pressure to the base of the lithosphere. The depth where these buoyancy stresses occur in a viscoelastic lithosphere may vary with position and time as the state of stress and character of the material changes from solid to fluid. Nonetheless, the model foundation is properly located at the base of the mechanical lithosphere with the approximation of an inviscid asthenosphere [*Nadai*, 1963, p. 284; *Turcotte and Schubert*, 1982, pp. 121–122; *Wallace and Melosh*, 1994]. The equivalence of a basal foundation to a sublithospheric pressure-induced restoring force has been demonstrated with finite element models of flexure of an elastic plate over an explicit isoviscous substrate. In the case of a continuous, thin, elastic plate, whether the restoring forces are applied at the top or bottom surface is of no consequence, but this choice is very significant in models with a fault, as we will explain below (section 4.3).

The far left and right vertical edges of the grid are initially constrained not to move horizontally. The left edge (of the hanging wall) is "tied" to the right edge (of the footwall) such that the vertical displacements are equal on these two edges. This condition simulates an infinitely long plate and prevents problems with different net vertical motions of these two edges. Initial lithostatic stresses and gravitational body forces are applied to the grid. A horizontal extensional displacement is applied incrementally (–100 m per increment) to the left edge of the hanging wall to induce slip on the fault. We use MARC's updated Lagrangian method (which computes the stiffness matrix at each increment using the current mesh coordinates) with the large displacement option (which accounts for large rotations). Our tests indicate that the solutions are sensitive to the large displacement effects and changes in the reference frame.

We obtain FEM solutions for a range of fault dips ($\theta = 45.0°$, 63.4°, and 76.0°) and elastic plate thicknesses (h_{fem} = 8, 16, and 32 km). At each increment of model deformation we calculate the heave of the fault (the relative horizontal displacement of the top two fault nodes on the hanging wall and footwall). We perform a nonlinear least-squares fit of the general thin-plate elastic flexure equation (1) to the footwall surface displacements. The horizontal origin of the analytic solution is defined as the footwall cutoff (point O_1 in Figure 5). The coefficients (A and B) and flexural wavelength (λ) are varied to obtain the best fit. The best-fit line load (V_0 of equation (4)) is compared to the horizontally integrated unloading stress acting on the footwall (V_{calc}):

$$V_{\mathrm{calc}} = (\rho_c - \rho_s) g e_0 \tan\theta \left(\frac{h_{\mathrm{fem}}}{\tan\theta} - \frac{1}{2} e_0 \right) + V_{\mathrm{erode}} \qquad (5)$$

where e_0 is the heave and V_{erode} is the footwall erosional load (if one is applied). We define the discrepancy between the analytic and calculated loads as $V_{\mathrm{err}} = (V_0 - V_{\mathrm{calc}})/V_{\mathrm{calc}}$. The best-fit elastic thickness (h_e) is compared to the true (FEM) plate thickness (h_{fem}) using the error $h_{\mathrm{err}} = (h_e - h_{\mathrm{fem}})/h_{\mathrm{fem}}$. The least-squares fit is repeated for the broken plate solution by fixing the coefficient $A = 0$.

We consider three separate loading configurations: extension alone, extension with basin infill, and extension with both infill and footwall erosion. In the first case unloading of the footwall by displacement of the hanging wall provides the only driving force for flexure. We model the effect of sediment loading by applying stresses on the top surface of the hanging wall and on the exposed fault surface of the footwall where deflections are negative. The sediment has density ρ_s (Table 1) and fills the basin to the datum. In the third case we apply a uniform stress 20 km wide on the footwall that increases linearly with heave to 50 MPa at e_0 = 1.5 km, roughly equaling the inferred Sacramento Mountains erosional load (section 3.1, Figure 4a). This is an ad hoc treatment of erosion; the results are sensitive to the load width, magnitude, and distribution, but they should give some guidance for flexural analyses of the SM.

4.2. FEM Results

FEM model results at e_0 = 1 km are summarized in Tables 2–4. For all loading cases the magnitude of footwall uplift increases linearly with heave (Figure 6a), but this relationship cannot be inferred for inelastic lithospheric rheologies or listric faults. Uplift increases with fault dip because a steeper fault places more of the load closer to the footwall cutoff [e.g., *Egan*, 1992]. Uplift is relatively insensitive to plate thickness because a thicker plate produces a larger load for a given fault dip and heave (equation (5)); sensitivity to h_{fem} increases as infill and erosional loads are added. Basin sediment loading acts to reduce footwall uplift, but it increases basin subsidence. The footwall erosional load causes shallowing of or no change to the basin depths.

The discrepancy between best-fit and FEM model loads might provide insight on the relationship between the shear force derived from an elastic fit to the actual stresses acting on the rift flank. Values of V_{err} are roughly constant with heave for extension alone; with addition of infill and erosion V_{err} becomes more dependent on e_0, but it behaves asymptotically with increasing heave (Figure 6b). The load discrepancy can be very large, although it is typically less than ±50% for cases in which the erosional load dominates. For all loading configurations the ratio V_0/V_{calc} increases with increasing uplift (and fault displacement). These observations hold for both the broken plate and general solutions.

The dependence of the elastic plate thickness error on heave for the different cases is similar to that of V_{err}. For models without erosion the broken plate fit systematically underestimates h_{fem} (Tables 2 and 3 and Figures 6c and 7), and $|h_{err}|$ is inversely correlated with uplift—greater fault displacement results in more "broken" plate behavior, reducing the best-fit errors. With erosion the best-fit thickness is usually an overestimate (Table 4), and the broken plate no longer even provides a lower bound on the true elastic thickness. The ratio h_e/h_{fem} increases with both decreasing plate thickness and decreasing fault dip when erosional loading is present. In all cases errors can reach many tens of percent, and the magnitude of the broken plate h_{err} increases with addition of infill and erosion. In contrast, the general solution almost always yields thicknesses that underestimate h_{fem} by no more than ~5% (Tables 2–4 and Figure 7). The one exception to this statement is the case in which the erosional load width is comparable to the flexural wavelength of the 8-km plate.

We have also tested FEM models with friction on the fault surface. Fault friction has a minimal effect on the flexural behavior of an elastic plate, but this finding cannot be extended to stress-sensitive rheologies without further study.

4.3. Implications

There are several possible reasons for the analytic broken plate misfits. (1) The elastic flexure equation is derived for a thin plate, while the FEM model has a finite plate thickness and properly accounts for the vertical and shear stresses. (2) The footwall is tapered beneath the fault, while the analytic solution assumes a plate of constant thickness. (3) We have approximated distributed loads on the footwall as a single line load at the origin. (4) The edge of the footwall is not truly free because normal stresses are transmitted across the fault. The fact that the general solution returns the true FEM plate thickness despite these differences demonstrates that points 1–3 are secondary: the broken plate model fails because the zero-curvature boundary condition at the fault is inappropriate. Hanging wall infill loading enhances coupling across the fault while footwall erosion diminishes it as exemplified by the coefficient ratios A/B in Tables 2–4. When the magnitude of A/B is smaller, the plate behavior is more "broken"; there is a direct correlation between the broken plate $|h_{err}|$ and $|A/B|$.

Bott [1996] also recognized discrepancies between FEM and broken plate solutions for a faulted elastic plate. Our results differ from his in a number of important respects. The broken plate model agreed very well with *Bott*'s [1996] FEM solution when infill loading was absent; this result was a consequence of placing restoring forces at the top surface of the plate. Using origin O_2 (Figure 5) and fitting to the bottom surface where restoring forces

Table 2. FEM Results for No Infill and No Erosion at e_0 = 1 km

			Broken Plate			General Solution			
h_{fem}, km	θ, deg.	Uplift, m	V_{err}	h_{err}	rms, m	A/B	V_{err}	h_{err}	rms, m
8	63.4	851	+0.46	–0.07	1.08	–0.06	+0.43	–0.02	0.99
16	45.0	313	–0.66	–0.26	0.83	–0.33	–0.71	–0.03	0.12
	63.4	814	+0.05	–0.13	0.78	–0.12	–0.00	–0.04	0.42
	76.0	—	—	—	—	—	—	—	—
32	63.4	771	–0.23	–0.17	0.75	–0.18	–0.29	–0.04	0.23

For h_{fem} = 16 km, θ = 76.0° the model fault gap elements open at $e_0 \approx$ 200 m.

Table 3. FEM Results for Infill but No Erosion at e_0 = 1 km

			Broken Plate			General Solution			
h_{fem}, km	θ, deg.	Uplift, m	V_{err}	h_{err}	rms, m	A/B	V_{err}	h_{err}	rms, m
8	63.4	506	+1.81	–0.30	1.99	–0.40	+1.19	–0.02	0.32
16	45.0	68	–0.87	–0.76	3.36	–2.41	–1.54	–0.01	0.06
	63.4	442	+0.76	–0.39	2.27	–0.55	+0.13	–0.02	0.14
	76.0	1141	+4.81	–0.21	1.96	–0.23	+4.21	–0.05	0.65
32	63.4	371	+0.09	–0.47	2.17	–0.73	–0.53	–0.03	0.10

are applied does yield a good match between FEM and analytic displacements (Figure 7a). *Bott*'s [1996] model predicted a nearly antisymmetric footwall uplift and hanging wall subsidence for no infill; the magnitudes of uplift and subsidence were the same. In contrast, our model displacements are quite different in amplitude on the footwall and hanging wall (Figure 7a). This difference is also explained by the placement of the restoring forces. For example, consider the restoring force applied to the base of the footwall beneath the fault; this force will not be fully transmitted to the hanging wall due to the decoupling effect of the fault, allowing greater basin subsidence. Basin subsidence is inhibited by placing restoring forces on the surface. The flexural deflections on the surface where the restoring forces are applied are nearly antisymmetric (Figure 7a). Thus placing restoring forces on the free surface causes overprediction of flank uplift.

Bott [1996] attempted to correct the discrepancy between FEM and analytic models with infill loading by deriving a new flexure equation subject to the requirement that the fault walls remain parallel. We have also fit *Bott*'s [1996] theory to our FEM results, but find, unfortunately, that it does not correctly determine the plate thickness under almost all conditions. We find that the only way in which to elicit the elastic plate thickness from fits to the FEM deflections is to retain both the sine and cosine terms in the analytic elastic plate solution, with both coefficients as free parameters. The two coefficients depend on many of the model parameters (heave, infill density, and plate thickness), precluding any simple relationship between them. The need to retain the sine term with $A \neq B$ demonstrates that the lithosphere is neither broken nor continuous at the master fault in these models; partial coupling on a dipping fault enables an intermediate condition. Interpretation of the loads acting on the rift flank through the best-fit shear force is ambiguous for both broken plate and general solutions.

5. Elastic Flexural Fits to the Sacramento Mountains

We have found the continuous plate flexure model to be inadequate at the Sacramento Mountains (section 2, Figure 4b). In addition, plate thickness estimates based on the broken plate solution are subject to large errors according to our finite element model results (section 4.2, Tables 2–4, and Figures 6 and 7). The alternative general analytic solution is more accurate, at the cost of an additional free parameter. In this section we fit both the general and broken plate elastic flexure equations as well as the finite element model to SM topographic profiles. Our aim is to evaluate the effective elastic plate thickness (h_e) and its uncertainty using three different measures: the change in rms error as a function of h_e, the variation in h_e between different cross sections, and the sensitivity of h_e to changes in the values of fixed parameters.

We perform these fits assuming the parameter values given in Table 1. Both the plate and the substrate have density ρ_c; the substrate density determines the restoring force. The origin (where the line load is applied) is defined by the surface trace of the fault, which we have approximated by a line trending N15°W (section 3.1). Models are fit to the residual topography (Figure 2) from the crest of the range to a distance of 200 km from the fault (the location of the Mescalero escarpment). Because of the likely contributions of erosion, salt dissolution, and collapse to Pecos Valley subsidence (section 2.7), we have also examined fits to a distance of 150 km, the base of the Pecos slope. These results, as well as fits to distances greater than 200 km, show only minor changes to the inferred h_e (less than ~2 km).

We first evaluate the accuracy of the elastic plate fits by examining the variation in rms misfit between the analytic equations and the observed topography (33°N profile) as a function of h_e.

Table 4. FEM Results for Infill and Erosion at e_0 = 1 km

			Broken Plate			General Solution			
h_{fem}, km	θ, deg.	Uplift, m	V_{err}	h_{err}	rms, m	A/B	V_{err}	h_{err}	rms, m
8	63.4	1091	–0.11	+0.91	3.98	+0.53	–0.02	+0.28	1.24
16	45.0	476	–0.45	+0.63	1.64	+0.64	–0.39	+0.03	0.19
	63.4	789	–0.33	+0.14	0.83	+0.18	–0.29	–0.01	0.29
	76.0	1499	+0.19	+0.04	1.09	+0.07	+0.22	–0.02	0.86
32	63.4	605	–0.38	–0.13	0.36	–0.10	–0.40	–0.05	0.20

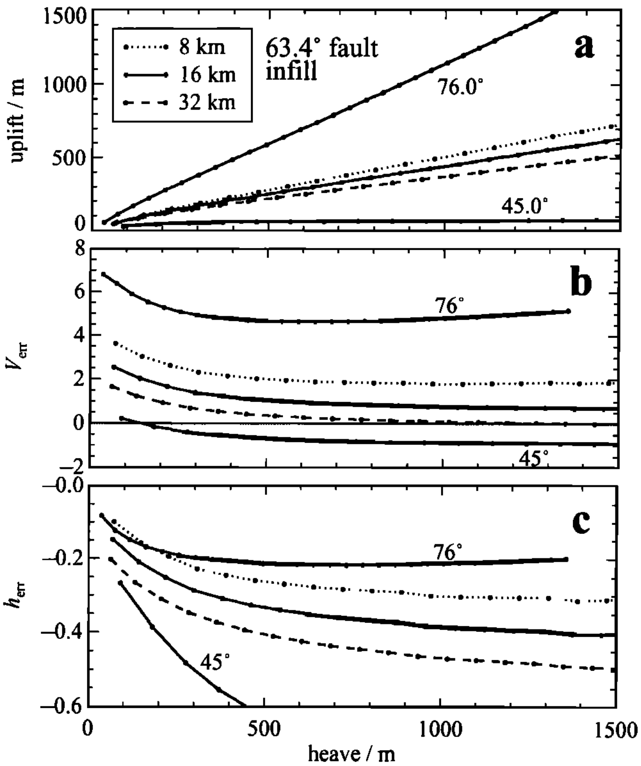

Figure 6. Effects of varying elastic plate thickness and fault dip on finite element results as a function of heave. Basin infill loading is included; denudational loading is not. Symbols mark 100-m increments of displacement at the far left edge of the hanging wall. (a) Maximum FEM footwall uplift. (b) Line load discrepancy (V_{err}) between analytic broken plate shear force and integrated load estimated from kinematic description of footwall unloading (equation (5)). (c) Fractional error in elastic plate thickness derived by broken plate analytic fit to FEM displacements relative to true FEM plate thickness (h_{err}). Broken plate origin defined at point O_1 in Figure 5. Compare Table 3.

We fix the datum elevation at −129 m, the height of the Southern High Plains in the residual topography (Figure 2d). We systematically vary the flexural wavelength. For the general solution and the broken plate equation we vary the cosine coefficient (B) to match the elevation of the crest; for the general solution we also perform a least squares fit to determine the sine coefficient (A). The results are shown in Figure 8. There is a fairly sharp lower bound on h_e of ~15 km from the general solution, and a much weaker constraint on the upper bound. The broken plate has a very pronounced minimum in rms error between $h_e \approx 18$ km and 25 km, and visual examination of the fits also shows that this is the most acceptable range of plate thicknesses.

The comparison of the general and broken plate solutions at the SM indicates that we can only establish a lower bound on the effective elastic thickness with an analytic model. This finding is consistent with the simulated broken plate FEM tests for h_{fem} greater than ~20 km (Table 4). Figure 9 shows a finite element model flexural profile for h_{fem} = 20 km and θ = 63.4° which provides a good fit to the SM. Greater plate thicknesses cause longer wavelength flexure, misfitting the Pecos slope. Thus, for this case of high-amplitude (~1-km) uplift the broken plate h_{err} is small, as seen in the simulations (Tables 2–4). The broken plate solution should provide accurate estimates of the elastic thickness and its uncertainty at the SM.

Next we fit the broken plate equation to 22 east–west profiles, from 32.76°N to 33.13°N, spaced about 2 km apart in latitude. The datum is a free parameter in the least squares analysis, along with the flexural wavelength and cosine coefficient. The mean elastic thickness of these 22 fits is 23.0 ± 2.3 km, ranging from 20.7 to 29.3 km. There is surprisingly little variation in h_e along strike of the range, despite the irregular topography on the Pecos slope. The standard deviation amounts to only 10% of h_e. Best-fit loads are about 1×10^{12} N m^{-1}.

We have also carried out sensitivity tests to determine the effect of parameter uncertainties on h_e. The parameters of concern are the datum elevation, the location of the origin, the

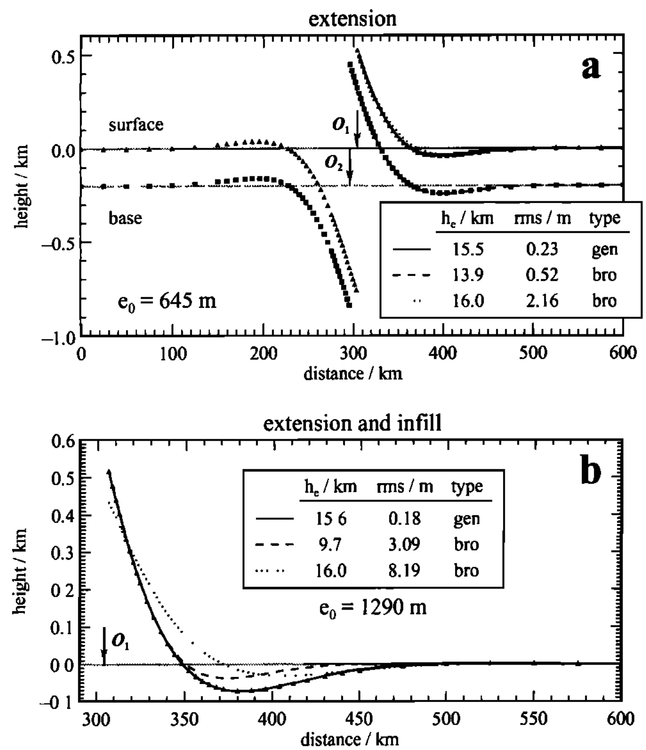

Figure 7. Analytic elastic plate equation least-squares fits to finite element model deflection profiles for a 16-km-thick plate with a 63.4° fault. Three cases are illustrated: the generalized equation ("gen") as well as the broken plate equation ("bro") with the elastic plate thickness a free parameter (dashed line) or fixed at 16 km (dotted line). Origins assumed for fits are marked by arrows (see Figure 5). (a) FEM model without basin infill loading; deflections at the surface (triangles) and base (squares) of the FEM plate are plotted. Latter profile is offset −200 m vertically for clarity. It is nearly antisymmetric across the fault, while the magnitude of surface footwall uplift is considerably less than the magnitude of surface hanging wall subsidence. The generalized and broken plate fits are indistinguishable on the plot. The broken plate solution with a forced 16-km thickness is acceptable, despite the much higher rms error. The broken plate fit to the base of the plate where the restoring forces are applied (with the origin at point O_2) produces an excellent fit (h_e = 16.1 km, rms = 0.32 m). (b) Same FEM model, but now including basin infill loading. The surface deflections of only the footwall are shown. In this case the broken plate fits are considerably worse.

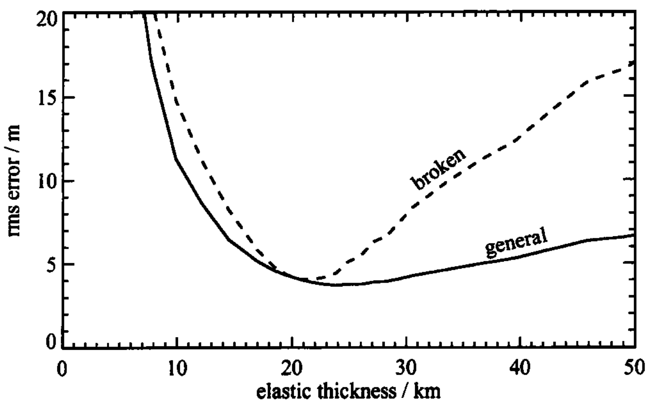

Figure 8. Root mean square (rms) misfit as a function of plate thickness for analytic elastic flexural fits to Sacramento Mountains residual topographic profile at 33°N (Figure 2). Solid curve corresponds to fits with the general solution, and the dashed curve corresponds to the broken plate solution. The minima for these two methods are the same, indicating the broken plate equation gives, at worst, a lower limit on h_e.

substrate density (restoring force stiffness), Young's modulus, and Poisson's ratio. We treat each of these in turn; the results of these tests are summarized in Table 5. The "nominal" model comprises a least squares fit of the broken plate with the cosine coefficient varied to best match the SM amplitude and with the datum and flexural wavelength free; it is plotted in Figure 9.

The appropriate datum for the differenced profile is not obvious (Figure 2d). Perhaps it is at zero residual elevation, where the SM profile and the averaged profile are at the same elevation (i.e., on the Great Plains, about 500 km from the SM). Or perhaps it belongs at the surface of the Pecos Valley (~150 km from the SM), at a residual elevation of –250 m. We find that these extremes for the reference elevation are not acceptable, resulting in large misfits to the Pecos Valley. The best fit datum is –129 m (the residual elevation of the Southern High Plains), and we consider a smaller range of –75 to –175 m. Even these datums produce flexural profiles that compare very poorly to the Pecos Valley, which would imply that it formed later, and by an entirely different process, than the young SM uplift. The Pecos Valley is a flexural downwarp for the –129-m datum (Figure 9). Nonetheless, these changes to the datum result in only ~10% changes in h_e.

The proper location of the horizontal origin, defined by the surface trace of the fault, is uncertain because of our linear approximation to the sinuous map trace and because multiple faults probably accommodated the SM uplift. We take the origin uncertainty to be ±5 km, yielding a <10% variation in h_e.

We have assumed that the lithosphere is confined to the crust, but the effective elastic thickness of ~20 km does not correspond to a true mechanical lithosphere thickness, which is undoubtedly greater accounting for frictional weakening near the surface and viscous creep at depth. Given a crustal thickness of ~30–50 km [*Keller et al.*, 1990; *Roberts et al.*, 1991], the lithosphere may include the upper mantle. Due to this uncertainty, we consider a mantle substrate density of 3300 kg m^{-3}, which determines the magnitude of the buoyant restoring forces. This higher density causes only a 5% change in the predicted h_e.

Altering Young's modulus and Poisson's ratio does not modify the elastic flexural fits. These parameters do, however, affect the conversion of flexural wavelength to elastic thickness. We have assumed a value of E = 65 GPa, representative of literature values for crustal rocks, but Young's modulus can vary by over a factor of 10 with rock type [*Turcotte and Schubert*, 1982, p. 432]. Changing E by ~50% can dramatically influence the derived value of h_e, from –13% to +31%. The elastic thickness is not sensitive to modest changes in Poisson's ratio.

6. Discussion and Conclusions

6.1. Rio Grande Rift Flank Tectonics

One goal of this research has been to identify synrift flank uplifts at the Rio Grande rift. While there are several examples of such uplifts, flexural footwall uplifts amenable to modeling are elusive. RGR flanks are very complex, reflecting their prolonged tectonic history (particularly Laramide deformation)—a fact apparent in the geology, topography, and apatite fission track measurements of the ranges. Those flanks with only small components of Laramide relief and the strongest evidence for rapid late Tertiary uplift—the Sandia Mountains, the Sierra Lucero, Ladron Peak, the Lemitar Mountains—are so pervasively faulted that models assuming mechanical continuity of the lithosphere are inappropriate. These uplifts stand apart even from Basin and Range metamorphic core complexes [e.g., *Davis and Lister*, 1988], which formed in very weak crust but have been modeled assuming a continuous lithosphere [*Buck*, 1988; *Wdowinski and Axen*, 1992]. For example, fitting the broken elastic plate analytic flexure equation to the Sandia Mountains yields an elastic thickness of only ~1 km, an implausible result given the seismic reflection observations of brittle faulting to depths of ~10 km in the Albuquerque Basin [*Russell and Snelson*, 1994]. The lithosphere is so highly bent in this fit that some of the assumptions of the analysis are not justifiable.

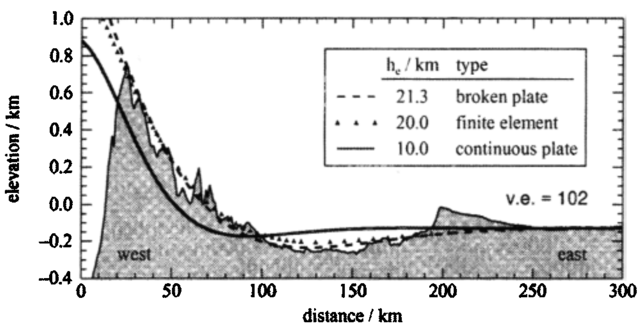

Figure 9. Residual Sacramento Mountains topography at 33°N (Figure 2d) with nominal broken elastic plate fit. The origin, near the surface trace of the master fault, is at the left edge of the plot. In this model, the flexural wavelength, line load (or cosine coefficient), and vertical datum are free parameters. The best fit values of these variables are 53.3 km (h_e = 21.3 km), 1.2 × 10^{12} N m^{-1}, and –129 m, respectively. The line load was constrained by the requirement that the solution pass through the range crest. The triangles mark the nodal displacements of a similar FEM solution, with h_{fem} = 20 km, θ = 63.4°, e_0 = 1.8 km, and a denudational line load of 1.2 × 10^{12} N m^{-1}. Also shown is a continuous plate solution with a distributed load comparable to the stresses applied to the FEM model.

Table 5. Flexure Sensitivity Test Results

Parameter	Value	Change*, %	h_e, km	h_e Change*, %	rms, m
Nominal model†	—	—	21.3	—	4.04
Datum	–75 m	+42	19.5	–8	5.42
	–175 m	–36	23.7	+12	4.89
Origin	–5 km	—	22.9	+8	3.86
	+5 km	—	20.2	–5	4.25
Substrate density	3300 kg m^{-3}	+18	22.4	+5	4.34
Young's modulus	100 GPa	+54	18.6	–13	4.02
	30 GPa	–54	27.8	+31	4.02
Poisson's ratio	0.20	–20	21.6	+2	4.02
	0.30	+20	21.2	–0.1	4.02

* Change in parameter value or elastic plate thickness relative to nominal model.

† For the nominal model (33°N Sacramento Mountains residual topographic cross section), the datum elevation is –129 m, the horizontal origin is defined as 0 km, the restoring force stiffness is $\rho_c g$, and all other parameters are as in Table 1.

The Sacramento Mountains (SM) in southeastern New Mexico are the only compelling example of flexural flank uplift. This range exhibits structural continuity both along strike and perpendicular to strike, legitimizing application of continuum mechanical models of the footwall. Several lines of evidence support an interpretation of synrift uplift little affected by Laramide deformation (section 2.6). The SM gradually increase in slope from the Pecos Valley to the crest, indicative of flexural uplift of a "broken" plate. Our focus has therefore been on flexural modeling of rift flank uplift at the SM.

6.2. Rift Flank Flexure Modeling

Further objectives of this work have been to understand the consequences of alternative boundary conditions and uplift mechanisms, as well as the sensitivity of flexure solutions to modeling approximations and parameter values. Arguably the worst supposition one could make when studying rift flank uplifts is that all the topographic relief is attributable to a single mechanism. We assert that it is essential to differentiate between relief arising from shallow, narrow loads (basins, erosion, faulting) and deep, wide loads (necking, compositional and thermal density anomalies). The former component of topography is potentially flexural and may avail itself to determination of lithospheric thickness; the latter is less well understood and provides poor constraints on lithospheric thickness. We accomplish separation of these components by subtracting the broad, unfaulted flank topography of the Mescalero arch from the SM cross sections (Figure 2).

This step is crucial: it alone is responsible for a factor of 2 decrease in estimated broken elastic plate thickness from 42 km (section 3.1) to a nominal 21 km (section 5). By extracting the short-wavelength flank topography we presumably remove longer wavelength components of uplift not specifically associated with normal faulting and basin formation, including topography arising from lateral heat conduction, small-scale convection, dynamic flow stresses, and lithospheric necking [*Alvarez et al.*, 1984; *Buck*, 1986; *Zuber and Parmentier*, 1986, *Chéry et al.*, 1992]. However, it is more common to explain all uplift at a rift flank with one mechanism alone [e.g., *Steckler*, 1985; *Villemin et al.*, 1986; *Ebinger et al.*, 1991]. We suggest that such models are prone to errors in estimates of lithospheric structure and driving stresses responsible for rift topography.

We have also identified problems with the continuous plate assumption in modeling flexural rift flank uplift. This model does not just predict an incorrect lithospheric thickness, it is seemingly unable to explain the Sacramento Mountains topography at all without special pleading (Figure 4b). Although we have liberally overestimated the applied loads, no elastic plate thickness can reproduce the position and amplitude of the SM; we return to this problem below. The continuous plate premise is common in the literature [*Weissel and Karner*, 1989; *Ebinger et al.*, 1991; *Kusznir et al.*, 1991; *Egan*, 1992; *Kusznir and Ziegler*, 1992]; again, we must question the results of such models.

With our finite element modeling (FEM) of flexure accompanying slip on a normal fault, we have examined the approximations inherent to analytic thin-plate flexure models that treat the fault only as a boundary condition, and we have estimated the errors in lithospheric thickness and applied loads associated with these simpler models. We emphasize that the restoring forces must be applied at the base of the lithosphere, not the surface (section 4.1); incorrect placement of the restoring forces results in erroneous flexural deflections (section 4.3). Our FEM simulations with and without basin infill, but no erosion, indicate that broken elastic plate fits to rift flank topography underestimate "true" elastic lithosphere thicknesses by tens of percent, the exact discrepancy depending primarily on the fault dip and plate thickness (Figure 6). A modified boundary condition proposed by *Bott* [1996] does not account for these errors. The inclusion of a footwall erosional load reveals large broken plate thickness errors that can be either positive or negative (Table 4). Therefore, the broken plate boundary assumption, employed by several workers [e.g., *Stern and ten Brink*; 1989; *Bott and Stern*, 1992; *Masek et al.*, 1994], is also generally not accurate.

A fundamental conclusion of this work is that the continuous and broken plate analytic rift flank flexure models cannot even provide consistent lower or upper bounds on the effective elastic lithosphere thickness. Interpretation of the loads acting on the flank are equally ambiguous. These shortcomings leave two alternatives. One may use the general flexure equation (1) with (at least) three free parameters: the coefficients (A and B) and the flexural wavelength (λ). In principle, B is fixed by the amplitude of the uplift and A and λ are determined by the combination of the back slope of the uplift and the location of the peripheral trough. However, peripheral troughs are not commonly recognized adjacent to rift flanks, and the applied forces derived from this model are also uninformative. The second choice is to explicitly model the fault as is done here (section 4) and by a few other workers [*King and Ellis*, 1990; *Bott*, 1997], which, while more physically robust, is a much less expedient alternative.

6.3. Sacramento Mountains Flexure

At the Sacramento Mountains we find that the broken plate solution does give a reasonable estimate of the effective elastic thickness because the large amplitude of the uplift causes significant decoupling across the fault (Figures 8 and 9). To test for sources of uncertainty in rift flank flexure, we have fit the broken plate equation to 22 SM profiles varying all relevant parameters. The effective elastic thickness (h_e) along strike is a surprisingly consistent 23.0 ± 2.3 km. The elastic thickness is subject to error on the <10% level for most fitting and physical parameters (Table 5), with the exception of Young's modulus, which potentially introduces a ~30% error. We cannot state with certainty what the net effect of all these errors might be. Perhaps 50% is a reasonable upper bound, corresponding to about ±12 km for the SM. The errors arising from parameter uncertainties are typically less than those from the fault boundary condition approximations for moderate flank uplifts (<1 km).

Our mean elastic plate thickness estimate for the SM, $h_e \approx 23$ km, is comparable to that of *Lowry and Smith* [1994] for the Archean Wyoming craton and northwest Colorado Plateau, and greater than their and *Stein et al.*'s [1988] values for the Basin and Range. It agrees with the spectrally derived thickness of *Bechtel et al.* [1990] for the RGR region, and seems to be appropriate for an area between the rift axis and the craton. Sacramento Mountains uplift and Pecos River Valley downwarping initiated in the late Miocene (<12 Ma); these events are associated with late-phase RGR extension, and they are probably recent. Our model of the SM implies that the Pecos Valley is a flexural trough (Figure 9). This result is supported by geologic information on the valley formation (section 2.7), although salt dissolution and erosion have also contributed to the observed subsidence. Rift tectonics probably controlled the development of both the Rio Grande and Pecos drainages.

The load balance for the SM is not easily interpreted using the shear force derived from analytic fits, as indicated by the FEM simulations. A direct FEM model of the flank uplift is required to ascertain if the model-derived loads match the geologically inferred stresses. An FEM model fit with $h_{fem} = 20$ km and $\theta = 63°$ (Figure 9) requires $e_0 = 1.8$ km and a 1.2×10^{12} N m^{-1} denudational force, exceeding the inferred heave and erosion (section 3.3). This result implies that we have not recognized all the loads present at the SM; the ~5×10^{11} N m^{-1} "missing" force is ~50% of the net estimated load. The continuous plate model was rejected for its inability to match the SM topography with "known" driving stresses, but the need for additional forces in the faulted-plate model obliges us to reconsider this judgement. If the additional stresses are applied to a continuous plate, a large misfit with the SM persists (Figure 9). However, our ignorance of the driving stresses leaves open the possibility of a still larger "missing" load that would allow the continuous plate solution to be acceptable. We conclude that the faulted plate model is preferable because it better accounts for the physics of a faulted upper crust and minimizes the anomalous stresses at the SM, but we cannot firmly reject the continuous plate approach. In any case, the contribution of erosion is important, and probably dominant, in the SM flexure.

6.4. Improved Rift Flank Modeling

Another aspiration of this study has been to advance beyond effective elastic thickness estimates to more relevant assessments of the lithospheric geotherm, which can then be compared to surface heat flow measurements or thermal structure inferred from xenolith geothermobarometry. Two methods that might be used to achieve geotherm estimates rely on constructing yield strength envelopes for the continental lithosphere [*Kohlstedt et al.*, 1995]. One approach is to take the maximum bending curvature and moment from an elastic fit and find the geotherm that gives an equivalent moment for an elastic–plastic lithosphere (in which the bending stresses are limited by the yield strength envelope) [*McNutt and Menard*, 1982; *Mueller and Phillips*, 1995]. Alternatively, one could generate the nonlinear moment–curvature function from the yield strength envelope and numerically solve the flexure equation with a finite difference routine [*Brown and Grimm*, 1996].

We have fit broken plate elastic–plastic flexural models to the SM flank uplift and find that the simpler moment–curvature matching technique is very accurate when compared to complete forward models. The maximum bending curvature (~4×10^{-7} m^{-1}) is predicted to occur on the Pecos slope, ~40 km east of the fault. However, the uncertainties in both the yield strength envelope and fitting parameters (i.e., datum, origin) produce a very large geotherm uncertainty, from 10 to 30 K km^{-1}. The most that can be said about these results is that they are consistent with heat flow [*Reiter et al.*, 1986] and xenolith [*Bussod and Williams*, 1991] information.

The future direction of rift flank modeling must be toward a more realistic representation of faulting within the lithosphere. While we favor the broken over the continuous plate model, the truth may lie somewhere in between. *Bott* [1997] included plasticity in his plate, but he neglected the role of viscous creep in the lower lithosphere. Our model, too, implicitly assumes penetrative faulting of the mechanically competent lithosphere and inviscid flow beneath this layer. But we recognize the nature of extension must transition from simple-shear normal faulting in the upper crust to pure-shear stretching or necking in the lower crust and upper mantle, and the mechanical response of the viscous lithosphere will influence the deformation and uplift observed at the surface [e.g., *Chéry et al.*, 1992]. The challenge is to satisfactorily simulate intralithospheric faults in the finite element model without introducing singularities or space problems [cf. *Melosh and Williams*, 1989; *Boutilier and Keen*, 1994].

Acknowledgments. We thank Michael Steckler, Scott Baldridge, and associate editor Carolyn Ruppel for their thorough reviews. This work was supported in part by NASA grant NAGW-3024 and NSF grant EAR-9706140.

References

Adams, D. C., and G. R. Keller, Crustal structure and basin geometry in south-central New Mexico, in *Basins of the Rio Grande Rift: Structure, Stratigraphy, and Tectonic Setting*, edited by G. R. Keller and S. M. Cather, *Spec. Pap. Geol. Soc. Am.*, *291*, 241–255, 1994.

Alvarez, F., J. Virieux, and X. Le Pichon, Thermal consequences of lithosphere extension over continental margins: The initial stretching phase, *Geophys J. R Astron. Soc.*, *78*, 389–411, 1984.

Bachman, G. O., Cenozoic deposits of southeastern New Mexico and an outline of the history of evaporite dissolution, *J. Res. U. S. Geol. Surv.*, *4*, 135–149, 1976.

Baldridge, W. S., Y. Bartov, and A. Kron, Geologic map of the Rio Grande rift and southeastern Colorado Plateau, New Mexico and Arizona, scale 1:500,000, in *Rio Grande Rift: Tectonics and Magmatism*, edited by R. E. Riecker, AGU, Washington, D. C., 1983.

Baldridge, W. S., G. R. Keller, V. Haak, E. Wendlandt, G. R. Jiracek, and K. H. Olsen, The Rio Grande rift, in *Continental Rifts: Evolution, Structure, Tectonics*, edited by K. H. Olsen, pp. 233–275, Elsevier, New York, 1995.

Bartsch-Winkler, S., Geology of east-central New Mexico, in *Mineral and Energy Resources of the Roswell Area, East-Central New Mexico*, edited by S. Bartsch-Winkler and A J. Donatich, *U. S Geol. Surv. Bull.*, *2063*, 5–34, 1995.

Bechtel, T. D., D. W. Forsyth, V. L. Sharpton, and R. A. F. Grieve, Variations in effective elastic thickness of the North American lithosphere, *Nature*, *343*, 636–638, 1990.

Bott, M H. P., Flexure associated with planar faulting, *Geophys. J Int.*, *126*, F21–F24, 1996.

Bott, M. H. P., Modeling the formation of a half graben using realistic upper crustal rheology, *J. Geophys. Res.*, *102*, 24,605–24,617, 1997.

Bott, M H. P., and T. A. Stern, Finite element analysis of Transantarctic Mountain uplift and coeval subsidence in the Ross Embayment, *Tectonophysics*, *201*, 341–356, 1992.

Boutilier, R. R., and C. E. Keen, Geodynamic models of fault-controlled extension, *Tectonics*, *13*, 439–454, 1994.

Bowsher, A L., Some effects of Precambrian basement on the development of the Sacramento Mountains, in *Geology of the Sierra Blanca, Sacramento and Capitan Ranges, New Mexico*, edited by J. M. Barker, B. S. Kues, G. S. Austin, and S. G. Lucas, *Field Conf Guideb. N. M Geol. Soc.*, *42*, 81–89, 1991

Bridwell, R. J., and C. A. Anderson, Thermomechanical models of the Rio Grande rift, in *Mechanisms of Continental Drift and Plate Tectonics*, edited by P. A. Davies and S. K Runcorn, pp. 41–59, Academic, San Diego, Calif., 1980.

Brister, B. S., and R. R. Gries, Tertiary stratigraphy and tectonic development of the Alamosa Basin (northern San Luis Basin), Rio Grande rift, south-central Colorado, in *Basins of the Rio Grande Rift. Structure, Stratigraphy, and Tectonic Setting*, edited by G R. Keller and S. M. Cather, *Spec Pap. Geol Soc. Am*, *291*, 39–58, 1994.

Brown, C. D., and R. E Grimm, Lithospheric rheology and flexure at Artemis Chasma, Venus, *J. Geophys. Res*, *101*, 12,697–12,708, 1996.

Buck, W. R., Small-scale convection induced by passive rifting: The cause for uplift of rift shoulders, *Earth Planet. Sci. Lett*, *77*, 362–372, 1986.

Buck, W. R., Flexural rotation of normal faults, *Tectonics*, *7*, 959–973, 1988.

Burchfiel, B. C., D S. Cowan, and G A. Davis, Tectonic overview of the Cordilleran orogen in the western United States, in *The Geology of North America*, vol G3, *The Cordilleran Orogen: Conterminous U S.*, edited by B. C. Burchfiel, P. W. Lipman, and M. L. Zoback, pp. 407–479, Geol. Soc. of Am., Boulder, Colo., 1992.

Bussod, G. Y. A., and D. R. Williams, Thermal and kinematic model of the southern Rio Grande rift: Inferences from crustal and mantle xenoliths from Kilbourne Hole, New Mexico, *Tectonophysics*, *197*, 373–389, 1991.

Caran, S. C., Cenozoic stratigraphy, southern Great Plains and adjacent areas, in *The Geology of North America*, vol. K2, *Quaternary Nonglacial Geology; Conterminous U. S.*, edited by R. B Morrison, plate 5, Geol. Soc of Am., Boulder, Colo., 1991.

Chapin, C. E., and S. M. Cather, Tectonic setting of the axial basins of the northern and central Rio Grande rift, in *Basins of the Rio Grande Rift: Structure, Stratigraphy, and Tectonic Setting*, edited by G. R. Keller and S. M. Cather, *Spec. Pap. Geol. Soc. Am*, *291*, 5–25, 1994.

Chapin, C. E., and W. R. Seager, Evolution of the Rio Grande rift in the Socorro and Las Cruces areas, in *Guidebook of the Las Cruces Country*, edited by W. R Seager, R. E. Clemons, and J. F. Callender, *Field Conf. Guideb. N. M. Geol. Soc.*, *26*, 297–321, 1975.

Chéry, J., F. Lucazeau, M. Daignières, and J. P. Vilotte, Large uplift of rift flanks: A genetic link with lithospheric rigidity?, *Earth Planet Sci. Lett.*, *112*, 195–211, 1992.

Coney, P. J., Structure, volcanic stratigraphy, and gravity across the Mogollon Plateau, New Mexico, in *Cenozoic Volcanism in Southwestern New Mexico*, edited by W. E. Elston and S. A. Northrop, *Spec. Publ. N. M. Geol. Soc.*, *5*, 29–41, 1976.

Cordell, L., Extension in the Rio Grande rift, *J. Geophys. Res.*, *87*, 8561–8569, 1982.

Davis, G. A., and G. S. Lister, Detachment faulting in continental extension; Perspectives from the southwestern U.S. Cordillera, in *Processes in Continental Lithospheric Deformation*, edited by S. P. Clark, B. C. Burchfiel, and J. Suppe, *Spec. Pap. Geol. Soc. Am.*, *218*, 133–159, 1988.

Davis, P. M., Continental rift structures and dynamics with reference to teleseismic studies of the Rio Grande and East African rifts, *Tectonophysics*, *197*, 309–325, 1991.

Eaton, G. P., Topography and origin of the southern Rocky Mountains and Alvarado Ridge, in *Continental Extensional Tectonics*, edited by M. P. Coward, J F. Dewey, and P. L. Hancock, *Spec. Publ. Geol. Soc.*, *28*, 355–369, 1987.

Ebinger, C. J., G. D. Karner, and J. K. Weissel, Mechanical strength of extended continental lithosphere: Constraints from the western rift system, East Africa, *Tectonics*, *10*, 1239–1256, 1991.

Egan, S. S., The flexural isostatic response of the lithosphere to extensional tectonics, *Tectonophysics*, *202*, 291–308, 1992.

Epis, R. C., and C. E. Chapin, Geomorphic and tectonic implications of the post-Laramide, late Eocene erosion surface in the southern Rocky Mountains, in *Cenozoic History of the Southern Rocky Mountains*, edited by B. F. Curtis, *Mem. Geol Soc. Am*, *144*, 45–74, 1975.

Frye, J C, A. B. Leonard, and H. D. Glass, Western extent of Ogallala Formation in New Mexico, *Circ. 175*, 41 pp., N. M Bur. Mines Min. Resour., Socorro, 1982.

Gilchrist, A. R., and M. A. Summerfield, Differential denudation and flexural isostasy in formation of rifted-margin upwarps, *Nature*, *346*, 739–742, 1990.

Gregory, K. M., and C. G. Chase, Tectonic and climatic significance of a late Eocene low-relief, high-level geomorphic surface, Colorado, *J. Geophys. Res.*, *99*, 20,141–20,160, 1994.

Gustavson, T. C., and R. J. Finley, Late Cenozoic geomorphic evolution of the Texas Panhandle and northeastern New Mexico, *Rep. of Invest. 148*, 42 pp., Bur. of Econ. Geol., Univ. of Tex., Austin, 1985.

Gustavson, T. C, V T. Holliday, and G. E. Schultz, Introduction, in *Tertiary and Quaternary Stratigraphy and Vertebrate Paleontology of Parts of Northwestern Texas and Eastern New Mexico*, edited by T. C. Gustavson, *Tex. Bur. Econ. Geol. Guideb.*, *24*, 1–21, 1990.

Harrison, R. W., Winston graben: Stratigraphy, structure, and tectonic setting, in *Basins of the Rio Grande Rift: Structure, Stratigraphy, and Tectonic Setting*, edited by G. R. Keller and S. M. Cather, *Spec. Pap. Geol. Soc. Am.*, *291*, 227–240, 1994.

Heywood, C. E., Isostatic residual gravity anomalies of New Mexico, *U. S. Geol. Surv. Water Resour. Invest. Rep.*, *91-4065*, 27 pp., 1992.

Ingersoll, R. V., W. Cavazza, W. S. Baldridge, and M. Shafiqullah, Cenozoic sedimentation and paleotectonics of north-central New Mexico: Implications for initiation and evolution of the Rio Grande rift, *Geol. Soc. Am. Bull.*, *102*, 1280–1296, 1990.

Keller, G. R., L Cordell, G. H. Davis, W. J. Peeples, and G. White, A geophysical study of the San Luis basin, in *Rio Grande Rift: Northern New Mexico*, edited by W. S. Baldridge, P. W. Dickerson, R. E. Riecker, and J. Zidek, *Field Conf. Guideb. N. M. Geol. Soc.*, *35*, 51–57, 1984.

Keller, G. R., P. Morgan, and W. R. Seager, Crustal structure, gravity anomalies and heat flow in the southern Rio Grande rift and their relationship to extensional tectonics, *Tectonophysics*, *174*, 21–37, 1990.

Keller, G. R., M. A. Khan, P. Morgan, R. F. Wendlandt, W. S. Baldridge, K. H. Olsen, C. Prodehl, and L. W. Braile, A comparative study of the Rio Grande and Kenya rifts, *Tectonophysics*, *197*, 355–371, 1991.

Kelley, S. A., and C. E. Chapin, Cooling histories of mountain ranges in the southern Rio Grande rift based on apatite fission-track analysis—A reconnaissance survey, *N. M. Geol.*, *19*, 1–14, 1997.

Kelley, S. A., and I. J Duncan, Late Cretaceous to middle Tertiary tectonic history of the northern Rio Grande rift, New Mexico, *J. Geophys. Res.*, *91*, 6246–6262, 1986.

Kelley, S. A, C. E. Chapin, and J. Corrigan, Late Mesozoic to Cenozoic cooling histories of the flanks of the northern and central Rio Grande rift, Colorado and New Mexico, *Bull 145*, 40 pp, N. M. Bur Mines Min. Resour., Socorro, 1992.

Kelley, V. C., Geology of the Pecos Country, southeastern New Mexico, *Mem. 24*, 75 pp., N. M. Bur. Mines Min. Resour., Socorro, 1971.

Kelley, V C., Tectonics, middle Rio Grande rift, New Mexico, in *Rio Grande Rift: Tectonics and Magmatism*, edited by R. E. Riecker, pp. 57–70, AGU, Washington, D. C., 1979.

Kelley, V. C., and S. A. Northrop, Geology of Sandia Mountains and vicinity, New Mexico, *Mem. 29*, 136 pp., N. M. Bur. Mines Min. Resour., Socorro, 1975.

King, G., and M. Ellis, The origin of large local uplift in extensional regions, *Nature*, *348*, 689–693, 1990.

Kohlstedt, D. L, B. Evans, and S. J Mackwell, Strength of the lithosphere: Constraints imposed by laboratory experiments, *J. Geophys. Res.*, *100*, 17,587–17,602, 1995.

Kooi, H., S Cloetingh, and J. Burrus, Lithospheric necking and regional isostasy at extensional basins, 1., Subsidence and gravity modeling with an application to the Gulf of Lions margin (SE France), *J. Geophys. Res*, *97*, 17,553–17,571, 1992.

Kusznir, N. J., and P. A. Ziegler, The mechanics of continental extension and sedimentary basin formation: A simple-shear/pure-shear flexural cantilever model, *Tectonophysics*, *215*, 117–131, 1992.

Kusznir, N. J., G. Marsden, and S. S. Egan, A flexural-cantilever simple-shear/pure-shear model of continental lithosphere extension: Applications to the Jeanne d'Arc Basin, Grand Banks and Viking Graben, North Sea, in *The Geometry of Normal*

Faults, edited by A. M Roberts, G. Yielding, and B. Freeman, *Spec. Publ. Geol. Soc*, *56*, 41–60, 1991.

Lewis, C J., and W. S Baldridge, Crustal extension in the Rio Grande rift, New Mexico: Half-grabens, accommodation zones, and shoulder uplifts in the Ladron Peak–Sierra Lucero area, in *Basins of the Rio Grande Rift Structure, Stratigraphy, and Tectonic Setting*, edited by G R. Keller and S. M. Cather, *Spec. Pap. Geol Soc. Am.*, *291*, 135–155, 1994.

Lowry, A. R., and R B. Smith, Flexural rigidity of the Basin and Range–Colorado Plateau–Rocky Mountain transition from coherence analysis of gravity and topography, *J. Geophys Res*, *99*, 20,123–20,140, 1994.

Lozinsky, R. P., Cross section across the Jornada del Muerto, Engle, and northern Palomas Basins, south-central New Mexico, *N. M. Geol.*, *9*, 55–63, 1987.

Lozinsky, R. P., and P. W. Bauer, Structure and basin-fill units of the Tularosa basin, in *Geology of the Sierra Blanca, Sacramento and Capitan Ranges, New Mexico*, edited by J. M. Barker, B. S. Kues, G. S. Austin, and S. G. Lucas, *Field Conf. Guideb. N. M. Geol. Soc.*, *42*, 7–9, 1991.

Machette, M. N., Preliminary assessment of paleoseismicity at White Sands Missile Range, southern New Mexico—Evidence for recency of faulting, fault segmentation, and repeat intervals for major earthquakes in the region, *U. S. Geol Surv Open File Rep.*, *87-444*, 46 pp., 1987.

Masek, J. G., B. L. Isacks, E. J. Fielding, and J. Browaeys, Rift flank uplift in Tibet. Evidence for a viscous lower crust, *Tectonics*, *13*, 659–667, 1994.

May, S J., S. A. Kelley, and L. R. Russell, Footwall unloading and rift shoulder uplifts in the Albuquerque Basin. Their relation to syn-rift fanglomerates and apatite fission-track ages, in *Basins of the Rio Grande Rift: Structure, Stratigraphy, and Tectonic Setting*, edited by G. R. Keller and S. M Cather, *Spec. Pap. Geol Soc. Am.*, *291*, 125–134, 1994.

McGookey, D A, T C. Gustavson, and A. D Hoadley, *Regional Structural Cross Sections, Mid-Permian to Quaternary Strata, Texas Panhandle and Eastern New Mexico*, 17 pp., 14 plates, Tex. Bur. of Econ Geol., Austin, 1988.

McNutt, M. K, Lithospheric flexure and thermal anomalies, *J Geophys Res*, *89*, 11,180–11,194, 1984.

McNutt, M. K, and H. W. Menard, Constraints on yield strength in the oceanic lithosphere derived from observations of flexure, *Geophys J R. Astron. Soc.*, *71*, 363–394, 1982.

Melosh, H. J, and C. A. Williams, Mechanics of graben formation in crustal rocks: A finite element analysis, *J Geophys. Res*, *94*, 13,961–13,973, 1989.

Moore, S. L., T. B. Thompson, and E. E. Foord, Structure and igneous rocks of the Ruidoso region, New Mexico, in *Geology of the Sierra Blanca, Sacramento and Capitan Ranges, New Mexico*, edited by J. M. Barker, B. S. Kues, G. S Austin, and S. G. Lucas, *Field Conf. Guideb N M. Geol. Soc.*, *42*, 137–145, 1991

Morgan, P., W. R. Seager, and M. P. Golombek, Cenozoic thermal, mechanical and tectonic evolution of the Rio Grande rift, *J. Geophys. Res.*, *91*, 6263–6276, 1986.

Mueller, S., and R. J. Phillips, On the reliability of lithospheric constraints derived from models of outer-rise flexure, *Geophys. J. Int.*, *123*, 887–902, 1995.

Nadai, A., *Theory of Flow and Fracture of Solids*, vol. 2, 348 pp, McGraw–Hill, New York, 1963.

Olsen, K. H., W. S. Baldridge, and J F. Callender, Rio Grande rift: An overview, *Tectonophysics*, *143*, 119–139, 1987.

Parker, E. C., P. M. Davis, J. R Evans, H. M. Iyer, and K. H. Olsen, Upwarp of anomalous asthenosphere beneath the Rio Grande rift, *Nature*, *312*, 354–356, 1984.

Polyak, V. J., W. C. McIntosh, N. Güver, and P. Provencio, Age and origin of Carlsbad Cavern and related caves from $^{40}Ar/^{39}Ar$ of alunite, *Science*, *279*, 1919–1922, 1998.

Pray, L. C., Geology of the Sacramento Mountains escarpment, Otero County, New Mexico, *Bull. 35*, 144 pp., N. M. Bur. Mines Min. Resour., Socorro, 1961.

Reiter, M., R. E. Eggleston, B. R. Broadwell, and J. Minier, Estimates of terrestrial heat flow from deep petroleum tests along the Rio Grande rift in central and southern New Mexico, *J. Geophys. Res.*, *91*, 6225–6245, 1986.

Roberts, D. G., D. C. Adams, and G. R. Keller, A geophysical analysis of crustal structure in the Ruidoso area, in *Geology of the Sierra Blanca, Sacramento and Capitan Ranges, New Mexico*, edited by J. M. Barker, B. S. Kues, G. S. Austin, and S. G. Lucas, *Field Conf. Guideb. N. M Geol. Soc*, *42*, 191–197, 1991.

Russell, L. R., and S. Snelson, Structure and tectonics of the Albuquerque Basin segment of the Rio Grande rift: Insights from reflection seismic data, in *Basins of the Rio Grande Rift. Structure, Stratigraphy, and Tectonic Setting*, edited by G. R. Keller and S. M. Cather, *Spec. Pap. Geol. Soc. Am.*, *291*, 83–112, 1994.

Slack, P. D., P. M. Davis, W. S. Baldridge, K. H. Olsen, A. Glahn, U. Achauer, and W. Spence, The upper mantle structure of the central Rio Grande rift region from teleseismic *P* and *S* wave travel time delays and attenuation, *J. Geophys Res.*, *101*, 16,003–16,023, 1996.

Steckler, M. S, Uplift and extension at the Gulf of Suez: Indications of induced mantle convection, *Nature*, *317*, 135–139, 1985.

Stein, R. S., G. C. P. King, and J. B. Rundle, The growth of geological structures by repeated earthquakes, 2. Field examples of continental dip-slip faults, *J Geophys Res.*, *93*, 13,319–13,331, 1988.

Stern, T., and U. ten Brink, Flexural uplift of the Transantarctic Mountains, *J Geophys. Res.*, *94*, 10,315–10,330, 1989.

Turcotte, D. L., and G Schubert, *Geodynamics*, 450 pp., John Wiley, New York, 1982.

Tweto, O., Laramide (late Cretaceous–early Tertiary) orogeny in the southern Rocky Mountains, in *Cenozoic History of the Southern Rocky Mountains*, edited by B. F Curtis, *Mem. Geol Soc Am.*, *144*, 1–44, 1975.

Tweto, O, The Rio Grande rift system in Colorado, in *Rio Grande Rift: Tectonics and Magmatism*, edited by R. E Riecker, pp. 33–56, AGU, Washington, D. C., 1979.

Villemin, T., F. Alvarez, and J. Angelier, The Rhinegraben: Extension, subsidence and shoulder uplift, *Tectonophysics*, *128*, 47–59, 1986.

Walker, J. R., Geomorphic evolution of the Southern High Plains, *Bull. 35*, 32 pp., Baylor Geol. Stud., Waco, Tex., 1978.

Wallace, M. H., and H. J. Melosh, Buckling of a pervasively faulted lithosphere, *Pure Appl. Geophys.*, *142*, 239–261, 1994.

Wdowinski, S, and G. J. Axen, Isostatic rebound due to tectonic denudation: A viscous flow model of a layered lithosphere, *Tectonics*, *11*, 303–315, 1992.

Weissel, J. K., and G. D. Karner, Flexural uplift of rift flanks due to mechanical unloading of the lithosphere during extension, *J. Geophys. Res.*, *94*, 13,919–13,950, 1989.

Wessel, P., Thermal stresses and the bimodal distribution of elastic thickness estimates of the oceanic lithosphere, *J. Geophys. Res.*, *97*, 14,177–14,193, 1992.

Winkler, D. A., Vertebrate-bearing eolian unit from the Ogallala Group (Miocene) in northwestern Texas, *Geology*, *15*, 705–708, 1987

Woodward, L. A., J F Callender, J. Gries, W. R. Seager, C. E. Chapin, W. L. Shaffer, and R. E. Zilinski, Tectonic map of the Rio Grande region, Colorado–New Mexico border to Presidio, Texas, scale ~1.1,000,000, in *Guidebook of the Las Cruces Country*, edited by W. R. Seager, R. E. Clemons, and J. F. Callender, *Field Conf. Guideb. N M. Geol. Soc.*, *26*, 239, 1975.

Zandt, G., and T. J. Owens, Crustal flexure associated with normal faulting and implications for seismicity along the Wasatch Front, Utah, *Bull. Seismol. Soc Am.*, *70*, 1501–1520, 1980.

Zuber, M T., and E. M. Parmentier, Lithospheric necking: A dynamic model for rift morphology, *Earth Planet. Sci. Lett.*, *77*, 373–383, 1986

C. D. Brown and R. J. Phillips, Department of Earth and Planetary Sciences, Washington University, Campus Box 1169, One Brookings Drive, Saint Louis, MO 63130-4899. (dbrown@geoid.wustl.edu)

(Received June 9, 1998;
revised May 12, 1999;
accepted May 27, 1999.)

TECTONICS, VOL. 18, NO. 6, PAGES 1064-1083 DECEMBER 1999

Lithosphere folding: Primary response to compression? (from central Asia to Paris basin)

S. Cloetingh

Faculty of Earth Sciences, Vrije Universiteit, Amsterdam

E. Burov[1]

Direction de la Recherche, Bureau de Recherches Géologiques et Minières, Orléans, France

A. Poliakov

UMR 5573, CNRS, University Montpellier II, Montpellier, France

Abstract. We examine the role of lithosphere folding in the large-scale evolution of the continental lithosphere. Analysis of the record of recent vertical motions and the geometry of basin deflection for a number of sites in Europe and worldwide suggests that lithospheric folding is a primary response of the lithosphere to recently induced compressional stress fields. Despite the widespread opinion, folding can persist during long periods of time independently of the presence of many inhomogeneities such as crustal faults and inherited weakness zones. The characteristic wavelengths of folding are determined by the presence of young lithosphere in large parts of Europe and central Asia and by the geometries of the sediment bodies acting as a load on the lithosphere in basins. The proximity of these sites to the areas of active tectonic compression suggests that the tectonically induced horizontal stresses are responsible for the large-scale warping of the lithosphere. Wavelengths and persistence of folding are controlled by many factors such as rheology, faulting, time after the end of the major tectonic compression, nonlinear effects, and initial geometry of the folded area. In particular, the persistence of periodical undulations in central Australia (700 Myr since onset of folding) or in the Paris basin (60 Myr) long after the end of the initial intensive tectonic compression requires a very strong rheology compatible with the effective elastic thickness values of about 100 km in the first case and 50-60 km in the second case.

1. Introduction

The lithosphere can undergo tectonic shortening in three principal ways: (1) volumetric shortening by distributed or localized thickening of the lithosphere due to compression, (2) folding, when shortening is accommodated by unstable, subperiodical, vertical upward and downward bending (escaping) of the lithosphere, and (3) underthrusting, subduction, when shortening is accommodated by localized, stable, downward escape of the lithosphere, i.e., by underthrusting of one block or plate along large thrust faults. The dynamics of lithosphere folding forms an important but hitherto largely underestimated component in models developed to study the evolution of the lithosphere in compressional regimes: until recently large-scale folding was accepted only for a few areas of tectonic compression such as the northeastern Indian Ocean or central Australia [*Turcotte and Schubert*, 1982; *Fleitout and Froidevaux*, 1982; *Lambeck*, 1983]. However, a number of recent data sets suggest that lithospheric folding may be a much more widespread mode of deformation than previously thought, though it may take less obvious forms than in the well-known "distinct" cases [*Ziegler et al.*, 1995; *Cloetingh and Burov*, 1996]. For this reason, a better understanding of processes controlling surface expressions of folding is required to address some of the recently raised questions (e.g., commonly inferred relationships between the folding wavelength and the age of the continental lithosphere do not explain some data from recently indicated areas of compressional instabilities [*Ziegler et al.*, 1995]).

It should be noted that at a small-scale, folding or buckling of layered mechanical structures is a typical response to horizontal shortening. For example, folding is largely observed in sedimentary layers, in outcrops exposing ductile shear bands, in clays, and in other superficial structures [*Johnson*, 1980; *Smith*, 1975]. Since the mechanism of folding is largely scale-independent, it is quite reasonable to suggest that folding may be reproduced on a lithospheric scale [e.g., *Biot*, 1961; *Stephenson and Lambeck*, 1985; *Stephenson and Cloetingh*, 1991]. Detailed small-scale studies of folding in the sedimentary cover, clays, soils, and other superficial materials [*Smith*, 1975, 1977, 1979] often consider sophisticated nonlinear rheologies in many aspects similar to those of the deep lithospheric materials. Thus it would be logical to assume that the transition from a small scale to a large scale will not change the characteristic response of the modeled system. The only really important difference, which might be expected, is associated with the effect of gravity, which is negligible for small systems and significant for large ones.

[1]Now at Department of Tectonics, University of Pierre and Marie Curie, Paris

Paper number 1999TC900040.
0278-7407/99/1999TC900040$12.00

The potential gravity energy scales as ρgh^2 per unit length, where $h(x)$ is surface elevation, ρ is the density, and g is the acceleration due to gravity, which requires a nonlinear increase in tectonic force needed to maintain continuously growing topographic uplift. Thus the influence of the gravity force on folding is negligible for the systems with $h < 10$-20 m but becomes important starting from $h > 50$-100 m. For this reason, small-scale folds may be of very large amplitude, a few times larger than the layer thickness and comparable to or exceeding the wavelength of folding. At lithospheric scale, upward elevations do not exceed 5 km, which is smaller than the thickness of the folded layers and less than 10% of the characteristic lithospheric folding wavelengths (30-600 km). Most lithospheric-scale studies used more simplified models than the small-scale studies; for example, a simplified elastic rheology was typically used as a first approximation of the lithospheric material properties. This approximation may work for the flexural models but predicts unrealistically high stresses for buckling models. Partly for this reason, models of lithospheric folding were put aside for quite a long time, just until the late seventies, when a number of authors [*McAdoo and Sandwell*, 1985; *Zuber*, 1987; *Turcotte*, 1979; *Fleitout and Froidevaux*, 1982, 1983] showed that the application of viscous or more realistic yield-stress rheologies can partly resolve the "high-stress" problems met in the elastic folding models. However, solution of the "high-stress" problem just freed space for another one, the "low-stress" problem. The latter is associated with the current wide-spread opinion that thrust faults, either preexisting or accompanying lithospheric shortening, may weaken the compressed layer so much that it will not be able to support stresses necessary to initialize and maintain folding (the latter requires a large competence contrast between the folded layer and the embedding).

Starting with early papers on the occurrence of lithospheric folding in the intracratonic lithosphere of central Australia [*Lambeck*, 1983] or on the folding of the oceanic lithosphere in the northeastern Indian Ocean [*Geller et al.*, 1983; *Stein et al.*, 1989], continental folding was subsequently recognized in the lithosphere of central Australia [*Stephenson and Lambeck*, 1985; *Beekman et al.*, 1997], central Asia [*Nikishin et al.*, 1993; *Burov et al.*, 1993; *Burg et al.*, 1994; *Cobbold et al.*, 1993; *Burov and Molnar*, 1998], Arctic Canada [*Stephenson et al.*, 1990], Iberia [*Waltham et al.*, 1999; S. Cloetingh et al., Late Cenozoic lithosphere folds in Iberia?, submitted to *Tectonophysics*, 1999, hereinafter referred to as Cloetingh et al., submitted manuscript, 1999] and the Paris basin [*Lefort and Agarwal*, 1996; J.-P. Brun, personal communication, 1994]. A surprising aspect of the outcome of these studies was that the occurrence of folding was not restricted to lithosphere with intrinsic zones of weakness but also occurred in areas characterized by the presence of cold and presumably strong lithosphere (see Figure 1 and Table 1).

More recently, evidence has also been put forward to support the occurrence of a component of lithosphere folding in some of the major extensional basins of Europe, such as the North Sea basin [*van Wees and Cloetingh*, 1996; *van Balen et al.*, 1998], the Pannonian basin [*Horváth and Cloetingh*, 1996; *van Balen et al.*, 1996; *Fodor et al.*, 1999; *Bada et al.*, 1998], and the Gulf of Lion's margin of the western Mediterranean [*Kooi et al.*, 1992; *Chamot-Rooke et al.*, 1999]. These basins are located on lithosphere with low rigidity, and the observed wavelengths seem at first hand to be at odds with these rheological contexts (see Figures 1 and 2).

However, the discrepancy with the theoretical predictions and the observations of the compressional deformation in the former extensional basins is not surprising, since in most of the "problematic" cases the geometry and other assumptions of the linear theory are poorly satisfied. The linear theory of folding developed in the sixties to seventies by *Biot* [1961], *Ramberg* [1961], *Smith* [1975], *Fletcher* [1974], and *Johnson* [1980] predicts development of sinusoidal undulations of a horizontally shortened competent layer embedded in less

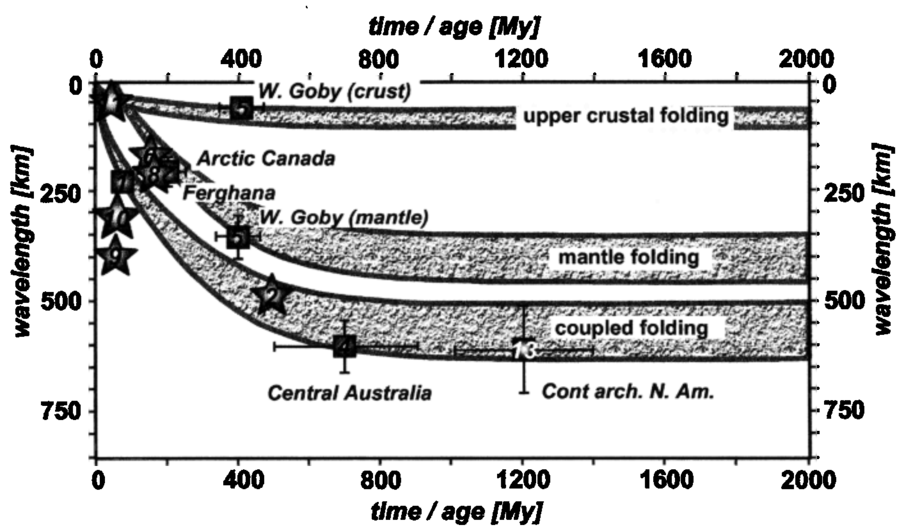

Figure 1. The observed wavelength of folding as a function of the thermal age (i.e., mechanical mantle thickness) calculated according to the model from *Burov et al.* [1993]. Numbers correspond to the ones used in Table 1. Squares show the cases of "regular" folding, whereas the stars mark "irregular" cases. Different theoretical curves correspond to crustal, mantle (supporting the presence of the decoupled rheology), and "welded" folding.

Table 1. Estimates for Wavelengths of Folding, Effective Elastic Thickness, Thermal Age, and the Onset of Folding

λ, km	EET, km	Thermal Age, Ma	t_0, Onset of Folding, Myr	Present State of Folding	Type
200-250 (1)	40	60	8	active deformation	B
500-600(2)	50	400-600	60	preserved	N
200 (3)	30	200	60	preserved	B
200 (present); > 400-500 (preserved) (4)	25 *	> 700	400-700	preserved	B
300-360 (5)	15	175 – 400	8-10	active deformation	B
100 –200 (6)	≥ 30	> 100	60	preserved	B/N
200 ? (7)	20-35	300	6	active subsidence	N
200–250 (8)	15	175	8-10	active deformation	B/N
350-400 (9)	6-9	< 20	4-6	active deformation	N
300 (10)	10-30	30	6-8	active deformation	B/N
40 (11)	20-25	< 20	6-8	active deformation	N
50 (12)	20-25	20	6-8	active subsidence	N
600 (13)	> 100	> 1200	1200	preserved ?	B
60 (14)	< 10	65	8-35	active deformation	B/N

EET, effective elastic thickness. Numbers in brackets refer to data sources: 1, Indian Ocean [*Cochran*, 1989; *Curray and Munasinghe*, 1989], (2) Russian platform [*Nikishin et al.*, 1997]; 3, Arctic Canada [*Stephenson et. al.*, 1990]; 4, central Australia [*Lambeck*, 1983; *Stephenson and Lambeck*, 1985; *Beekman et al.*, 1997]; 5, western Goby [*Nikishin et al.*, 1993; *Burov et al.*, 1993]; 6, Paris basin [*Lefort and Agarwal*, 1996]; 7, North Sea basin [*van Wees and Cloetingh*, 1996]; 8, Ferghana and Tadjik basins [*Burg et al.*, 1994; *Burov and Molnar*, 1998]; 9, Pannonian basin [*Horváth and Cloetingh*, 1996]; 10, Iberian continent [*Stapel et al.*, 1997; *Vegas et al.*, 1998; Cloetingh et al., submitted manuscript, 1999]; 11, southern Tyrrhenian Sea [*Mauffret et al.*, 1981]; 12, Gulf of Lion [*Kooi et al*, 1992]; 13, Transcontinental Arch of North America [*Ziegler et al.*, 1995]; 14, Norwegian sea [*Dore and Lundin*, 1996; *Vagnes et al.*, 1998]. "B" stands for regular folding style, "N" stands for "irregular" folding style, and "B/N" stands for the cases displaying both types of behavior.

*Value is for recent reheating at 200 Ma.

competent surroundings. This deformation is characterized by a single dominant wavelength between 3 and 50 km thickness of the competent layer. According to the linear theory, this dominant wavelength is time-independent and is mainly controlled by the thickness of the folded layer and much less by other parameters such as competence contrast or shortening rate. The linear analysis holds for many observed cases of folding but not for all. A number of very recent (generally small-scale) studies [*Davis*, 1994; *Zhang et al.*, 1996; *Mercier et al.*, 1997; *Bhalerao and Moon*, 1996; *Hunt et al.*, 1996; *Lan and Hudleston*, 1996] have shown that the wavelengths of folding may be significantly different from those inferred from the linear theory, if time-dependence and "non-sinusoidality" of deformation, realistic (elasto-plasto-ductile) rheologies, and layer geometries are taken into account. In particular, without any lateral inhomogeneities, depending only on the boundary conditions, time, rheology, and geometry, the wavelength of unstable plate deflections can significantly vary along the shortened plate, or even one single "megafold" can be formed [*Hunt et al.*, 1996; *Burg and Podladchikov*, 1999]. Regarding the frequently discussed influence of the preexisting faults on the development of folding, recent numerical experiments on folding of brittle-elasto-viscous lithosphere [*Gerbault et al.*, 1999] as well as previous analogue experiments on plasto-elastic lithosphere [*Shemenda*, 1989, 1992; *Burg et al.*, 1994; *Martinod and Davy*, 1994] have shown that (1) lithospheric folding and faulting can develop simultaneously and (2) preexisting crustal-scale faults do not prevent but participate in the development of folding instabilities. The instabilities, in turn, can provoke the formation of new faults at the inflection points of the folds. This disagreement with the usual expectations can be explained by the underestimated role of the gravity and friction in the behavior of the large-scale fault-and-fold systems. Yet most of the previous analogue studies were based on simplified pressure-, strain-, and temperature-independent rheologies, whereas the numerical studies employing nonlinear brittle-elasto-ductile rheology did not consider developed (large strain) stages of deformation. Consequently, a more thorough study is needed to verify the previous preliminary results and the hypothesis on folding and faulting interactions.

Based on the above mentioned new observational data sets and theoretical developments, the primary goal of our study is to demonstrate that lithospheric folding is much more widespread than is currently assumed. We propose that folding represents a rather typical initial and intermediate stage of tectonic compression, which may take quite different forms, which complicates its identification. For this reason, the cases of "irregular" folding were not recognized before. To explore this concept, we will discuss in the following the role of the nonlinear rheology, faulting, and other factors such as sediment loading and prefolding plate geometry in modifying the inferred wavelengths of lithosphere folds. In addition, we investigate further the role of coupled versus decoupled rheologies in the response of the lithosphere to large-scale compressional deformation. We will discriminate between the "typical," "regular," or "distinct" folding characterized by periodical deformation, which can be explained by the common linear theory, and "irregular" folding, which does not fit in the conventional theoretical scheme; for example, it may be aperiodical, polyharmonic, or have a much shorter or longer wavelength compared to the "linear" predictions.

2. Folding as a Mechanism of Shortening: Origin of Different Forms of Folding

Folding is commonly associated with periodical deformation of layered structures, and thus the periodicity is

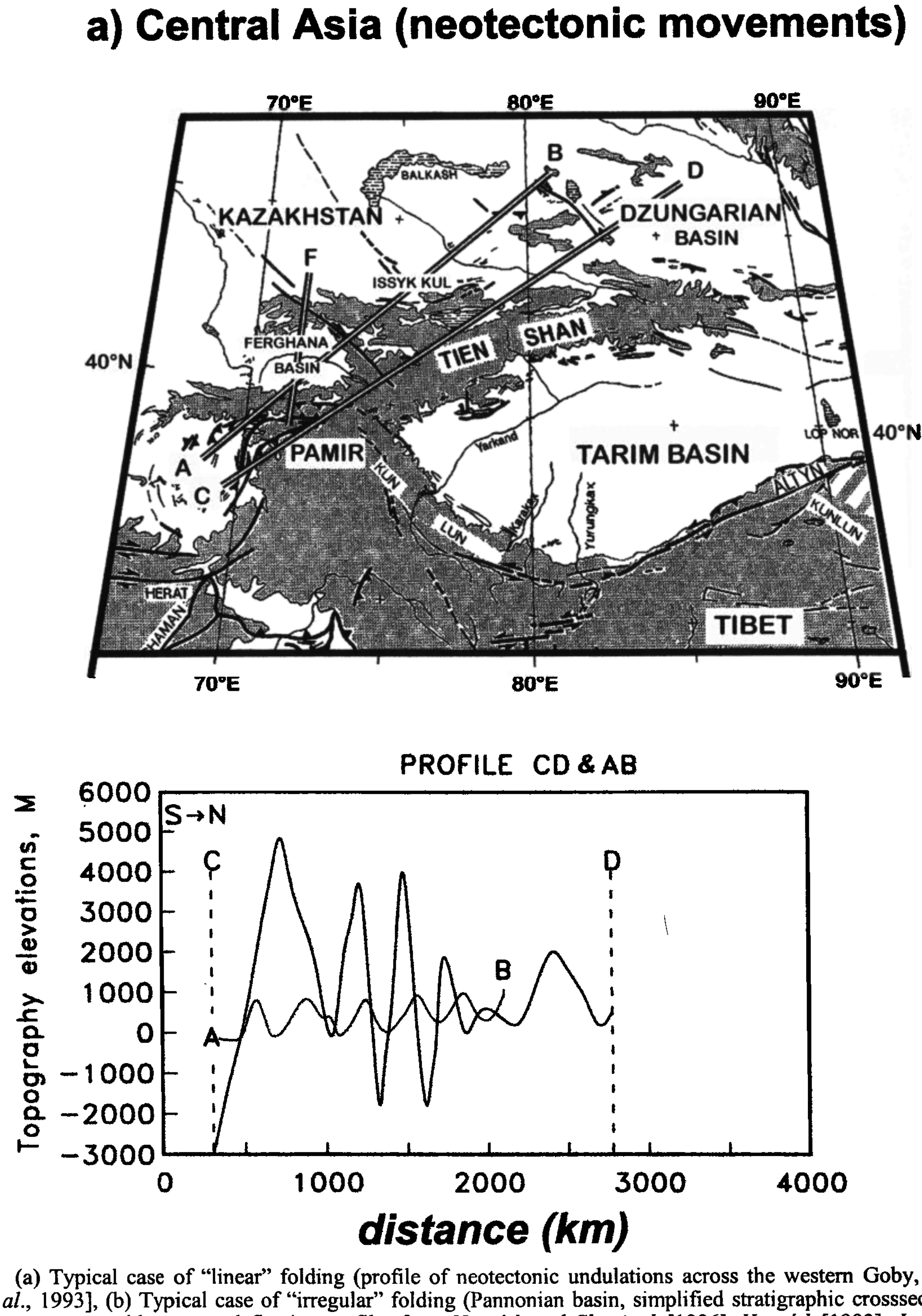

Figure 2. (a) Typical case of "linear" folding (profile of neotectonic undulations across the western Goby, central Asia [*Burov et al.*, 1993], (b) Typical case of "irregular" folding (Pannonian basin, simplified stratigraphic crosssections, recent vertical movements, and basement deflection profiles from *Horváth and Cloetingh* [1996], *Horváth* [1993], *Jaó* [1992], and *Bada et al.* [1998]), (c) Intermediate case of folding (gravity-based Moho deflection profile in the Ferghana basin, from *Burov and Molnar* [1998]).

often believed to be its primary, almost synonymous identifying feature. However, from a mechanical point of view, the periodicity is not a necessary requirement. For the mechanical theory, folding is just a compressional instability developing in stiff layers embedded in a weaker background, and the periodic, time-independent solution of the complete governing equilibrium and conservation equations is only the simplest one among the other possible solutions.

The physical mechanism of folding is well understood. In a continuum layered medium the stresses and strains must be

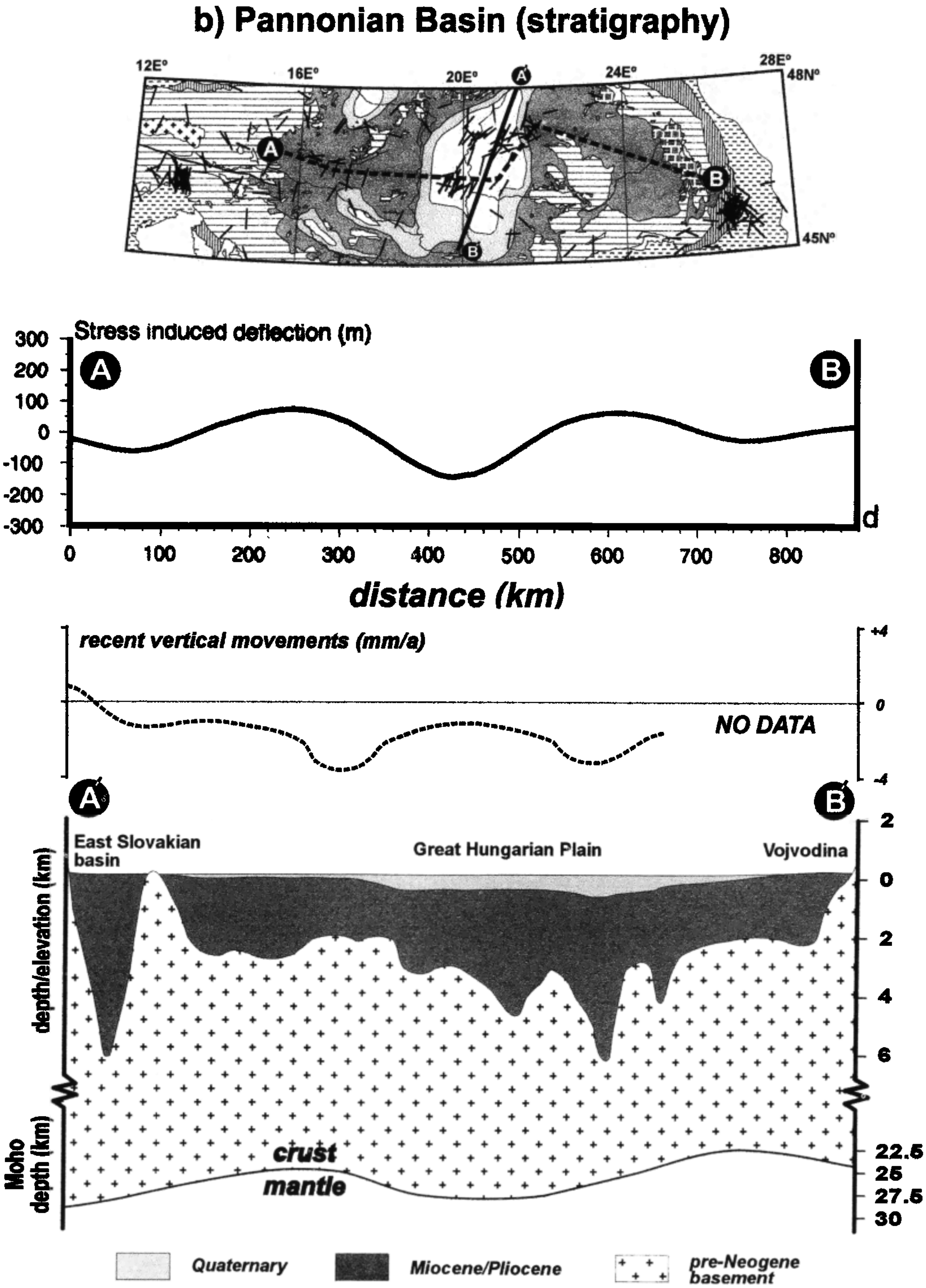

Figure 2. (continued)

continued across the interfaces between the layers. In compressed multilayers with contrasting mechanical properties (i.e., strong and weak layers), this requirement may be difficult to satisfy, because the same amount of shortening in a stiffer layer would require much larger stress than in the neighboring weaker layer. The system becomes unstable and, "trying" to reduce the stress or strain unconformities at the interfaces between the layers, starts to fold (buckle) in response to even negligibly low perturbations. In nonelastic media with strain-dependent properties, locally increased flexural strain at the fold limbs can create weakened zones significantly facilitating further deformation. These weak or softened plastic or viscous zones are often referred to as inelastic "hinges," since the system easily folds at such

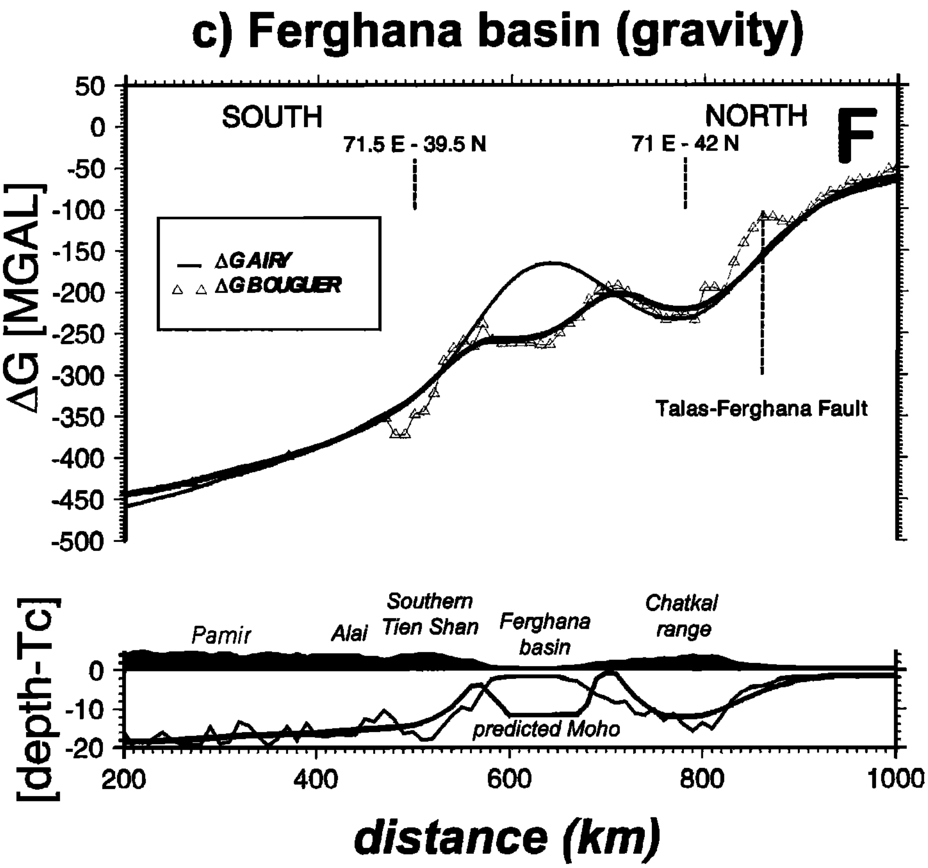

Figure 2. (continued)

weakened zones, similar to a carpenter's folding rule, under much lower compressional force than in the "normal" case. Homogeneous shortening of the lithosphere under horizontal compression requires a larger amount of work than that required by an equivalent amount of shortening by folding, whereas "shortening" by underthrusting/subduction of the lithosphere may be more advantageous then folding but cannot start immediately after the onset of shortening. For this reason, folding is likely to be a primary and even "standard" response to tectonic compression, which probably may continue, in an attenuated form, even after the beginning of subduction. As was noted in section 1, we subdivide the cases of lithosphere folding into two large, partly overlapping classes.

2.1. Linear, or Regular, Folding

"Biot's," or linear, folding encompasses the cases where compression of the lithosphere takes place from the beginning, leading to the formation of alternating basins and highs, and where the conditions of the linear theory are more or less satisfied (thin layer approximation, no strain-softening, plain layers, etc.). In the case of linear folding in a Newtonian media, an asymptotic relation derived from the thin layer equilibrium equation is quite simple [*Biot*, 1961; *Ramberg*, 1961]:

$$\lambda_l = 2\pi h\,(\mu_{l1}/6\mu_{l2})^{1/3}. \qquad (1)$$

Here λ_l is the "Laplacian" dominant wavelength of folding in the absence of gravity, h is the thickness of the competent layer (crustal or mantle), and (μ_{l1} and μ_{l2} are the effective viscosities (or competencies) of the strong layer and weak surrounds, respectively. Equation (1), derived assuming no gravity, gives estimates of λ_l/h = 20-40 for typical competence contrasts. This certainly does not hold for most lithospheric-scale cases, where λ/h = 4 - 6 is more common due to the participation of the gravity-dependent terms. In a simplest case of a single stiff layer embedded in inviscid medium, the dominant gravity-dependent harmonics can be accounted as [e.g., *Burov and Molnar*, 1998]

$$\lambda_g = 2\pi(2\,\dot{\varepsilon}\,\mu_{\mathrm{eff}}h^3/3n\,\Delta\rho g)^{1/4}, \qquad (2)$$

where $\Delta\rho$ is the density contrast, $\dot{\varepsilon}$ is the strain rate, μ_{eff} is the effective viscosity, n is the power law exponent (equating 1 in the Newtonian case), and h is the thickness of the competent layer. In a more general case, the term $2\,\dot{\varepsilon}\,\mu_{\mathrm{eff}}h^3/3n$ can be replaced with the term $G_{\mathrm{eff}}\,h^3/3$, where G_{eff} is the effective shear moduli, which can be used for any rheology. For example, in the elastic case, $G_{\mathrm{eff}} = 3D/h$, where $D = ET_e^3/12(1-\nu^2)$ is the flexural rigidity of the plate, E is Young's modulus, and ν is Poisson's ratio. For typical lithospheric h, $\Delta\rho$, $\dot{\varepsilon}$, and power law rheologies, the ratio λ_g/h is 3 - 6, which is compatible with many observations. For lithospheric parameters, λ_g grows faster than λ_l does, but

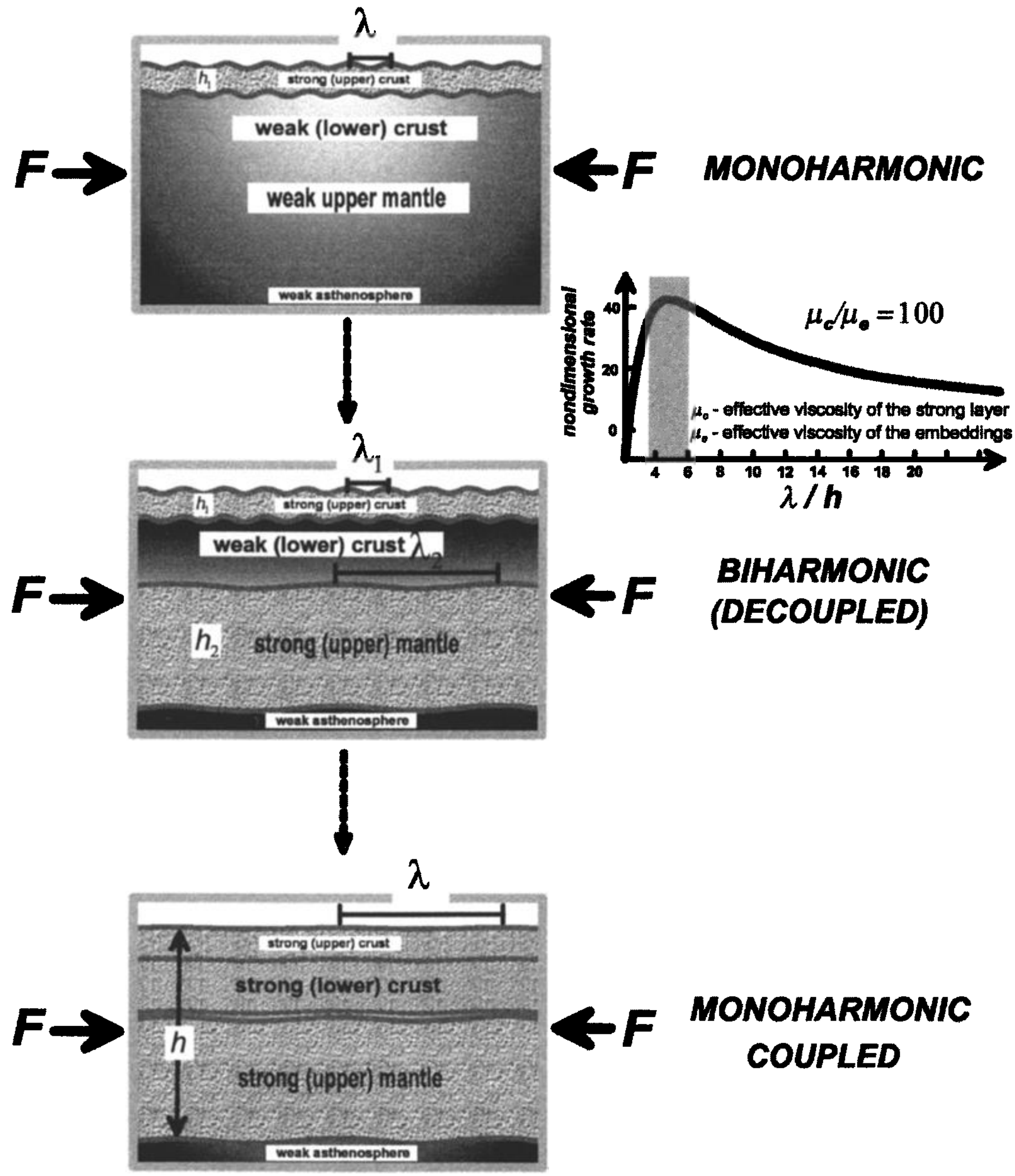

Figure 3a. Sketch of typical folding models (h_1 and h_2 are thicknesses of the competent crust and mantle, respectively). The system is submitted to compression by horizontal tectonic force *F*. In the case when the lower crust is weak, the upper crust may fold independently of the mantle part (wavelength λ_2), with a wavelength λ_1 (decoupled, or biharmonic folding). Young (< 150 Ma) and very old (> 1000 Ma) lithospheres (single competent layer or coupled crust and mantle) develop monoharmonic folding only. Inset shows the analytical estimate for the growth rate of strongly non-Newtonian folding (coupled layers, non-Newtonian rheology) as a function of λ/h for a typical ratio of the effective viscosities of the competent layer and embeddings (100). The ratio of the effective non-Newtonian power exponents is 100 [after *Burov et al.*, 1993]). Shaded rectangle shows the range of the dominating λ/h ratios (4-6).

naturally streams to infinity (flat surface) for small density contrasts. For more realistic cases, complex analytical relations based on the solution of full stress equations or at least taking account of gravity-load-dependent terms, multilayer structure and strongly non-Newtonian rheologies were proposed [*Smith*, 1975, 1977, 1979; *Martinod and Davy*, 1992, 1994; *Burov et al.*, 1993] (Figure 3a). However, even the most sophisticated analytical solutions are basically inadequate for large strain cases and faulted composite lithosphere. For these cases, pure numerical or laboratory experiments are indispensable [e.g., *Cobbold*, 1975, 1977; *Shemenda*, 1989; 1992; *Beekman*, 1994; *Burov and Molnar*, 1998; *Gerbault et al.*, 1999] (Figure 3b).

The "linear" cases generally involve strong lithosphere, the behavior of which is less affected by inhomogeneities, faulting, surface loads, and structural peculiarities. In these

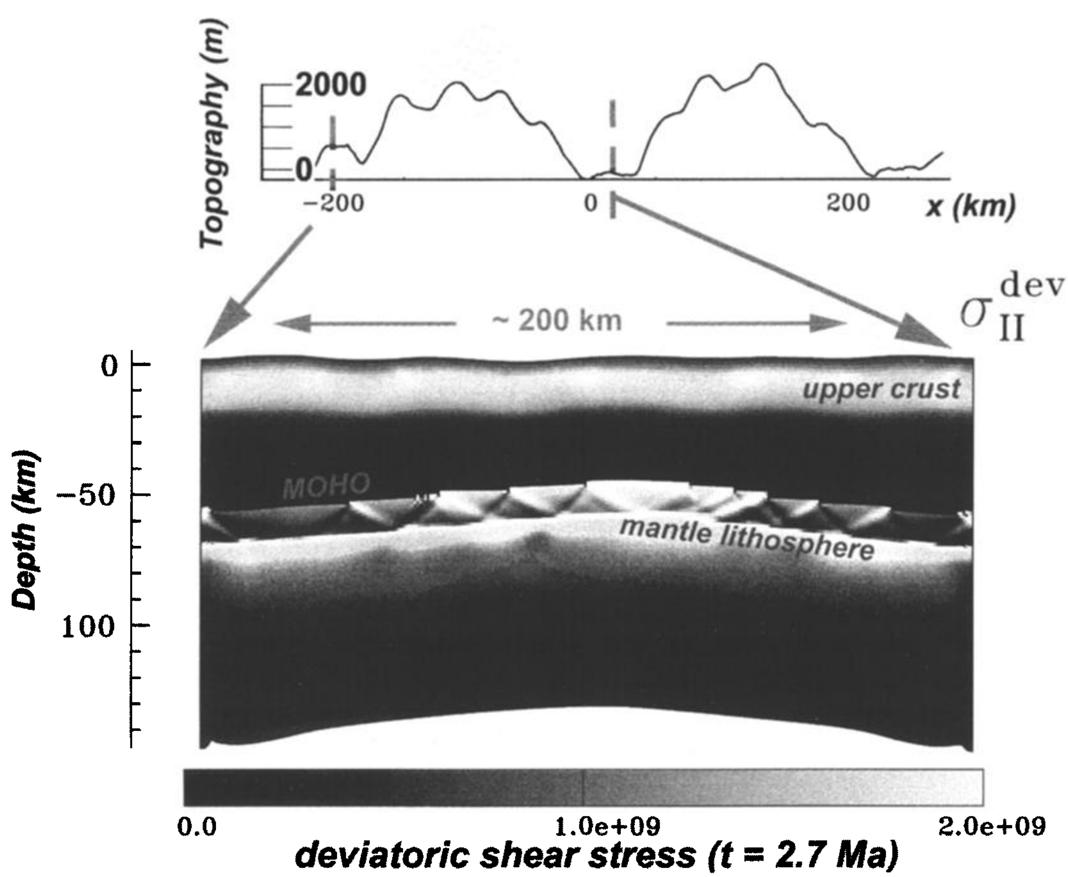

Figure 3b. Topography undulations and a "zoom" showing pattern of the second invariant of deviatoric shear stress (pascals) for the case of decoupled (biharmonic) folding of the middle-aged lithosphere (thermal age 250 Ma) with initial crustal thickness of 45 km, shortened at a rate of 2 cm/yr. Quartz (crust) -olivine (mantle) rheology is chosen (see Table 2 and the appendix for the parameters). Note the different wavelengths of crustal (40 - 50 km) and mantle (200 - 250 km) folding, as well as the intensive faulting in the upper mantle part. Crustal faults are as intensive as the mantle ones but not well imaged in Figure 3b, since the associated stresses are much lower than the mantle ones. See the strain rate patterns in Figure 4, which depict crustal faulting better than the stress patterns do.

cases, folding can be detected by matching the observed wavelengths of deformation and datings of the onset of folding (t_0) with the theoretical predictions (Indian Ocean, t_0=8 Myr, [*Cochran*, 1989; *Curray and Munasinghe*, 1989]; Russian platform, t_0=60 Myr, [*Nikishin et al.*, 1997]; Arctic Canada, t_0=60 Myr, [*Stephenson et al.*, 1990]; central Austaralia, t_0=400 Myr, [*Lambeck*, 1983; *Stephenson and Lambeck*, 1985; *Beekman et al.*, 1997]; western Goby, t_0=8-10 Myr, [*Nikishin et al.*, 1993; *Burov et al.*, 1993]; and Paris basin, t_0=60 Myr, [*Lefort and Agarwàl*, 1996]).

2.2. Irregular, or Nonlinear, Folding

The second class of folding refers to less distinguishable cases basically not covered by Biot's linear theory. Biot's theory assumes that the governing differential equations are linear and have a wavelength-dependent solution corresponding to time-independent dominant wavelength. Actually, (especially young) lithosphere may exhibit a significantly nonlinear response to the horizontal compression, resulting from various factors such as faulting, softening, strain rate dependence of the yield strength, or, finally, three-dimensional (3-D) effects. The last factor can not only affect the wavelength of folding but also lead to the appearance of a second dominant wavelength associated with out-of-plane deformation. All these factors would result in spatial distribution of folding, aperiodical time-dependent spacing of fold limbs, and strong lateral amplitude variations. The deviations from the assumptions of Biot's (or Ramberg's or Smith's) theory also include complex situations where folding (1) was followed or already preceded by distributed faulting [e.g., *Gerbault et al.*, 1999], (2) has been imposed on previously extended, predeformed lithosphere [e.g., *Brun and Nalpas*, 1996], (3) involved deformed layers that were too short compared to their thickness [e.g., *Burov and Molnar*, 1998], or (4) involved a part of the lithosphere that had too many lateral inhomogeneities, affected by significant sedimentation and erosion [e.g., *Cloetingh et al.*, submitted manuscript, 1999]. In these cases, folding instabilities can be poliharmonic or aharmonic or may exhibit much longer or shorter wavelengths than those of the theoretical predictions. For example, loading of a very young lithosphere by horizontally spreading sediments may increase the wavelength of the deformation (which is probably the case for the Pannonian basin). For these reasons, such folding instabilities are difficult to discriminate and to interpret using conventional criteria based on spectral analysis. Therefore we have to investigate some secondary characteristics of folding, such as, for example, an unusually high amplitude of undulations and accelerations of vertical motions (North Sea basin, 6 Myr, [*van Wees and Cloetingh*, 1996], Ferghana and Tadjik basins, 8-10 Myr, [*Burg et al.*, 1994; *Burov and Molnar*, 1998], Pannonian basin, 4-6 Myr, [*Horváth and Cloetingh*, 1996]; Iberian continent, 6-8 Myr, [Cloetingh et al., submitted manuscript, 1999; *Waltham et al.*, 1999]), southern Tyrrhenian Sea, 6-8 Myr, [*Mauffret et al.*, 1981], and Gulf of Lion, 6-8 Myr, [*Kooi et al*, 1992]). The use of these characteristics is based on the notion that vertical undulations due to compressional instability develop much faster (several times) than those produced by other mechanisms such as volumetric thickening and thermally or conventionally induced vertical movements [e.g., *Gerbault et al.*, 1999]. In most typical cases, only a few percent of shortening is sufficient to produce unstable undulations with an amplitude of a few kilometers, whereas other mechanisms would require more than 10% shortening. This is the case for the 3 - 5 km high Tien Shan range in central Asia, which was formed within approximately 10-15 Myr as a result of about 250 km plate shortening induced by the Indian–Eurasian collision, whereas the first buckling-induced neotectonic movements with amplitudes of a few kilometres developed in this area already after approximately 50 km shortening, several megayears before the creation of the mountain range [*Nikishin et al.*, 1993].

3. Geological and Geophysical Records of Folded Areas

3.1. New Observational Methods of Identification of Folding

The geological and geophysical recognition of folding requires a multidisciplinary approach. With the exception of the ocean lithosphere, folding is rarely reflected directly in the topography. Because of morphogenic activity modifying the surface topography and the possibility of crustal-mantle decoupling, folding is most times better reflected in the sedimentary records, differential subsidence and uplift data, fault spacing, seismic refraction and reflection profiles, and in the data on Moho topography (known from seismic reflection, gravity, and other data). The mantle deformation has normally very long wavelength characteristics requiring long geophysical and geological crosssections obtained using deep penetration techniques. For shallow crustal folding, high-resolution shallow seismics has proven to be a very important new diagnostic tool, additionally constraining the geometry of folding-associated crustal faulting. New petroleum industry data sets based on deep seismic reflection profiling such as those carried out along the Norwegian margin have also underlined the importance of the large-scale compressional deformation in passive margin settings, i.e., areas previously considered tectonically quiet [*Vagnes et al.*, 1998]. It should be realized that although the subtle geomorphic expressions of large-scale tilting have been recognized frequently by geomorphologists, the link with the intraplate deformation on the lithosphere and the crustal scale was often not made, since the supporting evidence from the geological and geophysical data sets were till recently lacking [*Horváth and Cloetingh*, 1996]. Only over the last few years, an integration of evidence from different data sets at different temporal and spatial scales has been made, which has provided a growing basis in support of folding as a key mechanism of continental intraplate deformation. Important differences were recently recognized between the wavelengths and durations of folding. In section 3.2 we will examine the different types of folding, particularly focusing on the atypical expressions of folding and the role of rheology and mechanical structure on the preservation of the folds.

3.2. Regular and Irregular Lithospheric Folding: Natural Examples and Predictions

In continental areas a number of examples of prominent periodical folding are found (which we call distinct or regular), such as Arctic Canada [*Stephenson and Cloetingh*, 1991], central Australia [*Stephenson and Lambeck*, 1985], central Asia [*Martinod and Davy*, 1992, 1994; *Nikishin et al.*, 1993; *Burov et al.*, 1993; *Cobbold et al.*, 1993], Tibetan plateau [*Burg et al.*, 1994], and Paris basin [*Lefort and Agarwal*, 1996]. Evidence for unstable lithospheric deformation in these areas is inferred from the presence of periodical undulations of the basement and Bouguer gravity anomalies, by indication of spatially periodic tectonic movements (with wavelengths matching the predictions of the linear theory of folding) and by rapidity of the growth of the vertical undulations. In the cases referred to as irregular or nonlinear, folding is aperiodic or has wavelengths significantly differing from the predictions of the linear theoretical model. Figures 1 and 2 and Table 1 summarize the regular and irregular cases of folding. Figure 1 displays observed wavelengths of folding plotted against the theoretical dependence between the wavelength of linear folding and thermotectonic age of the lithosphere, which reflects the thickness of the competent crust and mantle. As shown, most cases of irregular folding correspond to young, weak lithosphere, which is more affected by the side effects than the old and strong lithosphere is. Figure 2 demonstrates some representative data crosssections for regular and irregular folding. In the case of western Goby [*Burov et al.*, 1993], presented in Figure 2a, the wavelength of folding is close to the analytical solution for power law rheologies derived on the basis of the linear analysis by *Smith* [1975,1977,1979]. The young Pannonian basin [*Horváth and Cloetingh*, 1996] exhibits extremely long-wavelength deformation (300 km) compared with 50 km to the maximum 100 km predicted from the linear theory. The "intermediate" Ferghana basin in central Asia [*Burov and Molnar*, 1998] has a "correct" wavelength of deflection, but the ratio plate length/wavelength is too small to satisfy conditions of thin plate/layer approximation. The gravity signal over the Ferghana basin also has some peculiar short-wavelength features, which can result from plastic hinging or faulting on the sides of the basin.

In the present study we demonstrate the relative importance of lithospheric parameters on compressional basin deformation in terms of preexisting rheology, strain rate history, and the forces driving compression. To this aim, we have selected a number of areas in the Africa/Arabia -Eurasia plate collision zone and in the Alpine foreland (see Table 1 for the key parameters of folding) for a closer investigation of parameters characterizing their large-scale compressional deformation.

In section 3.2.1 we summarize geophysical evidences for folding in young extensional basins affected by late stage compression: the Gulf of Lion and the Tyrrhenian, Pannonian, and Transylvanian basins. We also describe in sections 3.2.2 – 3.2.6 the data related to other cases of irregular folding: the Iberia basin, the North Sea basin, the Helland-Hansen Arch, the Russian platform, and the Ferghana and Tadjik basins in central Asia.

3.2.1. Western Mediterranean and Pannonian basin. On the basis of seismic profiles in the western Mediterranean, *Mauffret et al.* [1981] pointed to strong evidence for late stage compressional basin deformation in this area. *Cloetingh and Kooi* [1992] noticed the simultaneous occurrence of accelerations in Pliocene-Quaternary subsidence with the onset of late stage compression, proposing large-scale downwarping as a mechanism. A more extensive investigation, backed up by large-scale modeling and gravity studies, was recently done for the Pannonian basin [*Vackarcs et al.*, 1994; *Horváth and Cloetingh*, 1996] and the Gulf of Lions [*Kooi et al.*, 1992; *Chamot-Rooke et al.*, 1999]. A modeling study, constrained by more recent seismic evidence for compressional deformation in the Tyrrhenian Sea [*Pepe,* 1998] is yet to come.

The Pannonian basin, formed by Neogene stretching and thinning of thickened Alpine lithosphere [*Horváth*, 1993], is presently probably the hottest basin of Europe. The crustal structure and subsidence history of the basin have been extensively documented through a large array of deep seismic reflection profiles, industry seismics [e.g., *Posgay et al.*, 1996], and boreholes [*Horváth*, 1993]. The Pannonian basin underwent a Pliocene-Quaternary reactivation, leading to large-scale warping of the lithosphere with a characteristic wavelength of several hundred kilometres [*Vackarcs et al.*, 1994; *Horváth and Cloetingh*, 1996]. The deformation has a clear expression in the topography of the area and has been recorded in tilted river terraces [*Horváth and Cloetingh*, 1996]. Seismic high-resolution shallow profiling has extensively documented the fine structure of the deformation [*Horváth and Cloetingh*, 1996]. The present-day stress field of the Pannonian basin has been studied extensively through focal mechanism studies and borehole breakout studies [*Gerner et al.*, 1999], demonstrating that the anomalous subsidence and uplift patterns occur in a regime of present-day compression. As illustrated by Figures 1-3, the first-order patterns of lithospheric deflection are consistent with an explanation in terms of late stage compression. Superimposed on the intralithospheric folding are contributions by slab detachment processes at the margins of the Pannonian basin, recorded by anomalous Pliocene-Quaternary uplift in the Styrian basin [*Sachsenhofer et al.*, 1997] and the Transylvanian basin. Within the Transylvanian basin itself, also a late stage deepening has been observed compatible with the documented stress field in the area [*Negut et al.*, 1997; *Ciulavu*, 1999]. As one can see on the profiles intersecting the Pannonian basin, there is no principal difference between the two orthogonal directions even though the major tectonic compression is roughly northward. This can be explained by important transpressional deformation of this three-dimensional basin, thus justifying the initial hypothesis of a folding mechanism. Of course, slab detachment or surface processes could also be responsible for the rapid vertical movements of the Pannonian basement but quite unlikely in both orthogonal directions. In contrast, a compressional instability in three dimensions would be a plausible mechanism, since, assuming "rigid" borders of the surrounding region, it may cause "circular" folding even due to unidirectional deformation.

3.2.2. Iberian continent. Another irregular case, Paleozoic Iberian continent is located at a very close distance to the African-Eurasian plate boundary. Iberia is surrounded by zones of a high level of recent tectonic activity, with late Neogene opening of extensional basins in the adjacent western Mediterranean [*Janssen et al.*, 1993; *Docherty and Banda*, 1995], the Betic and Pyrenees orogenies at its southern and northern margins [*Verges et al.*, 1995], and the Gibraltar-Azores deformation area in the southwest [*Masson et al.*, 1994]. The plate tectonic activity at Iberia's margins has gone through a time sequence starting in Eocene times in the north [*Roest and Srivastava*, 1991] and continuing until the present day at the southern plate boundary. Recently, the lack of data for the Iberian part of the World Stress Map has been compensated by a substantial body of new stress indicator data from borehole breakouts and structural analysis (see for an overview *Ribeiro et al.* [1996], *Jurado and Mueller* [1997], and *de Vicente et al.* [1996]). These data show the existence of consistently oriented stress fields in Iberia, with an orientation consistent with the plate interactions in the area. The central part of Spain occupies a position at the crossroads of the stresses propagated into the plate interior and provides a natural laboratory to examine the fine structure of intraplate deformation. Analysis of gravity, topography, and stratigraphy has shown the existence of large-wavelength folding with typical wavelengths of 300 km [*Stapel et al.*, 1997; *Waltham et al.*, 1999]. It is noteworthy that *Cobbold et al.* [1993] have already suggested possible folding scenarios for the deformation of the intra-Iberian Ebro basin, whereas the new data confirm that the same scenario can be applicable to the whole continent.

3.2.3. North Sea basin. The North Sea basin has, upon its formation by extension in Permo-Triassic time, been subjected to several phases in its basin evolution. The subsidence history is marked by a first initial phase of subsidence, compatible with predictions from stretching models, followed by a phase of thermal subsidence, interrupted by phases of atypical subsidence and uplift, with a timing and spatial distribution suggesting a far-field control by plate boundary forces operating at the Alpine collision zone [*Ziegler et al.*, 1995]. Particularly striking is the Pliocene-Quaternary acceleration of tectonic subsidence in the central part of the North Sea. As in the Pannonian basin, this acceleration in subsidence occurs at a time when according to predictions from stretching models subsidence should have decayed to essentially zero [*Cloetingh et al.*, 1990; *Cloetingh and Kooi*, 1992]. Two-dimensional (2-D) [*Kooi et al.*, 1991] and 3-D modeling studies [*van Wees and Cloetingh*, 1996] have demonstrated that the observed large-scale warping is compatible with present-day compression in NW Europe [*Muller et al.*, 1992]. The 3-D modeling has demonstrated that for stresses equivalent to those induced by ridge push forces, 700 m of accelerated subsidence in the North Sea basin can be induced [*van Wees and Cloetingh*, 1996]. Along with this downwarping in the central North Sea, an upwarping is generated at the margins of the North Sea basin, amplifying postglacial rebound, consistent with recent data [*Japsen*, 1998].

3.2.4. Helland-Hansen Arch. As a result of intensive petroleum exploration, detailed evidence has been found for the widespread occurrence of large-scale Cenozoic compressional domes associated with intensive crustal faulting on the margins of the northern Atlantic [*Dore and Lundin*, 1996]. The characteristic wavelength of these undulations over the southern part of the Helland-Hansen Arch is about 60 km, indicating that folding occurs in the upper crust only, as a result of crust-mantle decoupling due to very intensive thermal regime [*Vagnes et al.*, 1998].

3.2.5. Russian platform. With the advent of more detailed information of the crustal and sedimentary record of the Russian platform [*Nikishin et al.*, 1996] and the application of backstripping analyses techniques to the sedimentary record, it has become clear that the Russian platform over its long geological history has recorded important changes in stress propagated into this vast area from the plate boundaries. The present accelerations in neotectonic subsidence recorded in, for example, the Moscow basin appear to a large extent to be associated with the plate coupling processes in the Caucasus region [*Nikishin et al.*, 1996] and are possibly related to large-scale spatially periodic instabilities.

3.2.6. Ferghana and Tadjik basins, central Asia. The young Ferghana and Tadjik basins are two compressional basins northwest and north of Pamir and south of the Tien Shan ranges [*Burov and Molnar*, 1998]. They both underwent Jurassic rejuvenation and are characterized by very young thermal age (175 Ma) [*Burg et al.*, 1994; *Burov and Molnar*, 1998]. In addition to thermal weakening, these basins also probably have a weak lower crustal rheology (quartz), resulting, together with young thermal age, in low effective elastic thickness (EET) values of 15 km [*Burov and Molnar*, 1998]. The gravity data suggest that these two compressional basins are gravitationally overcompensated (i.e., the gravity anomalies indicate a several kilometres deeper Moho than that predicted by local isostatic models [*Burov and Kogan*, 1990; *Burg et al.*, 1994; *Burov and Molnar*, 1998]), which has lead to a hypothesis that these basins may result from unstable downwarping, possibly associated with deep mantle faulting.

It should be noted that the subdivision into regular and irregular folding is very approximate. For example, folding in the Ferghana and Tadjik basins can be treated as both regular (the wavelength roughly matches the linear theory predictions) and irregular (the area is faulted and probably was formed in a zone of preexisting weakness; formally, it is also too short to be analyzed using thin layer approximation, see Figure 2).

4. Mechanical Properties of the Lithosphere in Compressional Zones

Lithospheric folding is largely controlled by rheological and thermal structure. Effects of different initial crustal thickness and thermal state of the prefold lithosphere determine the effectiveness of far-field and near-field stresses and associated strain rates in the process of compressional basin deformation. Both these parameters control the prefold rheology, the material parameters of which are constrained by results of experimental rock mechanics data adopting the yield strength envelope concept [*Carter and Tsenn*, 1987; *Cloetingh and Banda*, 1992; *Ranalli*, 1994; *Burov and Diament*, 1995; *Cloetingh and Burov*, 1996]. The synthetic strength profiles derived for a representative background strain rate provide a qualitative picture of the distribution of lithospheric strength with depth, and they give a measure for the maximum stress levels to be supported by the lithosphere. In reality, strain rate may vary laterally and with depth, and for this reason, direct thermomechanical numerical calculations based on the explicit form of the rheological laws can give a more precise idea of strength and stress distribution in the lithosphere. Composition and temperature are controlling factors on bulk lithospheric strength [*Kusznir and Park*, 1987], reflected also in indirect observables such as EET [*Burov and Diament*, 1995] and distribution of intraplate seismicity [e.g., *Cloetingh and Banda*, 1992]. Important differences can be expected in the starting conditions for folding in relatively warm Alpine lithosphere such as that encountered in Iberia or the Pannonian basin, as opposed to cold foreland lithosphere such as that encountered in the North Sea basin and the Russian platform. The evidence for the rheological state of the lithosphere comes not only from these strength profiles but is also available through an extensive set of modeling studies carried out in Europe's main basins, formed by extensional processes in Mesozoic and Tertiary times but deformed by late stage compression only very lately in Pliocene-Quaternary times [e.g., *Horváth and Cloetingh*, 1996; *van Wees and Cloetingh*, 1996]. The kinematic models for extensional basin formation for the Alpine/Mediterranean and North Sea basins [e.g., *Kooi et al.*, 1992; *Cloetingh et al.*, 1995] and their validation through testing with data sets from rifted basins have yielded important constraints on the mechanics of the prefolding stage. In addition, questions have risen concerning the mantle part of the inferred strength distributions, suggesting that mantle strengths are possibly overestimated. For example, intraplate seismicity distributions do not show earthquake foci at the levels of the subcrustal mantle lithosphere, where rheological profiles predict considerable strength [*Cloetingh and Banda*, 1992].

Within the European lithosphere, considerable spatial variations in lithosphere rheology occur [*Cloetingh and Burov*, 1996]. In general, these variations follow the predictions of thermal models for continental lithosphere evolution, showing a clear increase of the bulk strength of the lithosphere with increasing thermotectonic age. As demonstrated by *Cloetingh and Burov* [1996], the predictions from strength profiles constructed from extrapolation of rock mechanics data are compatible with the outcomes of flexural studies of Europe's foreland basins. On a more regional scale, strength profiles have been constructed for a number of regions of Europe, including the Romanian part of the Pannonian basin and the Transylvanian basin [*Lankreijer et al.*, 1997], the Mediterranean margins of Iberia [*Cloetingh et al.*, 1992], and the Tyrrhenian Sea [*Spadini et al.*, 1995]. In general, the strength distribution patterns suggest a relatively low strength of the lithosphere in the near-field areas close to the African-European plate boundary.

Basically, the major differences in prefold rheology are the result of a cool versus a warm prefold lithosphere in the areas analyzed. Whereas Mesozoic and Paleozoic rifting and subsequent neotectonic folding probably took place under relatively stable thermal conditions, the Alpine/Mediterranean setting can be characterized by a transient thermotectonic regime. As observed from a comparison of the Alpine/Mediterranean basins and the cratonic basins, folding durations tend to be longer for the cratonic basins, probably reflecting a larger integrated strength for this class of basins.

5. Mechanical Model of Folding

In this section we conduct a number of numerical experiments allowing us to investigate the development of folding instabilities in "realistic" conditions, i.e., explicitly taking into account most of the factors that are thought to be responsible for deviations from the linear behavior. These factors include brittle-elasto-ductile rheology explicitly taken from the laboratory data, temperature, large strains, horizontally and vertically variable strain rates, and the possibility of lithospheric faulting during deformation.

5.1. Model Setup and Numerical Experiments on Regular Folding in Realistic Conditions

Figure 3 presents setups for both linear analytical and numerical models of folding. Figure 3a shows a sketch of typical monoharmonic and biharmonic folding models with an analytical estimate for the growth rate dependence on the λ/h ratio (λ is the wavelength of folding, and h is the thickness of the competent layer) [*Burov et al.*, 1993]. The brittle-elasto-ductile lithospheric rheology and lateral discontinuities strongly affect the dynamics of the lithospheric deformation [*Vilotte et al.*, 1993; *Burov et al.*, 1993]. For this reason, to investigate the development of folding instabilities in brittle-elasto-ductile multilayers, we adopted the Fast Lagrangian Analysis of Continua (FLAC)-based [*Cundall*, 1989] finite element code Paravoz [*Poliakov et al.*, 1993], which has a good record in modeling of folding and buckling instabilities in nonlinear media [*Burov and Molnar*, 1998; *Gerbault et al.*, 1999] (see appendix for the details on the numerical method).

The finite amplitude of deformation in an unstable compressive regime can be influenced by many usually negligible factors. Therefore our primary goal was only to obtain a reasonable amplitude of deformation applying reasonable forces (i.e., not exceeding mechanical strength of the lithosphere). For the layers with EET exceeding 15-20 km, the wavelength of the deformation is seemingly stable and is not significantly affected by variations in the loads (Figure 1). Thus the EET usually controls well the wavelengths that we can observe, but the magnitudes of deflections and corresponding gravity anomalies depend also on density contrasts and the magnitude of the horizontal force.

During our numerical experiments we have tested a significant number of situations encompassing most of the possible scenarios starting from relatively young continental lithosphere (thermotectonic age less than 150 Ma) and ending with very old lithosphere (thermotectonic age 2000 Ma). Figure 3b presents results of one of the series of experiments with non inear brittle-elastic-ductile rheology derived from rock mechanics data (Table 2, appendix. Figure 3b demonstrates the development of pronounced decoupled folding in a central Asia-type lithosphere (thermotectonic age from 175 to 450 Ma). These experiments were completed using quartz-olivine rheology from a previous study *by Burov et al.* [1993] (Table 2) that infers a weak lower crust promoting partial mechanical decoupling between the competent upper crust and the upper mantle. As can be seen, folding of a lithosphere with such a mechanically weak lower crust (of which there is a number of examples in central Asia, [*Sabitova*, 1986; *Roecker et al.*, 1993; *Burov and Molnar*, 1998]), is characterized by two characteristic wavelengths. The short one corresponds to crustal folding (30-60 km), and the larger one (200-350 km) corresponds to mantle folding. Figure 3b presents results for the thermotectonic age of 250 Ma, yielding 40-50 and 200-250 km wavelengths for the crust and mantle, respectively. Assumption of an older age (400 Ma) results in larger respective wavelengths of 60 and 350 km. In spite of the nonlinear rheology and intensive faulting, this experiment demonstrates good correspondence with the Biot - Smith's theory ($h_1 \approx$ 10-15 km, and $h_2 \approx$ 50-60 km; Figures 1, 2, and 3a), which confirms our recent result [*Gerbault et al.*, 1999] that faulted layers can effectively transmit horizontal stress. The next experiment (Figure 4) considers a coupled typical case of cold lithosphere (e.g., Australian craton before rejuvenation, age > 700 Ma; Table 1). The wavelength of the deformation is much larger (> 500 km) than that in the case of Figure 3b, since the crust is mechanically welded with the mantle lithosphere leading to total effective mechanical thickness of around 120 km. It can be seen that folding may activate intensive faulting in the crust and mantle and then continue for a very long time. In our longest experiments, folding persisted for 25 Myr before the final localization of the deformation on one single fault. Surface processes (erosion and sedimentation) may significantly prolong the lifetime of folding, since they decrease the effect of gravity by (1) filling the downward flexed basins and thus reducing the restoring force and (2) cutting the upward flexed basement and thus unloading the lithosphere in the uplifted areas.

5.2. Experiments on Irregular Nonlinear Folding

As was noted in the previous sections, various factors, such as nonlinear rheology, large surface loads, lateral inhomogeneities, and large strains may lead to significant

Table 2. Parameters of Dislocation Creep for Lithospheric Rocks and Minerals

Mineral/Rock	A, Pa^{-n}s^{-1}	H, kJ mol^{-1}	n
quartzite (dry)	5×10^{-12}	190	3
diorite (dry)	5.01×10^{-15}	212	2.4
diabase (dry)	6.31×10^{-20}	276	3.05
Olivine/dunite (dry)*	7×10^{-14}	520	3

Parameter values correspond to the lower bounds on the rock strength [*Brace and Kohlstedt*, 1980; *Carter and Tsenn*, 1987; *Tsenn and Carter*, 1987; *Kirby and Kronenberg*, 1987]. The elastic moduli used for all materials throughout this paper are E (Young's) modulus = 0.8 GPa and ν (Poisson's ratio) = 0.25. The brittle properties are represented by Mohr-Coulomb plasticity with friction angle 30° and cohesion 20 MPa [*Gerbault et al.*, 1999]. For olivine at σ_1-$\sigma_3 \geq 200$ MPa (Dorn's dislocation glide), $\dot{\varepsilon} = \dot{\varepsilon}_0 \exp\{-H^*[1-(\sigma_1-\sigma_3)/\sigma_0]^2/RT\}$, where $\dot{\varepsilon}_0 = 5.7\times10^{11}$ s^{-1}, $\sigma_0 = 8.5\times10^3$ Mpa, and $H = 535$ kJ/mol.
*Parameter values for dislocation climb at σ_1-$\sigma_3 < 200$ MPa

deviations of folding behavior from that predicted by the linear theory [*Davis*, 1994; *Zhang et al.*, 1996; *Mercier et al.*, 1997; *Bhalerao and Moon*, 1996; *Hunt et al.*, 1996; *Lan and Hudleston*, 1996]. Of course, this especially concerns young, thin lithosphere and much less old, strong continental plate segments. In the case of irregular folding (generally very young, weak lithosphere), the deformation may be very much affected by various factors (gravity-driven lateral spreading of the sedimentary infill, inhomogeneities, and nonlinear behavior). Consequently, the wavelength of the deformation can be much longer or shorter than that predicted by Biot's theory. The deformation may be highly aperiodic as well

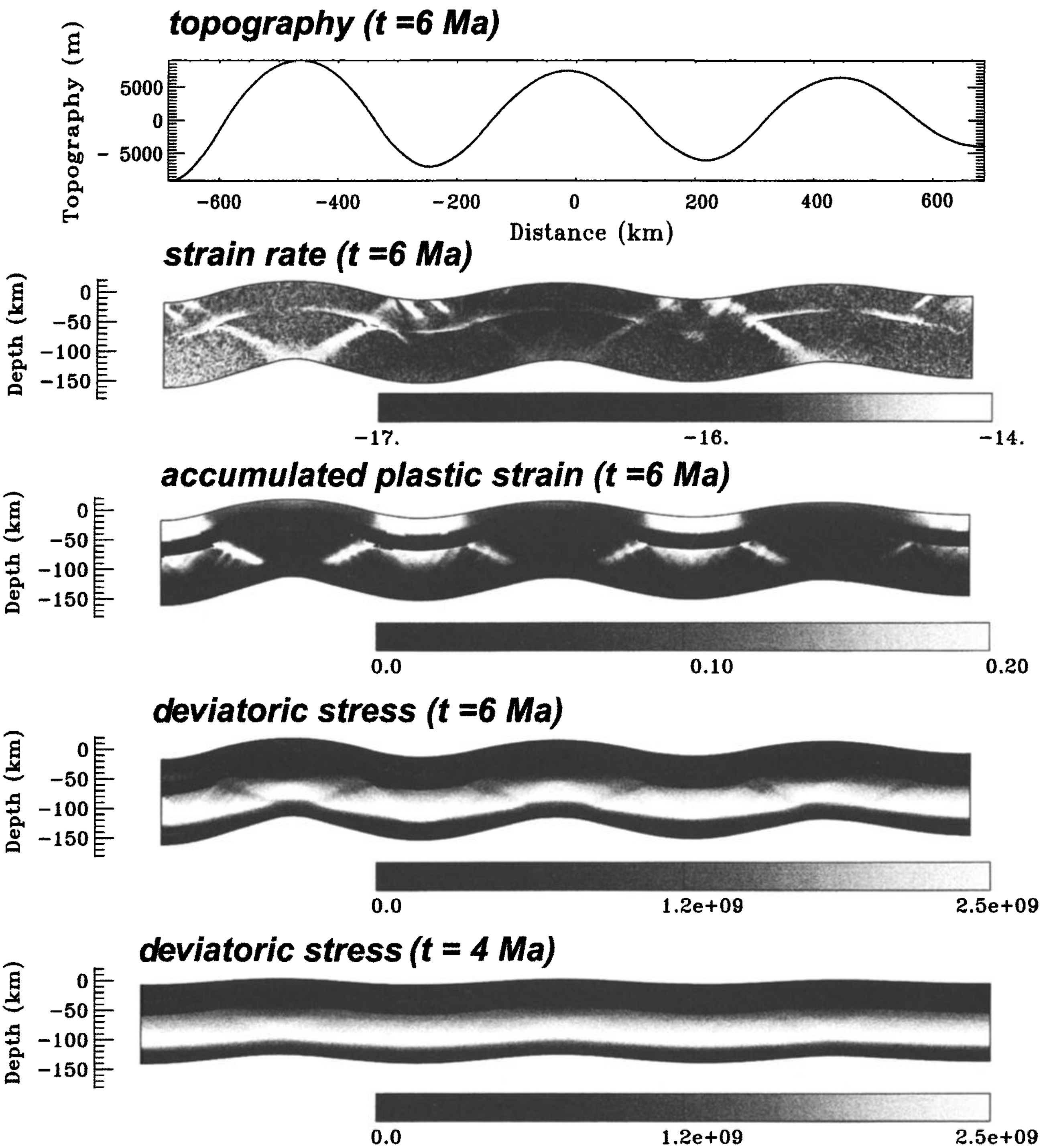

Figure 4. Coupled folding (old cratonic lithosphere with thermal age > 700 Ma and strong diabase lower crustal rheology; Table 2). Note the crustal and mantle faulting and a larger wavelength of the deformation (500 km). Shortening is at a rate of 1.5 cm/yr.

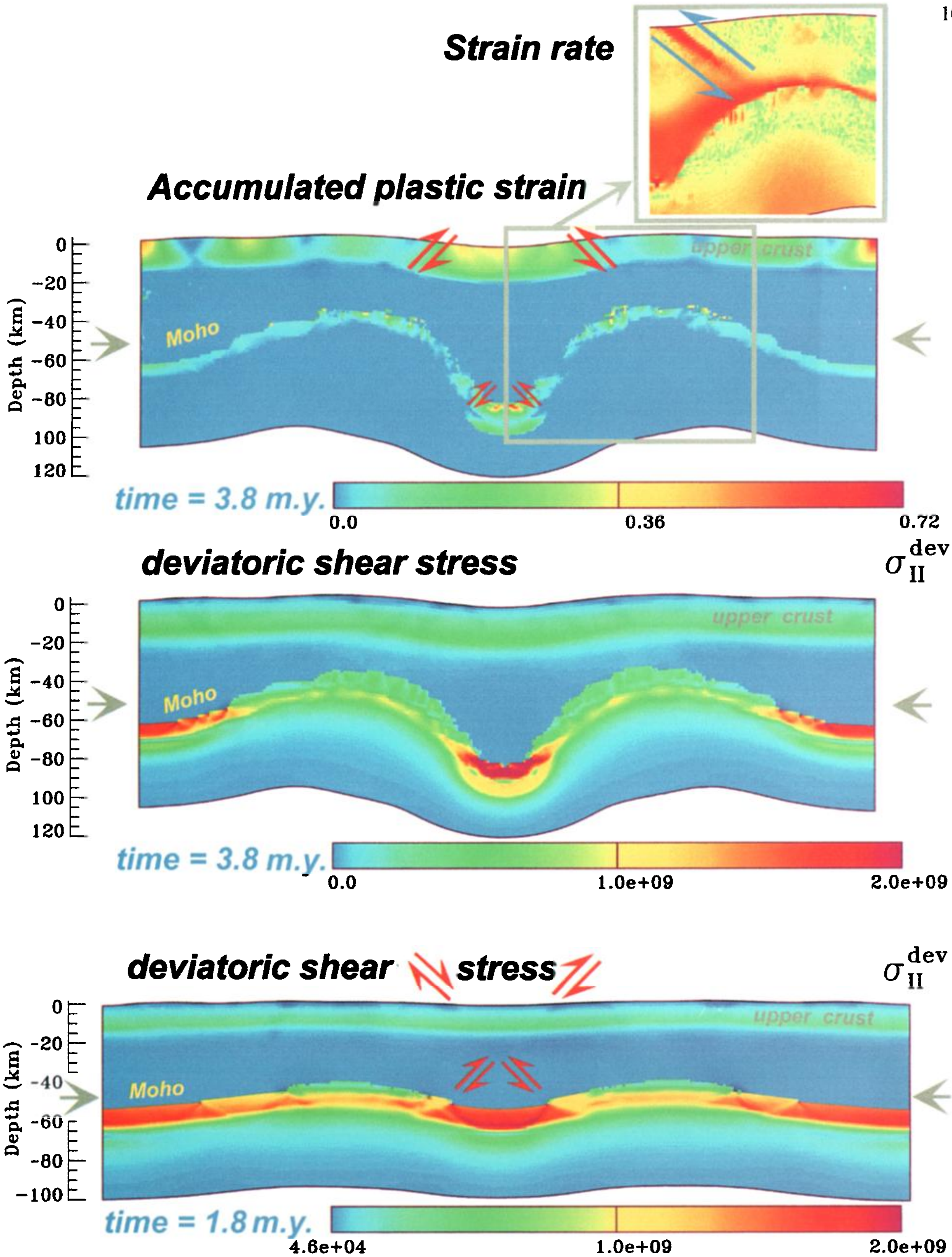

Plate 1. Numerical experiment demonstrating nonlinear, irregular folding: folding and faulting experiment (Ferghana/Tadjik basin type lithosphere, central Asia, quartz crustal rheology, olivine mantle rheology (Table 2), thermal age 175 Ma. The faults appear before the folding develops, but then the two processes, faulting and folding, can co-exist in such a way that folding is accommodated by faulting. Because of the weakness of the lower crust, the upper crust is completely decoupled from the mantle and interacts with it only by flow in the lower crust. The participation of the flow changes the wavelength and amplitude of folding, which finishes by the development of a single downwarped "megafold."

[*Hunt et al.*, 1996]. As noted in section 3.2, a new database including such irregular folding cases is now available for large areas of the European foreland and its margins as a result of intensive geophysical and geological studies carried out during the last decade, which have significantly enhanced the current understanding of the basin (de)formation mechanisms operating in these areas.

Plate 1 demonstrates the case of inverse "megafolding", the result of the prolongation of the numerical experiments considering simultaneous development of folding and faulting in a young Ferghana/Tadjik type basin (Figure 2c, [*Burov and Molnar*, 1998], which, as was mentioned above, possibly results from unstable downwarping, and may be associated with deep mantle faulting. Actually, for Ferghana-Tadjik settings our numerical experiments reproduce the formation of active crustal and mantle faults with characteristic spacing corresponding to the thicknesses of the brittle crustal and mantle domains. Surprisingly, the appearance of faults does not significantly influence the wavelength of folding: both processes continue to coexist for a long time, so that faulting serves as a mechanism of folding in the brittle domain [*Gerbault et al.*, 1999]. Also observed in some analogue experiments [*Martinod and Davy*, 1994], this "continuous" behavior of faulted lithosphere can be explained by fault locking due to gravity and friction: after some sliding (uplift) on the fault, the potential gravity energy and thus work against friction to be done by the forces of horizontal shortening become too high, and the fault locks and transmits the horizontal stress as a continuum medium. As soon as the compression continues, one of the folds finally starts to grow faster than the others, resulting in a loss of periodicity and the formation of a mega-fold (Plate 1), which can finish up by initialization of subduction and mountain building. In the case presented in Plate 1, large horizontal shortening also resulted in the decrease of the observed wavelength of mantle folding from the initial value of 250 km to approximately 150 km, and the increase of the crustal wavelength from 40-50 to 100 km. Note that the experiments shown in Figure 5 present a "developed" case with respect to that demonstrated by *Burov and Molnar* [1998]. Consequently, these results can be regarded as a possible scenario of the evolution of the deformation in the recently inverted basins.

As another possible example of irregular folding, Figure 5 demonstrates a case of demicoupled/demidecoupled lithosphere (similar to Figure 3b but with colder geotherm of 400 Ma). In the intermediate cases (between the coupled and decoupled state) the mantle lithosphere can be in some places coupled or decoupled with the upper crust, depending on the stress and strain rate. In this case, some parts of the plate may deform in a biharmonic mode whilst others will exhibit longer-wavelength monolayer folding.

5.3. Experiments on Preserved Folding

As was discussed by *Bird* [1991] and *Avouac and Burov* [1996], large-scale undulations of the lithosphere in the absence of sufficient compression cannot be preserved for a long time (> 10 Myr), except for very strong (especially low crustal) lithospheric rheology. Otherwise, they will be flattened owing to the gravity-driven crustal flow associated with the omnipresent large crust-mantle density contrast at the

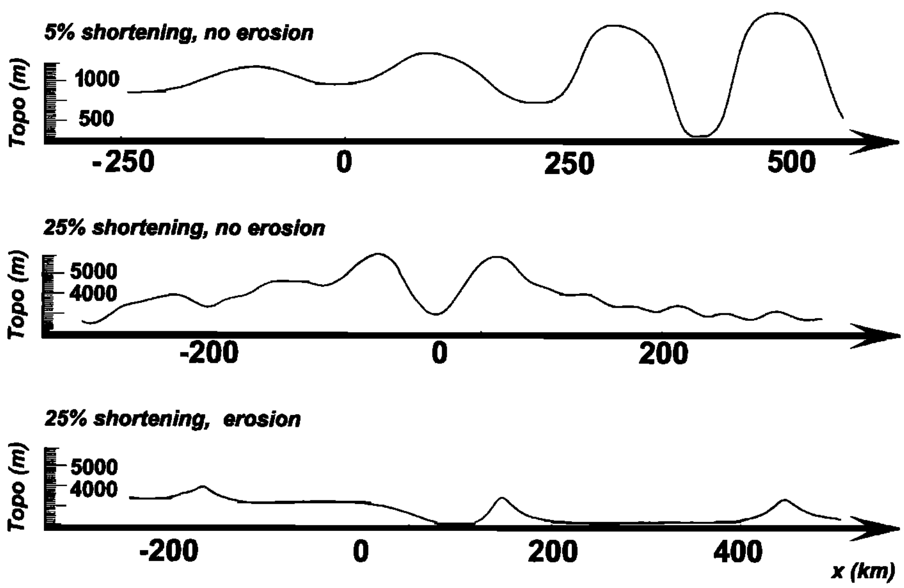

Figure 5. Numerical experiment demonstrating nonlinear, irregular folding. In some cases, the instabilities can be quite chaotic. Figure 5 demonstrates different cases of irregular folding with wavelength and amplitude varying along the plate on different stages of deformation due to partial crust-mantle coupling and strain localizations (400 Ma lithosphere with weak quartz-dominated crustal rheology; Table 2). After 5% shortening, (top), after 25% shortening, (middle), after 25% shortening (bottom), strong zero-order diffusional erosion [*Avouac and Burov*, 1996] tuned to keep mean elevations at the level of 3000 m. Erosion reduces the contribution of gravity-dependent terms (middle wavelength) and accelerates local deformations. Strong erosion, insufficiently compensated by the tectonic deformation (bottom), wipes out most of the topography. Yet, if the erosion is tuned to the average elevation rates, it may dramatically accelerate folding.

Moho boundary. Near the Moho, some parts of the folded crust occur at the same depth as the folded dense mantle, resulting in remarkable pressure differences (5 MPa per 1 km of Moho depression plus a contribution from the hydrostatically disbalanced part of the surface depression). These pressure differences in most cases are sufficient to overcome the yielding stress of the lower crust at Moho depth levels [*Bird*, 1991]. As a result, the crust would flow and flatten the bent layer. The occurrence of long - timescale preservation of folding after cessation of the compression (Figure 6) in the presumably strong Australian craton, Parisian basin or Russian platform points to a quite strong rheology yielding high EET values (> 60 km) and consequently confirming experimental estimates listed in Table 2. Yet the amplitude of the vertical deflection in the Paris basin is quite small, allowing for other mechanisms such as simple flexure due to the load by the Alpine system. However, the periodic deformation at the same wavelength is more or less well expressed to the northwest of the area, which would not be the case if the northeastern part of the basin was simply flexed down by the load of the Alps.

Most of the presently observed areas of folds coincide in time with the Alpine collision 60 Myr ago. It is thus reasonable to assume that the most typical characteristic timescale of the gravity collapse of the large-scale folds in the intermediate-age lithospheres is limited by this time, though in the cases of very weak quartz-dominated lower crust the folds may disappear within the following 8-15 Myr (analogously to the estimates made by *Bird* [1991] for the mountains). The experiment of Figure 6 (old 1000 Ma lithosphere with diabase lower crust; Table 2) demonstrates the preservation of folding-induced deformation for 10 Myr (potentially > 50 Myr) following the cessation of the tectonic compression. In this experiment we stopped the horizontal compression after the first 14 Myr of shortening and then studied the asymptotic behavior of the system in the next 10 Myr. During this period the amplitude of folds decreased by less than 10%, which yields at least 50 Myr decay time as an asymptotic prediction. The presence of the crustal faults, of course, may accelerate the gravity collapse of the folds, resulting in the creation of the inverted basins. For example, the experiment of Figure 6 predicts reactivation and inverted activity of some faults after the cessation of the tectonic compression.

6. Discussion

Up till now, we have discussed various parameters characterizing the rheological state of the folded lithosphere and the associated deformation signature. The initiation of folded basin formation depends on the interplay of forces operating on the continental lithosphere and the spatial distribution of the lithospheric strength. In platform settings a large distance away from plate boundaries, far-field lithospheric stresses should be relatively constant [*Zoback*,

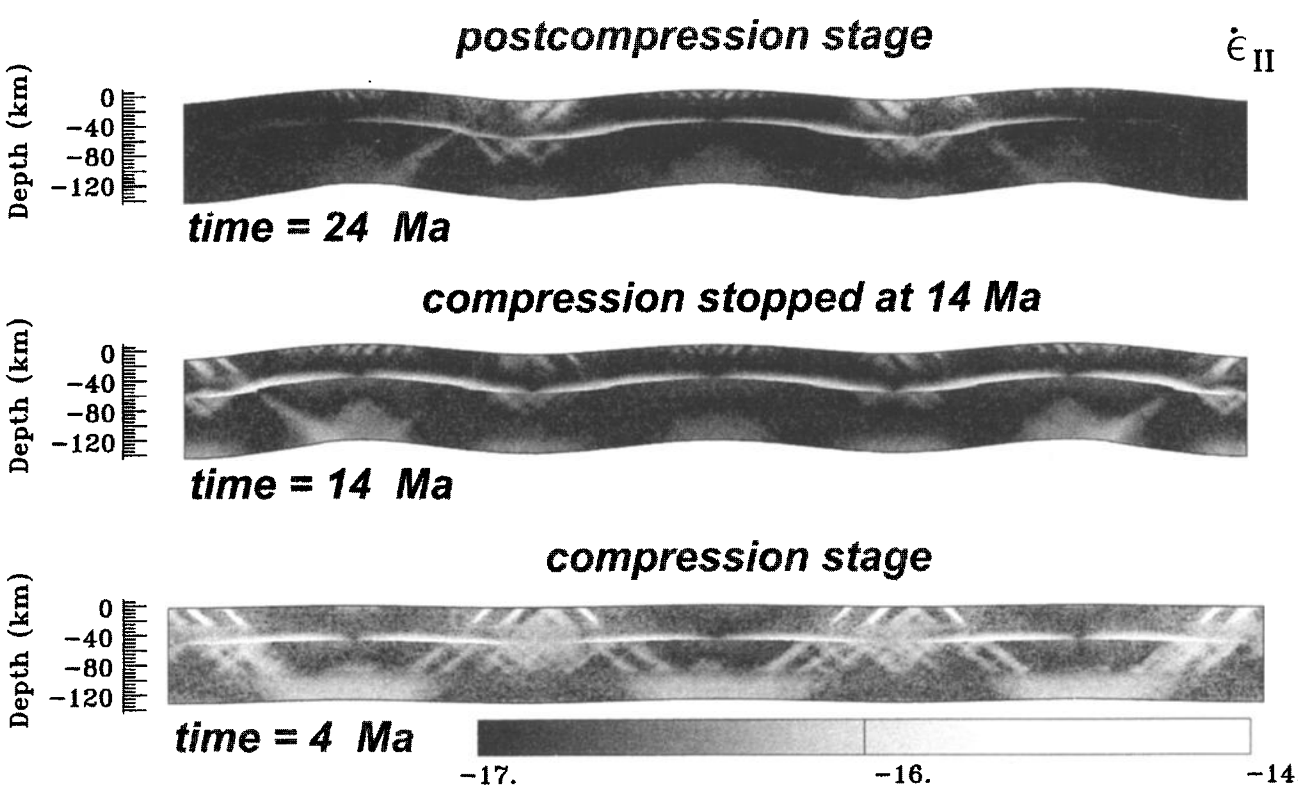

Figure 6. Strain rates for preserved folding. Preserved folding is an indicator of a strong lithospheric rheology (same parameters as those for the Figure 4, but with horizontal compression stopped after 14 Ma). It can be observed that for a strong cratonic-type rheology, folding may be frozen -in for a very long time.

1992], and therefore lithospheric deformation is expected to be primarily controlled by the initial distribution and subsequent evolution of lithospheric strength, possibly amplified by local sources of stresses. At plate margins, close to the main sources of intraplate stress, large horizontal and vertical fluctuations occur. For intraplate settings and adopting constant intraplate stresses, localization of extensional basin deformation is in agreement with a predicted reduction of extensional strength of the basin center relative to its margins [e.g., *Buck*, 1991; *Bassi*, 1995; *van Wees and Stephenson*, 1995].

Differences in the mode of folding between platforms and Alpine/Mediterranean basins appear to be primarily controlled by differences in (transient) thermal regime during the prefold phase and the duration of prefold lithospheric thinning, affecting the level of external stress required to result in folding. The latter is directly coupled to the presence of near-field versus far-field regional stresses.

6.1. Folding Wavelength

Folding of multilayers with lithospheric rheology can demonstrate good correspondence with Biot's linear theory only for small strains and relatively strong plates (EET > 15 km). Nevertheless, most of the cases presented in Figures 1 and 2 demonstrate more or less good correlation between the folding wavelength and crustal and lithospheric thickness (thermotectonic age). Inspection of the related field data reveals a particularly strong inverse correlation between the prefold crustal structure and wavelength in the Alpine/Mediterranean basins with an increasing thickness of the prefold crust, wavelengths are decreasing. This can be explained by the inverse dependence of the integrated lithospheric strength on the crustal thickness demonstrated by *Burov and Diament* [1995]. Thus lithosphere segments with thick crust are weaker and easier to fold. A less pronounced but similar correlation can also be observed between the lithospheric thickness and wavelength of folding. We infer from these findings that crustal control on folding wavelength prevails over the lithospheric control on this parameter, suggesting rheological decoupling in the prefold lithosphere. In contrast, and although characterized by a much larger scatter in the inferred parameter values, the case histories for foreland folding discussed here indicate a trend of an increase of the wavelength of folding with increasing lithospheric thickness, which may suggest that folding is primarily controlled by lithospheric thermal structure in these cases. This, however, does not apply to very young, weak basins, where the folding wavelength can also be strongly affected by factors other than the lithospheric strength (e.g., laterally spreading sedimentary infill, gravity-induced flattening of Moho due to weakly resisting lithosphere, heterogeneities, and basin geometry). In such areas the wavelength of folding can vary significantly, from a few to many hundreds of kilometers.

The data also show the absence of a correlation between prefold crustal thickness and wavelength in the Alpine foreland and platform areas. As pointed out by *Burov and Diament* [1995] and *Cloetingh and Burov* [1996], the highest lithospheric thickness values most likely reflect low mantle heat flow and a thermal structure, which would suppress intralithosphere decoupling during folding.

6.2. Folding Forces

Differences between the magnitudes of the driving forces for lithospheric folding can also be inferred from observations and models of folding. Whereas the Alpine foreland seems to have been predominantly affected by far-field stresses, in some cases possibly in combination with plume activity, the basins that formed in a regime of general convergence have mostly been affected by near-field stresses resulting from slab retreat [e.g., *Bassi and Sabadini*, 1994]. However, the estimation of actual forces may be complicated owing to the presence of various supplementary controls on their magnitudes. For example, sedimentary fill in the basins reduces the effect of gravity by decreasing the difference in density between the overlying and underlying material. As a result, buckling of a layer overlain by sediment that accumulates as buckling occurs can be initiated with a horizontal force lower than that for a layer that buckles into air. The presence of preexisting heterogeneities may also significantly reduce folding forces. The horizontal force required to buckle a plate with realistic brittle-elasto-ductile rheological structure is much lower than that which can be expected for folding of a plate with a linear rheology. In the experiments on the central Asian folding we concluded that folding of a brittle-elasto-ductile lithospheric plate with a Jurassic geotherm requires a horizontal force per unit length of the order of 10^{12} N/m, which is about one order lower than that in the conventional elastic models [e.g., *McAdoo and Sandwell*, 1985]. Finally, it should be noted that the 2-D models do not take into account out-of-plane stresses, which may lead to 2-3 times overestimated horizontal stresses [*van Wees and Cloetingh*, 1996].

In addition, rheological behavior at depth may exhibit some currently poorly constrained features such as strain softening and reduction of the brittle strength at significant depth. For example, the compressional brittle strength at the depth of 40-50 km may be 2-3 times lower than that induced from Byerlee's law [*Kirby et al.*, 1991; *Ranalli*, 1995]. However, a significant sharp competence contrast (> 10) between the stiff layer and embedding is always needed to maintain folding, which suggests the presence of strong lithospheric or crustal cores in folded areas (rather than strength distributed over the whole lithospheric thickness). For these reasons, further rheological investigations are needed to constrain horizontal tectonic forces operating in nature.

7. Conclusions

1. Folding (along with crustal and possibly mantle faulting) is a "standard" response of the lithosphere to tectonic compression, which is normally followed by localization of the deformation leading to orogeny and subduction. On a large scale, faulting does not prevent folding but actually serves as a mechanism of the unstable deformation in the brittle domain. This result is quite different from the small-scale studies of folding and faulting [e.g., *Johnson*, 1980] where the faults cannot be locked, owing to the little importance of gravity, and folding stops as soon as the system becomes faulted, just because sliding on the faults requires less energy than folding does. On a lithospheric scale, upward sliding on the faults is severely limited by the work against the gravity, friction, and

resistance of the embeddings. Thus the developed faults soon become locked, new faults form, and the system behaves as an essentially solid layered media.

We demonstrated the possibility of large-scale mantle faulting. This result is highly dependent on the applicability of the existing rheology laws at great depth. The indirect rheological data [*Kirby et al.*, 1991; *Ranalli*, 1995] suggest that the brittle strength might be much lower at the depths in excess of 40-50 km than the predictions of Byerlee's law. This boosts the importance of the brittle behavior on the sub-Moho depths and potentially resolves the problem of high horizontal stress required for the initialization of folding when commonly inferred Byerlee's brittle rheology is assumed.

2. The wavelength of the pronounced folding (strong lithosphere with competent layers with EET > 15 km) on the first stages follows the linear theory.

3. When irregular folding takes place, the wavelength of the "megafolds" is essentially determined by the geometry of the extensional basins; For example, weak, large basins may produce large-wavelength folding whilst strong, narrow basins may produce small-wavelength folding, with an important influence of the sedimentary load.

4. Developed stages of folding may be associated with lateral variations of the wavelength, irregular changes in the amplitude, and formation of megabuckles, etc. In the case of decoupled folding (weak lower crust), partial coupling with the mantle lithosphere may temporarily occur, owing to the ductile flow induced by folding of the mantle. This partial coupling may affect the wavelength of crustal folding and the amplitude of the basement subsidence.

5. Preservation of folding over large time spans > 20 Myr requires sufficiently strong rheology equivalent to that obtained for thermal age > 700-1000 Ma for the common rheological parameters from Table 2 (diabase lower crust). This explains why most of the known cases of folding are relatively recent. The relationship between the duration of preservation of folding and the age or EET of the lithosphere is nonlinear and is associated with short-lifetime spans of folds in the intermediate-age lithosphere and large-lifetime spans of folds in old lithosphere (cratons).

Appendix: Numerical Model

The plasto-elasto-viscous finite element code Paravoz [e.g., *Poliakov et al.*, 1993] is a fully explicit large-strain time-marching scheme, which solves the classical full Newton equations of motion (in a form adopted in the continuous mechanics) using fast Lagrangian analysis of continua (FLAC) [*Cundall*, 1989]:

$$\rho \partial v_i / \partial t - \partial \sigma_{ij} / \partial x_j - \rho g_i = 0,$$

where v is velocity, g is the acceleration due to gravity, and ρ is the density. This equation is written in small-strain formulation, but it can be used for large-strain problems if the local coordinates are dynamically updated to satisfy small strain conditions at grid points (large-strain deformation is modeled via sets of incremental small-strain deformations). This is achieved using the Lagrangian moving mesh method. In this method the numerical mesh moves with the material, and at each time step the new positions of the mesh grid nodes are calculated and updated in large-strain mode from the current velocity field using an explicit procedure (two-stage Runge-Kutta). Solution of these equations provides velocities at mesh points, which allows us to calculate element strains ε_{ij}. These strains are used in the constitutive relations to calculate element stresses σ_{ij} and equivalent forces $\rho \partial v_i / \partial t$, which form the basic input for the next calculation cycle. For elastic and brittle materials the constitutive relations have a linear form:

$$\varepsilon_{ij} = A\sigma_{ij} + A_0,$$

with A and A_0 being the constitutive parameters matrixes.

For the ductile rheology the constitutive relations become more complex:

$$\dot{\varepsilon}_{ij} = A\sigma^{n-1}\sigma_{ij},$$

where $\dot{\varepsilon}_{ij}$ is the strain rate, and $\sigma=(1/2\ \sigma_{ij}\sigma_{ij})^{1/2}$ is the effective stress (second invariant). The variables n (the effective stress exponent) and A (constitutive parameter) describe the properties of a specific material (Table 2). For ductile materials, n usually equals 2-4, and A is depth- and temperature-dependent. For the brittle and elastic materials, A is usually only depth-dependent. Yet A and A_0 can be functions of strain or stress for softening or hardening materials. To allow for explicit solution of the governing equations, the FLAC method employs a dynamic relaxation technique based on the introduction of artificial inertial masses in the dynamic system. Adaptive remeshing technique developed by A.N.B. Poliakov and Yu. Podladchikov [*Poliakov et al.*, 1993] permits us to resolve strain localizations, leading to formation of the faults. The solver of the FLAC method does not imply any inherent rheology assumptions, in contrast with the most common finite element techniques based on the displacement method.

For the elastic rheology we adopted the following values of the constitutive parameters: E (Young's) modulus = 0.8 GPa and ν (Poisson's ratio) = 0.25. The brittle behavior is modeled by Mohr-Coulomb plasticity with friction angle 30° and cohesion 20 MPa [*Gerbault et al.*, 1999].

Since some of the rheological parameters are temperature-dependent, the equations of motion are coupled with the heat transport equations:

$$\rho C_p\, \partial T / \partial t - div(\mathbf{k}\nabla T) + \mathbf{v}\nabla T = H,$$

where **v** is the velocity tensor, C_p is the specific heat, **k** is the thermal conductivity tensor, and H is the radiogenic heat production per unit volume (here we use the commonly inferred values adopted, e.g., by *Burov et al.* [1993]. The size of the finite elements was between 2.5x5 and 5x7.5 km.

Acknowledgements. G. Bertotti made a number of useful comments on the preliminary versions of the manuscript. G. Bada has kindly provided material for the Figure 2b. We also highly appreciated the comments by J. Martinod. Contribution NSG 981203 of the Netherlands Research School of Sedimentary Geology. BRGM contribution 98040. GeoFrance 3D contribution 72.

References

Avouac, J.-P., and E. B. Burov, Erosion as a driving mechanism of intracontinental mountain growth?, *J. Geophys. Res.*, *101*, 17,747-17,769, 1996

Bada, G., S. Cloetingh, P Gerner, and F Horváth, Sources of recent tectonic stress in the Panonnian region: Inferences from finite element modelling, *Geophys J. Int*, *134*, 87-101, 1998

Bassi, G., Relative importance of strain rate and rheology for the mode of continental extension, *Geophys J Int.*, *122*, 195-210, 1995.

Bassi, G., and R. Sabadini, The importance of subduction for the modern stress field in the Tyrrhenian area, *Geophys. Res. Lett.*, *21*, 329-332, 1994.

Beekman, F., Tectonic modelling of thick-skinned compressional intraplate deformation, Ph D thesis, 152 pp., Vrije Univ., Amsterdam, 1994.

Beekman, F., R.A. Stephenson, and R.J. Korsch, Mechanical stability of the Redbank Thrust Zone, central Australia: Dynamic and rheological implications, *Aust J Earth Sci.*, *44*, 215-226, 1997.

Bhalerao, M. S, and T J Moon, Micromechanics of local viscoelastic buckling in thick composites, *Composites Part B*, *27*, 561-568, 1996.

Biot, M. A., Theory of Folding of Stratified viscoelastic media and its implications in tectonics and orogenesis, *Geol Soc Am Bull.*, *72*, 1595-1620, 1961.

Bird, P., Lateral extrusion of lower crust from under high topography in the isostatic limit, *J. Geophys. Res.*, *96*, 10,275-10,286, 1991

Brace, W F, and D.L Kohlstedt, Limits on lithospheric stress imposed by laboratory experiments, *J. Geophys. Res.*, *85*, 6248-6252, 1980.

Brun, J.-P., and T Nalpas, Graben inversion in nature and experiments, *Tectonics*, *15*, 677-687, 1996.

Buck, W. R., Modes of continental lithospheric extension, *J Geophys Res.*, *96*, 20,161-20,178, 1991

Burg, J.-P, and Y Podladchikov, Lithospheric scale folding and rock exhumation: Numerical modelling and application to the Himalayan syntaxes, *Geol Rundsch.*, in press, 1999.

Burg, J.-P, P. Davy, and J. Martinod, Shortening of analogous models of the continental lithosphere: New hypothesis for the formation of the Tibetan plateau, *Tectonics*, *13*, 475-483, 1994.

Burov, E.B., and M Diament, The effective elastic thickness (T_e) of continental lithosphere: What does it really mean?, *J. Geophys. Res*, *100*, 3905-3927, 1995

Burov E. B., and M G Kogan, Gravitational-mechanical model of the continental plate collision in Tien Shan region, *Dokl Akad Nauk, SSSR Engl. Transl*, *Phys. Solid Earth*, *313(6)*, 1439-1444, 1990.

Burov E.B, and P. Molnar, Gravity anomalies over the Ferghana valley (central Asia) and intracontinental deformation, *J Geophys Res.*, *103*, 18,137-18,152, 1998.

Burov, E.B., L.I. Lobkovsky, S. Cloetingh, and A.M. Nikishin, Continental lithosphere folding in Central Asia (part 2), constraints from gravity and topography, *Tectonophysics*, *226*, 73-87, 1993

Carter, N.L., and M.C Tsenn, Flow properties of continental lithosphere, *Tectonophysics*, *136*, 27-63, 1987.

Chamot-Rooke, N, F Jestin, and J.M. Gaulier, From stretching to incipient closure in the Liguro-Provencal back-arc basin (western Mediterranean Sea): Constraints from a new subsidence analysis, *Geol Soc., Spec. Publ.*, in press, 1999.

Ciulavu, D., Tertiary tectonics of the Transilvania Basin, Ph.D thesis, 153 pp., Vrije Univ., Amsterdam, 1999.

Cloetingh, S., and E. Banda, Mechanical structure, *A Continent Revealed. The European Geotraverse*, edited by D. Blundell, R Freeman, and S Mueller, pp. 80-91, Cambridge Univ. Press, New York, 1992.

Cloetingh, S., and E B. Burov, Thermomechanical structure of European continental lithosphere: Constraints from rheological profiles and EET estimates, *Geophys J Int*, *124*, 695-723, 1996.

Cloetingh, S., and H. Kooi, Intraplate stresses and dynamical aspects of rifted basins, *Tectonophysics*, *215*, 167-185, 1992.

Cloetingh, S, H. Kooi, and W Groenewoud, Intraplate stresses and sedimentary basin evolution, in *Origin and Evolution of Sedimentary Basins and Their Energy and Mineral Resources, Geophys. Monogr., Ser.*, vol. 48, edited by R.A Price, pp. 1-16, AGU, Washington, D.C., 1989.

Cloetingh, S., F Gradstein, H. Kooi, A C. Grant, and M. Kaminski, Did plate reorganization cause rapid late Neogene subsidence around the Atlantic?, *J. Geol. Soc. London*, *147*, 495-506, 1990.

Cloetingh, S, P A van der Beek, D. van Rees, Th. B. van Roep, C. Beermann, and R.A. Stephenson, Flexural interaction and dynamics of Neogene extensional basin formation in Alboran-Betic region, *Geo-Mar. Lett*, *12*, 66-75, 1992.

Cloetingh, S., J.D. van Wees, P.A. van der Beek, and G. Spadini, Role of pre-rift rheology on extensional basin formation: Constraints from thermomechanical modeling of Alpine/ Mediterranean basins and intra-cratonic rifts, *Mar Petr. Geol*, *12*, 787-808, 1995

Cobbold, P.R., Fold propagation in single embedded layers, *Tectonophysics*, *27*, 333-351, 1975

Cobbold, P R., A finite-element analysis of fold propagation: A problematic application, *Tectonophysics*, *38*, 339-353, 1977

Cobbold, P R, P. Davy, D. Gapais, E. A. Rosello, E. Sadybakasov, J C Thomas, J. J. Tondji, and M. de Urreiztieta, Sedimentary basins and crustal thickening, *Sediment. Geol*, *86*, 77-89, 1993.

Cochran, J.R., Himalayan uplift, sea level and the record of the Bengal Fan sedimentation at the ODP Leg 116 Sites, *Proc. Ocean Drill. Program Sci. Results*, *116*, 397-414, 1989.

Cundall, P A, Numerical experiments on localization in frictional materials, *Ing-Arch*, *59*, 148-159, 1989.

Curray, J R., and T. Munasinghe, Timing of intraplate deformation, northeastern Indian Ocean, *Earth Planet. Sci Lett.*, *94*, 71-77, 1989.

Davis, D.M, Changing mechanical response during continental collision. Active examples from the foreland thrust belts of Pakistan, *J Struct Geol*, *16*, 21-34, 1994

de Vicente, G., J.L. Giner, A Munoz Martin, J.M Gonzalez-Casado, and R. Lindo, Determination of present-day stress tensor and neotectonic interval in the Spanish Central System and Madrid Basin, central Spain, *Tectonophysics*, *266*, 405-424, 1996.

Docherty, C, and E Banda, Evidence for the eastward migration of the Alboran Sea based ion regional subsidence analysis. Basin formation by delamination of the subcrustal lithosphere?, *Tectonics*, *14*, 804-818, 1995

Dore, A G., and E.R. Lundin, Cenozoic compressional structures on the NE Atlantic margin: Nature, origin and potential significance for hydrocarbon exploration, *Pet. Geosci.*, *2*, 299-311, 1996

Fleitout, L., and C Froidevaux, Tectonics and topography of the lithosphere containing density heterogeneities, *Tectonics*, *1*, 21-56, 1982.

Fleitout, L., and C. Froidevaux, Tectonic stresses in the lithosphere, *Tectonics*, *2*, 315-324, 1983.

Fletcher, R C, Wavelength selection in the folding of a single layer with power law rheology. *Am J Sci.*, *274*, 1029-1043, 1974.

Fodor, L., L. Csontos, G. Bada, I. Gyorfi, and L Bencovics, Tertiary tectonic evolution of the Pannonian basin system and neighbouring orogens: A new synthesis of paleostress data, *Geol Soc, Spec Publ.*, in press, 1999.

Geller, C.A., J.K. Weissel, and R N. Anderson, Heat transfer and intraplate deformation in the central Indian Ocean, *J. Geophys. Res.*, *88*, 1018-1032, 1983.

Gerbault, M., E. Burov, A.N.B Poliakov, and M Dagnières, Do faults trigger folding in the lithosphere ?, *Geophys Res. Lett*, *26*, 271-274, 1999

Gerner, P., G. Bada, P. Dovenyi, B. Muller, M.C. Onsescu, S. Cloetingh, and F. Horváth, Recent tectonic stress and crustal deformation in and around the Pannonian basin: Data and models, *Geol Soc Spec. Publ.*, in press, 1999.

Horváth, F, Towards a mechanical model for the deformation of the Pannonian basin, *Tectonophysics*, *226*, 333-357, 1993.

Horváth, F., and S. Cloetingh, Stress-induced late-stage subsidence anomalies in the Pannonian basin, *Tectonophysics*, *266*, 287-300, 1996.

Hunt, G., H Muhlhaus, B Hobbs, and A Ord, Localized folding of viscoelastic layers, *Geol Rundsch*, *85*, 58-64, 1996

Janssen, M.E, M Torne, S Cloetingh, and E Banda, Pliocene uplift of the eastern Iberian margin: Inferences from quantitative modelling of the Valencia Trough, *Earth Planet. Sci. Lett.*, *119*, 585-597, 1993

Jaó, I., Recent vertical surface movements in the Carpathian basin, *Tectonophysics*, *202*, 120-134, 1992.

Japsen P, Regional velocity depth anomalies, North Sea chalk: A record of overpressure and neogene uplift and erosion, *AAPG bulletin*, *82*, 2031-2074, 1998.

Johnson, A M., Folding and faulting of strain-hardening sedimentary rocks, *Tectonophysics*, *62*, 251-278, 1980.

Jurado, M J., and B Mueller, Contemporary tectonic stress in NE Iberia: New evidence from borehole breakout analysis, *Tectonophysics*, *282*, 99-115, 1997

Kirby, S. H., and A K Kronenberg, Rheology of the lithosphere: Selected topics, *Rev Geophys.*, *25*, 1219-1244, 1987.

Kirby S. H., W Durham, and L A. Stern, Mantle phase changes and deep earthquake faulting in subducting lithosphere, *Science*, *252*, 216-225, 1991.

Kooi, H., M. Hettema, and S. Cloetingh, Lithospheric dynamics and the rapid Pliocene-Quaternary subsidence phase in the southern North Sea Basin, *Tectonophysics*, *192*, 245-259, 1991.

Kooi, H., S Cloetingh, and J. Burrus, Lithospheric necking and regional isostasy at extensional basins, 1, Subsidence and gravity modeling with an application to the Gulf of Lions Margin (SE France), *J. Geophys. Res.*, *97*, 17,553-17,571, 1992.

Kusznir, N., and R G. Park, The extensional strength of the continental lithosphere: its dependence on geothermal gradient, crustal composition and thickness, in *Continental Extensional Tectonics*, edited by M.P.M

Coward, J F. Jewey, and P.I. Hancock, *Geol. Soc Spec Publ*, *28*, 35-52, 1987
Lambeck, K., Structure and evolution of intracratonic basins in central Australia, *Geophys J R Astron Soc*, *74*, 843-886, 1983.
Lan, L, and P Hudleston, Rock rheology and sharpness of folds in single layers, *J Struct Geol*, *18*, 925-931, 1996.
Lankreijer, A.C, Mocanu, V, and S. Cloetingh, Lateral variations in the lithosphere sstrength in the Romanian Carpathians: constraints on basin evolution, *Tectonophysics*, *272*, 269-290, 1997
Lefort, J.P., and B.N.P Agarwal, Gravity evidence for an Alpine buckling of the crust beneath the Paris Basin, *Tectonophysics*, *258*, 1-14, 1996.
Martinod, J., and P. Davy, Periodic instabilities during compression or extension of the lithosphere, 1, Deformation modes from an analytical perturbation method, *J. Geophys Res.*, *97*, 1999-2014, 1992.
Martinod, J., and P Davy, Periodic instabilities during compression of the lithosphere, 2, Analogue experiments, *J Geophys Res*, 99, 12,057-12,069, 1994
Masson, D G., J.A. Cartwright, L.M. Pinheiro, R.B. Whitmarsh, M.-O. Beslier, and H Roeser, Compressional deformation at the ocean-continent transition in the NE Atlantic, *J. Geol. Soc. London*, *151*, 607-614, 1994.
Mauffret, A, J.P. Rehault, M. Gennessaux, G. Bellaiche, M. Labarbarie, and D. Lefebvre, Western Mediterranean basin evolution: From a distensive to a compressive regime, in *Sedimentary Basins of Mediterranean Margins*, edited by F.C. Wezel, pp 67-81, Tectnoprint, Bologna, 1981.
McAdoo, D.,C, and D Sandwell, Folding of oceanic lithosphere, *J Geophys Res*, *90*, 8563-8569, 1985.
Mercier, E., F. Outtani, and D. Frizon de Lamotte, Late-stage evolution of fault propagation folds: principles and example, *J Struct Geol.*, *19*, 2185-2193, 1997
Muller, B., M.L., Zoback, K. Fuchs, L. Mastin, S. Gregersen, N Pavoni, O. Stephanson, and C. Ljunggren, Regional patterns of tectonic stress in Europe, *J. Geophys. Res.*, *97*, 11,783-11,803, 1992.
Negut, A., C. Dinu, I. Savu, R. Bardan, M-L. Negut, and I. Craicu, Stress orientation determination in Romania by borehole breakouts, geodynamic significance, *Rev. Rom. Geol*, *34*, 23-35, 1997.
Nikishin, A. M., L I Lobkovsky, S. Cloetingh, and E B. Burov, Continental lithosphere folding in central Asia, 2, Constraints from geological observations, *Tectonophysics*, *226*, 59-72, 1993.
Nikishin, A.M, et al, Late Precambrian to Triassic history of the east European Craton: Dynamics of sedimentary basin evolution, *Tectonophysics*, *268*, 23-63, 1996.
Nikishin, A.M., M.-F. Brunet, S. Cloetingh and A.V. Ershov, Northern Peri-Tethyan Cenozoic intraplate deformations· Influence of the Tethyan collision belt on the Eurasian continent from Paris to Tien-Shan, *C.R. Acad Sci*, *Ser. IIa, Terre Planetes*, *324*, 49-57, 1997.
Pepe, F., Structure and tectonics of the southern Tyrrhenian Sea inferred from a multichannel seismic reflection data, Ph.D. thesis, Univ of Palermo, Palermo, Italy, 1988.
Poliakov, A.N.B, Yu Podladchikov, and C Talbot, Initiation of salt diapirs with frictional overburden. numerical experiments, *Tectonophysics*, *228*, 199-210, 1993.
Posgay, K. et al., Internal deep reflection survey along the Hungarian Geotraverse, *Geophys Trans*, *40*, 1-44, 1996
Ramberg, H, Contact strain and folding instability of multilayered body under compression, *Geol. Rundsch*, *51*, 405-439, 1961.
Ranalli, G, Nonlinear flexure and equivalent mechanical thickness of the lithosphere, *Tectonophysics*, *240*, 107-114, 1994
Ranalli, G., *Rheology of the Earth*, 2nd ed, 413 pp, Chapman and Hall, New York, 1995
Ribeiro, A., R Baptista, J. Cabral, and L Matias, Tectonic stress patterns in Portugal Mainland and the adjacent Atlantic region (west Iberia), *Tectonics*, *15*, 641-659, 1996
Roecker, S. W, T. M. Sabitova, L P. Vinnik, Y. A Burmakov, M I Golvanov, R. Mamatkanova, and L. Munirova, Three-dimensional elastic wave velocity structure of the western and central Tien Shan, *J Geophys. Res*, *98*, 15,779-15,795, 1993.
Roest, W R., and S P. Srivastava, Kinematics of the plate boundaries between Eurasia, Iberia, and Africa in the North Atlantic from the Late Cretaceous to the present, *Geology*, *19*, 613-616, 1991
Royden, L.H., The tectonic expression of slab pull at continental margin boundaries, *Tectonics*, *12*, 303-325, 1993.
Sabitova, T.M, Structure of the Earth crust based on seismic data, in *The Lithosphere of the Tien Shan*, edited by I. Y. Gubin, pp. 31-33, Nauka, Moscow, 1986.
Sachsenhofer, R.F, A. Lankreijer, S Cloeingh, and F Ebner, Subsidence analysis and quantitative basin modelling in the Styrian basin (Pannonian Basin system, Austria), *Tectonophysics*, *272*, 175-196, 1997.
Seranne, M, Benedicto, A., Truffert, C., Pascal, G., and Labaume, P., Structural style and evolution of the Gulf of Lion Oligo-Miocene rifting. role of the Pyrenean orogeny. *Mar. Petrol Geol.*, *12*, 809-820, 1995.
Shemenda, A I, Results from physical modelling of horizontal lithosphere compression, *USSR Acad. Sci Rep.*, *307*(2), 345-350, 1989.
Shemenda, A I., Horizontal lithosphere compression and subduction: Constraints provided by the physical modeling, *J. Geophys Res.*, *97*, 11,097-11,116, 1992.
Smith, R B., Unified theory of the onset of folding, boudinage and mullion structure, *Geol. Soc. Am. Bull.*, 88, 1601-1609, 1975
Smith, R. B., Formation of folds, boudinage and mullions non-newtonian materials, *Geol. Soc Am Bull.*, *88*, 312-320, 1977.
Smith, R. B., The folding of a strongly non-Newtonian layer, *Am. J. Sci.*, *79*, 272-287, 1979
Spadini, G., S. Cloetingh, and G. Bertotti, Thermo-mechanical modeling of the Tyrrhenian Sea. Lithospheric necking and kinematics of rifting, *Tectonics*, *14*, 629-644, 1995.
Stapel, G., J.Verhoef, H. Kooi, and S. Cloetingh, Iberian crust analyzed by residual gravity anomalies: Moho prediction and isostasy, paper presented at 59th conference, EAGE, Geneva, Switzerland, 1997
Stein, C.A, S. Cloetingh, and R. Wortel, SEASAT-derived gravity constraints on stress and deformation in the northeastern Indian Ocean, *Geophys Res Lett.*, *16*, 823-826, 1989.
Stephenson, R.A., and S Cloetingh, Some examples and mechanical aspects of continental lithospheric folding, *Tectonophysics*, *188*, 27-37, 1991.
Stephenson, R.A., and K. Lambeck, Isostatic response of the lithosphere with in-plane stress: Application to central Australia, *J Geophys. Res.*, *90*, 8581-8588, 1985.
Stephenson, R.A., B.D. Ricketts, S.A. Cloetingh, and F. Beekman, Lithosphere folds in the Eurekan orogen, Arctic Canada?, *Geology*, *18*, 603-606, 1990.
Tsenn, M C., and N.L. Carter, Flow properties of continental lithosphere, *Tectonophysics*, *136*, 27-63, 1987.
Turcotte, D.L, Flexure, in *Advances in Geophysics*, *Acad Press*, 21, New York, 51-86, 1979.
Turcotte, D L, and G Schubert, *Geodynamics Applications of Continuum Physics to Geological Problems*, 450pp, John Wiley, New York, 1982.
Vackarcs, G., P.R. Vail, G. Tari, G., G Y. Pogacsas, R.E. Mattick, A Szabo, and S Bowman, Third-order Miocene-Pliocene sequences in the prograding delta complex of the Pannonian Basin, *Tectonophysics*, *240*, 81-106, 1994.
Vagnes, E., R.H. Gabrielsen, and P. Haremo, Late Cretaceous-Cenozoic intraplate contractional deformation at the Norwegian continental shelf: Timing, magnitude and regional implications, *Tectonophysics*, 300, 29-46, 1998.
van Balen, R.T., Y.Y. Podladchikov, and S. Cloetingh, A new multilayered model for intraplate stress-induced differential subsidence of faulted lithosphere applied to rifted basins, *Tectonics*, *17*, 938-954, 1998
van Wees, J. D., and S Cloetingh, 3D flexure and intraplate compression in the North Sea Basin, *Tectonophysics*, *266*, 343-359, 1996.
van Wees, J. D, and R Stephenson, Quantitative modelling of basin and rheological evolution of the Iberian Basin (central Spain): Implications for lithospheric dynamics of intraplate extension and inversion, *Tectonophysics*, *252*, 163-178, 1995.
Vegas, R., S. Cloetingh, G.D. Vincente, G.D., J. Giner, B. Andeweg, P. Rincon, P. and A. Munoz Martin, Accomodation de la deformation itraplace y la sismicidad resultante en la Peninsula Iberica. Fluxuras de la corteza y corredores de falla, paper presented at Primera asamblea Hispano-Portuguesa de Geodesia y Geofisica/IX Asamblea Espanola de Geodesia y geophysica, Aguadulce, Almeria, Spain, Feb. 9-13, 1998.
Vilotte, J.P., J. Melosh, W. Sassi, W, and G. Ranalli, Lithosphere rheology and sedimentary basins, *Tectonophysics*, *226*, 89-95, 1993
Waltham, D, C. Taberner, and C. Docherly, Intra-plate stress and basin formation by low strain rate flow of the upper crust: a mid-Eocene example from the south Pyrenean foreland, *Geophys. Research Abstr. Press*, p. 30, 1999.
Zhang, Y, B.E. Hobbs, A. Ord, and H.B. Muhlhaus, Computer simulation of single-layer buckling, *J. Struct Geol*, *18*, 5643-5655, 1996.
Ziegler P.A, S Cloetingh, and van J.D. Wees, Dynamics of intra-plate compressional deformation: The Alpine foreland and other examples, *Tectonophysics*, *252*, 7-60, 1995.
Zoback, M.L., First- and second-order patterns of stress in the lithosphere: The World Stress Map project, *J. Geophys. Res.*, *97*, 11,703-11,728, 1992.
Zuber, M. T., Compression of oceanic lithosphere. an analysis of intraplate deformation in the Central Indian Basin, *J. Geophys Res*, *92*, 4817-4825, 1987.

E. Burov, Department of Tectonics, T26-e1, Case 129, University of Pierre and Marie Curie, 75252 Paris, France. (burov@ipgp jussieu.fr)

S. Cloetingh, Faculty of Earth Sciences, De Boelelaan 1085, Vrije Universiteit, 1081HV Amsterdam, Netherlands.

A. Poliakov, UMR 5573, CNRS, University Montpellier II, 34090 Montpellier, France.

(Received January 5, 1999,
revised June 9, 1999, accepted June 17, 1999)

TECTONICS, VOL. 18, NO. 6, PAGES 1224-1244 DECEMBER 1999

Kinematics of basin development during the transition from terrane accretion to strike-slip tectonics, Late Cretaceous-early Tertiary Cantwell Formation, south central Alaska

Ronald B. Cole
Department of Geology, Allegheny College, Meadville, Pennsylvania

Kenneth D. Ridgway
Department of Earth and Atmospheric Sciences, Purdue University, West Lafayette, Indiana

Paul W. Layer and Jeffery Drake
Geophysical Institute, University of Alaska, Fairbanks

Abstract. The Cantwell basin was formed during Late Cretaceous time in the suture zone between the Wrangellia composite terrane and the former continental margin of southern Alaska. The Late Cretaceous (~80-70 Ma) lower Cantwell Formation represents the initial fill of this basin and includes ~4000 m of sedimentary rock. Between Maastrichtian and late Paleocene time (~70-60 Ma), rocks of the lower Cantwell Formation were deformed by nearly east-west trending folds and north vergent thrust faults. This deformation can be linked to the northward accretion and suturing of the Wrangellia composite terrane to southern Alaska. During late Paleocene to early Eocene time (~60-55.5 Ma), at least 2750 m of volcanic rocks of the upper Cantwell Formation were deposited above the folded lower Cantwell Formation. New $^{40}Ar/^{39}Ar$ ages for the upper Cantwell Formation range from 59.8+/-0.2 to 55.5+/-0.2 Ma and reveal that the unconformity between the lower and upper Cantwell Formations represents a 10-20 million year hiatus. Following volcanism the Cantwell Formation was crosscut by northeast trending folds, northwest trending normal faults, north trending left-lateral slip faults, northeast trending reverse faults, and east trending right-lateral slip faults. These structures are consistent with northwest-southeast compression in a zone of right-lateral simple shear along a fault with the same trend (east-northeast) as that of the present McKinley strand of the Denali fault system. Cantwell basin kinematics are compatible with an escape tectonics model for south central Alaska whereby the Cantwell basin was formed, folded, and partially uplifted during northward terrane accretion and suturing and was deformed again during the westward transfer of terranes along right-lateral strike-slip fault systems.

1. Introduction

The tectonic history of the northeastern Pacific margin is punctuated by periods of terrane accretion and subsequent dismemberment and orogen-parallel transport of these terranes along major strike-slip fault systems [*Coney et al.*, 1980; *Monger et al.*, 1982; *Howell et al.*, 1985; *Oldow et al.*, 1989]. This accretionary tectonic framework has led to such recent models as "hit and run" tectonics [*Maxson and Tikoff*, 1996] and has seeded much research and debate on the nature of terrane boundaries and terrane migration histories [see e.g., *Cowan et al.*, 1997]. Because terrane accretion is recognized as an important process along oblique slip convergent margins worldwide [e.g., *Debiche et al.*, 1987; *Leitch and Scheibner*, 1987], it is reasonable to infer that transitions between accretionary and strike-slip tectonics have been important during continental margin evolution throughout the geologic past. Yet a poorly documented component of accretionary tectonic models is the nature of the transition that must occur along continental margins from terrane collision to subsequent lateral slip along orogen-parallel fault systems. This type of transition should involve predictable kinematic responses in upper crustal deformation and basin development along terrane suture zones. We present new chronologic, structural, and stratigraphic data that define such an accretionary to strike-slip transition as recorded in rocks of the Cretaceous-Tertiary Cantwell basin in south central Alaska (Figure 1). Our study area lies within Denali National Park in the western Healy 1°x3° quadrangle (Figure 1) where rocks of the Cantwell Formation (the fill of the Cantwell basin) are well exposed.

Paper number 1999TC900033.
0278-7407/99/1999TC900033$12.00

2. Geologic Setting

2.1. Accreted Terranes

South-central Alaska is characterized as an amalgamation of accreted terranes, many of which are bound or crosscut by major fault systems. The three largest terranes in the region are the Wrangellia, Peninsular, and Alexander terranes [*Jones et al.*, 1981]. On the basis of stratigraphic, volcanic, and plutonic ties, these three terranes are interpreted to have been linked together between late Paleozoic and Late Triassic time to form a single composite terrane [*Pavlis*, 1983; *Gardner et al.*, 1988; *Plafker et al.*, 1989]. This composite terrane is most recently defined by *Nokleberg et al.* [1994] as the Wrangellia composite terrane (WCT), which generally occupies the area between the Denali and Border Ranges fault systems (Figure 1). The WCT is grossly characterized

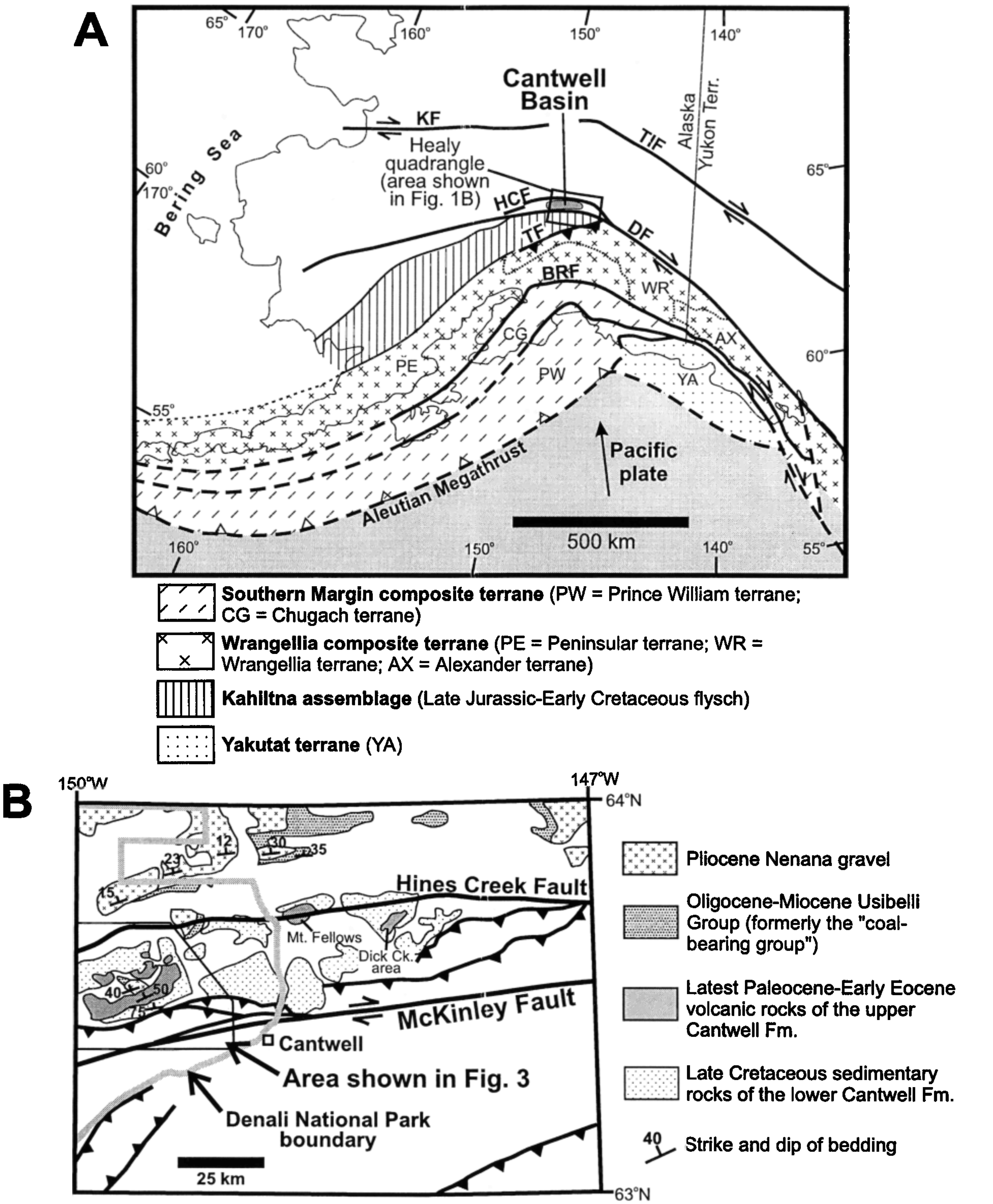

Figure 1. Map of south central Alaska showing the study area in the western Healy 1°x3° quadrangle. (a) Distribution of terranes and major faults in south central Alaska, from *Plafker and Berg* [1994]. Fault abbreviations are as follows: KF, Kaltag fault; TIF, Tintina fault; HCF, Hines Creek fault; DF, Denali fault system; TF, Talkeetna fault; BRF, Border Ranges fault. The motion of the Pacific plate, as shown by arrow, is from *Engebretson et al.* [1985]. (b) Simplified geologic map of the Healy quadrangle showing the Cantwell Formation and younger rock units. Modified from *Csejtey et al.* [1986, 1992].

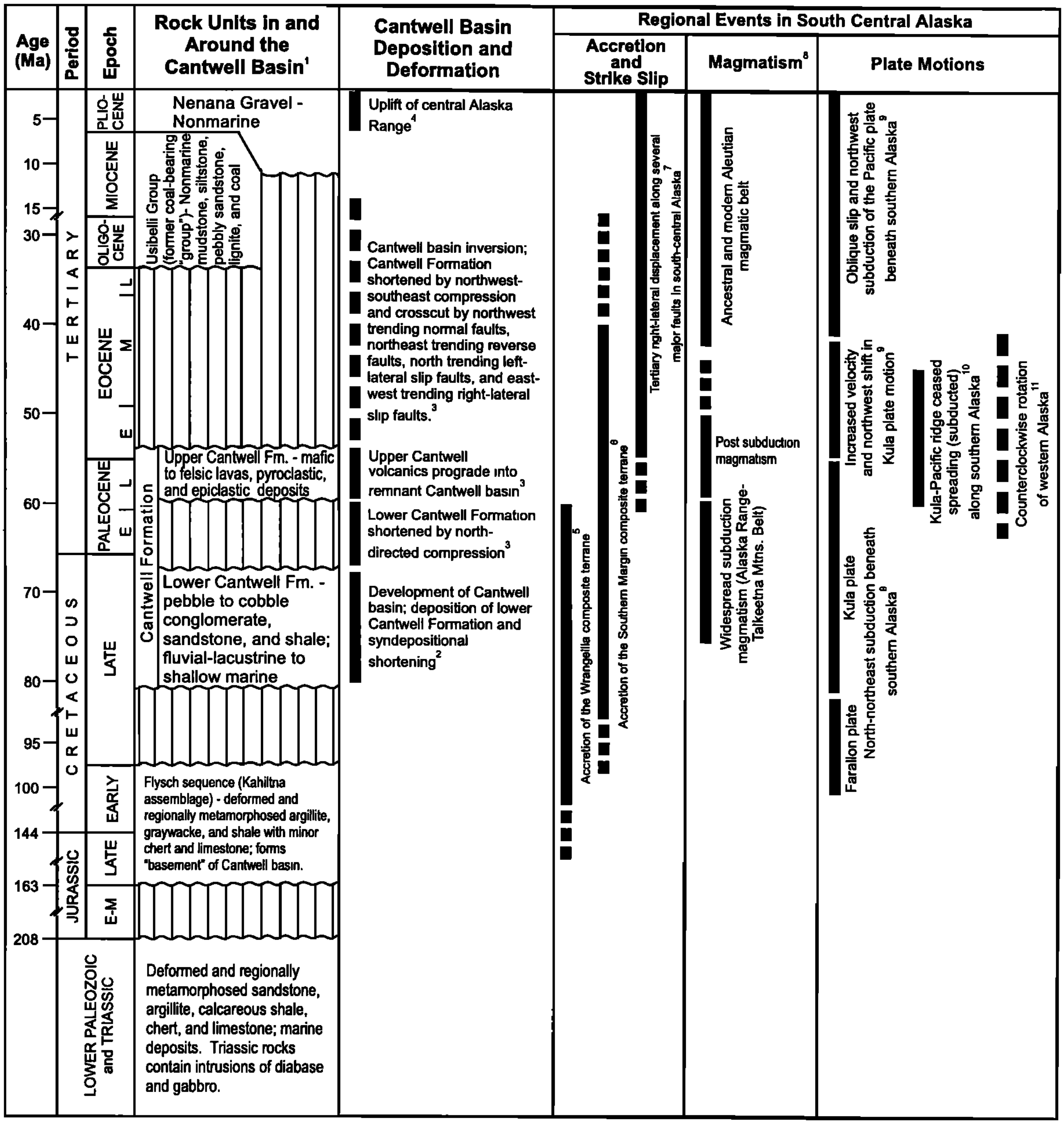

Figure 2. Age event diagram showing stratigraphy of rocks in and around the Cantwell basin, Cantwell basin history, and regional tectonic events. Timescale after *Palmer* [1983] and *Cande and Kent* [1992]. 1, rock units as described by *Csejtey et al.* [1992] except for Usibelli Group [*Wahrhaftig*, 1987] and age of Nenana Gravel [*Ager et al.* 1994]; 2, *Ridgway et al.* [1997]; 3, Cantwell deformation based on results of this study; 4, *Plafker et al.* [1991], *West* [1994], *West and Layer* [1994], *Fitzgerald et al.* [1995]; 5, *Csejtey et al.* [1982], *Nokleberg et al.* [1994]; 6, *Plafker et al.* [1994]; 7, includes Denali fault [*Lanphere*, 1978; *Nokleberg et al.*, 1994], Kaltag fault [*Patton and Hoare*, 1968], Tintina fault [*Gabrielse*, 1985; *Dover*, 1994], Castle Mtn. Fault [*Fuchs*, 1980; *Silberman and Grantz*, 1984], and Border Ranges fault [*Smart et al.*, 1996]; 8, after *Hudson* [1983], *Wallace and Engebretson* [1984], and *Moll-Stalcup* [1994]; 9, *Engebretson et al.* [1985]; 10, *Bradley et al.* [1993], *Plafker et al.* [1994], and *Pavlis and Sisson* [1995]; 11, timing and evidence summarized by *Hillhouse and Coe* [1994].

[*Plafker and Berg*, 1994, p. 996] by "Late Proterozoic(?) and younger magmatic arc, oceanic plateau(?), and rift-fill assemblages ... and the Late Jurassic to mid-Cretaceous magmatic arc and flysch deposits of the Gravina-Nutzotin belt." Paleomagnetic data, as summarized by *Hillhouse and Coe* [1994], show that the WCT was at least 25° south of its present position with respect to North America during Late Triassic time. This latitudinal gap was closed, and the WCT was accreted to western Canada and southern Alaska between Late Jurassic and Late Cretaceous time (Figure 2) [*Stone et al.*, 1982; *Csejtey et al.*, 1982; *Nokleberg et al.*, 1985, 1994; *Crawford et al.*, 1987; *Wallace et al.*, 1989; *McClelland et al.*, 1992]. The Late Jurassic-Early Cretaceous Kahiltna assemblage in south central and southwestern Alaska (Figure 1) represents a flysch basin which was tectonically collapsed along the leading edge of the WCT as it was accreted northward [*Csejtey et al.*, 1982; *Wallace et al.*, 1989]. The Chugach and Prince William terranes, which form most of the Southern Margin composite terrane (as summarized by *Plafker et al.* [1994]) (Figure 1) are largely subduction complex assemblages that were accreted northward along the trailing edge of the WCT between Late Cretaceous and middle Tertiary time. Rocks of the Chugach terrane have been underthrust at least 40 km beneath the WCT along the Border Ranges fault system [*Plafker et al.*, 1989].

2.2. Strike-Slip Fault Systems

Episodes of Late Cretaceous to early Tertiary dextral offset have been reported for major fault systems across south central and southeastern Alaska and the Yukon Territory, including the Border Ranges fault [*Roeske et al.*, 1993; *Smart et al.*, 1996], Denali fault [*Grantz*, 1966; *Turner et al.*, 1974; *Forbes et al.*, 1974; *Reed and Lanphere*, 1974; *Eisbacher*, 1976; *Sherwood*, 1979; *Brewer*, 1982; *Brewer et al.*, 1984; *Ridgway et al.*, 1992, 1995; *Cole*, 1999], Kaltag fault [*Patton and Hoare*, 1968], and Tintina fault [*Gabrielse*, 1985; *Dover*, 1994] (Figure 2). Of these, the Denali fault system is most relevant to this study because of its proximity to the southern margin of the Cantwell basin (Figure 1). Estimates for right-lateral displacement along the Denali fault vary and range from 300 to 400 km of Late Cretaceous-early Tertiary offset along the eastern segment [*Forbes et al.*, 1974; *Turner et al.*, 1974; *Eisbacher*, 1976] to tens and possibly up to 150 km along the western segment [*Grantz*, 1966; *Decker et al.*, 1994]. The strand of the Denali fault system that extends through the central Alaska Range is known as the McKinley fault and trends roughly east-northeast ~12-18 km south of the Cantwell Formation in our study area (Figure 3). The McKinley fault is a regional crustal structure that is identified on the basis of (1) fault zone rocks, including gouge, fracture zones, microbreccia, and mylonite [*Reed and Lanphere*, 1974; *Hickman et al.*, 1977; *Brewer*, 1982; *Brewer et al.*, 1984], (2) offset Quaternary landforms [*Richter and Matson*, 1971; *Stout et al.*, 1973; *Hickman et al.*, 1977], (3) a concentration of shallow seismic events (<50 km depth, $M \geq 2$) within 10 km of the McKinley fault trace [*Sherwood*, 1979], (4) a coincidence with the boundary between major magnetic domains in southern Alaska [*Saltus et al.*, 1999], and (5) a prominent 1- to 3-km-wide valley through the central Alaska Range [*Brewer, 1982*; *Riehle et al.*, 1997]. Estimates for offset along the McKinley fault consistently reveal that there has been ~35-40 km of right-lateral displacement since Eocene time [*Reed and Lanphere*, 1974; *Brewer*, 1982; *Cole*, 1999] including only ~1-6 km of Pliocene-Pleistocene displacement and tens to a few hundred meters of Holocene displacement [*Richter and Matson*, 1971; *Stout et al.*, 1973; *Hickman et al.*, 1977]. These estimates are consistent with interpretations for an episode of Oligocene strike slip along the Denali fault in the Yukon Territory [*Ridgway et al.*, 1995] and southwestern Alaska [*Ridgway et al.*, 1999] and collectively indicate that an episode of Oligocene strike slip occurred along nearly the entire Denali fault system. One estimate for offset along the McKinley fault (the offset Foraker-McGonnagal pluton as interpreted by *Reed and Lanphere* [1974]) has recently been disputed on the basis that at one location (Gunsight Pass) the McGonnagal pluton is interpreted to have an intrusive contact, not a fault contact, with rocks that should be on the opposite side of the McKinley fault [*Csejtey et al.*, 1997, 1998; *Ford et al.*, 1998; *Wrucke et al.*, 1998]. In contrast, *Reed and Lanphere* [1974, p. 1886] describe exposures of the McKinley fault to include steeply dipping and intensely sheared 30- to 40-m-wide zones of gouge and that "rocks of the Foraker pluton are mylonitized within 200 meters of the fault." Additional detailed mapping is required to evaluate this dispute and to accurately trace specific strands of the McKinley fault through the central Alaska Range. We argue though, on the basis of regional geologic evidence throughout Alaska and western Canada (see earlier references), that even if the McKinley fault is not located at Gunsight Pass, this fault does exist as a throughgoing structure of the Denali fault system, along which there were past episodes of strike-slip displacement.

Paleomagnetic data reveal that western Alaska had experienced between 30° and 50° of counterclockwise rotation between ~68 and 44 Ma (data summarized by *Hillhouse and Coe* [1994]). This rotation and regional strike-slip faulting were roughly coeval with the end of WCT accretion and a northwestward shift in Kula plate motion with respect to southern Alaska (Figure 2). While this broad framework for regional tectonic events has been established, the nature and timing of geologic events (e.g., Cantwell basin evolution) that occurred during the transition from WCT accretion to subsequent strike-slip deformation remain poorly defined [e.g., *Plafker and Berg*, 1994].

2.3. Cantwell Basin

The Cantwell basin was formed in an area to the north of the WCT and is generally bound between the McKinley and Hines Creek faults [*Hickman et al.*, 1990; *Ridgway et al.*, 1997]. In a study of the Cantwell Formation primarily in the eastern Healy 1°x3° quadrangle, *Hickman et al.*, [1990] have interpreted the Cantwell basin to have formed in response to Eocene dextral strike-slip along the Denali fault. More recently, on the basis of data from the Cantwell Formation primarily in the western Healy 1°x3° quadrangle, *Ridgway et al.*, [1997] proposed a model in which initial subsidence and sedimentation in the Cantwell basin were a response to northward vergent Late Cretaceous thrusting as opposed to strike-slip faulting. Their evidence includes palynologic ages, facies mapping, paleoflow data, petrography, and the mapping of rotated intraformational unconformities which collectively reveal that proximal synorogenic sediments were being shed from uplifted regions along the southern and northern basin margins and were subsequently deformed during successive shortening events. Results of this study support an interpretation of Late Cretaceous to early Paleocene north vergent shortening of the Cantwell basin followed by an episode of post-early Eocene right-lateral strike-slip deformation.

The Cantwell Formation, which is the fill of the Cantwell basin (Figures 2 and 3), has been divided into a lower

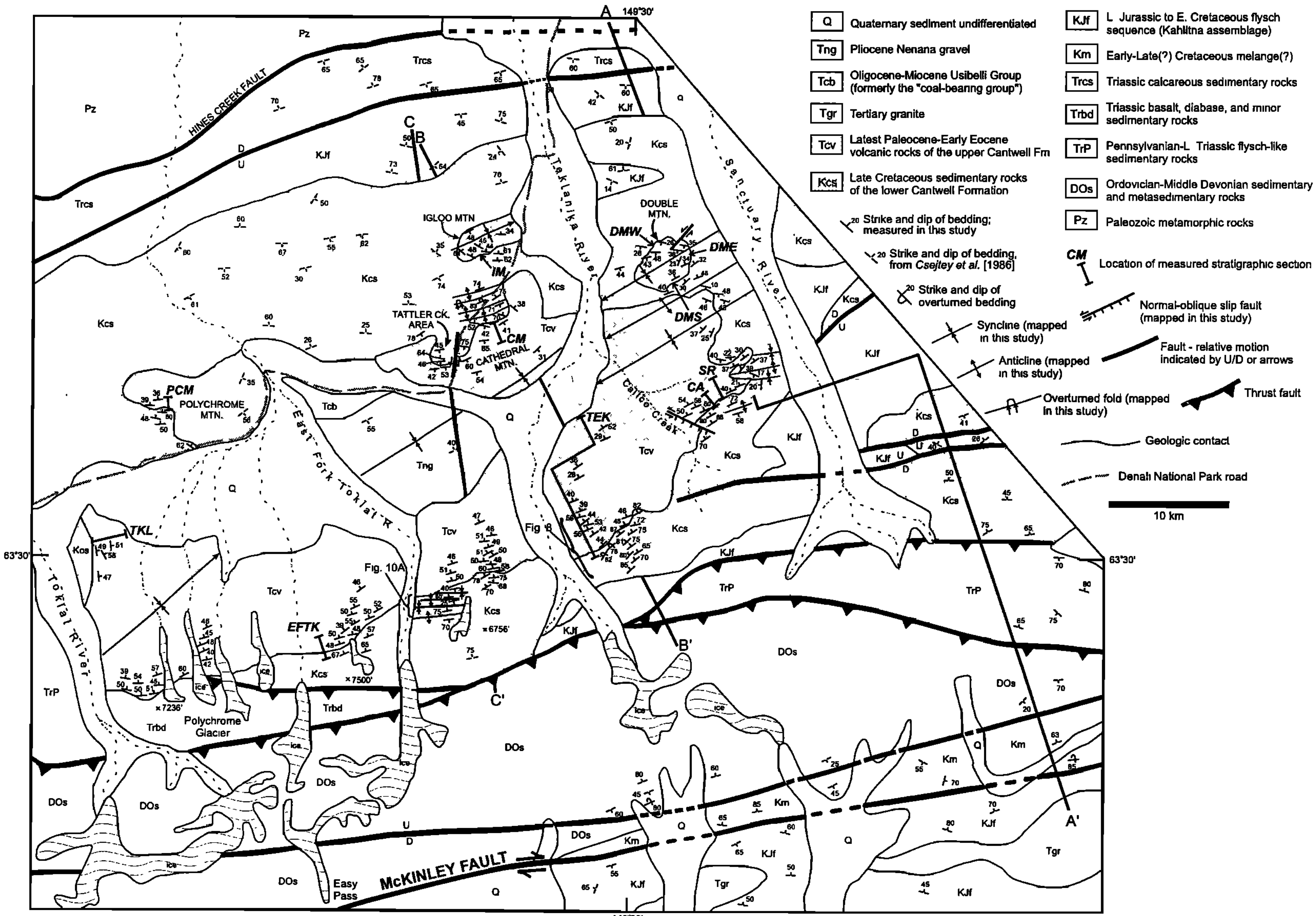

Figure 3. Geologic map of the study area. The geologic contact of the lower and upper Cantwell Formations and associated structures are based on mapping of this study. Other geologic contacts and structures are from *Csejtey et al.* [1986, 1992]. Cross sections are shown in Figure 7. Note the changes in dips between the lower and upper Cantwell Formations which represent an angular unconformity between these two units. CA, Calico Creek; CM, Cathedral Mountain; DME, Double Mountain east; DMS, Double Mountain south; DMW, Double Mountain west; EFTK, East Fork Toklat River; IM, Igloo Mountain; PCM, Polychrome Mountain; SR, Sanctuary River; TEK, Teklanika River; TKL, Toklat River.

sedimentary unit and an upper volcanic unit [*Wolfe and Wahrhaftig*, 1970]. The lower Cantwell Formation includes over 4000 m of conglomerate, sandstone, shale, and coal [*Hickman*, 1974; *Hickman et al.*, 1990]. Using palynologic data, *Trop* [1996] and *Ridgway et al.* [1997] document that the lower Cantwell Formation is of Late Cretaceous age (~80-70 Ma in the Campanian and Maastrichtian). The upper Cantwell Formation includes over 2750 m of basaltic to rhyolitic lavas, pyroclastic rocks, and minor interbedded sedimentary deposits [*Gilbert et al.*, 1976; *Nye*, 1978; *Cole et al.*, 1996] (Figure 4).

3. Age of Cantwell Volcanic Rocks

Eight K-Ar ages have previously been reported for the volcanic rocks of the upper Cantwell Formation at different locations across the Healy 1°x3° quadrangle (Table 1). These previous ages show a wide range from early Paleocene to middle Eocene (64.6 +/- 3.4 to 50.9 +/- 2.2 Ma). Of these ages, five are from volcanic rocks in the western Healy quadrangle (within the study area of this paper), and three are from volcanic rocks in the eastern Healy quadrangle, outside of our study area. *Gilbert et al.* [1976] consider two ages from their study to be minimum ages because of potential $^{40}Ar_{rad}$ loss during rock alteration. We determined new $^{40}Ar/^{39}Ar$ ages for the Cantwell volcanic rocks in order to test and refine the existing age data. Unlike previous reports of radiometric ages for volcanic rocks in the region, our age data are directly linked to the stratigraphy of the upper Cantwell Formation (Figure 4). Our new $^{40}Ar/^{39}Ar$ ages, from nine aphanitic lava samples, define a late Paleocene to early Eocene age for the Cantwell volcanic rocks in the western Healy quadrangle. Plateau ages from the base and near the top of the type section are 57.8 +/- 0.3 and 55.7+/- 0.3 Ma, respectively (Figure 5). Ages from the remaining samples range from 59.8+/-0.2 to 55.5+/-0.2 Ma (Table 1). In addition, ages were determined for two volcanic clasts from a conglomerate at the base of the upper Cantwell Formation at Double Mountain (Figure 4 and Table 1). Our $^{40}Ar/^{39}Ar$ ages are quoted to the +/- 1 sigma level and calculated using the standards of *Steiger and Jaeger* [1977]. For most samples, plateau ages are reported. These plateaus were identified on the basis of a sample having three or more contiguous fractions within 2 s of each other and constituting greater than 60% of gas release. Procedures for the $^{40}Ar/^{39}Ar$ analyses are presented in the appendix. In summary, our new age data show that the upper Cantwell Formation represents a period of volcanism ranging from ~59.8 to 55.5 Ma. The new dates also indicate that a previously unrecognized major hiatus exists between the Late Cretaceous lower Cantwell Formation and the late Paleocene-early Eocene upper Cantwell Formation.

4. Overview of Volcanic Stratigraphy

In our analysis we made bed-by-bed stratigraphic measurements across more than 7000 m of the upper Cantwell Formation using a Jacob staff at well-exposed sections across the western Healy quadrangle (Figure 4). This work was completed during the summers of 1994 through 1996. These new stratigraphic data, combined with the regional stratigraphic mapping of *Gilbert and Redman* [1975], *Gilbert et al.* [1976], and *Nye* [1978], provide the necessary details to evaluate correlations of volcanic rocks across the study area. The upper Cantwell Formation includes a complex stratigraphy dominated by lava flows (representing ~70% of the studied outcrops) and a lower proportion of volcaniclastic deposits (~20% pyroclastic and 10% epiclastic). Geochemically, the lavas can be grouped according to composition into mostly mafic (basalt and basaltic andesite) and felsic (rhyolite, dacite, and trachyte) types with fewer intermediate (andesite) units [*Cole et al.*, 1996; *Cole*, 1998]. Detailed petrographic and textural data of the upper Cantwell Formation lavas are described by *Gilbert et al.* and *Nye*. Some of the volcaniclastic deposits are described by *Cole et al.* [1996] and *Slaugenhoup et al.* [1997].

The thickest preserved section of the Cantwell volcanic rocks, which was designated as the type section by *Gilbert et al.* [1976], is located along the east side of the upper Teklanika River (section TEK in Figure 3). We concur with *Gilbert et al.* that this should be the type section for the upper Cantwell Formation because it includes the most complete representation of volcanic units. *Gilbert et al.* estimated an approximate minimum thickness of 3750 m for this section; we found, on the basis of our bed-by-bed measurements, that there are closer to 2750 m of continuous strata of volcanic rocks (Figure 6). Because the upper Cantwell Formation is unconformably overlain by upper Tertiary or Quaternary deposits, the total original thickness of volcanic rocks is not known.

The upper Cantwell Formation in the vicinity of the type section is divided by *Gilbert and Redman* [1975] and *Gilbert et al.* [1976] into six mappable units and is further divided by *Nye* [1978] into eight mappable units. For comparison purposes the divisions of *Gilbert et al.* [1976] are shown in Figure 6. We have found that correlations can be made across the study area for the broadly defined compositional units, but detailed correlations of individual beds or volcanic facies are hindered by complex lateral facies changes, especially in the lower portion of the upper Cantwell Formation (Figure 4). Above the laterally discontinuous lower volcanic deposits there is a more regionally continuous alternating succession of mafic- and felsic-dominated lavas with thinner localized intervals of fluvial volcaniclastic and felsic pyroclastic deposits.

Our new age data reveal that the lowermost volcanic rocks are older in the southwestern part of the basin (Figure 4), which suggests that volcanic activity began toward the southwest and prograded toward the northeast. Additionally, clast compositions and paleoflow data from a fluvial volcaniclastic conglomerate at the base of the upper Cantwell Formation at the Double, Igloo, and Cathedral Mountains (DM, IM, and CM in Figure 4) reveal that Cantwell volcanic rocks were being eroded and transported from sources to the west and south of these locations [*Cole et al.*, 1996; *Slaugenhoup et al.*, 1997]. The late Paleocene and Late Triassic ages that we obtained for two representative clasts from this conglomerate confirm this interpretation, whereby a combination of intraformational reworking of the upper Cantwell Formation and erosion of Mesozoic rocks from the southern margin of the Cantwell basin supplied detritus to the Cantwell basin during the early stages of volcanism. On the

Table 1. Compilation of Radiometric Ages for the Cantwell Formation Volcanic Rocks

Sample Number	Location	Stratigraphic Level Above Lower Cantwell Fm., m	Total Gas (Integrated) Age, Ma	Plateau or Isochron Age, Ma	Rock Type, Mineral[a]	Notes[b]
		This Study ($^{40}Ar/^{39}Ar$ Step Heating)[c]				
TEK-227	base of type section, upper Teklanika River	227	58.0±0.3	57.8±0.3 (p)[d]	basalt, wr	laser seven fraction plateau, 82% ^{39}Ar gas release
TEK-2400	top of type section, upper Teklanika River	2400	55.8±0.3	55.7±0.3 (p)[d]	basalt, wr	laser eight fraction plateau, 85% ^{39}Ar gas release
CM-319	Cathedral Mountain	319	56.9±0.3	57.1±0.3 (p)[d]	basalt, wr	furnace six fraction plateau, 81% ^{39}Ar gas release
CM-588	Cathedral Mountain	588	58.4±0.2	56.5±0.2 (p)[d]	rhyolite, wr	furnace some excess argon, nine fraction plateau, 90% ^{39}Ar gas release
DM3B-234	Double Mountain	234	57.6±0.5	57.7±0.4 (p)[d]	basalt, wr	furnace four fraction plateau, 65% ^{39}Ar gas release
EFTK-198	East Fork Toklat River	198	56.5±0.6	57.0±0.4 (p)[d]	basalt, wr	laser three fraction plateau, 84% ^{39}Ar gas release
TKL-17	upper Toklat River	17	59.2±0.2	58.3±0.2 (i)[d]	basalt, wr	laser slight excess argon; nine data point isochron
TKL-356	upper Toklat River	356	55.8±0.2	55.5±0.2 (p)[d]	rhyolite, wr	laser seven fraction plateau, 64% ^{39}Ar gas release
PCM-22B	Polychrome Mountain	52	61.9±0.3	59.8±0.2 (p)[d]	basaltic andesite, wr	laser nine fraction plateau; 66% ^{39}Ar gas release
DM96-3C	Double Mountain, volcanic conglomerate clast	40	58.7±0.2	59.4±0.2 (p)[d]	rhyolite, wr	laser six fraction plateau; 80% ^{39}Ar gas release
DM96-2C	Double Mountain, volcanic conglomerate clast	40	211.2±0.8[d]	–	basalt, wr	laser integrated age; poorly constrained isochron
		Previous K-Ar Studies[e]				
15	Dick Creek	?	64.6±3.4	-	dacite, hb	from *Sherwood* [1973]
18	Mount Fellows	?	50.9±2.2	-	basalt, wr	from *Bultman* [1972]
19	Mount Fellows	?	60.4±3.1	-	diabase, w	from *Bultman* [1972]
21	Igloo Mountain(?)	?	56.6±2.4	-	basalt, wr	original source of *Wegner* [1972] has sample located at Cathedral Mountain
22	Polychrome Mountain	?	58.7±3.5	-	qtz diorite, plag	from *Gilbert et al.* [1976]
23	upper East Fork Toklat River	?	>42.9	-	basalt, wr	from *Gilbert et al.* [1976]
24	Cathedral Mountain	?	>62.2	-	andesite, plag	from *Gilbert et al.* [1976]
25	Double Mountain	?	61.0±2.8	-	basalt, wr	from *Wegner* [1972]

Fm., Formation; p, plateau; i, isochron

[a] Abbreviations are as follows: wr, whole rock; hb, hornblende; plag, plagioclase; qtz, quartz.

[b] Laser is step-heated using an argon-ion laser, measured on a VG3600 spectrometer. Furnace is step-heated using a resistance-type furnace, measured on a Nuclide 6-60-SGA spectrometer.

[c] Ages of this study were run against the McClure Mountain hornblende standard (Mmhb-1) with an age of 513.9 Ma and processed using standards of *Steiger and Jager* [1977]. Errors are quoted at ± 1σ. Analytical data and age spectra are available from the authors on request.

[d] Preferred ages as reported in the text.

[e] Sample numbers represent age data as reported by *Csejtey et al.* [1992]; original sources of dates are also shown.

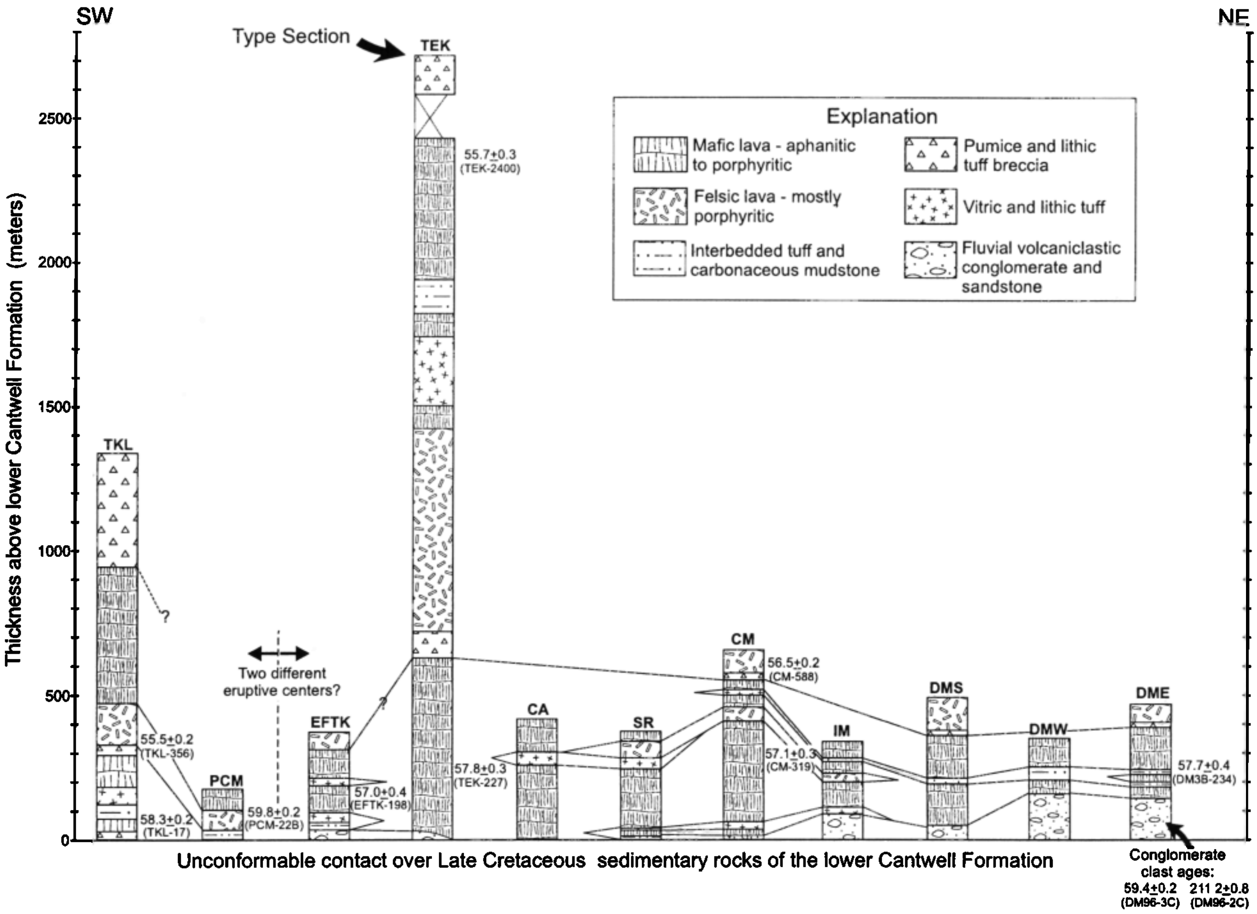

Figure 4. Stratigraphic sections, new $^{40}Ar/^{39}Ar$ age determinations, and possible correlations of volcanic assemblages in the upper Cantwell Formation. Stratigraphic sections are constructed from bed-by-bed measurements using a Jacob staff. Section TEK is the type section of the upper Cantwell Formation. See Figure 3 for section locations. CA, Calico Creek; CM, Cathedral Mountain; DME, Double Mountain east; DMS, Double Mountain south; DMW, Double Mountain west; EFTK, East Fork Toklat River; IM, Igloo Mountain; PCM, Polychrome Mountain; SR, Sanctuary River; TEK, Teklanika River; TKL, Toklat River.

basis of these predictable lateral volcanic facies changes, we suggest that an eruptive center with multiple vents was located in the vicinity of the southwestern margin of the Cantwell basin.

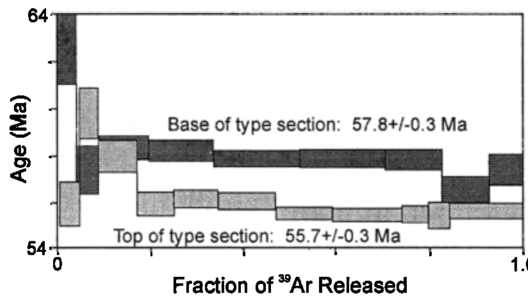

Figure 5. The $^{40}Ar/^{39}Ar$ age plateaus for aphanitic basalt samples from the base and top of the upper Cantwell Formation type section along the east side of the upper Teklanika River. See Figures 3 and 6 for section location and stratigraphic position of the samples.

5. Cantwell Formation Deformation

Detailed mapping, at a scale of 1:12,000, was conducted of the Cantwell Formation in the western Healy quadrangle during the summers of 1996-1998. The mapping reveals that in most parts of the study area the contact between the lower and upper Cantwell Formations is an angular unconformity (Figures 3, 7, and 8). In a few areas, for example at Double Mountain, the lower and upper Cantwell Formations are in disconformable contact (Figures 7 and 9). According to our new age data, which reveal that the base of the upper Cantwell Formation is ~60-58 Ma, this unconformity represents a 10-20 Ma hiatus above the lower Cantwell sedimentary rocks, which are Late Cretaceous in age (Campanian-Maastrichtian, ~80-70 Ma) [*Trop*, 1996; *Ridgway et al.*, 1997] (Figures 2, 4, and 7). We have been able to identify two separate deformational events that occurred before and after this unconformity developed. The first event occurred during Late Cretaceous and early Paleocene time and affected the lower Cantwell Formation. The second event occurred after Cantwell volcanism (after

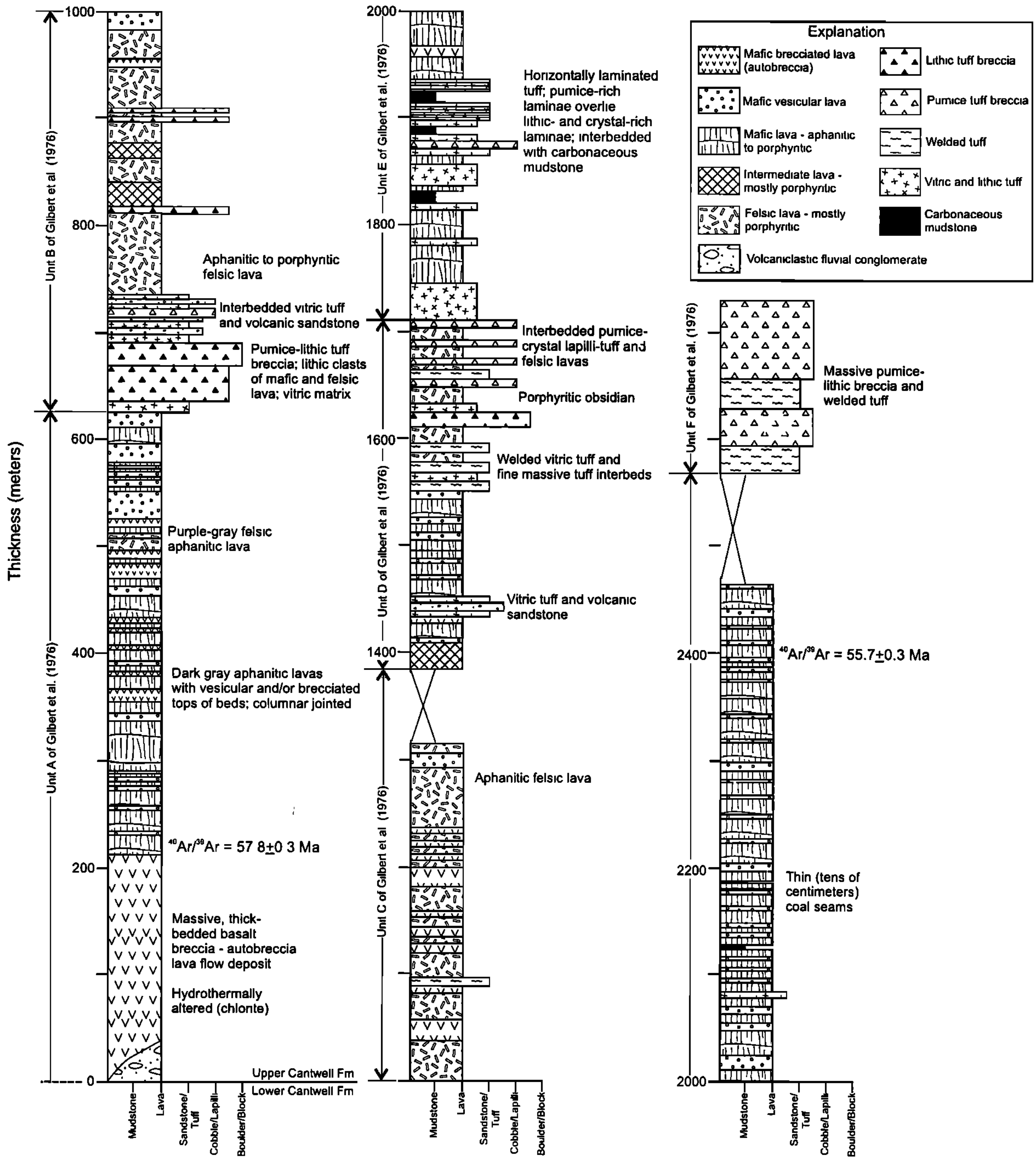

Figure 6. Detailed stratigraphy of the upper Cantwell Formation type section along the east side of the Teklanika River south of Calico Creek (see Figure 3 for section location). Data was collected as bed-by-bed measurements using a Jacob staff. Approximate boundaries of compositional units as defined by *Gilbert et al.* [1976] are shown for comparison. Radiometric ages shown were determined as part of this study (Table 1).

early Eocene time) and affected both the lower and upper Cantwell Formations.

5.1. Late Cretaceous-Early Paleocene (80-60 Ma) Deformation

This episode of deformation resulted in folding and thrust faulting of the lower Cantwell Formation. The lower Cantwell Formation folds vary from upright plunging, reclined, and recumbent and are open to isoclinal (interlimb angles from 10° to 95°) (Figures 7, 10a, and 10b). These folds have wavelengths of ~0.5-6 km and include symmetrical and asymmetrical forms with rounded to angular (kinked) hinge areas. *Hickman et al.* [1977, 1990] and *Sherwood* [1979] report similar fold styles and also chevron folds of the lower

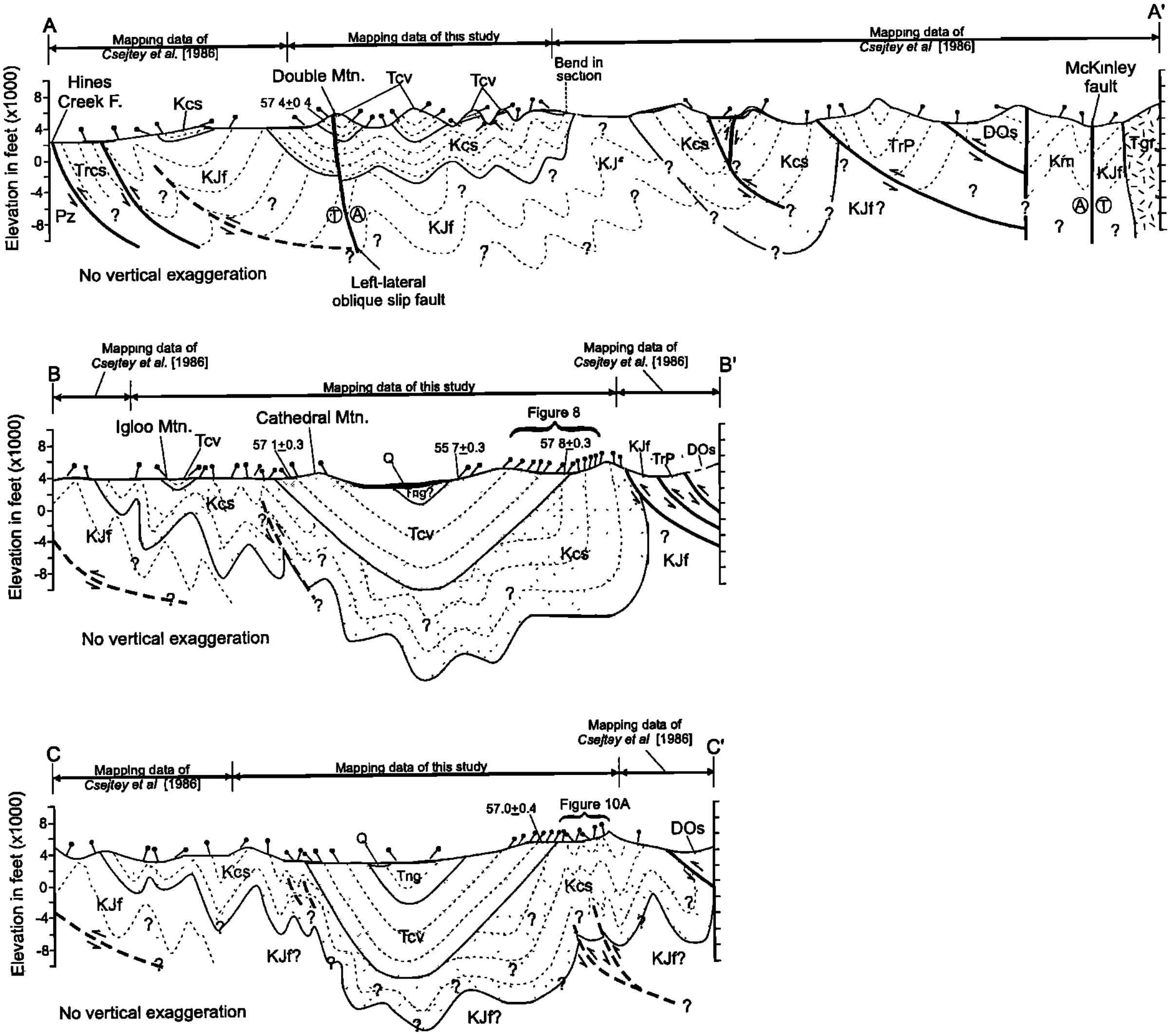

Figure 7. Cross sections showing structural relationships between the lower and upper Cantwell Formation and adjacent rock units. Cross sections are constructed from mapping data collected in this study and from mapping data of *Csejtey et al.* [1986] as shown. Note that the lower Cantwell Formation is shown to thicken toward the south, after *Ridgway et al.* [1997]. Inferred faults in the subsurface are dashed. Uncertain contacts and fold geometries in the subsurface are queried. Unit abbreviations are as shown in Figure 3. Dip isogons show distribution of surface data from which the cross sections are interpreted. Circled letters depict the sense of motion on strike-slip faults (T, toward; A, away). Locations of cross-section lines are shown in Figure 3.

Cantwell Formation in the eastern Healy quadrangle (~40-80 km east of our study area). Overall, lower Cantwell folding axes trend east to ENE across the study area (Figures 3 and 11a).

During this shortening event, the lower Cantwell Formation was also deformed by intraformational thrust faults and associated fault-related folding (Figures 7 and 10a). On the basis of outcrop exposures and our cross-section interpretations these intraformational thrust faults have offsets of tens of meters to a few hundred meters and most likely formed to accommodate tightening in the hinge areas of larger folds (Figure 10a). Blind thrust faults that we interpret to crosscut the lower Cantwell Formation could be imbricates of regional thrust faults that are exposed along the southern basin margin and which exhibit much greater stratigraphic separation (e.g., Paleozoic rocks placed over Cretaceous rocks) (Figure 7).

5.2. Post-Early Eocene (<55.5 Ma) Deformation

A second deformation event resulted in folding of the upper Cantwell Formation and further shortening (tightening) of older lower Cantwell folds. Folds in the upper Cantwell Formation are upright plunging and open (interlimb angles from 90° to 130°) with wavelengths of ~5-12 km (Figures 7 and 10c). These folds are generally parallel and symmetrical with rounded hinge areas and trend northeast-southwest. Note that there is a distinct difference in the geometry and orientation of lower Cantwell and upper Cantwell folds (Figures 3, 10, and 11). *Gilbert et al.* [1976] and *Nye* [1978] made similar observations and report that recumbent and

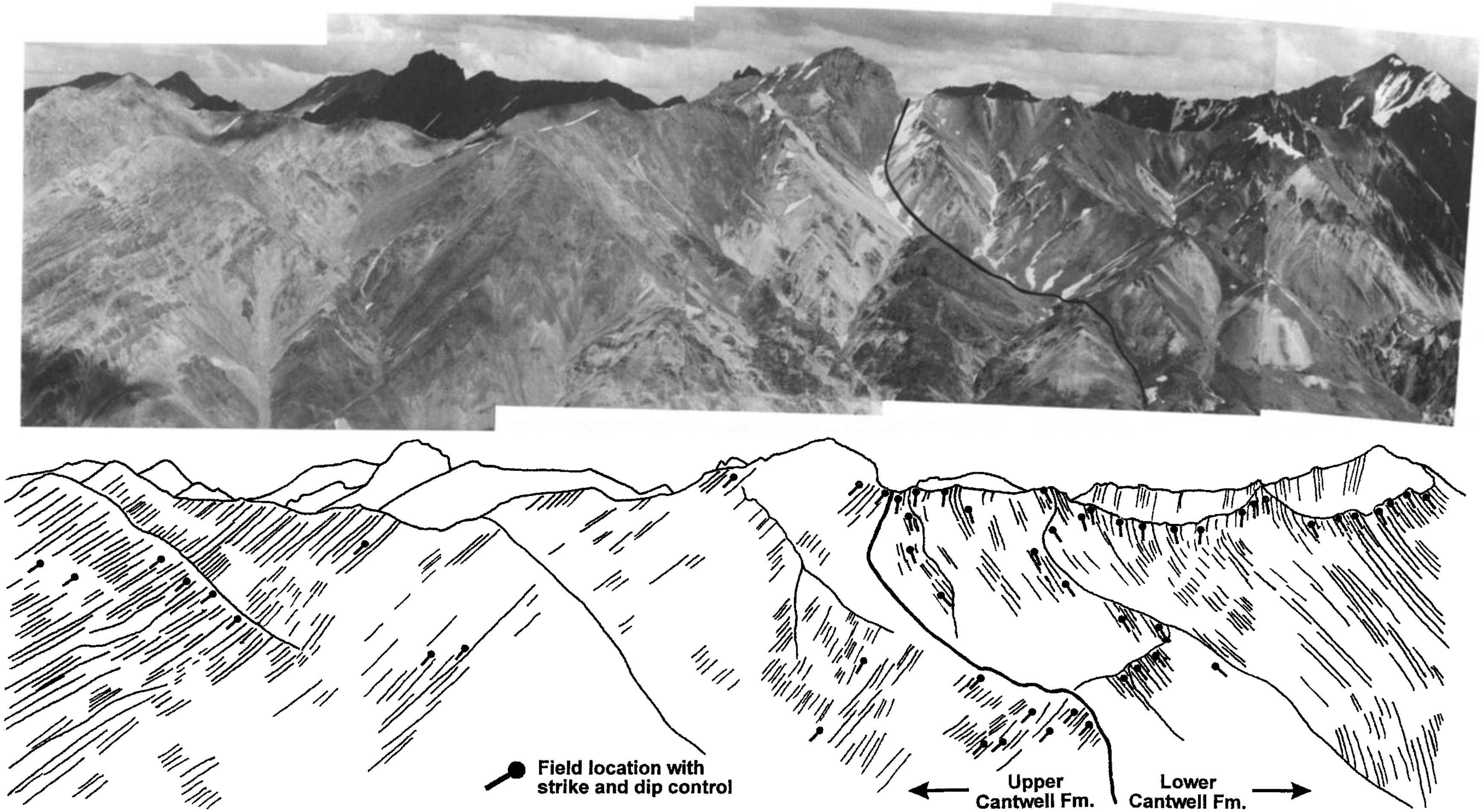

Figure 8. Photomosaic showing the lower and upper Cantwell Formations along the east side of the upper Teklanika River (view to the east). This is the type section for the upper Cantwell Formation. Note the angular unconformity between the lower and upper Cantwell Formations. The lower Cantwell Formation in this area is part of an overturned anticline, and the upper Cantwell strata dip uniformly ~40° to 50° toward the northwest. Location of photograph is shown in Figure 3.

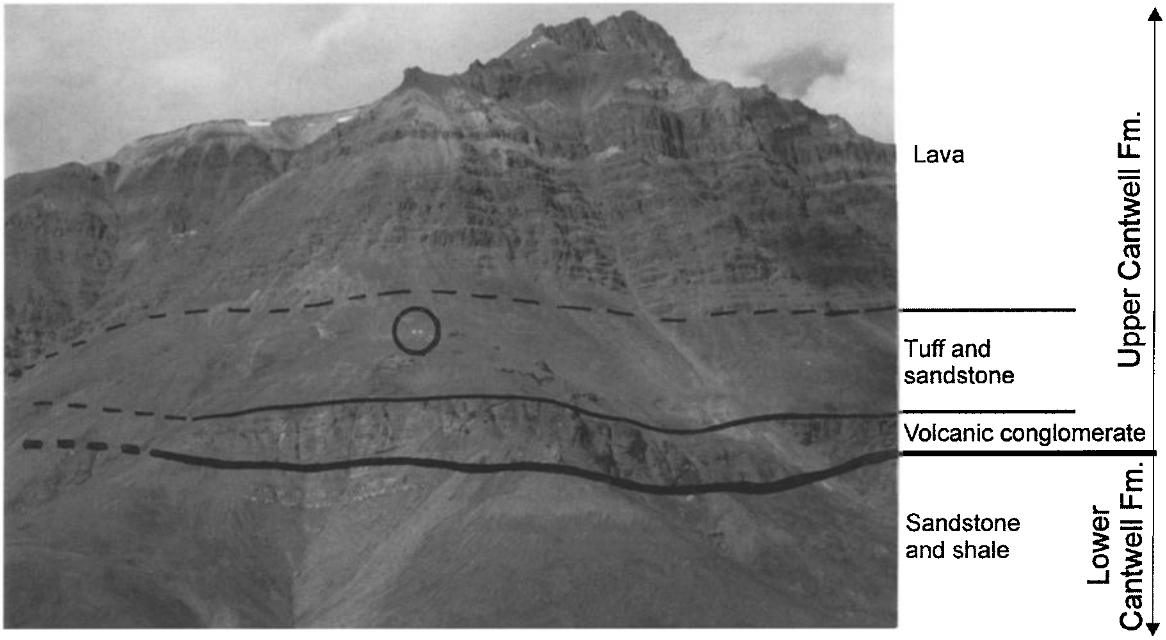

Figure 9. Disconformable contact (heavy line) between the lower and upper Cantwell Formations at Double Mountain. Contacts are dashed where covered. Tents (circled) are shown for scale.

isoclinal folds are present in the lower Cantwell Formation but are absent in the more openly folded upper Cantwell Formation. Some of the fold variations between the lower and upper Cantwell Formations could be attributed to lithologic competency contrasts where the thicker-bedded and more competent volcanic rocks of the upper Cantwell Formation might be expected to form larger-wavelength folds [e.g., *Curie et al.*, 1962]. We argue, however, that the discordant contact and the difference in folding axis orientation between these units indicate two distinct folding events. Furthermore, the unconformity that separates the lower and upper Cantwell Formations has been folded and rotated, which implies subsequent episode(s) of contractional deformation [e.g., *Riba*, 1976; *Ridgway et al.*, 1997]. Both fold generations display evidence for flexural slip folding mechanisms (bedding plane slip lineations with slip directions nearly perpendicular to hinge lines).

During this deformation event, rocks of the lower and upper Cantwell Formations were also crosscut by at least four sets of macroscopic-scale faults that we define on the basis of fault plane orientation, slip direction, and sense of motion (Figure 11b). One set of normal and normal oblique slip faults trends northwest-southeast; a second set of reverse oblique slip faults trends northeast-southwest; a third set of right-lateral slip faults trends nearly east-west; and a fourth set of left-lateral and left-lateral oblique slip faults trends nearly north-south. Most of these faults are steeply dipping (>45°) (Figure 11b), have well-developed slip lineations (Figure 12), and have stratigraphic separations of a few tens of meters (and therefore are not shown in Figure 3). On the basis of offset stratigraphic contacts and well-exposed fault planes, we were able to directly measure the net slip of steeply dipping reverse oblique and left-lateral faults at Double Mountain and at Tattler Creek (Figure 3) as ~250 m and 310 m with slip plunges of 27° and 15°, respectively. A fifth fault set, which was found only in the area of section SR along the west side of the Sanctuary River, consists of northeast trending normal faults (Figure 11b). Characteristics of each of these fault sets are typical of faults that form under shallow crustal conditions (generally less than ~5-km depth) [*Sibson*, 1977; *Scholz*, 1990]. Most of the observed faults, for example, show evidence for displacement by frictional sliding (smooth, polished surfaces with groove lineations) (Figure 12) and/or pressure solution slip (fault planes coated by elongate quartz mineral fibers).

5.3. Kinematic Interpretations of Cantwell Deformation

Deciphering the folding history of the rocks below and above the lower-upper Cantwell unconformity provides an opportunity to determine changes in Late Cretaceous to early Tertiary deformation in south central Alaska. *Hickman* [1974], *Sherwood* [1979], and *Hickman et al.* [1977, 1990] reported east-northeast trending fold axes for rocks of the lower Cantwell Formation in the eastern Healy quadrangle (between ~148° and 149° longitude), which they interpreted to be a result of middle Eocene or younger (post-Cantwell) north-northwest directed shortening. *Hickman et al.* [1977, 1990] also depict that the Cantwell volcanic rocks overlie the Cantwell sedimentary rocks with little or no discordance, thereby assuming that the entire Cantwell Formation has experienced the same deformation history. A different deformation history is apparent from results of our study. Poles to bedding for the lower Cantwell Formation in the western Healy quadrangle (Figure 11a) reveal a nearly east-west folding axis for these rocks which is consistent with results of *Hickman*, *Sherwood*, and *Hickman et al.* Our new

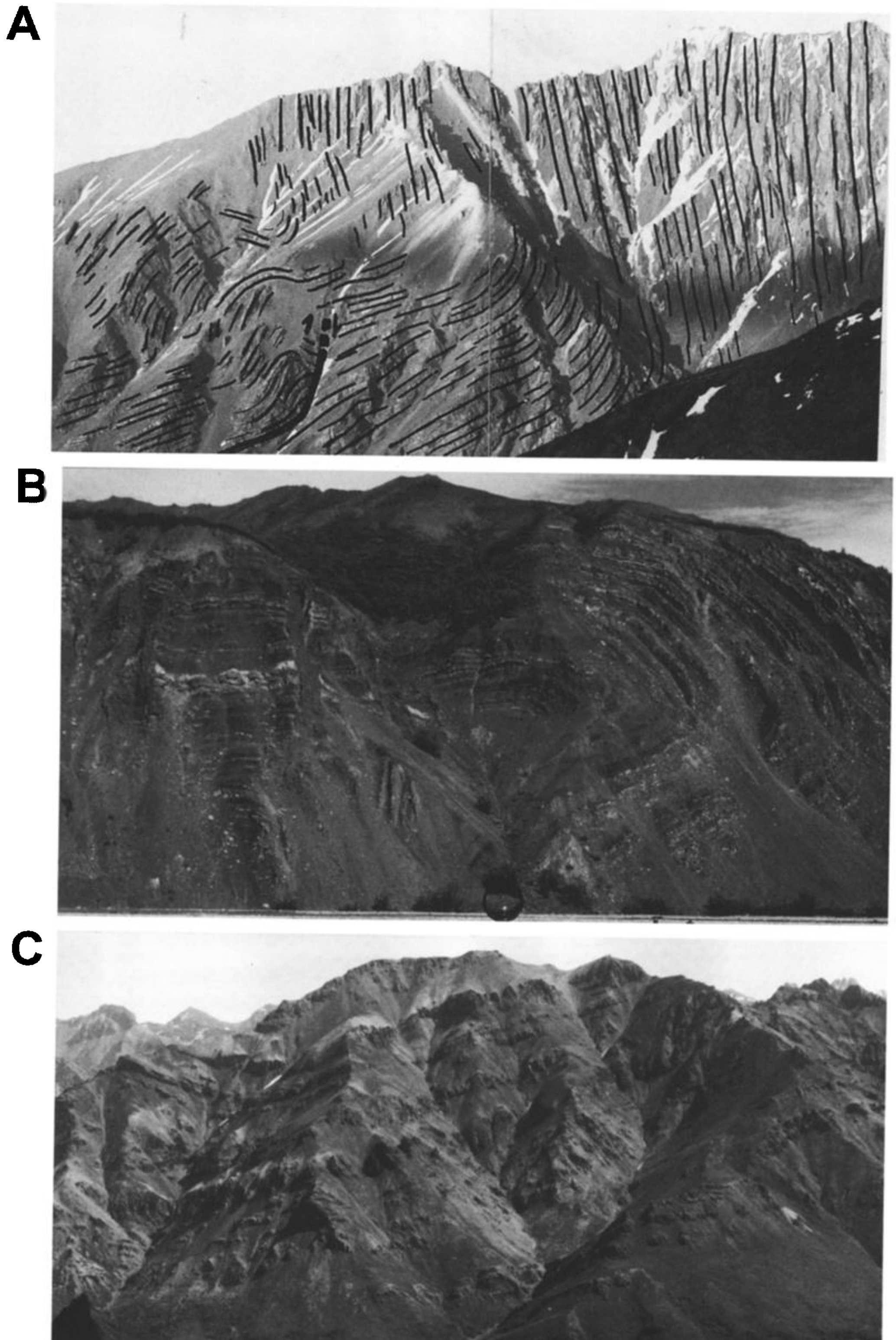

Figure 10. Photographs of folds in the Cantwell Formation. (a) Overturned syncline and intraformational thrust fault in the lower Cantwell Formation in the upper East Fork Toklat River area. View is toward the east; outcrop face is ~500 m from the valley to the ridge crest. Location of photograph is shown in Figure 3. (b) Recumbent fold of the lower Cantwell Formation crosscut by mafic dikes which are probably related to upper Cantwell magmatism. Person (circled) is shown for scale. (c) Broad, open fold of the upper Cantwell Formation at Cathedral Mountain. View is toward the northeast; exposed face is ~600 m in height.

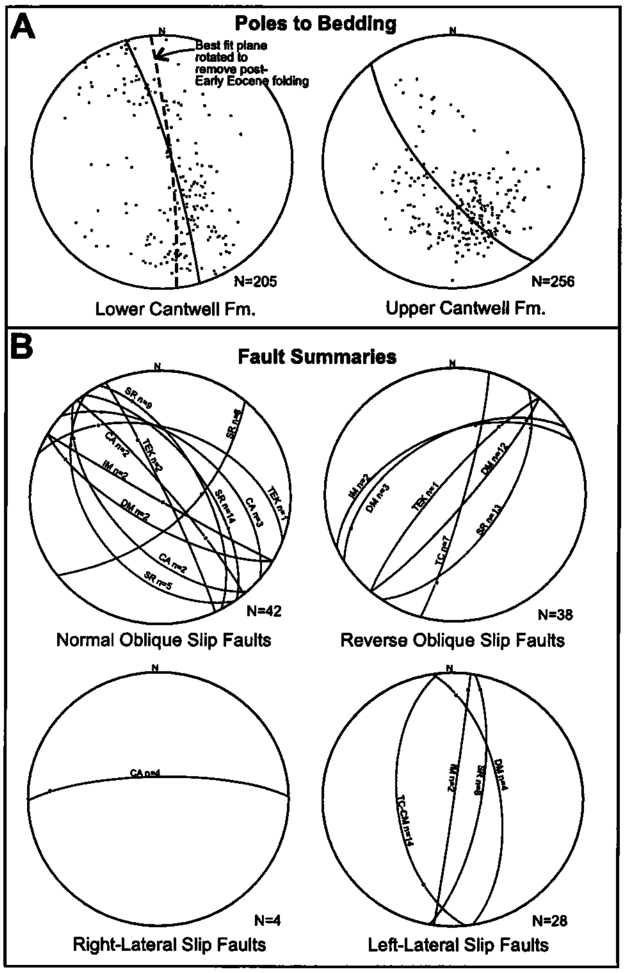

Figure 11. Patterns of deformation measured in rocks of the Cantwell Formation. All stereoplots are lower hemisphere equal area projections. (a) Poles to bedding showing a difference in average folding axis trends for the lower Cantwell Formation and upper Cantwell Formation. Characteristics of folds in each unit are discussed in the text. Also, see Figures 3 and 7 for the distribution and geometry of folds in the study area. (b) Summary of small-scale faults measured in the entire Cantwell Formation. Great circles represent the average fault trends for different locations in the study area. Points represent average slickenline trends on these faults. The number of faults measured at each field location is shown. Abbreviations are as follows: CA, upper Calico Creek area; CM, southern part of Cathedral Mountain; DM, Double Mountain; IM, Igloo Mountain; SR, area along west side of Sanctuary River in vicinity of section SR; TC, Tattler Creek area; TEK, upper Teklanika River area. Map locations are shown in Figure 3.

age and unconformity data show, however, that this folding must have occurred before late Paleocene time (before upper Cantwell volcanism) (Figure 13a). In contrast, upper Cantwell rocks (above the unconformity) have been folded along a northeast axis (Figure 11a), implying a change in the direction of maximum compression from north-south to northwest-southeast after upper Cantwell (early Eocene) time.

The northeast trending upper Cantwell folds, together with the orientations of the macroscopic normal, reverse, and strike-slip faults that crosscut the entire Cantwell Formation, are consistent with deformation in a zone of right-lateral simple shear that had the same orientation as that of the McKinley fault in the study area (Figure 13b). *Sherwood* [1979] and *Brewer* [1982] also interpret ENE-trending en echelon thrust faults and folds that crosscut the Cantwell Formation and older rocks in the eastern Healy quadrangle to have formed in response to right-lateral simple shear along the McKinley fault. Most major strike-slip faults around the world are in domains of simple shear [*Sylvester*, 1988]. On the basis of experimental models and observations of surface ruptures during earthquakes, there are predictable types and orientations of structures that form within regions of distributed shear along strike-slip faults [*Tchalenko*, 1970; *Tchalenko and Ambraseys*, 1970; *Wilcox et al.*, 1973; *Sharp*, 1976; *Harding et al.*, 1985] (also see summaries of *Christie-Blick and Biddle* [1985] and *Sylvester* [1988]). These predicted structures, as they might occur along the McKinley fault during an episode of right-lateral simple shear, are shown superimposed on a strain ellipse in Figure 13b; there is remarkable consistency between the set of structures measured in the Cantwell Formation and the predicted simple shear structures. Typically, geologic examples are more complicated than the simple shear models owing to the sequential, rather than instantaneous, development of structures, the potential for rotation of early formed structures during protracted deformation, and the heterogeneous nature of the rock record [*Harding et al.*, 1985; *Christie-Blick and*

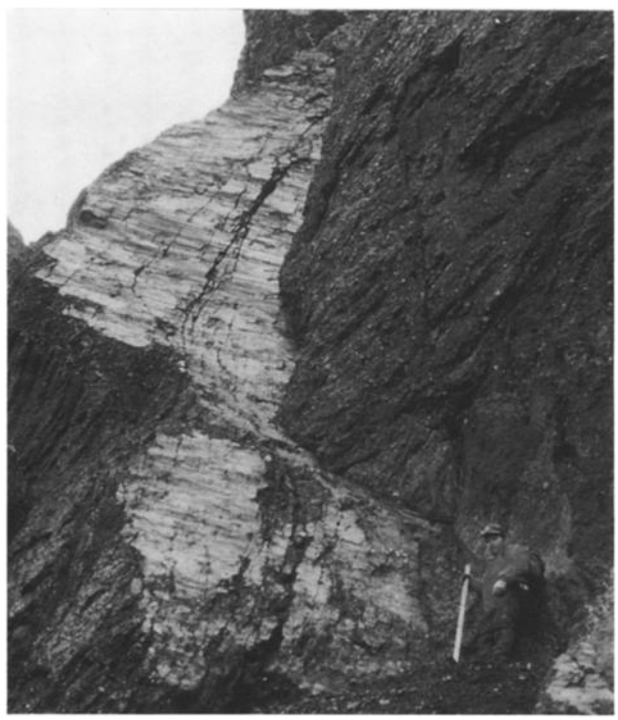

Figure 12. Oblique slip fault with grooved surface through the base of the upper Cantwell Formation at Double Mountain.

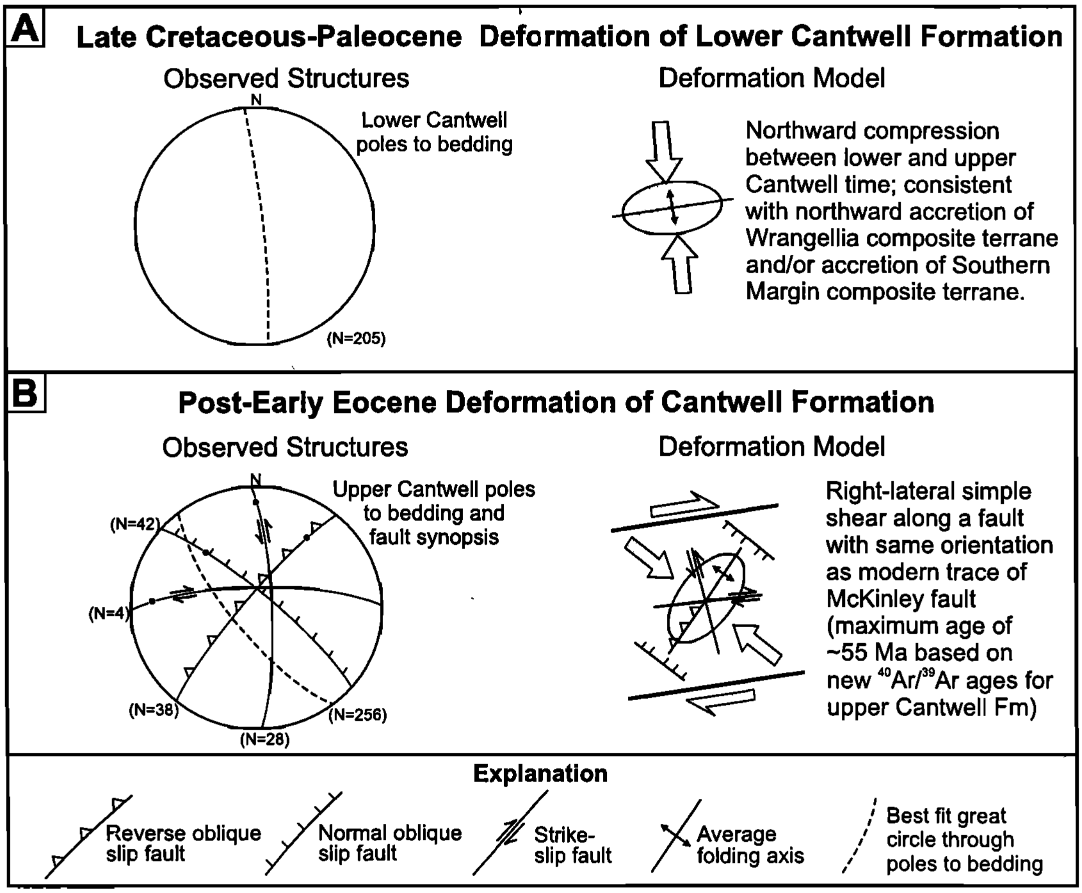

Figure 13. Synthesis and interpretation of deformation recorded in rocks of the Cantwell Formation in the western Healy quadrangle. (a) Deformation of the lower Cantwell Formation. (b) Deformation of the entire Cantwell Formation (based on folding of the upper Cantwell Formation and faults that crosscut the lower and upper Cantwell Formations). Synoptic diagram shows average trends of fault planes as single great circles; representative slickenline trends are shown as dots. Not shown is a normal slip fault set that trends northeast; interpretation for these faults is uncertain, but they most likely formed during an episode of deformation different from those shown above. All stereoplots are lower hemisphere equal area projections. Poles to bedding data reveal a change from northward to northwestward directed shortening between lower Cantwell and post-upper Cantwell time. Complete stereoplot data are shown in Figure 11. Deformation models show inferred strain ellipse for each episode of deformation. The predicted types and orientations of structures that are shown on the strain ellipse depicting right-lateral simple shear are from *Harding* [1974] and *Christie-Blick and Biddle* [1985].

Biddle, 1985]. The predictive models may therefore be most applicable to the early stages of simple shear during a single tectonic event [*Harding et al.*, 1985]. On this basis, if the observed Cantwell structures do represent simple shear deformation, then we suggest that they formed during the same non-protracted episode of right-lateral slip along the McKinley fault and have not subsequently been rotated by a significant amount with respect to the McKinley fault. Our $^{40}Ar/^{39}Ar$ ages for the Cantwell volcanic rocks show that right-lateral strike-slip deformation of the Cantwell Formation occurred after 55.5 Ma. The minimum timing for this deformation is not as well defined, but younger rocks in the study area (Usibelli Group and Nenana Gravel) (Figures 1 and 2) unconformably overlie the Cantwell Formation and are less deformed [*Wahrhaftig* 1970a, b, c; *Csejtey et al.*, 1986, 1992]. This implies that the episode of strike-slip deformation that affected the Cantwell Formation occurred sometime during middle Eocene through early Oligocene time.

5.4. Shortening Estimates

The total amount of shortening recorded by the lower Cantwell Formation in the study area ranges from 15 to 20 km (29-37%) on the basis of measuring bed lengths on our cross sections through the Cantwell Formation between the McKinley and Hines Creek faults (Figure 7). These faults mark the approximate north-south depositional limits of the Cantwell Formation within the Cantwell basin and provide a basis for estimating percent shortening. The amount of shortening of the lower Cantwell Formation (based on tighter folds and steeper fold limbs) increases toward the south in the vicinity of exposed thrust faults and the McKinley fault zone. *Hickman* [1974], *Sherwood* [1979], and *Hickman et al.* [1990]

found similar results for shortening of the lower Cantwell Formation in the eastern and central portion's of the Healy quadrangle; they estimated that shortening increased southward between the Hines Creek and McKinley faults from 24 to 50%. Our estimates for shortening of the upper Cantwell Formation range from 1 to 5 km (2-14%) also based on measuring bed lengths and assuming a north-south depositional limit between the McKinley and Hines Creek faults. Shortcomings in our restorations include uncertainty in the geometry of lower Cantwell beds projected into the subsurface, uncertainty of the presence of blind thrust faults that may have influenced folding of the lower Cantwell Formation, the absence of pinning points in correlative undeformed strata, and the lack of control on the amount of shortening accommodated by internal deformation [e.g., *Mitra*, 1994]. There are also inherent problems with restoring cross sections in areas of strike-slip deformation where the assumption of plane strain is questionable. Accordingly, we cannot consider our cross sections to be balanced. In addition, our estimates do not resolve shortening that may have occurred during uplift of the central Alaska Range over the past 5-6 Myr [*Plafker et al.*, 1991; *Fitzgerald et al.*, 1995]. We do consider our estimates of shortening to be first-order approximations that reveal a difference in the amount of contraction experienced by the lower and upper Cantwell Formations. From these estimates it appears that shortening of the lower Cantwell Formation due to northward compression was at a minimum of ~10-19 km (15-23%) and that shortening due to subsequent northwest-compression (consistent with right-lateral simple shear along the McKinley fault) was at a minimum of ~1-5 km (2-14%) (~15-20 km or 29-37% cumulative shortening of the lower Cantwell Formation).

6. Regional Tectonic Implications of Cantwell Basin Kinematics

Deformation of the Cantwell Formation can be partitioned into a phase of regional north-south shortening and a subsequent phase of northwest-southeast shortening that is consistent with right-lateral strike-slip deformation along the McKinley fault. We propose that this kinematic framework for Cantwell basin evolution serves as a template for linking events of terrane collision, strike-slip faulting, and regional plate motions which shaped south central Alaska.

6.1. Timing and Response to WCT Accretion

The WCT was accreted to southern Alaska during Late Jurassic through Late Cretaceous time [*Csejtey et al.*, 1982; *Nokleberg et al.*, 1985; *Plafker et al.*, 1989; *Wallace et al.*, 1989; *McClelland et al.*, 1992]. We attribute the initial development of the Cantwell basin between 80 and 70 Ma and subsequent north directed shortening of the lower Cantwell Formation between 70 and 60 Ma to the final accretion and suturing of the WCT to southern Alaska (Figure 14a). The driving force for final WCT suturing and resultant north-south compression during early Paleocene time was probably the continued northward underplating of the Kula plate beneath southern Alaska [*Wallace and Engebretson*, 1984; *Lonsdale*, 1988] along with accretion of the Southern Margin composite terrane to the trailing edge of the WCT (timing and events summarized by *Plafker et al.* [1994]).

Absence of evidence for north-south shortening of the upper Cantwell Formation indicates that northward displacement of the WCT and any associated deformation had ended by late Paleocene time (~59.8 Ma) at the onset of Cantwell volcanism. This is consistent with existing paleomagnetic data, which show that the Cantwell volcanic rocks and other early Tertiary volcanic rocks that crosscut the WCT to the south have not experienced any significant latitudinal drift with respect to each other and North America [*Hillhouse and Grommé*, 1982; *Hillhouse et al.* 1985; *Panuska et al.* 1990; *Hillhouse and Coe*, 1994].

6.2. Cantwell Volcanism and Regional Magmatism

Our new age data along with new geochemical data reported by *Cole* [1998, 1999] confirm that Cantwell volcanism immediately followed and was distinctive from a Late Cretaceous-early Paleocene episode of regional subduction-related magmatism in south central Alaska (Alaska Range belt of *Wallace and Engebretson* [1984] and Alaska Range-Talkeetna Mountains belt of *Moll-Stalcup et al.* [1994]). Our structural data indicate that this change from regional subduction magmatism to Cantwell volcanism coincided with the end of northward compression due to WCT accretion and preceded an episode of strike-slip deformation along the McKinley fault. Subsequently, the locus of subduction-related magmatism became reestablished to the south as the Oligocene to recent Alaska-Aleutian arc [*Scholl et al.*, 1986; *Wallace and Engebretson*, 1984; *Moll-Stalcup et al.*, 1994]. The southward shift in subduction magmatism was probably linked to the final accretion of the WCT and continued growth of the Southern Margin composite terrane during which the Kula trench shifted southward. In this scenario, Cantwell magmas could have originated as remnant Late Cretaceous-early Paleocene subduction-related magmas or perhaps were formed by partial melting of enriched subcontinental lithospheric mantle due to high heat flow caused by the preceding subduction magmatism [e.g., *Hudson*, 1994]. In either case, we propose that Cantwell magmas migrated through the crust along planes of weakness associated with the WCT suture zone and/or the incipient McKinley fault zone. This is supported by our volcanic stratigraphic and facies data (Figure 4) which indicate that Cantwell eruptive centers were located somewhere to the southwest of the present Cantwell outcrop belt (i.e., toward the McKinley fault zone) (Figure 14b) [*Cole et al.*, 1996].

6.3. Kula-North American Plate Interactions

The timing of Cantwell volcanism and the transition from north-south shortening to strike-slip deformation that we outline are consistent with several significant tectonic events that have shaped the northeastern Pacific margin. First, the episode of post-early Eocene (post 55.5 Ma) strike-slip deformation of the Cantwell Formation was coeval with dextral offset along several regional faults in south central and southeastern Alaska (Figure 2). For example, *Roeske et al.* [1993] and *Smart et al.* [1996] interpret that several hundred kilometers of dextral slip occurred along the Border Ranges

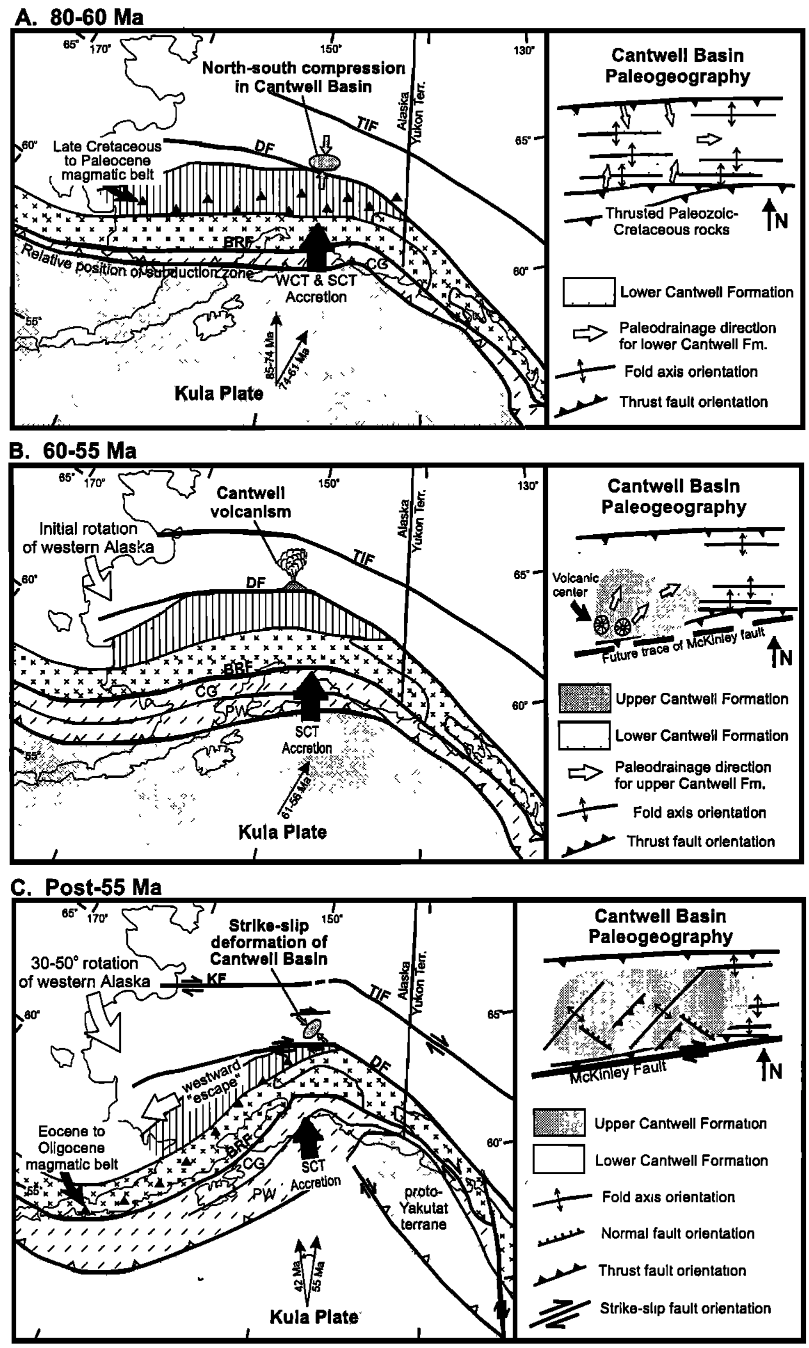

Figure 14. Late Cretaceous-early Eocene tectonic reconstruction diagrams for south central Alaska showing regional context of Cantwell basin development. Symbols and abbreviations for tectonic reconstruction maps are as shown in Figure 1. Schematic strain ellipses are shown for key deformation events. Tectonic reconstructions are modified from *Plafker and Berg* [1994]. Kula plate motions are from *Wallace and Engebretson* [1984], *Engebretson et al.* [1985], and *Lonsdale* [1988]. Magmatic belt positions are from *Wallace and Engebretson* [1984] and *Moll-Stalcup et al.* [1994]. Cantwell basin paleogeography and deformation data are from this study. The paleogeographic diagrams are meant to depict relative orientations and crosscutting relationships of stratigraphic units and sets of structures; these are not drawn to scale. See Figures 11 and 13 for the detailed structural data upon which these diagrams are based.

fault in southeastern Alaska at ~55-50 Ma. This is consistent with paleomagnetic data which reveal that parts of the SCT (Chugach-Prince William terranes) experienced 13+/-9° (minimum of ~400 km) of northward displacement from 57 to 45 Ma [*Coe et al.*, 1985; *Bol et al.*, 1992]. This episode of regional strike-slip faulting was coeval with a major northwestward shift in Kula plate motion which occurred at ~54 Ma (56 Ma event of *Wallace and Engebretson* [1984] and

Lonsdale [1988] recalibrated to new magnetic anomaly timescale of *Cande and Kent* [1992]). The plate shift resulted in a decrease in the convergence angle between the Kula plate and southeastern Alaska-western Canada (Figures 14b and 14c). With lower convergence angles there is a predictable increase in the amount of strain partitioning along continental margins from trench-parallel thrust faults to trench-parallel strike-slip faults [*Tikoff et al.*, 1994]. Accordingly, oblique subduction of the Kula plate was probably an important mechanism for post-early Eocene dextral slip and the northward transport of accreted terranes along strike-slip faults in southeastern Alaska.

The same argument that oblique plate convergence was a driving mechanism for strike-slip faulting in south central Alaska (i.e., along the McKinley fault) cannot be made as strongly as it can for southeast Alaska. Plate reconstruction models depict that even after the northwestward shift in Kula plate motion, there remained a high angle of convergence between the Kula plate and south central Alaska in the vicinity of present-day Cook Inlet (~150° longitude) (Figures 14b and 14c). High angles of convergence are not predicted to result in significant amounts of strike-slip along trench-parallel fault systems [*Tikoff et al.*, 1994]. Determining the precise convergence angle between the Kula plate and southern Alaska and therefore the potential degree of strike-slip strain partitioning, is complicated by uncertainties in the orientation of the southwestern margin of Alaska during the clockwise rotation that occurred between ~68 and 44 Ma (paleomagnetic data summarized by *Hillhouse and Coe* [1994]). Nevertheless, strike-slip faulting in south central Alaska can be linked to regional tectonic events through a model of escape tectonics whereby westward extrusion of crustal fragments from interior Alaska occurred along right-lateral slip faults in response to high-angle northward convergence in the Gulf of Alaska region [*Scholl and Stevenson*, 1991; *Scholl et al.*, 1994; *Dumitru et al.*, 1995]. In this hypothesis, northward directed terrane accretion along the Gulf of Alaska region resulted in "trench clogging" by early to middle Eocene time [*Scholl et al.*, 1994]. This resulted in intense northward compression and "indentation" along the Gulf of Alaska which, coupled with the northwestward shift in Kula plate motion, drove crustal fragments westward along right-lateral slip faults from interior Alaska toward the Bering Sea [*Scholl and Stevenson*, 1991; *Scholl et al.*, 1994]. In this context the Cantwell basin was folded and partially uplifted between Late Cretaceous and early Paleocene time during northward terrane accretion and suturing (trench clogging), and it was then deformed during the westward transfer of terranes along right-lateral strike-slip fault systems (escape tectonics).

We recognize that instead of right-lateral simple shear, an alternative hypothesis for post-early Eocene deformation of the Cantwell Formation might involve regional northwest-southeast compression of south central Alaska. During such an event the post-early Eocene structures that crosscut the Cantwell Formation could have formed in response to pure shear deformation. This alternative hypothesis, however, is not consistent with available plate reconstructions. For example, even after the Kula plate experienced a northwestward shift, there remained a relatively high convergence angle (north-northwestward) along the south central Alaska margin. In this case, there is not an obvious plate-scale driving mechanism for regional northwest-southeast shortening (i.e., pure shear deformation) in the region of the Cantwell basin. Our preferred hypothesis for deformation by right-lateral simple shear is most consistent with current plate reconstruction models and is also consistent with the large numbers of studies (discussed earlier) that document episodes of early Tertiary right-lateral slip along major fault systems in south central Alaska.

7. Summary of an Accretionary to Strike Slip Transition

The kinematics of Cantwell basin development provide evidence for a Late Cretaceous to early Tertiary transition from regional north directed compression to right-lateral strike-slip deformation along the McKinley fault in south central Alaska. We can summarize this transition as four stages of Cantwell basin evolution: (1) Late Cretaceous Cantwell basin development and synorogenic sedimentation of the lower Cantwell Formation during regional north directed compression, (2) Paleocene north directed shortening, uplift, and erosion of the lower Cantwell Formation, (3) late Paleocene to early Eocene volcanism and filling of the remnant Cantwell basin, and (4) post-early Eocene (middle Eocene to early Oligocene?) inversion of the Cantwell basin during northwest-southeast shortening due to right-lateral strike-slip deformation. These four stages constrain the kinematics of regional tectonic events which shaped the margin along southern Alaska. During both the first and second stages (80-60 Ma), rocks of the Cantwell basin (lower Cantwell Formation) were shortened at least 10-19 km (15-23%) by north directed compression. This shortening event can be attributed to northward accretion and suturing of the WCT to southern Alaska during northward motion of the Kula plate (Figure 14a). During the third stage, after north-south shortening, volcanism ensued along the southwestern margin of the Cantwell basin (Figure 14b). Lavas and volcaniclastic rocks filled the preexisting depocenter of the Cantwell basin in angular unconformity over the lower Cantwell Formation (hiatus of ~10-20 Ma). The absence of evidence for north-south shortening in the volcanic rocks constrains the final northward suturing of the WCT to ~60 Ma (our oldest age for the Cantwell volcanic rocks is 59.8 ± 0.2 Ma). The fourth stage of Cantwell basin development is consistent with deformation by right-lateral simple shear along the McKinley strand of the Denali fault system. During this stage, rocks of the Cantwell basin experienced a minimum of 1-5 km (2-14%) shortening (with cumulative shortening of the lower Cantwell Formation at a minimum of 15-20 km or ~29-37%). This episode of deformation along the McKinley fault occurred after 55.5 Ma (our youngest age for the Cantwell volcanic rocks) and probably ended sometime during early Oligocene time, after which the Usibelli Group and Nenana Gravel were deposited across the region (these younger units are less deformed than the Cantwell Formation).

The strike-slip deformation recorded in the Cantwell basin was coeval with several regional tectonic events, including a northwestward shift in Kula plate motion with respect to North America and strike-slip motion along several major fault systems in southeastern and south central Alaska. The kinematics of Cantwell basin deformation can be attributed to a combination of oblique convergence between the Kula plate and southern Alaska and escape tectonics whereby crustal fragments in south central Alaska were extruded westward along right-lateral strike-slip fault systems after northward impingement of accreted terranes. In this context, the first and second stages of Cantwell basin evolution represent a period of northward impingement of accreted terranes and the third and fourth stages represent the lateral displacement (escape) of these terranes.

Appendix: Methodology for $^{40}Ar/^{39}Ar$ Age Determinations

The $^{40}Ar/^{39}Ar$ age determinations were performed in the geochronology laboratory at the Geophysical Institute, University of Alaska, Fairbanks. The $^{40}Ar/^{39}Ar$ analyses were performed as two batches. The first batch included samples TEK-227, TEK-2400, DM3B-234, CM-319, CM-588, and TKL-356, and the second batch included samples TKL-17, PCM-22B, EFTK-198, DM96-2C, and DM96-3C. For both batches the samples were crushed and then washed in deionized water, dried, and sieved. Whole rock chips ~1 mm in diameter were selected. The samples were wrapped in aluminum foil and arranged in two levels, labeled top and bottom, within aluminum cans of 2.5-cm diameter and 4.5-cm height. Samples of McClure Mountain hornblende (MMhb-1) [*Samson and Alexander*, 1987] with an assumed age of 513.9 Ma [*Lanphere et al.*, 1990] were included on each level with each set of unknowns to monitor the neutron flux. The samples were sent to the uranium-enriched research reactor at McMaster University in Hamilton, Ontario, Canada, and irradiated for 70 mWh in position 5c.

Upon its return from the reactor, the first batch of samples and monitors was fused in a low-blank, double-wall tantalum furnace, connected "on-line" to an ultra-high vacuum extraction line. The monitors were fused in one step at 1600°C. The samples were step-heated from ~500 to 1600°C. Argon purification was achieved using a liquid nitrogen cold trap and a SAES Zr-Al getter at 400°C. The purified argon isotopes were then analyzed in a Nuclide 6-60-SGA mass spectrometer at the Geophysical Institute, University of Alaska, Fairbanks. The second batch of samples and monitors was analyzed at the Geophysical Institute using a laser heating system connected to a VG3600 mass spectrometer. The samples and monitors measured on this system were loaded into 2-mm diameter holes in a copper tray, which was then loaded into an ultra-high vacuum extraction line. The monitors were fused using a 6-W rated argon-ion laser (capable of 9-W output), and the samples were step heated [*York et al.*, 1981, *Layer et al.*, 1987] using laser powers between 100 mW and 9 W. For both sample batches the argon isotopes measured were corrected for system blank, mass discrimination, and calcium, potassium, and chlorine interference reactions following procedures outlined by *McDougall and Harrison* [1988]. The weighted mean of the results obtained on the monitor samples associated with each batch of samples was used in calculations. A summary of the $^{40}Ar/^{39}Ar$ results is given in Table 1.

Acknowledgments. Research was supported by the National Geographic Society (NGS-5650-96), Donors of the Petroleum Research Fund, administered by the American Chemical Society, and the Allegheny College Faculty Development Fund (all to RBC) for work during 1995-1998 and by the National Science Foundation (EAR-9406-78 and EAR-9725587) (KDR) for work during 1994 and 1995. We thank Phil Brease, Mark Keys, Garret Slaugenhoup, Chris Turner, and Michael Walker for field assistance. Chet Wrucke, Laura Serpa, Jeff Trop, Rick Hoy, and an anonymous reviewer provided insightful reviews of the manuscript. We also thank Dwight Bradley, Chris Nye, Alison Till, David Scholl, Phil Brease, Rick Hoy, and Jeff Trop for helpful discussions of this work. This research would not have been possible without the support of Denali National Park and Preserve, and for this we especially thank Phil Brease and Joe VanHorn.

References

Ager, T.A., J.V. Matthews, and W. Yeend, Pliocene terrace gravels of the ancestral Yukon River near Circle, Alaska: Palynology, paleobotany paleoenvironmental reconstruction and regional correlation, *Quat. Int., 22/23*, 185-206, 1994.

Bol, A.J., R.S. Coe, C. S. Gromme, and J.W. Hillhouse, Paleomagnetism of the Resurrection Peninsula, Alaska: Implications for the tectonics of southern Alaska and the Kula-Farallon Ridge, *J. Geophys. Res., 97*, 17,213-17,232, 1992.

Bradley, D.C., P.J. Haeussler, and T.M. Kusky, Timing of early Tertiary ridge subduction in southern Alaska, *U.S. Geol. Surv. Bull, 2068*, 163-177, 1993.

Brewer, W.M., Stratigraphy, structure, and metamorphism of the Mount Deborah area, central Alaska Range, Alaska, Ph.D. thesis, Univ. of Wis., Madison, 318 pp, 1982.

Brewer, W.M., K. Sherwood, C. Craddock, Metamorphic patterns in the central Alaska Range and the recognition of terrane-bounding faults, *Geol. Soc. Am. Abstr. Programs, 16*, 272, 1984.

Bultman, T.R., The Denali fault (Hines Creek strand) near the Nenana River, Alaska, M.S. thesis, 191 pp., Univ. of Wisconsin, Madison, 1972.

Cande, S.C., and D.V. Kent, A new geomagnetic polarity time scale for the Late Cretaceous and Cenozoic, *J. Geophy. Res., 97*, 13,917-13,951, 1992.

Christie-Blick, and K.T. Biddle, Deformation and basin formation along strike-slip faults, in *Strike-Slip Deformation, Basin Formation, and Sedimentation*, edited by K.T. Biddle and N. Christie-Blick, *Spec. Publ. 37*, pp. 1-34, Soc. of Econ. Paleontol. and Mineral., Tulsa, Okla., 1985.

Coe, R.S., B.R. Globerman, P.W. Plumley, and G.A. Thrupp, Paleomagnetic results from Alaska and their tectonic implications, in *Tectonostratigraphic Terranes of the Circum-Pacific Region, Earth Sci. Ser.*, vol. 1, edited by D.G. Howell, pp. 85-108, Circum-Pac. Counc. for Energy and Miner. Resour., Houston, Tex., 1985.

Cole, R.B., Early Tertiary post-subduction volcanism and deformation along the north side of the McKinley fault, Alaska, *Geol. Soc. Am. Abstr. Programs, 30*, 177, 1998.

Cole, R.B., Co-magmatic ties between the Cantwell volcanics and McKinley sequence plutons: Constraint on the early Tertiary offset history of the McKinley fault, central Alaska Range, *Geol. Soc. Am. Abstr. Programs, 31*, 46, 1999.

Cole, R.B., K.D. Ridgway, P.W. Layer, and J. Drake, Volcanic histroy, geochronology, and deformation of the upper Cantwell Formation, Denali National Park, Alaska: Early Eocene transition between terane accretion and strike-slip tectonics, *Geo. Soc. Am. Abst. Programs, 28*, 313, 1996.

Coney, P.J., D.L. Jones, and J.W.H. Monger, Cordilleran suspect terranes, *Nature, 288*, 329-333, 1980.

Cowan, D.S., M.T. Brandon, and J.I. Garver, Geologic tests of hypotheses for large coastwise displacements: A critique illustrated by the Baja British Columbia controversy, *Am. J. Sci., 297*, 117-173, 1997.

Crawford, M.L., L.S. Hollister, and G.J. Woodsworth, Crustal deformation and regional metamorphism across a terrane boundary, Coast plutonic complex, British Columbia, *Tectonics, 6*, 343-361, 1987.

Csejtey, B., Jr., D.P. Cox, R.C. Evarts, G.D. Stricker, H.L. Foster, The Cenozoic Denali fault system and the Cretaceous accretionary development of southern Alaska, *J. Geophy. Res., 87,* 3741-3754, 1982.

Csejtey, B., Jr., et al., in *Geology and Geochronology of the Healy Quadrangle, Alaska,* Additional bedding and structural data for the Healy quadrangle geologic map, scale 1:250,000, sheet 2, *U.S. Geol. Surv. Open File Rep., 86-396,* 1986.

Csejtey, B. Jr., M.W. Mullen, D.P. Cox, and G.D. Stricker, Geology and geochronology of the Healy quadrangle, south-central Alaska, *U.S. Geol. Surv. Map, I-1961,* 1992.

Csejtey, B., Jr., A.B. Ford, C.T. Wrucke, and J.G. Arth, The Denali fault in central Alaska: Fact or partly fiction?, *Geol. Soc. Am. Abstr. Programs, 29,* 9, 1997.

Csejtey, B., Jr., A.B. Ford, C.T. Wrucke, and P.F. Brease, The need to reevaluate the Denali fault in central and western Alaska, *Eos Trans. AGU, 79,* Fall Meet. Suppl , F876, 1998.

Curie, J.B., H.W. Patnode, and R.P. Trump, Development of folds in sedimentary strata, *Geol. Soc. Am. Bull., 73,* 655-674, 1962.

Debiche, M.G., A. Cox, and D.C. Engebretson, The motion of allochthonous terranes across the north Pacific basin, *Spec. Pap. Geol. Soc. Am. 207,* 49 pp., 1987.

Decker, J., et al., Geology of southwestern Alaska, in *The Geology of North America,* vol. G-1, *The Geology of Alaska,* edited by G. Plafker and H.C. Berg, pp. 285-310, Geol. Soc. of Am., Boulder, Colo., 1994.

Dover, J.H., Geology of part of east-central Alaska, in *The Geology of North America,* vol. G-1, *The Geology of Alaska,* edited by G. Plafker and H.C. Berg, pp. 153-204, Geol. Soc. of Am., Boulder, Colo., 1994.

Dumitru, T.A., E.L. Miller, P.B. O'Sullivan, J.M. Amato, K.A. Hannula, A.T. Calvert, and P.B. Gans, Cretaceous to Recent extension in the Bering Strait region, Alaska, *Tectonics, 14,* 549-563, 1995.

Eisbacher, G.H., Sedimentology of the Dezadeash flysch and its implications for strike-slip faulting along the Denali fault, Yukon Territory and Alaska, *Can. J. Earth Sci., 13,* 1495-1513, 1976.

Engebretson, D.C., A. Cox, and R.G. Gordon, Relative motions between oceanic and continental plates in the Pacific Basin, *Spec. Pap. Geol. Soc. Am., 206,* 59 pp., 1985.

Fitzgerald, P.G., R.B. Sorkhabi, T.F. Redfield, and E. Stump, Uplift and denudation of the central Alaska Range: A case study in the use of apatite fission track thermochronology to determine absolute uplift parameters, *J. Geophys. Res., 100,* 20,175-20,191, 1995.

Forbes, R.B., T.E. Smith, and D.L. Turner, Comparative petrology and structure of the Maclaren, Ruby Range, and Coast Range belts: Implications for offset along the Denali fault system, *Geol. Soc. Am. Abstr. Programs, 6,* 177, 1974.

Ford, A.B., B. Csejtey, Jr., C.T. Wrucke, and P.F. Brease, Oligocene pluton not offset 40 km by a Denali fault at Gunsight Pass, Denali National Park, Alaska, *Eos Trans. AGU, 79,* Fall Meet. Suppl., F876, 1998.

Fuchs, W.A., Tertiary tectonic history of the Castle Mountain-Caribou fault system in the Talkeetna Mountains, Alaska, Ph.D. thesis, 152 pp., Univ. of Utah, Salt Lake City, 1980.

Gabrielse, H., Major dextral transcurrent displacements along the northern Rocky Mountain trench and related lineaments in north-central British Columbia, *Geol. Soc. Am. Bull., 96,* 1-14, 1985.

Gardner, M.C., S.C. Bergman, E.M. MacKevett, Jr., G. Plafker, R.C. Campbell, G.W. Cushing, C.J. Dodds, and W.D. McClelland, Middle Pennsylvanian pluton stitching of Wrangellia and the Alexander terrane, Wrangell Mountains, Alaska, *Geology, 16,* 967-971, 1988.

Gilbert, W.G., and E. Redman, Geologic map and structure sections of Healy C-6 quadrangle, Alaska, 2 pp., scale 1:40,000, *Open File Rep. Alaska Div. Geol. Geophys. Surv., AOF-80,* 1975.

Gilbert, W.G., V.M. Ferrell, and D.L. Turner, The Teklanika Formation: A new Paleocene volcanic formation in the central Alaska Range, *Alaska Div. Geol. Geophys. Surv. Geol. Rep., 47,* 16 pp., 1976.

Grantz, A., Strike-slip faults in Alaska, *U.S. geol. Surv. Open File Rep , 276,* 82 pp., 1966.

Harding, T.P., Petroleum traps associated with wrench faults, *Am. Assoc. Pet. Geol. Bull., 58,* 1290-1304, 1974.

Harding, T.P., R.C. Vierbuchen, and N. Christie-Blick, Structural styles, plate-tectonic settings, and hydrocarbon traps of divergent (transtensional) wrench faults, in *Strike-Slip Deformation, Basin Formation, and Sedimentation,* edited by K.T. Biddle and N. Christie-Blick. *Spec. Publ. 37,* pp. 51-77, Soc. Of econ. Paleontol. And Mineral, Tulsa, Okla., 1985.

Hickman, R.G., Structural geology and stratigraphy along a segment of the Denali fault system, central Alaska Range, Alaska, Ph.D. thesis, 276 pp., scale 1:63,360, Univ. of Wis., Madison, 1974.

Hickman, R.G., C. Craddock and K.W. Sherwood, Structural geology of the Nenana River segment of the Denali fault system, central Alaska Range, *Geol. Soc. Am. Bull., 88,* 1217-1230, 1977.

Hickman, R.G., K.W. Sherwood, and C. Craddock, Structural evolution of the early Tertiary Cantwell Basin, south central Alaska, *Tectonics, 9,* 1433-1449, 1990.

Hillhouse, J.W., and R.S. Coe, Paleomagnetic data from Alaska, in *The Geology of North America,* vol. G-1, *The Geology of Alaska,* edited by G. Plafker and H.C. Berg, pp. 797-812, Geol. Soc. of Am., Boulder, Colo., 1994.

Hillhouse, J.W., and C.S. Grommé, Limits to northward drift of the Paleocene Cantwell Formation, central Alaska, *Geology, 10,* 552-556, 1982.

Hillhouse, J.W., C.S. Grommé, and B. Csejtey, Jr., Tectonic implications of paleomagnetic poles from early Tertiary volcanic rocks, south central Alaska, *J. Geophys. Res., 90,* 12,523-12,535, 1985.

Howell, D.G., D.L. Jones, and E.R. Schermer, Tectonostratigraphic terranes of the Circum-Pacific region, in *Tectonostratigraphic Terranes of the Circum-Pacific Region, Earth Sci. Ser.,* vol. 1, edited by D.G. Howell, pp. 3-30, Circum-Pac. Counc. for Energy and Miner. Resour., Houston, Tex., 1985.

Hudson, T.L., Calc-alkaline plutonism along the Pacific rim of southern Alaska, in *Circum-Pacific Plutonic Terranes,* edited by J.A. Roddick, *Mem. Geol. Soc. Am., 159,* 159-169, 1983.

Hudson, T.L., Crustal melting events in Alaska, in *The Geology of North America,* vol. G-1, *The Geology of Alaska,* edited by G. Plafker and H.C. Berg, pp. 657-670, Geol. Soc. of Am., Boulder, Colo., 1994.

Jones, D.L., N.J. Silberling, H.C. Berg, and G. Plafker, Map showing tectonostratigraphic terranes of Alaska, columnar sections, and summary description of terranes, 2 sheets, scale 1:2,500,000, *U.S. Geol. Surv Open File Rep., 81-792,* 20 pp., 1981.

Lanphere, M.A., Displacement history of the Denali fault system, Alaska and Canada, *Can. J. Earth Sci., 15,* 817-822, 1978.

Lanphere, M.A., G.B. Dalrymple, R.J. Fleck, and M.S. Pringle, Intercalibration of mineral standards for K-Ar and 40Ar/39Ar age measurements, *Eos Trans. AGU, 71,* 1658, 1990.

Layer, P.W., C.M. Hall, and D. York, The derivation of $^{40}Ar/^{39}Ar$ age spectra of single grains of hornblende and biotite by laser step-heating, *Geophys. Res. Lett., 14,* 757-760, 1987.

Leitch, E.C., and E. Scheibner, (Eds.), *Terraane Accretion and Orogenic Belts, Geodyn. Ser.,* vol. 19, 343 pp., AGU, Washington, D.C., 1987.

Lonsdale, P., Paleogene history of the Kula plate: Offshore evidence and onshore implications, *Geo. Soc. Am. Bull., 100,* 733-754, 1988.

Maxson, J., and B. Tikoff, 1996, Hit-and-run collision model for the Laramide orogeny, western United States, *Geology, 24,* 968-972, 1996.

McClelland, W.C., G E. Gehrels, and J.B. Saleeby, Upper Jurassic-Lower Cretaceous basinal strata along the Cordilleran margin: Implications for the accretionary history of the Alexander-Wrangellia-Peninsular terrane, *Tectonics, 11,* 823-835, 1992.

McDougall, I., and T.M. Harrison, *Geochronology and Thermochronology by the $^{40}Ar/^{39}Ar$ Method,* 212 pp., Oxford Univ. Press, New York, 1988.

Mitra, G., Strain variation in thrust sheets across the Sevier fold-and-thrust belt (Idaho-Utah-Wyoming): Implications for section restoration and wedge taper evolution, *J. Strct. Geol., 16,* 585-602, 1994.

Moll-Stalcup, E.J., Latest Cretaceous and Cenozoic magmatism in mainland Alaska, in *The Geology of North America,* vol. G-1, *The Geology of Alaska,* edited by G. Plafker and H.C. Berg, pp. 589-619, Geol. Soc. of Am., Boulder, Colo., 1994.

Moll-Stalcup, E.J., D.A. Brew, and T.L. Vallier, Latest Cretaceous and Cenozoic magmatic rocks of Alaska, in *The Geology of North America,* vol. G-1, *The Geology Alaska,* edited by G. Plafker and H.C. Berg, plate 5, 1 sheet, scale 1:2,500,000, Geol. Soc. of Am., Boulder Colo., 1994.

Monger, J.W.H., R.A. Price, and D.J. Tempelman-Kluit, Tectonic accretion and the origin of the two major metamorphic and plutonic welts in the Canadian Cordillera, *Geology, 10,* 70-75, 1982.

Nokleberg, W., D.L. Jones, and N.J. Silberling, Origin and tectonic evolution of the Maclaren and Wrangellia terranes, eastern Alaska Range, Alaska, *Geol. Soc. Am. Bull., 96,* 1251-1270, 1985.

Nokleberg, W.J., G. Plafker, and F.H. Wilson, Geology of south-central Alaska, in *The Geology of North America, vol. G-1, The Geology of Alaska,* edited by G. Plafker and H.C. Berg, pp. 311-366, Geol. Soc. of Am., Boulder Colo., 1994.

Nye, C., The Teklanika formation in the Calico Creek area Mt. McKinley National Park, Alaska, M.S. thesis, 68 pp., Univ. of Alaska, Fairbanks, 1978.

Oldow, J.S., A.W. Bally, H.G. Ave Lallemant, and W.P. Leeman, Phanerozoic evolution of the North American Cordillera; United States and Canada, in *The Geology of North America,* vol. A, *The Geology of North America: An Overview,* pp. 139-232, Geol. Soc. of Am., Boulder, Colo., 1989.

Palmer, A.R., *The Decade of North American Geology 1983 Geologic time Scale,* Geol. Soc. of Am., Boulder, Colo., 1983.

Panuska, B.C., D.B. Stone, and D.L. Turner, Paleomagnetism of Eocene volcanic rocks, Talkeetna Mountains, Alaska, *J. Geophys. Res., 95,* 6737-6750, 1990.

Patton, W.W., Jr., and J.M. Hoare, The Kaltag

fault, west-central Alaska, *U.S. Geol. Surv. Prof. Pap. 600-D*, D147-D153, 1968.
Pavlis, T.L., Pre-Cretaceous crystalline rocks of the western Chugach Mountains, Alaska: Nature of the basement of the Jurassic Peninsular terrane, *Geol. Soc. Am. Bull., 94*, 1329-1344, 1983.
Pavlis, T.L., and V.B. Sisson, Structural history of the Chugach metamorphic complex in the Tana River region, eastern Alaska: A record of Eocene ridge subduction, *Geol. Soc. Am. Bull., 107*, 1333-1355, 1995.
Plafker, G., and H.C. Berg, Overview of the geology and tectonic evolution of Alaska, in *The Geology of North America*, vol. G-1, *The Geology of Alaska*, edited by G. Plafker and H.C. Berg, pp. 989-1021, Geol. Soc. of Am., Boulder, Colo., 1994.
Plafker, G., W.J. Nokleberg, and J.S. Lull, Bedrock geology and tectonic evolution of the Wrangellia, Peninsular, and Chugach terranes along the Trans-Alaska Crustal Transect in the northern Chugach Mountains and southern Copper River basin, Alaska, *J. Geophys. Res., 94*, 4255-4295, 1989.
Plafker, G., C.W. Naeser, R.A. Zimmermann, J.S. Lull, and T. Hudson, Cenozoic uplift history of the Mount McKinley area in the central Alaska Range based on fission-track dating, *U.S. Geol. Surv. Bull., 2041*, 202-212, 1991.
Plafker, G., J.C. Moore, and G.R. Winkler, Geology of the southern Alaska margin, in *The Geology of North America*, vol. G-1, *The Geology of Alaska*, edited by G. Plafker and H.C. Berg, pp. 389-449, Geol. Soc. of Am., Boulder, Colo., 1994.
Reed, B.L., and M.A. Lanphere, Offset plutons and history of movement along the McKinley segment of the Denali fault system, Alaska, *Geol. Soc. Am. Bull., 85*, 1183-1892, 1974.
Riba, O., Syntectonic unconformities of the Alto Cardener, Spanish Pyrenees: A genetic interpretation, *Sediment. Geol, 15*, 213-233, 1976.
Richter, D.H., and N.A. Matson, Jr., Quaternary faulting in the eastern Alaska Range, *Geol. Soc. Am. Bull., 82*, 1529-1540, 1971.
Ridgway, K.D., P.G. DeCelles, A.R. Cameron, and A.R. Sweet, Cenozoic syntectonic sedimentation and strike-slip basin development along the Denali fault system, Yukon Territory, *Yukon Geol., 3*, 1-26, 1992.
Ridgway, K.D., A.R. Sweet, and A.R. Cameron, Climatically induced floristic changes across the Eocene-Oligocene transition in the northern high latitudes, Yukon Territory, Canada, *Geol. Soc. Am. Bull., 107*, 676-696, 1995.
Ridgway, K.D., J.M. Trop, and A.R. Sweet, Thrust-top basin formation along a suture zone, Cantwell Basin, Alaska Range: Implications for development of the Denali fault system, *Geol. Soc. Am. Bull., 109*, 505-523, 1997.
Ridgway, K.D., J.M. Trop, and A.R. Sweet, Stratigraphy, depositional systems, and age of the early Tertiary White Mountains basin, Denali fault system, southwestern Alaska, *Short Notes Alaska Geol.*, in press, 1999.
Riehle, J.R., M.D. Fleming, B.F. Molnia, J.H. Dover, J.S. Kelley, M.L. Miller, W.J. Nokleberg, G. Plafker, and A.B. Till, Digital shaded-relief image of Alaska, scale 1:2,500,000, *U.S. Geol. Surv. Misc. Invest. Ser. Map, I-2585*, 1997.
Roeske, S.M., L.W. Snee, and M.P. Bunds, $^{40}Ar/^{39}Ar$ dates from the Border Ranges fault system: A hydrothermally altered brittle-ductile transition strike-slip shear zone, southern Alaska, *Geol. Soc. Am. Abstr. Programs, 25*, 419, 1993.
Saltus, R.W., T.L. Hudson, and G.G. Connard, A new magnetic view of Alaska, *GSA Today, 9*, 1-6, 1999.
Samson, S.D., and E.C. Alexander, Jr., Calibration of the interlaboratory ^{40}Ar-^{39}Ar dating standard, MMhb-1, *Chem. Geol., 66*, 27-34, 1987.
Scholl, D.W., and A.J. Stevenson, Exploring the idea that early Tertiary evolution of the Alaska orocline and the Aleutian-Bering Sea region is a manifestation of Kula-plate-driven Cordilleran tectonism and escape tectonics?, *Geol. Soc. Am. Abst. Programs, 23*, 435, 1991.
Scholl, D.W. T.L. Vallier, and A.J. Stevenson, Geologic evolution and petroleum geology of the Aleutian ridge, in *Geology and Resource Potential of the Continental Margin of Western North America and Adjacent Ocean Basins: Beaufort Sea to Baja Californiania, Earth Sci. Ser.*, vol. 6, edited by D.W. Scholl, pp. 82-86, Circum-Pac. Coun. for Energy and Miner. Resour., Houston, Tex., 1986.
Scholl, D.W., A.J. Stevenson, S. Mueller, E. Geist, T.L. Vallier, and D.C. Engebretson, Regional-scale strain partitioning leading to escape tectonism and formation of offshore arc-trench systems, Alaska-Aleutian-Bering Sea region, *Geol. Soc. Am. Abstr. Programs, 26*, 110, 1994.
Scholz, C.H., *The Mechanics of Earthquakes and Faulting*, 439 pp., Cambridge Univ. Press, New York, 1990.
Sharp, R.V., Surface faulting in Imperial Valley during the earthquake swarm of January-February, 1975, *Seismol. Soc. Am. Bull, 66*, 1145-1154, 1976.
Sherwood, K.W., Stratigraphy, metamorphic geology, and structural geology of the central Alaska Range, Alaska, Ph.D. thesis, 692 pp., Univ. of Wisconsin, Madison, 1979.
Sibson, R.H., Fault rocks and fault mechanisms, *J. Geol. Soc. London, 133*, 190-213, 1977.
Silberman, M.L., and A. Grantz, Paleogene volcanic rocks of the Matanuska Valley area and the displacement history of the Castle Mountain fault, in *The United States Geological Survey: Accomplishments during 1981*, edited by W.L. Conrad and R.L. Elliot, *U.S. Geol. Surv. Circ., 868*, 82-86, 1984.
Slaugenhoup, G.L., R.B. Cole, and K.D. Ridgway, Change from terrane accretion to volcanism along the McKinley fault as recorded by conglomerate of the Cretaceous-Eocene Cantwell basin, south-central Alaska, *Geol. Soc. Am. Abstr. Programs, 29*, 80, 1997.
Smart, K.J., T.L. Pavlis, V.B. Sisson, S.M. Roeske, and L.W. Snee, The Border Ranges fault system in Glacier Bay National Park, Alaska: Evidence for major early Cenozoic dextral strike-slip motion, *Can. J. Earth Sci., 33*, 1268-1282, 1996.
Steiger, R.H., and E. Jäger, Subcommission on geochronology: Convention on the use of decay constants in geo- and cosmochronology, *Earth Planet. Sci. Lett., 36*, 359-362, 1977.
Stone, D.B., B.C. Panuska, and D.R. Packer, Paleolatitudes versus time for southern Alaska, *J. Geophys. Res., 87*, 3697-3707, 1982.
Stout, J.H., J.B. Brady, F. Weber, and R.A. Page, Evidence for Quaternary movement on the McKinley strand of the Denali fault in the Delta River area, Alaska, *Geol Soc Am. Bull, 84*, 939-948, 1973.
Sylvester, Arthur G., Strike-slip faults, *Geol. Soc. Am. Bull., 100*, 1666-1703, 1988.
Tchalenko, J.S., Similarities between shear zones of different magnitudes, *Geol. Soc. Am. Bull, 81*, 1625-1640, 1970.
Tchalenko, J.S., and N.N. Ambraseys, Structural analyses of the Dasht-e Bayaz (Iran) earthquake fractures, *Geol Soc Am. Bull., 81*, 41-60, 1970.
Tikoff, B., C. Teyssier, M. Markley, and S. McKinnon, The role of plate motion on strike-slip partitioning at zones of oblique convergence/divergence, *Geol. Soc. Am. Abstr. Programs, 26*, 110, 1994.
Trop, J.M., Sedimentological, provenance, and structural analysis of the lower Cantwell Formation, Cantwell Basin, central Alaska Range: Implications for the development of a thrust-top basin, M.S. thesis, 222 pp., Purdue Univ., West Lafayette, Indiana, 1996.
Turner, D.L., T.E. Smith, and R.B. Forbes, Geochronology of offset along the Denali fault system in Alaska, *Geol. Soc. Am. Abstr. Programs, 6*, 268-269, 1974.
Wahrhaftig, C., Geologic map of the Healy D-3 quadrangle, scale 1:63,360, *U.S. Geol. Surv. Geol. Map, GQ-805*, 1970a.
Wahrhaftig, C., Geologic map of the Healy D-4 quadrangle, scale 1:63,360, *U.S. Geol. Surv. Geol. Map, GQ-806*, 1970b.
Wahrhaftig, C., Geologic map of the Healy D-5 quadrangle, Alaska, scale 1:63,360, *U.S.. Geol. Surv. Geol. Map, GQ-807*, 1970c.
Wahrhaftig, C., The Cenozoic section at Suntrana, Alaska, in *Geological Society of America Centennial Field Guide: Cordilleran Section*, pp. 445-450, Geol. Soc. of Am., Boulder, Colo., 1987.
Wallace, W.K., and D.C. Engebretson, Relationship between plate motions and Late Cretaceous to Paleogene magmatism in southwestern Alaska, *Tectonics, 3*, 295-315, 1984.
Wallace, W.K., C.L. Hanks, and J.F. Rogers, The southern Kahiltna terrane: Implications for the tectonic evolution of southwestern Alaska, *Geol. Soc. Am. Bull., 101*, 1389-1407, 1989.
Wegner, W.W., The Denali fault (Hines Creek strand) in the northeastern Mount McKinley National Park, Alaska, M.S thesis, 74 pp., scale 1:63,360, Univ. of Wis., Madison, 1972.
West, A.W., A petrologic and geochronologic study of the McKinley Pluton, Alaska, M.S. thesis, 181 pp., Univ. of Alaska, Fairbanks, 1994.
West, A.W., and P.W. Layer, Thermochronologic history of the McKinley pluton, Denali National Park, Alaska, *U.S. Geol. Surv. Circ., 1107*, 351, 1994.
Wilcox, R.E., T.P. Harding, and D.R. Seely, Basic wrench tectonics, *Am. Assoc. Pet. Geol. Bull., 57*, 74-96, 1973.
Wolfe, J.A., and C. Wahrhaftig, The Cantwell Formation of the central Alaska Range, *U.S. Geol. Surv. Bull., 1294*-A, A41-A55, 1970.
Wrucke, C.T., B. Csejtey, Jr., A.B. Ford, and P.F. Brease, Rock units show no major lateral offset across the Denali fault as previously mapped, Mt. McKinley area, Alaska, *Eos Trans. AGU, 79*, Fall Meet. Suppl., F876, 1998.
York, D., C.M. Hall, Y. Yanase, J.A. Hanes, and W.J. Kenyon, $^{40}Ar/^{39}Ar$ dating of terrestrial minerals with a continuous laser, *Geophys. Res. Lett., 8*, 1136-1138, 1981.

R.B. Cole, Department of Geology, Allegheny College, Meadville, PA 16335. (rcole@alleg.edu)
J. Drake and P.W. Layer, Geophysical Institute, University of Alaska, Fairbanks, AK 99775. (jdrake@gi.alaska.edu; player@gi.alaska.edu)
K.D. Ridgway, Department of Earth and Atmospheric Sciences, Purdue University, West Lafayette, IN 47907. (ridge@)purdue.edu)

(Received January 25, 1999;
revised June 4, 1999;
accepted June 21, 1999.)

TECTONICS, VOL. 18, NO. 6, PAGES 1041-1063 DECEMBER 1999

Structure of the Castillo granite, Southwest Spain: Variscan deformation of a late Cadomian pluton

L. Eguíluz, A. Apraiz, and B. Ábalos

Departamento de Geodinámica, Universidad del País Vasco, Bilbao, Spain

Abstract. A geometrical reconstruction of the 500 Ma old Castillo granite pluton (SW Iberia) is completed on the basis of structural and geophysical (rock magnetism) techniques. The pluton is intrusive into latest Proterozoic-earliest Cambrian metasediments and conforms a tabular intrusion 6 km in diameter and 1.7 km thick that was emplaced at a depth of 10 km. Its magnetic fabric reveals that the strike of moderately to steeply dipping magmatic flow planes forms a high angle to the regional tectonic trends. Magnetic foliations and associated moderately to gently plunging magnetic lineations represent magmatic flow planes and directions. The internal anisotropy of the granite together with the structure shown by the country rocks attest the lateral propagation of the pluton and its latter inflation. The pluton's root zone would correspond to a likely thin, subvertical feeder structure initiated near the orientation of regional σ_1 at the time of emplacement. During the Variscan orogeny the pluton was tilted and underwent localized brittle-ductile strain in relation to shear zone deformation in the footwall of a major ductile thrust. Tilting permits the observation and study of a vertical profile of the intrusion. Localized deformation caused superposition of tectonic zonations on the magmatic ones, a reactivation of the basal contact of the pluton, and dismemberment from its root. This and other granitoid plutons of similar age emplaced at a similar depth constrained the creation of crustal mechanical heterogeneity and anisotropy. This controlled the site of pluton emplacement, the nucleation of a major ductile thrust, and localization of deformation and tectonic displacements along the pluton margins during later orogenic reactivation.

1. Introduction

Combined structural and geophysical measurements (gravity, geomagnetism, and flow heat) have been extensively carried out to determine the three-dimensional shape of granitoid plutons [*Miller and Tuach*, 1989; *Oliver et al.*, 1993; *Vigneresse* , 1995a, b, and references therein]. Measurement of rock magnetic susceptibility and its anisotropy (AMS) enables one to determine magnetic foliation planes and lineations, which are intrinsically related to magmatic flow structures reflecting frozen-in strain patterns [*Gléizes et al.*, 1993; *Bouillin et al.*, 1993; *Hippert*, 1994; *Neves et al.*, 1996]. These features delineate the pluton's internal organization and either permit localization of the root zones, establish likely mechanisms for pluton emplacement, or relate it to regional strain fields [*Schwerdner et al.*, 1983; *D'Lemos et al.*, 1992]. Consideration of the structure of the country rocks around plutons provides a complementary view of all these features [*Sanderson and Meneilly*, 1981; *Bateman*, 1985; *Brun and Pons*, 1981; *Van Berkel*, 1991; *Law et al.*, 1992].

The results of most of the aforementioned studies are relevant primarily to horizontal map views of the intrusions. Structural extrapolation to depth has led the scientific community to assume the widespread concept of inverted teardrop or large vertical diapirs when regarding pluton three-dimensional geometries [*Vigneresse*, 1995b]. Extrapolations to depth without direct evidence are a need in most field-based studies and are a reasonable approximation when geophysical techniques are employed.

Field examples where direct observation of the roof and the floor of a granite is possible are rare [*Rosenberg et al.*, 1995], or at least have not been realized so far. They have provided the opportunity to reconstruct the geometry of plutons on the basis of geometrical techniques and have highlighted the need of considering their horizontal and vertical dimensions at the same scale. According to *Vigneresse* [1995b], in this new perspective the vertical diapirs shown in many books turn into tabular intrusions with flattened cupolas.

In this paper we investigate the structure of the late Cadomian Castillo pluton, paying attention jointly to its internal structure and to the structural geology of its country rocks. This granite was partially gneissified during the late Paleozoic and tilted, the actual outcrop enabling one to study different depth levels of the intrusion. In addition to its conventional application, AMS is potentially useful for the recognition of superimposed deformation episodes in granites, too [*Bouchez and Gleizes*, 1995; *Riller et al.*, 1996]. In the case of the Castillo granite this technique has made it possible to separate the structures related to magma emplacement from those formed during tectonic reactivation and to relate each of them to regional strain fields and to a conceptual model for the segregation, ascent, and emplacement of this pluton.

2. Geological Setting

Latest Proterozoic-earliest Cambrian sequences within the Ossa-Morena Zone of the Iberian Massif constitute a basement recording a Cadomian tectonothermal evolution linked to Gondwana [*Quesada*, 1990a]. It is unconformably overlain by Cambrian successions [*Schäfer et al.*, 1992; *Liñán et al.*, 1993]. In the central area of the Ossa-Morena Zone (Figure 1) this basement is dissected by the Variscan Monesterio thrust,

Paper number 1999TC900037
0278-7407/99/1999TC900037$12.00

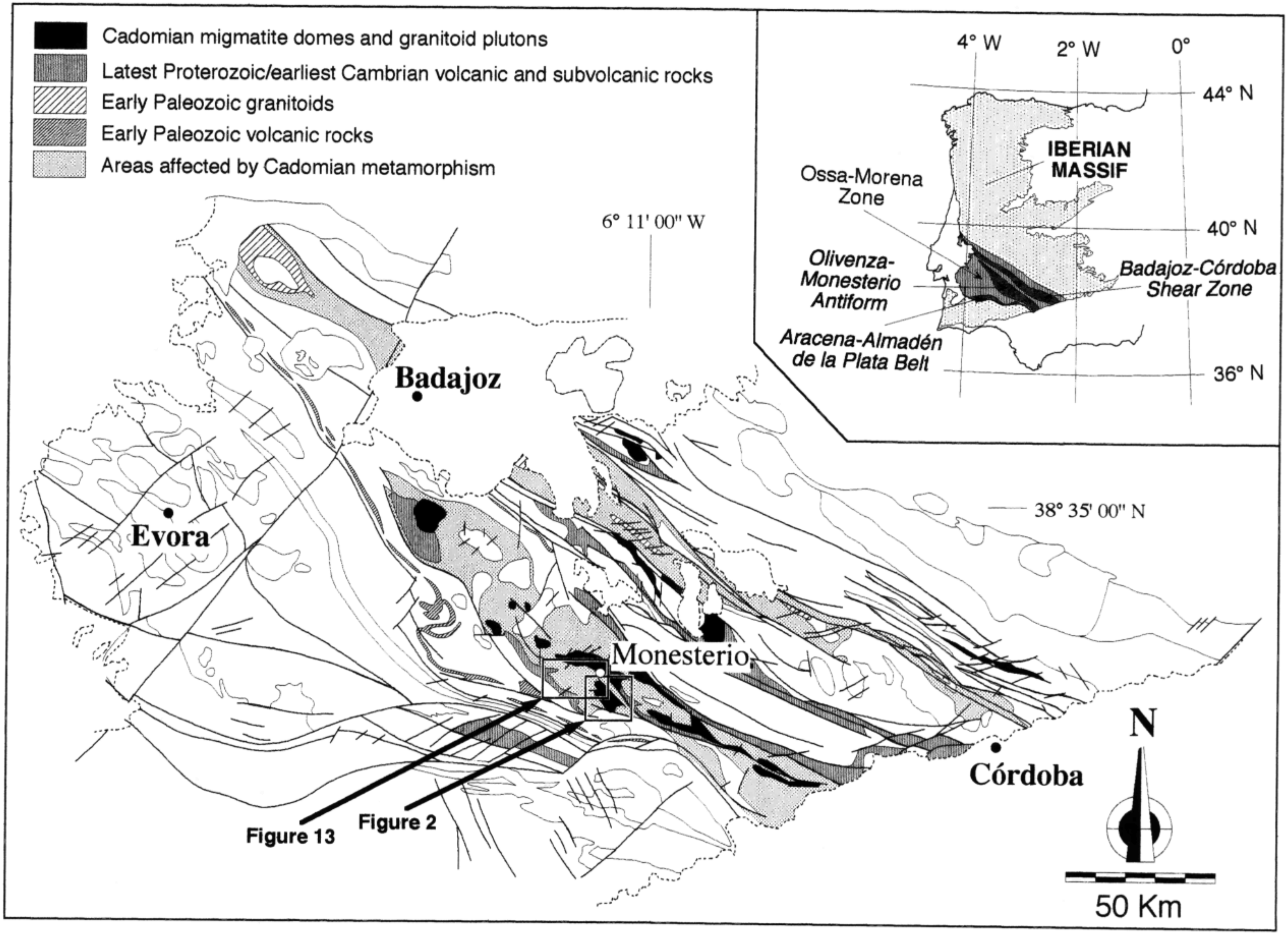

Figure 1. Sketch map of the Iberian Massif (inlet) showing the location of the Ossa-Morena Zone with its three metamorphic belts of latest Proterozoic-earliest Cambrian rocks and geological map of SW Iberian Massif showing the main Cadomian features.

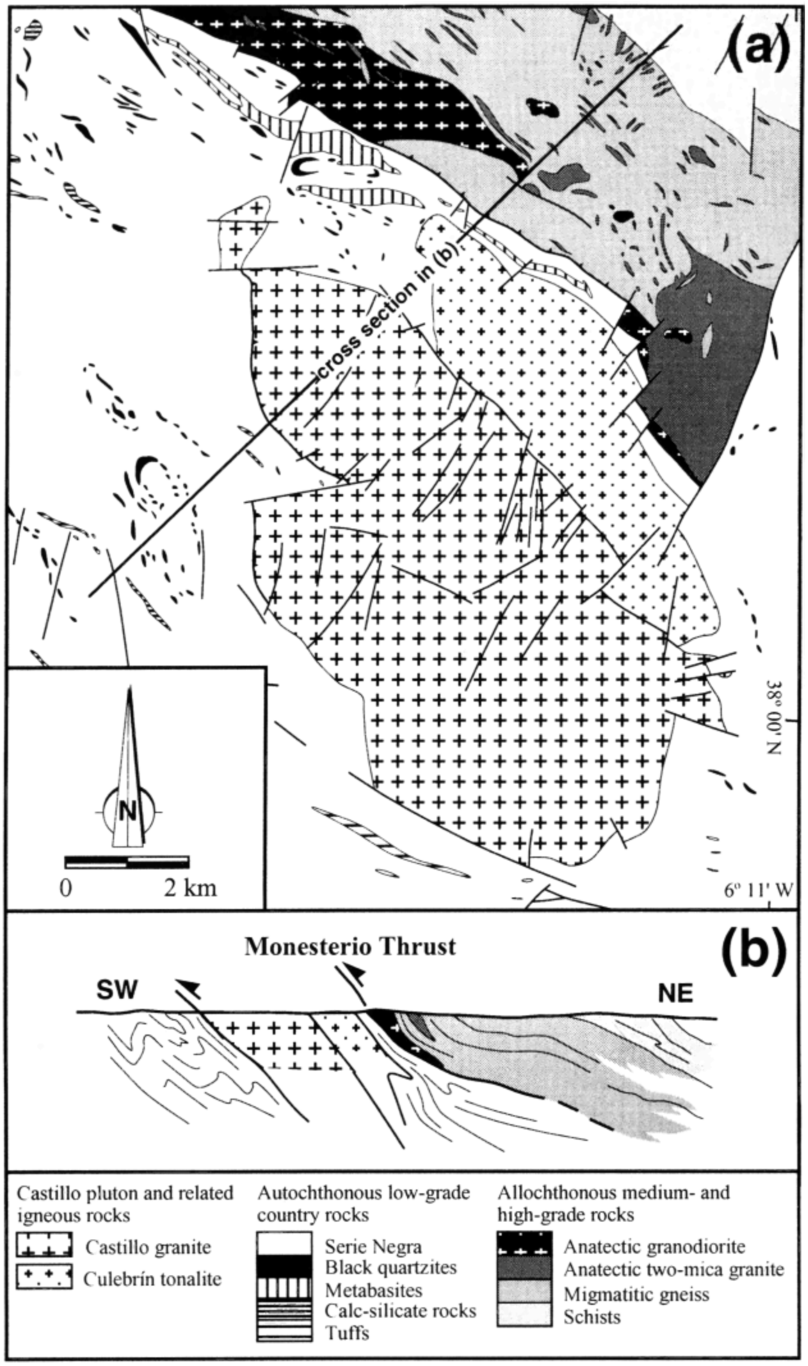

Figure 2. (a) Geological map and (b) schematic cross section of the Castillo pluton and its host rock units.

which separates two blocks with slightly different lithostratigraphic records of the Serie Negra [*Eguíluz and Quesada*, 1981; *Eguíluz et al.*, 1983; *Arriola et al.*, 1984; *Eguíluz*, 1988]. In the hanging wall the Serie Negra consists of a low-pressure metamorphic complex [*Eguíluz and Ábalos*, 1992] overlain by a metapelitic and volcanosedimentary epizonal ensemble. Intrusion of anatectic granodiorites and granitoid plutons has been dated there at 573±74 (Rb-Sr errorchron [*Cueto et al.*, 1983]), 550±16 (Rb-Sr [*Quesada*, 1990b]), and at 495±8 and 507±21 Ma (U-Pb and Sm-Nd systematics in zircon and apatite, respectively [*Schäfer*, 1990]). The $^{40}Ar/^{39}Ar$ cooling ages (449.7±7.2 and 552±3 Ma [Dallmeyer and Quesada, 1993]) suggest that the medium- and high-grade rocks underwent cooling below 400°C during latest Proterozoic-early Paleozoic times, cf. *D'Lemos et al.* [1990], *Bowring and Erwin* [1998], and *Landing et al.*, [1998]. In the footwall of the Monesterio thrust, only the metapelitic and volcanosedimentary epizonal ensemble of the Serie Negra

(500-3000 m in thickness) crops out. It is intruded by a number of granitoid plutons, including the Castillo granite (Figure 2).

Two major phases of Cadomian deformation (regional D1 and D2) and metamorphism (M1 and M2) are recognized in the area. M1 and D1 are mostly identified through S1 foliation relics within prophyroclasts or crenulations inside S2 microlithons. D1 mesoscopic structures are very rare. Only sporadic decimeter-sized fold hinges refolded by younger deformations have been recognized. Structures related to D2 are the most prominent: Southwest-ward verging, NW-SE trending recumbent folds coeval with the development of subhorizontal axial plane cleavage in the upper structural levels and penetrative tectonic banding/schistosity (that crenulate and transpose S1) in the lower structural levels. Mesoscopic structures are scarce, but some cartographic structures and occasional D1-D2 fold interference patterns have been delineated [*Eguíluz and Ramón-Lluch*, 1983] as marked by black quartzite horizons. Low-pressure, high-temperature M2 regional metamorphism reaching the high grade is associated with D2. M2-D2 tectonothermal activity in the lower structural levels is related to the generation of migmatitic domes and anatectic (paraautochthonous) granodiorite/granite plutons (Figure 2), some of which were subsequently emplaced at shallower structural levels.

Regional D3 (the first Variscan deformation phase) led to the deformation of both the early Paleozoic cover and the latest Proterozoic-earliest Cambrian basement. Occasional very low grade to low-grade metamorphism and overprinting of isotope systems were associated with it [*Schäfer et al.*, 1989; *Schäfer*, 1990; *Dallmeyer and Quesada*, 1993]. The Cadomian basement was dissected by a large NW-SE trending ductile thrust: the Monesterio thrust (Figures 1 and 2), which associates a SW directed tectonic displacement in excess of 20 km [*Eguíluz*, 1988]. The thickness of the thrust shear zone reaches up to 1 km in either the thrust footwall or the hanging wall. Cataclasites and mylonite series rocks are widespread and reflect moderate deformational pressure and temperature (P-T) conditions [*Eguíluz*, 1989]. Preexisting granitoids were transformed within this shear zone into orthogneisses and banded gneisses [*Eguíluz and Garrote*, 1983], whereas metasediments acquired a mylonitic foliation with S-C structures. In the unmetamorphosed lower Paleozoic cover, large fold nappes (up to 20 km inverted limbs) and thrusts were originated [*Eguíluz and Ramón-Lluch*, 1983; *Eguíluz*, 1988].

3. Castillo Granite

The Castillo granite is intrusive into the metapelitic and volcano-sedimentary epizonal ensemble of the Serie Negra in the footwall block of the Monesterio thrust. Its subelliptical shape is elongated NW-SE and occupies 40 km^2 (Figure 2). The NE contact of the pluton is mechanical against the Culebrín tonalite, considered a late Paleozoic intrusion in the literature [*Eguíluz*, 1988; *Sánchez-Carretero et al.*, 1990] on the basis of its petrographical and geochemical affinities with neighboring dated intrusions [*Bellon et al.*, 1979; *Brun and Pons* 1981; *Dupont et al.*, 1981]. The southern border corresponds to a left-lateral wrench fault. At the western contact the pluton is thrust onto the Serie Negra country rocks. Shear band development can be documented in the areas of the country rocks adjacent to these contacts. These are decimeter to meter thick shear zones with a composite, spaced secondary foliation and sheath folds with curved hinges whose orientation and kinematics are similar to those observed in the granite. The intrusive character of the pluton is preserved at the northern and southeastern areas, where apophyses, a finer-grained marginal leucocratic facies, and a thin contact aureole have been preserved (Figure 3). In the Castillo, pluton aureole static recrystallization of biotite as well as spotted slate development are recognizable. Rare andalusite occurrences are restricted to areas near the higher-temperature Culebrín tonalite. Formation of the aureoles of both plutons is separated 180 Myr. Their distinction in the field, however, is not straightforward at the areas equally distant to both plutons.

Geochemically, the Castillo pluton is a subalkaline granite with high SiO_2, K_2O, and Na_2O contents (71%, 5%, and 3.5% on average, respectively). Though variably deformed, no areal compositional variation has been recognized in this granite except for a volumetrically small marginal facies (Figure 3). Pluton crystallization (and subsequent intrusion) has been dated at 497.6 +9.5/-7.1 (U-Pb upper discordia-concordia intercept from zircon separates) by *Oschner* [1993], in accordance with the field criteria available.

From a petrographic point of view the Castillo pluton is a homogeneous, medium-grained, two-mica granite and contains occasional amphibole-rich microenclaves. It is composed of idiomorphic K feldspar (orthose and microcline), tabular crystals of sodic plagioclase, and xenomorphic quartz grains. The mafic minerals include hastingsitic hornblende and brownish biotite transformed to stilpnomelane. Accessory constituents include allanite, zircon, titanite, muscovite, and fluorine. Secondary alteration products are sericite, epidote, chlorite, and carbonates.

On petrographic/structural grounds a number of granite facies have been distinguished and mapped in this pluton [*Eguíluz and Garrote*, 1983; *Eguíluz et al.*, 1983; *Eguíluz*, 1988], each of them passing gradually into the other. They vary, as described below, from an undeformed facies lacking signs of plastic deformation to orthogneiss (Figure 3).

3.1. Undeformed Granite

This facies occupies the central southernmost portion of the pluton (Figure 3). As shown in the Figures 4a and 4b, it consists of apparently isotropic medium-grained (1-5 mm) granite with a conventional igneous texture. In detail, however, an ill-defined anisotropic structure can be recognized, as defined by the parallel disposition of tabular plagioclase grains. Irregular biotite and amphibole grains may conform ellipsoidal enclaves. These mafic minerals can show a weak shape fabric, too. Interstitial xenomorphic quartz grains can both fill submagmatic fractures [*Bouchez et al.*, 1992] and exhibit undulous extinction. The anisotropic microstructures described are interpreted as flow structures mostly inherited from internal magmatic movements, when over 35% of the granite body was in viscous state [*Bouchez and Gineberteau*, 1985]. These would comprise a badly defined magmatic flow plane and a ill-defined magmatic flow direction. Both are very difficult to recognize and measure in the field outcrops to the naked eye.

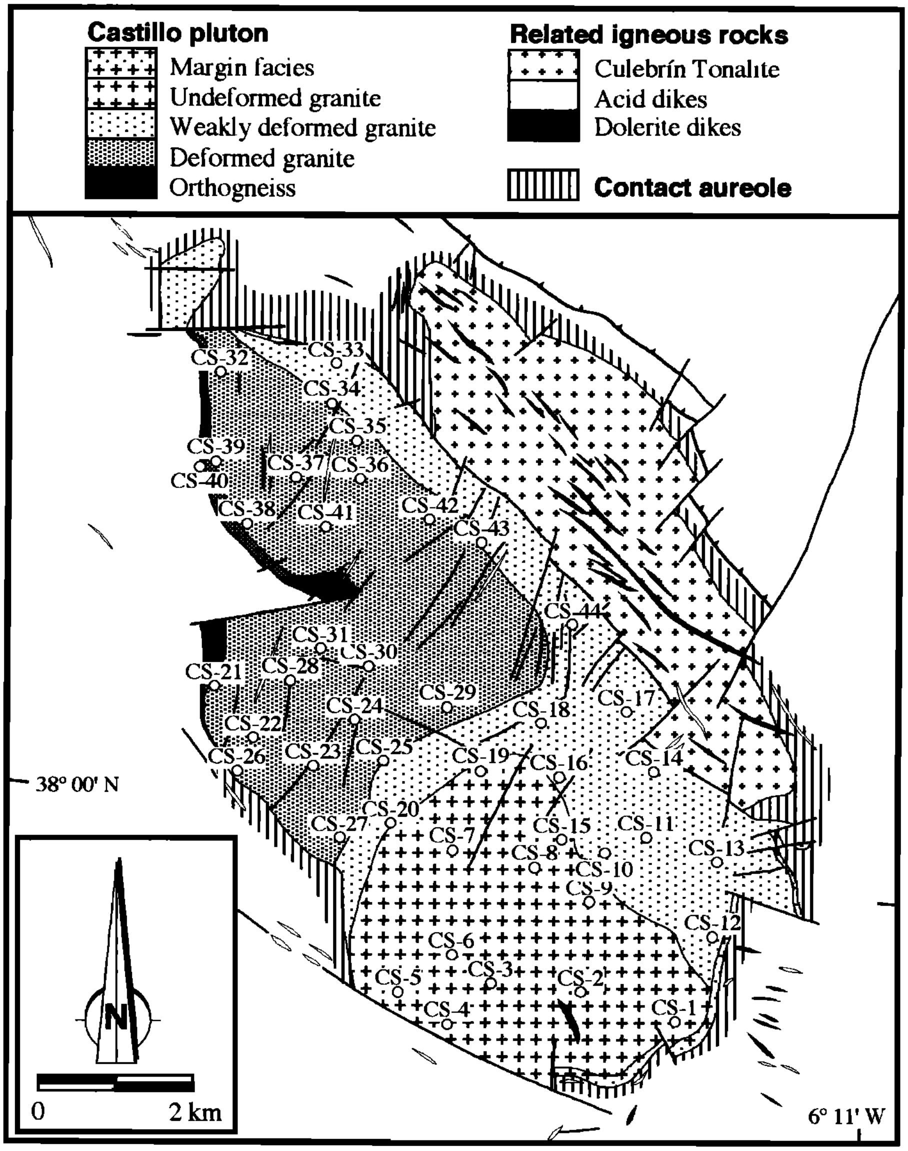

Figure 3. Geological map of the Castillo pluton showing its petrographic facies distribution, spatially related igneous rocks, contact aureole, and the drilling sites for anisotropy of magnetic susceptibility (AMS). Also shown is the late Paleozoic Culebrín tonalite.

3.2. Weakly Deformed Granite

This facies is characterized by the occurrence of nonpenetrative solid state deformation microstructures superimposed on the undeformed granite facies. It crops out as a 0.5-1.5 km envelope around the undeformed granite, which is extended to the NW along the northern contact of the pluton (Figure 3). In this facies a nonpenetrative discontinuous foliation and associated C-S structures can be observed occasionally. From the petrographic point of view the foliated domains are characterized by a protomylonitic microstructure where plagioclase porphyrocrystals (Figure 4c) are broken and stretched parallel to the structural X direction (XY is the plane of foliation and X is the lineation direction). The matrix contains fine-grained, irregular fragments of feldspar and quartz grains showing various microstructures due to cold working and recovery. The rock volumes not affected by foliation compare to the undeformed granite. On these grounds, and on the basis of the geometry of the contact between this and the previously described facies, the weakly deformed granite is interpreted as genetically related to the undeformed granite, with respect to which would represent an outer shell deformed in the solid state during later stages of granite emplacement.

3.3. Deformed Granite

This facies occupies most of the western portion of the pluton (Figure 3). It is characterized by the presence of a secondary tectonic foliation penetrative at the outcrop scale.

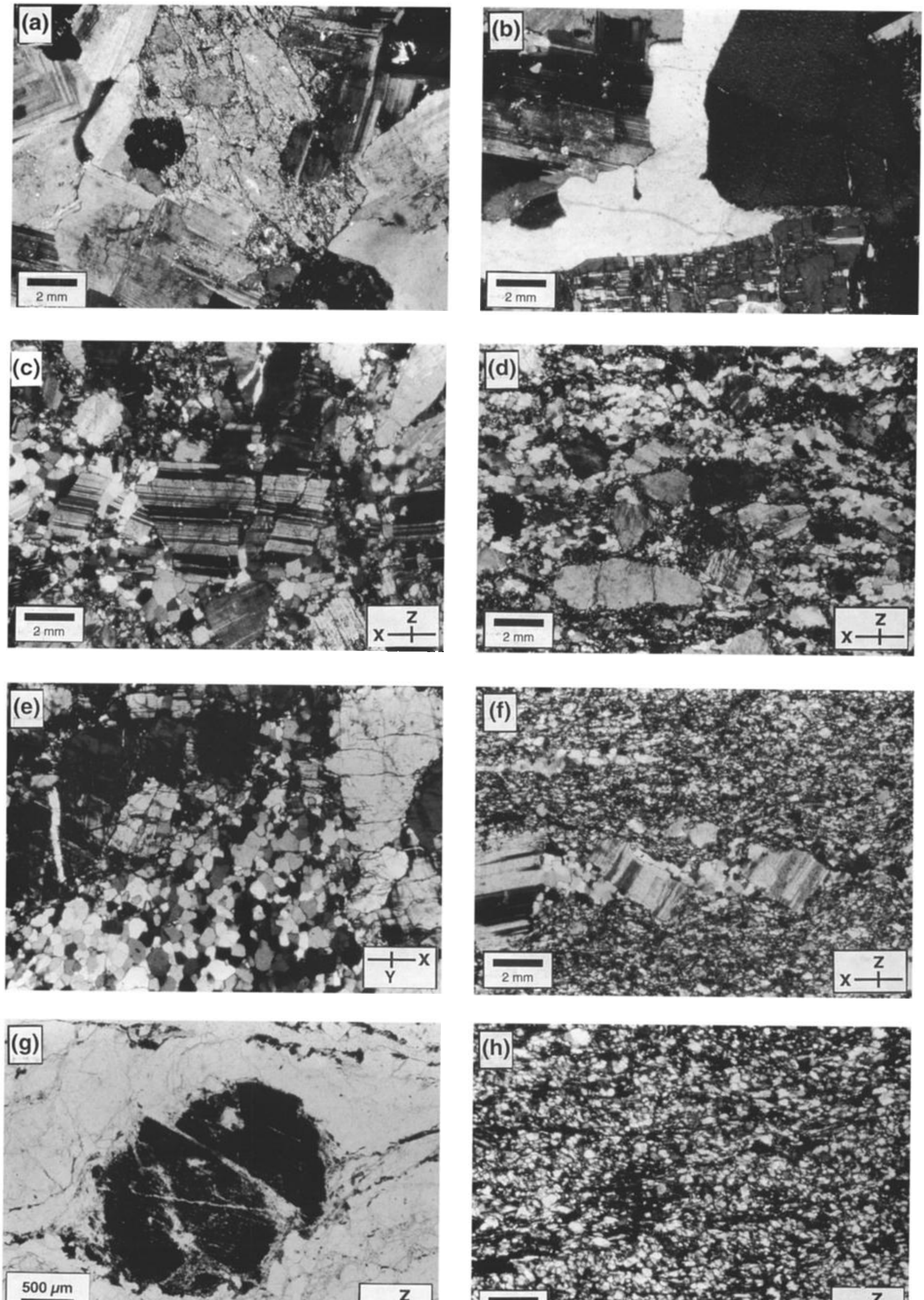

Figure 4.

This structure is more penetrative in the SW direction toward which a deformation gradient exists. A protomylonitic to mylonitic microstructure is defined by fractured feldspar and hornblende porphyroclasts (Figure 4d) embedded in a finer-grained, volumetrically dominant leucocratic matrix where quartz shows undulous extinction, subgrains (100-300 μm in grain size) and grain boundary migration recrystallization microstructures. Hornblende and biotite grains do not exhibit evidence of internal deformation. A stretching lineation (Figure 4e) can be observed and measured on the foliation planes, as defined by the elongation of fractured feldspar grains. The orientations of secondary foliation and lineation remain constant in this facies: foliation is parallel to the contact with the orthogneiss facies, parallel to the NE contact with the weakly deformed granite, and highly oblique to the SE contact with the latter facies.

3.4. Orthogneiss

Granite gneisses delineate the western thrust contact of the Castillo pluton with the (underlying) country rocks (Figure 3). It is a few tens of meters in thickness and is characterized by the occurrence of a penetrative, NW-SE trending, and NE dipping, gneissic foliation. C-S structures are common and penetrative at the outcrop scale, notably in the SW portion of this facies. Toward this direction the spacing of the C planes and the angle between C and S surfaces decrease (the latter from 45° to 25°). A prominent mineral and stretching lineation trending NE-SW occurs on the foliation and C planes, defined by stretched quartz and mafic aggregates. Under the microscope this is a pervasively foliated rock with a mylonitic microstructure. Fine-grained feldspar aggregates conform thin bands that alternate with recrystallized quartz ribbons. Scarce porphyroclasts (notably plagioclase and amphibole) show evidence of fragmentation, abrasion, recrystallization, and grain size reduction (Figures 4g and 4h). Quartz dynamic recrystallization, partial recrystallization of K feldspar, and myrmequite development in these rocks point to deformation conditions of the upper greenschists facies. Orientation of foliation and lineation and kinematic criteria [*Simpson and Schmid*, 1983; *Passchier and Simpson*, 1986] remain constant in this and the previous facies, all of them being congruent with the Monesterio thrust orientation and kinematics (Figure 2). Scarce and thin E-W trending and steeply dipping bands have been recognized where steeply plunging lineations and associated kinematic criteria indicate a downdip movement of hanging wall blocks, in contrast to the thrust relationships prevalent elsewhere.

4. Magnetic Susceptibility Data of the Pluton

The magnetic susceptibility of a rock is a measure of its in situ induced magnetization in the Earth's field. Since the work of *Graham* [1954] AMS is an established method of petrofabric analysis, as AMS arises from the preferred shape or crystallographic axis orientation of anisotropic magnetic minerals [*Borradaile*, 1988; *Tarling and Hrouda*, 1993]. The AMS is a second-rank tensor describable through a triaxial ellipsoid (with axes $K_{max} \geq K_{int} \geq K_{min}$) that is usually coaxial to the rock petrofabric. The magnetic fabric of a rock is defined by the K_{min} and the K_{max} axes of the AMS ellipsoid as follows: on one hand, the K_{min} axis (the pole to the magnetic foliation) is perpendicular to the macroscopic rock foliation; on the other hand, the K_{max} axis (the magnetic lineation) is parallel to the mineral/stretching lineation. The orientation of the magnetic fabric in a rock body can be related to the orientation of geologically plausible strain fields that could be responsible for its formation [*Rochette et al.*, 1992]. For the case of rock deformation this implies a direct relationship between AMS and strain which so far, however, remains poorly constrained [*Henry*, 1990; *Hrouda*, 1992; *Rochette et al.*, 1992; *Tarling and Hrouda*, 1993]. In spite of this, in the case of granitoid plutons the AMS technique is routinely applied for structural mapping provided that their microstructural state is well understood [*Guillet et al.*, 1983].

4.1. Field and Laboratory Methods

Samples were collected at 44 localities where the rock types covered the observed petrographic variety within the Castillo

Figure 4. (opposite) Optical micrographs of the relevant petrographic types and deformational microstructures of the Castillo granite pluton. (a) "Undeformed granite" with an igneous texture defined by idiomorphic feldspar crystals (zoned and twinned), xenomorphic hornblende (at the center of the micrograph), and interstitial quartz with slight undulous extinction (general section). (b) Undeformed granite with subidiomorphic plagioclase (left), microcline (bottom), hornblende (top right), and interstitial quartz without signs of solid-state deformation (general section). (c) Weakly deformed granite showing a fractured plagioclase crystal stretched parallel to the *X* structural direction. The matrix contains smaller-fractured feldspar clasts and plastically deformed quartz grains with various microtextures (*XZ* section). (d) Deformed granite showing a protomylonitic texture formed by feldspar and hornblende porphyroclasts embedded by a leucocratic matrix where quartz exhibits solid-state deformation microtextures (*XZ* section). (e) Microstructural detail of the deformed granite showing a profoundly fractured plagioclase crystal (top left) stretched parallel to the lineation, with voids filled by quartz, hornblende (right), and a completely recrystallized quartz matrix (*XY* section). (f) Deformed granite with a mylonitic texture. Plagioclase crystals have been substantially stretched and the fragments rotated. The foliated matrix is fine-grained and contains either feldspars, hornblende, biotite, or quartz (*XZ* section). (g) Rounded and fractured hornblende σ-type porphyroclast in orthogneiss derived of intense mylonitization of the Castillo granite at its western margin (*XZ* section). (h) Microtextural aspect of orthogneiss with a continuous foliation defined by alignment of feldspars, recrystallized quartz and oriented biotite and hornblende (*XZ* section). Except for the case of micrograph (Figure 4g), all the microstructures were taken under crossed nicols.

Table 1. Magnetic Susceptibility and Anisotropy of Magnetic Susceptibility (AMS) Data

Sample	X	Y	K_{mean}	$K1$	AZ	PL	$K2$	$K3$	AZ	PL	P%	L	F	Flinn [1962]
CS-1	744800	4208000	15.37	15.48	197	56	15.37	15.26	48	31	1.44	1.007	1.007	1.000
CS-2	743450	4208350	17.19	17.34	200	46	17.22	17.01	296	10	1.94	1.007	1.012	0.995
CS-3	742300	4208400	31.31	31.50	215	40	31.38	31.05	108	17	1.45	1.004	1.011	0.993
CS-4	741800	4207850	55.50	55.99	37	54	55.83	54.69	149	16	2.38	1.003	1.021	0.982
CS-5	741150	4208300	23 08	23.38	336	86	23.13	22.72	98	2	2.90	1.011	1.018	0.993
CS-6	741850	4208750	17.63	17.77	282	10	17.67	17.45	194	27	1.83	1.006	1.013	0.993
CS-7	741800	4210100	20.32	20.51	290	36	20.34	20.11	56	48	1.99	1.008	1.011	0.997
CS-8	742850	4209900	17.68	17.92	51	62	17.74	17.38	266	28	3.11	1.010	1.021	0.990
CS-9	743600	4209500	19.14	19.35	301	58	19.19	18.88	95	29	2.49	1.008	1.016	0.992
CS-10	743700	4210200	17.29	17.43	136	65	17.33	17.11	259	15	1.87	1.006	1.013	0.993
CS-11	744250	4210350	18.70	18 95	102	62	18.78	18.38	296	24	3.10	1.009	1.022	0.988
CS-12	745150	4209100	15.56	15 71	91	72	15.53	15.44	282	19	1.75	1.012	1.006	1.006
CS-13	745200	4210100	20.26	20.55	85	61	20.29	19.94	241	26	3.06	1.013	1.018	0.995
CS-14	744300	4211200	23.61	23 86	66	22	23.61	23.35	242	66	2.18	1.011	1.011	0.999
CS-15	743150	4210250	19.90	20.13	263	47	19.94	19.64	56	40	2.49	1.010	1.015	0.994
CS-16	743100	4211100	20.05	20.29	201	71	20.11	19.74	241	22	2.79	1.009	1.019	0.990
CS-17	743900	4211950	20.84	21.00	242	48	20.90	20.63	110	18	1 79	1.005	1.013	0.992
CS-18	742850	4211800	21.91	22.10	55	20	21.90	21.72	146	21	1.75	1.009	1.008	1.001
CS-19	742050	4211150	19 65	19.88	36	39	19.73	19.35	303	7	2.74	1.008	1.020	0.988
CS-20	740950	4210400	18.19	18.47	5	27	18.26	17.85	126	49	3.47	1.012	1.023	0.989
CS-21	738550	4212000	24.73	24.90	177	13	24.77	24 51	306	67	1.59	1.005	1.011	0.995
CS-22	739100	4211400	20.89	21.09	203	7	20.94	20.64	302	54	2.18	1.007	1.015	0.993
CS-23	739850	4210850	21.73	21.86	282	66	21.75	21.57	80	21	1.34	1.005	1.008	0.997
CS-24	740400	4211700	18.97	19 16	61	7	18.96	18.80	326	32	1 91	1.011	1.009	1.002
CS-25	740800	4211200	32.13	32.47	359	56	32.10	31 83	123	21	2.01	1.012	1.008	1.003
CS-26	738900	4210950	6.96	7.04	246	40	6.95	6.89	114	39	2 18	1.013	1.009	1.004
CS-27	740300	4210150	15 98	16.12	206	64	16.00	15.81	111	13	1.96	1.008	1.012	0.996
CS-28	739500	4212100	18.40	18.59	59	1	18.39	18.21	151	71	2.09	1.011	1.010	1.001
CS-29	741650	4211900	20.03	20 12	291	52	20.04	19.93	162	25	0.95	1.004	1.006	0.998
CS-30	740500	4212400	27.90	28.20	331	55	27.86	27.64	122	28	2.03	1.012	1.008	1.004
CS-31	739900	4212550	20.77	21 01	92	54	20.77	20.52	319	29	2.39	1.012	1.012	0.999
CS-32	738350	4216000	18.69	18.89	126	7	18.68	18 51	268	77	2.05	1.011	1.009	1.002
CS-33	739850	4216200	23.05	23.24	178	84	23.09	22.81	291	1	1.89	1.006	1.012	0.994
CS-34	739800	4215700	28.41	28.78	178	8	28.54	27.90	71	50	3.15	1.008	1.023	0.986
CS-35	740150	4215250	22 82	23.01	201	11	22.88	22.56	105	33	1.99	1.006	1.014	0.992
CS-36	740300	4214800	19.59	19.84	280	55	19.56	19.38	52	24	2.37	1.014	1.009	1.005
CS-37	739450	4214700	21.22	21.47	138	71	21.21	20.98	258	6	2.34	1.012	1.011	1.001
CS-38	738850	4214050	19.75	20.05	108	37	19.81	19.40	309	52	3.35	1.012	1.021	0.991
CS-39	738400	4214850	22.85	23.12	135	0	22.89	22.54	237	78	2 57	1.010	1.016	0.995
CS-40	738150	4214700	23.61	23.93	142	21	23.78	23 11	14	50	3.55	1.006	1.029	0.978
CS-41	739850	4214150	18 17	18.46	272	5	18.18	17.86	138	7	3.36	1.015	1.018	0.998
CS-42	741200	4214350	18.50	18.66	90	29	18.56	18.28	198	28	2.08	1.005	1.015	0.990
CS-43	741900	4214100	17.81	17.99	118	52	17.85	17.60	199	19	2.22	1.008	1.014	0 994
CS-44	743100	4213050	33.98	34.26	25	50	34.06	33 62	280	12	1.90	1.006	1.013	0.993

Magnetic susceptibility and anisotropy of magnetic susceptibility (AMS) results obtained for the samples studied. $K1$, $K2$ and $K3$ are the values of the principal axes of the magnetic susceptibility ellipsoid. K_{mean} is the arithmetic mean of $K1$, $K2$ and $K3$. X and Y are the Universal Transverse Mercator (UTM) geographic coordinates of the sampling sites. L and F are the lineation and foliation parameters, as defined by *Tarling and Hrouda* [1993]. Anisotropy degree (P%) and *Flinn*'s [1962] parameters were calculated after *Jelinek* [1978]. AZ and PL refer to the azimuth and plunge of the AMS axes, respectively.

granite (Figure 4). The samples were oriented and drilled in the field. Two cores were collected at each site. Each core was subsequently cut with a saw to form two 2.5 cm diameter and 2.2 cm long cylinders, the result obtained representing four samples at each station. The magnitude of the magnetic susceptibility and the anisotropy of magnetic susceptibility of every specimen were measured in the laboratory at room temperature with the Kappabridge KLY-2 susceptometer of the University of Salamanca (manufactured by Geofyzika Brno), working at a low alternating inductive magnetic field of ±4 x 10^{-4} T at 920 Hz. The sensibility of the KLY-2 susceptibility bridge is 5 x 10^{-8} SI, which allows one to determine reliable AMS directions in practically every rock type down to an anisotropy ratio of 1.002. Measurements provide the magnitude and orientations of the $K_{max} \geq K_{int} \geq K_{min}$ axes of the AMS ellipsoid. The bulk susceptibility is defined as $K_{mean} = (K_{max} + K_{int} + K_{min})/3$.

4.2. Magnetic Susceptibility Magnitudes

Table 1 gives the magnitude of the bulk magnetic susceptibility (K_{mean}) for the sites sampled, after correction of the constant contribution of diamagnetic minerals (-1.4 x 10^{-5} SI cf. *Rochette* [1987]). K_{mean} varies between absolute

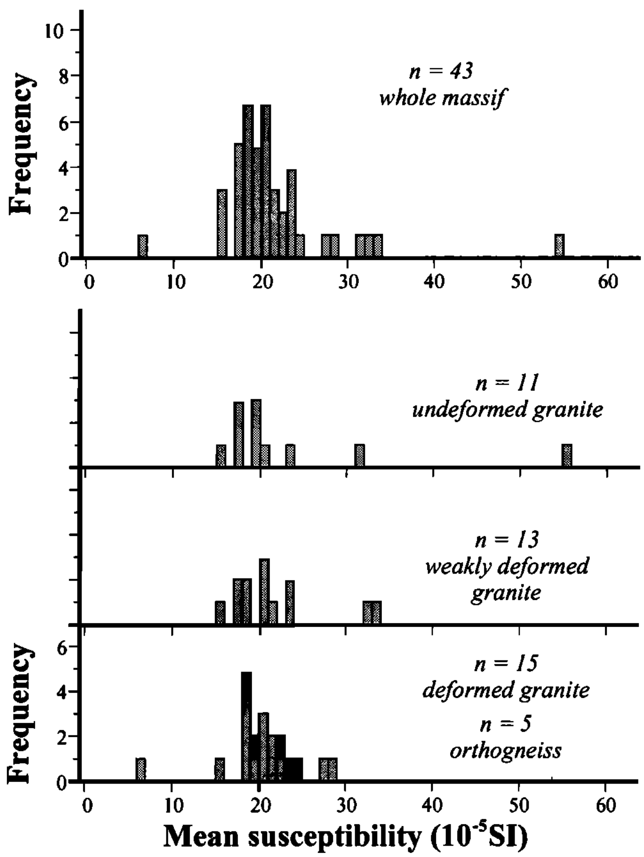

Figure 5. Frequency distribution histograms of mean magnetic susceptibility in the Castillo granite. Plots correspond to (top) all the samples studied and (bottom) to each one of the petrographic/deformational types described in the text.

extremes of 6.96 x 10^{-5} (site CS-26) and 55.50 x 10^{-5} SI (site CS-4). Nevertheless, K_{mean} of most samples ranges between 15 and 34 x 10^{-5} SI, with a maximum near 20 x 10^{-5} SI. The different deformational granite varieties recognized contain essentially the same mineral constituents and share a similar geochemical composition. Accordingly, K_{mean} exhibits comparable variation ranges in every rock type (Figure 5). Nevertheless, a distinguishable zonation of the K_{mean} values exists throughout the Castillo granite (Figure 6), which could be related to its petrographic constitution and ultimately to its structure.

On the basis of available chemical analyses of this granite [*Eguíluz*, 1988], and admitting that all Fe^{2+}, Fe^{3+}, and Mn^{2+} are contained in paramagnetic mineral species, the theoretical magnetic susceptibility [cf. *Rochette*, 1987] calculated for these rocks (the diamagnetic contribution being considered) ranges between 6.1 x 10^{-5} SI and 14.4 x 10^{-5} SI. These values compare to those actually measured.

The reported low magnetic susceptibility (measured and calculated $K_{mean} \ll 10^{-3}$ SI), usually found in granites, reflects the magnetic contribution of paramagnetic minerals [*Rochette*, 1987; *Tarling and Hrouda*, 1993], notably hornblende (and biotite) for the case of the Castillo pluton. Also, there is a lack of substantial ferromagnetic contribution among the principal magnetic susceptibility carriers in the pluton. The anisotropy of magnetic susceptibility in these rocks is therefore expected to be due to the crystallographic preferred orientation of the paramagnetic minerals cited.

4.3. Anisotropy of Magnetic Susceptibility Data

Inspection of the anisotropy degree *P*(%) as a function of K_{mean} (Table 1) shows that samples exhibit a wide variety of *P*(%) values (0.95-3.55) independent of their magnetic susceptibility. It is only noticeable that the sites with larger *P*(%) values tend to show a smaller degree of variation of K_{mean} (around 20 x 10^{-5} SI), while sites with smaller *P*(%) exhibit K_{mean} values spread over a wider range (between 15 and 35 x 10^{-5} SI). *Jelinek*'s [1978] *P'* and *T* parameters range between 1.01 and 1.04 and -0.33 and 0.76, respectively.

Distinct zonation patterns can be observed in the Castillo granite with regard to its AMS signature. Magnetic foliations (Figure 7a) and lineations (Figure 7b), as well as derived anisotropy degree *P*(%) (Figure 7c) and *Flinn*'s [1962] *k* parameters (Figure 7d), tend to be more intensely defined either in the areas where the secondary structural fabrics are better defined or at not so explicitly deformed areas whose location, however, can be related to magmatic pluton emplacement.

4.4. Magnetic Structure of the Granite: Directional and Regionalized Data

Orientation diagrams for the K_{max} (the magnetic lineation) and K_{min} (the pole to the magnetic foliation) axes of the magnetic fabric of the Castillo granite (Figure 8) reflect its internal structure. Gently or steeply dipping magnetic foliations tend to define an incomplete girdle oriented ESE-WNW. The strike of this foliations is approximately normal to the trend of regional structures and fabrics in the granite country rocks. In detail, some additional interesting conclusions can be gained from inspection of the foliation map in Figure 9. Gently dipping foliations concentrate at the NW contacts of the pluton, where orthogneiss is the dominant rock type. The remainder of the granite exhibits magnetic foliations dipping, often >60°. The strike of these foliations is more or less parallel with the contacts between the granitoid petrographic types distinguished, notably with the contact between the undeformed and weakly deformed facies. This would suggest a genetic relationship (in addition to the geometric) between them.

Magnetic lineations tend to plunge steeply (often ≥45°) throughout the pluton (Figure 8). The exception of this occurs at the northwestern margins, where granite gneissiffication is widespread and magnetic lineations are gently dipping to the NNE (Figure 10). The variability in the direction of magnetic lineations contrasts with the constancy of mineral and stretching lineations measured in the field in the northwestern margin of the pluton. Furthermore, these orthogneiss lineations are parallel with mineral and stretching lineations formed in the footwall and hanging wall of the Monesterio ductile thrust (Figure 10). These geometrical relationships enable us to interpret that magnetic lineations in the areas of the pluton not affected by gneissification could be related to magmatic emplacement of the pluton, while those formed in

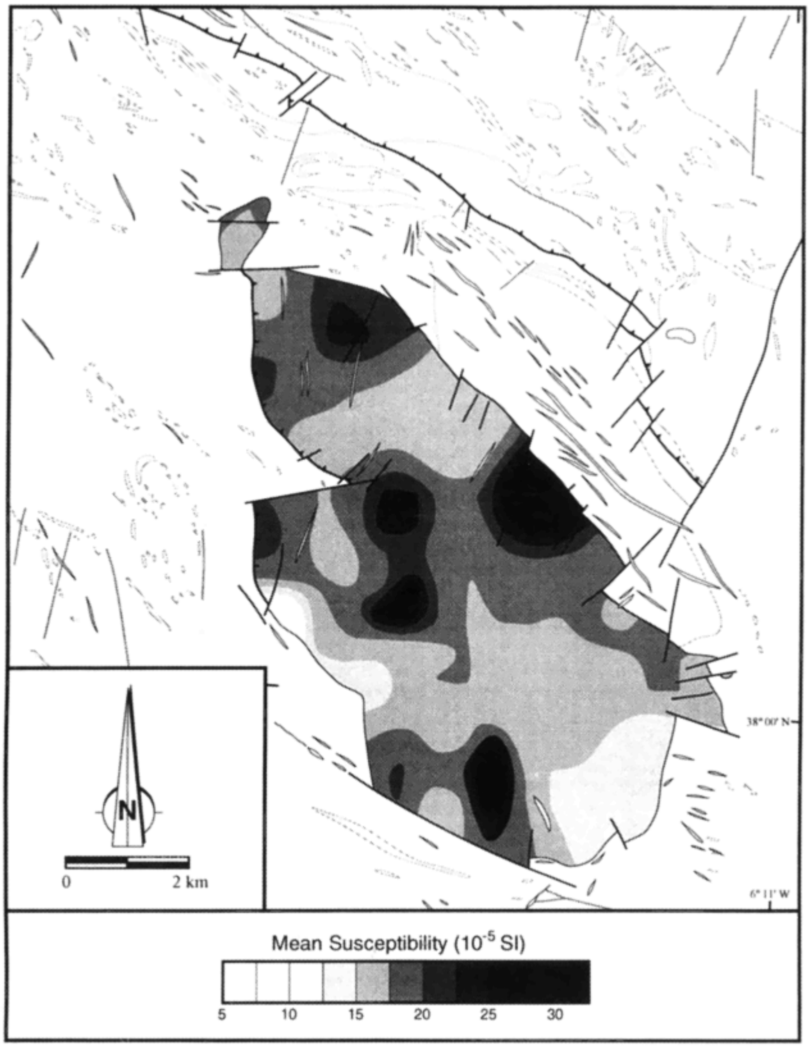

Figure 6. Areal distribution of mean magnetic susceptibility across the Castillo pluton. See text for further details.

the NW margin relate to later solid-state deformations not linked to pluton emplacement.

In the foliation trajectory map shown in Figure 11a the superimposition of solid-state deformation fabrics on magmatic ones and the parallelism of the latter with the contacts between the different facies recognized are highlighted. Structural superposition is also clear from Figure 11b. Here strike constancy of mineral and stretching lineations (NE-SW traces in the shadowed areas) in the Monesterio thrust and the NW margin of the Castillo pluton contrasts with the variation in orientation shown by lineation trajectories within the pluton.

Superposition of fabrics in the NW margin of the pluton deserves further attention. The stereoplot presented in Figure 12 contains a gray patterned girdle with a point maxima. The girdle represents the trace of the Monesterio thrust and the ±5° and ±10° orientation intervals around it. The heavily shaded point maxima represents the mean stretching lineation associated with the thrust, whereas the shaded areas around it represent 5° and 10° confidence cones for such orientations. Also plotted are the traces of magnetic foliations and the contained magnetic lineations for the 17 samples located in the NW margin of the pluton or near it. It is clear from the figure that both magnetic foliations and lineations plot at high angles with respect to mean mesoscopic foliation and lineation orientations in the same area. It must be emphasized that the magnetic axes of these samples were tested for axis inversion prior to this analysis.

Since the Monesterio thrust postdates the Castillo pluton emplacement by 180 Myr, the structures related to it should be expected to reorientate and/or obliterate any structure previously formed. It is surprising, however, that strong solid-state secondary deformation has not reoriented (at least noticeably) the magnetic fabric of the Castillo granite in its NW margin. As far as we are aware, relationships such as described have not been reported in the literature so far. *Riller et al.*, [1996] give evidence of the converse: A complete reorientation of magnetic fabrics during a deformation episode without accompaniment of reorientation/transposition of the preexisting mesoscopic foliations/lineations, which are thus

Figure 7. Areal distribution of (a) the foliation, (b) lineation, (c) anisotropy degree, and (d) *Flinn*'s [1962] parameters across the Castillo pluton. See text for further details.

intersected at high angles. Their interpretation of the cited geometrical relationships (noncoaxial superimposition of two separate deformation pulses resulting in overprinting of the earlier fabrics) can be proposed for the case of the Castillo granite as well.

5. Discussion: Structure of the Castillo Pluton

Previous structural and kinematic interpretation of the Castillo pluton [*Eguiluz*, 1988, and references therein] considered it as an initially subcircular Cadomian intrusion deformed during Variscan orogeny. As a result, the pluton would have acquired a subelliptical external morphology elongated roughly subparallel to the Monesterio thrust, whose emplacement was the driving force for pluton internal deformation and thrusting onto its country rocks. In detail, however, this interpretation fails to explain some capital structural features of the granite, such as (1) the obliquity between the pluton maximun elongation direction and the strike of the Monesterio thrust, (2) the location of the pluton's thrust contacts only at its western margins instead of along its whole SW facing margins, and (3) the geometry of the internal strain facies distribution of the granite (Figures 2 and 3).

The magnetic structure of the pluton and its interpretation based on microstructural observations enables us to delineate, as shown in the section 4, the fundamental features of the granite's internal structure. In this regard, the structural signatures due to pluton emplacement can now be separated from those due to its subsequent tectonic deformation. Nevertheless, in order to kinematically interpret the shape of the intrusion, as well as its internal structure, it is necessary to ascertain whether the pluton has undergone solid body rotations, and to this end, a structural inspection of the country rocks is essential.

Inspection of the foliation map shown in Figure 9 enables one to realize that the main attitude of foliations in the

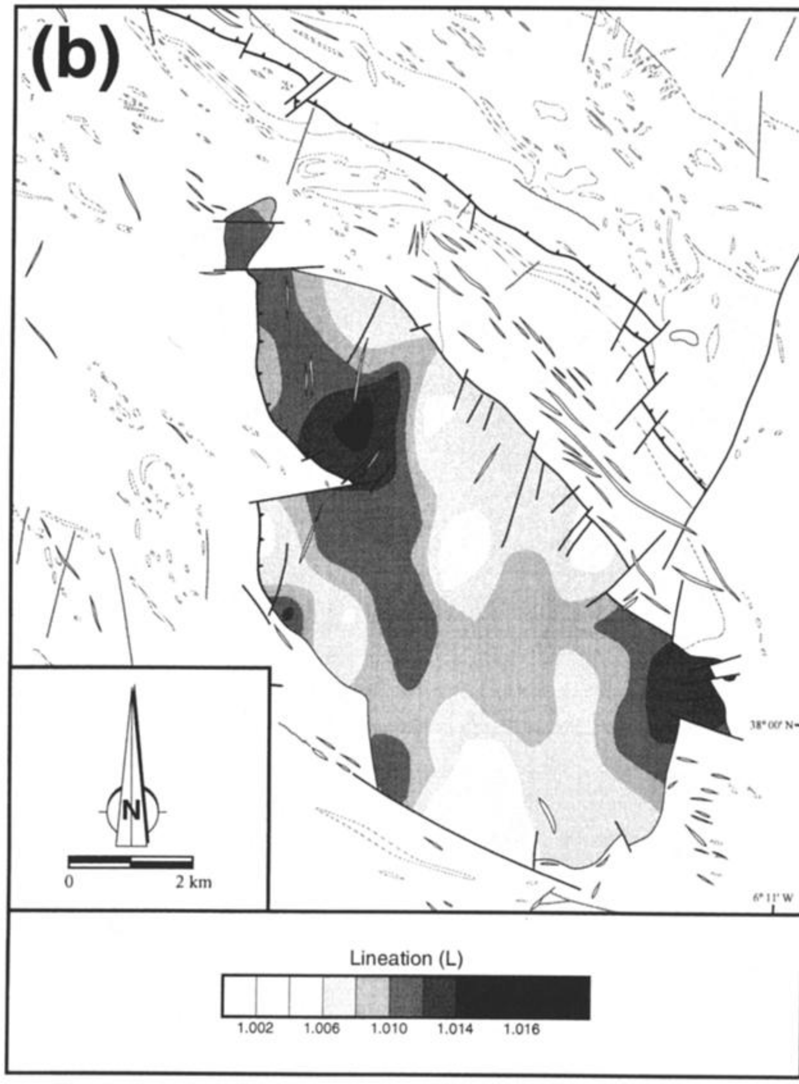

Figure 7. (continued)

country rocks of the Castillo pluton (apart from minor refolding areas) consists in a NE dip of NW-SE trending planes. This occurs both in the northern and the southern areas of the map, the aforementioned orientations being parallel to the orientation of the Monesterio thrust, to the attitude of foliations in the thrust hanging wall, and to the western thrust contact of the Castillo granite. Figure 13 presents a structural map of the studied area at a larger scale where structural relationships between the Monesterio thrust, the Castillo pluton (as well as neighboring granitoid intrusions), and the internal structure of the Serie Negra are shown. Superimposed deformations in the Serie Negra are evident from foliation trajectory patterns and the complexly refolded geometry of black quartzite layers (Figure 14). Orientation analysis of these structures (stereoplots in Figure 13) enable us to clearly identify the signature of the superimposed Variscan deformation: S_0+S_1 planes tend to dip moderately to the NE, and fold axes have been reoriented to that orientation, which corresponds to the regional strike (N110°-140°E) and dip (30°-40°) of the Monesterio thrust [*Eguiluz and Ramón-Lluch*, 1983]. Also noticeable in this map is the fact that foliations in the southwestern portions of the Serie Negra dip to the NE, in spite of the SW directed dip of the unconformable overlying rocks, which were affected only by the Variscan deformations. All this denotes, on one hand, a likely genetic relationship between the reorientation of regional foliations in the Serie Negra and the Monesterio thrust (and related structures) and, on the other hand, the structural contrast between a larger-scale, younger (Variscan) antiformal structure cut across by the Monesterio thrust (also Variscan) and the more complex internal geometry of the Serie Negra in the core of the antiform (with superimposed deformations). If the Monesterio thrust was, reasonably, a subhorizontal ductile shear zone conforming the base of a metamorphic nappe, its current attitude would denote its basculation around a subhorizontal NW-SE trending axis and therefore the ensuing passive rotation of the hanging wall and footwall blocks adjacent to the thrust zone. This would also have been the case for the

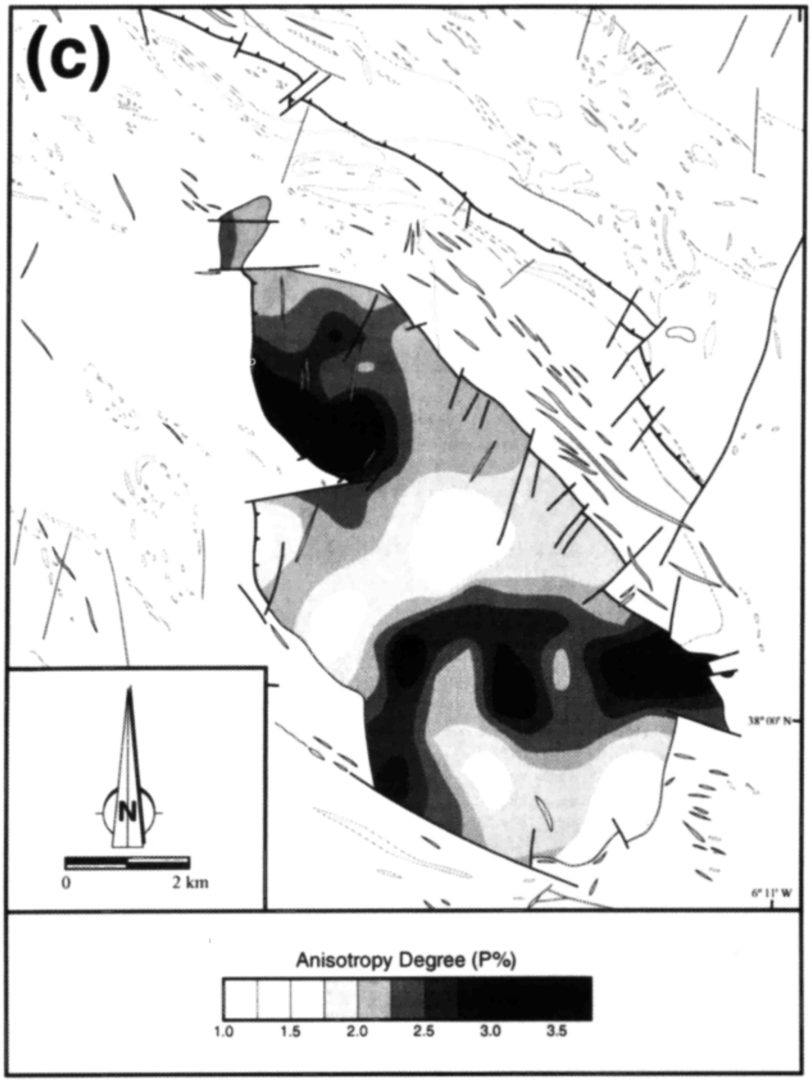

Figure 7. (continued)

Castillo pluton. Thus in order to reconstruct its geometry and to decipher its kinematic evolution a restoration to its original emplacement situation is needed.

Structural reconstructions of the geometry of tilted plutons are rare. *Rosenberg et al.*, [1995] present such a study on the Bergell pluton (central Alps). On the basis of a downplunge projection of the cartographic data they reconstruct the geometry of the intrusion from its root zone to its cap in a structural section whose vertical depth attains 20 km. *Ague and Brandon* [1996] document regional batholith tilting based on variations observed in aluminum-in-hornblende barometry. However, these authors discuss the tectonic implications of their data from a paleomagnetic perspective

In the Figure 15 a digitally drawn downplunge projection of the map area shown in Figures 2 and 3 is presented. The map was projected onto a plane normal to the mean orientation of stretching lineation in the Monesterio thrust, with the latter structure placed subhorizontal. In this projection the Castillo pluton appears as a tabular intrusion of 6 km in diameter and 1.7 km thick, thus with a 3.5:1 width-thickness ratio. In the following the geometry of the pluton's contacts and its internal structure will be reevaluated from this new perspective.

The outcrops of the orthogneissic granite correspond here to two basal flat areas of the pluton, which are parallel to the trace of the overlying Monesterio thrust, with respect to where the kinematic relationship is clear in addition to the geometrical. Other flat contacts of the pluton parallel to the principal thrust, as is the case for the top of the intrusion, were not reactivated by thrusting, likely because of the shadow effect induced by the attached and overlying Culebrín tonalite, which localized thrusting above. The basal contact of the pluton deserves further attention. It is shown in the Figure 2 that it is cut by a late wrench fault. Areal variation of magnetic susceptibility and other derived parameters (Figures 6 and 7) toward the southern border of the pluton as well as the attitude of magnetic foliations there (Figures 9 and 11a) could be interpreted jointly as the reflection of the occurrence of the

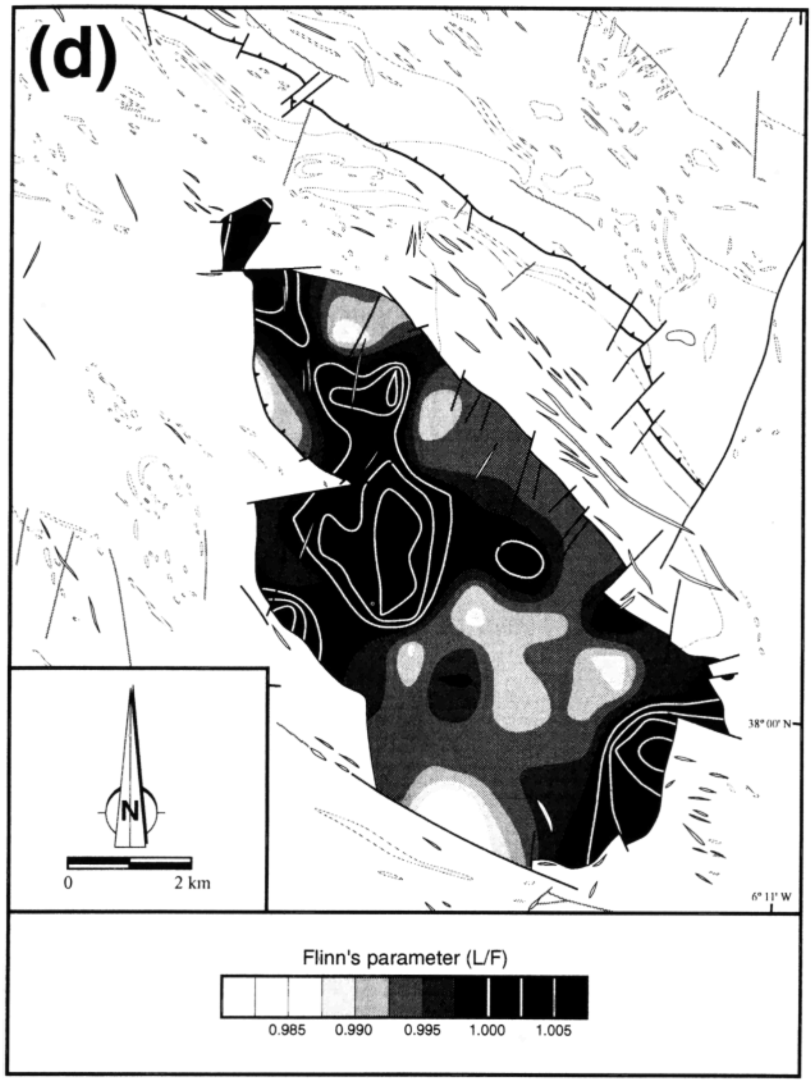

Figure 7. (continued)

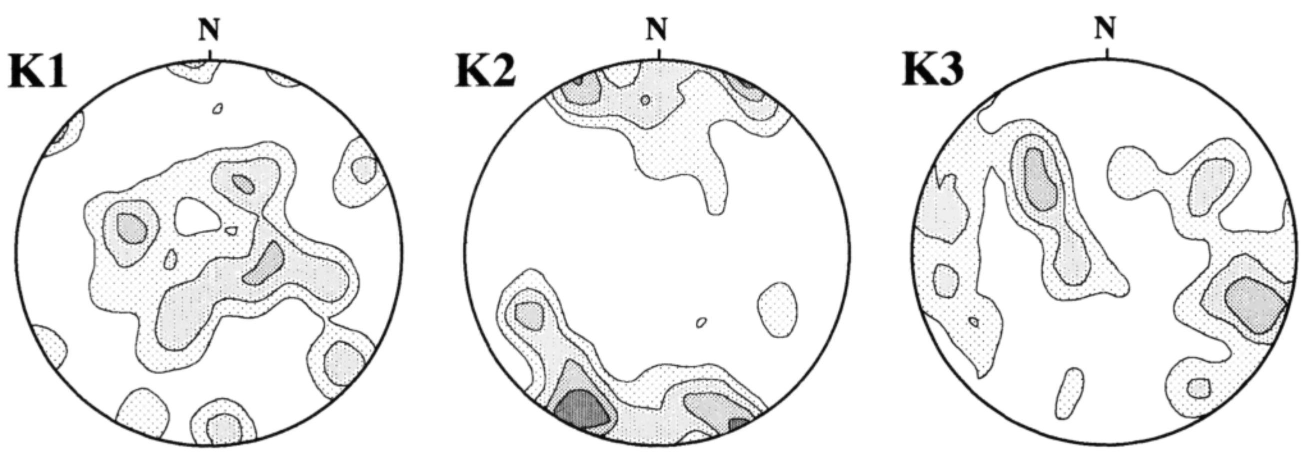

Figure 8. Stereographic projection (equal area, lower hemisphere) of the orientations of the $K1$, $K2$, and $K3$ magnetic anisotropy axes. Contours are in multiples of uniform distribution.

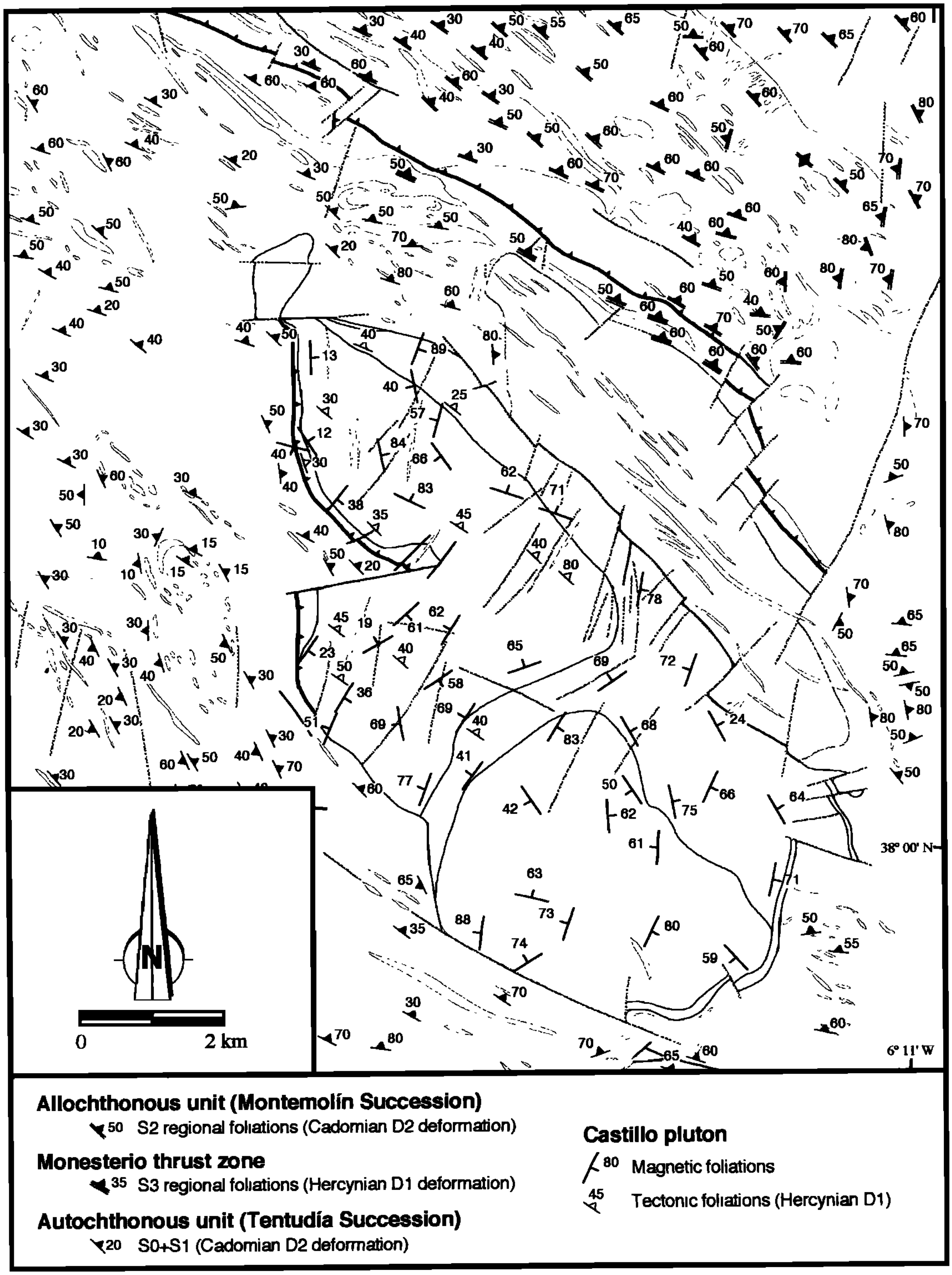

Figure 9. Structural map showing the attitudes of magnetic foliations in the Castillo pluton and of tectonic foliations in the western margin of the pluton and the country rocks.

pluton's root zone there. The transition of the tabular morphology of the main body of the granite to a likely thin, subvertical feeder dike structure would occur here. It is reasonably expected that localization of deformation along such a weak structural zone would occur under tectonic reactivation, thus leading to dismemberment of the pluton from its root.

The lateral contacts of the pluton remained apparently intact during the superimposed Variscan deformation, enabling preservation of the contact aureole. Foliation

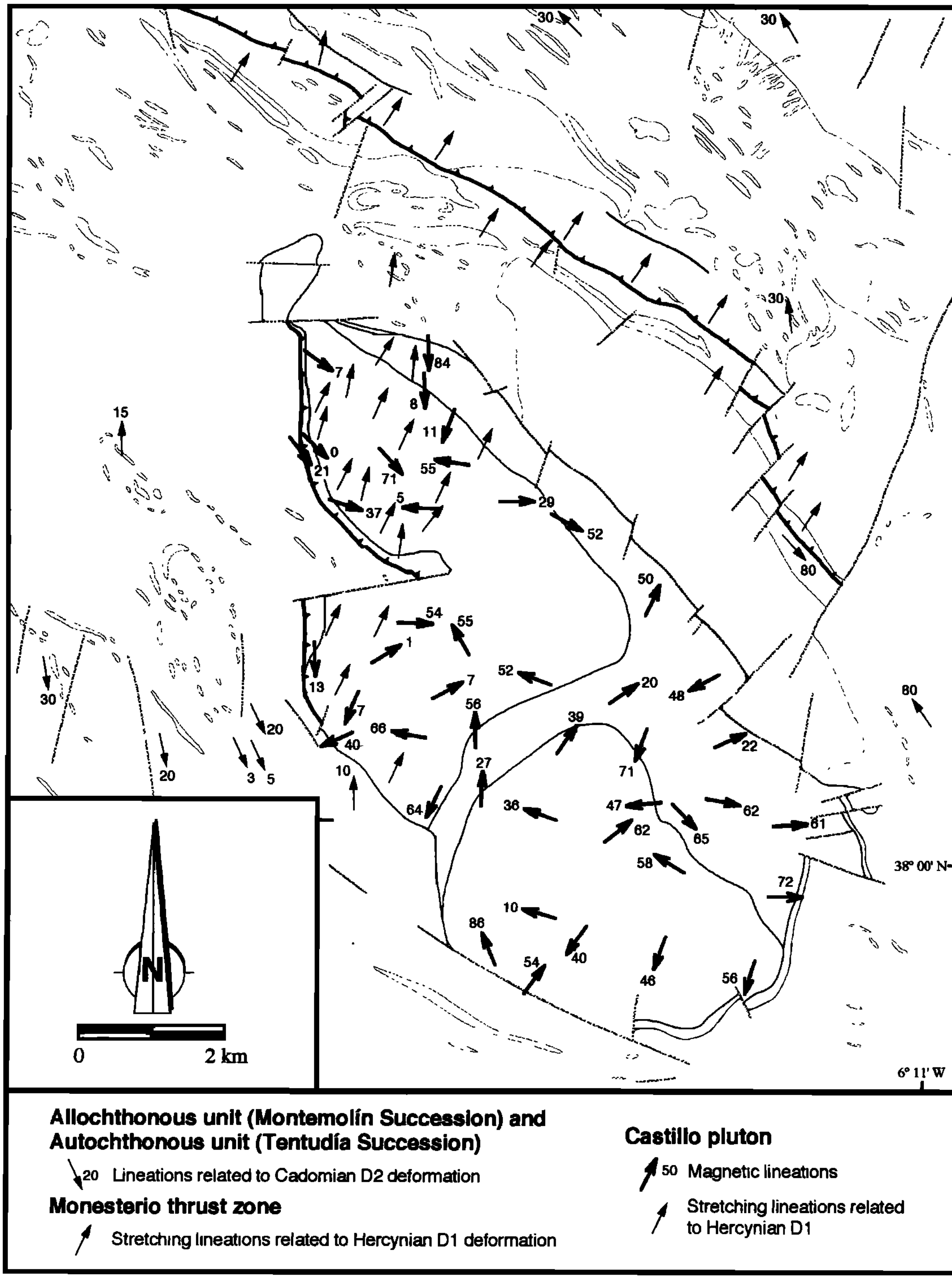

Figure 10. Structural map showing the attitudes of magnetic lineations in the Castillo pluton and of mineral and stretching lineations in the western margin of the pluton and the country rocks.

trajectories around the intrusion (Figure 15) reflect the accommodation of the country rocks to its shape as a tectonic foliation does around a porphyroclast in thin section.

As regards the internal geometry of the pluton, the magnetic foliation and lineation trajectories redrawn in the new projection plane in Figure 16 clearly locate the root of the Castillo granite at its actual southern border (Figure 2). The root can be tentatively identified as a subvertical dike on the basis of the concentric vertical wall geometry described by the magnetic foliation trajectories. In Figure 16 the length of the arrows depicting magnetic lineations is inversely proportional to its plunge in the projection plane. Bearing

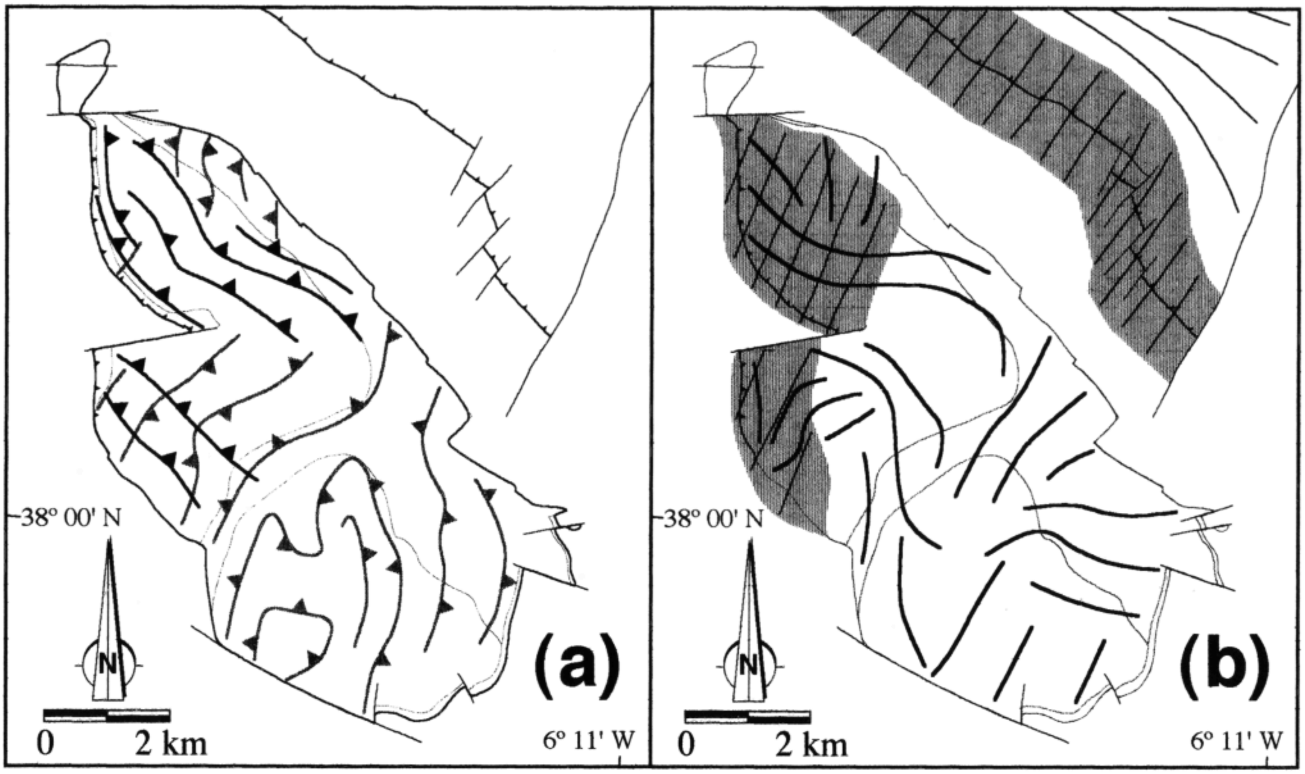

Figure 11. (a) Structural map of the Castillo pluton showing the attitudes of inferred magmatic foliation trajectories (shaded trajectories) and observed solid state deformation fabrics (bold black trajectories). The geometrical relationships of superimposed fabrics can be observed in the western area of the pluton. (b) Trajectory map showing the attitudes of inferred magmatic (bold black curved lines) and tectonic lineations (thick black lines in the shaded areas) for the Castillo pluton and selected units of its country rocks. The contacts between the different granite facies recognized are depicted by thin lines both in Figures 11a and 11b.

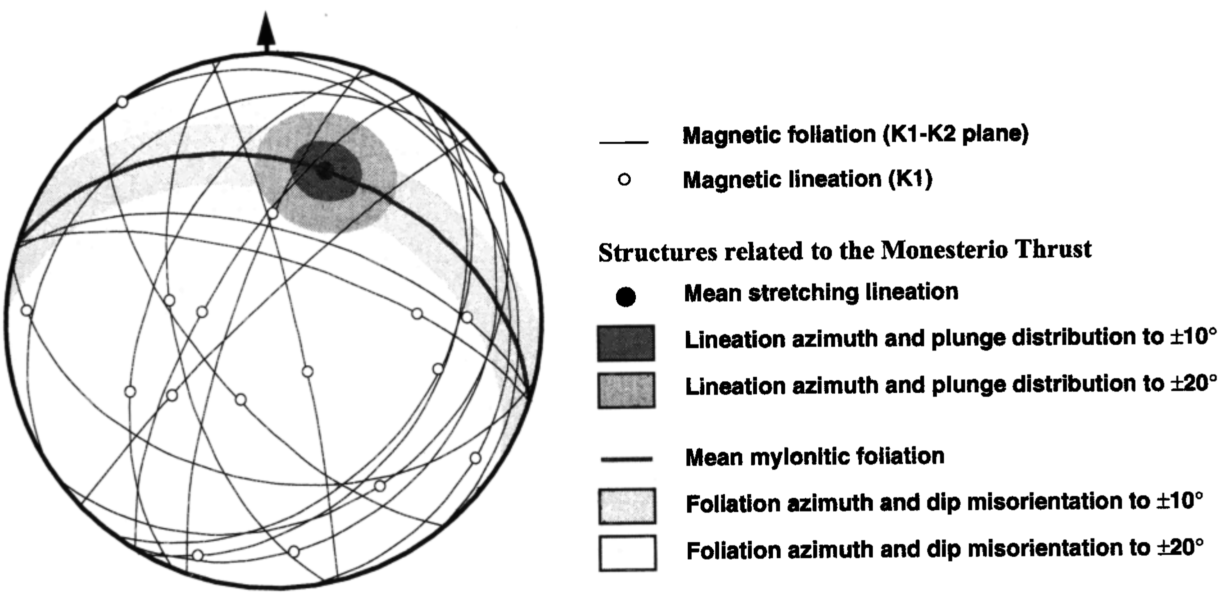

Figure 12. Stereographic projection (lower hemisphere) of the orientations of the magnetic foliations ($K1$-$K2$ planes, great circles) and lineations (open dots) for 17 samples located in the NW margin of the Castillo pluton. The shaded girdle represents the trace (heavily shaded great circle) of the Monesterio thrust and the ±5° (dark shading) and ±10° (light shading) orientation intervals around it. The heavily shaded point maxima represents the mean stretching lineation associated to the thrust, whereas the shaded areas around it represent 5° and 10° confidence cones for such orientations.

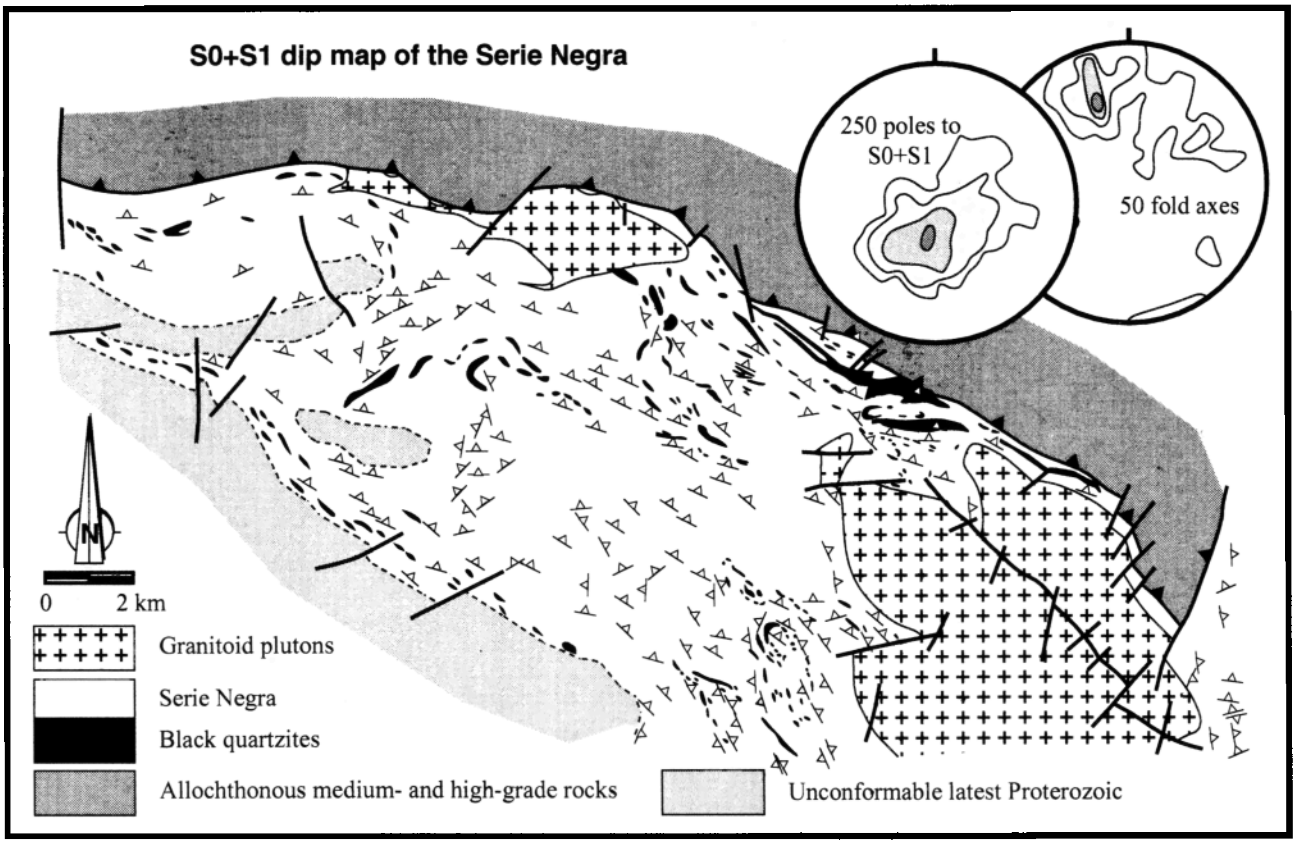

Figure 13. Structural map depicting the intricate patterns of superimposed folding in the country rocks of the Castillo pluton (the Serie Negra) and the geometrical relationships with discordant latest Proterozoic units and the late Paleozoic Monesterio thrust. Stereographic projections (equal area, lower hemisphere) correspond to the orientations of structural elements of the Serie Negra. Contours are in multiples of uniform distribution.

this in mind, it is remarkable that the dominance of vertical "tangential" displacements near the root zone and horizontal tangential displacements at the pluton's edges in the perspective shown. This structural geometry, together with the wrapped geometry shown by the country rocks, could attest the lateral propagation of the pluton and its latter inflation [*McCaffrey and Petford*, 1997].

The shallow depth of emplacement of the Castillo pluton can be inferred either from the thermobaric signature of the greenschists facies country rocks or from the use of aluminum-in-Hornblende barometers in the granite. On one hand, according to *Eguíluz and Ábalos* [1992], the upper temperature constraints are between 390°±50°C and 460°±50°C, whereas maximum pressures of metamorphism did not exceed 3500-4000 MPa. On the other hand, since aluminum content in hastingsitic hornblende of the granite varies between 1.382 and 1.653 atoms per formula unit, the pressures calculated by use of the barometers of *Johnson and Rutherford* [1989] and *Schmidt* [1992] oscillate around 4400±500 MPa on average. These pressures should be interpreted as upper constraints as well, as they are higher than the pressures undergone by coeval, higher-grade metamorphic rocks in the hanging wall of the Monesterio thrust. All this evidence suggests that assuming a density of 2700 kgr/m^3 for a model crust and a lithostatic pressure, the depth of emplacement of the Castillo granite was of the order of 10 km, close to the ductile-brittle transition zone [*Vigneresse*, 1995a].

The N190°-200°E trending magnetic lineations and subvertical magnetic foliations that dominate the southern area of the pluton (Figure 9) form a high angle to the regional structures present in the country rocks. This southern area was affected only by structures of magmatic origin and would reasonably relate to emplacement processes operative in the originally deeper portions of the pluton, close to the root zone. We interpret these structures as related to the magma feeder zone [*Vigneresse*, 1995a], likely a feeder dike whose orientation would thus be close to N190°-200°E, according to present-day geographical coordinates. Since the Castillo pluton is a Cadomian intrusion, that orientation could reflect the regional stress field prevalent at that time. According to *Vigneresse* [1995b], and given the shallow level of emplacement within the Serie Negra, this root zone would have initiated and remained at or near the orientation of σ_1 but would have penetrated deep enough to involve the ductile crust. This is in good agreement with the lithospheric-scale late Cadomian NNE-SSW compressional tectonic regime

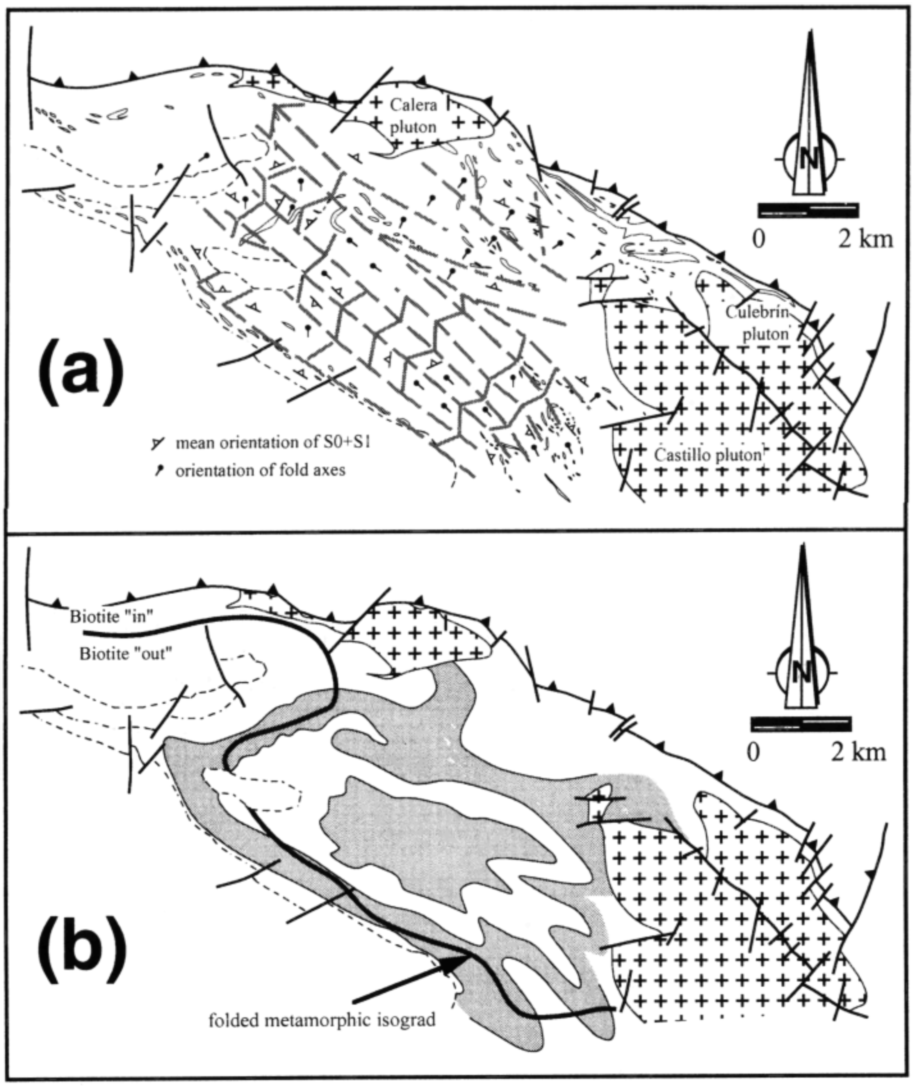

Figure 14. Interpretative structural maps of the area shown in Figure 13 after *Eguíluz and Ramón-Lluch* [1983]. (a) Delineation of homogeneous fold domains. (b) Idealized reconstruction of superimposed fold geometries affecting latest Proterozoic-earliest Cambrian bedding surfaces (gray stippled area) and metamorphic isograds (thick black line). The geometrical relationships of these structures with the post-Cadomian discordance, the Castillo pluton, and the Monesterio thrust are highlighted.

which has been documented in this and other areas of SW Iberia through geological field data and geophysical investigations [*Ábalos and Díaz-Cusí*, 1995].

Brittle deformation in deeper crustal levels can be demonstrated in the study area. A close inspection of northeastern area of the Figure 2 shows NE-SW trending dikes of anatectic two-mica granites intruding migmatitic gneisses at the map scale. These dikes are spatially related to other planar anatectic bodies trending NW-SE which are concordant with the principal foliation as well as to structurally underlying anatectic mobilisates with larger and more complex geometries. The down plunge projection of these features of anatectic origin shown in Figure 15 highlights the described geometrical relationships. In this regard, the relationships shown by the different kinds of anatectic mobilisates and their gneissic country rocks in the Monesterio thrust hanging wall could be considered as a frozen image of the process of granitic magma segregation and initial upwelling. Though a direct physical connection does not exist between the lower crustal realms cited (source of granitic magma) and the shallower crustal levels preserved in the Monesterio thrust footwall (where magma emplacement gave rise to the Castillo pluton) a conceptual model can be proposed to relate them (Figure 17), as ultimately both are the result of Cadomian high-grade metamorphism.

6. Conclusions

The late Cadomian Castillo granite is a tilted pluton. Geometrical reconstruction on the basis of structural and

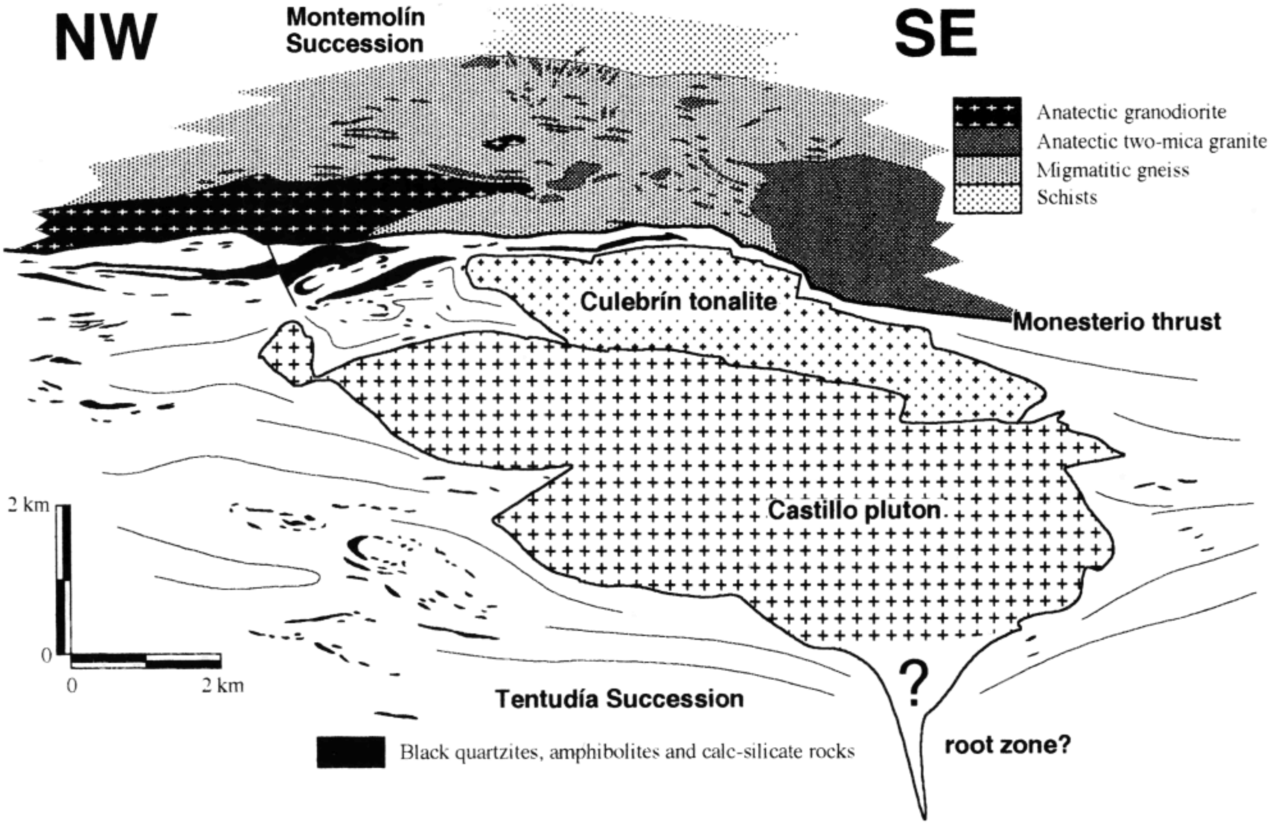

Figure 15. Downplunge plot of the area shown in Figure 2. The projection section (oriented NW-SE) is normal to the direction of stretching lineations associated to both the Monesterio thrust and the western margin of the Castillo pluton. Note the subhorizontal, tabular geometry of the pluton, its emplacement within a medium dominated by a flat-lying mechanical anisotropy, and the accommodation of such anisotropy to the pluton geometry at its edges. Note also the geometry and orientation of anatectic mobilisates (two-mica granites) in the hanging wall of the Monesterio thrust.

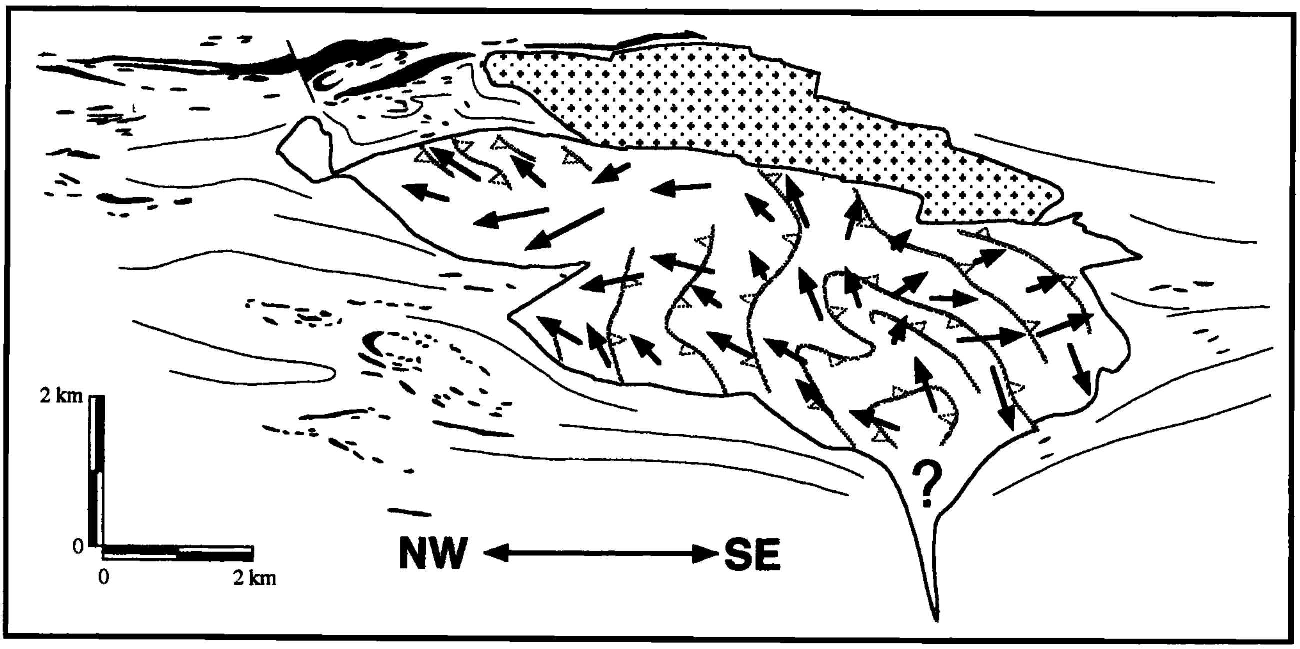

Figure 16. Sketched downplunge projection of the Castillo pluton (and its country rocks in the footwall of the Monesterio thrust) showing the geometry inferred for magmatic, emplacement-related structures inside the pluton. Stippled lines with triangles are magnetic foliation trajectories. Black arrows are magnetic lineation trajectories whose length is inversely proportional to their plunge out of the plane of the section.

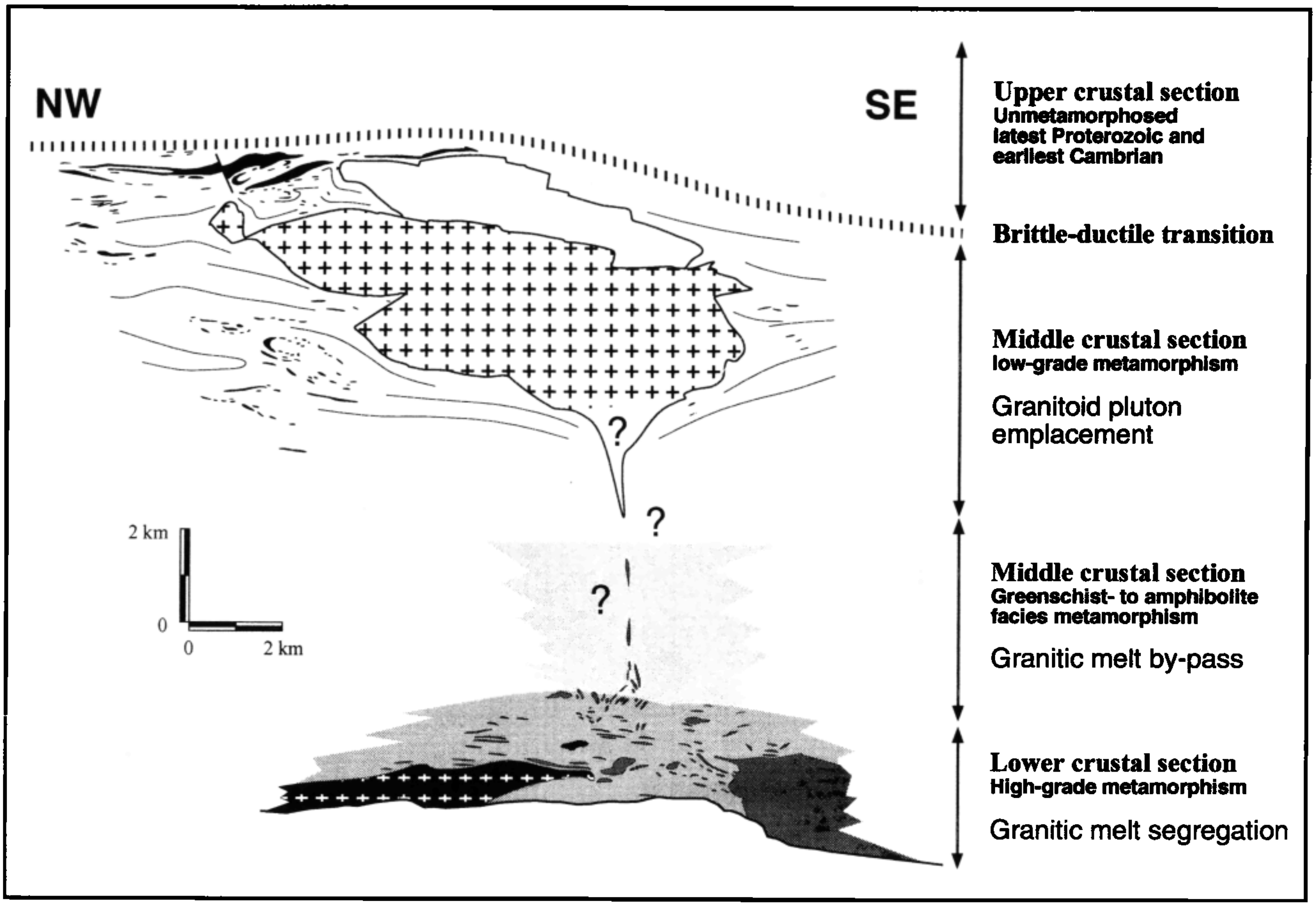

Figure 17. Idealized model of the emplacement and vertical structure of the Castillo pluton. The allochthonous block of the Monesterio thrust, representing lower crustal structural levels with widespread anatexis, is presented as an hypothetical source region for the granite pluton. See text for further details.

geophysical techniques enables us to describe its emplacement-related internal structure as well as accommodation of the country rocks around it in different depth levels. Originally it was a tabular intrusion 6 km in diameter and 1.7 km thick emplaced at a depth of the order of 10 km, close to the ductile-brittle transition zone. Its internal structure is characterized by moderately to steeply dipping magmatic flow planes whose strike is normal to the regional tectonic trends and moderately to gently plunging flow directions, as deduced from its magnetic structure. This geometry, together with that shown by the country rocks, could attest to the lateral propagation of the pluton and its latter inflation. The tabular morphology of the main granite body relates to a likely thin, subvertical feeder dike structure that constitutes its root zone. This root would have initiated and remained near the orientation of regional σ_1 at the time of emplacement (the latest stages of the Cadomian orogeny) and would have penetrated deep enough to involve the ductile crust.

Subsequent to its emplacement and after intrusion of the Culebrín Variscan pluton at the contact between the Castillo granite and the overlying country rocks, the Castillo pluton underwent localized fragile-ductile deformation in relation to Variscan shear zone deformation. This caused a superposition of tectonic zonations on the magmatic ones, a reactivation of the basal contact of the pluton, and dismemberment of the pluton from its root. Also, the occurrence of these and other granitoid plutons emplaced at a similar depth was likely a major constraint for the nucleation of the Variscan Monesterio thrust.

Acknowledgments. Financial support for this paper was provided by the Spanish DGICYT projects PB95/1035 and PB98/0143. We are indebted to A. Ribeiro, A. Pérez-Estaún, and an anonymous referee for their constructive reviews and advice on improving the manuscript.

References

Ábalos, B., and J. Díaz-Cusí, Correlation between seismic anisotropy and major geological structures in SW Iberia: a case study on continental lithosphere deformation, *Tectonics*, *14*, 1021-1040, 1995.

Ague, J.J., and M.T. Brandon, Regional tilt of the Mount Stuart batholith, Washington, determined using aluminum-in-hornblende barometry: Implications for northward translation of Baja British Columbia. *Geol. Soc. Am. Bull.*, *108*, 471-488, 1996.

Arriola, A., L Eguíluz, J. Fernández Carrasco, A. Garrote, and R. Sánchez-Carretero, Zonación metamórfica en el área de Monesterio-Fuente de Cantos; criterios texturales y mineralógicos, *Cuad. Lab. Geol. Laxe*, *8*, 17-46, 1984.

Bateman, R., Aureole deformation by flattening around a diapir during in situ ballooning: The Cannibal Creek Granite, *J. Geol.*, *93*, 293-310, 1985

Bellon, H., H. Blanchere, M. Crousilles, C. Deloche, C. Dixsaut, B. Hertritch, V. Prost-Dame, P Rossi, D. Simon, and G. Tamain, Radiochronologie, évolution téctono-magmatique et implications métallogéniques dans les cadomo-variscides du sud-est Hespérique. *Bull. Soc. Geol. Fr.*, *21*, 113-120, 1979

Borradaile, G.J., Magnetic susceptibility, petrofabrics and strain, *Tectonophysics*, *156*, 1-20, 1988.

Bouchez, J.L., and B. Gineberteau, Ecoulement dans les granitoides: De l'état visqueux a l'état solide, in *Uranium et granitoides*, Centre de Recherche et d'Etude sur la Géol. de l'Uranium, Nancy, France, 1-19, 1985.

Bouchez, J.L., and Gleizes, G, Two-stage deformation of the Mount-Louis-Andorra granite pluton (Variscan Pyrenees) inferred from magnetic susceptibility anisotropy, *J. Geol. Soc. London*, *152*, 669-679, 1995.

Bouchez, J.L., C. Delas, G. Gleizes, A. Nédélec, and M. Cuney, Submagmatic microfractures in granites, *Geology*, *20*, 35-38, 1992.

Bouillin, J.-P., J.-L. Bouchez, P. Lespinasse, P., and A. Pêcher, Granite emplacement in an extensional setting: An AMS study of the magmatic structures of Monte Capanne (Elba, Italy), *Earth Planet. Sci. Lett.*, *118*, 263-279, 1993.

Bowring, S.A., and D.H. Erwin, A new look at evolutionary rates in deep time: Uniting paleontology and high-precision geochronology, *GSA Today*, *8*, 1-7, 1998.

Brun, J.P., and J. Pons, Strain patterns of pluton emplacement in a crust undergoing noncoaxial deformation, Sierra Morena, Spain, *J Struct. Geol*, *3*, 219-229, 1981.

Cueto, L A., L. Eguíluz, F.J. Llamas, and C Quesada, La granodiorita de Pallares, un intrusivo Precámbrico en la alineación Olivenza-Monesterio (Zona de Ossa-Morena), *Comun Serv. Geol. Port.*, *69*, 219-226, 1983.

Dallmeyer, R.D., and C. Quesada, Cadomian versus Variscan evolution of the Ossa-Morena Zone: Field and $^{40}Ar/^{39}Ar$ mineral age constraints, *Tectonophysics*, *216*, 339-364, 1993.

D'Lemos, R.S., R.A. Strachan, and C.G. Topley, *The Cadomian Orogeny*, Geol. Soc. Spec Publ., *51*, 1-423, 1990.

D'Lemos, R.S., M. Brown, and R.A. Strachan, Granite magma generation, ascent and emplacement within a transpressional orogen, *J. Geol. Soc. London*, *149*, 487-490, 1992.

Dupont, R., E. Linares, and J. Pons, Premières datations radiométriques par le méthode potassium-argon des granitoides de la Sierra Morena Occidentale (Province de Badajoz, Espagne). Conséquences géologiques et métallogéniques, *Bol. Geol. Min.*, *92*, 370-374, 1981.

Eguíluz, L., Petrogénesis de rocas ígneas y metamórficas en el Anticlinorio Burguillos-Monesterio, Macizo Ibérico Meridional, Ph.D. thesis, 694 pp., Univ. del País Vasco, Bilbao, Spain, 1988.

Eguíluz, L., Lineación de estiramiento, estructuras C-S y sentido de movimiento en el granito del Castillo (Zona de Ossa-Morena, España), *Stvd. Geol. Salmant.*, *4*, 205-215, 1989.

Eguíluz, L., and B. Ábalos, Tectonic setting of Cadomian low-pressure metamorphism in the central Ossa-Morena Zone (Iberian Massif, SW Iberia), *Precambrian Res.*, *56*, 113-137, 1992.

Eguíluz, L., and A Garrote, Procesos cataclásticos en el stock granítico de la Sierra del Castillo (Monesterio), *Com. Serv. Geol. Port.*, *69*, 235-248, 1983

Eguíluz, L., and C. Quesada, La sucesión precámbrica de la transversal de Monesterio (Badajoz): Nota preliminar, *Temas Geol. Min.*, *1*, 123-141, 1981.

Eguíluz, L., and R. Ramón-Lluch, La estructura del sector central del dominio de Arroyomolinos: Anticlinorio Olivenza-Monesterio, Ossa-Morena, *Stvd. Geol. Salmant.*, *18*, 171-192, 1983.

Eguíluz, L., J. Fernández Carrasco, J.L. Collaut, A. Garrote, E. Liñán, and T. Palacios, *Mapa y memoria explicativa de la Hoja 897 (Monesterio) del Mapa Geol. Nac.* (scale 1:50.000). Ins. Geol. y Minero de Esp., Madrid, 1983.

Flinn, D., On folding during three-dimensional progressive deformation, *Q. J. Geol Soc. London*, *118*, 385-428, 1962.

Gléizes, G., A. Nédélec, J.-L. Bouchez, A. Autran, and P. Rochette, Magnetic susceptibility of the Mount-Louis Andorra illmenite-type granite (Pyrenees): A new tcol for the petrographic characterization and regional mapping of zoned granite plutons, *J Geophys. Res*, *98*, 4317-4331, 1993.

Graham, J.W., Magnetic susceptibility anisotropy, an unexploited petrofabric element, *Geol. Soc. Am. Bull.*, *65*, 1257-1258, 1954.

Guillet, P., J.-L. Bouchez, and J.J. Wagner, Anisotropy of magnetic susceptibility and magmatic structures in the Guérande granite massif, *Tectonics*, *2*, 419-429, 1983.

Henry, B., Magnetic fabric implications for the relationships between deformation mode and grain growth in slates from the Borrowdale volcanic group in the English Lake District, *Tectonophysics*, *178*, 225-230, 1990.

Hippert, J.F., Structures indicative of helicoidal flow in a migmatitic diapir (Bação Complex, southeastern Brazil), *Tectonopphysics*, *234*, 169-196, 1994.

Hrouda, F, Separation of a component of tectonic deformation from a complex magmatic fabric. *J. Struct. Geol.*, *14*, 65-71, 1992.

Jelinek, V, Statistical processing of magnetic susceptibility measured in groups of specimens, *Stud. Geophys. Geod.*, *22*, 50-62, 1978.

Johnson, M.C., and M.J Rutherford, Experimental calibration of the aluminium-in hornblende geobarometer with application to Long Valley caldera (California) volcanic rocks, *Geology*, *17*, 837-841, 1989.

Landing, E, S.A. Bowring, K.L. Davidek, S.R. Westrop, G Geyer, and W. Heldmaier, Duration of the Early Cambrian: U-Pb ages of volcanic ashes from Avalon and Gondwana, *Can. J. Earth Sci.* *35*, 329-339, 1998.

Law, R.D., S.S. Morgan, M. Casey, A.G Sylvester, and M. Nyman, The Papoose flat pluton of eastern California: A reassessment of its emplacement history in the light of new microstructural and crystallographic fabrics observations, *Tans. R. Soc. Edinburgh Earth Sci.*, *83*, 361-375, 1992.

Liñán, E., A. Perejón, and K. Sdzuy, The Lower-Middle Cambrian stages and stratotypes from the Iberian Peninsula: A revision, *Geol. Mag.*, *130*, 817-833, 1993.

McCaffrey, K.J.W., and N Petford, Are granitic intrusions scale invariant?, *J. Geol. Soc. London*, *154*, 1-4, 1997.

Miller, H.G., and J. Tuach, Gravity and magnetic signatures of the Ackley Granite Suite, southeastern Newfoundland: Implications for magma emplacement, *Can. J. Earth. Sci.*, *26*, 2697-2709, 1989.

Neves, S.P., A. Vauchez, and C.J. Archanjo, Shear-zone controlled magma emplacement or magma-assisted nucleation of shear zones? Insights from northeast Brazil, *Tectonophysics*, *262*, 349-364, 1996.

Ochsner, A, U-Pb geochronology of the upper proterozoic-lower paleozoic geodynamic evolution in the Ossa-Morena Zone (SW Iberia): Constraints on the timing of the Cadomian orogeny, Ph.D. dissertation, 249 pp., Swiss Fed. Inst. of Technol., Zürich, Switzerland, 1993.

Oliver, H.W., J G. Moore, and R.F. Sikora, Internal structure of the Sierra Nevada Batholith based on specific gravity and gravity measurements, *Geophys. Res. Lett.*, *20*, 2179-2182, 1993.

Passchier, C.W., and C. Simpson, Porphyroclast systems as kynematic indicators, *J. Struct. Geol.*, *8*, 831-843, 1986.

Quesada, C., Precambrian successions in SW Iberia: Their relationship to cadomian orogenic events, in *The Cadomian Orogeny*, edited by R.S. D'Lemos, R.A. Strachan, and C.G. Topley, *Geol. Soc. Spec. Publ.*, *51*, 553-562, 1990a.

Quesada, C., Geological constraints on the Paleozoic tectonic evolution of tectonostratigraphic terranes in the Iberian Massif, *Tectonophysics*, *185*, 225-245, 1990b.

Riller, U., A.R. Cruden, and W.M. Schwerdtner, Magmatic fabric and microstructural evidence for a tectonothermal overprint of the early Proterozoic Murray pluton, central Ontario, Canada, *J. Struct. Geol.*, *18*, 1005-1016, 1996.

Rochette, P., Magnetic susceptibility of the rock matrix related to magnetic fabric studies, *J. Struct Geol.*, *9*, 1015-1020, 1987.

Rochette, P., M Jackson, and C. Aubourg, Rock magnetism and the interpretation of anisotropy of magnetic susceptibility, *Rev. Geophys.*, *30*, 209-226, 1992.

Rosenberg, C.L., A. Berger, and S.M. Schmid, Observations from the floor of a granitoid pluton: Inferences on the driving force of final emplacement, *Geology*, *23*, 443-446, 1995.

Sánchez-Carretero, R., L. Eguíluz, E. Pascual, and M. Carracedo, Ossa-Morena Zone: Igneous rocks, in. *Pre-Mesozoic Geology of Iberia*, edited by R.D Dallmeyer, and E. Martínez-García, 292-313, Springer-Verlag, New York, 1990.

Sanderson, D.J., and A.W. Meneilly, Analysis of three-dimensional strain modified uniform distribution. Andalusite fabrics from a granite aureole, *J. Struct. Geol.*, *3*, 109-116, 1981.

Schäfer, H.-J., Geochronological investigations in the Ossa-Morena Zone, SW Spain, Ph.D. dissertation, 153 pp., Swiss Fed. Inst. of Technol., Zürich, Switzerland, 1990.

Schäfer, H.-J., D. Gebauer, and T.F. Nägler, Pan-African and Caledonian ages in the Ossa-Morena Zone (southwest Spain): A U-Pb zircon and Sm-Nd study, *Terra Abstr.*, *1*, 350-351, 1989.

Schäfer, H.-J., D. Gebauer, T.F. Nägler, and L

Eguíluz, Conventional and ion-microprobe U-Pb dating of detrital zircons from the Tentudía Formation (SW Spain): Possible implications for the stratigraphy and the Precambrian-Cambrian boundary, *Contrib. Mineral. Petrol*, *113*, 289-299, 1992.

Schmidt, M.W., Amphibole composition in tonalite as a function of pressure: An experimental calibration of the Al-in-hornblende barometer, *Contrib. Mineral Petrol.*, *110*, 304-310, 1992.

Schwerdner, W.M., G.M. Scott, and R.H. Sutcliffe, Strain patterns of crescent granitoid plutons in the Archaean greenstone terrain of Ontario, *J. LStruct. Geol.*, *5*, 419-430, 1983.

Simpson, C., and S.M. Schmid, An evaluation of criteria to deduce the sense of movement in sheared rocks, *Geol. Soc Am. Bull.*, *9*, 1281-1288, 1983.

Tarling, D.H. and F. Hrouda, *The Magnetic Anisotropy of Rocks*, 217 pp., Chapman and Hall, New York, 1993.

Van Berkel, J.T., Influence of pre- or post-diapiric deformation on the foliation and strain pattern of a diapiric ridge, *Tectonophysics*, *190*, 315-329, 1991.

Vigneresse, J.L., Control of granite emplacement by regional deformation, *Tectonophysics*, *249*, 173-186, 1995a.

Vigneresse, J.L., Crustal regime of deformation and ascent of granitic magma, *Tectonophysics*, *249*, 187-202, 1995b.

B. Ábalos, A. Apraiz, and L. Eguíluz, Departamento de Geodinámica, Universidad del País Vasco, P.O.Box 644, E-48080 Bilbao, Spain (e-mail: gppabvib@lg.ehu.es)

(Received May 12, 1998;
revised April 6, 1999;
Accepted May 28, 999.)

TECTONICS, VOL. 18, NO. 6, PAGES 1004-1026 DECEMBER 1999

Evolution of the Kap Cannon Thrust Zone (north Greenland)

W. von Gosen

Geological Institute, University of Erlangen, Erlangen, Germany

K. Piepjohn

Geological Institute, University of Münster, Münster, Germany

Abstract. In North Greenland, early Paleozoic metamorphic successions of the north Greenland fold belt are carried along the Kap Cannon Thrust Zone northward over the Late Cretaceous Kap Washington Group and Permo-Carboniferous strata. Ellesmerian deformations and metamorphism occurred prior to ductile deformation in the Kap Cannon mylonites, which developed from shear zones in the hanging wall metamorphics Heterogeneous shearing affects the Ellesmerian structures, with shear sense indicators suggesting top-to-north displacements in the mylonites. Late Cretaceous mafic dikes and sills record intense ductile deformation in the mylonites and incipient shearing within distinct zones of the hanging wall metamorphics. In the footwall of the mylonite zone, approximately NW directed thrusting with the formation of imbricates in Permo-Carboniferous strata on Lockwood Ø is related to an oblique ramping beneath and in front of the Kap Cannon Thrust Zone. Since the Kap Washington volcanics are mostly affected by brittle deformation, the onset of thrusting occurred in a deeper crustal level. Condensed ductile deformation within the mylonites, shear zones, and an additional oblique to lateral ramp suggest that shear/strain heating contributed to a local rise in temperature. Continuing displacement led to uplift of the thrust zone bounded block of metamorphic rocks with a final emplacement over the northern volcanics under brittle conditions. According to the age of the magmatic rocks in the footwall, the evolution of the Kap Cannon Thrust Zone probably took place during early Tertiary (Eurekan) times The regional implications are briefly discussed

1. Geological Overview

North Greenland is dominated by the W-E trending north Greenland fold belt, which continues westward into Ellesmere Island (Figure 1). There several branches of the mid-Paleozoic to late Paleozoic orogen have been distinguished [compare, e g , *Higgins et al.*, 1982, *Trettin*, 1991], and the terminal deformation took place in late Devonian-early Carboniferous time (Ellesmerian Orogeny in a strict sense). In the north Greenland fold belt, Ellesmerian deformation and metamorphism are most intense in the north, and three phases of coaxial deformation and amphibolite facies metamorphic grade are recognized in northern Johannes V Jensen Land (Figure 2) [*Soper et al.*, 1980; *Higgins et al*, 1981, *Soper and Higgins*, 1987, *Higgins and Soper*, 1991; *Soper and Higgins*, 1991a]. The southern part of the north Greenland fold belt is a southward directed, thin-skinned fold-and-thrust zone [*Soper and Higgins*, 1985, 1987, 1990, 1991a] The lack of clear Devonian deposits in the north Greenland fold belt [e.g , *Dawes*, 1971; *Higgins*, 1986a] and a few radiometric data [e g , *Springer*, 1981, 1982, *Pedersen and Holm*, 1983; *Springer and Friderichsen*, 1994] broadly indicate that Ellesmerian deformation and metamorphism took place in the Devonian to early Carboniferous time interval [e.g , *Dawes and Peel*, 1981; *Higgins and Soper*, 1991, *Soper and Higgins*, 1991a]

Deformation and metamorphism affect early Paleozoic sediments of the W-E trending Franklinian Basin, which continues westward into the Canadian Arctic Islands. The basin is characterized by a division into a southern shallow water carbonate platform and a northern deepwater trough (Figure 2) [e g , *Dawes and Peel*, 1981, *Higgins et al*, 1991a, b; *Surlyk*, 1991; *Trettin*, 1991] In north Greenland this division broke down in the Silurian when turbidites flooded the former platform areas [e.g., *Hurst and Surlyk*, 1982, *Surlyk*, 1982; *Higgins*, 1986a; *Soper and Higgins*, 1990, *Higgins et al.*, 1991a, b; *Surlyk*, 1991].

Post-Ellesmerian (Carboniferous-Tertiary) sediments and volcanics in north Greenland are collectively assigned to the Wandel Sea Basin [*Dawes and Soper*, 1973; *Håkansson et al.*, 1981; *Håkansson and Stemmerik*, 1989], the principal exposures occur in Kronprins Christian Land, eastern Peary Land, along the Harder Fjord Fault Zone, and between Lockwood Ø and Kap Cannon (Figures 2 and 3) The Wandel Sea Basin successions were variously affected by a complex pattern of latest Cretaceous to Tertiary compressive and transpressive events known as the Eurekan deformation on the Canadian Arctic Islands [e.g., *Higgins*, 1986a; *De Paor et al*, 1989; *Okulitch and Trettin*, 1991], associated with the opening of the Arctic and North Atlantic Oceans

One of the most prominent Eurekan structures at the north Greenland coast is the Kap Cannon Thrust Zone (KCTZ) discovered in 1969 [*Soper and Dawes*, 1970]. It can be traced from Kap Cannon in the northeast across the southern parts of Kap Washington and Kap Kane to Lockwood Ø in the southwest (Figure 3). Along the KCTZ, early Paleozoic metamorphic sequences of the fold belt override Permo-Carboniferous sediments, which are exposed on Kap Kane and Lockwood Ø, and a thick volcanic suite with intercalated and underlying clastic sediments (Late Cretaceous Kap Washington Group) The thrust zone and adjacent units have been described by, for example, *Dawes and Soper* [1970], *Soper and Dawes* [1970], *Dawes* [1971], *Brown and Parsons* [1981], *Soper et al.* [1982], *Brown et al.* [1987], and *Soper and Higgins* [1987, 1991b].

The effects, distribution, and significance of these young compressive structures at and around the KCTZ, with respect to the Paleozoic deformations and metamorphic overprint in the north Greenland fold belt to the south, are not well understood [see, e.g., *Dawes and Peel*, 1981]. Structures of a comparable age can be found at the

Paper number 1999TC900035.
0278-7407/99/1999TC900035$12.00

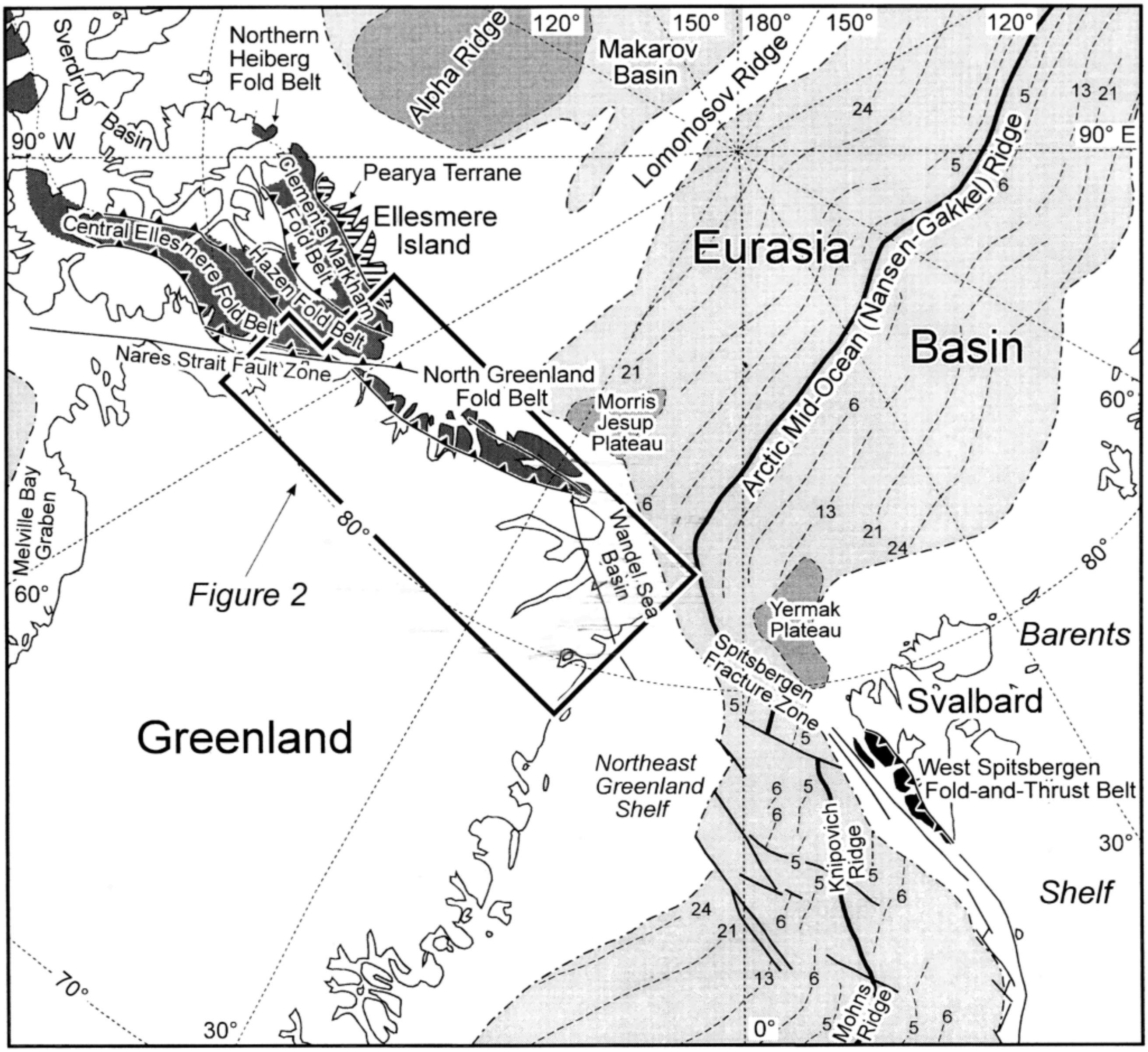

Figure 1. Sketch map of the Arctic areas with north Greenland fold belt, its continuation in different branches of the mid-Paleozoic to late Paleozoic orogen on Ellesmere Island (dark shading), and Paleogene West Spitsbergen Fold-and-Thrust Belt (solid). Prominent magnetic lineations (dashed lines) on oceanic crust of the Eurasia Basin and Norwegian-Greenland Sea (light shading) are numbered. Map is compiled after *Vogt et al.* [1982a, b], *Sundvor and Austegard* [1990], *Trettin* [1991], and *Scott et al.* [1995]. Frame depicts location of map of Figure 2.

Harder Fjord Fault Zone in the south and probably in the Wandel Hav Mobile Belt in the southeast. Within the reconstruction of Eurekan (Tertiary) contraction and related plate tectonic configurations of the Arctic areas, the KCTZ plays an important role.

The present paper is based on two NW-SE profiles across the KCTZ, located at Kap Cannon and on Lockwood Ø, and additional study areas in the footwall of the KCTZ (Figure 3). The descriptions follow the chronological order of events with (1) the Ellesmerian structures and metamorphic overprint, (2) the development of Eurekan shearing and mylonite formation in the KCTZ, and (3) the structures within the different units of its footwall. They will lead to an interpretative model of the evolution of the thrust zone and finally to some regional implications. In the text the additional subscript P refers to Paleozoic (Ellesmerian) structures.

2. Lithological Units

The early Paleozoic succession in the hanging wall of the KCTZ consists of phyllites, micaschists, quartzites, marbles, and carbonate schists of the Lower Cambrian Polkorridoren and Paradisfjeld Groups (Figure 3) [cf. *Surlyk*, 1991]. The rocks were affected by Ellesmerian deformations and metamorphism [e.g., *Dawes and Soper*, 1973, *Dawes*, 1976; *Soper et al.*, 1980; *Dawes and Peel*, 1981; *Higgins et al.*, 1982, 1985; *Higgins and Soper*, 1991].

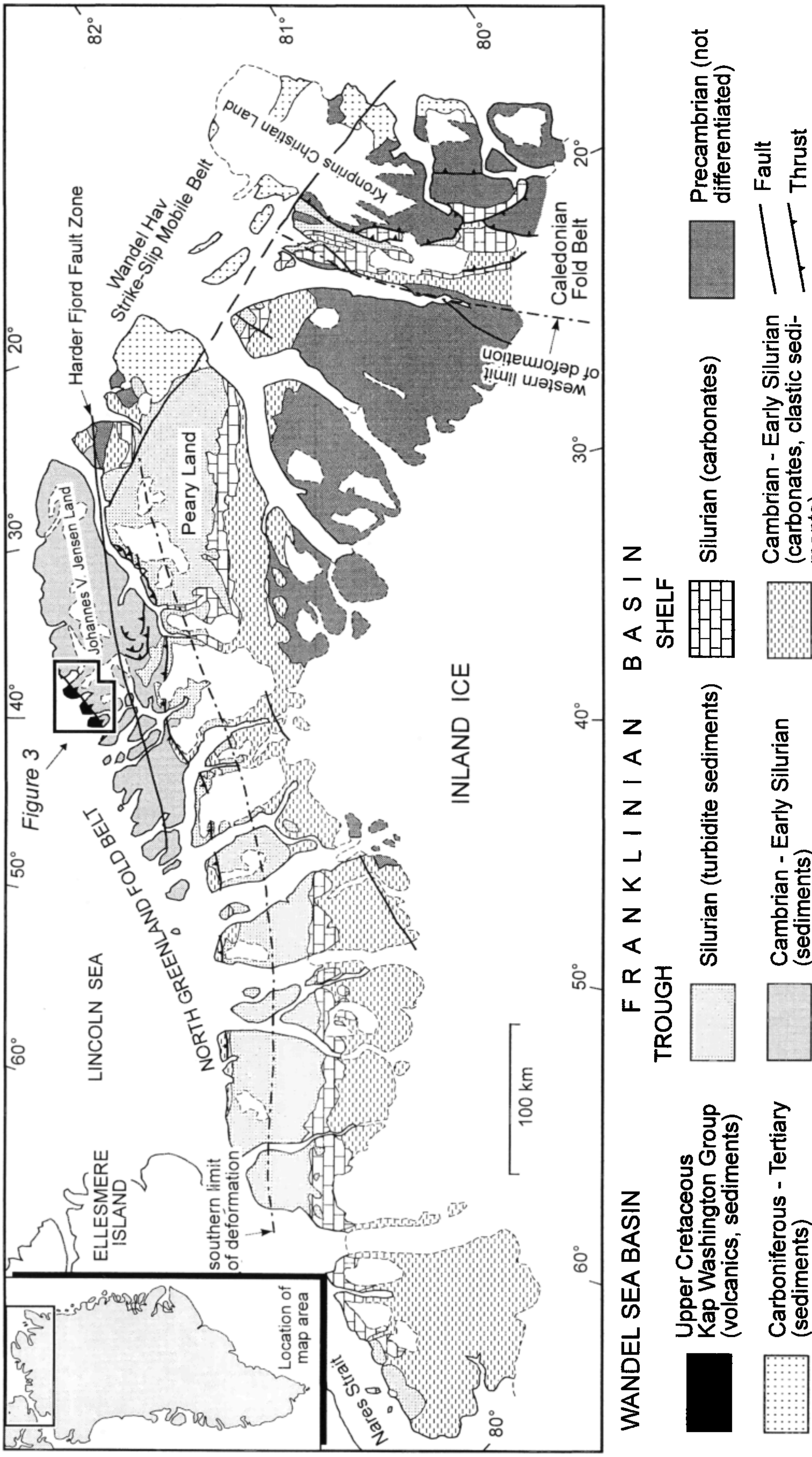

Figure 2. Geological map of north Greenland [after *Henriksen*, 1992]; frame shows location of map of Figure 3

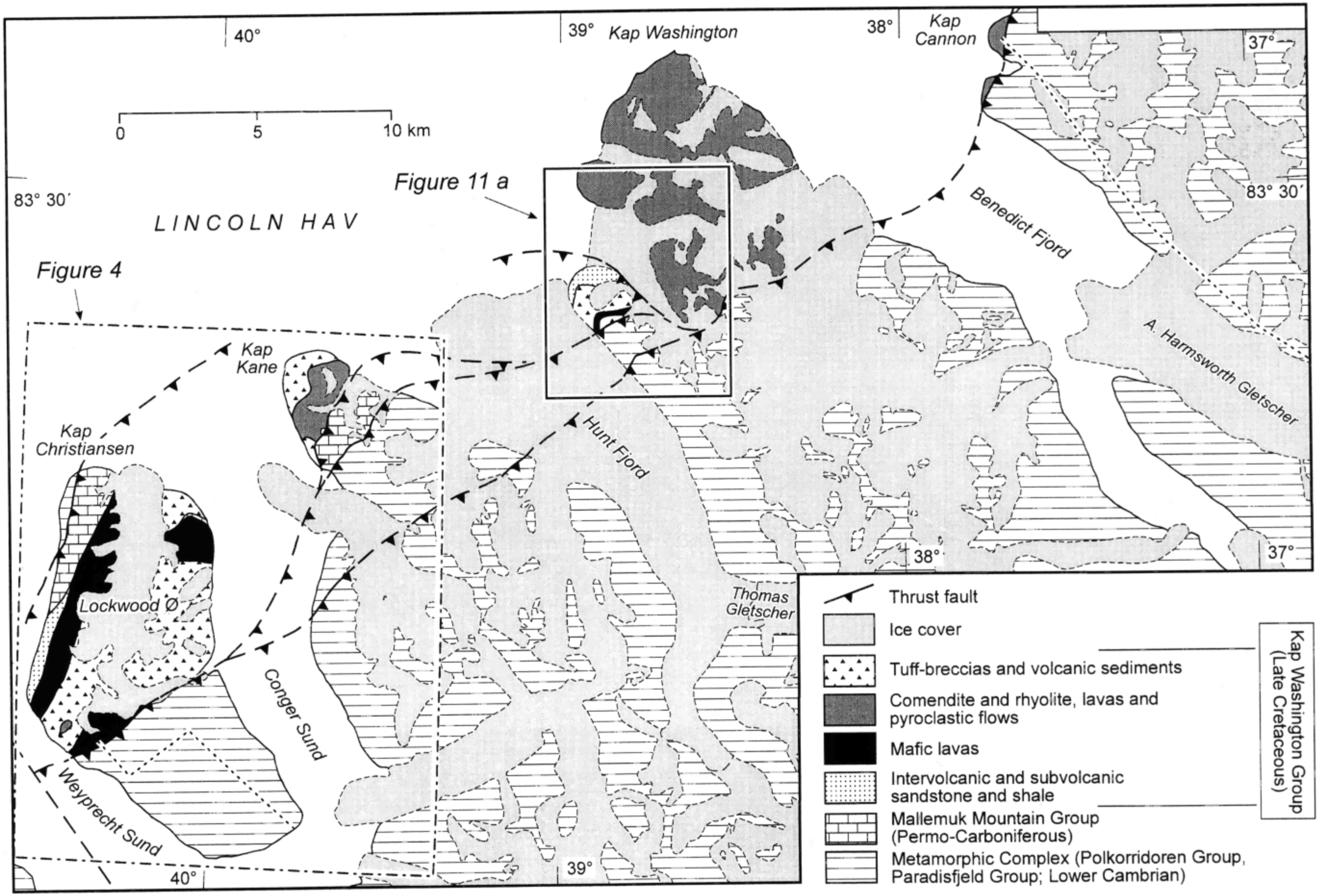

Figure 3. Geological sketch map of the Kap Cannon Thrust Zone (north Greenland), compiled and adapted after *Higgins* [1986b] and own investigations (for location, see Figure 2). Dash-dotted and solid frames depict locations of maps of Figures 4 and 11a, respectively. Stippled lines indicate locations of studied profiles across the Ellesmerian metamorphic complex in the southeastern part of Lockwood Ø and SE of Kap Cannon (compare Figures 7 and 10, respectively).

At the northwestern margin of Lockwood Ø (Figure 4), monotonous slates with a few intercalated siltstone layers are assigned to the Frigg Fjord mudstone [*Brown and Parsons*, 1981], which is part of the lower Cambrian Polkorridoren Group. To the east of this N-S trending strip, coarse-grained and partly red conglomerates are exposed at Kap Christiansen. Upward, they grade into sandstones and siltstones which are overlain by fossiliferous, cherty limestones and dolomitic carbonates. The unit has been briefly described by *Soper et al.* [1980] and *Håkansson et al.* [1981] and assigned to the Mallemuk Mountain Group (late Carboniferous-early Permian) by, for example, *Håkansson* [1979] and *Stemmerik and Håkansson* [1989].

The Kap Washington Group [*Dawes and Soper*, 1970] has been described in detail by *Brown and Parsons* [1981], *Soper et al.* [1982], and *Brown et al.* [1987]. At the western margin of Lockwood Ø the section starts with grey sandstones and up to tens of meters thick layers of grey to black siltstones. Within the upper part of the clastic sediments, layers of acid and mafic volcanics are intercalated. They grade into the thick volcanic sequence, which generally consists of subaerial basaltic, trachytic, and rhyolitic lavas, rhyolite tuffs, and pyroclastic flows, with interbedded breccias and agglomeratic layers [*Brown and Parsons*, 1981; *Brown et al.*, 1987]. Intercalated layers of sandstones and dark shales yielded pollen and spores of probable Late Cretaceous age (Campanian or Maastrichtian) [*Batten*, 1982]. *Batten et al.* [1981] report the occurrence of leaf fragments in the sediments beneath the volcanic rocks, indicating a mid-Cretaceous or younger age. Rb-Sr dating of rhyolite volcanics gave an approximate age of 63 Ma [*Larsen et al.*, 1978], which later was confirmed at 64±3 Ma by *Larsen* [1982] and *Estrada et al* [1998]. Both radiometric and palynological data suggest a generation of the Kap Washington Group of volcanics and sediments during the Late Cretaceous up to the Cretaceous-Tertiary boundary.

The early Paleozoic metamorphic rocks and late Carboniferous-early Permian sediments are crosscut by widely distributed and several centimeters to tens of meters thick mafic dikes and sills with chilled margins. Within the metamorphic complex the dikes strike approximately NW-SE to N-S (Figures 4 and 5a). They are part of a widely distributed dike swarm north of the Harder Fjord Fault Zone with a general approximately N-S trend [e.g., *Higgins et al.*, 1981; *Soper et al.*, 1982; *Brown et al.*, 1987; *Soper and Higgins*, 1991b] whilst south of the fault zone a more scattered swarm of WNW-ESE and W-E trending dikes occurs [*Higgins et al*, 1981]. According to a few radiometric data, the dikes are also assigned to the Late Cretaceous magmatic activity [e.g., *Henriksen and Jepsen*, 1970, *Dawes*, 1971; *Dawes and Soper*, 1971; *Higgins et al.*, 1981; *Dawes et al.*, 1983; *Manby et al.*, 1998].

The direct relationship of the dikes to the Kap Washington Group volcanics and sediments is uncertain. As *Brown et al* [1987], we did not find dikes cutting across the volcanics and/or sediments However, *Batten et al.* [1981] mention that dikes cut Cretaceous sediments but not the volcanics. Hence it can be assumed that the dikes are slightly older than, and sometimes related to, the generation of the Kap Washington volcanics On the basis of the minor element chemistry, Brown et al. regard the dikes as precursors of the Kap Washington volcanics

3. Deformations in the Early Paleozoic Metamorphic Complex

The widespread Late Cretaceous dike swarms and sills, cutting across pre-middle Carboniferous Ellesmerian structures of the early Paleozoic rocks [e.g., *Dawes*, 1971, *Soper et al.*, 1982], provide a simple means of distinguishing Ellesmerian deformation from Eurekan (post-Late Cretaceous) deformation Ellesmerian structures are well preserved in the southeastern parts of the studied profiles. Downsection toward the KCTZ they are successively overprinted by Eurekan structures.

3.1. Ellesmerian Structures

The first recognizable deformation (D_{P1}) is documented by a planar foliation fabric (S_{P1}) in the quartzites and phyllite layers on southern Lockwood Ø. It crosscuts bedding at low angles. Axes of relict B_{P1} folds and the intersection lineation between bedding and S_{P1} planes (δ_{P1}) plunge between NE and SE (Figure 5c). In the marbles the penetrative S_{P2} foliation is combined with isoclinal F_{P2} folds on a centimeter to meter size with approximately NE-SW trending B_{P2} axes (Figure 5b) In more competent quartzites no clear F_{P2} folds were found There the S_{P2} foliation is oriented parallel to relics of bedding planes. Aligned sericite and elongated quartz in a few outcrops indicate a poorly preserved L_{P2} lineation plunging toward approximately SE

Within more incompetent marbles and carbonate phyllites, S_{P2} foliation planes and isoclinal F_{P2} folds interfere with open and tight F_{P3} folds on a centimeter to meter scale (Figure 6a). The F_{P3} folds have a gently inclined, S_{P3} axial plane cleavage. A poorly defined NW-SE trending L_{P3} lineation indicated by aligned muscovite is sporadically developed. In the other rock types, north to NW vergent F_{P3} folds are combined with an approximately SSE dipping, axial plane S_{P3} crenulation cleavage (Figures 5b and 5c). On the planes, aligned muscovite and elongated quartz define the L_{P3} lineation with a gentle to moderate plunge toward east to SE (Figure 5b).

On Lockwood Ø, B_{P3} axes strike W-E to WSW-ENE (Figure 5c). In the southeastern part of the Kap Cannon profile they plunge toward approximately SW Farther northward they trend N-S with a general plunge toward approximately south (Figure 5b). This slight change in trend of the fold axes is associated with a change from NW to approximately west vergent fold structures

In the profiles studied, Ellesmerian folds are developed on a decimeter to several meters scale. In the southwestern coast cliffs of the Hunt Fjord (between Kap Washington and Kap Kane; Figure 3), however, tight to iscoclinal (? F_{P2}) or open and NW vergent (? F_{P3}) folds reach tens of meters to hundreds of meters scale within semipelitic units with quartzites of the Cambrian Polkorridoren Group. They suggest that Ellesmerian contraction resulted in large-scale folding of the early Paleozoic pile of rocks [cf. also, e.g., *Soper and Higgins*, 1987]. The three fold generations, found in this northern part of the fold belt, also support the evidence described by, for example, *Soper et al.* [1980], *Higgins et al.* [1981], and *Soper and Higgins* [1987, 1990, 1991a].

Unlike the southern margin of the north Greenland fold belt, which is characterized by thin-skinned southward directed thrusting [*Soper and Higgins*, 1987, 1990], we saw no evidence in our study areas in the northern part of the fold belt for the presence of significant Ellesmerian thrusts, reverse faults, or strike-slip faults. In some outcrops, however, single and small detachments are parallel to S_{P2} planes and combined with NW vergent F_{P3} folds and C_{P3} planes in the hanging wall

Late Ellesmerian brittle movements are indicated by quartz-filled extension veins which mostly occur in quartzites They are oriented perpendicular to B_{P3} axes and S_{P3} foliation planes and indicate final extension during and after cessation of the folding event.

3.1.1. Microfabrics. In the schists and phyllites on southeastern Lockwood Ø, quartz was flattened between S_{P1} foliation planes and

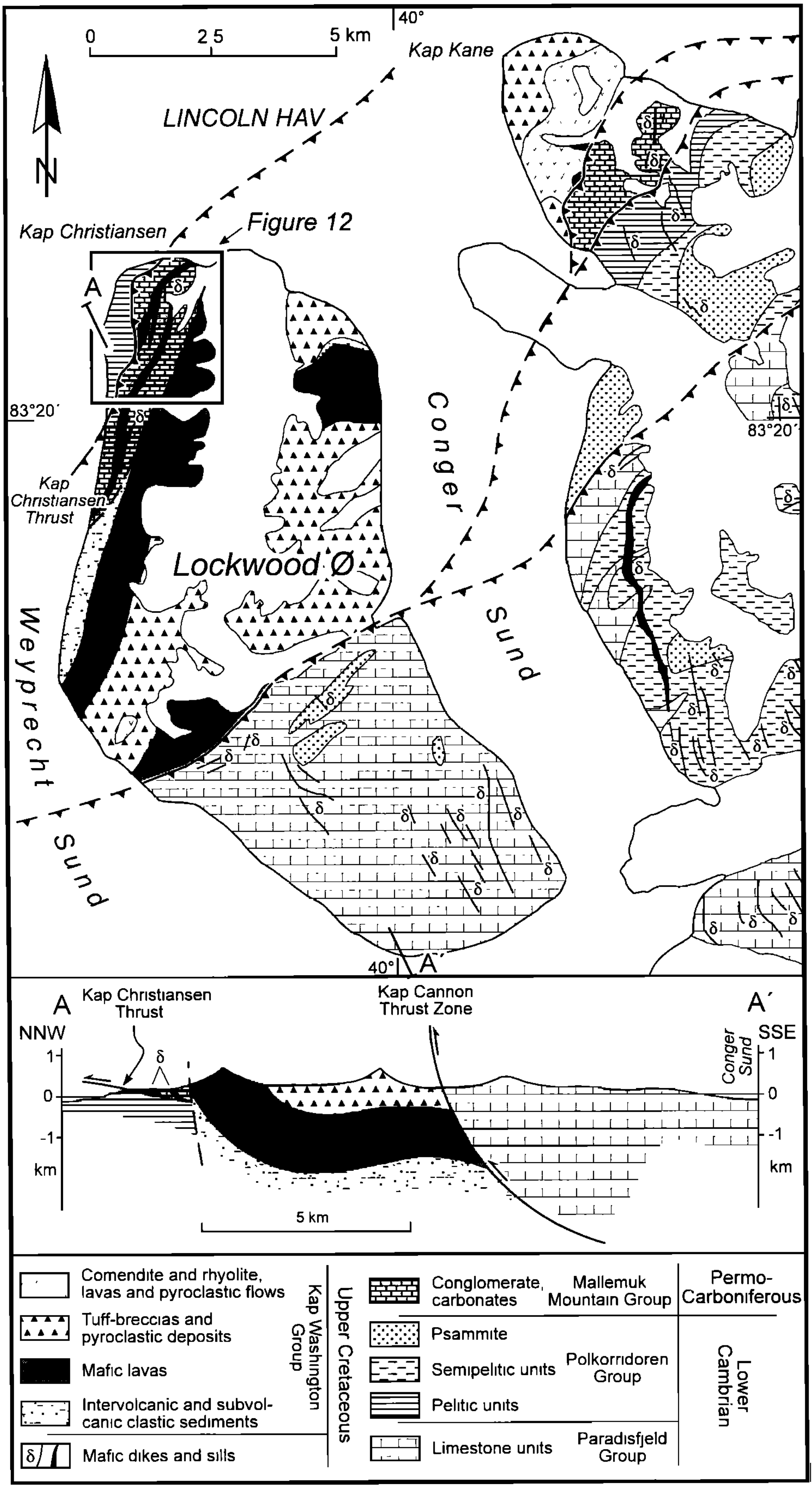
0
2 5
5 km
40°
Kap Kane
LINCOLN HAV
Kap Christiansen
Figure 12
A
83°20´
Kap Christiansen Thrust
Lockwood Ø
Conger Sund
Weyprecht Sund
83°20´
40°
A´
A
Kap Christiansen Thrust
Kap Cannon Thrust Zone
A´
NNW
SSE
Conger Sund
1
0
-1
km
5 km
Comendite and rhyolite, lavas and pyroclastic flows
Tuff-breccias and pyroclastic deposits
Mafic lavas
Intervolcanic and subvolcanic clastic sediments
Mafic dikes and sills
Kap Washington Group
Upper Cretaceous
Conglomerate, carbonates
Mallemuk Mountain Group
Permo-Carboniferous
Psammite
Semipelitic units
Pelitic units
Polkorridoren Group
Limestone units
Paradisfjeld Group
Lower Cambrian

Figure 4.

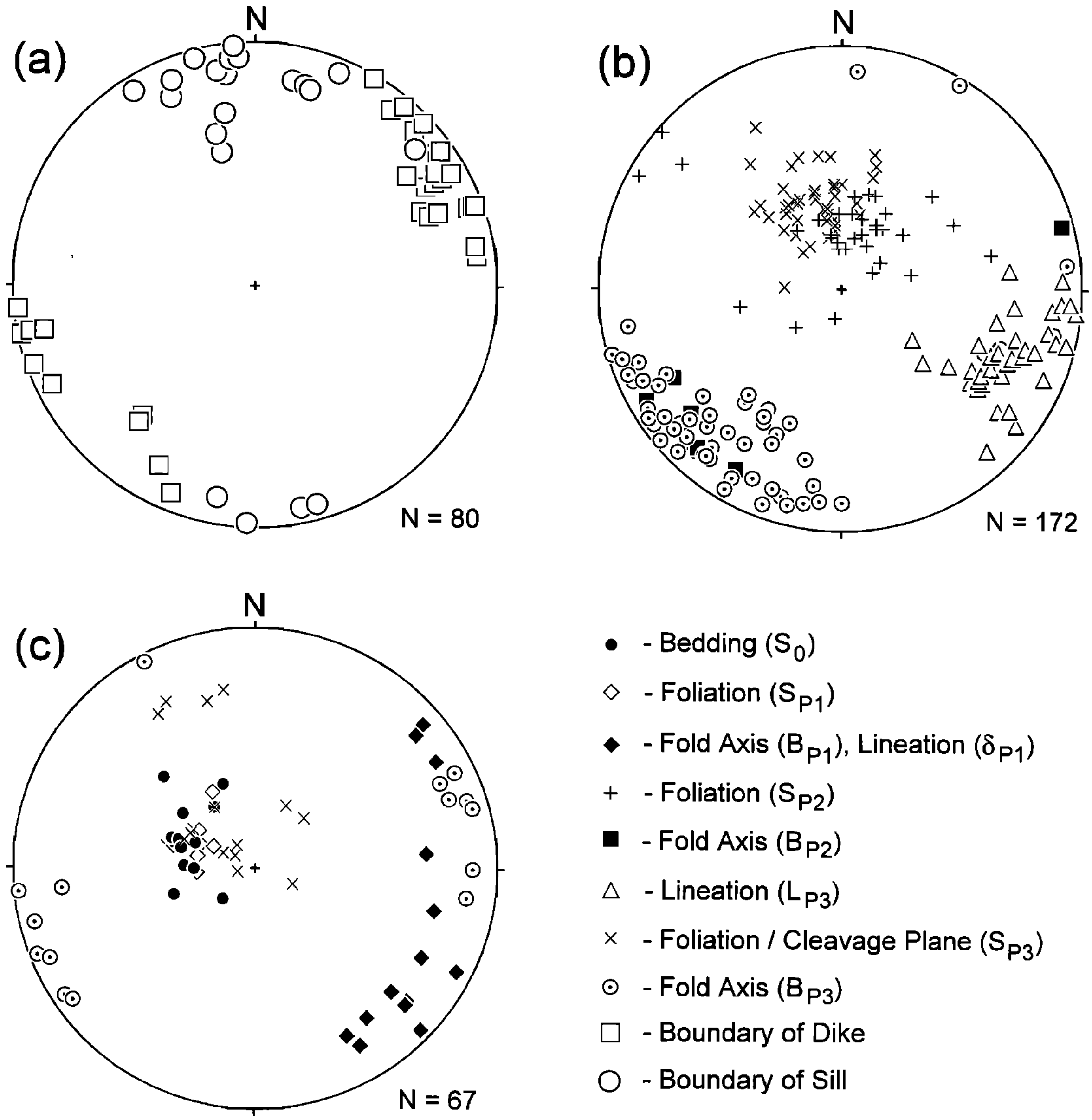

Figure 5. Stereoplots of structural elements in the hanging wall of the Kap Cannon Thrust Zone (lower hemisphere, equal-area projections) (a) Boundaries of mafic dikes and sills. (b,c) Ellesmerian structural elements in the metamorphic complex. Figures 5a and 5c are for Lockwood Ø, and Figure 5b is for the Kap Cannon area.

affected by pressure solution. Muscovite, sericite, and biotite grew parallel to S_{P1}. Thin layers, composed of predominantly quartz and phyllosilicates, are relics of bedding Larger quartz grains are probably of clastic origin.

Within the S_{P2} foliation of the marbles, defined by recrystallized calcite, relics of larger calcite grains are sheared and flattened. Between S_{P2} planes of sandy schists, quartz is sheared, flattened, and recrystallized Boundaries between recrystallization grains are straight to slightly curved and record widely distributed triple junctions. Such fabrics were also found in S_{P3} cleavage planes and microscale shear zones related to F_{P3} folds. Large quartz grains and grain aggregates within the S_{P3} foliation, however, record an internal strain and suggest that complete recrystallization took place to a variable extent.

In the schists, new and reoriented older muscovite and biotite are aligned parallel to S_{P3}. Older plates are deformed and recrystallized syn-D_{P3} to post-D_{P3}. Within F_{P3} fold hinges and between S_{P3} crenula-

Figure 4. Geological map of Lockwood Ø and surrounding areas (adapted after *Higgins* [1986b] and own investigations) with a simplified geological profile. For location of map, see Figure 3, frame shows location of map of Figure 12

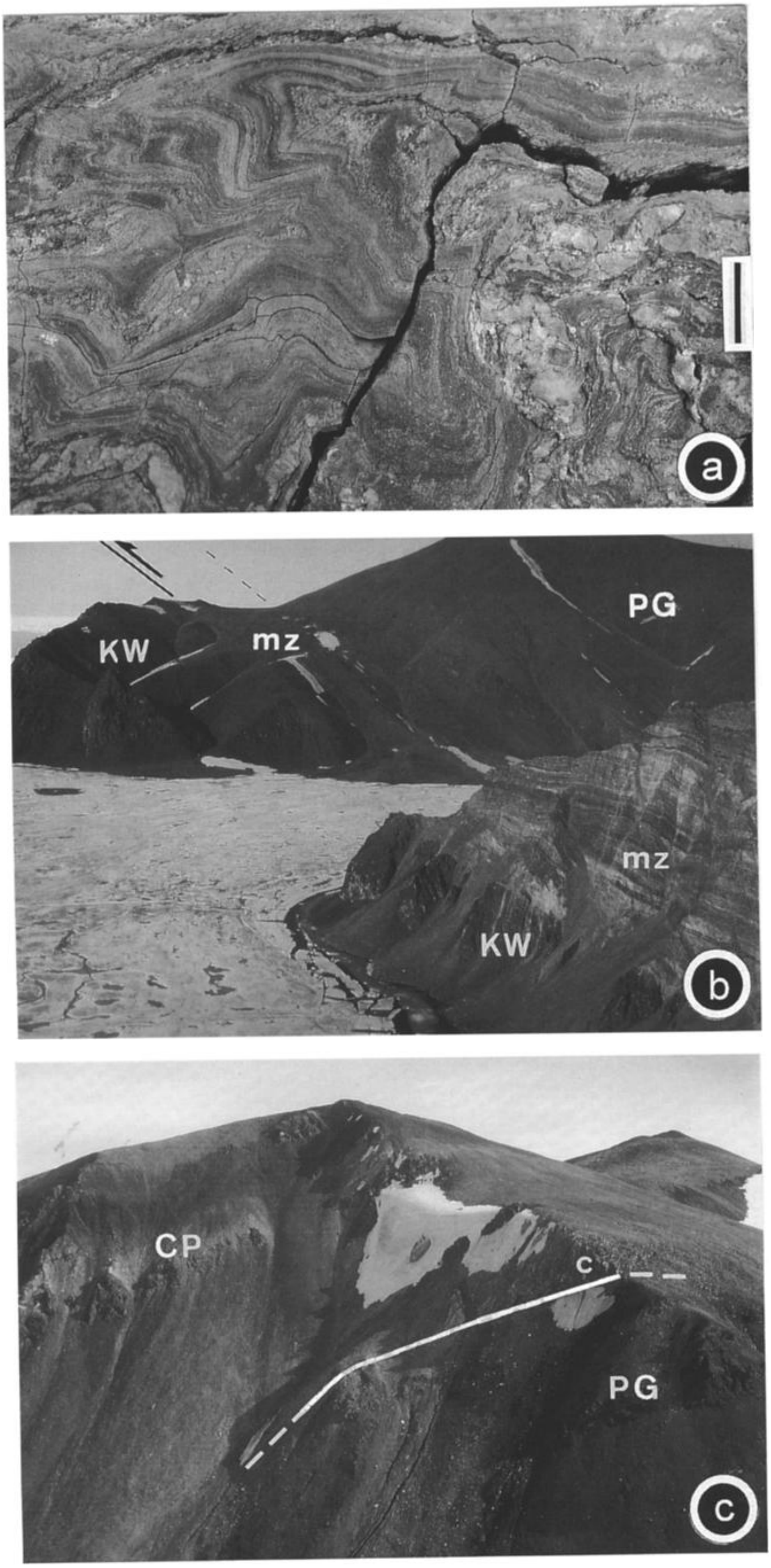

Figure 6.

tion cleavage planes, muscovite, sericite, and biotite are bent and partly to entirely recrystallized, which is indicated by polygonal fabrics. The latter and chlorite plates parallel to S_{P3} planes are overgrown mostly by biotite, which postdates the D_{P3} event

3.1.2. Metamorphism. The microfabrics suggest that Ellesmerian deformation was accompanied by the growth of biotite, muscovite, and also chlorite. Recrystallization of quartz, calcite, biotite, and muscovite outlasts the third deformational event. Static metamorphic conditions after cessation of the D_{P3} deformation are indicated by grain growth of quartz, leading to the formation of triple junctions and strain-free quartz aggregates. All this suggests that deformations took place at least under upper greenschist facies metamorphic conditions. Previous workers have described the metamorphic variations in the north Greenland fold belt in terms of E-W trending metamorphic zones, from nonmetamorphic in the south to amphibolite facies in a narrow zone along the northern coast of Johannes V. Jensen Land [e.g., *Dawes*, 1971; *Dawes and Soper*, 1973, *Dawes*, 1976; *Dawes and Peel*, 1981; *Higgins et al.*, 1982, 1985; *Soper and Higgins*, 1987; *Higgins and Soper*, 1991]. Although we did not find clear evidence in our study area, an amphibolite facies overprint cannot be excluded.

3.2. Eurekan Structures

Within the early Paleozoic metamorphic complex, the effects of Eurekan deformation increase from SE to NW. In the southern parts of the Kap Cannon and Lockwood Ø areas, mafic dikes cut across Ellesmerian structures without being deformed significantly. In and around the KCTZ, three phases of Eurekan deformation (D_{1-3}) are recognized which also affect the mafic dikes and sills. Shearing of the dikes as well as schistose fabrics and greenschist facies assemblages have been mentioned by, for example, *Soper et al.* [1982]. Eurekan ductile and brittle shearing dies away south of the thrust zone.

3.3. D_1 Structures

3.3.1. Shear planes and shear zones. In the southern part of Lockwood Ø, Late Cretaceous dikes are crosscut by several and mostly conjugate sets of W-E trending shear planes (C_1) which are spaced on a decimeter scale (Figure 7). The relative sense of shear indicates approximately N-S compression. The planes can be traced into the country rocks (phyllites) and there are replaced by S_1 crenulation cleavage planes which cut across the planar S_{P1} fabric. Compression is also accommodated by W-E trending kink bands, and the dikes are partly displaced along shear planes parallel to the boundaries. To the north a slight bending of thin sills on a centimeter scale indicates a small amount of compression. In the country rocks the main foliation is crosscut by S_1 crenulation cleavage planes which are restricted to single and decimeter wide zones

In the central parts of the Kap Cannon and Lockwood Ø profiles, C_1 planes increase in abundance and are more densely spaced On the planes, aligned sericite and elongated quartz define the L_1 lineation which plunges between SE and SW (Figures 8a and 8b) Sills approximately parallel to long limbs of NW vergent F_{P3} folds and cutting through short limbs are sheared more or less parallel to S_{P3} foliation planes along the margins as a result of competence contrast with the country rocks (Figure 9a). Within the sills, single C_1 shear zones connect decimeter thick shear zones along the upper and lower margins.

In the metasediments, shear zone deformation is indicated by C_1 planes which are parallel to S_{P2} foliation planes or cut across under small angles S/C fabrics, σ-clasts, and duplex structures on a centimeter scale indicate top-to-NW-to-north sense of displacements of the hanging wall (Figures 7 and 10) parallel to the L_1 lineation.

Northwestward and downsection toward the Kap Cannon Thrust Zone, C_1 planes are more densely spaced and dip moderately toward the SSE Shearing is concentrated in shear zones which are parallel or oblique to S_{P2} foliation planes. S/C fabrics, shear bands, and single σ-clasts indicate top-to-NNW displacements of the hanging wall. As in the upper parts of the metasedimentary pile, shearing took place parallel to the pronounced L_1 lineation The intersection lineation (δ_1) between S_1/C_1 planes and the Ellesmerian foliation (S_{P2}) mostly plunges toward ENE to ESE (Figures 8a and 8b). Between the shear zones, slices of metamorphic rocks record (relics of) Ellesmerian structures.

Toward the underlying mylonites, C_1 planes and shear zones continuously pass into a penetrative S_1 foliation within more incompetent phyllites or micaschists (Figures 7 and 10). In the transitional zone, S_1 planes are parallel to the S_{P2} foliation and only relics of F_{P3} hinge zones are preserved On S_1 planes the L_1 lineation is defined by aligned sericite and reoriented older muscovite and plunges to the south. Within penetratively sheared parts, S/C fabrics and shear bands indicate north directed displacements of the hanging walls. Quarz veins are isoclinally folded and record curving fold axes within the S_1 foliation

Intercalated mafic sills are intensely sheared along their chilled margins Foliation-parallel sills are disrupted into lens- and angular-shaped, isolated boudins on a decimeter to several meters size. Dikes are juxtaposed along centimeter to decimeter thick shear zones which are parallel to S_{P2} foliation planes within the country rocks (Figure 7) In the sills, shear zones display anastomosing fabrics on a scale of several meters around lens-shaped magmatic bodies (Figure 9b) Comparable fabrics were found in sandy phyllites within the hanging wall and indicate the transition from single C_1 shear zones to a penetrative S_1 foliation. Generally, the entire D_1 deformation above the mylonite zone is characterized by heterogeneous C_1 shear zone deformation with an increase downward to the mylonites (Figures 7 and 10).

3.3.2. Mylonite zone. At the contact between the overthrust Paleozoic metasediments and underlying Kap Washington Group and Permo-Carboniferous rocks, Eurekan deformation is concentrated within the ~50-100 m thick mylonites of the KCTZ (Figure 6b). There the internal strain increases from top to bottom In the upper

Figure 6 (a) Interference pattern of F_{P2} and F_{P3} folds in marbles of the Paradisfjeld Group north of A Harmsworth Gletscher (SE of Kap Cannon, view toward SW; scale bar is ~4 cm). (b) View from helicopter toward NE on the Kap Cannon Thrust Zone at Kap Cannon with Kap Washington Group volcanics (KW) beneath and metamorphic rocks of the Lower Cambrian Polkorridoren Group (PG) above the mylonite zone (mz). Dark strips in the mylonites above the cliff in the foreground partly represent sheared mafic sills (c) View from helicopter toward approximately SW on exposed Kap Christiansen Thrust at Kap Christiansen (northern cliff of Lockwood Ø). Carboniferous-Permian carbonates (CP) with mafic sills and a wedge of conglomerates (c) at the base override Lower Cambrian slates of the Polkorridoren Group (PG; bottom right).

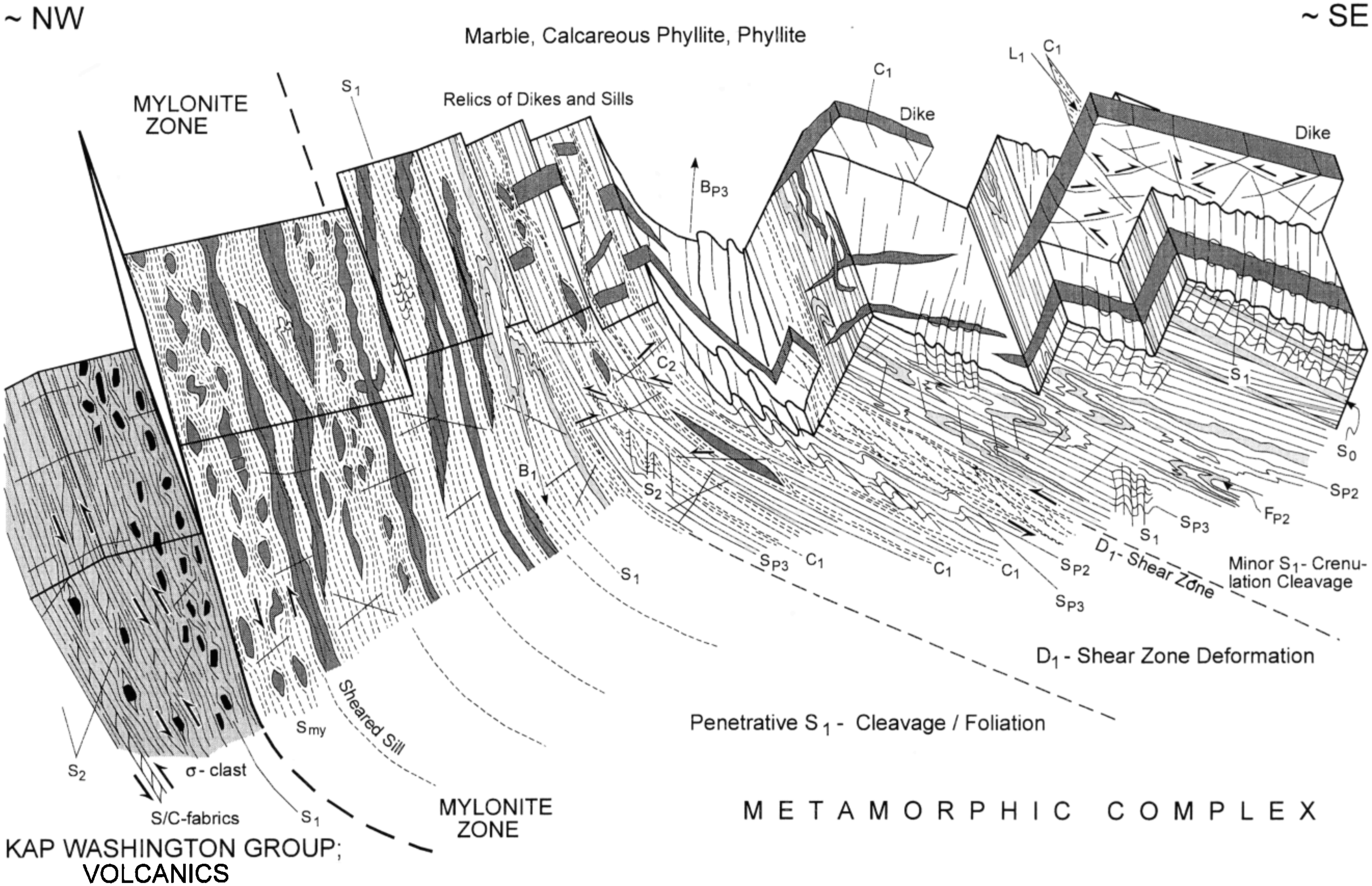

Figure 7. Schematic, simplified, and composite block profile across the Ellesmerian metamorphic complex, mylonite zone, and adjacent volcanic rocks in the southern part of Lockwood Ø, summarizing the main structural elements (for location of profile, see Figure 3). Cartoon is not to scale; see text for explanations.

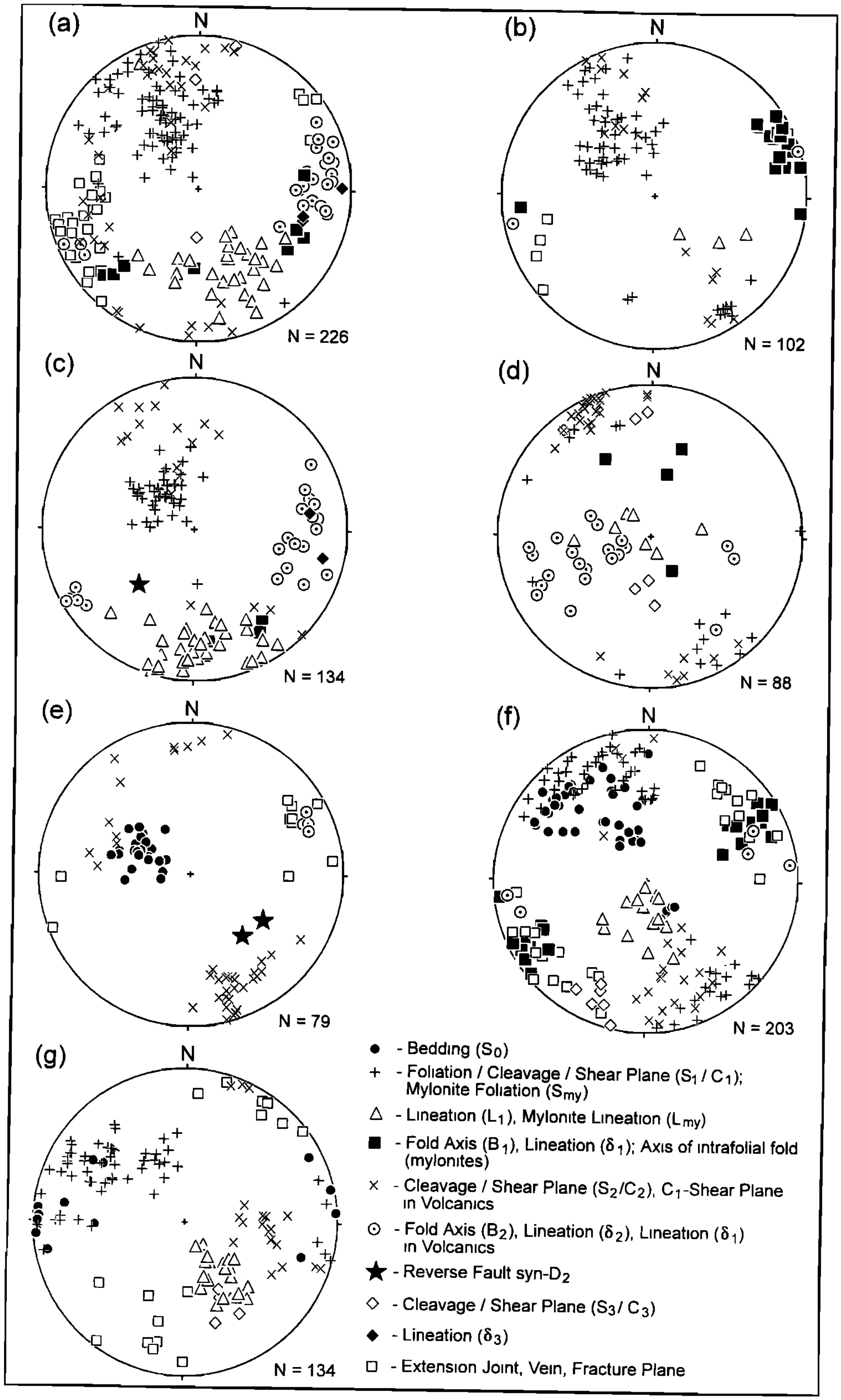

Figure 8. Stereograms of Eurekan structural elements (lower hemisphere, equal-area projections). (a,b) Ellesmerian metamorphic complex, (c,d) Mylonite zone, (e) Kap Washington Group, (f) Kap Washington Group with sediments, (g) Permo-Carboniferous sediments. Figures 8a, 8c, and 8e are for Kap Cannon, and Figures 8b, 8d, 8f, and 8g are for Lockwood Ø.

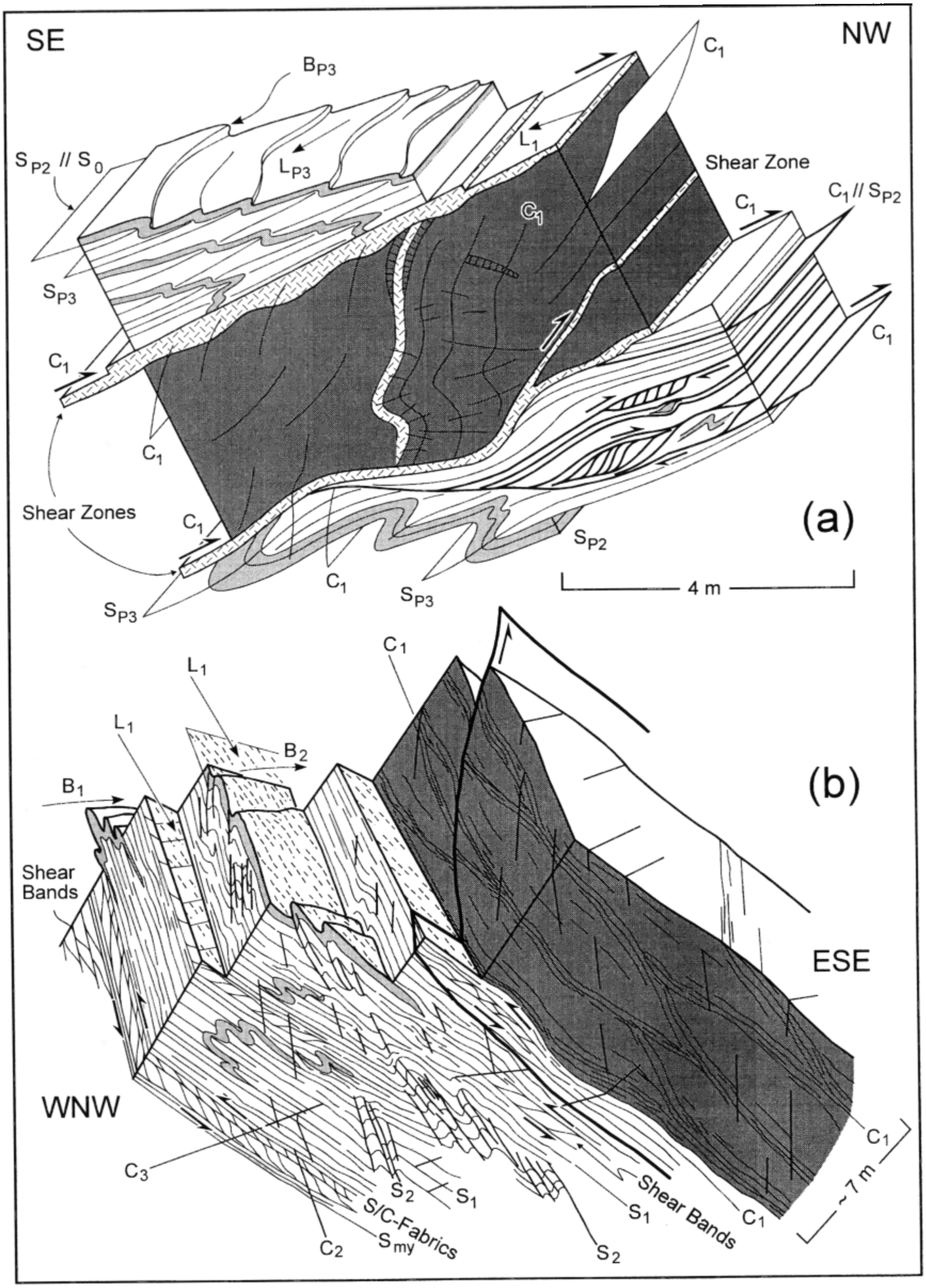

Figure 9. (a) Simplified block sketch of a sheared Upper Cretaceous mafic sill within marbles and carbonate micaschists of the Paradisfjeld Group (Lower Cambrian) northeast of the A. Harmsworth Gletscher. Note Ellesmerian F_{P3} folds with an S_{P3} cleavage being crosscut by shear zones along the sill margin and within the lowermost part of the carbonate schists. There S/C fabrics and asymmetric clasts indicate a top-to-the northwest sense of shear parallel to the L_1 stretching lineation. (b) Simplified and schematic block sketch of intense C_1 shearing just above the Kap Cannon mylonite zone (southeast of Kap Cannon). Shear zones with S/C fabrics and shear bands partly record a mylonite fabric (bottom) and downward grade into the Kap Cannon mylonite zone. In the central part the shear planes are replaced by a penetrative S_1 foliation fabric with relics of folded quartz veins On top of the outcrop a mafic sill is crosscut by anastomosing C_1 shear zones. C_2 shear planes and S_2 crenulation cleavage planes, combined with small-scale F_2 crenulation folds, are the result of continuing compression.

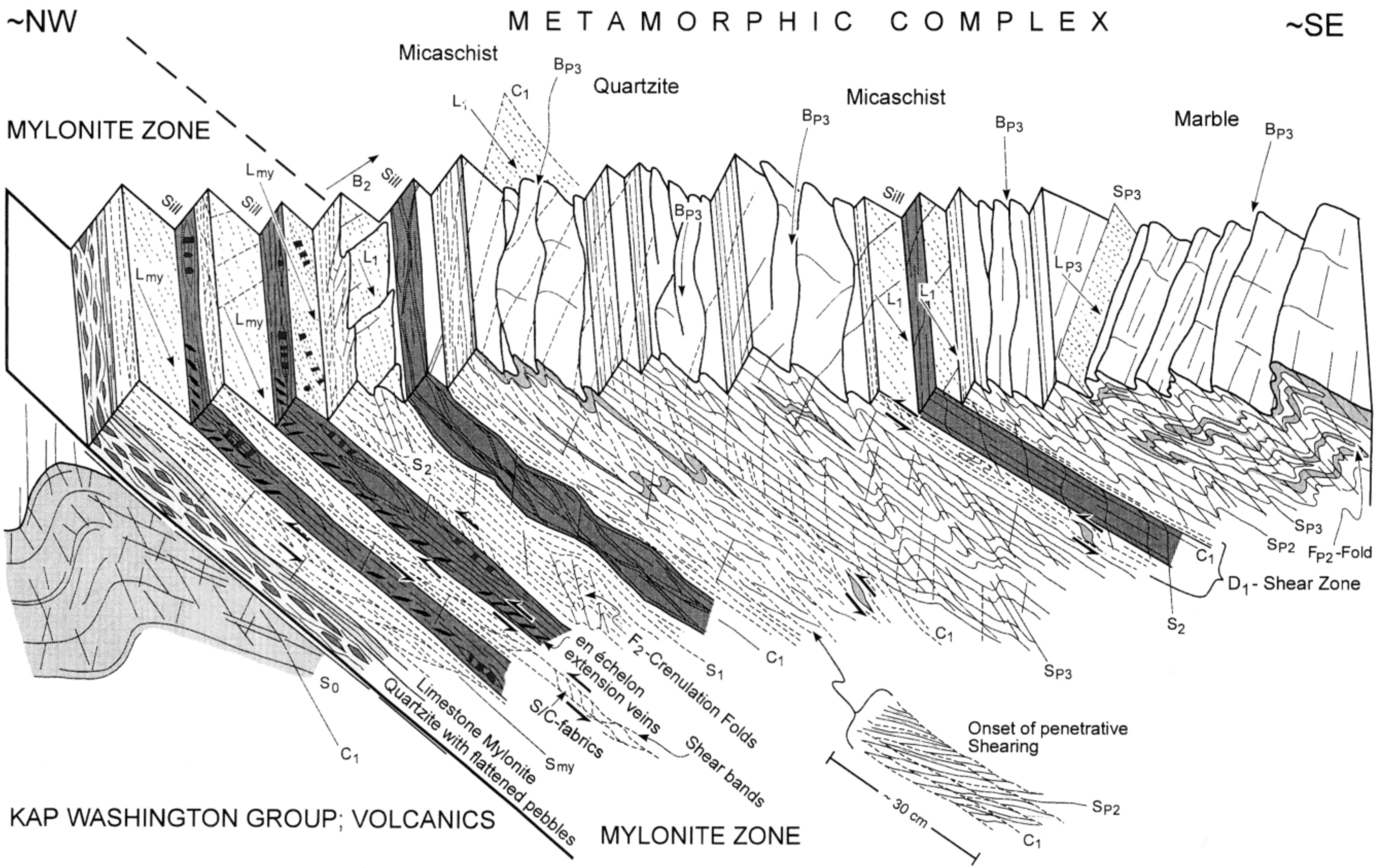

Figure 10. Simplified, schematic, and composite block profile summarizing the main structural elements in the studied section from Kap Cannon toward the area north of A. Harmsworth Gletscher (for location of profile, see Figure 3). Cartoon is not to scale; see text for explanations.

parts, shearing is condensed within distinct, centimeter to decimeter thick layers recording a protomylonite to mylonite foliation (S_{my}) which developed from the S_1 foliation

In the mylonite zone, mylonitic quartzites alternate with phyllosilicate-rich mylonites on a scale of several meters to tens of meters, indicative of different compositions of the metamorphic rocks prior to mylonite formation Relic isoclinal, intrafolial, and rootless F_1 folds with variable orientations of the axes are related to the foliation. On S_{my} planes the pronounced mylonite lineation (L_{my}) is indicated by aligned phyllosilicates with different size, elongated quartz, and disrupted feldspar The lineation plunges southward (Figure 8c and 8d). On Lockwood Ø, marbles of the Paradisfjeld Group are converted to marble mylonites

Intercalated mafic sills and dikes are penetratively affected by the mylonite foliation or densely spaced shear planes and record ductile deformation (Figure 10). Magmatic feldspar is disrupted between S_{my} planes. Its extended and isolated pieces lie in the pronounced L_{my} lineation which is also defined by aligned chlorite. Sills record pinch-and-swell structures and, like the dikes, are boudinaged and disrupted into lens- or angular-shaped, isolated, and decimeter to meter long bodies (Figure 7). At the cliff SW of Kap Cannon a mafic sill is bent around a NNW-SSE trending, tight fold structure within the foliation.

In the mylonites the relative sense of shear is indicated by shear bands within phyllosilicate-rich layers Additional σ-clasts (feldspar, quartz lenses, and asymmetric mafic boudins) and centimeter thick S/C fabrics are indicators in quartzitic mylonites. In ductilely deformed sills, σ-clasts (feldspar) and en echelon extension joints record the same sense of shear (see Figure 10). All indicators prove a general transport of the hanging wall to the north, parallel to the pronounced L_{my} lineation.

On Lockwood Ø the S_{my} foliation is locally folded around open to tight folds with steeply inclined to almost vertical axes. The folds are combined with ductile shear planes. These structures are related to continuing compression within the mylonite zone.

At the base of the mylonite zone at Kap Cannon, single exposures of mylonite quartzites contain layers of pebble quartzites The centimeter long pebbles of dark pelites and polycrystalline quartz are sheared and flattened within the foliation. Above this horizon, widely distributed blocks and boulders of limestone mylonite display a pronounced lineation. We assume that both rocks represent slices of intensely sheared Permo-Carboniferous rocks at the base of the mylonite zone (Figure 10).

3.4. D_2 and D_3 Structures

Within areas of incipient to intense D_1 shear zone deformation, single and widely spaced C_2 shear planes cut across C_1 planes and Ellesmerian structures. The steeply southward inclined planes are associated with F_2 folds and kinks on a centimeter scale around approximately WSW-ENE striking axes (Figures 8a and 8b).

Above the mylonite zone, C_2 planes are replaced by south dipping S_2 crenulation cleavage planes which cut across the S_1 foliation (Figure 9b). They are associated with north to NNW vergent F_2 crenulation folds overprinting the L_1 lineation around subhorizontal axes. Within mafic sills, small listric reverse faults ramp up from an S_1 parallel orientation and are combined with C_2 planes

In more incompetent, phyllosilicate-rich layers of the mylonite zone, a crosscutting S_2 crenulation cleavage is combined with north to NNE vergent F_2 crenulation folds. The B_2 axes mostly plunge toward east and ESE. Within these parts of the mylonite zone, brittle C_3 shear planes cut across the older structures They strike W-E, are steeply inclined to the north or south, and indicate the final stage of compression.

On Lockwood Ø, S_1 foliation planes, C_1 shear planes, and shear zones steepen toward the mylonite zone Within the thrust zone the mylonite foliation is vertical or steeply dips to the south (Figure 7). It is crosscut by northward and southward inclined and conjugate sets of C_2 planes with slickensides indicating approximately N-S compression.

The semiductile to brittle structures of the D_{2+3} deformations are interpreted as the result of continuing compression after cessation of the mylonite formation. Since they are concentrated within the basal parts of the overthrust complex, they can be related to final movements of the entire block of metamorphics above the Kap Washington volcanics. This conclusion is supported by blocks of a brown and fine-grained, tectonic carbonate breccia within a several meters wide zone found at the boundary between the mylonite zone and overridden Kap Washington volcanics in the cliff SW of Kap Cannon. As a thin and grey layer on top of the volcanics, it could be traced southwestward along the steep cliffs. The breccia represents either crushed marbles of the Paradisfjeld Group (Cambrian) or relics of Permo-Carboniferous carbonates.

3.5. Microfabrics and Metamorphism

Above the mylonite zone the onset of C_1 shearing is indicated by undulation, flattening, strain-induced boundary migration, subgrain formation, and also incipient dynamic recrystallization of quartz. In the marbles, calcite records internal deformation and dynamic recrystallization. Feldspar is affected by stretching and partly converted into sericite. Small chlorite grows parallel to C_1 planes whilst older flakes are reoriented.

The foliation of marble mylonites is indicated by elongated and dynamically recrystallized calcite or submicroscopical calcite recrystallization grains. The matrix contains larger clasts of calcite, quartz, and polycrystalline aggregates.

In the foliation of mylonite quartzites at Kap Cannon, quartz is reduced in grain size, flattened, and replaced by submicroscopical subgrains and dynamically generated recrystallization grains. Extremely elongated quartz lenses and layers contain thin strips of parallel and crosscutting kink bands and shear planes, both being covered by recrystallization grains. Within phyllosilicate-rich mylonites the foliation records a slight bending, which led to the formation of shear bands. Beside aligned sericite and muscovite, chlorite occurs parallel to foliation planes.

In the pebbly quartzite mylonites of (?) Permo-Carboniferous, different clasts could be detected: (1) single quartz grains, (2) polycrystalline quartz clasts, partly indicating relics of a former static annealing by triple junctions between adjacent grains (along boundaries of intraclast grains, new recrystallization grains occur), and (3) fine-grained clasts consisting of submicroscopical quartz, a few sericite, and finest-grained opaque material. They could have been derived from (?) cherts and the finest-grained types also from dark slates.

Larger clasts record ductile (flattening with internal strain) and brittle deformation of quartz (disrupted clasts). Dynamically generated quartz recrystallization grains are concentrated along intracrystalline deformation zones (kink bands and shear planes) and grain boundaries. Smaller clasts are flattened within the main foliation and bent along the boundaries of larger quartz clasts. Aligned sericite, chlorite, and reoriented muscovite are parallel to the S_{my} foliation within phyllosilicate-rich layers.

In the limestone mylonite at Kap Cannon the foliation is indicated by small, elongated calcite recrystallization grains. Shearing was condensed within finest-grained parts of the matrix which are completely recrystallized.

At the margins of sheared mafic dikes and sills above the mylonite zone, the S_1 foliation is indicated by aligned chlorite and flattened and sheared fine-grained quartz. The shear zone and mylonite foliations of the marbles flow along the boundaries of isolated fragments of dikes and sills on a millimeter to centimeter size.

Within the mylonite zone the penetrative S_{my} foliation is recorded by aligned, dense chlorite which contains strips of opaque and epidote grains. It flows around sheared and disrupted feldspar and feldspar aggregates. As in sheared magmatics above the mylonite zone, they also record isolated relics of intersertal textures. Fine-grained sericite occurs within feldspar aggregates. Mafic minerals or their relics could not be detected within thin section and presumably are entirely converted into chlorite.

The microfabrics generally indicate ductile deformation of quartz and calcite with continuing dynamic recrystallization. Feldspar records only brittle deformation phenomena. The growth of phyllosilicates and recrystallization of quartz suggest that a slight greenschist facies metamorphism accompanied the D_1 deformation ($T \geq 300°C$).

During the D_2 event, growth of sericite and chlorite along S_2 crenulation cleavage planes and incipient ductile deformation of quartz without recrystallization suggest a slight temperature overprint in the field of the deeper anchizone. Quartz- and calcite-filled, approximately NNW-SSE trending and steeply inclined extension veins show that subsequent brittle conditions were accompanied by pressure solution (shear and cleavage planes) with mass transfer.

4. Eurekan Deformation in the Footwall of the Mylonite Zone

4.1. Kap Washington Group

4.1.1. Kap Cannon. At Kap Cannon the volcanic rocks below the mylonite zone are not affected by ductile deformation. Bedding planes gently to moderately dip to approximately SE (Figure 8e) and are cross-cut by W-E to NE-SW trending, densely spaced C_1 planes. These are steeply inclined and partly represent conjugate sets. The intersection lineation between bedding and C_1 planes (δ_1) plunges toward the ENE. In the cliff of Kap Cannon the volcanics are folded around an approximately NNW vergent F_1 fold on a ~50 m size. The structure is combined with C_1 planes dipping toward SSE. The finite extension is documented by steeply inclined and NNW-SSE to N-S trending extension fracture planes and joints.

4.1.2. South of Kap Washington. Southwest of Kap Cannon the thrust zone continues across the Benedict Fjord to the area south of Kap Washington There it splits into several branches (Figure 3) which continue toward Kap Kane in the southwest From the westernmost volcanic rocks on Kap Washington, *Brown and Parsons* [1981] report a tectonized junction between the sediments and volcanics and a strong slaty cleavage in the shales At the northeastern margin of the mountain range south of Kap Washington, intervolcanic clastic sediments (Figure 11a) consist of phyllites, quartz phyllites, and quartzites. They are underlain by chlorite schists with intercalated and several meters long, lens-shaped bodies of mafic metavolcanics (Figure 11c).

Within distinct layers, the sandy metasediments contain small clasts of sandstones, dark shales, single quartz grains, polycrystalline quartz, and finest-grained, chert-like types. The penetrative S_1 foliation is displayed by aligned chlorite and sericite, which forms beards at quartz clasts. Ductilely deformed quartz indicates strain-induced boundary migration; however, recrystallized quartz could not be detected. Larger quartz is dissected by extension veins or ductilely stretched. Calcite is concentrated within thin layers. Its bending and flattening is accommodated by deformation twins, kink bands, and shear planes. Recrystallization grains occur at grain boundaries and along zones of intracrystalline deformation. Continuing dynamic recrystallization could be detected in adjacent shear zones.

Shearing and flattening led to boudinage of the more competent magmatic layers within the chlorite schists. On SW dipping S_1 planes an L_1 lineation is defined by aligned sericite, elongated quartz, lens-shaped clasts, flattened chlorite flakes (? former lapilli of pyroclastics), and single disrupted feldspar grains. It gently plunges toward SSE (10°-30°, Figure 11b). Within more intensely sheared layers, single S/C fabrics and shear bands indicate an oblique, top-to-NNW sense of shear parallel to the L_1 lineation (Figure 11c). This is supported by single en echelon extension veins.

The chlorite matrix of the mafic metamagmatics is crosscut by distinct C_1 shear planes. In undeformed parts, small feldspars partly indicate relics of intersertal textures and are replaced by chlorite, epidote, and sericite/muscovite.

The planar S_1 foliation planes are crosscut by widely spaced, brittle C_2 shear planes dipping steeply to NE or SW. They are combined with single F_2 folds on a centimeter scale. Both B_2 axes and intersection lineations between S_1 and C_2 planes strike parallel to the L_1 lineation (Figure 11b).

The metasediments and metavolcanics represent a specific strip of rocks We relate the structures as well as the slight metamorphic overprint to the formation of the KCTZ because the SW dip of the S_1 foliation planes and oblique top-to-NNW sense of shear suggest that the sequence lies within a NW-SE trending ductile fault zone. The fault is interpreted as an oblique or lateral ramp in front of the KCTZ proper with an oblique dextral displacement It branches from the main thrust zone in the SE and, as a NW-SE trending line, cuts through the Kap Washington volcanics and sediments (Figure 11a) It can be assumed that the fault line turns into an approximately NE-SW strike north of Hunt Fjord.

The microstructural observations from the sediments with intercalated magmatics suggest a deformation under elevated temperatures. Sericite beards, ductile deformation and recrystallization of calcite, ductile deformation of quartz with incipient subgrain formation and strain-induced boundary migration, and the generation of sericite plus chlorite within the main foliation broadly indicate a temperature at the boundary between very low and low grade metamorphism.

The ductile deformation within this small strip of rocks suggests that the slight metamorphic overprint was a limited phenomenon related to the fault zone. Local and condensed "shear/strain heating" seems to have occurred in addition to burial-related heating. In general, however, no penetrative, ductile cleavage or foliation was found in the Kap Washington volcanics (e g , at Kap Cannon). Thus there is a discrepancy compared to the mylonite zone in the hanging wall of the volcanics, and the brittle fabrics of the volcanics do not represent direct equivalents of the ductile D_1 fabrics in the mylonites

4.1.3. Lockwood Ø. Just beneath the marble mylonites of the KCTZ, an S_1 cleavage cuts across bedding of rhyolitic tuffs and tuff breccias and more steeply dips southward (Figure 7). It displays the growth of parallel and fine-grained sericite. Single quartz grains or grain aggregates record pressure solution, a slight undulation, however, without strain-induced boundary migration or recrystallization. The south plunging L_1 lineation is defined by aligned sericite (Figure 8f). Rock fragments on a centimeter size are surrounded by S_1 planes.

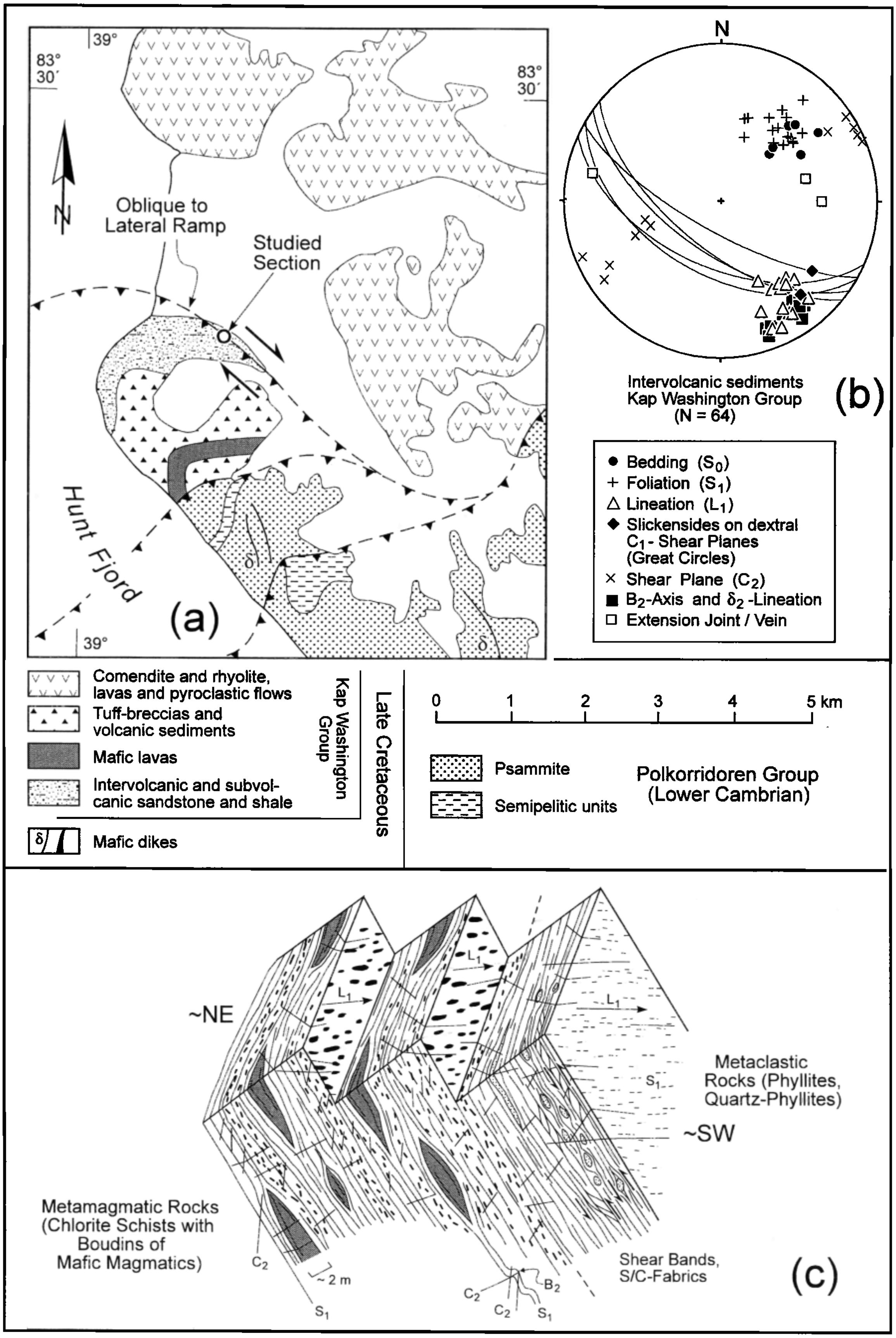

Figure 11. (a) Geological map of the area south of Kap Washinton [after *Higgins*, 1986b] (for location, compare Figure 3). The thrust plane is interpreted as an oblique to lateral ramp with respect to the main Kap Cannon Thrust in the southeast. (b) Lower hemisphere, equal-area fabric diagram depicts the orientations of structural elements in the studied section NE of Hunt Fjord. (c) Simplified and schematic block diagram illustrating the main structures in the studied section in Figure 11a (see text for explanations).

Both together display asymmetric shapes (σ-clasts) indicating a top-to-north transport of the hanging wall which is supported by S/C fabrics. Thus both indicators suggest a sense of shear comparable to that found in the mylonites just above.

Farther to the north of the thrust zone, the volcanics and some intercalated layers of clastic sediments are crosscut by approximately SW-NE striking and steeply southeastward inclined C_1 planes. Within finer-grained pyroclastic rocks and black siltstones, C_1 planes are replaced by an S_1 pencil cleavage. In the siltstones, submicroscopical sericite is aligned parallel to bedding. Only in some parts, finest-grained chlorite could be detected along S_1 cleavage planes. D_1 fabrics in the intercalated sandstones can be compared with those of the slightly deformed parts of the Permo-Carboniferous conglomerates (see section 4.2.). In the volcanic rocks and sediments, folds were not found. In contrast to the mylonites of the KCTZ, deformation within these strata took place under brittle conditions.

At the west coast of Lockwood Ø, grey sandstones with thick layers of black siltstones below the volcanics (Figure 4) are affected by a few cleavage and shear planes or a penetrative S_1 cleavage, respectively, dipping toward SE. The SE plunging L_1 lineation is recorded by aligned clastic sericite and small, quartz-filled pressure shadows around pyrite. C_2 planes partly represent a conjugate set indicating approximately NNW-SSE compression.

Within the sediments and partly also the magmatics, the development of an S_1 cleavage and growth of sericite depend on the tectonic position Near and at the KCTZ, sericite plus chlorite growth is accompanied by the development of undulose extinction in quartz Away from the KCTZ only a few shear or cleavage planes could be detected with minor sericite growth. As in the Permo-Carboniferous sediments, the metamorphic overprint can be interpreted to lie in the field of the anchizone and probably was concentrated along and near fault zones.

4.2. Late Carboniferous to Permian Sediments

In the northwestern part of Lockwood Ø (Figure 12), dolomitic layers are crosscut by widely distributed, brittle C_1 planes dipping steeply toward SSE to SE. In the limestones, a penetrative S_1 pressure solution cleavage affects sheared and bent relics of fossils. On a microscale it is indicated by thin strips and bands of dynamically recrystallized calcite. Sericite is aligned parallel to penetrative S_1 cleavage planes within more silty layers.

Up to several tens-of-meters thick mafic sills, intercalated in the carbonate sequence, are penetratively sheared along the margins whereas central parts are crosscut by C_1 planes. The orientations of the planes are comparable with those of the cleavage and shear planes within the carbonates

Near the northwest coast of the island the carbonate sequence is partly underlain by vertical red conglomerates with intercalated sandstone layers and lenses In the coarse conglomerates, sericite forms beards at smaller quartz pebbles. Single C_1 planes are indicated by aligned sericite and opaque dust At pebble contacts these are further developed as pressure solution planes, and adjacent quartz was bent and partly kinked. Within fine-grained parts, incipient S_1 planes with sericite growth and pressure solution phenomena are developed.

At the base of the conglomerates no original sedimentary contact with the Lower Cambrian Polkorridoren slates in the west could be found (Figure 12). In agreement with the maps of *Håkansson and Pedersen* [1982] and *Håkansson et al.* [1991] we interpret this contact as a thrust fault (Kap Christiansen Thrust) This interpretation is supported by observations from the contact's southward continuation which is underlain by and partly connected with at least six approximately NE-SW trending imbricate slices These slices consist of isolated conglomerates with sandstone and siltstone layers, or carbonates with cross-cutting mafic dikes and sills and are separated by incompetent Cambrian slates. At the bases of the imbricate slices no sedimentary contacts are preserved.

The internal deformation is characterized by an intense C_1 shear or S_1 foliation fabric which caused flattening of conglomerate pebbles. The planar foliation is recorded by newly grown sericite, chlorite, and sericite beards at quartz clasts. Undulation, bending, and kink bands within quartz pebbles of different size are due to shearing and tectonic compaction. The clasts content can be compared with that of the pebbly quartzite mylonite at Kap Cannon (single quartz crystals, polycrystalline quartz, and finest-grained quartz-rich rocks which possibly are chert pebbles).

These imbricates just below the gently inclined Kap Christiansen Thrust probably represent a duplex structure (Figure 12, profile). Their southern continuation and footwall thrust are unclear since the western slope to the coast line is covered by scree. At the northern cliff of Kap Christiansen, however, a vertical wedge of conglomerates and gently dipping carbonates with intercalated sills is displaced northwestward along the exposed Kap Christiansen Thrust over pelitic units of the Polkorridoren Group (Figure 6c).

The entire situation in the northwestern part of Lockwood Ø, north of the Kap Cannon Thrust Zone proper, suggests that approximately NW directed thrusting occurred during the D_1 event within the sediments. It can be related to an oblique ramping of the strata from a flooring décollement in the subsurface which propagated northward from the main thrust (mylonite) zone in the south.

Generally, the Permo-Carboniferous rocks indicate different intensities in C_1 shearing and/or S_1 cleavage development with sericite and ±chlorite growth and dynamic recrystallization of calcite. No evidence was found for subgrain formation or recrystallization of quartz. Hence it can be estimated that the temperature overprint did not reach greenschist facies conditions but was in the field of the lower anchizone.

4.3. Early Paleozoic Strata at the NW Coast of Lockwood Ø

At the northwestern margin of Lockwood Ø, grey slates of the Polkorridoren Group (Figure 12) contain small-scale cross beds and graded bedding (microscale), which indicate the sequence is right way up. The rocks are crosscut by WNW-ESE trending dikes. Good exposure of one dike records C_1 planes which are concentrated within several decimeters wide shear zones. There chlorite flakes are flattened within the shear plane fabric and define an L_1 lineation plunging toward approximately SE S/C fabrics record a top-to-NW sense of displacement parallel to the lineation In addition to the shear zones, parallel C_1 planes cut across the dike

The C_1 planes could be compared with the foliation planes in the more incompetent slates of the Polkorridoren Group which also dip toward approximately SE The foliation is related to a few tight folds on a meter scale with NNW-SSE trending axes. They affect silty layers and are combined with small-scale accommodation faults. Thin quartz veins are oriented parallel to the foliation planes and do not record an older folding event. A lineation is defined by aligned sericite and pressure shadows around pyrite. As in the dike, it plunges to the SE.

The penetrative foliation is recorded by sericite which grew during deformation, suggesting a slight metamorphic overprint Within thin quartz-rich layers. microscale quartz records incipient ductile

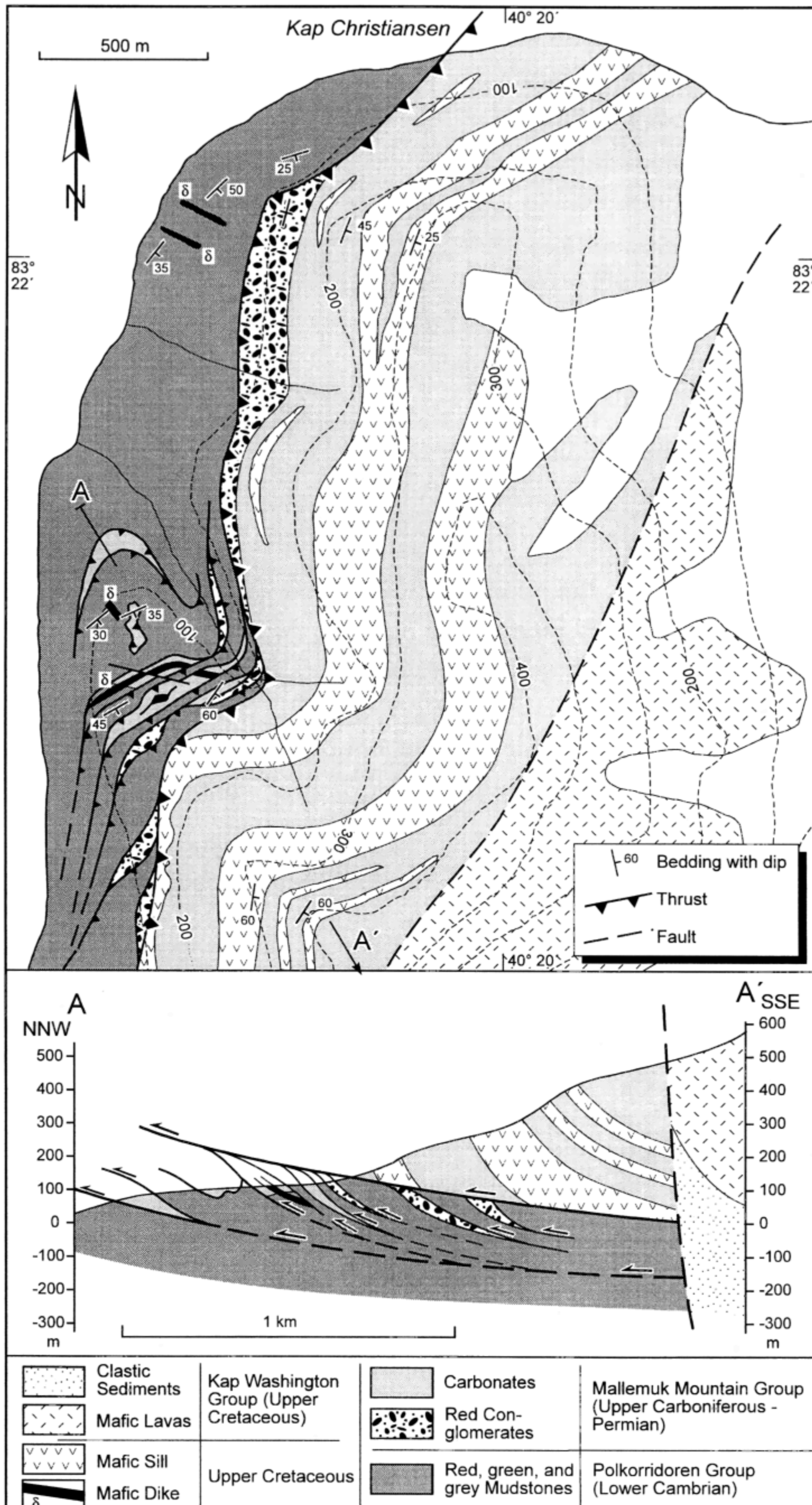
Kap Christiansen
500 m
N
40° 20´
83° 22´
83° 22´
A
A´
Bedding with dip
Thrust
Fault
NNW
SSE
1 km
m
Clastic Sediments
Mafic Lavas
Kap Washington Group (Upper Cretaceous)
Mafic Sill
Mafic Dike
Upper Cretaceous
Carbonates
Red Conglomerates
Mallemuk Mountain Group (Upper Carboniferous - Permian)
Red, green, and grey Mudstones
Polkorridoren Group (Lower Cambrian)

Figure 12.

deformation; however, recrystallization could not be detected. Several lens-shaped quartz aggregates display σ-clast geometries with a top-to-NW sense of shear. The chlorite matrix of a crosscutting mafic dike is affected by several C_1 planes, which can be compared with the foliation planes in the Cambrian slates.

Within single, decimeter thick silty layers, more widely spaced S_2 planes cut across bedding-parallel S_1 planes at high angles. They are related to small-scale, NNE vergent F_2 crenulation folds with axes plunging toward ESE Single and parallel C_2 planes also cut through the dikes. As do S_2 planes, they dip toward approximately SSW. The occurrence of two sets of foliation and cleavage planes within the Cambrian slates and C_1 planes in the Late Cretaceous dikes to our impression suggests that Ellesmerian structures in the slates have been reactivated and partly overprinted during Eurekan shearing.

5. Synthesis of the Structural Evolution

The deformations within the overthrust metamorphic complex and the different units below it suggest that the KCTZ developed during a continuous process within different crustal levels. In the metamorphic complex the mylonite zone was generated by an increase in shearing from the upper to the lower part of the displaced block. Transitions from single shear planes to shear zones, separating slices of metamorphic rocks, indicate the onset of Eurekan deformation A downward transition to an S_1 foliation and a mylonite foliation at the base record the increase in strain. The entire deformation is interpreted as the result of an overall simple shear mechanism.

Since a southward shallowing of dip in the thrust sheet is evident on Lockwood Ø, a broad listric shape of the thrust zone (Figure 13a) is assumed here. This is indirectly supported by the trend of the (oblique) thrusts to the northwest (in the footwall) of the mylonite zone. They join the latter along strike [see also, e.g., *Håkansson and Pedersen*, 1982] and make it possible to assume "spoon-shaped" geometries for their spatial arrangements also in the subsurface. The precise deep trajectory of the thrust zone, however, is unclear [*Soper and Higgins*, 1991b].

If the slices of limestone mylonites and mylonitic pebble quartzites at the base of the mylonite zone (Kap Cannon) represent relics of Permo-Carboniferous sediments, then the KCTZ must have overridden also late Paleozoic deposits to the south of the present Kap Washington volcanics. The slices were displaced below the overriding block of metamorphic rocks, affected by ductile deformation, and amalgamated with the base of the mylonites (Figure 13a).

Ductile deformation and dynamic recrystallization of quartz suggest that shearing and mylonite formation must have taken place in a deeper crustal level A temperature of ~300°C can be roughly estimated. Since ductile deformation is restricted to distinct zones within the pile of rocks (e.g., mylonites) and also occurs within an oblique to lateral ramp fault (Kap Washington Group), an additional contribution of "shear/strain heating" within the thrust and shear zones can be assumed

During continuing displacement along the basal mylonite zone, the block of early Paleozoic metasediments was displaced along the thrust plane cutting upsection (Figure 13a) By this the brittle-ductile transition was crossed. Further advance and uplift of the thrust sheet plus basal mylonites (Figure 13b) had to be accomplished by semi-ductile to brittle structures, which developed during the D_{2+3} events. These can be compared with equivalents within the volcanics and sediments in the footwall. There, thrusting propagated northward along a subsurface décollement in front of the mylonite zone (Figures 13a - 13c). A comparable propagation of the main basal décollement is reasonable for the area between Lockwood Ø and Kap Washington, which led to the formation of an oblique to lateral ramp south of Kap Washington

During the later stage of thrusting, deformation in the footwall of the thrust zone continued, which can be described as high-level thrusting and shearing This is exemplified by the final generation of the Kap Christiansen Thrust with imbricates (duplex) at the NW coast of Lockwood Ø As Permo-Carboniferous strata override Cambrian rocks (Figure 12), it can be assumed that ramping of the Kap Christiansen Thrust partly took place along a reactivated older normal fault The precise dip of the ramp, however, is unclear. A steeply inlined fault, cutting across the thrust (Figure 12), could not be observed in outcrop It could either represent a younger normal fault or a reverse fault related to reactivation of a normal fault during thrust tectonics.

In the Kap Cannon area the final emplacement of the metasediments over the Kap Washington volcanics took place on a thin strip of brecciated carbonates between the volcanics and the mylonite zone. Thus the mylonites represent passively carried relics of the former mylonite zone which was generated in a deeper crustal level. This also suggests that fabrics of the D_2 and D_3 events in the hanging wall block of metasediments are equivalents of the brittle deformational structures in the Kap Washington volcanics, and both are related to final, higher-level displacements

Whilst the initial displacement of the metamorphic complex along the basal mylonite zone (D_1) was directed northward, the final and semiductile to brittle thrusting (D_{2+3}) within its footwall on Lockwood Ø and south of Kap Washington was directed toward NNW to NW. This is supported by the present NE-SW trend of the mylonite zone, together with the imbricate slices of the Kap Christiansen Thrust, as well as the pattern of shear planes, cleavage planes, and lineations Continuing compression in the footwall led to the formation of oblique ramp structures with respect to the orientation of the main thrust (mylonite) zone.

The amount of displacement along the thrust zone is difficult to estimate. Given an onset of mylonite formation in a depth of ~7-8 km, then a displacement of more than 10 km can be assumed. *Soper and Higgins* [1991b] estimate a minimum of 15 km

The thrust faulting can be no older than earliest Tertiary because it affects strata as young as the Cretaceous-Tertiary boundary (Kap Washington Group) [cf., e.g., *Larsen et al.*, 1978; *Batten*, 1982; *Larsen*, 1982; *Soper et al.*, 1982; *Estrada et al.*, 1998]. On the basis of $^{40}Ar/^{39}Ar$ age spectra, *Estrada et al.* [1998] interpret a date of circa 38 Ma as a minimum age for the thermal overprint of the volcanic rocks during compression This date is in good agreement with two K/Ar whole rock determinations from volcanic lavas at 34.9±3.5 and 32.3±3.2 Ma [*Dawes*, 1971; *Dawes and Soper*, 1971] K/Ar age determinations from metamorphic rocks in northern Peary Land have

Figure 12. Geological map of the northwestern part of Lockwood Ø with Kap Christiansen Thrust leading to the formation of imbricate slices in the southern part (map compiled after *Higgins* [1986b] and own field mapping, for location, see Figure 4). Interpretative profile summarizes the geometry of the thrust

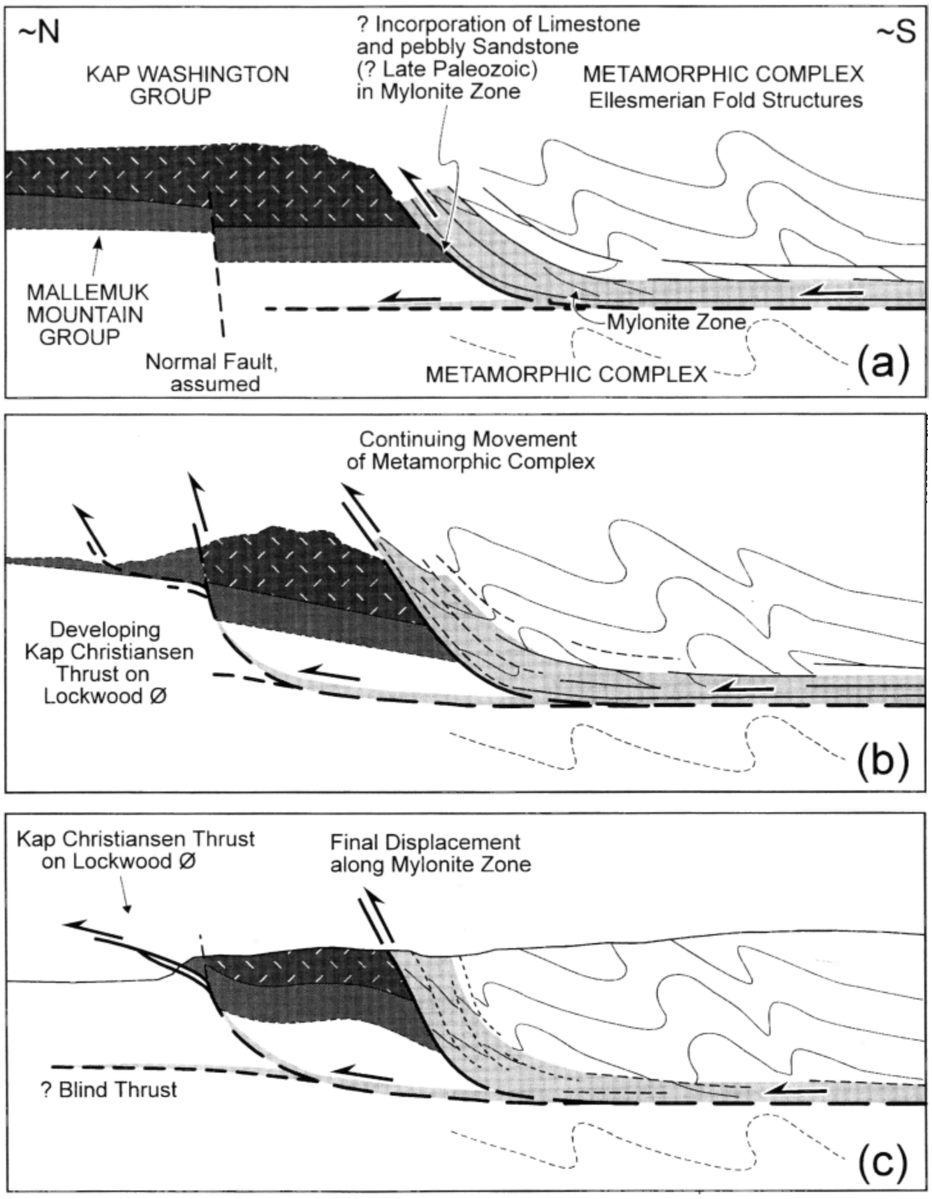

Figure 13. Simplified and interpretative cartoons (not to scale) to illustrate the evolution of the Kap Cannon Thrust Zone. (a) Development of the mylonite zone. (b) Continuing displacement of the metamorphic complex and ramping of the Kap Christansen Thrust on Lockwood Ø. (c) Final displacement along the Mylonite Zone and Kap Christansen Thrust (see text for further explanations). Penetrative ductile deformation at the thrusts is indicated by light shading. The older normal fault as location for ramping of the Kap Christiansen Thrust is assumed.

given Cretaceous to Tertiary ages [*Dawes*, 1971; *Dawes and Soper*, 1971] and suggest the influence of a younger thermal overprint in the northern part of the north Greenland fold belt.

6. Regional Implications

The Devonian-early Carboniferous compression led to the generation of the north Greenland fold belt with a complex pattern of structures and a metamorphic overprint following at least four different zones [e.g., *Higgins et al.*, 1982; *Soper and Higgins*, 1987, 1991a].

The late Carboniferous-early Permian sedimentation at the north Greenland coast (Lockwood Ø and Kap Kane) can be compared with that in other parts of the Wandel Sea Basin where late Paleozoic sedimentation was accompanied by fault tectonics [e.g., *Stemmerik and Håkansson*, 1991]

The mafic dikes and sills are part of the ~N-S trending dike swarm in north Greenland [*Higgins et al.*, 1981], which is related to Late Cretaceous approximately W-E crustal extension [e.g., *Soper and Higgins*, 1991b]. This dike swarm can be traced from north of the Harder Fjord Fault Zone to the Kap Washington area. It is reasonable to assume that the dikes are precursors of and/or are related to the generation of the subaerial Kap Washington volcanic suite The emplacement of the dikes and extrusion of the Kap Washington volcanics have been related to a rifting process [*Batten et al*, 1981; *Dawes and Peel*, 1981, *Soper et al.*, 1982; *Soper and Higgins*, 1991b] Geochemical data also show that the magmatics were generated during continental crustal extension [e.g , *Soper et al.*, 1982, *Brown et al.*, 1987] The northern offshore continuation of crustal dilation can be linked to extension (? rifting or spreading) in the Makarov Basin [see, e g , *Kovacs*, 1982, *Larsen*, 1982; *Brown et al.*, 1987] Magnetic anomalies offshore to the west and east of the Kap Washington volcanics are probably associated with them [*Kovacs*, 1982, see also *Feden et al.*, 1979]; however, the precise extent of rift volcanics and oceanic basalts beneath the shelf remains a matter of speculation [*Dawes*, 1990]

After generation of the Kap Washington volcanics plus dikes and sills, the early Paleozoic metamorphic complex was thrust northward along the KCTZ. Ductile deformation within the thrust zone indicates an important intraplate suture. On the basis of the age of the Kap Washington Group, thrusting took place during early Tertiary times (late Paleocene-Eocene) [*Soper et al.* 1982].

The timing of compressive deformation in north Greenland suggests a relation to the onset of separation of the Lomonosov Ridge from Eurasia. This possibly took place during anomaly 25 or a bit later [*Srivastava*, 1985] and was followed by spreading along the Nansen Ridge with anomaly 24 being the first recognized. Depending on the different magnetic polarity timescales, the anomaly 25-24 interval falls into the late Paleocene or late Paleocene-early Eocene intervals [see, e.g., *Dawes*, 1982]

These first movements in the Arctic Basin along the Nansen Ridge coincide with the onset of spreading in the Norwegian-Greenland Sea in the anomaly 25-24 interval [*Srivastava*, 1985; *Roest and Srivastava*, 1989]. *Roest and Srivastava* [1989] have shown that in the above interval a counterclockwise change in the direction of spreading took place in the Labrador Sea It led to a north-northeast directed drift of Greenland with respect to North America and compression in the Arctic archipelago. Hence this northward movement of Greenland is related to the onset of spreading in the Norwegian-Greenland Sea and Arctic Basin and compression in north Greenland [see also, e.g., *Soper et al*, 1982]. By this the displacement along the KCTZ can be interpreted as a within-plate accommodation of northward movements of Greenland [*Soper and Higgins*, 1991b].

Within many predrift plate tectonics' reconstructions the Svalbard archipelago, as part of the Barents Shelf, is placed opposite to and in connection with northeastern north Greenland [e g , *Kristoffersen and Talwani*, 1977; *Talwani and Eldholm*, 1977, *Birkenmajer*, 1981; *Håkansson and Stemmerik*, 1984, *Srivastava*, 1985; *Srivastava and Tapscott*, 1986; *Brown et al.*, 1987, *Rowley and Lottes*, 1988; *Stemmerik and Håkansson*, 1991]. In such an arrangement the NW-SE trending Wandel Hav Strike-Slip Mobile Belt [*Håkansson and Pedersen*, 1982] with its NW-SE fault lines is oriented parallel to the inferred offshore plate boundary Dextral transpressive deformation in this belt ("Kronprins Christian Land Strike-Slip Orogeny" of *Pedersen* [1988]) terminates its deformational history, which also comprises two events in the Jurassic and Late Cretaceous [e.g., *Pedersen*, 1988; *Håkansson et al.*, 1991]

A connection of thrusting along the KCTZ with dextral transpressive displacements in the Wandel Hav Mobile Belt has been described by *Håkansson and Pedersen* [1982] [see also *Dawes and Peel*, 1981]. Both can be linked with N-S compression along the Harder Fjord Fault Zone

In this configuration the KCTZ with northward directed displacements could broadly represent the western continuation of the Paleogene West Spitsbergen Fold-and-Thrust Belt on the opposite side of the plate boundary where ENE-WSW compression (present coordinates) dominated. This would suggest a more or less coeval Eurekan belt of compressive movements in this west Spitsbergen-north Greenland strip which extends farther westward into Ellesmere Island (compare also interpretation of *Soper et al.* [1982]).

It should be stated, however, that the timing of compression in these different areas is far from being precise and is still a matter of debate [see, e.g , *Håkansson and Stemmerik*, 1984, 1989; *Håkansson*, 1988, *Soper and Higgins*, 1991b] On the basis of undeformed sediments of the late Paleocene-early Eocene Thyra Ø Formation [*Boyd et al.*, 1994], transpressive deformation in the Wandel Hav Mobile Belt has been interpreted as Late Cretaceous-earliest Tertiary in age followed by a post-Paleocene extensional event [e.g., *Håkansson and Pedersen*, 1982, *Håkansson et al*, 1991, 1994]. The possibility that offshore strike-slip fault lines exist, which separate undeformed blocks of these sediments, however, suggests that transpressive deformation could also have continued through post-Paleocene times. In such a view, dextral transpression in the Wandel Hav Strike-Slip Mobile Belt was the result of northward movement of Greenland combined with north directed diplacements in the west (Kap Cannon Thrust Zone) and compression in the West Spitsbergen Fold-and-Thrust Belt.

7. Conclusions

The studies at the Kap Cannon Thrust Zone (KCTZ) suggest several stages of deformation and metamorphism and partly confirm earlier work:

1. In the early Paleozoic strata, Ellesmerian compression is documented by three deformational events which were accompanied by at least greenschist facies metamorphism. The third deformation led to approximately NW vergent folding.

2. During Late Cretaceous times, the early Paleozoic metamorphic complex and Permo-Carboniferous sediments were injected by mafic dikes and sills It is assumed that the emplacement of the magmatics took place under an approximately NE-SW to E-W extensional regime and partly coincided with the formation of the Late Cretaceous volcanic rocks and clastic sediments (Kap Washington Group).

3. The onset of ductile deformation within the metamorphic complex, leading to the generation of the KCTZ, took place in a deeper crustal level. It was characterized by an increase in shear zone deformation from the upper to the lower part, following a simple shear mechanism, and led to the formation of a mylonite zone at the base. Shear sense indicators prove a north directed transport of the entire block along the basal mylonite Mylonitic pebble quartzites and limestone mylonites at the base of the KCTZ could have been derived from overridden Permo-Carboniferous sediments. The latter then had a wider distribution in the subsurface to the south of Kap Washington.

South of Kap Washington an oblique or lateral ramp is interpreted as a branch of the main thrust zone and cuts through the Kap Washington Group Ductile deformation indicates a local rise in temperature. As in the KCTZ proper this suggests the influence of a local "shear/strain heating"

4. During transport of the block of metamorphic rocks into higher crustal levels, ductile deformation successively changed to semiductile and final brittle conditions This suggests that the thrust sheet and

basal mylonites were passively carried over the Kap Washington Group, and a listric shape of the thrust zone is assumed here

In the footwall and in front of the mylonite zone on Lockwood Ø, the cover sediments record brittle deformation phenomena and ductile effects only at and in fault zones They are thrust and imbricated northwestward. This is interpreted as the result of an oblique ramping from a basal décollement along the Kap Christiansen Thrust, which presumably reactivated an older normal fault.

Thrust faulting and related structures are not older than earliest Tertiary, because they affect the Kap Washington Group. Thus a Paleocene and/or younger age seems realistic.

It is reasonable to relate the emplacement of the volcanics and mafic dikes to extension along the Makarov Basin, which was combined with a dilation of the north Greenland crust [e.g. *Brown et al*, 1987]. The onset of spreading activity along the Nansen Ridge, the northward movement of Greenland, and the combined lateral displacement within the Wandel Hav Strike-Slip Mobile Belt presumably coincided with the important northward directed thrust tectonics

Acknowledgments. We are grateful to the Federal Institute for Geosciences and Natural Resources (BGR, Hannover, Germany) for the invitation to participate in the CASE 2-Expedition to north Greenland in 1994, led by F Tessensohn Thanks to him and all members of the CASE 2-group for many discussions about the evolution of Ellesmerian and Eurekan structures in the study areas. We are grateful to H P Trettin and an anonymous reviewer for remarks and suggestions which improved the manuscript. We gratefully acknowledge financial support from the German Research Foundation (DFG, projects Go 405/3-1 and Th 126/26-2) which enabled the studies to be carried out

References

Batten, D J, Palynology of shales associated with the Kap Washington Group volcanics, central north Greenland, *Rapp. Groenl. Geol. Unders., 108,* 15-23, 1982

Batten, D J, P E Brown, P R Dawes, A K Higgins, B Eske Koch, I Parsons, and N J Soper, Peralkaline volcanicity on the Eurasia Basin margin, *Nature, 294,* 150-152, 1981

Birkenmajer, K, The Geology of Savalbard, the western part of the Barents Sea, and the continental margin of Scandinavia, in *The Ocean Basins and Margins,* vol 5, *The Arctic Ocean,* edited by A E M Nairn, M Churkin, and F G Stehli, pp 265-329, Plenum, New York, 1981

Boyd, A, E Håkansson, and L Stemmerik, Preliminary age considerations and descriptions of the early Tertiary Thyra Ø flora from eastern north Greenland, in *Wandel Sea Basin: Basin Analysis, EFP-91, Proj. 0012, Sci. Rep 15,* pp 1-32, Univ of Copenhagen, Copenhagen, 1994

Brown, P E, and I Parsons, The Kap Washington Group volcanics, *Rapp. Groenl. Geol. Unders., 106,* 65-68, 1981

Brown, P E, I Parsons, and S M Becker, Peralkaline volcanicity in the Arctic basin - the Kap Washington volcanics, petrology and palaeotectonics, *J. Geol. Soc. London, 144,* 707-715, 1987

Dawes, P R, The north Greenland fold belt and environs, *Bull. Geol. Soc. Den., 20,* 197-239, 1971

Dawes, P R, Precambrian to Tertiary of northern Greenland, in *Geology of Greenland,* edited by A Escher and W S Watt, pp 248-303, Geol Surv of Greenland, Copenhagen, 1976

Dawes, P R, Note on the magnetic polarity time scales used in the Nares Strait volume, in *Nares Strait and the Drift of Greenland: A Conflict in Plate Tectonics,* edited by P R Dawes and J W Kerr, *Medd Groenl., Geosci., 8,* 389-392, 1982

Dawes, P R, The north Greenland continental margin, in *The Geology of North America,* vol L, *The Arctic Ocean Region,* edited by A Grantz, L Johnson, and J F Sweeney, pp 211-226, Geol Soc of Am, Boulder, Colo, 1990

Dawes, P R., and J S Peel, The northern margin of Greenland from Baffin Bay to the Greenland Sea, in *The Ocean Basins and Margins,* vol 5, *The Arctic Ocean,* edited by A E M Nairn, M Churkin, and F G Stehli, pp 201-264, Plenum, New York, 1981

Dawes, P R, and N J Soper, Geological investigations in northern Peary Land, *Rapp. Groenl Geol. Unders., 28,* 9-15, 1970

Dawes, P R, and N J Soper, Significance of K/Ar age determinations from northern Peary Land, *Rapp Groenl. Geol Unders., 35,* 60-62, 1971

Dawes, P R, and N J Soper, Pre-Quaternary history of Greenland, in *Arctic Geology,* edited by M G Pitcher, *AAPG Mem., 19,* 117-134, 1973

Dawes, P R, D C Rex, and N J Soper, Routine K/Ar age determinations on post-Silurian dolerite dykes, north Greenland fold belt, *Rapp Groenl Geol. Unders, 115,* 9-114, 1983

De Paor, D G, D C Bradley, G Eisenstadt, and S M Phillips, The Arctic Eurekan orogen A most unusual fold-and-thrust belt, *Geol. Soc Am. Bull., 101,* 952-967, 1989

Estrada, S, A Hohndorf, and F Henjes-Kunst, Cretaceous/Tertiary volcanism in north Greenland, paper presented at International Conference on Arctic Margins (ICAM III), Fed Inst Geosci Natur Resour, Celle, Germany, Oct 12 to 16, 1998

Feden, R H, P R Vogt, and H S Fleming, Magnetic and bathymetric evidence for the "Yermak Hot Spot" northwest of Svalbard in the Arctic Basin, *Earth Planet. Sci. Lett., 44,* 18-38, 1979

Håkansson, E, Carboniferous to Tertiary development of the Wandel Sea Basin, eastern north Greenland, *Rapp. Groenl. Geol. Unders., 88,* 73-83, 1979

Håkansson, E, Did Tertiary compressional tectonics affect north Greenland? Summary of the evidence, *Nor Polarinst Rapp., 46,* 101-104. 1988

Håkansson, E, and S A S Pedersen, Late Paleozoic to Tertiary tectonic evolution of the continental margin in north Greenland, in *Arctic Geology and Geophysics,* edited by A F Embry and H R Balkwill, *Mem. Can. Soc Pet. Geol, 8,* 331-348, 1982

Håkansson, E, and L Stemmerik, Wandel Sea Basin The north Greenland equivalent to Svalbard and the Barents Shelf, in *Petroleum Geology of the North European Margin,* edited by A M Spencer et al, pp 97-107, Graham and Trotman, Norwell, Mass, 1984

Håkansson, E, and L Stemmerik, Wandel Sea basin A new synthesis of the late Paleozoic to Tertiary accumulation in north Greenland, *Geology, 17,* 683-686, 1989

Håkansson, E, C Heinberg, and L Stemmerik, The Wandel Sea Basin from Holm Land to Lockwood Ø, eastern north Greenland, *Rapp. Groenl. Geol. Unders., 106,* 47-63, 1981

Håkansson, E, C Heinberg, and L Stemmerik, Mesozoic and Cenozoic history of the Wandel Sea Basin area, north Greenland, in *Sedimentary Basins of North Greenland,* edited by J S Peel and M Sønderholm, *Bull Groenl. Geol. Unders., 160,* 153-164, 1991

Håkansson, E, C Heinberg, L Madsen, S Mølgaard, S A S Pedersen, S Piasecki, J A Rasmussen, L Stemmerik, and K Zinck-Jørgensen, Wandel Sea Basin Basin analysis - Project Summary, in *Wandel Sea Basin: Basin Analysis, EFP-91, Proj. 0012,* pp 1-11, Univ of Copenhagen, Copenhagen, 1994

Henriksen, N, Geological map of north Greenland, scale 1 500,000, Nyboe Land sheet 7, Peary Land sheet 8, descriptive text, Geol Surv of Greenland, Copenhagen, 1992

Henriksen, N, and H F Jepsen, K/Ar age determinations on dolerites from southern Peary Land, *Rapp Groenl. Geol. Unders, 28,* 55-58, 1970

Higgins, A.K., Geology of central and eastern north Greenland, *Rapp Groenl. Geol. Unders, 128,* 37-54, 1986a

Higgins, A K (ed), Geological map of Greenland. Harder Fjord, scale 1 100,000, Geol Surv of Greenland, Copenhagen, 1986b

Higgins, A K, and N J Soper, Devonian-early Carboniferous deformation and metamorphism, North Greenland, B, Metamorphism, in *Geology of the Innuitian Orogen and Arctic Platform of Canada and Greenland, Geol. Can.,* vol 3, edited by H P Trettin, pp 289-291, Geol Surv of Can, Min Supply Serv of Can, 1991

Higgins, A K, J D Friderichsen, and N J Soper, The north Greenland fold belt between central Johannes V Jensen Land and eastern Nansen Land, *Rapp. Groenl. Geol. Unders., 106,* 35-45, 1981

Higgins, A K, U Mayr, and N J Soper, Fold belts and metamorphic zones of northern Ellesmere Island and north Greenland, in *Nares Strait and the Drift of Greenland A Conflict in Plate Tectonics,* edited by P R Dawes and J W Kerr, *Medd. Groenl, Geosci., 8,* 159-166, 1982

Higgins, A K, N J Soper, and J D Friderichsen, North Greenland fold belt in eastern north Greenland, in *The Caledonide Orogen. Scandinavia and Related Areas,* edited by D G Gee and B A Sturt, pp 1017-1029, John Wiley, New York, 1985

Higgins, A K, J Ineson, J S Peel, F Surlyk, and M Sønderholm, Lower Palaeozoic Franklinian Basin of north Greenland, in *Sedimentary Basins of North Greenland,* edited by J S Peel and M Sønderholm, *Bull. Groenl. Geol. Unders., 160,* 71-139, 1991a

Higgins, A K, J R Ineson, J S Peel, F Surlyk, and M Sønderholm, Cambrian to Silurian basin development and sedimentation, North Greenland, in *Geology of the Innuitian Orogen and Arctic Platform of Canada and Greenland, Geol. Can.,* vol 3, edited by H P Trettin, pp 111-161, Geol Surv of Can, Min Supply Serv of Can, 1991b

Hurst, J M, and F Surlyk, Stratigraphy of the Silurian turbidite sequence of north Greenland, *Bull. Groenl. Geol. Unders., 145,* 1-121, 1982

Kovacs, L C, Motion along Nares Strait recorded in the Lincoln Sea Aeromagnetic evidence, in *Nares Strait and the Drift of Greenland. A Conflict in Plate Tectonics,* edited by P R Dawes and J W Kerr, *Medd Groenl, Geosc., 8,* 275-290, 1982

Kristoffersen, Y, and M Talwani, Extinct triple junction south of Greenland and the Tertiary motion of Greenland relative to North America, *Geol. Soc. Am. Bull, 88,* 1037-1049, 1977

Larsen, O, The age of the Kap Washington Group volcanics, north Greenland, *Bull. Geol. Soc. Den., 31,* 49-55, 1982

Larsen, O, P R Dawes, and N J Soper, Rb/Sr age of the Kap Washington Group, Peary Land, north Greenland and geotectonic implication, *Rapp. Groenl. Geol Unders, 90,* 115-119, 1978

Manby, G M, S Estrada, M Thirlwall, N Lyberis, and A N Baxter, Geochemical and isotopic constraints on the age and origins of Kap Washington Group volcanic rocks and related dykes of north Greenland, paper presented at International Conference on Arctic Margins (ICAM III), Fed Inst Geosci Natur Resour Celle, Germany, Oct 12 to 16, 1998

Okulitch, A V, and H P Trettin, Late Cretaceous - early Tertiary deformation, Arctic Islands, in *Geology of the Innuitian Orogen and Arctic Platform of Canada and Greenland, Geol. Can*, vol 3, edited by H P Trettin, pp 469-489, Geol Surv of Can, Min Supply Serv of Can, 1991

Pedersen, S A S, Model of structural events in the late Mesozoic platform break up between Greenland and Svalbard, *Nor. Polarinst. Rapp., 46*, 99-100, 1988

Pedersen, S A S, and P M Holm, The significance of a Middle Devonian K/Ar age of an intrusive rock in the southern part of the north Greenland fold belt, *Bull. Geol Soc. Den., 31*, 121-127, 1983

Roest, W R, and S P Srivastava, Sea-floor spreading in the Labrador Sea A new reconstruction, *Geology, 17*, 1000-1003, 1989

Rowley, D B. and A L Lottes, Plate-kinematic reconstructions of the North Atlantic and Arctic Late Jurassic to present, *Tectonophysics, 155*, 73-120, 1988

Scott, R A, L M Natapov, L M Anderson, J C Stewart, and C F H Willan, Tectonic elements of the Arctic, Reg. Arctic Proj Ser, scale 1 10,000,000, Cambridge Arctic Shelf Progr, Cambridge, UK, 1995

Soper, N J, and P R Dawes, A section through the north Peary Land fold belt, *Proc. Geol. Soc. London, 1662*, 60-61, 1970

Soper, N J, and A K Higgins, Thin-skinned structures at the basin-shelf transition in north Greenland, *Rapp. Groenl Geol. Unders., 126*, 87-94, 1985

Soper, N J, and A K Higgins, A shallow detachment beneath the north Greenland fold belt Implications for sedimentation and tectonics. *Geol. Mag, 124*, 441-450, 1987

Soper, N J, and A K Higgins, Models for the Ellesmerian mountain front in north Greenland A basin margin inverted by basement uplift, *J. Struct. Geol., 12*, 83-97, 1990

Soper, N J, and A K Higgins, Devonian - early Carboniferous deformation and metamorphism. north Greenland, A. Deformation, in *Geology of the Innuitian Orogen and Arctic Platform of Canada and Greenland, Geol. Can.*, vol 3, edited by H P Trettin, pp 283-288, Geol Surv of Can. Min Supply Serv of Can, 1991a

Soper, N J, and A K Higgins, Late Cretaceous - early Tertiary deformation, north Greenland, in *Geology of the Innuitian Orogen and Arctic Platform of Canada and Greenland, Geol Can.*, vol 3, edited by H P Trettin, pp 461-465, Geol Surv of Can, Min Supply Serv of Can, 1991b

Soper, N J, A K Higgins, and J D Friderichsen, The north Greenland fold belt in eastern Johannes V Land, *Rapp. Groenl. Geol. Unders., 99*, 89-98, 1980

Soper, N J, P R Dawes, and A K Higgins, Cretaceous-Tertiary magmatic and tectonic events in north Greenland and the history of adjacent basins, in *Nares Strait and the drift of Greenland: A Conflict in Plate Tectonics*, edited by P R Dawes and J W Kerr, *Medd. Groenl., Geosci, 8*, 205-220, 1982

Springer, N, Preliminary Rb-Sr age determination from the north Greenland fold belt, Johannes V Jensen Land with comments on the metamorphic grade, *Rapp. Groenl. Geol. Unders., 106*, 77-84, 1981

Springer, N, Rb-Sr age determinations on low-grade metasediments from the north Greenland fold belt, *Terra Cognita, 2*, 63, 1982

Springer N, and J D Friderichsen, Age of low-grade regional metamorphism in the north Greenland fold belt Mineralogical and Rb-Sr-isotope evidence from pelitic metasediments, *Can J. Earth Sci., 31*, 358-368. 1994

Srivastava. S P, Evolution of the Eurasian Basin and its implications to the motion of Greenland along Nares Strait, *Tectonophysics, 114*. 29-53, 1985

Srivastava, S P, and C R Tapscott, Plate kinematics of the North Atlantic. in *The Geology of North America*, vol M, *The Western North Atlantic Region*, edited by P R Vogt and B E Tucholke, pp 379-404, Geol Soc of Am. Boulder. Colo, 1986

Stemmerik, L, and E Håkansson, Stratigraphy and depositional history of the upper Palaeozoic and Triassic sediments in the Wandel Sea Basin, central and eastern north Greenland, *Rapp Groenl Geol Unders, 143*, 21-45, 1989

Stemmerik. L and E Håkansson, Carboniferous and Permian history of the Wandel Sea Basin, north Greenland. in *Sedimentary Basins of North Greenland* edited by J S Peel and M Sønderholm, *Bull Groenl Geol. Unders, 160*, 141-151, 1991

Sundvor, E, and A Austegard, The evolution of the Svalbard margins Synthesis and new results, in *Geological History of the Polar Oceans: Arctic versus Antarctic*, edited by U Bleil and J Thiede, pp 77-94, Kluwer Acad, Norwell, Mass, 1990

Surlyk, F, Nares Strait and the down-current termination of the Silurian turbidite basin of north Greenland, in *Nares Strait and the Drift of Greenland· A Conflict in Plate Tectonics*, edited by P R Dawes and J W Kerr, *Medd. Groenl., Geosci., 8*, 147-150, 1982

Surlyk, F, Tectonostratigraphy of north Greenland, in *Sedimentary Basins of North Greenland*, edited by J S Peel and M Sønderholm, *Bull. Groenl. Geol Unders., 160*, 25-48, 1991

Talwani, M, and O Eldholm, Evolution of the Norwegian-Greenland Sea, *Geol. Soc Am. Bull, 88*, 969-999, 1977

Trettin, H P, Tectonic framework, in *Geology of the Innuitian Orogen and Arctic Platform of Canada and Greenland, Geol. Can.*, vol 3, edited by H P Trettin, pp 59-66, Geol Surv of Can, Min Supply Serv of Can, 1991

Vogt, P R, L C Kovacs, C Bernero, and S P Srivastava, Asymmetric geophysical signatures in the Greenland - Norwegian and southern Labrador Seas and the Eurasian Basin, *Tectonophysics, 89*, 95-160, 1982a

Vogt, P R, P T Taylor, L C Kovacs, and G L Johnson, The Canada Basin Aeromagnetic constraints on structure and evolution, *Tectonophysics, 89*, 295-336, 1982b

K Piepjohn, Geological Institute, University of Munster, Corrensstrasse 24, D-48149 Munster, Germany (piepjoh@uni-muenster de)

W von Gosen, Geological Institute, University of Erlangen, Schlossgarten 5, D-91054 Erlangen, Germany (vgosen@geol uni-erlangen de)

(Received January 5. 1999,
revised April 26, 1999,
accepted May 3, 1999)

Multistage accretion and exhumation of the continental crust (Ivrea crustal section, Italy and Switzerland)

M. R. Handy,[1] L. Franz,[2] F. Heller,[3] B. Janott,[1] and R. Zurbriggen[4]

Abstract. The Ivrea crustal section exposes in map view all levels of the southern Alpine continental crust, from ultramafic, mafic, and felsic granulite facies rocks of the deep crust (Ivrea-Verbano Zone), through medium-grade basement rocks (Strona-Ceneri Zone and Val Colla Zone), to unmetamorphosed Permo-Mesozoic sediments. The oldest part of the crustal section is preserved in the medium-grade basement units, which are interpreted to be the overprinted remains of an Ordovician (440-480 Ma) magmatic arc or forearc complex. During Variscan subduction this arc was tectonically underplated by a Carboniferous accretion-subduction complex (320-355 Ma) containing metasediments and slivers of Rheic oceanic crust presently found in the Ivrea-Verbano Zone. During the late stages of Variscan convergence (290-320 Ma), lithospheric delamination triggered magmatic underplating and lead to polyphase deformation under amphibolite to granulite facies conditions. This was broadly coeval with extensional exhumation and erosion of the Variscan-overprinted Ordovician crust presently exposed in the Strona-Ceneri and Val Colla Zones. Post-Variscan transtensional tectonics (270-290 Ma) were associated with renewed magmatic underplating, mylonitic shearing, and incipient exhumation of the lower crust in the Ivrea-Verbano Zone. This coincided with the formation of elongate basins filled with volcanoclastic sediments in the upper crust. Early Mesozoic, Tethyan rifting of the southern Alpine crust (180-230 Ma) reduced crustal thickness to 10 km or less. In the lower crust, most of this thinning was accommodated by granulite to retrograde greenschist facies mylonitic shearing. The lower crust was exhumed along a large, noncoaxial mylonitic shear zone that was linked to asymmetrical rift basins in the upper crust. The composite structure resulting from this complex evolution is probably typical of thinned, late Variscan continental crust on the passive margins of western Europe. Alpine faulting and folding (20-50 Ma) fragmented the crustal section. The originally deepest levels of the crustal section in the Ivrea-Verbano Zone as well as some segments of the basement-cover contact were steepened, whereas other parts of the crustal section, particularly the Strona-Ceneri Zone, underwent only minor to moderate Alpine rotation.

[1]Institut für Geowissenschaften, Giessen, Germany.
[2]Mineralogisches Institut, Bergakademie, Freiberg, Germany.
[3]Institut für Geophysik, Eidgenossische Technische Hochschule Hönggerberg, Zurich, Switzerland.
[4]Geologisches Institut, Bern.

Paper number 1999TC900034
0278-7407/99/1999TC900034$12.00

1. Introduction

Continental crust is generally considered to form at convergent plate margins, where sediments accrete above subduction zones and then are deformed, metamorphosed, and sometimes melted during continental collision [*Dewey and Bird*, 1970]. Yet coherent cross sections of exposed continental crust [*Fountain and Salisbury*, 1981] reveal that crust also forms in other tectonic environments, including divergent settings within and along plate boundaries [*Percival et al.*, 1992]. In particular, magmatic underplating associated with asthenospheric upwelling and lithospheric attenuation is thought to be an important mechanism in forming and transforming the continental crust [*Furlong and Fountain*, 1986; *Fountain*, 1989; *Asmerom et al.*, 1990]. Lithospheric attenuation has also been proposed as a mechanism for exhuming coherent tracts of deep continental crust and upper mantle [*Wernicke*, 1990]. This paper examines the relative roles of accretion, magmatism, and attenuation in the formation and exhumation of the southern Alpine crust. Do these processes affect all levels of the crust similarly or do some of these processes act selectively on certain levels of the crust? How are these processes related to the regional tectonic framework?

The Ivrea crustal section at the western end of the southern Alps (Figure 1) is an excellent place to seek answers to these questions. This crustal section reveals different levels of the continental crust, from granulite facies metasediments and mafic and ultramafic intrusive rocks of the Ivrea-Verbano Zone in the northwest, through amphibolite facies metasediments and granitoids of the Strona-Ceneri Zone and Val Colla Zone, to unmetamorphosed upper Carboniferous, Permian, and Mesozoic sediments in the south and southeast (Figure 1). The general coincidence of these changes in metamorphic grade with density and seismic velocity gradients across the crustal section has lead to its interpretation as an upended section of continental crust [*Mehnert*, 1975; *Fountain*, 1976] that formed part of the rifted, Apulian margin in early Mesozoic time [*Zingg et al.*, 1990]. However, a consensus on the Paleozoic evolution of the Ivrea crustal section has proved elusive so far.

Debate centers on the ages of pre-Mesozoic sedimentation and regional metamorphism and especially on the relationship of the latter to magmatism in the crustal section (reviews by *Zingg et al.* [1990], *Gebauer* [1993], and*Schmid* [1993]). The metasediments are interpreted to have accreted in Proterozoic to early Paleozoic time [*Gebauer*, 1993] before experiencing regional metamorphism, variously dated as Ordovician [*Hunziker and Zingg*, 1980] or late Carboniferous [*Boriani et al.*, 1990; *Boriani and Villa*, 1997] in both the Ivrea-Verbano Zone and the Strona-Ceneri Zone. Other workers favor an

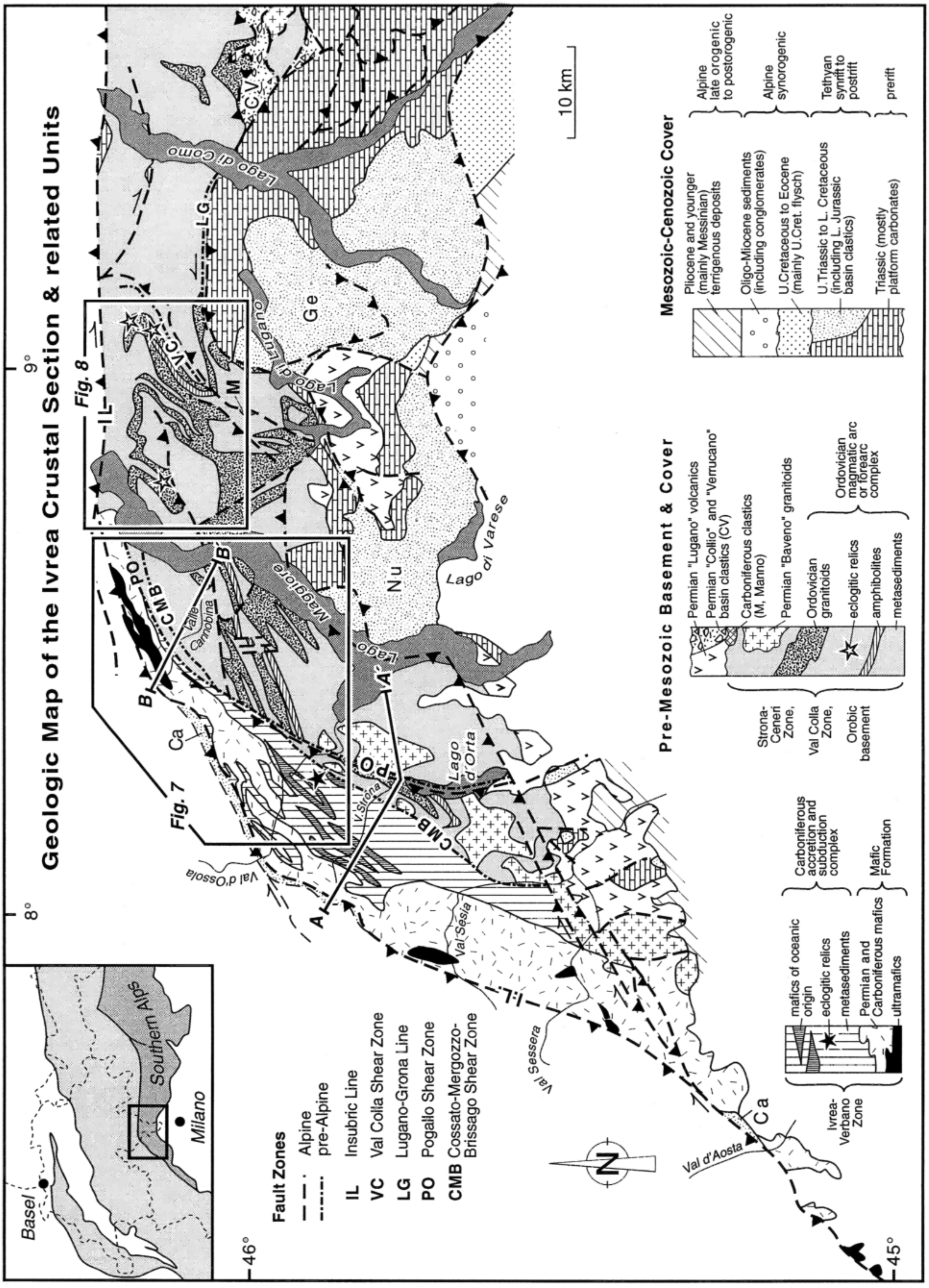
Geologic Map of the Ivrea Crustal Section & related Units
Fig. 7
Fig. 8
10 km
8°
9°
46°
45°
Basel
Southern Alps
Milano
Fault Zones
Alpine
pre-Alpine
IL Insubric Line
VC Val Colla Shear Zone
LG Lugano-Grona Line
PO Pogallo Shear Zone
CMB Cossato-Mergozzo-Brissago Shear Zone
Ivrea-Verbano Zone
mafics of oceanic origin
eclogitic relics
metasediments
Permian and Carboniferous mafics
ultramafics
Carboniferous accretion and subduction complex
Mafic Formation
Pre-Mesozoic Basement & Cover
Strona-Ceneri Zone, Val Colla Zone, Orobic basement
Permian "Lugano" volcanics
Permian "Collio" and "Verrucano" basin clastics (CV)
Carboniferous clastics (M, Manno)
Permian "Baveno" granitoids
Ordovician granitoids
eclogitic relics
amphibolites
metasediments
Ordovician magmatic arc or forearc complex
Mesozoic-Cenozoic Cover
Pliocene and younger (mainly Messinian) terrigenous deposits
Oligo-Miocene sediments (including conglomerates)
U.Cretaceous to Eocene (mainly U.Cret. flysch)
U.Triassic to L. Cretaceous (including L. Jurassic basin clastics)
Triassic (mostly platform carbonates)
Alpine late orogenic to postorogenic
Alpine synorogenic
Tethyan synrift to postrift
prerift
Lago di Como
Lago di Lugano
Lago Maggiore
Lago di Varese
Lago d'Orta
Val d'Ossola
Val Sesia
Val Sessera
Val d'Aosta
Valle Cannobina
V. Strona
Ca
Ge
Nu
CV
M
A
A'
B
B'
N

Figure 1.

Early Permian age for this metamorphism, attributing it to the intrusion of mafic melts in the Ivrea-Verbano Zone [*Pin*, 1986; *Fountain*, 1989; *Teufel and Schärer*, 1989]. Clearly, insight into deep crustal processes can only be gained if these discrepancies are reconciled.

The controversies above stem partly from the contrasting approaches and interpretations of specialists working in different parts of the crustal section. They also reflect the inherent difficulty of correlating tectonothermal events across a lithologically and structurally heterogeneous exposure of crust that occupied different depths during its evolution. A given tectonothermal event is recorded differently in different parts of the section. Conversely, different levels of the crust experienced similar deformational and metamorphic conditions at various times during exhumation. Added to this problem are the complex, Alpine emplacement tectonics, which in our case dismembered and selectively reoriented parts of the crustal section.

A prime goal of this paper is therefore to present a tectonic model of the Ivrea crustal section that is based on a first attempt to correlate structures, metamorphic mineral assemblages, and magmatic rocks across the entire section, from its base to its unmetamorphic cover. To this end, we synthesize new and existing structural, petrological, geochronological and paleomagnetic data. In section 2, we present the salient arguments and overprinting relationships used to relate pre-Alpine structures and metamorphism within the crustal section. Structural and paleomagnetic information in section 3 constrain differential rotations of parts of the section during Alpine emplacement tectonics and allow us to reconstruct the original orientation of pre-Alpine structures. The tectonic model of the Ivrea crustal section presented in section 4 serves as a vehicle for a discussion of deep-seated processes involved in the formation and exhumation of the southern Alpine continental crust. We conclude in section 5 by showing how consideration of these processes might inspire more realistic geophysical models of the continental crust.

2. Correlation of Pre-Alpine Events in Different Crustal Levels

Figure 2 summarizes the available age constraints on tectonometamorphic phases in the Ivrea-Verbano Zone, the Strona-Ceneri Zone, and adjacent units. The pre-Alpine phases are numbered sequentially for each unit. To help distinguish tectonometamorphic phases with identical numbers in different units, all phases are also named after their type localities within the two outlined areas in Figure 1. The criteria for determining the kinematics and age of the phases within these areas are discussed in sections 2.1-2.4. Note that identically numbered phases in different units are neither temporal nor kinematic equivalents. This reflects the contrasting Paleozoic histories of the Ivrea-Verbano and Strona-Ceneri Zones, as well as the fact that different levels of the crust reacted differently to the same crustal-scale events.

2.1. Ordovician Events

2.1.1. Sedimentation, accretion, and high-pressure metamorphism. A first stage of crustal accretion is restricted to the Strona-Ceneri and Val Colla Zones. It is marked by at least one phase of deformation (D1, Cannobio Phase) and by the intercalation of micaschist, banded amphibolite, and fine-grained gneiss containing quartz-rich bands and calc-silicate nodules. Very locally, these rocks preserve sedimentary features (compositional banding, graded bedding, cross-bedding) [*Origoni Giobbi et al.*, 1982; *Zurbriggen et al.*, 1998] and contain altered mafic and ultramafic lenses, some of which bear relict eclogite facies assemblages (open stars in Figure 1) [*Bächlin*, 1937; *Spicher*, 1940; *Borghi*, 1988]. These high-pressure relics reequilibrated partially under amphibolite to greenschist facies conditions [*Zurbriggen et al.*, 1997]. The trace element characteristics of the garnet amphibolites indicate that they originally comprised tholeiitic, ocean floor basalt [*Buletti*, 1983]. The imbrication of such mid-ocean ridge basalt type (MORB-type), eclogitic amphibolites with former pelites, greywackes, and carbonates is diagnostic of an accretionary sedimentary wedge, possibly containing older passive margin lithologies, that incorporated both obducted and exhumed, metamorphosed fragments of oceanic crust [*Giobbi et al.*, 1995].

Figure 3a shows that the clockwise pressure-temperature (P-T) path of the eclogites ends with nearly isothermal decompression prior to the onset of D2, Ceneri Phase deformation and metamorphism. During D1 most metasediments underwent prograde amphibolite facies metamorphism at a minimum depth of 15 km [*Zurbriggen*, 1996]. The absolute age of accretion and subduction is unknown but must predate Ordovician granitoids in the Strona-Ceneri Zone, because the imbricated rocks described above occur as xenoliths within these granitoids (Figure 4a).

2.1.2. Magmatism and regional metamorphism. Large volumes of granitic melts in the Strona-Ceneri Zone (Figure 1) intruded the accretionary wedge sequence described in section 2.1.1 sometime within the time span of 430-510 Ma (Figure 2, discussion below), although most such granitoids range in age from 440 to 480 Ma. These granitoid bodies are inferred to have intruded during D2, because they have high ratios, because their contacts are parallel to the main S2 schistosity in the Strona-Ceneri Zone and because large, euhedral feldspar phenocrysts in some granitoid bodies define a magmatic shape-preferred orientation that is coplanar with S2 [*Zurbriggen et al.*, 1997].

Figure 1. Map of western part of southern Alps. Box in small inset map shows location of large map within the Alpine chain (shaded); dashed lines indicate national boundaries. Traces of transects A-A' and B-B' are shown in Figure 5. Framed areas are shown in detail in Figures 7 and 8. Abbreviations of basins are as follows: Ca, Canavese; Ge, Generoso; Nu, Nudo; CV, Collio-Verrucano. Map is modified from *Bigi et al.* [1983], *Handy and Zingg* [1991], *Hermann* [1937], and *Schumacher et al.* [1997].

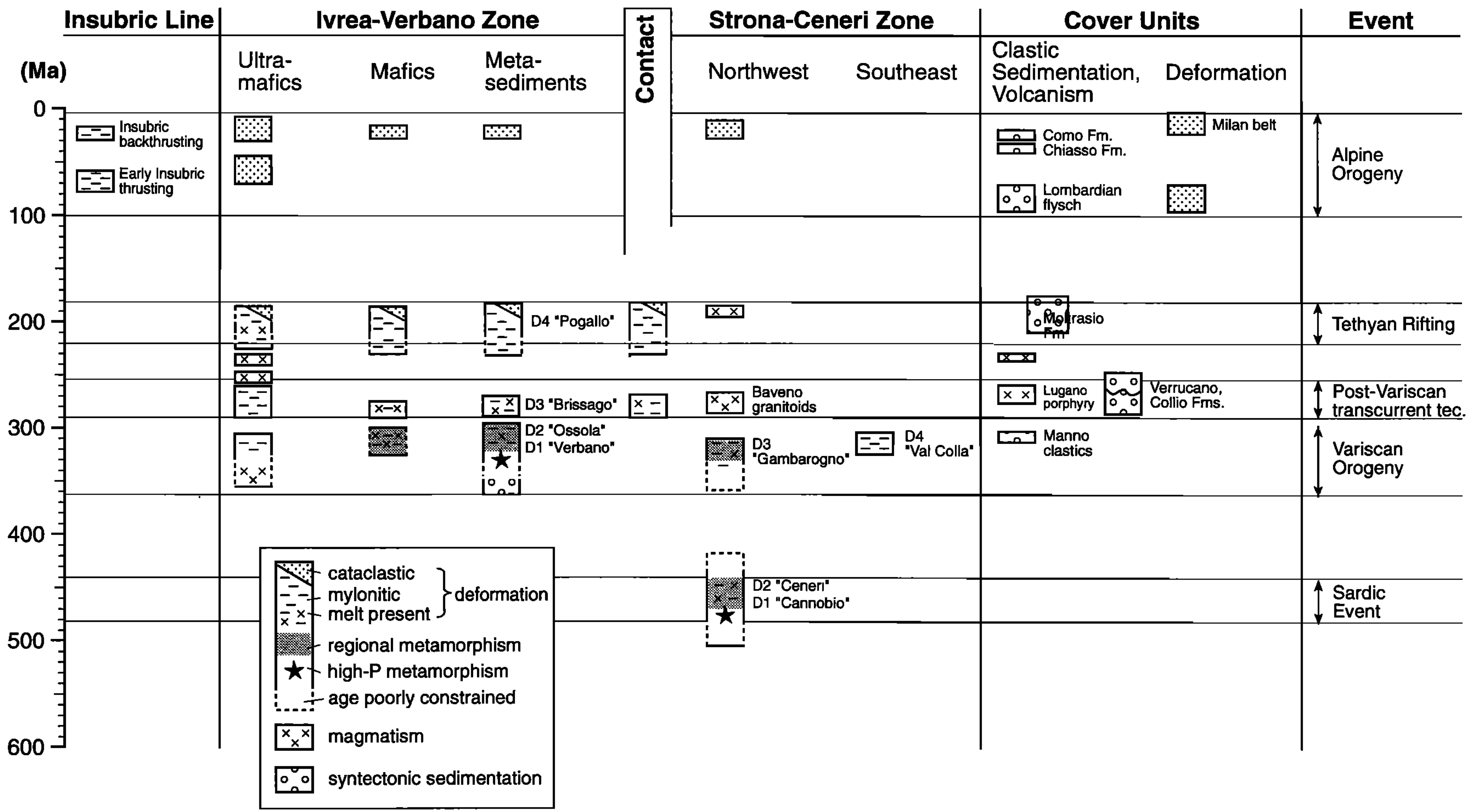

Figure 2. Ages of deformation, magmatism, and syntectonic sedimentation in basement units of the southern Alps, their sedimentary cover, and along the Insubric Line. Age criteria are discussed and cited in the text. Additional references used in Figure 2 but not cited in the text include the following: *Bernoulli et al.* [1993], *Brodie et al.* [1989], *Hofmann et al.* [1992], *Hunziker and Zingg* [1982], *Jäger et al.* [1967], *Lu et al.* [1994, 1997], *Miller and Jäger* [1968], *Schönborn* [1992], *Stähle et al.* [1986], *Wagner and Reimer* [1972], *Wright and Shervais* [1980], and *Zingg et al.* [1976]. Fm., Formation.

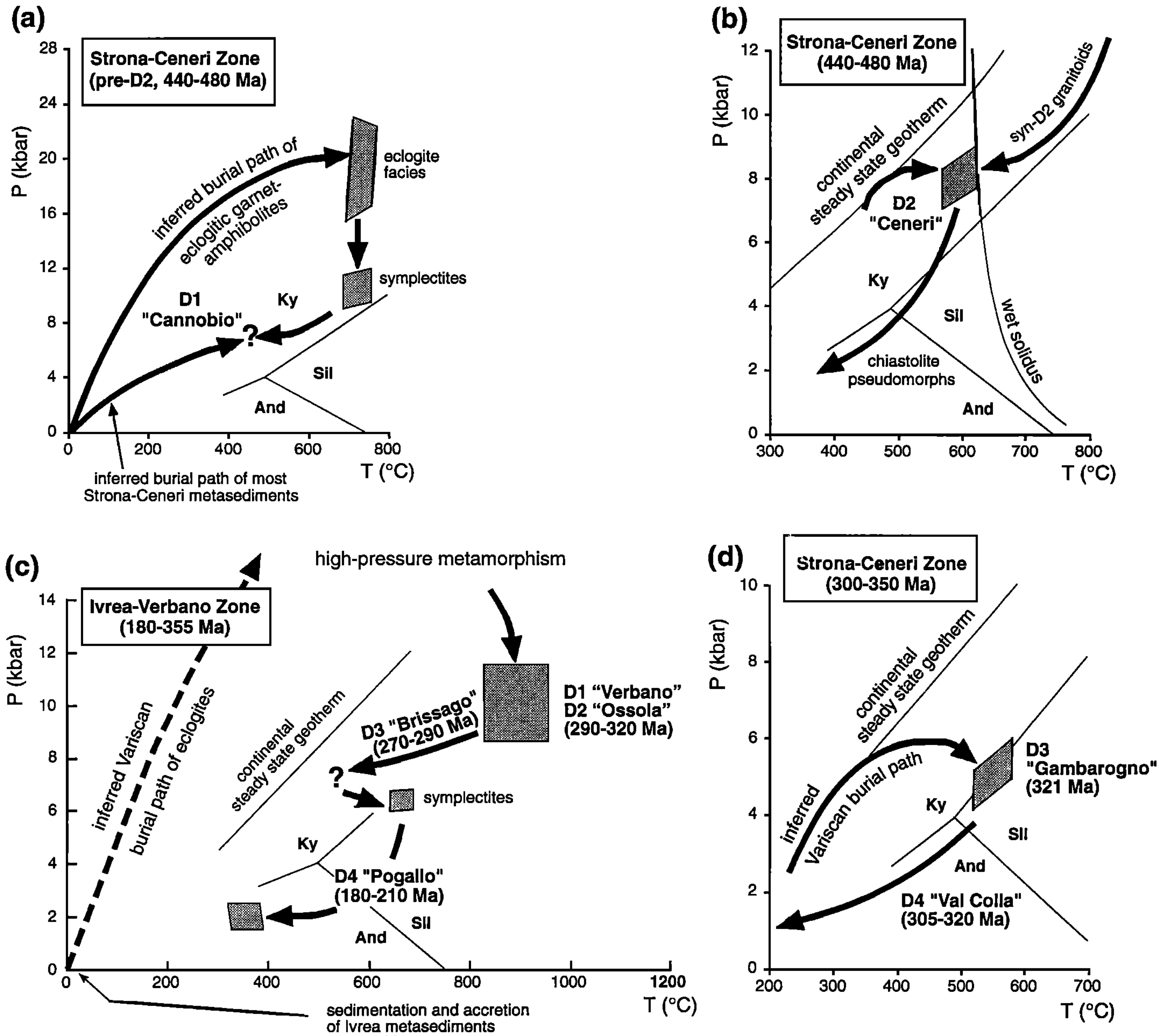

Figure 3. Pressure-temperature (P-T) paths for rocks in the Ivrea-Verbano and Strona-Ceneri Zones: (a) Ordovician paths of metasediments and eclogitic amphibolites in the Strona-Ceneri Zone simplified from *Borghi* [1988] and *Zurbriggen et al.* [1997]; (b) Ordovician paths of metasediments and granitoids in the Strona-Ceneri Zone from Zurbriggen et al.; (c) early Carboniferous to Jurassic paths of metasediments in the granulite facies part of the Ivrea-Verbano Zone synthesized from own data and that of *Franz et al.* [1994, 1996], *Handy* [1986], *Henk et al.* [1997], *Lu* [1994], *von Quadt et al.* [1992], and *Vogler* [1992]; (d) early Carboniferous to early Mesozoic paths of rocks in the Strona-Ceneri Zone from own unpublished thermobarometric data. Continental steady state geotherm is from *Peacock* [1989].

The intrusion of the granitoids was probably coeval with regional, amphibolite facies metamorphism in the Strona-Ceneri Zone, as evidenced by severe Pb loss in the U-Pb systems in zircon and monazite from both granitoids and metasediments of the Strona-Ceneri Zone at about 430-490 Ma [*Pidgeon et al.*, 1970; *Köppel and Grünenfelder*, 1971; *Köppel*, 1974; *Ragettli*, 1993]. The U-Pb and Pb-Pb systematics of staurolite oriented within the S2 foliation of metasediments in the Strona-Ceneri Zone suggest that this staurolite grew in Ordovician time and lost Pb during a later (D3, Variscan) thermal overprint (minimum 385±6 Ma $^{206}Pb/^{238}U$ staurolite age in the work of *Romer and Franz*

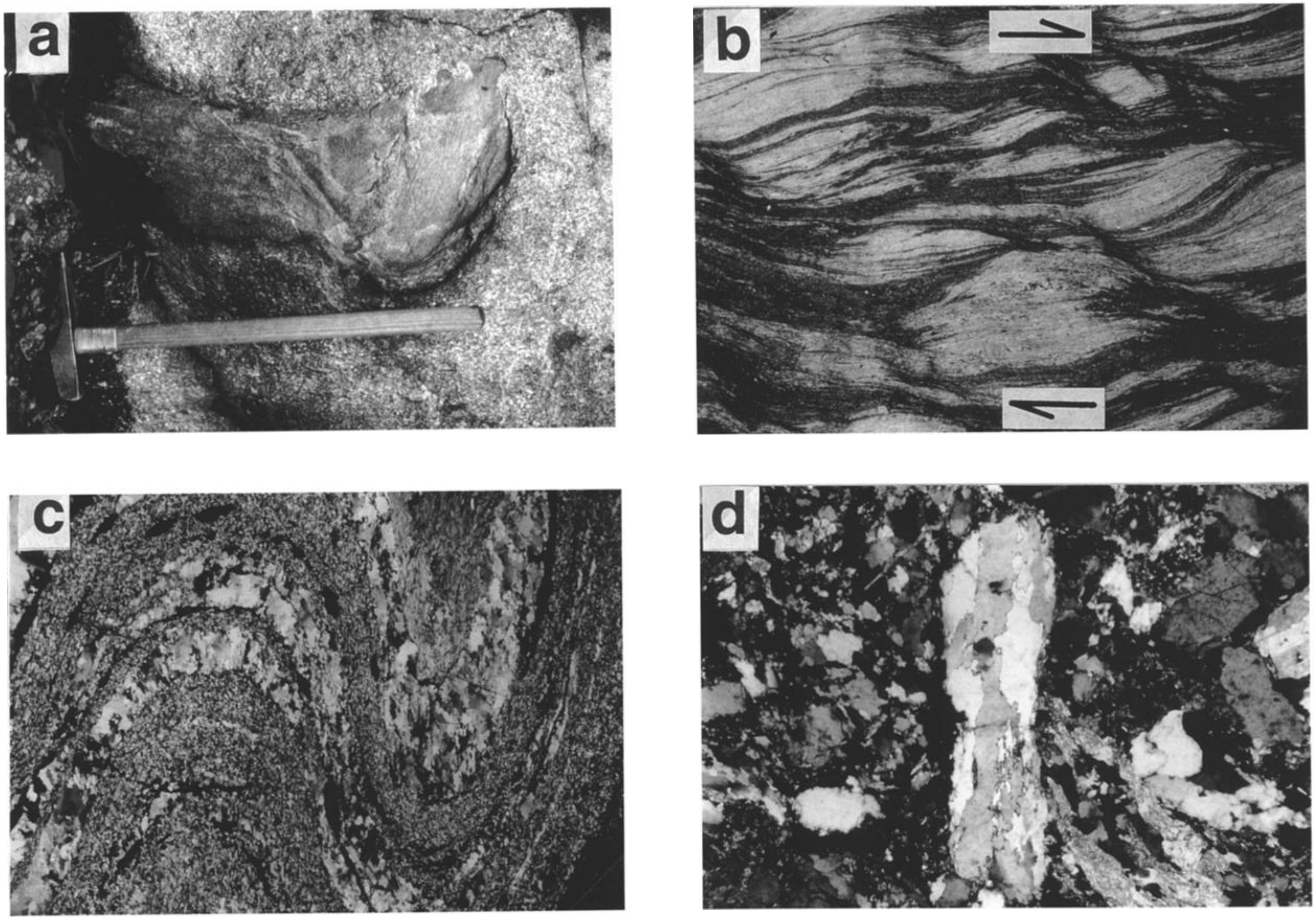

Figure 4. Key structural relationships in the Strona-Ceneri Zone: (a) xenolith of foliated (S1) metasediment within weakly foliated (S2) Ordovician granitoid; (b) shear bands in Val Colla mylonite with half arrows indicating top-to-SW shear sense as viewed in the XZ fabric plane, with crossed polarizers, frame length of 225 mm; (c) F3, Gamborogno Phase fold overprinted by D4 mylonitic deformation in the Val Colla Shear Zone; Note the shape-preferred orientation of dynamically recrystallized quartz grains, with crossed polarizers, frame length of 275 mm; (d) component of Val Colla mylonite with dynamically recrystallized quartz grains embedded in unmetamorphosed Westphalian conglomerate, with crossed polarizers, frame length of 6.8 mm.

[1998]). Indeed, thermobarometric studies on D2 and D3 mineral assemblages in the Strona-Ceneri Zone indicate that temperatures reached 500°-600°C during both tectonometamorphic phases (Figures 3b and 3d).

We note that our interpretation of the mineral ages in the Strona-Ceneri Zone in terms of separate Ordovician and Carboniferous (Variscan) metamorphic events with roughly equal thermal peaks contradicts *Boriani et al.*'s [1990] interpretation of a solely Variscan peak of regional metamorphism based on mid-Carboniferous K-Ar and Ar-Ar hornblende [*McDowell*, 1970; *Boriani and Villa*, 1997] and Rb-Sr white mica ages [*Boriani et al.*, 1983]. The structural setting of the hornblende and white mica dated in these studies is not clear (growth during D2 or D3?), however. The fact that U-Pb zircon and monazite systems in the granitoids of the Strona-Ceneri Zone were not reset in Carboniferous time may reflect the paucity of volatiles in the Variscan crust owing to Ordovician metamorphism and anatexis.

The Ordovician granitoids comprise both S-type, tonalitic to granodioritic gneisses and subordinate, mantle-derived, hornblende-bearing tonalitic gneisses. *Zurbriggen et al.* [1997] propose that the formation of the peraluminous, S-type granitoids involved the melting of substantial volumes of metapelite and/or metagreywacke at high-pressure, granulite facies conditions (10-14 kbar, 800°-900°C) in deeper levels of the crust originally underlying the Strona-Ceneri Zone in Ordovician time. The schists and fine-grained gneisses presently exposed in the Strona-Ceneri Zone may represent the shallower, compositional equivalents of these anatectic metasediments. The granitoid melt path in Figure 3b shows that these melts rose to the 8 kbar, D2 Ordovician isobar presently exposed at the surface in the Strona-Ceneri Zone. Pre-Carboniferous, D3-deformed augengneisses ("Gneiss Chiari") in the Val Colla Zone and Orobic basement are interpreted as volcanic or subvolcanic equivalents of the Ordovician granitoids [*Zurbriggen et al.*, 1997].

2.1.3. Deformation. Unfortunately, structural information regarding early Paleozoic tectonics in the Strona-Ceneri Zone is limited. Xenoliths in the Ordovician granitoids contain at least one preintrusive, amphibolite facies schistosity (S1, Figure 4a) parallel to the axial plane of isoclinal F1 folds. In most rocks the S2 schistosity of the Strona-Ceneri and Val Colla Zones completely transposes S1, obliterating the original S1 orientation and precluding kinematic reconstructions of D1 tectonics. Similarly, the kinematics of D2, Ceneri Phase deformation are masked by strong Variscan (D3, Gambarogno Phase) and Alpine structural overprints. The main S2 schistosity in the Strona-Ceneri Zone is characterized by mylonitic microstructures that were extensively annealed under D2 and/or D3, amphibolite facies conditions [*Handy and Zingg*, 1991, Figure 5c].

An Ordovician age for the D2, Ceneri Phase is inferred from the aforementioned parallelism of S2 with magmatic foliation in some granitoids. White micas aligned parallel to S2 have Si values that are consistent with the thermobarometrically derived 8 kbar pressure estimate for D2 metamorphism (Figure 3b). This pressure clearly exceeds the 4-5 kbar values obtained for D3, Gambarogno Phase assemblages in the same area (L. Franz et al., manuscript in preparation, 1999). If one assumes a crustal density of 2.8 g/cm^3, the 3-4 kbar difference in pressure estimates on D2 and D3 assemblages indicates that the Strona-Ceneri Zone underwent at least 9-12 km of exhumation before the baric peak of Carboniferous, D3 metamorphism. Most of this exhumation is inferred to have occurred already in Ordovician time, because pseudomorphs of D2 chiastolites that are transformed to kyanite and deformed during D3 (Figure 3b; see also *Zurbriggen et al.* [1997]) document post-D2 decompression prior to prograde D3 metamorphism.

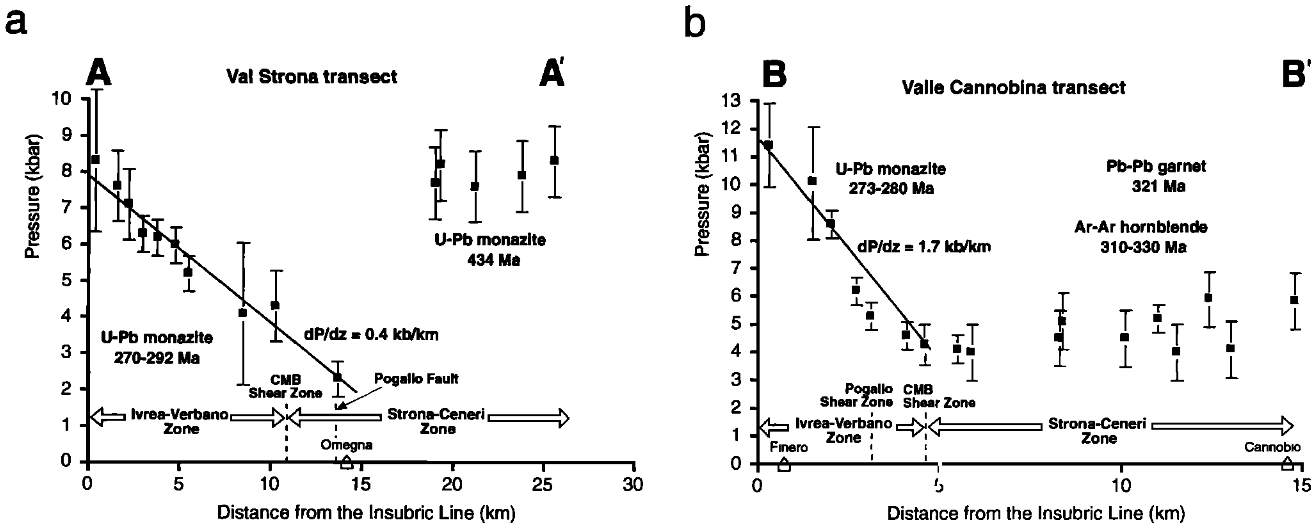

Figure 5. Metamorphic pressures across the Ivrea crustal section: (a) Val Strona transect (A-A') and (b) Valle Cannobina transect (B-B'). Trace of transects is shown in Figure 1. The U-Pb monazite ages and metamorphic pressures for Figure 5a are taken from *Henk et al.* [1997], and those for Figure 5b are taken from own data and *Franz et al.* [1994, 1996]. The Ar-Ar hornblende ages are from *Boriani and Villa* [1997], and the Pb-Pb garnet age is from *Zurbriggen et al.* [1998]. CMB, Cossato-Mergozzo-Brissago Shear Zone.

2.2. Carboniferous Events

2.2.1. Sedimentation and accretion. The deformed and metamorphosed remains of a second accretionary complex are preserved in the Ivrea-Verbano Zone (Figure 1). This complex is a highly deformed sequence of semipelitic gneiss and schist (so-called kinzigites) locally containing calc-silicate bands. The sequence alternates with amphibolite layers that show trace element characteristics of both normal MORB and enriched tholeiitic or alkalic MORB (type 1 mafic rocks of *Zingg et al.* [1990], *Sills and Tarney* [1984], and *Mazzucchelli and Siena* [1986]). There is no evidence for pre-existing continental basement underlying this complex. In fact, the accretionary complex probably formed above oceanic crust, represented by the amphibolite layers with MORB chemistry. The complex is overprinted by amphibolite to granulite facies, regional metamorphism and deformation in the Ivrea-Verbano Zone, and it is intruded by gabbroic and dioritic rocks of the Mafic Formation (Figure 1).

Up to now, accretion of the Ivrea metasediments is generally regarded to have occurred in early Paleozoic time [*Sills and Tarney*, 1984; *Zingg et al.*, 1990; *Zingg*, 1990; *Schmid*, 1993] on the basis of 480-700 Ma Sr model ages from Ivrea metasediments that are interpreted as sedimentation ages [*Hunziker and Zingg*, 1980]. However, we believe that sedimentation and accretion of the Ivrea metasediments is much younger for the following reasons:

1. The Ivrea-Verbano and Strona-Ceneri Zones comprise different lithologies with contrasting metamorphic histories. In particular, metasediments in the Ivrea-Verbano Zone differ both mineralogically and compositionally from those in the Strona-Ceneri Zone, even at comparable metamorphic grade. Unlike the Strona-Ceneri Zone, the Ivrea-Verbano Zone yields no mineral ages older than Carboniferous [*Zingg*, 1990]. This suggests that the two basement units underwent different Paleozoic evolutions,

2. The Ordovician Sr model ages are based on the extrapolation of a 478 ± 20 Ma, Rb-Sr whole rock isochron that may not be geologically relevant, given the differences cited above. *Hunziker and Zingg* [1980] obtained this isochron from a mixture of Ivrea metasediments, Strona-Ceneri metasediments, and Ordovician granitoids of the Strona-Ceneri Zone. They interpreted this mixed source isochron as the common age of regional metamorphism in the two zones. The Sr model ages of Hunziker and Zingg therefore overestimate the age of sedimentation.

In fact, there is compelling evidence that sedimentation and accretion of the Ivrea metasediments occurred in Early Carboniferous time: *Vavra et al.* [1996] found that the oldest cores of zircons in Ivrea metasediments yield a concordant, 355 ± 6 Ma U-Pb sensitive high-resolution ion microprobe (SHRIMP) age and have a prismatic morphology that is diagnostic of calk-alkaline magmatism. The occurrence of these zircons in both anatectic and metapelitic layers of the Ivrea schists reflects the admixture of the zircons in a sedimentary environment [*Vavra et al.*, 1996], indicating that the protolith was deposited in a volcanic setting in early Carboniferous time. Both metasediments and amphibolite layers of MORB affinity experienced 290-320 Ma regional metamorphism in the Ivrea-Verbano Zone (see dating of regional metamorphism in section 2.2.3). Thus accretion of the Ivrea metasediments at an active margin must have occurred sometime between 320 and 355 Ma.

2.2.2. High-pressure metamorphism. High-pressure metamorphism documenting the subduction of crustal and upper mantle rocks is manifest locally by eclogitic amphibolites [*Boriani and Peyronel Pagliani*, 1968] and kelyphitic peridotites [*Lensch and Rost*, 1972] in the Ivrea-Verbano Zone. These retrogressed high-pressure rocks occur along the southeastern border of the Ivrea-Verbano Zone (solid star in Figure 1), where they are imbricated with metasediments and amphibolites of MORB affinity. Other relics of pressure-dominated metamorphism, also arrayed along the southeastern margin of the Ivrea-Verbano Zone, include kyanites that are overgrown by sillimanite in metasediments [*Bertolani*, 1959; *Capedri*, 1971; *Boriani and Sacchi*, 1973; *Handy*, 1986]. None of these high-pressure assemblages has been dated yet. However, the high-temperature overgrowth textures of these assemblages indicate that pressure-dominated metamorphism preceded temperature-dominated, amphibolite to granulite facies, regional metamorphism (Figure 2 and section 2.2.3). The distribution of the high-pressure relics at and near the tectonic contact between the Ivrea-Verbano and Strona-Ceneri Zones suggests that this contact was originally a Variscan suture, as discussed in section 2.2.3. Suturing must have occurred sometime after the accretion of the Ivrea metasediments but before the onset of regional metamorphism in the Ivrea-Verbano Zone.

2.2.3. Regional metamorphism and magmatism in the Ivrea-Verbano Zone. Regional metamorphism in the Ivrea-Verbano Zone serves as an important time marker for magmatism and deformation. This Barrovian-type metamorphism increases from amphibolite facies along the tectonic contact with the Strona-Ceneri Zone to granulite facies along the Insubric Line (Figure 1). Thermobarometers record an increase of peak pressure with regional metamorphism from southeast to northwest across the Ivrea-Verbano Zone, as shown in Figures 5a and 5b, respectively, for the Val Strona and Valle Cannobina transects (lines A-A' and B-B' in Figure 1). Crustal thickness at the time of regional metamorphism was at least 30-40 km, as estimated from the peak pressures (8.5-11.5 kbar) recorded by granulite facies assemblages (Figures 3c and 6) [*Zingg*, 1983; *Henk et al.*, 1997] and an assumed, average crustal density of 2.8 g/cm^3.

Several isotopic systems have been used in attempts to determine the age of this regional metamorphism [*Zingg et al.*, 1990], but the U-Pb monazite system has proved to be the most reliable so far, because the ages it yields can be readily interpreted in a petrogenetic context. Monazites aligned parallel to the main, S1 schistosity in amphibolite facies metasediments and mafics in the southeastern part of the Ivrea-Verbano Zone yield 290-310 Ma U-Pb ages [*Köppel and Grünenfelder*, 1978/1979; *Henk et al.*, 1997]. This is corroborated by 296 ± 12 Ma U-Pb SHRIMP ages on zircon overgrowths from anatectic leucosomes in Ivrea metapelites [*Vavra et al.*, 1996]. We interpret the monazite ages to date the regional metamorphism, because the peak temperatures attained in the amphibolite facies rocks (550°-600°C [*Zingg*, 1983, and references therein]) did not exceed the estimated 600° ± 50°C closure temperature of the U-Pb system in deformed monazite [*Smith and Barreiro*, 1990]. Peak conditions in the granulite facies part of the Ivrea-Verbano

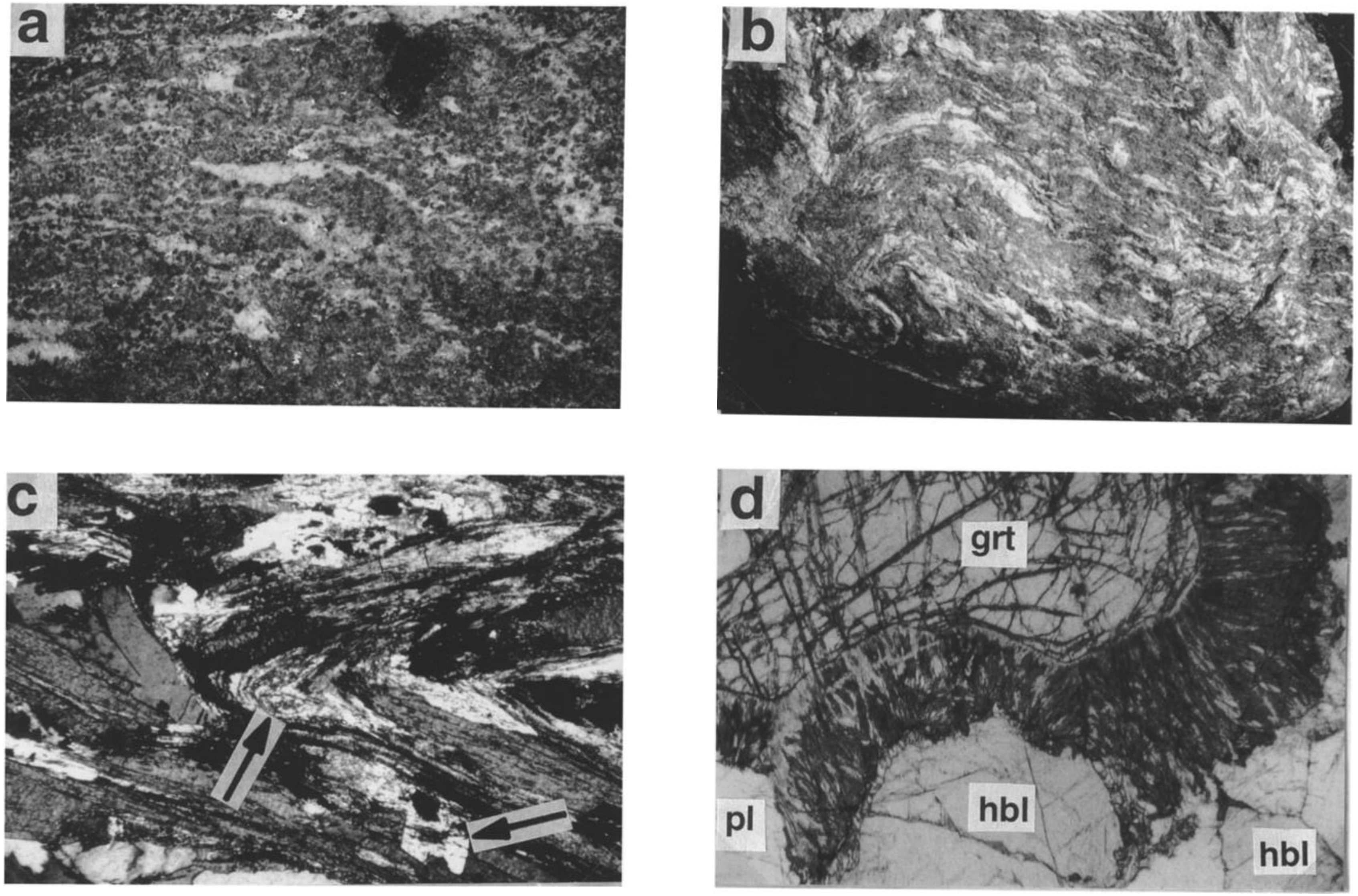

Figure 6. Key structural and metamorphic relationships in the Ivrea-Verbano Zone: (a) euhedral garnets that overgrow S1 and leucosomes in metasediment, with frame length of approximately 20 cm; (b) F2 folds that deform S1 containing leucosomes, with frame length of approximately 50 cm; (c) cross white mica (arrows) that overgrows fibrolite deformed by F2 fold in metasediment, with crossed polarizers, frame length of 2 mm; (d) garnet and hornblende rimmed by symplectites of orthopyroxene, spinel (hercynite) and anorthitic plagioclase in a hornblende-gabbro that underwent prograde metamorphism during D4. Abbreviations are as follows: grt, garnet; hbl, hornblende; pl, anorthitic plagioclase. Frame length is 1 cm.

Zone were attained some 5-10 Myr earlier (i.e., 300-320 Ma) according to the thermal modeling of *Henk et al.* [1997]. The range of U-Pb monazite ages (270-290 Ma) along the two transects of the Ivrea-Verbano Zone in Figure 5 is interpreted either to reflect cooling after regional metamorphism [*Henk et al.*, 1997] or to reflect fluid circulation after the thermal peak of this metamorphism [*Vavra et al.*, 1996]. The youngest, circa 270 Ma ages from the granulite facies part of the Ivrea-Verbano Zone therefore postdate this thermal peak by approximately 20-40 Myr.

When assessing the role of magmatic underplating and its relationship to regional metamorphism, it is important to remember that the Mafic Formation is a composite of three, differently aged suites of mantle-derived intrusive rock [*Zingg et al.*, 1990]. Most of the Mafic Formation comprises large gabbroic bodies and banded mafic rocks interlayered with ultramafics (type 2 and type 3 mafic rocks of *Zingg et al.* [1990], respectively). These rocks intruded the Ivrea metasediments but equilibrated at the conditions of regional metamorphism [*Zingg*, 1980]. The intrusive age of these mafic rocks is poorly constrained in the absence of isotopic age work on their relict magmatic minerals. If the intrusion of these mafic rocks triggered regional metamorphism as is indicated by the field relations cited above, then their crystallization must have only just preceded the attainment of peak temperatures in granulite facies metasediments at the base of the Ivrea-Verbano Zone some 300-320 Myr ago.

The youngest suite of mafic rocks comprises gabbro-diorites (type 4 mafic rocks of *Zingg et al.* [1990]) within the southeastern part of the Mafic Formation (Val Sesia in Figure 1). These rocks contain fresh magmatic structures [*Rivalenti et al.*, 1975] and magmatic zircons that yield concordant 285 Ma U-Pb ages [*Pin*, 1986]. Granodioritic to tonalitic intrusive breccias forming the rim of these mafic intrusions yield 274 Ma, Rb-Sr whole rock ages [*Bürgi and Klötzli*, 1990]. The intrusive contacts of these rocks are discordant to and truncate the regional metamorphic isograds [*Zingg*, 1980, 1983]. The relationships discussed above indicate at least two mafic, magmatic underplating events in the Ivrea-Verbano Zone: a massive, late Carboniferous pulse that triggered regional metamorphism and a smaller, Early Permian pulse that postdated, and was therefore unrelated to, the peak of regional metamorphism.

2.2.4. Deformation in the Ivrea-Verbano Zone. The structural and radiometric age constraints on metamorphism and magmatism help bracket the age of deformation in the Ivrea-Verbano Zone. At least two generations of nearly coaxial, isoclinal to tight folds (D1, Verbano Phase, and D2, Ossola Phase) developed in the Ivrea metasediments and pre-Permian mafic rocks of the Mafic Formation. The S1 axial planar foliation in the paragneisses is overgrown by high-grade minerals (e.g., euhedral garnet in Figure 6a), indicating that it developed prior to or during regional metamorphism. F2 folds clearly deform and therefore postdate leucosomes related to initial anatexis and regional metamorphism in the Ivrea-Verbano Zone (Figure 6b). However, the microstructures of rocks with F2 folds were annealed under regional metamorphic conditions [*Handy and Zingg*, 1991, Figure 5b] and overgrown by cross white micas (Figure 6c).

Taken together, these observations indicate that both D1 and D2 deformations in the Ivrea-Verbano Zone are broadly coeval with late Carboniferous regional metamorphism. Unfortunately, the kinematics of these deformations are ambiguous, because F1 and F2 folds were highly susceptible to reorientation during D3 and D4 deformations in the Ivrea-Verbano Zone.

2.2.5. Deformation and regional metamorphism in the Strona-Ceneri Zone. Across the crustal section in the Strona-Ceneri Zone the main Carboniferous structures include kilometer-scale folds (D3, Gambarogno Phase) and the Val Colla Shear Zone (D4, Val Colla Phase, Figure 2). The F3 folds have moderate to steep axes and axial planes and deform the main S2 schistosity in the Strona-Ceneri Zone (stereoplots labeled Gi in Figure 7 and Ga in Figure 8a). D3 folding was locally accompanied by the intrusion of tonalitic dikes derived from the anatexis of metasediments underlying the present erosional surface of the Strona-Ceneri Zone [*Zurbriggen et al.*, 1998]. By dating magmatic garnets in these dikes, *Zurbriggen et al.* [1998] determined that the F3 folds formed about 321 Myr ago under prograde, amphibolite facies conditions (Figure 3d). The peak temperatures of this metamorphism (500°-600°C) outlasted folding, as is inferred from the polygonization of micas and amphibole grains around F3 folds [*Zurbriggen*, 1996, Figure 4-10]. F3 folds rarely have an axial planar schistosity, except at the northwestern and southeastern limits of the Strona-Ceneri Zone where they are overprinted by mylonites of the Cossato-Mergozzo-Brissago (CMB) and Val Colla Shear Zones, respectively (Figure 1). The formation of the folds at or slightly before the thermal peak of D3 metamorphism together with the lack of vergence of these folds on the kilometer-scale suggests that they formed during subhorizontal shortening of a moderately to steeply dipping, S2 schistosity prior to exhumation during D4.

D4, Val Colla Phase mylonitic deformation affects the southeastern margin of the Strona-Ceneri Zone and the adjacent Val Colla Zone (Figure 1). There a 5 km thick zone of retrograde, amphibolite to greenschist facies mylonites, the Val Colla Shear Zone (labeled VC in Figures 1 and 8a), overprints the gradational lithological contact between these units. Kinematic indicators in these mylonites (Figure 4b) are consistent with top-to-the-south to -southwest displacement of the overlying Val Colla Zone with respect to the Strona-Ceneri Zone (Figure 8a). Extensional exhumation and cooling of the Strona-Ceneri Zone during Val Colla shearing is inferred from the successive closure of K-Ar hornblende and biotite systems in the footwall of the Val Colla Shear Zone (Figure 8b). Correlating the temperatures of mylonitization in the Val Colla Shear Zone (300°-500°C [*Janott*, 1996]) with the radiometrically derived temperature-time curve for this part of the Strona-Ceneri Zone in Figure 8b constrains Val Colla Phase shearing to have occurred sometime between 330 and 305 Ma.

A maximum age of 320 Ma for D4 extension is consistent with field relations which indicate that the Val Colla mylonites overprint F3, Gambarogno Phase folds in the Strona-Ceneri Zone. In the footwall of the Val Colla Shear Zone the axial planes and axes of F3 folds are reoriented to be coplanar and parallel to the foliation and stretching lineations

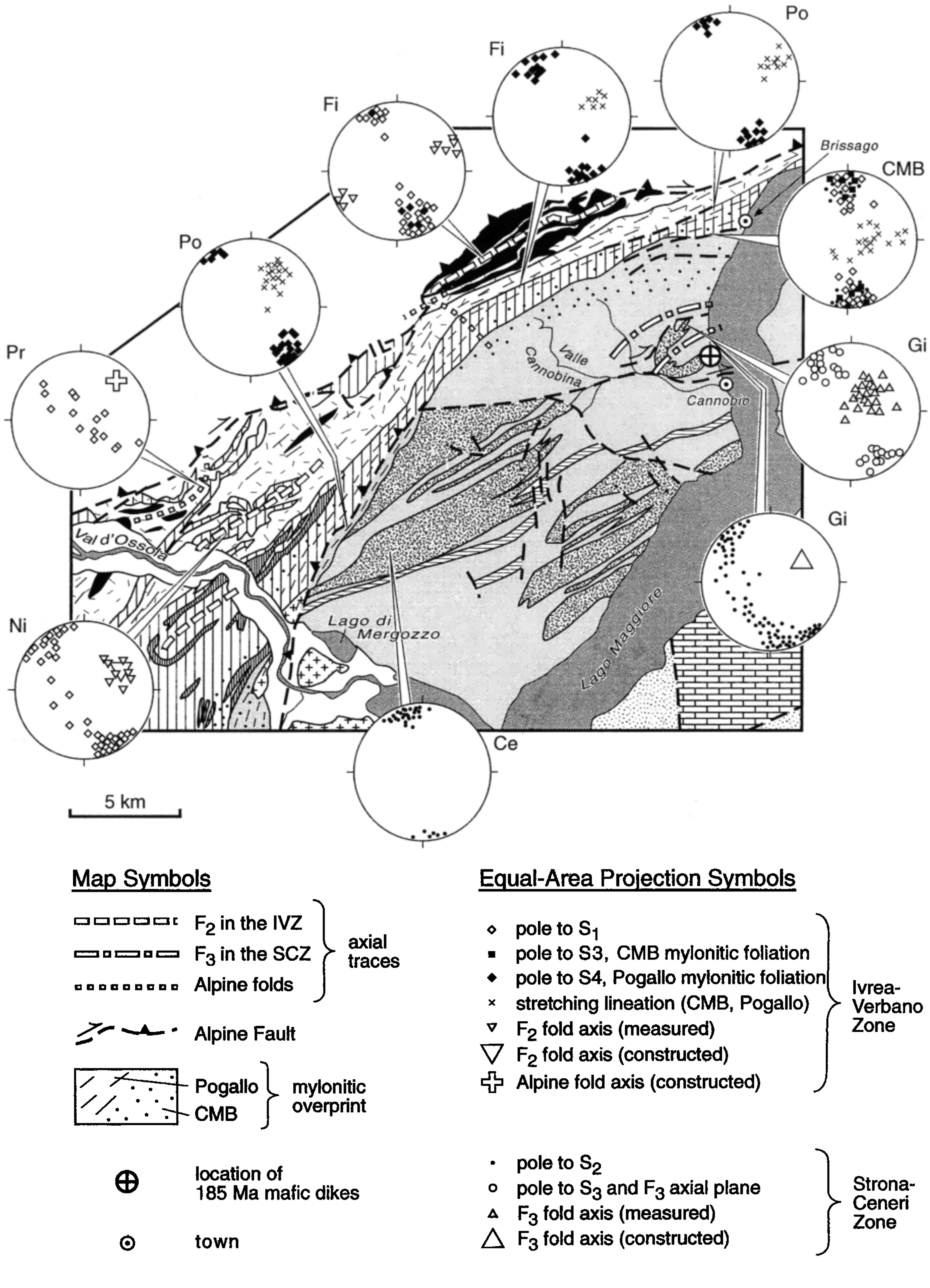

Figure 7. Structural map with contact of Ivrea-Verbano and Strona-Ceneri Zones. Lithological symbols and map location are given in Figure 1. Stereoplot abbreviations are as follows: Pr, Proman fold; Po, Pogallo Shear Zone; Fi, Finero complex; CMB, Cossato-Mergozzo-Brissago Shear Zone; Gi, Giove fold; Ni, Nibbio fold. Stereoplots are lower hemisphere equal-area projections. Map is based on own mapping and structural data and modification of maps by *Boriani et al.* [1977], *Handy* [1986, 1987], *Schmid* [1967], *Steck and Tièche* [1976], *Vogler* [1992], *Walter* [1950], and *Zurbriggen* [1996]. Structural data for Proman fold are taken from *Schmid et al.* [1987] and *Zingg et al.* [1990]. IVZ, Ivrea-Verbano Zone; SCZ, Strona-Ceneri Zone.

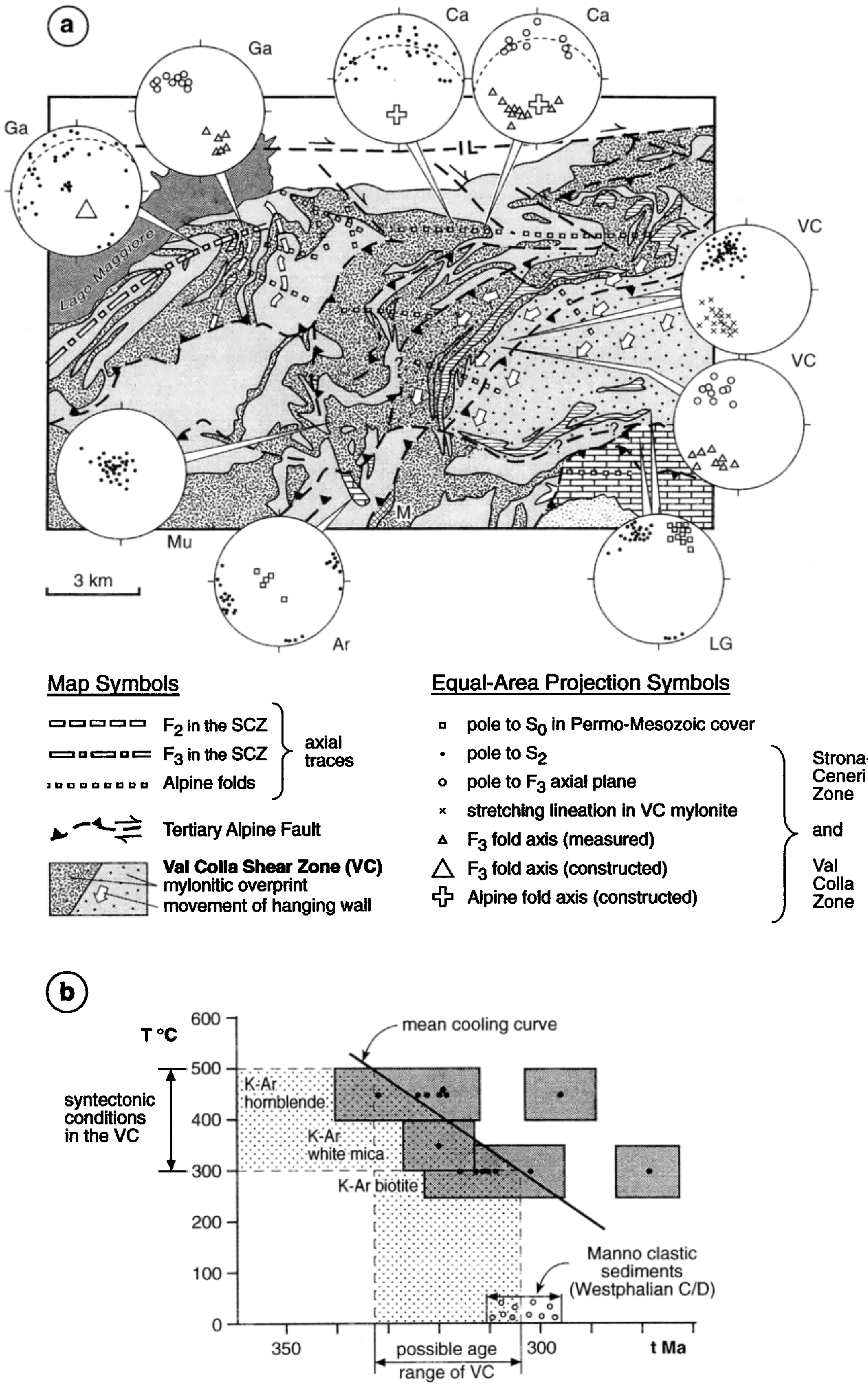
a
Ga
Ga
Ca
Ca
VC
VC
Lago Maggiore
IL
M
Mu
Ar
LG
3 km
Map Symbols
F2 in the SCZ
F3 in the SCZ
Alpine folds
axial traces
Tertiary Alpine Fault
Val Colla Shear Zone (VC)
mylonitic overprint
movement of hanging wall
Equal-Area Projection Symbols
pole to S0 in Permo-Mesozoic cover
pole to S2
pole to F3 axial plane
stretching lineation in VC mylonite
F3 fold axis (measured)
F3 fold axis (constructed)
Alpine fold axis (constructed)
Strona-Ceneri Zone
and
Val Colla Zone
b
T °C
600
500
400
300
200
100
0
syntectonic conditions in the VC
mean cooling curve
K-Ar hornblende
K-Ar white mica
K-Ar biotite
Manno clastic sediments (Westphalian C/D)
350
300
t Ma
possible age range of VC

Figure 8.

in the Val Colla mylonites, respectively (stereoplots marked VC in Figure 8a). The annealed, amphibolite facies microstructure typical of F3 folds in other parts of the Strona-Ceneri Zone is overprinted by mylonitic fabrics of the Val Colla Shear Zone (Figure 4c).

Conglomerates that unconformably overlie the Strona-Ceneri Zone at Manno (location marked M in Figures 1 and 8a) contain unmetamorphosed Westphalian plant remains [*Jongmans*, 1960] and components of Val Colla mylonite (Figure 4d). The Westphalian conglomerates also contain clasts of gneiss from the Val Colla and Strona-Ceneri Zones, indicating that these basement units were exposed to erosion by late Carboniferous time [*Graeter*, 1951; *Zingg*, 1983]. Independently of the radiometric data, these sediments place a minimum age limit of 305 Ma for the activity and exhumation of the Val Colla Shear Zone.

2.3. Early Permian Events

2.3.1. Deformation and magmatism in the Ivrea-Verbano Zone. Early Permian magmatism and deformation affected all levels of the Ivrea crustal section but in different ways. In the Ivrea-Verbano Zone the aforementioned intrusion of 285 Ma, gabbroic to gabbro-dioritic melts in parts of the Mafic Formation was contemporaneous with and transitional to localized mylonitic shearing and renewed anatexis of the contacting metasediments [*Rutter et al.*, 1993; *Quick et al.*, 1994]. Higher up in the crustal section along the contact between the Ivrea-Verbano and Strona-Ceneri Zones, mutually crosscutting relationships between anatectic, upper amphibolite facies mylonites of the CMB Shear Zone and 270-280 Ma, mafic and aplitic veins [*Pinarelli et al.*, 1988; *Mulch et al.*, 1999] document coeval mylonitization and Early Permian magmatism [*Handy and Streit*, 1999]. The vein geometry and mylonitic fabrics in the subvertically dipping CMB mylonites indicate a strong component of flattening normal to schistosity combined with a component of sinistral noncoaxial shear parallel to predominantly east-northeast plunging mineral stretching lineations (stereoplot marked CMB in Figure 7). Large-scale, D2, Ossola Phase folds in the Ivrea-Verbano Zone are acylindrical with steep axial planes and have axes aligned subparallel to this stretching lineation (stereoplot labeled Ni in Figure 7). This indicates that F2 folds may have been reoriented during D3 shearing, such that their axial planes became subparallel to the CMB mylonitic foliation [*Handy and Zingg*, 1991].

The pressure-temperature-time (P-T-t) path for the Ivrea-Verbano Zone in Figure 3c shows that the D3, Brissago Phase is associated with decompression and cooling from peak metamorphic conditions. The D3 decompression of 1.3 kbar in Figure 3c is obtained from element zonation patterns in garnets in local equilibrium with plagioclase and hornblende in garnet-bearing amphibolites of the Val Strona transect [*Henk et al.*, 1997]. This is a minimum estimate of D3 decompression, because a single thermobarometer can record only part of the exhumation. A much greater decompression of approximately 7 kbar to pressures of at most 3 kbar (not shown in Figure 3c) can be inferred from the occurrence of cordierite and andalusite in Ivrea metapelites that experienced contact metamorphism adjacent to Early Permian, gabbro-dioritic intrusions at the rim of the Mafic Formation in Val Sesia [*Zingg*, 1980].

Petrologic evidence for decompression during D3 is consistent with several independent lines of evidence for crustal attenuation in Early Permian time: (1) Discrepant temperature-time cooling curves for the adjacent parts of the Ivrea-Verbano and Strona-Ceneri Zones in the Val d'Ossola transect (Figure 1) indicate that at least 3 km of crust were excised from the crustal section along the CMB Shear Zone at about 280 Ma [*Handy*, 1987]. (2) The metamorphic pressure gradients across the Ivrea-Verbano Zone in Figure 5 are anomously high (0.4 kbar/km in Val Strona and 1.7 kbar/km in Valle Cannobina), suggesting heterogeneous stretching subparallel to the length of the Ivrea-Verbano Zone during and/or after Permian cooling through the 600° ± 50°C closure temperature for the U-Pb monazite system. On the basis of the high pressure gradient in the Val Strona transect, *Henk et al.* [1997] estimated that approximately 4 km of crust were thinned from the Ivrea-Verbano Zone in Permian time, although an early Mesozoic age for this thinning cannot be ruled out. We attribute the even higher metamorphic pressure gradient in the Valle Cannobina transect to later crustal extension during D4, Pogallo Phase deformation, as discussed in section 2.4. The lack of a break in metamorphic pressure gradients across the CMB Shear Zone (Figure 5) indicates that it accommodated little, if any, vertical throw after the thermobarometers equilibrated during regional metamorphism. Therefore the CMB Shear Zone was subhorizontal while active in Early Permian time. Today, Alpine faults truncate the southeastern end of the CMB Shear Zone (Figure 1), preventing us from tracing it into shallower levels of the Early Permian crust exposed at the basement-cover contact.

2.3.2. Structures in the Strona-Ceneri Zone and upper crustal units. Except for the CMB Shear Zone, all post-Carboniferous structures in the Strona-Ceneri Zone are brittle and therefore difficult to distinguish from later structures. The Strona-Ceneri Zone contains Early Permian granitoid bodies that cut the S2 schistosity (Baveno granitoids in Figure 1), and it is unconformably overlain by rhyolitic to andesitic, Permian Lugano volcanics [*Graeter*, 1951; *Hunziker*, 1974; *Stille and Buletti*, 1987]. The occurrence of miarolitic cavities

Figure 8. Structural relations and isotopic ages in the Strona-Ceneri Zone, Val Colla Zone, and cover units. (a) Structural map based on own data and modification of maps by *Reinhard* [1964], *Janott* [1996], *Bertotti* [1991], and *Schumacher et al.* [1997]. Lithological symbols and map location are given in Figure 1. Structural abbreviations are as follows: Ga, Gambarogno fold; Ca, Camoghé fold; VC, Val Colla Shear Zone; Ar, Arosio basement-cover contact; Mu, Mugena valley; LG, Lugano-Grona Line. Stereoplots are lower hemisphere equal-area projections. (b) Cooling curve for the Strona-Ceneri Zone in the footwall of the Val Colla Shear Zone; K-Ar isotopic ages are from *McDowell* [1970]. C/D, subseries of the Westphalian.

in these granites [*Köppel*, 1974] indicates that these intrusive bodies and the surrounding gneisses in the Strona-Ceneri Zone already occupied relatively shallow levels (approximately 10 km) when the granitoids were emplaced.

2.4. Early Mesozoic Events

Early Mesozoic deformation (Figure 2) is strongly partitioned within the crustal section and occurred under widely varied conditions in different crustal levels. In the originally deepest parts of the Ivrea-Verbano Zone, high-grade mylonites in anastomozing shear zones (D4, Pogallo Phase) overprint the regional metamorphic fabric in granulite facies paragneisses and mafic rocks [*Brodie and Rutter*, 1987; *Zingg et al.*, 1990]. This structural and metamorphic overprint is strongest in the narrow, northeastern segment of the Ivrea-Verbano Zone shown in Figure 7.

The mineral assemblages in some of these high-grade mylonites are diagnostic of a renewed increase in metamorphic grade from amphibolite to granulite facies conditions at the onset of D4 shearing. In Figure 6d, for example, the prograde reaction of garnet to symplectitic orthopyroxene, hercynite, and plagioclase in a garnet-hornblende gabbro indicates temperatures of at least 650°-700°C [*Spear*, 1995]. The contacting garnet and orthopyroxene in this rock are not in chemical equilibrium, indicating that subsequent cooling under static (i.e., stress-free) conditions must have been rapid. In general, however, high-grade mylonitization continued under retrograde, amphibolite facies conditions, as was already documented in several studies [*Handy and Zingg*, 1991, and references therein]. Retrograde mylonitization is concentrated in quartz-bearing rocks, especially along the part of the rim of the Ivrea-Verbano Zone in contact with the Strona-Ceneri Zone (dashed lines in Figure 7). This 1-3 km wide zone of retrograde mylonites defines the Pogallo Shear Zone (marked PO in Figure 1). The replacement of syn-tectonic sillimante by postkinematic andalusite in amphibolite facies, Pogallo mylonites near Brissago (Figure 7) documents D4 decompression and cooling. Retrograde, amphibolite to greenschist facies mylonites and cataclasites of the Pogallo Shear Zone overprint the CMB mylonites and associated Early Permian intrusive rocks [*Handy*, 1987]. Crossing the Ivrea-Verbano Zone across its strike from northwest to southeast, only 5 km separates the granulite facies mylonites from the cataclasites along the southern margin of the Pogallo Shear Zone. This small separation indicates an abnormally high D4, metamorphic field gradient of approximately 80°C/km. Southwest of the Val d'Ossola, the Pogallo Shear Zone is poorly exposed but appears to continue as a brittle fault within the Strona-Ceneri Zone (Figure 1).

The microstructures above indicate a clockwise P-T exhumation path for the Ivrea-Verbano 'Zone during D4, Pogallo Phase deformation (Figure 3c). The Pogallo Shear Zone was active sometime between 180 and 230 Ma, as is constrained by correlating the temperature range of retrograde, syntectonic metamorphism in the Pogallo mylonites with the temperature-time cooling curves constructed from the successive closures of the Rb-Sr and K-Ar white mica and biotite systems from the Ivrea-Verbano Zone [*Handy*, 1987]. High-grade D4 mylonites have not been satisfactorily dated but were probably coeval with Pogallo mylonitization on the basis of the lack of strong annealing in D4 mylonites and the aforementioned, high D4, metamorphic field gradient across the Ivrea-Verbano Zone.

Kinematic indicators in the high-grade mylonites are ambiguous and indicate foliation-parallel stretching parallel to moderately northeast plunging mineral and stretching lineations (stereoplots marked Fi in Figure 7) [*Brodie and Rutter*, 1987]. The Pogallo mylonites, however, yield a sinistral sense of shear parallel to a similarly northeast plunging stretching lineation (stereoplots marked Po in Figure 7) [*Handy and Zingg*, 1991]. The significance of this kinematic framework for early Mesozoic tectonics in the southern Alps becomes clear only when the Ivrea-Verbano Zone is back-rotated into its pre-Tertiary orientation, as is discussed in section 3. The Pogallo mylonitic foliation then accommodated east-west directed crustal extension.

The structural evidence for lateral crustal extension in early Mesozoic time is consistent with the idea that the D4 mylonites attenuated the lower crust while exhuming the Ivrea-Verbano Zone from beneath the Strona-Ceneri Zone along the Pogallo Shear Zone [*Handy and Zingg*, 1991]. D4 thinning is most pronounced in the northeastern part of the Ivrea-Verbano Zone, where it telescoped the crustal section and caused the anomalously high metamorphic pressure gradient in the Valle Cannobina transect (Figure 5b).

In the upper crust, Pogallo Phase deformation involved brittle faulting along north-south trending normal faults. Such faults are ubiquitous in the southern Alps [*Winterer and Bosellini*, 1981] and bound asymmetrical basins (marked Nu and Ge in Figure 1) containing unmetamorphosed, Early to Middle Jurassic rift sediments [*Bernoulli*, 1964; *Bertotti et al.*, 1993]. This is best seen in map view along the Lugano-Grona Line (LG in Figures 1 and 8a) where cataclasites and mylonites that accommodated east-west extension along the verticalized basement-cover contact [*Bertotti*, 1991] form a low-angle discordance with tilted, Upper Triassic carbonates and Lower Jurassic clastics of the Generoso basin.

Only limited calc-alkaline to alkaline magmatism and metasomatism accompanied D4 deformation. Most of this activity is restricted to the Ivrea-Verbano Zone for the time span 200-230 Myr [*Stähle et al.*, 1990; *von Quadt et al.*, 1992; *Vavra et al.*, 1996], although 185 Ma mafic dikes also intruded the Strona-Ceneri Zone (see *Zurbriggen* [1996] and section 3). Minor volumes of mid-Triassic intrusive [*Sanders et al.*, 1996] and extrusive [*Hellmann and Lippolt*, 1981] rock in other middle to upper crustal units of the southern Alps are interpreted as harbingers of Late Triassic to Early Jurassic extension.

3. Alpine Tectonics

Any attempt to reconstruct the original structure of the Ivrea crustal section must begin by subtracting the effects of Alpine folding and faulting. These effects vary strongly with location in the crustal section. Figure 9 summarizes various criteria that serve as guides to the original orientation of pre-Alpine structures. Only the newest or most reliable of these are described below.

3.1. Pre-Tertiary Orientation of the Ivrea-Verbano Zone

In the Ivrea-Verbano Zone several independent observations indicate that compositional banding and the

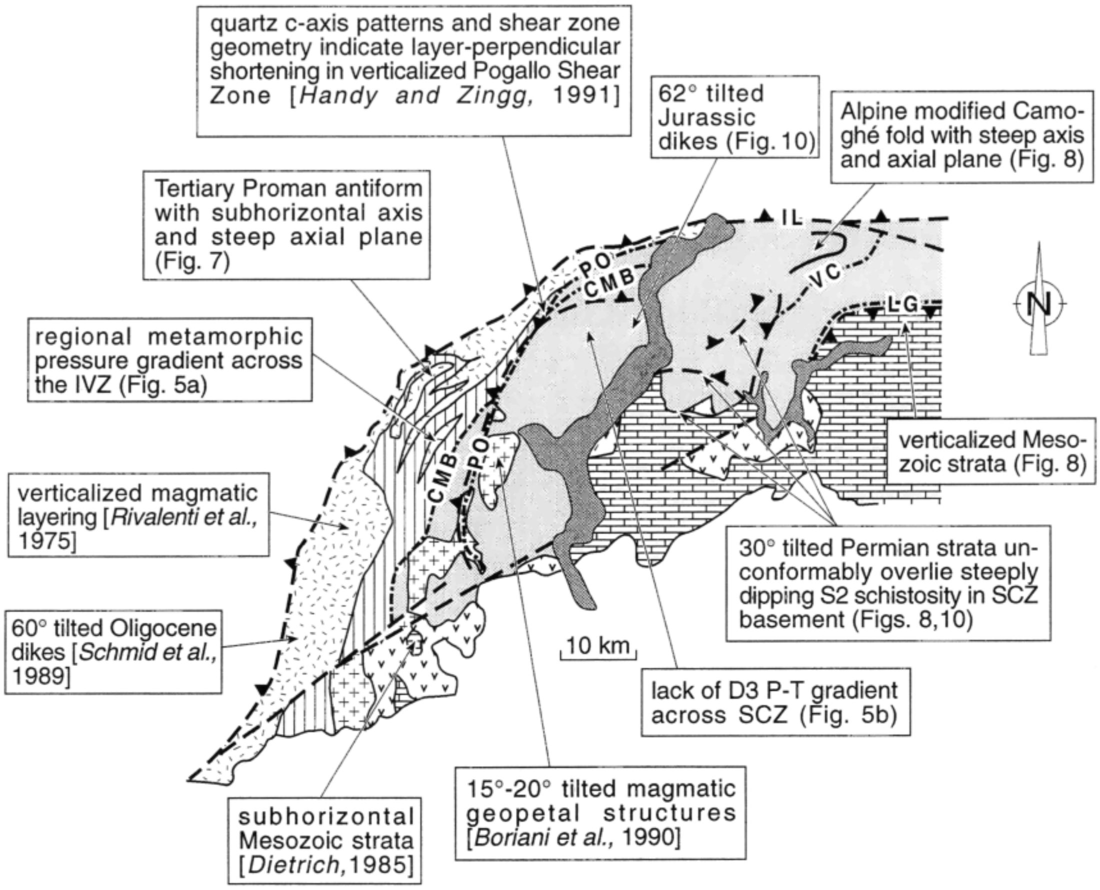

Figure 9. Criteria for determining pre-Tertiary orientation of basement and cover units in the Ivrea crustal section (see text for explanation).

main foliation (S1) was subhorizontal prior to Tertiary time:

1. Regional metamorphic pressure gradients from thermobarometry across the Ivrea-Verbano Zone (Figure 5) trend perpendicular to the strike of the S1 foliation. Except in the vicinity of Early Permian mafic intrusives, regional metamorphic isograds run parallel to this foliation and to the compositional banding [*Zingg*, 1980].

2. The pre-Alpine foliation adjacent to the Insubric Line is deformed by flexural slip folds with steep axial planes and gently plunging fold axes (Proman fold with stereoplot marked Pr in Figure 7; greenschist facies folds of *Kruhl and Voll* [1978/1979] and *Steck and Tièche* [1978/1979]). Folds with this attitude could only have formed if the pre-Alpine foliation was originally horizontal to moderately dipping. They are related to south to southeast directed, Tertiary shortening and backthrusting [*Schmid et al.*, 1987].

3. Natural remanent magnetization (NRM) directions from discordant dikes of inferred Oligocene age within the Ivrea-Verbano Zone along the southwestern part of the Insubric Line (Figure 9) indicate a 60° clockwise rotation (looking northeast about a horizontal axis) since early Tertiary time [*Schmid et al.*, 1989]. Back-rotating these dikes into concordance with the NRM direction for stable Europe indicates that the compositional banding and schistosity in the southwestern part of the Ivrea-Verbano Zone was moderately to gently inclined to the southeast.

4. Quartz *c* axis fabrics of the early Mesozoic, Pogallo Shear Zone indicate combined simple shear parallel to the shear zone boundary and shortening perpendicular to the steeply northwest dipping Pogallo mylonitic foliation [*Handy and Zingg*, 1991, Figure 8]. Shortening perpendicular to the Pogallo mylonitic foliation in the Ivrea-Verbano Zone is only compatible with east-west crustal extension documented by early Mesozoic sediments of the southern Alps if the Pogallo mylonites were gently to moderately dipping in Early Jurassic time.

3.2. Pre-Tertiary Orientation of the Strona-Ceneri Zone, Val Colla Zone, and Cover Units

In the Strona-Ceneri Zone the following arguments based on new structural and paleomagnetic information indicate that the main schistosity (S2) was moderately to steeply dipping already before Alpine deformation:

1. The large Camoghé fold in the northeastern part of the Strona-Ceneri Zone (marked Ca in Figure 8a) deforms S2. The Camoghé fold was originally an F3 fold like the Gambarogno fold to the southwest (marked Ga in Figure 8a), but on the basis of its box-shaped hinge and the abundance of brittle accommodation structures in its core, we believe that it tightened and became isoclinal in response to north-south directed, Tertiary Insubric thrusting under sub-greenschist-

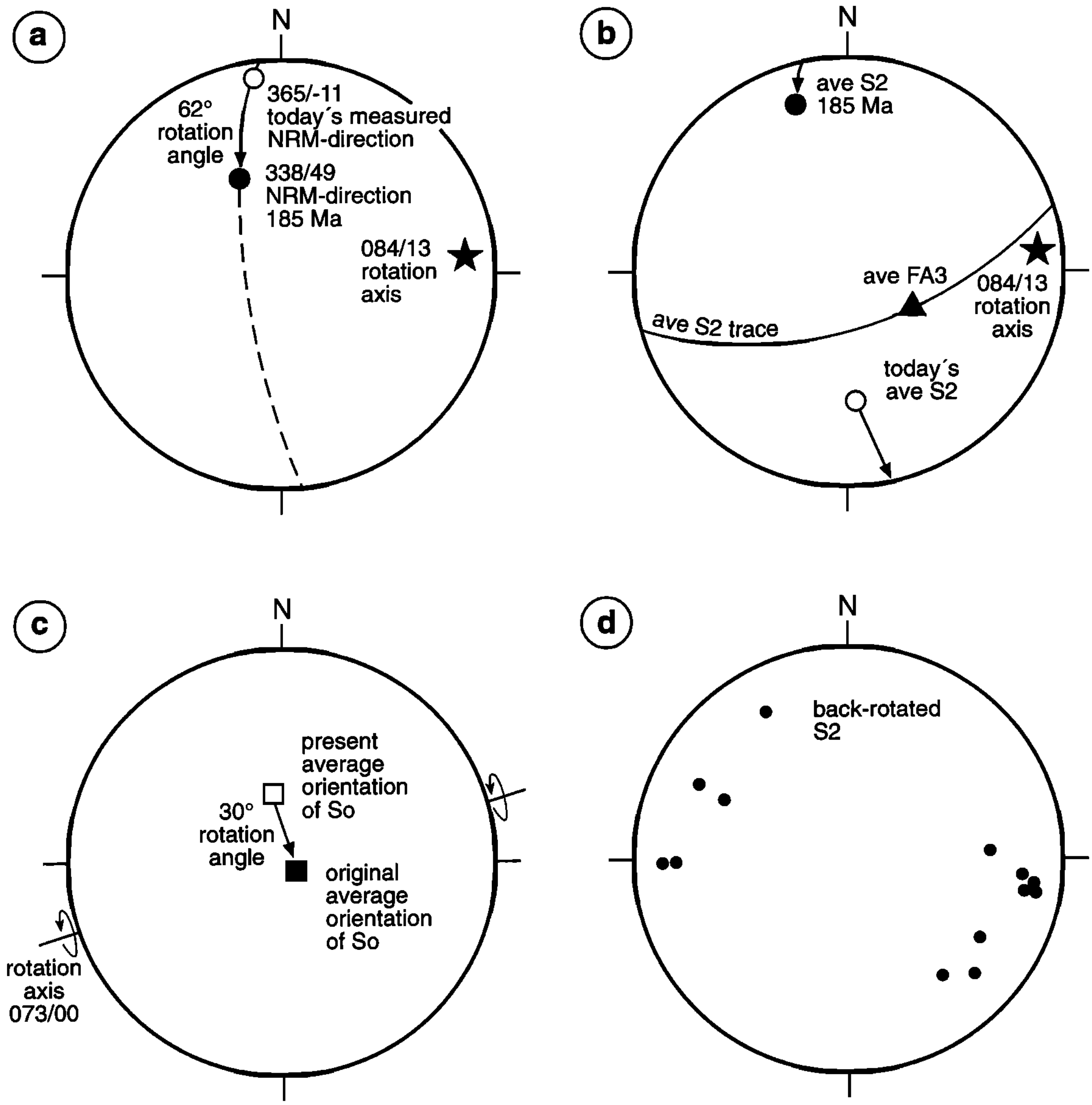

Figure 10. Present and back-rotated orientations of structures in the Strona-Ceneri Zone: (a) characteristic natural remanent magnetization (NRM) directions in 185 Ma mafic dikes from the Strona-Ceneri Zone (location in Figure 7); (b) back-rotated, pre-Jurassic orientations of S2 and F3 fold axis (FA3) in the Strona-Ceneri Zone; (c) back rotation of sedimentary bedding (So) in Permian strata unconformably overlying the Strona-Ceneri Zone; (d) back-rotated, Permian orientation of S2 in the Strona-Ceneri Zone beneath the Lower Permian unconformity. Stereoplots are lower hemisphere equal-area projections. See text for explanation.

facies conditions. The Camoghé fold is truncated by and therefore predates dextral Riedel faults associated with late Insubric, strike-slip faulting (Figure 8a). A 60°-70° dip for S2 and F3 fold axial planes in the Strona-Ceneri Zone prior to Insubric shortening and folding is inferred from the moderate attitude of the fold's axis and axial plane (Figure 8a).

2. NRM directions from discordant, 185 Ma mafic dikes in the northern part of the Strona-Ceneri Zone (circled cross in Figur 7; Ar-Ar hornblende ages by *Zurbriggen* [1996]) indicate that there, D2 and D3 structures underwent a post-Jurassic, clockwise rotation of 62° looking down a rotation axis oriented 084°/13° (Figure 10a). When back-rotated, the S2 schistosity in the northern part of the Strona-Ceneri Zone acquires a 70°, pre-Jurassic dip (Figure 10b), and F3 fold axes acquire the same orientation as that in southern parts of the Strona-Ceneri Zone.

3. The high-angle erosional unconformity between S2 schistosity in the southern part of the Strona-Ceneri Zone and subhorizontal bedding in the overlying Permian sediments (steroplot marked Ar in Figure 8a; stereoplot in Figure 10c) indicates that S2 was inclined 60°-80° at the time of sedimentation (Figure 10d).

4. The lack of D3 thermobarometric gradients across the northwestern part of the Strona-Ceneri Zone (Figure 5) indicates that the 4-5 kbar, D3 isobar is roughly parallel to the present erosional surface and that D2 and D3 structures in this part of the Strona-Ceneri Zone (stereoplots marked Gi in Figure 7) had attained their steep orientation prior to the equilibration of the thermobarometers in Carboniferous time.

The evidence in the Ivrea-Verbano Zone for originally subhorizontal foliations and regional metamorphic isobars indicates that large parts of the Ivrea-Verbano Zone were rotated some 60°-80° into a subvertical attitude with respect to the already moderately to steeply dipping, intermediate crustal units to the south. Most of this differential rotation was probably accommodated by numerous steep faults that transect the northwestern part of the Strona-Ceneri Zone [*Zurbriggen*, 1996] and overprint parts of the Pogallo Shear Zone [*Handy and Zingg*, 1991], but the kinematics of this faulting have yet to be worked out in detail.

The K-Ar mica ages along the Insubric Line [*Zingg and Hunziker*, 1990] and fission track ages from zircons and apatites within the Ivrea-Verbano and Strona-Ceneri Zones [*Hurford et al.*, 1989; *Hunziker et al.*, 1992] indicate that

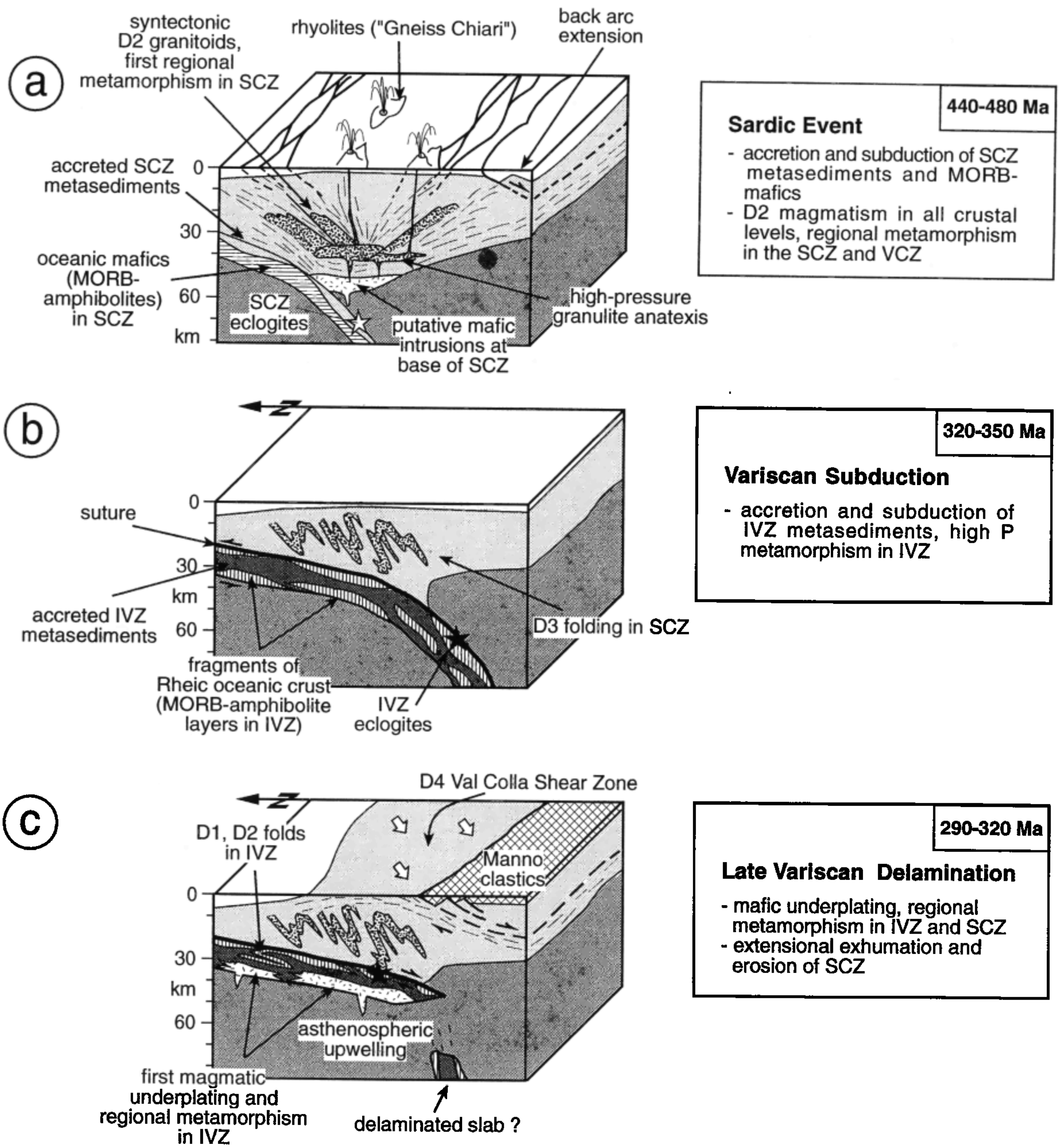

Figure 11. Evolution of the Ivrea crustal section described in text: (a) Sardic event, (b) Variscan subduction, (c) late Variscan delamination, (d) Permian transtension, (e) Tethyan rifting, and (f) Alpine emplacement. Abbreviations are as follows: IVZ, Ivrea-Verbano Zone; SCZ, Strona-Ceneri Zone; VCZ, Val Colla Zone.

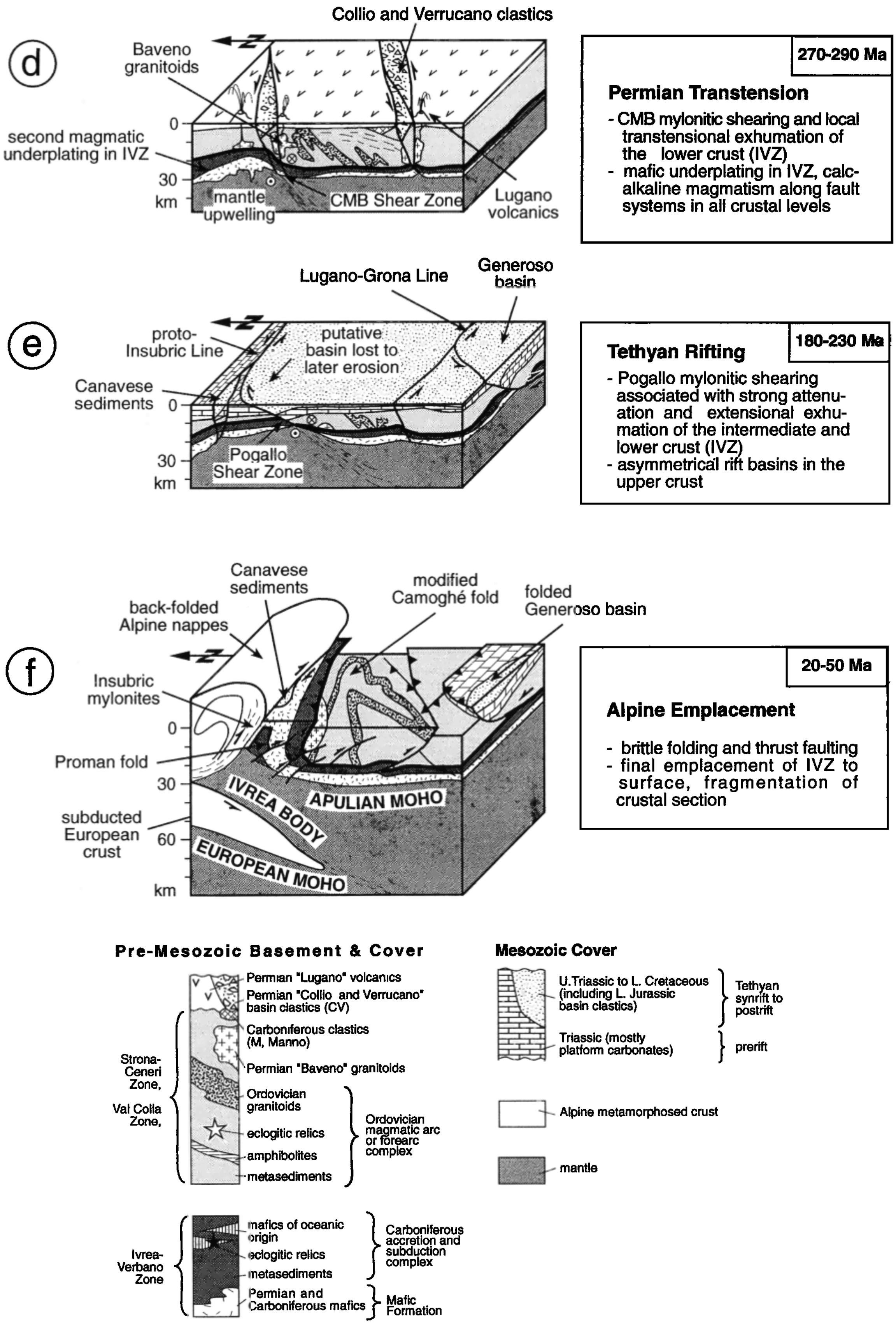

Figure 11. (continued)

northern parts of the crustal section including the Ivrea-Verbano Zone were exhumed in Late Cretaceous time and finally emplaced in early Tertiary to Mid-Tertiary time (Figure 2). In the southern part of the crustal section the basement-sediment contact is segmented into fault-bounded blocks with orientations varying from subvertical to horizontal (stereoplots marked Mu and Ar in Figure 8a). This complex local structure reflects the interference of north-south trending, early Mesozoic normal faults with both north and south directed Alpine folding and faulting [*Bertotti*, 1991]. The Alpine faulting is mid-Tertiary to late Tertiary on the basis of seismic and borehole information in the sedimentary cover to the south [*Bernoulli et al.*, 1989; *Schumacher et al.*, 1997].

4. A Model for the Evolution of the Southern Alpine Lithosphere

The evolution depicted in Figure 11 derives from the successive retrodeformation of Alpine and pre-Alpine structures. We emphasize that uncertainties in the local kinematics of Alpine deformation render any such reconstruction qualitative at best. In particular, the pre-Variscan structure of the crust is conjectural, based as it is on interpretations of thermobarometric and geochemical data in the context of actualistic models of crustal subduction and accretion.

4.1. Sardic Arc Tectonics

We envisage two possible scenarios for the pre-Variscan evolution of the southern Alps, depending on the ages of the eclogites and the D1, Cannobio Phase in the Strona-Ceneri Zone: (1) Subduction, high-pressure metamorphism, and exhumation (D1) are closely related in space and time to D2, Ceneri Phase deformation and magmatism in an Ordovician forearc or magmatic arc located at or near the northern margin of Gondwanaland (Figure 11a). (2) D1 occurred much earlier, during Cadomian orogenesis (520-580 Ma) and is unrelated to D2. We favor the first scenario (Figure 11a) because in pre-Alpine basement units of the Alps that are similar to the Strona-Ceneri Zone (e.g., the Gotthard Massif), eclogite facies metamorphism, felsic magmatism, and high-temperature metamorphism occurred within the relatively short span of 440-470 Ma [*Oberli et al.*, 1994]. Alternative scenarios involving rifting [*Ziegler*, 1990] are unlikely given the paucity of mantle-derived intrusives and the minimum crustal thickness of 35-50 km estimated above for the generation of S-type granitoids in the Strona-Ceneri Zone.

A magmatic arc setting has also been proposed to explain the felsic, subalkaline character of Early to Middle Ordovician magmatic suites in southern Sardinia [*Carmignani et al.*, 1994] and in the Central Iberian Zone of central Spain [*Valverde-Vaquero and Dunning*, 1999]. Relating these Ordovician events with those in the southern Alps, though speculative, is consistent with paleogeographic reconstructions locating the southern Variscides (including Alpine basement units) along the peri-Gondwanan margin of the Iapetus Ocean in mid-Ordovician time [*von Raumer*, 1998]. We therefore adopt the term "Sardic event" to refer to Ordovician tectonometamorphism in the southern Alps. This term is more appropriate than the term "Caledonian" for Ordovician events in units which, like most pre-Variscan basement of the Alps at that time, occupied the opposite (Gondwanan) side of the Iapetus Ocean to the Caledonides of Scotland and Scandinavia [*Ziegler*, 1990; *Torsvik et al.*, 1996].

The thickened Ordovician crust shown in Figure 11a was modified prior to the onset of Variscan accretion and subduction, as is evidenced by the aforementioned post-D2, pre-D3 decompression of 3-4 kbar and cooling of 200°C in the Strona-Ceneri Zone. The nature and exact timing of this modification are unconstrained but we speculate that the modification may be related to the breakup of the northern margin of Gondwana [*Ziegler*, 1990; *von Raumer*, 1998], possibly behind the retreating subduction zone and magmatic arc illustrated in Figure 11a.

4.2. Variscan Convergent Tectonics

Variscan accretion and subduction are shown in Figure 11b. Slivers of oceanic crust and upper mantle were subducted to depths consistent with eclogite facies metamorphism, as preserved in MORB-mafic layers along the southeastern margin of the Ivrea-Verbano Zone. These oceanic fragments of subducted, pre-Variscan mafic crust are interpreted as remnants of the Rheic Ocean between Avalonia and Gondwana. Tectonic underplating of imbricated Ivrea metasediments and MORB-mafic layers to the Ordovician crust in the Strona-Ceneri Zone was sited along a predecessor to the CMB Shear Zone (suture in Figure 11b). Relics of prograde, pressure-dominated amphibolite facies metamorphism in the Ivrea metasediments testify to this accretion and underplating along the crustal roof of the subduction zone. In the overlying Strona-Ceneri Zone, D3, Gambarogno Phase folds formed during subhorizontal shortening of the steeply dipping, Ordovician S2 foliation (Figure 11b).

The direction of Variscan subduction in the southern Alps is poorly constrained. *Vai and Cocozza* [1986] proposed west directed subduction on the basis of the assumption that the Ivrea-Verbano Zone was verticalized and emplaced in the core of the Variscan orogen, where it was supposedly flanked to the east by more external units with westward increasing Variscan metamorphic grade (Orobic basement, Val Colla and Strona-Ceneri Zones in Figure 1). However, the abundant evidence for an Alpine rather than Variscan emplacement age of the Ivrea-Verbano Zone refutes this hypothesis [*Zingg et al.*, 1990; *Schmid*, 1993]. According to the orientational criteria discussed in section 4.1, back-rotating the Ivrea-Verbano Zone into its pre-Alpine attitude yields a southeastward dip of the Ivrea-Verbano - Strona-Ceneri contact. This is consistent with a southeast dipping Variscan subduction zone, as drawn in Figure 11b.

Figure 11c depicts a late stage of Variscan convergence during the time span 290-320 Ma. We speculate that events in the Ivrea crustal section during this time (Figure 2) were triggered by some kind of lithospheric delamination, for example, slab break-off [*von Blanckenburg and Davies*, 1995], that lead to asthenosheric upwelling, mantle anatexis, and advection of heat into the thickened crust. A similar mechanism has been proposed to explain late Carboniferous magmatism and regional metamorphism in other parts of the Variscan orogen, such as the Moldanubian domain in the

Vosges and Schwarzwald of France and southern Germany [*Eisbacher et al.*, 1989]. Isostatic rebound of the delaminated Variscan crust may have been partly responsible for the exhumation and overprinting of Variscan high-pressure rocks presently exposed in the southern part of the Ivrea-Verbano Zone (Figure 11c). Lithospheric delamination also provides a plausible explanation for the general simultaneity of regional metamorphic deformation in the Ivrea-Verbano Zone and extensional unroofing of the Strona-Ceneri Zone. The latter lead to the subaerial erosion of basement into intramontane basins filled with Manno clastic sediments (Figure 11c). These events preceded peneplainization of the southern Alpine basement, as is marked by the Lower Permian erosional unconformity at the top of the Strona-Ceneri Zone [*Graeter*, 1951]. We note that presently observed differences in the style and orientation of late Carboniferous structures in the Ivrea-Verbano and Strona-Ceneri Zones reflect the fact that these two basement units originally occupied different levels of the Variscan crust and were juxtaposed much later during early Mesozoic extensional shearing along the Pogallo Shear Zone (see section 4.4).

4.3. Early Permian Transtensional Tectonics

Figure 11d shows the southern Alpine crust during Early Permian, oblique-slip tectonics and magmatism. Sinistral transtension in the western part of the southern Alps is inferred from kinematic restoration of the steeply dipping CMB mylonites in the Ivrea-Verbano Zone to their subhorizontal, pre-Alpine attitude [*Handy and Zingg*, 1991]. We propose that the CMB Shear Zone steepened upward to merge with oblique-slip faults which bound elongate, Permian basins in the intermediate to upper crust (Figure 11d). Today, these faults are marked by ENE-WSW trending facies boundaries in Lower Permian basinal sediments overlying the Strona-Ceneri Zone [*Kälin and Trümpy*, 1977] and the Orobic basement [*Cassinis et al.*, 1986]. Pronounced, north-south variations in facies and thickness of the Permian, Collio, and Verrucano formations in the southern Alps (marked CV in Figure 1) are diagnostic of strong subsidence within narrow, fault-bounded basins [*Schönborn and Schumacher*, 1994]. This evidence for localized subsidence in the upper crust is consistent with exhumation of the lower crust in the Ivrea-Verbano Zone.

The Early Permian crustal section was approximately 30 km thick, as is inferred from the 600° ± 50°C closure temperature of the U-Pb monazites that yield 270-280 Ma ages at the base of the crustal section in the Ivrea-Verbano Zone [*Henk et al.*, 1997] and the assumption of a moderate to high geothermal gradient (20°-30°C/km) at this time [*Handy*, 1987]. Magmatic underplating of mantle-derived, mafic melts probably played an important role in maintaining this thickness where parts of the lower crust, like the Ivrea-Verbano Zone, were locally stretched and exhumed during transtensional mylonitic shearing (Figure 11d). The concentration of syn-mylonitic mafic veins and granitoids along the CMB Shear Zone suggests that this shear zone channeled mantle- and crust-derived melts upward from deep to shallow crustal levels. The Baveno intrusives adjacent to the CMB Shear Zone and the Lugano volcanics discordantly overlying the Strona-Ceneri basement (Figure 1) represent such middle to upper crustal magmatic rocks. Although Early Permian magmatism affected all levels of the Ivrea crustal section, its obvious effects (renewed metamorphism and anatexis) were restricted to parts of the lower crust in the vicinity of post-regional-metamorphic, mafic intrusives.

We emphasize that Early Permian magmatism and oblique-slip tectonics are temporally and kinematically distinct from Variscan convergent tectonics. This fact has been overlooked or even obscured in the literature by misleading use of the term "late Variscan" or "late Hercynian" for Early Permian events. As shown above, Early Permian intrusives and structures overprint truly late Variscan features in the Ivrea crustal section. These overprinting relationships are clearly incompatible with the idea, inspired by geophysical and petrological models [*Furlong and Fountain*, 1986; *Huppert and Sparks*, 1988], that Early Permian mafic intrusions within parts of the Mafic Formation affected amphibolite to granulite facies, regional metamorphism and anatexis in the entire Ivrea-Verbano Zone [*Fountain*, 1989; *Voshage et al.*, 1990].

Handy and Zingg [1991] proposed that Early Permian sinistral transtension in the southern Alps was conjugate to dextral strike-slip shearing across Europe within an overall regime of post-Variscan, right-lateral strike slip between Gondwana and Laurussia, linking convergence in the Uralides and the Appalachians [*Arthaud and Matte*, 1975; *Ziegler*, 1990]. Alternatively, transtension in the southern Alps was related to oblique spreading behind an eastwardly retreating convergent margin in the western Paleotethys [*Stampfli*, 1996]. Whatever its cause, oblique-slip tectonics ended in Early Triassic time with the transition from clastic sedimentation to carbonate precipitation on gradually and differentially subsiding, marine platforms [*Winterer and Bosellini*, 1981]. This subsidence continued into Middle Triassic time, when it was complicated by strike-slip tectonics [*Bertotti et al.*, 1993]. Structures related to this event are abundant farther to the east in the Dolomites [*Doglioni*, 1984] but have not yet been identified in the Ivrea crustal section.

4.4. Tethyan Rifting

Figure 11e shows the Ivrea crustal section toward the end of Pogallo Phase deformation in Early to Middle Jurassic time. The Pogallo Shear Zone itself is depicted as a moderate- to low-angle, oblique-normal fault that accommodated noncoaxial, east-west directed, extensional exhumation of the Ivrea-Verbano Zone to depths of 10 km or less. This kinematic reconstruction is based on a backrotation of the D4, Pogallo mylonitic foliation and stretching lineations into their pre-Alpine orientations, as discussed by *Handy* [1987] and in section 3. The rift basin and upper crustal normal faults that were linked to the Pogallo Shear Zone at depth have been lost to Tertiary erosion but probably had a geometry similar to that of the Monte Nudo and Generoso basins presently exposed in the southern part of the crustal section (Figures 1 and 11e). The putative basin may have been bounded to the north by an east-west trending, early Mesozoic predecessor of the Insubric Line (proto-Insubric Line in Figure 11e), whose former existence is inferred from the highly deformed "Canavese" sediments preserved locally along the Insubric Line (marked Ca in Figure 1). In the southwestern part of the Ivrea-Verbano Zone these sediments represent a very condensed, early Mesozoic passive margin facies [*Bertotti et al.*, 1993] and rest in tectonic contact with relics of their granitoid basement and with late Carboniferous, granulite facies mafic rocks of the Ivrea-Verbano Zone [*Biino et al.*, 1988]. The juxtaposition of attenuated rocks from such disparate levels of the Ivrea crustal section may be due to early Mesozoic thinning [*Handy and Zingg*, 1991].

The kinematics of early Mesozoic deformation in the Ivrea crustal section are consistent with widespread evidence in the Alps for east-west directed crustal extension within a sinistral pull-apart margin at the northwestern corner of the Apulian promontory of Africa in Early to Middle Jurassic time [*Weissert and Bernoulli*, 1985]. Given the location of the Ivrea crustal section in the distal parts of the Apulian continental margin, Pogallo Phase extensional exhumation of the lower crust probably occurred during the advanced stages of rifting, when necking of the distended margin was accommodated by conjugate faulting and highly noncoaxial shearing in the upper and lower crust, respectively [*Handy*, 1987; *Bertotti et al.*, 1993].

4.5. Alpine Emplacement Tectonics

Figure 11f depicts the Ivrea crustal section in late Tertiary time, after it had been modified by Tertiary, Insubric faulting and brittle folding. Some of the faults that transect the crustal section are reactivated structures that helped to accommodate differential rotation of crustal blocks. For example, brittle reactivation of parts of the Pogallo Shear Zone accommodated differential rotation of the Ivrea-Verbano Zone into its present, subvertical attitude (Figure 11f). Similarly, reactivation of the Lugano-Grona Line accommodated folding and verticalization of the northern part of the early Mesozoic Generoso basin (Figure 11f).

Early Alpine tectonics are not shown in Figure 11, because of the difficulty of determining the precise age of Alpine faults within the basement units of the Ivrea crustal section. The lack of fission track analyses in traverses across such faults and the complexity of Tertiary tectonics render Late Cretaceous reconstructions south of the Insubric Line [*Schumacher et al.*, 1997] highly speculative.

5. Implications for Crustal Processes and Seismic Imaging of the Crust

The evolution outlined above has several interesting implications, first for the processes which formed the continental crust in western Europe and second for the interpretation of seismic profiles of such crust. The southern Alpine crust has a composite structure, comprising an older intermediate crust sandwiched between much younger segments of the lower and upper crust. This kind of structural zonation appears to be a general characteristic of continental crust in western Europe [*Costa and Rey*, 1993], although the age range of early deformation and metamorphism in the Strona-Ceneri Zone (440-480 Ma) is somewhat older than that of the earliest events in some other exposed Variscan basement terrains (e.g., Massif Central, Eo-Variscan phase of *Ledru et al.* [1994]). In the case of the Ivrea crustal section this zonation results primarily from Variscan suturing of a Carboniferous accretion-subduction complex in the Ivrea-Verbano Zone to an Ordovician magmatic arc in the Strona-Ceneri and Val Colla Zones.

This structural zonation only partly corresponds to the distribution of metamorphic facies and isotopic ages observed today in the crustal section. This discrepancy is testimony to the three ways in which deformation, metamorphism, and magmatism selectively modified different levels of the crust at different times:

1. Main elements of the Sardic magmatic arc and Variscan accretion-subduction complex that make up the Ivrea crustal section were modified or lost, probably during the late stages of Variscan convergence. The Ordovician lower crust that originally underlay the Strona-Ceneri Zone was delaminated, whereas the Ordovician upper crust was lost to extensional and erosional denudation. In contrast, the intermediate crust represented by the Strona-Ceneri Zone survived despite overprinting by Variscan folds and amphibolite facies metamorphism.

2. Early Permian magmatic underplating and transtensional shearing locally overprinted late Variscan structures and regional metamorphism that had already modified the Variscan lower crust (Ivrea-Verbano Zone) during the main pulse of late Carboniferous magmatic underplating. Permian magmatism lead to a further reconstitution of the crust and reequilibration of the petrological crust-mantle boundary at approximately 30 km. This is the average depth of continental crust beneath large parts of western central Europe, i.e., crust that was unaffected by rifting or the Alpine orogeny [*Ansorge et al.*, 1992].

3. Low-angle normal faulting associated with early Mesozoic, Tethyan rifting excised at least 10-20 km of mostly intermediate to lower crust from the section. Together with Early Permian transtensional shearing, early Mesozoic extension sheared out up to two thirds of the late Variscan crust while juxtaposing pieces of this crust that originally occupied different lateral positions. The Strona-Ceneri Zone is therefore the lateral equivalent of intermediate crust that once overlay the Ivrea-Verbano Zone and has since been faulted out and/or eroded.

The late Paleozoic exhumation of the Ivrea crustal section is polyphase and corresponds closely to that outlined by *Burg et al.* [1994] for continental crust across western Europe: Late Variscan (Westphalian) extensional unroofing of the intermediate crustal Strona-Ceneri Zone yielded to post-Variscan (Early Permian) transtensional exhumation of the deep crustal Ivrea-Verbano Zone. Most exhumation of the deep crust occurred during Early Jurassic rifting, however, and was accommodated along the continentward-dipping Pogallo Shear Zone. The southern Alpine crust is therefore typical of thinned, late Variscan continental crust within Tethyan and Atlantic passive margins.

The crustal evolution of the southern Alps has several implications for the interpretation of seismic reflection profiles of "Variscan" crust in western Europe: Seismic reflectivity of the lower crust can be attributed to the subhorizontal geometry of flattened and sheared, late Variscan mafic intrusives and Carboniferous metasediments [Figure 3.10 by *Ansorge et al.*, 1992, and references therein]. In contrast, the relative seismic transparence of the intermediate crust probably stems from the moderate to steep attitude of Sardic and Variscan structures. Reflectivity of the upper crust is due to Early Permian and early Mesozoic faults and basins.

Finally, we note that the Ivrea crustal section is transected by numerous Alpine faults and was not uniformly steepened during Tertiary, Insubric tectonics. Only the originally deepest levels of the section in the Ivrea-Verbano Zone and some shallow parts of the section along the basement-cover contact are presently verticalized. Other parts, particularly the Strona-Ceneri Zone, underwent only minor to moderate Alpine rotation [*Boriani et al.*, 1990] and have an erosional surface that is generally parallel to the late Carboniferous, metamorphic isobars. Unfortunately, some geophysical models that have used the Ivrea crustal section to simulate the seismic reflective properties of continental crust are implicitly or explicitly based on the assumption that a uniform, en bloc Alpine rotation affected all the basement units, including the Strona-Ceneri Zone [*Burke and Fountain*, 1990; *Holliger and Levander*, 1994; *Rutter et al.*, 1999]. Future modeling will no doubt take into account the abundant evidence for varied, differential rotations within the Ivrea crustal section.

Acknowledgments. We are indebted to Ivan Mercolli, Stefan Schmid, Jürgen von Raumer, and Pablo Valverde-Vaquero for animated discussions and to Paul Graeter, Andreas Mulch, Matthias Rosenau, and Jürgen Streit for companionship and discourse in the field. Markus Albertz patiently drew several versions of our figures. Matthias Rosenau rendered this manuscript camera-ready. Thanks also go to Igor Villa for aiding us with Ar-Ar radiometric dating of the mafic dikes and to Klaus Holliger for letting M.H. use his quiet flat to write this paper on a visit to Zürich. This paper was first presented at EUG in 1997. Unfortunately, *Tectonics* lost track of the manuscript with the result that it spent more than 13 months in review! We thank Neil Mancktelow for his substitute review and Dennis Brown for constructive remarks. The generous support of the Swiss National Science Foundation (grants 21-30598.91 and 21-33814.92) and the Deutsche Forschungsgemeinschaft (grant HA 2403/2-1, SPP Orogene Prozesse...) are acknowledged with gratitude.

References

Ansorge, J., D. Blundell, and S. Mueller, Europe's lithosphere. Seismic structure, in *A Continent Revealed. The European Geotraverse*, edited by D. Blundell, R. Freeman, and S Mueller, pp. 33-70, Cambridge Univ. Press, New York, 1992.

Arthaud, F , and P. Matte, Les décrochements Tardi-Hercynian du sud-ouest de l'Europe Geometrie et essai de reconstitution des conditions de la deformation, *Tectonophysics*, *25*, 139-171, 1975

Asmerom, Y., J.K. Snow, D.K Holm, S.B Jacobsen, B.P. Wernicke, and D.R Lux, Rapid uplift and crustal growth in extensional environments· An isotopic study from the Death Valley region, California, *Geology*, *18*, 223-226, 1990.

Bächlin, R., Geologie und Petrographie des M. Tamaro-Gebietes (südliches Tessin), *Schweiz. Mineral. Petrogr. Mitt.*, *17* (1), 1-79, 1937.

Bernoulli, D., Zur Geologie des Monte Generoso, *Beitr. Geol. Karte Schweiz, N.F*, *118*, 1-113, 1964.

Bernoulli, D., G. Bertotti, and A Zingg, Northward thrusting of the Gonfolite Lombarda ("South-Alpine Molasse") onto the Mesozoic sequence of the Lombardian Alps: Implications for the deformation history of the southern Alps, *Eclogae Geol. Helv*, *82* (3), 841-856, 1989

Bernoulli, D., M. Giger, D W Müller, and U R.F Ziegler, Sr-isotope-stratigraphy of the Gonfolite Lombarda Group ("South-Alpine Molasse", northern Italy) and radiometric constraints for its age of deposition, *Eclogae Geol. Helv.*, *86* (3), 751-767, 1993.

Bertolani, M., La formazione basica "Ivrea-Verbano" e la sua posizione nel quadro geologico-petrografico della Basse Valsesia del Biellese, *Period Mineral.*, *28*, 151-209, 1959

Bertotti, G., Early Mesozoic extension and Alpine shortening in the western southern Alps The geology of the area between Lugano and Menaggio (Lombardy, northern Italy), *Mem. Sci. Geol*, *43*, 17-123, 1991

Bertotti, G., V. Picotti, D Bernoulli, and A. Castellarin, From rifting to drifting: Tectonic evolution of the South-Alpine upper crust from the Triassic to the Early Cretaceous, *Sediment Geol.*, *86*, 53-76, 1993.

Bigi, G , A. Castellarin, M. Coli, G.V Dal Piaz, R Sartori, P. Scandone, and G.B. Vai, Structural model of Italy, map, sheet 1, Cons Naz.delle Ric.,Rome, Italy, 1983

Biino, G., R. Compagnoni, and M. Naldi, The Canavese Zone near Ivrea (western Alps), *Rend. Soc. Geol Ital*, *11*, 85-88, 1988

Borghi, A , Evoluzione metamorfica del settore nord-est della Serie dei Laghi (Alpi Meridionali-Canton Ticino), *Rend Soc. Geol. Ital.*, *11*, 165-170, 1988.

Boriani, A., and G. Peyronel Pagliani, Rapporti fra le plutoniti erciniche e le metamorfiti del "Massiccio dei Laghi" nella zona del M. Cerano (bassa Val d'Ossola), *Rend. Soc Ital Mineral. Petrol.*, *24*, 111-142, 1968.

Boriani, A , and R Sacchi, Geology of the junction between the Ivrea-Verbano and Strona-Ceneri Zones, *Mem. Ist. Geol Mineral. Univ. Padova*, *28*, 1-35, 1973

Boriani, A , and I.M Villa, Geochronology of regional metamorphism in the Ivrea-Verbano Zone and Serie dei Laghi, Italian Alps, *Schweiz Mineral. Petrogr. Mitt.*, *77* (3), 381-402, 1997

Boriani, A., B. Bigioggero, and E Origoni Giobbi, Metamorphism, tectonic evolution and tentative stratigraphy of the Serie dei Laghi: Geologic map of the Verbania area (northern Italy), *Mem. Sci. Geol.*, *32*, 1-26, 1977.

Boriani, A., E Origoni Giobbi, and A. Del Moro, Composition, level of intrusion and age of the "Serie dei Laghi" orthogneisses (northern Italy - Ticino, Switzerland), *Rend Soc. Ital. Mineral Petrol.*, *38* (1), 191-205, 1983.

Boriani, A., E. Origoni Giobbi, A. Borghi, and V. Caironi, The evolution of the "Serie dei Laghi" (Strona-Ceneri and Schisti dei Laghi)· The upper component of the Ivrea-Verbano crustal section, southern Alps, north Italy and Ticino, Switzerland, *Tectonophysics*, *182*, 103-118, 1990.

Brodie, K.H., and E.H. Rutter, Deep crustal extensional faulting in the Ivrea Zone of northern Italy, *Tectonophysics*, *140*, 193-212, 1987

Brodie, K.H , D Rex, and E.H. Rutter, On the age of deep crustal extensional faulting in the Ivrea Zone, northern Italy, in *Alpine Tectonics*, edited by M P. Coward, D Dietrich, and R G. Park, *Geol Soc. Spec. Publ.*, *45*, 203-210, 1989.

Buletti, M , Zur Geochemie und Entstehungsgeschichte der Granat-Amphibolite des Gambarognogebietes, Ticino, Südalpen, *Schweiz Mineral. Petrogr Mitt.*, *63* (2-3), 233-247, 1983.

Burg, J P , J Driessche, and J.P. Brun, Syn- to post-thickening extension in the Variscan belt of western Europe· Modes and structural consequences, *Geol Fr*, *3*, 33-51, 1994.

Bürgi, A., and U. Klötzli, New data on the evolutionary history of the Ivrea Zone (northern Italy), *Bull. Swiss Assoc. of Pet Geol and Eng*, *56* (103), 49-105, 1990.

Burke, M.M., and D.M. Fountain, Seismic properties of rocks from an exposure of extended continental crust: New laboratory measurements from the Ivrea Zone, *Tectonophysics*, *182*, 119-146, 1990.

Capedri, S., Sulle rocce della formazione basica Ivrea-Verbano, 2, Petrografia delle granuliti e rocce derivate affioranti nella Val Mastallone (Vercelli) e loro evoluzione petrogenetica, *Mem. Soc Geol. Ital.*, *10*, 277-312, 1971.

Carmignani, L , G. Oggiano, and P C Pertusati, Geological outline of the Hercynian basement of Sardinia, in *Guidebook to the Field Excursion. Petrology, Geology and Ore Deposits of the Paleozoic Basement of Sardinia*, edited by L Carmignani et al., pp. 9-20, Int Mineral Assoc , Pisa, 1994.

Cassinis, G., et al., Report on a structural and sedimentological analysis in the uranium province of the Orobic Alps, Italy, *Uranium*, *2*, 241-260, 1986

Costa, S., and P. Rey, Lower crustal rejuvenation and crustal growth during post-thickening collapse· The example of the Variscan crust in the eastern French Massif Central, in *Late Orogenic Extension in Mountain Belts*, edited by M. Seranne and J. Malavieille, Bur. de Rech. Geol. et Minières, Paris, France, 1993.

Dewey, J.F., and J M. Bird, Mountain belts and the new global tectonics, *J. Geophys. Res*, *75*, 2625-2647, 1970

Dietrich, A , Zur Geologie des Monte Fenera (untere Val Sesia, Piemont, Norditalien), diploma thesis, Univ of Basel, Basel, Switzerland, 1985

Doglioni, C , Tettonica triassica transpressiva nelle Dolomiti, *G. Geol.*, *3*, 47-60, 1984.

Eisbacher, G.H., E Lüschen, and F. Wickert, Crustal-scale thrusting and extension in the Hercynian Schwarzwald and Vosges, central Europe, *Tectonics*, *8* (1), 1-21, 1989.

Fountain, D M., The Ivrea-Verbano and Strona-Ceneri Zones, northern Italy. A cross section of the continental crust - new evidence from seismic velocities, *Tectonophysics*, *33*, 145-166, 1976.

Fountain, D.M., Growth and modification of lower continental crust in extended terrains The role of extension and magmatic underplating, in *Properties and Processes of Earth's Lower Crust*, Geophys. Monogr Ser., Vol. 51, edited by R F. Mereu, S Mueller, and D.M Fountain, pp 287-299, AGU, Washington, D.C., 1989

Fountain, D.M., and M.H Salisbury, Exposed cross sections through the continental crust. Implications for crustal structure, petrology and evolution, *Earth Planet. Sci Lett.*, *5*, 263-277, 1981.

Franz, L., S Teufel, and O Oncken, Die Abkühlungsgeschichte orogen gestörter Kruste - das Ivrea-Krustensegment (Norditalien), erste Ergebnisse, *Göttinger Arb. Geol. Palaontol.*, *1*, 129-131, 1994

Franz, L., S. Teufel, and O. Oncken, Thermische Entwicklung der Ivrea- und Strona-Ceneri-Zone (N-Italien), *Terra Nostra*, *96* (2), 58-60, 1996

Furlong, K P., and D M. Fountain, Continental crustal underplating: Thermal considerations and seismic-petrologic consequences, *J. Geophys Res*, *91*, 8285-8294, 1986.

Gebauer, D., The Pre-Alpine evolution of the continental crust of the central Alps. An overview, in *Pre-Mesozoic Geology in the Alps*, edited by J.F von Raumer and F Neubauer, pp 93-117, Springer-Verlag, New York, 1993

Giobbi, E., A. Zappone, R Bocchio, and L. Morten, Pre-Alpine ophiolites from Serie dei Laghi (western southern Alps),*Terra Nova*, *7*, Abstr. suppl. 1, 182, 1995

Graeter, P., Geologie und Petrographie des Malcantone (südliches Tessin), *Schweiz. Mineral. Petrogr Mitt.*, *31* (2), 361-482, 1951.

Handy, M.R., The structure and rheological evolution of the Pogallo fault zone: A deep crustal dislocation in the southern Alps of northwestern Italy (prov. Novara), Ph D thesis, Univ of Basel, Switzerland, 1986.

Handy, M R., The structure, age, and kinematics of the Pogallo fault zone, southern Alps, northwestern Italy, *Eclogae Geol. Helv.*, *80* (3), 593-632, 1987.

Handy, M R., and J.E Streit, Mechanics and mechanisms of magmatic underplating: Inferences from mafic veins in deep crustal mylonite, *Earth Planet Sci. Lett.*, *165*, 271-286, 1999

Handy, M R, and A. Zingg, The tectonic and rheological evolution of an attenuated cross section of the continental crust: Ivrea crustal section, southern Alps, northwestern Italy and southern Switzerland, *Geol. Soc. Am. Bull.*, *103*, 236-253, 1991.

Hellmann, K.N , and H.J Lippolt, Calibration of the Middle Triassic time scale by conventional K-Ar and $^{40}Ar/^{39}Ar$ dating of alkali feldspars, *J. Geophys.*, *50*, 73-88, 1981

Henk, A , L Franz, S. Teufel, and O Onken, Magmatic underplating, extension, and crustal reequilibration: Insights from a cross-section through the Ivrea Zone and Strona-Ceneri Zone, northern Italy, *J Geol*, *105*, 367-377, 1997.

Hermann, F , Carta Geologica delle Alpi Nord-Occidentali, map, scale 1.200,000, Ufficio Cart.^{co}, Milano, 1937.

Hofmann, A.W., M. Lu, W. Obermiller, G Rivalenti, and M Mazzuchelli, Contrasting styles of crustal contamination in Ivrea magma chambers and peridotites, *U S Geol. Surv. Circ.*, *1089*, 10, 1992

Holliger, K., and A Levander, Structure and seismic response of extended continental crust Stochastic analysis of the Strona-Ceneri and Ivrea Zones, Italy, *Geology*, *22*, 79-82, 1994

Hunziker, J.C., Rb-Sr and K-Ar age determinations and the Alpine tectonic history of the western Alps, *Mem. Ist Geol. Mineral Univ Padova*, *31*, 1-55, 1974.

Hunziker, J C , and A Zingg, Lower Paleozoic amphibolite to granulite facies metamorphism in the Ivrea Zone (southern Alps, northern Italy), *Schweiz Mineral. Petrogr Mitt.*, *60* (2-3), 181-213, 1980.

Hunziker, J.C., and A Zingg, Zur Genese der ultrabasischen Gesteine der Ivrea-Zone, *Schweiz Mineral Petrogr. Mitt.*, *62* (3), 483-486, 1982.

Hunziker, J.C , J. Desmons, and A J Hurford, Thirty-two years of geochronological work in the central and western Alps: A review on seven maps, *Mem. Geol Lausanne*, *13*, 1-59, 1992.

Huppert, H.E , and S J. Sparks, The generation of granitic magmas by intrusion of basalt into continental crust, *J. Petrol.*, *29*, 599-624, 1988.

Hurford, A.J., M Flisch, and E Jäger, Unravelling the thermo-tectonic evolution of the Alps: A contribution from fission track analysis and mica dating, in *Alpine Tectonics*, edited by M.P. Coward, D. Dietrich, and R.G. Park, *Geol. Soc. Spec. Publ*, *45*, 369-398, 1989

Jäger, E., E. Niggli, and E. Wenk, Rb-Sr Altersbestimmungen an Glimmern der Zentralalpen, *Beitr. Geol Karte Schweiz, N F*, *134*, 1-67, 1967

Janott, B., Kinematik und Metamorphose der Val Colla Mylonitzone im Südalpinen Grundgebirge (Tessin, Schweiz), diploma thesis, Justus-Liebig-Univ. Giessen, Germany, 1996.

Jongmans, W J., Die Karbonflora der Schweiz, *Beitr. Geol. Karte Schweiz*, *N.F*, *108*, pp. 1-97, 1960

Kälin, O., and D.M. Trümpy, Sedimentation und Paläotektonik in den westlichen Südalpen. Zur triassisch- jurassischen Geschichte des Monte Nudo-Beckens, *Eclogae Geol Helv.*, *70* (2), 295-350, 1977.

Köppel, V , Isotopic U-Pb ages of monazites and zircons from the crust-mantle transition and adjacent units of the Ivrea and Strona-Ceneri Zones (southern Alps, Italy), *Contrib Mineral. Petrol.*, *43*, 257, 1974

Köppel, V , and M Grünenfelder, A study of inherited and newly formed zircons from paragneisses and granitized sediments of the Strona-Ceneri Zone (southern Alps), *Schweiz Mineral Petrogr. Mitt.*, *51* (2-3), 385-409, 1971

Koppel, V , and M Grünenfelder, Monazite and zircon U-Pb ages from the Ivrea and Ceneri Zones (southern Alps, Italy), *Mem Sci. Geol.*, *33*, 55-70, 1978/1979.

Kruhl, J.H , and G. Voll, Deformation and metamorphism of the western Finero complex, *Mem. Sci. Geol.*, *33*, 95-109, 1978/1979

Ledru, P., S Costa, and H Echtler, Structure, in *Pre-Mesozoic Geology in France and Related Areas*, edited by J D. Keppie, pp 305-323, Springer-Verlag, New York, 1994.

Lensch, G., and F Rost, Kelyphitperidotit in der mittleren Ivrea Zone zwischen Val d'Ossola und Val Strona. Ein Beitrag zur Herkunftstiefe der Ultramafitite der Ivreazone, *Schweiz Mineral. Petrogr Mitt*, *52* (2), 237-250, 1972

Lu, M , Geochemistry and geochronology of the mafic-ultramafic complex near Finero, Ivrea-Verbano Zone, northern Italy, Ph D thesis, Univ. Mainz, Germany, 1994.

Lu, M, A.W. Hofmann, G. Rivalenti, and M Mazzuchelli, Geochemistry of the lower crustal mafic-ultramafic complex at Finero, Ivrea Zone, N Italy, *Mineral. Mag*, *58A*, 537-538, 1994

Lu, M , A W Hofmann, M Mazuchelli, and G. Rivalenti, The mafic-ultramafic complex near Finero (Ivrea-Verbano Zone), II, Geochronology and isotope geochemistry, *Chem. Geol*, *140*, 223-235, 1997.

Mazzucchelli, M, and F. Siena, Geotectonic significance of the metabasites of the kinzigitic series, Ivrea-Verbano Zone (western Italian Alps), *Tschermaks Mineral. Petrogr Mitt.*, *35*, 99-116, 1986

McDowell, F W , Potassium-Argon ages from the Ceneri Zone, southern Swiss Alps, *Contrib Mineral Petrol.*, *28*, 165-182, 1970

Mehnert, K , The Ivrea Zone. A model of the deep crust, *Neues Jahrb. Mineral Abh*, *125*, 156-199, 1975.

Miller, D S , and E. Jäger, Fission track ages of some Alpine micas, *Earth Planet Sci Lett.*, *4*, 375-378, 1968.

Mulch, A , M.R. Rosenau, W. Dörr, U Haack, and M R. Handy, U-Pb ages of syn-mylonitic mafic and granitoid veins in the middle to lower continental crust (Ivrea-Verbano Zone, Switzerland and Italy), *Terra Nostra*, *99* (1), 150, 1999.

Oberli, F., M. Meier, and G G. Biino, Time constraints on the pre-Variscan magmatic/metamorphic evolution of the Gotthard and Tavetsch units derived from single-zircon U-Pb results, *Schweiz Mineral Petrogr Mitt*, *74* (3), 483-488, 1994.

Origoni Giobbi, E., B Testa, and R. Carimati, Contributo alla ricostruzione stratigrafica della "Serie dei Laghi". Litofacies principali della "Strona-Ceneri" a NE del Lago Maggiore (Alpi Meridionali - Italia), *Rend Soc Ital. Mineral. Petrol.*, *38*, 1337-1350, 1982.

Peacock, S M., Thermal modelling of metamorphic pressure-temperature-time paths: A forward approach, in *Metamorphic Pressure-Temperature-Time Paths*, *Short Course Geol. Ser*, Vol. 7, edited by F.S Spear and S M. Peacock, pp. 57-102, AGU, Washington, D.C , 1989

Percival, J.A., D M Fountain, and M H. Salisbury, Exposed crustal cross sections as windows on the lower crust, in *Continental Lower Crust*, *Dev Geotectonics*, Vol 23, edited by D.M. Fountain, R Arculus, and R W Kay, pp 317-362, Elsevier, New York, 1992

Pidgeon, R T , V. Köppel, and M Grünenfelder, U-Pb isotopic relationships in zircon suites from a para- and ortho-gneiss from the Ceneri Zone, southern Switzerland, *Contrib Mineral. Petrol*, *26*, 1-11, 1970.

Pin, C , Datation U-Pb sur zircons à 285 Ma du complexe gabbro-dioritique du Val Sesia -Val Mastallone et age tardi-hercynien du métamorphisme granulitique de la zone Ivrea-Verbano (Italie), *C R. Acad Sci Ser 2*, *303* (9), 827-830, 1986

Pinarelli, L., A Del Moro, and A Boriani, Rb-Sr geochronology of lower Permian plutonism in Massiccio dei Laghi, southern Alps (NW-Italy), *Rend Soc Ital Mineral Petrol.*, *43* (2), 411-428, 1988.

Quick, J E , S. Sinigoi, and A Mayer, Emplacement dynamics of a large mafic intrusion in the lower crust, Ivrea-Verbano Zone, northern Italy, *J. Geophys Res*, *99*, 21,559-21,573, 1994

Ragettli, R A., Vergleichende U-Xe und U-Pb Datierung an Zirkon und Monazit, Ph D thesis, Eidg. Techn. Hochsch Zurich, Switzerland, 1993

Reinhard, M, Ueber das Grundgebirge des Sottoceneri im Süd-Tessin und die darin auftretenden Ganggesteine, *Beitr Geol. Karte Schweiz*, *N F*, *117*, 1-89, 1964

Rivalenti, G , G. Garuti, and A Rossi, The origin of the Ivrea-Verbano basic formation (western Italian Alps): Whole-rock chemistry, *Boll. Soc. Geol. Ital*, *94*, 1149-1186, 1975.

Romer, R.L , and L Franz, Ordovician Barrow-type metamorphism in the Strona-Ceneri Zone (northern Italy) dated by U-Pb on staurolite, *Schweiz. Mineral. Petrogr Mitt.*, *78* (3), 383-395, 1998

Rutter, E H , K H. Brodie, and P J Evans, Structural geometry, lower crustal magmatic underplating and lithospheric stretching in the Ivrea-Verbano Zone, northern Italy, *J Struct Geol*, *15* (3-5), 647-662, 1993

Rutter, E H , J Khazanehdari, K H Brodie, D.J Blundell, and D A Waltham, Synthetic seismic reflection profile through the Ivrea Zone - Serie dei Laghi continental crustal section, northwestern Italy, *Geology*, *27*, 79-82, 1999.

Sanders, C A E , G Bertotti, G R Davies, and J R Wijbrans, Triassic pegmatites in the Mesozoic middle crust of the southern Alps (Italy) Fluid inclusions, radiometric dating and tectonic implications, *Eclogae Geol. Helv*, *89* (1), 505-525, 1996

Schmid, R., Zur Petrographie und Struktur der Zone von Ivrea-Verbano zwischen Valle d'Ossola und Val Grande (Prov Novara, Italien), *Schweiz. Mineral. Petrogr. Mitt.*, *48* (2), 305-314, 1967

Schmid, S M., Ivrea zone and adjacent southern Alpine basement, in *Pre-Mesozoic Geology in* *the Alps*, edited by J.F. von Raumer and F Neubauer, pp 567-583, Springer-Verlag, New York, 1993

Schmid, S.M., A. Zingg, and M.R. Handy, The kinematics of movements along the Insubric Line and the emplacement of the Ivrea Zone, *Tectonophysics*, *135*, 47-66, 1987

Schmid, S. M., H R. Aebli, F Heller, and A Zingg, The role of the Periadriatic Line in the tectonic evolution of the Alps, in *Alpine Tectonics*, edited by M.P Coward, D Dietrich, and R.G Park, *Geol Soc. Spec Publ*, *45*, 153-171, 1989.

Schönborn, G., Alpine tectonics and kinematic models of the central southern Alps, *Mem Sci Geol.*, *54*, 229-393, 1992.

Schönborn, G, and M E Schumacher, Controls on thrust tectonics along basement-cover detachment, *Schweiz Mineral Petrogr. Mitt*, *74* (3), 421-436, 1994

Schumacher, M E, G Schönborn, D Bernoulli, and H.P Laubscher, Rifting and collision in the southern Alps, in *Results of NRP-20 "Deep Structure of the Alps"*, edited by O A. Pfiffner et al, pp 186-204, Birkhäuser, Basel, Berlin, Boston, 1997

Sills, J D., and J Tarney, Petrogenesis and tectonic significance of amphibolites interlayered with meta-sedimentary gneisses in the Ivrea Zone, N.W Italy, *Tectonophysics*, *107*, 187-206, 1984

Smith, H A., and B. Barreiro, Monazite U-Pb dating of staurolite-grade metamorphism in pelitic schists, *Contrib. Mineral. Petrol*, *101*, 149-164, 1990

Spear, F., *Metamorphic Phase Equilibria and Pressure-Temperature-Time Paths, Monogr. Mineral Soc. Am.*, vol. 1, Mineral. Soc of Am, Washington, D.C., 1995

Spicher, A., Geologie und Petrographie des oberen Val d'Isone (südliches Tessin), *Schweiz. Mineral. Petrogr Mitt.*, *20* (1), 17-100, 1940

Stähle, V., G. Frenzel, and D F Mertz, Retrograde Metamorphose in anorthositischen Lagen von Finero (Zone von Ivrea), *Schweiz. Mineral Petrogr. Mitt.*, *66* (1-2), 73-98, 1986

Stähle, V, G. Frenzel, B Kober, A Michard, H. Puchelt, and W Schneider, Zircon syenite pegmatites in the Finero peridotite (Ivrea zone) Evidence for a syenite from a mantle source, *Earth Planet Sci. Lett*, *101*, 196-205, 1990.

Stampfli, G M., The Intra-Alpine Terrain. A Paleotethyan remnant in the Alpine Variscides, *Eclogae Geol Helv*, *89* (1), 13-42, 1996.

Steck, A, and J.-C. Tièche, Carte géologique de l'antiforme peridotique de Finero avec des observations sur les phases de deformation et de recristallisation, *Bull Mineral Petrogr. Suisse*, *56*, 501-512, 1976.

Steck, A, and J-C Tièche, Geologic Guide to the Testa di Misello Region, Finero Peridotitic Massif, Ivrea Zone, *Mem Sci. Geol*, *33*, 11-16, 1978/1979

Stille, P., and M Buletti, Nd-Sr isotopic characteristics of the Lugano volcanic rocks and constraints on the continental crust formation in the south Alpine domain (N-Italy, Switzerland), *Contrib. Mineral. Petrol.*, *96*, 140-150, 1987

Teufel, S, and U Schärer, Unravelling the age of high-grade metamorphism of the Ivrea Zone. A monazite single-grain and small fraction study, *Terra Abstr.*, *1*, 350, 1989.

Torsvik, T.H., M.A. Smethurst, J G Meert, R. Van der Voo, W.S McKerrow, M D. Brasier, B.A. Sturt, and H J Walderhaug, Continental break-up and collision in the Neoproterozoic and Paleozoic: A tale of Baltica and Laurentia, *Earth Sci Rev.*, *40*, 229-258, 1996

Vai, G.B, and T. Cocozza, Tentative schematic zonation of the Hercynian chain in Italy, *Bull Soc. Geol Fr*, *8*, 95-114, 1986

Valverde-Vaquero, P, and G.R. Dunning, New U-Pb ages from the Sierra de Guadarrama (Central Spain) Evidence for Early Ordovician "Sardic" magmatism in the Ollo de Sapo Domain of the central Iberian Zone (Iberian Massif), *J Geol. Soc London*, in press, 1999.

Vavra, G, D Gebauer, R Schmid, and W Compston, Multiple zircon growth and recrystallization during polyphase late Carboniferous to Triassic metamorphism in granulites of the Ivrea Zone (southern Alps). An ion microprobe (SHRIMP) study, *Contrib Mineral. Petrol*, *122*, pp. 337-358, 1996

Vogler, R., Die Ivrea Zone zwischen Val Grande und Val Pogallo (Provinz Novara, Italien), *Schweiz. Mineral Petrogr. Mitt.*, *72* (2), 241-249, 1992.

von Blanckenburg, F., and J.H. Davies, Slab breakoff A model for syncollisional magmatism and tectonics in the Alps, *Tectonics*, *14* (1), 120-131, 1995

von Quadt, A, A. Ferrario, V. Diella, W Hansmann, G. Vavra, and V. Köppel, U-Pb ages of zircons from chromites of the phlogopite peridotite of Finero, Ivrea Zone, northern Italy: Abstracts from the Ivrea-Verbano Zone Workshop, Varallo, Italy, *U.S. Geol. Surv. Circ.*, *1089*, 20, 1992

von Raumer, J, The Paleozoic evolution in the Alps From Gondwana to Pangea, *Geol Rundsch.*, *87*, 407-435, 1998

Voshage, H., A.W Hofman, M. Mazucchelli, G Rivalenti, S. Sinigoi, I. Raczek, and G. Demarchi, Isotopic evidence from the Ivrea Zone for a hybrid lower crust formed by magmatic underplating, *Nature*, *347*, 731-736, 1990.

Wagner, G A., and G M Reimer, Fission track tectonics: The tectonic interpretation of fission track apatite ages, *Earth Planet Sci Lett.*, *14*, 263-268, 1972

Walter, P., Das Ostende des basischen Gesteinszuges Ivrea-Verbano und die angrenzenden Teile der Tessiner Wurzelzone, *Schweiz Mineral. Petrogr Mitt.*, *30* (1), 1-144, 1950.

Weissert, H J, and D. Bernoulli, A transform margin in the Mesozoic Tethys: Evidence from the Swiss Alps, *Geol Rundsch.*, *74*, 665-679, 1985.

Wernicke, B, The fluid crustal layer and its implications for continental dynamics, in *Exposed Cross-Sections of the Continental Crust*, edited by M.H. Salisbury and D.M. Fountain, *NATO ASI Ser.*, *Ser C*, *317*, 509-544, 1990

Winterer, E.L., and A. Bosellini, Subsidence and sedimentation on Jurassic passive continental margin, southern margin, southern Alps, Italy, *Am. Assoc. Pet Geol. Bull.*, *65*, 394-421, 1981.

Wright, J.E, and J W Shervais, Emplacement age of the Balmuccia lherzolite massif, N W Italy, *Int Geol Congr 26th 1980. Precambrian*, *2*, 804, 1980

Ziegler, P.A, *Geological Atlas of Western and Central Europe*, 2nd ed., 239 pp., Shell Int Pet, Maatschappij B V, The Hague, 1990.

Zingg, A., Regional metamorphism in the Ivrea Zone (southern Alps, N-Italy): Field and microscopic investigations, *Schweiz. Mineral. Petrogr Mitt*, *60* (2-3), 153-179, 1980.

Zingg, A, The Ivrea and Strona-Ceneri Zones (southern Alps, Ticino and N-Italy): A review, *Schweiz. Mineral Petrogr Mitt.*, *63* (3), 361-392, 1983

Zingg, A., The Ivrea crustal cross-section (northern Italy and southern Switzerland), in *Exposed Cross-Sections of the Continental Crust*, edited by M.H Salisbury and D M Fountain, *NATO ASI Ser*, *Ser C*, *317*, 1-20, 1990

Zingg, A., and J C Hunziker, The age of movements along the Insubric Line west of Locarno (northern Italy and southern Switzerland), *Eclogae Geol. Helv*, *83* (3), 629-644, 1990.

Zingg, A., J C Hunziker, M Frey, and H Ahrendt, Age and degree of metamorphism of the Canavese Zone, *Schweiz. Mineral Petrogr. Mitt*, *56* (2), 361-375, 1976

Zingg, A., M.R. Handy, J.C. Hunziker, and S.M. Schmid, Tectonometamorphic history of the Ivrea Zone and its relationship to the crustal evolution of the southern Alps, *Tectonophysics*, *182*, 169-192, 1990.

Zurbriggen, R, Crustal genesis and uplift history of the Strona-Ceneri Zone (southern Alps), Ph D. thesis, Univ of Bern, Switzerland, 1996

Zurbriggen, R., L. Franz, and M.R Handy, Pre-Variscan deformation, metamorphism and magmatism in the Strona-Ceneri Zone (southern Alps of northern Italy and southern Switzerland), *Schweiz Mineral Petrogr. Mitt*, *77* (3), 361-380, 1997

Zurbriggen, R, B Kamber, M.R. Handy, and R. Nägler, Dating syn-magmatic folds A case study of Schlingen structures in the Strona-Ceneri Zone (southern Alps, northern Italy), *J Metamorph Geol.*, *16* (3), 403-414, 1998.

L. Franz, Mineralogisches Institut, Bergakademie, Brennhausgasse 14, D-09596 Freiberg, Germany

M. R Handy and B Janott, Institut für Geowissenschaften, Senckenbergstr. 3, D-35390 Giessen, Germany. (mark handy@geo.uni-giessen.de)

F. Heller, Institut für Geophysik, ETH-Hönggerberg, CH-8093 Zürich, Switzerland

R Zurbriggen, Geologisches Institut, Balzerstr 1, CH-3012 Bern, Switzerland

(Received January 5, 1998,
revised May 13, 1999;
accepted June 3, 1999.)

TECTONICS, VOL. 18, NO. 6, PAGES 950-966 DECEMBER 1999

Arc-continent collision in Papua Guinea: Constraints from fission track thermochronology

Kevin C. Hill and Asaf Raza[1]

Australian Geodynamics Cooperative Research Centre, Department of Earth Sciences, La Trobe University, Melbourne Victoria, Australia

Abstract. The Papua New Guinea (PNG) Mobile Belt adjacent to the Finisterre Arc was formerly the leading NE corner of the Australian plate that converged obliquely with the Pacific plate. Forty new apatite and zircon fission track analyses of Mobile Belt rocks previously dated by K-Ar and Rb-Sr analyses constrain Neogene time-temperature paths and tectonic models. The Paleogene arc along the southern margin of the Caroline plate was juxtaposed against PNG in the early Miocene, coeval with locking up of the west dipping Solomon subduction zone by the Ontong Java Plateau. These events initiated wrenching along the northern PNG margin and increased westward subduction of the Solomon Sea plate beneath the eastern margin. The Mobile Belt underwent extension above the downgoing slab with rapid cooling of metamorphic rocks at ~17 Ma, immediately prior to emplacement of the Maramuni Arc from 17 to 12 Ma. A change in plate motion at ~12-10 Ma terminated the arc and caused PNG-Caroline plate convergence, creating the orogenic belt in New Guinea from 12 to 4 Ma. This resulted in ~4.5 km of uplift and ~3 km of denudation and cooling of the entire Mobile Belt in the late Miocene, propagating westward along the Mobile Belt at 8-5 Ma and southward into the Fold Belt at 5-4 Ma. The compression caused thrusting of Miocene strata within the Mesozoic type section. A further change in plate motion at 4-3 Ma returned the margin to transpression with local compression along strike-slip faults and ongoing collision of the Finisterre Arc terrane.

1. Introduction

Understanding the collision of the Finisterre Arc with Papua New Guinea (PNG) and the timing and nature of deformation in the adjacent Mobile Belt is crucial to any tectonic reconstruction of New Guinea (Figure 1). Located on the NE corner of the Australian craton, the Finisterre area is a sensitive recorder of Pacific-Australia convergence throughout the Tertiary, particularly Neogene changes in plate motion and arc-continent collision. Using fission track analysis to determine the Neogene low-temperature cooling history of rocks of known stratigraphic or emplacement age, mainly Mesozoic, it is possible to date tectonic events and estimate their magnitude. This in turn allows construction of a new tectonic model.

The orogenic belt through PNG records the Neogene to Recent collision of an arc and/or terranes with the northern margin of the Australian continent, a modern analogue for Mesozoic orogenesis in western North America [*Silver and Smith*, 1983]. The driving force for the collisions has been Eocene to Recent oblique convergence between the Australian and Pacific plates. Within that regional context the PNG margin has directly interacted with the intervening Philippine, Caroline, Bismarck, and Solomon plates/microplates (Figure 1).

North of New Guinea, a subduction zone was lost in the late Oligocene - early Miocene, commensurate with the onset of arc-continent collision [e.g., *Jaques and Robinson*, 1977; *Hall*, 1997], which in the PNG Mobile Belt is recorded by rapid early Miocene cooling of medium- to high-grade metamorphic rocks (Figure 2). Middle Miocene intrusion of the Maramuni Arc along the PNG margin followed (see Figure 2 for references). This preceded middle to late Miocene-Pliocene thrusting and folding of the Mobile and Fold Belts in PNG, interpreted by many authors to have been due to collision with the Finisterre Arc (Figures 1 and 2).

Studies of earthquake focal plane solutions and restoration of present plate motions have constrained models of the collision process, particularly that of the Finisterre Arc with PNG, overriding the doubly subducting Solomon Sea Plate (Figure 1) [e.g., *Ripper and McCue*, 1983; *Pegler et al.*, 1995; *Hall*, 1997]. This area is well constrained geophysically, but the onshore geology and structural events are less well known owing to poor exposure and difficult access to the jungle-covered, equatorial mountains. It is generally agreed that the Finisterre and Adelbert Ranges were part of a Paleogene volcanic arc [*Jaques*, 1976] that, following late Oligocene plate realignment, collided with PNG in the Neogene, but the exact timing of collision and its relation to the deformation in PNG are contentious (Figure 2).

Application of zircon and apatite fission track (ZFT and AFT) analyses can constrain the time, amount, and rate of cooling of samples which, in turn, can constrain the time(s) and style(s) of deformation and/or igneous activity. ZFT and AFT analyses have closure temperatures of 280°±30°C and 110°±10°C, respectively [e.g., *Stockhert et al.*, 1999]. In the PNG context, ZFT analysis constrains the time of postmetamorphic or igneous cooling. As the PNG samples are mainly Mesozoic and lie at surface in a mountain belt in which denudation rates are amongst the highest in the world

[1]Now at School of Earth Sciences, University of Melbourne, Parkville, Victoria, Australia.

Paper number 1999TC900043.
0278-7407/99/1999TC900043$12.00

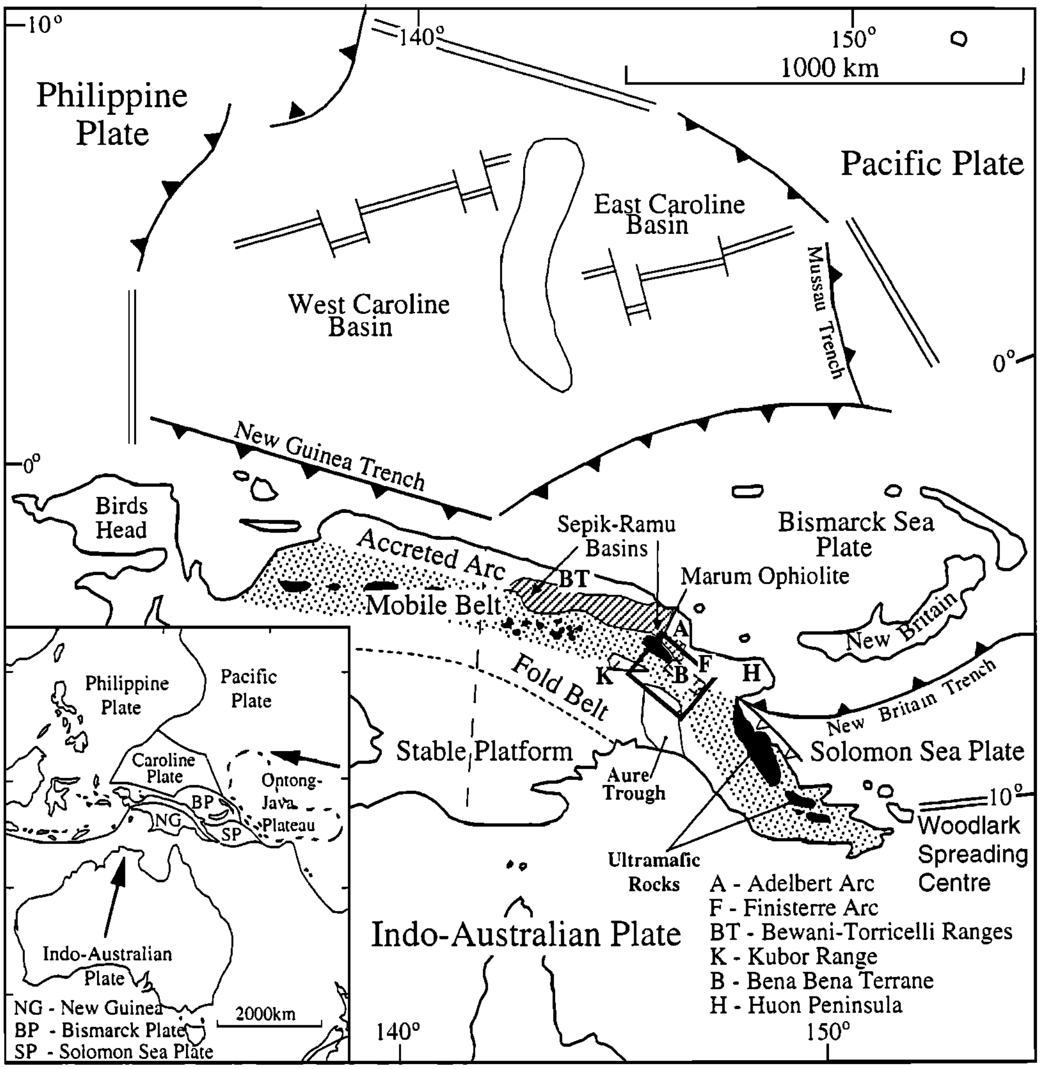

Figure 1. Plate tectonic setting of New Guinea. The box outlines the study area. Pacific-Australian plate convergence has occurred since at least the Eocene and is recorded by the structural belts in Papua New Guinea (PNG): the continental Fly Platform/Fold Belt in the south; the igneous, metamorphic and ophiolitic Mobile Belt in the center; and in the north the Neogene Sepik and Ramu Basins bound by the accreted Volcanic Arc along the north coast [after *Dow*, 1977] (details of the Caroline plate after *Hegarty and Weissel* [1988]). Collision of the Volcanic Arc occurred in the Neogene-Recent, and collision of the Finisterre Arc is ongoing.

[*Ludwig and Probst*, 1998; *Milliman*, 1995], the Neogene cooling from AFT analysis can reasonably be attributed to mountain building and denudation, resulting from orogenesis. When both analyses are applied to samples for which other radiometric ages have been obtained, the resulting time-temperature history strongly constrains models of the tectonic events.

Previous AFT studies in NW PNG indicated cooling in response to uplift and denudation mainly between 8 and 5 Ma [*Crowhurst et al.*, 1996] while those in the Fold Belt throughout New Guinea yielded cooling ages of 4±1 Ma and younger [*Hill and Gleadow*, 1989; *Kendrick et al.*, 1995; *Weiland and Cloos*, 1996]. In the present study of the Mobile Belt adjacent to the Finisterre Range, AFT and ZFT analyses have been carried out on a wide range of previously dated rock types [*Page*, 1976] to determine the time-temperature history and hence the geodynamics of arc-continent collision. In this study, the Australian Geological Survey Organization (AGSO) time-scale [*Young and Laurie*, 1996] is used, particularly important for the start of the early Miocene (23.8 Ma), middle Miocene (16.4 Ma), late Miocene (11.2 Ma), Pliocene (5.32 Ma) and Pleistocene (1.78 Ma).

2. Study Area and Sampling

The study area in northern PNG includes part of the Mobile Belt and the accreted Volcanic Arc (Figures 1 and 3). The area was geologically mapped at a 1:250,000 scale by the Australian Bureau of Mineral Resources (now AGSO) in the 1970s and 1980s, including considerable K-Ar and Rb-Sr

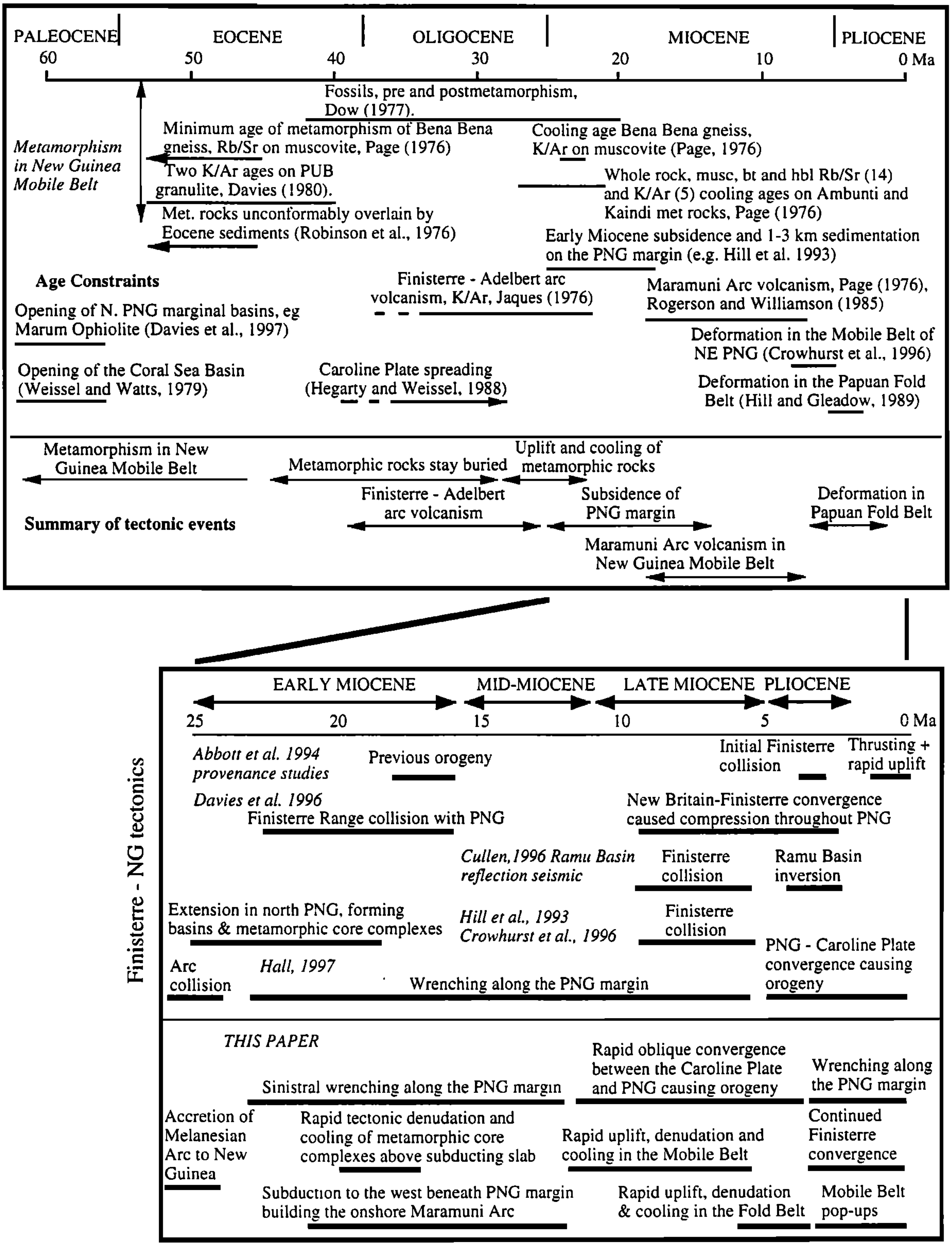

Figure 2. (top) A summary of the main tectonic events in Papua New Guinea and relevant literature. Note particularly the early Miocene cooling of metamorphic rocks and subsidence of the PNG margin, the middle Miocene Maramuni Arc along the PNG margin, and the late Miocene-Pliocene deformation in PNG. PUB, Papuan Ultramafic Belt. (bottom) Recent models for collision of the Finisterre Arc with PNG, including the one presented here.

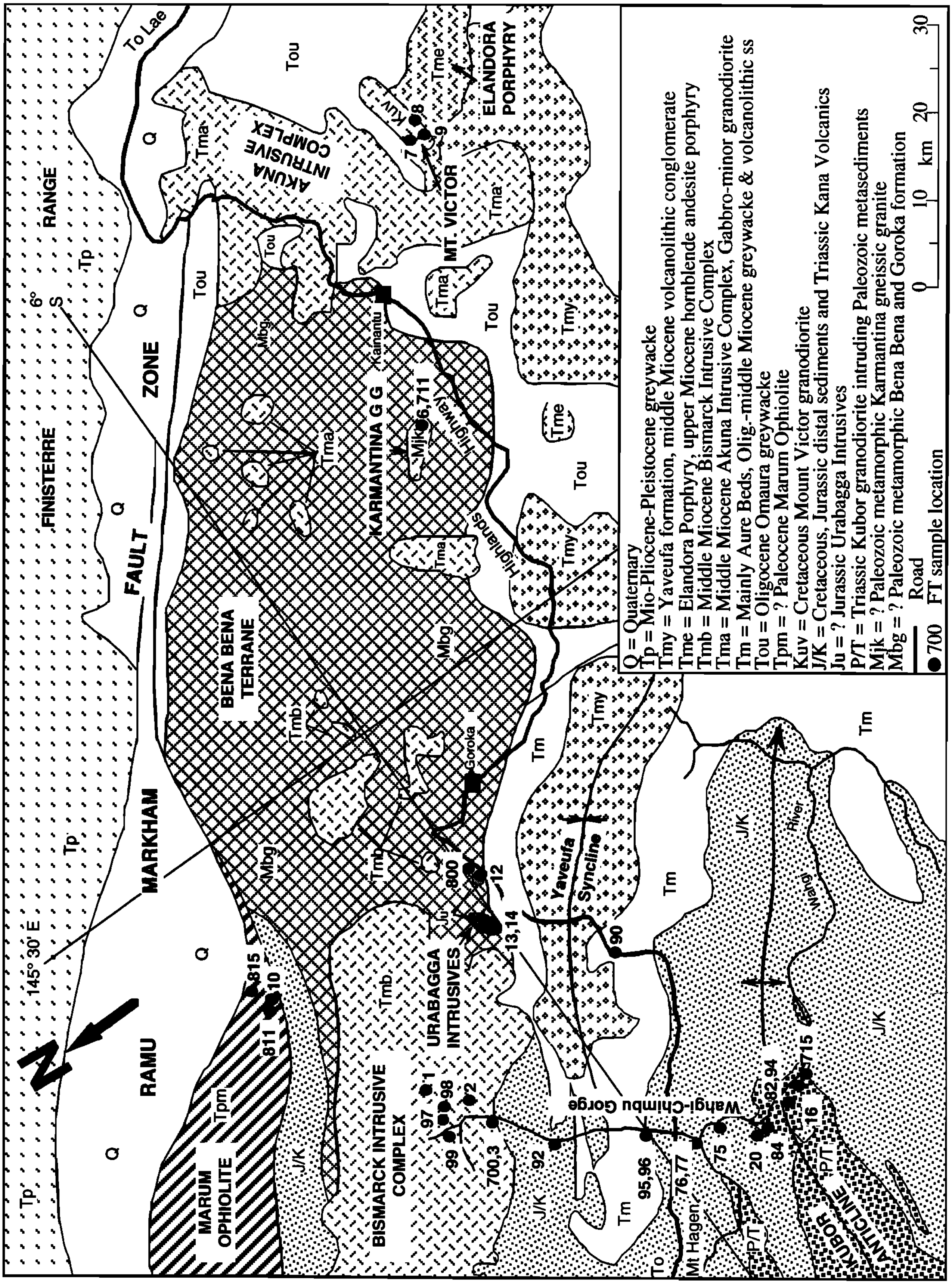

Figure 3. Summary geological map of the study area showing the main tectono-stratigraphic units and the location of samples analyzed. Sedimentary samples were collected along the Wahgi-Chimbu Gorge, the type section, between the Kubor Anticline and Bismarck Intrusive Complex. See Figure 1 for location and Figure 4 for stratigraphic relationships. ss, sandstone.

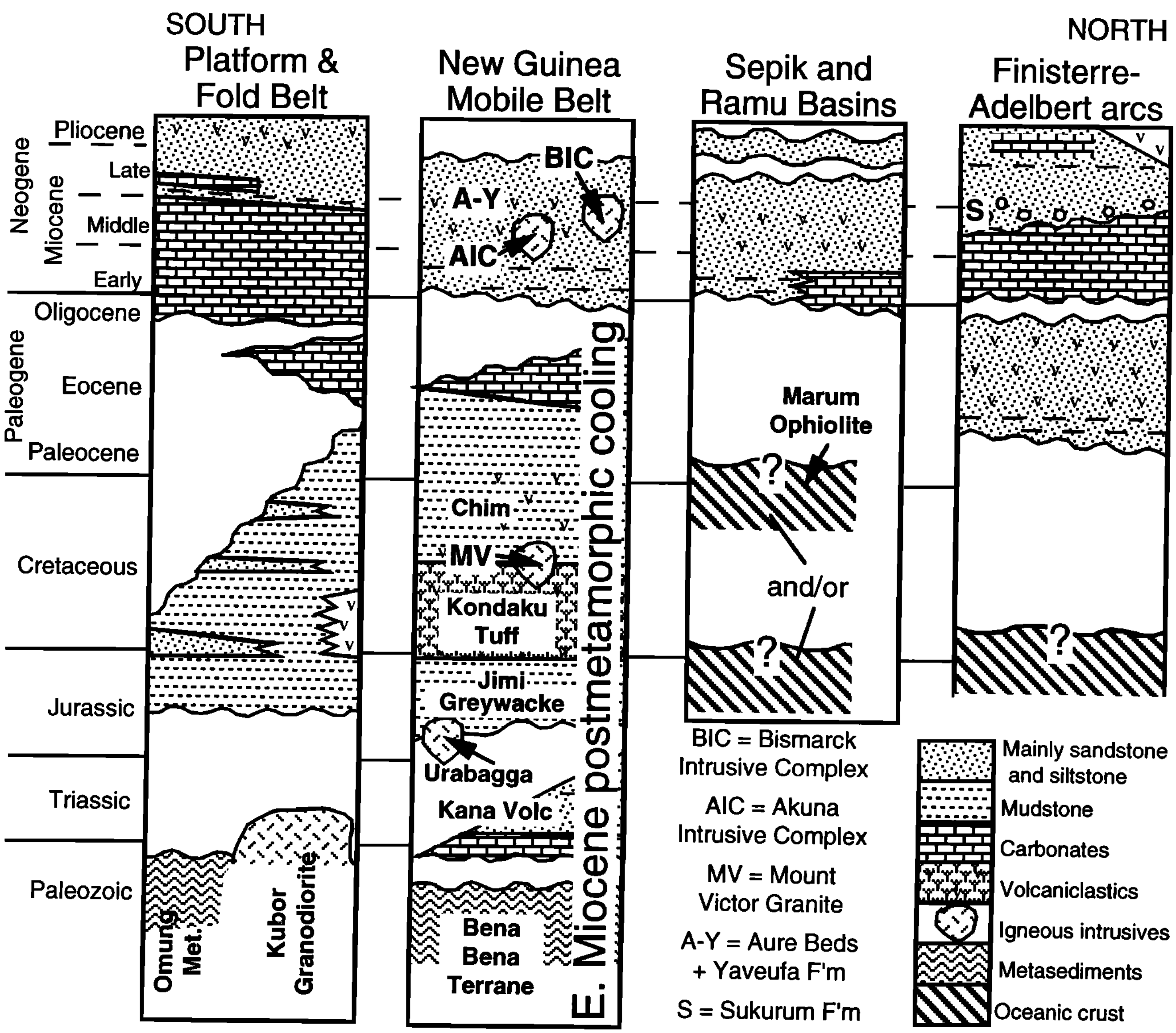

Figure 4. Simplified stratigraphic sections for the main orogenic belts in Papua New Guinea (see Figure 1), showing the units analyzed in this study.

dating by *Page* [1976], which laid the foundation for all subsequent tectonic models.

The area is bound to the SW by the ~1250 km^2 upthrust basement outcrop that makes up the 3000 m high Kubor Ranges (Figures 1 and 3). These comprise Triassic Kubor Granodiorite intruding the less well exposed Paleozoic greenschist-grade Omung Metamorphics [*Page*, 1976]. The NE portion of the study area is bound by the Ramu-Markham Valley, which overlies the suture between the accreted arc and the Mobile Belt. Along strike the Ramu Basin contains early Miocene carbonates and basinal sediments overlain by volcaniclastics thought to be derived from the late early to middle Miocene Maramuni Arc.

Between the Kubor Range and the Ramu-Markham Valley are five tectonostratigraphic units or terranes (Figures 3 and 4). The Bena Bena terrane in the east largely consists of low- to medium-grade ?Paleozoic metamorphic rocks such as the Bena Bena and Goroka Formations and the Karmantina Gneissic Granite, although isotopic dating of the latter indicated subsequent early Miocene cooling [*Page*, 1976]. The Bena Bena terrane was intruded by the Akuna Intrusive Complex in the middle Miocene (17-14 Ma), but there is also a Cretaceous granite at Mount Victor.

West of the Bena Bena terrane is the Bismarck Intrusive Complex of middle to late Miocene age (12.5 - 8 Ma) [*Page*, 1976], a few million years younger than the Akuna Intrusive Complex, although part of the same Maramuni Arc system. South of the Bena Bena terrane, overlying Oligocene greywackes, are extensive middle Miocene volcanolithic sediments of the Yaveufa Formation, probably the surface expression of the adjacent Akuna and Bismarck Intrusive Complexes. The northern margin of the Bismarck Intrusive Complex is overthrust by the Paleocene or older Marum Ophiolite. In contrast, between the Bismarck Intrusive Complex and the Kubor Range, highly faulted distal Mesozoic sediments crop out, including the type section along the Wahgi-Chimbu Gorge (Figure 3).

Utilizing the limited road network, *Forwood* [1990] and *Rodda* [1990] collected samples from each of the above units/terranes, which have been used for fission track analysis. Where possible, the areas sampled were the same as those analyzed by *Page* [1976] so that the intrusion/protolith age of the rocks was known and the fission track analyses could be used to determine the low-temperature history. The location of the samples and their ages and lithologies are shown in Figures 3 and 4 and Table 1, with detailed information in appendix A[1].

3. Fission Track Analysis

In many heavy minerals, such as apatite and zircon, trace amounts of ^{238}U undergo spontaneous fission, leaving tracks of radiation damage that can be made visible under the microscope by etching with acid [*Gleadow et al.*, 1986]. In apatite the tracks are initially 16±1 μm long. The number of tracks accumulated in a mineral can be related to the Uranium content and the time over which they have been retained, a measure of the geological age [*Naeser*, 1979; *Gleadow et al.*, 1983, 1986]. At high temperatures the radiation damage is rapidly repaired, so the tracks are annealed, but at more moderate temperatures the tracks are only partially annealed. The partial annealing zone (PAZ) for zircon is ~210°-320°C for geological heating times of the order of 10^7 years [*Tagami et al.*, 1998]. For samples that cooled rapidly through the PAZ and remain below PAZ temperatures, the fission track age records the time of cooling below ~280°C [*Stockhert et al.*, 1999]. In this study the ZFT ages are interpreted to date the postigneous or postmetamorphism cooling age of the rock.

The PAZ for apatite is ~60°-110°C [*Laslett et al.*, 1987], and samples that cooled rapidly and remain below those temperatures record the time of cooling below ~100°C and retain mean fission track lengths of >13 μm [*Gleadow et al.*, 1983]. If the apatites are subsequently heated to PAZ temperatures, for instance, because of burial or nearby igneous intrusion, the tracks are partially annealed, giving reduced ages and often a wide spread in track lengths and single-grain ages [e.g., *Green et al.*, 1986, 1989]. Such samples are termed partially annealed and commonly yield a mixed AFT age that is intermediate between the original cooling age and the cooling age following subsequent heating. Such an AFT age cannot be used directly to date a geologic cooling event, but analysis of the age distributions from many crystals in one sample can constrain the interpretation [*Galbraith*, 1990].

To obtain and interpret an AFT age, the track densities from 20 or more crystals from a sample are determined, and 100 or more track lengths are measured to specify the mean length and the length distribution. The chi-square probability relates to the dispersal of the single-grain results within each fission track age determination. If *P*(chi-square) is >5% and the track length is ≥13 μm (volcanic distribution of *Gleadow et al.* [1983]), then the central age [*Galbraith and Laslett*, 1993] is likely to record a discrete cooling event. Lower probabilities and shorter mean track lengths imply that there is real variation in the fission track ages of individual grains, which usually results from a mixed source, a significant degree of thermal annealing, or compositional variation.

Apatites and zircons were separated from 1-2 kg samples using standard heavy liquid and magnetic techniques. Samples were irradiated in a well-thermalized neutron flux in the X-7 position at the High Flux Australian Reactor at Lucas Heights. The fission track ages and lengths were determined using the zeta calibration and external detector methods. Ages were determined by K. C. Hill using an apatite zeta = 350±5 and a zircon zeta = 84 ± 3 for U3 glass or = 118 ± 3 for Corning (CN) 1 glass. The lengths were determined by A. Raza. The results were analyzed following the principles of *Naeser* [1979], *Gleadow et al.* [1983, 1986], and *Green et al.* [1986, 1989]. Track lengths were not measured for zircons as the annealing temperature versus length relationships are not well constrained. During zircon counting several samples were found to be partially underetched as old grains with substantial radiation damage etch faster than less damaged younger grains and the old grains are destroyed by the long etching time needed to reveal the tracks in the younger grains. New mounts were made and etched for a more appropriate period.

4. Modeling

The results below were modeled using the understanding of the AFT system described by *Green et al.* [1989], based on an empirical kinetic description of laboratory annealing data in Durango apatite [*Green et al.*, 1986; *Laslett et al.*, 1987]. A best fit thermal history, consistent with the data, was obtained using the *Laslett et al.* [1987] quantitative treatment of annealing to forward computer model track shortening and age evolution through likely thermal histories, for an apatite composition equal to that of Durango (0.4 wt % Cl). The geological constraints were input, such as the age of the rock, the known cooling to surface temperatures for plutons and metamorphic rocks, heating due to burial by adjacent sedimentary packages, and exhumation to the surface at the present day. Within those constraints the Monte Carlo simulation technique of *Gallagher* [1995] was applied, which statistically tests numerous possible thermal histories against the observed AFT data, including a genetic algorithm to rapidly converge on an acceptable fit.

It is important to note that such modeling is normally only considered valid if at least 50 and preferably 100 AFT length measurements have been obtained. In this study only two samples, both Miocene granites, met those criteria.

[1] Supporting appendix A is available on diskette or via Anonymous FTP from kosmos.agu.org, directory APEND (Username=anonymous, Password=guest). Diskette may be ordered by mail from AGU, 2000 Florida Ave, NW, Washington, DC 20009 or by phone at 800-966-2481; $15.00. Payment must accompany order.

Table 1. Analytical, Apatite and Zircon Fission Track Age for 33 Outcrop Samples From the New Guinea Mobile Belt

Sample Number	Lat and Long, deg	Elevation, m	Formation	Stratigraphic Age	No of Grains/ Count Quality	Standard Track Density, 10^6 cm^{-2}	Fossil Track Density, 10^6 cm^{-2}	Induced Track Density, 10^6 cm^{-2}	Uranium Content, ppm	Age Dispersion $P(\chi^2)$, %	Age Dispersion RE, %	Fission Track Central Age, Ma	Mean Track Length, µm	s d, µm
				Kubor Granite and Omung Metamorphics										
715Z	144°56 2'E, 6°9 9'S	1645	Kubor Granodiorite	Triassic (240 Ma)	5	0 590 (4297)	13 33 (1754)	1 702 (224)	154	41	0 5	191±14		
715A	144°56 2'E, 6°9 9'S	1645	Kubor Granodiorite	Triassic (240 Ma)	20-G	1 158 (2602)	0 016 (15)	0 497 (460)	6	67	10	6 6±1 7	7 8 ± 0 9 (31)	4 8
16A	144°56 1'E, 6°9 4'S	1569	Kubor Granodiorite	Triassic (240 Ma)	20-E	1 170 (2602)	0 025 (23)	0.524 (483)	6	56	16	9 8±2 1	13 0 ± 0 5 (40)	3 3
82A-F	144°55 6'E, 6°8 0'S	1602	Omung? Metamorphics	Paleozoic	9-P	1 146 (2602)	0 184 (43)	0 646 (151)	7	7	45	57 2±15	13 7 ± 0.0 (1)	-
94A	144°55 6'E, 6°8 0'S	1488	Omung Metamorphics	Paleozoic	11-P	1 181 (2602)	0 045 (13)	0 540 (156)	6	21	65	16 1±6	-	-
84Z	144°55 2'E, 6°6 2'S	1428	Omung Metamorphics	Paleozoic	6	0 604 (4297)	17 83 (2808)	2 05 (323)	181	0	30	242±34	-	-
84A	144°55 2'E, 6°6 2'S	1428	Omung Metamorphics	Paleozoic	19-P	1 192 (2602)	0 024 (17)	0 476 (342)	5	0	108	12 1±4 5	14 1 ± 0 6 (7)	1 6
				Mount Victor Granodiorite										
7A	145°59 3'E, 6°25 7'S	1620	Mt Victor granodiorite	Cretaceous (95 Ma)	16-G	1 188 (5488)	0 079 (27)	1 935 (660)	21	22	35	8 6±1 9	12 8 ± 0 5 (46)	3 5
8A	145°59 5'E, 6°25 1'S		Mt Victor granodiorite	Cretaceous (95 Ma)	20-E	1 266 (5488)	0 140 (108)	2 917 (2258)	30	34	6	10 6±1 1	13 6 ± 0 7 (27)	3 6
8Z	145°59 5'E, 6°25 1'S		Mt Victor granodiorite	Cretaceous (95 Ma)	10	0 639 (4297)	8 514 (1068)	1 937 (243)	162	8	16	113±11	-	-
9Z	145°59 5'E, 6°25 1'S		Mt Victor granodiorite	Cretaceous (95 Ma)	9	0 646 (4297)	10 74 (1315)	2 499 (306)	206	27	4	115±8	-	-
				Goroka Formation, Urabagga Intrusives and Karmantina Gneissic Granite										
800A	145°18 3'E, 6°0 5'S	1453	Goroka Formation	Mesozoic	14-P	1 165 (5488)	0 014 (5)	0 568 (205)	6	95	0 2	5 0±2 2	15 5 ± 1 3 (2)	1 8
12A	145°18 0'E, 6°0 9'S	1635	Urabagga intrusives	E Jurassic (185 Ma)	20-M	1 173 (5488)	0 002 (2)	0 189 (155)	2	83	2 5	2 6±1 9	11 5 ± 1 1 (12)	3 8
711Z-F	145°42 9'E, 6°13 9'S	1490	Karmantina gneiss	Jurassic (170 Ma)	10	0 784 (3723)	4 922 (2497)	12 16 (6169)	604	0	98	34 7±27	-	-
				Mesozoic Sediments										
92A-F	145°2 6'E, 5°54 6'S	1785	Kana Volcanics	Triassic	25-E	1 433 (2987)	0 035 (50)	0 688 (975)	6	0	76	13 6±3 0	13 7 ± 1 8 (2)	2 5
81Z	145°3 5'E, 5°54 1'S	1950	Kana Volcanics???	L Miocene	2	0 471 (1804)	1 045 (75)	4 764 (342)	395	0	35	6 1±1 7	-	-
20A	144°55 5'E, 6°5 8'S	1534	Jimi Greywacke	Jurassic	15-M	1 204 (2602)	0 110 (53)	1 013 (489)	11	0	129	24 2±8 9	14 5 ± 0 0 (1)	-
75A	144°56 9'E, 6°4 3'S	1495	Kondaku Tuff	E Cretaceous	15-P	1 112 (2602)	0 045 (13)	0 517 (149)	6	0	141	20 1±9 5	-	-
76Z	144°57 0'E, 6°2 2'S	1315	Base Chim???	L Miocene	20	0 900 (3723)	0 392 (293)	2 621 (1961)	114	96	0 0	7 9±0 5	-	-
76A	144°57 0'E, 6°2 2'S	1315	Base Chim???	L Miocene	22-G	1 124 (2602)	0 228 (159)	1 076 (750)	13	0	71	34 9±6 5	14 5 ± 0 5 (29)	2 8
95Z	144°59 2'E, 6°0 2'S	1538	Chim formation	L Cretaceous	8	0 618 (4297	5 667 (612)	1 194 (129)	103	0	49	97±21	-	-
95A	144°59 2'E, 6°0 2'S	1538	Chim formation	L Cretaceous	20-G	1 462 (2987)	0 016 (21)	0 234 (306)	2	26	68	16 3±4 9	16 2 ± 0 0 (1)	-
96A	144°59 2'E, 6°0 2'S	1779	Chim formation	L Cretaceous	21-G	1 492 (2987)	0 015 (12)	0 261 (203)	2	4	123	14 3±5 9	13 3 ± 1 9 (7)	4 9
77Z	144°57 0'E, 6°2 2'S	1345	Chim Formation	L Cretaceous	10	0 584 (4297)	5 731 (2907)	0 530 (269)	47	0	77	215±55	-	-
77A	144°57 0'E, 6°2 2'S	1345	Chim Formation	L Cretaceous	20-G	1 135 (2602)	0 050 (54)	0 813 (876)	9	0	104	14 3±4 3	14 1 ± 0 6 (15)	2 4
				Marum Ophiolite										
10A	145°18 4'E, 5°44 8'S	735	Marum Ophiolite	Paleocene	15-M	1 200 (5488)	0 183 (66)	0 967 (348)	11	0	73	35 9±8 7	-	-
811A	145°18 2'E, 5°44 5'S	710	Marum Ophiolite	Paleocene	30-G	1 212 (5488)	0 015 (14)	0 638 (615)	7	10	47	5 1±1 5	16 00 ± 0 1 (2)	0 2
815A	145°19 2'E, 5°43 7'S	228	Marum Ophiolite	Paleocene	7-P	1 239 (5488)	0 138 (32)	0 778 (180)	8	0	92	63 7±24	-	-
				Akuna and Bismarck Intrusive Complexes										
6A-F	145°42 9'E, 6°13 9'S	1490	Akuna Intrusive	Miocene	20-G	1 180 (5488)	0 089 (32)	2 195 (789)	24	0	53	12 7±3 0	13 3 ± 2.8 (4)	5 6
1A	145°8 1'E, 5°49 7'S	2987	Bismarck Intrusive	Miocene	15-P	1 256 (2987)	0.199 (55)	1 602 (442)	17	0	133	25 7± 10	13 7 ± 0 8 (2)	1 2
2A-F	145°7 2'E, 5°51 5'S	2524	Bismarck Intrusive	Miocene	19-G	1 315 (2987)	0 057 (52)	1 942 (1746)	19	45	13	6 8±1	14 7 ± 0 5 (29)	2 6
3Z-F	145°5 7'E, 5°52 4'S	2017	Bismarck Intrusive?	Miocene	9	0 842 (3723)	1 559 (648)	3 161 (1314)	146	54	0 1	24 7±1 3	-	-
3A-F	145°5 7'E, 5°52 4'S	2017	Bismarck Intrusive?	Miocene	20-E	1 403 (2987)	0 075 (65)	2 302 (1983)	22	26	31	8 1±1 2	14 3 ± 0 3 (70)	2 1
13A-F	145°15 3'E, 5°59 9'S	1640	Bismarck Intrusive	Miocene	20-E	1 251 (5488)	0 237 (221)	5 416 (5045)	57	26	11	9 6±0 7	14 8 ± 0 2 (100)	1 8
14Z-F	145°15 3'E, 5°59 9'S	1640	Bismarck Intrusive	Miocene	5	0 632 (4297)	4 467 (932)	9 515 (1985)	803	78	0 0	12 4±0 5		
97A-F	145°7 0'E, 5°49 8'S	2514	Bismarck Intrusive	Miocene	22-E	1 216 (2602)	0 048 (53)	1 457 (1611)	16	88	1 0	7 0±1 0	14 8 ± 0 36 (20)	1 2
98Z	145°7 3'E, 5°49 9'S	2581	Bismarck Intrusive	Miocene	22	0 484 (1804)	0 288 (275)	1 395 (1330)	112	29	11	6 3±0 5	-	-
98A	145°7 3'E, 5°49 9'S	2581	Bismarck Intrusive	Miocene	20-G	1 286 (2987)	0 012 (8)	0 634 (440)	7	20	67	4 2±1 6	13 0 ± 0 6 (35)	3 6
99A-F	145°6 5'E, 5°49 7'S	2489	Bismarck Intrusive	Miocene	20-G	1 345 (2987)	0 048 (37)	0 706 (544)	7	8	60	15 2±3 4	14 9 ± 0 4 (23)	1 8
700A-F*	145°5 7'E, 5°52 4'S	2017	Bismarck Intrusive	Miocene										
				Miocene Sediments-Volcanics										
90A	145°9 1'E, 6°5 1'S	1500	Yaveufa Formation	Miocene	13-M	1 157 (5488)	0 224 (93)	1 097 (456)	7	0	65	35 0±7 8	12 6 ± 0 7 (7)	1 8

See Appendix A and the work of *Forward* [1990] and *Rodda* [1990] for full sample details Good to excellent quality samples with chi-square probabilities >5% record the time of significant geological cooling events Errors are quoted at the level of one standard deviation throughout The quality of each apatite mount is assessed in terms of the number of fractures and dislocations present, the number of apatite grains present and the average size of the apatite grains E, excellent, G, good, M, moderate, P, poor The chi-square probability relates to the dispersal of the single-grain results within each fission track age determination The P(chi-square) value gives a measure of the probability that all grains belong to a single population If P(chi-square) is >5%, then the central age [*Galbraith and Laslett*, 1993] is likely to record a single cooling event Lower probabilities imply that there is real variation in the fission track ages of individual grains, which usually results from a mixed source or from a significant degree of thermal annealing The following ages were determined by K C Hill apatite zeta, 350±5 for nbs glass, zircon zeta, 84 ± 3 for U3 glass, except Z-2 samples where zeta = 118 ± 3 for CN I glass Lengths were determined by A Raza Z, zircon, A, apatite, Lat, latitude, Long, longitude, RE, relative error

* Sample had insufficient apatite for determining count quality

Table 2. A Summary of the Main FT Results Reported Here and Their Interpretation

Rock	Previous Age	FT Samples	ZFT Interpretation	AFT Interpretation
Kubor Granite intruding Omung Metamorphics	Triassic (244 Ma) intruding late Paleozoic	715Z, 715A 16A, 82A 84A, 94A	slow cooling of Triassic intrusion passing through ~200°C isotherm in the Early Jurassic	burial to <3 km prior to late Miocene uplift and erosion at 7-10 Ma
Mount Victor Granodiorite	Mid-Cretaceous 90-95 Ma	8Z, 9A, 7A, 8A	cooling below ~200°C in the Aptian, 115±6 Ma	Uplift and erosion in the late Miocene at 9-11 Ma
Karmantina Gneissic Granite	Jurassic but cooled at 23 Ma	711Z	Mesozoic intrusion but cooled below 200°C at 17 Ma	
Urabagga Granite intruding Goroka Formation	Early Jurassic intruding late Paleozoic	800A, 12A		latest Miocene - Pliocene cooling due to uplift and erosion
Kondaku Tuff - Chim Formation boundary	Mid-Cretaceous	76Z, 76A	late Miocene Aure Group inlier, 8 0±0 5 Ma	Late Cretaceous and Miocene provenances, not significantly heated after deposition
Chim Formation	Late Cretaceous	77Z, 95Z, 77A, 95A, 96A	Late Cretaceous deposition with late Paleozoic-Triassic grains one sample possibly Oligocene?	burial to temperatures of <120°C prior to middle to late Miocene cooling
Jimi Greywacke, Kana Volcanics, and Kondaku Tuff	Jurassic, Triassic, and Early Cretaceous	20A, 92A, 75A, 81Z	Kana sample is really Aure Beds, ~6 Ma, overthrust by Kana Volc at <6 Ma	burial to temperatures of <120°C prior to late Miocene to Pliocene cooling
Marum Ophiolite	Paleocene or Mesozoic	10A, 811A, 815A		Paleogene ophiolite, uplift at 5 1±1 5 Ma
Akuna Intrusive Complex	15-17 Ma	6A		middle - late Miocene uplift and erosion and Pliocene reactivation
Bismarck Intrusive Complex	12 5 Ma with pegmatites at 8-9 Ma	3Z, 14Z, 98Z, 1A, 2A, 3A 97A, 98A, 99A, 13A	Oligocene diorite in S, 25±1 Ma middle Miocene monzodiorite in SE at 12 4±0 5 Ma, late Miocene diorite in center at 6 3±0 5 Ma	Rapid uplift and erosion at 10-7 Ma

The estimated amounts of burial and denudation are derived from temperature estimates assuming paleotemperature gradients of 30°C/km FT, fission track

5. Results and Interpretation

A total of 33 samples were processed, 28 for AFT analysis and 12 for ZFT analysis. Sixteen of the apatite samples yielded enough apatite to count 20 or more grains, and only three samples had <10 grains. Seventeen were of good to excellent quality, while 11 were moderate to poor, based on the number of fractures and dislocations present and the size and number of apatite grains present. The good to excellent samples are emphasized in the interpretation. Because of the young AFT ages and low Uranium content, there was a paucity of measurable track lengths. In only one AFT sample were the desired 100 track lengths measured, while the average number measured was 29. Six of the zircon samples had a total of ≥10 crystals counted, while five had between 5 and 10 crystals counted. The full analytical results are shown in Table 1 with a summary of the interpretations in Table 2; the detailed FT age, length and radial plots, as well as the full modeling results are shown in Figures A1 and A2.

The results are reported in sections 5.1-5.8 in order from the stratigraphic oldest to youngest samples. Sample numbers are followed by an A or Z for AFT and ZFT analyses. Note that for all analyses the central age is used [*Galbraith and Laslett*, 1993], and 1σ error is quoted unless otherwise stated. In the absence of measured data, when calculating the amount of rock eroded from maximum paleotemperature estimates, temperature gradients of 30°C/km are assumed. This estimate is higher than the typical ≤25°C/km gradients in the Fold Belt, owing to the presence of the middle Miocene Maramuni Arc throughout the Mobile Belt.

5.1. Kubor Granodiorite and Omung Metamorphics

The Triassic Kubor Granodiorite crops out over ~900 km^2 in east central PNG (Figures 3 and 4) and attains elevations of over 3000 m. On the basis of Rb-Sr and K-Ar dating, *Page* [1976] considered the emplacement age to be 244 Ma, intruding the upper Paleozoic greenschist-grade Omung Metamorphics. Samples 715 and 16 were from the Kubor Granodiorite, and samples 82, 84 and 94 were from the Omung Metamorphics (Table 1).

ZFT dating of the Kubor Granodiorite sample 715Z yielded an age of 191±14 Ma that passed the chi-square test, suggesting that the sample cooled through the ~280°C isotherm in the Early Jurassic. This indicates a protracted cooling from the 244 Ma emplacement age, consistent with the 31 K-Ar ages on hornblende, muscovite and biotite from *Page* [1976] which ranged from 217 to 242 Ma.

ZFT dating of the Omung Metamorphic sample 84Z failed the chi-square test, indicating a complex cooling history and/or zircons of different provenance, but still yielded an age of 242±34 Ma, consistent with Triassic intrusion into late Paleozoic strata.

AFT dating of the good-excellent Kubor Granodiorite samples 715A and 16A passed the chi-square test with ages of 7±2 and 10±2 Ma, indicating late Miocene cooling through the ~100°C isotherm. Modeling of sample 16A suggests a maximum temperature of ~113°C in the middle Miocene followed by rapid middle-late Miocene cooling with minimal Pliocene cooling (Figure 5). Modeling of sample 715A suggests a maximum temperature of ~111°C in the late Miocene, with rapid cooling in the late Miocene-Pliocene (appendix A). The mean lengths of 8±1 and 13±0.5 μm for 715A and 16A suggest that the cooling histories were different, but modeling suggests that AFT lengths are highly susceptible to 1°-2°C changes at these high temperatures so the predicted thermal histories are similar. Thus, assuming 30°C/km temperature gradients and equatorial surface temperatures, the results are interpreted to show ~3 km of burial by Mesozoic and Tertiary rocks in the middle Miocene,

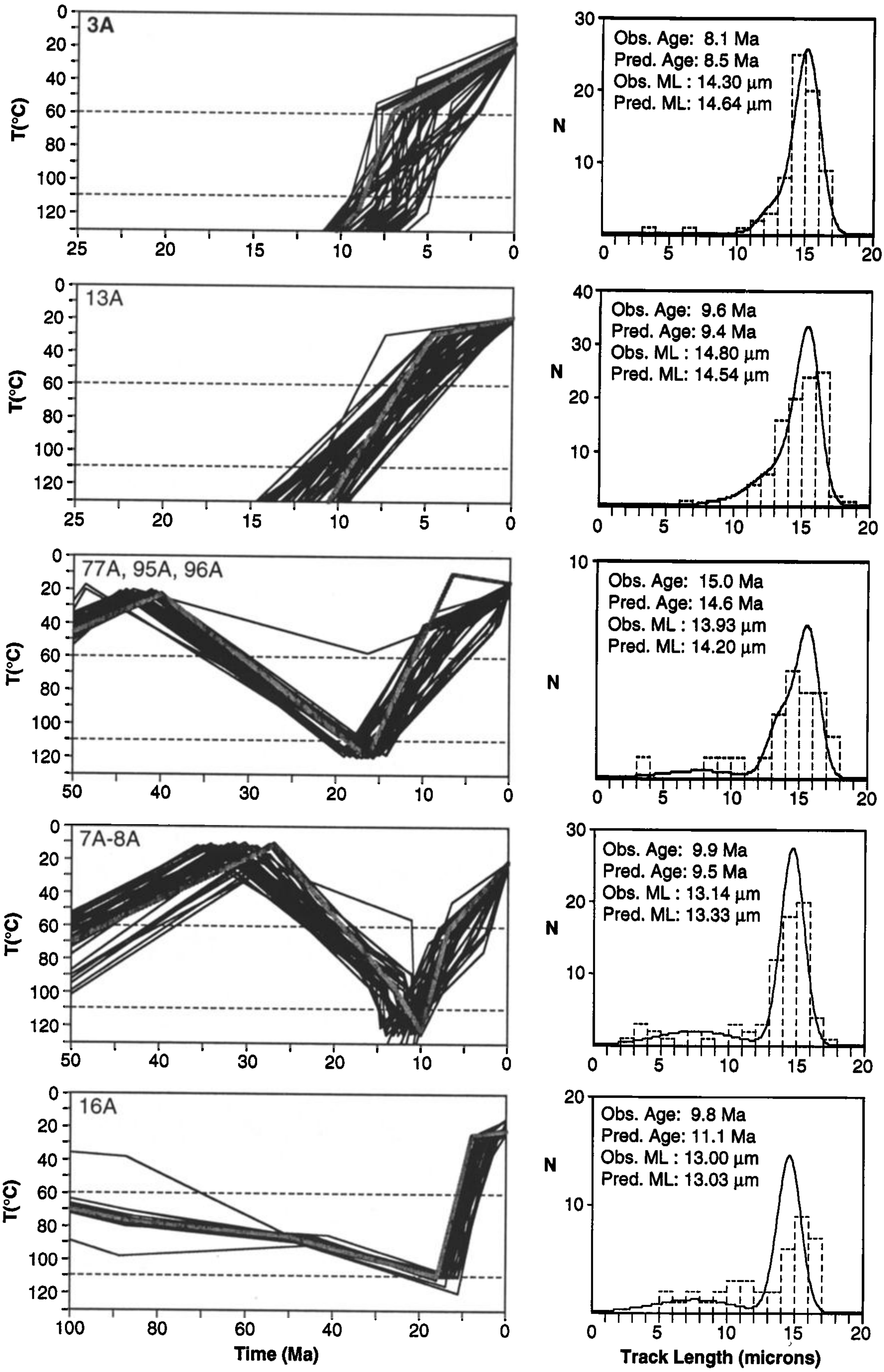
3A
13A
77A, 95A, 96A
7A-8A
16A
T(°C)
Time (Ma)
N
Track Length (microns)
Obs. Age: 8.1 Ma
Pred. Age: 8.5 Ma
Obs. ML : 14.30 μm
Pred. ML: 14.64 μm
Obs. Age: 9.6 Ma
Pred. Age: 9.4 Ma
Obs. ML : 14.80 μm
Pred. ML: 14.54 μm
Obs. Age: 15.0 Ma
Pred. Age: 14.6 Ma
Obs. ML : 13.93 μm
Pred. ML: 14.20 μm
Obs. Age: 9.9 Ma
Pred. Age: 9.5 Ma
Obs. ML : 13.14 μm
Pred. ML: 13.33 μm
Obs. Age: 9.8 Ma
Pred. Age: 11.1 Ma
Obs. ML : 13.00 μm
Pred. ML: 13.03 μm

Figure 5.

with subsequent cooling due to uplift and erosion in the late Miocene, with reduced erosion in the Pliocene. As the Kubor Granite and Omung Metamorphic sampled areas are currently at ~1500 m, this suggests uplift of ~4.5 km in the late Miocene.

AFT dating of the three poor Omung Metamorphic samples 82A, 84A, and 94A gave ages of 57±15, 12±5, and 16±6 Ma, with only sample 84A failing the chi-square test. Although two samples pass the chi-square test and the eight measurable lengths are long, the ages are interpreted to be mixed ages, lying between the Triassic cooling age indicated from ZFT analysis and the interpreted late Miocene cooling, consistent with the modeling of sample 16A. This suggests maximum temperatures of ≤~120°C between the Triassic and the late Miocene and is consistent with burial to ~3 km prior to late Miocene cooling.

The burial by only 3 km of Mesozoic-Tertiary sediment is significant as the thicknesses of these units are far greater in adjacent areas. *Bain et al.* [1975] inferred 7000 m of Jurassic and Cretaceous sediments on the flanks of the Kubor Anticline and a further 4500 m of Tertiary volcaniclastics; however, they recognized that the sediments thinned and onlapped onto the Kubor High. The AFT analyses confirm the latter interpretation and demonstrate that the Kubor area was a basement high throughout the Mesozoic and Tertiary.

5.2. Mount Victor Granodiorite

The Mount Victor Granodiorite, southeast of Kainantu, was dated by *Page* [1976] using K-Ar on nine hornblendes and biotites, giving an emplacement age of 90-95 Ma. The granodiorite is unconformably overlain by a late Oligocene to middle Miocene volcano-sedimentary sequence and intruded by middle - late Miocene stocks and dikes equivalent to the Elandora Porphyry. The latter have associated hydrothermal gold mineralization, which has been subject to small-scale mining [*Samuel and Sie*, 1991]. Currently, the Mount Victor Granodiorite is the only known Cretaceous intrusive in PNG. One surface sample, 7, and two shallow drill cores, 8 and 9, were analyzed.

ZFT analyses of samples 8Z and 9Z yielded ages of 113±11 and 115±8 Ma, both of which passed the chi-square test. The weighted mean age of the two samples is 115±6 Ma, which is Aptian and significantly older than the Cenomanian emplacement age indicated by K-Ar dating. This suggests that the K-Ar dates may have been affected by excess argon.

AFT analysis of the good to excellent samples 7A and 8A yielded ages of 9±2 and 11±1 Ma, both of which passed the chi-square test, and mean track lengths of 12.8±3.5 and 13.6±1.8 μm although with only 46 and 27 lengths measured (Table 1). The samples were combined for modeling to give a mean age of 9.9±1.0 Ma and mean length of 13.14± 0.4 μm with 73 lengths measured. Other constraints for modeling included the ZFT age and closure temperature and surface temperatures for the granite in the Oligocene as Oligocene sediments onlap it. The modeling yields an excellent fit to the observed data and confirms rapid Oligo-Miocene heating to ~124°C in the late Miocene followed by rapid cooling in the late Miocene (Figure 5) with reduced cooling in the Pliocene.

As the Cretaceous granite was at surface in the Oligocene, the model indicates rapid burial during the early-middle Miocene followed by rapid uplift, denudation and cooling in the late Miocene. Assuming temperature gradients of ~30°C/km the granite was buried by >3 km of Oligocene-middle Miocene sediment. Regionally, the lower-middle Miocene Aure and Wogamush Beds are marine, probably bathyal sediments [eg. *Francis*, 1990; *Hill et al.*, 1990], so the 1600 m elevation of the Mount Victor Granite indicates ≥4.5 – 5 km of uplift in the late Miocene-Pliocene.

5.3. Urabagga Intrusives, Karmantina Gneissic Granite, and the Goroka Formation.

The Urabagga intrusives comprise a suite of small granodiorite bodies that intrude the ?Paleozoic amphibolite-grade metamorphics of the Goroka Formation and are overlain by Oligocene limestone [*Page*, 1976]. On the basis of whole rock Rb-Sr dating and K-Ar dating of a hornblende, *Page* [1976] interpreted the emplacement age of the granodiorite to be Early Jurassic (180-190 Ma).

Approximately 45 km ESE of Urabagga Hill, the Karmantina Gneissic Granites intrude the greenschist facies metasediments of the Bena-Bena Formation, which was thought to be older than Early Jurassic and probably Paleozoic in age [*Page*, 1976]. A Rb-Sr age for the gneissic granite of 172±27 Ma (2 sigma) was interpreted by *Page* [1976] either to be the emplacement age or to indicate a strong metamorphic event. K-Ar ages on muscovite from the same rock yielded cooling ages of 23 Ma, indicating early Miocene uplift and cooling [*Page*, 1976].

ZFT analysis of Karmantina Gneissic Granite sample 711 yielded a central age of 35±8 Ma and a mean age of 101±45 Ma due to a scatter of individual grain ages from 727 to 12 Ma. The data suggest partially reset zircons, with compositions resistant to annealing recording Mesozoic and older ages, while the less resistant compositions record early Miocene cooling. The radial plot illustrates a marked peak at 17 Ma, which strongly indicates early Miocene cooling below ~280°C. The age is significantly younger than the 23 Ma from K-Ar dating on muscovite, perhaps owing to a lower closure temperature for ZFT or to argon loss in the latter. Unfortunately, sample 711 did not yield any apatite.

Figure 5. Modeled time-temperature histories for five selected samples, generated using a genetic algorithm [*Gallagher*, 1995] to forward model the fission track data, inputting all the geological constraints (see text). Each plot shows the envelope of possible solutions with the best fit thermal model superimposed. Samples 77A, 95A, and 96A, and 7A and 8A use the combined fission track parameters of these samples. All models only show the low-temperature and Cretaceous-Neogene stages of the thermal history. For full details of the thermal history, see appendix A. ML, mean length.

AFT analysis of the poor to moderate Goroka Formation and Urabagga Granite samples 800A and 12A yielded ages of 5±2 and 3±2 Ma, both of which passed the chi-square test. This indicates cooling below ~100°C in the latest Miocene to Pleistocene, although the low number of track counts reduces the confidence in the result. The mean track length of 11.5±3.8 μm for Urabagga sample 12 may indicate a multiphase cooling history.

5.4. Mesozoic Sediments

Eight samples were collected along the Wahgi-Chimbu Gorge section, considered to be the type section for the distal Mesozoic facies [e.g., *Francis et al.*, 1990]. The samples were collected in 1990 during a Geological Survey of PNG field trip to examine those sections. The samples collected were from Triassic Kana Volcanics, 92 and 81, the Jurassic Jimi Greywacke, 20, the Lower Cretaceous Kondaku Tuff, 75, and the Upper Cretaceous Chim Formation, 76, 77, 95, and 96. Descriptions of the samples are recorded in Table A1.

Sample 76 was noteworthy as being the stratotype marking the mid-Cretaceous Kondaku Tuff - Chim Formation boundary in the lowermost Chim Formation. In fact, it yielded a late Miocene zircon age, so is probably part of a Miocene fault slice within the Cretaceous units. Similarly the "Triassic" Kana Volcanics sample 81 yielded a late Miocene zircon age. Both samples are discussed with the Miocene samples in section 5.8.

ZFT analysis of eight zircons from Chim sample 95Z yielded an age of 97±21 Ma, but the sample failed the chi-square test. More significantly, two grains yielded Oligocene ages, although with large error bars. The Cretaceous and older grains may be explained as detrital grains in an Upper Cretaceous sediment, but the Oligocene grains suggest either resetting during low-grade metamorphism or an Oligocene sediment with Cretaceous and older detritus. AFT analysis of the same sample, 95A, yielded an age of 16±5 Ma, indicating middle - early Miocene cooling below ~100°C but not differentiating between the above alternatives.

ZFT analysis of Chim sample 77Z yielded an age of 215±55 Ma, with grain ages ranging from Late Cretaceous to Triassic or older. This is consistent with the Late Cretaceous depositional age of the Chim Formation but indicates that it contains zircons of late Paleozoic-Triassic provenance.

AFT analysis of the good quality Chim Formation samples 77A, 95A, and 96A yielded ages of 14±4, 16±5, and 14±6 Ma, although only 95A passed the chi-square test. The relatively few track lengths measured are all long, and suggest late early to late Miocene cooling. Significantly, the two grains with highest precision in sample 77A have ages of 4±2 and 6±2 Ma, indicating late Miocene to Pliocene cooling, recorded in grains less resistant to annealing. The fact that two of these samples fail the chi-square test and retain older grain ages suggests that the samples were not completely annealed prior to the middle-late Miocene, with maximum temperatures probably <120°C, assuming some grains are Cl-rich.

To model the data, the three samples 77A, 95A, and 96A were combined giving an AFT age of 15±3 Ma and mean track length of 13.93±1 μm from 23 track lengths. Modeling assumed a Late Cretaceous age for the Chim Formation but took account of it being unconformably overlain by mid-Eocene beds. The results show a good fit to the data, given the paucity of length measurements, and indicate rapid Oligocene-early Miocene heating of the Chim Formation to ~119°C at the end of the early Miocene, followed by rapid middle-late Miocene cooling to surface temperatures with minimal Pliocene cooling (Figure 5). The data are consistent with ~3 km of Oligocene-early Miocene burial, followed by uplift, denudation, and cooling in the middle to late Miocene. The outcrops lie >15 km from the middle Miocene Bismarck intrusives and were probably farther away prior to late Miocene shortening, so heating is unlikely to have been due to intrusion of the plutons.

This interpretation is confirmed by AFT analysis of Jurassic Jimi Greywacke sample 20A, Triassic Kana Volcanics sample 92A, and the poor quality Lower Cretaceous Kondaku Tuff sample 75A with ages of 24±9, 14±3, and 20±10 Ma. All three samples fail the chi-square test suggesting a mixed AFT age lying between the original Mesozoic cooling age and a subsequent middle to late Miocene cooling age. The radial plots of single grain ages for samples 20A and 92A (see Appendix A) reveal prominent clusters of late Miocene-Pliocene single-grain ages, indicating the time of cooling.

Thus the AFT analyses indicate partial annealing of the Mesozoic sediments most likely due to Oligocene-early Miocene burial and late Miocene to Pliocene cooling due to uplift and denudation. As the sediments were not completely annealed prior to the late Miocene, maximum temperatures were probably between 110° and 120°C suggesting burial of ~3 km. The present elevation of >1300 m of the sampled area indicates ~4.5 km of uplift in the late Miocene-Pliocene.

5.5. Marum Ophiolite

The Marum Ophiolite is one of a series of ultramafic bodies in northern New Guinea separating the accreted volcanic arcs and Sepik and Ramu Basins from the Mobile Belt. The ultramafic bodies include the large Papuan Ultramafic Belt on the Papuan Peninsula to the east and the disaggregated slices of April Ultramafics to the west. These ophiolites have been interpreted as being Miocene, Paleocene, or Mesozoic in age, although with few constraints owing to the general paucity of radiogenic elements [e.g., *Davies and Jaques*, 1984]. *Davies et al.* [1997] determined that some of the ultramafics in northern PNG were Paleocene in age, and *Pigram and Symonds* [1991] suggested that the Marum Ophiolite was a continuation of the Paleocene Coral Sea opening, offset along the Aure Continental Transform.

Several samples were processed for zircons, but none was found, owing to the ultramafic nature of the rocks. However, three samples yielded apatite, albeit low in uranium, a dunite 10A, a dioritic tectonite 811A, and a serpentinite 815A (Table 1).

The moderate to poor quality samples 10A and 815A had low amounts of apatite and yielded ages of 36±9 and 64±24 Ma. Both failed the chi-square test, indicating partial annealing, confirmed by the mix of zero-age grains and early Tertiary grains. The AFT ages are thus interpreted as mixed ages, lying between the crystallization age of the ophiolite and the subsequent cooling age due to tectonism. Sample 10A contains a number of grains with latest Cretaceous to early Tertiary ages, consistent with the Paleocene age of the Marum Ophiolite. These single-grain ages indicate that the igneous emplacement of the ophiolite was Paleogene or earlier.

The good quality dioritic tectonite sample 811A yielded abundant apatite, although with low uranium, compensated for by counting 30 grains. The sample gave an age of 5.1±1.5 Ma and passed the chi-square test, indicating that this was the age of cooling below ~100°C. This suggests that the ophiolite was structurally emplaced in the late Miocene to Pliocene or that the sampled shear zone associated with the ophiolite was last active at around 5 Ma.

5.6. Akuna Intrusive Complex

The Akuna Intrusive Complex, a Miocene complex near Kainantu, was reported to comprise porphyritic dolerites and granodiorites, the dolerites giving 17 mineral and whole rock K-Ar ages between 14 and 16.5 Ma [*Page*, 1976]. *Page* [1976] suggested the possibility of separate cooling ages at 15 and 17 Ma.

A float sample, 6A, was collected from the Karmantina River and was originally thought to be part of the Karmantina Gneissic Granite; however, it was found to lack gneissic texture and be a monzonite rather than a granite, so it was interpreted to be part of the Akuna Intrusive Complex. This good quality sample gave an AFT age of 13±3 Ma and failed the chi-square test. The sample had only four measurable lengths with a mean of 13.25 μm indicating partial annealing. It also had one high-precision grain with more than half the tracks for the whole sample, yielding an age of 4±1 Ma, suggesting a Pliocene event following ?mid-Miocene cooling.

5.7. Bismarck Intrusive Complex

The Bismarck Intrusive Complex is a 65 km x 25 km, northwest trending batholith composed predominantly of granodiorite and monzonite with minor gabbro and diorite. It includes Mount Wilhelm, the highest peak in PNG at 4510 m. *Page* [1976] dedicated a substantial amount of effort to dating this complex, as it had been considered to be Mesozoic. He completed more than 50 K-Ar ages on hornblende, biotite, and muscovite and five Rb-Sr analyses. Page observed a spread in ages from 7 to 13.5 Ma due to a complex emplacement and cooling history. However, his best estimates for the initial postemplacement cooling were 12.4±0.8 Ma from Rb-Sr and the mean K-Ar age of 12.7 Ma for hornblendes. The 8 - 9 Ma ages obtained on pegmatites were interpreted to represent the final stages of cooling. Page also inferred that the 5 Ma spread in ages for different minerals represented the time for the whole of the batholith to cool below ~240°C. He suggested uplift rates of ~1 mm/yr through the Miocene to bring these rocks to their present elevation of up to 4000 m above sea level.

Two monzodiorites, 13 and 14, from the Urabagga Hill region were originally thought to be part of the Urabagga Granite, but five zircons counted from sample 14Z gave an age of 12.4±0.5 Ma, passing the chi-square test. This suggests intrusion in the middle Miocene, consistent with the 12.5 Ma age of the Bismarck Intrusives indicated by *Page* [1976].

The excellent sample 13A gave an AFT age of 10±1, passing the chi-square test. The mean length of 14.8±1.8 μm derived from 100 track length measurements indicates the age can be interpreted as a true cooling age. Modeling of the sample (Figure 5) confirmed rapid cooling in the late Miocene consistent with late Miocene uplift and erosion, rather than a continuation of slow cooling after middle Miocene intrusion of the Bismarck Intrusive Complex. Importantly, modeling suggests that cooling in the Pliocene was much slower. Rapid late Miocene cooling associated with bringing the Miocene granite to surface at >1600 m is consistent with 3-5 km of uplift and 3+ km of late Miocene denudation.

ZFT analysis 3Z passed the chi-square test and yielded an age of 25±1 Ma. The data indicate that this quartz diorite float sample, which was slightly gneissic, cooled below ~280°C in the latest Oligocene, suggesting that it was intruded in the Oligocene. AFT analysis of the same sample 3A, which was excellent, passed the chi-square test and gave an age of 8±1 Ma. The long mean length of 14.3±2.1 μm from 70 length measurements indicates rapid cooling from temperatures >100°C, indicating a significant late Miocene cooling event, with reduced cooling in the Pliocene, confirmed by modeling (Figure 5). Given the Oligocene ZFT intrusion age of the granite, the 8 Ma AFT age indicates that this rock cooled rapidly in the late Miocene owing to uplift and erosion from depths >3 km. The elevation of >2000 m from which the sample was collected indicates 3-5 km of uplift in the late Miocene.

ZFT and AFT dating of sample 98 from the center of the Bismarck Intrusive Complex show that it cooled below ~280°C at 6.3 ± 0.5 Ma and below ~100°C at 4.2 ± 1.6 Ma. As these ages are within ±2_ error, this probably indicates rapid cooling of a diorite intruded in the late Miocene, consistent with modeling (appendix A).

AFT analysis of the three good to excellent diorite samples 2A, 97A, and 99A resulted in ages of 7±1, 7±1, and 15±3 Ma. The first two samples had long lengths and easily passed the chi-square test, indicating a significant rapid cooling event in the late Miocene. Sample 99A had a mean length of 14.9±0.4 μm, indicating a significant cooling event. The age of 15.2±3.4 Ma may indicate middle Miocene cooling, but it is just within ±2_ error of the 7 Ma ages, so is consistent with late Miocene cooling.

AFT analysis of the poor ?aplite sample 1A failed the chi-square test with an age of 26±10 Ma and several early Tertiary to Mesozoic individual grain ages. The sample, which is 95% quartz, may have been a Mesozoic sediment close to an intrusion, which was not totally reset to the Miocene age.

Overall, the analyses of the Bismarck Intrusive Complex indicate Oligocene intrusion and late Miocene intrusion of at least some of the complex, although most of it is probably middle Miocene in age as dated by *Page* [1976]. The three most reliable AFT ages indicate 3+ km of rapid denudation and cooling in the late Miocene, probably at 7-10 Ma, and the other data are consistent with this. As the intrusive rocks are currently at elevations of >2 km and denudation rates are high in equatorial regions, the denudation was probably associated with 3-5 km of uplift in the late Miocene. This time of rapid uplift is coeval with the emplacement of pegmatites in the Bismarck Ranges and the intrusion of the gold-bearing Elandora Porphyry.

5.8. Miocene Sediments and Volcanics

Sample 76Z, thought to be from the mid-Cretaceous Kondaku Tuff - Chim Formation boundary, yielded a ZFT age of 8±0.5 Ma that passed the chi-square test. Clearly, this sample contained only late Miocene zircons and was therefore part of the upper Miocene Aure Beds, probably as a fault slice within the Cretaceous units.

Interestingly, AFT analysis of the same good quality sample, 76A, yielded an age of 35±7 Ma, significantly older than the late Miocene zircon age despite the much lower closure temperature. The radial plot suggests two apatite provenances, Late Cretaceous and Miocene as opposed to only a late Miocene zircon provenance. The preservation of the Late Cretaceous apatite ages indicates that the upper Miocene Aure Beds received some apatites from erosion of a Late Cretaceous source area and that the Aure Beds were not significantly heated after deposition.

Kana Volcanics sample 81 yielded only two zircons, but they had an age of 6 Ma, indicating that they, too, are part of the upper Miocene Aure Beds. The sample lies just south of very weathered thrust sheets of Kana Volcanics. If these are thrust over the Aure Beds, it suggests that the thrusting occurred after 6 Ma.

AFT analysis of the moderate quality andesitic sample, 90A, yielded a mixed age of 35±8 Ma that failed the chi-square test with a mean length of 12.6±1.8 μm from seven track lengths. The radial plot shows strong age peaks in the Late Cretaceous and Miocene, indicating either a Miocene sample with two provenances or a Late Cretaceous sample partially reset in the Miocene.

6. Discussion

6.1. The Kubor Basement High

Several AFT analyses of the Kubor basement and adjacent Mesozoic sediments indicate that samples were not totally overprinted prior to uplift, indicating maximum burial of ~3 km in the middle Miocene. It is notable that this is true for Paleozoic basement, Triassic, Jurassic and Cretaceous sediments, which is surprising given the estimated 7 km thick Mesozoic section [*Bain et al.*, 1975]. If the sediment thickness were constant, the Triassic and Jurassic beds ought to have been heated to temperatures well over 120°C and been totally annealed prior to late Miocene denudation and cooling. The fact that maximum burial was ~3 km supports *Bain et al.*'s [1975] contention that the Mesozoic and Tertiary strata onlapped the Kubor High. Thus the Kubor High was long-lived and partially emergent in the Mesozoic and possibly part of the Tertiary. This geometry is a useful template when reconstructing sections across the adjacent Papuan Fold Belt.

6.2. ZFT Analysis

In general, the zircon fission track dating confirms the K-Ar and Rb-Sr dating of *Page* [1976], although it suggests that the Mount Victor Granodiorite may have been intruded in the Aptian rather than the Cenomanian. The fission track dating also indicates that the Bismarck Intrusive Complex was intruded over a long period, from the Oligocene to the late Miocene, although most of the intrusion is probably middle Miocene as determined by Page. In the Mesozoic type section along the Wahgi-Chimbu Gorge, the boudinaged sandstone at the mid-Cretaceous boundary between the Kondaku Tuff and the Chim Formation appears to be a fault slice of upper Miocene Aure Beds. In the same section the siltstones just south of overthrust Triassic Kana Volcanics are also late Miocene. The structural location of these samples indicates that thrusting occurred after 8±1 and 6±3 Ma, respectively (±2σ). The data suggest that the type section needs reevaluating, given the likely late Miocene faulting.

6.3. The Bena Bena Terrane and Finisterre Ranges

The single Tertiary metamorphic sample dated is from the Karmantina Gneissic Granite, which is surrounded by Paleozoic metasediments of the Goroka and Bena Bena Formations in the core of the Bena Bena terrane. ZFT analysis indicates cooling below ~280°C at 17±1 Ma, younger than the ~27-23 Ma metamorphic cooling ages previously inferred [*Page*, 1976; *Rogerson et al.*, 1987] but consistent with the initial supply of metasedimentary detritus to the Sukurum Formation at 16-18 Ma, exposed on the southern flank of the Finisterre Range 100 km to the east (Figure 4) [*Abbott et al.*, 1994].

Regardless of the precise time-temperature path, the 17 Ma age indicates substantial cooling and exhumation of metamorphic rocks of the Bena Bena terrane in the early Miocene. Cooling to surface from temperatures of ~280°C implies removal of several kilometers of overburden, which *Crowhurst et al.* [1996] argued was due to extensional tectonic unroofing of deep crustal rocks above a subducting slab. This exhumation is coeval with or immediately prior to emplacement and cooling of the Akuna Intrusive Complexes at 17-14 Ma as part of the Maramuni Arc, suggesting that it may have been related to the rising plutons.

It is probable that a plate realignment at the end of the Oligocene, perhaps related to the collision between the Solomons and the Ontong Java Plateau [*Kroenke*, 1984; *Hall*, 1997], initiated subduction of the Solomon Sea plate beneath the PNG margin. The overriding plate was in extension [e.g., *Hamilton*, 1994], causing tectonic unroofing and denudation of deep crustal rocks such as the Karmantina Gneissic Granite around 17 Ma. This was immediately prior to emplacement of the Maramuni Arc along the PNG margin.

6.4. Timing of Compressional Deformation

The main result to emerge from the AFT analyses is that the entire study area underwent rapid cooling in the late Miocene interpreted to be due to ~4.5 km of uplift and ~3 km of denudation, assuming paleotemperature gradients of

30°C/km. This equates to average uplift rates for northern New Guinea of ≤1 mm/yr during the late Miocene.

As several of the samples are near the Bismarck Intrusive Complex or from the Intrusives, the possibility of postintrusive cooling needs to be considered. This study and *Page* [1976] dated cooling from magmatic temperatures through to temperatures of <240°C to have occurred by 12.5 Ma for most Bismarck Intrusive Complex samples. However, the cooling through the 100°C isotherm occurred in the late Miocene, apart from the late Miocene-Pliocene intrusion of sample 98. Importantly, samples well removed from the Bismarck Intrusive Complex show the same cooling age, for instance, the Triassic Kubor Granite 30 km to the SW and the Cretaceous Mount Victor Granite 60 km to the SE. Thus it seems likely that the cooling is due to regional tectonic uplift and denudation, probably associated with compression.

The late Miocene cooling in the Mobile Belt is consistent with the Pliocene to Recent cooling in the Fold Belt to the SW, interpreted to be due to uplift and erosion associated with fold and thrust deformation of the Miocene limestones [*Hill and Gleadow*, 1989]. This timing relationship suggests that compressional deformation in the Mobile Belt occurred in the late Miocene and that the deformation migrated toward the undeformed foreland in the southwest in the Pliocene.

The regional late Miocene uplift and denudation event in the Mobile Belt is also consistent with that postulated by *Crowhurst et al.* [1996] for northwest PNG, although they considered the event to have occurred mainly from 8 to 5 Ma. If so, then the uplift and denudation may have been migrating from east to west as well as to the south into the Fold Belt.

These timing relationships place significant constraints on tectonic models for the area, indicating that the major compressional pulse in PNG commenced in the northeast at ~12-10 Ma and migrated to the southwest and west in the latest Miocene to Pliocene. This immediately followed intrusion and cooling of the Akuna Intrusive Complex at ~17-14 Ma and most of the Bismarck Intrusive Complex at ~12.5 Ma [*Page*, 1976], indicating a linkage between the end of plutonism and the start of compressional deformation. The timing is consistent with the observation of *Hamilton* [1994] that in areas of subduction the overriding plate is commonly in extension and that continental margins are only crumpled during collisions. This suggests that the middle Miocene magmatism in northern New Guinea occurred during extension above the subducting Solomon Sea slab and was terminated by late Miocene arc collision and resultant compression commencing at ~12-10 Ma. *Jaques and Robinson* [1977] and *Hall* [1997] proposed that the accreted arc was adjacent to the New Guinea margin thoughout the early Miocene, so the late Miocene compression was probably initiated by a change in plate motion vectors at ~12 Ma.

6.5. Pliocene Reactivation

In general, the AFT data indicate that the acme of denudation and cooling in the Mobile Belt was in the late Miocene, with relatively little cooling and denudation since. In contrast, *Hill and Gleadow* [1989] found that the peak of denudation in basement outcrops in the Fold Belt was in the Pliocene at ~4 Ma. However, some samples from the Mobile Belt, presented here, yielded Pliocene ages or high-precision single-crystal ages indicating Pliocene reactivation. Along strike to the NE in the Frieda River area, on the basis of structural and fission track data, *Crowhurst et al.* [1997] suggested that compressional deformation had terminated by ~4 Ma and was replaced by strike-slip faulting in the Mobile Belt. They suggested that local transpressional reactivation against a buttress gave rise to 3 Ma AFT cooling ages in the Landslip Ranges. Extending this model further, it is quite plausible that the Pliocene transition from compression to strike-slip deformation caused local reactivation and hence the local Pliocene cooling ages throughout the Mobile Belt.

7. Tectonic Model

The cooling ages determined from fission track analyses place constraints on the times of magmatism and postmetamorphic cooling and the time of regional low-temperature cooling demonstrated to be due to uplift and denudation, resulting from mountain building. Applying these new age constraints, it is possible to test and refine tectonic models for the area, such as the recent Tertiary plate tectonic reconstructions of *Hall* [1997]. He developed a kinematic plate reconstruction model of the tectonic history of northern New Guinea and showed that an arc was accreted along the northern margin of New Guinea in the late Oligocene, but the arc was originally along the southern margin of the Caroline plate [*Hegarty and Weissel*, 1988; *Hill et al.*, 1993]. Hall inferred sinistral strike-slip motion along the northern margin of New Guinea until the Pliocene when plate convergence generated the orogenic belt. The work presented here indicates early Miocene extension and middle Miocene volcanism in PNG prior to the main compressional pulse in New Guinea in the late Miocene-earliest Pliocene, from ~12 to 4 Ma. Since 4 Ma, the deformation in the Mobile Belt has been dominated by transpression [*Crowhurst et al.*, 1997].

Figure 6 shows the inferred plate tectonic configuration of New Guinea from 20 Ma to the present. In the early Miocene, Halmahera and the southern Caroline Arc impinged on the New Guinea margin, and the Ontong Java Plateau collided with the Solomon Arc. The loss of these subduction zones resulted in a plate realignment with a new subduction zone developed along the NE PNG margin. The Philippine and Caroline plates moved west with respect to New Guinea, creating a wrench fault zone along the northern margin of New Guinea and initiating westward subduction of the Solomon Sea beneath NE PNG [*Hall*, 1997].

In the early Miocene, extension is inferred in the PNG margin overriding the Solomon Sea plate, giving rise to regional subsidence and local metamorphic core complexes, causing the 17 Ma cooling of the Karmantina Gneissic Granite [*Crowhurst et al.*, 1996; *Hill et al.*, 1993]. The extension was the precursor to rising magmas above the downgoing Solomon Sea slab, generating the Akuna and Bismarck Intrusive Complexes in the Bena Bena terrane, as part of the Maramuni Arc. In the middle Miocene the

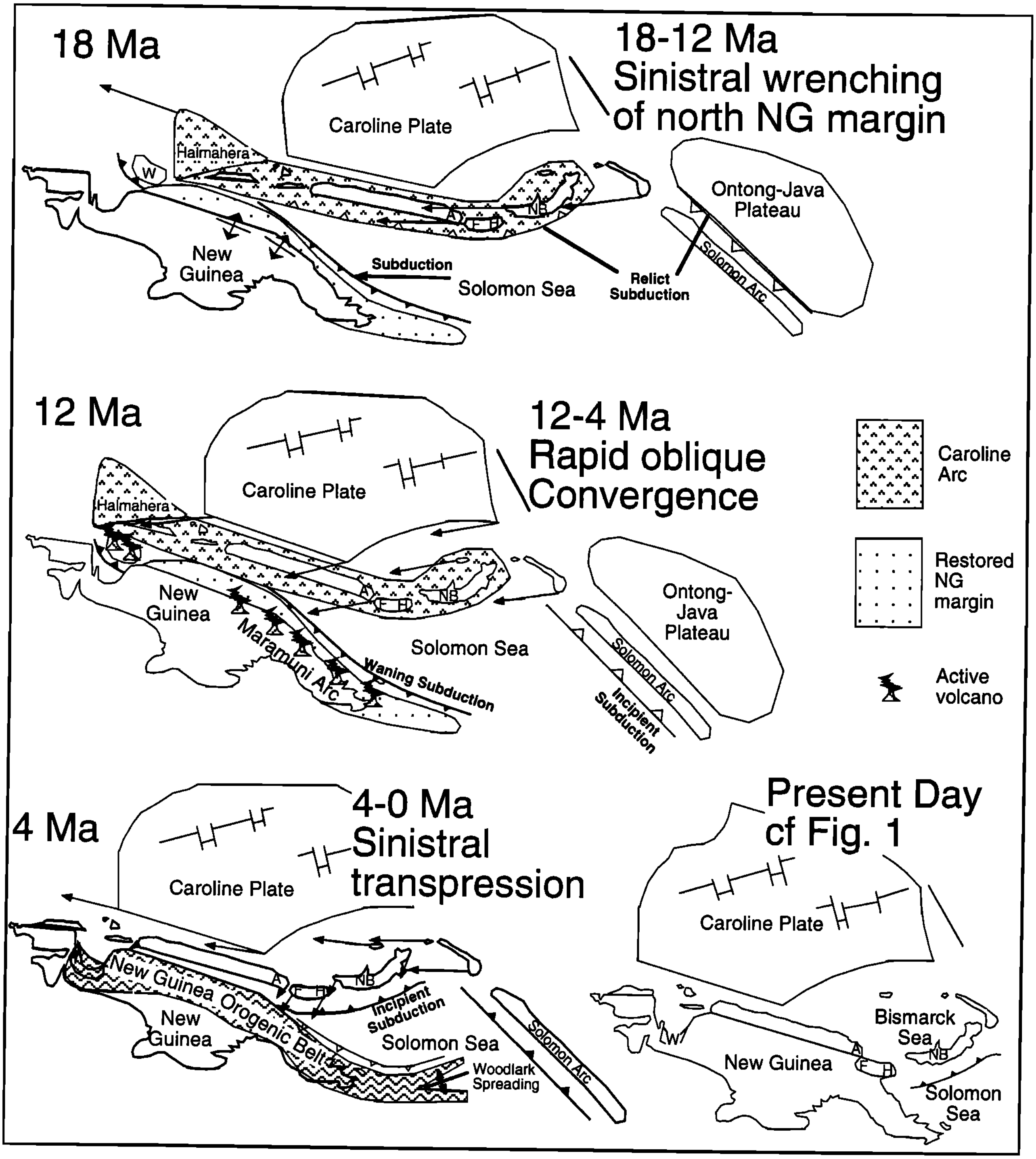

Figure 6. A plate tectonic model for the evolution of PNG incorporating the fission track results from this study. The diagrams illustrate the inferred positions of the microplates at 18, 12, 4, and 0 Ma, following *Hall* [1997] but modified to allow the main compressional pulse between 12 and 4 Ma. The arrows indicate the vectors of movement, with PNG fixed, from 18-12, 12-4, and 4-0 Ma. From 18 to12 Ma the PNG margin was in extension, overriding the westerly subducting Solomon Sea plate and being intruded by the Maramuni Arc. The majority of the compressional deformation, uplift, and denudation occurred between 12 and 4 Ma. From 4 to 0 Ma the margin was subject to transpression, except for rapid convergence of the Finisterre Range. See text for details. A, Adelbert Range; F, Finisterre Range; H, Huon Peninsula; NB, New Britain; W, Weyland Overthrust.

Maramuni Arc was fully developed along the PNG margin, and sediments from the arc and core complexes were deposited in the forearc region as the Sukurum Formation [*Abbott et al.*, 1994].

At ~12 Ma another change in plate motion, perhaps related to developing northeasterly subduction of the Solomon Sea plate beneath the Solomon Arc, resulted in more rapid convergence between the Caroline plate and New Guinea. It is likely that this oblique convergence was partitioned with transpression along and north of the arc-continent suture and compression to the south, giving rise to deformation in the Mobile Belt and Fold Belt from 12 to 4 Ma. This caused late Miocene uplift of ~4.5 km throughout northern PNG and ~3 km of denudation and cooling. The deformation propagated into the Fold Belt in the early Pliocene.

At ~4 Ma a further change in plate motion resulted in the present situation with more oblique convergence between New Guinea and the Caroline plate. Transpression continued in the Mobile Belt but with less convergence, hence less uplift, denudation, and cooling. Renewed subduction of the Solomon Sea plate beneath New Britain and the Finisterre Arc accompanied back arc spreading in the Bismarck Sea [*Taylor*, 1979]. The subduction also juxtaposed the Sukurum Formation against the Finisterre terrane, which subsequently overrode the PNG margin on the Ramu-Markham Fault [e.g., *Pegler et al.*, 1995]. At present the Finisterre terrane is still rising rapidly on the Ramu-Markham Fault, and there is ongoing transpression in mainland New Guinea.

The model proposed here illustrates that from the accretion of the arc the arc-continent collision spanned 25 Myr. It involved wrenching, extension, ~10 Myr of oblique subduction beneath the continental margin generating a volcanic arc, ~8 Myr of folding, thrusting, uplift and denudation, and then transpression with ongoing convergence of the Finisterre Arc.

Acknowledgments. The original fieldwork and sample collection by John Forwood and Chris Rodda were sponsored by BP Australia, with assistance in the field from the Geological Survey of PNG. Neutron irradiations for fission track studies are supported by a grant from the Australian Institute of Nuclear Science and Engineering. The draft paper benefited by reviews from Barry Kohn and Bob Findlay. It is published with the approval of the Director of the Australian Geodynamics Cooperative Research Centre. The three reviewers are thanked for their constructive comments which improved the paper.

References

Abbott, L. D., E A. Silver, P R. Thompson, M. V Filewicz, C Schneider, and Abdoerrias, Stratigraphic constraints on the development and timing of arc-continent collision in northern Papua New Guinea, *J Sediment. Res Sect B, B64*(9), 169-183, 1994.

Bain, J. H. C., D. E. MacKenzie, and R J. Ryburn, Geology of the Kubor Anticline, Central Highlands of Papua New Guinea, *Bull Bur Miner. Res Aust. 155*, 106 pp , Canberra, 1975.

Crowhurst, P V., K. C. Hill, D. A. Foster, and A. P. Bennett, Thermochronological and geochemical constraints on the tectonic evolution of northern Papua New Guinea, in *Tectonic Evolution of SE Asia*, edited by R Hall and D. Blundell, *Geol. Soc. Spec. Pub., 106*, 525-537, 1996.

Crowhurst, P. V., K. C. Hill, and D A. Foster, Thermal history of northern Papua New Guinea implication for tectonics and mineral exploration, in *Proceedings of the PNG Geology, Exploration and Mining Conference, 1997, Madang*, edited by G E. Hancock, pp. 51-60, Aust. Inst. of Min. and Metal., Melbourne, Victoria, 1997.

Cullen, A. B., Ramu Basin, Papua New Guinea· A record of late Miocene terrane collision, *AAPG Bull., 80*, 663-684, 1996.

Davies, H. L., Crustal structure and emplacement of ophiolite in southeastern Papua New Guinea, *Collo. Int. C. N. R. S., 272*, 17-33, 1980.

Davies, H. L., and A. L. Jaques, Emplacement of ophiolite in Papua New Guinea, In *Ophiolites and Oceanic Lithospheree*, edited by I.G Gass, S. J. Lippard, and A. W. Shelton, *Geol. Soc. Spec Publ., No. 13*, 341-349, 1984.

Davies, H. L., R. D. Winn, and P Kengemar, Evolution of the Papuan Basin. - A view from the orogen, in *Petroleum Exploration, Development and Production in Papua New Guinea: Proceedings of the Third PNG Petroleum Convention, Port Moresby September 1996*, edited by P.G. Buchanan, pp. 53-62, PNG Chamber of Mines and Petroleum, Port Moresby, 1996.

Davies, H. L., R C. B. Perembo, R D. Winn, and P. Kengemar, Terranes of the New Guinea Orogen, in *Proceedings of the PNG Geology, Exploration and Mining Conference 1997, Madang*, edited by G. E Hancock, pp. 61-66, Aust Inst. of Min and Metal. Melbourne, Victoria, 1997

Dow, D. B., Geological synthesis of Papua New Guinea, *Bull. Bur. Miner Res. Geol. and Geophys. Aust., 201*, 41 pp., Canberra, 1977.

Forwood, J , The geology and structure of the Egele south area, Papua New Guinea and the geochemistry and tectonic affinities of five intrusives from the New Guinea Mobile Belt, Honours thesis, 122 pp, La Trobe Uni , Melbourne, Victoria Australia, 1990

Francis, G. The North New Guinea Basin and associated infra-basins, in *Petroleum Exploration in Papua New Guinea: Proceedings of the First PNG Petroleum Convention, 1990, Port Moresby*, edited by G. J. Carman and Z Carman, pp. 445-460, PNG Chamber of Mines and Petroleum, Port Moresby, 1990.

Francis, G., R. Rogerson, D Hilyard, and D. W. Haig, *Excursion Guide to the Wahgi and Chimbu Gorges, First PNG Pet. Conv Excursion Guide Ser* Edited by R. Rogerson, Geol. Surv. of Papua New Guinea, Port Moresby, 1990.

Galbraith, R F., The radial plot: Graphical assessment of spread in ages, *Nucl Tracks Radiat Meas., 17*, 207-214, 1990.

Galbraith, R F, and G. M Laslett, Statistical models for mixed fission track ages *Nucl Tracks Radiat. Meas., 21*, 459-470, 1993

Gallagher, K., Evolving temperature histories from apatite fission track data, *Earth Planet Sci Lett., 136*, 421-435, 1995.

Gleadow, A. J W., I. R Duddy, and J. F Lovering, Fission track analysis· A new tool for the evaluation of thermal histories and hydrocarbon potential, *Aust Pet. Explor. Assoc. J, 23*, 93-102, 1983.

Gleadow, A. J W, I R. Duddy, P. F. Green, and J. F. Lovering, Confined fission track lengths in apatite A diagnostic tool for thermal history analysis, *Contrib. Mineral Petrol., 94*, 405-415, 1986.

Green, P. F, I. R Duddy, A. J. W. Gleadow, P. T Tingate, and G M Laslett, Thermal annealing of fission tracks in apatite, 1, A qualitative description *Chem. Geol., 59*, 237-253, 1986.

Green, P F, I. R Duddy, A. J W Gleadow, and J F. Lovering, Apatite fission track analysis as a palaeotemperature indication for hydrocarbon exploration, in, *Thermal History of Sedimentary Basins· Methods and Case Histories*. edited by N.D. Naeser, pp. 181-195, New York, Springer-Verlag, 1989

Hall, R, Cenozoic tectonics of SE Asia and Australasia, in *Petroleum Systems of SE Asia and Australasia Indonesian Petroleum Association Conference, Jakarta, May 1997*, edited by J.V.C. Howes and R.A. Noble pp. 47-62, Indonesian Pet. Assoc., Jakarta, 1997.

Hamilton, W. B Subduction systems and magmatism, in *Volcanism Associated With Extension at Consuming Plate Margins*, edited by Smellie, J.L. *Geol Soc. Spec Publ, No. 81*, 3-28, 1994.

Hegarty, K. A , and J. K Weissel, Complexities in the development of the Caroline Plate region, western equatorial Pacific, in *The Ocean Basins and Margins*, vol 7B, *The Pacific Ocean*, edited by A.E.M. Nairn, F.G. Stehli, and S Uyeda, pp 277-301, *Plenum, New York*, 1988

Hill, K. C., and A. J. W. Gleadow, Uplift and thermal history of the Papuan Fold Belt, Papua New Guinea: Apatite fission track analysis. *Aust. J Earth Sci., 36*, 515-539, 1989.

Hill, K. C., D. Medd, and P. Darvall, Structure, stratigraphy, geochemistry and hydrocarbons in the Kagua-Kubor area, Papua New Guinea, in *Petroleum Exploration in Papua New Guinea: Proceedings of the First PNG Petroleum Convention, 1990, Port Moresby*, edited by G J Carman and Z Carman, pp. 351-368, PNG Chamber of Mines and Petroleum, Port Moresby, 1990.

Hill, K. C., A. Grey, D. A. Foster, and R. Barrett, An alternative model for the Oligo-Miocene evolution of northern PNG and the Sepik-Ramu Basins, in *Petroleum Exploration and Development in Papua New Guinea· Proceedings* *of the Second PNG Petroleum Convention, Port Moresby*, edited by G. J. Carman and Z Carman, pp. 241-259, PNG Chamber of Mines and Petroleum, Port Moresby, 1993.

Jaques, A L, High K_2O-island arc volcanics from the Finisterre and Adelbert Ranges, northern Papua New Guinea, *Geol Soc. Am. Bull., 87*, 861-867, 1976

Jaques, A. L., and G. P. Robinson, Continent/island arc collision in northern Papua New Guinea, *BMR J. Aust Geol. Geophys, 2*, 289-303, 1977

Kendrick, R D, K. C Hill, K Parris, I Saefudin, and P. B O'Sullivan, Timing and style of Neogene regional deformation in the Irian Jaya Fold Belt, Indonesia, *in The Petroleum Industry's Contribution to Indonesia's Development: Past, Present and Future: Proceedings of the 24th Annual Convention Jakarta, October 10-12, 1995*, pp 249-261, Indonesian Pet Assoc, Jakarta, 1995.

Kroenke, L W, Cenozoic tectonic development of the southwest Pacific, *Tech. Bull. 6*, Comm for Coord. of Joint Prospe. in S. Pac. Offshore Areas, CCOP/SOPAC, Suva, Fiji, 1984

Laslett, G. M., P. F. Green, I. R. Duddy, and A J W. Gleadow, Thermal annealing of fission tracks in apatite, 2, A quantitative analysis. *Chem Geol 59*, 237-253, 1987.

Ludwig, W., and J L. Probst, River sediment discharge to the oceans: Present-day controls and global budgets, *Am J of Sci. 298*(4), 265-295, 1998.

Milliman, J D., Sediment discharge to the ocean from small mountainous rivers: The New Guinea example, *GeoMar Lett., 15*(3-4), 127-133, 1995.

Naeser, C W., Thermal history of sedimentary basins from fission track dating of subsurface rocks, in *Aspects of Diagenesis, Spec. Publ. Soc Econ. Paleontol. and Miner., 26*, 109-112, 1979

Page, R W, Geochronology of igneous and metamorphic rocks in the New Guinea Highlands, *Bull Bur Miner Res Geol. and Geophys. Aust, 162*, 117 pp., 1976.

Pegler, G., S. Das, and J. H Woodhouse, A seismological study of the eastern New Guinea and the western Solomon Sea regions and its tectonics implications, *Geophys J Int, 122*, 961-981, 1995.

Pigram, C. J, and P. A. Symonds, A review of the timing of the major tectonic events in the New Guinea Orogen, *J Southeast Asian Sci, 6*, 307-318, 1991

Ripper, I., and K. F McCue, The seismic zone of the Papuan Fold Belt, *BMR J. Aust. Geol. and Geophys, 8*, 147-156, 1983.

Robinson, G. P, A. L. Jaques and C. M. Brown. Madang, geological map and explanatory notes, 1.250,000 sheet SB/55-6, Dep. of Miner and Energy, Geol. Surv. of Papua New Guinea, Port Moresby, 1976

Rodda, C W., Petrogenesis of the Wahgi-Chimbu Gorge and geology and structure of the Egele Anticline, Papua New Guinea Honours thesis, 68 pp., La Trobe Univ., Melbourne, Victoria, Australia, 1990.

Rogerson, R., and A. Williamson, Age, petrology and mineralisation associated with the two Neogene intrusive types in the Eastern Highlands of Papua New Guinea, *Open File Rep. Geol. Surv. Papua New Guinea, 85 2*, 1985

Rogerson, R. J., D B. Hilyard, E. J. Finlayson, D. J Holland, S T S Nion, R M Sumaiang, J. Duguman, and C D. C. Loxton, The geology and mineral resources of the Sepik Headwaters region, Papua New Guinea, *Mem. Geol. Surv Papua New Guinea, 12*, 130 pp, 1987.

Samuel, K., and A Sie, The Mount Victor Gold Mine, Eastern Highlands Province, Papua New Guinea, in *Proceedings of the PNG Geology, Exploration and Mining Conference, 1991, Rabaul*, edited by R Rogerson, pp 125-131, Aust. Inst Min. and Metall, Melbourne, 1991.

Silver, E A, and R. B Smith, Comparison of terrane accretion in modern Southeast Asia and the Mesozoic North American Cordillera, *Geology, 11*, 198-202, 1983.

Stockhert, B., M. R. Brix, R. Kleinschrodt, A. J. Hurford, and R. Wirth, Thermochronometry and microstructures of quartz. A comparison with experimental flow laws and predictions on the temperature of the brittle-plastic transition, *J Struct Geol., 21*, 351-369, 1999.

Tagami, T, R. F Galbraith, G M. Yamada, and G. M. Laslett, Revised annealing kinetics of fission tracks in zircon and geological implications, in *Advances in Fission-Track Geochronology*, edited by P. Van den Haute and F De Corte, pp 99-112, Kluwer Acad., Norwell, Mass, 1998

Taylor, B, Bismarck Sea. Evolution of a back-arc basin, *Geology, 7*, 171-174, 1979

Weiland, R J, and M. Cloos, Pliocene-Pleistocene asymmetric unroofing of the Irian Jaya fold belt, Irian Jaya, Indonesia: Apatite fission-track thermochronology, *Geol Soc Am. Bull., 108*, 1438-1449, 1996

Weissel, J K., and A. B. Watts, Tectonic evolution of the Coral Sea Basin, *J. Geophys Res., 84*(B9), 4572-4582, 1979.

Young, G. C., and J R. Laurie (Eds) *An Australian Phanerozoic Time-Scale*, 279 pp., Oxford Univ. Press, New York, 1996.

K.C. Hill, Australian Geodynamics Cooperative Research Centre, Department of Earth Sciences, La Trobe University, Bundoora, Victoria 3083, Australia.(email: khill@latrobe.edu.au)

A Raza, School of Earth Sciences, University of Melbourne, Parkville, Victoria 3052, Australia.

(Received August 3, 1998;
revised July 13, 1999;
accepted July 13, 1999.)

TECTONICS, VOL. 18, NO. 6, PAGES 1120-1138 DECEMBER 1999

Evolution of the transport direction of the Carpathian belt during its collision with the east European Platform

J.-C. Hippolyte[1]
URA 1759 CNRS, University of Paris VI, Paris

D. Badescu and P. Constantin
Institute of Geology, Bucharest

Abstract. The evolution of the Carpathians is in its final stage with intermediate seismic activity (70-200 km, M_w= 4-7.7) localized beneath its southeastern salient (Vrancea zone). Our analysis, in the transition area between south Carpathians and east Carpathians, reveals that the termination of convergence is characterized by a clockwise rotation of the Carpathian belt transport direction. Using structural maps and cross sections, we show that this change of convergence direction had several structural consequences including (1) the Pliocene-Quaternary activation of out-of-sequence structures in the southern east Carpathians and (2) the creation of dextral strike-slip faults bounding the mobile belt to the west, in the south Carpathians. Our fracture analysis in syntectonic deposits allows us to distinguish and stratigraphically date two fanning stress patterns, corresponding to the two last transport directions of the Carpathian system (1) a Burdigalian to early Tortonian stress field with compression directions rotating along with the Carpathian curved orogenic belt but with transpression (NW-SE compression) and a low-strain partitioning along east trending internal strike-slip faults in the south Carpathians and (2) a late Tortonian to Pleistocene rotated and smaller radial stress pattern, with N-S compression in the south Carpathians. The rotation of the convergence direction is interpreted as the result of the Miocene migration and progressive collision of the Carpathian system with the thick crust of the NW trending Tornquist-Teisseyre line and its prolongation in Romania. The area able to subduct, determined by thickness of crust entering the subduction zone, was progressively restricted to a foreland corner in front of the southeastern Carpathians. The progressive collision forced the convergence to slow down and rotate from eastward to southeastward in late Miocene. The Dobrogea hills in front of the latest migrating system may represent the late Neogene NE-SW flexural bulge of the subducting foreland panel. This clockwise rotation of the transport direction can be compared with the clockwise rotation that occurred in other subduction systems (Tyrrhenian subduction, Caribbean subduction, etc.) which were controlled by the location of oceanic versus continental crust in front of the orogenic belt.

1. Introduction

Within the Alpine mountain belt system the Carpathians form a great Z-bend chain connecting the eastern Alps to the Balkans (inset of Figure 1a). The Carpathians globally constitute a north and east verging structure that wraps to the north around the Pannonian and Transylvanian Basins (Figure 1b) and to the south around the Moesian foreland platform. The definitive shape of this double-loop belt was obtained during Neogene times when the intra-Carpathian area moved laterally both away from the central and eastern Alps collision zone [*Tapponnier*, 1977; *Ratschbacher et al.*, 1991] and toward the east and northeast (Figure 1a) where lithosphere could be subducted beneath the arc [*Royden et al.*, 1982]. These models of block transport predict large dextral movements, located north of the Moesian platform and south of the Transylvanian Basin (Figure 1b) [e.g., *Airinei*, 1983], trending parallel to the transport direction, and accommodating >100 or 200 km of displacement mostly during the middle Miocene [*Royden*, 1988]. However, while the hypothesis of such dextral movements is consistent with paleostress orientations in the central part of the south Carpathians (Figure 1b) [*Ratschbacher et al.*, 1993], more to the east, the published maps [e.g., *Sandulescu et al.*, 1978] do not indicate the presence of E-W strike-slip faults with significant offset (Figure 1a).

The intermediate-depth seismic activity of the Vrancea zone (Figure 1b) and the Pliocene-Quaternary "Wallachian folds" (Figure 1a) show that the tectonic activity continued until present times. However, the Pliocene-Quaternary compression, which is only identified in the southeastern Carpathian salient, is usually considered a minor and local deformational event, and the last 9 m.y. evolution of the Carpathians is not well integrated in the geodynamical models of migration of the Carpathian-Pannonian system.

In this paper we present a structural analysis of the transition area (Figure 2) between the south Carpathians, where strike-slip faulting is supposed to be dominant, and the east Carpathians, where thrusts are the main structures. In particular, we try to characterize the strike-slip fault pattern and unravel its relationships with the thrust deformation nearby. The study of this Carpathian area, where the tectonic

[1]Now at UMR CNRS 5025, Laboratoire de Géodynamique des Chaînes Alpines, Université de Savoie, Campus Scientifique Technolac, Le Bourget du Lac, France.

Paper number 1999TC900027
0278-7407/99/1999TC900027$12.00

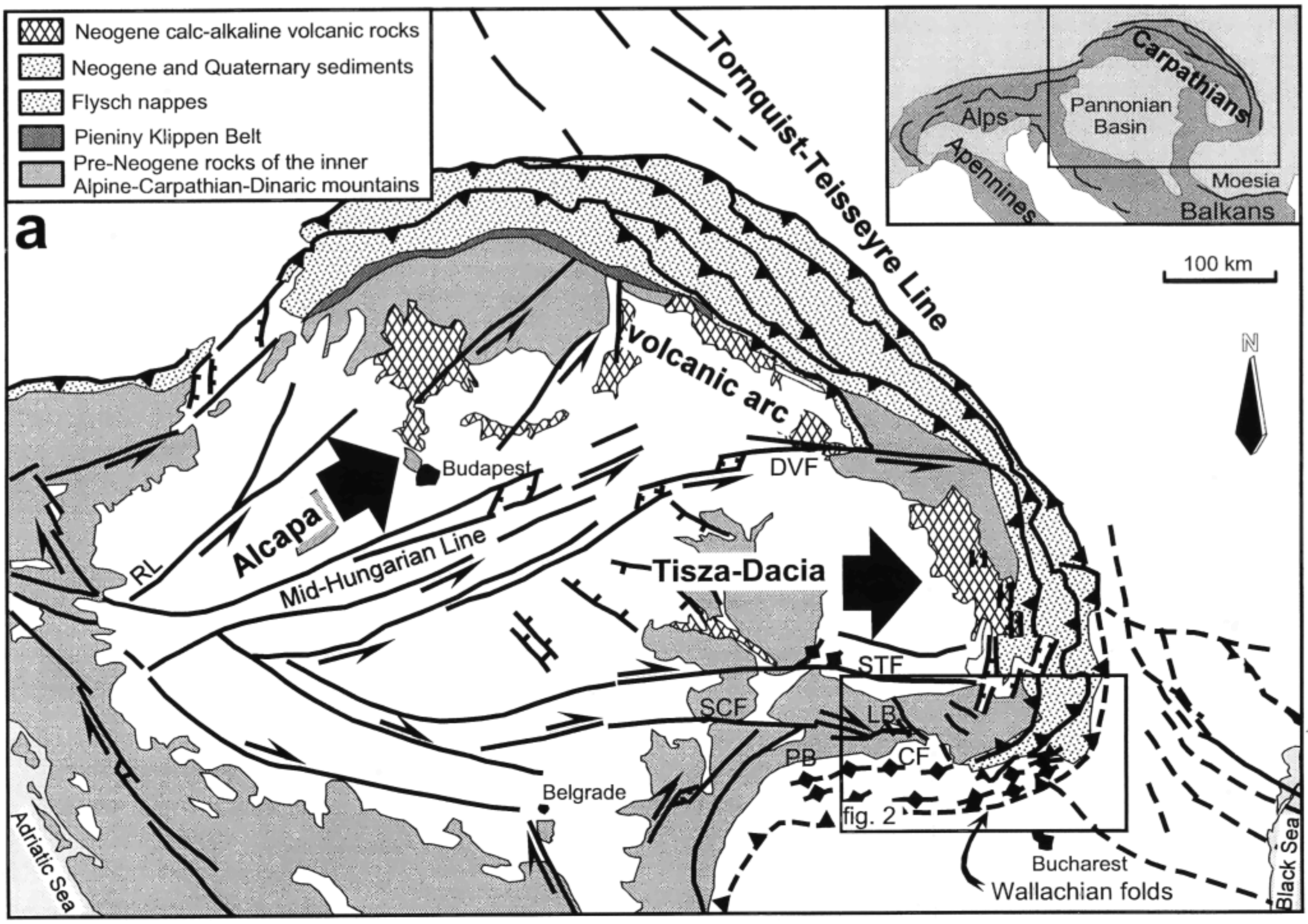

Figure 1. (a) Structural units of the Carpathian area with middle Miocene kinematics according to *Royden et al.* [1982], *Csontos et al.* [1991], and *Fodor et al.* [1996]. The intra-Carpathian Alcapa and Tisza-Dacia blocks moved toward the northeast and east, respectively. The inset shows the location of the Carpathians within the European Alpine system. Abbreviations are defined as follows: CF, Cozia fault; DVF, Dragos-Voda fault; LB, Lovistei Basin; PB, Petrosani Basin; RL, Rába Line; SCF, south Carpathian fault; STF, south Transylvanian fault. (b) Principal crustal domains and sedimentary basins. Seismicity is from *Cornea et al.* [1979]. Crustal thicknesses are from *Guterch et al.* [1986] and *Mocanu and Radulescu* [1994]. Thickness of Neogene sediments are according to *Dumitrescu and Sandulescu* [1970] and *Royden et al.* [1982]. Age of calc-alkaline rocks is according to *Royden et al.* [1982] and *Szakács and Seghedi* [1995]. Note the eastward progression of the age in Carpathian arc calc-alkaline volcanism. Note also the trend of the east Carpathians, parallel to the NW trending faults of the Tornquist-Teisseyre line and the thick crust at the southwestern border of the east European platform (Laramian Polish swell and North Dobrogea Kimmerian orogen).

activity is the most complete with Pliocene-Quaternary deformation, is aimed at understanding the evolution of the Carpathian belt transport during all of the Neogene.

2. Geological Framework

The Carpathian chain is a thin-skinned fold-and-thrust belt that overlies the autochtonous east European and Moesian platforms (Figure 1b). Its formation was contemporaneous with the filling of two main Neogene intra-Carpathian basins, the Pannonian Basin and the Transylvanian Basin, and of a foreland basin with up to 8 km of Neogene sediments in the Focsani depression (Figure 1b) [*Dumitrescu and Sandulescu*, 1970; *Sandulescu*, 1975].

The major factors that have contributed to the formation of the Carpathian-Pannonian system are the N-S convergence between the Adriatic and Eurasian plates [*Le Pichon et al.*, 1988], the collision in the Alps and the lateral escape of crustal wedges toward the east and north [*Tapponnier*, 1977; *Ratschbacher et al.*, 1991; *Kázmér and Kovács*, 1985; *Balla*, 1987; *Csontos et al.*, 1992], the extensional collapse of the thickened Alpine crust [*Ratschbacher et al.*, 1991; *Horváth*, 1993], the subduction and rollback of the Eurasian plate [*Royden et al.*, 1982; *Royden*, 1993, *Csontos*, 1995], and the

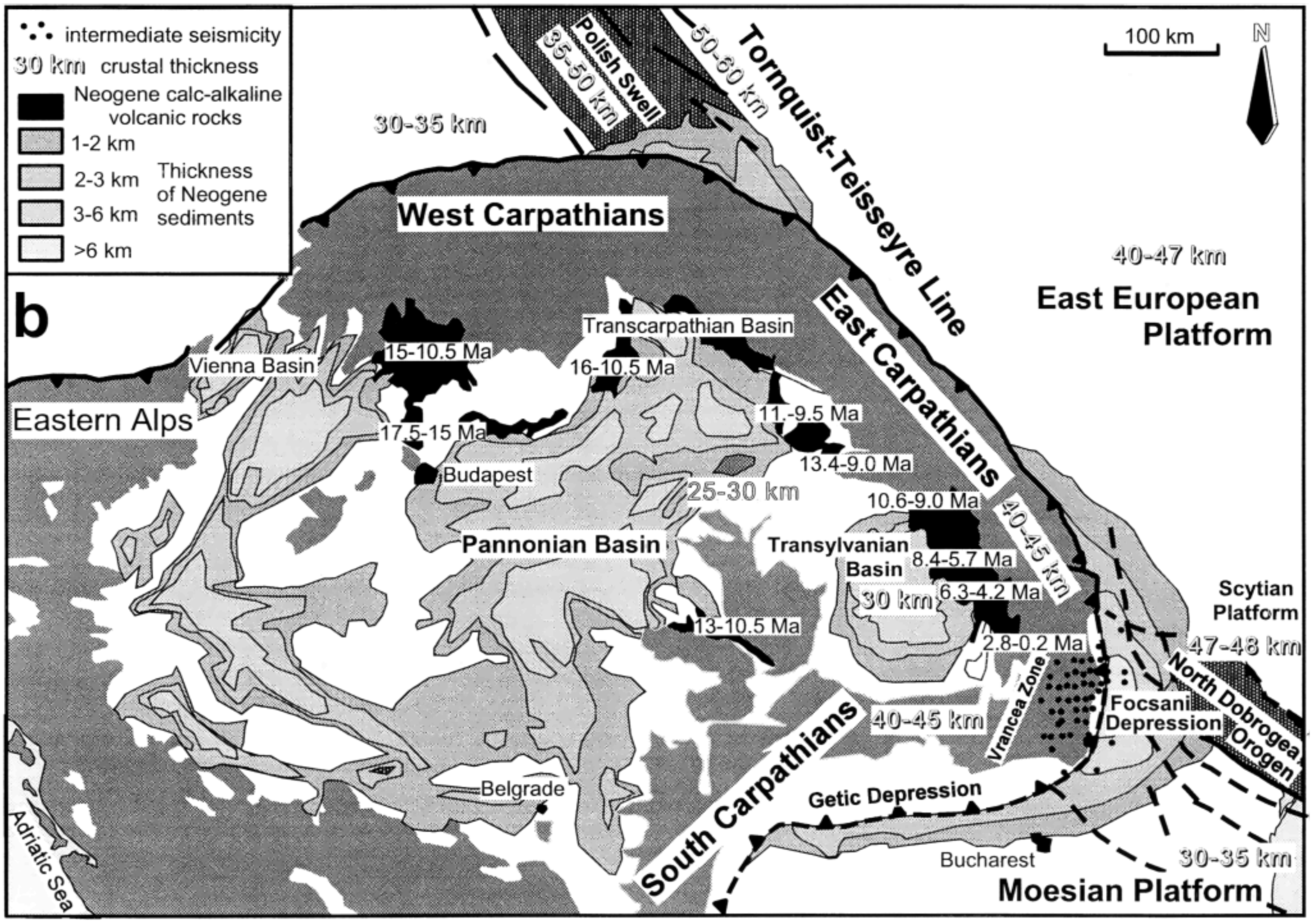

Figure 1. (continued)

shape and structures of the Eurasian margin with its northwest trending faults prolonging to the southeast the Polish Tornquist-Teisseyre line [*Sandulescu and Visarion*, 1988; *Ellouz and Roca*, 1994; *Hippolyte et al.*, 1996; *Horváth and Cloetingh*, 1996; *Roure et al.*, 1996].

A set of large strike-slip faults running through the Pannonian Basin (Figure 1a) recorded the late Tertiary northeastward and eastward transport of crustal material away from the central and eastern Alps collision zone [*Royden et al.*, 1982; *Balla*, 1987; *Horváth*, 1988; *Royden*, 1988; *Csontos et al.* 1991; *Ratschbacher et al.*, 1991]. This displacement was contemporaneous with the migration of the subduction zone toward the east, associated with the steepening of a west dipping subducted slab [*Spakman et al.*, 1993], which is, at present, known in a nearly vertical position in the Vrancea seismic zone (Figure 1b) [*Roman*, 1970; *Royden et al.*, 1982; *Oncescu*, 1984]. The subduction and rollback of this oceanic or thinned continental European crust was recorded in a volcanic arc, where the calc-alkaline Miocene rocks are progressively younger toward the southeast (Figure 1b) [*Radulescu and Sandulescu*, 1973; *Royden et al.*, 1982; *Szakács and Seghedi*, 1995].

The Carpathian belt includes two major structures (Figure 1a): an inner orogenic belt deformed during Cretaceous and early Paleogene and an outer belt that results from the Neogene subduction and that is composed of Cretaceous to Miocene flysch and molasse [e.g., *Sandulescu*, 1975]. The nappes of this latter belt display a piggyback sequence of thrusting. The nappe emplacement becomes younger from more internal to more external parts of the flysch belt, attesting to a continuous eastward progression of deformation [*Dumitrescu and Sandulescu*, 1970; *Sandulescu*, 1988; *Roure et al.*, 1993]. Moreover, timing of nappe transport within the outer Carpathians varies along the strike of the orogenic belt [*Sandulescu*, 1975; *Jîricek*, 1979; *Oszczypko and Slaczka*, 1985; *Royden*, 1988]. The termination of thrusting is younger toward the southeast, and the most recent deformation is a Pliocene-Quaternary folding and thrusting confined in the southern east Carpathians [*Stille*, 1924; *Mrazec*, 1927; *Dumitrescu and Sandulescu*, 1968; *Hippolyte and Sandulescu*, 1996]. This folding (Figure 1a) allowed *Stille* [1924] to define the term "Wallachian phase", which is still used in geological timescales to name a Pliocene-Quaternary event.

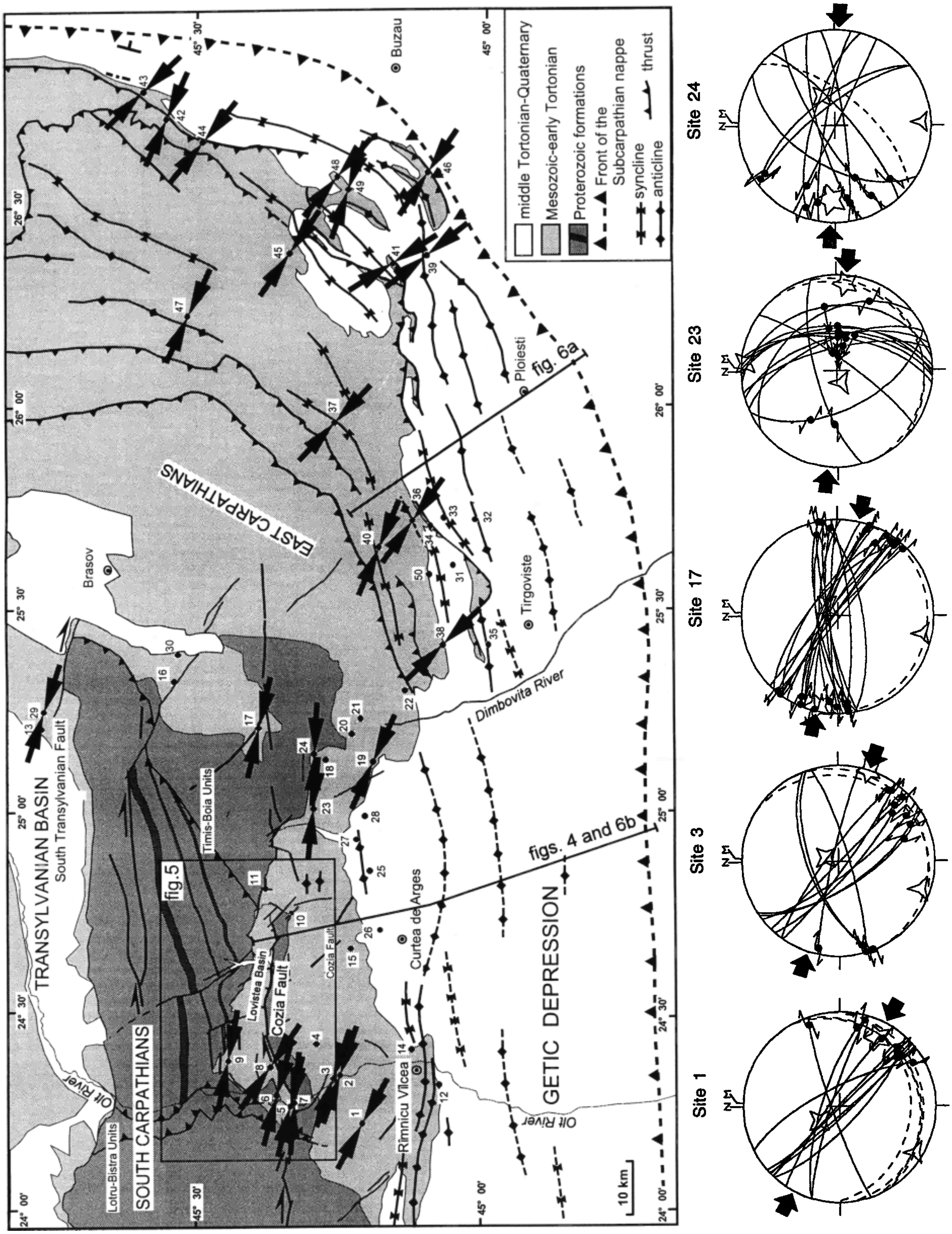

Figure 2. Structural sketch of the southeastern Carpathians (location in Figure 1a) with the Miocene directions of compression (see also Table 1). The directions of compression are perpendicular to thrust faults and the deformation front in the east Carpathians, but they are oblique to the deformation front in the south Carpathians.

The Miocene convergence in the outer Carpathians was synchronous to lithosphere stretching in the intra-Carpathian basins [*Royden*, 1988]. Royden showed that in the Pannonian plate the locus of major extensional activity migrated progressively southward and that this change through time of the location of active extension was consistent with the coeval change in the location of active thrusting along the Carpathian belt. Extension began in the Pannonian Basin in the early Miocene but was confined along major faults in the northern area (Vienna and Transcarpathian Basins) (Figure 1b). It was synchronous with the Burdigalian northward to eastward thrusting along the west and east Carpathians [e.g., *Sandulescu*, 1975; *Jîricek*, 1979; *Royden*, 1988; *Morley*, 1996]. At that time, the Pannonian plate was divided into two main blocks, Tisza-Dacia to the south and Alcapa to the northwest (Figure 1a), [*Csontos et al.*, 1992; *Fodor et al.*, 1996]. The Alcapa block, in which 35°-90° counterclockwise block rotations were evidenced [*Márton and Mauritsh*, 1990], contrasts with the Tisza-Dacia block, where clockwise rotations up to 60°-80° have been determined [*Patrascu et al*, 1994], and moved northeastward along the dextral mid-Hungarian line [e.g., *Fodor et al.*, 1996], (Figure 1a).

The regional "back arc" extension [*Royden et al.*, 1982] only began in the middle Miocene when tectonic activity migrated southward and generated deep basins along major strike-slip faults over much of the Pannonian region (Figure 1). The strike-slip faults that connected areas of coeval extension to one another form a conjugate set with northeast trending sinistral faults and northwest trending dextral faults [*Royden et al.*, 1982] (Figure 1a) that correspond to roughly east-west extension and north-south shortening across the Pannonian region [*Bergerat*, 1989; *Royden*, 1988; *Peresson and Decker*, 1997]. The major displacement of the Tisza-Dacia block toward the east reversed the slip on the Dragos-Voda fault from a dextral to a sinistral sense [*Morley*, 1996] (Figure 1a) and resulted in the middle to late Miocene (i.e., Badenian-Sarmatian in the Paratethys chronostratigraphy of the Dacian Basin [*Steininger et al.*, 1988] shortening in the east Carpathians [*Sandulescu*, 1988; *Roure et al.*, 1993; *Artyushkov et al.*, 1996]. Most researchers agree that the compressional stress trajectories, contemporaneous with this shortening, are radial, trending approximately perpendicular to the main structures of the east Carpathian belt (A. Caire as discussed by *Bouillin and Caron* [1975], *Hippolyte and Badescu* [1993], *Hippolyte and Sandulescu* [1996], *Linzer* [1996], and *Morley* [1996]).

In the intra-Carpathian domain the main strike-slip fault activity [*Royden*, 1988] and its related block rotations [*Patrascu et al.*, 1994; *Márton and Mauritsh*, 1990] terminated ~10-12 m.y. ago (late Serravallian-early Tortonian), and largely undeformed late Miocene sedimentary units lie on top of the fault bounded early to middle Miocene basins. In the east Carpathians the emplacement of the outermost thrust sheet (sub-Carpathian nappe) also ended during late Serravallian-early Tortonian (middle Sarmatian in the Paratethys chronostratigraphy) [*Dicea and Tomescu, 1969*; *Sandulescu*, 1975], but the direction of compression remained the same until early Tortonian (late Sarmatian in the Paratethys chronostratigraphy) [*Hippolyte and Sandulescu*, 1996]. *Peresson and Decker* [1997] proposed that this late Miocene end or slowdown of tectonic activity corresponds to a soft collision in the east Carpathians, during which the compressive east directed principal stress was transferred through the earlier extended Pannonian region into the eastern Alps, up to 1400 km behind the subduction zone. The late Miocene compression would have caused the pronounced postrift subsidence by stress-induced flexure of the Pannonian lithosphere [*Horváth and Cloetingh*, 1996]. Even if much of the thrust activity terminated in Tortonian times in the Carpathians belt, compressional deformation proceeded until Quaternary times in the southeastern Carpathian salient characterized by the Wallachian folds (Figure 1a) [*Stille*, 1924].

3. Problems and Method

Determination of the block movement directions is a major issue for understanding the formation of the Carpathian belt. It is also important for map and cross-section restoration because in restoring a curved orogenic belt, one faces the problem of convergent restoration paths with artificial overlap of structural units [e.g., *Ellouz et al.*, 1996; *Morley*, 1996]. Taking as restoration directions the compression direction determined by several authors in the south and east Carpathians [*Ratschbacher et al.*, 1991; *Hippolyte and Sandulescu*, 1996; *Linzer*, 1996; *Morley*, 1996; *Matenco et al.*, 1997] does not solve this problem because the pattern of Miocene stress trajectories is radial, partly due to the combination of forces produced by plate convergence and body forces acting normal to the trend of the mountain belt [*Platt et al.*, 1989], and therefore the restoration paths are also convergent. Effectively, in the south Carpathians the maximum horizontal principal stress (σ_1) is trending NW-SE and is oblique to the main structures, but toward the north it is perpendicular to the main structures of the east Carpathians and rotates along with the trend of this orogenic belt.

Studies of major intra-Carpathian strike-slip faults were more conclusive because they revealed that major blocks moved between parallel sinistral and dextral strike-slip faults [*Royden*, 1988; *Csontos et al.*, 1992; *Horváth*, 1993] (Figure 1a). These strike-slip faults, probably connecting areas of extension in the intra-Carpathian domain to areas of coeval shortening within the thrust belt, help in understanding the kinematics of the thrust belt. Even if a few faults previously considered as subvertical, in particular, the "Rába line" (Figure 1a), are now interpreted as low-angle thrusts reactivated as extensional faults [*Tari et al.*, 1992; *Horváth*, 1993], the strike-slip pattern as presented in Figure 1a remains globally valid and indicates the major directions of block movements.

The displacement magnitude of these faults is more difficult to determine. However, the estimations of the east to northeast Miocene shortening within the east Carpathians, from >100 km to >200 km [*Burchfiel*, 1980; *Royden*, 1988; *Ellouz and Roca*, 1994; *Ellouz et al.*, 1996; *Morley*, 1996], are indicative of their high values. It is usually recognized that the Miocene shortening in the east Carpathians was accommodated by right-lateral slips in the south Carpathians [e.g., *Airinei*, 1983; *Royden*, 1988; *Csontos et al.*, 1992]. More precisely, movements on parallel dextral (to the south)

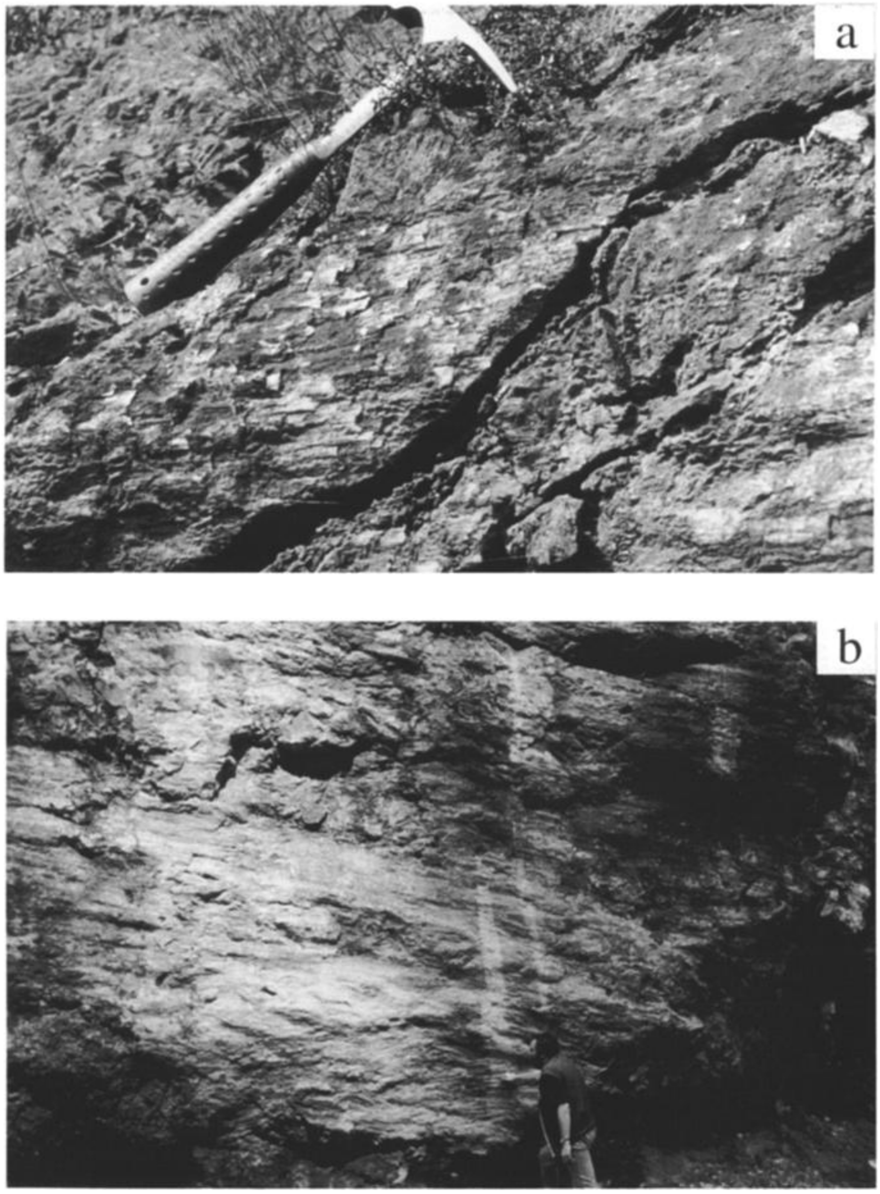

Figure 3. Examples of strike-slip fault used for stress inversion. (a) Mesoscale northwest trending fault with steps of calcite indicating a sinistral movement (site 6 in Figure 2). This fault cuts the tilted Campanian-Maastrichtian formation. The corresponding Schmidt diagram in Figure 5 shows that this fault moved with the WNW-ESE Miocene compression. (b) Dextral strike-slip fault at site 10 (Figure 7). The sense of movement was indicated by fibrous calcite and Riedel criteria. The corresponding direction of compression is N-S (Figure 5b).

and sinistral (to the north) faults seem to have participated in the Tisza-Dacia block transport (Figure 1a). The presence of pull-apart-like basins at the northern edge of the Tisza-Dacia block and along the east trending Dragos-Voda fault effectively suggests a sinistral strike-slip movement and eastward block transport during the middle to late Miocene [*Royden*, 1988; *Csontos et al.*, 1992]. However, the counterpart of this movement and the thrusting in the east Carpathians, which is expected to be >100-200 km [*Royden*, 1988], is not well documented. According to *Royden* [1988], this movement may have occurred at the front (to the south) of the south Carpathian thrust sheets. However, *Ratschbacher et al.* [1993] propose that some east trending faults in the south Carpathians underwent large-scale Miocene dextral wrenching. The main argument to suggest this dextral movement on east trending faults during the Miocene is the existence of a southeast trending compression in the central south Carpathians (Figure 1a) [*Ratschbacher et al.*, 1993; *Matenco et al.*, 1997]. However, an analysis around the Transylvanian Basin [*Huisman et al.*, 1997] concludes that NW-SE and E-W trends of compression correspond to a late Oligocene and to a Pliocene event, respectively, whereas the

Table1. Paleostress Tensors Computed from Fault Slips Measured at the Sites of Figures 2 and 7

Site	Age of Rocks	T	N	σ_1, deg		σ_2, deg		σ_3, deg		Φ	ANG, deg
				Trend	Plunge	Trend	Plunge	Trend	Plunge		
1	Ypresian-Lutetian	S	10	119	19	324	69	212	08	0.43	06
		E	09	339	85	101	03	191	04	0.46	10
		E	09	332	84	156	06	066	01	0.40	11
2	Ypresian-Lutetian	S	14	109	15	294	75	199	01	0.40	07
		E	17	342	83	087	02	177	07	0.26	11
3	Ypresian-Lutetian	S	12	109	00	017	79	199	11	0.56	09
		E	10	334	69	164	20	073	03	0.51	05
4	Ypresian-Lutetian	E	08	310	88	062	01	152	01	0.35	08
5	Campanian-Maastrichtian	S	16	104	04	007	57	197	33	0.31	09
6	Campanian-Maastrichtian	S	21	105	06	343	79	196	09	0.43	15
7	Late Proterozoic	S	13	095	11	345	61	190	27	0.23	13
8	Paleocene-Ypresian	S	15	125	01	360	88	215	02	0.71	07
		E	08	167	81	296	06	027	07	0.28	15
9	Paleocene-Ypresian	S	06	101	24	323	59	199	18	0.20	15
		E	20	350	77	238	05	147	12	0.28	13
		E	11	305	74	154	14	062	08	0.36	08
10	Paleocene-Ypresian	S	14	170	17	040	65	265	18	0.24	07
		E	08	280	83	058	05	149	05	0.44	05
11	Oligocene	E	05	269	79	082	11	172	01	0.51	07
12	Badenian (middle Miocene)	C	25	207	06	298	06	072	82	0.24	09
		E	10	355	62	230	17	133	22	0.53	11
13	Badenian (middle Miocene)	S	17	356	26	145	60	260	14	0.44	11
		E	23	203	69	022	21	112	00	0.55	07
14	Badenian (middle Miocene)	C	10	211	10	119	13	337	74	0.13	08
15	Burdigalian-Langhian	C	25	164	04	255	06	039	82	0.43	06
16	Lutetian-Priabonian	S	14	343	02	097	86	253	04	0.51	06
17	Kimmeridgian-Portlandian	C	06	339	01	070	43	248	47	0.10	12
		S	22	283	06	042	78	192	10	0.39	09
18	Oligocene-Burdigalian	C	11	346	15	080	13	209	71	0.29	11
19	Burdigalian-Langhian	C	12	164	09	074	01	336	80	0.50	11
		S	15	295	01	027	81	205	09	0.46	06
20	Albian	C	05	155	01	245	05	058	85	0.43	07
21	Albian	S	14	155	09	043	67	249	21	0.14	10
22	Lutetian	S	13	203	06	103	61	296	28	0.16	10
23	Eocene	C	13	096	10	005	05	250	79	0.50	10
24	Late Jurassic	S	10	273	25	066	63	178	11	0.25	09
		S	07	351	22	130	62	254	17	0.15	11
25	Dacian (early Pliocene)	C	10	324	01	054	13	232	77	0.10	05
26	Pontian (late Miocene)	S	10	010	11	158	77	278	07	0.64	09
		E	06	143	78	022	06	291	10	0.23	06
27	Pontian (late Miocene)	E	21	336	70	093	09	186	17	0.27	10
		E	10	057	69	181	13	275	17	0.57	07
28	Dacian (early Pliocene)	S	09	162	10	042	72	255	16	0.32	12
		E	15	147	72	001	15	268	09	0.41	10
29	Burdigalian	S	20	289	14	149	71	021	11	0.21	09
		C	17	285	05	016	16	180	73	0.50	10
30	Paleocene-Ypresian	E	05	181	80	026	28	290	11	0.21	09

See *Hippolyte and Sandulescu* [1996] for sites 31-50. Abbreviations are defined as follows: T, type of deformation; S, strike-slip; C, compressional; E, extensional; N, number of faults used for tensor calculation; $\Phi = (\sigma_2 - \sigma_3)/(\sigma_1 - \sigma_3)$; ANG, average angle between computed shear stress and observed slickenside lineations.

early Miocene is characterized by a N-S to NNE-SSW compression all around the Transylvanian Basin (Figure 1b). In fact, most of the fault planes analyzed [*Ratschbacher et al.*, 1993; *Matenco et al.*, 1997; *Huisman et al.*, 1997] are measured in Proterozoic to Mesozoic rocks. The discrepancies in the interpretations show the need for precise stratigraphic dating of these states of stress using faults measured in syntectonic deposits. Moreover, the continuation toward the nappe structure of the strike-slip faults presented in Figure 1a needs to be analyzed, and the displacement on these faults needs to be evaluated to validate the models.

Taking into account the classical geographic and geologic distinction of the south Carpathian belt from the east Carpathian belt, we consider the transition area (Figure 2) a key for understanding the formation of the Carpathians. Not even this transition area allows us to study the eastward extension of the east trending faults, but it includes the most recent deformation of the Carpathian belt and therefore gives access to the longest record of tectonic activity of the Carpathians. We used mapping of major faults and observations of slip indicators in the field to determine the direction of block movements. Measurements of kinematic indicators and palaeostress determinations are used to confirm the sense of movement of major faults, assuming that the fault movements at various scales (Figure 3a and 3b) are consistent with the determined stress field. We determined the orientations of the stress axes σ_1, σ_2, and σ_3 ($\sigma_1 \geq \sigma_2 \geq \sigma_3$, and pressure is considered positive) and the ratio $\Phi = (\sigma_2-\sigma_3)/(\sigma_1-\sigma_3)$ using the inversion technique of *Angelier* [1984]. Results of the stress tensor analyses and their quality estimators are listed in Table 1. Displacements on strike-slip faults are estimated using offset relationships. The late Neogene shortening in the nappe structures is determined on cross sections [*Stefanescu*, 1984]. This study, incorporating fracture measurement in the synorogenic late Neogene rocks, shows that two main periods can be distinguished in the late Tertiary geodynamic evolution of the Carpathian belt.

4. Early to Middle Miocene Kinematics

4.1. Structures

The south Carpathian range (Figure 2), constituted by nappes of Proterozoic metamorphic rocks overlain by a Mesozoic sequence [e.g., *Sandulescu*, 1975; *Berza*, 1994], contrast with the mountains of the outer east Carpathians, which are principally made of nappes of Cretaceous, Paleogene, and Neogene flysch. These flysch nappes, emplaced during the Neogene, were first thought to narrow and disappear at the southern edge of the east Carpathians (Figure 1). However, seismic profiles and drill cores [*Dicea and Tomescu*, 1969; *Paraschiv*, 1975; *Stefanescu*, 1984; *Dicea*, 1995] demonstrate that Neogene thrusts continue to the west beneath the late Miocene-Quaternary deposits of the Getic depression (Figure 2). *Stefanescu* [1984] made cross sections of the Carpathians, integrating most of the available seismic profiles (especially at the leading edge thrust) and drill core data issue from a long period of petroleum exploration in Romania. The cross section presented in Figure 4 shows that there is a buried Miocene fold-and-thrust belt at the southern edge of the south Carpathians that we can partly study in outcrops along the Olt and Dimbovita Rivers (Figure 2).

The northern (outcropping) part of the south Carpathians (Figure 2) is composed of two main groups of basement units, the Lotru-Bistra units and the Timis-Boia units [e.g., *Gheuca*, 1988; *Berza*, 1994]. Their contact zone is exposed along the Olt River. Both groups of nappes belong to the Getic-supra-Getic terrane that was thrusted, probably during the latest Cretaceous to earliest Tertiary times, over the Severin terrane with oceanic affinities, itself thrusted over the Danubian continental terrane [e.g., *Burchfiel*, 1976; *Berza*, 1994]. This Mesozoic nappe pile is uncomformably overlain by Paleogene to Quaternary sediments in the Getic depression and in the Lovistei Basin (Figures 2 and 4). As compressional faults cutting the Eocene to recent sedimentary sequence refer to the Neogene geodynamics [*Sandulescu*, 1975], these basins represent the areas of the south Carpathians where a fault analysis can reveal compression directions of certain Miocene to Recent age, without possible confusion with compression directions of the Cretaceous events. The compression directions determined in these formations will therefore indicate the Neogene possible kinematics of their neighboring major faults.

Two main east trending faults are known at the south of the Tisza-Dacia block and are supposed to move dextrally [*Sandulescu*, 1975; *Royden*, 1988; *Csontos et al.*, 1992; *Horváth*, 1993; *Ratschbacher et al.*, 1993]: the south Transylvanian fault and the south Carpathian fault (Figure 1a). This latter fault is prolonged in the eastern south Carpathians by the Cozia fault (Figures 1a and 2).

4.2. Geodynamics

To determine the Miocene geodynamics of the southeastern Carpathian salient, we measured fault planes with striations and movement sense indicators (Figure 3) and we computed paleostress axes. Except for two mutually perpendicular directions of extension (NNW-SSE and ENE-WSW, see Table 1) that we ascribe to the Paleogene subsidence, the Eocene to Recent rocks are characterized by strike-slip to reverse deformation. In contrast to most of the east Carpathians, in the Carpathian salient, while the trend of the orogenic belt rapidly changes from N-S to E-W (Figure 1), the direction of compression we date as Miocene does not rotate and remains with a WNW-ESE trend (Figure 2). The obliquity between the compression and the trend of the orogenic belt (Figure 2), together with the predominance of strike-slip faults in the observed mesoscale faults, indicate that the south Carpathian range is a transpressional orogenic belt. A similar NW-SE direction of compression was found in the central south Carpathians and was attributed to the Miocene tectonics [*Ratschbacher et al.*, 1993]. Because in our study area most of the faults were measured in Paleogene and Miocene rocks (Table 1) and because the most recent rocks recording this trend of compression are of early Tortonian (late Sarmatian in the Paratethys chronostratigraphy, sites 39, 41, 46, 48, and 49 in Figure 2, from *Hippolyte and Sandulescu*, [1996]), we confirm and specify a Miocene and premiddle Tortonian (Meotian in the

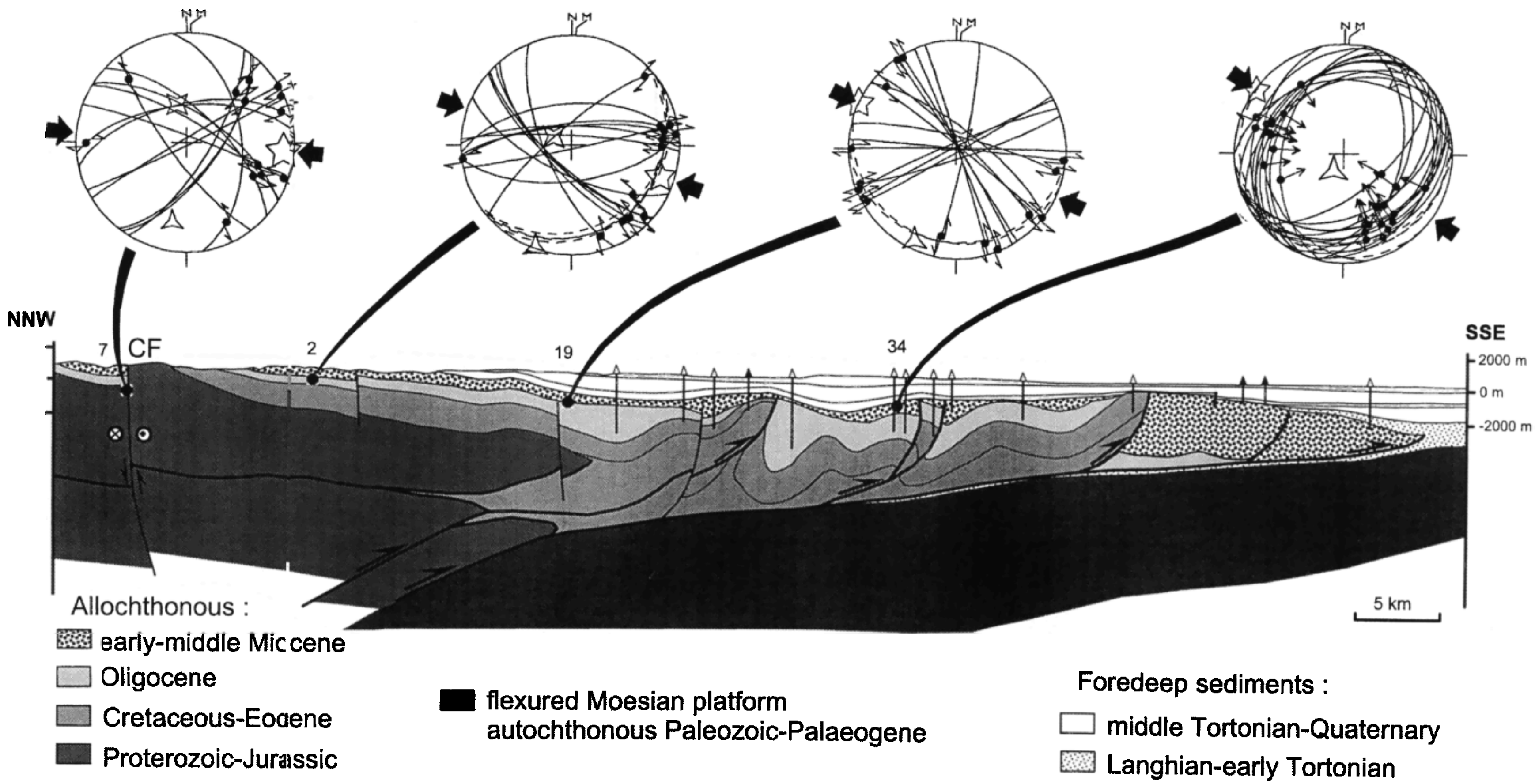

Figure 4. Cross section of the south Carpathians (see location on Figure 2) with Miocene kinematics and examples of Schmidt diagrams (lower hemisphere) with faults and computed stress axes (see Table 1). Bedding planes are represented by dashed lines. Computed paleostress axes are as follow: five-branch star represents σ_1, four-branch star represents σ_2, and three-branch star represents σ_3. Note the strain partitioning between the Cozia dextral fault (CF) in the inner Carpathians and the Miocene thrusts in the outer Carpathians. Modified from *Stefanescu* [1984], reprinted with permission.

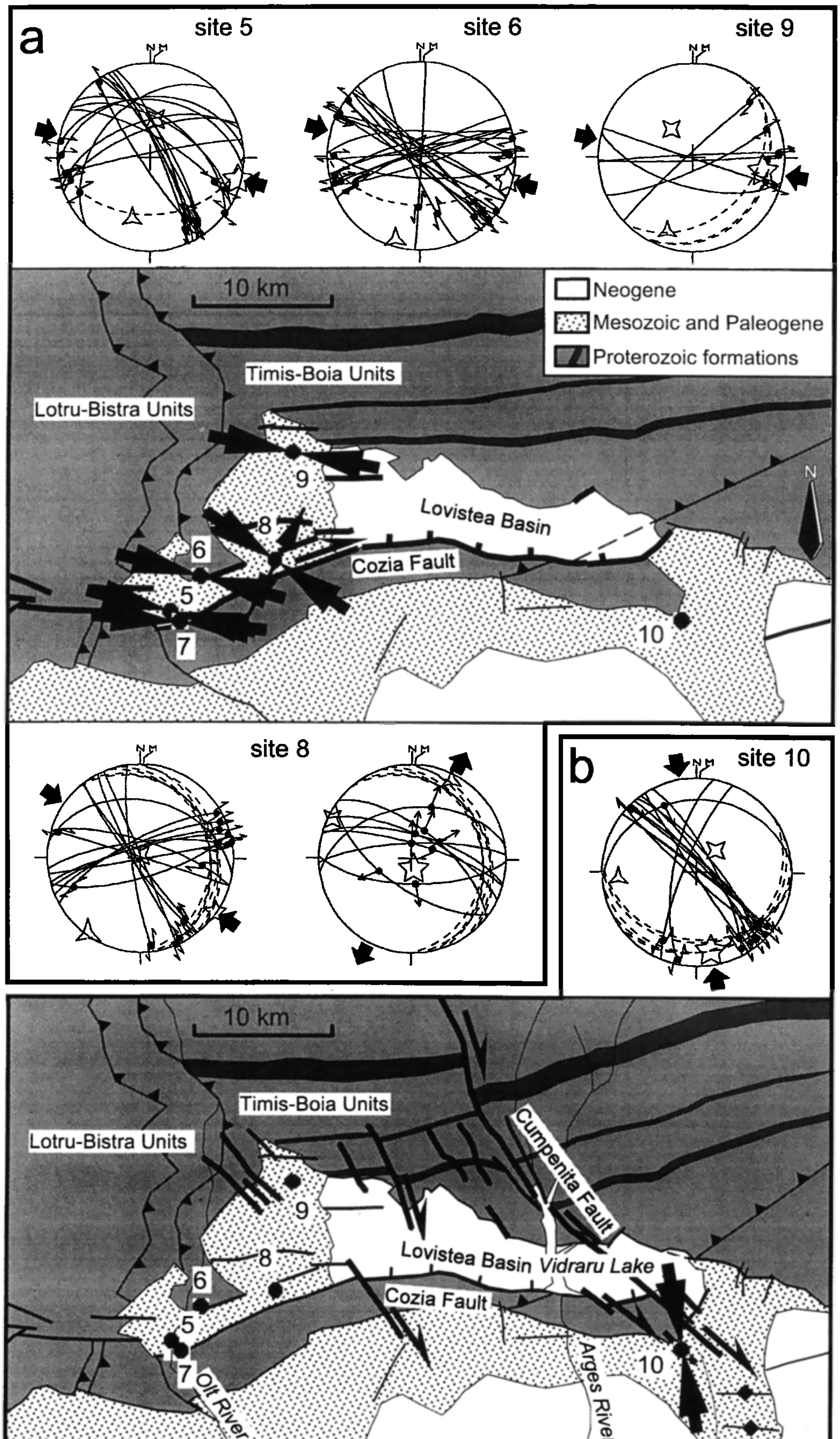
a
site 5
site 6
site 9
10 km
Neogene
Mesozoic and Paleogene
Proterozoic formations
Timis-Boia Units
Lotru-Bistra Units
9
8
6
5
7
10
Lovistea Basin
Cozia Fault
N
site 8
b
site 10
10 km
Timis-Boia Units
Lotru-Bistra Units
Cumpenita Fault
Lovistea Basin
Vidraru Lake
Cozia Fault
Olt River
Arges River

Figure 5.

Paratethys chronostratigraphy) age for this transpressional deformation.

Among the observed faults the Cozia fault (Figures 2 and 5), which borders to the south the Lovistei Basin, is of particular interest. It is the largest fault of the eastern south Carpathians, and it prolongs the south Carpathian fault to the east (Figure 1a). It is therefore the favorite candidate for the few hundred kilometer displacement considered in models. Observations of striated surfaces in the fault zone (site 7 in Figure 5a) indicate that the Cozia fault moved dextrally (Figure 5a ; see the diagram in Figure 4). Moreover, paleostress orientations near the fault (sites 5 and 8 in Figure 5a) and within a parallel fault zone (site 6 in Figure 5a) confirm that the Cozia fault moved dextrally with an ESE trending compression. A Miocene age for this dextral fault movement is clear both because the fault cuts the early Miocene sediments of the Lovistei Basin and because it moved consistently with the Miocene premiddle Tortonian stress field.

Unexpected, however, is the low displacement on this fault. In the eastern south Carpathians, steeply dipping Cretaceous thrust contacts are obliquely cut by the Cozia fault (Figures 2 and 5b) and an estimate of the fault displacement is possible. In agreement with the dextral movement observed in the field, the Cozia fault displaces >2 km and, in a dextral sense, the thrust contact of the Timis-Boia units onto the Lotru-Bistra units along the Olt River (Figure 5b). A northeast trending thrust contact within the Timis-Boia units (Figure 5b) is also cut and offset in a dextral sense by the Cozia fault [*Gheuca*, 1988] but no more than 6 km. This movement, estimated between 2 and 6 km, is much lower than expected. Moreover, we think that the strike-slip movement of the east trending south Carpathian fault (Figure 1a) ends along the Cozia fault and the Lovistei Basin. From west to east the strike of the Cozia fault changes (Figure 5a) and its movement changes from dextral to normal dextral (Figure 4). In a similar way the deformation is strike slip at sites 5 and 7 (Figure 5a) and becomes strike slip normal at site 8, where normal faults indicate a stress permutation [*Angelier and Bergerat*, 1983; *Hippolyte et al.*, 1992], which is a switch of the σ_1 and σ_2 stress axes (see the diagrams in Figure 5a). The low displacement on one of the most important east trending strike-slip faults in the south Carpathians does not account for the expected 100 or 200 km dextral movement [*Royden*, 1988]. Even if a dextral movement of the south Transylvanian fault (Figure 1a) seems to be confirmed by the direction of the maximum principal stress at site 29 (Figure 2), this other fault cannot account for the expected large eastward movement of the south Carpathians either, because it is located too far north (Figure 1a). We conclude that much of the dextral movement between the Tisza-Dacia block and the Moesian platform was accommodated by oblique thrusting in the fold-and-thrust belt presently buried beneath the late Miocene-Quaternary Getic depression (Figure 4).

The Miocene dextral movement of the Cozia fault was contemporaneous with the Miocene thrusting in the more external, buried fold-and-thrust belt (Figure 4). We point out that, as in many other transpressional orogenic belts, in the south Carpathians the deformation was partitioned between thrust and strike-slip faults active at the rear of thrust units. The low displacement on the Cozia strike-slip fault (a few kilometers) compared to a few tens to a hundred kilometer thrust displacement of the south Carpathian units (Figure 4) indicates that this orogenic belt is characterized by a low degree of strain partitioning that might be related to its Miocene low coupling with its foreland [*Hippolyte et al.*, 1996].

5. Late Neogene Kinematics

5.1. Structures

Several seismic profiles located around the Carpathian belt show that the front of the sub-Carpathian nappe is stratigraphically overlain by foredeep sediments, indicating that the outermost thrusts of the east and south Carpathians stopped during late Serravallian-early Tortonian (middle Sarmatian in the Paratethys chronostratigraphy) (Figure 6) [*Dicea and Tomescu*, 1969; *Mocanu and Radulescu*, 1994; *Dicea*, 1995]. A post-Tortonian deformation is, however, well known in the southeastern Carpathian salient where folds and thrusts are classically attributed to the Wallachian Pliocene-Quaternary phase (Figures 1a, 2, and 6a). *Hippolyte and Sandulescu* [1996] emphasize that the Wallachian folds are associated to out-of-sequence faults active from middle Tortonian to Quaternary times (Figure 6a). Recent seismic profiles in the Carpathian salient confirm this age and indicate that within this reverse fault set the activity also migrated toward the internal area [*Stefanescu and Dicea*, 1995]. *Hippolyte and Sandulescu* [1996] demonstrate that the out-of-sequence character of the deformation during the late Neogene must be related to a clockwise rotation of the stress field, from NW-SE (Figure 2) to N-S (Figure 7), in the southern east Carpathians.

In the south Carpathians, where strike-slip deformation was dominant (Figure 2), the deformation pattern also changed during the late Miocene. Detailed mapping shows that the Miocene Cozia fault is cut and offset in the dextral sense by northwest trending faults [*Stefanescu et al.*, 1982; *Dimitrescu et al.*, 1985] (Figure 5b). Observations of striated surfaces confirm that they are strike-slip faults that moved dextrally (Figure 3b). As these faults cut various formations

Figure 5. Polyphase strike-slip deformation in the Lovistei Basin. (a) Fault kinematics in early to middle Miocene (the blocks are moved back to their middle Miocene position). The Cozia fault moved dextrally with a NW-SE orientation of σ_1, and the Lovistei Basin opened under a local NE-SW extension resulting from the change in strike of the main fault in its eastern part. (b) Late Miocene-Quaternary kinematics. A set of parallel northwest trending faults cuts and offsets, in a dextral sense, the preexisting Miocene Cozia fault and the metamorphic units (Proterozoic metamorphic formations from *Gheuca* [1988]).

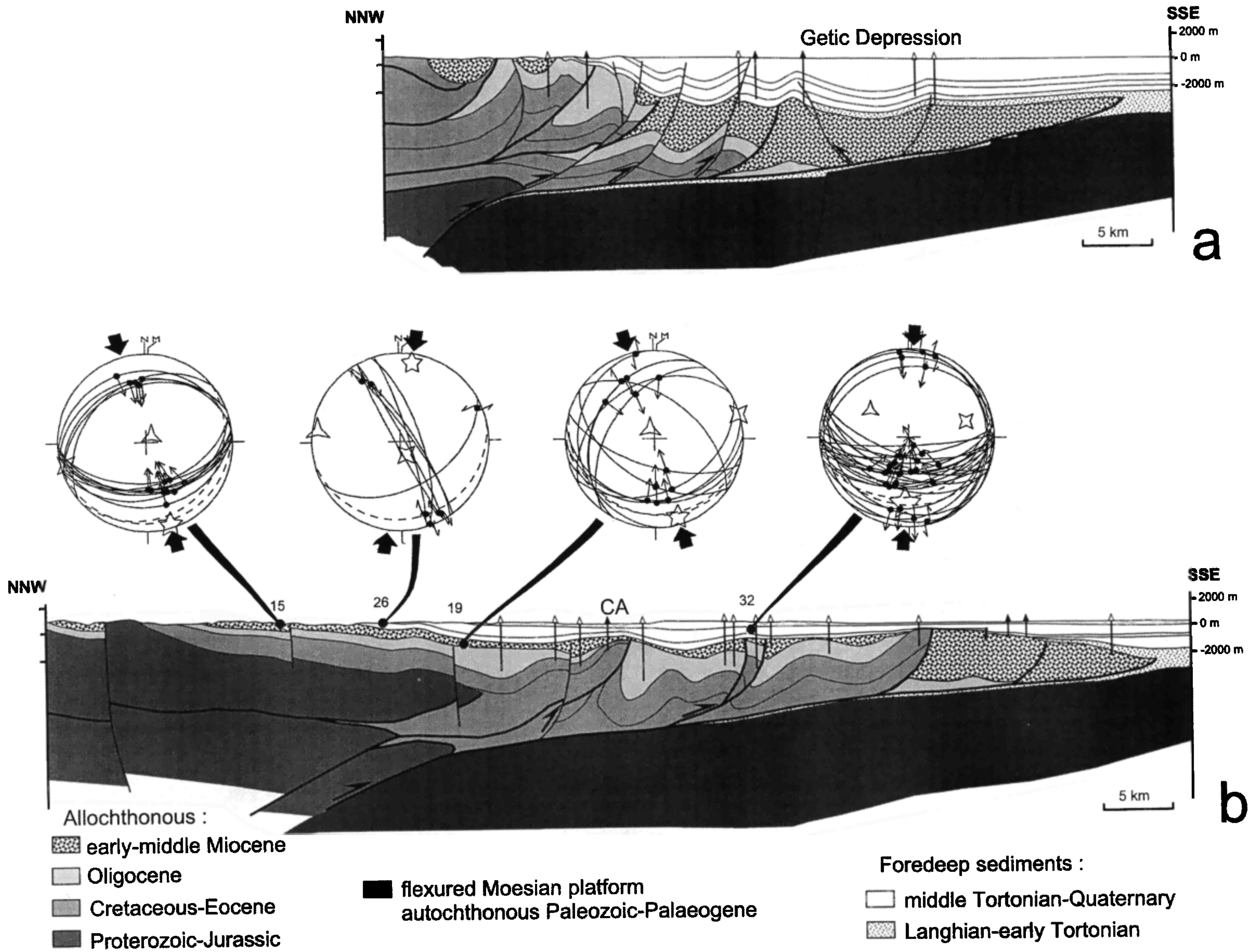

Figure 6. Cross sections (a) in the east Carpathians and (b) in the south Carpathians (see locations on Figure 2), with late Miocene to Quaternary kinematics. CA is Curtea de Arges. As in the east Carpathians (Figure 6a), the compressional deformation visible in the middle Tortonian-Quaternary sequence of the south Carpathians (Figure 6b) occurred in the internal position. Modified from *Stefanescu* [1984], reprinted with permission.

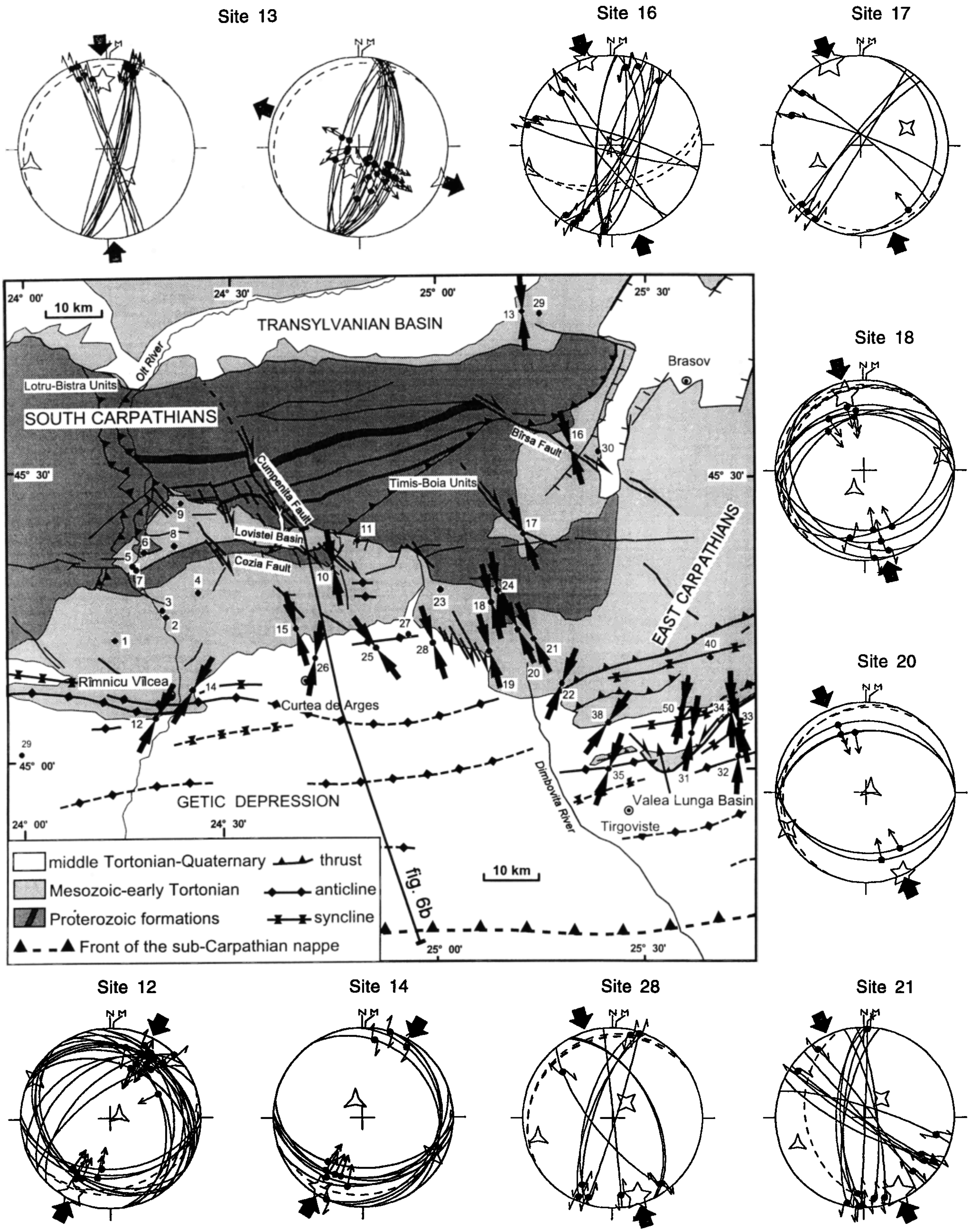

Figure 7. Structural sketch of the eastern south Carpathians with the computed late Miocene to Quaternary directions of compression (see also Table 1). The directions of compression are globally trending N-S in the late Neogene sequence. This direction allows the Cumpenita, the Bîrsa, and other faults to move in a right-lateral sense.

of metamorphic rocks with vertical foliation (Figure 5b), their horizontal displacement can be estimated [*Gheuca*, 1988]. The Cumpenita fault (Figure 5b), which is the most important of these northwest trending faults, cuts and offsets the Cozia fault and the metamorphic formations of the Timis-Boia units to up to 4 km. Note that this fault also participates in the dextral offset of the northeast trending thrust contact within the Timis-Boia units (Figure 5b). Moving back the blocks to their middle Miocene position (Figure 5a), one can see that the displacement on the Cozia fault, considered between 2 and 6 km, is no larger than 2 km. Farther to the east, the Bîrsa fault (Figure 7) also cuts and offsets a Cretaceous-Paleocene thrust contact ~2 km in a dextral sense.

Taking into account that the NW trending faults cut and offset the Cozia fault that borders the Miocene Lovistei Basin (Figure 5b), a post early Miocene age must be considered for this second strike-slip deformation. This age indicates that the crosscut strike-slip deformation may have participated in the late Neogene evolution of the Carpathians together with the out-of-sequence late Neogene thrusts in the east Carpathians (Figure 6a).

5.2. Geodynamics

Paleostress determinations confirm that the northwest trending faults moved dextrally with a globally N-S oriented compression (Figures 6b and 7). In pre-Eocene rocks, like at site 17 (Figure 7), superposition of slickenside lineations, styloliths, and fibrous calcite on previous striations indicates the chronology between the two states of stress and confirms that the N-S compression (Figure 7) postdates the NW-SE transpression (Figure 2). The reverse and strike-slip faults measured in middle Tortonian to Quaternary rocks (sites 25, 26, 28, 35, 31, 32, 33, and 50 in Figure 7) only indicate a N-S compression and therefore confirm that during the middle Tortonian-Quaternary time span the compression was no longer trending NW-SE. The direction of the last compression is perpendicular to the trend of the south Carpathians and the axes of the open folds in the late Neogene sequence of the Getic depression (Figure 7). Syndepositional folds, together with the age of the Valea-Lunga piggyback basin (Figure 7), indicate that the N-S compression lasted from middle Tortonian to early Quaternary [*Hippolyte and Sandulescu*, 1996].

Local variations in the trend of compression and the change in strike of the subvertical metamorphic units across the Cumpenita fault (Figures 5b and 7) suggest that its 4 km movement produced a block rotation. The strike of the metamorphic units indicates that, locally, up to 20° counterclockwise block rotations may have occurred relative to the central south Carpathians. Such rotations may be one cause of the discrepancy between the NNE-SSW directions of compression on the left-hand side of Figure 7 (sites 12 and 14) and NNW-SSE (rotated) or NNE-SSW (postrotation) directions in the middle and right-hand sides of Figure 7. Note that if this event locally rotated blocks, it also rotated, in a counterclockwise sense, the older, early to middle Miocene faults and determined directions of compression, which are E-W along the Dimbovita River and WNW-ESE to NW-SE elsewhere (Figure 2). The magnitude of older block rotations is discussed below.

The northwest trending strike-slip faults of south Carpathians and the east trending Wallachian folds of the south and east Carpathians (Figure 7) formed after the NW-SE Miocene compression. Their common age, together with their similar trend of compression and their geometrical relationships (see below), indicate that these structures formed during the same deformation event. On cross section in Figure 6b one can note that the east trending folds in the middle Tortonian-Quaternary sequence did not develop at the front of the orogenic belt but were generated in an internal area. Similarly, on a more easterly section (Figure 6a) one can see that the Wallachian folds are internal structures and that the Wallachian thrusts are in out-of-sequence positions. On both sections (Figure 6) the area of maximum deformation (near Curtea de Arges on Figure 6b) is internal and located ~40 km north of the Miocene outermost thrust. On the map in Figure 7 this area is running E-W through the Rîmnicu Vîlcea and Curtea de Arges anticline and the Valea Lunga thrust. This zone of recent deformation may represent the emergence of a deep thrust, which was active during the uplift of the inner part of the south Carpathians (Figure 6). The Getic depression, with its puzzling location above the foreland and above the outer south Carpathian nappes (Figures 6 and 7), is located in front of the late Neogene out-of-sequence structures and can be considered as a part of the flexural basin of the late Miocene-Quaternary deformation.

The geometric relationship between the contemporaneous Wallachian thrusts and strike-slip faults can be understood if one compares the values of the Wallachian NW-SE shortening (parallel to the strike of the faults) in different cross sections along the orogenic belt (Figure 8b). We made this comparison using the NW-SE cross sections of *Stefanescu* [1984], which are well controlled by drill core data, field data, and seismic profiles and which precisely represent the Pliocene-Quaternary deformation. On cross section b, presented in Figure 6, the late Miocene-Quaternary shortening is only 1.5 km. To the west the cross sections indicate that the NW-SE shortening diminishes to only a few hundred meters (Figure 8b). On the contrary, the shortening increases to the east, is of 6 km on section a (Figures 6 and 8b), and reaches 11 km in the southeastern Carpathian salient (Figure 8b). These values are quite similar to the total displacement on the northwest trending strike-slip faults (Figure 7). The 4 km offset of the Cumpinita fault can explain much of the 4.5 km increase of shortening between sections b and a (Figures 6 and 8b). The maximum shortening in the Carpathian salient (11 km) is approximately equivalent to the cumulated horizontal displacement on the Wallachian northwest trending strike-slip faults (mainly the Cumpenita fault, 4 km, and the Bîrsa fault, 4 km) added to the 1.5 km shortening of section b. We conclude that the late Neogene strike-slip faulting in the south Carpathians was accommodated by folding and thrusting in the Wallachian fold area. The late Miocene-Quaternary Wallachian deformation is the consequence of the southeastward transport of an intra-Carpathian block, named here the Transylvanian block, along parallel northwest trending dextral strike-slip faults in the south Carpathians and along sinistral faults and probable reactivated thrusts in the east Carpathians (Figure 8b). Even if the Wallachian deformation rapidly diminishes to the west, a N-S direction of compression that

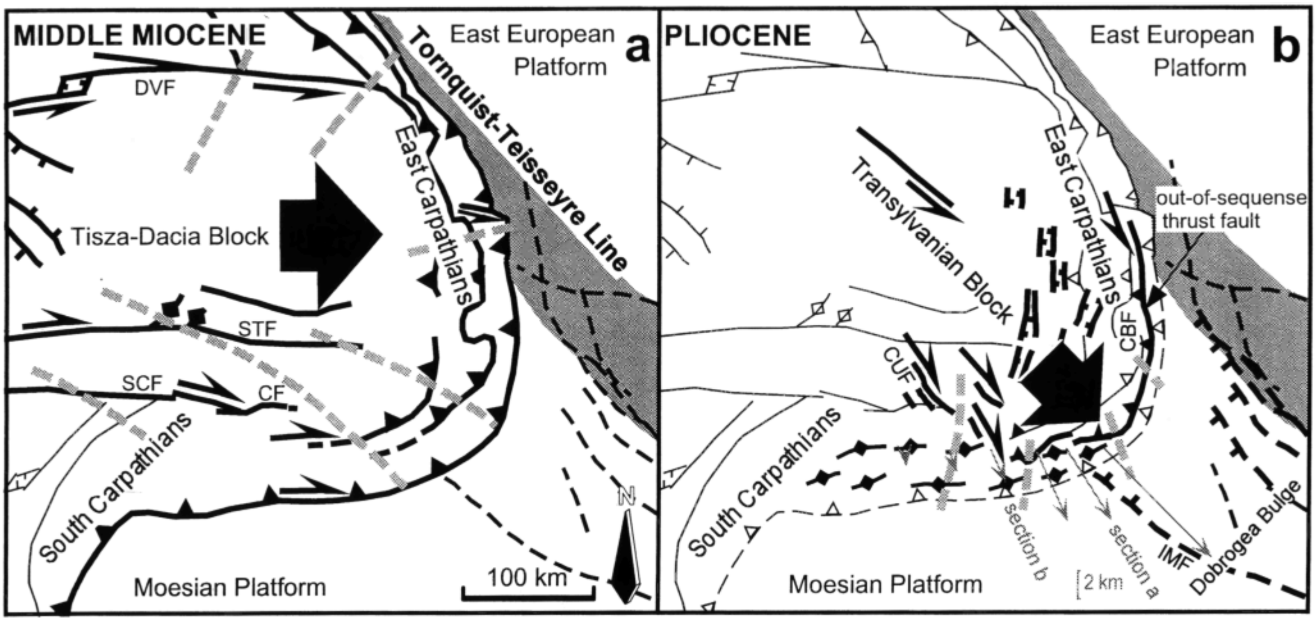

Figure 8. Geodynamical evolution of the east and south Carpathians in the (a) middle Miocene and (b) Pliocene. Stippled dashed lines represent orientations of σ_1 axes (from A. Caire as discussed by *Bouillin and Caron* [1975], *Hippolyte and Badescu* [1993], *Hippolyte and Sandulescu* [1996], *Linzer* [1996], *Morley* [1996], *Matenco et al.* [1997], and J.-C. Hippolyte, personal data 1999). Stippled arrows of Figure 8b shows the amount of shortening on different cross sections. Abbreviations are defined as follows: CBF, Casim-Bisoca fault; CF, Cozia fault; CUF, Cumpenita fault; DVF, Dragos-Voda fault; IMF, Intra-Moesian fault; SCF, south Carpathian fault; and STF, south Transylvanian fault. Figure 8a shows that during the middle Miocene the Tisza-Dacia block moved eastward and produced a radial pattern of stress trajectories with frontal compression in the east Carpathians and transpression in the south Carpathians. The shortening and collision along the Romanian prolongation of the Tornquist-Teisseyre line reduced the area able to subduct to a foreland corner in front of the southeastern Carpathian salient. Figure 8b shows that from the middle Tortonian to the Quaternary a more reduced eastern area (Transylvanian block) migrated to the southeast along NW-SE dextral faults and produced the Wallachian out-of-sequence structures localized in the southeastern Carpathian salient. Note that the deformation pattern and the stress field can be superimposed on the middle Miocene through a change of scale and a rotation.

could be correlated to this event was also determined in the central south Carpathians [*Ratschbacher et al.*, 1993; *Matenco et al.*, 1997].

6. Carpathian Belt Transport

Shortening in the Carpathians results from the northeastward and eastward displacement of Pannonian-Transylvanian crustal blocks (Figure 1a) [e.g., *Csontos*, 1995]. This displacement was probably driven mainly by the gravitational sinking of dense lithosphere beneath the arc [*Royden et al.*, 1982; *Royden*, 1993]. The subduction is now in its final stage. In the Carpathian belt the locus of active thrusting was progressively confined to the southeast. The progressive steepening of the subducted slab was recorded in the southeastward younging of the calc-alkaline volcanic activity [e.g., *Szakács and Seghedi*, 1995], and a subducted slab remnant is present in a nearly vertical position in the Vrancea seismic zone in the Carpathian salient (Figure 1b) [*Roman*, 1970; *Royden et al.*, 1982; *Oncescu*, 1984].

Taking into account the geometric characteristics of the compressional structures in the orogenic belt, the directions of compression, and the age of the deformation, we could distinguish the two last periods of the Carpathian evolution (Figure 8). Our analysis of the Carpathian belt evolution leads to the conclusion that the direction of the intra-Carpathian block transport rotated clockwise during the Neogene (Figure 9). This rotation results from the progressive collision of the Carpathians belt with the thick continental crust of the northwest trending Tornquist-Teisseyre line and its prolongation in Romania [*Ellouz and Roca, 1994*; *Roure et al.*, 1996] (Figure 9). This collision is diachronous as attested by the progressive younger age of the termination of thrusting from northwest to southeast along the west and east Carpathians (Figure 9) [e.g., *Royden*, 1988]. Finally, the evolution of the Carpathian system agrees well with a model of progressive reorientation of convergence direction (Figure 9) as proposed by *Mann* [1997].

During most of the Miocene the Carpathian belt is characterized by a piggyback sequence of thrusting. In the early to middle Miocene the Pannonian plate (Alcapa and Tisza-Dacia intra-Carpathian blocks) moved to the northeast [*Csontos*, 1995] (Figure 9, arrow 1). In the middle to late Miocene, while collision occurred in the west Carpathians, the southern part of the Pannonian plate (Tisza-Dacia block), which was split along the mid-Hungarian line, underwent a

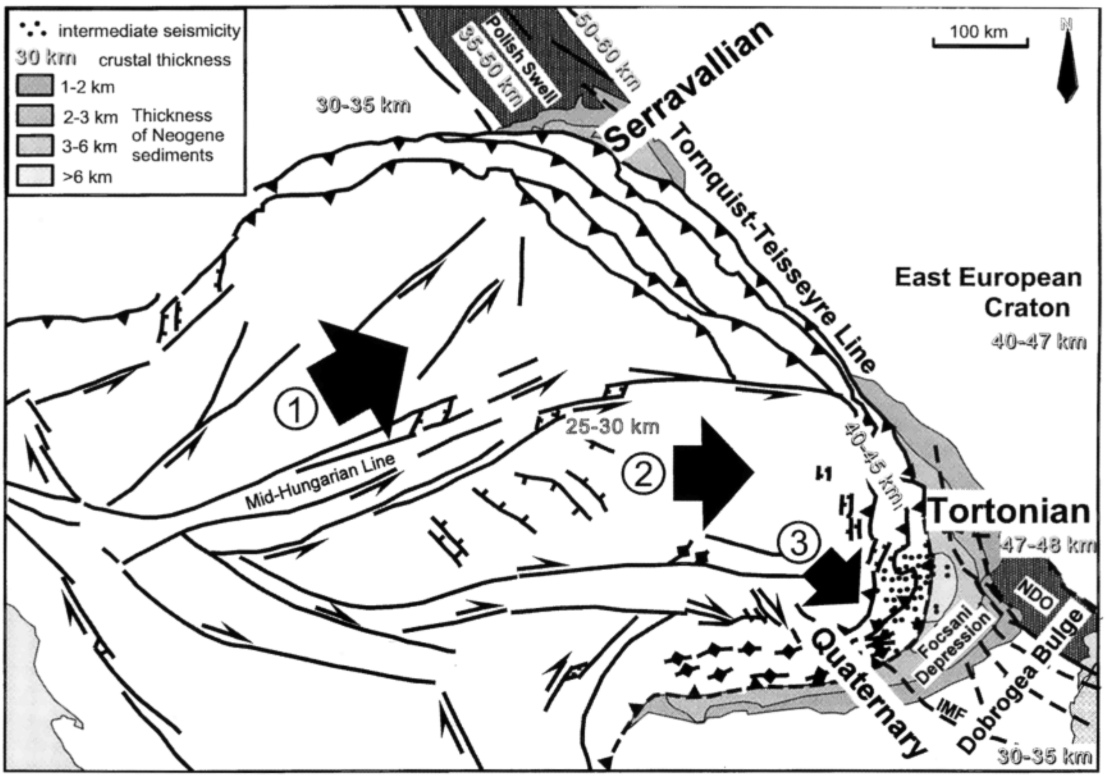

Figure 9. Model of reorientation of the convergence direction during progressive collision of the Carpathian belt with the thick crust of the Tornquist-Teisseyre line. Ages of termination of thrusting are according to *Royden* [1988], and *Sandulescu* [1988]. Arrow 1 indicates northeastward early to middle Miocene convergence direction between the Pannonian and Eurasian plates. Arrow 2 indicates eastward middle to late Miocene convergence direction between the Tisza-Dacia block and Eurasian plates. Arrow 3 indicates southeastward late Miocene-Quaternary convergence direction of the Transylvanian block and the Eurasian plate. The thicker crust of the Polish Tornquist-Teisseyre line and its prolongation in north Dobrogea guided the Carpathians to its last phase of southeast motion. The Dobrobea hills represent the NE trending bulge of the latest, SE directed, subduction. NDO is north Dobrogea orogen, and IMF is intra-Moesian fault.

larger displacement reoriented toward the east (Figure 9, arrow 2). During this period the Dragos-Voda fault was sinistral (Figure 8a). The Miocene progressive collision of the Pannonian plate with the northwest trending margin of the east European Craton resulted in the dominant NW-SE trend of the east Carpathians (Figure 9).

The contemporaneous stress field was radial, with a direction of maximum horizontal stress swinging from NE-SW in the northern east Carpathians to NW-SE in the southern east Carpathians and south Carpathians (Figure 8a). These directions of σ_1 axes can be traced in the intra-Carpathian area where the stress regime was strike slip (Figure 8a) [*Hippolyte and Badescu*, 1993]. The middle Miocene radial stress field (Figure 8a) was not largely modified by block rotations similar to those determined by paleomagnetism in the intra-Carpathian area [e.g., *Patrascu et al.*, 1994]. Our recent results in paleomagnetically controlled, nonrotated middle Miocene rocks [*Patrascu et al.*, 1994] near the south Transylvanian fault and near the Dragos-Voda fault (Figure 8a) give orientations quite similar to the paleomagnetically uncontrolled areas. This lack of evidence of large (>30°) rotations of kinematics indicators in the uncontrolled areas suggests that the mesoscale faults we measured in Tertiary rocks formed mostly at the end of, or after, large possible block rotations that terminated during the middle Miocene in the Tisza-Dacia block [*Patrascu et al.*, 1994]. Another hypothesis would be that in the uncontrolled areas, early clockwise block rotations rotated the early formed fault planes to a present orientation similar to those of the later (nonrotated) fault planes. This hypothesis would explain why we could not distinguish, from their present orientations, the early Miocene stress field (northeastward transport) from the middle Miocene one (eastward transport).

It is important to note that the stress orientations we determined do not correspond to directions of movement (Figure 8). During the middle to late Miocene the Tisza-Dacia block moved toward the east along parallel strike-slip faults, and the resulting radial stress field is consistent with an opposite sense of movement on these parallel faults, sinistral to the north and dextral to the south. In the late Miocene, when most of the east Carpathians had collided with the east European platform, an E-W compression was probably transferred through most of the upper plate [*Peresson and Decker*, 1997] and replaced the strike-slip regime characterized by N-S compression and E-W extension in the Pannonian Basin [*Bergerat*, 1989; *Csontos et al.*, 1991]. The piggyback progression of thrusting stopped in the Carpathian belt, and a largely undeformed "postrift" sequence was deposited in the intra-Carpathian basins.

During the 9 m.y. period from late Miocene to Quaternary the tectonic activity did not stop but was largely reduced, and the direction of convergence rotated clockwise (Figure 9, arrow 3). Effectively, a new set of dextral strike-slip faults limiting the deformation area to the west indicates that a localized block displacement also occurred during this period, but this time, the transport was toward the southeast. This transport was probably guided by the flexure of a foreland panel limited to the south by the intra-Moesian fault and to the north by the Tornquist-Teisseyre line (Figures 8b and 9). As a consequence of the rotation of the block transport direction and the size reduction of the active curved mobile belt, the new compressional structures formed out of sequence (e.g., the Wallachian faults and the Casim-Bisoca fault, Figure 8b). All these structures moved consistently with a more localized radial stress field (Figure 8b) characterized in the south Carpathians by N-S compression, which strongly differs from the Miocene E-W to NW-SE directions of compression. The strike-slip movement on northwest trending dextral faults (8 km on the two larger faults) was accommodated by the Wallachian folds and thrust faults of the southern east Carpathians (11 km of shortening in the southeastern Carpathian salient).

At the end of this period, in Pliocene time, several en echelon grabens were generated (Figure 8b). They opened with a NW-SE direction of σ_3 [*Girbacea and Har*, 1997]. We also found evidence of this extension in the Transylvanian Basin (site 13 in Figure 7 and Table 1), and we note that the direction of σ_3 (N112°) is close to the direction of extension of the strike-slip stress regime in the southern Transylvanian Basin (Figure 7 and Table 1). Despite several observations of slickenside superpositions at site 13 that indicate that this extension postdates the strike-slip movements (Figure 7), the Pliocene age of the graben filling and the consistent orientations of the minimum and maximum horizontal stress axes suggest that the strike-slip and the extensional movements of the inner Carpathians are interconnected (Figure 8b). These grabens may result either from the progression of an intra-Carpathian extensional tectonics at the end of the southeastward crustal block transport or from recent gravitational movements localized in the Carpathian belt. The opening of these grabens may have contributed in the rotation of the direction of compression from N-S to NW-SE in the Carpathian salient (Figure 8b). The morphology of the normal faults indicates that they are probably still active, and their movement may also result in the ESE directed convergence determined in a 15 km wide Global Positioning System (GPS) network in the east Carpathians [*Schmidt et al.*, 1990].

It is noteworthy that the Pliocene deformation is similar to the middle Miocene one. In both cases the stress pattern is radial (Figures 8a and 8b). The deformation is compressional in the outer Carpathians but is strike-slip and extensional in the intra-Carpathian area. Furthermore, normal faults located in the internal area terminate close to the dextral strike-slip faults and strike at 40° to them (Figures 8a and 8b). Finally, the middle Miocene (Figure 8a) and Pliocene (Figure 8b) deformation patterns are superposable on each other, provided that the scale is changed and a rotation is made. We conclude that the mechanism of block transport did not change in late Miocene, but the direction changed, resulting in peculiar structures including out-of-sequence thrusts and crosscutting dextral faults. Moreover, our analysis confirms that thrusting of the Carpathians was contemporaneous with strike-slip and extensional deformation in the intra-Carpathian area [*Royden*, 1988] and also gives an insight into their relationships.

7. Conclusions

The Carpathian belt was considered a result of a regional Miocene shortening and a more localized Pliocene-Quaternary shortening. We show that these two "phases" correspond to the same continuous mechanism of block transport toward a heterogeneous foreland. The displacement of intra-Carpathian blocks and, consequently, the direction of convergence of the Carpathian belt were controlled in the subduction front by the thickness of the incoming crust. During the reduction of the foreland surface that was able to subduct, the active front was progressively confined to the southeast.

In the early and middle Miocene times the south Carpathian chain was a transpressional orogen. The dextral oblique collision of the south Carpathians with the Moesian platform was resolved mostly by oblique thrusting rather than by strike-slip faulting. In the late Miocene, when most of the belt had collided along the Moesian platform and along the strike of the Tornquist-Teisseyre line that acted as a barrier, subduction was possible only in a narrow zone in the southeastern Carpathians. The deformation system was forced to rotate clockwise for a last reduced convergence from late Miocene to Quaternary times. The Wallachian folds represent this final stage of shortening. We showed that this event was not limited to these folds but includes out-of-sequence thrusts (mainly in the east Carpathians) and a set of Wallachian dextral strike-slip faults in the south Carpathians.

The Carpathian belt can be compared to other arc-shaped orogenic belts generated within converging continental blocks. In particular, in the Mediterranean region, striking similarities exist between the Carpathian belt and the Apennines (Figure 1a) [e.g., *Tapponnier*, 1977]. During the Apennines transport the locus of extension in the Tyrrhenian Basin moved to the southeast (from the Vavilov to the Marsili Basin) and the direction of extension probably rotated clockwise [*Sartori*, 1989]. In the Carpathian-Pannonian system and the Apennines-Tyrrhenian system, during the final stage of shortening, a similar foreland geometry forced the system to rotate clockwise. Other examples of reorientation of the direction of escape were found in the Anatolia plate and in the Caribbean plate [e.g., *Gordon et al.*, 1997; *Mann*, 1997]. In all these examples, after local collision the reoriented direction of the "escaping" plate was determined by the presence of a "free face" or subductable oceanic crust [*Mann*, 1997]. These examples of subduction demonstrate the important control that foreland geometry has on belt deformation. In the Carpathians the location of the latest block transport, far from the Alps, suggests that after extrusion of crustal wedges in the early Miocene the transport can continue with extensional collapse and subduction rollback of dense lithosphere as main mechanisms.

Acknowledgments. This work was supported by the Peri-Tethys program and was partly realized at the University of Paris VI (URA CNRS 1759) and at the University of Savoie (UMR CNRS 5025). We used SPOT images obtained through the ISIS program (CNES). We are grateful to Mircea Sandulescu, Nicoleta Badescu, Mihai Turturanu, and Ion Gheuca for their help during data acquisition and constructive discussions. Special thanks go to L. Csontos and P. Mann for their constructive reviews.

References

Airinei, S., Rapports géodynamiques entre la microplaque Moesienne et l'arc Carpatho-Balkanique sur le territoire de la Roumanie, *Anu. Inst. Geol. Geofiz.*, *60*, 7-14, 1983.

Angelier, J., Tectonic analysis of fault-slip data sets, *J. Geophys. Res.*, *89*, 5835-5848, 1984.

Angelier, J., and F. Bergerat, Systèmes de contrainte et extension intracontinentale, *Bull. Centr. Rech. Explor. Prod. Elf Aquitaine*, *7*(1), 137-147, 1983.

Artyushkov, E.V., M.A. Baer, and N.-A. Mörner, The east Carpathians: Indications of phase transitions, lithospheric failure and decoupled evolution of the thrust belt and its foreland, *Tectonophysics*, *262*, 101-132, 1996.

Balla, Z., Neogene kinematics of the Carpatho-Pannonian Region, *Mag. All. Foldt. Intez. Evk.*, *70*, 193-199, 1987.

Bergerat, F., From pull-apart to the rifting process: The formation of the Pannonian Basin, *Tectonophysics*, *157*, 271-280, 1989.

Berza, T. (Ed.), Geological Evolution of the Alpine-Carpathian-Pannonian System. Alcapa II. Field Guidebook, *Rom. J. Tectonics Reg. Geol.*, *75(2)*, 148 pp., 1994.

Bouillin, J.-P., and J.-M. Caron, Les Carpathes Roumaines: Réunion extraordinaire de la société géologique de France, *Bull. Soc. Geol. Fr.*, *7*, 267-298, 1975.

Burchfiel, B.C., Geology of Romania, *Spec. pap. Geol. Soc. Am.*, *158*, 82 pp., 1976.

Burchfiel, B.C., Eastern European Alpine system and the Carpathian orocline as an example of collision tectonics, *Tectonophysics*, *63*, 31-61, 1980.

Cornea, I., I. Dragoescu, M. Popescu, and M. Visarion, Harta miscarilor crustale verticale recente pe teritoriul R. S. Romania, *Stud. Cercet. Geol. Geofiz. Geogr. Geofiz.*, *17*, 3-20, 1979.

Csontos, L., Tertiary tectonic evolution of the Pannonian-Carpathian area: A review, *Acta Vulcanol.* *7*, 1-13, 1995.

Csontos, L., G. Tari, F. Bergerat, and L. Fodor, Evolution of the stress fields in the Carpatho-Pannonian area during the Neogene, *Tectonophysics*, *199*, 73-91, 1991.

Csontos, L., A. Nagymarosy, F. Horváth, and M. Kovác, Tertiary evolution of the intra-Carpathian area: A model, *Tectonophysics*, *208*, 221-241, 1992.

Dicea, O., The structure and hydrocarbon geology of the Romanian east Carpathian border from seismic data, *Petrol. Geosc.*, *1*, 135-143, 1995.

Dicea, O., and L. Tomescu, Tectonica zonei externe a avanfosei Carpatice din sectorul Motru-Buzau, in lumina datelor prospectiunii seismice, *Stud. Cercet. Geol. Geofiz. Geogr. Geofiz.*, *7*, 73-78, 1969.

Dimitrescu, R., H.P. Hann, I. Gheuca, M. Stefanescu, L. Szasz, M. Marunteanu, E. Serban, and G. Dumitrascu, Harta geologica scara 1:50.000, *109c*, Inst. de Geol. si Geofiz., Bucharest, 1985.

Dumitrescu, F., and M. Sandulescu, Problèmes structuraux fondamentaux des Carpathes roumains et de leur avant-pays, *Annu. Com. Geol. Rom.*, *36*, 195-218, 1968.

Dumitrescu, F., and M. Sandulescu, Harta tectonica scara 1:1.000.000, Romania, in *Atlas Geologic*, foaia 6, Inst. Geol., Bucharest, 1970.

Ellouz, N., and E. Roca, Palinspastic reconstructions of the Carpathians and adjacent areas since the Cretaceous: A quantitative approach, in *Peri-Tethyan Platforms*, edited by F. Roure, 51-77, Technip, Paris, 1994.

Ellouz, N., F. Roure, M. Sandulescu, and D. Badescu, Balanced cross sections in the eastern Carpathians (Romania): A tool to quantify Neogene dynamics, in *Geodynamics Evolution of Sedimentary Basins*, edited by F. Roure et al., 305-325, Technip, Paris, 1996.

Fodor, L., L. Csontos, G. Bada, I. Györfi, and L. Benkovics, Tertiary paleostress and kinematic evolution of the Pannonian basin and neighbouring orogens, paper presented at *The Mediterranean Basins: Tertiary Extension within the Alpine Orogen*, Univ. de Cergy-Pontoise, Paris, Dec. 11-13, 1996.

Gheuca, I., Versantul sudic al muntilor Fagaras, litostratigrafie si tectonica. *D. S. Inst. de Geol. si Geofiz.*, *72-73*, 93-117, 1988.

Girbacea, R., and N. Har, Extension and magmatism in a convergent tectonic setting (the East Carpathians, Romania), *Terra Nova Abstr.*, *9*, 156, 1997.

Gordon, M., P. Mann, D. Cáceres, and R. Flores, Cenozoic tectonic history of the North America-Caribbean plate boundary zone in western Cuba, *J. Geophys. Res.*, *102*, 10,055-10,082, 1997.

Guterch, A., M. Grad, R. Materzok, and E. Perchuç, Deep structure of the Earth's crust in the contact zone of the Palaeozoic and Precambrian platforms on Poland (Tornquist-Teisseyre zone), *Tectonophysics*, *128*, 251-279, 1986.

Hippolyte, J.-C., and D. Badescu, Preliminary results of paleostress and structural analyses in the eastern Carpathians, *Terra Nova, Abstr.*, *7*, 218-219, 1993.

Hippolyte, J.-C., and M. Sandulescu, Paleostress characterization of the "Wallachian phase" in its type area (southeastern Carpathians, Romania), *Tectonophysics*, *263*, 235-248, 1996.

Hippolyte, J.-C., J. Angelier, and F. Roure, Les permutations de contraintes: Exemples dans des terrains quaternaires du sud de l'Apennin (Italie), *C. R. Acad. Sci., Ser. II*, *315*, 89-95, 1992.

Hippolyte, J.-C., M. Sandulescu, D. Badescu, and N. Badescu, L'activité d'un segment de la ligne Tornquist-Teisseyre depuis le Jurassique supérieur: La faille de Peceneaga-Camena (Roumanie), *C. R. Acad. Sci., Ser. II*, *323*, 1043-1050, 1996.

Horváth F., Neotectonic behavior of the Alpine-Mediterranean region, in *The Pannonian Basin: A Study in Basin Evolution*, edited by L. H. Royden and F. Horváth, *AAPG Mem.*, *45*, 49-55, 1988.

Horváth, F., Toward a mechanical model for the formation of the Pannonian Basin, *Tectonophysics*, *226*, 333-357, 1993.

Horváth, F., and S. Cloetingh, Stress-induced late-stage subsidence anomalies in the Pannonian Basin, *Tectonophysics*, *266*, 287-300, 1996.

Huisman, R.S., G. Bertotti, D. Ciulavu, C.A.E. Sanders, S. Cloetingh, and C. Dinu, Structural evolution of the Transylvanian Basin (Romania): A sedimentary Basin in the bend zone of the Carpathians, *Tectonophysics*, *272*, 249-268, 1997.

Jiricek, R., Tectonic development of the Carpathian arc in the Oligocene and Neogene, in: *Tectonic Profiles Through the West Carpathians*, edited by M. Mahel, 583-622, Geol. Ustav Dionysa Stura, Bratislava, 1979.

Kázmér, M. and S. Kovács, Permian-Paleogene paleogeography along the eastern part of the Insubric-Periadriatic lineament system: Evidence for continental escape of the Bakony-Drauzug unit, *Acta Geol. Hung.*, *28*, 69-82, 1985.

Le Pichon, X., F. Bergerat, and M.J. Roulet, Plate kinematics and tectonics leading to the Alpine belt formation: A new analysis, in *Processes in Continental Lithosphere Deformation*, edited by S.P. Clark, B.C. Burchfiel and J. Suppe, *Spec. Pap., Geol. Soc. Am.* *218*, 111-131, 1988.

Linzer, H.-G., Kinematics of retreating subduction along the Carpathian arc, Romania, *Geology*, *24*, 167-170, 1996.

Mann, P., Model for the formation of large, transtensional basins in zones of tectonic escape, *Geology*, *25*, 211-214, 1997.

Márton, E., and H. J. Mauritsh, Structural applications and discussion of a paleomagnetic post-Paleozoic database for the central Mediterranean, *Phys. Earth Planet. Inter.*, *62*, 46-59, 1990.

Matenco, L., G. Bertotti, C. Dinu, and S. Cloetingh, Tertiary tectonic evolution of the external South Carpathians and the adjacent Moesian platform (Romania), *Tectonics*, *16*, 896-911, 1997.

Mocanu, V., and F. Radulescu, Geophysical features of the Romanian territory, in: *Geological Evolution of the Alpine-Carpathian-Pannonian System: Alcapa II Field Guidebook*, edited by T. Berza, *Rom. J. Tectonics Reg. Geol.*, *75(2)*, 17-36, 1994.

Morley, C.K., Models for relative motion of crustal blocks within the Carpathian region, based on restorations of the outer Carpathian thrust sheets, *Tectonics*, *15*, 885-904, 1996.

Mrazec, L., Les plis diapirs et le diapirisme en général, *C. R. Seances Inst. Geol. Roum., Fr. Ed.*, *6*, 215-255, 1927.

Oncescu, M.C., Deep structure of the Vrancea region, Romania, inferred from simultaneous inversion for hypocenters and 3-D velocity structure, *Ann. Geophys.*, *2*, 23-28, 1984.

Oszczypko, N., and A. Slaczka, An attempt to palinspastic reconstruction of Neogene basins in the Carpathian foredeep, *Ann. Soc. Geol. Pol.*, *55*, 55-75, 1985.

Paraschiv, D., Geologia zăcămintelor de hidrocarburi din România: Prospectiuni si explorari geologice, *Stud. Teh. Econ. Inst. Geol. Geofiz. Bucharest*, *10*, 1-363, 1975.

Patrascu, S., C. Panaiotu, M. Seclaman, and C.E. Panaiotu, Timing of rotational motion of the Apuseni Mountains (Romania): Paleomagnetic data from Tertiary magmatic rocks, *Tectonophysics, 233*, 163-176, 1994.

Peresson, H., and K. Decker, Far-field effects of late Miocene subduction in the eastern Carpathians: E-W compression and inversion of structures in the Alpine-Carpathian-Pannonian region, *Tectonics, 16*, 38-56, 1997.

Platt, J.P., J.H. Behrmann, P.C. Cunningham, J.F. Dewey, M. Helman, M. Parish, M.G. Shepley, S. Wallis, and P.J. Weston, Kinematics of the Alpine arc and the motion history of Adria, *Nature, 337*, 158-161, 1989.

Radulescu D.P., and M. Sandulescu, The plate-tectonics concept and the geological structure of the Carpathians, *Tectonophysics, 16*, 155-161, 1973.

Ratschbacher, L., W. Frisch, H.-G. Linzer, and O. Merle, Lateral extrusion in the eastern Alps, 2, Structural analysis, *Tectonics, 10*, 257-271, 1991.

Ratschbacher, L., H.-G. Linzer, F. Moser, R.-O. Strusievicz, H. Bedelean, N. Har, and P.-A. Mogos, Cretaceous to Miocene thrusting and wrenching along the central south Carpathians due to a corner effect during collision and orocline formation, *Tectonics, 12*, 855-873, 1993.

Roman, C., Seismicity in Romania: Evidence for the sinking lithosphere, *Nature, 228*, 1176-1178, 1970.

Roure, F., E. Roca, and W. Sassi, The Neogene evolution of the outer Carpathians flysch units (Poland, Ukraine and Romania): Kinematics of a foreland/fold-and-thrust belt system, *Sediment. Geol., 86*, 177-201, 1993.

Roure, F., J. Kusmierek, G. Bessereau, E. Roca, and W. Strzetelski, Initial thickness variations and basement-cover relationships in the western outer Carpathians (southeastern Poland), in *Geodynamic Evolution of Sedimentary Basins*, edited by F. Roure et al., 255-279, Technip, Paris, 1996.

Royden, L.H., Late Cenozoic tectonics of the Pannonian basin system, in *The Pannonian Basin: A Study in Basin Evolution*, Edited by L.H. Royden and F. Horváth, *AAPG Mem. 45*, 27-48, 1988.

Royden, L.H., The tectonic expression of slab pull at continental convergent boundaries, *Tectonics, 12*, 303-325, 1993.

Royden, L.H., F. Horváth, and B.C. Burchfiel, Transform faulting, extension and subduction in the Carpathian Pannonian region, *Geol. Soc. Am. Bull., 93(8)*, 717-725, 1982.

Sandulescu, M., Essai de synthèse structurale des Carpathes, *Bull. Soc. Geol. Fr., 17*, 299-358, 1975.

Sandulescu, M., Cenozoic tectonic history of the Carpathians, in *The Pannonian Basin: A Study in Basin Evolution*, edited by L.H. Royden and F. Horváth, *AAPG Mem., 45*, 17-25, 1988.

Sandulescu, M., and M. Visarion, La structure des plate-formes situées dans l'avant-pays et au dessous des nappes du flysch des Carpathes orientales, *Stud. Teh. Econ. Inst. Geol. Geofiz. Bucharest, 15*, 61-70, 1988.

Sandulescu, M., et al., Geological map of Romania, Inst. de Geol. si Geofiz , Bucharest, 1978.

Sartori, R., Evoluzione Neogenico-recento del bacino Tirrenico e suio rapporti con la geologia delle aree circonstanti, *G. Geol, 51*, 1-30, 1989.

Schmidt, G., T. Moldoveanu, V. Nica, and R. Jäger, Deformation analysis of local terrestrial network in Romania with respect to the Vrancea earthquake of August 30, 1986, in *Global and Regional Geodynamics*, edited by P. Vyskocil, C. Reigber, and P.A. Cross, 211-222, Springer-Verlag, New York, 1990.

Spakman, W., S. Van der Lee, and R. Van der Hilst, Travel-time tomography of the European-Mediterranean mantle down to 1400 km, *Phys. Earth Planet. Inter., 79*, 3-74, 1993.

Stefanescu, M., Elaborarea profilelor, scara 1:200.000 pentru completarea imaginii geologice a teritoriului R. S. Romania, A17-A20, Inst. de Geol. si Geofiz., Bucharest, 1984.

Stefanescu, M., and O. Dicea, Multiple thrust events at the Carpathian orogen/foreland contact in Romania, paper presented at *Managing Change at the Turn ot the Century*, Am. Assoc. of Petrol. Geol., Nice, Sept. 10-13, 1995.

Stefanescu, M., H.P. Hann, I. Gheuca, L. Szasz, and M. Stefanescu, Harta geologica scara 1:50.000, *108d*, Inst. de Geol. si Geofiz., Bucharest, 1982.

Steininger, F.F., C. Müller, and F. Rögl, Correlation of central Paratethys, eastern Paratethys, and Mediterranean: Neogene Stages, in *The Pannonian Basin, A Study in Basin Evolution*, edited by L.H. Royden, and F. Horváth, *AAPG Mem., 45*, 79-87, 1988.

Stille, H., *Grundfragen der Vergleichenden Tektonik*, edited by Borntraeger, 443 pp., Berlin, 1924.

Szakács, A., and I. Seghedi, Time-space evolution of Neogene-Quaternary volcanism in the Calimani-Giurghiu-Harghita volcanic chain, *Rom. J. Stratigr., 76*, 1-24, 1995.

Tapponnier, P., Evolution tectonique du système Alpin en Méditerranée: Poinçonnement et écrasement rigide-plastique, *Bull. Soc. Geol. Fr., 7*, 437-460, 1977.

Tari, G., F. Horváth, and J. Rumpler, Styles of extension in the Pannonian Basin. *Tectonophysics, 208*, 203-219, 1992.

D. Badescu and P. Constantin, Institute of Geology, Str. Caransebes, sector 1, 78344 Bucharest, Romania.

J.-C. Hippolyte, UMR CNRS 5025, Laboratoire de Géodynamique des Chaînes Alpines, Université de Savoie, Campus Scientifique Technolac, 73376 Le Bourget du Lac Cedex, France. (e-mail: Jean-Claude.Hippolyte@univ-savoie.fr)

(Received November 17, 1997;
revised March 2, 1999;
accepted March 16, 1999.)

TECTONICS, VOL. 18, NO. 6, PAGES 1292-1304 DECEMBER 1999

Erosional control on the geometry and kinematics of thrust belt development in the central Andes

Brian K. Horton

Department of Geology and Geophysics, Louisiana State University, Baton Rouge

Abstract. Long-term erosion rates in the central Andes may have influenced not only mean elevation and relief but also the regional geometry and kinematic history of the orogenic belt. A drastic along-strike erosional gradient exists in the modern central Andes, from a high-erosion region directly north of the 17.5°S bend in the Andes to a low-erosion region south of the bend. This gradient has existed since ~10-15 Ma based on fission track analyses of middle Miocene to Holocene denudation and qualitative evaluations of the preservation potential of middle-late Tertiary volcanic edifices and synorogenic sediment. Global positioning system velocity data indicate conflicting patterns of active surface shortening north and south of the 17.5°S bend. Whereas present-day shortening in the thrust belt north of the bend is distributed over much of the width of the belt, south of the bend it is concentrated near the eastern frontal margin. Structural data suggest a similar kinematic situation during late Miocene to Holocene shortening: an out-of-sequence chronology of thrusting in the narrow (200 km wide) thrust belt to the north versus a forward-breaking sequence of thrusting in the relatively wide (350 km wide) thrust belt to the south. The long-term internal deformation and limited width of the thrust belt north of the bend are attributed to prolonged subcritical thrust-wedge conditions, induced by rapid erosion rates since ~10-15 Ma. Such conditions inhibit thrust-front advance and favor distributed deformation within the thrust-belt interior. In the thrust belt south of the bend, a progressive eastward migration of thrusting is interpreted to be the result of long-term critical thrust-wedge conditions promoted by extremely low rates of denudation since middle Miocene time.

1. Introduction

At 17.5°S the central Andes exhibit an abrupt bend in surface orientation and a substantial change in width (Figure 1). South of the bend, the mountain belt trends N-S and has a width of ~550 km (measured perpendicular to tectonic strike from the volcanic arc to the front of the thrust belt). North of the bend, the mountain belt trends NW-SE and has a width of ~350 km. The change in trend directly overlies a similar-magnitude bend in the subducted Nazca slab, suggesting that the surface orientation of the central Andes is fundamentally related to the dynamics of subduction [*Cahill and Isacks*, 1992; *Gephart*, 1994; *Tinker et al.*, 1996]. The variation in width, however, cannot be attributed to the geometry of subduction because the Wadati-Benioff zone consistently dips ~30° under the South American plate directly north and south of the bend [*Barazangi and Isacks*, 1976; *Cahill and Isacks*, 1992; *Tinker et al.*, 1996]. Moreover, an along-strike variation in total shortening, which could potentially explain the change in width [*Isacks*, 1988], is not observed in regional balanced cross sections constructed directly north and south of the bend [*Roeder*, 1988; *Roeder and Chamberlain*, 1995; *Dunn et al.*, 1995; *Kley et al.*, 1996; *Schmitz and Kley*, 1997; *Schmitz*, 1994; *Sheffels*, 1990; *Baby et al.*, 1997; *Allmendinger et al.*, 1997].

This paper explores the hypothesis that the change in orogen width as well as variations in thrust-belt geometry and kinematics north and south of the 17.5°S bend are controlled by long-term erosional processes. A synthesis of different central Andean data sets for both the modern system (topography, precipitation, fluvial denudation rates, GPS-derived shortening rates) and ancient, middle Miocene to Holocene system (long-term denudation rates, sediment depositional patterns, fold-thrust kinematics) provides a compelling case for inhibited thrust-front advance in a high-erosion region (north of the bend) versus significant thrust-front propagation in a low-erosion region (south of the bend). This situation is consistent with an orogenic belt governed by maintenance of critical taper whereby high erosion rates prevent the thrust belt from gaining sufficient topographic slope to induce forward propagation of the thrust front and overall widening of the orogen [e.g., *Dahlen and Suppe*, 1988; *Beaumont et al.*, 1992; *DeCelles*, 1994; *DeCelles and Mitra*, 1995; *Norris and Cooper*, 1997; *Pavlis et al.*, 1997].

2. Regional Geologic Setting

The central Andes display the highest average elevation, greatest width, thickest crust, and maximum shortening of the Andean orogenic belt [*Isacks*, 1988; *Sheffels*, 1990; *Schmitz*, 1994; *Zandt et al.*, 1994; *Beck et al.*, 1996; *Allmendinger et al.*, 1997; *Baby et al.*, 1997]. From west to east, the central Andes (Figure 1) include the Western Cordillera, a magmatic arc; the Altiplano, a high-elevation hinterland plateau; the Eastern Cordillera, the uplifted interior of the thrust belt; the Subandean Zone, the seismically active frontal part of the thrust belt; and the Chaco-Beni Plain, the undeformed foredeep overlying basement rocks of the Brazilian shield. This overall geometry represents a noncollisional orogenic belt associated with subduction of an oceanic plate beneath a continent [*Dewey and Bird*, 1970; *James*, 1971]. The subducted Nazca plate dips ~30° under most of the central Andes (Figure 2); however, north of 15°S and south of 28°S, slab dip becomes much less and is nearly horizontal [*Barazangi and Isacks*, 1976; *Cahill and Isacks*, 1992].

The cross-sectional asymmetry of the central Andes is defined by a short, steep western slope (western flank of the Western Cordillera), a high axial plateau (Altiplano), and a long, rugged

Paper number 1999TC900051.
0278-7407/99/1999TC900051$12.00

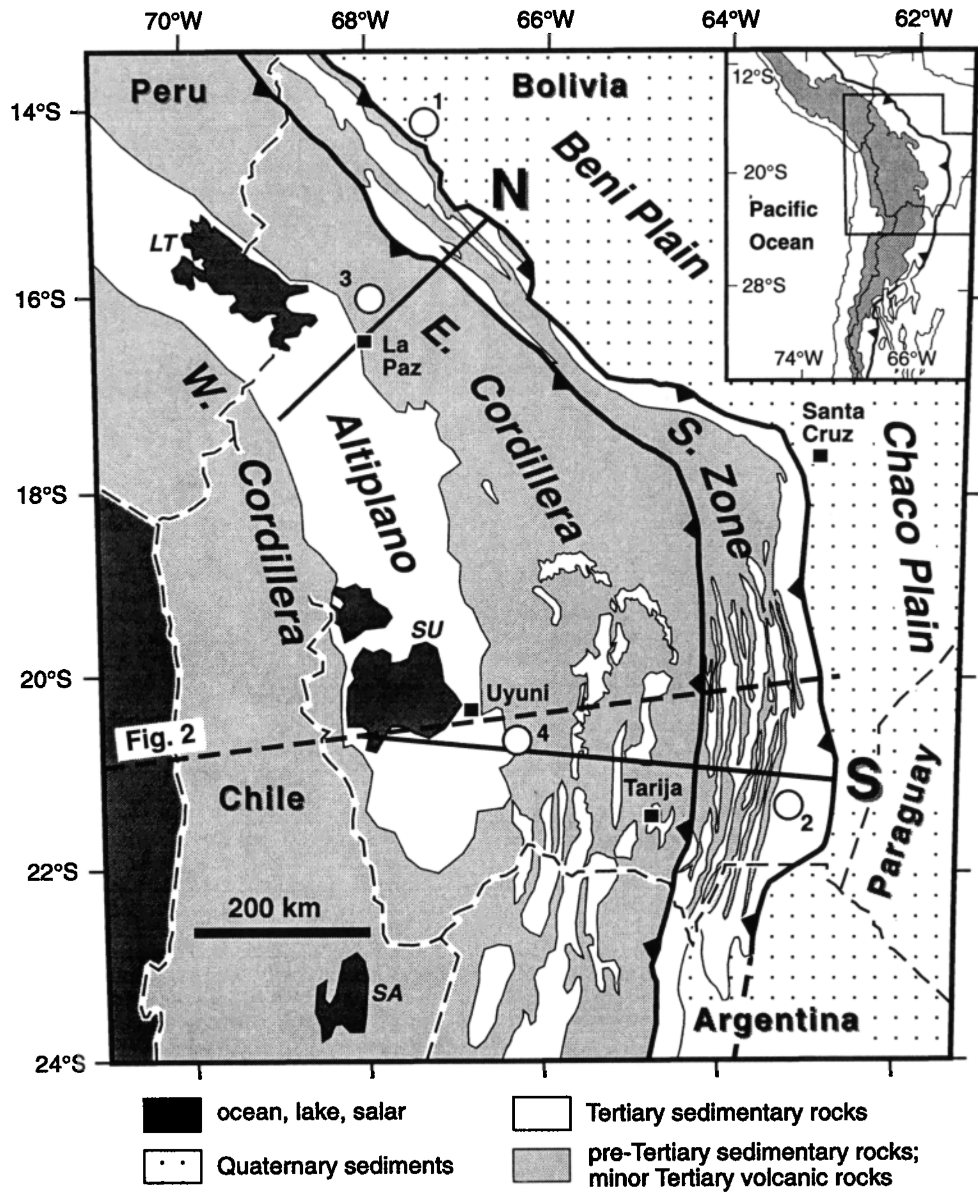

Figure 1. Map of central Andes displaying major geological, physiographic, and political boundaries and locations of a lithospheric profile (Figure 2) and topographic profiles N and S (Figure 3). The Subandean Zone is situated between two major thrust faults (barbed lines): a frontal thrust to the east and the Main Andean thrust (and equivalent "Interandean Zone" of southern Bolivia) to the west. Note the greater amount of Tertiary sedimentary rocks within the Eastern Cordillera and Subandean Zone south of the 17.5° bend in the Andes. Circles denote sites with denudation information (1, gauging station near Rurrenabaque; 2, gauging station at Villamontes; 3, Zongo and Huayna Potosi granites; 4, Cerro Chorolque). Major lakes and salars include Lake Titicaca (LT), Salar de Uyuni (SU), and Salar de Atacama (SA). Inset map (upper right) shows location of areas above 3 km elevation (shaded), thrust front (barbed line), and basement uplifts (outlined areas).

eastern slope (Eastern Cordillera and Subandean Zone) (Figures 1 and 2). The steep western slope is not extensively disrupted by upper-crustal structures, and therefore exhibits a smooth, continuous morphology for hundreds of kilometers along strike [*Isacks*, 1988]. The internally drained Altiplano has an average elevation of 3.7 km and remarkably subdued relief (Figure 3). The rough topography of the eastern slope represents a series of primarily E-vergent fold-thrust structures in the Eastern Cordillera and Subandean Zone (Figures 1 and 2).

Whereas thrust-belt structures north of 17.5°S strike NW-SE, those south of 17.5°S strike N-S (Figure 1). Development of these structures and associated evolution of the bend in the Andes (referred to as the "Bolivian orocline") are generally attributed to late Cenozoic shortening [*Isacks*, 1988; *Sempere et al.*, 1990;

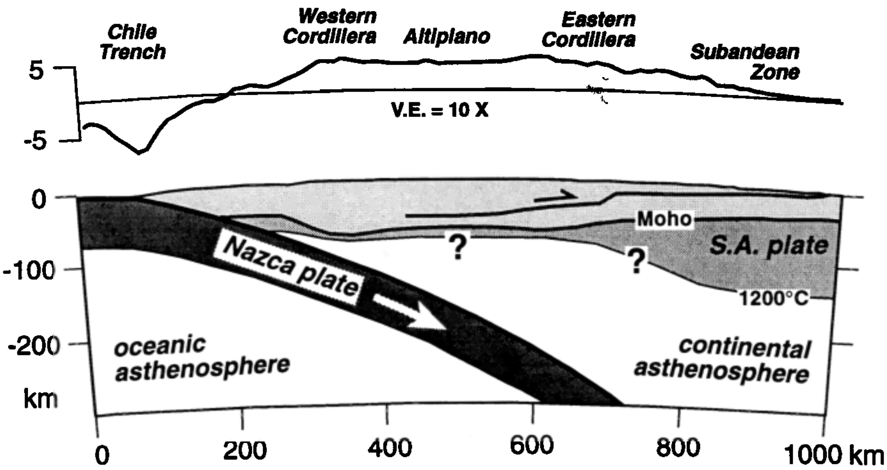

Figure 2. Lithospheric cross section (location in Figure 1) showing asymmetric topography and structure of central Andes [after *Isacks*, 1988]. A smooth, steep western slope contrasts with rough topography of the shallow eastern slope. A schematic regional decollement depicts crustal shortening and thickening associated with numerous E-vergent structures of the thrust belt along the eastern slope of the Andes. The western slope lacks major upper-crustal structures and potentially represents a crustal-scale monocline above a thickened lower crust.

Butler et al., 1995; *MacFadden et al.*, 1995; *Tinker et al.*, 1996]. Ages of coarse-grained, foreland-basin deposits indicate that shortening has taken place in the Eastern Cordillera since the late Oligocene [*Sempere et al.*, 1990; *Horton*, 1998] and in the Subandean Zone since the late Miocene [*Gubbels et al.*, 1993; *Hernández et al.*, 1996; *Moretti et al.*, 1996; *Jordan et al.*, 1997].

3. Erosion in the Central Andes

3.1. Modern Topography, Precipitation, and Denudation

Two profiles through the central Andes (Figure 3) reveal drastic differences in topography and precipitation north and south of the 17.5°S bend [*Masek et al.*, 1994]. Most striking is the topographic divide along the eastern margin of the Altiplano which exhibits significantly greater relief and higher average elevation to the north than to the south (Figure 3). In fact, the maximum values of elevation and relief in the entire Eastern Cordillera-Subandean Zone thrust belt occur north of the bend. This includes a belt of high rugged peaks (~5.5-6.5 km elevation) in the Cordillera Real region (westernmost Eastern Cordillera) that extends from La Paz northwestward into Peru (Figure 1). The gradient of the eastern, foreland-dipping slope is much greater along the northern profile than the southern profile (Figure 3). To the north, average elevation drops 3 km in a horizontal distance of 60 km from the topographic divide (3° average slope). A similar 3-km drop in average elevation takes place over a horizontal distance of 225 km along the southern profile (0.8° average slope).

The topographic contrast between the northern and southern profiles correlates with a pronounced change in precipitation patterns near the 17.5°S bend. Annual precipitation along the northern profile is typically 2-4 times the value for the southern profile (Figure 3). Within the Eastern Cordillera-Subandean Zone thrust belt in particular, precipitation of ~1.4-2.4 m yr^{-1} to the north contrasts with ~0.2-1.1 m yr^{-1} precipitation to the south (Figure 3). *Masek et al.* [1994] discuss the positive correlation between amounts of precipitation and relative slope and relief. They attribute the development of high-relief peaks and a steep frontal slope in the northern region to high precipitation and associated high rates of erosion. The differences in precipitation also appear to be manifest in stream discharge, as measured by two gauging stations at the front of the thrust belt. The first station is situated at the exit point of the Rio Beni from the northern thrust belt (site 1, Figure 1) [*Guyot et al.*, 1993], and the second station resides at the exit point of the Rio Pilcomayo from the southern thrust belt (site 2, Figure 1) [*Guyot et al.*, 1990]. At 67,500 km^2 and 81,300 km^2 the drainage basins defined by the Beni and Pilcomayo river systems, respectively, cover the greatest area of any drainage networks in the central Andean thrust belt. Despite the slightly smaller area of the Beni drainage basin, it has an average discharge of 2050 m^3 s^{-1}, much higher than the 260 m^3 s^{-1} average discharge for the Pilcomayo [*Guyot et al.*, 1990, 1993].

The observed precipitation change in the central Andes may reflect a regional climatic boundary that approximately coincides with the drainage divide between the Amazon and Parana drainage basins (Figure 4). The Amazon drainage basin (5.98 x 10^6 km^2) occupies most the northern part of the continent (Figure 4) and exhibits high precipitation rates (>1.5-3.0 m yr^{-1} or 4-8 mm d^{-1}). In contrast, the Parana drainage basin (2.86 x 10^6 km^2), which drains the majority of the craton south of ~15°-20°S (Figure 4), is generally characterized by low precipitation rates (<0.75-1.5 m yr^{-1} or 2-4 mm d^{-1}). Fluvial denudation data [from *Summerfield and Hulton*, 1994, and references therein] that have been normalized to basin area indicate that the Amazon basin undergoes greater erosion and sediment transport per unit area than the Parana basin, as shown by mean annual specific solid load (221 t km^{-2} yr^{-1} versus 30 t km^{-2} yr^{-1}) and total (mechanical and chemical) denudation rate (93 mm kyr^{-1} versus 14 mm kyr^{-1}). Furthermore, stream power, defined as the product of average discharge and average slope, is substantially higher for the Amazon (149,736 m^3 s^{-1} x 0.842 = 126,078 m^3 s^{-1}) than the Parana

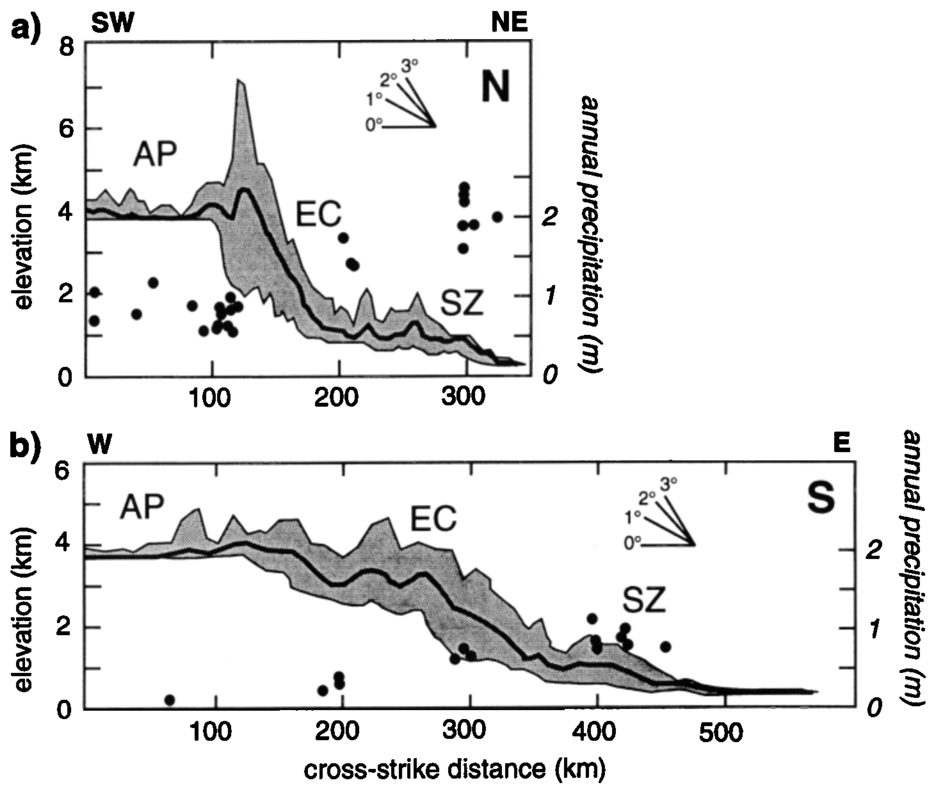

Figure 3. Topography and mean annual precipitation along (a) N profile and (b) S profile (locations in Figure 1) (modified from *Masek et al.* [1994]). Topography is based on elevation data from a 100-km-wide swath along the trend of each profile. Upper and lower limits of the shaded envelope represent maximum and minimum elevations, respectively, within each swath. Vertical extent of the envelope represents topographic relief. Swath-averaged elevation is shown by dark line within envelope. Precipitation data (circles) have been projected from stations within a 200-km-wide swath. Abbreviations are as follows: AP, Altiplano; EC, Eastern Cordillera; SZ, Subandean Zone.

($13,594\ m^3\ s^{-1} \times 1.22 = 16,585\ m^3\ s^{-1}$) (J. Pelletier, California Institute of Technology, unpublished data, 1998). Similar trends are observed for the Rio Beni, a major tributary of the Amazon, relative to the Rio Pilcomayo, a major tributary of the Parana [*Guyot et al.*, 1990, 1993; *Aalto and Dunne*, 1998]. Mean annual specific solid load, measured at gauging stations at the front of the thrust belt (Figure 1), is higher for the Beni than the Pilcomayo (74 t $km^{-2}\ yr^{-1}$ versus 36 t $km^{-2}\ yr^{-1}$) [*Guyot et al.*, 1990, 1993]. The combination of a steeper slope (Figure 3) and higher discharge for the Beni (mentioned previously) also ensures a greater average stream power than the Pilcomayo. In sum, the north-to-south transition from the Amazon drainage basin (and smaller Beni basin) to the Parana drainage basin (and smaller Pilcomayo basin) at ~15°-20°S (Figure 4) exhibits strong spatial correspondence with the differences in precipitation, discharge, and erosion observed north and south of the bend in the Andes. These transitions may be ultimately attributable to zonal (latitudinally controlled) atmospheric circulation in the southern hemisphere [*Trewartha*, 1966] combined with possible circulation effects related to the narrow width (and decreased land area) of the continent south of ~15°-20°S [*Meehl*, 1992; *Clapperton*, 1993].

3.2. Long-Term Denudation

Amounts of middle Miocene to Holocene denudation have been relatively high north of 17.5°S and extremely low south of 17.5°S, suggesting that the erosional contrast observed in the modern central Andes has existed since ~10-15 Ma. Apatite and zircon fission track data from several plutons in the Cordillera Real (westernmost Eastern Cordillera) near La Paz (site 3, Figure 1) provide constraints on the rates of Tertiary denudation (rates recalculated by *Masek et al.* [1994] from *Benjamin* [1986] and *Benjamin et al.* [1987]). Fission track ages represent the time at which apatite and zircon cooled through the ~100°C and ~200°C isotherms, respectively. In the case of the Zongo and Huayna Potosi granites in the Cordillera Real, apatite samples yield ages ranging from ~5 to 20 Ma and zircon samples yield much older ages, from ~25 to 100 Ma. Assuming a reasonable geothermal gradient (25°-30°C km^{-1}), these data indicate denudation rates of 50-160 m Myr^{-1} prior to ~10-15 Ma [*Masek et al.*, 1994]. Rapid denudation rates of 200-900 m Myr^{-1} have characterized the middle-late Miocene to Holocene history of the Cordillera Real, requiring erosional removal of ~4-8 km of rock mass from the

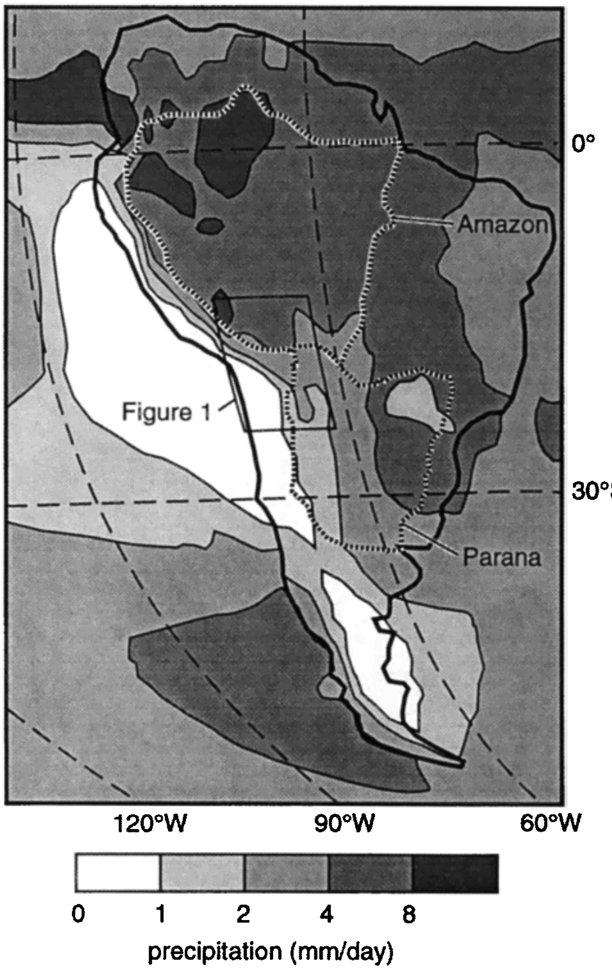

Figure 4. Precipitation in South America and adjacent areas based on global mean annual precipitation data from *Legates and Willmott* [1990], copyright John Wiley & Sons Limited, reproduced with permission. Outlines of the high-precipitation Amazon drainage basin and low-precipitation Parana basin (redrawn from *Summerfield and Hulton* [1994]) define an E trending drainage divide at ~15°-20°S.

thrust belt in the past 10-15 Myr [*Benjamin*, 1986; *Benjamin et al.*, 1987; *Masek et al.*, 1994]. Preliminary modeling of additional apatite fission track data and construction of a channel network incision model for this region [*Safran*, 1998; *Safran and Dunne*, 1998] confirm the high denudation rates (values ranging from 200-600 m Myr^{-1} since 10 Ma) and suggest a moderate downstream increase in rates within the first ~20 km of headwater reaches.

South of the bend in the Andes, there are several lines of evidence that indicate limited erosion since ~15 Ma. First, major middle Miocene volcanic edifices such as Cerro Chorolque and the Chocaya stock [*Francis et al.*, 1983; *Gubbels*, 1993], remain largely intact in the westernmost Eastern Cordillera of southern Bolivia. Cerro Chorolque (site 4, Figure 1) is a shallow subvolcanic intrusion dated as 16.2 ± 0.3 Ma [*Grant et al.*, 1979; *Schneider and Halls*, 1986] which retains its original volcanic morphology and reaches an elevation of 5552 m (Figure 5a). The elevation difference between the summit of Cerro Chorolque and the surrounding region is ~1750 m, comparable to the relief of the largest modern volcanoes of the active arc in the Western Cordillera. The fact that this ~16 Ma volcanic edifice remains virtually unaltered from its original state suggests extremely low rates of denudation since middle Miocene time. A second point concerns the large volume of Miocene and younger synorogenic sediment preserved within the Eastern Cordillera-Subandean Zone thrust belt in southern Bolivia and northern Argentina (see discussion by *Horton* [1998]). Numerous N trending belts of Tertiary strata are preserved within this region (Figure 1), including deposits above and below the San Juan del Oro geomorphic surface in the Eastern Cordillera (Figure 5b). The surface is a regional erosion surface located at ~2-4 km elevation and capped by late Miocene and younger deposits [*Gubbels et al.*, 1993; *Kennan et al.*, 1997]. Collectively, the preservation of such large amounts of sediment and a geomorphic surface at high elevations within the uplifted hinterland of an orogenic belt, a region typically characterized by large amounts of denudation rather than deposition, suggests special conditions in which extremely limited erosion has taken place since ~10-15 Ma. In direct contrast, the Eastern Cordillera north of the 17.5°S bend contains almost no Tertiary sediment, and the Subandean Zone has less Tertiary sediment than areas to the south (Figure 1). Possible supporting evidence for limited erosion south of the bend comes from estimates of Tertiary erosion rates based on mineralization pressure-temperature conditions for a porphyry-copper deposit in the Western Cordillera near the Salar de Atacama (Figure 1). These data indicate a middle Miocene decrease from maximum values of 190 m Myr^{-1} to 10 m Myr^{-1} [*Alpers and Brimhall*, 1988]. This decrease, combined with oxygen isotopic evidence for middle Miocene cooling of the Pacific and Atlantic Oceans [*Miller et al.*, 1987], may point to regional onset of arid conditions over part of South America at ~15-13 Ma [*Alpers and Brimhall*, 1988].

The N-S contrast in erosion since middle Miocene time also may have affected large-scale sediment accumulation histories within the adjacent foreland basin. North of the 17.5°S bend, the Beni Plain foredeep (Figure 1) is filled with 4-7 km of mostly Neogene sediment, whereas the Chaco Plain foredeep south of the bend contains a maximum Neogene thickness of only 3 km [*Watts et al.*, 1995; *Horton and DeCelles*, 1997]. This contrast could be related purely to differences in accommodation space due to variations in thrust-load distribution or effective elastic thickness of the lithosphere [e.g., *Watts et al.*, 1995]. An intriguing alternative, however, that may explain part of the difference is the possibility that relatively higher denudation rates in the northern part of the thrust belt resulted in higher sediment yields, greater sediment loading, and more sediment accumulation in the Beni Plain foredeep than the Chaco Plain foredeep.

4. Synthesis of Thrust Belt Evolution

4.1. Critical Taper Theory

Theoretical models state that a fold-thrust wedge strives for a stable or critical condition in which the net force driving the wedge forward, the sum of a gravitational body force and a horizontal compressive force, is exactly balanced by the basal friction force resisting advance of the wedge [*Davis et al.*, 1983; *Dahlen and Suppe*, 1988; *Dahlen*, 1990]. The critical condition is de-

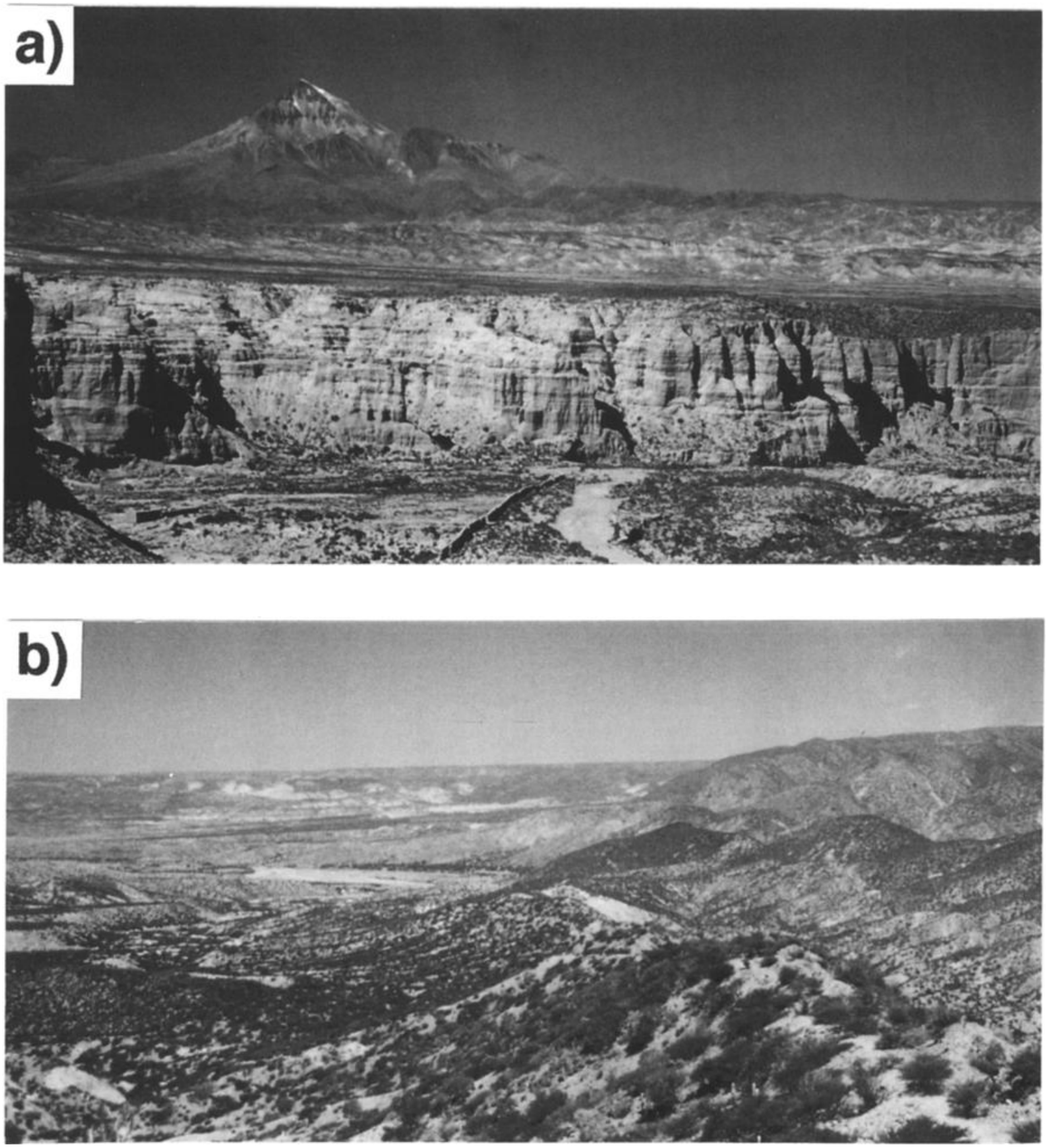

Figure 5. Photographs representing minimal erosion in southern Bolivia from middle Miocene to Holocene time. (a) View eastward of Cerro Chorolque volcanic edifice (subvolcanic intrusion dated as 16.2 ± 0.3 Ma) and its ejected volcanic deposits (Quehua Formation) in the foreground (site 4, Figure 1). Neither the more-resistant edifice (with peak elevation of 5552 m) nor the less resistant volcanic deposits (at 3800 m elevation) have been significantly incised since their middle Miocene emplacement. (b) View southward of San Juan del Oro geomorphic surface preserved near the Bolivia-Argentina border (21.7°S, 65.6°W). Surface is located 500 m above valley floor, dips <3° eastward (left), and is capped regionally by late Miocene to Holocene volcanic and sedimentary strata.

pendent on several mechanical properties of the wedge, including basal strength, internal wedge strength, basal pore fluid pressure, and internal pore fluid pressure. For a given set of these values, the critical condition will be attained only if the sum of surface slope (α) and decollement slope (β) reaches a specific value, or "critical taper." Because numerous combinations of α and β may sum to this specific value, the critical condition is represented by a line in α-β space (Figure 6). When changes in any of the geometric parameters (α and β) or mechanical parameters force the wedge out of the critical state into a "supercritical" or "subcritical" state (Figure 6), the wedge responds by deforming to alter its geometry (α and/or β) until the critical condition is regained. For instance, an orogenic wedge that becomes subcritical may attempt to regain a critical state through internal deformation by

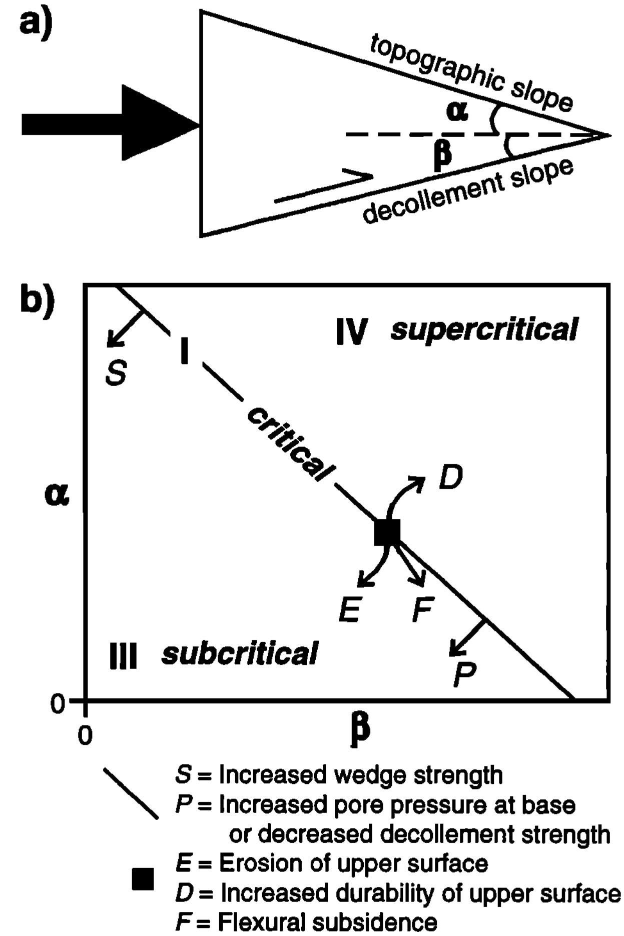

Figure 6. Critical taper theory for thrust wedges (modified from *DeCelles and Mitra* [1995]). (a) Geometry of a thrust wedge being pushed from behind (arrow). Wedge taper equals the sum of the surface slope (α) plus the angle of the basal decollement (β). (b) Diagram depicting wedge behavior in α-β space in response to variations in some key parameters. I, critical, wedge advances in self-similar form by accretion of new material at base; III, subcritical, insufficient taper prevents advance and promotes internal deformation; IV, supercritical, stable sliding is possible along a single basal thrust. Variations S and P alter the mechanical properties of the wedge and affect the location of the critical-taper line in α-β space. Variations E, D, and F modify the geometry of a specific wedge (represented by the solid square) that initially has critical taper.

out-of-sequence thrusting, synchronous thrusting, or duplexing [e.g., *Boyer*, 1992; *DeCelles and Mitra*, 1995; *Mitra*, 1997; *Mitra and Sussman*, 1997]. An implication of this sort of thrust-wedge behavior is that processes, such as erosion, which reduce surface slope may ultimately tend to induce internal deformation within the wedge [*DeCelles*, 1994; *DeCelles and Mitra*, 1995; *Norris and Cooper*, 1997; *Pavlis et al.*, 1997].

The exact mechanical properties and thrust-wedge geometries are nearly impossible to retrieve from an orogenic wedge, modern or ancient [e.g., *Meigs and Burbank*, 1997]. Nevertheless, it is possible to use a symptomatic approach in which wedge behavior (defined by regional patterns of thrusting and erosion) is interpreted in terms of critical taper models [e.g., *DeCelles and Mitra*, 1995; *Mitra*, 1997]. Since the central Andean thrust belt is still active, a first-order question concerns the present-day conditions of the thrust belt north and south of the bend in the Andes at 17.5°S. Specifically, is the wedge internally deforming (consistent with a subcritical condition) or is deformation concentrated at or near the thrust front (consistent with a critical condition)? Evaluating the current thrust-wedge conditions in these two regions of the thrust belt requires data on the active deformational processes within the orogenic belt. Furthermore, are modern kinematics of the thrust belt similar to the ancient, Miocene and younger history of deformation?

4.2. Active Tectonics: Global Positioning System (GPS) Velocity Data

The condition of a modern thrust wedge may potentially be evaluated with surface velocity data from a collection of sites along a transect through the wedge. For a subcritical wedge, continuous internal shortening by thrust-sheet translation will result in a distinctive velocity profile. Internal shortening requires that the distance between sites on the surface of the wedge will be decreased (Figure 7a). Therefore surface velocities relative to the stable foreland will be progressively lower from the hinterland to the thrust front, yielding a foreland-sloping line in a velocity profile across the thrust belt (Figure 7a). Figure 7 shows a specific case in which total displacement (18 mm) of the rear of the wedge is accommodated by synchronous displacement on three active thrusts (with displacements of 9, 6 , and 3 mm) in the frontal part of the wedge. For a critical wedge, most deformation will be concentrated at the thrust front (Figure 7b). Therefore the velocity relative to the stable craton will be uniform for all sites in the thrust belt, yielding a straight horizontal line in a velocity profile across the thrust belt (Figure 7b). In effect, this situation represents a single intact thrust sheet sliding toward the craton with no internal deformation of the sheet. The example in Figure 7 presents the particular case in which all sites within the thrust belt have moved the same distance (18 mm in this case) toward the craton within a given amount of time (say, a single year). Thus the total displacement (18 mm) at the rear of the wedge is entirely accommodated by displacement (18 mm) on a single frontal thrust. It should be cautioned that self-similar growth of a thrust wedge at critical-taper conditions over geologic time frames (> 1-5 Myr), although dominated by thrust-front deformation, may include modest internal shortening.

Space geodetic observations provide an excellent opportunity to determine the velocity of points on Earth's surface relative to each other on a very short timescale (several years) and, in this case, attempt to evaluate the present-day condition of the thrust wedge. Recent GPS studies in the central Andes provide modern surface velocities for numerous sites within the orogenic belt [*Leffler et al.*, 1997; *Norabuena et al.*, 1998] which are utilized here to evaluate the thrust wedge north and south of the 17.5°S bend in the Andes. The entire GPS data set published by *Norabuena et al.* [1998] ranges from 8°S to 22°S and extends from the west coast to the craton. The following analysis utilizes the GPS data for all sites that are east of the axis of the Western Cordillera and between 13°S and 22°S (Table 1). Velocity data are grouped into two populations in order to construct two profiles perpendicular to the strike of the orogenic belt: a NE-SW profile north of the bend (using data from 13°S to 17.5°S) and an

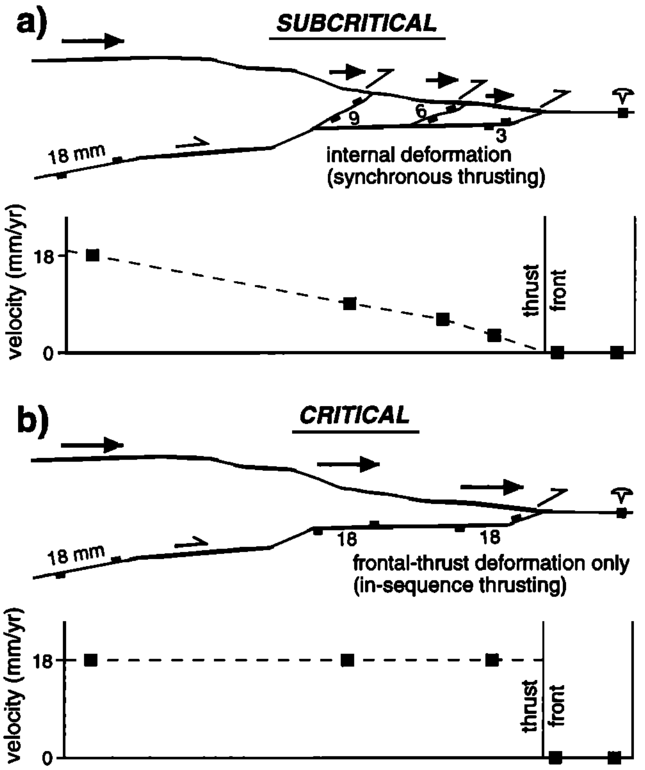

Figure 7. Idealized representation of expected horizontal surface velocities relative to a stable craton (bold arrows) within a thrust wedge that is (a) subcritical or (b) critical. In both cases, the rear of the thrust belt (left) has been displaced 18 mm toward the stable cratonic foreland (right) in a single year. In Figure 7a, internal shortening within the wedge requires that surface velocities become progressively lower toward the thrust front and an 18 mm displacement at the rear of the thrust belt is distributed on a suite of faults (three, in this case) in the frontal part of the thrust belt. In Figure 7b, the 18 mm yr^{-1} velocity is constant throughout the wedge, there is no internal deformation within the wedge, and shortening is taken up exclusively on the frontal thrust.

Table 1. GPS Velocities Relative to Stable South America

Site	Distance from Thrust Front, km	Velocity, mm yr^{-1}	Velocity Error, mm yr^{-1}
Western Cordillera and Altiplano Sites (13°-17.5°S)			
AREQ	459	18.19	± 2.09
BAJO	409	15.73	± 2.53
COTA	340	25.00	± 3.72
CANA	310	16.14	± 2.75
LAMP	284	11.55	± 2.57
COMA	269	14.16	± 2.85
Eastern Cordillera and Subandean Sites (13°-17.5°S)			
PNAS	210	10.31	± 3.01
CUSO	132	11.51	± 2.46
LEON	123	13.39	± 2.59
CNOR	112	11.07	± 2.55
SAPE	83	4.42	± 2.70
TUNA	38	8.00	± 2.61
CHIM	9	4.70	± 2.34
REYE	-26	9.19	± 2.71
FITZ	-65	2.19	± 2.15
Western Cordillera and Altiplano Sites (17.5°-22°S)			
SACA	589	23.87	± 4.79
OLLA	513	24.59	± 4.63
CORQ	472	19.66	± 4.12
CHTA	397	19.04	± 4.62
ORUR	370	14.76	± 4.31
Eastern Cordillera and Subandean Sites (17.5°-22°S)			
CSUR	325	12.29	± 3.37
POTO	266	16.06	± 4.52
SUCR	213	16.12	± 3.86
TARI	196	14.14	± 3.98
ENRI	109	15.62	± 4.17
VAGR	101	10.12	± 18.46
INGM	-8	5.90	± 3.95
PSUC	-60	6.55	± 3.80

GPS velocity data from *Norabuena et al.* [1998] (available in table format from http://www.earth.nwu.edu/research/snapp.html) are resolved into their velocity components in two profiles. Northern data set (13°-17.5°S) is projected onto a NE-SW profile and southern data set (17.5°-22°S) is projected onto an E-W profile. Reported distance from thrust front is measured parallel to each profile (positive for Andean sites, negative for foreland sites).

E-W profile south of the bend (using data from 17.5°S to 22°S). The absolute velocities from *Norabuena et al.* [1998] are resolved into their appropriate components in the plane of each profile (Table 1). It is important to point out that the approach utilized here, resolving the GPS velocities into the plane of the appropriate profile, only evaluates plane strain (surface motions perpendicular to strike) for each of the two profiles. However, the assumption of plane strain may be justified in this case since a summary by *Meijer et al.* [1997] of the present-day stress field in the central Andes (including analyses of borehole breakouts, earthquake focal mechanisms, and fault kinematics) indicates maximum horizontal compression perpendicular to strike both north and south of the 17.5°S bend (i.e., NE-SW compression north of the bend and E-W compression south of the bend).

Although the analytical details of the GPS analyses are available in other sources [*Leffler et al.*, 1997; *Norabuena et al.*, 1998; *Dixon et al.*, 1997], several key points are addressed here. All velocities are reported relative to a stable South America reference frame which is defined by minimizing the horizontal velocities (in a least squares sense) of four permanent GPS sites along the eastern margin of the craton, ranging from 5°N to 35°S, and two survey sites within the western craton at 11°S to 18°S, ~200-400 km east of the thrust front [*Norabuena et al.*, 1998]. The residual velocities are zero (within error) for each of the six cratonic sites [*Norabuena et al.*, 1998]. Subsequent GPS analyses for South America by *Kendrick et al.* [1999] and *Angermann et al.* [1999] include the same four permanent sites in the eastern craton, and there are no discrepancies among the residual velocities calculated by the three different studies [*Kendrick et al.*, 1999]. However, a discrepancy does exist for the magnitude of the horizontal velocity at the only Andean site common to all three studies, the Arequipa (AREQ) site at 16.5°S in the Western Cordillera of southern Peru. The directions are fairly uniform at ~073°-082° azimuth, but the magnitudes are 10.2 ± 0.3 mm yr^{-1} [*Kendrick et al.*, 1999], 11.9 ± 0.6 mm yr^{-1} [*Angermann et al.*, 1999], and 22.6 ± 1.7 mm yr^{-1} [*Norabuena et al.*, 1998]. In the *Norabuena et al.* [1998] analysis, velocities for the nearest three sites within the Western Cordillera and forearc region (including

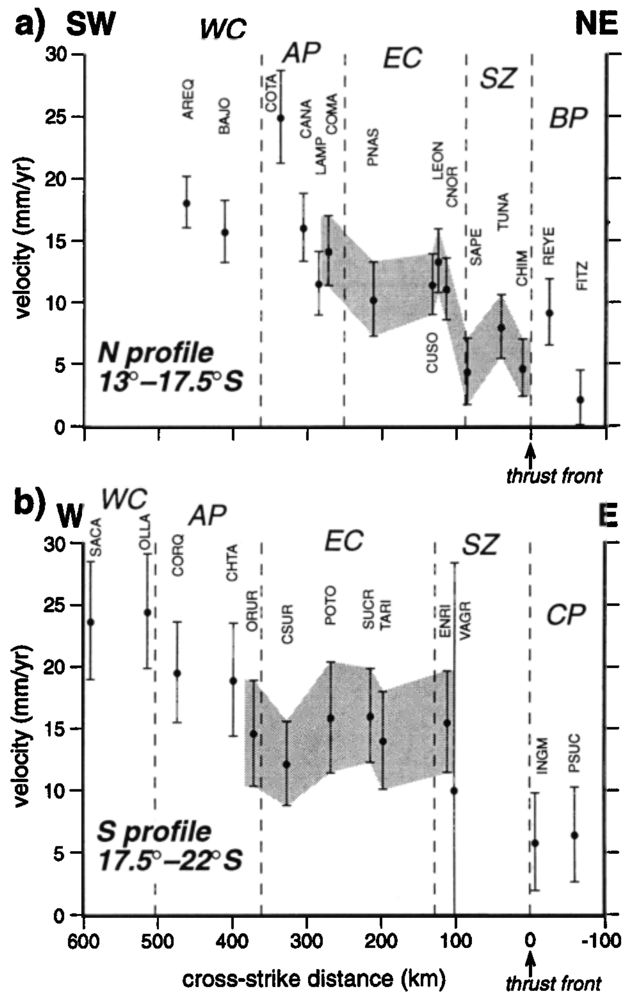

Figure 8. Surface velocity profiles (with error bars) for GPS sites across the central Andes, calculated from data of *Norabuena et al.* [1998]. (a) Sites north of the bend in the Andes (13°-17.5°S) are resolved into a strike-perpendicular profile trending 045° (NE-SW). (b) Sites south of the bend in the Andes (17.5°-22°S) are resolved into a strike-perpendicular profile trending 090° (E-W). Shaded regions highlight trends in surface velocities within the fold-thrust belt: variable velocities to the north and uniform velocities to the south. Following the concept in Figure 7, these data suggest significant internal deformation (subcritical state) to the north and relatively little internal deformation (critical state) to the south. Abbreviations are as follows: WC, Western Cordillera; AP, Altiplano; EC, Eastern Cordillera; SZ, Subandean Zone; BP, Beni Plain; CP, Chaco Plain.

JHAI, BAJO, and POCO, all within 150 km of AREQ) exhibit ~19-33 mm yr^{-1} velocities, notably higher than the AREQ velocities of *Kendrick et al.* [1999] and *Angermann et al.* [1999]. In addition, four distant sites from *Kendrick et al.* [1999] which span the Western Cordillera and forearc region from IQQE (20.3°S) to ANTC (37.3°S) have azimuths of ~073°-092° and velocities of ~16-24 mm yr^{-1}. Thus the ~10-12 mm yr^{-1} AREQ velocities conflict with other GPS velocity data from both proximal and distal sites in the Western Cordillera and forearc region. Moreover, an independent estimate of AREQ motion based on very long baseline interferometry (VLBI) indicates a velocity of 19.0 ± 3.0 mm yr^{-1} relative to stable South America [*Robaudo and Harrison*, 1993], matching the velocity of *Norabuena et al.* [1998]. The lower velocities of the other two studies could potentially reflect a time series which is, to this point, insufficient in length to reduce time-correlated noise [e.g., *Mao et al.*, 1999]. A case example of such noise, and its elimination with a longer time series, may be the preliminary study of *Leffler et al.* [1997] in which a velocity of 13.3 ± 1.5 mm yr^{-1} was calculated for AREQ, but with additional data was updated by *Norabuena et al.* [1998] to 22.6 ± 1.7 mm yr^{-1}. Given the internal consistency and agreement with VLBI data, the GPS data set of *Norabuena et al.* [1998] is considered to be robust and appropriate for the simple analysis considered here.

Two velocity profiles constructed perpendicular to strike (Figure 8) sample the orogenic belt from the Western Cordillera active magmatic arc to the foreland basin of the Chaco-Beni Plain, crossing the Altiplano hinterland plateau and Eastern Cordillera-Subandean Zone thrust belt. In both the northern and southern profiles, maximum velocities are observed in the Western Cordillera or westernmost Altiplano and minimum velocities are observed in the Chaco-Beni Plain. Following *Norabuena et al.* [1998], the observed velocities are interpreted as (1) deformation associated with shortening in the fold-thrust belt and (2) locking along the plate boundary zone. Surface shortening represents a permanent change in the position of sites on the surface of the mountain belt relative to stable South America. Thus site velocities in the Eastern Cordillera-Subandean Zone thrust belt, a region of active upper-crustal shortening, may be regarded as rates of surface shortening in the plane of the given cross section. Measurable non-zero velocities for sites directly east of the thrust front may indicate surface shortening along blind thrusts within the proximal foreland basin [e.g., *Horton and DeCelles*, 1997] or possibly intracratonic deformation. The high velocities within the Western Cordillera and Altiplano, a region that is not known to be undergoing active upper crustal shortening [*Lamb and Hoke*, 1997], are tentatively interpreted as recorders of transient elastic deformation that will be released (and the deformation recovered) during future earthquakes.

Surface velocities within the Eastern Cordillera-Subandean Zone are most relevant to this discussion as they best define cross-strike variations in surface shortening, an important parameter in evaluating the condition of a thrust wedge (Figure 7). For the northern profile, site velocities are higher in the Eastern Cordillera than in the Subandean Zone (Figure 8), requiring internal shortening within the thrust belt. For the southern profile, more or less uniform site velocities across the Eastern Cordillera and western Subandean Zone require no internal shortening over most of the thrust belt; however, the frontal 100 km of the Subandean Zone has no well-constrained velocity data (Figure 8). Nevertheless, an important conclusion can be drawn for the southern profile based on the uniform velocities across the Eastern Cordillera-Subandean Zone boundary (Figure 8). This boundary contains one of the major structural elements of the thrust belt, a feature called the "Interandean Zone" which accommodated 80-90 km of shortening, roughly half of the total shortening in the thrust belt [*Kley*, 1996; *Kley et al.*, 1996; *Schmitz and Kley*, 1997]. This zone is defined by two basement-involved thrusts and associated smaller structures expressed at or near the surface ~5-50 km west of the town of Entre Rios (ENRI). The uniform GPS velocity data among all Eastern Cordillera sites and the ENRI site in the western Subandean Zone indicate that this structural system, as well as the entire Eastern Cordillera, are not undergoing internal shortening along the southern profile (Figure 8b). In direct contrast, velocity data for the northern profile (Figure 8a) require internal shortening across the Eastern Cordillera-Subandean Zone boundary. The Main Andean thrust [*Roeder*, 1988; *Sempere et al.*, 1990; *Roeder and Chamberlain*, 1995] approximates this boundary, and based on the velocity difference between the easternmost Eastern Cordillera sites (CUSO, LEON, and CNOR) and the western Subandean Zone site (SAPE) (Figure 8a), it appears to be accommodating active internal shortening.

The GPS velocity data clearly show that part of the thrust belt to the north is being internally shortened, a feature suggestive of subcritical thrust-wedge conditions (Figure 7a). To the south, all velocity data indicate a thrust belt that is translating as an intact sheet undergoing no internal deformation, implying critical thrust-wedge conditions (Figure 7b). However, additional velocity data are needed for the eastern Subandean Zone to confirm that the entire thrust belt to the south is at critical conditions. This speculation that the present-day central Andes are characterized by an active subcritical thrust belt north of the 17.5°S bend and an active critical thrust belt south of the bend can be tested for the Neogene history of the thrust belt through structural analysis on thrust-belt rocks.

4.3. Structural Geometries and Kinematics

The Eastern Cordillera-Subandean Zone thrust belt displays differences in broad-scale structural geometries and fold-thrust kinematics north and south of the 17.5°S bend. The most obvious geometric difference is the cross-strike width of the thrust belt (as measured perpendicular to tectonic strike from the deformation front to the Altiplano-Eastern Cordillera boundary). This width is 350 km to the south and only 200 km to the north (Figure 1). In addition, the slopes of the upper topographic surface (Figure 3) and basal decollement (where known) are different in the two regions. The northern thrust belt has a high wedge taper characterized by a 4° decollement slope [*Roeder*, 1988; *Roeder and Chamberlain*, 1995], a 0.5°-1° surface slope from the thrust front to the central Eastern Cordillera, and a 3° surface slope in the western Eastern Cordillera (Figure 3). In contrast, the southern thrust belt has an extremely low taper defined by a 2° decollement slope [*Dunn et al.*, 1995; *Kley*, 1996], a 0.5° surface slope in the Subandean Zone, and a 0.7°-1.5° surface slope in the Eastern Cordillera (Figure 3). Despite these differences, some large-scale structural geometries are similar throughout the thrust belt. To both the north and south, the majority of contractional structures are E-vergent and ultimately related to thrust faults that root in a regional basal decollement primarily in Silurian strata [*Roeder*, 1988; *Roeder and Chamberlain*, 1995; *Baby et al.*, 1992, 1995, 1997; *Dunn et al.*, 1995]. W-vergent backthrusts are common along the western margin of the thrust belt (Eastern Cordillera-Altiplano boundary) in the north, including the Huarina fold-thrust belt near La Paz [*Sempere et al.*, 1990; *Roeder and Chamberlain*, 1995], and in the south, including the San Vicente thrust at 21°-22°S [*Baby et al.*, 1990; *Kley et al.*, 1997]. Furthermore, estimates of total shortening within the Eastern Cordillera-Subandean Zone thrust belt are approximately the same to the north and south, ranging from 177 to 230 km [*Roeder*, 1988; *Roeder and Chamberlain*, 1995; *Dunn et al.*, 1995; *Kley et al.*, 1996; *Schmitz and Kley*, 1997; *Schmitz*, 1994; *Sheffels*, 1990; *Baby et al.*, 1997; *Allmendinger et al.*, 1997].

The kinematic evolution of the thrust belt has been markedly different to the north and south. During the late Oligocene to middle Miocene, contractional deformation was limited to the Eastern Cordillera in areas to both the north and south [*Roeder*, 1988; *Baby et al.*, 1990; *Sempere et al.*, 1990; *Roeder and Chamberlain*, 1995; *Horton*, 1998]. Initial deformation in the Subandean Zone began during late Miocene time, roughly between 12 and 6 Ma [*Gubbels et al.*, 1993; *Hernández et al.*, 1996; *Kley*, 1996; *Moretti et al.*, 1996; *Jordan et al.*, 1997]. In southern Bolivia, the undeformed, late Miocene San Juan del Oro geomorphic surface covers much of the Eastern Cordillera, suggesting that no upper-crustal deformation has taken place in that region since ~10 Ma [*Gubbels et al.*, 1993]. In the Eastern Cordillera to the north, however, no evidence exists for such a cessation of upper-crustal deformation.

Detailed analyses of the structural geometries in the Subandean Zone indicate out-of-sequence thrusting to the north and generally in-sequence thrusting to the south. Major E directed thrusts in the southern Bolivian Subandean Zone cut continuously upsection to the east and root into local decollements in Devonian strata and a regional basal decollement in Silurian strata [*Dunn et al.*, 1995]. Although local out-of-sequence thrusts characterize the Eastern Cordillera-Subandean Zone boundary in places [*Kley*, 1996], overall thrust kinematics in the easternmost Eastern Cordillera and Subandean Zone of southern Bolivia have been attributed to an in-sequence, eastward progression of deformation during late Miocene to Holocene time [*Hérail et al.*, 1990; *Baby et al.*, 1992; *Dunn et al.*, 1995; *Kley*, 1996]. In contrast, the thrust belt north of 17.5°S contains several thrusts that cut downsection in the direction of transport (to the east), requiring earlier deformation in locations to the east. These out-of-sequence thrusts include the Main Andean thrust near the Eastern Cordillera-Subandean Zone boundary [*Roeder*, 1988], thrusts within the western Subandean Zone [*Baby et al.*, 1995], and faults which define the deformation front [*Roeder and Chamberlain*, 1995]. These thrust faults indicate that late Miocene and younger contraction in the thrust belt north of 17.5°S was not recorded by a simple eastward progression of deformation.

5. Discussion

For the central Andes, long-term erosion rates are considered to be a key element governing the geometry and kinematic history of the orogenic belt. In this sense, rapid erosion north of 17.5°S since ~10-15 Ma may be regarded as a principal cause of subcritical thrust-wedge conditions in which internal deformation is promoted. Similarly, extremely low denudation rates to the south may facilitate critical conditions that favor a continuous eastward progression of thrusting. However, a host of other variables, in addition to erosion, potentially influence thrust-wedge behavior [*Davis et al.*, 1983; *Dahlen and Suppe*, 1988; *Boyer*, 1995; *DeCelles and Mitra*, 1995; *Mitra*, 1997; *Mitra and Sussman*, 1997].

Boyer [1995] and *Mitra* [1997] identified the initial slope of the preorogenic sedimentary prism as an important variable which determines the initial decollement slope (β), and therefore influences the overall taper in a thrust wedge. In the central Andes, a much greater thickness of lower Paleozoic strata accumulated in the region north of the 17.5°S bend [*Hérail et al.*, 1990], creating a steeper sloping sedimentary prism to the north than to the south. This is exemplified by a change in the decollement slope (β) from a northern value of 4° to a southern value of 2° [*Roeder*, 1988; *Roeder and Chamberlain*, 1995; *Dunn et al.*, 1995; *Kley*, 1996; *Allmendinger et al.*, 1997]. In general, regions with a more steeply sloping sedimentary prism and higher β will have a relatively higher taper (sum of α and β), thereby promoting more critical conditions than adjacent areas with gently sloping sedimentary prisms [*Boyer*, 1995; *Mitra*, 1997]. In the central Andes, however, the high-β northern region exhibits a kinematic history that is consistent with subcritical thrust-wedge conditions. Moreover, the average surface slope (α) in the north (0.5°-3° range) is greater than to the south (0.5°-1.5° range), a condition which ought to, but apparently does not, promote critical conditions to the north.

If the thrust belt is governed by maintenance of critical taper, these observations imply that some mechanical differences exist between the northern and southern regions such that the value of critical taper is higher to the north. Potential differences include but are not limited to (1) reduced internal strength of the northern wedge (possibly related to incorporation of greater amounts of weak sedimentary rocks), (2) increased strength of the basal decollement to the north (due to strain hardening or buttressing by basement rocks), or (3) decreased pore fluid pressure along the basal surface of the northern wedge (possibly due to erosional breaching of the decollement) [*DeCelles and Mitra*, 1995; *Mitra*, 1997]. The first alternative may be most appropriate because the degree of involvement of strong Precambrian crystalline basement and Ordovician metasedimentary rocks in the southern thrust belt exceeds that of the northern thrust belt. In southern Bolivia, gravity anomalies, electrical resistivities, seismic velocities, and balanced cross sections indicate that the upper ~10 km of crystalline basement is involved in thrust-belt deformation in the easternmost Eastern Cordillera [*Kley*, 1996; *Kley et al.*, 1996]. Farther west in the central Eastern Cordillera, seismic reflection data suggest a major footwall ramp that penetrates to ~20-40 km beneath the surface [*Allmendinger and Zapata*, 1996], depths well below the basement-cover interface. In contrast, balanced cross sections for the northern thrust belt indicate incorporation of only the upper few kilometers of crystalline basement [*Roeder*, 1988; *Roeder and Chamberlain*, 1995]. In addition, the majority of surface exposures across the Eastern Cordillera of southern Bolivia are penetratively deformed, Ordovician low-grade metasedimentary rocks, whereas the Eastern Cordillera to the north is primarily comprised of relatively weaker, lesser deformed Ordovician to Devonian strata. Therefore it is reasonable to suggest that greater involvement of crystalline basement and deformed metasedimentary rocks in the thrust belt to the south may have imparted higher internal strength to the southern wedge. However, without quantitative information on the specific mechanical properties of the northern and southern parts of the wedge and their basal decollements, it is difficult to rule out the other possibilities. At this point, the situation may be summarized as follows: (1) differences in mechanical properties between the northern and southern thrust belts produce a situation in which the northern wedge requires a higher taper than the southern wedge to achieve critical conditions; and (2) erosion significantly modifies the geometry of the upper surface of the wedge, thereby affecting taper, and promoting subcritical conditions in the high-erosion thrust belt to the north and critical conditions in the low-erosion thrust belt to the south.

6. Conclusions

Erosion may exert a strong control on the regional cross-sectional geometry and long-term kinematic evolution of the thrust belt on the eastern slope of the central Andes. This is exemplified by a remarkably sharp contrast in net erosion along the strike of the orogenic belt and corresponding variation in the width and kinematic history of the thrust belt. North of the 17.5°S bend in the Andes, rapid erosion rates have prevailed since middle Miocene time. The region south of the bend has exhibited extremely low erosion rates from ~10-15 Ma to present. In general, rapid denudation within the narrow (200 km wide) northern thrust belt has apparently promoted a subcritical thrust-wedge condition in which internal contractional deformation is required to build taper prior to forward advance of the thrust belt. Modern surface velocities based on GPS data confirm that the northern thrust belt is currently experiencing internal shortening. To the south, a wider (350 km wide) thrust wedge has expanded by continuous eastward migration of the thrust front with little or no internal deformation. Available GPS data reveal that the majority of the thrust belt is presently translating eastward without internal shortening, consistent with a critical wedge condition. The erosional gradient and associated variation in thrust-belt geometry and kinematics in the central Andes suggest that along-strike variations in erosion within an orogenic belt can potentially modify the tectonic processes associated with contractional mountain building.

Acknowledgments. Seth Stein and Tim Dixon are gratefully acknowledged for discussions regarding GPS velocity data acquired through SNAPP (South America-Nazca Plate Motion Project). Jon Pelletier, Rolf Aalto, and Elizabeth Safran graciously provided unpublished erosion data. I thank Ramiro Suárez of Yacimientos Petrolíferos Fiscales Bolivianos for a discussion which led to consideration of precipitation and erosion patterns in the Amazon and Parana drainage basins. Informal reviews by Peter DeCelles and Aviva Sussman and discussions with Carmala Garzione, Scott Miller, Clem Chase, and An Yin are greatly appreciated. The manuscript also benefited from constructive reviews by Rick Allmendinger and Dan Davis.

References

Aalto, R., and T. Dunne, Geomorphic controls on erosion rates in the Bolivian Andes (abstract), *Eos Trans. AGU, 79* (45), Fall Meet. Suppl., F306, 1998.

Allmendinger, R.W., and T.R. Zapata, Imaging the Andean structure of the Eastern Cordillera on reprocessed YPF seismic reflection data, *Congr. Geol. Argentino, 8* (2), 125-134, 1996.

Allmendinger, R.W., T.E. Jordan, S.M. Kay, and B.L. Isacks, The evolution of the Altiplano-Puna plateau of the Central Andes, *Annu. Rev. Earth Planet. Sci., 25*, 139-174, 1997.

Alpers, C.N., and G.H. Brimhall, Middle Miocene climatic change in the Atacama Desert, northern Chile: Evidence from supergene mineralization at La Escondida, *Geol. Soc. Am. Bull., 100*, 1627-1639, 1988.

Angermann, D., J. Klotz, and C. Reigber, Space-geodetic estimation of the Nazca-South America Euler Vector, *Earth Planet. Sci. Lett., 171*, 329-334, 1999.

Baby, P., T. Sempere, J. Oller, L. Barrios, G. Hérail, and R. Marocco, A late Oligocene-Miocene intermontane foreland basin in the southern Bolivian Altiplano, *C. R. Acad. Sci. Ser. II, 311*, 341-347, 1990.

Baby, P., G. Hérail, R. Salinas, and T. Sempere, Geometry and kinematic evolution of passive roof duplexes deduced from cross section balancing: Example from the foreland thrust system of the southern Bolivian Subandean Zone, *Tectonics, 11*, 523-536, 1992.

Baby, P., I. Moretti, B. Guillier, R. Limachi, E. Mendez, J. Oller, and M. Specht, Petroleum system of the northern and central Bolivian Sub-Andean Zone, in *Petroleum Basins of South America*, edited by A.J. Tankard, R. Suárez, and H.J. Welsink, *AAPG Mem., 62*, 445-458, 1995.

Baby, P., P. Rochat, G. Mascle, and G Hérail, Neogene shortening contribution to crustal thickening in the back arc of the Central Andes, *Geology, 25*, 883-886, 1997.

Barazangi, M., and B.L. Isacks, Spatial distribution of earthquakes and subduction of the Nazca Plate beneath South America, *Geology, 4*, 686-692, 1976.

Beaumont, C., P. Fullsack, and J. Hamilton, Erosional control of active compressional orogens, in *Thrust Tectonics*, edited by K.R. McClay, pp. 1-18, Chapman and Hall, New York, 1992.

Beck, S., G. Zandt, S.C. Myers, T C. Wallace, P.G. Silver, and L. Drake, Crustal-thickness variations in the central Andes, *Geology, 24*, 407-410, 1996.

Benjamin, M.T., Fission-track ages on some Bolivian plutonic rocks: Implications for the Tertiary uplift and erosion history of the Altiplano-Cordillera Real, M.S thesis, 58 pp., Dartmouth Coll., Hanover, N. H., 1986.

Benjamin, M.T., N.M. Johnson, and C.W. Naeser, Recent rapid uplift in the Bolivian Andes: Evidence from fission-track dating, *Geology, 15*, 680-683, 1987.

Boyer, S.E., Geometric evidence for synchronous thrusting in the southern Alberta and northwest Montana thrust belts, in *Thrust Tectonics*, edited by K.R. McClay, pp. 377-390, Chapman and Hall, New York, 1992.

Boyer, S.E., Sedimentary basin taper as a factor controlling the geometry and advance of thrust belts, *Am. J. Sci., 295*, 1220-1254, 1995.

Butler, R.F., D.R. Richards, T. Sempere, and L.G. Marshall, Paleomagnetic determinations of vertical-axis tectonic rotations from Late Cretaceous and Paleocene strata of Bolivia, *Geology, 23*, 799-802, 1995.

Cahill, T., and B.L. Isacks, Seismicity and shape of the subducted Nazca plate, *J. Geophys. Res., 97*, 17,503-17,529, 1992.

Clapperton, C., *Quaternary Geology and Geomorphology of South America*, 779 pp., Elsevier, New York, 1993.

Dahlen, F.A., Critical taper model of fold-and-thrust belts and accretionary wedges, *Annu. Rev. Earth Planet. Sci., 18*, 55-99, 1990

Dahlen, F.A., and J. Suppe, Mechanics, growth, and erosion of mountain belts, in *Processes in Continental Lithospheric Deformation*, edited by S P. Clark Jr., B.C. Burchfiel, and J. Suppe, *Spec. Pap. Geol. Soc. Am., 218*, 161-178, 1988.

Davis, D., J. Suppe, and F.A. Dahlen, Mechanics of fold-and-thrust belts and accretionary wedges, *J. Geophys. Res., 88*, 1153-1172, 1983.

DeCelles, P.G., Late Cretaceous-Paleocene synorogenic sedimentation and kinematic history of the Sevier thrust belt, northeast Utah and southwest Wyoming, *Geol. Soc. Am. Bull., 106*, 32-56, 1994.

DeCelles, P.G., and G. Mitra, History of the Sevier orogenic wedge in terms of critical taper models, northeast Utah and southwest Wyoming, *Geol. Soc. Am. Bull., 107*, 454-462, 1995.

Dewey, J.F., and J.M. Bird, Mountain belts and the new global tectonics, *J. Geophys. Res., 75*, 2625-2647, 1970.

Dixon, T.H., A. Mao, M. Bursik, M. Heflin, J. Langbein, R. Stein, and F. Webb, Continuous monitoring of surface deformation at Long Valley Caldera, California, with GPS, *J. Geophys. Res., 102*, 12,017-12,034, 1997.

Dunn, J.F., K.G. Hartshorn, and P.W. Hartshorn, Structural styles and hydrocarbon potential of the Sub-Andean thrust belt of southern Bolivia, in *Petroleum Basins of South America*, edited by A.J. Tankard, R. Suárez, and H.J. Welsink, *AAPG Mem., 62*, 523-543, 1995.

Francis, P.W, C. Halls, and M.C.W. Baker, The Kari-kari caldera, Bolivia, and the Cerro Rico stock, *J. Volcanol. Geotherm. Res., 10*, 113-124, 1983.

Gephart, J.W., Topography and subduction geometry in the central Andes: Clues to the mechanics of a noncollisional orogen, *J. Geophys. Res., 99*, 12,279-12,288, 1994.

Grant, J.N., C. Halls, W.A. Salinas, and N J. Snelling, K-Ar ages of igneous rocks and mineralization in part of the Bolivian tin belt, *Econ. Geol., 74*, 838-851, 1979.

Gubbels, T.L., Tectonics and geomorphology of the eastern flank of the Central Andes, 18° to 23° south latitude, Ph.D. thesis, 211 pp., Cornell Univ., Ithaca, N. Y., 1993.

Gubbels, T.L, B.L. Isacks, and E. Farrar, High-level surfaces, plateau uplift, and foreland development, Bolivian central Andes, *Geology, 21*, 695-698, 1993.

Guyot, J.L., H. Calle, J. Cortes, and M. Pereira, Transport of suspended sediment and dissolved material from the Andes to the Rio Plata by the Bolivian tributaries of the Rio Paraguay (Rios Pilcomayo and Bermejo), *Hydrol. Sci. J., 35*, 653-665, 1990.

Guyot, J.L., J.M. Jouanneau, J. Quintanilla, and J.G. Wasson, Dissolved and suspended sediment loads exported from the Andes by the Beni river (Bolivian Amazonia), during a flood, *Geodi. Acta, 6*, 233-241, 1993.

Hérail, G., P. Baby, J.M. López, J. Oller, O. López, R. Salinas, T. Sempere, G. Beccar, and H. Toledo, Structure and kinematic evolution of Subandean thrust system of Bolivia, in *International Symposium on Andean Geodynamics*, pp. 179-182, ORSTOM, Paris, 1990.

Hernández, R.M., J. Reynolds, and A. Disalvo, Análisis tectosedimentario y ubicación geocronológica del Grupo Orán en el Río Iruya, *Bol. Inf. Petrol., 12*, 80-93, 1996.

Horton, B.K., Sediment accumulation on top of the Andean orogenic wedge: Oligocene to late Miocene basins of the Eastern Cordillera, southern Bolivia, *Geol. Soc. Am. Bull., 110*, 1174-1192, 1998.

Horton, B.K., and P.G. DeCelles, The modern foreland basin system adjacent to the Central Andes, *Geology, 25*, 895-898, 1997.

Isacks, B.L., Uplift of the central Andean plateau and bending of the Bolivian Orocline, *J. Geophys. Res., 93*, 3211-3231, 1988.

James, D.E., Plate-tectonic model for the evolution of the central Andes, *Geol. Soc. Am. Bull., 82*, 3325-3346, 1971.

Jordan, T E., J.H. Reynolds, and J.P. Erikson, Variability in age of initial shortening and uplift in the central Andes, 16-33°30' S, in *Tectonic Uplift and Climate Change*, edited by W.F. Ruddiman, pp. 41-61, Plenum, New York, 1997.

Kendrick, E.C., M. Bevis, R.F. Smalley Jr., O. Cifuentes, and F. Galban, Current rates of convergence across the Central Andes: Estimates from continuous GPS observations, *Geophys. Res. Lett., 26*, 541-544, 1999.

Kennan, L., S.H. Lamb, and L. Hoke, High-altitude palaeosurfaces in the Bolivian Andes: Evidence for late Cenozoic surface uplift, in *Palaeosurfaces: Recognition, reconstruction and palaeoenvironmental interpretation*, edited by M Widdowson, *Geol. Soc. Spec. Publ., 120*, 307-323, 1997.

Kley, J., Transition from basement-involved to thin-skinned thrusting in the Cordillera Oriental of southern Bolivia, *Tectonics, 15*, 763-775, 1996.

Kley, J., A.H. Gangui, and D Krüger, Basement-involved blind thrusting in the eastern Cordillera Oriental, southern Bolivia: Evidence from cross-sectional balancing, gravimetric and magnetotelluric data, *Tectonophysics, 259*, 179-184, 1996.

Kley, J., J. Müller, S. Tawackoli, V. Jacobshagen, and E. Manutsoglu, Pre-Andean and Andean-age deformation in the Eastern Cordillera of southern Bolivia, *J. S. Am. Earth Sci, 10*, 1-19, 1997.

Lamb, S, and L. Hoke, Origin of the high plateau in the Central Andes, Bolivia, South America, *Tectonics, 16*, 623-649, 1997.

Leffler, L, S. Stein, A. Mao, T. Dixon, M.A Ellis, L. Ocola, and I.S. Sacks, Constraints on present-day shortening rate across the central eastern Andes from GPS data, *Geophys. Res. Lett., 24*, 1031-1034, 1997.

Legates, D.R., and C.J. Willmott, Mean seasonal and spatial variability in gauge-corrected, global precipitation, *Int. J. Climatol., 10*, 111-127, 1990.

MacFadden, B J., F. Anaya, and C.C. Swisher III, Neogene paleomagnetism and oroclinal bending of the central Andes of Bolivia, *J Geophys. Res., 100*, 8153-8167, 1995.

Mao, A., C.G.A. Harrison, and T H. Dixon, Noise in GPS coordinate time series, *J. Geophys. Res., 104*, 2797-2816, 1999.

Masek, J.G, B.L. Isacks, T.L. Gubbels, and E.J Fielding, Erosion and tectonics at the margins of continental plateaus, *J. Geophys. Res., 99*, 13,941-13,956, 1994.

Meehl, G.A., Effect of tropical topography on global climate, *Annu. Rev. Earth Planet. Sci., 20*, 85-112, 1992.

Meigs, A.J., and D.W. Burbank, Growth of the south Pyrenean orogenic wedge, *Tectonics, 16*, 239-258, 1997.

Meijer, P.T., R. Govers, and M.J.R. Wortel, Forces controlling the present-day state of stress in the Andes, *Earth Planet. Sci. Lett, 148*, 157-170, 1997.

Miller, K.G., R.G. Fairbanks, and G.S. Mountain, Tertiary oxygen isotope synthesis, sea level history, and continental margin erosion, *Paleoceanography, 2*, 1-19, 1987.

Mitra, G., Evolution of salients in a fold-and-thrust belt: The effects of sedimentary basin geometry, strain distribution and critical taper, in *Evolution of Geological Structures in Micro- to Macro-Scales*, edited by S. Sengupta, pp. 59-90, Chapman and Hall, New York, 1997.

Mitra, G., and A.J. Sussman, Structural evolution of connecting splay duplexes and their implications for critical taper: An example based on geometry and kinematics of the Canyon Range culmination, Sevier Belt, central Utah, *J. Struct. Geol., 19*, 503-521, 1997.

Moretti, I., P. Baby, E. Mendez, and D. Zubieta, Hydrocarbon generation in relation to thrusting in the Sub Andean Zone from 18 to 22°S, Bolivia, *Petrol. Geosci., 2*, 17-28, 1996.

Norabuena, E., L. Leffler-Griffin, A Mao, T. Dixon, S. Stein, I.S. Sacks, L. Ocola, and M. Ellis, Space geodetic observations of Nazca-South America convergence across the Central Andes, *Science, 279*, 358-362, 1998.

Norris, R.J., and A.F. Cooper, Erosional control on the structural evolution of a transpressional thrust complex on the Alpine Fault, New Zealand, *J. Struct. Geol., 19*, 1323-1342, 1997.

Pavlis, T.L., M.W. Hamburger, and G.L. Pavlis, Erosional processes as a control on the structural evolution of an actively deforming fold and thrust belt: An example from the Pamir-Tien Shan region, central Asia, *Tectonics, 16*, 810-822, 1997.

Robaudo, S., and C.G.A. Harrison, Plate tectonics from SLR and VLBI data, in *Contributions of Space Geodesy to Geodynamics: Crustal Dynamics, Geodyn. Ser.*, vol. 23, edited by D.E. Smith and D.L. Turcotte, pp. 51-71, AGU, Washington, D. C., 1993.

Roeder, D., Andean-age structure of Eastern Cordillera (province of La Paz, Bolivia), *Tectonics, 7*, 23-39, 1988.

Roeder, D., and R.L. Chamberlain, Structural geology of Sub-Andean fold and thrust belt in northwestern Bolivia, in *Petroleum Basins of South America*, edited by A.J. Tankard, R. Suárez, and H.J. Welsink, *AAPG Mem., 62*, 459-479, 1995.

Safran, E.B., Channel network incision and patterns of mountain geomorphology, Ph.D. thesis, 326 pp., Univ. Calif., Santa Barbara, 1998.

Safran, E., and T. Dunne, Channel network incision and regional patterns of channel and ridge morphology in the Bolivian Andes (abstract), *Eos Trans. AGU, 79* (45), Fall Meet. Suppl., F358, 1998.

Schmitz, M., A balanced model of the southern Central Andes, *Tectonics, 13*, 484-492, 1994.

Schmitz, M., and J. Kley, The geometry of the central Andean backarc crust: Joint interpretation of cross-section balancing and seismic refraction data, *J. S. Am. Earth Sci., 10*, 99-110, 1997.

Schneider, A., and C. Halls, Eruptive processes, mineralization and isotopic evolution of the Los Frailes Karikari region/Bolivia, *Berl. Geowiss Lateinam.-Kolloq., 10*, 182-184, 1986

Sempere, T., G. Hérail, J. Oller, and M G. Bonhomme, Late Oligocene-early Miocene major tectonic crisis and related basins in Bolivia, *Geology, 18*, 946-949, 1990.

Sheffels, B.M., Lower bound on the amount of crustal shortening in the central Bolivian Andes, *Geology, 23*, 812-815, 1990.

Summerfield, M.A., and N.J. Hulton, Natural controls of fluvial denudation rates in major world drainage basins, *J. Geophys. Res., 99*, 13,871-13,883, 1994.

Tinker, M.A., T.C. Wallace, S.L. Beck, S. Myers, and A. Papanikolas, Geometry and state of stress of the Nazca plate beneath Bolivia and its implication for the evolution of the Bolivian orocline, *Geology, 24*, 387-390, 1996.

Trewartha, G.T., *The Earth's Problem Climates*, 334 pp., Univ. of Wis. Press, Madison, 1966.

Watts, A.B., S.H. Lamb, J.D. Fairhead, and J.F. Dewey, Lithospheric flexure and bending of the Central Andes, *Earth Planet. Sci. Lett., 134*, 9-21, 1995.

Zandt, G., A.A. Velasco, and S.L. Beck, Composition and thickness of the southern Altiplano crust, Bolivia, *Geology, 22*, 1003-1006, 1994.

B. K. Horton, Department of Geology and Geophysics, Louisiana State University, Baton Rouge, LA 70803-4101. (horton@geol.lsu.edu)

(Received December 15, 1998;
revised June 22, 1999;
accepted July 27, 1999.)

TECTONICS, VOL. 18, NO. 6, PAGES 1027-1040 DECEMBER 1999

Palinspastic restoration of a post-Taconian successor basin deformed within a transpressive regime, northern Appalachians

Donna Kirkwood

Département de géologie et de génie géologique, Université Laval, Sainte-Foy, Québec, Canada

Abstract. Restoration of transpressional orogens requires a three-dimensional analysis of the strain state in order to take into account both the pure shear and simple shear components of the deformation and assess their relative contribution throughout the deformation history. Restoration of the post-Taconian successor basin, the Gaspé Belt located within the external part of the Acadian orogen in the Canadian Appalachians, was performed by using a step-by-step method based on the successive removal of strain increments. The pure shear component contributed 70% of the total strain during the first stages of the deformation whereas the simple shear component contributed 30% of the total strain during the last stages. Three retrodeformation steps are defined, starting with restoration of the last deformation stage and working back to the first deformation stage. The first step is to restore slip along Acadian strike-slip faults. The second step is to restore shortening related to the horizontal extension during the Acadian regional simple shear event. Finally, the third step is to restore vertical extension related to the pure shear event by removing slip along the reverse faults, unfolding and removing internal strain associated with cleavage development. Retrodeformation of the simple shear component of the transpressive deformation during the first two steps is performed on a horizontal view of the Gaspé Belt basin which contains the horizontal extension direction and which is perpendicular to the Acadian NW-SE directed compression. Likewise, restoration of the pure shear component is performed in vertical sections which contain the vertical extension and which are perpendicular to the Acadian NW-SE directed compression. The palinspastic map presented here is a much more appropriate base map for the basin and allows for a more realistic paleogeographic interpretation of the Gaspé Belt.

1. Introduction

Historically, palinspastic reconstructions or restorations of deformed parts of orogens have been attempted in thrust belts or in regions affected by strike-slip tectonics [*Gratier et al.*, 1989; *Levy and Christie-Blick*, 1989; *Protzman and Mitra*, 1990; *Stockmal and Waldron*, 1993; *Richard*, 1993; *Mitra*, 1994]. These reconstructions are two dimensional and are performed either on cross sections for thrust belts or on horizontal map views of the given area for strike-slip systems. The sections or maps to restore are necessarily parallel to the transport direction, affording for no motion of material into or out of the section plane. As such, restorations within thrust belts are based on balanced cross sections drawn perpendicular to a plane of no finite extension and perpendicular to regional fold axes and constructed by bed length or area balancing [see *De Paor*, 1988]. In strike-slip fault systems, reconstructions are performed on geological maps and take into account vertical axis rotations and lateral movement along the faults within the map plane. However, these two-dimensional restorations cannot accommodate out-of-section material movement, and they do not seem appropriate when dealing with more complexly deformed terrains such as transpressional orogens.

Oblique convergence and the related notion of dip-slip and strike-slip motion play an important role in the evolution of many collisional orogens [see *Platt*, 1993]. Attempting restorations in these settings is very problematic because material has moved both vertically and horizontally owing to the convergent and transcurrent components of the transpressive deformation. Thus movement cannot be contained within a single two-dimensional section. However, the problem may be partially resolved by considering how the deformation is partitioned in time within these settings. Such an approach was undertaken for the Gaspé part of the northern Appalachians by using incremental strain data, which helped define the progressive deformation history of the area. In this paper, I will demonstrate how restoration of the basin was accomplished by successively removing strain increments while taking into account both the pure shear and simple shear components of the transpressive deformation.

2. Geological Setting

The reconstruction is performed on rocks of the Gaspé Belt, located within the Acadian deformation belt of the Gaspé Peninsula, in the Canadian Appalachians (Figure 1). Rocks of the Gaspé Belt are part of a single depositional basin which formed south of the Cambro-Ordovician allochthonous belt, also known as the Humber zone [*Williams*, 1979], following the Middle to Late Ordovician Taconian orogeny. Deposition of sedimentary and more rarely volcanic rocks occurred throughout the Upper Ordovician to Middle Devonian time span [*Malo and Bourque*, 1993]. Rocks of the basin were subsequently deformed and metamorphosed to anchimetamorphic and lower greenschist grade [*Hesse and*

Paper number 1999TC900039
0278-7407/1999TC900039$12.00

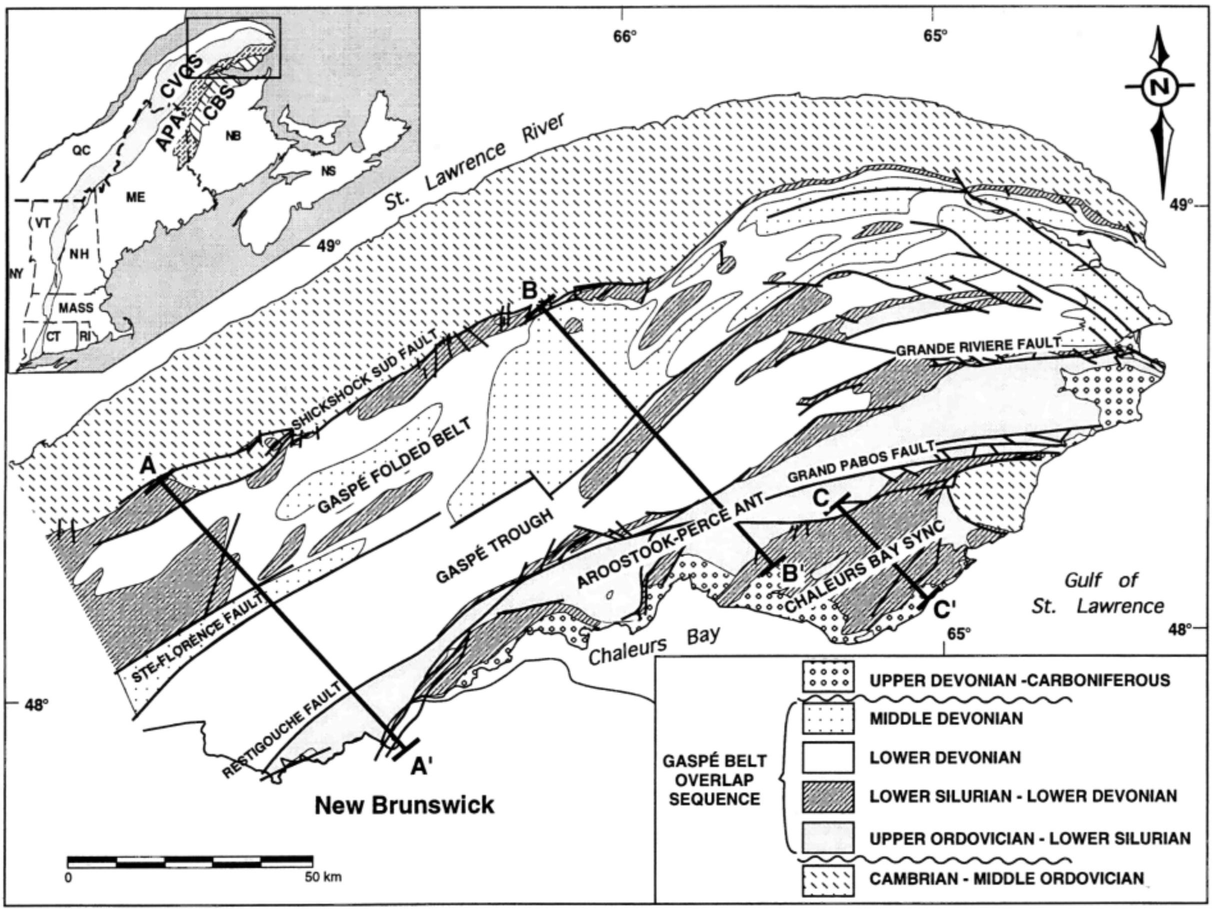

Figure 1. Geological map of the Gaspé Peninsula and location of cross sections presented in Figure 2. The inset shows the extent of the Connecticut Valley-Gaspé synclinorium (CVGS), Aroostook-Percé anticlinorium (APA) and Chaleurs Bay synclinorium (CBS).

Dalton, 1991] during the Acadian orogeny, which is well constrained to mid-Devonian in this part of the orogen [*Malo and Kirkwood*, 1995].

Rocks of the Gaspé Belt are bracketed between two major unconformities. In the northern part of the Gaspé Peninsula, Lower Silurian rocks of the Gaspé Belt rest unconformably over Cambro-Ordovician allochthonous rocks (Figure 1). Undeformed Upper Devonian and Carboniferous strata unconformably overlie rocks of the Gaspé Belt in the southern part of the peninsula.

Rocks of the Gaspé Belt are divided into four broad temporal and lithological sequences (Figure 1). The first sequence consists of Upper Ordovician to lowermost Silurian deep water fine-grained siliciclastic and carbonate facies of the Honorat and Matapedia Groups. The second sequence is made up of Silurian to lowermost Devonian shallow to deep carbonate shelf facies of the Chaleurs Group. The upper Gaspé limestones and the Fortin Group, composed of Lower Devonian mixed siliciclastic and carbonate fine-grained deep shelf and basin facies, make up the third sequence. Finally, the fourth sequence comprises the Lower to Upper Devonian near shore to terrestrial coarse-grained facies of the Gaspé sandstones.

Rocks of the Gaspé Belt can be divided into four geologic domains characterized by differing stratigraphy and structural features. The regional structure of the belt is dominated by regional NE trending Acadian folds, with fold wavelengths and interlimb angles that differ in each domain, and a cleavage which also varies in intensity in the different domains. The domains are, from north to south, the Gaspé Folded Belt (GFB), the Gaspé Trough (GT), the Aroostook-Percé anticlinorium (APA), and the Chaleurs Bay synclinorium (CBS) (Figure 1). The GFB and the GT form the Connecticut Valley-Gaspé synclinorium. The GFB is restricted to the Gaspé Peninsula whereas the GT extends southwest for approximately 1200 km along the strike of the northern Appalachians (Figure 1). Regional faults either border the domains, as for the Shickshock Sud and Sainte-Florence faults, or cut across them, as does the Grand Pabos fault in southern Gaspé (Figure 2). Most of the regional faults are dextral strike-slip faults [*Malo et al.*, 1992]. An exception is the Sainte-Florence fault, a reverse fault which separates the GFB from the GT. Recent work has established that a bulk dextral transpressive regime is responsible for the development of folds and faults in the Gaspé Belt [*Kirkwood and Malo*, 1993; *Malo and Bourque*, 1993]. The deformation within the transpressive belt was initially accommodated and distributed over the entire area through the development of compressive structures such as folds and reverse faults [*Kirkwood*, 1995]. Continued

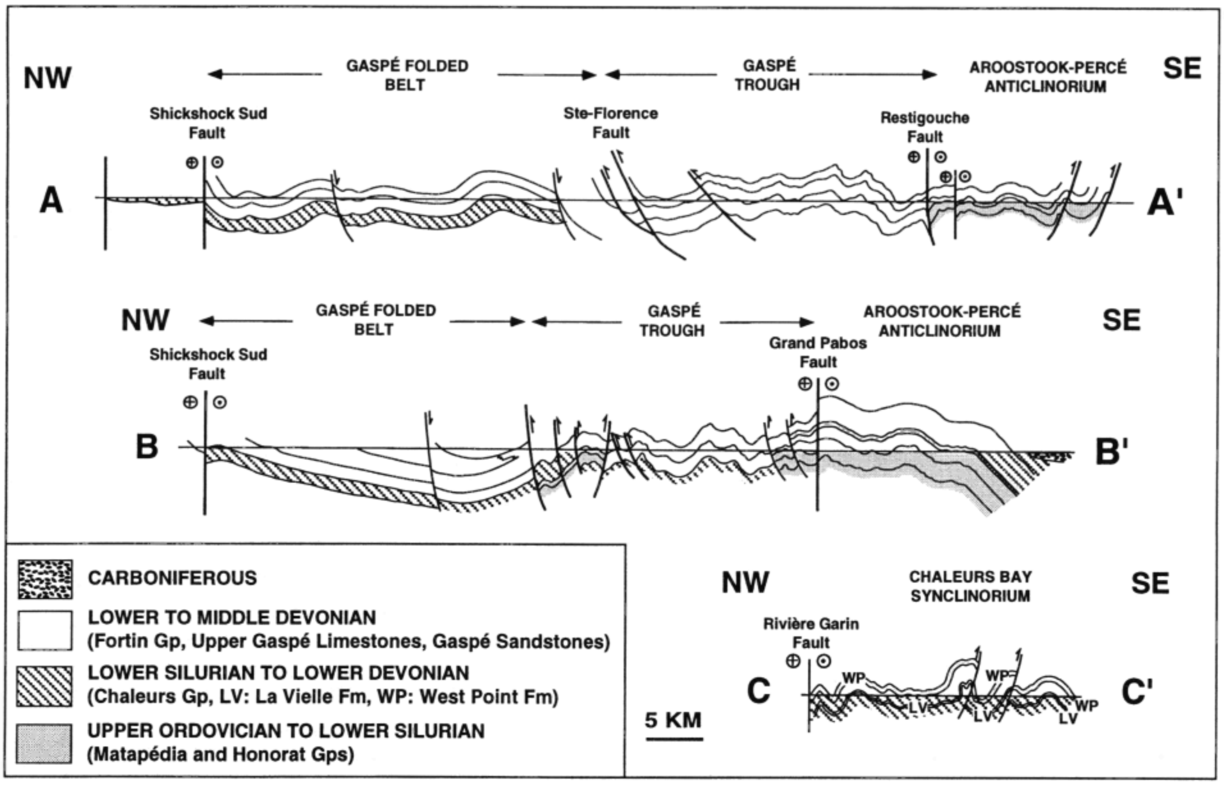

Figure 2. Structural cross-sections across the Gaspé Peninsula. See Figure 1 for location.

deformation brought about further flattening of the folds and resulted in dextral transcurrent faulting along steeply dipping east to ENE striking brittle-ductile shear zones. The Acadian folds and cleavage are oriented approximately 30° to the major strike-slip faults and can be seen to rotate clockwise near the major faults. Chronological and spatial relationships between compressive structures, i.e., folds and cleavage, and strike-slip faults in the Gaspé Belt are compatible with a dextral transpressive regime [*Malo and Béland*, 1989]. The Middle Devonian structural history of equivalent strata in northern New Brunswick, i.e., the Matapedia Cover Sequence, is also explained in terms of dextral transpression [*van Staal and de Roo*, 1995]. Thus this part of the northern Appalachians was the site of NW-SE compression due to oblique convergence during the Acadian orogeny.

3. Progressive Deformation History of the Gaspé Belt

The importance of including strain data in the restoration of cross sections has been discussed and demonstrated by many authors [*Hossack*, 1978; *Woodward et al.*, 1986; *Geiser*, 1988; *Protzman and Mitra*, 1990; *Mitra*, 1994]. First, strain data provide important information concerning the amount of strain, including internal strain that cannot be evaluated otherwise. Second, a careful analysis of the incremental strain data can help define the progressive deformation history and the deformation path followed by the rocks, which in turn provides additional information concerning both the kinematics of the deformation and the relative chronology of structural elements. Using this information, the stepwise restoration of a given area can be performed by successively removing strain increments [*Mitra*, 1994].

In view of the transpressive nature of the Acadian deformation in the Gaspé Peninsula, a correct restoration must take into account both the pure shear and simple shear components of the deformation and assess their relative contribution throughout the deformation history. Transpression as first introduced by *Harland* [1971] simply describes the form of deformation imposed on obliquely converging plates. *Sanderson and Marchini* [1984] kinematically modeled transpression by factorizing the deformation into pure and simple shear components. In their model, different values of shear strain and shortening across the transpressive zone produced flattening strains (oblate, finite strain ellipsoids) responsible for the development of structural features such as a steep cleavage, vertical or horizontal stretching lineations and folds and thrust faults at oblique angles to the zone. The importance of the deformation path for the progressive development of structures during a transpressive deformation is mentioned by *Sanderson and Marchini* [1984] and further discussed by *Treagus and Treagus* [1992] and *Robin and Cruden* [1994]. Basically, a finite transpressive state can be produced by a constant progressive transpression, with equal components of pure shear and simple shear, or by an infinity of more complex deformation paths characterized by variable components of pure shear and simple

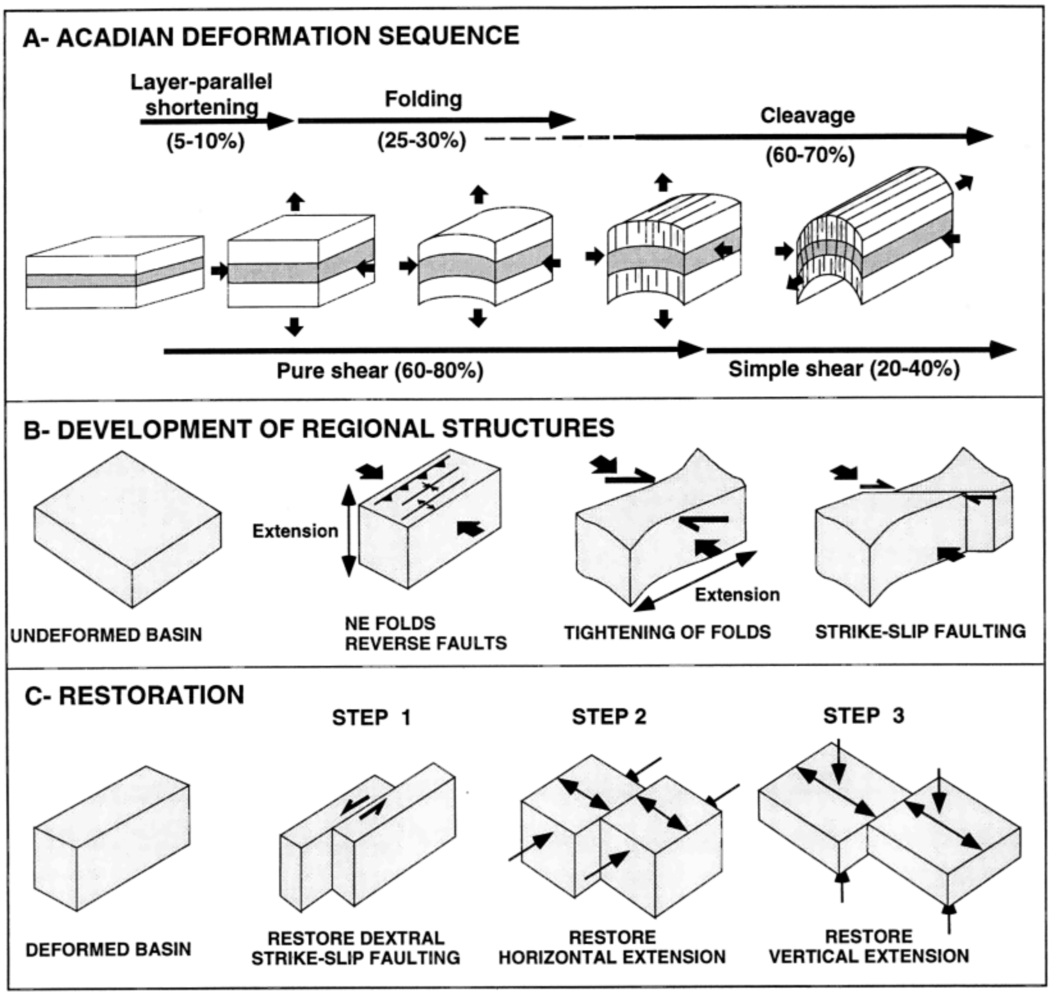

Figure 3. (a) The Acadian deformation sequence within the Gaspé Belt, involving layer-parallel shortening, folding, and cleavage development. The relative contribution of the pure shear and simple shear components of the deformation is indicated. (b) Schematic representation of the three regional Acadian deformation stages within the Gaspé Belt. (c)Three restoration steps are defined by reversing the deformation sequence. See text for further discussion. Reprinted from *Kirkwood* [1995], with permission from Elsevier Science.

shear. Because of the combined effects of convergence and transcurrent motion in transpressive settings, a three-dimensional analysis of the strain state in these belts is absolutely necessary.

The kinematic history of the Gaspé Belt was determined by a detailed analysis of structural features such as folds, faults, and cleavage combined with regional and local three-dimensional strain analysis [*Malo and Kirkwood*, 1995]. Map- and outcrop-scale structural features, kinematic indicators, deformed markers, and strain patterns within the Gaspé Belt demonstrate that both pure shear and simple shear components affected rocks of the belt during the Acadian orogeny. Syntectonic fibre segments in pressure shadows adjacent to pyrite grains were used to record the complex extension history in the southwestern part of the belt and helped to separate the deformation sequence into distinct structural stages all related to the Acadian progressive deformation [*Kirkwood*, 1995]. The extension history within the GT and the APA is consistent and can be divided into a vertical component followed by a horizontal component. The Acadian progressive deformation sequence in this part of the Appalachians consists of three main stages: (1) layer-parallel shortening followed by folding, cleavage development, and reverse faulting, (2) tightening of folds due to enhanced cleavage development and initiation of strike-slip faulting, and (3) slip along strike-slip faults (Figure 3). The first part of the deformation sequence is mainly characterized by the vertical extension during coaxial shortening. Fold tightening, cleavage enhancement, and strike-slip faulting are related to regional simple shearing during which the extension direction changed progressively from dominantly subvertical to dominantly subhorizontal and fold axis parallel (Figure 3). This interpretation suggests that strain within the transpressional regime is partitioned in time and that the pure shear component dominated over the simple shear component during the early stages of the deformation whereas the simple shear component was dominant during the last part of the progressive deformation. Although the strain history could also be explained by a superposed structural pattern resulting from a change in direction of convergence, field evidence gathered in the Gaspé and in New Brunswick all clearly point toward a transpressive regime during the Acadian orogeny [*Kirkwood and St-Julien*, 1987; *van Staal and Williams*, 1988; *Malo and Béland*, 1989; *Dostal et al.*, 1993; *Kirkwood and Malo*, 1993; *de Roo and van Staal*, 1994; *Sacks and Malo*, 1994; *van Staal and de Roo*, 1995].

4. Strain Data

Different methods were used to record strain within rocks of the Gaspé Belt. Syntectonic fibres in pressure shadows adjacent to pyrite framboids were used where available in the GT and the APA to compute extension. The Fry center-to-center technique was used on sandstone beds in the GT and the APA. This method yields strain axial ratios in the plane of measurement which were converted to shortening values by assuming plane strain. Strain axial ratios were only computed on *XZ* sections since the calculated shortenings were considerably lower than those computed from other methods (see below). Shortening values were also obtained by measuring the length of tightly folded, thin, competent beds (veins, fossil hash layers, and sandstones) and by comparing the original length to the folded length. Cleavage does not cut through the competent layers, and strain within the more competent layers is almost entirely accommodated by small-scale folding, whereas in the less competent argillaceous layers, strain is accommodated both by folding and by cleavage development. Strain related to regional folding was estimated by the sinuous bed length method along three regional cross sections (Figure 2). This method simply computes shortening related to the regional folding and faulting ignoring, however, strain related to layer-parallel shortening and cleavage development.

Results vary considerably for each method and for each structural domain (Table 1). Highest values were obtained with the *Ramsay and Huber* [1983] method on syntectonic fibres, which computes the main elongation from the measured length of fibres adjacent to pyrite framboids (Table 1). This method is considered to be the most reliable of the four since it records the entire strain, including strain related to the penetrative deformation, and this method offers the greatest potential for the calculation of incremental strain histories [*Ellis*, 1986; *Spencer*, 1991]. As discussed by *Kirkwood* [1995], problems intrinsic to and limitations of the technique have been the subject of discussion [*Cox and Etheridge*, 1983; *Williams and Urai*, 1989]. However, detailed analysis of the studied fibres within the Gaspé Belt has revealed that in many cases the optically continuous curved fibres connect small pyrite grains which were detached from the parent pyrite cluster, and the shape of the pressure shadows mimics the shape of the pyrite cluster [*Kirkwood*, 1995; *Kirkwood et al.*, 1995]. As discussed by *Urai et al.* [1991], such evidence substantiates the fact that the fibres track the instantaneous stretching direction and thus can be confidently used to analyze the progressive deformation history in the Gaspé Belt. Also, this method has been shown to be a sensitive indicator of finite strain when used on syntectonic fibres within pyrite-type pressure shadows as opposed to vein fibres [*Etchecopar and Malavieille*, 1987; *Spencer*, 1991]. Strain data obtained by this method for sandstone and mudstone beds of the Gaspé Belt are consistent with the fact that sandstone beds have recorded less strain [*Kirkwood*, 1995], the sandstones being more competent than the mudstone beds. A method of strain integration [*Hossack*, 1978] was used to calculate the mean shortenings across the GT and the APA from the fibre extension values. Following this method, the undeformed length of a profile can be computed by simple integration of the measured reciprocal stretch (expressed as $\sqrt{\lambda'_1}$) for each locality along the profile in the deformed state [*Woodward et al*, 1986]. The advantage of the integration method is to obtain a regional or average strain by integrating all the finite strains determined from point to point along a given section and thus maintaining strain compatibility between the different sample locations and the corresponding finite strains, which when taken one by one do reflect slight heterogeneity of the deformation (see *Kirkwood et al.* [1995]) for complete strain data for the GT). Calculated mean shortenings across the GT and the APA are 77% and 65%.

Shortening values estimated by combining results from small- and large-scale folds are similar to those obtained by

Table 1. Estimated Shortening Values for Each Structural Domain

	Shortening value, %			
Strain Method	Gaspé Folded Belt	Gaspé Trough	Aroostook-Percé Anticiclinorium	Chaleurs Bay Synclinorium
Syntectonic fibres	_	77	65	_
Fry center-to-center technique	_	22*	5*	_
Unfolding, small-scale folds	_	38	44	_
Section restoration	5	15	15	30
Cleavage intensity	15	_	_	15

* Results are compiled from *XZ* sections and represent only partial strains

Table 2. Partial and Total Shortenings for Each Structural Domain

	Gaspé Folded Belt	Gaspé Trough	Aroostook-Percé Anticlinorium	Chaleurs Bay Synclinorium
Partial shortening, %				
Horizontal extension	_	46	33	_
Vertical extension	20	31	32	45
Total shortening, %	20	77	65	45

the fibre method. A mean shortening of 59% is estimated for the APA when combining 44% (small-scale folding) and 15% (section restoration) shortening. For the GT a mean shortening of 53% can be estimated when combining strain related to small-scale folding (38% shortening) and regional folding (15%). These results represent 92% and 68% of the total strain estimated by the fibre method for the APA and the GT, respectively. The difference between both methods, i.e. 8% for the APA and 32% for the GT, can be partially attributed to strain related to layer-parallel shortening during the first stage of the progressive deformation, which is not computed when estimating shortenings from folded layers. Larger amounts of layer-parallel shortening are to be expected in the GT compared to the APA because of the lower competency contrast between the different layers in the Fortin Group Folding does occur almost immediately in rock sequences of highly contrasting competencies [*Hudleston*, 1973] such as for the Matapedia Group of the APA.

Shortenings obtained by the Fry center-to-center technique are considerably lower than those computed from the syntectonic fibres (22% versus 77% for the GT, Table 1). However, results were obtained by computing strain in vertical *XZ* sections, perpendicular to fold axes, which do not contain the late subhorizontal, fold-axis parallel extension. Consequently, these values do not reflect the strain related to the simple shear component of the transpressive deformation. When compared only to the mean shortenings obtained in the *XZ* sections by the fibre method, the Fry center-to-center technique still grossly underestimates strain (22% versus 55% for the GT, see *Kirkwood* [1993]). This is to be expected since the Fry method has been shown to underestimate strain when performed on sandstones containing a high percentage of matrix or on rocks deformed by pressure solution [*Crespi*, 1986; *Onasch*, 1986; *Erslev and Ge*, 1990], both cases encountered in the studied rocks [*Kirkwood*, 1993]. This method was not used to compute strain in horizontal (*YZ*) or vertical cleavage-parallel (*XY*) sections, because results in *XZ* sections were unsatisfactory.

Because of the lack of reliable strain markers within the GFB and the CBS, only the cross-section restoration method was used to compute strain; mean shortenings of 5% and 30% were obtained for the GFB and the CBS, respectively. These results represent the partial strain related to regional folding and faulting and do not include deformation accommodated by cleavage development. However, rough estimates of shortening due to cleavage strain can be obtained by evaluating the intensity of cleavage development [*Ramsay and Huber*, 1983; *Reks and Gray*, 1983]. Following *Alvarez et al.* 's [1978] scale, which relates cleavage intensity to shortening, an additional 15% shortening can be added for rocks of the GFB and the CBS which present anastomosing to disjunctive pressure solution cleavages [*Kirkwood and St-Julien*, 1987]. This gives a combined mean shortening of 20% for the GFB and 45% for the CBS. Total shortenings for each structural domain are given in Table 2. Mean shortenings of 77% and 65% were estimated from syntectonic fibres for the GT and the APA, respectively. Eighty percent shortening has also been attributed to Acadian deformation in an outcrop-scale duplex within the Lower Devonian flysch of the northern Maine Appalachians, a correlative of the Fortin Group (GT) in the Gaspé Peninsula [*Bradley and Bradley*, 1994].

Strain measurements presented here are only estimates of true strain, because of errors in applying the techniques, strain heterogeneity, inaccuracy of the strain markers, and unknown volume change. However, the application of the strain integration method does help minimize some of the inconsistencies. The scale of the problem considered here, i.e., the paleogeographic interpretation of the Gaspé basin, does permit errors of 10-15% total shortening, which are indeed much greater than the errors encountered when gathering the strain data. Also, shortening values are surprisingly consistent at different scales of observation. Shortening values deduced at the scale of the thin section (65% shortening for the APA, deduced from measured extensions of syntectonic fibres) are quite consistent with those obtained from unfolding mesoscopic and regional folds on cross sections (59% shortening for the APA).

5. Three Steps Toward the Restoration of the Basin

Even though transpressive belts are the result of combined pure and simple shear components, the finite transpressive state of rocks in the Gaspé belt seems to have been produced by a complex deformation path characterized by shear components that were dominantly the result of pure shear during the early stages of the deformation and simple shear during the last part of the progressive deformation. Extension and strain components within the Gaspé Belt can thus be separated in time, and restoration of the basin can be performed within two different sections, each of which is parallel to the movement direction during a specific part of the

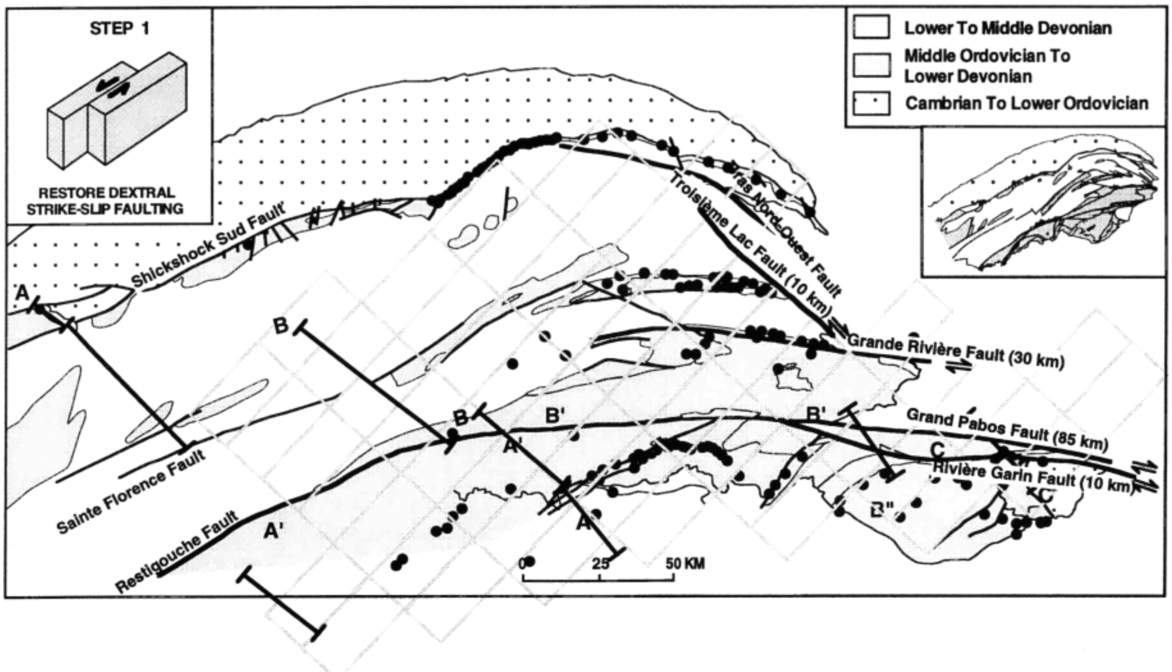

Figure 4. Step 1 of the restoration, involving restoring slip along the Acadian strike-slip faults. This step is performed on a horizontal view of the Gaspé Belt basin which contains the horizontal extension direction and which is perpendicular to the Acadian NW-SE directed compression. Present-day map of the Gaspé Peninsula is shown in inset. Solid circles represent the geographic location of stratigraphic sections.

Acadian progressive deformation. Correct restoration of the basin must be performed (1) in a vertical cross section perpendicular to the regional structural trend (*XZ*) in order to consider the vertical movement of rock particles during the first stages of the deformation, in a way similar to the restoration of balanced cross sections in fold and thrust belts, and (2) on a horizontal map view of the basin, parallel to the horizontal extension and slip along major strike-slip faults during the last part of the deformation history. This last step is somewhat similar to restoration in strike-slip terranes which consider the horizontal movement of rock particles.

The Acadian progressive deformation sequence is separated into three regional deformation stages (Figure 3b). Partial strains associated with each deformation stage have been computed, and each stage corresponds to a step toward the retrodeformation of the basin. The restoration can be performed by reversing the deformation sequence (Figure 3c). The first step consists of restoring the slip along the Acadian strike-slip faults, the second step consists of restoring the shortening related to the horizontal extension during the Acadian regional simple shear event, and the third step consists of restoring the vertical extension related to the pure shear event by removing slip along the reverse faults, and unfolding and removing internal strain associated with cleavage development. Three cross sections were constructed across the Siluro-Devonian rocks of the Gaspé Peninsula in order to illustrate the regional structures and the relationship between the different structural domains. The azimuth of the sections is perpendicular to the regional Acadian structural trend. These cross sections will be used to restore strain related to the pure shear component of the deformation. For the purpose of the reconstruction, the northern and northeastern margins of the basin are considered stable and were fixed during the restoration. In northeastern Gaspé the Siluro-Devonian cover sequence rests unconformably on rocks of the Taconian nappe domain, which consists of a series of imbricated thrusts emplaced during the Taconian orogeny [*Slivitzky et al.*, 1991]. The Saint Lawrence Promontory, which parallels the northeastern margin of the basin, is a paleogeographic feature inherited from the rifting of the North American margin during the Early Cambrian, and it has had a major influence on the development of the orogen during the entire Paleozoic [*Stockmal et al.*, 1987; *van der Pluijm and van Staal*, 1988; *Malo et al.*, 1995]. Sequential stratigraphic analysis of the Siluro-Devonian rocks has demonstrated the importance of the promontory during the sedimentation of the rocks, acting as a source area for the sediments and a boundary along which synsedimentary faults developed [*Malo and Kirkwood*, 1995].

Step 1 is performed on a horizontal map view of the Gaspé Peninsula and consists of restoring the translation or lateral displacement along strike-slip faults. Estimated displacements across the regional strike-slip faults and resulting geometry of the basin helped redefine the pre-Middle-Devonian position of the Baie Verte-Brompton Line in this part of the northern Appalachians (Figure 4). Offset of stratigraphic markers indicates apparent dextral displacements of 85, 22, and 10 km for the Grand Pabos, Grande Rivière, and Rivière Garin faults, respectively [*Malo et al.*, 1992]. Displacement along the Troisième Lac and Bassin Nord-Ouest faults has been estimated between a few hundred meters to a few kilometers [*Kirkwood*, 1989].

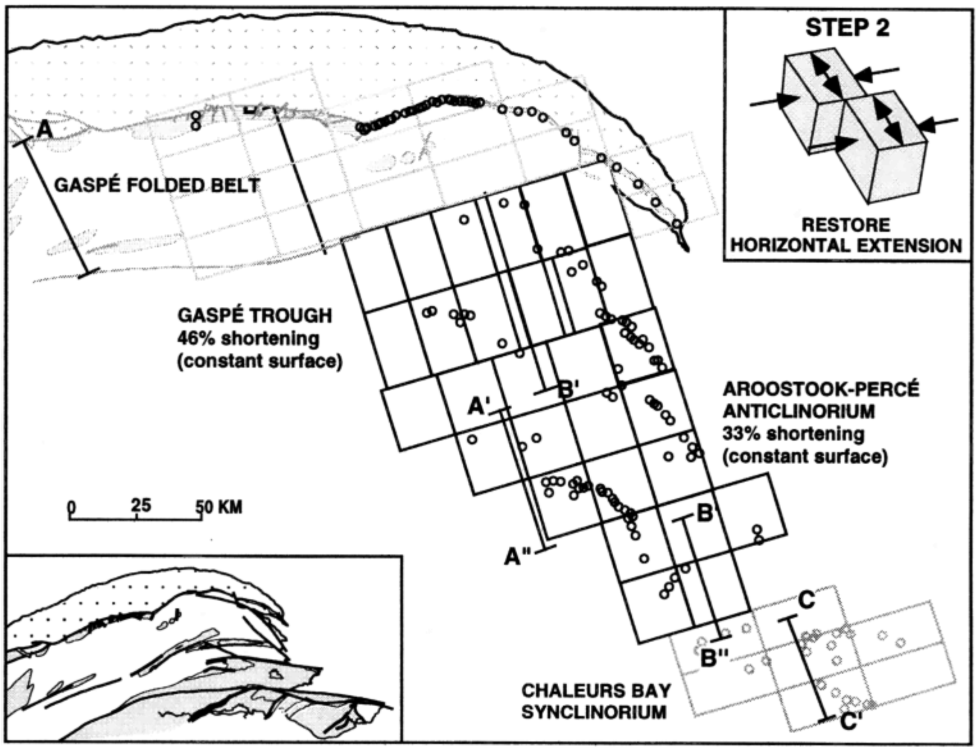

Figure 5. Step 2 of the restoration, involving restoring shortening related to the horizontal extension during the Acadian regional simple shear event. Restoration is performed on a horizontal view of the Gaspé Belt basin which contains the horizontal extension direction and which is perpendicular to the Acadian NW-SE directed compression. Partially restored map of Figure 4 is shown in the bottom left corner.

A method of strain reversal first described by *Schwerdtner* [1977] and *Cobbold* [1979] was used to unstrain the rocks within each domain of the Gaspé Belt during steps 2 and 3. A grid of rectangular elements was drawn on the partially restored map of Figure 4 with the sides of the elements parallel to the strain trajectories, i.e., parallel and perpendicular to the regional fold axes. In order to obtain a more realistic stratigraphic interpretation of the Gaspé Belt basin, the geographic location of the Siluro-Devonian stratigraphic sections [see *Bourque et al.*, 1993], shown as solid circles within the rectangular elements of Figure 4, were used as reference points to unstrain rocks of the basin. Each specific section was displaced accordingly within the rectangular element.

Step 2 involves the removal of internal strain related to the regional simple shearing event and is performed on a horizontal map view of the basin. Since the northern and northeastern margins of the basin are fixed, the horizontal extension was restored toward the northeast, and consequent contraction was restored by unstraining the rectangular elements towards the southeast. The assumption of plane strain deformation with a vertical Y axis necessitates that the surface of each element remains constant during this step (Figure 5). The partial strain related to this part of the deformation was calculated by considering only strain computed from the horizontal extension values, i.e., 85% and 49% for the GT and the APA, respectively (Table 2). These values correspond to mean shortenings of 46% and 33%. Horizontal extensions were not computed within the CBS and the GFB, because no suitable strain markers were found in these domains. As a consequence, rectangular elements within these domains remain unchanged. However, the position of the CBS is affected by the subsequent unstraining of the GT and the APA (Figure 5). Even though no suitable strain markers were found within the CBS, its position south of the APA and more proximal with respect to the Acadian internal zone, located just 25 km farther south in northern New Brunswick (Miramichi anticlinorium [*Malo et al.*, 1995; *van Staal and de Roo*, 1995]), suggests that this domain was also affected by the simple shear component of the transpressive deformation and must have recorded some horizontal extension. As shown in Figures 5 and 6, step 2 modifies the geometry of the basin by reducing its NE-SW width and by extending its NW-SE length. Fold interlimb angles increase during step 2 since the strain related to this part of the deformation is mostly accommodated by cleavage development and consequent fold tightening [*Kirkwood*, 1995] (Figure 6).

Step 3 toward the restoration of the Gaspé Belt involves removal of strain related to reverse faulting, folding, and cleavage development during the pure shear dominated event. This step was performed in vertical sections containing the vertical extension and which are perpendicular to the Acadian NW-SE directed compression. In cross section, displacement along faults is first restored by pinning the footwall and restoring the structures back from the fault, ensuring stratigraphic continuity between the hanging wall and the

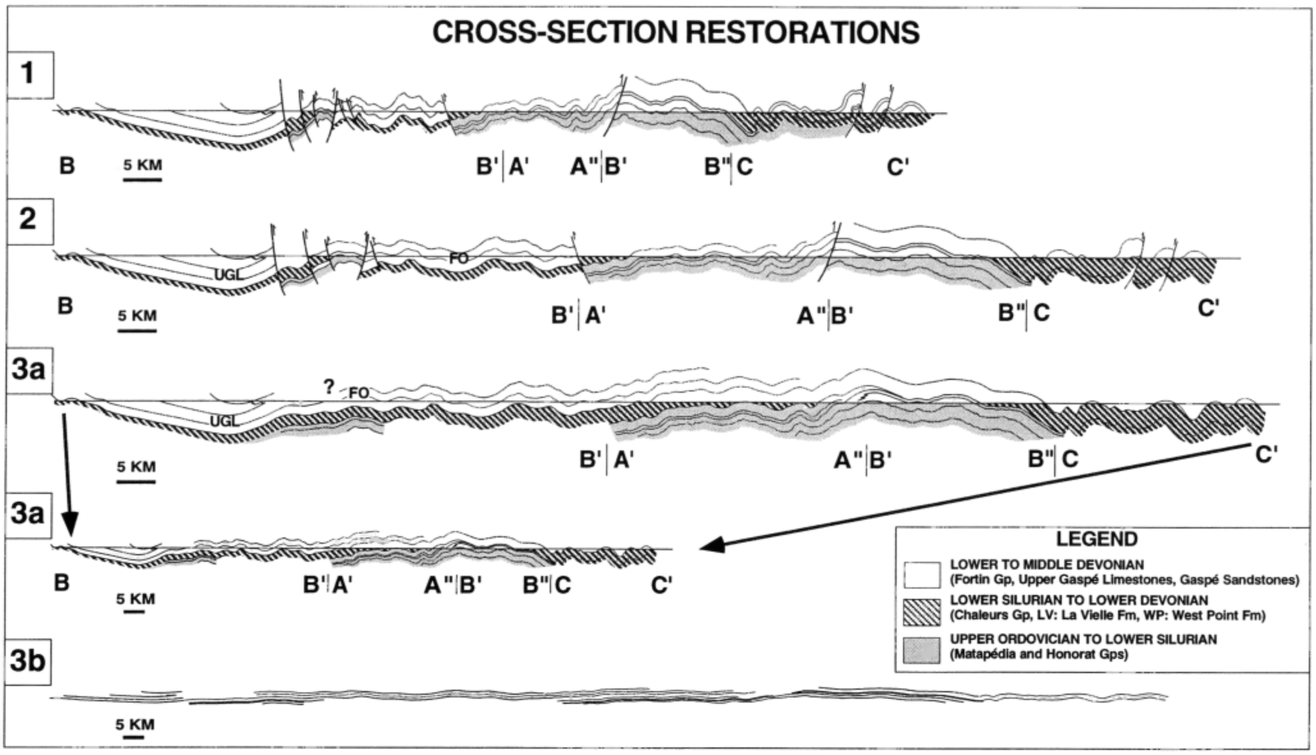

Figure 6. 1, composite cross section across the partially restored Gaspé Belt, following the removal of slip along strike-slip faults (step 1) (see location of line segments in Figure 4); 2 , composite cross section across the partially restored Gaspé Belt, following the removal of shortening related to the horizontal extension during the Acadian regional simple shear event (step 2) (see location of line segments in Figure 5); 3a and 3b, cross sections of step 3, which consists of restoring the vertical extension related to the pure shear event by removing slip along the reverse faults (illustrated in Figure 3b) and unfolding and removing internal strain associated with cleavage development (illustrated in Figure 3c). Restoration of the pure shear component is performed on the composite section which contains the vertical extension and which is perpendicular to the Acadian NW-SE directed compression. Note change of scale in cross section 3a.

footwall (Figure 6). Since structures are progressively younger from the internal to the external part of an orogen, elements within the most southeastern structural domain (CBS) are restored first, and those within the most northwestern domain are restored last (GFB). The partial strains related to this part of the deformation for the GT and the APA were determined by considering vertical extensions of 125% and 90% and resulting shortenings of 56% and 47%, respectively (Table 2). The northern margin of the basin being fixed, shortening was restored toward the southeast (Figure 7). During this step, movement is contained within a vertical plane, perpendicular to fold axes, and the assumption of plane strain necessitates that the vertical surface remains constant in cross section. However, in the horizontal plane, only the width of the rectangular elements remains constant, with a consequent gain in surface compensated by the reduction of stratigraphic thicknesses in cross section (Figures 7 and 8). The complete restoration presented in Figure 7 shows the undeformed dimension of the Gaspé Belt basin in pre-Devonian times. This paleogeographic map clearly shows that the basin was much larger than its present size and extended farther southeast as far as the present-day location of Cape Breton Island.

6. Discussion

6.1. Displacement Fields

A schematic view of the relative displacement during the Acadian progressive deformation can be obtained by comparing points of the unstrained grid after each partial restoration. In order to construct the displacement field related to the last deformation stage, i.e., slip along regional strike-slip faults, the rectangular elements of Figure 4 were cut where necessary, displaced, and adjusted by slight rotations in order to fit within the boundaries on the Gaspé geological map (Figure 8). Although the actual displacement path of the Siluro-Devonian sequence is likely to be far more complicated than the model presented in Figure 9, this example does demonstrate the importance and necessity of considering the tectonic evolution of an orogen in a three-dimensional frame. The partial displacement fields shown in Figure 9 can be related to the motion of the Silurian to Devonian cover sequence after each successive stage of the Acadian deformation. Overlaps occur within the GFB as well as throughout the basin when fitting the rectangular elements of

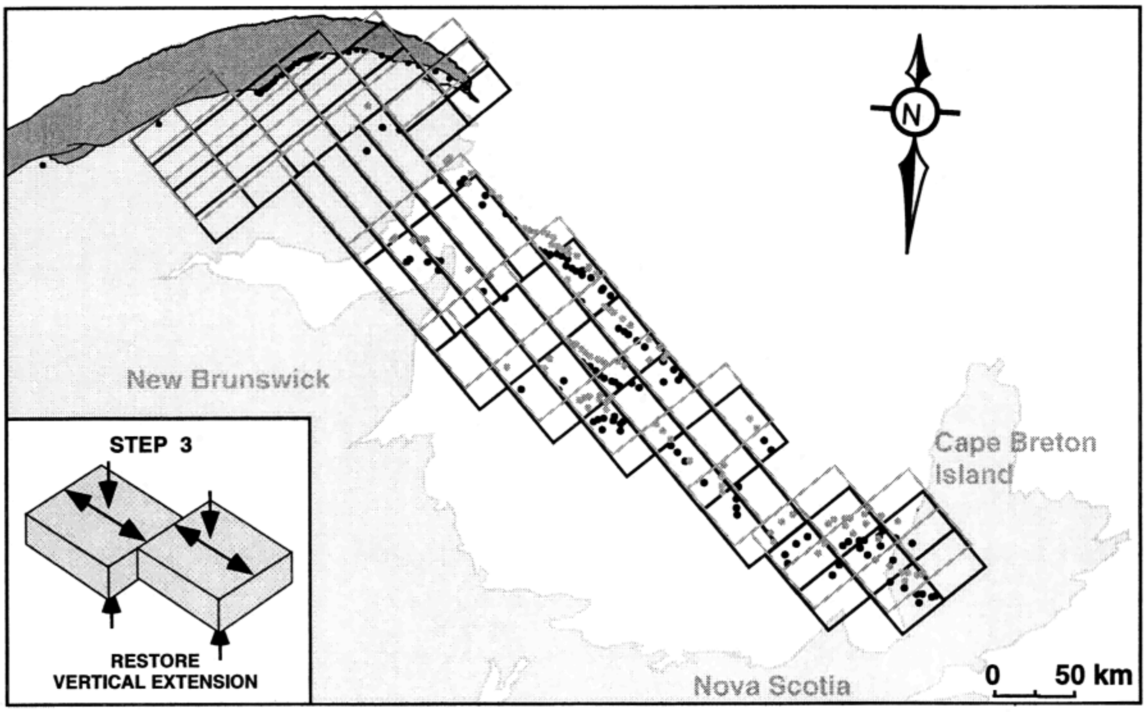

Figure 7. Palinspastic map of the Gaspé Belt basin after complete restoration (solid rectangular elements and solid circles) shown on a present-day map of northeastern Canada for scale. The shaded rectangular grid and shaded circles represent the true palinspastic map after consequent removal of the shortening strain within the Gaspé Folded Belt, which in fact is unstrained during step 1 simply by restoring slip along the regional strike-slip faults. See text for further discussion.

the partially restored state (strike-slip faulting) on the present (deformed) geological map (Figure 8). Obviously, the orientation of these overlaps is parallel to the long side of the rectangles, since the rectangles were constructed parallel to the strain trajectories, i.e., parallel and perpendicular to the regional fold axes. It is interesting to note, however, that these overlaps are also located where NE trending reverse faults affect rocks of the GT, the APA, and the CBS. As proposed by *Malo and Béland* [1989] and *Kirkwood and Malo* [1993], most of these reverse faults are compatible with strike-slip faulting and could have developed as a result of the west directed expulsion during the transpressive deformation (see below).

NW-SE convergence during the initial stages of the Acadian deformation produced a NW directed displacement of the Gaspé Belt cover sequence, the amount of which decreases towards the NW or toward the northern stable margin (Figure 9a). Although these displacement paths indicate greater displacement in the SW, i.e., in the CBS, strain estimates and the amount of shortening suggest a more symmetrical pattern with greater shortening in the central part of the basin (APA and GT) and decreasing strain toward the margins of the belt (CBS and GFB)(see Table 2). This supports the fact that the Gaspé Belt was caught between two rigid walls with the greatest amount of strain partitioned in the central part of the basin and that the southern margin of the belt acted as a rigid piston that converged obliquely toward the northern stable margin. It is possible, however, that deformation within the GFB was restricted to the last stage of the deformation sequence as suggested by the displacement field linked to strike-slip faulting. As shown in Figure 9c, deformation (by folding) in the cover sequence seems to be necessary to accommodate the transcurrent displacements within the southern domains. In fact, the amount of deformation is approximately equivalent to the 20% estimated shortening for the GFB. Thus, by restoring slip along the regional strike-slip faults during step 1, rocks of the GFB are automatically unstrained. If this is the case, then unstraining of the GFB rocks is restricted to step 1, and the undeformed state of the basin should be modified as shown in Figure 7, i.e., by removing the unstraining of the GFB rocks.

The NW-SE convergence also induced transcurrent motion along the northeastern stable margin, parallel to the Saint Lawrence Promontory, as proposed by *Stockmal et al.* [1990] along the hypothetical Canso fault. Although continued NW-SE contraction also produces NW directed motion within the cover sequence in the southernmost part of the basin and transcurrent motion along the Saint Lawrence Promontory, the displacement pattern changes drastically toward the northern stable margin where a progressively increasing west directed displacement is noted (Figure 9b). The presence of the northern stable domain inhibits further NW directed displacement and induces lateral expulsion of the sedimentary cover sequence toward the west. Mechanisms such as cleavage development and folding are not efficient enough to accommodate further convergence within the Siluro-Devonian cover sequence. Westerly expulsion is accommodated by

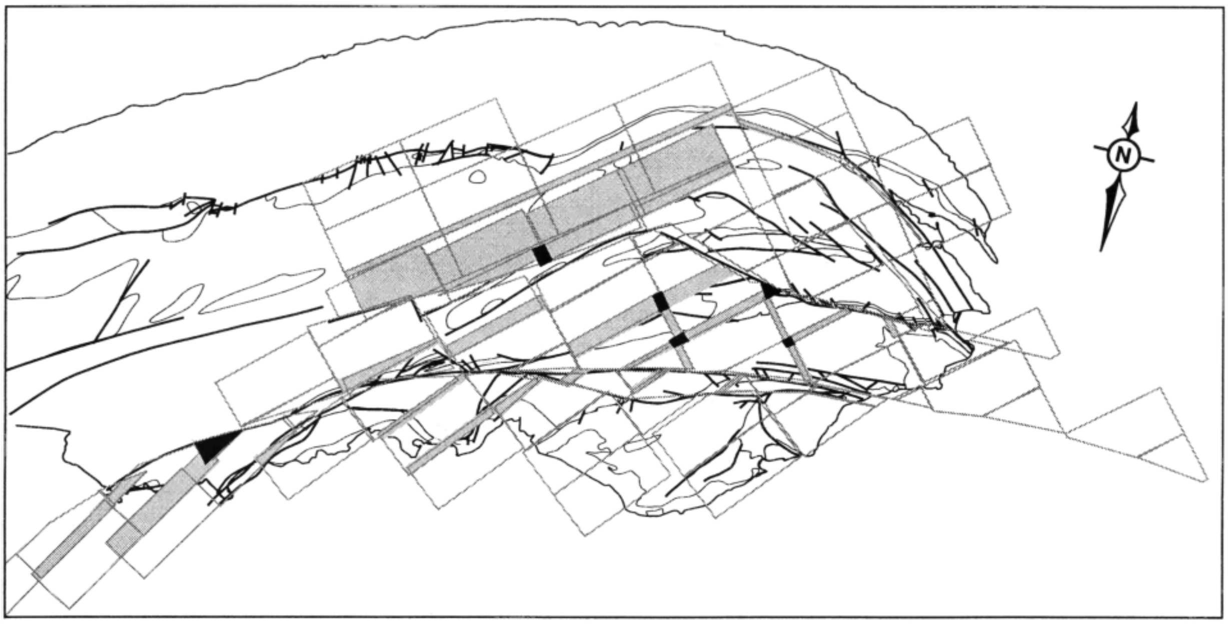

Figure 8. Grid of rectangular elements of Figure 5 deformed to fit within the geological boundaries on the Gaspé geological map. The rectangular elements of Figure 5 were cut where necessary, displaced, and adjusted by slight rotations. Superposition of rectangular elements is illustrated by shaded (two elements) or solid areas (three elements) and represents areas where space problems occur during strike-slip faulting, which must be compensated by either folding or faulting.

transcurrent movement along dextral strike-slip faults, subparallel to the northern stable margin, such as the Grande-Rivière, Grand Pabos, and Rivière Garin faults in the Gaspé Peninsula and the Rocky Brook-Milstream and Catamaran faults in New Brunswick (Figure 9c). The displacement is gradually transferred from one structure to another, i.e., from folds to cleavage and eventually to strike-slip faults. This displacement pattern is consistent with the geology of this part of the Appalachians. In response to west directed motion, regional northeasterly trending reverse faults developed to the west and SW of the study area. Some of these structures merge with the regional dextral strike-slip faults, as, for example, the Restigouche fault in western Gaspé. Furthermore, the northeasterly trend of the APA and the CBS to the southwest of the Gaspé Peninsula is quite unique to this part of the northern Appalachians (see inset in Figure 1), where anticlinoria and synclinoria trends are usually orogen-parallel [*Williams*, 1978]. A plausible explanation for this irregular trend could be the indentation of the Miramichi Highlands, which most probably followed the same displacement path during the Acadian orogeny as that of the Silurian to Devonian cover sequence of the Gaspé.

6.2. Plane Strain and Constant Volume

The attempt at retrodeforming rocks of the Gaspé basin was performed by assuming plane strain and constant volume throughout deformation. However, important volume losses have been documented in many fold belts [*Wright and Platt*, 1982; *Beutner and Charles*, 1985; *Henderson et al.*, 1986; *Wright and Henderson*, 1992; *Onasch*, 1994], and dilatation is an important factor to consider when retrodeforming a given area. Three-dimensional analysis of the fibres within rocks of the Gaspé Belt has shown that for each successive increment of the deformation, extension occurred in only one direction parallel to the maximum principal extension ($e1$) and that no extension occurred parallel to the intermediate principal extension ($e2$), confirming the plane strain deformation [*Kirkwood et al.*, 1995]. At the scale of the hand specimen, deformation associated with folding and cleavage development within rocks of the Gaspé Belt basin seems to have been of constant volume [*Kirkwood*, 1995]. Many cases have been documented where material lost at dissolution sites is compensated for by local precipitation within sinks [*Waldron and Sandiford*, 1988; *Protzman and Mitra*, 1990; *Wintsch et al.*, 1991], the volume flux being restricted to a few centimeters at best. More recently, *Erslev and Ward* [1994] documented compositional changes associated with the development of slaty cleavage and demonstrated that depletion in cleavage zones is balanced by enrichments in adjoining microlithons. Such transfers can be accomplished via diffusion in a stationary fluid and do not require large-scale fluid transport [*Waldron and Sandiford*, 1988]. At the basin scale, volume loss within one horizon can be easily compensated by volume gain elsewhere within the stratigraphic column. However, more important volume loss is expected during the development of regional shear zones in the Gaspé Belt as documented in numerous studies (*Etheridge et al.*, [1983], *Kerrich and Kamineni* [1988], *O'Hara* [1988], *Marquer* [1989], *Carter and Dworkin* [1990], and *Newman and Mitra*, [1993], to name only a few). Such volume losses are restricted to fault zones and would not significantly affect restoration of the

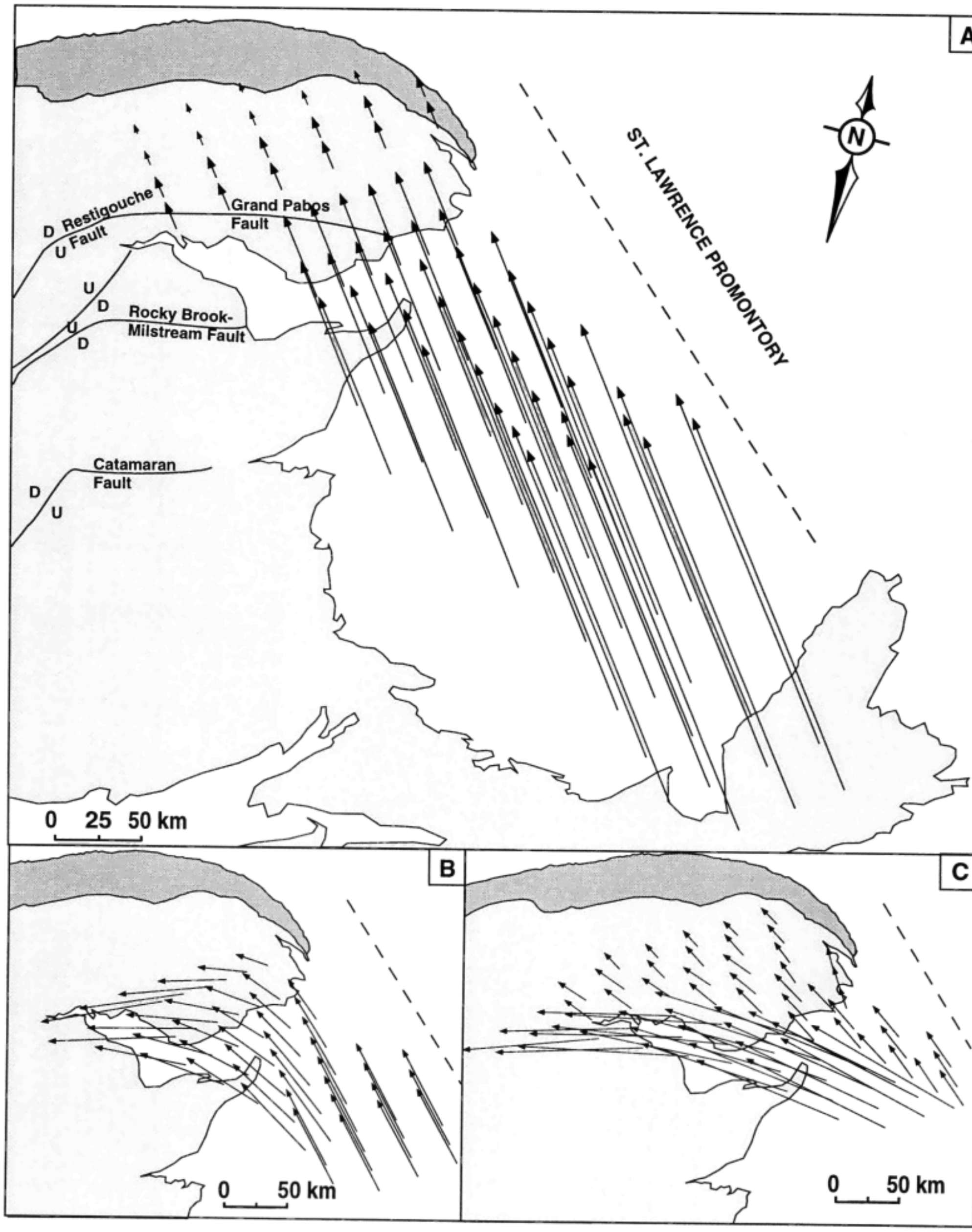

Figure 9. A schematic view of the relative displacement of the Siluro-Devonian cover sequence after each successive stage of the Acadian deformation obtained by comparing points of the unstrained grid after each partial restoration. (a) NW directed displacement of the cover sequence, accomplished by folding, reverse faulting and cleavage development during pure shear deformation. (b) NW directed displacement of the cover sequence, accomplished by continued cleavage development and consequent tightening of folds during a dominantly simple shear deformation. West directed displacement is initiated because of the horizontal, orogen-parallel extension. (c) Horizontal slip along Acadian strike-slip faults during regional simple shear deformation producing west directed expulsion. D, down; U, up.

Gaspé Belt basin at the chosen scale. In any case, if deformation in the Gaspé Belt was accompanied by important volume losses during cleavage development, then the computed strain values presented here would represent minimum estimates and the restored basin would be even larger.

7. Conclusions

The example presented in this paper shows that it is possible to restore basins which have suffered complex deformation histories, provided both finite and incremental strain data are gathered and the progressive deformation history of the area is well known. This is the case even in transpressional orogens, such as the Gaspé Belt, in as much as the incremental strain analysis can help establish the relative contribution of the pure shear and simple shear components of the transpressive deformation in order to propose a step-by-step restoration compatible with the development of the structures within the belt. The method proposed here for the Gaspé Belt takes into account horizontal displacements along strike-slip faults and internal strain related to the simple shear deformation as well as vertical displacements along reverse faults and internal strain due to folding and cleavage development. Chronologically and kinematically distinct deformation components are restored within separate sections, each parallel to the transport direction, thus ensuring no motion of material into or out of the section plane.

The Gaspé Belt example clearly demonstrates that when strain is incorporated into a restoration, the initial basin geometry is quite different from the actual basin geometry and that paleogeographic interpretations in complexly deformed basins can be greatly improved by such restorations. The restoration of the Gaspé Belt basin does present a more realistic picture of the geometry of the post-Taconian successor basin located in the Québec Reentrant at the southwest margin of the Saint Lawrence Promontory than the one reflected by the present-day geological map of this part of the orogen [see *Bourque et al.*, 1993]. This reconstruction considers that the Gaspé Belt acted as a soft deformable zone caught between two rigid pistons with the southern margin converging obliquely toward the relatively stable northern margin, i.e., the Humber zone, during the Acadian orogeny. However, it has been demonstrated elsewhere within the Canadian Appalachians that thrusting, reverse faulting, cleavage development, and folding within rocks of the Humber zone developed during the Acadian Orogeny [*Cawood*, 1993; *Stockmal and Waldron*, 1993]. Indeed, more attention should be given to the extent of Acadian deformation within rocks of the Humber zone to the north of the Gaspé Belt.

The restoration of the Gaspé Belt basin places additional constraints on the interpretation of the Paleozoic geology before and during the development of the mid-Devonian Acadian orogeny. Earlier analyses of the tectonic evolution of the Acadian orogeny have presented the evolutionary cross sections of the orogen, neglecting to incorporate orogen-parallel motion and lateral variations, even though the importance of oblique collision and transpressive motion has long been demonstrated in this part of the Appalachians [*Léger and Williams*, 1986; *van Staal and Williams*, 1988; *Malo and Béland*, 1989; *Stockmal et al.*, 1990].

Acknowledgements. Discussions with M. Malo, P. St-Julien, P.A. Bourque, J.P. Gratier, and C. van Staal have been instrumental in shaping the ideas presented here. Constructive criticism by F. Roure, K. Schulmann, and L. Ratschbacher helped improve the manuscript. Research was funded by NSERC and FCAR through individual and team grants to M. Malo and P.A Bourque. The Ministère de l'Énergie et des Ressources du Québec funded part of the field work The NSERC, FCAR, and INRS-Géoressources are acknowledged for scholarships and post doctoral fellowships to the author.

References

Alvarez, W., T. Engelder, and P.A. Geiser, Classification of solution cleavage in pelagic limestone, *Geology*, *6*, 263-266, 1978.

Beutner, E.C., and E.G. Charles, Large volume loss during cleavage formation, Hamburg sequence, Pennsylvania, *Geology, 13*, 803-805, 1985.

Bourque, P.A., M. Malo, and D. Kirkwood, Sedimentary history and paleogeography of a shelf segment at the NW margin of Iapetus during Silurian to Early Devonian time. GSA Bull., in press 1999.

Bradley, D.C., and L.M. Bradley, Geometry of an outcrop-scale duplex, Maine, *J. Struct Geol., 16*, 371-380, 1994.

Carter, K.E., and S.I. Dworkin, Channelized fluid flow through shear zones during fluid-enhanced dynamic recrystallization, northern Appenines, Italy, *Geology, 18*, 720-723, 1990.

Cawood, P.A., Acadian orogeny in west Newfoundland: Definition, character, and significance, in *The Acadian Orogeny: Recent Studies in New England, Maritime Canada, and the Autochtonous Foreland*, edited by D.C. Roy and J.W. Skeenan, *Spec. Pap. Geol. Soc. Am., 275*, 135-152, 1993.

Cox, S.F., and M.A. Etheridge, Crack-seal fibre growth mechanisms and their significance in the development of oriented layer silicate microstructures, *Tectonophysics, 92*, 147-170, 1983.

De Paor, D.G., Balanced section in thrust belts, 1, Construction, *AAPG Bull., 72*, 73-90, 1988.

de Roo, J.A., and C.R. van Staal, Transpression and recumbent folding: Steep belts and flat belts in the Appalachian Central Mobile Belt of northern New Brunswick, Canada. *Geol. Soc. Am. Bull., 106*, 541-552, 1994

Dostal, J.R., R. Laurent, and J D. Keppie, Late Silurian-early-Devonian rifting during dextral transpression in the southern Gaspé Peninsula (Québec): Petrogenesis of volcanic rocks, *Can. J. Earth Sci., 30*, 2283-2294, 1993.

Ellis, M.A., The determination of progressive deformation histories from antiaxial syntectonic crystal fibers, *J. Struct. Geol., 8*, 701-709, 1986.

Erslev, E.A., and H. Ge, Least-squares center-to-center and mean object ellipse fabric analysis, *J. Struct. Geol., 12*, 1047-1059, 1990.

Erslev, E.A., and D.J Ward, Non-volatile element and volume flux in coalesced slaty cleavage, *J. Struct. Geol., 16*, 531-554, 1994.

Etchecopar, A., and J. Malavieille, Computer models of pressure shadows: A method for strain measurement and shear-sense determination, *J. Struct. Geol., 9*, 667-677, 1987.

Etheridge, M.A., V.J. Wall, and R H Vernon, The role of the fluid phase during regional metamorphism and deformation, *J. Metamorph. Geol., 1*, 205-226, 1983.

Geiser, P.A., The role of kinematics in the construction and analysis of geological cross sections in deformed terranes, in *Geometries and Mechanisms of Thrusting, With Special Reference to the Appalachians*, edited by G Mitra and S. Wojtal, *Spec Pap. 222, Geol. Soc. Am*, 47-76, 1988.

Gratier, J.P., G. Ménard, and R. Arpin, Strain-displacement compatability and restoration of the Chaines Subalpines of the western Alps, in *Alpine Tectonics*, edited by M.P. Coward, D. Dietrich, and R.G. Park, *Spec. Publ. Geol. Soc. London, 45*, 65-81, 1989

Harland, W.B., Tectonic transpression in Caledonian Spitsbergen, *Geol. Mag., 108*, 27-42, 1971.

Henderson, J.R., T.O. Wright, and M.N. Henderson, A history of cleavage and folding: An example from the Goldenville Formation, Nova Scotia, *Geol. Soc. Am Bull., 97*, 1354-1366, 1986.

Hesse, R., and E. Dalton, Diagenetic and low-grade metamorphism terranes of the Gaspé Peninsula related to the geological structure of the Taconian and Acadian orogenic belts, Québec Appalachians, *J. Metamorph, Geol, 9*, 775-790, 1991.

Hossack, J.R., The correction of stratigraphic sections for tectonic finite strain in the Bygdin area, Norway, *Q. J. Geol. Soc London, 135*, 229-241, 1978.

Hudleston, P.J., An analysis of "single layer" folds developed in a viscous media, *Tectonophysics, 16*, 189-214, 1973.

Kerrich, R., and D.C. Kamineni, Characteristics and chronology of fracture-fluid infiltration in the Archean, Eye-Dashwa Lakes pluton, Superior province: Evidence from H, C, O-isotopes and fluid inclusions, *Contrib. Mineral. Petrol., 99*, 430-445, 1988.

Kirkwood, D., Géologie structurale de la région de Percé, *ET 87-17*, Minist de L'Éner. et des Ressources du Québec, Qué , Canada, 1989

Kirkwood, D., Étude qualitative et quantitative de la déformation acadienne du bassin siluro-dévonien de la péninsule gaspésienne, Appalaches du Nord, Ph.D. thesis, Univ. Laval, Quebec, Canada, 1993.

Kirkwood, D., Strain partitioning and progressive deformation history of a transpressive belt, northern Appalachians, *Tectonophysics, 242*, 15-35, 1995.

Kirkwood, D., and M. Malo, Across-strike geometry of the Grand Pabos fault zone. Evidence for Devonian dextral transpression in the Québec Appalachians, *Can. J Earth Sci, 30*, 1363-1373, 1993.

Kirkwood, D., and P. St-Julien, Analyse structurale du Siluro-dévonien dans la vallée de la Matapédia, *MB 87-33*, Minist. de L'Éner. et des Ressources du Québec, Qué., Canada, 1987

Kirkwood, D., M. Malo, P St-Julien, and P Therrien, Vertical and fold-axis parallel extension within a slate belt in a transpressive setting: Northern Appalachians, *J. Struct. Geol., 17*, 329-343,1995.

Léger, A., and PF. Williams, Transcurrent faulting history of southern New Brunswick *Open File, Pap. 86-1B, Geol. Surv. Can*, 111-120, 1986.

Levy, M, and N.,Christie-Blick, Pre-Mesozoic palinspastic reconstruction of the Eastern Great Basin (western United States), *Science, 245*, 1454-1462, 1989

Malo, M., and J Béland, Acadian strike-slip tectonics in the Gaspé Region, Québec Appalachians, *Can. J Earth Sci., 26*, 1764-1777, 1989

Malo, M., and P.A Bourque, Timing of the deformation events from Late Ordovician to Mid-Devonian in the Gaspé Peninsula, in *The Acadian orogeny: Recent Studies in New England, MaritFme Canada, and the Autochtonous foreland*, edited by D.C. Roy and J.W Skeenan, *Spec Pap. Geol. Soc Am., 275*, 101-122, 1993.

Malo, M., and D. Kirkwood, Faulting and progressive strain history of the Gaspé Peninsula in post-Taconian time: A review, in *Current Perspectives in the Appalachian-Caledonian Orogen*, edited by J. Hibbard, C.R. van Staal, and P.A. Cawood,*Geol. Assoc Can. Spec. Pap.*, 41, 267-282, 1995

Malo, M, D. Kirkwood, G DeBroucker, and P. St-Julien, A re-evaluation of the position of the Baie Verte-Brompton Line in the Québec Appalachians: The influence of Middle Devonian strike-slip faulting in Gaspé Peninsula, *Can J. Earth Sci., 29*, 1265-1273, 1992.

Malo, M., A. Tremblay, D. Kirkwood, and P Cousineau, Along-strike Acadian structural variations in the Québec Appalachians· Consequence of a collision along an irregular margin, *Tectonics, 14*, 1327-1338, 1995

Marquer, D., Transfert de matière et déformation des granitoides. Aspects méthodologiques, *Scheweiz. Mineral Petrogr. Mitt, 69*, 15-35, 1989.

Mitra, G, Strain variation in thrust sheets across the Sevier fold-and-thrust belt (Idaho-Utah-Wyoming)· Implications for section restoration and wedge taper evolution, *J. Struct. Geol, 16*, 585-602, 1994.

Newman, J., and G Mitra, Lateral variations in mylonite zone thickness as influenced by fluid-rock interactions, Linville Falls fault, North Carolina, *J. Struct. Geol., 15*, 849-863, 1993.

O'Hara, K., Fluid flow and volume loss during mylonitization: An origin for phyllonite in an overthrust setting, North Carolina, U.S.A., *Tectonophysics, 156*, 21-36, 1988.

Onasch, C.M., Ability of the Fry method to characterize pressure-solution deformation, *Tectonophysics, 122*, 187-193, 1986.

Onasch, C.M., Assessing brittle volume-gain and pressure solution volume-loss processes in quartz arenite, *J Struct. Geol., 16*, 519-530, 1994

Platt, J.P., Mechanics of oblique convergence, *J Geophys Res, 98*, 16,239-16,256, 1993

Protzman, G.M and Mitra G., Strain fabric associated with the Meade thrust sheet implications for cross-section balancing, *J. Struct. Geol, 12*, 403-417, 1990.

Ramsay, J G., and M. Huber, *The Techniques of Modern Structural Geology. Vol. 1: Strain Analysis*, 307 pp., Academic, San Diego, Calif., 1983.

Reks, I J., and D.R. Gray, Strain patterns and shortening in a folded thrust sheet. An example from the Southern Appalachians, *Tectonophysics, 93*, 99-128, 1983.

Richard, S.M., Palinspastic reconstruction of southeastern California and southwestern Arizona for the middle Miocene, *Tectonics, 12*, 830-854, 1993.

Robin, P Y., and A R. Cruden, Strain and vorticity patterns in ideally ductile transpression zones, *J. Struct. Geol., 16*, 447-466, 1994

Sacks, P, and M. Malo, Taconian and Acadian transpressional faulting, Mont Albert and Mont Logan nappes and along the Shickshock sud fault, Gaspé Appalachians, Quebec (abstract), *Geol. Soc. Am, Abstr. Programs,. 26*, p. A196, 1994.

Sanderson, D.J., and W.R.D. Marchini, Transpression, *J. Struct. Geol., 6*, 449-458, 1984.

Schwerdtner, W.M., Geometric interpretation of regional strain analysis, *Tectonophysics, 39*, 97-120, 1977.

Slivitzky, A., P. St-Julien, and G. Lachambre, Synthèse géologique du Cambro-Ordovicien du nord de la Gaspésie, *ET 88-14*, Minist. de L'Éner. et des Ressources du Québec, Qué., Canada, 1991.

Spencer, S, The use of syntectonic fibres to determine strain estimates and deformation paths. An appraisal, *Tectonophysics, 194*, 13-34, 1991

Stockmal, G.S., and J.W.F. Waldron, Structural and tectonic evolution of the Humber zone, western Newfoundland, 1, Implications of balanced cross sections through the Appalachian structural front, Port au Port Peninsula, *Tectonics, 12*, 1056-1075, 1993.

Stockmal, G.S., S.P. Colman-Sadd, C.E. Keen, S J O'Brien, and G Quinlan, Collision along an irregular margin: A regional plate tectonic interpretation of the Canadian Appalachians, *Can J. Earth Sci, 24*, 1098-1107, 1987.

Stockmal, G S., S.P. Colman-Sadd, C.E. Keen, F Marillier, S.J. O'Brien, and G Quinlan, Deep seismic structure and plate tectonic evolution of the Canadian Appalachians, *Tectonics, 9*, 45-62, 1990.

Treagus, S.H., and J.E. Treagus, Transected folds and transpression: how are they associated?, *J. Struct. Geol., 14*, 361-367, 1992

Urai, J.L., P.F. Williams, and H.L.M. van Roermund, Kinetics of crystal growth in syntectonic fibrous veins, *J. Struct. Geol., 13*, 823-836, 1991.

van der Pluijm, B A., and C.R. van Staal, Characteristics and evolution of the Central Mobile Belt, Canadian Appalachians, *J Geol., 96*, 535-547, 1988.

van Staal, C R., and J.A. de Roo, Mid-Paleozoic tectonic evolution of the Appalachian Central Mobile Belt in northern New Brunswick, Canada: Collision, extensional collapse and dextral transpression, *in Current Perspectives in the Appalachian-Caledonian Orogen*, edited by J. Hibbard, C.R van Staal, and P.A. Cawood,*Geol. Assoc. Can. Spec Pap., 41*, 367-390, 1995.

van Staal, C R., and P.F. Williams, Collision along an irregular margin: A regional plate tectonic interpretation of the Canadian Appalachians: Discussion, *Can. J. Earth Sci, 25*, 1912-1916, 1988.

Waldron, H.M., and M. Sandiford, Deformation volume and cleavage development in metasedimentary rocks from the Ballarat slate belt, *J. Struct. Geol., 10*, 53-62, 1988.

Williams, H. (Comp.), Tectonic lithofacies map of the Appalachian Orogen, Map 1a, scale 1 2,000,000, Mem. Univ., St. John's, Newfoundland, 1978.

Williams, H, Appalachian orogen in Canada, *Can J. Earth Sci., 16*, 770-791, 1979

Williams, PF., and J.L Urai, Curved vein fibres An alternative explanation, *Tectonophysics, 158*, 311-333, 1989.

Wintsch, R P., C.M. Kvale, and H.J. Kisch, Open-system, constant-volume development of slaty cleavage, and strain induced replacement reactions in the Martinsburg Formation, Lehigh Gap, Pennsylvania, *Geol. Soc. Am. Bull, 103*, 916-927, 1991.

Woodward, N.B., D R. Gray, and D.B. Spears, Including strain data in balanced cross-sections, *J. Struct. Geol., 8*, 313-324, 1986.

Wright, T.O., and J.R. Henderson, Volume loss during cleavage formation in the Meguma Group, Nova Scotia, Canada, *J. Struct Geol., 14*, 281-290, 1992.

Wright, T.O., and L.B. Platt, Pressure dissolution and cleavage in the Martinsburg shale, *Am. J. Sci., 282*, 122-135, 1982.

Donna Kirkwood, Département de géologie et de génie géologique, Université Laval, Sainte-Foy, Québec, Canada, G1K 7P4 (Donna Kirkwood @ggl ulaval ca)

(Received August 15, 1997;
revised January 5, 1999,
accepted June 21, 1999)

TECTONICS, VOL. 18, NO. 6, PAGES 1198-1223 DECEMBER 1999

Geometry and Quaternary kinematics of fold-and-thrust units of southwestern Taiwan

O. Lacombe, F. Mouthereau, B. Deffontaines, and J. Angelier

Département de Géotectonique, Université Pierre et Marie Curie, Paris

H. T. Chu

Central Geological Survey, Ministry of Economic Affairs, Taipei

C. T. Lee

Institute of Applied Geology, National Central University, Chungli

Abstract. Structural and paleostress analyses provide new insights into the Quaternary kinematics of the outermost fold-and-thrust units of southwestern Taiwan Foothills. The frontal folds are interpreted as fault-related folds, and their tectonic evolution through space and time is tightly constrained. Fold development is correlated with reef building on top of the anticlines. Moreover, we provide field evidence that NW-SE fault zones oblique to the structural grain of the belt probably acted as transfer fault zones during the the Quaternary fold-thrust emplacement. Two successive Quaternary stress regimes are evidenced in southwestern Taiwan: A NW-SE compression, followed by a recent nearly E-W compression. The latter shows an along-strike change from pure E-W contraction to the north to perpendicular N-S extension in the south. This southward decrease in N-S confinement probably represents the on-land signature of the incipient Quaternary tectonic escape predicted by analogue and numerical modelling and evidenced at present-day by Global Positioning System data.

1. Introduction

Arc-continent collision is occurring in the Taiwan segment of the active convergent plate boundary between the Philippine Sea plate and Eurasia [*Suppe*, 1984; *Ho*, 1986a, b; *Barrier and Angelier*, 1986; *Angelier et al.*, 1986, 1990; *Teng*, 1990]. This collision segment connects the south verging Ryukyu subduction zone, where the Philippine Sea Plate is subducting beneath the Eurasian Plate, and the west verging Manila subduction zone, where the Philippine Sea Plate is overriding the crust of the South China Sea (Figure 1). The orogen which developed in Taiwan during the late Cenozoic, mainly since 5 Ma [*Ho*, 1986a, b], is consequent to this collision between the Luzon arc and the Chinese passive margin.

Because of the obliquity of the convergence between the Philippine Sea Plate and the Eurasian Plate, subduction within the Manila trench evolves northward into incipient collision south of Taiwan, near the transition between oceanic and continental crust within the subducting Eurasian lithosphere; active collision culminates on-land within the southwestern part of the island (Figure 1). The northern part of Taiwan was deforming until recent times but is presently less active because of the southward propagation of the collision through time.

In this paper, we focus on the geometry and kinematics of the outermost units of the southwestern Taiwan Foothills: This is the key region to understand how the offshore Manila subduction and related accretionary wedge evolves northward to the oblique collision prevailing in southwestern Taiwan (Figure 1). Our aim is to provide a complete structural map of southwestern Taiwan and to discuss the geometry and kinematics of tectonic features related to the collision. For this purpose, structural analyses were carried out on the basis of subsurface data, satellite imagery, digital elevation models and fieldwork. Paleostress reconstructions were performed in order to define the orientation of the tectonic forces responsible for mountain building in the area investigated and to constrain both the tectonic mechanisms prevailing during the Quaternary and the kinematics of the westward propagating units.

2. Sedimentary and Structural Setting

The investigated area of southwestern Taiwan corresponds to the southern part of a Plio-Pleistocene foreland basin which developed in response to lithospheric flexure due to the tectonic loading of the Central Range orogenic belt. The nearly 5 km thick sediments of the foredeep consist of Pliocene bathyal to shallow marine and Pleistocene neritic to fluvial deposits; they unconformably overlie the precollisional Miocene shelf to bathyal deposits of the Chinese passive margin. These formations were deformed and partially exposed because of the westward propagation of the collision: They are deformed by stacked west vergent folds and thrust sheets resulting from the late Cenozoic collisional shortening. This deformation decreases toward the still slightly deformed but progressively deforming western Coastal Plain, where the Pleistocene formations are generally unconformably overlain by Holocene terrace deposits.

Paper number 1999TC900036.
0278-7407/99/1999TC900036$12.00

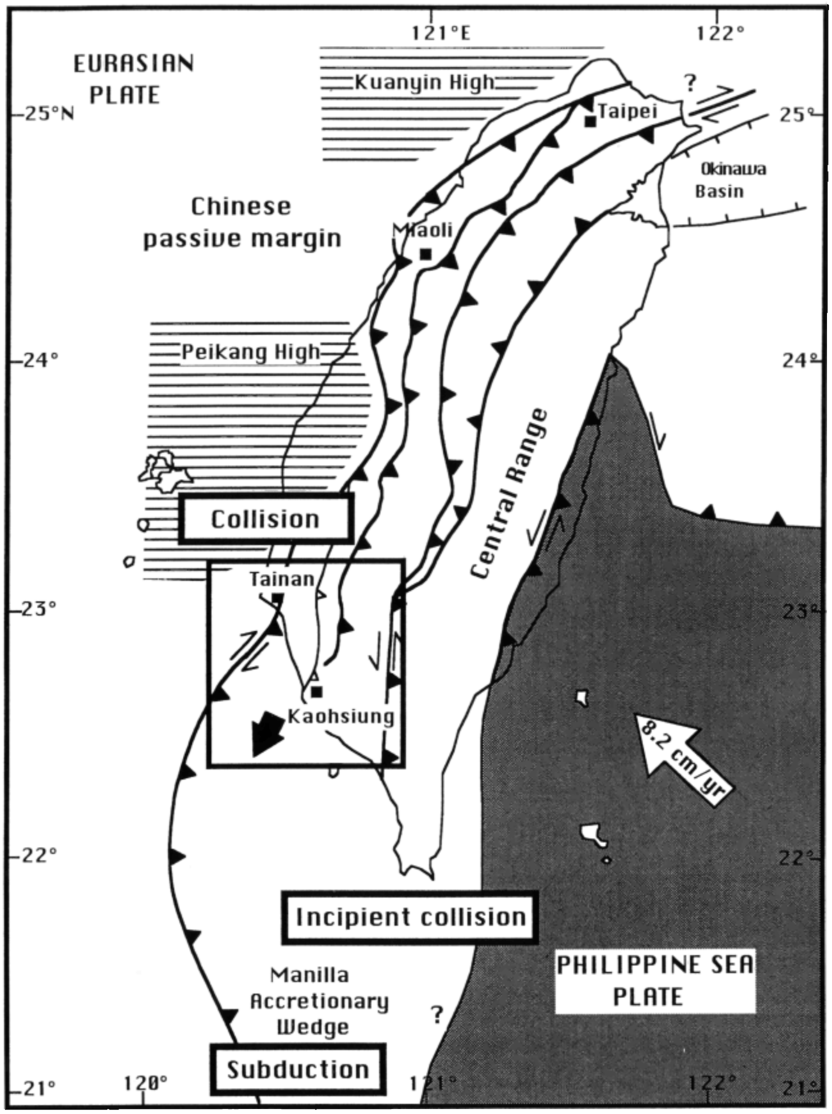

Figure 1. Geotectonic setting and main structural features of Taiwan. The large open arrow shows the present direction of convergence of the Philippine Sea Plate (shaded) relative to south China; velocity is after *Yu et al.*, [1997]. Heavy lines indicate major thrusts; triangles are on upthrown side. Hatched areas correspond to basement highs of the Chinese margin which underlie the deposits of the foreland basin. The frame indicates the location of the area investigated.

Most of the formations cropping out in the study area are thus detritic deposits of late Pliocene-Pleistocene age; they correspond to the sedimentary record of the collision. Precollisional Miocene formations may locally be found at the surface but only in the vicinity of major thrusts (Figure 2). In the northern part of our study region (domain 1, Figure 2), the late Pliocene lithostratigraphic units consist of the Chutouchi Formation (Nannoplankton Zones: NN15-NN17) and the overlying Liuchungchi Formation (NN18), made of sandy shales and muddy sandstones (Figure 3, column A). These late Pliocene formations are overlain by the Pleistocene formations, which are, from base to top, the Kanhsialiao and the Erchungchi Formations (NN19), mainly composed of interbedded shales and sandstones, and the Liushuang Formation (NN20), composed mostly of gray mudstones and shales [*Ho*, 1986a, b].

In contrast, the late Pliocene-Pleistocene formations in the southern Tainan-Kaohsiung area (domain 2, Figure 2) mainly consist of the thick Gutingkeng Formation, ranging in age from NN13 to NN19 (Figure 3, column B). It is mostly composed of dark gray mudstones interbedded with thin bedded sandstones. It is generally overlain by the Liushuang and the Erchungchi Formations. The upper Gutingkeng Formation, the Erchungchi Formation, and the lower Liushuang Formation change laterally to the southeast (Figure 3, column C) to the NN19-NN20 Lingkou Conglomerate, which locally may directly overlie the NN14 Nanshihlun Formation. The lateral changes in facies and thickness between these formations as

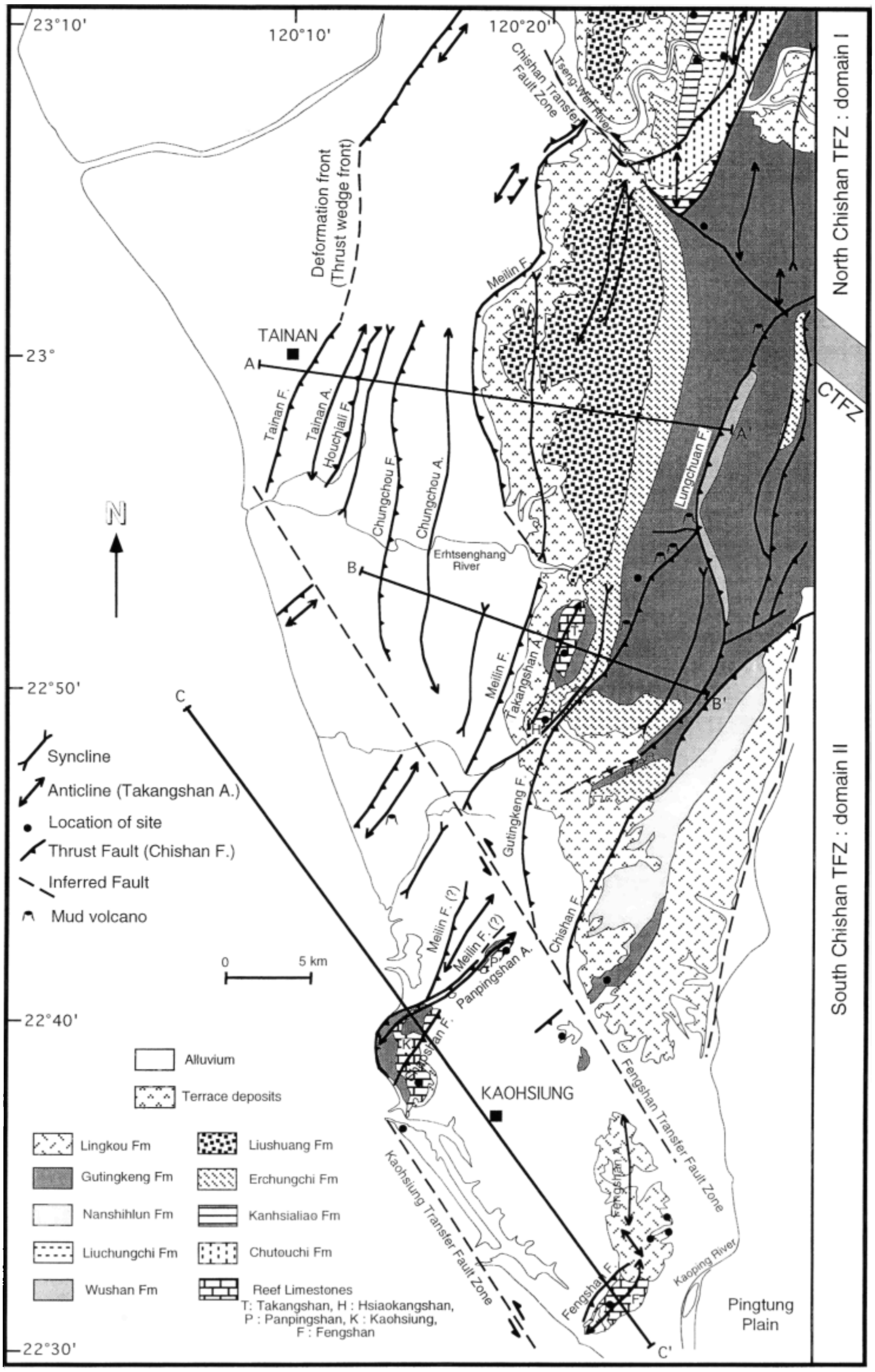

Figure 2. Structural map of southwestern Taiwan (*Chinese Petroleum Corporation*, [1974] and this work). The investigated area is divided into a domain 1, north of the Chishan Transfer Fault Zone (CTFZ)(outlined by the shaded area on the right), and a domain 2, south of it. See Figure 3 for thickness of sedimentary formations and time correlations. The names of major faults and anticlines used in the text and in the sections of Figure 5 are reported. Note the transverse fault zones (dashed lines) which are interpreted as transfer fault zones. A-A', B-B', and C-C' show location of cross sections of Figure 5.

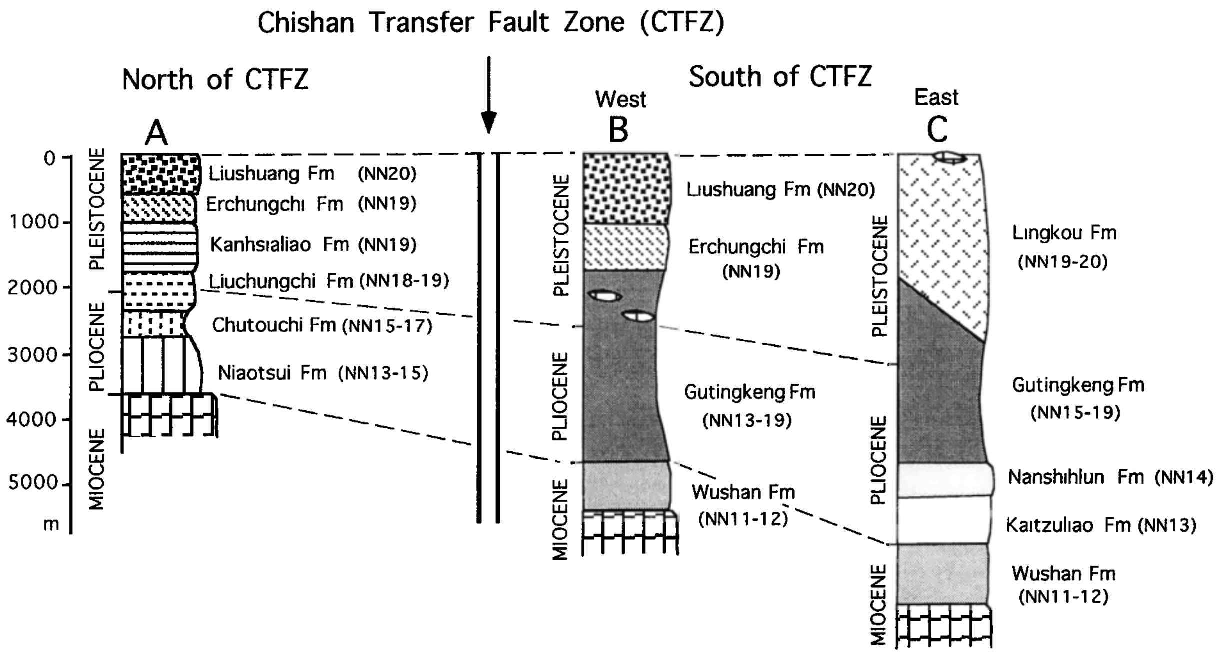

Figure 3. Stratigraphic columns showing time correlations between Neogene sedimentary formations in southwestern Taiwan. Ages are after *Chinese Petroleum Corporation*, [1974], *Chi*, [1979], *Chang and Chi*, [1983], *Ho*, [1986a, b], *Chi*, [1989], *Lee*, [1990], *Lin*, [1991], *Gong et al.*, [1996]. Column A is located north of the CTFZ; columns B and C are south of it. Note the lateral variations of type and thickness of formations across the CTFZ, as well from NW to SE south of it (columns B and C). The patterns are the same as those in Figure 2. Note the lenses of reef limestones (see Figure 2 for localities).

well as their local conformable or unconformable attitude with respect to the underlying ones reflect the dynamics of the foredeep basin with depocenters changing in space and time in response to the westward propagation of thrust units and the southward migration of the collision.

Reef limestones are distributed sparsely in the Pleistocene rocks of southwestern Taiwan [*Ho*, 1986a, b]. These limestone lenses vary from several meters to nearly 100 m in thickness and from 10 m to several thousand meters in length; they often thin out laterally over short distances and grade into the poorly stratified muddy sediments (Figure 3). The main reef localities are Takangshan, Hsiaokangshan, Panpingshan, Kaohsiung, and Fengshan (Figure 2). For instance, the NN19 Kaohsiung limestone is nearly 300 m thick and mainly composed of corals, bryozoairs, foraminifera, molluscs, and numerous thin mudstone layers; the NN20 Fengshan limestone is composed of gray coral reef limestone, with a total thickness of nearly 30 m. These recently uplifted limestones provide a very suitable material for analyzing brittle deformation.

3. Methods Used in Structural Analysis

Our structural analysis of the tectonic features of the Foothills of southwestern Taiwan combines fieldwork, new interpretations of already published structural data, and morphostructural studies. The occurrence, geometry, and mechanism of major features inferred from morphological and remote-sensing data (Figure 4) were checked and characterized in the field, and these new data were used to improve the regional structural mapping (Figure 2). Geological cross sections constrained by drill holes and seismic profiles where available (Chinese Petroleum Corporation, unpublished data, 1997) describe the geometry at depth of frontal fold-and-thrust units (Figure 5). Finally, tectonic analyses based on fault slip data and calcite twin data reveal the Quaternary stress patterns and bring constraints on the kinematics of propagating units. These methods are briefly summarized in sections 3.1-3.3.

3.1. Digital Elevation Model (DEM) and SPOT-Panchromatic Image Analysis

Because the recent age of deformation in Taiwan makes possible a rather good correlation between tectonics and morphology, we carried out a study of a digital elevation model (DEM) of southwestern Taiwan in order to decipher structural information through the outermost geomorphological features of the Foothills. Such data were obtained by numerical autocorrelation of aerial photographs of the western Foothills of Taiwan. The ground resolution of the DEM presented in Figure 4a is 40x40 m. This analysis provides additional information with respect to previous subsurface data and photogeologic interpretations [*Sun*, 1963, 1964].

Two types of major features could be recognized. The first type consists of features striking parallel to the belt; most of them correspond to major anticlines and thrusts (Figure 4b). The second type of features strikes obliquely to the structural grain of the belt. Where lithological contrasts are absent and thus cannot account for differential erosion, these transverse features correspond to fault zones [*Deffontaines et al.*, 1994]. Additional field studies (this work) resulted in identification of

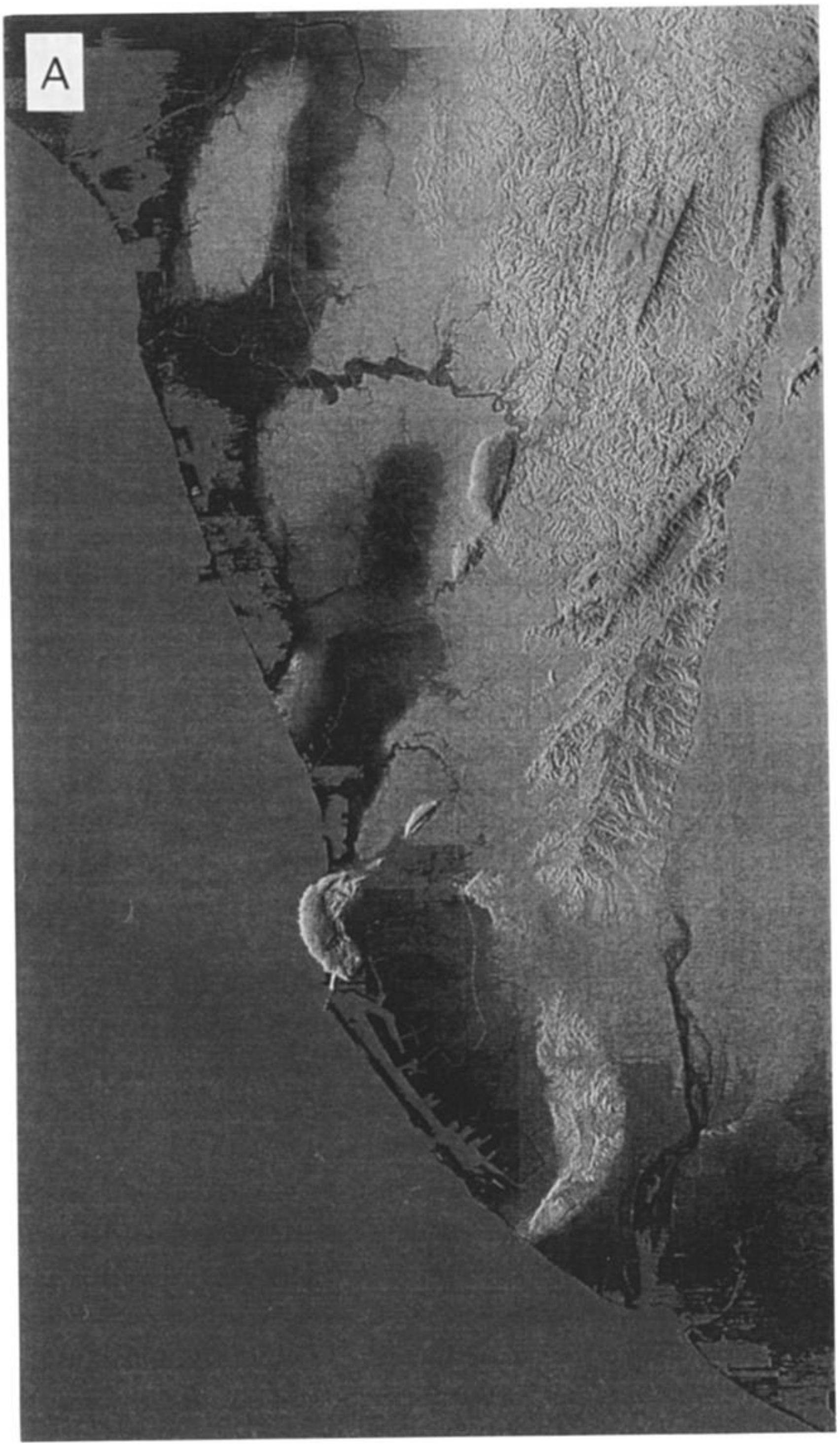

Figure 4. (a) Digital elevation model of southwestern Taiwan. (b) Structural interpretation of morphologic features.

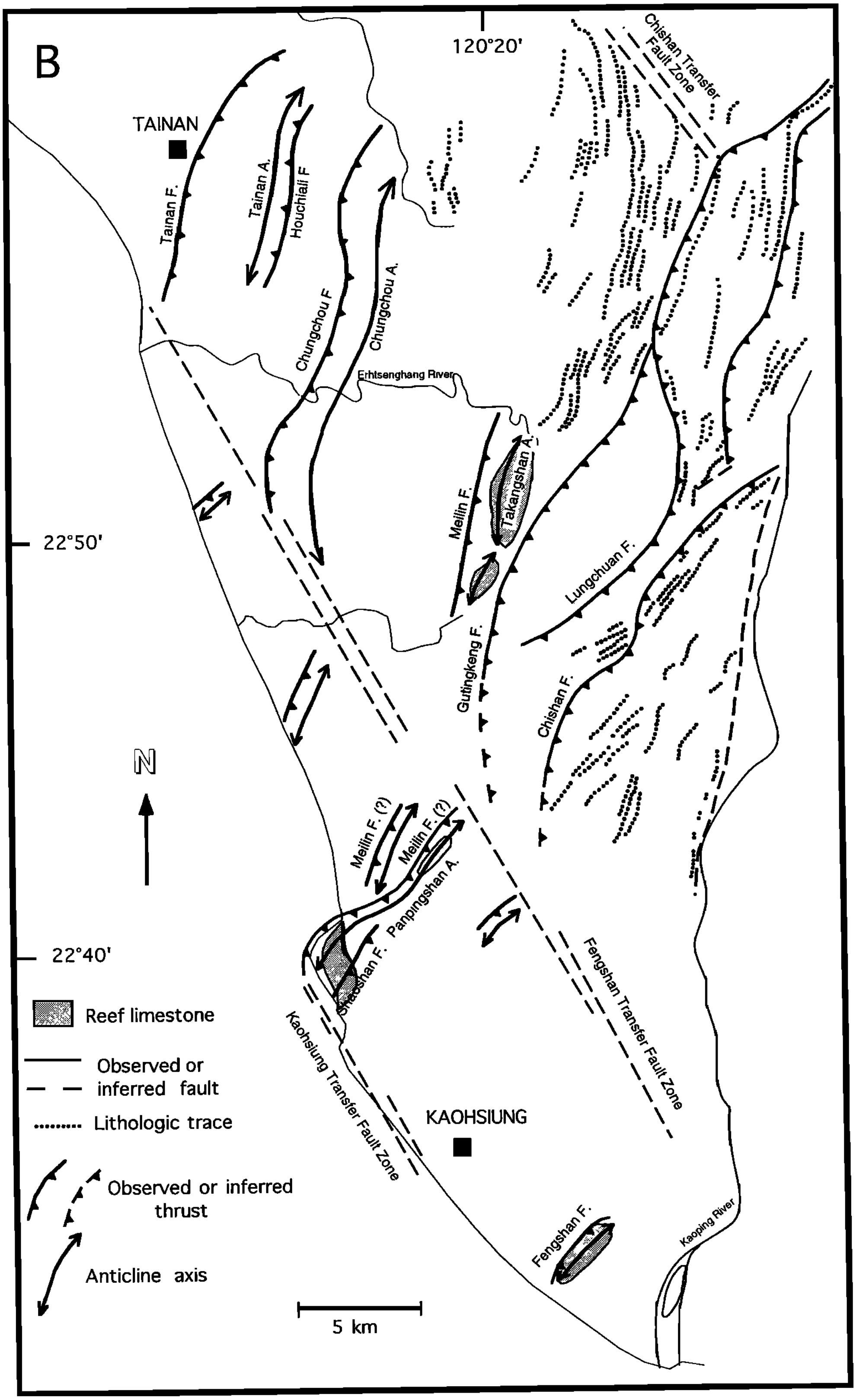

Figure 4. (continued)

major and minor fracture sets along such oblique trends, and brought constraints on both their kinematics and tectonic significance.

These geomorphological studies were complemented by interpretations of high-resolution SPOT panchromatic scenes (10x10 m ground resolution) of western Taiwan. Both analyses allow improvement of the structural information reported on previous geological maps [Chinese Petroleum Corporation, 1974; *Ho*, 1986a, b](Figure 2).

3.2. Construction of Geological Cross Sections

Three geological cross sections were constructed perpendicular to the outermost fold-and-thrust units (Figure 5). The control at depth of these sections was provided by well data (location on cross sections) and seismic profiles (Chinese Petroleum Corporation, unpublished data, 1997) where available. The Plio-Pleistocene synorogenic deposits provide time constraints on the structural evolution of the units. As discussed in sections 4.2.1-4.2.3, these cross sections highlight the geometry, extension at depth, and spacing of fold-thrust systems and the lateral changes in thickness and type of sedimentary formations. They provide evidence for the regional along-strike change in kinematics and structural style of the deformed units. At a more local scale they highlight the close relationships between reefs and fault-related folds (Figure 5).

3.3 Paleostress Analyses

The analysis of macrostructures was combined with a detailed study of small-scale brittle deformation, such as striated microfault surfaces, stylolites, joints, and tension gashes. The location of sites is reported in Figure 2. The dynamic interpretation of these microstructures in terms of tectonic stress patterns brought constraints on both the Quaternary tectonic mechanisms and the kinematics of propagating units.

Computation of paleostress tensors was performed on the basis of inversion of fault slip data [*Angelier*, 1984]. The basic principle consists of finding the best fit between the observed directions and senses of slip on numerous faults and the theoretical shear stress induced on these planes by the tensor solution of the inverse problem. The results are the orientation (trend and plunge) of the three principal stress axes σ_1, σ_2, and σ_3 (with $\sigma_1 \geq \sigma_2 \geq \sigma_3$, pression considered positive) and the Φ ratio between differential stress magnitudes ($\Phi=(\sigma_2-\sigma_3)/(\sigma_1-\sigma_3)$, with $0 \leq \Phi \leq 1$). Additional information is obtained from stylolites, tension gashes, and joints. The procedure for separating successive stress tensors and related subsets of fault slip data is based on both mechanical reasoning [e.g., *Angelier*, 1984] and relative tectonic chronology data (superimposed striations on fault surfaces, crosscutting relationships between faults, ...).

In order to establish a time distribution of tectonic regimes, dating of the brittle structures also requires stratigraphic information about the age of the deformed units and/or evidence of syndepositional tectonism. Particular attention was also paid to rotations of rock masses due to folding. Reconstruction of the original attitudes of minor structures and related paleostress axes with respect to fold axes and bedding attitudes was thus performed in the following way: Where tilted bedding is observed as a result of folding, several cases deserve consideration, because faults may have formed before, during or after folding. Following *Anderson* [1951], we assumed that one of the three principal stress axes of a tensor is generally vertical. If a fault set formed before folding and was secondarily tilted with the bedding, the tensor calculated on this set does not display a vertical axis. Instead, one of the stress axes is generally found perpendicular to bedding, whereas the two others lie within the bedding plane. Accordingly, the conjugate fault systems do not display vertical planes of symmetry. In such a case, it is necessary to back tilt the whole system (faults, tensor, and bedding) in order to put it back in its initial position. Within a heterogeneous fault population this geometrical reasoning allows separation of data subsets based on their age relative to fold development. For simplicity we only provide examples of the most significant diagrams illustrating fault slip data. The corresponding stress tensors are listed in Table 1.

The reef limestones also provide a suitable material for paleostress reconstructions based on inversion of mechanical twins in calcite [*Etchecopar*, 1984; *Laurent*, 1984]. They contain large sparry calcite crystals resulting from recrystallization during diagenesis of the primary aragonitic material and micritic calcite. These sparry grains are of nearly homogeneous size and developed independently with respect to the initial organic network (Figure 6); they display nearly random crystallographic orientations, which is appropriate for calcite twin analysis. Twin lamellae within these grains are straight and narrow, indicating low strain (less than 2 or 3%) and low temperature (<200°C). Paleostress reconstructions were thus carried out on the basis of inversion of mechanical calcite twin data [*Lacombe et al.*, 1993; *Rocher et al.*, 1996; this work].

4. Geometry and Kinematics of Fold-and-Thrust Units

The study area is limited to the north by an oblique fault zone, the Chishan Transfer Fault Zone (CTFZ) [*Deffontaines et al.*, 1997] (Figure 2), whose tectonic significance will be discussed in section 5. This oblique fault zone corresponds to the surface expression of a broader transition area underlined by numerous earthquakes (some of them as deep as 80 km [*Wu et al.*, 1997]) which clearly separates a northern domain (domain 1 in Figure 2) in front of the Peikang High, which displays high seismic activity, and a southern region (domain 2 in Figure 2) where shallow (between 0 and 20-25 km depth) earthquakes are scarce [*Wu et al.*, 1997]. This zone corresponds to the transition between a northern region where collision is taking place and involves the deformation of the continental basement (and the whole crust [*Wu et al.*, 1997]), and a southern region which can be described as the on-land extension of the Manila accretionary wedge, where shortening occurs while the deformation front moves westward toward the Eurasiatic continental shelf. From structural and sedimentary points of view this zone is also marked by an important lateral variation in type and thickness of sedimentary formations (Figure 3) as well as contrasting styles of deformation [*Mouthereau et al.*, 1999a, b].

In this paper, we focus on the southern region, but we briefly present the results of tectonic analyses carried out just north and along the surface trace of the so-called Chishan Transfer Fault Zone, in order to allow comparison with the southern area. For the sake of simplicity, sections 4.1-4.2 report separately the results obtained in the two subregions located north and south of the CTFZ, respectively (domains 1 and 2 in Figure 2).

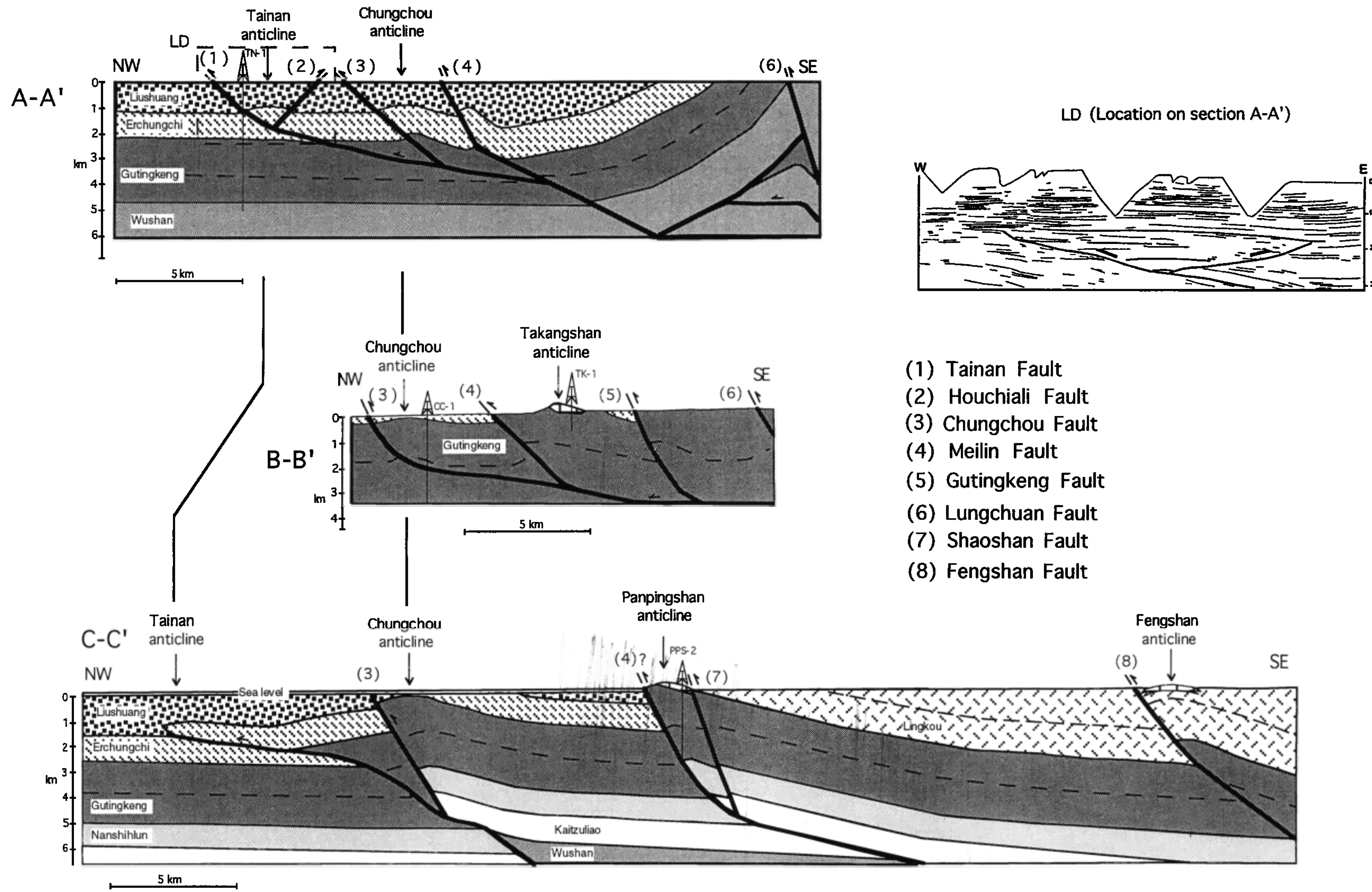

Figure 5. Geological cross sections through the area investigated (location in Figure 2), constrained by well data (projected on the sections) and seismic lines. The patterns used for sedimentary formations are the same as those used for the map of Figure 2 and the stratigraphic columns of Figure 3. The Holocene formations have not been represented. Note the particular location of the reefs and the fault-propagation fold geometry. LD, Line drawing (upper right), located on section A-A'. In the offshore part of section C-C', the Tainan and Chungchou anticlines have been extrapolated. The numbers refer to faults located in Figure 2.

Table 1. Results of Stress Tensor Determination Based on Fault Slip Data

Site	Diagram	Trend (Plunge) of the Principal Stress Axes σ_1	σ_2	σ_3	Ratio Between Differential Stresses (Φ)	Total Number of Faults (F)	Quality of Tensor (Q)
1	b*	092 (27)	325 (38)	207 (30)	0.3	6	c
	c*	085 (01)	355 (19)	178 (71)	0.3	22	a
	d*	089 (08)	358 (06)	233 (81)	0.2	11	a
2	*	107 (17)	231 (62)	010 (22)	0.4	7	c
3		287 (16)	080 (72)	194 (08)	0.2	6	c
4	a*	111 (16)	300 (74)	202 (02)	0.2	22	a
	b*	082 (03)	288 (87)	172 (02)	0.4	46	a
5	a	274 (03)	037 (84)	183 (05)	0.1	89	a
	b	127 (17)	324 (72)	218 (05)	0.5	23	a
	c	288 (74)	066 (12)	158 (10)	0.2	9	a
6	a	270 (04)	029 (81)	179 (08)	0.1	46	a
	b	148 (70)	016 (14)	283 (03)	0.3	5	b
7	a	334 (72)	236 (03)	145 (18)	0.4	11	a
	b	132 (02)	011 (87)	222 (03)	0.0	30	a
8	a	131 (03)	338 (87)	221 (02)	0.3	36	a
	b	025 (69)	192 (21)	284 (04)	0.2	22	a
	c	073 (03)	306 (85)	164 (04)	0.2	13	b
9		302 (03)	184 (85)	033 (05)	0.4	34	a
10		111 (11)	229 (66)	017 (20)	0.2	13	b
13	b	254 (80)	084 (10)	354 (02)	0.4	12	a
14	a	170 (76)	022 (12)	291 (07)	0.3	6	c
	b	188 (88)	083 (01)	353 (02)	0.3	22	a
	c	305 (02)	208 (76)	035 (12)	0.2	10	b
15	b	290 (01)	033 (86)	200 (04)	0.5	19	b

Trend and plunge of each stress axis are given in degrees. Ratio Φ is defined in text. F, number of faults consistent with the tensor; and Q, quality of the tensor (a to c) estimated according to the number of faults explained, the variety of their orientations, and intraprogram numerical quality estimators [*Angelier,* 1984].

* Back tilted stress axes.

4.1. Area North of the Chishan Transfer Fault Zone (Domain 1 in Figure 2)

Immediately north of the CTFZ (Figure 2), Pleistocene mudstones display steep dips to the west as a consequence of the development of NNE trending folds and thrusts (Figure 7). At the outcrop scale, brittle features reveal a dominating nearly E-W compression. Three main types of fracture sets could be observed in this area.

The first set consists of subvertical E-W trending tension joints (Figure 7, diagram a at site 1), consistent with a mean E-W compression. The second type includes N140°-160°E left-lateral strike-slip faults and N70°E right-lateral ones. The striations are often non horizontal and parallel with the bedding. We infer that these strike-slip faults developed before folding and were secondarily tilted. Such patterns should therefore be analyzed in their initial attitude. Thus bedding was back tilted along the local strike of beds (because the folds are generally cylindric), which allowed restoration of the original attitude of fault patterns (e.g., Figure 7, diagram b at site 1 and diagram at site 2). In contrast, some strike-slip faults exhibit nearly horizontal striae oblique to tilted bedding (Figure 7, diagram at site 3) and should thus be interpreted as faults which developed after folding. The third type of brittle structures consists of apparent normal fault patterns, associated with a steeply plunging σ_1 axis, and a shallowly plunging, N80°E trending σ_3 axis. These normal faults do not reflect extension: Backtilting the strata as before restores the initial pattern, a simple system of reverse faults consistent with a subhorizontal E-W compression (Figure 7, diagrams c and d at site 1). This compression is nearly perpendicular to fold axes and similar to that deduced from tension joints and strike-slip faults.

We conclude that a nearly E-W compression accounts for all the tectonic features observed at different scales. Faulting and folding occurring during the same compressional event produce apparently complicated fault patterns; however, the geometrical-mechanical analysis provides a key to identify and interpret these patterns, thus revealing that the stress regimes remained rather constant during folding.

Seismic investigations as well as mapping of the top of the pre-Miocene basement using well data in this northern region emphasize the involvement of the basement in the thrust wedge and the superimposition of shallow décollement and deep-seated décollement tectonics. It is not the aim of this paper to discuss the structural style of this northern area in

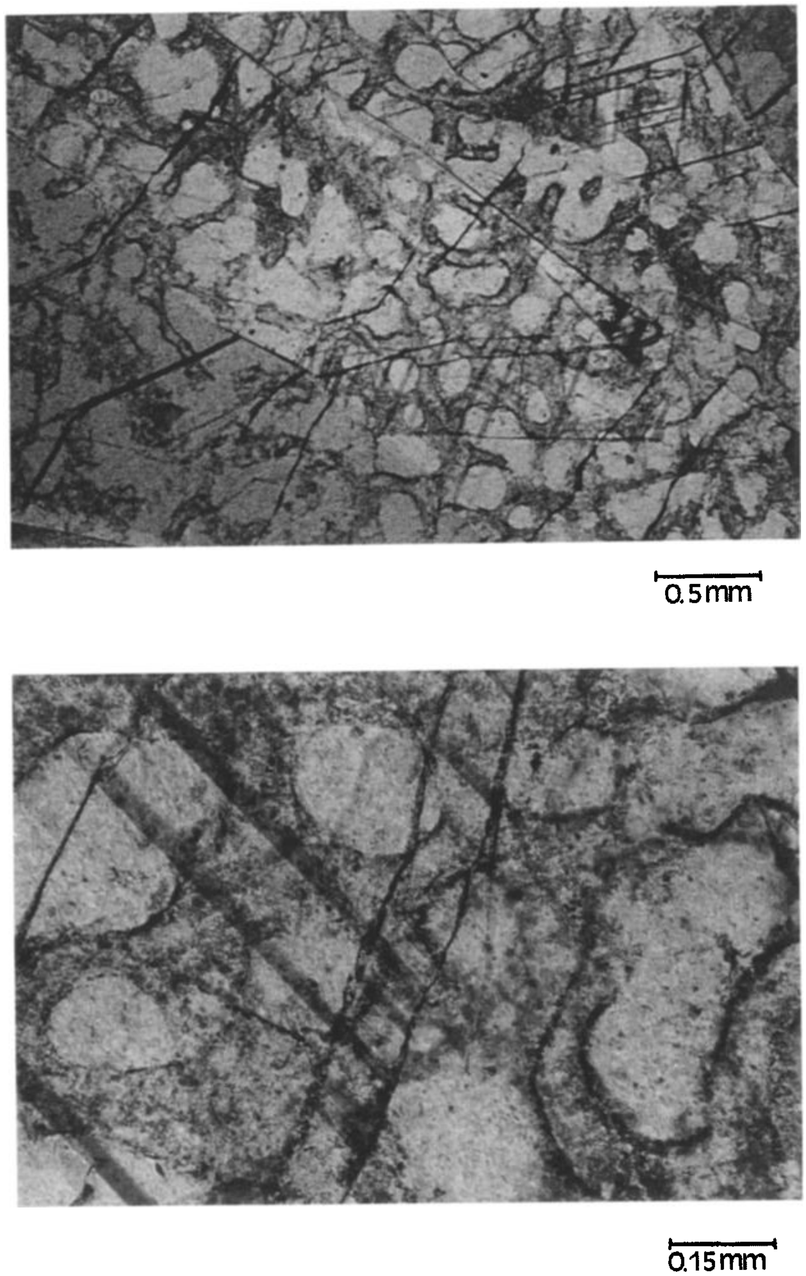

Figure 6. Microphotographs (in natural light) of a coral limestone showing twin lamellae cross cutting sparry calcite crystals resulting from recrystallisation regardless of the initial coralline organic network.

detail (see *Mouthereau et al.* [1999a, b] for cross sections and review of previous works).

4.2. Area South of the Chishan Transfer Fault Zone (Domain 2 in Figure 2)

In contrast to the northern domain, where the basement is involved in collisional shortening [*Mouthereau et al.*, 1999a, b], deformation in the Tainan-Kaohsiung province did not involve the pre-Miocene basement. The propagation of frontal thrust units probably occurred above a low dipping and shallow décollement surface, above the pre-Miocene basement (Figure 5): Structures consist of regularly spaced fault-propagation folds and pop-up structures, which usually develop in relation to flat detachments with low-friction conditions [*Huiqi et al.*, 1992] such as for accretionary wedges. This deformation style is therefore largely controlled by high-fluid-pressure conditions, as shown by the thick poorly consolidated muddy Quaternary deposits and the numerous mud volcanoes (Figure 2). This confirms that this province can be regarded as the onshore extension of the submarine Manila accretionary wedge [*Sun and Liu*, 1993; *Liu et al.*, 1997], so

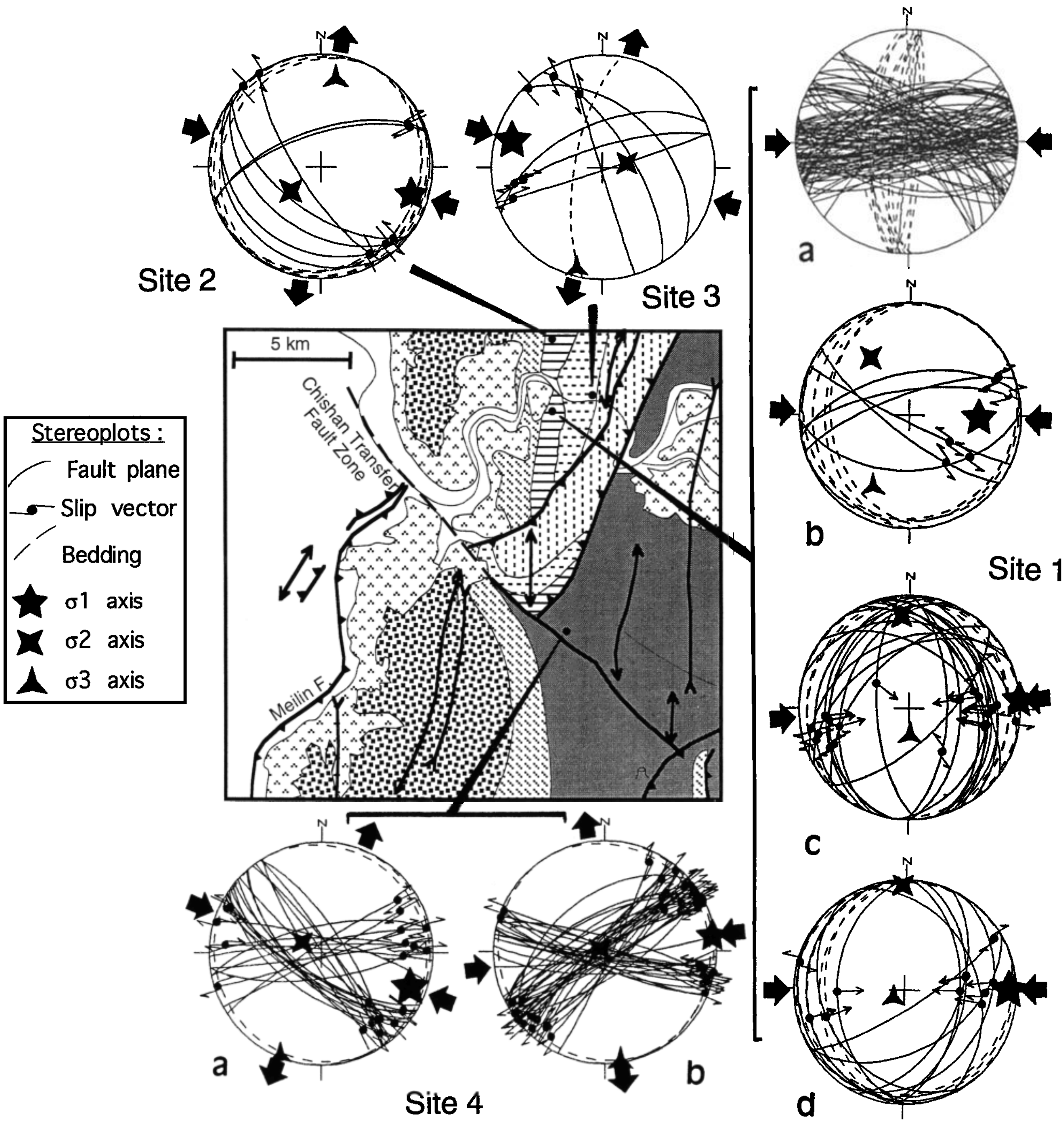

Figure 7. Results of stress reconstruction based on fault slip analysis along and away from the surface trace of the Chishan Transfer Fault Zone.
The map is part of that of Figure 2 (Longitude: 120°20'-120°30'; Latitude: 23°-23°10') and uses the same key. Site numbers refer to sites of Figure 2 and of Table 1.

that the deformation front defined on-land (Figure 2) can be correlated with the offshore northern extension of the Manila trench.

4.2.1. Tainan and Chungchou anticlines. The analysis of the high-resolution DEM of southwestern Coastal Plain of Taiwan (Figure 4) provides evidence of slightly elevated, asymmetric hills, striking parallel to the NE trend of the known folds and thrusts. There is no significant drainage parallel to the NE direction to explain these features in terms of erosion. Therefore we consider that these morphologic features are of tectonic origin and cannot result from erosion solely: They are interpreted as the outermost west vergent folds.

Available well data and seismic reflection profiles (Chinese Petroleum Corporation, unpublished data, personal communication, 1997) confirm the tectonic origin of these features (Figure 5): In the western part of the A-A' section, two shallow thrust-related folds were identified in the Pleistocene cover (Liushuang-Erchungchi Formations). The Tainan Fault is considered as the outermost thrust and corresponds to the so-called deformation front, which is therefore located farther NW than in previous locations (e.g., near Kaohsiung according to *Lee et al.* [1995]). The Tainan thrust (and the Houchiali backthrust) connects to a thrust flattening at nearly 3 km depth, within the thick, fluid-rich poorly consolidated muddy Quaternary deposits of the Gutingkeng Formation which behave as an intermediate mechanical decoupling level (sections A-A' and B-B'). At greater depth (nearly 6 km) this thrust roots within a low-dipping decollement surface above the pre-Miocene basement. Section A-A' (Figure 5) additionally shows that the Tainan anticline corresponds to a small pop-up structure (line drawing in figure 5). This structure was previously identified on the basis of the radial centrifugal drainage pattern and the morphologic trace of the Houchiali Fault [*Sun*, 1964] but not interpreted in terms of deformation front.

The Chungchou anticline exhibits a morphological signature (Figure 4) which suggests a west verging asymmetric anticline. Its rectilinear western limit indicates that it is closely related to the motion of the Chungchou Fault, which also corresponds to a west vergent thrust flattening within the Gutingkeng Formation (Figure 5, section B-B'). The close spacing of the thrusts along the section is consistent with a shallow location of this intermediate decoupling level.

The Meilin thrust separates a slightly deformed western domain from an eastern domain characterized by well-expressed folds and faults (Figure 2). It probably corresponds to a steep thrust surface dipping toward the east, in relation to which a fault-propagation fold developed. At depth, however, the relation between the Meilin thrust and the décollement level is unclear; it is only tentatively extrapolated in section A-A'.

4.2.2. Takangshan and Panpingshan anticlines. The Takangshan and Panpingshan anticlines, trending NE-SW, provide good examples of fault-propagation folds commonly observed in southwestern Taiwan (Figure 2). The steeply dipping NW flanks of these anticlines are limited by NW vergent thrusts (such as the Meilin Fault), whereas their eastern flanks dip gently to the southeast.

Near the top of these anticlines, thick Pleistocene reefal limestones interbedded within the clastic layers of the Gutingkeng Formation crop out [e.g., *Heim and Chung*, 1962; *Chen et al.*, 1994]. The Takangshan and Hsiaokangshan reefs (T and H in Figure 2) are located on top of the Takangshan anticline, whereas the Panpingshan and Kaohsiung reefs (P and K on Figure 2) cover the top of the Panpingshan anticline. The age of the reefs ranges from 1.2 to 0.45 Ma and is younger from south (Kaohsiung) to north (Takangshan).

Tectonic analyses and paleostress reconstructions based on fault slip data and calcite twin data were carried out within the areas of the Takangshan and Panpingshan anticlines (Figures 2 and 8), especially in the reef material which is suitable for tectonic record. The reconstructed tectonic regimes and the corresponding data are briefly summarized in Figure 8. For details, refer to *Rocher et al.* [1996] and *Lacombe et al.* [1997].

In Panpingshan, normal faults trending N60°E to E-W and dipping gently to the north or steeply to the south revealed a NW-SE extension (Figure 8, diagram a at site 7). The σ_2 axis of the tensor is nearly parallel to bedding (hence to the anticline axis), while the σ_3 axis trends perpendicular to bedding strike. At least part of these normal faults developed contemporaneously with mud deposition and reef building [*Chen et al.*, 1994; *Lacombe et al.*, 1997]. We conclude that normal faulting was partly syndepositional and occurred during folding. In the Takangshan, Hsiaokangshan, and Kaohsiung reefs (Figure 2), some normal faults also indicate a WNW-ESE to NW-SE extension (Figure 8, diagrams c at site 5, b at site 6, and b at site 8).

Compressional features were also observed. In the Panpingshan quarry, left-lateral strike-slip faults trending N150°-160°E and right-lateral strike-slip faults trending N110°-130°E indicate a NW-SE compression (Figure 8, diagram b at site 7). This compression is perpendicular to the fold axis and related to folding. Two systems of large subvertical fractures were also measured; although striations are absent, they probably correspond to conjugate strike-slip faults related to a nearly E-W compression (Figure 8, diagram c at site 7). In site 8 a NW-SE compression has also been identified, marked in the field by both strike-slip and reverse faults (Figure 8, diagram a at site 8). A few tension gashes and strike-slip faults additionally indicate a N80°E compression (Figure 8, diagram c at site 8). In Hsiaokangshan most of the measured strike-slip faults are consistent with an E-W compression (Figure 8, diagram a at site 6). In Takangshan, two different systems of strike-slip faults could be identified. The first set is similar to the system of strike-slip faults identified in Hsiaokangshan and is also related to a nearly E-W compression (Figure 8, diagram a at site 5). The second set comprises conjugate right-lateral E-W strike-slip faults and left-lateral N160°E to N200°E strike-slip faults associated with N130°E trending tension gashes; these structures are consistent with a NW-SE compression (Figure 8, diagram b at site 5).

Closer inspection of the normal fault systems reveals a large dispersion in trend relative to the orientation of the fold axes; in detail, the normal fault sets include E-W trending and highly dipping faults, as well as nearly N-S to N40°E trending faults subparallel to bedding. Despite this azimuthal dispersion, the slips along these planes are mechanically consistent with a nearly NW-SE extension, which is the reason why they were not separated into subsets in Figure 8. This azimuthal dispersion could be tentatively related to the heterogeneity of the poorly lithified limestone material and/or to a gentle collapse (or differential compaction?) of the recently built, protruding coral reef on top of the poorly lithified mudstones. Rather, we consider that the E-W trending faults oblique at large angle to bedding are related to a nearly N-S extension, perpendicular to, and associated with, the E-W to WNW-ESE compression; the normal faults striking parallel to fold axis being related to local NW-SE extension in response to stretching at the hinge of the growing anticlines.

Relative chronology criteria, such as cross cutting relationships between faults, superimposed striations on fault surfaces, or attitude of minor structures and related paleostress axes with respect to fold axes and bedding provide constraints on stress evolution through time. In several cases, normal faults were reactivated as strike-slip faults under NW-SE (Figure 8, diagrams a and b at site 7) or E-W compressions (Figure 8, diagrams a and c at site 5). Concerning the compressions, diagrams a at site 5, a at site 6, c at site 7 and c at site 8 (Figure 8) show that the intersection of the conjugate families of strike-slip faults marking the E-W compression is vertical and that most striations on the fault planes are subhorizontal (and therefore less tilted than the bedding), so that this compression is likely to have prevailed after folding; in contrast, the NW-SE compression probably occurred during and after folding (Figure 8, diagrams b at site 5 and b at site 7

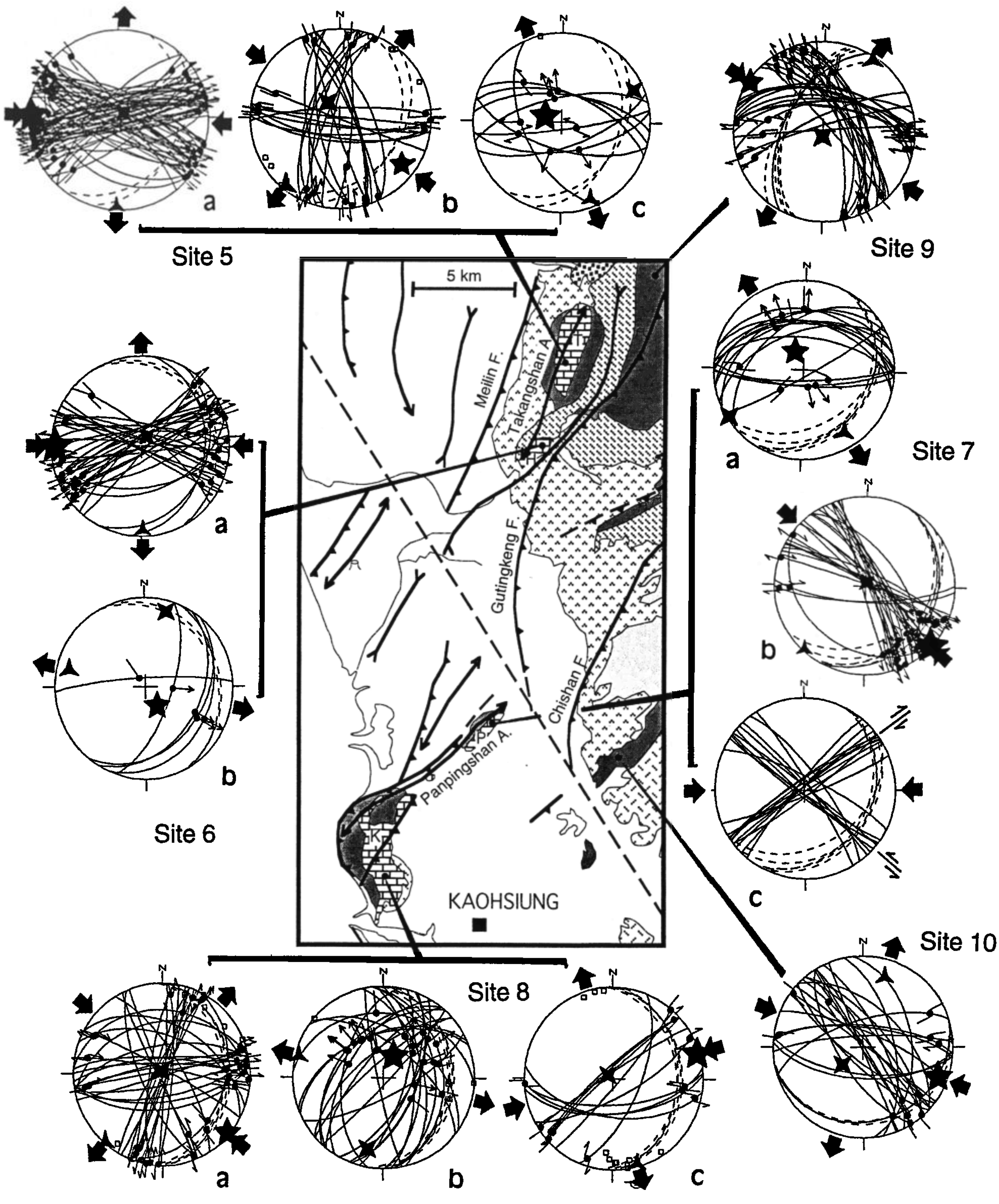

Figure 8. Results of stress reconstruction based on fault slip analysis in the vicinity of the Takangshan and Panpingshan anticlines. The map is part of that of Figure 2 (Longitude: 120°15'-120°25'; Latitude: 22°35'-22°55') and uses the same key as in Figures 2 and 7. Small open squares in diagrams represent poles to tension gashes.

and diagrams at sites 9 and 10). This suggests that the E-W compression postdated the NW-SE compression.

In summary, two compressional stress regimes have been identified: A NW-SE compression, followed by an E-W compression. The NW-SE compression is associated with the major stage of fold development and associated reef building; it is marked by strike-slip faults. Under this compression, early normal faults, sometimes syndepositional, locally developed in response to stretching at the hinge of the growing anticlines. The E-W compression mainly prevailed during the latest stages of folding; it is associated with a component of perpendicular N-S extension.

At the northeastern tip of the Takangshan anticline, microtectonic measurements were carried out in the Quaternary mudstones on the western side of the Guntingkeng Fault. In these mudstones, which display high dips to the west (65°-85°), conjugate strike-slip faults were observed, consistent with a N130° trending compression. These faults show non horizontal striations that dip more shallowly than bedding, which suggests that strike-slip faulting occurred during folding. The diagram at site 9 (Figure 8) illustrates the attitude of the fault set at a stage of limited back tilt, the calculated stress axes being horizontal (σ_1 and σ_3) and vertical (σ_2). This demonstrates the importance of the syn folding NW-SE compression in this area.

4.2.3. Fengshan anticline. The Fengshan anticline is one of the innermost features of the southwestern Taiwan Foothills (Figure 2). It bounds the Pingtung Plain to the west. The northern part of the Fengshan anticline trends N170°E to N-S. In the northern part of the fold most of the outcropping formations consist of the lower member of the Lingkou conglomerate (Figures 2 and 3).

To the south, the anticline axis turns from N-S to N110°E and becomes NE-SW where the anticline is covered by the Fengshan NN20 limestone. This limestone unconformably overlies the NN19 mudstones equivalent to the lower member of the Lingkou conglomerate [*Gong et al.*, 1996; this work]. Aerial photograph analyses suggest that this southern part is limited to the west by a west vergent thrust: the Fengshan Fault (section C-C'). Compressional features along the northern side of this thrust indicate that the NE oriented southern part has moved northwestward and has overthrust the N-S trending part of the fold. This may suggest a two-phase fold development.

Tectonic analyses of minor fault patterns have been performed in this fold (Figures 2 and 9). In its northern part, tension joints oriented N110°-120°E (Figure 9, diagrams at sites 11 and 12) probably mark a regional N110°-120°E strike-slip regime, consistent with the average trend of the Fengshan anticline. In site 13, E-W trending tension joints (Figure 9, diagram a at site 13) and normal faults (Figure 9, diagram b at site 13) are interpreted in terms of a NNE extension accompanying the WNW-ESE compression (σ_1-σ_2 stress permutation).

In the southern part of the anticline, a large quarry allows observation of the Fengshan reef limestone covering the crest of the anticline and its erosional contact with the underlying mudstones (Figure 10a). Calcite twin analysis reveals two states of stress: a NW-SE compression (with vertical σ_2 axis) as well as a NW-SE extension, consistent with those reconstructed in the other reef formations. In the mudstones, nearly E-W trending, low-dipping normal faults were predominantly observed (Figure 9, diagrams a and b at site 14 and Figure 10c), compatible with normal faults observed along the erosional contact between the limestones and the underlying mudstones (Figure 10b). On the highest part of the quarry a nearly E-W graben filled with limestone conglomerates shows channel-like sedimentary features (Figure 10d): It is bounded by normal faults associated with carbonate breccia, indicating that these normal faults acted as the graben filled up. The graben is sealed by continental red soils and conglomerates, whereas red clays have filled solution cavities developed within the limestone. These observations suggest that most extensional features prevailed during deposition of the upper part of the NN19 mudstones and building and emergence above sea level of the NN20 reef. Most normal faults trend E-W (Figure 9, diagram b at site 14); only few trend subparallel to bedding (Figure 9, diagram a at site 14). As already proposed by *Lacombe et al.* [1997] for the Takangshan and Panpingshan anticlines, the few normal faults parallel to fold axis are probably related to fold development, in response to tensional stresses initiated at the hinge of the growing anticline.

The WNW-ESE to E-W trending normal faults are tentatively interpreted in terms of extensional stresses perpendicular the WNW-ESE compression prevailing during and after folding in the Fengshan area. Some of these normal faults display evidence for a late reactivation as right-lateral strike-slip faults, consistent with a WNW-ESE directed compression (Figure 9, diagram c at site 14). We conclude that the WNW-ESE compression was responsible for both the development of the northern part of the Fengshan anticline and the associated fracturing (sites 11, 12, and 13) and the northwestward thrusting of its southern part (associated with reef building). This compression prevailed until recently after folding (site 14). In contrast to the clear contractional character of the NW-SE compression, the widespread occurrence of extensional features indicating a late N-S to NNE-SSW extension may reveal a situation of low N-S confinement during the recent WNW-ESE to E-W compression, a tectonic regime which may reflect the incipient tectonic escape in southwestern Taiwan (see section 6.3).

5. Geometry, Kinematics and Tectonic Significance of NW-SE Trending Fault Zones

5.1. Chishan Transfer Fault Zone (CTFZ)

Structural mapping reveals the existence north of our study area of a NW-SE structural trend, previously identified and called by *Deffontaines et al.* [1997] the Chishan Transfer Fault Zone (Figure 2), on both sides of which contrasting styles of deformation and mismatches of anticline axes occur. On the basis of new accurate analysis of DEM we propose that this zone extends farther west along the NW-SE branch of the Tsengwen river and accompanies the left-lateral offset of the deformation front to the north with respect to the frontal thrust of the Tainan anticline (Figure 2).

In the field the NW-SE Chishan Transfer Fault Zone (CTFZ) crops out as an elongated bulge, more than 20 km long and 1 km wide. This area contains several closely spaced NW-SE shear zones, associated with a variety of normal and reverse components of motion, along which most of the deformation has been accommodated. Wrench deformation zones are underlined in the field by highly deformed black clays which appear as black oblique stripes cutting through the light gray mudstones (Figure 11a). These sheets of highly sheared clays display narrow-spaced shear cleavages and small truncated elements, contrasting with the absence of large deformation in

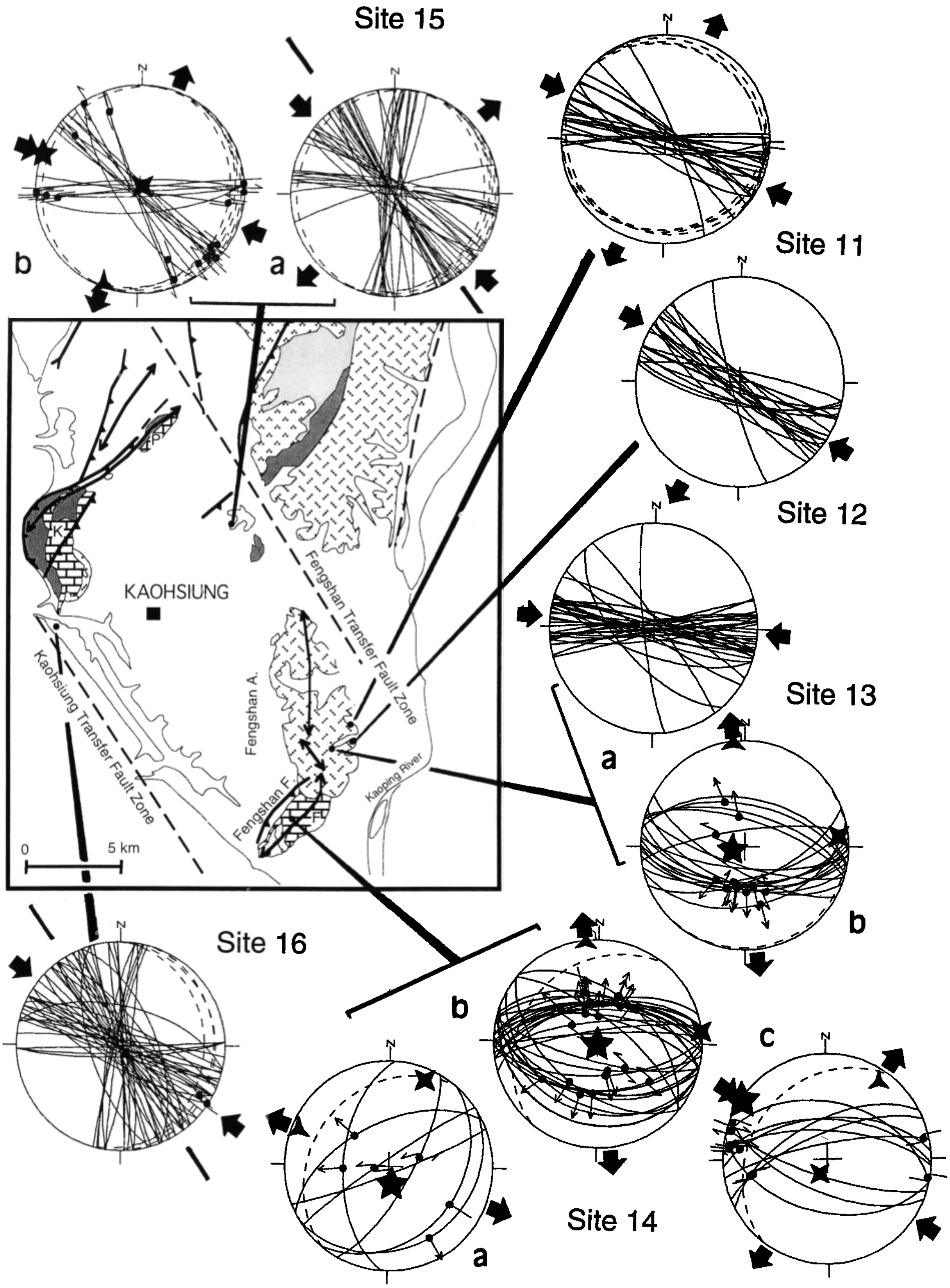

Figure 9. Results of stress reconstruction based on fault slip analysis within the Fengshan area. The map is part of that of Figure 2 (Longitude: 120°10'-120°25'; Latitude: 22°30'-22°45') and uses the same key as in Figures 2, 7, and 8.

A

B

Figure 10. Field observations from the Fengshan anticline. (a) Erosional contact between the Fengshan NN20 reef limestone and the underlying NN19 mudstones. (b) Normal faults along the erosional contact between the Fengshan reef limestones and the mudstones. (c) E-W trending syndepositional normal fault within the Fengshan mudstones. (d) E-W trending graben at the top of the Fengshan quarry. Cartoons provide simplified interpretations of photographs.

the surrounding mudstones (Figure 11a). The passive rotation and offsets of markers as well as S-C relationships within the shear bands consistently indicate a left-lateral sense of transpressive shear. At a wider scale the upward divergent geometry of these faults suggests that the whole pattern is a positive "flower structure", consistent with the wrench movement recognized in individual shear zones.

Microtectonic analyses carried out within the mudstones lead us to identify two systems of strike-slip faults (Figure 7). A N80°E compression is marked in the field by a system of conjugate left-lateral strike-slip faults trending N110°-120°E and right-lateral strike-slip faults trending N40°-60°E (Figure 7, diagram b at site 4, and Figure 11b). The striations on these fault planes lie within the bedding plane, and the intersection of the fault planes is not vertical; in addition, the σ_1 axis of the stress tensor is not horizontal, but is parallel to the dip direction of the beds, whereas σ_3 axis is parallel to the strike of beds. Back tilting fault slip data, hence the calculated stress axes, along the local strike of beds restores the initial attitude

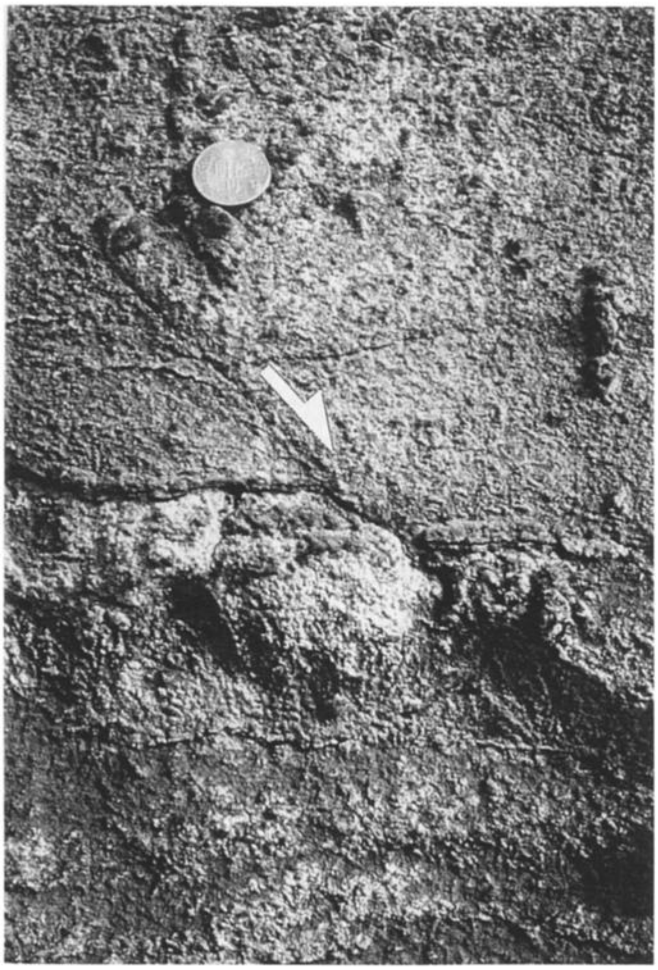

C

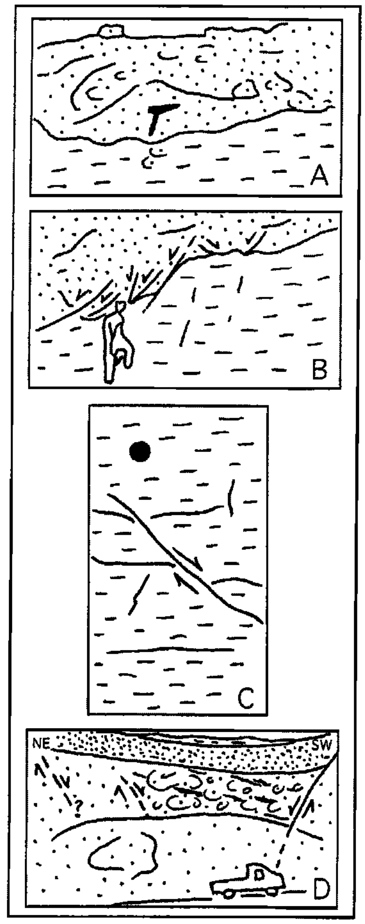

D

Figure 10. (continued)

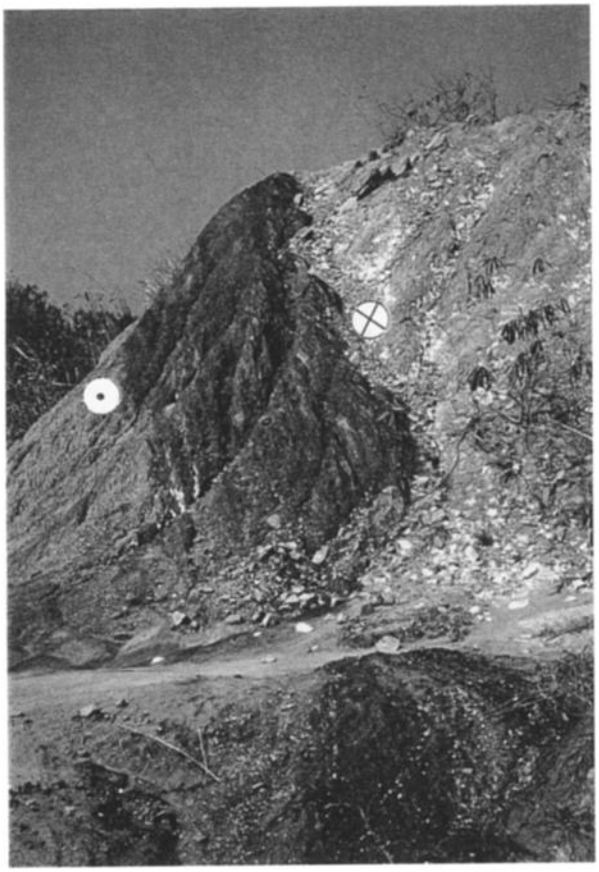

A

Figure 11. Field observations from the Chishan Transfer Fault Zone. (a) View of a NW-SE shear zone along the Chishan Transfer Fault Zone. The deformation zone is underlined by highly deformed stripes of black clays which cut and offset the light gray mudstones and show narrow-spaced shear cleavages. (b) Tilted set of minor conjugate N110°-120°E left-lateral and N40°-60°E right-lateral strike-slip faults observed within sandstones beds within the Chishan Transfer Fault Zone. Back tilting fault slip data along the local strike of beds restores the initial attitude of fault pattern; these are consistent with a σ_1 axis oriented N80°E and a σ_3 axis oriented N170°E (Figure 7, diagram b at site 4).

B

of fault pattern and stress axes (σ_1 and σ_3 axes horizontal), that is, a σ_1 axis trending N80°E and a σ_3 axis trending N170° (Figure 7, diagram b at site 4). This indicates that strike-slip faulting occurred probably in the earliest stage of folding, in response to N80°E compression. The second stress regime is marked by left-lateral strike-slip faults striking parallel to the NW-SE fault zone associated with conjugate right-lateral strike-slip faults trending N50°-80°E. Tensor determination [*Angelier*, 1984] indicates a N110°E compressional strike-slip stress regime (Figure 7, diagram a at site 4). Although the calculated σ_1 axis is nearly horizontal, the slip vectors on the strike-slip faults marking this compression display a variety of orientations, ranging from parallel to bedding to horizontal, which indicates that the N110°E compression probably prevailed before and after folding.

Both these stress orientations are similar to those identified away from the fault zone (Figure 7). Note that these stress regimes (and the related data subsets) were separated in the site considered on the basis of their relative chronology with respect to folding and of mechanical considerations (similar value of the acute angle between conjugate shear planes [*Anderson*, 1951]. If one accepts a dispersion of fault plane orientations, taking into account the dispersion range of stress orientations recognized away from the shear zone, both these fault systems can be gathered and accounted for by a single average N100°E compression.

Comparison between these reconstructed compressional trends and previous findings in the Foothills [*Angelier et al.*, 1986; *Chu*, 1990; *Lee*, 1994] leads us to conclude that at the regional scale the average N100°E compression probably reflects the Quaternary far-field state of stress. At the local scale, the occurrence of N80°E and N115°E compressions may be interpreted in terms of trend dispersion around a mean regional N100°E compression but it may also reveal occurrence of a regional N100°-110°E compression locally perturbed into a N80°E trend in the vicinity of the fault zone.

5.2. Fengshan Transfer Fault Zone (FTFZ)

Geomorphological and remote-sensing data combined with structural mapping emphasized the sigmoidal virgation and mismatches of most of the N20°-40°E trending thrusts and anticlines close the Fengshan N140°E Transfer Fault Zone inferred by *Deffontaines et al.* [1997](Figure 2). For instance, to the west the NE trending Chungchou thrust and the related anticline, as well as the Gutingkeng and the Chishan Faults, turn to the south and tend to become parallel to the N140°E direction (Figure 2). To the southeast the Fengshan anticline, which is oriented NE-SW to the south, turns to N-S close to the inferred fault zone (Figures 2 and 4). Cross sections of Figure 5 underline the slight difference in structural style between the sections A-A' and B-B' located north of the Fengshan Transfer Fault Zone (see section 5.4) and the section C-C'.

From a morphological point of view this fault zone has no clear straight surface expression: Its signature on the DEM (Figure 4) only consists of a roughly linear, NW-SE oriented depression zone. On the map of Figure 2 this subsiding area filled with Holocene deposist corresponds to the limit of the outcrops of Pleistocene Gutingkeng and Lingkou Formations. Few suitable outcrops are thus available along this inferred fault zone.One outcrop of Gutingkeng mudstones (Figure 9, site15) allowed measurements of striated faults and joint patterns. Four main sets of subvertical joints could be separated on the basis of the orientations of fracture planes: A dominant N120-150°E trending subset and second order subsets trending N-S, N100°E and N50°E. The geometry of the first three sets suggests that the N120°-150°E planes correspond to tension fractures, whereas N-S and N110°E fractures may correspond to conjugate shear fractures, all consistent with a NW-SE directed compression (Figure 9, diagram a at site 15). This is confirmed by observations of minor striated faults associated with joints, left lateral trending N130°-150°E and right lateral trending N090°-110°E, also consistent with a NW-SE compression (Figure 9, diagram b at site 15). The clustering of fracture orientations along the N140°E direction supports the occurrence of a major N140°E fault zone; the reconstructed N120°E compression indicates that this fault zone may have locally undergone a left-lateral motion.

5.3. Kaohsiung Transfer Fault Zone (KTFZ)

South of the Kaohsiung city and harbor, the rectilinear, NW-SE trending shape of the shoreline and the sigmoidal shape of the Shaoshan hill covered on its eastern side by the Kaohsiung limestone led *Deffontaines et al.* [1997] to suspect the occurrence of a NW-SE fault zone (Figure 2). New field observations carried out within the reef limestones on the southern part of the Kaohsiung harbor entrance, along the shoreline, enable us to discuss the probable existence of an offshore, nearly coast-parallel, fault zone. Tectonic measurements carried out on the coastline provide evidence that the local shape of the coast results from the occurrence of a dominant set of N125°-145°E large fracture planes. Despite dispersion (Figure 9, diagram at site 16), a clustering of fracture trends occurs along a N140°E direction, as noticed for the Fengshan Transfer Fault Zone. This dominant set of fractures forms a conjugate pattern with a minor set of N90°-110°E oriented fractures, suggesting that both sets originated in response to strike-slip fault regime, with σ_1 oriented N115°-120°E. This is confimed by numerous tension gashes, brecciated or filled with calcite, oriented N120°E, and by some evidence of left-lateral shear along N125°E directed planes interpreted as Riedel shears along a major N140°E fault zone. These field observations argue in favor of the existence of a major N140°E fault zone, with a possible left-lateral sense of motion.

5.4. Significance of the NW-SE Fault Zones

The interpretation of the Chishan, Fengshan, and Kaohsiung N140°E trending structures as transfer fault zones [*Deffontaines et al.*, 1997; this work] was based on the identification of thrust sheet segments displaying differential displacement / shortening on both sides of the fault zones. The sigmoidal shape of thrusts and fold axes, the contrasting styles and amplitude of deformation, the mismatches of compressional structures on both sides of the fault zone, as well as the different senses and rates of displacement between adjacent blocks argue in favor of transfer faulting. According to this interpretation these transfer fault zones are expected to trend approximately parallel (or oblique at small angle) to the direction of displacement of the tectonic units. The N140°E direction thus corresponds to the Quaternary regional direction of emplacement of tectonic units [*Mouthereau et al.*, 1996], slightly oblique to the direction of the reconstructed compressional trends (NW-SE and E-W).

The origin of such transfer fault zones deserves discussion. Experimental and analytical modelings coupled with field studies have resulted in a better understanding of the geometry and mechanism of transverse zones [e.g., *Apotria et al.*, 1992; *Calassou et al.*, 1993; *Philippe*, 1994; *Baby et al.*, 1994; *Apotria*, 1995]. Such domains are characterized by structures oblique to the front belt. Sandbox modeling revealed that a thrust sheet moving over a décollement level may exhibit development of transverse structures in response to a lateral change in cover thickness due to basement geometry or basin boundary or to the lateral termination of the main décollement surface, which can be viewed as a high/low friction boundary. A primary tear fault may thus appear contemporaneously with fold-thrust development and be associated with a curvature of these structures as soon as they form; on both sides the amount of shortening is the same, but it may be accommodated in a different way. Such a system may secondarily evolve gradually into a transfer (or tear) fault, associated with a clear offset of already formed or currently forming folds. On both sides of the fault, differential displacement / shortening may be accommodated.

In Taiwan, the obliquity of the collision as well as the structural inhomogeneity of the Chinese margin colliding with the Luzon arc have played a major role in the structural style of the Foothills, resulting in an along-strike variation of thrust wedge geometry and kinematics of the frontal units [*Mouthereau et al.*, 1999a, b]. The precollisional structural pattern of the margin consists of a series of ENE oriented Miocene basins (e.g., the Tainan basin) and horsts resulting from the opening of the South China Sea, associated with NNW-SSE transfer faults. Revisited isobath maps of the top of the pre-Miocene rocks (Figure 12a) emphasize the occurrence of a major horst underlying the Taiwan Strait and the Coastal Plain: the Peikang High (Figure 1). Such a lateral change in basement geometry had a great influence on the geometry and kinematics of the west verging thrust sheets. Analogue modelings [*Lu et al.*, 1998] show that the Peikang High probably acted as a buttress for the west verging thrust units; the authors suggest that this structural high may have partially controlled the tectonic escape in southwestern Taiwan (see section 6.3) but also may have induced transfer zones in the frontal thrust belt. The influence of the basement on development of transfer zones has been highlighted for the Pakuashan Transfer Fault Zone [*Mouthereau et al.*, 1999c]: Detailled analyses have shown that the kinematic evolution of this area was, effectively, mainly controlled by the geometry of the Peikang High, acting as a buttress for the propagating thrusts; the Pakuashan transverse zone accommodated the motion of connected thrust sheets moving over an oblique ramp linked to the hinge fault of the Peikang High.

Immediately north of our study area, the Miocene Tainan basin underwent oblique inversion tectonics during the arc-continent collision, indicating that the basement was involved in collisional shortening [*Mouthereau et al.*, 1999a, b]. The southern limit of this area of basement-involved tectonics roughly corresponds to the Chishan Transfer Fault Zone (Figure 12b). Along this major boundary, probably inherited from the rifting period, an important lateral change of basement depth and thickness of Neogene sediments occurs (Figure 12b). This lateral change in the cover thickness probably localized a primary tear fault which accompanied thrust emplacement; this zone secondarily evolved into a transfer fault zone, on both sides of which largely contrasting styles of deformation occur. Field evidence additionally indicates local left-lateral wrench deformation, consistent with the regional stress field. At a broader scale this major fault zone is delineated by seismic activity and corresponds to the transition from subduction (or incipient collision) to the south to culmination of collision to the north. At the present-day this fault zone consists of a major crustal (lithospheric?) left-lateral wrench boundary, as suggested by earthquake focal mechanisms [*Yeh et al.*, 1991; *Rau and Wu*, 1998].

The Fengshan Transfer Fault Zone is clearly of second order compared with the Chishan Transfer Fault Zone. For this transfer fault zone, a primary tear fault nature can be proposed. Figure 12b shows no important change of Neogene deposit thickness beneath the inferred transfer zone. However, a slight change in basement topography, not visible at the scale of the section of Figure 12b, may have occurred, possibly across an inherited NNW-SSE transfer fault of the Chinese margin: Such a weakness zone in the basement may have localized such a primary tear fault in the cover. In contrast to the CTFZ this primary system has probably evolved poorly: The analysis of small-scale brittle deformation (Figure 9, site 15) suggests an incipient left-lateral component of strike-slip motion; consistent with the regional stress field, but the absence of clear straight signature of the fault zone at the surface and the lack of data do not allow us to draw definite conclusions.

6. Discussion and Conclusions

In this section, we aim at discussing the different possible interpretations concerning the relations in space and time and the genesis of tectonic structures within the outermost Foothills of the southwestern Taiwan belt and at placing the tectonic evolution of this key region within the framework of a lateral evolution from subduction (Manila trench) to oblique collision (prevailing in southern Taiwan).

6.1. Anticlines in Southwestern Taiwan: Tectonic or Diapiric?

Seismic surveys carried out offshore southwestern Taiwan have led to identification of mud diapirs [*Lee*, 1992; *Huang*, 1993; *Chang and Liu*, 1993]. These diapirs appear as elongated ridges running in a NNE-SSW direction, parallel to fold structures, faults, and diapir alignments observed on-land [*Sun and Liu*, 1993; *Liu et al.*, 1997]. These authors relate the diapiric movement to unbalanced loading caused by fast deposition of recent channel deposits along the syncline structures; they propose that faults alongside of the mud diapirs formed first in response to the Pliocene compression and later by the Pleistocene diapiric movement. The rapidly accumulated thick muddy sediments of the subsiding Taiwan foredeep provide a source material for these mud diapirs.

Such a diapiric origin has also been proposed for the on-land anticlines trending NE-SW in southwest Taiwan. As an example, *Wu* [1959] suggests that the lack of seismic reflectivity in the Panpingshan anticline reflects an intrusion of the mudstone of the lower member of the Gutingkeng Formation and concludes that the Panpingshan anticline is a diapiric structure. *Pan* [1968], *Hsieh* [1972] and *Huang* [1995] also consider the on-land Tainan, Chungchou, Panpingshan and Fengshan anticlines as mud diapiric anticlines.

These interpretations of the origin of on-land anticlines, according to which the driving mechanism is mud diapirism, do not account for the striking structural characteristics of the onland anticlines. Offshore, the elongated character of the ridges formed by diapir alignments argues in favor of a tectonic origin with initiation along NE trending folds and thrusts. Onshore, the general asymmetry of west vergent thrust-related anticlines (Figure 5), underlined by location of reefs on the eastern flanks of the folds [*Gong et al.*, 1996; *Lacombe et al.*, 1995, 1997] is difficult to explain through a simple model of mud diapirism, which usually results in more

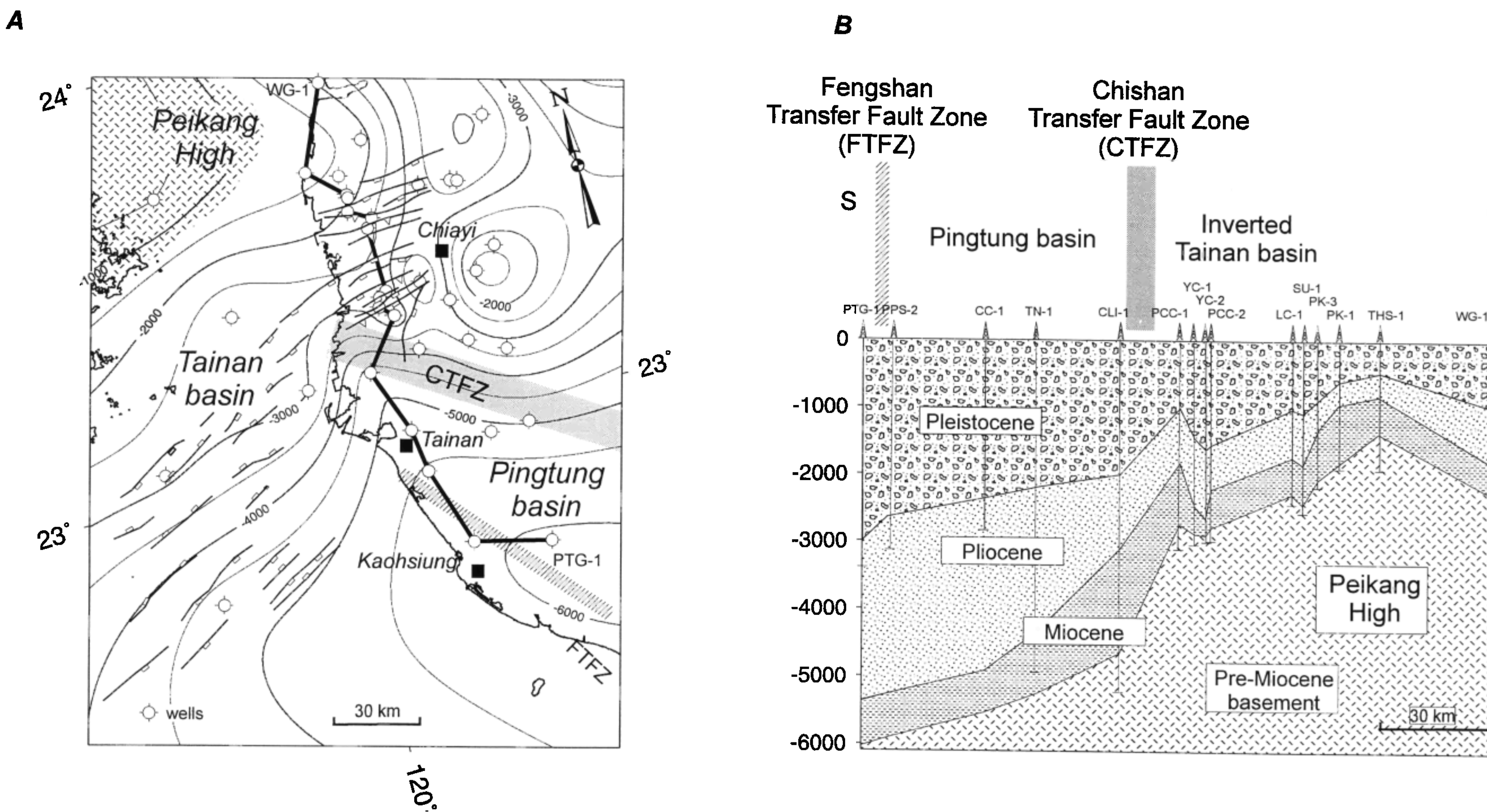

Figure 12. (a) Isobath map of the top of the pre-Miocene basement in southwestern Taiwan, based on correlation between well data [after *Mouthereau et al.*, 1999a, b]. Shaded areas show location of the Chishan and Fengshan Transfer Fault Zones (CTFZ and FTFZ). (b) Along-strike section showing the Neogene basins and highs along the profile connecting the wells of Figure 12a. Note (1) the location of the inverted Tainan basin on the southern edge of the Peikang High, and (2) the important change in basement geometry and Neogene deposit thickness across the CTFZ.

symmetric features. Furthermore, the regional consistency of the tectonic mechanisms and stress orientations identified within the fold structures indicate that onshore and offshore Taiwan the tectonic forces related to the Plio-Pleistocene collision are the major factor controlling structural evolution in this region.

As a consequence, mud diapirism is thought herein to be a second order phenomenon associated with folding and thrusting. Numerous mud volcanoes can be observed along major faults, such as the Gutingkeng and the Lungchuan Faults (Figure 2). This indicates that fluid and mud emergences are guided along major décollement and tectonic contacts, as commonly observed in subduction zones throughout the world (e.g., Barbados ridge [*Screaton et al.*, 1990; *Le Pichon et al.*, 1990; *Lallemant et al.*, 1990], and Nankai accretionary prism [*Henry et al.*, 1989]). Mud diapirism is basically initiated by upward migration of fluids and of fluid-saturated mud material in response to contraction due to thrusting and folding; a second possible step can be the enhancement of diapirism by loading of recent deposits over poorly consolidated muddy sediments [*Liu et al.*, 1997].

6.2. Reef Development in Southwestern Taiwan and Its Relation in Space and Time to Fold-and-Thrust Tectonics and Southward Propagating Collision

Recent papers provided significant results in terms of relationships between the reef limestones and the surrounding formations. *Chen et al.* [1994] demonstrated the conformable contact relationships between the early Pleistocene limestone of Panpingshan and the Gutingkeng Formation. *Gong et al.* [1995, 1996] emphasize some characteristics of these lenticular limestones, which are (1) rapid transition from underlying deep-water siliciclastic mudstones of the Gutingkeng Formation upward to reef limestones, (2) lateral interfingering with deep-water siliciclastics, and (3) no cover or else overlay by only terrestrial deposits, implying emergence above sea level since reef formation. These observations, as well as the close geographical relationship between reefs and anticlines and the results of tectonic analyses carried out within the reef limestones [*Lacombe et al.*,1995, 1997] have led to a model summarized below, which considers that reefs developed on structural highs raised by folding, on top of which decreasing clastic flow induced local favorable paleoecological environment for reef-building organisms.

According to this model, reefs developed on top of folds related to west vergent thrusts under a regional compressional stress. Continuing folding resulting from westward propagating thrusting allowed reef growth. During reef development, local syn folding extension may have occurred nearly perpendicular to fold axis, in response to tensile stresses at the hinge of the anticline. Additionally, an eastward migration of the climax of reef development is likely to have occurred at this stage because of the hinge migration and asymmetry of the fault-propagation fold, as well as some collapse along the eastern flank of the fold. Reefs developed until they reached water level and emerged. At this step, folding progressively slowed down and shortening in the reefs was achieved mainly by strike-slip faulting. Emergence of the reefs was accompanied by karst development (as observed in Takangshan and in Fengshan), marked by local dissolution of the limestones and deposition of red clays within cavities and former fractures.

If this model of tectonically controlled reef development is valid, the reefs are expected to provide time constraints on southwestward thrust migration. The relationship between the age of the reefs and the age of the thrust-related folds on the top of which they developed therefore needs a detailed discussion. The age of the reefs decreases northward, from Kaohsiung (middle NN19) to Panpingshan/ Hsiaokangshan (middle-late NN19) and to Takangshan (late NN19) (ages are after *Chang and Chi* [1983], *Chi* [1989] and *Lee* [1990]). Two hypotheses which may account for this age-spatial relationship are (1) a diachronic fold development from south to north during early Pleistocene times and a correlative thrust activation occurring later to the north (Takangshan and Hsiaokangshan) than to the south (Panpingshan and Kaohsiung), and/or (2) an uplift rate higher to the south than to the north. These hypotheses contradict somewhat the well-established southward migration through time of the Taiwan collision. According to a third hypothesis the age of the reefs may not exactly reflect the age of thrust development because in addition to the fold growth control on reef building, local changes of paleoecological environments in the foreland basin may also have occurred. In this latter case, the Meilin Fault, in relation to which the Takangshan and Panpingshan anticlines probably developed (Figure 2), would have initiated as early as 1 Myr ago, but lateral change in sedimentary conditions and paleoecological environments could have led to a reef development younger from south to north (from Kaohsiung to Takangshan). Sedimentary studies effectively suggest that the Tainan area was an early Pleistocene depocenter in the foreland basin [e.g., *Lin*, 1991]: This means that while sediments prograded the shoreline advanced toward the depocenter [*Gong et al.*, 1996], so that the favorable environmental conditions for reef building migrated with time from Kaohsiung to Takangshan (i.e., northward). This last hypothesis implies that the folds and associated NN19 reefs are accounted for by a single episode of thrust development around 1 Ma and that the time migration of reef development only reflects basin sedimentary dynamics.

Southwestern Taiwan also displays evidence for reef development younger than NN19. The Fengshan limestone and the Shaoshan limestone are dated NN20 (the latter cannot be shown at the scale of Figures 2 and 5). In contrast to the Takangshan, Hsiaokangshan, Panpingshan and Kaohsiung limestones both of them unconformably overlie the underlying formations: The folded Fengshan limestone is in erosional contact with the underlying gray siliciclastic mudstones, dated NN19, equivalent to the lowest member of the Lingkou conglomerates [*Chi*, 1979] (Figure 10a), whereas the non folded Shaoshan limestone unconformably overlies the Kaohsiung limestones and the Chichiao Formation (local equivalent of the upper Gutingkeng Formation, not distinguished in Figure 2). According to the model of reef development related to fault-propagation folds, the Shaoshan and Fengshan limestones probably formed in the same way. We consequently expect an episode of thrust-fold activation during the late Pleistocene, in agreement with the southward migration of the collision proposed by *Suppe* [1984] and in agreement with the two-phase fold development proposed for the Fengshan anticline.

Because of the more eastern location of the Fengshan anticline covered by the reefs with respect to the Kaohsiung area this late Pleistocene reef and fold development requires an out-of-sequence thrusting. A similar hypothesis can be drawn for the Shaoshan limestone which is located on the hanging-wall of the late high-angle reverse fault (the Shaoshan Fault) which cuts the eastern flank of the Panpingshan anticline, south of Kaohsiung (Figure 5, section C-C').

The unconformable overlay of the Kaohsiung limestones by the NN20 Shaoshan limestones, containing blocks of NN19 Kaohsiung limestones [*Sun*, 1963], may be interpreted either as resulting from the development of this reverse fault or in terms of slope-related deposition (talus deposit). The unconformable attitude of the Shaoshan limestones thus does not imply emergence of the Kaohsiung limestones and the Chichiao Formation above sea level and subsequent erosion. However, the unconformable attitude of the NN20 Fengshan limestone on the underlying NN19 mudstones (Figure 10a) needs explanation. As seen earlier, the southern Fengshan area provides evidence of a two-phase fold development, that is, the reactivation and the overthrust of the former Fengshan anticline. This implies that the deformed mudstones and the lower Lingkou conglomerates were (1) first folded and eroded during early Pleistocene times contemporaneously with the formation of the Panpingshan (and Takangshan?) anticlines, then (2) secondarily newly immerged (foreland subsidence of the Pingtung basin or sea level rise?) and (3) refolded, giving rise to reef development in southern Fengshan; this sequence of events may explain the erosional contact between reefs and underlying mudstones.

Summarizing, the age of the reefs in southwestern Taiwan (which ranges from nearly 1 Ma to 0.2 Ma), the location of these reefs on the top of anticlines, and the conformable or unconformable attitude of these reefs with respect to the underlying formations provide convincing evidence for two episodes of folding, during the early and late Pleistocene. However, two tectonic scenarios can be proposed: The first one relates the formation of the Takangshan and Panpingshan anticlines and the early folding in the Fengshan area to the same event, around 1 Ma, with a later reef development to the north in response to lateral variations of depositional environments within the foreland basin. This event would have been followed by out-of-sequence thrusting in southern Fengshan area (and possibly in the Shaoshan area), ~0.5 Myr ago. The second possible scenario relates the formation of the Panpingshan anticline and early folding in Fengshan area to the same event, associated with reef development at nearly 1 Ma; this event was followed by in-sequence thrusting, folding, and reef development in the Takangshan area at ~0.7-0.5 Myr, contemporaneous with out-of-sequence thrusting in southern Fengshan area.

6.3. Quaternary and Present-Day Stress and Strain Patterns and Tectonic Evolution of Southwestern Taiwan: Propagating Collision and Lateral Escape.

The synthesis of paleostress reconstructions carried out in Quaternary formations allows a tentative mapping of Quaternary σ_1 stress patterns in southwestern Taiwan (Figures 13a and 13b). A striking result of our study is that two compressional stress regimes have regionally prevailed. Despite difficulties in separation of data subsets and relative dating, we identified a NW-SE compression followed by a nearly E-W (WNW-ESE to ENE-WSW) compression. The first regime was clearly contractional and associated with the major stage of fold development, whereas the second regime generally prevailed during the latest stages of folding (at least south of the CTFZ) and was associated from north to south with an increasing component of perpendicular N-S extension; the related structures evolving southward from strike-slip and reverse faults north of Tainan (Figure 7) to strike-slip and normal faults in the Takangshan area (Figure 8) and to tension joints and normal faults in the Fengshan area (Figure 9).

These contrasting compressional trends, NW-SE and E-W on average, probably followed each other rapidly during the Pleistocene. They may reflect local changes in the kinematics of thrust units without any really significant change in the N309°E direction of plate convergence during the Pleistocene. This is confirmed by magnetic susceptibility anisotropy analyses which indicate that Quaternary deformation was dominated by an average N100°-110°E recent shortening [*Lee and Angelier*, 1995], nearly parallel to the average of the two Quaternary compressional trends (Figures 13a and 13b). This may indicate that in a setting of average regional N100°-110°E shortening, stresses are sensitive to slight changes in the kinematics of individual thrust sheets. However, relating precisely a given direction of stress to the Quaternary development and the kinematics of a given major structural unit still remains difficult: South of the CTFZ, the NW-SE compression was probably responsible for the major west-northwestward displacement of thrust sheets and related folding, whereas the late E-W compression only accompanied the latest stages of fold evolution and induced a late right-lateral/reverse motion along NNE thrusts. In contrast, north of the CTFZ, the NW-SE compression was not clearly identified, and folding was apparently mainly related to E-W to N100°E shortening (Figure 7).

The present-day kinematics and crustal strain distribution are documented by Global Positioning System data [*Yu and Chen*, 1992; *Yu and Kuo*, 1993; *Yu et al.*, 1995, 1997]. These data suggest that in contrast to the central part of the island where displacements of structural units are presently toward the WNW, the structural units of southwestern Taiwan are moving toward the WSW: This pattern of displacement velocities is illustrated by GPS displacement velocity vectors and trajectories of Figure 13d. This deflection of displacement trajectories has been interpreted in terms of a southwestward incipient tectonic escape in response to the ongoing WNW convergence, by comparison with the "so-called" concept of tectonic escape [*Sengör et al.*, 1985] or tectonic extrusion [*McKenzie*, 1972; *Tapponnier et al.*, 1983; *Ratschbacher et al.*, 1991] which is referred to the lateral motion of structural units toward a free boundary in response to collisional shortening. Analogue modeling experiments [*Lu and Malavieille*, 1994; *Lu et al.*, 1998] suggest that this lateral escape is greatly controlled by the structural inhomogeneity of the Chinese margin: The Peikang High probably acted as a buttress for the advancing thrust units, causing contraction against it and localizing a large dextral transfer zone around the shelf-slope break of the Chinese continental margin, along which the structures to the south were dragged to the southwest. Numerical modeling [*Hu et al.*, 1997] suggests that this escape may be enhanced by the decreasing confinement related to the Manila subduction zone.

Crustal strain orientations and magnitudes deduced from Global Positioning System data effectively indicate an average N110°E trending shortening, as well as a southward increasing magnitude of the perpendicular extension (Figures 13d and 13e, *Yu and Chen* [1996]) which probably reflects the southward escape. Concerning the present-day stress pattern, it is dominated by a N105°E compressional trend (Figure 13c) and is thus in good agreement with the present-day shortening; in this framework, local ENE-WSW oriented σ_{hmax} deduced from borehole breakouts [*Suppe et al.*, 1985] and ENE σ_1 trends deduced from earthquake focal mechanisms [*Yeh et al.*, 1991] (Figure 13c) could be partially interpreted as local stress reorientation at different depths of the present-day compression along NNE thrusts undergoing a right-lateral component of motion, consistent with the tectonic escape.

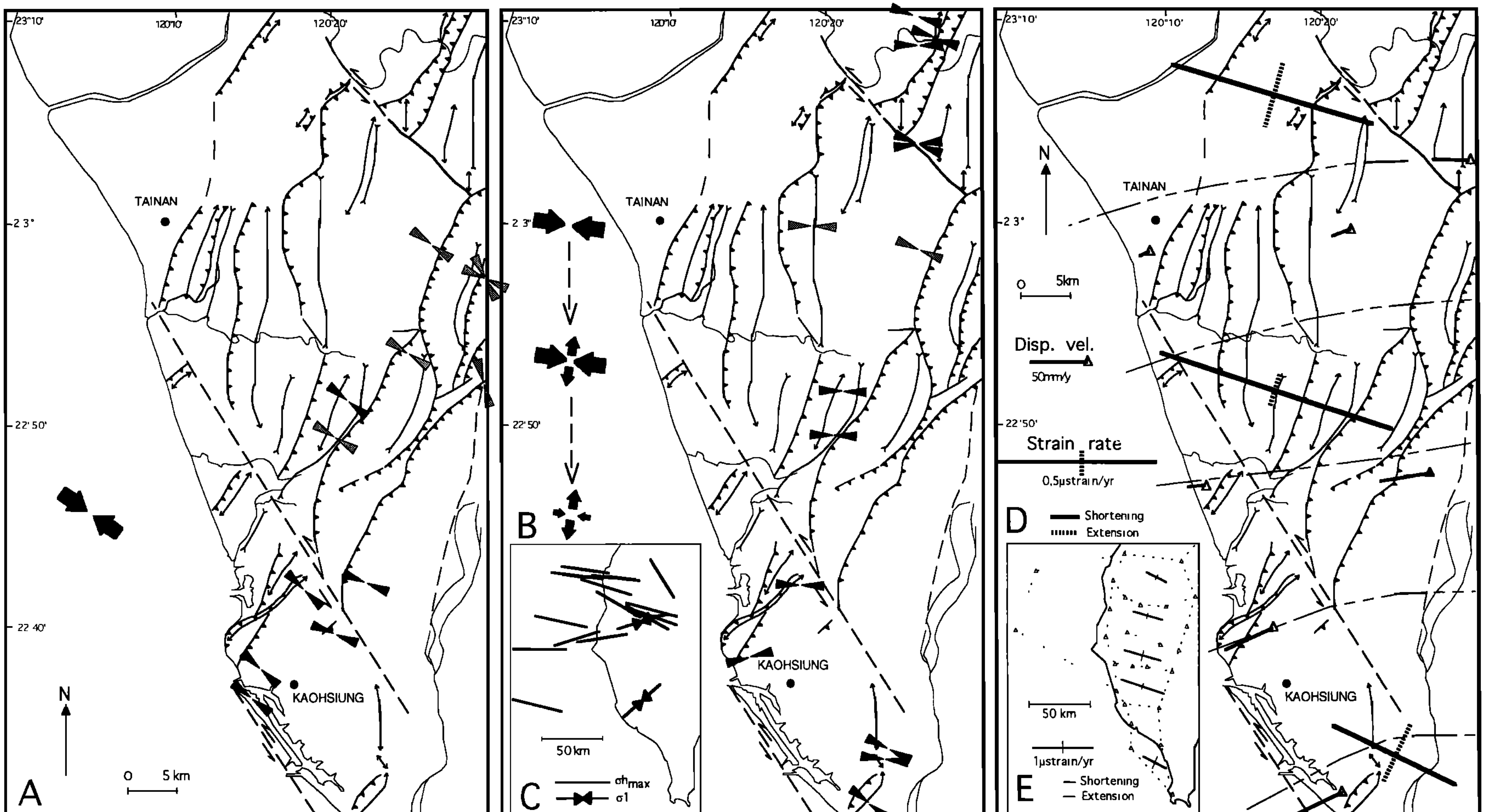

Figure 13. Pleistocene and present-day stress patterns and present-day crustal strain in southwestern Taiwan. Structural framework: same key as in Figure 2. (a) Pleistocene NW-SE compression. Convergent arrows indicate directions of σ_1 (shaded, data after *Rocher et al.*, [1996] and *Mouthereau et al.*, [1998]; solid, this work). The large solid convergent arrows indicate the average regional compression. (b) Late (?) Pleistocene WNW-ESE to E-W compression. Same key is used as in Figure 13a. Note the southward change in the relative stress magnitudes (convergent arrows, compression; divergent arrows, extension) accompanying the regional E-W regional compression. (c) Present-day stress pattern deduced from borehole breakouts (σ_{hmax})[*Suppe et al.*, 1985] and earthquake focal mechanisms (σ_1)[*Yeh et al.*, 1991]. (d) Displacement field and average principal strain rates in the area investigated. Triangles, GPS stations; heavy solid lines connected to triangles, displacement velocity vectors, with length proportional to velocity; dashed lines, extrapolated displacement trajectories from GPS stations. Note the southwestward present-day displacement, suggesting tectonic escape. Heavy lines, strain axes in the area investigated, length proportional to magnitude (see scale). (e) Average principal strain rates within Global Positioning System (GPS) subnets in southwestern Taiwan [*Yu and Chen*, 1996]. Triangles, GPS stations.

Comparison between Quaternary and present-day stress and strain patterns allows discussion of whether or not the kinematics of structural units has recently changed in southwestern Taiwan. It is clear that the E-W to WNW-ESE contraction prevailed both during the late Quaternary and at present-day. Is there evidence for a tectonic escape occurring (or beginning) during the Quaternary, and if so, is there any relation to the identified change in Quaternary stress regimes? The escape should have been accommodated by a Quaternary right-lateral component of motion along the southern edge of the Peikang High [*Lu and Hsü*, 1992; *Lu*, 1994; *Lu et al.*, 1998] and along the NNE trending thrusts on-land. This has been evidenced at the present-day from Global Positioning System data [*Angelier et al.*, 1999], but a clear component of right-lateral motion along on-land NNE thrusts during the Quaternary has never been clearly identified in the field, although suspected offshore southwestern Taiwan [*Liu et al.*, 1997]. The absence of clear signature of the tectonic escape in the on-land Quaternary deformation may be accounted for by a very recent beginning of this escape, which would have not markedly influenced the already existing structural pattern. However, the signature of the onset of tectonic escape may correspond to the change from the NW-SE to the nearly E-W (and locally ENE-WSW to NE-SW) compression, the latter being consistent with (or maybe resulting from) an incipient Quaternary right-lateral component of motion along NNE thrusts. Another possible signature could be the southward increasing occurrence of extensional features related to a nearly N-S Quaternary extension during the latest stage of (or after) fold development that we have documented in this paper. This along-strike change may indicate a southward decrease in N-S confinement, allowing σ_2/σ_1 stress permutations during the late E-W shortening. This is consistent with the present-day southward increase in extensional crustal strain relative to the regional N100°E shortening deduced from Global Positioning System (Figures 13d and 13e).

As a result, our structural and paleostress analyses provide a very efficient tool for deciphering the complex tectonic evolution of southwestern Taiwan: The results are in good agreement with the present-day stress-strain patterns and demonstrate that southwestern Taiwan is undergoing since the Pleistocene both a collisional shortening and an incipient lateral escape.

Acknowledgments. The work was supported by the French Institute of Taipei - National Science Council of Taiwan cooperation framework, by the Central Geological Survey of Taiwan, and by the Institut Français du Pétrole. The authors would like to thank A. Pfiffner and an anonymous reviewer for their constructive comments on the manuscript.

References

Anderson, E. M, The Dynamics of Faulting, 2nd ed., 206 pp, Oliver and Boyd, White Plains, N Y., 1951.

Angelier, J., Tectonic analysis of fault slip data sets, *J Geophys Res*, *89* (B7), 5835-5848, 1984.

Angelier, J, E Barrier, and H T. Chu, Plate collision and paleostress trajectories in a fold-thrust belt The Foothills of Taiwan, *Tectonophysics*, *125*, 161-178, 1986

Angelier, J., S B Yu, J. C. Lee, J C Hu, and H. T. Chu, Active deformation of Taiwan collision zone: Discontinuities in GPS displacement field, paper presented at International Symposium on Subduction and Active collision in SE Asia, 4th Colloquium on Sino-French Cooperation Program in Earth Sciences, *Geol. Soc of France*, Montpellier, 1999.

Apotria, T G, Thrust sheet rotation and out-of-plane strains associated with oblique ramps: An example from the Wyoming salient, USA, *J. Struct. Geol*, 17 (5), 647-662, 1995.

Apotria, T. G., W T. Snedden, J H Spang, and D. V. Wiltchensko, Kinematic models of deformation at an oblique ramp. In *Thrust Tectonics*, edited by K R Mc Clay, pp 141-154, Chapman and Hall, New York, 1992.

Baby, P, M. Specht, J Oller, G. Montemurro, B. Colletta, and J Letouzey, The boomerang Chapare transfer zone (recent oil discovery trend in Bolivia): Structural interpretation and experimental appproach, In *Geodynamic Evolution of Sedimentary Basins*, edited by F. Roure et al, pp 203-222, France, Technip, 1994.

Barrier, E, and J. Angelier, Active collision in eastern Taiwan The Coastal Range, *Tectonophysics*, *125*, 39-72, 1986

Calassou, S, C Larroque, and J. Malavieille, Transfer zones of deformation in thrust wedges: An experimental study, *Tectonophysics*, *221*, 325-344, 1993

Chang, S. S. L, and W R. Chi, Neogene nannoplankton biostratigraphy in Taiwan and the tectonic implications, *Pet Geol Taiwan*, *19*, 93-147, 1983

Chang, C H, and C. S Liu, Mud diapirs in offshore southwestern Taiwan, paper presented at Annual Meeting, Geol Soc of China, Taipei, 1993

Chen, H. W, L C. Wu, and H H Tsien, The contact relationship between the Early Pleistocene Panpingshan Limestone and Gutingkeng Formation in the Kaohsiung area, southern Taiwan (in Chinese), *Cent. Geol Surv Spec Publ.*, *8*, 101-119, 1994

Chi, L. M., Sedimentological study of limestones at southern Shaoshan, Kaohsiung (in chinese) M Thesis, Nat Sun Yat-Sen Univ, Kaohsiung, Taiwan, 1989

Chi, W. R, A biostratigraphic study of the late Neogene sediments in the Kaohsiung area based on calcareous nannofossils, *Proc. Geol. Soc China*, 22, 121-144, 1979.

Chinese Petroleum Corporation (CPC), Geological maps of Kaohsiung and Tainan, scale 1 100000, Taiwan, 1974

Chu, H T, Néotectonique cassante et collision plio-quaternaire à Taiwan, Ph D. Thesis, *Mem Sci Terre, 90-28*, 292 pp, Univ P. et M Curie, Paris, 1990

Deffontaines, B., J. C Lee, J Angelier, J. Carvalho, and J. P Rudant, New geomorphic data on the active Taiwan orogen. A multisource approach, *J. Geophys Res*, *99* (B10), 20,243-20,266, 1994.

Deffontaines, B, O Lacombe, J Angelier, H. T. Chu, F. Mouthereau, C. T Lee, J Deramond, J F. Lee, M S. Yu, and P. M. Liew, Quaternary transfer faulting in Taiwan Foothills: Evidence from a multisource approach, *Tectonophysics*, *274*, 61-82, 1997

Etchecopar, A, Etude des états de contraintes en tectonique cassante et simulation de déformations plastiques (approche mathématique), Ph D Thesis, 270 pp., Univ Sci et Techn du Languedoc, Montpellier, France, 1984

Gong, S Y, T Y Lee, J C Wu, S W Wang, and K M Yang, Possible links between Plio-Pleistocene reef development and thrust migration in the southwestern Taiwan, paper presented at International Conference and 3rd Sino-French Symposium on Active Collision in Taiwan, *Geol Soc of China*, Taipei, March 22-23, 1995

Gong, S Y, T Y Lee, J C Wu, S. W. Wang, and K M Yang, Possible links between the development of Plio-Pleistocene coral reef limestones and thrust migration in southwestern Taiwan, *J Geol Soc China*, *39* (2), 151-166, 1996

Heim, A., and C T Chung, Preliminary observations on the structure of the Kaohsiung limestone mountains, *Pet Geol Taiwan*, *1*, 23-30, 1962.

Henry, P, S Lallemant, X Le Pichon, and S Lallemand, Fluid venting along Japanese trenches Tectonic context and thermal modelling, *Tectonophysics*, *160*, 277-291, 1989

Ho, C S, Geological map of Taiwan, scale 1 500,000, Cent Geol Surv, Minist. of Econ Affairs, Taipei, 1986a

Ho, C S, A synthesis of the geologic evolution of Taiwan, *Tectonophysics*, *125*, 1-16, 1986b

Hsieh, S H, Subsurface geology and gravity anomalies of the Tainan and Chungchou structures of the Coastal Plain of southwestern Taiwan, *Pet. Geol Taiwan*, 10, 323-338, 1972

Hu, J C, J Angelier, and S B. Yu, An interpretation of the active deformation of southern Taiwan based on numerical simulation and GPS studies, *Tectonophysics*, *274*, 145-169, 1997

Huang, W L, Distribution of mud diapirs offshore southwestern Taiwan, their relationships to the onland anticlinal structures and their effects on the deposition environment in southwest Taiwan (in Chinese), M Thesis, Inst. Oceanogr., Nat. Taiwan Univ, Taipei, 1995

Huang, Y L., Analysis of geological structure in offshore southwestern Taiwan (in Chinese), M Thesis, Nat Taiwan University, Taipei ,1993

Huiqi, L, K R McClay, and D Powell, Physical models of thrust wedges In *Thrust Tectonics*, edited by K R McKlay, pp 71-81, Chapman and Hall, New York, 1992

Lacombe, O, J Angelier, and P Laurent, Les macles de la calcite, marqueurs des compressions récentes dans un orogène actif. L'exemple des calcaires récifaux du sud de Taiwan, *C R Acad Sci*, *Ser.II*, *316*, 1805-1813, 1993

Lacombe, O., J Angelier, M Rocher, H W Chen, H T Chu, B. Deffontaines, J C Hu, and J. C. Lee, Calcite twin analysis A key to the recent stress fields at the front of the Taiwan Collision belt, paper presented at International Conference and 3rd Sino-French Symposium on Active Collision in Taiwan, *Geol Soc of China*, Taipei, March 22-23, 1995

Lacombe, O, J Angelier, H W Chen, B Deffontaines, H T Chu, and M Rocher, Syndepositional tectonics and extension-compression relationships at the front of the Taiwan collision belt: A case study in the Pleistocene reefal limestones near Kaohsiung, SW Taiwan, *Tectonophysics, 274,* 83-96, 1997

Lallemant, S., P Henry, X. Le Pichon, and J P Foucher, Detailed structure and possible fluid paths at the toe of the Barbados accretionary wedge (ODP Leg 110), *Geology, 18,* 854-857, 1990

Laurent, P., Les macles de la calcite en tectonique· Nouvelles méthodes dynamiques et premières applications, Ph D Thesis, 324 pp, Univ Sci. et Techn. du Languedoc, Montpellier, France, 1984.

Lee, J C, Structure et déformation active d'un orogène Taiwan, Ph D Thesis, *Mem Sc Terre, 94-10,* 281 pp, Univ P et M Curie, 1994

Lee, T Q and J Angelier, Analysis of magnetic susceptibility anisotropy of the sedimentary sequences in southwestern Foothills of Taiwan and its tectonic implications, paper presented at International Conference and 3rd Sino-French Symposium on Active Collision in Taiwan, *Geol Soc of China,* Taipei, March 22-23, 1995

Lee, T Y., Cenozoic plate reconstruction of southeast Asia and sequence stratigraphy and tectonics in the Tainan basin, offshore southwestern Taiwan, PhD Thesis, 240 pp, Univ of Texas at Austin, 1992.

Lee, T. Y, Y. Y Hsu, and C H Tang, Structural geometry of the deformation front between 22°N and 23°N and migration of the Penghu Canyon, offshore Southwestern Taiwan Arc-continent Collision Zone, paper presented at International Conference and 3rd Sino-French Symposium on Active Collision in Taiwan, *Geol. Soc. of China,* Taipei, March 22-23, 1995.

Lee, Y H, Nannobiostratigraphy, age correlation and paleoenvironments of the limestones in Kaohsiung area (in Chinese), M Thesis, Nat Sun Yat-Sen Univ, Kaohsiung, Taiwan, 1990

Le Pichon, X, P Henry, and S Lallemant, Water flow in the Barbados accretionary complex, *J Geophys Res., 95* (B6), 8945-8967, 1990.

Lin, D S, Lithofacies and the sedimentary environment evolution of the Plio-Pleistocene series in the southwestern Taiwan Foothills region, M. Thesis, 93 pp., Nat. Taiwan Univ., Taipei, 1991.

Liu, C. S., I L. Huang, and L. S. Teng, Structural features off southwestern Taiwan, *Mar. Geol, 137,* 305-319, 1997

Lu, C. Y, Neotectonics in the foreland thrust belt of Taiwan, *Pet. Geol. Taiwan, 29,* 1-26, 1994

Lu, C. Y, and K. J Hsu, Tectonic evolution of the Taiwan Mountain belt, *Pet Geol. Taiwan, 27,* 21-46, 1992

Lu, C Y., and J. Malavieille, Oblique convergence, indentation and rotation tectonics in the Taiwan Mountain belt Insights from experimental modeling, *Earth Planet. Sci Lett., 121,* 477-494, 1994

Lu, C Y, F. S Jeng, K J Chang, and W. T Jian, Impact of basement high on the structure and kinematics of the western Taiwan thrust wedge : insights from sandbox models, *Ter. Atm Oc., 9* (3), 533-550, 1998.

McKenzie, D., Active tectonics of Mediterranean region, *Geophys. J.R Astron. Soc, 30* (2), 109-185, 1972.

Mouthereau, F., J Angelier, B. Deffontaines, O Lacombe, H T. Chu, B. Colletta, J. Déramond, M S Yu, and J F Lee, Cinématique actuelle et récente du front de chaîne de Taiwan, *C R Acad Sci, Ser II, 323,* 713-719, 1996

Mouthereau, F., J Angelier, B Deffontaines, S. Brusset, O Lacombe, H T Chu, and J Deramond, Folds and fault kinematics and tectonic evolution of the southwestern thrust belt of onshore Taiwan, paper presented at Annual Meeting, Geol Soc. of China, Chungli, Taiwan, March 20-21, 1998

Mouthereau, F, B Deffontaines, O. Lacombe, and J Angelier, Basement control on structural style, wedge geometry and kinematics at the front of the Taiwan mountain belt, paper presented at International Conference on Thrust Tectonics, *Royal Holloway Univ. of London,* April 26-29, 1999a.

Mouthereau, F., B Deffontaines, O. Lacombe, and J. Angelier, Along-strike variations of the Taiwan belt front: Basement control on structural style, wedge geometry and kinematics, *Geol. Soc Am Spec. Pub,* 1999b (in press).

Mouthereau, F, O Lacombe, B. Deffontaines, J Angelier, H T. Chu, and C. T Lee, Quaternary transfer faulting and belt front deformation at Pakuashan (western Taiwan), *Tectonics, 18,* (2), 215-230, 1999c

Pan, Y. S., Interpretation and seismic coordination of the Bouguer gravity anomalies obtained in southern Taiwan, *Pet. Geol Taiwan, 6,* 197-207, 1968.

Philippe, Y, Transfer zone in the southern Jura thrust belt (eastern France) Geometry, development and comparison with analogue modeling experiments, In *Hydrocarbon and Petroleum Geology of France,* edited by A Mascle, *EAPG Spec. Publ. 4,* 327-346, 1994

Ratschbacher, L., W Frisch, H. G Linzer, and O Merle, Lateral extrusion in the Eastern Alps, 2, Structural analysis, *Tectonics, 10* (2), 245-256, 1991

Rau, R J, and F T. Wu, Active tectonics of Taiwan orogeny from focal mechanisms of small-to-moderate-sized earthquakes, *Ter Atm Oc., 9* (4), 755-778, 1998

Rocher, M, O Lacombe, J Angelier, and H. W. Chen, Mechanical twin sets in calcite as markers of recent collisional events in a fold-and-thrust belt: Evidence from the reefal limestones of southwestern Taiwan, *Tectonics, 15* (5), 984-996, 1996

Screaton, E. J, D. R. Wuthrich, and S. J. Dreiss, Permeabilities, fluid pressures, and flow rates in the Barbados Ridge Complex, *J Geophys Res., 95,* 8997-9007, 1990

Sengör, A. M. C., N. Görür, and F. Saroglu, Strike-slip faulting and related basin formation in zones of tectonic escape: Turkey as a case study, *SEPM Spec. Publ., 37,* 227-264, 1985

Sun, S. C., The reef limestones and the geologic structures in the vicinity of Kaohsiung City, Taiwan, *Pet. Geol. Taiwan, 2,* 47-64, 1963

Sun, S C., Photogeologic Study of the Tainan-Kaohsiung Coastal Plain Area, Taiwan, *Pet. Geol. Taiwan, 3,* 39-51, 1964.

Sun, S. C. and C S Liu, Mud diapirs and submarine channel deposits in offshore Kaohsiung-Hengchun, southwest Taiwan, *Pet. Geol Taiwan, 28,* 1-14, 1993

Suppe, J, Kinematics of arc-continent collision, flipping of subduction, and back-arc spreading near Taiwan, *Mem Geol. Soc of China., 4,* 67-90, 1984

Suppe, J, C. T Hu, and Y J Chen, Present-day stress directions in western Taiwan inferred from borehole elongation, *Petr. Geol Taiwan, 21,* 1-12, 1985.

Tapponnier, P., A. Peltzer, Y Le Dain, R Armijo, and P Cobbold, Propagating extrusion tectonics in Asia new insights from simple experiments with plasticine, *Geology, 10,* 611-616, 1983

Teng, L. S, Geotectonic evolution of late Cenozoic arc-continent collision in Taiwan. *Tectonophysics, 183,* 57-76, 1990

Wu, C. S., Final report on seismic survey conducted on the Kaohsiung prospect, Taiwan, Int. Rep Chinese Petroleum Corporation, 1959.

Wu, F., R J Rau, and D. Salzberg, Taiwan orogeny: Thin-skinned or lithospheric collision?, *Tectonophysics, 274,* 191-200, 1997

Yeh, Y. H, E. Barrier, and J Angelier, Stress tensor analysis in the Taiwan area from focal mechanisms of earthquakes: *Tectonophysics, 200,* 267-280, 1991

Yu, S. B and H. Y. Chen, A global positioning system network for crustal deformation study in Taiwan, *Bull. Inst Earth Sci Acad Sinica, 12,* 52-55, 1992.

Yu, S B. and H Y. Chen, Spatial variation of crustal strain in the Taiwan area, paper presented at 6th Taiwanese Geophysical Meeting, *Univ. Chiayi,* Chiayi, November 1996

Yu, S B., and L. C. Kuo, Utilizing continuous GPS data for study the crustal deformation in Taiwan, *Bull Inst. Earth Sci. Acad. Sinica, 13,* 77-82, 1993.

Yu, S. B., H. Y. Chen, and L. C. Kuo, Velocity field of GPS stations in the Taiwan area, paper presented at International Conference and 3rd Sino-French Symposium on Active Collision in Taiwan, *Geol. Soc of China,* Taipei, March 22-23, 1995

Yu, S. B., H Y. Chen, and L. C Kuo, Velocity field of GPS stations in the Taiwan area, *Tectonophysics, 274,* 41-59, 1997.

J. Angelier, B. Deffontaines, O Lacombe, and F. Mouthereau, Département de Géotectonique, Université Pierre et Marie Curie, T26-25, E1, Boîte 129, 4 place Jussieu, 75252 Paris Cedex 05, France. (olivier.lacombe@lgs jussieu fr)

H T. Chu, Central Geological Survey, MOEA, P.O. Box 968, Taipei, Taiwan (chuht@linx.moeacgs.gov.tw)

C T. Lee, Institute of Applied Geology, National Central University, Chungli, Taiwan. (ct@gis geo.ncu.edu.tw)

(Received December 10, 1998,
revised May 6, 1999,
accepted May 27, 1999.)

TECTONICS, VOL. 18, NO. 6, PAGES 1139-1153 DECEMBER 1999

Rheology predictions across the western Carpathians, Bohemian massif, and the Pannonian basin: Implications for tectonic scenarios

Anco Lankreijer,[1] Miroslav Bielik,[2] Sierd Cloetingh,[1] and Dušan Majcin[2]

Abstract. On the basis of extrapolation of failure criteria, lithology, and temperature models, we predict the rheology of the lithosphere for several sections through the Carpathians and surrounding regions. Our models show significant lateral variations in rheology for the different tectonic units, with important implications for the tectonic evolution. The rheologically strong lithosphere of the Polish Platform area contrasts with the weak lithosphere of the Pannonian basin, indicating that the arcuate shape of the Carpathian orogen is primarily caused by an inherited curvature of an ancient embayment in the foreland, with the Pannonian units passively filling the space. The Polish Platform and the Moesian Platform exhibit a similar rheological anisotropy caused by NW-SE trending weakness zones paralleling the Tornquist - Teisseyre zone. This anisotropy was the main controlling factor on the behavior of the lithosphere in this area since Cadomian times, as documented by the geological evolution of the Sudety Mountains and the Mesozoic Polish Trough, including the Late Cretaceous Alpine inversion and the Neogene development of the Carpathian foreland. This rheological anisotropy appears to have a major controlling impact on the development of at least the eastern part of the European lithosphere. Rheology predictions for the Bohemian massif support the idea that the rigid lithosphere of the Bohemian massif governed the bending of the Alpine-Carpathian transition zone, expressed in the large-scale wrench movements opening the Vienna basin. In the foreland area, detachment levels are predicted for upper and lower crustal levels, leading to a decoupling of crustal and subcrustal flexure in most areas. Comparison with basin formation models indicates that our predictions for effective elastic thickness (EET) are similar to those derived from flexural models for the foreland area. Also, EET predictions from extensional basin models in the Pannonian region yield values close to our findings.

1. Introduction

The Carpatho-Pannonian region provides a key area to study the influence of different parameters on the rheology of the lithosphere. In a relatively small area, many different thermotectonic units occur. Many extensional basins characterize the young and hot Pannonian lithosphere, whereas the young Carpathian-thickened crust shows mainly strike slip related basins. The thermotectonically old lithosphere underlying the foreland area on the Bohemian massif and the European platform area form a sharp rheological contrast to the former two lithospheric units.

Furthermore, the abundance of geophysical data such as deep seismic reflection profiles, gravity surveys, and surface heat flow data provide valuable constraints on tectonic models of the area. To this purpose, we selected two profiles. The westernmost profile is based on the Deep Seismic Section VI (DSS VI) [*Beránek and Zátopek,* 1981], running WNW-ESE, starting in the Czech Republic, crossing the Bohemian massif, the Vienna basin, and the Malé Karpaty Mountains, and ending in the Danube basin (NW Pannonian basin) (Figure 1). The eastern profile, which includes deep seismic line 2T [*Tomek et al.,* 1989], starts on the Polish Platform, crosses the foreland basin and the western Carpathians, and ends in the Pannonian basin (Figure 1).

Finally, the inferences from many generations of numerical basin models for both the foreland and the extensional hinterland area provide independent constraints on lithospheric rheology. Lateral and temporal changes in lithosphere rheology have been documented to have pronounced effects on lithosphere dynamics [*Lankreijer et al.,* 1997; *Sachsenhofer et al.,* 1997]. Therefore rheological constraints on the proposed geodynamic models for the area are important.

Several authors [*Burov and Diament,* 1995; *Ranalli and Murphy,* 1987] have documented the methods for calculating lithospheric rheology during the last few years. Incorporating rheology predictions into tectonic models has yielded important constraints on those models [*Bassi,* 1995; *Buck,* 1991]. Incorporating lithosphere rheology into regional geodynamic and tectonic studies has only recently started [*Cloetingh and Banda,* 1992; *van Wees and Cloetingh,* 1996]. This approach allows a better quantitative understanding of the role of the lithosphere in tectonic processes such as basin formation and continental collision. We use a fully two-dimensional approach to predict rheology along selected lithospheric profiles, thus allowing a detailed study on the nature of variations in rheology across different tectonic units. Our approach predicts effective elastic thickness (EET) variations and detachment levels in the lithosphere, which are validated by comparison with EET estimates derived from other tectonic modeling techniques and which can be compared to interpretations of deep reflection seismic sections.

[1]Faculty of Earth Sciences, Vrije Universiteit, Amsterdam.
[2]Geophysical Institute, Slovak Academy of Sciences, Bratislava, Slovakia.

Paper number 1999TC900023.
0278-7407/99/1999TC900023$12.00

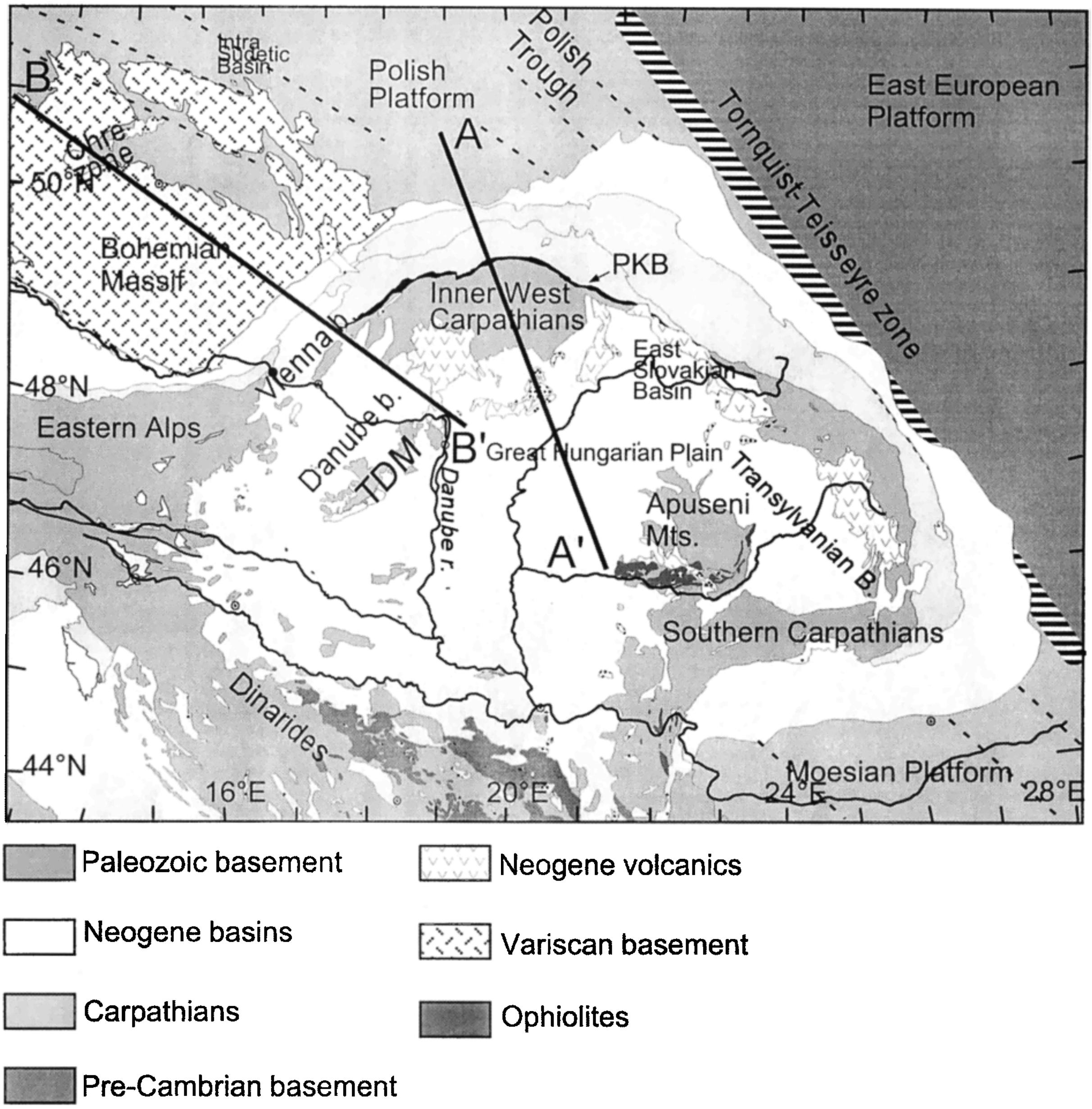

Figure 1. Tectonic map of central Europe. Solid lines show the location of the lithospheric crosssections A-A' and B-B'. TDM, Trans-Danubian Mountain Range; PKB, Pieniny Klippen belt.

2. Tectonic setting

The study area (Figure 1) allows the study of many different tectonic units in close spatial distribution. Tectonic units of different thermotectonic age, lithologic stratification, and crustal and lithospheric thicknesses cause significant variations in rheology with important implications for the tectonic behavior of each unit.

2.1. Bohemian Massif

The Bohemian massif (Figure 1) forms a Variscan and possibly Cadomian core [*Zoubek and Malkovský,* 1974], with an Alpine overprint, resulting in a cold and thickened crust. Surface heat flow values are typically low on the Bohemian massif (45 - 60 mW m^{-2}), especially in the Moldanubian unit.

The Bohemian massif appears to have played an important role in the bending of the Alpine-Carpathian junction and the associated strike-slip motions which opened the Vienna basin [*Royden,* 1988]. The rigidity of the Bohemian massif has a pronounced effect on the width of the foreland basin. Crustal-scale NE-SW strike slip faults of Hercynian age characterize the Saxothuringian part of the Bohemian massif and form major terrane boundaries [*Maheľ and Malkovský,* 1984]. NW-SE trending faults are mainly found in the central Bohemian massif [*Franke et al.,* 1993]. Tertiary reverse movements along the NW-SE trending Franconian lineament are evidenced from fission-track analyses of the German Kontinentales Tiefbohrungsprogramm (KTB) borehole [*Coyle et al.*, 1997]. Quaternary faulting has been observed in the Bohemian massif (Diendorf Fault) [*Hejl et al.*, 1997].

2.2. Polish Platform

The Polish Platform is of Precambrian age [*Znosko*, 1974]. Crustal-scale NW-SE strike-slip zones (Elbe-Hamburg fracture zone, Odra Fracture zone, Main Intra-Sudetic fault, and Lusatian main fault), parallel to the Tornquist-Teisseyre zone crosscut the Polish foreland. A similar set of NW-SE trending shear zones can be observed in the Moessian platform. These weakness zones create a large-scale anisotropic fabric, governing the rheologic behavior of the Polish platform through time. The Polish foreland shows low surface heat flow values and intermediate crustal and lithospheric thicknesses. The Polish Platform is characterized by low surface heat flow values (~ 60 mW m^{-2}). Foreland basin modeling [*Zoetemeijer et al.*, 1999] predicts values for the effective elastic thickness (EET) in the order of 15 km, to explain the bending of the lithosphere along the western Carpathian foreland.

2.3. Western Carpathians

The western Carpathians are the northernmost spur of the central European Alpides. The formation of its structure was influenced by complex processes such as convergence, lateral displacement, collision suturing, accretion, and transpression - transtension [e.g., *Andrusov*, 1968; *Plašienka*, 1997; *Soták*, 1992]. The fundamental feature of the western Carpathians is their nappe structure [e.g., *Mahel'*, 1974; *Sandulescu*, 1994; *Sandulescu and Bercia*, 1974]. The western Carpathian lithosphere has been thermotectonical rejuvenated during the volcanic episodes associated with the Carpathian convergence (22-15 Ma). The mean value of surface heat flow in the central western Carpathians amounts to 60 - 70 mW m^{-2}. However, the heat flow density in the Neogene Danube basin is noticeably higher (70 - 80 mW m^{-2})[*Bodri*, 1981; *Čermák*, 1994].

2.4. Pannonian Basin

The Pannonian basin is a young basin (17-10 Ma), with associated high surface heat flow values (85 - 95 mW m^{-2}). Numerical basin models for the Pannonian basin predict low values for the EET of the order of 5-7 km [*Lankreijer et al.*, 1995; *van Balen and Cloetingh*, 1995]. Earthquake focal depths are limited to the upper 6 km of the crust of the Pannonian basin [*Horváth and Cloetingh*, 1996], supporting this thin upper crustal strong layer. The thickness of the Neogene fill in the Pannonian basin amounts to 9 km in the deepest troughs, but on average, the Neogene sequences are only 2-3 km thick. Lithospheric and crustal thickness maps [*Horváth*, 1988; 1993; *Szafian*, 1999] show a close spatial coupling between thinned crust and the main depocenters in the Neogene Pannonian basin. The lithosphere in the Pannonian area is extremely thin (60 km), giving rise to very high crustal temperature in the region [*Dövényi and Horváth*, 1988; *Lenkey*, 1999]. Crustal thickness amounts to 25-28 km [*Kilènyi et al.*, 1989; *Lillie et al.*, 1994]. Neogene core-complex style deformation along the western margin of the Pannonian basin [*Tari*, 1993] indicates a weak lower part of the crust in these areas during Neogene deformation [*Sachsenhofer et al.*, 1997].

2.5. Vienna Basin

The Vienna basin is a Neogene extensional pull-apart basin located on top of Alpine-Carpathian thrustsheets. Large-scale sinistral strike-slip faults decouple the basin from the surrounding lithosphere. The discussion on the penetration depth of the basin-bounding faults is still going on [*Lankreijer et al.*, 1995; *Royden*, 1985; *Wessely*, 1992].

The Vienna basin opened during Karpatian / early Badenian times (17.5 - 15.5 Ma) and shows a passive postrift subsidence since Sarmatian (14 Ma) times. Changes in the paleostress field, in Pannonian and Pliocene times, are documented by microtectonic fabric analyses [*Bada*, 1999; *Decker and Peresson*, 1996; *Fodor et al.*, 1999].

Paleogeography of the basin [*Seifert*, 1992] indicates an isostatic compensation, where the basin is decoupled along the master faults. A flexural response to loading of the basin [*Watts et al.*, 1982] predicts a general widening of the basin. The paleogeography of the Vienna basin [*Seifert*, 1992] shows a stable position of the paleocoastline through time. Measured surface heat flow values in the basin are relatively low (50 - 60 mW m^{-2}) [*Dövényi and Horváth*, 1988], but this could be due to the effect of blanketing by the sediment pile, which is in places more than 6 km thick.

Many different tectonic models have been proposed for the Carpatho-Pannonian area [*Csontos et al.*, 1992; *Ratschbacher et al.*, 1991a, b; *Royden*, 1988; *Soták*, 1992; *Tari et al.*, 1992]. It is clear that around 20 Ma several microplates filled the space inside the Carpathian arc. Collision ceased diachronously along the Carpathian belt between 22 Ma (in the west) and 5- 0 Ma (in the southern Carpathians). After 17 Ma, extension started in the Pannonian basin system, thinning the crust in general with a factor 1.6 and extending the

Table 1. Thermal Parameters

Parameter	Value
Thermal base depth, km	250
Depth increment, m	1000
Surface temperature, °C	0
Temperature at base of the plate (mantle melt temperature), °C	1300

Thickness, km	Density, kg m^{-3}	Conductivity, W m^{-1} K^{-1}	Capacity, J kg^{-1} K^{-1}	Heat Production, W m^{-3}	Skindepth, km
Upper crust	2650	2.5	1136	2.00×10^{-6}	10
Lower crust	2900	2.0	1029	0.50×10^{-6}	0
Mantle	3300	3.5	1212	0.0	0

Table 2a. General Properties Used for Rheology Models

Definition	Parameter	Value
Acceleration of gravity, m s^{-2}	g	9.81
Universal gas constant, J mol K^{-1}	R	8.314
Surface heat flux, W m^{-2}	q_s	30-100
Temperature base lithosphere, °C	T_m	1300
Static friction coefficient	f_s	0.6
Strain rate, s^{-1}	$\dot{\varepsilon}$	10^{-15}
Hydrostatic pore fluid factor (ρ_w/ρ)	λ	≈0.35

subcrustal lithosphere by a much higher factor [*Lankreijer et al.*, 1995; *Lenkey*, 1999; *Royden and Dövenyi*, 1988].

3. Method

A dependence of rock strength on temperature and pressure has been demonstrated by laboratory experiments [e.g., *Goetze and Evans*, 1979; *Ranalli and Murphy*, 1987]. In the upper region of the mechanically strong part of the lithosphere, rheology is generally governed by brittle failure (Byerlee's law). At temperatures exceeding roughly half the melting temperature of rock, ductile creep processes become the dominant deformation mechanism [*Carter and Tsenn*, 1987]. Therefore the strength in the lower part of the lithosphere and the lower parts of the Earth's crust is mainly governed by the temperature distribution. *Ord and Hobbs* [1989] argue that there must be a breakdown stress for Byerlee's brittle failure law. They infer a value of ~ 260 MPa for this breakdown stress.

Extrapolation of flow laws and laboratory failure criteria [*Brace and Kohlstedt*, 1980; *Byerlee*, 1978], adopting estimates for tectonic strainrates and thermal gradients, provides a firs-order description for the strength distribution within the lithosphere. For each depth interval, strengths for both brittle and ductile deformation are calculated (taking into account the brittle failure breakdown stress), with the lesser of these representing the limiting strength (yield strength) of the lithosphere at that particular depth interval [e.g., *Beekman*, 1994; *Burov and Diament*, 1995; *Cloetingh and Burov*, 1996; *Ranalli*, 1995]. Critical input data for the prediction of lithospheric strength are crustal composition and thermal structure of the lithosphere (Table 1).

Furthermore, predictions of lithospheric strength are strongly influenced by the adopted strain rate. We adopted a bulk lithospheric strain rate for our calculations of $\dot{\varepsilon} = 10^{-15}$ s^{-1}, which is commonly observed in extensional and compressional settings [*Carter and Tsenn*, 1987; *Okaya et al.*, 1996]. Observations on strain rates indicate a range of 10^{-17} s^{-1} $< \dot{\varepsilon} < 10^{-12}$ s^{-1} [*Carter and Tsenn*, 1987; *van den Beukel*, 1990]. Faster strain rates produce greater predicted strengths. Strain rates are typically assessed within the accuracy of an order of magnitude. Such uncertainties in estimation change the predicted lithospheric strength by no more than 10%.

Although the construction of lithospheric strength profiles invokes a number of intrinsic uncertainties, the results of many recent studies support the extrapolation of microphysical models from a laboratory scale to a lithosphere scale [e.g., *Burov and Diament*, 1995; *Cloetingh and Banda*, 1992; *Lankreijer et al.*, 1997; *Ranalli and Murphy*, 1987]. Furthermore, hydraulic fracture tests in the KTB borehole (SW Germany) demonstrate that such an extrapolation is valid for the tested interval (4-6 km) [*Zoback et al.*, 1993a].

We adopted a five-layer rheologic model for the lithosphere along our profiles, consisting of a sedimentary layer (where present), a quartzite layer (representing superficial sedimentary nappes, i.e., Tatric nappe), a granite layer (representing the upper crust), a diorite layer (for the lower crust), and a dunite layer representing the lithospheric mantle. Mantle xenolites indicate a mantle composition beneath the study area consisting of Lherzolite and Habsburgite [*Downes and Vaselli*, 1995]. Tables 2a and 2b summarize the material properties for the adopted lithologies. We adopted a wet rheology for these lithologies, since most recent studies support "wet" rheology rather than the stronger "dry" variant [*Beekman et al.*, 1994; *Cloetingh and Burov*, 1996; *Lankreijer et al.*, 1997].

3.1. Temperature Model

A lithology model, based on gravity and geological interpretation of deep reflection seismic [*Bielik et al.*, 1995; *Tomek et al.*, 1987] served as a base for assigning thermal properties to individual blocks in a model of the lithosphere [*Kutas et al.*, 1989; *Majcin*, 1993]. The temperature distribution was calculated following *Kutas et al.* [1989] and *Majcin and Tsvyashcheko* [1994].

The stationary component of the temperature field is determined as a result of both the effect of heat sources and of background heat flow density from the lower mantle. A second component of the thermal field corresponds to thermotectonic rejuvenation of the area [*Čech*, 1988; *Horváth et al.*, 1989; *Jiříček*, 1979; *Kováč et al.*, 1993].

Table 2b. Material Properties used in Rheology Models

	Upper Crust		Lower Crust		Mantle	
	Granite Dry	Granite Wet	Diabase Dry	Diorite Wet	Dunite Dry	Dunite Wet
Density (ρ), kg m^{-3}	2700	2700	2900	2900	3300	3300
Young's modulus (E), Gpa	50	50	70	90	70	70
Poisson's ratio (ν)	0.25	0.25	0.25	0.25	0.25	0.25
Power law exponent (n)	3.3	1.9	3.05	2.4	4.5	3.6
Power law activation energy (E_p), kJ mol^{-1}	186	140	276	212	535	498
Pre-exponential constant (power law) (A_p), Pa^{-N} s^{-1}	3.16×10^{-26}	7.94×10^{-16}	6.31×10^{-20}	1.26×10^{-16}	7.94×10^{-18}	3.98×10^{-25}

The brittle failure Function is $\sigma_{brittle} = \alpha\rho g z\,(1-\lambda)$, where $\alpha = R-1/R$ for normal faulting, R-1 for thrust faulting, and $(R-1)/[1+\beta(R-1)]$ for strike-slip faulting and $R = [(1+f_s^2)^{1/2} - f_s]^{-2}$. The power law creep function used is $\sigma_{creep} = (\dot{\varepsilon} / A_p)^{1/n} \exp[E_p / nRT]$. after *Carter and Tsenn* [1987] and *Goetze and Evans* [1979]

Table 3. Comparison Between Tectonics Units

Tectonic Unit	HF, mW m^{-2}	EET, km	Thermo Tectonic Age, Ma	Bouguer, mGal
Bohemian Massif (core)	45-50	20-40	660-550	-10 - 20
Bohemian Massif (Tepla-Barrandian)	55-60	8-12	320-260	-20 - 10
Foreland area (Polish Platform)	50-60	7-8	320-260	0 - 20
Vienna Basin	50-60	18-22*	17-15	-40 - 0
Pannonian basin	70-100	5-10	17-14	-40 - 20
West Carpathians	60-70	15-23	22-7	-50 - 0

HF, Heat flow; EET, effective elastic thickness.

* note that the measured heatflow for the Vienna basin reflects the surface heatflow only. The thick sedimentary fill of the basin isolates the basement; therefore thermal and rheological predictions yield estimates that are too cold, i.e., too strong.

The reliability of a temperature model depends mainly on the accuracy and density of measurements of heat flow density in the surroundings of the profile [*Hurtig et al.*, 1992]. The reliability of the temperature model was further increased by fitting the lithosphere thickness along the profile to seismic data [*Babuška et al.*, 1988]. Therefore the relative inaccuracy is not in excess of 10%. Temperature calculations for the Bohemian massif [*Čermák*, 1994], yield values very close to ours. Differences are mainly in temperature predictions for the deepest parts of the model (>150 km), where the effect on rheology is minimal.

3.2. Gravity Model

Gravity modeling along section A-A' was performed using the GM-SYS™ programs of Northwest Geophysical Associates, Inc. Thicknesses of the Pannonian basin sediments are derived from the maps of *Kilényi et al.* [1991]. The thickness of the sediments in the Carpathian foreland and the thickness of Tatricum are taken from deep seismic profile 2T [*Tomek et al.*, 1987; 1989]. Depths of the upper to lower crust boundary are deduced from *Bielik et al.* [1990]. Depths to the Moho and lithosphere / asthenosphere boundary were taken from *Horváth* [*1993*] and *Babuška et al.* [1988], respectively. Density contrasts of the different bodies are similar to those of *Lillie et al.* [1994], *Szafián et al.* [1997] and *Szafian* [1999].

For calculation of the gravimetric model along section B-B', the method of *Talwani* [1973] was used. Density contrasts for the anomalous bodies are relative to the reference model defined by *Bielik et al.* [1994]. The interpretation was based

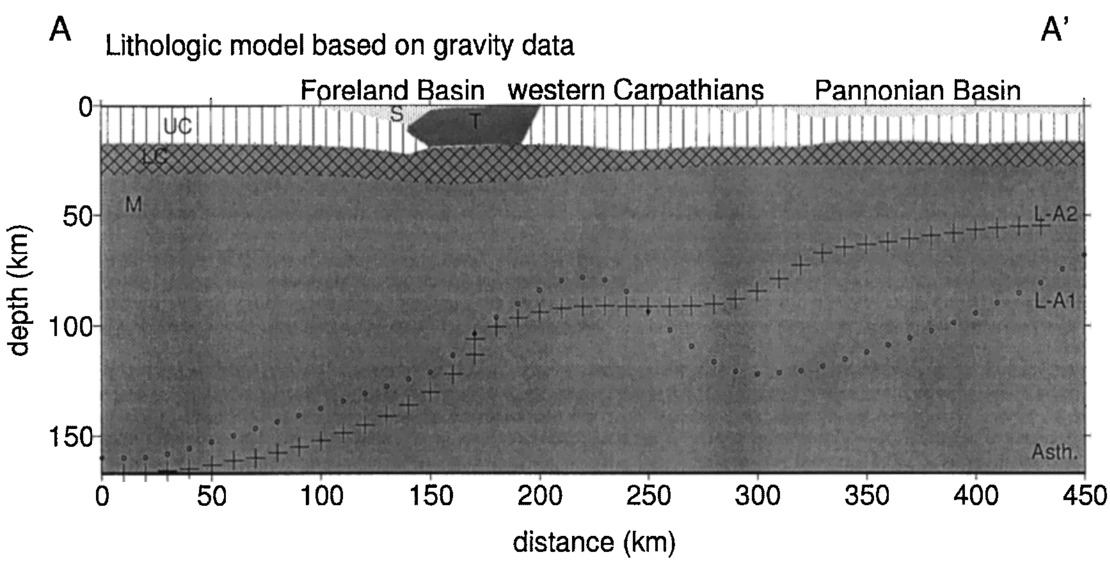

Figure 2. Lithospheric crosssection A-A' through the western Carpathians (For location, see Figure 1.). Lithologic differentiation is based on gravity modelling [*Bielik et al.*, 1994]. Lithologic units as used for rheology calculations: S, sediments; T, Tatricum (quartzite); UC, upper crust (granite); LC, lower crust (diorite); M, upper mantle (olivine); Asth, asthenosphere; L-A1, lithosphere - asthenosphere boundary based on gravity model; L-A2, thermally defined lithosphere – asthenosphere boundary based on model in Figure 3. Lithospheric crosssection cuts, from north to south, the following tectonic units: between km 0 and 130 is the Polish Platform, forming the substratum for a well-developed foreland basin of the outer Carpathians. Between km 130 and 230 is the central western Carpathians, consisting of a series of nappes related to different Alpine convergence events. Between km 230 and 270 is the inner western Carpathian system, probably thermotectonically rejuvenated by Neogene convergence-related intrusions. Farther southward, between km 270 and 450, is the Pannonian basin, consisting of several individual mountain ranges (Matra – Bükk) and grabens (Szolnock and Békés).

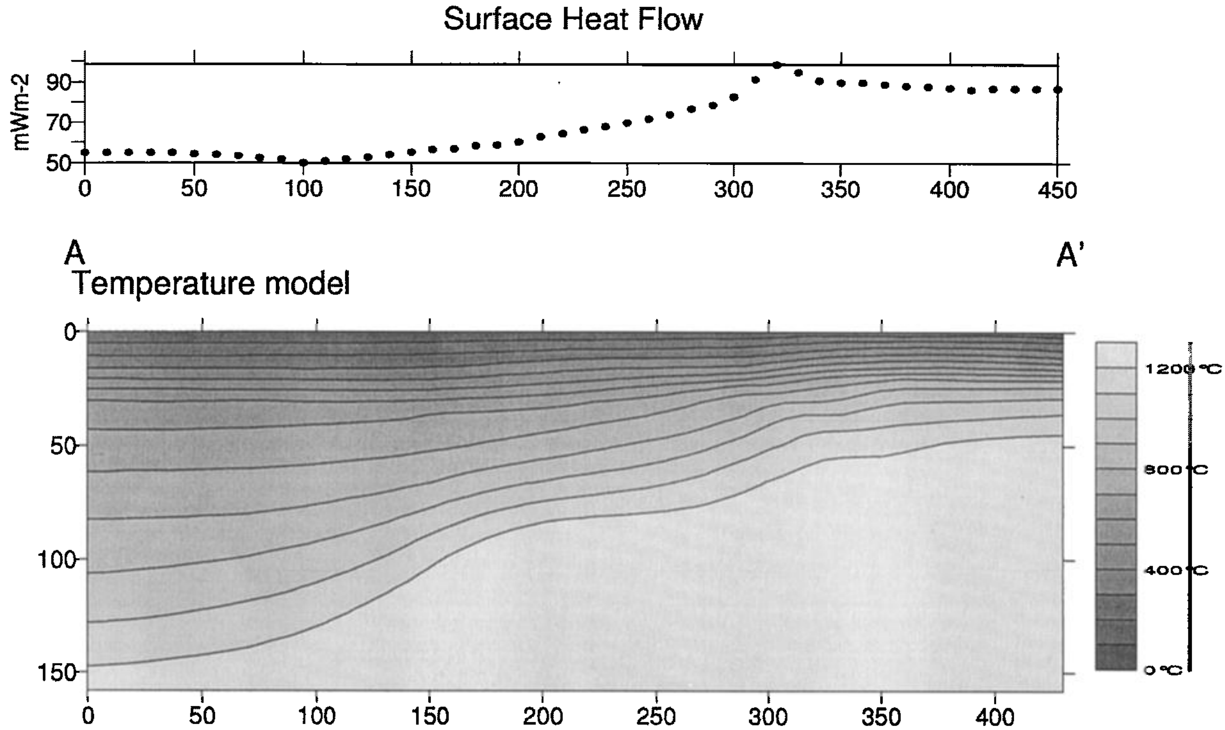

Figure 3. Temperature field calculated for the studied crosssection A-A'. Surface heat flow is from *Hurtig et al.*, [1992]. Crustal heat production is taken into account (model after *Majcin*, [1993] and *Kutas et al.* [1989]). Thermophysical properties are assigned to lithologic units defined by gravity modeling and deep seismics [*Bielik et al.*, 1995; *Tomek et al.*, 1987].

on the following input data: information on the geologic structure to a depth of ~ 5 km, densities of rocks defined according to *Eliaš and Uhmann* [1968], *Ondra and Hanák* [1981], the Moho after *Beránek* [1980], and the seismic velocity after *Beránek and Zátopek* [1981].

3.3. EET

According to *Burov and Diament* [1995], the effective elastic thickness of the continental lithosphere can be calculated from the combined effect of the thicknesses (h_i) of the individual strong layers:

$$EET = (\sum_{i=1}^{n} \Delta h_i^3)^{1/3}$$

Definition of the exact thickness of the strong layers (values of h_1, h_2, etc.,) remains a matter of debate [*Burov and Cloetingh*, 1997; *Burov and Diament*, 1995; *Cloetingh and Burov*, 1996]. The criterion of *Ord and Hobbs'* [1989] for Byerlee brittle failure breakdown, at ~ 260 MPa, would imply that EET values cannot be higher than 26 km, under the condition that we adopt a pressure-scaled minimum yield strength or minimum vertical stress gradient of 10 Mpa km^{-1}. The conversion of strength predictions to EET values is useful since the latter can be directly compared to inferences from basin modeling and lithospheric flexure studies, providing a means to quantitatively test the merits of the individual modeling techniques (Table 3).

4. Lateral Variations in Lithospheric Properties Along the Profiles

4.1. Western Carpathian Profile

The profile through the western Carpathians (A-A') (Figures 2 and 3) can roughly be subdivided into three zones i.e., the Polish platform - foreland area, the Carpathians, and the Pannonian region. The Polish platform - foreland area is characterized by a relatively thick crust, overlain in the foreland area by a thick sedimentary pile (6 km). Surface heat flow values are intermediate (40 - 60 mW m^{-2}).

In the Carpathian unit, the crustal thickness is notably increased (32 - 35 km). Our model assumes a large body of Tatric low-density material to form the upper crust in the outer part of the central western Carpathians.

The Pannonian region is characterised by a relatively thin crust (25-28 km) and high surface heat flow values (90 - 100 mW m^{-2}). The thickness of the lithosphere is also very small (50 - 80 km).

Profile A-A' (across the western Carpathians) shows a general decrease in strength toward the Pannonian basin (Figure 4). The Polish foreland area (between km 0 and 130) shows a horizontal rheological stratification of the lithosphere. Mechanically strong behavior is predicted for the upper part of the crust, the uppermost part of the lower crust, and the uppermost part of the mantle. The weak lower part of the lower crust is predicted as the most obvious detachment level;

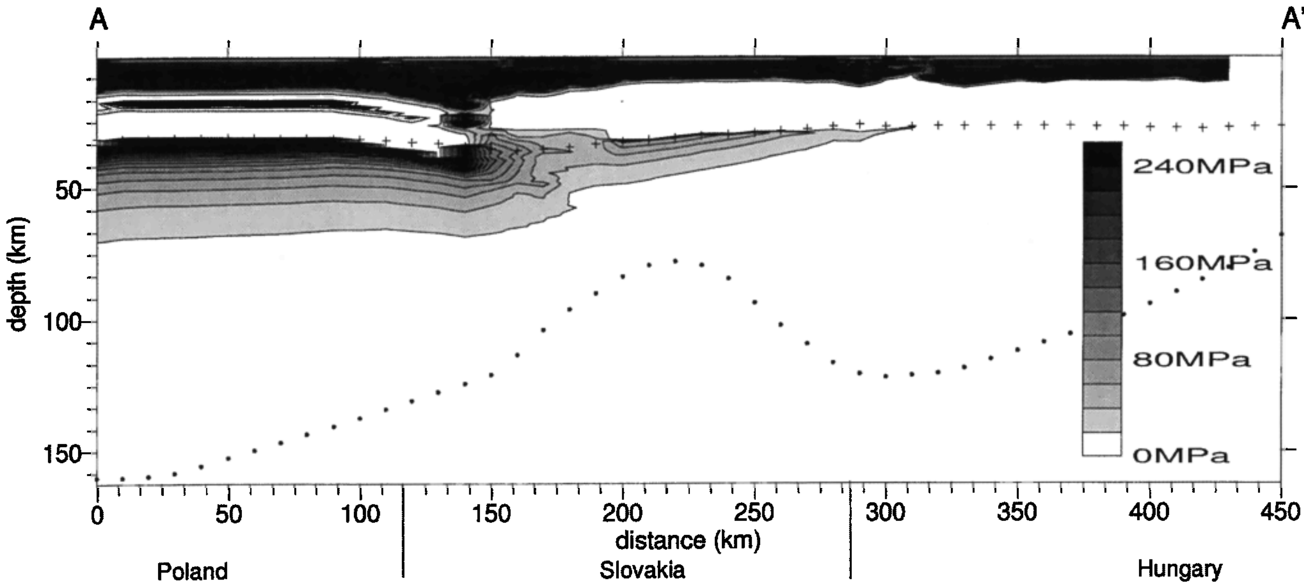

Figure 4. Yield-strength contour plot for compressional deformation. For rheological cross-section A-A', at a strain rate of $\dot{\varepsilon} = 10^{-15}\,s^{-1}$. A clear rheological stratification of the lithosphere is visible. In the foreland area, three individual strong layers are predicted, whereas in the Pannonian part of the profile only one thin strong layer is predicted. Clearly visible is also the lower crustal detachment level in the foreland area. Moho and base of the lithosphere are indicated by crosses and dots, respectively [after *Bielik et al.,* 1995].

possibly also the lower part of the upper crust will act as a detachment level for the adopted strain rate of $\dot{\varepsilon} = 10^{-15}\,s^{-1}$. The combined elastic effect of the three strong layers in this region will govern the flexural behavior of the foreland in this region. An EET of 12 km is predicted for this region on the basis of our strength predictions. Flexural models for this area [*Krzywiec and Jochym,* 1997; *Zoetemeijer et al.,* 1999] predict values between 6 and 15 km for this area.

In the Carpathian part of the profile (km 150-250), lower crustal strength completely disappears as a result of crustal thickening and increased crustal temperatures. The lithospheric strength gradually decreases toward the SE along this profile; this is a direct result of the increasing temperatures toward SE and the corresponding decrease of the (thermally defined) lithospheric thickness. The EET for this region is mainly governed by the thickness of the upper crustal brittle part; we predict an EET of 15 - 23 km. There are no independent estimates for EET in this area.

The Pannonian part of the profile (km 300-450) displays a typical Pannonian rheological structure, characterized by one relatively thin strong layer in the uppermost 10 km of the crust and a complete absence of strength in the lower crust and lower lithosphere. The extreme weakness of the Pannonian lithosphere is a direct result of the high heat flow density and it is related to the extremely shallow asthenosphere in this area. EET values of 5 - 10 km are predicted. Results from extensional basin modeling in the Pannonian basin yield EET values of 5 -10 km [*van Balen et al.,* 1999]. Rheology predictions based on a technique similar to that adopted here yield EETs of 8 km for the Romanian part of the Pannonian basin [*Lankreijer et al.,* 1997]. Earthquakes in the Pannonian basin are limited to the upper 6 – 10 km of the crust [*Szíros et al.,* 1987], supporting the interpretation of a thin strong layer.

4.2. Bohemian Profile

The profile through the Bohemian massif (B-B') (Figures 5 and 6) can be subdivided into three main different units, based on crustal structure: the Krušné hory - Saxothuringian zone, the Bohemian core zone (includes Tepla-Barrandian, Moldanubicum, and Brunovistulicum) and the Carpathians - Pannonian zone [*Bielik et al.,* 1994]. The Krušné hory - Saxothuringian zone is characterised by a relatively thick upper crust (16-20 km) in comparison to the thin lower crust (12-14 km), resulting in negative Bouguer anomalies. Intermediate surface heat flow values (60 -70 mW m^{-2}) are found in this unit, whereas the Cretaceous basin shows slightly increased heat flow values. The Ohre zone, a whole crustal fault zone, is characterized by a steep gravity gradient and separates this unit from the Bohemian core unit.
The Bohemian core unit shows a thicker crust (30 - 39 km), whereas the upper crust is remarkably thinner (9 - 15 km). The gravity effect of the depressed Moho is almost completely compensated by the presence of high-density rocks in the upper and lower crust [*Bielik et al.,* 1994]. The Bohemian core typically shows low heat flow values (40 - 60 mW m^{-2}).

The Carpathian - Pannonian area is characterized by a reduced crustal thickness (25 - 28 km) and a thinner lower crust in comparison with that of the Bohemian unit. The upper crust is ~ 16 km thick in this unit. The Pannonian unit especially is characterized by extremely high surface heat flow values (85 - 95 mW m^{-2}).

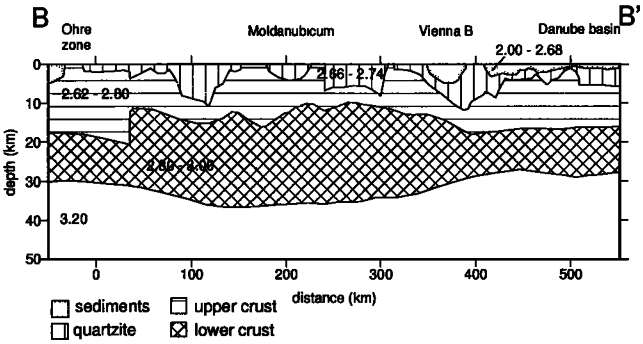

Figure 5. Lithologic stratification of crosssection B-B' (For location, see Figure 1) based on gravity models of Deep Seismic Section VI, [*Bielik et al.,* 1994]. Densities are in kg m^{-3}. The profile shows three different tectonic units, separated by the Ohře zone and the Peripienian lineament, which are interpreted as whole crustal faults. The Ohře zone marks the sharp transition between the Krušné hory - Thuringian region (characterized by a thick upper crust and a relative thin lower crust) and the Bohemian core (with its thickened lower crust and thinned upper crust). The Bohemian core consists of the Teplá-Barrandian, the Moldanubicum, and the Brunovistulicum regions. The third region comprises the Carpathians and the Pannonian basin system (including the Vienna basin).

The profile through the Bohemian massif (B-B') shows a three-layer rheological stratification in the Saxothuringian part of the profile (km -50 - 0). EET values predicted for this area are 8 - 12 km.

Underneath the Cretaceous basin (km 0-50) and the Ohre zone, an absence of strength in the lower crust and mantle is predicted associated with the high surface heat flow values [*Čermák,* 1994] measured in this area (Figure 7). We predict EET's between 5 and 8 km for this area (Figure 8a and 8b).

The remarkable increase in thickness of the lower crust on the SE side of the Ohře fault is also visible in the predicted strength distribution, since lower crustal material is present at shallower depths, causing strong layers. This exceptionally thick and shallow lower crust continues along the entire Moldanubicum and is possibly a result of earlier crustal thickening.

The Moldanubicum (km 150 - 300) displays the mechanical strong core of the Bohemian massif. At the adopted strain rate, only a very thin zone in the lowest part of the lower crust allows detachment between crust and mantle. All other crustal layers are nondetached and behave as one single thick, rigid layer. Additionally, the lower lithosphere shows a very strong and deep keel, with a thickness of over 60 km. We predict EETs of the order of 20 – 40 km for this area. Extremely low heat flow density values, a shallow lower crust, and a cool mantle are the main causes for the predicted extreme values of lithospheric strength. The stiff behavior of the Bohemian massif allowed transmission of Alpine compressional stresses far from the orogenic front, causing inversions of the northern margins of the Bohemian massif (P.A. Ziegler, personal communication 1997).

In the Bohemian foreland area (km 300-350), we still observe the shallow lower crust, producing a strong upper layer in the lower lithosphere. The lower part of the lower crust is again a weak zone. The seismically observed Moho in

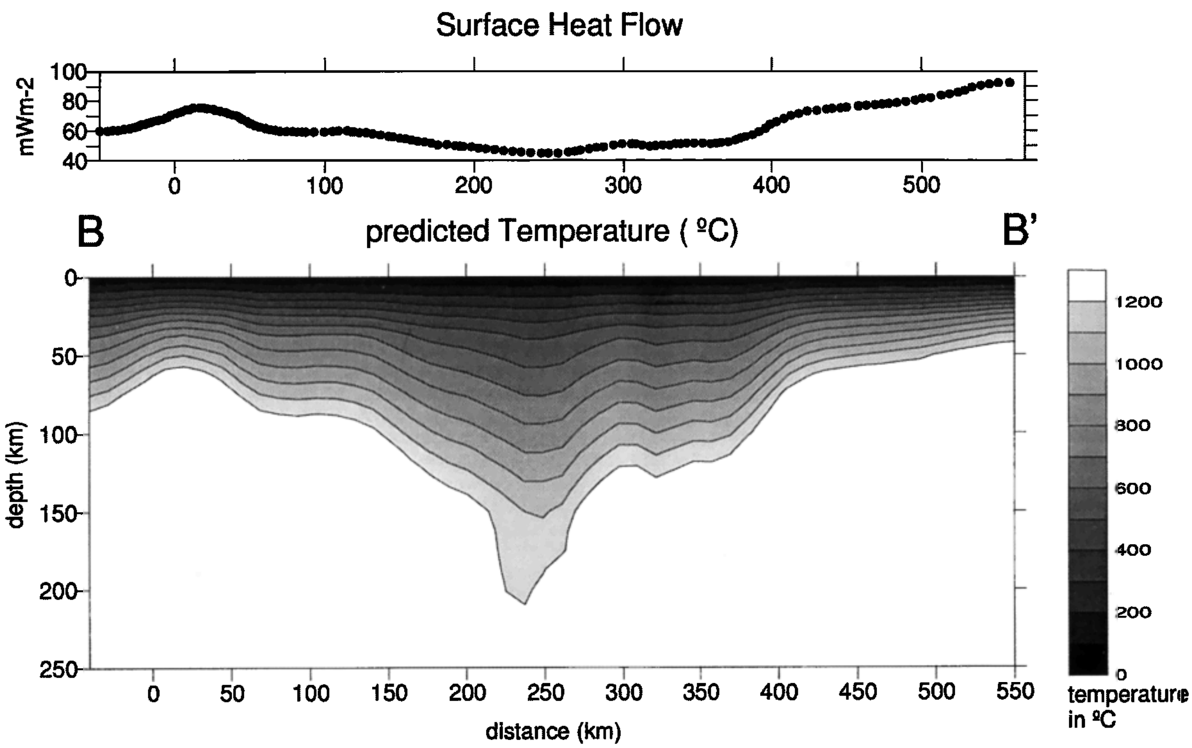

Figure 6. Temperature distribution along section B-B'. Model is partly based on the work of *Čermák* [1994]. Crustal heat production is taken into account. Surface heat flow and crustal structure are after *Čermák* and *Bielik et al.* [1994].

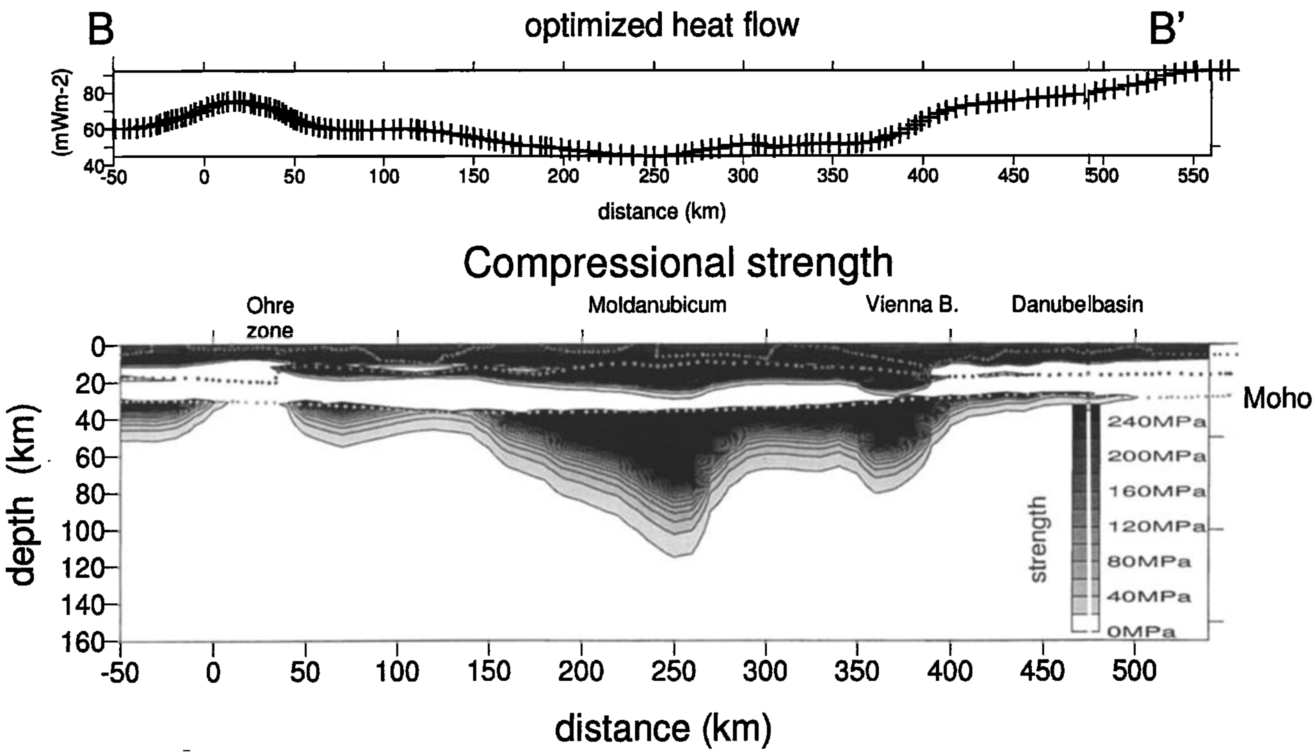

Figure 7. Yield-strength contour plot for compressional deformation for cross section B-B', at a strain rate of $\dot{\varepsilon} = 10^{-15}\ s^{-1}$. A clear rheological stratification of the lithosphere is visible. The Moldanubian core of the Bohemian massif shows a strong keel, where crustal layers are mechanically attached to lower lithospheric layers. The strength rapidly decreases away from the strong center toward SE and NW. The Carpathian foreland area is, however, still relatively strong. The Vienna basin shows a remarkably strong lithosphere owing to the fact that we did not correct for the insulation effect of thermal blanketing of the over 6 km sedimentary fill of the basin. The Pannonian basin typically only displays lithospheric strength in the uppermost parts of the crust.

this area is supposed to be of very recent age, since it is not down-flexed, as is the case in all other Carpathian foreland areas [*Tomek et al.,* 1987; *Tomek and Hall,* 1993]. The predicted weak lower crusts possibly aided the process of the formation of a new Moho after flexure and possibly slab detachment. We predict EET values of 10 km for this area.

Strength values inferred for the Vienna basin are assumed to be overestimated, since the relatively low surface heat flow values do not take the thermal effect of sediment blanketing into account. Basement heat flow values are probably much higher than the used surface heat flow, since the basin is filled with over 6 km of Neogene sediments. EET values based on our strength estimates are 18 – 22 km.

Basin models show a southward increase of detachment depth in the Vienna basin [*Lankreijer et al.,* 1995]. However, since our profile crosses the basin at an unfavorable angle, no lateral changes can be observed in the rheology of the lithosphere underneath the Vienna basin.

The Danube basin, on the SE side of the profile, shows very low values of lithospheric strength, associated with the increased heat flow density and deeper lower crust. Only the upper part of the upper crust and the uppermost part of the lower lithosphere show some strength in our calculations. The EET is mainly governed by the thickness of the strong part of the upper crust and amounts to 8 km.

Seismic interpretations of the Danube basin [*Posgay et al.,* 1986; 1996; *Tari,* 1994; 1996] show SE dipping crustal detachments. Detachment along discrete deep faults is not completely in accordance with the predicted recent rheology. On the basis of the recent crustal strength predictions, a shallower detachment (at the base of the strong part of the upper crust) is expected. Furthermore, these detachments show a synsedimentary behavior for Karpatian - Sarmatian times and do not affect Pannonian strata. Therefore the deep detachments represent an earlier (Karpatian - Sarmatian) rheological situation.

The absence of lithospheric strength in the lower crust and upper mantle has major implications for basin models. Lithospheric loads, imposed by sedimentary fill of the basins overlying this extremely weak lithosphere, must be largely compensated in a local isostatic manner, that is, flexural support of the lithosphere is almost absent. However, the predicted rheology is only valid for the present situation, and caution must be taken in extrapolating these findings to previous times. The Pannonian part of the profile (km 500 - 550) shows the typical Pannonian rheology, a total absence of

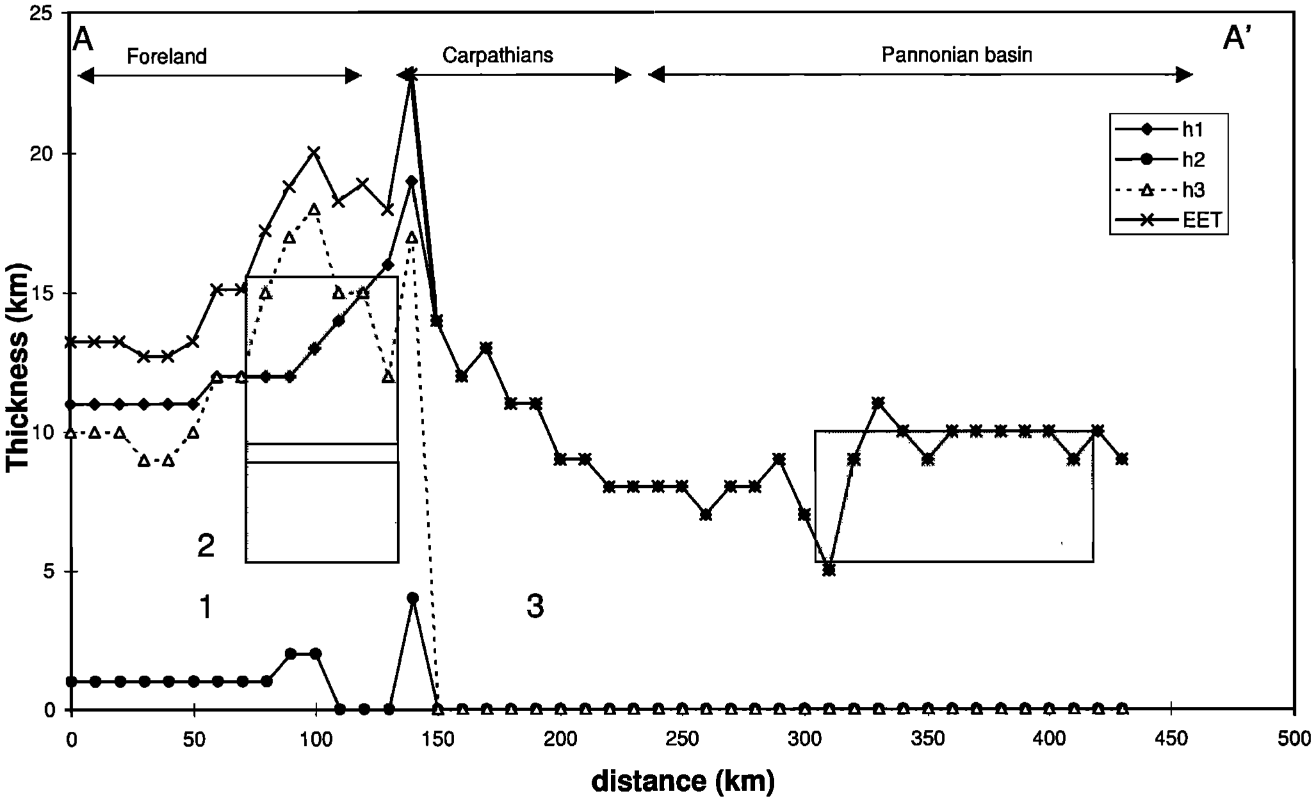

Figure 8a. Effective elastic thickness (EET)(T_e) distribution along profile A-A'. The thicknesses of the mechanically strong layers h_i are shown. The combined effect of n detached layers can be calculated using $Te = (\Sigma \Delta h_i^3)^{1/3}$ [*Burov and Diament,* 1995]. The EET is mainly governed by the thickness of the uppermost strong layer h_1. In the Polish Platform, a significant contribution to EET is also added by the strong part of the mantle (h_3). Boxes indicate independent EET estimates based on foreland basin models (EET 6-10 km [*Zoetemeijer et al.,* 1999] and EET 10-15 km [*Krzywiec and Jochym,* 1997]) and extensional basin models (EET 5-10 km, [*van Balen et al.,* 1999; *van Balen and Cloetingh,* 1995]).

lithospheric strength except for the uppermost few kilometers of the crust, similar to that observed in section A-A' and described by *Lankreijer et al.,* [1997] and *Lankreijer* [1998].

5. Discussion

5.1. Validation

As pointed out in section 4, EET predictions derived from alternative modeling techniques like extensional basin modeling and those from flexural modeling yield independent estimates on the lithospheric rheology in the studied area. The observed close fit between the rheology predictions obtained using the different methods makes us confident in our own rheology predictions, which not only predict EET but also allow identification of detachment zones.

The predicted EETs for the foreland areas do not take into account the weakening effect imposed by the bending of the lithosphere. The effect of far-field stresses causing weakening was also not taken into account, since the predictions reflect a static situation in the absence of actual deformation and stress. Incorporation of these effects requires limiting the calculations to a single well-defined tectonic scenario, with its intrinsic uncertainties. Furthermore, the complex feedback mechanisms operating in the relation between stress and strain through rheology do not permit such complex calculations. The stress field is directly influenced by the strength distribution, and the predicted rheology is partially dependent on the applied stress. Deformation induces direct geometrical changes, thus influencing the strength distribution. Additionally, strain hardening, weakening, or localization as a function of deformation is difficult to quantify in a kinematic model. Far-field stresses do probably play an important role in the areas where the lithosphere is weak, i.e., the central parts of the Pannonian basin system. In order not to make too many concessions on the spatial geometry of the system, a static model was used, rather than a dynamic model that would take into account the above mentioned processes.

Deformation velocities can be derived from extensional basin models [*Lankreijer,* 1998]. Typical extension values for the Pannonian basin system are of the order of β=1.6 [*Horváth et al.,* 1975; *Lankreijer et al.,* 1995; *Royden and Dövenyi,* 1988; *Sclater et al.,* 1980; *Stegena et al.,* 1975]. The duration of the rift period in the Pannonian basin system is ~ 2 Myr

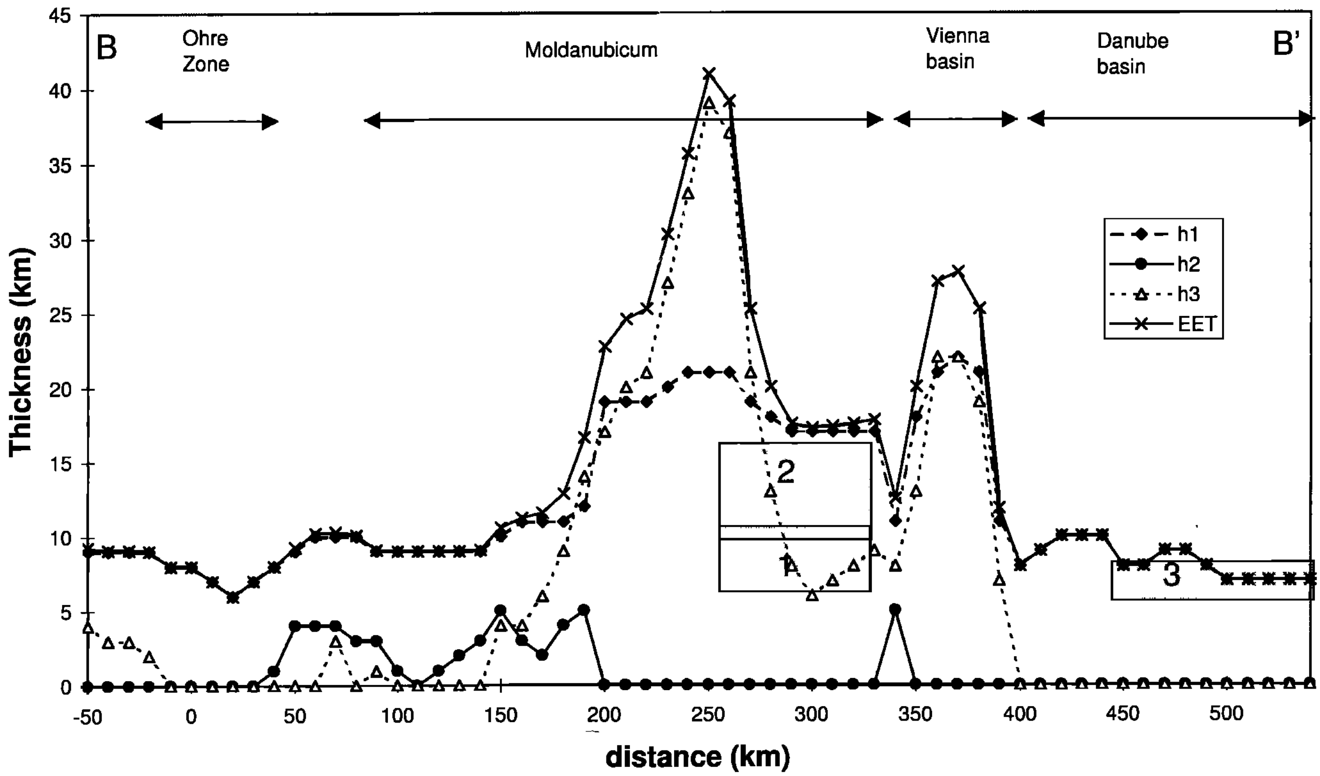

Figure 8b. EET ditribution along profile B-B'. EET is mainly governed by the uppermost part of the crust (h_1). In the Bohemian massif, however, the EET is controlled by the mantle rheology (h_3), although the upper crust also adds considerably to the EET. The strong layers of the upper and lower crust underneath the Bohemian massif are attached and have a combined thickness (h_1) of ~ 20 km, leaving the thickness of h_2 as zero. Boxes 1, 2, and 3 indicate independent EET estimates based on foreland basin models of 5 – 10 km [*Zoetemeijer et al.,* 1999] and 8 – 16 km [*Krzywiec and Jochym,* 1997] and extensional basin models yielding an EET of 7 km [*Lankreijer et al.,* 1995; *van Balen et al.,* 1999], respectively.

(Karpatian and early Badenian). This yields a strain rate of 9.5×10^{-15} s^{-1}.

Palinspastic reconstructions of the late Oligocene - early Badenian deformation in the Carpathian thrust belt yield shortening values of between 130 km (original length of 190 km) and 180 km (original length of 230 km) [*Ellouz and Roca,* 1994; *Roure,* 1994]. This produces strain rates of 3.6×10^{-15} s^{-1} and 4.1×10^{-15} s^{-1}. Strainrates for Magura and Silesian nappe deformation amount to 10^{-15} s^{-1} - 10^{-16} s^{-1} [*Nemčok et al.,* 1997].

Geodynamic reconstructions provide similar amounts of displacement. *Csontos et al.* [1992] shows an estimate of 150 km displacement for the Carpathian front during mid-Miocene and younger times. The deformed area includes in Csontos et al.'s model the extensional basin areas in the Pannonian basin system, ~ 400 - 600 km . The time involved in this displacement is difficult to quantify and is dependent on the location in the Carpathian arc due to the migration of thrusting along the arc. Estimates are of the order of 3 - 6 Myr, yielding strain rates roughly between 1.3×10^{-15} s^{-1} and 3.9×10^{-15} s^{-1}. Short-term strain rates, based on seismicity of the Vrancea area, yield estimates of 1.1×10^{-14} s^{-1} [*Oncescu and Bonjer,* 1997].

Since most observed deformation related to the formation of the Neogene Pannonian-Carpathian system is of the order of between 20 and 60% and the time involved is of the order of a few million year, strain rates typically are of the order of 10^{-15} s^{-1} to 10^{-14} s^{-1}. In summary, differences in strain rate of one order of magnitude induce differences in strength predictions of no more than 10%, which is well within the uncertainties introduced by the thermal model and the gravity model.

5.2. Tectonic Implications

The Polish Platform is characterized by significant NW-SE trending shear zones parallel to the Tornquist - Teisseyre zone (e.g., Odra Fracture zone, Elbe Fracture zone, Main Intra-Sudetic fault, and Lusatian main fault), possibly of Cadomian or older origin [*Żelaźniewicz and Bankwitz,* 1995]. These zones have been reactivated by subsequent various stress regimes.

During Variscan times, large-scale dextral strike-slip movements (up to 300 km [*Aleksandrowski,* 1995]) along these faults occurred, accommodating the northward Variscan compression [*Franke et al.,* 1993]. Also, the dextral Intra-Sudetic strike-slip basin opened along the Intra-Sudetic NW-SE trending strike-slip fault. The Polish Trough opened

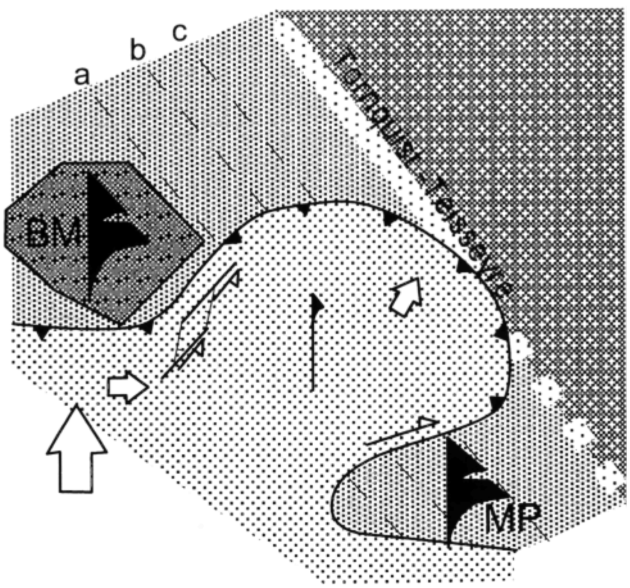

Figure 9a. Tectonic sketch of the effect of the rigid Bohemian massif (BM) and Moesian Platform (MP) on the north-south compression in the Alpine-Carpathian transition zone.

parallel to the Tornquist-Teiseyre zone in Mesozoic times [*Ziegler*, 1990].

Alpine inversion movements inverted the Polish Trough and the northern Bohemian margin, including the Intra-Sudetic basin, reactivating these NW-SE trending faults. Carpathian foreland flexure is largely governed by these NW-SE trending weakness zones [*Krzywiec*, 1997]. Large lateral displacements along the Odra fault zone [*Mastalerz and Wojewoda*, 1990] and the Diendorf Fault [*Leichman and Hejl*, 1996] occurred during Quaternary. In Tertiary times, the western border of the Bohemian massif (Franconian lineament) was heavily inverted [*Coyle et al.*, 1997].

In the Moesian Platform (Romania), similar NW-SE trending shear zones, influencing to a large extent the flexure of the foreland, have been documented [*Maţenco*, 1997; *Sandulescu and Visarion*, 1978; *Visarion and Sandulescu*, 1979]. We can only speculate on the extent of this fault system, since the basement areas do not outcrop.

Ziegler's [1990] map of Permian paleogeography indicates that it is likely that this fault system coincides with the northern boundary of the London-Brabant massif and that the entire area northward of the Alpine - Carpathian orogenic front and south of the Tornquist-Teisseyre line, including the west Netherlands basin, is influenced by this fault system. There could be a causal relation between the dominant NW-SE direction of the recent stress field [*Müller et al.*, 1992; *Zoback et al.*, 1993b] and the main direction of large-scale basement shear zones in this area still governing the recent rheology.

These shear zones are not manifested as discrete faults, but in the case of the Polish Platform, it is better to refer to an anisotropic fabric with two different axes. This implies that because of this megascale foliation, material properties like grain size and thus rheology are different for shear zone parallel and shear zone perpendicular directions. In shear zone perpendicular directions (NE-SW), extensional stresses will be able to reactivate the inherited shear fabric as normal faults, thus utilizing the minimal yield strength. NW-SE oriented extensional stresses will have to overcome the maximum strengths.

The rheology we predict for the Polish foreland does not take into account the above described NW-SE trending rheology anisotropy but only describes the maximum strengths. Since it is difficult to assess the actual failure mechanisms in the NW-SE shear zones with depth, the calculation of failure envelopes will not provide a satisfactory minimum yield-strength envelope.

Studies of extensional basins, like the Polish Trough, can provide this minimum rheology. The anisotropy of the rheology of the Polish Platform will have important consequences for the flexural behavior of the foreland downbending underneath the arc-shaped Carpathians, thus loading in different directions with respect to the weakest direction.

The strength maximum calculated in the foreland area of the Carpathians (Figures 4 and 7) places important constraints on the evolution of foreland basins. Downbending of the lower plate implies the introduction of relative cool material at greater depths, thus increasing the strength. This mechanism puts a limit to the rate of downbending. Bending rates in excess of the thermal relaxation rate will lead to an increase of strengths in the plate automatically blocking the movement by the increased flexural rigidity. The vertical loads associated with flexural basins induce fiber stresses that reduce the strength of a bending lithosphere severely [*Bertotti et al.*, 1997; *Cloetingh and Burov*, 1996]. If we can extrapolate our rheology predictions to the geologic past, they may shed some light on tectonic models for the area during Neogene times.

A striking feature in our predictions of lithospheric strength is the extremely strong Bohemian core, rooting deep into the lower lithosphere. It is likely that its core acted as a rigid anchor, blocking the northward movement of the colliding Alpine region, causing for example, large-scale sinistral strike-slip movements in the eastern Alps (Salzachtal – Ennstal fault and Mur – Mürz fault zone) opening the Vienna basin in Karpatian times (Figure 9a).

The proposed rheologic anisotropy in the Polish Platform and the Moesian Platform has probably determined the precollisional continental margin in the western and southern Carpathians. The NW-SE trending weakness zones favor a jagged edge (Figure 9b) to a straight or slightly curved edge. How such a margin with internal weakness zones reacts to loading is unclear. Each slab, separated by major shear zones, probably flexes individually as a reaction to the load. This creates a distinct shape of reactivated structures perpendicular to the axis of the foreland basin, like that described by *Krzywiec* [1997]. In the eastern Carpathians, the weakness zones run parallel to the margin, favoring a staircase geometry. Furthermore, differences in foreland basin development [*Zoetemeijer et al.*, 1999] between the western Carpathians, where the foreland basin axis is at high angles to the trend of the anisotropy, and the eastern Carpathians, where the foreland basin axis runs parallel to the anisotropy, can be due to this effect.

The predicted weakness of the lithosphere underlying the Pannonian basin makes it highly unlikely that it can

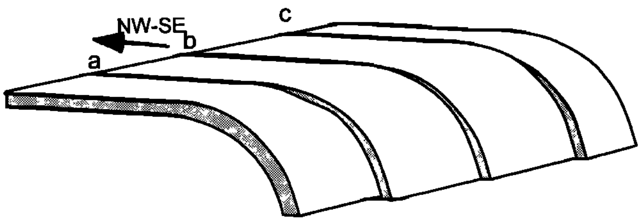

Figure 9b. Tectonic sketch of the effect of rheologic anisotropy on the precollisional margin of the Polish platform and the Moesian Platform. NW-SE trending, inherited weakness zones cleave the slab into separated segments, causing differential flexing of the separate parts along the western and southern Carpathian margin, where the rheologic anisotropy is at high angle to the margin. Along the eastern Carpathians margin, the anisotropy is parallel to the margin.

compensate the load of the shallow asthenosphere, which produces a gravity effect of +50 mGal at least [*Bielik et al.*, 1994]. Therefore a passive subsidence mechanism, caused by re-equilibration of the thinned lithosphere, as described by *Huismans et al.* [*1999*] is likely to occur in the Pannonian basin. The two-phase subsidence history of the Neogene Pannonian basin system [*Lankreijer et al.*, 1999] and the spatial correlation of the youngest extension phase with the weakest lithosphere [*Lankreijer*, 1998] indicates a causal relationship between the asthenospheric dome, the extension processes, and the weak rheology. The observed good fit between our strength predictions and those inferred from the approaches of others (Figure 8a and 8b) provides an independent validation of our results.

6. Conclusions

We predict a detached behavior of the crust and mantle for all study areas for the adopted strain rate. However, a faster strain rate will cause coupling of the strong lithosphere in the Bohemian massif. We speculate that the stiff Bohemian massif causes major implications for the eastern Alpine – Carpathian tectonic evolution. A similar behavior was predicted for the Moesian Platform [*Lankreijer et al.*, 1997]. Furthermore, the strong rheologic contrast between the Pannonian area and the surrounding platform areas supports scenarios in which the shape of the Pannonian embayment was predetermined by the passive margins of the lithosphere surrounding the present-day Carpathian arc. We also predict a strong anisotropy in the rheology of the Polish Platform, possibly extending to the North Sea area, directly linked to the occurrence of NW-SE basement faults, parallel to the Tornquist-Teisseyre zone.

Large lateral variations in present-day lithospheric rheology are predicted for the study area, corresponding to the broad spectrum of thermotectonic ages encountered. The Bohemian massif forms a relatively strong lithospheric block. The rigid behavior is responsible for complex large-scale strike-slip movements along these blocks in order to accommodate the emplacement of the internal microplates of the Pannonian system.

The Polish platform is characterized by a rheologic anisotropy induced by large-scale NW-SE trending shear zones that form prominent weakness zones controlling reactivation since Variscan times. This anisotropy controls the shape of the Carpathian foreland basin, the tectonic history of the Polish Trough in Mesozoic times, and the Intra-Sudetic basin in Paleozoic times. The Pannonian basin system is dominated by a weak rheology, owing to high lithospheric temperatures. In general, the peripheral basins of the Pannonian basin show a relatively stronger present-day rheology than the central basins do.

The inferred large variations in lithospheric strength suggest that tectonic models should be based on units with similar rheology (i.e., the strong part of the Bohemian massif or the Polish Platform - Moesian Platform rheologic anisotropy), rather than primarily based on geographical units. Additionally, temporal changes of rheology should be taken into account in such models.

Acknowledgments. Reviews by G. Tari and E. Burov were very helpful. M. Bielik thanks the Slovak Grant Agency for Science (grant 95/53005/418) for partial support of this work. Netherlands Research School of Sedimentary Geology (NSG) publication 980805.

References

Aleksandrowski, P., The significance of major strike-slip displacements in the development of Variscan structure of the Sudetes (SW Poland), *Przegl. Geol.*, *43*, 745-754, 1995.

Andrusov, D.(Ed.), *Grundriss der Tektonik der Nördlichen Karpaten*, 188 pp., VEDA, Bratislava, Slovakia, 1968.

Babuška, V., J. Plomerová, and P. Pajdušák, Lithosphere - asthenosphere in central Europe model derived from P-residuals, in *Proceedings of the 4th EGT Workshop*, edited by G. Nolet and B. Dost, pp. 37-48, ESF, Strasbourg, France 1988.

Bada, G., Cenozoic stress field evolution in the Pannonian basin and surrounding orogens, Ph.D. thesis, 218 pp., Vrije Universiteit, Amsterdam, 1999.

Bassi, G., Relative importance of strain rate and rheology for the mode of continental extension, *Geophys. J. Int.*, *122*, 195-210, 1995.

Beekman, F., Tectonic modelling of thick-skinned compressional intraplate deformation, Ph.D. thesis, 152 pp., Vrije Universiteit, Amsterdam, 1994.

Beekman, F., R.A. Stephenson, S.A.P.L. Cloetingh, and R.J. Korsch, Dynamic and rheological implications of crustal structure in central Australia: Numerical modelling results, *Abst. Geol. Soc. Austr.*, *36*, 5-6, 1994.

Beránek, B., Investigation of deep-seated structure of the Earth's crust in Czechoslovakia, *Geol. Průzkum*, *23*, 98-101, 1980.

Beránek, B., and A. Zátopek, Earth's crust structure in Czechoslovakia and in central Europe by methods of explosion seismology, in *Geophysical Syntheses in Czechoslovakia*, edited by A. Zátopek, pp. 243-264, VEDA, Bratislava, Slovakia, 1981.

Bertotti, G., M. ter Voorde, S. Cloetingh, and V. Picotti, Thermomechanical evolution of the South Alpine rifted margin (north Italy): Constraints on the strength of passive continental margins, *Earth Planet. Sci. Lett.*, *146*, 181-193, 1997.

Bielik, M., O. Fusán, M. Burda, M. Hübner, and V. Vyskočil, Density models of the western Carpathians, *Contrib. Geophys. Inst. Slov. Acad. Sci.*, *20*, 103-113, 1990.

Bielik, M., M. Blížkovský, M. Burda, O. Fusán, M. Hübner, H. Herrmann, A. Novotný, M. Suk, Č. Tomek, and V. Vyskočil, Density models of the Earth's crust along seismic profiles, in *Crustal Structure of the Bohemian Massif and the West Carpathians*, edited by V. Bucha and M. Blížkovský, pp. 177-187, Academia, Prague, 1994.

Bielik, M., J. Šefara, V. Bezak, and P. Kubeš, Deep-seated models of the western Carpathians, in *Proceedings of the 1st Slovak Geophysical Conference:GISAS*, edited by M.B. I. Túnyi, et al., pp. 7-11, Slovak Academic Press, Bratislava, Slovakia, 1995.

Bodri, L., Geothermal model of the Earth's crust in the Pannonian basin, *Tectonophysics, 7*, 61-73, 1981.

Brace, W.F., and D.L. Kohlstedt, Limits on lithospheric stress imposed by laboratory experiments, *J. Geophys. Res., 85*, 6248-6252, 1980.

Buck, W.R., Modes of Continental Lithospheric Extension, *J. Geophys. Res., 96*, 20161-20178, 1991.

Burov, E., and S. Cloetingh, Erosion and rift dynamics: New thermomechanical aspects of post-rift evolution of extensional basins, *Earth Planet. Sci. Lett., 150*, 7-26, 1997.

Burov, E.B., and M. Diament, The effective elastic thickness (T_e) of continental lithosphere: What does it really mean?, *J. Geophys. Res., 100*, 3905-3927, 1995.

Byerlee, J.D., Friction of rocks, *Pure Appl. Geophys., 116*, 615-626, 1978.

Carter, N.L., and M.C. Tsenn, Flow properties of continental lithosphere, *Tectonophysics, 136*, 27-63, 1987.

Čech, F. (Ed.), ***Dynamics of the Neogene Carpathian Basins in Relation to Deep Structure, Crustal Type and Fuel Deposits***, 253 pp., Bratislava, Slovakia, 1988.

Čermák, V., Results of heat flow studies in Czechoslovakia, in ***Crustal structure of the Bohemian Massif and the Western Carpathians***, edited by V.Bucha and M. Blížkovský, pp. 85-120, Springer-Verlag, Berlin, 1994.

Cloetingh, S., and E. Banda, Europe's lithosphere: Physical properties, mechanical structure, in *A Continent Revealed: The European Geotraverse*, edited by D. Blundell, R. Freeman, and S. Mueller, pp. 80-91, Cambridge Univ. Press, New York, 1992.

Cloetingh, S., and E.B. Burov, Thermomechanical structure of European continental lithosphere: Constraints from rheological profiles and EET estimates, *Geophys. J. Int., 124*, 695-723, 1996.

Coyle, D.A., G.A. Wagner, E. Hejl, R. Brown, and P. van den Haute, The Cretaceous and younger thermal history of the KTB site (Germany): Apatite fission-track data from the Vorbohrung, *Geol. Rundsch., 86*, 203-209, 1997.

Csontos, L., A. Nagymarosy, F. Horváth, and M. Kováč, Tertiary evolution of the intra-Carpathian area: A model, *Tectonophysics, 208*, 221-241, 1992.

Decker, K., and H. Peresson, Tertiary kinematics in the Alpine-Carpathian-Pannonian system: Links between thrusting, transform faulting and crustal extension, in *Oil and Gas in Alpidic Thrust Belts and Basins of Central and Eastern Europe, EAGE Spec. Pub.*, vol. 5, edited by G. Wessely and W. Liebl, pp. 69-77, Geol. Soc., London, 1996.

Dövényi, P., and F. Horváth, A review of temperature, thermal conductivity, and heat flow data for the Pannonian Basin, *AAPG Mem., 45*, 195-233, 1988.

Downes, H., and O. Vaselli, The lithospheric mantle beneath the Carpathian-Pannonian region: A review of trace element and isotopic evidence from ultramafic xenoliths, *Acta Vulcanol., 7*, 219-229, 1995.

Eliáš, M., and J. Uhmann (Ed.), *Density of Rocks of Czechoslovakia*, 60 pp., ÚÚG, Prague, 1968.

Ellouz, N., and E. Roca, Palinspastic reconstructions of the Carpathians and adjacent areas since the Cretaceous: A quantitative approach, in *Peri-Tethyan Platforms*, edited by F. Roure, pp. 51-78, Editions Technip, Paris, 1994.

Fodor, L., L. Csontos, G. Bada, I. Györfi, and L. Benkovics, Tertiary tectonic evolution of the Pannonian basin and neighbouring orogens: A new synthesis of paleostress data, *Geol. Soc., Spec. Publ., In press*, 1999.

Franke, W., A. Żelaźniewicz, S.J. Porebski, and B. Wayspych, Saxothuringian zone in Germany and Poland: Differences and common features, *Geol. Rundsch., 82*, 583-599, 1993.

Goetze, C., and B. Evans, Stress and temperature in the bending lithosphere as constrained by experimental rock mechanics, *Geophys. J. R. Astron. Soc., 59*, 463-478, 1979.

Hejl, E., D. Coyle, N. Lal, P. von der Haute, and G.A. Wagner, Fission-track dating of the western border of the Bohemian massif: Thermochronology and tectonic implications, *Geol. Rundsch., 86*, 210-219, 1997.

Horváth, F., Neotectonic behavior of the Alpine-Mediterranean region, *AAPG Mem., 45*, 49-55, 1988.

Horváth, F., Towards a kinematic model for the formation of the Pannonian basin, *Tectonophysics, 226*, 333-357, 1993.

Horváth, F., and S. Cloetingh, Stress-induced late-stage subsidence anomalies in the Pannonian Basin, *Tectonophysics, 266*, 287-300, 1996.

Horváth, F., L. Stegena, and B. Géczy, Geophysical and geological characteristics of the ensialic interarc basins, (abstract), *Eos Trans. AGU, 56*, 166, 1975.

Horváth, F., A. Szalay, P. Dövenyi, and J. Rumpler, Structural and thermal evolution of the Pannonian basin, in ***Thermal Modelling in Sedimentary Basins***, edited by J. Burrus, pp. 339-358, Editions Technip, Paris, 1989.

Huismans, R.S., Y.Y. Podladchikov, and S. Cloetingh, The transition from passive to active rifting. FEM modelling of convective upwelling of mantle lithosphere beneath rift zones, *Tectonophysics, In press*, 1999.

Hurtig, E., V. Čermák, R. Haenel and V.I. Zvi, ***Geothermal Atlas of Europe***, Herman Haack Verlag, Potsdam, Germany, 1992.

Jiříček, R., Tectonogenetic development of the Carpathian arc in the Oligocene and Neogene, in *Tectonic Profiles Through the West Carpathians*, edited by M. Mahel', pp. 205-215, Geol. Inst. of Dionýz Štúr, Bratislava, Slovakia, 1979.

Kilényi, E., A. Kröll, D. Obernauer, J. Šefara, P. Steinhauser, Z. Szabó, and G. Wessely, Pre-Tertiary basement contour map of the Carpathian basin beneath Austria, Czechoslovakia and Hungary, *Geofiz. Kozl., 36*, 15-36, 1991.

Kováč, M., A. Nagymarosy, J. Sotak, and K. Sutovska, Late Tertiary paleogeographic evolution of the western Carpathians, *Tectonophysics, 226*, 401-415, 1993.

Krzywiec, P., Large-scale tectono-sedimentary middle Miocene history of the central eastern Polish Carpathian foredeep basin: Results of seismic data interpretation, *Przeglad Geol., 10*, 1039-1054, 1997.

Krzywiec, P., and P. Jochym, Characteristics of the Miocene subduction zone of the Polish Carpathians: Results of flexural modeling, *Przeglad Geol., 45*, 785-792, 1997.

Kutas, R.I., V.A. Tschviastchenko, and I.I. Korchagin (Eds.), *Modelling of the Thermal Field of the Continental Lithosphere*, 191 pp., Nauka Dumka, Kiev, 1989.

Lankreijer, A.C., Rheology and basement control on extensional basin evolution in central and Eastern Europe: Variscan and Alpine - Carpathian - Pannonian tectonics, 158 pp., Ph.D. thesis, Vrije Universiteit, Amsterdam, 1998.

Lankreijer, A., M. Kováč, S. Cloetingh, P. Pitoňák, M. Hlôška, and C. Biermann, Quantitative subsidence analysis and forward modelling of the Vienna and Danube basins: Thin-skinned versus thick-skinned extension, *Tectonophysics, 252*, 433-451, 1995.

Lankreijer, A., V. Mocanu, and S. Cloetingh, Lateral variations in lithosphere strength in the Romanian Carpathians: Constraints on basin evolution, *Tectonophysics, 272*, 269-290, 1997.

Lankreijer, A., P. Müller, L. Kovács, and E. Juhász, A two-phase asymmetric extension model for the tectonic evolution of the Kisalföd basin NW Pannonian basin): Inferences from subsidence analyses and basin modelling, *Mar. Pet. Geol., in press*, 1999.

Leichman, J., and E. Hejl, Quaternary tectonics at the eastern border of the Bohemian massif: New outcrop evidence, *Geol. Mag., 133*, 103-105, 1996.

Lenkey, L., Geothermics of the Pannonian basin and its bearing on the tectonics of basin formation, Ph.D. thesis, 227 pp., Vrije Universiteit, Amsterdam, 1999.

Lillie, R.J., M. Bielik, V. Babuska, and J. Plomerova, Gravity modelling of the lithosphere in the eastern Alpine-western Carpathian-Pannonian Basin region, *Tectonophysics, 231*, 215-235, 1994.

Mahel', M., Tectonics of the Carpathian Balkan system, explanation of the tectonic map, Carpathian Mountain system, and adjacent areas, Geol. úst. Dionyzs Štúra, Bratislava, Slovakia, 1974.

Mahel', M., and M. Malkovský (Eds.), Explanations to the tectonic map of Czechoslvakia, 50 pp., 1:500,000, Geol. úst. Dionyzs Štúra, Bratislava, Slovakia, 1984.

Majcin, D., Thermal state of the west Carpathian lithosphere, *Stud. geophys. Geod., 37*, 345-364, 1993.

Majcin, D., and V.A. Tsvyashcheko, Effects of magmatism on temperature field in the northern part of the Transcarpathian depression, *Contrib. Geophys. Inst. Slov. Acad. Sci., 24*, 72-86, 1994.

Mastalerz, K., and J. Wojewoda, The pre-Kaczawa alluvial fan: An example of sedimentation in the active wrench zone, Plio-Pleistocene age, Sudeten Mountains, *Przeglad Geol., 38*, 363-370, 1990.

Maţenco, L., Tectonic evolution of the outer Romanian Carpathians; constraints from kinematic analyses and flexural modelling, Ph.D. thesis, 160 pp., Vrije Universiteit, Amsterdam, 1997.

Müller, B., M.L. Zoback, K. Fuchs, L. Mastin, S. Gregersen, N. Pavoni, O. Stephanson, and C. Ljunggren, Regional patterns of tectonic stress in Europe, *J. Geophys. Res., 97*, 11783-11803, 1992.

Nemčok, M., J. Nemčok,M. Wojtaszek, L. Ludhova, N. Oszczypko, W. Sercombe, M. Cieskovski, Z. Paul, M. Coward and A. Ślączka, Recontruction of Cretaceous rifts incorporated in the outer west Carpathian wedge by balancing, in *EUROPROBE, PANCARDI Workshop*, 10, edited by M. Krobicki and W. Zuchiewicz, *Przegl. Geol.*, 1093-1094, 1997.

Okaya, N., S. Cloetingh, and S. Mueller, A lithospheric cross-section through the Swiss Alps: II, Constraints on the mechanical structure of a continent-continent collision zone, *Geophys. J. Int., 127*, 399-414, 1996.

Oncescu, M.C., and K.P. Bonjer, A note on the depth recurrence and strain release of large Vrancea earthquakes, *Tectonophysics, 272*, 291-302, 1997.

Ondra, P., and J. Hanák, Mapa hustot geologicko: petrografických jednote Českého masívu, map, Geol. Průzk, Prague, 1981.

Ord, A., and B.E. Hobbs, The strength of the continental crust, detachment zones and the development of plastic instabilities, *Tectonophysics, 158*, 269-289, 1989.

Plašienka, D., Cretaceous tectonochronology of the central western Carpathians, Slovakia, *Geol. Carpathica, 48*, 99-111, 1997.

Posgay, K., I. Albu, G. Ráner, and G. Varga, Characteristics of the reflecting layers in the Earth's crust and upper mantle in Hungary, in *Reflection Seismology: A Global Perspective, Geodyn. Ser.*, Vol. 13, edited by M. Barazangi and L. Brown, pp. 55-65, AGU, Washinton D.C., 1986.

Posgay, K., et al., International deep reflection survey along the Hungarian geotraverse, *Geophys. Trans.*, *40*, 1-44, 1996.

Ranalli, G., (Ed.), *Rheology of the Earth*, 413 pp., Chapman and Hal, New York 1995.

Ranalli, G., and D.C. Murphy, Rheological stratification of the lithosphere, *Tectonophysics*, *132*, 281-295, 1987.

Ratschbacher, L., W. Frisch, H.G. Linzer, and O. Merle, Lateral extrusion in the Eastern Alps: 2, Structural analysis, *Tectonics*, *10*, 257-271, 1991a.

Ratschbacher, L., O. Merle, P. Davy, and P. Cobbold, Lateral extrusion in the Eastern Alps: 1, Boundary conditions and experiments scaled for gravity, *Tectonics*, *10*, 245-256, 1991b.

Roure, F., *Peri-Tethyan Platforms*, pp. 275, Editions Technip, Paris, 1994.

Royden, L.H., The Vienna basin: A thin-skinned pull-apart basin, in *Strike Slip Deformation, Basin Formation and Sedimentation*, edited by K. Biddle and K. Christie-Blick, *SEPM Spec. Publ.*, 37, 317-339, 1985.

Royden, L.H., Late Cenozoic tectonics of the Pannonian basin system, *AAPG Mem.*, *45*, 27-48, 1988.

Royden, L.H., and P. Dövenyi, Variations in extensional styles at depth across the Pannonian basin system, *AAPG Mem.*, *45*, 235-255, 1988.

Sachsenhofer, R.F., A. Lankreijer, S. Cloetingh, and F. Ebner, Subsidence analysis and quantitative basin modeling in the Styrian basin (Pannonnian basin system, Austria), *Tectonophysics*, *272*, 175-196, 1997.

Sandulescu, M., Overview of Romanian geology, *Rom. J. Tectonics Reg. Geol.*, *75*, 3-15, 1994.

Sandulescu, M., and O. Bercia, Regions of Alpine folding; Rumanian Carpathians: The east Carpathians, the crystalline-Mesozoic zone, in *Tectonics of the Carpathian Regions*, edited by M.Mahel', Geol. Ust. Dionyzs Stur, Bratislava, Slovakia, 240-253, 1974.

Sandulescu, M., and M. Visarion, Considerations sur la structure tectonique du soubassement de la depression de Transylvanie, *Tecton. Geol. Reg*, *64*, 153-173, 1978.

Sclater, J.G., L. Royden, F. Horváth, B.C. Burchfiel, S. Semken, and L. Stegena, The formation of the intra-Carpathian basins as determined from subsidence data, *Earth Planet. Sci. Lett.*, *51*, 139-162, 1980.

Seifert, P., Palinspastic reconstruction of the easternmost Alps between upper Eocene and Miocene, *Geol. Carpathica*, *43*, 327-333, 1992.

Soták, J., Evolution of the western Carpathian sutural zone, principal geotectonic events, *Geol. Carpathica*, *43*, 355-362, 1992.

Stegena, L., B. Geczy, and F. Horváth, Late Cenozoic evolution of the Pannonian basin, *Tectonophysics*, *26*, 71-90, 1975.

Szafián, P., Gravity and tectonics: A case study from the Pannonian basin and the surrounding mountain belt, Ph.D. thesis, 164 pp., Vrije Universiteit, Amsterdam, 1999.

Szafián, P., F. Horváth, and S. Cloetingh, Gravity constraints on the crustal structure and slab evolution along a transcarpathian transect, *Tectonophysics*, *272*, 233-248, 1997.

Szíros, T., P. Mónus, and L. Tóth, Focal depth of Hungarian earthquakes, *Gerlands Beitr. Geophys.*, *98*, 146-154, 1987.

Talwani, M., Computer usage in the computation of gravity anomalies, in *Method in Computational Physics*, vol. 13, edited by B. Alder, pp. 425-426, Academic Press, New York, 1973.

Tari, G., Alpine tectonics of the Pannonian Basin, *AAPG Bull.*, *77*, 1669-1673, 1993.

Tari, G., Alpine tectonics of the Pannonian basin, Ph.D. thesis 501 pp., Rice Univ., Houston, Tex., 1994.

Tari, G., Neoalpine tectonics of the Danube basin (NW Pannonian basin, Hungary), in *Peri-Tethys Memoir 2: Structure and Prospects of Alpine basins and Forelands*, edited by P.A. Ziegler and F. Horváth, , *Mém. Mus. Natn. Hist. Nat*, *170*, 439-454, 1996.

Tari, G., F. Horváth, and J. Rumpler, Styles of extension in the Pannonian basin, *Tectonophysics*, *208*, 203-219, 1992.

Tomek, Č., and J. Hall, Subducted continental margin imaged in the Carpathians of Czechoslovakia, *Geology*, *21*, 535-538, 1993.

Tomek, Č., L. Dvořáková, J. Ibrmajer, R. Jiříček, and T. Koráb, Crustal profiles of active continental collisional belt: Czechoslovak deep seismic reflection profiling in the west Carpathians, *Geophys. J. R. Astron. Soc.*, *89*, 383-388, 1987.

Tomek, Č., I. Ibrmajer, and T. Korab, Crustal structure of the western Carpathians as determined by deep seismic sounding, (in Czech), *Miner. Slovaca*, *21*, 3-26 1989.

van Balen, R.T., and S. Cloetingh, Neural network analyses of stress-induced overpressures in the Pannonian basin, *Geophys. Jl Int.*, *121*, 532-544, 1995.

van Balen, R., L. Lenkey, F. Horváth, and S. Cloetingh, Numerical modelling of stratigraphy and fluid flow in the Pannonian Basin, *Geol. Soc. Spec. Publ.*, in press, 1999.

van den Beukel, J., Thermal and mechanical modelling of convergent plate margins, Ph.D. thesis, *Geol. Ultraiectina*, *62*, 126 pp., Utrecht, 1990.

van Wees, J.D., and S. Cloetingh, 3D flexure and intraplate compression in the North Sea basin, *Tectonophysics*, *266*, 343-359, 1996.

Visarion, M., and M. Sandulescu, Structura subasmentuui depresiunii Panonice in Romania, *St. Cerc. Geol. Geofiz. Geogr.*, *17*, 191-201, 1979.

Watts, A.B., G.D. Karner, and M.S. Steckler, Lithosphere flexure and the evolution of sedimentary basins, *Philos. Trans. R. Soc. London, Ser. A*, *305*, 249-281, 1982.

Wessely, G., The Calcareous Alps below the Vienna basin in Austria and their structural and facial development in the Alpine Carpathian border zone, *Geol. Carpathica*, *43*, 347-354, 1992.

Żelaźniewicz, A., and P. Bankwitz, Cadomian basement of the Paleozoic platform in Central Europe, *Stud. Geophys. Geod.*, *39*, 302-308, 1995.

Ziegler, P.A., (Ed.), *Geological Atlas of Western and Central Europe*, 239 pp., Geol. Soc. London / SIPM, London, 1990.

Znosko, J., Polish Carpathian foreland, in *Tectonics of the Carpathian Balkan regions*, edited by M. Maheľ, pp. 431-442, Geol. Úst. Dionzs Štúr, Bratislava, Slovakia, 1974.

Zoback, M.D., et al., Upper crustal strength inferred from stress measurements to 6 km depth in the KTB borehole, *Nature*, *365*, 633-635, 1993a.

Zoback, M.D., R.A. Stephenson, S. Cloetingh, B.T. Larsen, B. Van Hoorn, A. Robinson, F. Horváth, C. Puigdefabregas, and Z. Ben Avraham, Stresses in the lithosphere and sedimentary basin formation, *Tectonophysics*, *226*, 1-4, 1993b.

Zoetemeijer, R., Č. Tomek, and S. Cloetingh, The flexural expression of European continental lithosphere under the The western outer Carpathians, *Tectonics*, *in press*, 1999.

Zoubek, V., and M. Malkovský, Czechoslovakian part of the Bohemian massif, in *Tectonics of the Carpathian Balkan Regions*, edited by M. Maheľ, pp. 407-414, Geol. úst. Dionýzs Štúr, Bratislava, Slovakia, 1974.

M. Bielik and D. Majcin, Geophysical Institute, Slovak Academy of Sciences, 842 28 Bratislava, Slovakia.

S. Cloetingh and A. Lankrijer, Faculty of Earth Sciences, Vrije Universiteit, 1081 HV Amsterdam Netherlands. lana@geo.vu.nl

**(Received June 16, 1997;
revised February 23, 1999;
accepted March 8, 1999.)**

TECTONICS, VOL. 18, NO. 6, PAGES 1099-1119 DECEMBER 1999

Architecture and tectonic evolution of nonvolcanic margins: Present-day Galicia and ancient Adria

Gianreto Manatschal,[1] and Daniel Bernoulli

Geologisches Institut, Eidgenössische Technische Hochschule, Zurich

Abstract. A comparison of the reconstructed southeastern margin of the Tethys ocean with the present-day Galicia margin shows that although both margins are of different age and had a different fate, their architectures and tectonic evolutions are very similar. Along both non-volcanic margins the site of rifting shifted from a broad area in the future proximal margins to a localized area in its distal parts, accompanied by a change in the mode of extension. During the initial phase of rifting, extension was accommodated by symmetrically arranged listric faults which soled at midcrustal levels, indicating that deformation in the upper crust was decoupled from deformation in the upper mantle along a hot and weak lower crust. During advanced rifting, extension was dominated by simple shear along low-angle detachment faults with a top-to-the-ocean sense of movement. These shallow crustal structures formed a series of breakaways in the continental crust and cut into mantle rocks, indicating that now deformation in the upper crust and in the upper mantle was no longer decoupled. Cooling and strengthening of the lower crust during an initial stage of rifting apparently led to localization of deformation and a different style of deformation, documenting that the tectonic evolution of nonvolcanic margins is largely controlled by the thermal state of the lithosphere. Seafloor spreading initiated only after exhumation and exposure of the subcontinental mantle on the ocean floor and may have been accompanied by a loss of the yield strength of the upper mantle, due to a combination of simple shear extension, asthenospheric uplift, and increased melt production.

1. Introduction

Present-day divergent, nonvolcanic margins record one of the major plate tectonic processes, i.e., the rifting and breakup of continental lithosphere and the exhumation of subcontinental mantle preceding the onset of seafloor spreading. In present-day passive margins the reconstruction of their early histories relies mainly on the interpretation of reflection seismic profiles, magnetic and gravity data, and, in a few places along sediment-starved margins like the one of Galicia, on the analysis of samples collected by deep-sea drilling and from submersibles. By contrast, mountain belts provide extensive outcrops of oceanic and continental basement rocks, of overlying prerift, synrift, and postrift sediments, and of associated fault rocks. However, in these areas the continent-ocean transition is often tectonically decoupled, the elements of the former margin are dismembered, and only under favorable conditions can the history of the margin be reconstructed. This is the case in a few segments of the Alps, particularly in the south Pennine-Austroalpine boundary zone of the eastern Alps and in the southern Alps, where well-preserved rift-related faults allow for the palinspastic reconstruction of the passive margin and the ocean-continent transition zone.

One of the best investigated present-day continental margins is the nonvolcanic margin west of Iberia from which a wealth of data from deep-sea drilling, submersibles, and reflection seismic profiling is avalaible. Although the overall structure of the margin is well known and a large amount of excellent data exists, several contrasting models for the evolution of this margin have been proposed (compare Figure 3 of *Reston et al.* [1996]), and there appears to be little consensus on important questions such as the mode of extension (pure shear versus simple shear or a combination of both, symmetrical or asymmetrical margins) and the kinematics of the fault systems involved.

In this paper we shall compare the early history of the Cretaceous nonvolcanic margin of Galicia with that of a Jurassic margin of the Alpine Tethys which was involved in Alpine thrusting and nappe formation. Our comparison is based on stratigraphic, structural, petrological, and geochronological data from the eastern and southern Alps, both published and our own, on published geophysical and deep-sea drilling material and on personal observations of deep-sea drilling cores. We shall document the striking analogies in the architecture of these margins and reconstruct their tectonic and kinematic evolution from initiation of rifting to mantle exhumation and beginning seafloor spreading. Also, we shall discuss the mode and kinematics of detachment faulting and the role of the lower crust during rifting. We postulate that the similarities between the two margins and their common evolution from rifting distributed over a wide area to localized extension along low-angle detachment systems may be explained by a model that includes changes in the rheology of the continental lithosphere during progressive rifting. We argue for asymmetric rifting dominated by simple shear extension during the late phases of rifting, leading to the exhumation of subcontinental mantle, and for a lower plate position of both margins as opposed to the Newfoundland and Briançonnais margins. We further document in detail the analogies between the Galicia and Adriatic margins, whereas in an earlier short contribution [*Manatschal and Bernoulli*, 1999] we outlined the general situation of the Galicia-Newfoundland and Adria-Briançonnais margin pairs without a detailed reference to their structural, sedimentological, and metamorphic evolution.

[1]Now at Ecole et Observatoire des Sciences de la Terre UMR 7517, Université Louis Pasteur, Strasbourg, France.

Paper number 1999TC900041.
0278-7407/99/1999TC900041$12.00

2. Paleogeographic and Tectonic Framework

2.1. General Situation

Late Triassic to Early Cretaceous rifting and opening of the different segments of the Mesozoic (Neo-)Tethys spatially followed, in the Atlantic and western Mediterranean area, approximately the Variscan orogeny. The resulting ocean basins were part of an equatorial spreading system which extended from the Caribbean to the eastern Mediterranean area and beyond, including the central Atlantic, the eastern Mediterranean, the Liguria-Piemonte ocean, and the Vardar-Meliata ocean to the east (Figure 1c). The evolution of these different branches of Tethys was determined by the movements of the North American, the African, the Eurasian, and the smaller Iberia and Adria plates (Figure 1c) [cf. *Ricou*, 1994]. The evolution of the Liguria-Piemonte ocean, from which most of the Alpine ophiolites are derived, was contemporaneous with and kinematically linked to the opening of the central Atlantic in the Jurassic and separated Eurasia from Adria. In the Early Cretaceous the Iberian plate separated from Laurasia and migrated eastward, leading to the opening of the Iberian Atlantic, the Bay of Biscay, and possibly also of another small ocean basin, the Valais ocean (Figure 1b) [cf. *Stampfli*, 1993]. Rotation of Iberia was kinematically linked with the opening of the Bay of Biscay and may have been associated with minor margin-parallel transfer movements along the west Iberian margin; however, most of the admittedly oblique extension was accommodated by the emplacement of oceanic crust and lithosphere. The different segments of the Atlantic-Tethyan ocean system opened at different times, and the closing of the Liguria-Piemonte segment was contemporaneous with ongoing spreading in the central and Iberian Atlantic and the opening of the North Atlantic (Figure 1b).

2.2. The Galicia Margin

The Galicia margin off NW Spain and Portugal (Figure 2) is a typical example of a non-volcanic, sediment-starved margin. It resulted from rifting and final breakup between the North American and the Iberian plates during Early Cretaceous time (Figure 1b). From this margin and its southern prolongation, a wealth of reflection seismic, magnetic, and gravity data were published, and rock samples are available from expeditions of the Deep Sea Drilling Project and the Ocean Drilling Program (Legs 47B, 103, 149, and 173), dredging, and submersible cruises. In this paper we shall concentrate on the northern portion of the Iberian margin, id est the Galicia margin west of the Galicia province in northwestern Spain. This portion of margin can be subdivided into three segments: the Interior and Porto Basins, Galicia Bank, and the Deep Galicia Margin (Figure 2). These segments can be distinguished by their different bathymetry and geological evolution during rifting.

2.2.1. The Interior and Porto Basins. The north-south trending Interior and Porto Basins form the proximal part of the margin and are considered to be the northward extension of the on-land Lusitanian Basin [*Montenat et al.*, 1988]. The two basins are bounded by normal faults which trend NNE-SSW and NW-SE and dip toward the basin centers, resulting in an assembly of moderately tilted blocks along the flanks and near-symmetrical grabens in the basin centers (Figure 2c). Transfer faults with a NE-SW to ENE-WSW orientation segment the basins. As no wells have been drilled in the Interior Basin, the reconstruction of its sedimentary and stratigraphic evolution is based mainly on correlation with

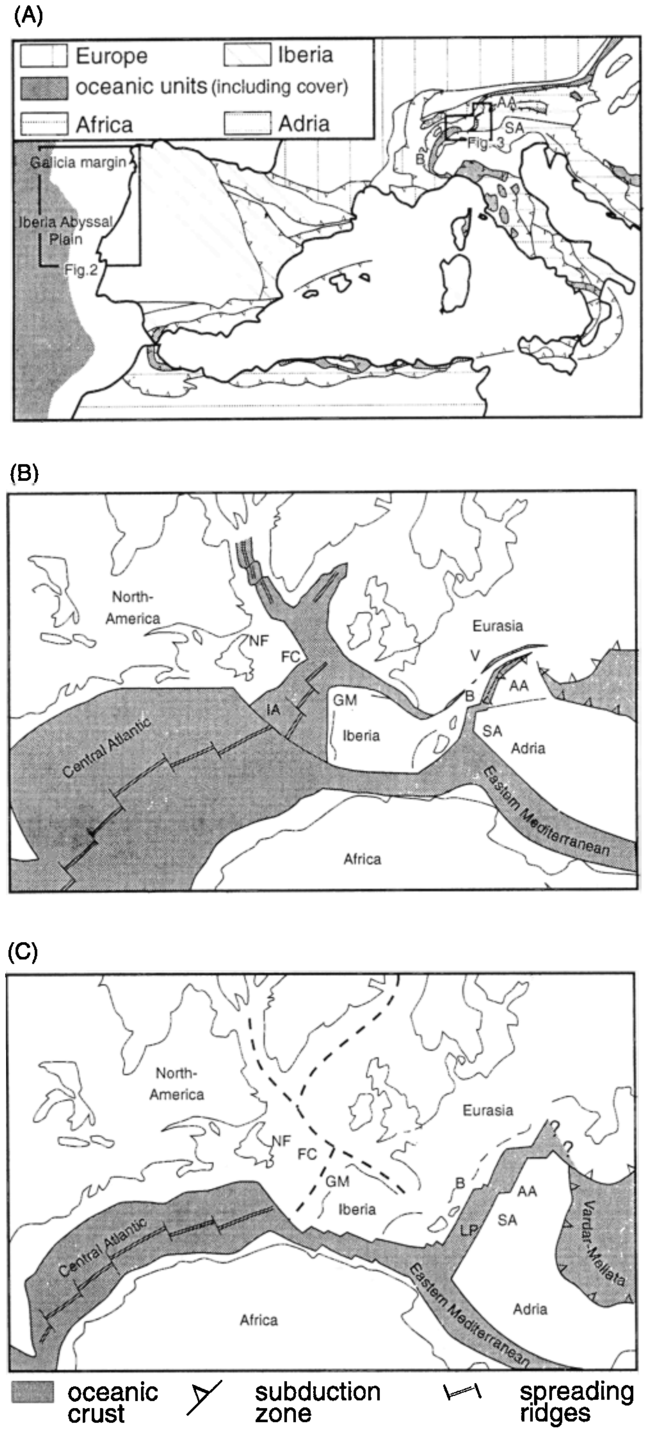

Figure 1. (a) Tectonic sketch map of the present-day west Mediterranean area showing the distribution of the European, Iberian, Adriatic, and African continental areas and the distribution of the tectonic elements derived from them. Oceanic units are remnants of the Mesozoic Tethys. (b,c) Large-scale paleogeography reconstructed for the Late Cretaceous (Figure 1b) and for the Late Jurassic (Figure 1c). AA, Austroalpine; B, Briançonnais; FC, Flemish Cap; GM, Galicia margin; IA, Iberian Atlantic; LP, Liguria-Piemonte ocean; NF, Newfoundland; SA, southern Alps, V, Valais ocean.

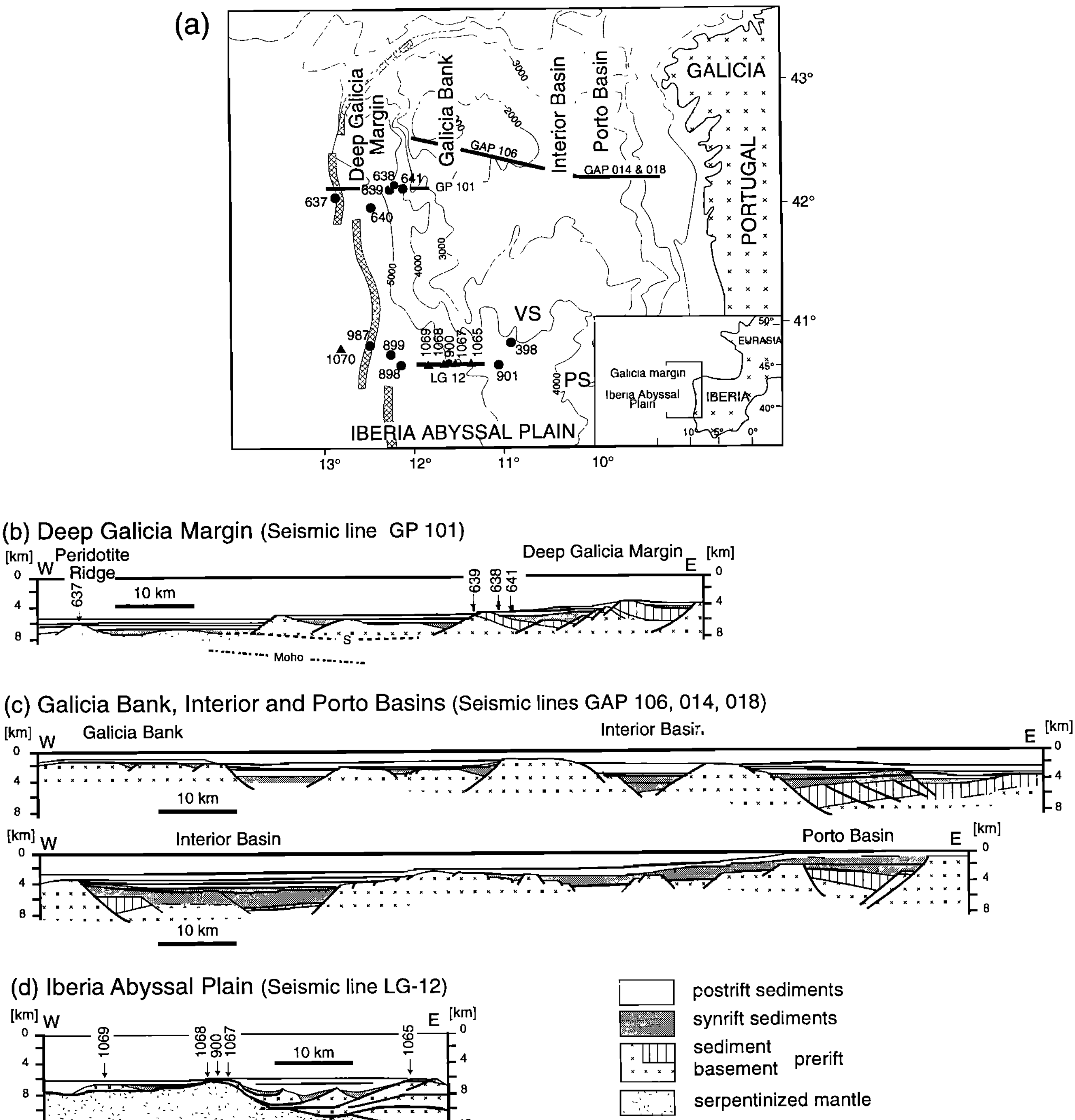

Figure 2. (a) Map of the Iberian margin west of Galicia and Portugal with the locations of Deep Sea Drilling sites and of seismic lines GP 101 and GAP 106, 014, and 018. Cross-hatched band marks the peridotite ridge. PS, Porto seamount; VS, Vigo seamount. (b) Seismic line GP 101 across the Deep Galicia Margin (after the work of *Mauffret and Montadert* [1987], discussed by *Pinheiro et al.* [1996]. Numbers refer to Ocean Drilling Program (ODP) Leg 103 Sites. S, *S* reflector. (c) Seismic lines GAP 106, 014, and 018 across the Galicia Interior Basin (after the work of *Murillas et al.* [1990], discussed by *Pinheiro et al.* [1996]). (d) Seismic line LG-12 across the Iberia Abyssal Plain after *Krawczyk et al.* [1996] with new interpretation.

wells in the Porto Basin and in the Deep Galicia Margin and on seismic stratigraphic correlation. In the Interior Basin, several events of extensional deformation can be defined, of which the most important is interpreted to be of Valanginian age [*Murillas et al.*, 1990].

2.2.2. Galicia Bank. Together with the Vigo and Porto seamounts, Galicia Bank forms a NNW-SSE trending alignment of elevated highs which separate the Interior Basin from the Deep Galicia Margin. Several authors [e.g., *Boillot et al.*, 1979] interpreted these highs as former horsts originating from Mesozoic rifting and uplifted during Tertiary compression. However, the geometry of the reflections, the nature of the seismic stratigraphic units, and the architecture of the basins are different east and west of Galicia Bank, suggesting that this ridge separates two different tectonic provinces of the margin.

2.2.3. Deep Galicia Margin. The Deep Galicia Margin includes the distal part of the margin and the continent-ocean transition, and it is characterized by N-S trending tilted fault blocks of continental basement and prerift sediments overlain by relatively thin synrift and postrift sequences. These tilted blocks are underlain by a prominent reflection, the so-called *S* reflector (Figure 2b) [*de Charpal et al.*, 1978; *Boillot et al.*, 1988]. The *S* reflector can be followed oceanward toward a ridge consisting of serpentinized peridotites, the so-called peridotite ridge [*Boillot et al.*, 1980]. This ridge is supposed to separate true oceanic crust to the west from a "transitional" and thinned continental crust to the east. Rifting in the distal margin and breakup between Newfoundland and Iberia are thought to have taken place from Valanginian to Aptian times [*Boillot et al.*, 1988].

2.3. The Adriatic Margin

2.3.1. Alpine tectonic evolution. By and large, the Alps are the product of continental collision between the Eurasian, the Iberian, and the Adriatic plates (Figure 1). This collision was preceded by the opening of three different oceans, the Vardar - Meliata (-Hallstatt) ocean to the east of Adria, the Liguria-Piemonte ocean between Adria and Briançonnais (a possible promontory of the Iberian plate), and the Valais ocean between Briançonnais and Europe. In the Alps, convergence started in the Early Cretaceous with the elimination of the Vardar - Meliata ocean and the collision with another microplate to the east [*Froitzheim et al.*, 1996]. As part of this orogeny, a thrust wedge propagated from the northeastern margin of Adria to the west, leading to a nappe edifice in the Austroalpine complex and its margin to the Liguria-Piemonte ocean. During this event the ocean-continent transition of the Piemonte-Adriatic boundary zone was telescoped into a number of thrust sheets.

During the Late Cretaceous and early Tertiary, tectonic activity shifted to the west, and most of the Liguria-Piemonte ocean was subducted below the Adriatic plate (Figure 1b). During the Eocene, subduction and related metamorphism affected also parts of the Briançonnais, the Valais ocean, and, later on, the lower part of the European lithosphere, whereas the upper crust was delaminated and accumulated in a number of crystalline basement and sedimentary decollement nappes [*Pfiffner et al.*, 1997]. The thrust sheets derived from the Adriatic margin including the most continentward parts of the Liguria-Piemonte ocean, i.e., the Platta nappe, were always part of the upper plate and escaped subduction and high-pressure metamorphism.

The Tertiary continent-continent collision with the Briançonnais and with Europe affected the south Pennine-Austroalpine boundary zone of Grisons only weakly. The Cretaceous nappe edifice was thrust more or less "en bloc" to the north and over the middle and north Penninic units (Briançonnais and Valais). In contrast, a southward propagating thrust wedge affected the domains of the Adriatic margin located today in the southern Alps, which were less deformed by the previous Late Cretaceous orogeny [*Schumacher et al.*, 1997].

2.3.2. The south Pennine-Austroalpine transect. The evolution of the Adriatic margin can be reconstructed along two transects in the Alps (Figures 3 - 5). In Grisons the elements of the former margin have been telescoped by thrusting during the Late Cretaceous; however, the ocean-continent transition has never been subducted to great depth, and metamorphism did not exceed lower greenschist facies along our transect [*Ferreiro Mählmann*, 1995, and references therein]. West directed shortening was of the order of 200 - 300% (about 100 - 150 km). The resulting nappe edifice includes (from top to bottom) the upper Austroalpine (Ötztal, Silvretta-Sesvenna, and Campo-Ortler), the lower Austroalpine (Bernina-Ela and Err nappes), and the south Pennine nappes (Arosa zone, Platta nappe, and Forno-Malenco complex) (Figures 3a and 3b).

Late Cretaceous nappe stacking was followed by extension which occurred still during the Late Cretaceous [*Froitzheim et al.*, 1994, 1996]. The amount of extension, however, was small compared with the amount of previous shortening. Compression and extension were parallel to previous extension during Jurassic rifting, and part of the Jurassic basins was inverted along rift-related east dipping faults. During this process, higher crustal levels including sediments and shallow basement were detached from their original basement; however, the coaxial Cretaceous phases of deformation allowed us to visualize a relatively straightforward kinematic inversion of the margin (for details, see *Froitzheim et al.* [1994] and *Manatschal and Nievergelt* [1997]). According to this kinematic reconstruction, the higher nappe units are derived from the proximal margin (upper Austroalpine) whereas the lower nappes represent the distal margin (lower Austroalpine, Err and Bernina nappes) and the transitional crust (Platta nappe). Because of the detachment of shallow crust and sediments, the deep structures of the margin are not preserved in our transect; however, deeper crustal levels of the prerift stage are exposed to the south in the Austroalpine Margna nappe and the ultramafic Malenco complex [*Hermann et al.*, 1997; *Müntener et al.*, 1999]. In contrast, shallow crustal structures of the proximal margin (Ortler-Silvretta) [*Eberli*, 1988; *Froitzheim*, 1988; *Conti et al.*, 1994], the distal margin (Err) [*Handy et al.*, 1993; *Manatschal and Nievergelt*, 1997) and of the ocean

Figure 3. (a) Tectonic sketch map and distribution of early Mesozoic faults of the western southern Alps and the south Pennine-Austroalpine boundary zone, Italy, and southeastern Switzerland (modified after *Bernoulli et al.* [1990] and *Schönborn* [1992]). (b) Profile across the south Pennine-Austroalpine units in Grisons (modified after *Froitzheim et al.* [1994] and *Manatschal and Nievergelt* [1997]). (c) Profile across the southern Alps [after *Schönborn*, 1992]. For traces of the profiles, see Figure 3a.

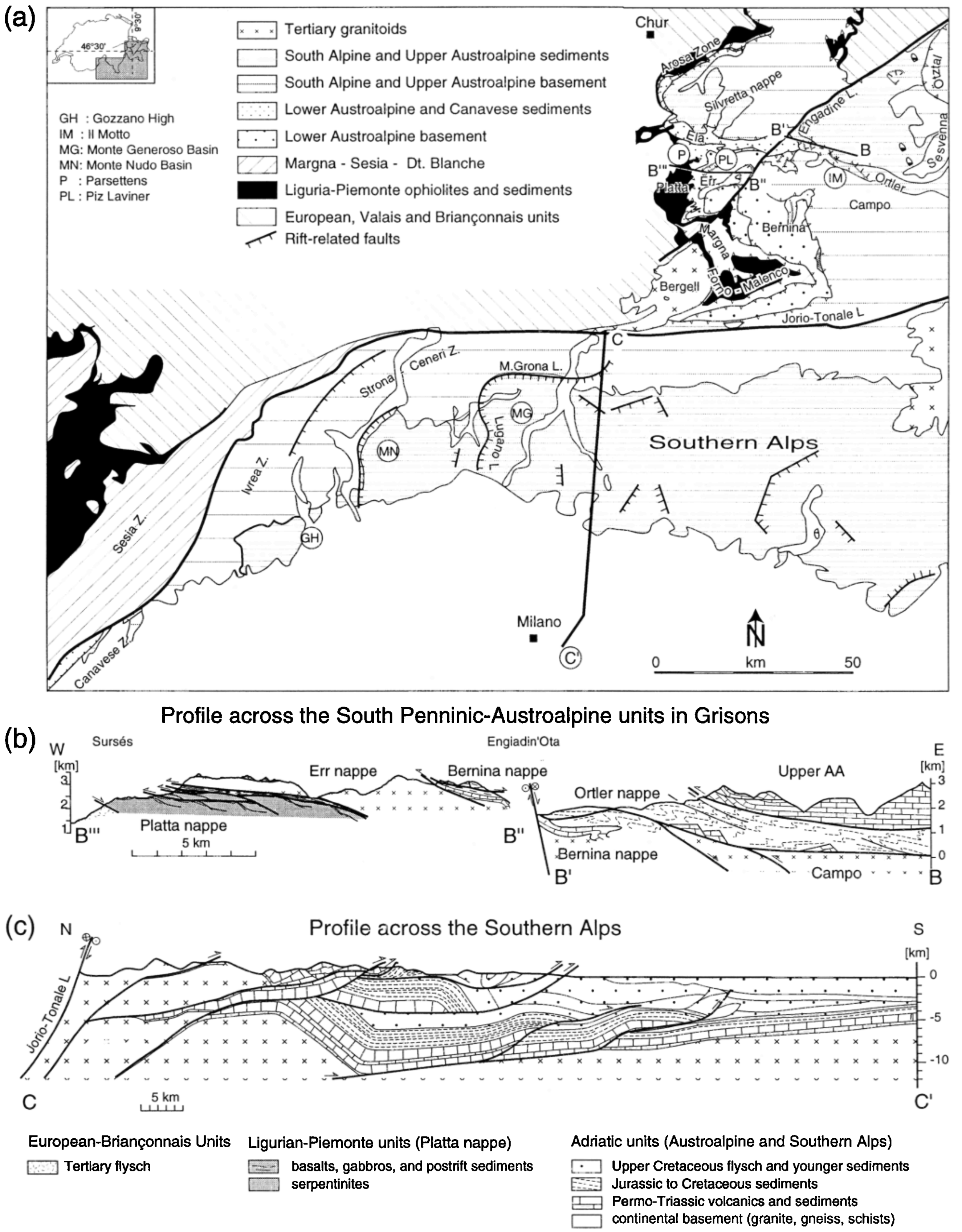
(a)
GH : Gozzano High
IM : Il Motto
MG: Monte Generoso Basin
MN: Monte Nudo Basin
P : Parsettens
PL : Piz Laviner
Tertiary granitoids
South Alpine and Upper Austroalpine sediments
South Alpine and Upper Austroalpine basement
Lower Austroalpine and Canavese sediments
Lower Austroalpine basement
Margna - Sesia - Dt. Blanche
Liguria-Piemonte ophiolites and sediments
European, Valais and Briançonnais units
Rift-related faults
Chur
Arosa Zone
Silvretta nappe
Engadine L.
Ela
Err
Platta
Bernina
Margna
Forno - Malenco
Bergell
Ortler
Campo
Sesvenna
Ötztal
Jorio-Tonale L
M.Grona L.
Ceneri Z.
Strona
Lugano L
Ivrea Z.
Sesia Z.
Canavese Z.
Southern Alps
Milano
0 km 50
Profile across the South Penninic-Austroalpine units in Grisons
(b)
W E
Sursés
Engiadin'Ota
Err nappe
Bernina nappe
Platta nappe
Ortler nappe
Upper AA
Bernina nappe
Campo
5 km
[km]
(c)
N S
Profile across the Southern Alps
Jorio-Tonale L
5 km
C C'
European-Briançonnais Units
Tertiary flysch
Ligurian-Piemonte units (Platta nappe)
basalts, gabbros, and postrift sediments
serpentinites
Adriatic units (Austroalpine and Southern Alps)
Upper Cretaceous flysch and younger sediments
Jurassic to Cretaceous sediments
Permo-Triassic volcanics and sediments
continental basement (granite, gneiss, schists)

floor sequence (Platta) (*Dietrich* [1969, 1970] and this paper) are well preserved along our transect. Younger, N-S directed shortening and associated transcurrent faulting during Tertiary time are of subordinate importance within our transect [*Froitzheim et al.*, 1994] and are not considered in the kinematic inversion and palinspastic reconstruction.

2.3.3. The southern Alps transect. The southern Alps in southern Switzerland and northern Italy preserve another transect across the same margin to the south (Figures 1, 3a, and 3c) [*Bernoulli et al.*, 1979; *Winterer and Bosellini*, 1981]. Basement and sediments of the proximal margin segment are well exposed in the central portion of the southern Alps north of Milano, but the distal part, situated in the Canavese zone, is poorly outcropping and heavily deformed (Figure 3a). A precise reconstruction of the distal margin is therefore not possible along this transect. In the central Lombardian segment, north-south shortening during the Late Cretaceous and Tertiary was between 80 and 100 km and parallel to the strike of the Jurassic rift faults which were partly reactivated as transcurrent faults and oblique ramps within the east-west trending fault-and-thrust belt (Figure 3c) [*Schönborn*, 1992]. Nevertheless, a few of the Jurassic rift faults can be followed into the basement [*Bertotti*, 1991], and the anatomy of the proximal margin can be reconstructed from the depositional geometries of the well-exposed synrift sediments [*Bertotti et al.*, 1993].

Both sectors of the margin, the northern and the southern transect, are divided into segments with a characteristic structural and sedimentary evolution which is discussed in section 3. These segments are from west to east (1) a distal margin (Err in the north and Canavese in the south), (2) a boundary zone between the distal and the proximal margins (Bernina-Ela in the north and Gozzano in the south); and (3) a proximal part of the margin (Ortler-Silvretta in the north and Lombardian basin in the south) (Figures 4b and 4C).

3. Anatomy of the Margins

3.1. Continental Crust and Prerift Sediments

3.1.1. Galicia margin. The continental basement of the Galicia margin is known from very limited samples from drill holes and submersible dives, and its age and tectonic evolution are not well defined. Plutonic and metamorphic rocks [e.g., *Capdevila and Mougenot*, 1988] are locally overlain by thick, weakly metamorphosed sandstones, dolomites, and volcanoclastics of Late Devonian-early Carboniferous age [*Mamet et al.*, 1991]. A similar sequence is found in the Ossa-Morena zone in Portugal and southern Spain. This suggests that the Galicia margin is underlain by the northwestward prolongation of this external zone of the Variscan orogen. The occurrence of undeformed lower Paleozoic rocks at Flemish Cap in the conjugate Newfoundland margin [*King et al.*, 1986] indicates that this latter area was situated outside the Variscan belt and that the breakup between Newfoundland and Iberia followed more or less the Variscan front [*Capdevila and Mougenot*, 1988].

Lower crustal rocks have not been found so far along the Deep Galicia Margin, except for a few granulite samples. Fission track ages on zircons from two of them were Carboniferous to Early Permian [*Fuegenschuh et al.*, 1998], indicating that these rocks cooled to about 250°C at this time and were at upper crustal levels when rifting initiated.

Little is also known about the prerift sediments. In the Deep Galicia Margin, sandstones with volcanic detritus, interbedded with shaly dolomites and conglomerates, are overlain by about 400 m of Tithonian shallowwater carbonates. On Galicia Bank the basement is separated from these carbonates by a horizon which shows evidence of soil development during Mesozoic emergence [*Mamet et al.*, 1991]. Thus the area occupied by the Galicia margin was in shallow water or at sea level before rifting started in Cretaceous time.

3.1.2. Continental crust and prerift sediments of the Adriatic margin. In the southern Alps a pre-upper-Carboniferous (Variscan) metamorphic basement underlies the upper Paleozoic and Mesozoic formations. Some controversies exist about the importance and significance of earlier, Cadomian or early Paleozoic events which are documented by an increasing amount of radiometric data. Amphibolite-grade metamorphic mineral assemblages in the Variscan basement document extremely low-pressure (p), high-temperature (T) metamorphism as it is characteristic for extensional areas with a high heat flow [e.g., *Lardeaux and Spalla*, 1991]. Post-Variscan, Early Permian (290 Ma) extension is also documented by syntectonic intrusions of gabbros along the crust-mantle transition in the Ivrea zone [*Quick et al.*, 1994], accompanied by granulite formation and partial melting in the lower crust and the emplacement of granitic batholiths in the middle and upper crust, both contemporaneous with the formation of sedimentary basins and the extrusion of andesitic, dacitic, and rhyolitic volcanic rocks at the surface.

Like in the Ivrea zone, gabbros intruded during the Permian at the crust-mantle transition of the Malenco complex [Hermann *et al.*, 1997]. These gabbros crystallized at 10 - 12 Kbar, indicating that the Moho was at that time at about 30 km depth. Pressure-temperature-time data obtained from the gabbros and the surrounding granulites and ultramafic rocks document isobaric cooling which lasted for about 50 Myr, before these rocks were exhumed during Late Triassic and Early Jurassic rifting [*Müntener et al.*, 1999].

The sedimentary prerift sequence of the Adriatic margin starts with Upper Permian to Middle Triassic continental clastics of variable thickness. These subaerial deposits are overlain by Middle to Upper Triassic dolomites, limestones, and minor evaporites and shales. Varying thicknesses indicate differential subsidence and local tectonic activity, possibly in connection with ongoing transtensional/ transpressional movements [*Handy and Zingg*, 1991] or events connected with the evolution of the Vardar-Meliata ocean to the east [*Bertotti et al.*, 1993]. The prerift sequence is generally thicker (1 - 5 km) in the east (upper Austroalpine) and south (southern Alps) and thinner (< 500 m) in the lower Austroalpine in the northwest.

3.1.3. Similarities in the prerift history of the two margins. The very different quality and density of data, as well as the poorly known crustal evolution of the Austroalpine and south Alpine areas during the Permian and Triassic, make a direct comparison of the continental basement and the prerift sedimentary sequence of the two margins difficult. There are, however, important similarities at least as far as the lower Austroalpine and the western south Alpine basement are concerned. For both margins we can assume (1) a Variscan overprint of the continental crust and (2) an isostatically equilibrated, about 30 km thick continental crust before initiation of rifting, as is indicated by limited subsidence and shallow water conditions prevailing over a long time before initiation of rifting and by the p-T-t data of the mantle-crust boundary in the Malenco area [*Müntener et al.*, 1999]. We therefore think that the continental crust underlying the two margins had a similar

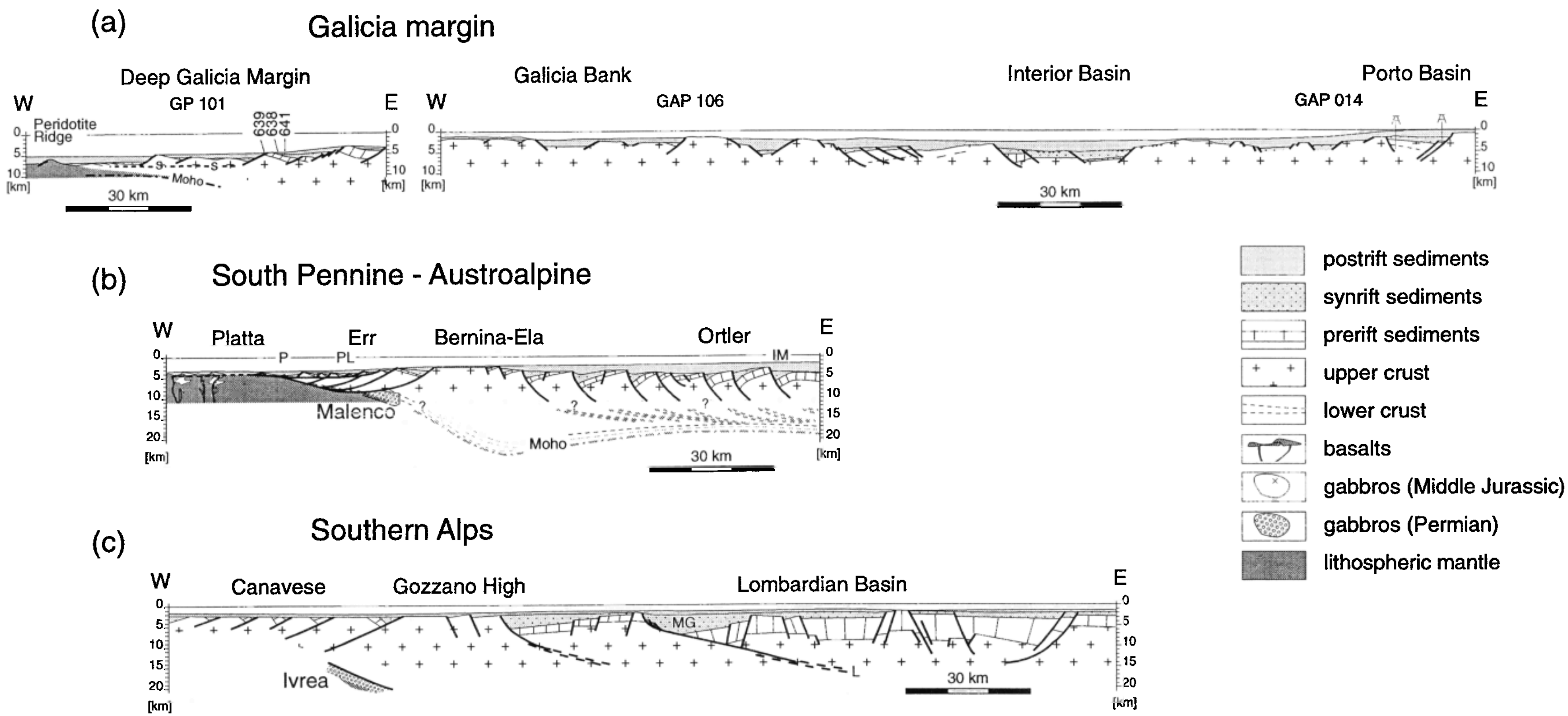

Figure 4. Reconstructed geological profiles across the Iberian (today) and Adriatic margins (Late Jurassic). (a) Galicia margin (modified after *Murillas et al.* [1990]). (b) South Pennine-Austroalpine boundary zone. IM, Il Motto; P, Parsettens; PL, Piz Laviner. (c) Southern Alps (modified after *Bertotti et al.* [1993]). MG, Monte Generoso Basin; L, Lugano-Monte Grona fault.

tectonic and thermal evolution before the onset of rifting and that the conditions at the onset of rifting were similar for the two margins.

3.2. Rift Basins and Synrift Sediments

Rift basins, bounded by normal faults and tilted blocks, are the most prominent structures defining the architecture of rifted margins (e.g., Figures 2b and 2c). Because the formation of basins and the deposition of synrift sediments are closely linked, they will be discussed together in this section. Rift-related structures, such as the intrabasement reflections and detachment faults, will be discussed in section 4.

The age of the onset of rifting and therefore also the duration of rifting depends on the way rifting is defined. In the Alpine Tethys, Permian and Middle Triassic extension have been interpreted by several authors as precursors of the opening of the Tethyan ocean [e.g., *Winterer and Bosellini*, 1981]. Likewise, Late Triassic to Early Jurassic crustal extension and basin formation in the Iberian and North Atlantic area have been related to the later opening of the corresponding ocean basins; however, these early extensional events are separated from break-up by a time interval of some 100 Myr during which tectonic activity and subsidence were discontinuous. Moreover, Permian and Triassic extension and related subsidence occur over large areas of northern Europe which never evolved into oceanic areas. In this paper we shall refer to rifting as the extensional processes continuously and progressively leading to break-up and continental separation. In the Alpine Tethys and along the Iberian margin, crustal extension leading to continental separation lasted about 30 - 50 Myr.

3.2.1. Rift basins and synrift sediments along the Galicia margin. Along the Galicia margin, rifting apparently started in the Interior Basin during the Valanginian, as postrift sedimentary sequences of assumed Hauterivian to Aptian age drape the rift basins [*Murillas et al.*, 1990]. Data from Deep Sea Drilling Project (DSDP) Leg 47B and Ocean Drilling Project (ODP) Leg 103 indicate that rifting along the Deep Galicia Margin was later, from Hauterivian to Aptian time [*Boillot et al.*, 1989a]. These scanty data suggest that rifting along the Galicia margin was diachronous, beginning in the Interior Basin and shifting only later to the Deep Galicia Margin. A similar spatial and temporal evolution of rifting is reported from the transect farther to the south between the Iberian Abyssal Plain and the Lusitanian Basin. In this transect, rifting started in late Oxfordian-early Kimmeridgian time in the proximal Lusitanian Basin [*Wilson et al.*, 1989] and shifted after the Tithonian, probably during the early Valanginian, to the distal Iberian Abyssal Plain [*Wilson et al.*, 1996]. Likewise, the formation of oceanic crust started earlier in the south (136 Ma) from where it propagated to the north [*Whitmarsh and Miles*, 1995].

In the Interior and Porto Basins most of the basins are bounded by antithetic high-angle and/or listric normal faults, and the overall geometry is that of a horst and graben structure (Figure 2c). The sedimentary fill is much thicker than that in the more distal basins of the Deep Galicia Margin (Figures 2b and 2c). Initial faulting led to drowning as well as to uplift and erosion of parts of the Tithonian-Lower Cretaceous carbonate platform and to the accumulation of a thick clastic sequence in the depocenters of the Porto Basin. Toward Galicia Bank the rift basins become shallower, and normal faulting appears to have been of lesser importance.

In the Deep Galicia Margin, rift basins are bounded by west dipping normal faults separating fault blocks tilted toward the east, i.e., toward the continent. These blocks are underlain by a strong reflection, the so-called *S* reflector. The size of the blocks decreases toward the ocean. The fault blocks are cut off and/or slightly offset by a discrete pattern of transfer faults which strike east-northeast or east-southeast and show a quite regular spacing of about 20 km. The blocks overlying the *S* reflector consist of continental basement rocks and prerift sediments and are unconformably overlain by a synrift sequence including marlstones, turbiditic sandstones, claystones, and hemipelagic limestones interbedded with debris flow deposits of Hauterivian to early Barremian age. In the half grabens these synrift sediments are up to 1 km thick but thin and locally pinch out toward the highs of the tilted blocks along onlap surfaces and internal unconformities [*Boillot et al.*, 1989a]. Quartzo-feldspatic sandy turbidites in the basins west of Galicia Bank are derived from the erosion of a subaerial, narrow high occupying the present area of Galicia Bank [*Winterer et al.*, 1988]. This implies tectonic uplift of Galicia Bank simultaneously with rifting and subsidence in the Deep Galicia Margin.

3.2.2. Rift basins and synrift sediments of the Adriatic margin. In the Alpine transect, rifting started in the areas which were to become the proximal parts of the future margin(s). In the Adriatic margin the geometry of the rift basins can be reconstructed from the relationships between prerift, synrift, and postrift sediments, their depositional geometries, and their relations to Jurassic fault scarps. At places, the Jurassic faults have not been reactivated, and their geometry can be observed directly [*Eberli*, 1988; *Froitzheim*, 1988; *Bertotti*, 1991; *Conti et al.*, 1994].

The first rift basins formed during the latest Triassic. They were depressions only a few kilometers wide in which coarse resediments, derived from active fault scarps, were deposited [*Bertotti*, 1991]. The shape and orientation of these basins could suggest a left-lateral component in their formation. During the Rhaetian, extension continued; however, because of high sedimentation rates, the faults had no major morphological expression [*Bertotti et al.*, 1993].

In the early Liassic the number of active faults decreased, and strain was gradually concentrated along a few major crustal faults. These faults controlled the sedimentation in the adjacent basins, which was characterized by olistoliths, coarse lithic breccias, slump complexes, and calcareous turbidites interbedded with hemipelagic spongolithic limestones [*Bernoulli*, 1964; *Eberli*, 1988]. Locally, these basinal deposits reach a thickness of a few kilometers. On the sediment-starved highs, submarine faulting produced a network of sediment-filled fractures (neptunic dikes) and complex tectono sedimentary breccias. Rifting in the proximal parts of the future margin ceased in the middle to late Liassic; however, some of the faults became inactive even earlier and were sealed by lower Liassic (upper Sinemurian) sediments (Figures 5 and 6f) [*Eberli*, 1988; *Conti et al.*, 1994].

In the southern Alps, facies and thickness of the synrift sediments abruptly change across these Jurassic faults, and their depositional geometries define the rift basins as half-grabens, up to 30 km wide (Figure 4c) [*Bernoulli*, 1964; *Bertotti*, 1991]. The Lugano-Monte Grona fault bounding the Late Triassic-early Liassic Generoso basin to the west can be traced from the surface into the Variscan basement over a horizontal distance of more than 30 km (Figure 7). This fault was active as a top-to-the-east normal fault and can be traced from the brittle into the ductile field where quartz mylonites formed. On the basis of the depositional geometry of the synrift sediments and on the temperature conditions during deformation, *Bertotti* [1991] could show that the fault had a listric geometry and soled out at a depth of about 15 km.

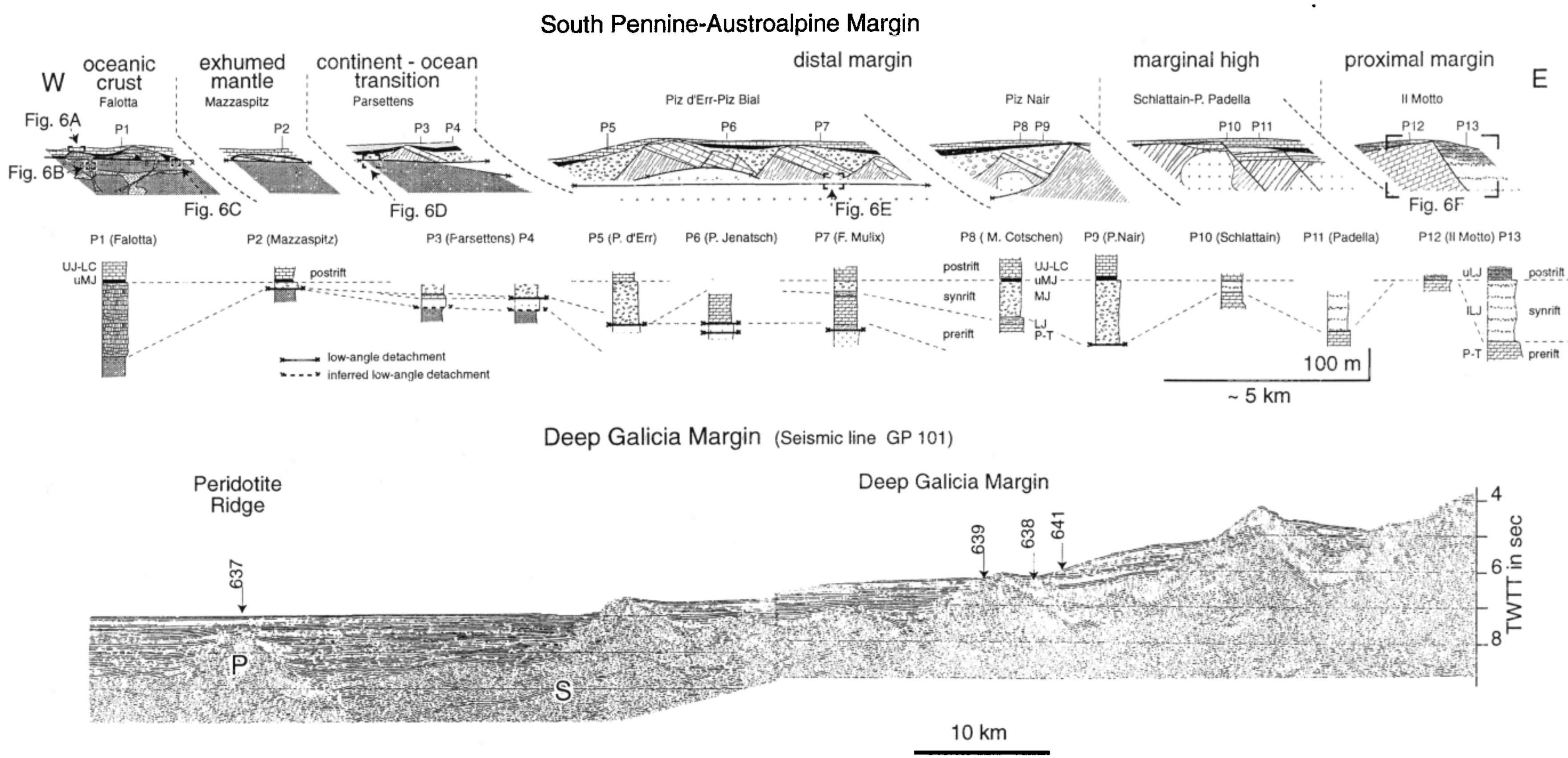

Figure 5. (top) Relationships between sediments, fault zones, and exhumed mantle rocks along the south Pennine-Austroalpine margin and (bottom) comparison with the Deep Galicia Margin. The top section represents portions of the margin, now in different tectonic imbricates, which preserve rift-related structures and depositional contacts with sediments. The corresponding lithostratigraphic columns document measured sections. For further reference to the stratigraphic columns, see *Eberli* [1988] and *Manatschal and Nievergelt* [1997]. Abbreviations are as follows: LC, Lower Cretaceous; UJ, Upper Jurassic; uMJ, upper Middle Jurassic; MJ, Middle Jurassic; LJ, Lower Jurassic; uLJ, upper Lower Jurassic; lLJ, lower Lower Jurassic; P-T, Permian-Triassic. The reflection seismic section below shows a portion of the Deep Galicia Margin including transitional crust in the peridotite ridge and continentward tilted blocks overlain by synrift and postrift sediments in the distal continental margin. P, peridotite ridge; S, *S* reflection, TWTT, two-way travel time. Numbers show locations of ODP sites. From *Boillot et al.* [1988].

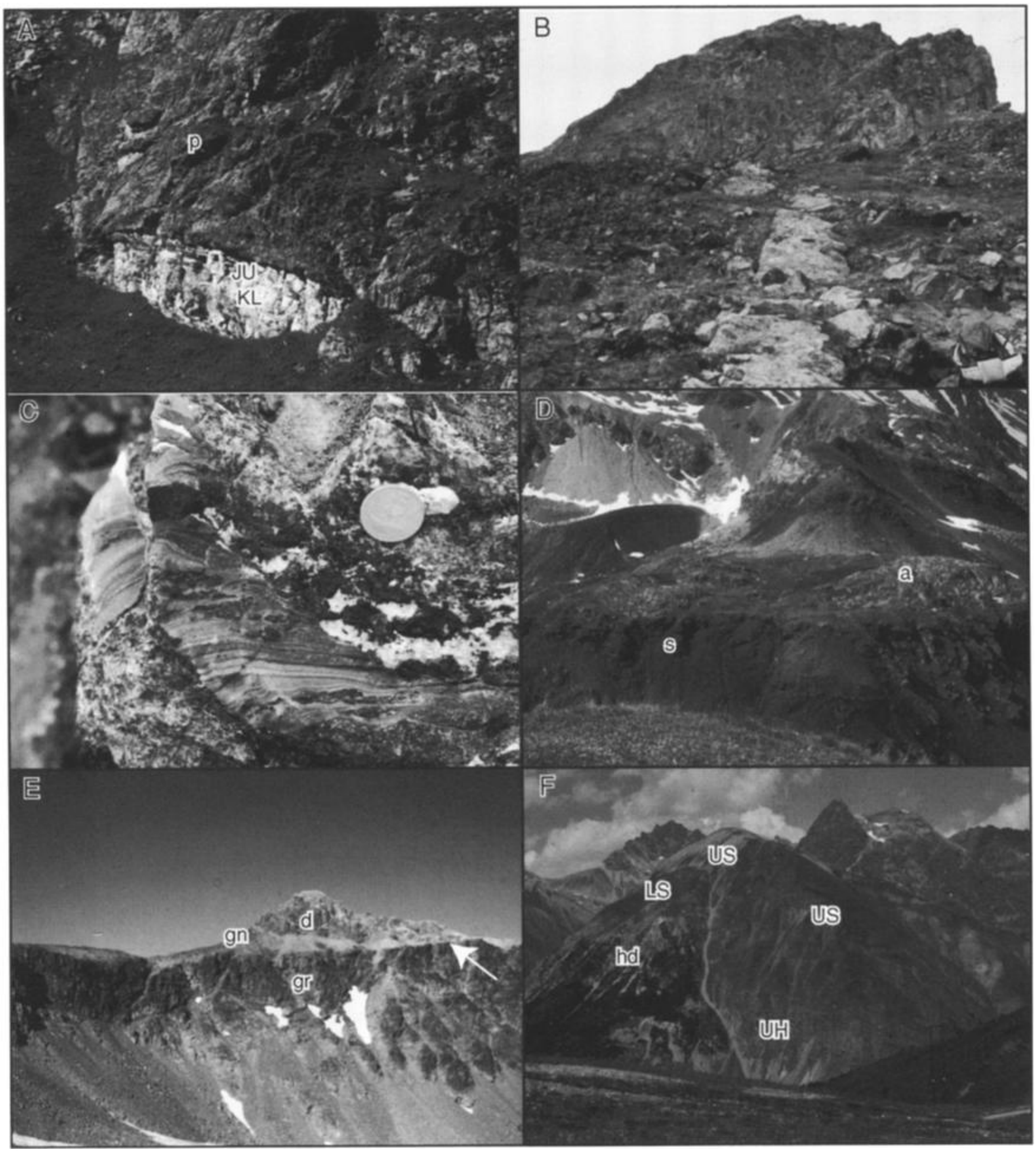

Figure 6. Geometrical relationships between postrift, synrift, and prerift sediments, continental, transitional and oceanic crust, and rift-related faults. (a) Pillow basalt (p), stratigraphically overlain by about 3 m of uppermost Middle to Upper Jurassic radiolarites (JU), and Lower Cretaceous white pelagic limestones (KL). The sequence is overturned. Platta nappe, Val Savriez, Grisons. (b) Undeformed, nonrodingitized basaltic dike cutting across serpentinized peridotites. Serpentinization predates emplacement of the dike (and extrusion of pillow lavas). Platta nappe, Starschagns, Grisons. (c) Pocket in serpentinized peridotite filled by internally deposited sediment. Layers and laminae of serpentinitic arenite with limestone matrix show distinct size-grading and lamination. Together with the radiolarites stratigraphically overlying the serpentinites, these internal sediments document exposure of the serpentinites at the seafloor. Coin is 2 cm in diameter. Arosa zone (lateral equivalent of Platta nappe), Totalp, Grisons. (d) Serpentinized peridotite (s), overlain by an extensional allochthon (a) composed of brittlely deformed granite and orthogneiss. The subhorizontal contact between the serpentinites and the allochthon is locally marked by a black fault gouge, clasts of which also occur in synrift debris flow breccias, documenting the Mesozoic age of emplacement of the allochthon. (e) Low-angle detachment fault (arrow) separating Variscan continental basement (Err granite, gr) below from tilted block composed of Variscan gneiss (gn) and prerift sediments (Lower Triassic sandstones and Middle Triassic dolomites (d), Err nappe, Piz Lavinèr, Grisons. (f) Jurassic high-angle fault separating Upper Triassic prerift sediments (Norian Hauptdolomit Formation (hd) to the left) from Liassic synrift sediments (Allgäu Formation, upper Hettangian (UH), lower Sinemurian (LS), upper Sinemurian (US)) to the right. Synrift sediments are hemipelagic spiculitic limestones with intercalations of thick debris flow breccias and proximal turbidites. The prerift sediments to the left are unconformably overlain by lower Sinemurian breccias, and the fault is sealed by upper Sinemurian basinal limestones. Il Motto, Sondrio Province, Italy.

Fault geometry and basin fill architecture of the south Alpine basins are conspicuously similar to that observed in reflection seismic profiles across the Jeanne d'Arc basin of the Newfoundland margin (Figure 7) [*Keen et al.*, 1987]. This basin is situated on the conjugate margin of the Iberian Atlantic; however, it evolved during early rifting when the evolution of the future margins was still symmetrical (see below).

In the Austroalpine proximal margin, exceptional exposures in the Ortler nappe allowed scientists to identify several high-angle normal faults [*Froitzheim*, 1988; *Conti et al.*, 1994]. Here the different subbasins appear to be smaller than those in the southern Alps; spacing between the faults is only of the order of 5 - 10 km, and the thickness of the basin fill is less than 1 km. At Il Motto (Figures 5 and 6f), one of these high-angle normal faults separates prerift Upper Triassic dolomites to the west from lower Liassic fault scarp-derived breccias interbedded with turbidites and hemipelagic sediments to the east. The synrift sediments show thinning and fining upward cycles and are overlain by pelagic and hemipelagic sediments of late Sinemurian age which also overlie the dolomites to the west sealing the fault. The reconstruction of the original fault geometry shows that near the surface the fault was dipping 60° - 70° toward the east.

In contrast to the basins in the proximal margin, the basins in the distal margin are less well preserved. The reconstruction of the basin geometry is mainly based on the depositional geometries of the synrift sediments which show that these basins were smaller [*Finger et al.*, 1982]. Their spacing was of the order of 3 - 5 km, and the sedimentary fill was only a few hundred meters thick. In many places, the synrift sediments overlie directly low-angle detachment faults exposed at the seafloor.

Rifting along the distal part of the margin (Err domain) initiated later than in the proximal margin, during the late Liassic (Toarcian) or earliest Middle Jurassic: middle Liassic hemipelagic cherty limestones (Agnelli Formation) show a constant thickness across the entire distal margin and no indication of synsedimentary faulting. The limestones terminate with a typical submarine hard ground and are unconformably overlain by deep-water clastics, interbedded with hemipelagic marls and between 200 and 450 m thick (Figure 5, Saluver Formation) [*Finger et al.*, 1982]. The formation includes siliciclastic turbidites, often with a reddish matrix and coarse, unsorted, polygenic breccias with variable amounts of matrix and clasts predominantly derived from the basement. The frequent occurrence of clasts of alkali granite, characteristic for the Bernina nappe [*Spillmann and Büchi*, 1993], indicates uplift and subaerial exposure of parts of the Bernina domain contemporaneous with downfaulting of the Err domain. The age of the Saluver Formation is weakly constrained; it is younger than the lower Pliensbachian hard ground along the top of the Agnelli Formation (H. Furrer, personal communication, 1997) and older than the overlying upper Middle Jurassic Radiolarite Formation [*Baumgartner*, 1987]; therefore a late Liassic (Toarcian) to early Middle Jurassic age may be assumed for these synrift sediments. Contemporaneous with initial faulting in the distal margin, a second pulse of gravity flow sedimentation is noted in the distal part of the proximal margin (eastern Bernina-Ela) [*Eberli*, 1988]. This late Liassic event may be associated with the uplift of the Bernina domain reactivating the fault(s) bounding the adjacent basin to the east. However, in contrast to the siliciclastic gravity flow deposits of the Saluver Formation, fault scarp derived breccias and turbidites of the proximal margins yield no basement clasts but only fragments of Triassic dolomites and limestones and penecontemporaneously displaced carbonate material.

3.2.3. Similarities in the synrift evolution of the two margins. Although the age of rifting is different in the two margins, there are remarkable analogies in their evolution. The duration of rifting along both margins is of the order of some 40 Myr. Along both margins, rifting shifted to the distal margin about 20 Myr before onset of seafloor spreading, reflected by the younging of the synrift and postrift sediments toward the ocean. A similar sedimentary evolution is suggested by comparable facies and thickness variations across the margins, in turn suggesting a similar isostatic response to extension. Another similarity is the change of the basin architecture from large-scale and overall symmetrical in the proximal margin to small-scale and asymmetrical in the distal margin.

3.3. Transitional and Oceanic Crust

3.3.1. Transitional and oceanic crust along the Galicia margin. A major result of ODP Leg 103 was the discovery of serpentinized mantle rocks exposed at the seafloor. The serpentinized mantle rocks occur along a 10 - 12 km wide segmented "ridge" [cf. *Boillot et al.*, 1987] which can be followed over 125 km parallel to the continent-ocean boundary. Basalts and gabbros occur only locally on the ridge itself [*Boillot et al.*, 1995b] but are more common along its western slope. Refraction seismic and magnetic data suggest the existence of a thin oceanic crust west of the peridotite ridge [*Whitmarsh et al.*, 1993]. On the eastern flank of the ridge the Galinaute II submersible cruise [*Boillot et al.*, 1995b] sampled a breccia with fragments of ultramafic, mafic, and continent-derived rocks. This breccia has been interpreted by *Boillot et al.* [1995b] as a tectonic breccia formed during Early Cretaceous rifting along a low-angle, brittle detachment fault.

The seismic velocity structure and magnetic anomalies of the peridotite ridge are distinctly different from those expected from either a true oceanic crust or a thinned continental crust [e.g., *Discovery 215 Working Group*, 1998]. Therefore this type of crust has been termed transitional [*Whitmarsh and Sawyer*, 1996]. The transitional crust is assumed to consist mainly of serpentinized peridotites separating thinned continental crust to the east from true ocean crust to the west. The serpentinization front is assumed to lie, on the basis of the seismic velocity structure, at 5 - 6 km below the seafloor [*Boillot et al.*, 1988] and to coincide with the Moho reflection observed in seismic profiles.

Samples collected by dredging, by drilling, and from submersibles show that the transitional crust consists of serpentinized plagioclase-bearing harzburgite and lherzolite [*Beslier et al.*, 1990], locally cut by rare plagioclase-rich veins and dioritic intrusions. The petrological and structural evolution of the serpentinized peridotite documents the following history of exhumation: (1) partial melting of the peridotite at temperatures of 1250° - 970°C, (2) formation of mylonites at temperatures decreasing from about 1000° to 850°C; (3) crystallization of pargasite (900° - 800°C) and other amphiboles under static conditions (750°C), (4) beginning hydrothermal alteration, (5) serpentinization (<300°C), and (6) brittle fracturing and filling of the fractures with serpentinite fragments and calcite cements (Figure 8), [cf. *Evans and Girardeau*, 1988; *Girardeau et al.*, 1988; *Beslier et al.*, 1990).

Foliated dikes of dioritic composition cutting across the serpentinites include brown amphibole overgrowing a high-

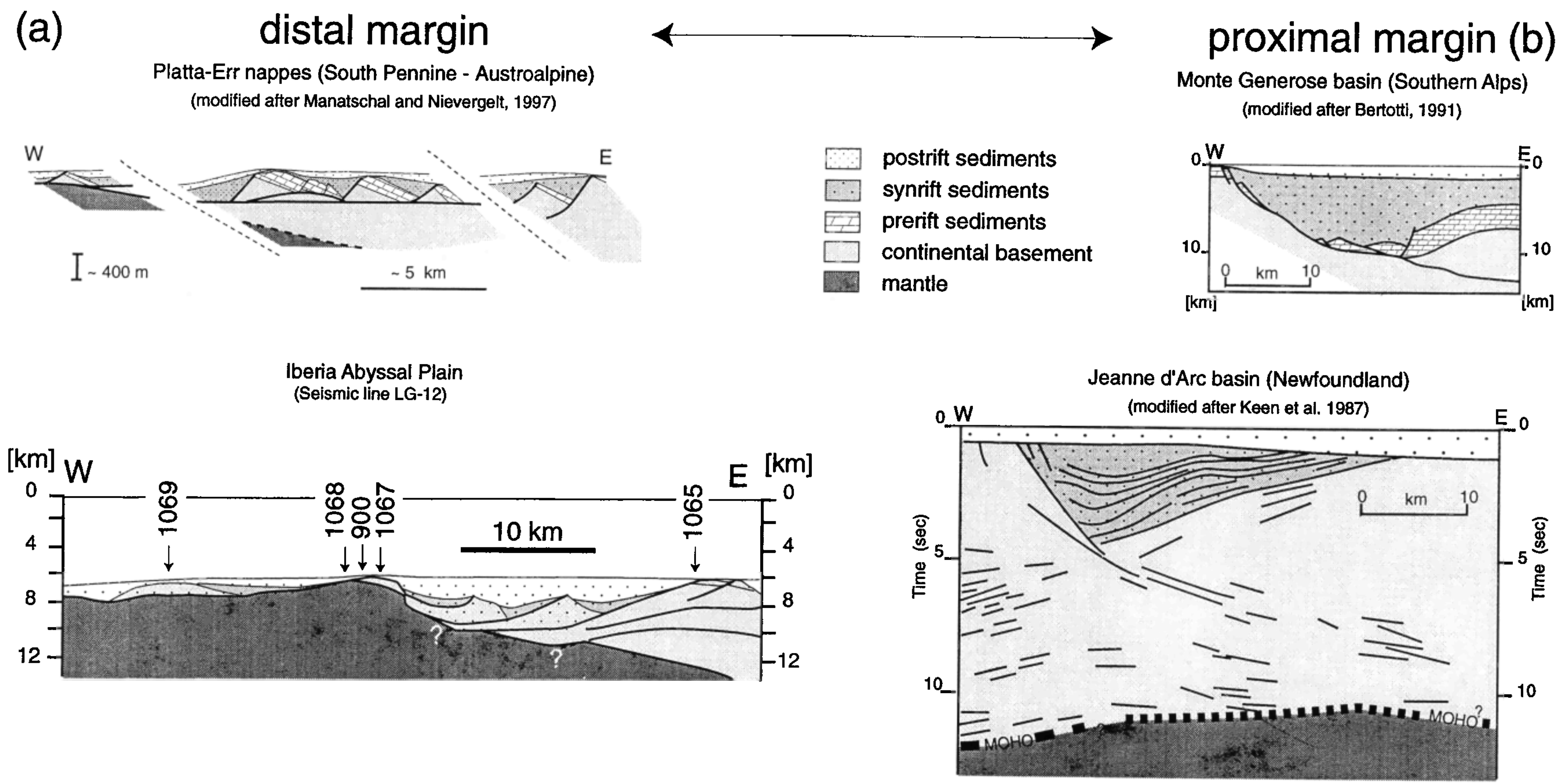

Figure 7. Architecture of rift basins in (a) distal margins and (b) proximal margins. Margins of the Liguria-Piemonte ocean (top cross sections) and the Atlantic (bottom cross sections) are shown, documenting different styles of extensional faulting, basin geometries, and mantle exhumation during early and late rifting. Examples in top cross sections are based on field studies from the Alps, and those in the bottom cross sections are based on seismic profiles from present-day margins.

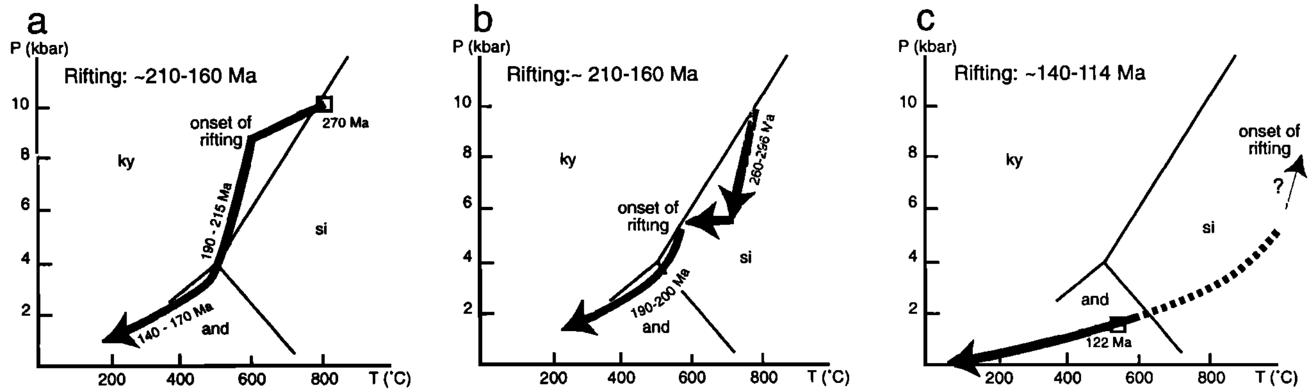

Figure 8. P-T-t paths of lower crustal and mantle rocks from the Adriatic and Galicia margins: (a) Malenco (granulites), (b) Ivrea (granulites), and (c) Galicia (peridotite). The examples of the Malenco and Ivrea granulite terrains have been compiled by *Hermann* [1997]. For locations, see Figures 3 and 4, and for details and further references, see *Müntener et al.* [1999] for Malenco and *Handy and Zingg* [1991, and references therein] for Ivrea. For the Galicia margin, see *Boillot et al.* [1995a, and references therein].

temperature foliation. The $^{39}Ar/^{40}Ar$ dating of amphiboles from one of these dikes yielded a well-constrained plateau age of 122±0.6 Ma [*Féraud et al.*, 1988]. This age is compatible with the U-Pb ages of 13 different zircon fractions from a gabbro and a sheared chlorite-bearing schist from the same locality, which yielded an identical age of 122±0.3 Ma [*Schärer et al.*, 1995]. Thus dike and gabbro emplacement predates the breakup, generally assumed to occur at 114 Ma along the Galicia margin [*Boillot et al.*, 1988], indicating the occurrence of synrift magmatic activity.

Basalts collected during submersible dives along the northwestern Galicia margin and from the peridotite ridge show a tholeiitic signature free of continental contamination [*Kornprobst et al.*, 1988; *Malod et al.*, 1993; *Charpentier et al.*, 1998]. Rare earth element patterns and isotopic ratios (Nd and Sr) grade from gently enriched to moderately depleted. Two basalt samples from the oceanward slope of the peridotite ridge yielded an $^{39}Ar/^{40}Ar$ age of 100±5 Ma [*Malod et al.*, 1993], indicating that the emplacement of these basalts postdated the gabbro intrusion and the breakup which occurred at 114 Ma [*Boillot et al.*, 1988].

3.3.2. Transitional ocean floor sequences of the Liguria-Piemonte ocean in Grisons. Relatively complete ocean floor sequences of the Liguria-Piemonte ocean are preserved in the Platta nappe in Grisons. The weak Alpine metamorphic overprint and the strongly localized Alpine deformation led to the preservation of primary contacts between ultramafic and mafic rocks and postrift sediments.

The ultramafic rocks are serpentinized harzburgites and lherzolites. Pyroxenite layers occur within the serpentinites and are commonly subparallel to the locally preserved spinel foliation. In high-temperature mylonitic shear zones, pyroxene shows crystal plastic deformation indicative of temperatures above 700°C, whereas low-temperature mylonitic shear zones are composed of strongly foliated serpentinite (< 350°C) and are usually overprinted by hydrothermal alteration and late brittle deformation. Both types of shear zones are scarce, showing that deformation was localized. Fragments of serpentinite mylonites occur as clasts in cataclastically deformed serpentinite and document progressive deformation under decreasing temperatures. Replacement of serpentine minerals by calcite occurred under still lower temperatures.

Tectonosedimentary breccias, so-called ophicalcites, typically occur along the top of the serpentinites. They include serpentinite clasts embedded in a fine-grained, microsparitic, typically red-stained calcite matrix or white sparry calcite often preserving typical cement fabrics [*Bernoulli and Weissert*, 1985]. The fabric of these breccias varies considerably from serpentinite host rock with fractures filled by red limestone and/or white sparry calcite (Figure 6c), to clast-supported breccias with in situ fragmented serpentinite clasts (ophicalcites I of *Lemoine et al.* [1987]), to coarse, unsorted, matrix-supported breccias with fragments of serpentinite, gabbro, and continent-derived basement rocks and prerift sediments (ophicalcites II of *Lemoine et al.* [1987]). Clasts of basalts are conspicuously absent in these breccias. The amount of matrix within these tectonosedimentary breccias typically increases away from the hostrock and upsection. Geopetal infill of sediment into crevasses and pockets of the mantle rocks indicates that these rocks were exposed at the seafloor (Figure 6c) [*Bernoulli and Weissert*, 1985]. Ophicalcites I are very similar to tectonosedimentary breccias overlying exhumed serpentinites at Site 1070 (Iberia Abyssal Plain) [cf. *Whitmarsh et al.* 1998].

Gabbro bodies occur but are not very common. Part of them are isotropic and show intrusive contacts with the enclosing serpentinites, whereas others have been deformed under high-temperature conditions. Gabbros are also found as clasts in tectonosedimentary breccias and pillow breccias. Two gabbro samples from an intrusion in the Platta nappe were dated by U-Pb on zircons and yielded an age of 161±1 Ma [*Desmurs et al.*, 1999]. This age is almost identical with ages obtained from other gabbros from the Liguria-Piemonte ocean [*Bill et al.*, 1997; *Rubatto et al.*, 1998] and is close to the age of the oldest postrift sediments overlying the serpentinites (late Middle Jurassic) [*Baumgartner*, 1987].

Basaltic dikes cut across the serpentinites (Figure 6b), and the gabbros and basaltic flows overlie stratigraphically the tectonosedimentary breccias and serpentinized mantle rock (Figure 5), however, they do not occur as clasts in tectonosedimentary breccias. The basalts are obviously the youngest rocks within the ultramafic-mafic sequence, and their extrusion post-dated mantle exposure at the seafloor. Thickness and volume of the basalts increase oceanward over 10 - 20 km from zero to a few hundred of meters, whereas the volume of gabbros remains small (< 5%). Nd-isotope data from basalts of the Platta nappe show εNd values ranging from +7 to +9.9, indicating a depleted mantle source for these basalts [*Stille et al.*, 1989].

3.3.3. Similarities between the ocean floor sequences of the Galicia and Adriatic margins. The transitional ocean floor sequences of the two margins show a similar spatial distribution and analogous crosscutting and stratigraphic relationships between serpentinites, ophicalcites, gabbros, and basalts. This sequence is characterized by (1) the exhumation of mantle rocks from deep lithospheric levels to the ocean floor as documented by their deformation under decreasing temperatures indicated by serpentinization, the formation and subsequent cataclastic reworking of serpentinite mylonites, and low-temperature replacement by calcite, (2) the formation of tectonosedimentary breccias reworking and/or overlying serpentinites, (3) scarce magmatic activity before breakup, as indicated by the rare occurrence of gabbros with a prebreakup age, and (4) increasing amounts of basalt toward the ocean.

3.4. Postrift Sediments

Both the Galicia and Adriatic margins are sediment-starved with a discontinuous sedimentary cover of postrift sediments (0-4 km thick). Toward the ocean, the oldest postrift sediments become younger. Along the Galicia margin the oldest postrift sediments are of Hauterivian age and drape the Interior Basin, whereas on the Deep Galicia Margin they are of Albian age. Along the Adriatic margin a similar trend can be observed. In the east the oldest postrift sediments are of Sinemurian age, whereas in the distal margin the first postrift sediments are upper Middle to Upper Jurassic radiolarian cherts (Figures 5 and 6a). In general, the thickness of the postrift sedimentary sequence is strongly variable, and local facies variations or hiatuses occur.

3.5. Detachment Structures in the Distal Margins

3.5.1. The *S* reflector of the Galicia margin. The so-called *S* reflector is a characteristic feature of the nonvolcanic margins associated with the opening of the Iberian Atlantic and the Bay of Biscay. It represents a prominent reflection or a bundle of reflections and was first described in the distal continental margin of the Bay of Biscay by *de Charpal et al.* [1978]. Along the Galicia margin the *S* reflector is well imaged; it is a prominent reflection underlying the tilted fault blocks of the distal margin [*Boillot et al.*, 1980; *Mauffret and Montadert*, 1987]. Toward the peridotite ridge, the *S* reflector shows an upward-convex shape, and at places it appears to have emerged at the seafloor and to be directly overlain by synrift or postrift sediments [*Boillot et al.*, 1988]. Toward the continent, its geometry becomes more complex, and its continuation is unclear. *Reston et al.* [1995, 1996] thought the *S* reflector branches continentward into several reflections whereby the lowest reflection would lead to a breakaway in the east. *Boillot et al.* [1995a] and *Brun and Beslier* [1996] suggested that the *S* reflector belongs to a conjugated fault system with a brittle fault along the base of the tilted blocks showing a top-to-the-ocean sense of shear and a deeper fault zone showing a top-to-the-continent sense of movement.

In seismic profiles, the intensity of the *S* reflector is strongly variable, and its relation to the high-angle faults bounding the tilted blocks is not clear. *Reston et al.* [1995, 1996] were able to demonstrate, on the basis of constructed true depth profiles, that the *S* reflector represents a continuous, locally updomed structure. Thus the high-angle faults and the fault blocks of continental basement rocks and prerift sediments are clearly truncated along the *S* reflector. On the basis of its waveform, Reston et al. interpreted the *S* reflector as a reflection from a discrete interface, i.e., from a fault zone, rather than the result of gradually changing material properties (e.g., downward decreasing serpentinization of ultramafic mantle rocks).

Another controversy related to the *S* reflector concerned the type of material underlying it. *Sibuet* [1992] assumed lower crustal rocks, whereas *Boillot et al.* [1989b] suggested serpentinized peridotite. Since these lithologies are difficult to distinguish by their seismic velocities, drilling will be the only method to obtain a clear answer.

Although most authors agree at present that the *S* reflector images a rift-related detachment structure associated with mantle exhumation, the dynamic significance of this structure is still a matter of debate (see the different models in Figure 3 in the work of *Reston et al.* [1996] and our discussion in section 4). A major reason for the different interpretations is the ambiguity of the kinematic data. The few data available (see Table 1, p. 335, in the work of *Beslier et al.* [1990]) show top-to-the-NE, top-to-the-NW, top-to-the-SE, and top-to-the-west senses of shear, all of them recording deformation under different metamorphic conditions, i.e., at different crustal levels.

3.5.2. The low-angle detachment system in the Err and Platta nappes. In the distal Austroalpine margin, exhumation of the mantle and final emplacement of the tilted fault blocks are connected with the evolution of a low-angle detachment system. The geometry of this detachment system is spectacularly exposed and preserved in the area of Piz d'Err-Piz Bial in the Err nappe (Figures 5 and 6e) [*Froitzheim and Eberli*, 1990]). Except for a few gaps due to Quaternary erosion, the detachment system is exposed over 18 km, parallel to the E-W transport direction. Its hanging wall is formed by fault blocks of continental basement rocks and prerift sediments, tilted toward the east, i.e., toward the continent along west dipping high-angle faults. The fault blocks are of variable size (100 m to a few kilometers across) and become generally smaller toward the ocean. Within the study area the high-angle faults and associated tilted fault blocks are systematically cut by the low-angle detachment faults. An incisement structure is preserved at Piz Jenatsch where a higher detachment fault is cut by a younger lower one (Figure 5). For one of the fault planes a displacement of more than 10 km can be determined [*Manatschal and Nievergelt*, 1997]; however, no mylonites were found to be associated with the detachment system along the whole length of outcrop. The fault rocks associated with the detachment system consist of up to 50 m thick green cataclasites which gradually pass downward into massive, undeformed post-Variscan granite. The detachment planes themselves are sharp and well-defined horizons marked by a characteristic black fault gouge, which accommodated most of the displacement [*Manatschal*, 1999]. Shear sense criteria from fault rocks indicate a top-to-the-west, i.e., a top-to-the-ocean, sense of shear.

Relics of the same fault system, marked by the same characteristic black gouge, can be traced from the Err nappe into the Platta nappe [*Manatschal and Nievergelt*, 1997]. Here the black gouge occurs at the base or within blocks of continental basement and prerift sediments emplaced onto the serpentinized mantle peridotites (Figures 5 and 6d) or as clasts in tectono-sedimentary breccias; however, also here no mylonites were observed. Postrift sediments overlie the allochthonous fault blocks ("extensional allochthons") and the exhumed mantle rocks.

From our observations it becomes clear that the detachment faults are late, shallow crustal structures with a top-to-the-ocean sense of shear. They formed breakaways in the continental crust to the east and penetrated oceanward, i.e., to the west, into deeper crustal levels (Figure 7). This is compatible with the observed top-to-the-ocean sense of shear. The footwall rocks are upper crustal granites and gneisses in the east and serpentinized mantle rocks in the west. Prerift lower crustal rocks were not observed in the footwall.

3.5.3. Similarities between the *S* reflector and the low-angle detachment system. The dynamic interpretation of the *S* reflector and its comparison with the low-angle detachment faults of the Austroalpine margin is hampered by the lack of kinematic data; however, the geometrical similarities of the two sets of structures go, in our opinion, beyond chance. It is undisputed that both kinds of structure (1) are related to rifting, (2) occur and were active at a shallow crustal level, (3) can be traced toward exhumed mantle, and (4) are overlain by continentward rotated tilted fault blocks.

Reston et al. [1996] interpreted the *S* reflector as a continuous fault zone truncating older high-angle faults and associated tilted fault blocks and forming incisement structures. These authors implied a top-to-the-ocean sense of shear on the basis of the continentward tilting of the hanging wall blocks and the inferred occurrence of breakaway structures to the east. Furthermore, they suggested that the *S* reflector forms the base of the synrift sediments at the continent-ocean transition. All these inferences fit exactly with our observations in the Err and Platta nappes. Therefore we think that the detachment system in the Err-Platta nappes and the *S* reflector in the Iberian margin are analogous structures.

The overall observations made along the Err-Platta detachment system fit extremely well with the results of ODP Leg 173 along the Iberia Abyssal Plain (Figures 2a and 2d) [*Whitmarsh et al.*, 1998]. Along this more southern transect, deep-sea drilling penetrated a detachment surface separating exhumed mantle rocks below from tectono-sedimentary breccias above (Site 1068). Further oceanward, an isolated continental block was drilled (Site 1069). This block is soled by a reflection which can be traced eastward toward the exhumed tectonized mantle at Site 1068. This isolated block of continental material therefore represents an extensional allochthon comparable with the analogous "klippen" of the Platta nappe (Figure 7).

4. Discussion

In the following we discuss the temporal and spatial evolution of rifting, in particular the kinematics and the polarity of crustal-scale detachment faulting, and the processes controlling the observed shift of rifting from a wide zone of extension to a localized area in the future distal margin. We also discuss the processes controlling the transition from rifting to seafloor spreading and propose that the thermal evolution and associated changes in the rheology of the lithosphere control the evolution of rifting.

4.1. Early Rifting

In the Tethyan area, basins evolving during the early phase of rifting were distributed over a wide zone which was to become the proximal parts of the future margins (Figure 9a). The basins were bounded by high-angle faults, which had a listric geometry and which can be traced into basement (Figure 7) [e.g., *Bertotti*, 1991]. During this phase, synrift sediments in the hanging wall basins and on the footwall shoulders were marine, and in general, a stratigraphically reduced but deepening-upward sequence from carbonate platform to lithohermal limestones and pelagic deposits is observed on the submarine highs of the footwall blocks [*Bernoulli et al.*, 1990]. No basement rocks were reworked during this phase. This documents that the entire future margin was subsiding. Although the individual basins are half grabens, east and west dipping master faults occur, and the basins are symmetrically arranged along preexisting zones of weakness, showing an overall symmetric structure of the margin (Figure 9a). Pure shear-dominated symmetric rifting on a lithospheric scale during this initial phase is consistent with the subsidence history and the reconstructed stretching factors. For the proximal Adriatic margins, β values of about 1.5 have been estimated by *Froitzheim* [1988] and *Bertotti et al.* [1993]. On the basis of the seismic interpretation of *Murillas et al.* [1990], reproduced in our Figure 2b, a β value of 1.4 can be determined for the Interior and Porto Basins. Thinning of the crust associated with the uplift of mantle material and simultaneous cooling of the crust during this initial rift phase are supported in the Adriatic margin by the evolution of different isotope systems [e.g., *Handy and Zingg*, 1991], by fission track data [*Sanders et al.*, 1996] and by the P-T-t path of a Permian crust-mantle boundary (Figure 8) [*Hermann et al.*, 1997; *Müntener et al.*, 1999].

4.2. Advanced Rifting

About 20 - 30 Myr after the initiation of rifting, the rifting site was shifted to the previously not or only weakly extended areas that became the distal margin (i.e., to the Err domain and the Deep Galicia Margin) whereas the proximal basins to the east were draped by postrift sediments. The new basins in the distal margin were distinctly smaller and bounded by west dipping high-angle normal faults (Figures 7 and 9b). The tilted blocks of continental basement and prerift sediments separated by the high-angle faults are underlain by an oceanward dipping low-angle detachment system along which subcontinental mantle rocks eventually were exhumed and exposed to the seafloor (Figures 7 and 9b). Where detachment structures are exposed, like in the Err and Platta nappes, the shear sense indicators along them show a top-to-the-ocean sense of shear. This sense of shear is consistent with the continentward tilting of the hanging wall blocks, with the observation that the detachment system forms a breakaway in the east and cuts downward into mantle rocks toward the west, and finally with the occurrence of continent-derived extensional allochthons overlying the mantle rocks (Figure 5). In the Deep Galicia Margin the shear sense along the inferred detachment fault underlying the continental fault blocks (*S* reflector) is not known; however, a top-to-the-ocean sense of shear is consistent with the overall geometry observed [*Reston et al.*, 1995, 1996].

In contrast to the initial phase of rifting, during which the entire margin subsided, the subsidence/uplift pattern during the advanced stage of rifting was more complex. Subsidence in the distal margins was contemporaneous with uplift and subaerial exposure of small domains continentward of the distal margins which became the local source area of siliciclastic sediments with reworked basement clasts (Galicia Bank [*Winterer et al.*, 1988]; and Bernina domain [*Finger et al.*, 1982]). This uplift is possibly related to the breakaway along the oceanward dipping detachment faults leading to an isostatic "edge effect" caused by the removal of the hanging wall block. The uplift and the unconformity associated with it

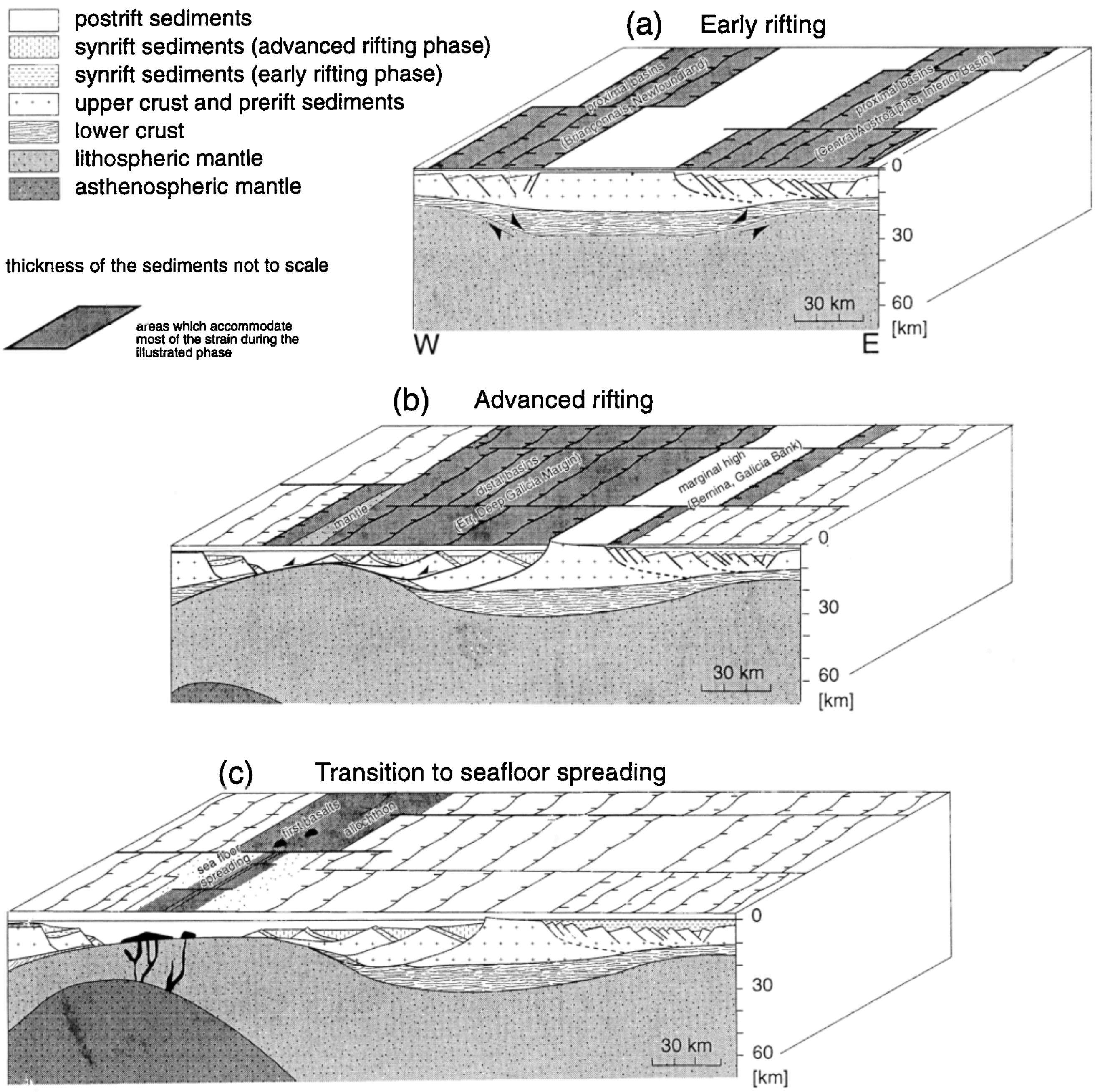

Figure 9. Model presenting the temporal and spatial evolution from (a) initial rifting to (b) advanced rifting to (c) final seafloor spreading.

and the small amount of internal extension allow one to distinguish these highs as characteristic segments of the margins, separating their proximal and distal parts. Along the Galicia Margin the high isolated the distal margin from the continent, which may explain why the distal margin became sediment-starved; in the Tethyan realm a much wider area of the Adria microplate was submerged during Liassic rifting and subsided to subphotic depth [*Bernoulli and Jenkyns*, 1974].

4.3. Mantle Exhumation

The p-T-t data of mantle rocks from the Adriatic and the Galicia margins document a similar exhumation history. In the south Pennine-Austroalpine Malenco complex, a large volume of gabbroic rocks intruded along the crust-mantle boundary during Permian time [*Hermann et al.*, 1997], documenting that the mantle rocks already occupied a shallow position in the subcontinental mantle lithosphere at that time [*Müntener et al.*, 1999]. After this the mantle and lower crustal rocks cooled more or less isobarically, until decompression accompanied by increased cooling occurred during initial rifting in latest Triassic to Early Jurassic times (Figure 8). Cooling of lower crustal rocks below 300°C is documented for this period in the southern Alps [*Handy and Zingg*, 1991] and in the Malenco complex [*Muntener et al.*, 1999].

In the south Pennine Platta nappe the widespread preservation of a high-temperature spinel foliation in many of the mantle rocks finally exposed on the seafloor shows that deformation during uplift was not pervasive but localized along fault zones. Decreasing temperatures during exhumation are documented by (1) serpentinization of mantle peridotites and their subsequent mylonitization, (2) brecciation of the former serpentine mylonites leading to serpentinite breccias with a serpentine matrix, and (3) low-temperature replacement of serpentine minerals by calcite. All these transformations predate final exposure at the seafloor documented by the different types of tectonosedimentary breccias ("ophicalcites") described above. The occurrence of clasts of continental basement rocks, of Triassic prerift sediments, and of fault rocks typically associated with the low-angle detachment faults in these breccias shows that mantle exhumation was closely associated with the emplacement of the extensional allochthons [*Froitzheim and Manatschal*, 1996].

On the Deep Galicia Margin, breccias resembling ophicalcites were interpreted as extensional mélanges following the trace of a brittle detachment fault [*Boillot et al.*, 1995b]. To the south, along the Iberian Abyssal Plain, breccias with clasts of continental basement rocks overlying exhumed mantle rocks were drilled at Site 1068, ODP Leg 173 [*Whitmarsh et al.*, 1998]. Seaward of this window of exhumed subcontinental mantle, continental basement rocks were drilled again at Site 1069. These continental rocks are underlain by a prominent reflector which we interpret as the trace of a low-angle detachment fault underlying an extensional allochthon, forming an isolated klippe on the exhumed mantle rocks (Figure 7). Like *Reston et al.* [1995, 1996], we interpret the *S* reflector as an oceanward dipping crustal-scale detachment fault, forming a breakaway in the continental crust to the east and cutting across mantle rocks, exhuming and exposing them on the seafloor. In our interpretation the *S* reflector is thus analogous to the detachment fault system in the south Pennine-Austroalpine margin.

4.4. Magmatic Evolution and Transition to Seafloor Spreading

The large volumes of gabbroic rocks occurring in Alpine sections along the mantle-crust boundary are associated with magmatic underplating in Permian times [*Quick et al.*, 1994; *Hermann et al.*, 1997] and clearly not related to Mesozoic rifting. During late rifting and mantle exhumation the production of melt was apparently very limited along the continent-ocean transition zone. In this transitional part of the margin the crust is formed mainly by serpentinized mantle rocks containing only small portions of magmatic rocks. Apparently, a diffuse magmatic activity penetrated and overprinted the exhumed subcontinental mantle during the rise of the asthenosphere before seafloor spreading initiated along a mid-ocean ridge. Along the Deep Galicia Margin the intrusion of rift-related gabbros (121 Ma) [*Schärer et al.*, 1995] predates the formation of true oceanic crust to the west (114 Ma [*Boillot et al.*, 1995a]) by several millions of years.

In the Platta nappe, basalts with a mid-ocean ridge (MOR) signature locally overlie the serpentinites adjacent to the thinned continental crust. Their volume increases oceanward, but the amount of gabbro remains small, suggesting a gradational transition to a true oceanic crust. As along the Iberian margins the intrusion of gabbros into the Platta serpentinites predates the extrusion of basaltic pillow lavas and flows. For the pillow lavas no geochronological data are available, but their relative age with respect to the gabbros (161±1 Ma [*Desmurs et al.*, 1999]) becomes clear from stratigraphic and crosscutting relationships. The gabbros intruded the already serpentinized mantle rocks (L. Desmurs, personal communication, 1998) and were locally deformed under high-temperature conditions. In contrast to the basalts, the gabbros occur also as clasts in tectonosedimentary breccias and were exposed on the seafloor, where they were covered by pillow lavas and breccias. Locally, undeformed basaltic dikes cut across gabbros deformed under high temperatures. A combination of the geochronological data from the Deep Galicia Margin and of the stratigraphic relationships in the Platta nappe suggests that along both margins the gabbros were emplaced during the transition from rifting to the formation of new oceanic crust. The similar age of all gabbros determined so far from south Pennine ophiolites in the Alps (165-161 Ma [*Bill et al.*, 1997; *Rubatto et al.*, 1998]) further suggests that in the Alps the oldest parts of the ocean were preferentially preserved and that if a slow-spreading ridge eventually developed, it was largely subducted. In any case, a classical oceanic crust with a sheeted dike complex and a substantial gabbroic layer has not been observed in the Alps, and many of the preserved Alpine ophiolites may therefore represent transitional rather than "true" oceanic crust accreted along a spreading ridge.

4.5. Shallow and Deep Detachment Structures

Whereas the shallow structures of the Galicia margin and of the south Pennine-Austroalpine margins can be reconstructed with some confidence, the deep structure of the margins and their kinematic evolution is still a matter of controversy. Indeed, many different models which are incompatible with each other exist for the polarity and kinematics of the low-angle detachment faults of the continent-ocean transition (for Galicia see Figure 3 in the work of *Reston et al.* [1996]; for the Adriatic margins, compare, e.g., the work of *Lemoine et al.* [1987], *Trommsdorff et al.* [1993], and *Frotzheim and Manatschal* [1996]).

Where, like in the Err-Platta nappes, shallow detachment structures are exposed, the shear sense indicators show a top-to-the-ocean sense of shear. This sense of shear is compatible with the observation of continentward tilting of the hanging wall blocks, the occurrence of normal faults forming a sequence of breakaways in the east, and of continent-derived extensional allochthons overlying the detachment which oceanward cuts down into mantle rocks. However, this sense of shear records only late deformation occurring at shallow crustal levels. In the Alps, kinematic data recording deformation deeper in the crust (>10 km) associated with mantle exhumation are not available either because the deep crustal levels are not exposed (Err, Bernina, and other Austroalpine nappes) or because the structures were strongly overprinted by Alpine deformation and metamorphism and their interpretation is therefore ambiguous (Malenco complex).

For the Deep Galicia Margin most of the authors accept a late top-to-the-ocean sense of shear for the detachment fault(s) underlying the tilted blocks at a shallow crustal level. This top-to-the-ocean sense of shear is in line with kinematic indicators observed in chloritized and strongly altered gabbroic schists which yielded a protolith age of 122 Ma [e.g., *Boillot et al.*, 1995a] and the continentward tilting of the fault blocks overlying the *S* reflector. However, locally, a top-to-the-continent, i.e., top-to-the-east, sense of shear was determined in peridotite mylonites [*Beslier et al.*, 1990]. These mylonites were formed at 1000° - 850°C and are therefore older than 122 Ma, the time when the $^{39}Ar/^{40}Ar$ system in amphibole crossed its blocking temperature, which is about 550°C [*Féraud et al.*, 1988]. The movements associated with the two opposite shear sense indicators are therefore of different age.

In an analog experiment, *Brun and Beslier* [1996] produced a conjugate set of faults with opposite shear senses as considered by some authors for the Deep Galicia Margin. In their experiment they obtained a top-to-the-ocean movement in the upper crust and a conjugate top-to-the-continent one in the lower crust. On the basis of the analogy between their experiment and the shear sense distribution in the Galicia margin, they concluded that mantle exhumation was controlled by boudinage of the lithosphere. However, in contrast to the analog model, the shear senses established along the Deep Galicia Margin are not of the same age and therefore are not necessarily part of the same kinematic system. Moreover, in the analog experiment the change during exhumation of the rheological properties of, for example, the lower crust, cannot be taken into account during the experiment, which leads to unrealistic conditions during the final stages of the experiment. In fact, cooling of the lower crust during early rifting is documented along the Adriatic margin (Figure 8).

A model including an east, i.e., continentward, dipping detachment has been proposed for the Adriatic margin by *Trommsdorff et al.* [1993]; this model was later modified by *Hermann and Müntener* [1996]. These authors assumed that a first, top-to-the-east directed detachment fault system became inactive and further extension was accommodated by a younger, west dipping one. This model is mainly based on the observation that a crust-to-mantle boundary, i.e., part of the former Adriatic Moho, was exposed along the Adriatic margin. This observation may, in our opinion, be explained in a much simpler and coherent way by only one west dipping detachment fault system (see Figure 4b). The most important argument against the model of Hermann and Müntener is its incompatibility with the overall geometrical and uplift subsidence patterns observed along the asymmetrical Tethyan margins [see *Manatschal and Bernoulli*, 1999, Figure 3). Moreover, extension along one single low-angle detachment fault cutting across the entire crust during early rifting (1) is in conflict with the observation that early faults are listric and sole out at midcrustal levels (Figure 7) and (2) is also not realistic from a mechanical point of view as long as the lower crust was hot and behaved in a ductile way (see below).

An indirect way to determine the polarity of detachment systems along nonvolcanic margins is to consider the asymmetry of pairs of margins. *Lister et al.* [1986, 1991] showed that depending on the polarity of the detachment system, an upper plate margin can be distinguished from a lower plate margin on the basis of their architecture and subsidence/uplift patterns. Lower plate margins are characterized by basement rocks exhumed from deeper crustal levels and overlain by highly faulted remnants of the upper plate, the so-called extensional allochthons. These rotated blocks and half grabens of the upper plate, left behind on the lower plate, are bounded by oceanward dipping high-angle faults. The faults are truncated along their base by one or several low-angle detachment faults with a complex geometry. The uplift/subsidence pattern of lower plate margins is characterized by a small and localized shoulder uplift continentward of the subsiding basins of the distal margin (Figure 9b). In contrast, the upper plate margins tend to be relatively narrow and structurally simpler and show pronounced regional uplift during late rifting. Using these criteria, the Adriatic and Galicia margins represent typical lower plate margins characterized by low-angle detachment faults at a shallow crustal level, the widespread occurrence of tilted blocks, the exhumation of serpentinized mantle rocks at the seafloor, and subsidence of the distal basins bounded by a small rift shoulder. Likewise, the Briançonnais and Newfoundland margins are interpreted as upper plate margins [*Manatschal and Bernoulli*, 1999, and references therein].

A lower plate position of the Galicia and the Adriatic margins implies a west dipping detachment system with a top-to-the-ocean sense of shear as proposed by *Reston et al.* [1996] for Galicia and by *Froitzheim and Manatschal* [1996] for the south Pennine-Austroalpine margin. These authors suggested that over the entire lithosphere, extension was accommodated by a detachment system with a top-to-the-west sense of movement resulting in a strong asymmetry of the pairs of margins [*Manatschal and Bernoulli*, 1999]. However, the (low) continentward dip of the *S* reflector seems to be at odds with a top-to-the-ocean sense of shear during extension and exhumation of mantle rocks; indeed, a top-to-the-ocean sense of shear seems to imply that the extensional allochthons were moved uphill during extension. To explain this apparent paradox, a comparison with the evolution of metamorphic core complexes might be helpful; these complexes show many geometrical similarities with the extensional systems of our continental margins [*Davis and Lister*, 1988], although their tectonic setting is very different. Metamorphic core complexes show a progressive warping of the initial detachment system and the inactivation of older breakaways during this process. To generate this type of structural geometry, a strong vertical force driven by the buoyancy of the footwall rocks must lead to the upwarping of the originally planar or listric detachment surface. Upwarping of the detachment surface leads to a geometry mechanically not suitable for further movement along the original fault, favoring the stepwise initiation of new faults and an oceanward shift of the breakaways (compare, Figure 11 in the work of *Lister and Davis* [1989]). The oceanward migration of detachment faulting, together with simultaneous uplift of the footwall rocks, can explain many of the complex geometries observed in seismics profiles or in the field, such as incisement structures, tilted blocks truncated by detachment faults, the oceanward decreasing size of fault blocks, and the extensional allochthons of continental crust overlying exhumed mantle rocks (Figure 4b). We also suggest that with the evolution of new faults, the lower crustal rocks of the continent-ocean transition zone were covered and hidden at depth by later emplaced blocks of upper crustal rocks.

Isostatic uplift of mantle rocks may be related to the removal of overlying crustal material during extension, to serpentinization of mantle rocks leading to a strong increase in volume and consequently to lower densities, or to the uplift of a hot, less dense asthenospheric mantle. Although all three processes appear to be involved during the latest stages of rifting, the rates of extension and the driving forces are not yet determined.

The occurrence of the high-temperature, top-to-the-continent directed shear zones in the mantle rocks of the Deep Galicia Margin is not explained by our model. A possible explanation for these shear zones and their direction of movement could be that they formed during updoming of the mantle during initial stages of symmetrical rifting (Figure 9a).

4.6. Extensional Decoupling During Rifting: The Role of the Lower Crust

One of the most enigmatic features of the Galicia and Adriatic margins is that the site of final continental breakup is not located within the zone of initial rifting (Figure 9). Riftactivity shifted from the future proximal margins and localized in the previously not or only weakly extended future distal margins. Associated with this shift of rifting is a change in the tectonic style from symmetric pure shear to asymmetric and localized simple shear extension. Most of the models used to explain the formation of rifted margins do not take this change into account, although it appears to be a common feature along nonvolcanic margins.

The shift of the site of rifting shows that the response of the lithosphere to extension changed through time. We think that these changes were strongly controlled by the thermal state of the lithosphere during extension, a view also supported by numerical modeling [*Hopper and Buck*, 1996]. The thermal history of the Adriatic margins clearly shows that cooling of the lithosphere started immediately after the onset of rifting. This is indicated by the p-T path of lower crustal rocks and their cooling ages (Figure 8) and the cooling history of upper crustal rocks below the Lombardian basin [*Sanders et al.*, 1996]. Fault zones developing during this initial stage of rifting sole out at middle- to lower crustal levels (see Figure 7b), and reflection seismic profiles across early rift basins do not show a displacement of the Moho (see, e.g., Jeanne d'Arc basin of the Newfoundland margin) [*Keen et al.*, 1987]). Obviously, the lower crust was weak, and extension in the upper crust decoupled from pure shear extension in the lower crust and in the upper mantle.

Cooling of the lithosphere changed its rheological properties and led to strengthening, which eventually forced rifting to shift into previously not or weakly extended areas. Also, the geometry of the fault zones changed: Fault systems developing during late stages of rifting in the distal margin are low-angle detachment faults which cut across the lower crust and into mantle rocks (Figures 5 and 7). During this stage, extension was no longer decoupled between the upper and lower crust, and the faults could exhume mantle rocks directly to the seafloor. Whether the low-angle detachment faults cut across the entire lithosphere, as suggested by most of the simple shear models, or merged with a network of ductile shear zones in the upper mantle is beyond observation. Finally, ongoing extension together with heat advected by melts derived from the rising asthenosphere might have eliminated the remaining yield strength of the subcontinental lithosphere, resulting in final breakup and seafloor spreading.

5. Conclusions

Although the Galicia and Adriatic margins are of different age and ultimately had a different fate, the spatial and temporal evolution of rifting and the duration of its different stages are very similar. The similar tectonic evolution resulted in a similar architecture of the margins with different segments showing specific basin geometries and a characteristic sedimentary evolution. The tectonic evolution is characterized by a shift of the site of rifting from a broad zone of deep-seated pure shear extension below the future proximal margins to a localized area in the future distal margin, which previously had undergone distinctly lesser extension. During this later phase, extension was accommodated by low-angle detachment faults with a top-to-the-ocean sense of movement that is in line with a lower plate position of the Galicia and the Adriatic margins, likewise compatible with the subsidence-uplift pattern observed along the margins and their conjugate counterparts (Newfoundland and Briançonnais). Seafloor spreading initiated only after exhumation of the subcontinental mantle to the ocean floor requires, on a lithosphereic scale, a mechanism of simple shear extension in the lower crust and uppermost mantle. During rifting, the style of large-scale deformation thus changed from symmetric and homogeneous (pure shear) to asymmetric and localized (simple shear).

An important factor controlling the evolution of the margin appears to be the thermal state of the lithosphere. Cooling and strengthening of the lower crust may control localization of deformation and the changing style of deformation. Therefore models in which the rheological properties do not change as a function of cooling may not be appropriate for the study of processes leading to the formation of passive continental margins.

Acknowledgments. Our work is part of the research project "Comparative anatomy of passive continental margins: Iberia and Eastern Alps", supported by the Swiss National Science Foundation, project 21-049117 96/1. We thank L. Desmurs, N. Froitzheim, G. Bernasconi-Green, U. Schaltegger, G. Boillot, J. Hermann, O. Müntener, V. Trommsdorff, and the Scientific Party of ODP Leg 173 for stimulating discussions and helpful suggestions, and A.W. Bally, C. Doglioni, and F. Roure for critically reading the manuscript.

References

Baumgartner, P O, Age and genesis of Tethyan radiolarites, *Eclogae Geol. Helv*, *80*, 831-879, 1987

Bernoulli, D., Zur Geologie des Monte Generoso, *Beitr Geol. Karte Schweiz*, *118*, 134 pp., 1964.

Bernoulli, D, and H C Jenkyns, Alpine, Mediterranean and central Atlantic Mesozoic facies in relation to the early evolution of the Tethys, in *Modern and Ancient Geosynclinal Sedimentation*, edited by R.H. Dott Jr and R.H. Shaver, *Spec. Publ Soc Econ. Paleontol Mineral*, *19*, 129-160, 1974.

Bernoulli, D., and H Weissert, Sedimentary fabrics in Alpine ophicalcites, South Pennine Arosa zone, Switzerland, *Geology*, *13*, 755-758, 1985

Bernoulli, D., C Caron, P. Homewood, O Kälin, and J van Stuijvenberg, Evolution of continental margins in the Alps, *Schweiz Mineral. Petrogr. Mitt.*, *59*, 165-170, 1979.

Bernoulli, D, G Bertotti, and N Froitzheim, Mesozoic faults and associated sediments in the Austroalpine-south Alpine continental margin, *Mem. Soc Geol Ital.*, *45*, 25-38, 1990

Bertotti, G, Early Mesozoic extension and Alpine shortening in the western southern Alps: The geology of the area between Lugano and Menaggio (Lombardy, northern Italy), *Mem Sci. Geol. Padova*, *43*, 17-123, 1991

Bertotti, G, V Picotti, D Bernoulli, and A. Castellarin, From rifting to drifting Tectonic evolution of the south-Alpine upper crust from the Triassic to the Early Cretaceous, *Sediment Geol*, *86*, 53-76, 1993

Beslier, M-O., J. Girardeau, and G Boillot, Kinematics of peridotite emplacement during North Atlantic continental rifting, Galicia, northwestern Spain, *Tectonophysics*, *184*, 321-343, 1990.

Bill, M, F. Bussy, M Cosca, H. Masson, and J Hunziker, High-precision U-Pb and $^{40}Ar/^{39}Ar$ dating of an Alpine ophiolite (Gets nappe, French Alps), *Eclogae Geol. Helv.*, *90*, 43-54, 1997.

Boillot, G, J L Auxietre, J P. Dunand, P A. Dupeuble, and A. Mauffret, The northwestern Iberian Margin: A Cretaceous passive margin deformed during Eocene, in *Deep Drilling Results in the Atlantic Ocean. Continental Margins and Paleoenvironment, Maurice Ewing Ser., vol 3*, edited by M. Talwani, W.W Hay, and W B F Ryan, pp. 138-153, AGU, Washington, D.C, 1979

Boillot, G, S. Grimaud, A. Mauffret, D Mougenot, J. Kornprobst, J Mergoil-Daniel, and G Torrent, Ocean-continent boundary off the Iberian margin: A serpentinite diapir west of the Galicia Bank, *Earth Planet Sci Lett., 48*, 23-34, 1980

Boillot, G., et al., Tectonic denudation of the upper mantle along passive margins: A model based on drilling results (OPD Leg 103, western Galicia margin, Spain), *Tectonophysics, 132*, 335-342, 1987

Boillot, G, et al, *Proceedings of the Ocean Drilling Program: Scientific Results*, vol.*103*, 858 pp, Ocean Drill. Program, College Station, Texas, 1988.

Boillot, G., D Mougenot, J Girardeau, and E L. Winterer, Rifting processes on the west Galicia margin, Spain, in *Extensional Tectonics and Stratigraphy of the North Atlantic Margins*, edited by A J. Tankard and H R. Balkwill, *AAPG Mem., 46*, 363-377, 1989a

Boillot, G, G Féraud, M. Recq, and J. Girardeau, Undercrusting by serpentinite beneath rifted margins, *Nature, 341*, 523-525, 1989b.

Boillot, G., M.-O Beslier, and J. Girardeau, Nature, structure and evolution of the ocean-continent boundary. The lesson of the west Galicia margin (Spain), in *Rifted Ocean-Continent Boundaries*, edited by E Banda, M Talwani, and M Torne, *NATO ASI Ser, Ser C, 463*, 219-229, 1995a

Boillot, G et al, A lithospheric syn-rift shear zone at the ocean-continent transition Preliminary results of the GALINAUTE II cruise (Nautile dives on the Galicia Bank, Spain), *C. R. Acad. Sci., Ser IIa Sci Terre Planetes, 321*, 1171-1178, 1995b.

Brun, J P, and M.-O Beslier, Mantle exhumation at passive margins, *Earth Planet Sci. Lett, 142*, 161-173, 1996.

Capdevila, R., and D Mougenot, Pre-Mesozoic basement of the western Iberian continental margin and its place in the Variscan belt, *Proc Ocean Drill. Program Sci Results, 103*, 3-12, 1988

Charpentier, S., J. Kornprobst, G Chazot, G. Cornen, and G Boillot, Interaction entre lithosphère et asthénosphère au cours de l'ouverture océanique Données isotopiques préliminaires sur la Marge passive de Galice (Atlantique-Nord), *C R Acad. Sci, Ser IIa Sci.Terre Planetes, 326*, 757-762, 1998

Conti, P, G Manatschal, and M Pfister, Synrift sedimentation, Jurassic and Alpine tectonics in the central Ortler Nappe (eastern Alps, Italy), *Eclogae Geol Helv., 87*, 63-90, 1994

Davis, G.A, and G S. Lister, Detachment faulting in continental extension Perspectives from the southwestern U S Cordillera, *Spec Pap Geol Soc. Am., 218*, 133-159, 1988

de Charpal, O, P Guennoc, L Montadert, and D G. Roberts, Rifting, crustal attenuation and subsidence in the Bay of Biscay, *Nature, 275*, 706-711, 1978

Desmurs, L, U Schaltegger, G. Manatschal, and D Bernoulli, Geodynamic significance of gabbros along ancient ocean-continent transitions Tasna and Platta nappes, eastern Alps, *Terra Nova Abstr., 10*, 1999

Dietrich, V, Die Ophiolithe des Oberhalbsteins (Graubünden) und das Ophiolithmaterial der ostschweizerischen Molasseablagerungen, ein petrographischer Vergleich, 179 pp, Verlag Herbert Lang & Cie. AG, Bern, 1969

Dietrich, V., Die Stratigraphie der Platta-Decke, *Eclogae Geol Helv., 63*, 631-671, 1970.

Discovery 215 Working Group, Deep structure in the vicinity of the ocean-continent transition zone under the southern Iberia Abyssal Plain, *Geology, 26*, 743-746, 1998.

Eberli, G.P, The evolution of the southern continental margin of the Jurassic Tethys Ocean as recorded in the Allgau Formation of the Austroalpine nappes of Graubünden (Switzerland), *Eclogae Geol. Helv, 81*, 175-214, 1988

Evans, C Y, and J Girardeau, Galicia margin peridotites: Undepleted abyssal peridotites from the North Atlantic, *Proc. Ocean Drill Program Sci. Results, 103*, 195-207, 1988

Féraud, G, J. Girardeau, M.-O Beslier, and G. Boillot, Datation ^{39}Ar-^{40}Ar de la mise en place des péridotites bordant la marge de la Galice (Espagne), *C.R. Acad. Sci., Ser. IIa* Sci. Terre Planetes, *307*, 49-55, 1988.

Ferreiro Mählmann, R, Das Diagenese-Metamorphose-Muster von Vitrinitreflexion und Illit-"Kristallinität" in Mittelbünden und im Oberhalbstein, 1, Bezüge zur Stockwerktektonik, *Schweiz Mineral. Petrogr. Mitt., 75*, 85-122, 1995

Finger, W, I. Mercolli, R. Kündig, A. Stäubli, C De Capitani, P. Nievergelt, T. Peters, and V Trommsdorff, Bericht über die gemeinsame Exkursion der Schweizerischen Geologischen Gesellschaft und der Schweizerischen Mineralogischen und Petrographischen Gesellschaft ins Oberengadin vom 21 bis 24. September 1981, *Eclogae Geol Helv., 75*, 199-222, 1982

Froitzheim, N, Synsedimentary and synorogenic normal faults within a thrust sheet of the eastern Alps (Ortler zone, Graubünden, Switzerland), *Eclogae Geol Helv., 81*, 593-610, 1988.

Froitzheim, N, and G.P Eberli, Extensional detachment faulting in the evolution of a Tethys passive continental margin, eastern Alps, Switzerland, *Geol Soc Am Bull, 102*, 1297-1308, 1990.

Froitzheim, N., and G Manatschal, Kinematics of Jurassic rifting, mantle exhumation, and passive-margin formation in the Austroalpine and Penninic nappes (eastern Switzerland), *Geol. Soc Am. Bull, 108*, 1120-1133, 1996

Froitzheim, N., S M. Schmid, and P Conti, Repeated change from crustal shortening to orogen-parallel extension in the Austroalpine units of Graubünden, *Eclogae Geol. Helv, 87*, 559-612, 1994.

Froitzheim, N, S.M Schmid, and M. Frey, Mesozoic paleogeography and the timing of eclogite-facies metamorphism in the Alps: A working hypothesis, *Eclogae Geol Helv, 89*, 81-110, 1996

Fuegenschuh, B, N. Froitzheim, and G. Boillot, Cooling history of granulite samples from the ocean-continent transition of the Galicia margin Implications for rifting, *Terra Nova, 10*, 96-100, 1998

Girardeau, J, C A Evans, and M-O Beslier, Structural analysis of plagioclase-bearing peridotites emplaced at the end of continental rifting Hole 637, ODP Leg 103 on the Galicia margin, *Proc. Ocean Drill Program Sci Results, 103*, 209-223, 1988

Handy, M R, and A Zingg, The tectonic and rheological evolution of an attenuated cross section of the continental crust. Ivrea crustal section, southern Alps, northwestern Italy and southern Switzerland, *Geol. Soc Am. Bull., 103*, 236-253, 1991.

Handy, M R, M. Herwegh, and R Regli, Tektonische Entwicklung der westlichen Zone von Samedan (Oberhalbstein, Graubünden, Schweiz), *Eclogae Geol Helv, 86*, 785-818, 1993.

Hermann, J., The Braccia Gabbro (Malenco, Alps): Permian intrusion at the crust to mantle interface and Jurassic exhumation during rifting, Ph.D. thesis, 194 pp, Eidg. Tech. Hochsch, 1997

Hermann, J., and O. Muntener, Extension-related structures in the Malenco-Margna-system Implications for paleogeography and consequences for rifting and Alpine tectonics, *Schweiz. Mineral Petrogr. Mitt., 76*, 501-519, 1996.

Hermann, J, O. Müntener, V Trommsdorff, W. Hansmann, and G.B. Piccardo, Fossil crust-to-mantle transition, Val Malenco (Italian Alps), *J. Geophys Res, 102*, 20,123-20,132, 1997

Hopper, J.R., and W R. Buck, The effect of lower crustal flow on continental extension and passive margin formation, *J. Geophys. Res., 101*, 20,175-20,194, 1996

Keen, C.E., R. Boutilier, B De Voogd, B. Mudford, and M.E Enachescu, Crustal geometry and extensional models for the Grand Banks, eastern Canada. Constraints from deep seismic reflection data, in *Sedimentary Basins and Basin-Forming Mechanisms*, edited by C. Beaumont and A J. Tankard, *Mem Can. Soc. Petr. Geol., 12*, 101-115, 1987.

King, L.H, G B J Fader, V.A.M Jenkins, and E L. King, Occurrence and regional geological setting of Paleozoic rocks on the Grand Banks of Newfoundland, *Can. J Earth Sci, 23*, 504-526, 1986.

Kornprobst, J., P Vidal, and J A Malod, Les basaltes de la marge de Galice (NO de la Péninsule Ibérique): Hétérogénéité des spectres de terres rares au niveau de la transition continent/océan: Données géochimiques préliminaires, *C R Acad Sci., Ser IIa Sci. Terre Planetes, 306*, 1359-1364, 1988

Krawczyk, C.M., T J Reston, M.-O. Beslier, and G Boillot, Evidence for detachment tectonics on the Iberia Abyssal Plain rifted margin, Proc Oceanic Drill Program Sci Results, 149, 603-615, 1996.

Lardeaux, J M., and M I. Spalla, From granulites to eclogites in the Sesia zone (Italian western Alps): A record of the opening and closure of the Piedmont ocean, *J. Metamorph. Geol., 9*, 35-59, 1991.

Lemoine, M, P. Tricart, and G Boillot, Ultramafic and gabbroic ocean floor of the Ligurian Tethys (Alps, Corsica, Apennines): In search of a genetic model, *Geology, 15*, 622-625, 1987.

Lister, G S., and G.A Davis, The origin of metamorphic core complexes and detachment faults formed during Tertiary continental extension in the northern Colorado River region, U.S.A., *J. Struct Geol, 11*, 65-94, 1989.

Lister, G.S., M A Etheridge, and P A Symonds, Detachment faulting and the evolution of passive continental margins, *Geology, 14*, 246-250, 1986.

Lister, G.S, M.A. Etheridge, and P A Symonds, Detachment models for the formation of passive continental margins, *Tectonics, 10*, 1038-1064, 1991.

Malod, J.A, J Murillas, J Kornprobst, and G. Boillot, Oceanic lithosphere at the edge of a Cenozoic active continental margin (northwestern slope of Galicia Bank, Spain), *Tectonophysics, 221*, 195-206, 1993

Mamet, B., M C Comas, and G. Boillot, Late Paleozoic basin on the west Galicia Atlantic margin, *Geology, 19*, 738-741, 1991

Manatschal, G, Fluid-and reaction-assisted low-angle normal faulting: Evidence from rift-related brittle fault rocks in the Alps (Err nappe, Switzerland), *J Struct. Geol, 21*, 777-793, 1999.

Manatschal, G., and D. Bernoulli, Rifting and early evolution of ancient ocean basins: The record of the Mesozoic Tethys and of the Galicia-

Newfoundland margins, *Mar. Geophys Res*, in press, 1999.
Manatschal, G, and P Nievergelt, A continent-ocean transition recorded in the Err and Platta nappes (eastern Switzerland), *Eclogae Geol Helv*, *90*, 3-27, 1997.
Mauffret, A., and L Montadert, Rift tectonics on the passive continental margins off Galicia (Spain), *Mar. Petr. Geol.*, *4*, 49-70, 1987.
Montenat, C, F Guery, and P Y Berthou, Mesozoic evolution of the Lusitanian basin: comparison with the adjacent margin, *Proc Ocean Drill. Program Sci Results*, *103*, 757-776, 1988.
Müntener, O., J. Hermann, and V. Trommsdorff, Cooling history and exhumation of lower crustal granulites and upper mantle (Malenco, eastern central Alps), *J. Petrol.*, in press, 1999
Murillas, J, D. Mougenot, G Boillot, M C Comas, E Banda, and A Mauffret, Structure and evolution of the Galicia Interior Basin (Atlantic western Iberian continental margin), *Tectonophysics*, *184*, 297-319, 1990
Pfiffner, O.A., P Lehner, P Heitzmann, S Mueller, and A. Steck (Eds.), *Deep Structure of the Swiss Alps: Results Fom the National Research Program 20 (NRP 20)*, 380 pp, Birkhäuser, Boston, Cambridge, Mass, 1997
Pinheiro, L.M., R C L. Wilson, R Pena dos Reis, R B. Whitmarsh, A Ribeiro, The western Iberia margin A geophysical and geological overview, Proc Ocean Drill Program Sci Results, 149, 3-23, 1996.
Quick, J E., S. Sinigoi, and A Mayer, Emplacement dynamics of a large mafic intrusion in the lower crust, Ivrea-Verbano zone, northern Italy, *J Geophys. Res*, *99*, 21,559-21,573, 1994.
Reston, T.J., C.M Krawczyk, and H J. Hoffmann, Detachment tectonics during Atlantic rifting Analysis and interpretation of the S reflection, the west Galicia margin, in *The Tectonics, Sedimentation and Palaeoceanography of the North Atlantic Region*, edited by R A. Scrutton et al, *Geol Soc. Spec Publ.*, *90*, 93-109, 1995
Reston, T.J., C.M. Krawczyk, and D Klaeschen, The S reflector west of Galicia (Spain) Evidence from prestack depth migration for detachment faulting during continental breakup, *J Geophys Res.*, *101*, 8075-8091, 1996
Ricou, L.-E., Tethys reconstructed Plates, continental fragments and their boundaries since 260 Ma from Central America to southeastern Asia, *Geodin. Acta*, *7*, 169-218, 1994
Rubatto, D., G Gebauer, and M Fanning, Jurassic formation and Eocene subduction of the Zermatt-Saas Fee ophiolites: Implications for the geodynamic evolution of the central and western Alps, *Contrib. Mineral. Petrol*, *132*, 269-287, 1998.
Sanders, C A E, G Bertotti, S Tommasini, G R Davies, and J.R. Wijbrans, Triassic pegmatites in the Mesozoic middle crust of the southern Alps (Italy): Fluid inclusions, radiometric dating and tectonic implications, *Eclogae Geol Helv.*, *89*, 505-525, 1996.
Schärer, U, J Kornprobst, M-O Beslier, G. Boillot, and J. Girardeau, Gabbro and related rock emplacement beneath rifting continental crust. U-Pb geochronological and geochemical constraints for the Galicia passive margin (Spain), *Earth Planet Sci Lett*, *130*, 187-200, 1995.
Schönborn, G., Alpine tectonics and kinematic models of the central southern Alps, *Mem. Sci. Geol Padova*, *44*, 229-393, 1992
Schumacher, M.E, G Schönborn, D Bernoulli, and H Laubscher, Rifting and collision in the southern Alps, in *Deep Structure of the Swiss Alps: Results From the National Research Program 20 (NRP 20)*, edited by O A Pfiffner et al, pp 186-204, Birkhäuser, Boston, Cambridge, Mass, 1997
Sibuet, J C, New constraints on the formation of the non-volcanic continental Galicia-Flemish Cap conjugate margins, *J Geol. Soc London*, *149*, 829-840, 1992.
Spillmann, P., and H.J Büchi, The pre-Alpine basement of the Lower Austroalpine nappes in the Bernina Massif (Grisons, Switzerland; Valtellina, Italy), in *Pre-Mesozoic Geology in the Alps*, edited by J F von Raumer and F. Neubauer, pp. 457-467, Springer-Verlag, New York, 1993.
Stampfli, G M, Le Briançonnais Terrain exotique dans les Alpes?, *Eclogae Geol. Helv*, *86*, 1-45, 1993
Stille, P., N. Clauer, and J Abrecht, Nd isotopic composition of Jurassic Tethyan sea water and the genesis of Alpine Mn-deposits: Evidence from Sr-Nd isotope data, *Geochim Cosmochim Acta*, *53*, 1095-1099, 1989
Trommsdorff, V., G.B. Piccardo, and A Montrasio, From magmatism through metamorphism to sea floor emplacement of subcontinental Adria lithosphere during pre-Alpine rifting (Malenco, Italy), *Schweiz Mineral Petrogr Mitt*, *73*, 191-203, 1993.
Whitmarsh, R B, and P.R. Miles, Models of the development of the West Iberia rifted continental margin at 40°30'N deduced from surface and deep-tow magnetic anomalies, *J Geophys Res.*, *100*, 3789-3806, 1995
Whitmarsh, R B, and D S. Sawyer, The ocean/continent transition beneath the Iberian Abyssal Plain and continental-rifting to seafloor-spreading processes, *Proc. Ocean Drill Program Sci Results*, *149*, 713-733, 1996.
Whitmarsh, R B, L.M. Pinheiro, P.R. Miles, M Recq, and J C Sibuet, Thin crust at the western ocean-continent transition and ophiolites, *Tectonics*, *12*, 1230-1239, 1993.
Whitmarsh, R B. et al., *Proceedings of the Ocean Drilling Program: Initial Reports*, vol 173, pp 1-493, Ocean Drill Program, College Station, Tex, 1998
Wilson, R.C.L., R.N. Hiscott, M G Willis, and F.M. Gradstein, The Lusitanian Basin of west-central Portugal: Mesozoic and Tertiary tectonic, stratigraphic, and subsidence history, in *Extensional Tectonics and Stratigraphy of the North Atlantic Margins*, edited by A J Tankard and H R Balkwill, *AAPG Mem*, *46*, 341-361, 1989
Wilson, R.C L., D S Sawyer, R.B Whitmarsh, J Zerong, and J. Carbonell, Seismic stratigraphy and tectonic history of the Iberia Abyssal Plain, *Proc. Ocean Drill Program Sci Results*, *149*, 617-633, 1996.
Winterer, E L, and A. Bosellini, Subsidence and sedimentation on a Jurassic passive continental margin, southern Alps, Italy, *AAPG Bull.*, *65*, 394-421, 1981
Winterer, E L, J S Gee, and R.J. Van Waasbergen, The source area for Lower Cretaceous clastic sediments of the Galicia margin: Geology and tectonic and erosional history, *Proc Ocean Drill Program Sci Results*, *103*, 697 - 732, 1988

D. Bernoulli, Geologisches Institut, ETH Zentrum, 8092 Zurich, Switzerland.
G. Manatschal, Ecole et Observatoire des Sciences de la Terre, UMR 7517, Université Louis Pasteur, 1 rue Blessig, F-67084 Strasbourg Cedex, France.

(Received February 11, 1999;
revised June 17, 1999,
accepted June 28, 1999)

TECTONICS, VOL. 18, NO. 6, PAGES 977-1003 DECEMBER 1999

Paleozoic rocks of northern Chukotka Peninsula, Russian Far East: Implications for the tectonics of the Arctic region

Boris A. Natal'in,[1] Jeffrey M. Amato,[2] Jaime Toro,[3,4] and James E. Wright[5]

Abstract. Paleozoic rocks exposed across the northern flank of the mid-Cretaceous to Late Cretaceous Koolen metamorphic dome make up two structurally superimposed tectonic units: (1) weakly deformed Ordovician to Lower Devonian shallow marine carbonates of the Chegitun unit which formed on a stable shelf and (2) strongly deformed and metamorphosed Devonian to Lower Carboniferous phyllites, limestones, and andesite tuffs of the Tanatap unit. Trace element geochemistry, Nd isotopic data, and textural evidence suggest that the Tanatap tuffs are differentiated calc-alkaline volcanic rocks possibly derived from a magmatic arc. We interpret the associated sedimentary facies as indicative of deposition in a basinal setting, probably a back arc basin. Orthogneisses in the core of the Koolen dome yielded a Devonian (between ~369 and ~375 Ma) U-Pb zircon age which is similar to the ages of the Tanatap tuffs as well as granitic plutons formed within a Devonian active continental margin of northern Alaska. The stratigraphy of the Chegitun unit is similar to that of the Novosibirsk carbonate platform which overlies the Late Precambrian Bennett-Barrovia block. The basement of the block is exposed in Chukotka where ortogneiss in the Chegitun River valley yielded Late Proterozoic (~650 to 550 Ma) U-Pb ages. These two tectonic units form the shelf of the Chukchi and East Siberian Seas and may continue into northern Alaska as the Hammond subterrane. The deep-water Tanatap unit can be traced along the southern boundary of the Bennett-Barrovia block from the Novosibirsk Islands to northern Alaska. This basin was paired with a Devonian magmatic arc that existed farther to the south. The northern margin of the Bennett-Barrovia block collided with North America in the Late Silurian to Early Devonian. In Chukotka, during Middle to Late Carboniferous time the reconstructed Devonian arc-trench system at the southern edge of the Bennett-Barrovia block collided with an unknown continental object, fragments of which now occur to the south of the South Anyui suture. Triassic to Cretaceous deformation strongly modified the Paleozoic units. Our results provide new constraints on the geometry and Paleozoic history of the Chukotka-Arctic Alaska block, the essential element involved in the opening of the Canada basin.

[1] Department of Geology, Istanbul Technical University, Istanbul, Turkey.
[2] Department of Geological Sciences, New Mexico State University, Las Cruces.
[3] Department of Geological and Environmental Sciences, Stanford University, Stanford, California.
[4] Now at Department of Geology and Geography, West Virginia University, Morgantown.
[5] Department of Geology and Geophysics, Rice University, Houston, Texas.

Paper number 1999TC900044
0278-7407/99/1999TC900044$12.00

1. Introduction

Interest in stratigraphic and tectonic correlations between the Russian Far East and Alaska recently has been revived as the result of collaboration between North American and Russian geologists. This paper presents the results of one such study from the Chegitun River valley, Russia, where field work was carried out to establish the stratigraphic, structural, and metamorphic relationships in the northern part of the Chukotka Peninsula (Figure 1). The Chegitun River region exposes an Ordovician to Lower Carboniferous carbonate and metacarbonate, shale, phyllite, and thin-bedded turbidite sequence with rare interbedded tuffs that were metamorphosed and deformed during the Cretaceous. This sequence is in fault contact with a mid-Cretaceous to Late Cretaceous high-grade metamorphic complex, the Koolen dome. The geology of the high-grade complex was discussed by the *Bering Strait Geological Field Party* (BSGFP) [1997].

Stratigraphic correlations between Paleozoic sequences in the Chegitun River region and similar successions in Chukotka, in the various islands of the Chukchi and East Siberian Seas, and in northern Alaska bear on an important unsolved problem for this region: the presence or absence of a large Precambrian block on which these lower Paleozoic carbonate platform deposits accumulated.

The Paleozoic framework of the region sheds light on the geometry and size of the Chukotka-Arctic Alaska microplate whose Early Cretaceous displacement is thought to be responsible for the opening of the Canada Basin (Figure 1) (see *Lawver et al.* [1990] for a review of the different models proposed for the opening of the Canada Basin). In this paper we investigate the correlation of Late Proterozioc and Paleozoic rocks of the Chegitun River valley with rocks of similar ages in the Siberian/northern Alaska sector of the Arctic region, the depositional setting of these strata, and the geochemistry and geochronology of Devonian magmatism on the Chukotka Peninsula. These data are then used to discuss the Paleozoic tectonic evolution of northeastern Russia and northern Alaska. We will address the Cretaceous thermal evolution and structural history of the Chegitun River valley metamorphic rocks in a later paper.

2. Tectonic Setting of the Study Area

Prior to the now widely accepted hypothesis of the counterclockwise rotation of the Chukotka-Arctic Alaska block for 60° about a pole at the McKenzie delta (Figure 1) [e.g., *Tailleur and Brosge*, 1970], the idea of a Hyperborean platform underlain by Precambrian basement in the central part of the Arctic Ocean was

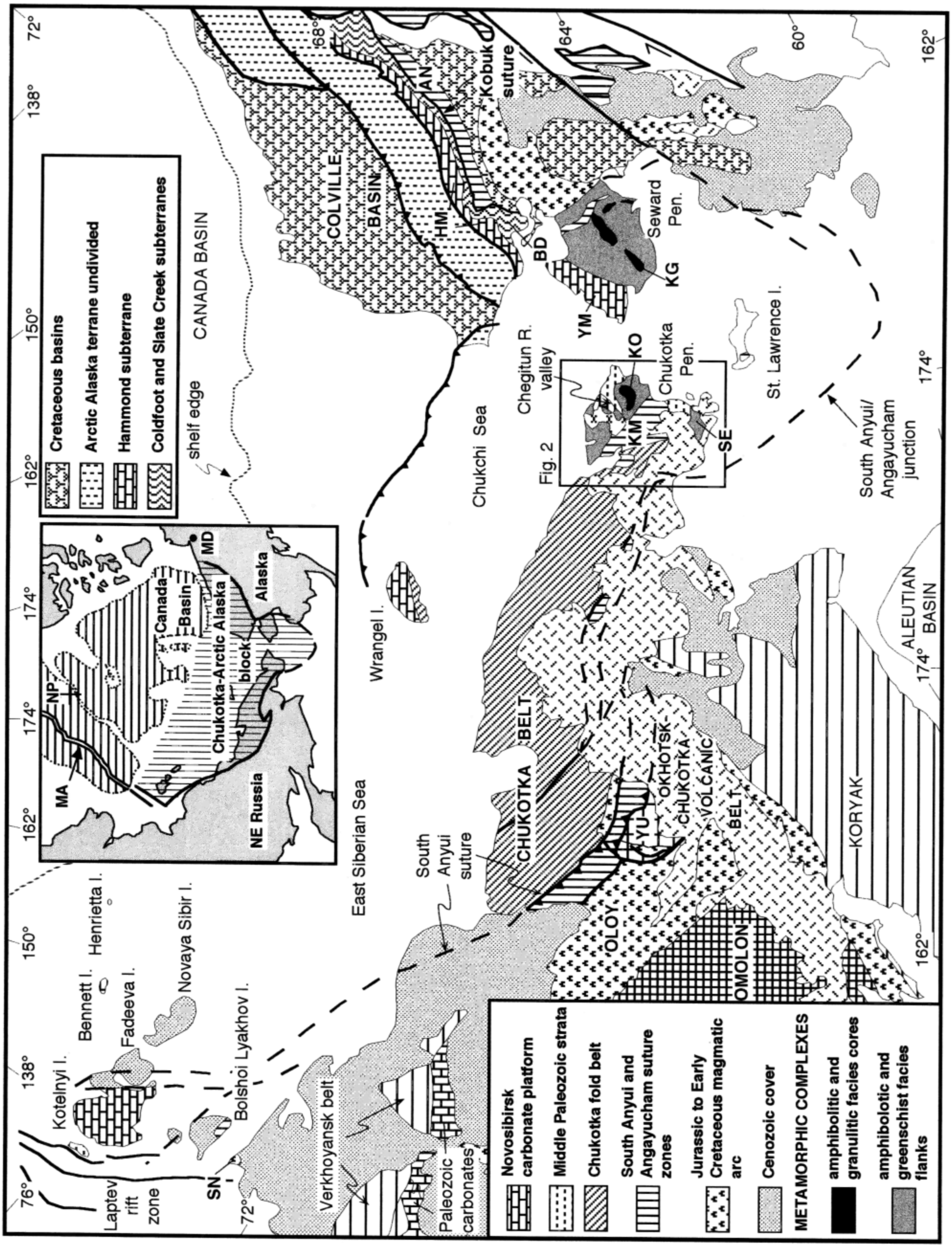
Cretaceous basins
Arctic Alaska terrane undivided
Hammond subterrane
Coldfoot and Slate Creek subterranes
CANADA BASIN
shelf edge
COLVILLE BASIN
HM
AN
Kobuk suture
BD
Seward Pen.
KG
YM
KO
Chegitun R. valley
Chukotka Pen.
St. Lawrence I.
KM
SE
Fig. 2
Chukchi Sea
South Anyui/ Angayucham junction
Wrangel I.
NE Russia
Chukotka-Arctic Alaska block
Canada Basin
Alaska
MA
NP
MD
East Siberian Sea
South Anyui suture
CHUKOTKA BELT
YU
OKHOTSK-CHUKOTKA VOLCANIC BELT
OLOY
OMOLON
KORYAK
ALEUTIAN BASIN
Laptev rift zone
SN
Kotelnyi I.
Bennett I.
Henrietta I.
Fadeeva I.
Novaya Sibir I.
Bolshoi Lyakhov I.
Verkhoyansk belt
Paleozoic carbonates
Novosibirsk carbonate platform
Middle Paleozoic strata
Chukotka fold belt
South Anyui and Angayucham suture zones
Jurassic to Early Cretaceous magmatic arc
Cenozoic cover
METAMORPHIC COMPLEXES
amphibolitic and granulitic facies cores
amphibolotic and greenschist facies flanks

proposed by *Shatsky* [1935] to explain the sinuosity and disposition of fold belts (e.g., Chukotka fold belt, the Brooks Range) and high-grade metamorphic rocks in the Arctic region. *Eardley* [1948] referred to this Precambrian platform as "Ancient Arctica." American geologists proposed the existence of an area called "Barrovia Land" to provide a northern source region for Paleozoic and Mesozoic clastic rocks in northern Alaska [e.g., *Tailleur*, 1973]. However, if a rotational origin for the Chukotka-Arctic Alaska block about a pole in the McKenzie delta is assumed, the North American craton is a suitable source for these sediments. *Zonenshain et al.* [1990] defined a microcontinent, "Arctida," as one of several Precambrian cratons, such as the East European and Siberian cratons, which was later disrupted owing to the opening of the oceanic basins in the Arctic Ocean. *Şengör and Natal'in* [1996] supported the necessity of an old continental block but defined it with a shape and size different from that of Arctida. They named it after the Bennett massif which is located in the northwestern part of the East Siberian Sea [*Vinogradov et al.*, 1974] but noted that it may be contiguous with Precambrian crust in the northeastern part of the Chukchi Sea [*Grantz et al.*, 1990]. In this paper we use the term Bennett-Barrovia block for this Precambrian block. It should be stressed that the Bennett-Barrovia block is not the same as the Arctic Alaska terrane [*Newman et al.*, 1977; *Moore et al.*, 1994]. The latter is a younger tectonic element not assembled until Devonian time (see below).

The Chegitun River valley exposes carbonate and metacarbonate rocks which we correlate with the early to middle Paleozoic Novosibirsk carbonate platform. The Novosibirsk carbonate platform covers the Bennett-Barrovia block as defined by *Şengör and Natal'in* [1996]. This platform includes rocks exposed on the Novosibirsk (New Siberian) Islands of the East Siberian Sea, on Wrangel Island, and in several localities of northern Alaska including the Seward Peninsula and the western and central Brooks Range (YM and HM, Figure 1). The wide geographic distribution of rocks of similar age and composition, in addition to geophysical data, suggests that this early Paleozoic carbonate platform underlies the entire East Siberian shelf. On the basis of stratigraphic and fossil evidence, both *Dumoulin and Harris* [1994], for the Alaskan terranes, and Şengör and Natal'in, for the whole region, agree that these widely scattered pre-Middle-Devonian carbonate successions were part of a single carbonate platform, rather than disparate, far-traveled terranes as had been previously proposed [*Fujita and Cook*, 1990]. However, the Paleozoic tectonic history of this extensive platform has not been investigated in great detail.

The Paleozoic rocks of northern Chukotka Peninsula are in fault contact with the Koolen metamorphic dome (Figure 2) [*Natal'in*, 1979], one of several high-grade metamorphic complexes on the Chukotka and Seward Peninsulas [*Belyi*, 1964; *Drabkin*, 1970b; *Tilman*, 1973; *Shuldiner and Nedomolkin*, 1976; *Nedomolkin*, 1977; *Natal'in*, 1979; *Amato et al.*, 1994]. These metamorphic complexes expose Late Proterozoic to Paleozoic igneous and sedimentary protoliths metamorphosed to upper amphibolite and locally granulite grade. The age of metamorphism was previously estimated to range from Archean [*Shuldiner and Nedomolkin*, 1976; *Nedomolkin*, 1977] to Paleozoic [*Gnibidenko*, 1969; *Bunker et al.*, 1979] or with an additional episode in the Mesozoic [*Gelman*, 1973; *Natal'in*, 1979], but it is now known to have occurred during mid-Cretaceous time on both the Chukotka Peninsula [*BSGFP*, 1997] and on the Seward Peninsula [*Amato et al.*, 1994; *Amato and Wright*, 1998].

Paleozoic rocks and high-grade metamorphic complexes on the Chukotka Peninsula comprise part of a broader tectonic province in the Russian Far East and northern Alaska: the former Chukotka-Arctic Alaska microplate. The southern boundary of this ancient microplate is defined by the Neocomian South Anyui suture in northeast Russia and the Late Jurassic to Neocomian Kobuk suture in Alaska (Figure 1). For a review of the tectonics of northeast Asia, see the work of *Parfenov and Natal'in* [1985], *Zonenshain et al.* [1990], *Fujita and Cook* [1990], and *Şengör and Natal'in* [1996]. For a review of the tectonics of northern Alaska, see the work of *Moore et al.* [1994, 1997b].

3. Lithotectonic units of the Chegitun River Valley

From the southeast to the northwest, three principal fault-bounded lithotectonic units are exposed in the Chegitun River valley (Figure 3): (1) the High-Grade unit, which consists of upper amphibolite facies metamorphic rocks along the northern flank of the Koolen metamorphic dome; (2) the Tanatap unit, which consists of Devonian to Lower Carboniferous greenschist facies metasedimentary rocks; and (3) the Chegitun unit, which consists of virtually unmetamorphosed Ordovician through Lower Devonian shallow marine carbonate rocks. It was previously believed that the high-grade rocks represented the Precambrian depositional basement for the Paleozoic sedimentary rocks [*Belyi*, 1964; *Tilman*, 1973; *Shuldiner and Nedomolkin*, 1976; *Nedomolkin*, 1977]. In this framework the Tanatap and Chegitun units were regarded as a continuous Paleozoic succession [*Nedomolkin*, 1977; *Oradovskaya and Obut*, 1977]. However, although the High-Grade unit does include Late Proterozoic protoliths, our research has shown that there is no evidence of a straightforward basement/cover relationship between the high-grade metamorphic rocks and the weakly metamorphosed sedimentary rocks that bear Paleozoic fossils. In addition, both the lithology and paleodepositional environment of the Tanatap unit are significantly different from those of the Chegitun unit and the inferred sedimentary protoliths for the high-grade metamorphic rocks. These differences in lithology and depositional environment allow us to define three fault-bounded lithotectonic units which have internal contacts that are truncated by the bounding faults. These units are described in sections 3.1-3.3 in order of decreasing metamorphic grade.

Figure 1. Principal tectonic units of northeastern Russia and northern Alaska [after *Natal'in*, 1981, 1984; *Moore et al.*, 1994, *Plafker and Berg*, 1994]). The inset shows the Chukotka-Arctic Alaska block. AN, Angayucham terrane; BD, Baird Group; HM, Hammond subterrane; KG, Kigluaik dome; KO, Koolen dome; KM, Kolyuchin-Mechigmen zone; MA, Arctic mid-ocean ridge; MD, McKenzie delta; NP, North Pole; PR, Primorsk Basin; SE, Senyavin Uplift; SN, Svaytoy Nos; YM, York terrane; YU, Paleozoic Yarakvaam and Aluchin blocks.

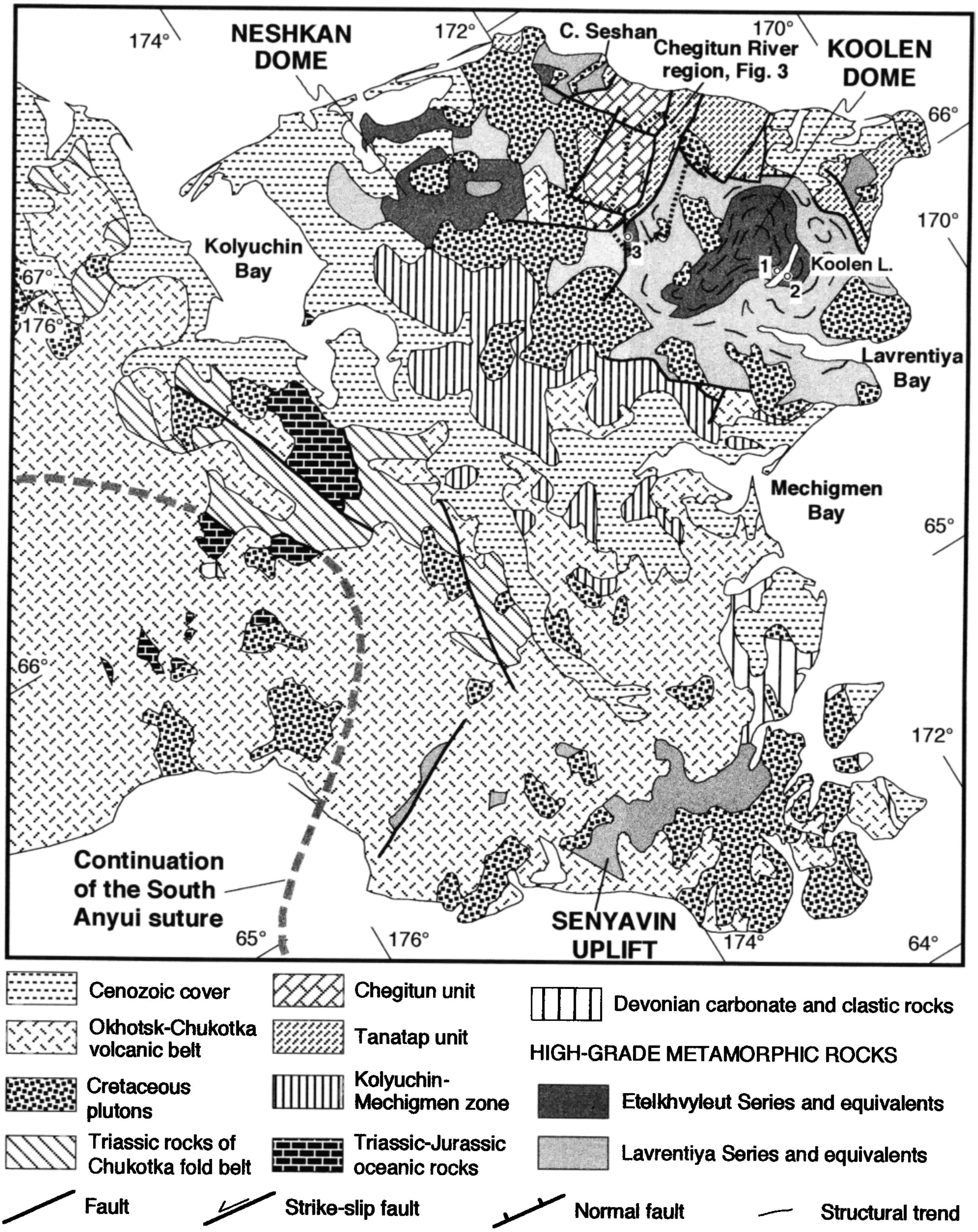

Figure 2. Geologic map of the Chukotka Peninsula modified after *Gorodinsky* [1980] showing the location of detailed geologic mapping in the Chegitun River valley area of Figure 3. The Etelkhvyleut Series is exposed in the core of the Koolen dome and the Lavrentiya Series represents flanks of the dome. Circles indicate locations of samples for U-Pb age determination: 1, M18-94K; 2, F45-94K; and 3, 95JT4a.

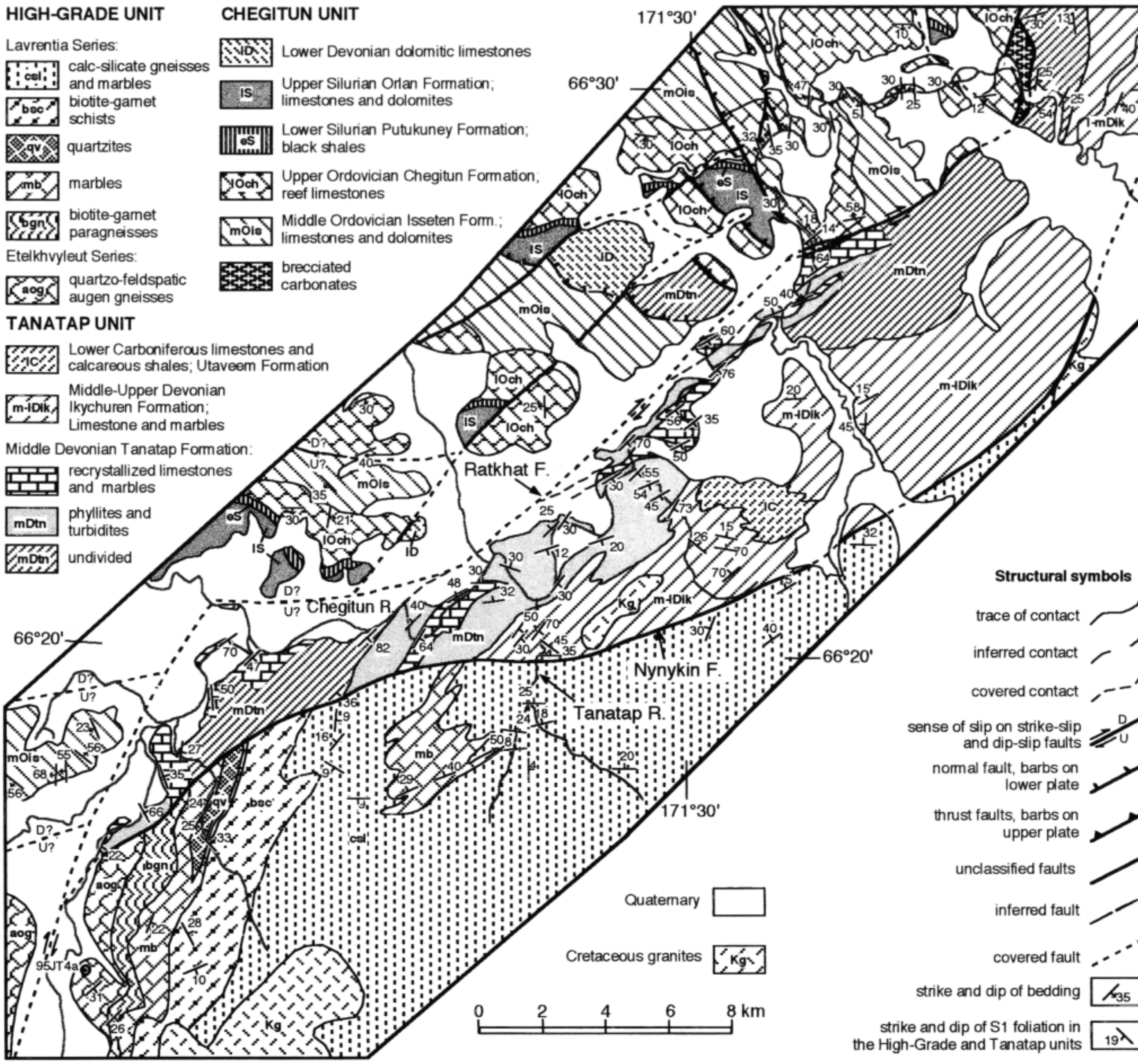

Figure 3. Geologic map of the Chegitun River valley.

3.1. High-Grade Unit

The high-grade metamorphic rocks in the Chegitun River valley are very similar to rocks in the core and southern flank of the Koolen dome that are exposed in the Koolen Lake region (Figure 2) [*Shuldiner and Nedomolkin*, 1976; *Nedomolkin*, 1969, 1977; *Gelman*, 1973; *Natal'in*, 1979; *BSGFP*, 1997]. The Koolen metamorphic complex was divided into two major units by *Shuldiner and Nedomolkin* [1976]. A structurally lower succession of mostly orthogneiss is called the Etelkhvyleut Series, and a structurally higher, dominantly paragneiss, schist, and marble-bearing succession is called the Lavrentiya Series. In the Koolen Lake region, three types of rock assemblages have been observed in ascending order: (1) granitic orthogneisses of Cretaceous [*BSGFP*, 1997] and Devonian ages (see below) within both the Etelkhvyleut Series and the Lavrentiya Series; (2) thinly banded schists and quartzofeldspathic paragneisses that include lenses of ultramafic rocks, marbles, amphibolites, and rare quartzite (metachert?) [*BSGFP*, 1997], which together may represent accretionary prism material [*Şengör and Natal'in*, 1996]; and (3) marble and calc-silicate rocks that resemble the less metamorphosed lower to middle Paleozoic shallow marine sequence of the Novosibirsk carbonate platform as exposed on the Chukotka Peninsula [*Şengör and Natal'in*, 1996]. Mid-Cretaceous granites intrude the Koolen metamorphic complex [*Shuldiner and Nedomolkin*, 1976; *Nedomolkin*, 1977; *BSGFP*, 1997] and the Tanatap unit in the Chegitun River area.

Along the Chegitun valley, in the southwestern part of the map area (Figure 3), biotite-bearing granitic augen gneisses interlayered with 3- to 30-m-thick horizons of coarse-grained white mar-

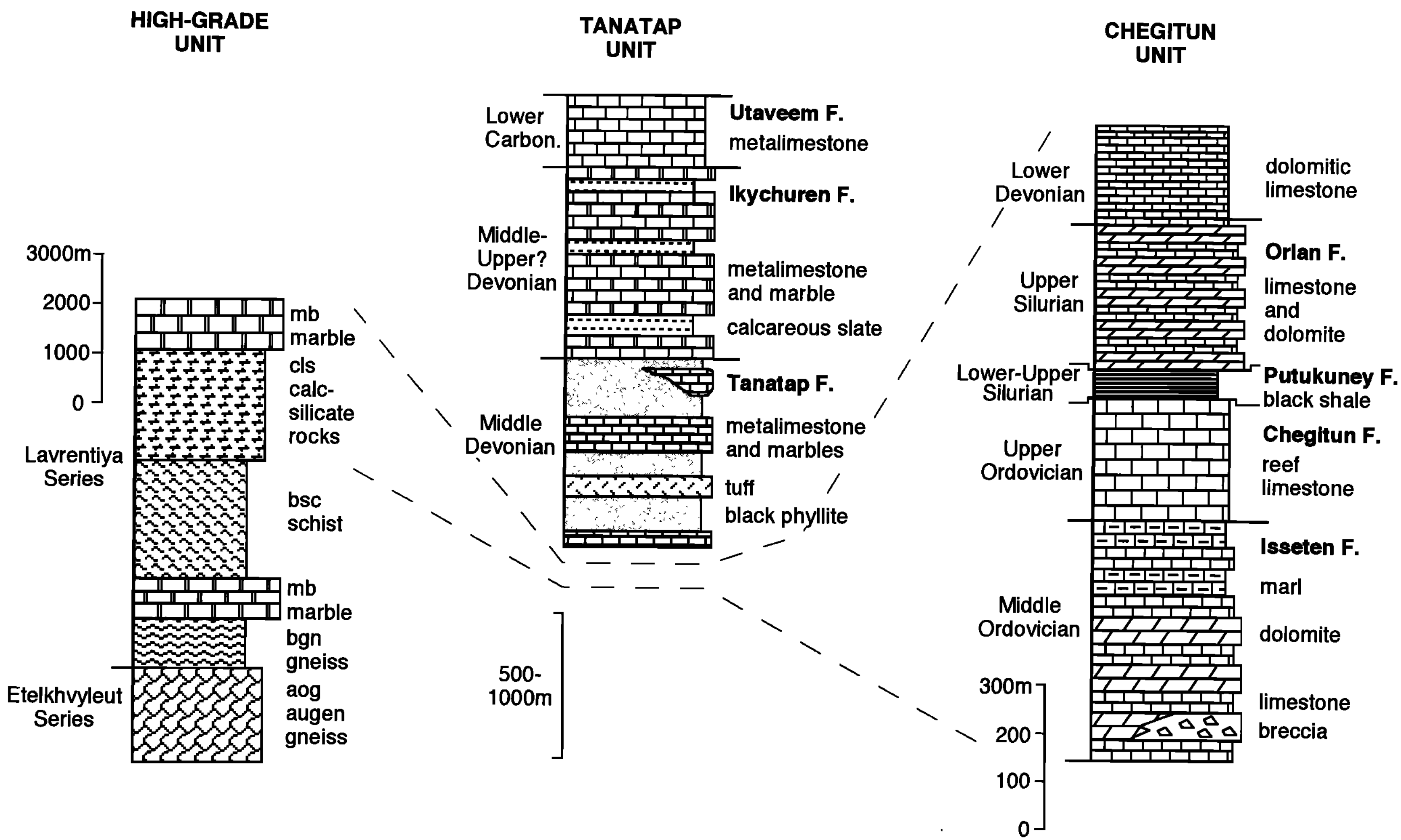

Figure 4. Stratigraphic columns of the tectonic units in the Chegitun River valley compiled taking into account data of *Oradovskaya and Obut* [1977] and *Nedomolkin* [1977].

ble constitute the lowest exposed structural unit (map unit "aog" in Figures 3 and 4). We carried out ion microprobe (super high resolution ion microprobe-reverse geometry (SHRIMP-RG)) U-Pb dating of zircon grains from this augen gneiss (sample 95JT4a) and obtained $^{206}Pb/^{238}U$ ages between ~650 and ~540 Ma (refer to Table 1 for analytical methods and to Figures 5a and 5b for data plots). This broad range of ages from a single sample is probably due to a combination of two effects: (1) the incorporation of somewhat older zircons by a latest Proterozoic granitic magma (inheritance) and (2) loss of radiogenic lead during younger metamorphic events. These two phenomena will conspire to spread the ages parallel to concordia (Figure 5a), making it impossible to assign a precise crystallization age to the protolith of the augen gneiss. In any case, these new data demonstrate the occurrence of Late Proterozoic granitic magmatism in Chukotka Peninsula.

A few lenses of plagioclase-bearing amphibolites, probably metagabbro, occur within the marbles. We correlate these rocks with the Etelkhvyleut Series of the Koolen Lake region [*Shuldiner and Nedomolkin*, 1976; *Nedomolkin*, 1969, 1977; *BSGFP*, 1997], but the augen gneisses and interlayered metasedimentary rocks of the Chegitun valley contain less pegmatite or other evidence for partial melting than equivalent units of the Koolen Lake region. The augen gneiss unit is overlain by a poorly exposed section of biotite gneisses containing subordinate horizons of augen gneisses (map unit "bgn"). Overlying rocks, from the structural base upward, include intercalated biotite gneisses, calc-silicate rocks, and marbles that grade upward to pure coarse-grained marbles (map unit "mb"). Muscovite-bearing garnet schists and quartzites form a lenticular body in the marbles in the upper part of the structural section (map unit "qv"). Biotite and garnet-bearing schists (map unit "bsc") overlie the marble unit. Peak metamorphism reached upper amphibolite facies in the deepest part of the structural section exposed in the Chegitun valley and in the core of the Koolen dome. This metamorphic event has been dated as occurring between 104 and 94 Ma in the Koolen Lake region [BSGFP, 1997].

In the Chegitun area, *Nedomolkin* [1969, 1977] assigned all rocks that lie structurally above the augen gneiss unit to the Lavrentiya Series. In general, we agree with this correlation, but the lithology and succession of the rocks in the Chegitun valley are different in detail from those of the Lavrentiya Series in the Koolen Lake region where thick quartzo-feldspatic paragneisses

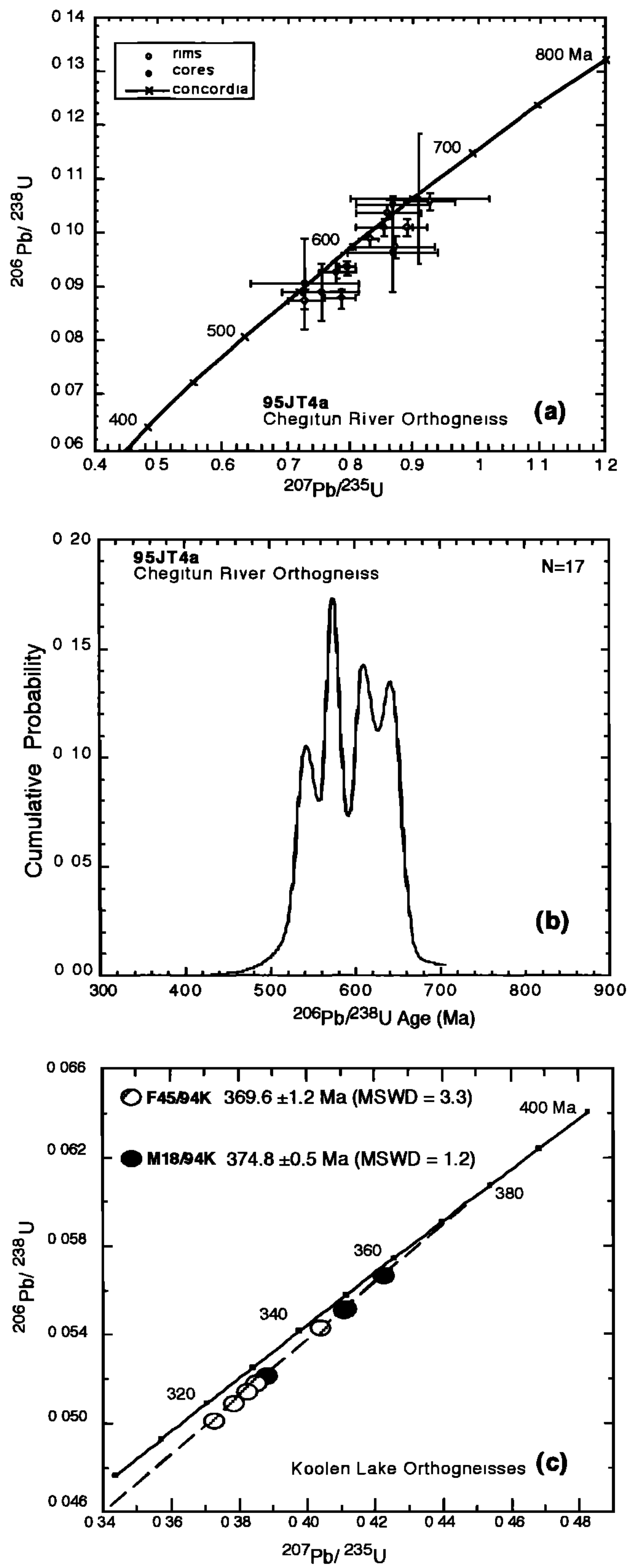

Figure 5. U-Pb concordia diagrams from the Koolen orthogneiss. (a) Concordia diagram of ion microprobe (super high resolution ion microprobe-reverse geometry (SHRIMP-RG)) data from sample 95JT4a of Late Proterozoic augen gneiss from the Chegitun valley. Each data point represents a single ~20 μm spot on a zircon crystal. The discordance and wide spread of ages is probably due to the combined effects of inheritance of older zircon and lead loss during Cretaceous high-grade metamorphism. (b) Cumulative probability diagram of $^{206}Pb/^{238}U$ ages of zircons from sample 95JT4a from the Chegitun valley. This histogram is calculated by taking the individual data points and assuming a Gaussian distribution of unit area with width proportional to the error. (c) U-Pb concordia diagrams from the Koolen orthogneiss, F45/94K and M18/94K. MSWD stands for mean standard weighted deviation, a measure of the goodness of fit of the chord. Both sets of analyses are discordant, but upper intercepts of 376 and 375 Ma agree within analytical error. These data show that the orthogneiss of the Etelkhvyleut Series is neither Precambrian nor Cretaceous as has been previously speculated. These Devonian ages are within the stratigraphic age limits of the Tanatap metatuff. See text and Table 3 for details.

Table 1. Ion Microprobe U-Pb Isotopic Data Etelvekhvyleut Series Orthogneiss, Sample 95JT4a, Chegitun Valley

	Concentrations			Isotopic Ratios						Apparent Ages, Ma					
Grain Spot	U, ppm	Th, ppm	^{204}Pb, ppb	$^{207}Pb/^{206}Pb$	Error, ±	$^{238}Pb/^{206}Pb$	Error, ±	$^{235}U/^{207}Pb$	Error, ±	$^{206}Pb/^{238}U$	Error, ±	$^{207}Pb/^{235}Pb$	Error, ±	$^{207}Pb/^{206}Pb$	Error, ±
6 Rim	52.1	25.3	0	0.0609	0.0009	10.12	0.12	1.21	0.02	607.6	7.2	613.1	9.3	633.8	31.1
7 Rim	60.9	26.7	1	0.0604	0.0018	11.42	0.23	1.37	0.05	541.1	10.4	556.1	16.1	618.2	64.2
7 Core	41.3	18.1	0	0.0648	0.0013	11.38	0.23	1.27	0.04	543.0	10.4	588.3	13.6	767.2	43.7
8 Rim	27.9	16.1	0	0.0638	0.0020	9.90	0.17	1.13	0.04	620.3	10.2	645.6	18	735.1	67.1
9 Rim	18.5	12.2	1	0.0599	0.0034	9.62	0.13	1.16	0.07	637.4	8.3	629.6	28.6	601.5	128.3
10 Rim	30.0	12.8	3	0.0584	0.0034	11.03	1.04	1.37	0.16	559.5	50.5	556.5	51.2	544.5	132.1
10 Core	103.6	27.0	4	0.0608	0.0020	10.76	0.14	1.28	0.05	573.0	7.1	585.4	16.6	633.7	72.9
11 Core	116.1	30.2	1	0.0617	0.0007	10.69	0.14	1.26	0.02	576.5	7.1	594.7	8.1	664.8	23.4
11 Rim	35.0	10.8	0	0.0620	0.0016	9.40	1.07	1.10	0.13	651.5	71.1	656.5	59.7	673.8	54.9
13 Rim	26.3	14.7	3	0.0648	0.0044	10.27	0.22	1.15	0.08	599.3	12.3	635.8	35.5	768.0	150.2
13 Core	54.1	31.5	2	0.0613	0.0029	9.90	0.16	1.17	0.06	620.1	9.9	626.7	24.3	650.4	103.3
14 Rim	35.3	26.0	1	0.0633	0.0025	9.44	0.14	1.08	0.05	649.2	9.2	664.7	21.6	717.5	85.9
14 Rim	45.0	33.4	2	0.0614	0.0030	11.22	0.64	1.32	0.11	550.4	30.1	571.0	35.2	653.8	107.5
15 Rim	40.1	28.2	1	0.0653	0.0013	10.39	0.79	1.15	0.09	592.1	43.3	633.8	39.1	785.5	43.4
16 Core	651.5	825.6	32	0.0607	0.0006	10.80	0.24	1.29	0.03	571.1	12.3	582.9	11.4	629.4	20.6
17 Rim	37.2	15.4	2	0.0597	0.0037	9.50	0.14	1.15	0.08	645.4	8.9	633.5	31.2	591.5	139.7

Analytical procedure was as follows: Zircons were obtained from the orthogneiss sample through standard heavy liquid and magnetic separation techniques. Zircons from the least magnetic fraction produced by a Frantz magnetic separator were mounted on epoxy without any hand-picking. The 95JT4a zircons are euhedral, translucent, light gold color with small dark inclusions. They are between 200 and 100 μm in length. The mount was polished to expose the mid-section of the grains. Cathodoluminescense images were used to characterize the zircon zoning and to identify the cores and rims. The zircons were then analyzed on the Stanford University/U.S. Geological Survey ion microprobe (super high resolution ion microprobe-reverse geometry (SHRIMP-RG)) using zircon AS57, with a known age of 1099 Ma, as a standard. The analytical techniques used are similar to those described by *Muir et al.* [1996]. The spot bore onto the zircon grains by the primary beam is ~ 25 μm in diameter. Therefore the spots analyzed are small enough relative to the size of the zircon grains to resolve the cores from the rims. The ion probe data were corrected for common Pb using the ^{204}Pb measured during the analysis and assuming a Pb isotopic composition according to the *Cumming and Richards* [1975] Pb evolution model. Overall, the U concentrations of 95JT4a zircons are low, leading to relatively large analytical errors for individual analyses.

separate the augen orthogneisses from the overlying marbles [see *BSGFP*, 1997].

A thick structural section of calc-silicate rocks and marble is exposed in the upper reaches of the Tanatap River (Figure 3). Individual horizons of foliated marble are internally homogeneous and often more then 10 m thick, suggesting that their protoliths were shallow water carbonate rocks. Lower-grade metamorphism may indicate that the calc-silicate rocks and marbles belong to the upper part of the structural section (Figure 4). This conclusion is supported by the correlation with the Koolen Lake region where marbles occur at the highest structural level [*BSGFP*, 1997].

The $^{40}Ar/^{39}Ar$ analyses indicate that the high-grade rocks near the Chegitun River cooled from 500°C to 350°C between 108 and 104 Ma [*Natal'in et al.*, 1997]. These cooling ages are slightly older than those (90-92 Ma) of the southern flank of the Koolen dome.

Sense of shear determined from stretching lineations is dominantly top-to-south, similar to the kinematics previously described for the southern flank of the dome [*BSGFP*, 1997]. Taking into consideration the structural relationships and lithologic similarity, the calc-silicate and carbonate units of the Lavrentiya Series are tentatively correlated with the Ordovician to Lower Devonian carbonate rocks of the Chegitun unit (see below), which are exposed to the northwest. Both of these units are interpreted to represent part of the Novosibirsk carbonate platform of *Şengör and Natal'in* [1996] (Figure 1).

Despite poor outcrops, the map pattern, together with structural data (B.A.Natal'in et al., manuscript in preparation, 1999) and the fact that internal contacts of the High-Grade unit are at an angle to the contact with the Tanatap unit, indicates that a fault (here named the Nynykin fault) separates the two tectonic units (Figure 3). The Nynykin fault cuts the mid-Cretaceous foliation in the high-grade rocks and is conjugate with north-west striking extensional faults and dikes. The dikes have been dated as Late Cretaceous [*Nedomolkin*, 1969]. On the other hand, the extensional structures have the same orientation as Tertiary extensional structures in the Hope Basin (Figure 1) [*Grantz et al.*, 1990]. Thus we infer the Late Cretaceous to Tertiary age of the Nynykin fault. Kinematic criteria indicate that the fault has a right-lateral sense of displacement.

3.2. Tanatap Unit

The Tanatap unit (Figure 3) consists of polydeformed greenschist facies rocks exposed along the Chegitun River from the southwestern corner of the map area to the Chukchi Sea coast. Similar rocks are also exposed along the northern flank of the Koolen dome (Figure 2) [*Nedomolkin*, 1969, 1977; *Natal'in*, 1979]. According to previous accounts and unpublished geologic maps, three stratigraphic units metamorphosed to lower greenschist facies have been recognized within the Tanatap unit (Figure 4) [*Drabkin*, 1970a; *Nedomolkin*, 1969, 1977; *Oradovskaya and Obut*, 1977; *Krasny and Putintsev*, 1984]: (1) the Tanatap Formation, consisting of graphitic phyllite, calcareous slate, limestone turbidites, and recrystallized limestone dated as early Middle Devonian (Eifelian) on the basis of extremely rare brachiopods and coral remnants; (2) the Ikychuren Formation, consisting of thinly bedded limestone and calcareous shale with rare late Middle Devonian (Givetian) corals and brachiopods; and (3) the Utaveem Formation, consisting of Lower Carboniferous gray to black fine-grained fossiliferous limestone, calcareous sandstone, and phyllite (Figures 3 and 4). *Drabkin* [1970a] and *Markov et al.* [1980] infer that Upper Devonian rocks are present in the Ikychuren Formation, although no Late Devonian fossils have been found so far in northern Chukotka.

In the Chegitun River region (Figure 3) the Tanatap unit is bounded by the Nynykin fault to the southeast and by what we call the Ratkhat fault in the northwest, which are both interpreted as right-lateral strike-slip faults (Figure 3). Rocks of the Tanatap unit possess an intricate structure produced by polyphase, inhomogenous deformation and greenschist facies metamorphism that resulted in formation of muscovite, chlorite, albite, and actinolite. Numerous isoclinal folds, shear zones, and faults make it impossible to reconstruct details of the initial stratigraphic succession. An unconformity was proposed to exist at the base of the Utaveem Formation [*Drabkin*, 1970a; *Nedomolkin*, 1969, 1977]. In our field area the Lower Carboniferous rocks indeed occupy the highest structural level (Figure 3); however, the lower contact of the Utaveem Formation is not exposed. Like the underlying Devonian rocks, the limestones of the Utaveem Formation display spaced anastomosing cleavage, and the calcareous phyllites have a penetrative foliation. This indicates that the Utaveem Formation was deformed and metamorphosed together with underlying Devonian rocks. If the unconformity does exist, it does not likely reflect a penetrative deformational event.

In general, graphitic phyllites and thinly bedded metacarbonates are the predominant lithologies of the Tanatap Formation. In zones of lower strain, sedimentary structures are locally well preserved. Turbidites consisting of Bouma C, D, and E intervals are commonly observed. In a few localities, flame structures and matrix-supported debris flow deposits several meters thick and rich in limestone pebbles were observed.

Metalimestone of the Tanatap and Ikychuren Formations is mainly thinly bedded and often interbedded with clear examples of carbonate turbidites. Medium- and thick-bedded metalimestone is rare. The metalimestone contains little terrigenous material and very few macrofossils. Both formations contain uniformly disseminated sulfides that, together with a high content of carbon in metapelitic rocks, are interpreted as evidence of an anoxic depositional environment. These sedimentological features suggest that they were deposited in a deep-water restricted marine basin.

In the Tanatap Formation we found 2- to 35-m-thick horizons of reddish and green andesite tuff containing abundant volcanic clasts (see below). Gray and dark gray metalimestone of the Lower Carboniferous Utaveem Formation is rich in macrofossils, mainly shallow marine corals [*Drabkin*, 1970a]. We recovered *Cavusgnathus unicornis, Cavusgnathus, and Bispathodus stabilis or Bispathodus utahensis conodonts* from this unit, thus corroborating a mid-Famennian to Meramecian age (latest Devonian to early late Mississippian) (A. Harris, written communication, 1997).

Middle to Upper (?) Devonian and Lower Carboniferous rocks are also exposed along the Chukchi sea coast to the southeast of the Chegitun River region (Figure 2). In that area, Devonian rocks that are similar to those of the Chegitun River valley are overlain by Lower Carboniferous (Visean) limestones that are rich in shallow marine fossils. The limestones grade up into thin intercalated black phyllites and slates, sericitic and chloritic phyllite, and quartzo-feldspathic sandstones [*Drabkin*, 1970a]. Cleavage and schistosity developed at greenschist facies metamorphic conditions are reported from these rocks [*Drabkin*, 1970a; *Natal'in*, 1979]. Thus we assign these rocks to the Tanatap unit.

We infer that greenschist facies metasedimentary and metavolcanic rocks that are exposed to the northwest and north of the Chegitun unit, in the Seshan Cape region (Figure 2), are equivalent to those of the Tanatap unit. *Oradovskaya and Obut* [1977] distinguished there the Seshan Formation, which contains phyllites, rhyolites, and probably basaltic tuffs, and overlying, dark gray to black shale, phyllites, and limestones of the Ikoluvrun Formation. No fossils have been found in either of these formations. Their Cambrian-Early Ordovician age was inferred from their structural position beneath fossil-bearing Upper Ordovician rocks at Seshan Cape [*Oradovskaya and Obut*, 1977]. However, the lithological similarity of the Ikoluvrun Formation to the Tanatap Formation as well as strong deformation at the contact with the overlying Ordovician rocks [see *Oradovskaya and Obut*, 1977, Figure 7] allows the inference that there is a fault contact between the Ikoluvrun Formation and the Ordovician rocks. Thus an age determination based on structural position may not be valid. The lithologic and structural features, greenschist facies metamorphism and fault relationships with the Ordovician rocks of the Chegitun unit, as well as the presence of volcanic horizons in the Seshan Formation, indicate that the Seshan and Ikoluvrun Formations may also correlate with the Tanatap Formation.

Some researchers believe that the southern part of the Tanatap unit contains Riphean rocks. This belief is based on findings of oncolites [*Ivanov and Kryukov*, 1973] or acritarchs [*Gorodinsky*, 1980; *Krasny and Putintsev*, 1984], the location of which have not been specified. Within the area of supposedly Riphean rocks we observed rocks that are lithologically identical to rocks of the Tanatap Formation and in places containing remnants of crinoids. Thus we dispute the existence of the Riphean rocks in the Tanatap unit.

The $^{40}Ar/^{39}Ar$ dating of metamorphic white mica from the Tanatap unit has shown that the age of deformation and metamorphism in the Chegitun River valley is Early Cretaceous at 124 Ma [*Natal'in et al.*, 1997]. No traces of earlier deformational events have been detected by structural analysis.

3.3. Chegitun Unit

The Chegitun unit is represented by unstrained, fossil-rich, shallow marine Middle Ordovician to Lower Devonian limestone, dolomite, and minor shale (Figures 3 and 4). The base of the Chegitun unit is not exposed in the Chegitun River valley, but *Oradovskaya and Obut* [1977] assume that the unit rests upon the inferred Upper Cambrian to Lower Ordovician Seshan and Ikoluvrun Formations. These relationships have been disputed in section 3.2, in which the Seshan and Ikoluvrun Formations are correlated with the Middle Devonian Tanatap Formation.

At the base of the Chegitun unit lies the 430 - to 540-m-thick Isseten Formation (Figure 4), which consists of dark gray to gray pelitomorphic and bioclastic limestone (locally argillaceous), dolomite, marl, and rare sedimentary breccia with clasts of limestone, and dolomite. Marl is present in the upper part of the section and reflects the deepening of the basin over time. To the northwest of the Chegitun River, limestone breccia with a dolomite matrix is reported as the most abundant rock type within the lower part of the formation. The rocks contain Middle Ordovician corals (Late Llanvirnian to Llandeilo), graptolites, brachiopods, gastropods, and trilobites which are very similar to the faunal assemblages of the Siberian platform and Kolyma region [*Oradovskaya and Obut*, 1977]. A Middle Ordovician conodont assemblage was recovered from this unit, including *Protopanderodus* sp. indet., *Panderodus* sp. indet., *Acanthocodina (?)* sp. indet., *Acanthocordylodus* sp. indet., *Drepanoistodus* sp., and possibly *Erismodus* sp. (A. Harris, written communication, 1997). This Middle Ordovician conodont assemblage is characteristic of warm shallow water environments of the Siberian platform.

The Upper Ordovician Chegitun Formation (225-350 m) (Figure 4) conformably overlies the Isseten Formation and is represented by medium- to coarse-grained dark gray bioclastic and reefal limestone and rare dolomite. Dark, organic-rich silicified concretions are commonly present in reefal limestones. Bedding surfaces within this unit are wavy. Reefal limestones form lenses several meters thick. The rocks are generally rich in recrystallized pentamerids, corals, and gastropods of Ashgilian (Upper Ordovician) age which are similar to those of the Kolyma region [*Oradovskaya and Obut*, 1977]. *Oradovskaya and Obut* [1977] infer a disconformity at the base of the Chegitun Formation.

The Chegitun Formation is, in turn, conformably overlain by the Silurian Putukuney Formation (60-70 m) (Figure 4). The contact between formation is very sharp. The Putukuney Formation consists of black calcareous shale and dark, thinly bedded, flaggy argillaceous limestone which contains numerous graptolites indicating Late Llandoverian, Wenlockian, to Early Ludlovian age. Light gray to yellowish thick-bedded limestone and dolomite (300-315 m) of the Late Silurian (Upper Ludlow) Orlan Formation overlies the Putukuney Formation. Lacking fossil evidence, *Oradovskaya and Obut* [1977] determined the age of the Orlan Formation on the basis of its structural position between the Putukuney Formation and fossil-bearing Lower Devonian rocks. Silurian conodonts recovered from our samples of the Orlan Formation include *Ozarkodinus* sp. indet and *Walliserodus* sp. indet (A. Harris, written communication, 1997). At the top of the Chegitun unit are Lower Devonian (200-250 m) dolomitic limestones containing stromatoporoid corals [*Oradovskaya and Obut*, 1977; *Krasny and Putintsev*, 1984].

In contrast to the Tanatap unit, the internal structure of the Chegitun unit is very simple. There are northwest and north-south striking open folds, wavelength of which is of hundreds of meters to kilometer scale. These folds are oblique to the boundaries between the lithotectonic units and to the principal northeastern trends in the Tanatap units. Northwest striking normal faults and northeast striking steeply dipping strike-slip faults are superimposed on the above mentioned folds. Despite the simple map- and outcrop-scale structure and the lack of any penetrative metamorphic fabric, the conodonts recovered from rocks of the Chegitun unit have conodont alteration indexes (CAIs) ranging from 5 to 6 (A. Harris, written communication, 1997). These values correspond to paleotemperatures of 300°-435°C [*Rejebian et al.*, 1987]. We attribute this high CAIs to local heating of the Chegitun unit during emplacement of the mid-Cretaceous granitic intrusions that rim the Koolen and Neshkan metamorphic domes (Figure 2).

4. Devonian Magmatism on the Northern Chukotka Peninsula

The correlation of Paleozoic magmatic events between the Russian Far East and North America and the search for a tectonic framework that can help us to understand the disposition and origin of Paleozoic magmatic belts remain an outstanding problem. This is especially important in Chukotka where pre-Triassic rocks are generally buried by the Mesozoic sedimentary rocks of the Chukotka fold belt and by the mid-Cretaceous Okhotsk-Chukotka volcanic belt. Devonian volcanic and plutonic rocks of the Russian Far East have been correlated with similar rocks known from California to northern Alaska [e.g., *Tilman*, 1973; *Rubin et al.*, 1990]. We provide here new ages for Devonian orthogneisses from the core of the Koolen dome, and we report andesitic tuffs from the Tanatap unit of the Chegitun River valley. These Devonian magmatic rocks are the first recognized from the Chukotka Peninsula and provide an important link between the mid-Paleozoic tectonic history of Chukotka and northern Alaska.

4.1. The Etelkhvyleut Series Orthogneiss

The Etelkhvyleut orthogneiss of the Koolen dome (Figure 2) consists of metamorphosed and deformed biotite granodiorite and granite, in places exhibiting migmatization [*Shuldiner and Nedomolkin*, 1976]. Protolith ages for this unit were suspected to be Precambrian, but *BSGFP* [1997] considered the possibility that some of these orthogneisses were highly deformed and metamorphosed Paleozoic or Mesozoic plutonic rocks. U-Pb geochronology revealed that most of the orthogneisses are highly deformed Cretaceous granites related to the high-grade metamorphic event [*BSGFP*, 1997]. However, samples F45-94K and M18-94K yielded Devonian ages. These two samples are from a metaluminous biotite granitic orthogneiss (unit Egog) [see *BSGFP*, 1997, Figure 4]. SiO_2 is 60 wt % and 64 wt % in the two rocks, respectively, so the original composition was likely a granodiorite (Table 2). Accessory phases include sphene, zircon, and apatite.

We dated six fractions of zircon from each of two Etelkhvyleut Series orthogneisses along the north and southern sides of Koolen Lake (Table 3 and Figure 2). Because of the fairly limited spread in U-Pb dates and the complete agreement within analytical error of the $^{207}Pb^*/^{206}Pb^*$ dates from analyzed fractions of each sample we interpret the age of these samples to be the weighted mean of the $^{207}Pb^*/^{206}Pb^*$ dates. The six zircon fractions analyzed from sample F45-94K give an age of 369.6 ± 1.2 Ma (MSWD = 3.3) whereas the 5 zircon fractions from sample M18-94K give an age of 374.8 ± 0.5 Ma (MSWD = 1.2). These data establish a Devonian age for the Etelkhvyleut Series orthogneisses in this area. The initial Sr for these two samples is 0.706, and the ε_{Nd} is +0.2 (F45) and -0.3 (M18, Table 4).

4.2. The Tanatap Series Metatuff

At least four distinct horizons of alternating red and green andesite tuffs 2 - 35 m thick are present in the Tanatap Formation in the Chegitun River valley; whereas a thicker (340 m) body of volcanic rocks has been reported off Seshan Cape [*Oradovskaya and Obut*, 1977]. In places, these horizons contain altered clasts with relict porphyritic texture. The tuffs have been metamorphosed to greenschist facies, and the identifiable mineralogy is mainly white mica, calcite/dolomite, and chlorite. The layered fabric is similar to unmetamorphosed volcanoclastic rocks, al-

Table 2. Major and Trace Element Geochemistry for Devonian Igneous Rocks

	Koolen Lake Orthogneiss		Tanatap Metatuff	
	F45-94K	M18-94K	95JT-39	95JT-48
SiO_2†	60.37	64.02	57.27	58.91
Al_2O_3	17.39	16.27	20.03	20.02
TiO_2	1.04	0.89	1.05	1.06
FeO*	5.16	4.81	7.12	4.99
MnO	0.11	0.11	0.06	0.05
CaO	4.28	3.36	2.34	2.60
MgO	1.96	1.57	3.53	3.84
K_2O	3.57	4.45	4.42	3.48
Na_2O	4.43	3.88	0.44	1.08
P_2O_5	0.39	0.33	0.15	0.15
Sum	98.70	99.69	96.41	96.18
Ba‡	1271	1540	460	500
Rb	199.30	140.40	177.90	137.20
Th	58.20	18.38	11.19	12.18
Nb	8.52	16.97	17.37	18.28
Ta	2.56	2.69	1.17	1.25
Sr	360	536	172	479
Zr	460	339	162	188
Hf	9.79	7.40	4.58	5.20
Tb	0.88	1.10	1.08	1.06
Y	18.62	32.23	35.25	33.83
La		82.89	36.04	49.59
Ce		155.35	71.08	93.36
Pr		15.77	8.04	10.44
Nd		57.81	31.60	40.63
Sm		10.44	7.00	8.54
Eu		2.41	1.56	1.34
Gd		7.70	6.01	6.28
Tb		1.10	1.08	1.06
Dy		6.10	6.54	6.48
Ho		1.17	1.31	1.29
Er		3.03	3.71	3.71
Tm		0.45	0.51	0.53
Yb		2.67	3.20	3.40
Lu		0.43	0.49	0.53
Ni			68	63
Cr			118	126
Sc			15	13
V			184	184
Ga			27	31
Cu			1	487
Zn			33	37
Pb			1.6	1.3
U			3.5	3.5
Cs			6.9	6.3

† Major element data were collected by XRF.
* All Fe was calculated as FeO.
‡ Trace element data were collected by inductively coupled plasma mass spectrometry except for metatuff rare earth element (REE) data, which were collected by isotope dilution at the University of Wisconsin using a mixed REE spike.

Table 3. U-Pb Isotopic Data from Koolen Lake Orthogneiss

Sample†	U, ppm	$^{206}Pb^*$, ppm	Measured Ratios‡			Atomic Ratios			Apparent Ages,§ Ma		
			$^{206}Pb/^{204}Pb$	$^{207}Pb/^{206}Pb$	$^{208}Pb/^{206}Pb$	$^{206}Pb^*/^{238}U$	$^{207}Pb^*/^{235}U$	$^{207}Pb^*/^{206}Pb^*$	$^{206}Pb^*/^{238}U$	$^{207}Pb^*/^{235}U$	$^{207}Pb^*/^{206}Pb^*$
F45/94K +100A	542.8	25.31	734	0.07390	0.22148	0.05428(27)	0.40417(230)	0.05400(15)	340.8	344.7	371.1 ±6.1
F45/94K +100	577.8	25.71	7692	0.05585	0.16927	0.05179(26)	0.38524(194)	0.05395(4)	325.5	330.9	369.0 ±1.5
F45/94K100-150A	680.8	32.24	9455	0.05555	0.19451	0.05512(28)	0.41085(206)	0.05401(3)	345.9	349.5	371.3 ±1.1
F45/94K 100-150	642.6	27.65	15385	0.05492	0.18732	0.05008(25)	0.37271(187)	0.05398(2)	315.0	321.7	369.9 ±1.1
F45/94K 150-210	699.7	30.90	21323	0.05464	0.19331	0.05141(26)	0.38243(192)	0.05395(2)	323.2	328.8	369.1 ±1.0
F45/94K 210-325	748.9	32.74	28634	0.05445	0.20330	0.05088(25)	0.37843(190)	0.05394(2)	319.9	325.9	368.5 ±1.0
M18/94K+100A	559.1	27.21	6550	0.05635	0.19370	0.05666(28)	0.42278(213)	0.05412(3)	355.3	358.0	376.0 ±1.4
M18/94K +100	576.2	27.27	5280	0.05685	0.18835	0.05509(28)	0.41078(207)	0.05408(4)	345.7	349.4	374.4 ±1.5
M18/94K 100-150	636.3	30.13	12686	0.05523	0.20365	0.05513(28)	0.41110(207)	0.05408(3)	345.9	349.7	374.5 ±1.1
M18/94K 150-210	712.3	31.88	22521	0.05473	0.21943	0.05210(26)	0.38850(195)	0.05408(2)	327.4	333.3	374.3 ±1.1
M18/94K 210-325	889.3	31.80	21323	0.05478	0.21213	0.04163(21)	0.31050(156)	0.05410(3)	262.9	274.6	375.1 ±1.1

† Value >100, <200, etc., refer to size fractions in mesh size. All analyzed zircon fractions consisted of the least magnetic crystals that could be fractionated on a Frantz magnetic separator. "A" refers to the fraction that was air abraded prior to dissolution. See *Wright and Fahan* [1988] and *Dilles and Wright* [1988] for details of the analytical procedure. The sample locations are F45/94K (65°55.7'-N, 171°7.32'-W) and M18/94K (65°57.12'-N, 171°57.12'-W).

* Radiogenic Pb is used, corrected for common Pb using the isotopic composition of $^{206}Pb/^{204}Pb = 18.6$ and $^{207}Pb/^{204}Pb = 15.6$.

‡ Isotopic compositions are corrected for mass fractionation of 0.11%. Sample dissolution and ion exchange chemistry are modified from *Krough* [1973].

§ Ages were calculated using the following constants: decay constants for ^{235}U and $^{238}U = 9.8485 \times 10^{-10}$ yr^{-1} and 1.55125×10^{-10} yr^{-1} respectively; $^{238}U/^{235}U = 137.88$. Precessions on $^{206}Pb^*/^{238}U$ ratios are ~ 0.2 - 0.3% based on the replicate analysis of two "standard" zircon fractions. Accuracy of the $^{206}Pb^*/^{238}U$ dates, including uncertainties in spike calibration, are estimated to be of the order of 0.5%. The two-sigma uncertainties in the $^{207}Pb^*/^{206}Pb^*$ ages were calculated from the combined uncertainties in mass spectrometry and an assumed uncertainty of ± 0.1 in the $^{207}Pb/^{204}Pb$ ratio used for the common Pb correction [*Mattinson*, 1987].

Table 4. Rb-Sr and Sm-Nd Isotopic Data From Devonian Igneous Rocks

Sample	Age, Ma	Rb, ppm	Sr, ppm	Atomic Ratio $^{87}Rb/^{86}Sr$	Measured Ratio* $^{87}Rb/^{86}Sr$	Initial Ratio $^{87}Rb/^{86}Sr$	Sm, ppm	Nd, ppm	Atomic Ratio $^{147}Sm/^{144}Nd$	Measured Ratio† $^{143}Nd/^{144}Nd$	Initial Ratio $^{143}Nd/^{144}Nd$	ε_{Nd}‡
Koolen Orthogneiss												
F45/94K	376	122.0	585.0	0.604	0.70938 (8)	0.70615	11.2	67.2	0.101	0.512411 (20)	0.512167	0.2
M18/94K	375	144.0	575.0	0.725	0.71007 (8)	0.70620	10.2	61.7	0.100	0.512383 (20)	0.512138	-0.3
Tanatap Metatuff												
95JT-39	~380	172.0	153.2	3.25	0.71935 (7)	0.7018	6.6	28.1	0.142	0.512125 (20)	0.511781	-7.3
95JT-48	~380	134.6	448.1	0.870	0.71277 (7)	0.70806	8.0	35.6	0.135	0.512119 (20)	0.511791	-7.1

Koolen orthogneiss was analyzed at Rice University by J. Wright. Tanatap metatuff was analyzed at the University of Wisconsin, Madison, by J. M. Amato. Values used for chondritic uniform reservoir (CHUR) are $^{143}Nd/^{144}Nd = 0.512638$ and $^{147}Sm/^{144}Nd = 0.1967$. Decay constants are the following: Sm, 6.54×10^{-2} yr^{-1}; Rb, 1.42×10^{-11} yr^{-1}. Rb, Sr, Sm, and Nd concentrations were determined by isotope dilution by the addition of a mixed spike prior to the sample dissolution. At Rice University, Nd was measured as Nd^+; at the University of Wisconsin, Nd was measured as NdO. Repeated analysis of NBS-987 yielded $^{87}Sr/^{86}Sr = 0.710247 \pm 10$ (Rice University, >80 analyses) and 0.710257 ± 18 (University of Wisconsin, 30 analyses). Repeated analysis of BCR-1 yielded $^{143}Nd/^{144}Nd = 0.512633 \pm 10$ (Rice University, >20 analyses) and 0.512630 ± 20 (University of Wisconsin, 4 analyses). Tanatap ages are assumed to be ~ 380 Ma on the basis of the orthogneiss ages and stratigraphic constraints (Middle Devonian: 377-386 Ma).

* Ratios are corrected for mass fractionation by normalizing to $^{86}Sr/^{88}Sr = 0.1194$.

† All errors in measured isotopic ratios are at the 95% confidence limit. Ratios are corrected for mass fractionation by normalizing to $^{146}Nd/^{144}Nd = 0.72190$.

‡ $\varepsilon_{Nd}(T) = \{[^{143}Nd/^{144}Nd(T)_{sample}/^{143}Nd/^{144}Nd(T)_{CHUR}] - 1\} \times 10,000$.

though subsequent tectonic deformation may have contributed to the formation of the foliation.

Major element geochemistry on two of the volcanic samples indicates that the tuffs are calc-alkaline andesites (SiO_2 = 59-61 wt % anhydrous) significantly enriched in potassium (Table 1). Because of greenschist facies metamorphism, it is not known to what degree this potassium enrichment is the result of posteruptive metasomatic processes. Some notable aspects of the geochemistry include Cr concentrations of 118 and 126 ppm and Ni concentrations greater than 60 ppm. It is unclear what phases are responsible for these concentrations, which are elevated with respect to normal andesites [e.g., *Ewart*, 1982]. It is possible, however, that the whole rock SiO_2 concentration is elevated because of the inadvertent inclusion of felsic clasts in the whole rock analysis. If this is true, the tuffs may be of a more basaltic-andesite composition, for which such high Cr and Ni concentrations may be more characteristic. These rocks are enriched in the light rare earth elements (LREE) (Figure 6), with La/Lu ratios of 74-94 and a negative Eu anomaly.

Although we report Sr isotopic data for the tuffs (Table 2), the mobility of Rb during greenschist facies metamorphism may have affected the measured Sr ratios. Nd and the REE are less mobile during metamorphism, so we believe the Nd isotopic data is much more robust. Although the tuffs are foliated, there are no structural discontinuities or shear zones between the tuffs and the surrounding rocks of the Tanatap Formation from which rare findings of Middle Devonian fossils have been reported [*Nedomolkin*, 1969, 1977; *Oradovskaya and Obut*, 1977]. So if we assume an age for the tuffs similar to that for the orthogneisses (~375 Ma), the initial ε_{Nd} for both metatuff samples is about -7. This is significantly different from the values measured from the Koolen Lake orthogneiss and would seem to preclude a common source region. However, the tuffs could have interacted with significant amounts of older crustal material during their ascent and eruption. Alternatively, the isotopic analysis of the tuff could have been contaminated by the inclusion of crustal material of a different age or origin. These two possibilities could have the effect of decreasing the ε_{Nd}. The question of

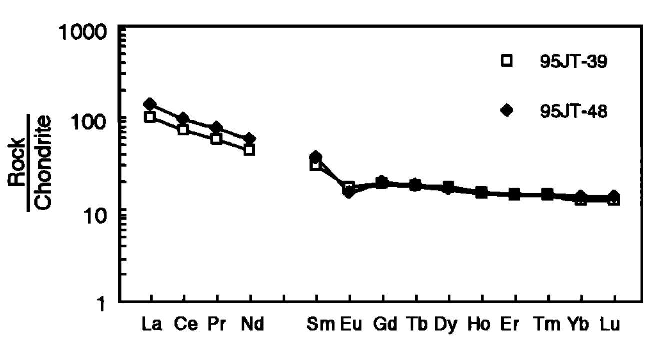

Figure 6. Rare earth element pattern from Tanatap metatuff. Light rare earth element enriched pattern with a negative Eu anomaly is commonly observed in continental arc volcanic rocks and may reflect derivation from an already fractionated source or a mixture of a primary magma with older, evolved crustal partial melts. Normalization factors are from *Anders and Ebihara* [1982].

whether or not the tuff and the orthogneiss are comagmatic is thus not resolvable using the isotopic data. We believe that the spatial relationships and the similar compositions point to a common origin for the orthogneiss and tuff.

Trace element geochemistry can be useful for identifying the tectonic setting of volcanic rocks, though large-ion lithophile elements such as Ba and Rb are to be avoided owing to both post-depositional alteration and the likelihood that the primary magma interacted with continental crust during its ascent. This crustal interaction may significantly alter the magmatic values and thus provide misleading information. High field strength elements and REE are less affected by alteration and metamorphism, and a comparison of the La/Th and La/Nb ratios with other orogenic andesite compositions indicates that the Tanatap tuffs overlap with high-K andesites from other areas [*Gill*, 1981].

Textural evidence, major and trace element chemistry, and Nd isotopic data all suggest that the Tanatap Series tuffs are differentiated calc-alkaline andesites possibly derived from a continental margin magmatic arc. The degree of metamorphism and alteration precludes a more rigorous assessment of the tectonic setting based on the tuffs alone. If we take into consideration the deep-water, anoxic, fine-grained nature and the lack of a terrigenous clastic component in the host rocks, it seems possible that these arc volcanic rocks were deposited in a back arc basin.

5. Paleozoic and Mesozoic Tectonic Units and Correlation of the Structures of Chukotka and Northern Alaska

The rocks exposed in the Chegitun River valley are an important element in Paleozoic tectonic reconstructions, because in many other areas of Chukotka and northern Alaska, Mesozoic magmatism, metamorphism, and deformation obscure earlier tectonic features. In addition, important tectonic elements may lie hidden within the broad continental shelves of the region. In this section we describe the important tectonic units of this region, attempt to correlate these features between Russia and Alaska, and propose a Paleozoic tectonic evolution for the region.

The major Paleozoic tectonic units of the Russian sector of the Chukotka-Arctic Alaska microplate are the following (Figure 7): (1) Precambrian crust which is inferred to underlie the Paleozoic and Mesozoic sedimentary cover (the Bennett-Barrovia block), (2) Ordovician to Devonian shelf carbonates and shales (the Novosibirsk carbonate platform) [*Şengör and Natal'in*, 1996], and (3) a middle Paleozoic arc-trench system stretching along the southern boundary of the Novosibirsk carbonate platform [*Natal'in et al.*, 1997]. Triassic-Early Jurassic passive continental margin deposits which now make up the Chukotka fold belt overlie these units and are bounded in the south by the Neocomian South Anyui suture [*Parfenov and Natal'in*, 1977, 1985; *Natal'in*, 1981, 1984].

In northern Alaska all Proterozoic to Early Cretaceous tectonic units located to the north of the Angayucham terrane (Figure 7) are assigned to the Arctic Alaska terrane [*Moore et al.*, 1994; *Plafker and Berg*, 1994]. The Seward Peninsula is generally correlated with the southern part of the Arctic Alaska terrane [*Moore et al.*, 1994; *Plafker and Berg*, 1994]. The Arctic Alaska terrane is unified by its Late Devonian through Jurassic passive margin stratigraphy (the Ellesmerian sequence). This sequence is predated by Middle (in places upper Lower Devonian) to Upper Devonian clastic rocks, shale, and mafic igneous rocks which formed in extensional environment and accumulated atop of strongly deformed basement [*Anderson et al.*, 1994; *Moore et al.*, 1994; 1997b]. *Grantz et al.* [1991] and *Moore et al.* [1994] suggest that pre-Middle-Devonian tectonic history of northern Alaska was a result of accretion of continental fragments of Siberian affinity to the continental margin of North America. Following this interpretation, the most significant pre-Middle-Devonian tectonic units are the following (Figure 7): (1) a fragment of the upper Proterozoic to lower Paleozoic passive continental margin rocks of the North American craton exposed in the Sadlerochit and Shublik mountains, northeastern Brooks Range; (2) lower Paleozoic rocks of oceanic and island arc affinity that are tectonically mixed with upper Proterozoic to lower Paleozoic passive continental margin deposits in the Franklinian fold belt (Figure 7) and which are exposed to the south of this fragment of the North American margin in the Romanzoff Mountains and in the Doonerak window of the Brooks Range and underlie part of the Colville Basin; (3) a complexly imbricated and metamorphosed assemblage of upper Proterozoic to Mississippian rocks mostly of continental affinity that make up the Hammond subterrane of the Brooks Range; and (4) Proterozoic to Mississippian (protolith age) schist, phyllite, metasandstone, and metacarbonate rocks with subordinate metaquartzite, metabasite, and felsic metavolcanic rocks of the Coldfoot subterrane. Units 3 and 4 and at least part of unit 2 have been considered as being of Siberian origin [*Grantz et al.*, 1991]. To the south of the Coldfoot subterrane there are quartzose phyllite, schist, slate, quartzite, minor metabasite, and chert of the Slate Creek subterrane which yield sparse Early and Middle Devonian and Mississippian fossils. The Hammond, Coldfoot, and Slate Creek subterranes were affected by intense deformation and blueschist to greenschist facies metamorphism during the Brookian orogeny in Late Jurassic to Early Cretaceous time.

The Late Jurassic to Early Cretaceous Kobuk suture, reactivated by mid-Cretaceous normal faulting [*Grantz et al.*, 1991], separates Arctic Alaska from the Angayucham terrane and, together with the South Anyui suture, defines the southern boundary of the Chukotka-Arctic Alaska block [*Parfenov and Natal'in*,

Figure 7. Tectonic map of the Siberian-Alaskan sector of Arctic. Abbreviations are as follows: AM, Alyarmaut Uplift; AN, Angayucham terrane; BD, Baird Mountains; BF, Barrow fault zone; BI, Belkov Island, BN, Belkovskyi-Nerpalakh Trough; DN, Doonerak window; HM, Hammond subterrane; HRT, Herald thrust; HT, Henrietta Island; KC, Kiber Cape; KG, Kigluaik dome; KI, Kotel'nyi Island; KM, Kolyuchin-Mechigmen zone; KO, Koolen dome; KU, Kuyul Uplift; NT, Nutesyn; PR, Primorsk Basin; RC, Rauchua Basin; RZ, Romanzof Mountains; SA, South Anyui suture zone; SE, Senyavin Uplift; SS, Shublik and Sadlerochit mountains; TP, Topolevka; YR, York Mountains; YU, Yarakvaam Uplift.

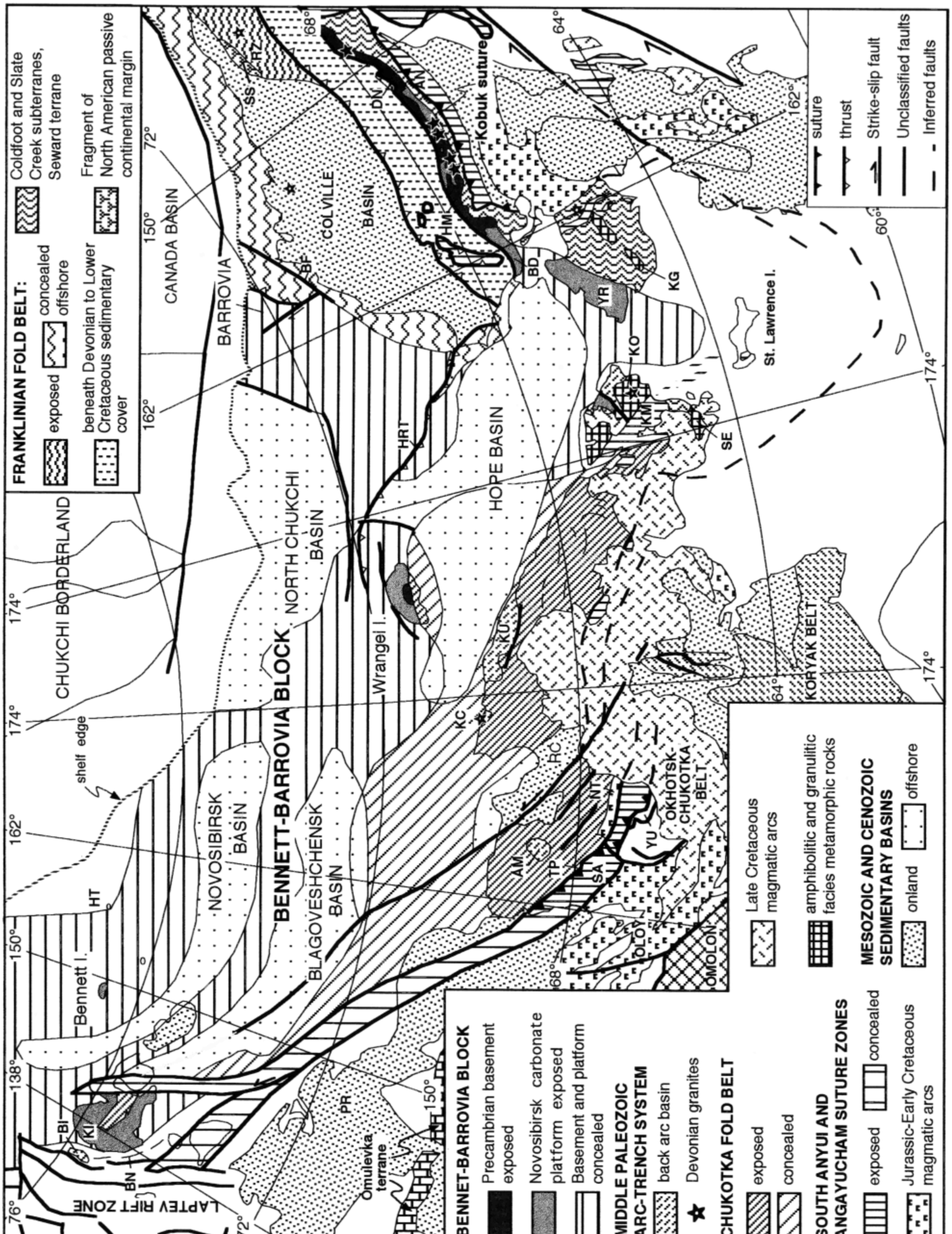
FRANKLINIAN FOLD BELT:
exposed
concealed offshore
beneath Devonian to Lower Cretaceous sedimentary cover
Coldfoot and Slate Creek subterranes, Seward terrane
Fragment of North American passive continental margin
suture
thrust
Strike-slip fault
Unclassified faults
Inferred faults
BENNET-BARROVIA BLOCK
Precambrian basement exposed
Novosibirsk carbonate platform exposed
Basement and platform concealed
MIDDLE PALEOZOIC ARC-TRENCH SYSTEM
back arc basin
Devonian granites
CHUKOTKA FOLD BELT
exposed
concealed
SOUTH ANYUI AND ANGAYUCHAM SUTURE ZONES
exposed
concealed
Jurassic-Early Cretaceous magmatic arcs
Late Cretaceous magmatic arcs
amphibolitic and granulitic facies metamorphic rocks
MESOZOIC AND CENOZOIC SEDIMENTARY BASINS
onland
offshore
CHUKCHI BORDERLAND
CANADA BASIN
BARROVIA
COLVILLE BASIN
Kobuk suture
BENNETT-BARROVIA BLOCK
NORTH CHUKCHI BASIN
HOPE BASIN
NOVOSIBIRSK BASIN
BLAGOVESHCHENSK BASIN
Wrangel I.
Bennett I.
St. Lawrence I.
LAPTEV RIFT ZONE
Omulevka terrane
OKHOTSK-CHUKOTKA BELT
KORYAK BELT
OMOLON
shelf edge

Figure 7.

1977, 1985; *Natal'in*, 1984, *Rowley and Lottes*, 1988]. In the sections 5.1-5.4 we discuss mainly the Russian sector of the region. Details of the geological structure of the Alaskan sector (the Arctic Alaska terrane) are given by *Moore et al.* [1994, 1997b] and *Grantz et al.* [1990].

5.1. Bennett-Barrovia Block

Two distinct tectonic hypotheses have been proposed for the evolution of this portion of the Arctic. In one, an intact Precambrian basement block forms the basement of the Novosibirsk Islands, Wrangel Island, the Chukchi and East Siberian Seas, and the Hammond subterrane in northern Alaska [e.g., *Zonenshain et al.*, 1990; *Şengör and Natal'in*, 1996]. In the other, this same region is an amalgamation of terranes that accreted to Asia or North America during Paleozoic-Mesozoic time and then rifted away during a subsequent event [*Fujita and Newberry*, 1982; *Fujita and Cook*, 1990]. We believe the "intact Precambrian basement block" hypothesis is valid for the following reasons: (1) The lower Paleozoic stratigraphy and lithology indicates a tectonically stable shallow marine environment that persisted throughout the area, from the Novosibirsk Islands to the Hammond subterrane in Alaska (see below), thus the different exposures are not likely to represent disparate terranes, but rather reflect deposition on a unified basement block; (2) faunal evidence places these exposures near each other and adjacent to Siberia during Paleozoic time [*Oradovskaya and Obut*, 1977; *Krasny and Putintsev*, 1984; *Moore et al.*, 1994]; and (3) low-amplitude, broad E-W or NW striking magnetic anomalies over most of the central and southern Chukchi and East Siberian Seas [*Vinogradov et al.*, 1974; see also *Fujita and Cook*, 1990] indicate an absence of sutures, which would be required in the terrane hypothesis.

The Bennett-Barrovia block underlies the shelf of the East Siberian and Chukchi Seas (Figure 7). The boundaries of the block and its main components can be inferred from (1) exposures of Paleozoic rocks, which reveal no evidence of extensive pre-Late Jurassic to Early Cretaceous deformation and thus formed in rather stable tectonic environment [*Kos'ko et al.*, 1993]; (2) disposition and geometry of the wide Mesozoic extensional basins (Figure 7); and (3) similarity of geophysical characteristics of the underlying basement [*Vinogradov et al.*, 1974, *Gramberg and Pogrebitzkiy*, 1984]. The boundaries and description of this block will be separately described for Russia, Alaska, and the Canadian Arctic islands.

5.1.1. Russia. The western boundary of the Bennett-Barrovia block coincides with the Laptev rift zone, which is a continuation of the Arctic mid-ocean ridge (Figure 9). *Zonenshain et al.* [1990] included the North Taimyr Peninsula and the Severnaya Zemlya Archipelago within their Arctida microcontinent, but both of these regions are characterized by a thick, strongly deformed succession of Riphean to Lower Ordovician flysch and rare red beds deposited on a passive continental margin. Such rocks are completely absent from the regions that we include in the Bennett-Barrovia block. In the Bennett Island region, in the East Siberian Sea (Figure 7), consolidated Precambrian crust underlying Paleozoic and Mesozoic sedimentary cover can be inferred from gravity and aeromagnetic anomalies [*Tkachenko and Egiazarov*, 1970; *Vinogradov et al.*, 1974; *Gramberg and Pogrebitzkiy*, 1984]. We infer that this basement is exposed in Wrangel Island where a Late Precambrian fold belt constitutes the basement for less deformed and less metamorphosed Silurian to Lower Devonian and younger rocks [*Kos'ko et al.*, 1993]. The fold belt consists of felsic to intermediate metavolcanic rocks, slate, schist, quartzite, and conglomerate, intruded by mafic sills and dikes as well as by small bodies of granite yielding a U-Pb age of 699 Ma [*Cecile et al.*, 1991b]. The discovery of Late Proterozoic protolith ages in the Etelkhvyleut orthogneiss in the Chegitun River valley indicates that a Late Proterozoic granitic magmatic belt extends to Chukotka.

In the eastern Chukchi Sea (Barrovia in Figure 7), another fragment of Precambrian crust covered by undeformed Upper Proterozoic to Cambrian [*Grantz et al.*, 1990] or lower Paleozoic [*Sherwood*, 1994] carbonate rocks can be inferred from seismic reflection profiling. Dips of foreset beds in overlying Paleozoic clastic rocks indicate that the source area for them was to the northwest (in the internal part of the Bennett-Barrovia block).

In the Chukotka sector the northern boundary of the Bennett-Barrovia block is masked by deep Cretaceous to Cenozoic basins which stretch along the shelf edge. On the basis of geophysical data, *Vinogradov et al.* [1974] defined the Henrietta fold belt to the northeast of Bennett Island (Figures 7 and 9). The only exposure of the belt in Henrietta Island is represented by sandstone, tuffaceous sandstone, shale, conglomerate with numerous lavas, sill, and dikes of basalt, andesite, and diabase. Conglomerate contains pebbles of granite, greenschist, and gneiss. A Paleozoic age is evidenced from recrystallized, presumably Carboniferous, foraminifera and K-Ar ages of volcanic rocks of 450-310 Ma [*Vinogradov et al.*, 1975]. The Ordovician age of volcanic rocks has been confirmed by recent $^{40}Ar/^{39}Ar$ dating (A. Kaplan, oral communication, 1998). The rocks of the Henrietta Island are markedly different from the Paleozoic cover of the Bennett-Barrovia block and have previously been interpreted as an independent terrane [*Fujita and Cook*, 1990]. We infer here that Ordovician basalt to andesite volcanic rocks of the Henrietta belt may indicate a magmatic arc along the northern side of the Bennett-Barrovia block

5.1.2. Canadian Arctic Islands. The lower Paleozoic rocks of Henrietta Island may represent a link to Arctic Canada, where the exotic Pearya terrane (PE in Figure 9) provides a record of a Middle Ordovician collision of a Precambrian block with an Early to Middle Ordovician island arc [*Trettin*, 1991]. After their collision a new Middle Ordovician to Silurian arc of southern polarity [*Klaper*, 1992; *Bjørnerud and Bradley*, 1994] was constructed above the suture within the Pearya terrane [*Trettin*, 1991]. Another arc (CM in Figure 9) was active in the area between the Pearya terrane and the passive continental margin of North America during the Ordovician and Silurian. This arc also had southern polarity, as is indicated by the vergence of the Clements Markham fold belt [*Trettin*, 1991; *Klaper*, 1992].

Trettin [1991] correlated pre-Middle-Ordovician rocks of the Pearya terrane with the Caledonides of the northern Atlantic. He inferred that the collision of Pearya with the Clements Markham arc happened before the Late Silurian in a sinistral transpressional environment . In turn, the Clements Markham arc collided with the passive continental margin of Arctic Canada in the Late Silurian to Early Devonian. Structural studies revealed no evidence of sinistral regime of these collisions [*Klaper*, 1992]. Consequently, we infer that the Pearya terrane and Clements Markham arc were at least in the position between Bennett-Barrovia and Arctic Canada and thus relevant to the Bennett-Barrovia block evolution.

5.1.3. Alaska. Proterozoic rocks have been found in two structurally imbricated units in the western part of the Hammond subterrane in northern Alaska [*Moore et al.*, 1994]. The lower unit consists of metacarbonate rocks with subordinate siliciclastic and metavolcanic rocks. The upper unit is made up of metasedimentary rocks and metabasites. The rocks of the upper unit are intruded by granitic rocks yielding a U-Pb age of 750 Ma. The amphibolitic facies metamorphism that affected these rocks occurred at about 655-594 Ma [*Moore et al.*, 1994]. These rocks are very different from a more or less continuous succession of Proterozoic to lower Paleozoic carbonate rocks of the North American continental margin that are exposed in the Sadlerochit Mountains in the northeastern Brooks Range.

Granitoids yielding a 705 Ma U-Pb age also have been reported as intruding metasedimentary and metavolcanic rocks in the Coldfoot terrane [*Moore et al.*, 1994]. In addition, Nd and Sr isotopic data from younger magmatic rocks, as well as Proterozoic inherited zircons found in the Devonian orthogneisses, suggest that these magmatic rocks were in part derived from Proterozoic crust [*Dillon et al.*, 1987; *Nelson et al.*, 1993; *Toro*, 1998]. In Alaska, these rocks form the most probable basement for the Paleozoic Baird Group carbonate rocks [*Nelson et al.*, 1993; *Moore et al.*, 1994]. The timing of Late Proterozoic granitoid magmatism in the Brooks Range is similar to a magmatic event recorded in rocks found on Wrangel Island [*Kos'ko et al.*, 1993] and Chukotka. Late Proterozoic orthogneisses also have been reported from the Seward Peninsula [*Till and Dumoulin*, 1994; *Amato and Wright*, 1998].

In Alaska, Cambrian to Silurian rocks of island arc and oceanic origin are exposed between the Hammond subterrane and the fragment of the North America continental margin in the northeastern Brooks Range (the Franklinian belt in Figure 7) [*Grantz et al.*, 1991; *Moore et al.*, 1994]. These rocks mark an ocean which was closed at the end of the Silurian to Early Devonian, as it is evidenced by a sharp unconformity at the base of the Middle Devonian rocks [*Anderson et al.*, 1994]. The suture between the Bennett-Barrovia block and North America is inferred to be located at the northern boundary of the island arc and oceanic rocks [*Grantz et al.*, 1991]. This conclusion is supported by Cambrian fossils of Siberian type found in the island arc rocks [*Dutro et al.*, 1984] and by their position near the boundary with the Hammond subterrane.

5.2. Novosibirsk Carbonate Platform

The early to middle Paleozoic Novosibirsk carbonate platform was defined by *Şengör and Natal'in* [1996] as cover deposits of the Bennett-Barrovia block. The platform includes mainly shelf and lagoonal carbonate rocks that are exposed in both Russia and Alaska (Figures 7 and 8).

5.2.1. Russia. Ordovician to Lower Devonian shallow marine and lagoonal carbonate rocks and shales have been described from Kotel'nyi Island within the Novosibirsk Archipelago [*Tkachenko and Egiazarov*, 1970; *Volnov*, 1975; *Kos'ko*, 1977; *Kos'ko et al.*, 1990]. On Kotel'nyi Island the oldest rocks are Lower to Middle Ordovician, but farther to the north, on Bennett Island, shale and siltstone are interbedded with rare limestone containing Middle Cambrian trilobites. These rocks are unconformably (?) overlain by Lower to Middle Ordovician shale, siltstone, and quartzose sandstone [*Tkachenko and Egiazarov*, 1970; *Kos'ko et al.*, 1990]. Thin beds of limestone and the presence of quartzose sandstones in the Ordovician rocks on Bennett Island may be interpreted as evidence of facies changes from an area of carbonate deposition in Kotel'nyi Island toward an uplifted area in the north [*Kos'ko*, 1994]. Starting in the Early Silurian, two depositional zones existed in Kotel'nyi Island [*Kos'ko*, 1977; *Kos'ko et al.*, 1990]. In the northwestern zone, shallow marine and lagoonal carbonate accumulated while in the southwestern zone fine-grained limestone was deposited with deep-water shale, siltstone, and siliceous shale. Middle Devonian limestone, debris flow deposits, and conglomerate conformably or unconformably overlie the older rocks of both zones and mark another tectonic cycle [*Kos'ko et al.*, 1990].

Silurian to Lower Devonian shallow marine carbonates and clastic rocks on Wrangel Island which formed in stable shelf, shallow marine environments [*Kos'ko et al.*, 1993] can also be assigned to the Novosibirsk platform. The unconformably lying on the Proterozoic rocks the Lower to Upper Devonian unit (the oldest fauna is Givetian) consists of conglomerates and sandstones. Silurian to Lower Devonian sandstones consist predominantly of quartz and feldspar and are compositionally similar to the Ordovician sandstones in the Bennett Island. Conglomerate and sandstone of the Lower to Upper Devonian unit, in contrast, are lithic and include fragments of volcanic, volcanoclastic, and granitic rocks derived from the underlying basement [*Kos'ko et al.*, 1993].

5.2.2. Alaska. A characteristic succession of lower to middle Paleozoic shallow marine carbonate rocks is found in the York Mountains of the Seward Peninsula [*Till and Dumoulin*, 1994], in the Baird Mountains of the western Brooks Range, and in several localities in the central and eastern Brooks Range within the Hammond subterrane [*Dumoulin and Harris*, 1994; *Moore et al.*, 1994] (Figures 7 and 8). In the York Mountains the succession starts with Arenigian deepening-upward subtidal to supratidal limestones which are overlain by shallowing-upward Lower Llanvirnian shales and thin-bedded limestones [*Dumoulin and Harris*, 1994]. Rocks of this age are missing on Chukotka Peninsula but exist on the Kotel'nyi Island [*Kos'ko*, 1977]. The Upper Llanvirnian to Lower Llandeilian black limestone of the York Mountains correlates well with the Isseten Formation of Chukotka. The overlying Upper Ordovician bioclastic fossiliferous limestones are similar to the Chegitun Formation of the Chukotka Peninsula. Lower Upper Ordovician rocks are not documented or missing in both regions. Silurian (Ludlovian) dolostone of the York Mountains may be correlated with the dolomites of the Orlan Formation of Chukotka. *Till and Dumoulin* [1994] reported that in addition to carbonate rocks the Silurian section of the York Mountains includes mudstone and that Middle Silurian fossils have been documented from this section. These rocks may be equivalent to the Putukuney Formation shales of the Chegitun River area.

In the Baird Mountains there are two fault-bounded carbonate sequences. The west central sequence consists of Lower Ordovician to Devonian shallow to deeper water platformal carbonate rocks, and its stratigraphy is very similar to that of the York Mountains on the Seward Peninsula [*Dumoulin and Harris*, 1994] and the Chegitun unit on the Chukotka Peninsula (Figure 8). The Lower to Middle Ordovician and Upper Silurian rocks are represented by limestone and dolomite, and the Upper Ordovician consists of limestone. The northeastern sequence of the Baird Mountains consists of Lower to Middle Ordovician shale and chert which grade up into inner shelf metalimestone

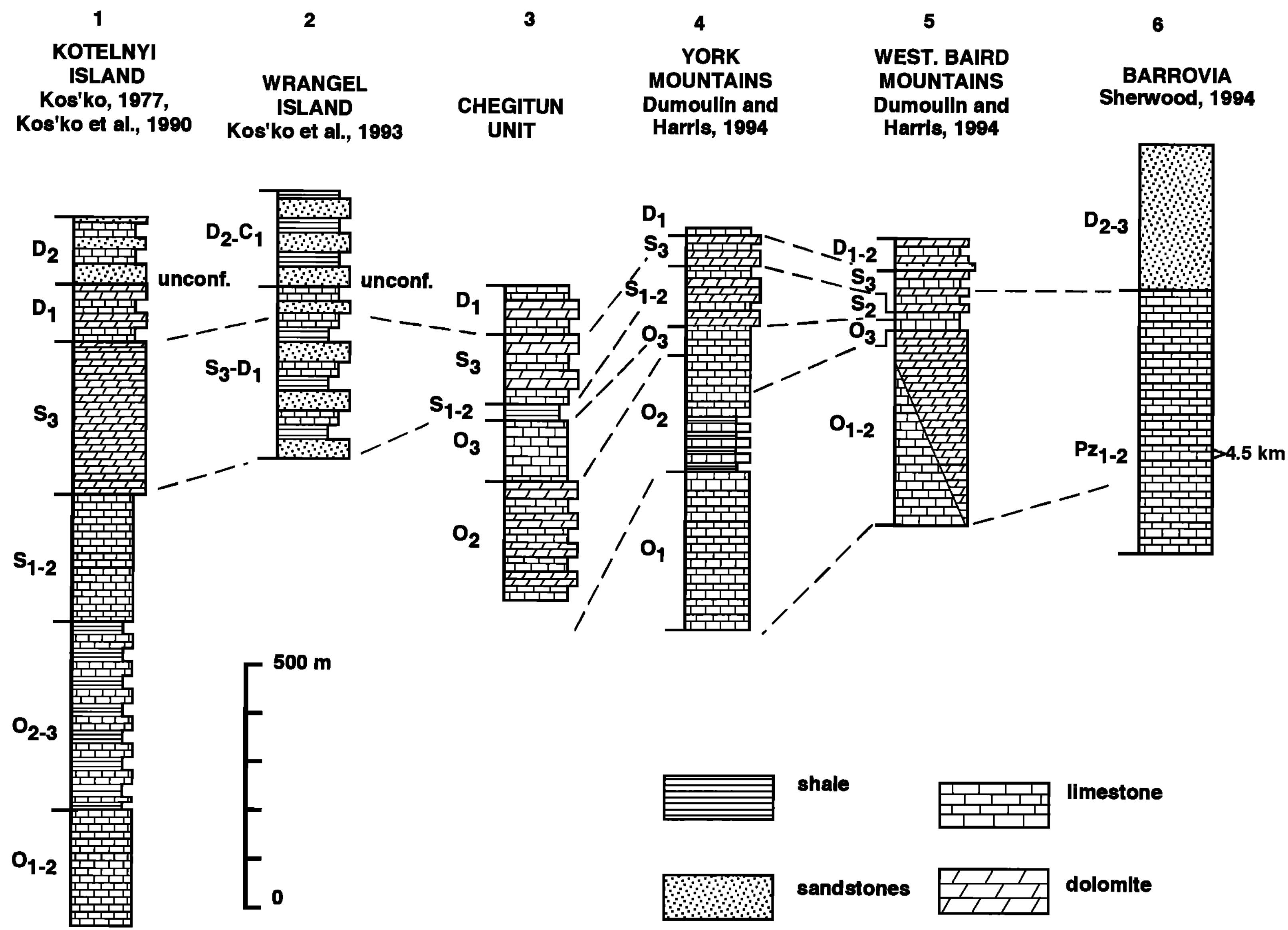

Figure 8. Stratigraphic correlation of lower and middle Paleozoic rocks of the Novosibirsk carbonate platform.

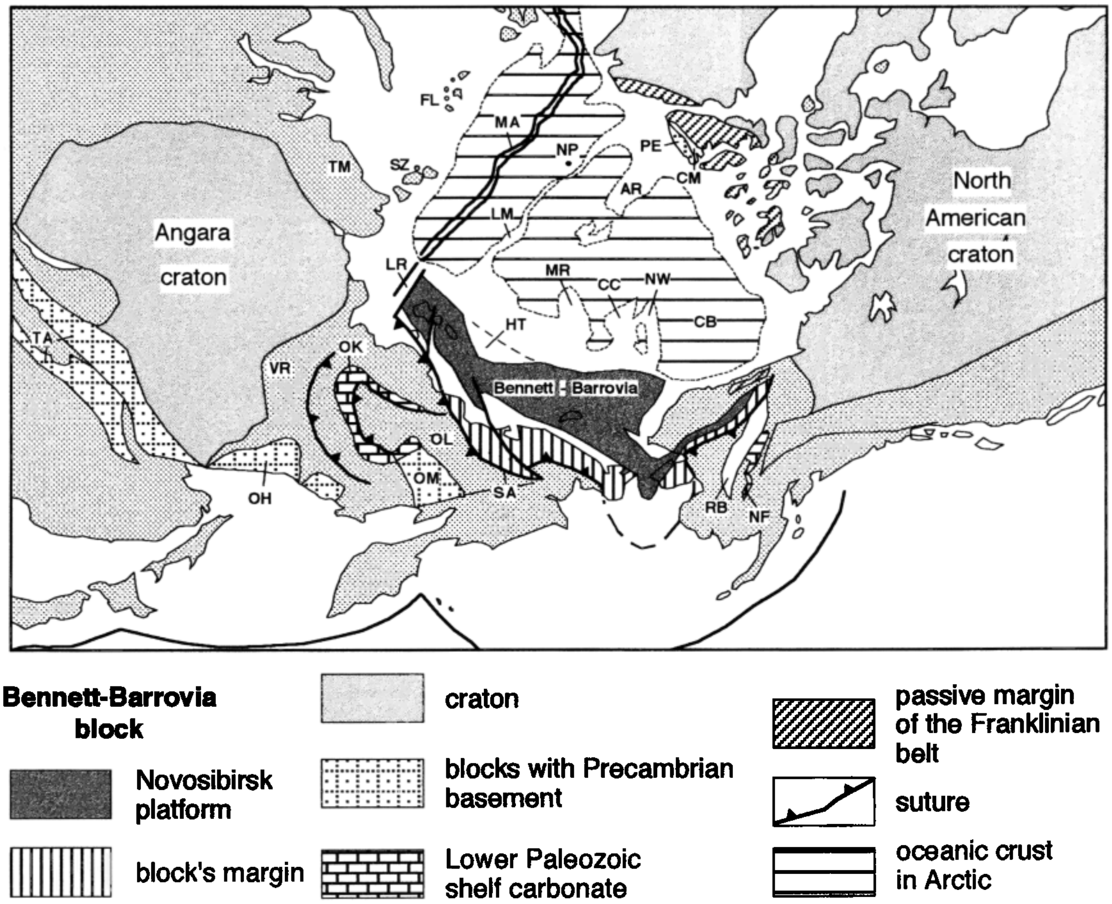

Figure 9. The Bennett-Barrovia block and tectonic units used in the paleotectonic reconstructions. Abbreviations are as follows: AR, Alpha Ridge; CB, Canada basin; CC, Chukchi Cap; CM, Clements Markham belt; FL, Franz Josef Land; HT, Henrietta fold belt; LM, Lomonosov ridge; LR, Laptev rift; MA, Arctic mid-ocean ridge; MR, Mendeleev Ridge; NF, Nixon Fork terrane; NP, North Pole, NW, Northwind Ridge; OH, Okhotsk massif; OK, Omulevka terrane; OL, Oloy zone; OM, Omolon massif; PE, Pearya terrane; RB, Ruby terrane; SA, South Anyui suture; SZ, Severnaya Zemlya; TA, Tuva-Mongol arc; TM, Taimyr; VR, Verkhoyansk passive continental margin.

[*Dumoulin and Harris*, 1994]. This change of facies is different than that of the previously described regions. The upper Upper Ordovician to Lower Devonian carbonate rocks are represented by shallow marine facies. The Middle to Upper Cambrian metalimestone have been described from this region. *Dumoulin and Harris* [1994] report that the Cambrian and the Ordovician to Lower Devonian rocks of the eastern Baird Mountains are similar to the rocks of the Snowden Mountain in the eastern part of the Hammond terrane.

Lower Paleozoic fauna from rocks of the Novosibirsk platform reveal a similarity with the Siberian fauna [*Tkachenko and Egiazarov*, 1970; *Oradovskaya and Obut*, 1977; *Krasny and Putintsev*, 1984; *Moore et al.*, 1994; *Till and Dumoulin*, 1994]. *Oradovskaya and Obut* [1997] emphasized a similarity of Chukotkan and Alaskan (Kuskokwim and Yukon-Porcupine regions (NF in Figure 9) and Seward Peninsula) Middle Ordovician brachiopods, Late Ordovician corrals, and Silurian graptolites. *Rozman* [1977] determined the Kolyma-Alaska region (Novosibirsk Islands, Chukotka and Seward Peninsula, Kuskokwim, and Yukon-Porcupine regions) as a unique one in northern Asia and North America for the Late Ordovician brachiopods. *Dumoulin and Harris* [1994, p.56] noted that "both 'Siberian' and 'North American' faunal affinities occur at different times and in different fossil groups within all of the (meta)carbonate successions" in northern Alaska making it likely that the Novosibirsk platform formed in a position between Siberia and North America.

In the northeastern corner of the Chukchi Sea (Barrovia in Figure 7), seismic reflection profiling revealed two [*Grantz et al.*, 1990] or three [*Sherwood*, 1994] subhorizontal pre-Mississippian seismostratigraphic units. There is a controversy in the age determination of these units. *Grantz et al.* [1990] infer, on the basis of seismic velocities and the character of the reflectors, that the lower unit is made up of Precambrian or Cambrian carbonate rocks and that the upper unit consists of Ordovician to Silurian clastic rocks. In contrast, *Sherwood* [1994] infers a Proterozoic (?) to Middle Devonian age for the carbonate unit and a Middle to Late Devonian age for the clastic rocks in which he recognized two units separated by a low-angle thrust. Both authors agree that the NW striking Barrow fault (BF in Figure 7) separates these units from strongly deformed and slightly metamorphosed Ordovician to Silurian argillite, phyllite, slate, chert, and graywacke in the basement of the Colville basin. Regardless of the age determination, both interpretations corroborate the idea of the Novosibirsk carbonate platform as the sedimentary cover of the Bennett-Barrovia block.

We consider the regions listed above in Russia, Seward Peninsula, and northern Alaska as part of the continuous Bennett-Barrovia block covered by the Novosibirsk carbonate platform (Figure 9). The original size of this block could have been much larger, as other exposures of similar rocks may also be a part of these tectonic units. For example, in Alaska the Nixon Fork terrane (Figure 9) consists of the Ordovician to Lower Devonian shallow marine carbonate, calcareous turbidite, and shale. Fossils from these rocks indicate a link to Siberia [*Dumoulin et al.*, 1998], and thus this terrane could also be a part of the Novosibirsk platform.

5.3. Middle Paleozoic Arc-Trench System

5.3.1. Magmatic arc. Devonian and lower Mississippian volcanic and plutonic rocks are found throughout the North American Cordillera, from California to northern Alaska [*Rubin et al.*, 1990]. These magmatic rocks and related basinal strata have been interpreted as remnants of an arc system developed near the edge of the Proterozoic craton on continental crust, transitional crust, or oceanic crust [*Dusel-Bacon and Aleinikoff*, 1985; *Dillon et al.*, 1987; *Rubin et al.*, 1990; *Plafker and Berg*, 1994]. Devonian plutonic rocks from both northern Alaska and Russia are briefly described here.

In northern and central Alaska, Devonian granites are widely scattered through the Hammond and Coldfoot subterranes (recently, parts of the Hammond subterrane where granites are exposed were assigned to the Coldfoot subterrane [*Moore et al.*, 1997a]) and on the Seward Peninsula [*Till and Dumoulin*, 1994; *Miller*, 1994] (Figure 7). A few granitic bodies of uncertain origin are known from the North Slope subterrane [*Moore et al.*, 1994]. Felsic to intermediate volcanic rocks in the eastern part of the Hammond terrane (Nutirwik Creek unit) yield the Early to Middle Devonian U-Pb zircon ages [*Moore et al.*, 1997b]. Middle Frasnian conodonts have been collected from the upper part of their section. Petrologic features of these rocks indicate a subduction-related origin of the rocks. Their age partly overlaps the age of the extension-related igneous rocks of the Hammond subterrane. Early to Middle Devonian granitoids (now orthogneiss) vary in composition from diorite to granite [*Moore et al.*, 1994]. They yield U-Pb ages of 398-383 Ma and reveal a subduction-related signature although mixing of some other magma type with partial melts from preexisting subduction-related rocks is possible [*Moore et al.*, 1997b]. Younger granitic rocks in the Coldfoot terrane are Late Devonian (discordant U-Pb zircon age is 366 Ma) [*Moore et al.*, 1994]. Their major element and isotopic composition indicates that these granites incorporated large components of continental crust [*Nelson et al.*, 1993]. Euhedral detrital zircons from quartzites in the Coldfoot subterrane varying in age from 370 to 360 Ma may have various igneous sources, and granite plutons are considered among the possible ones [*Moore et al.*, 1997a]. Orthogneiss on the Seward Peninsula yields a 381 Ma U-Pb zircon age [*Till and Dumoulin*, 1994].

In Chukotka the knowledge of the distribution of Devonian plutonic and volcanic rocks is limited by the scarcity of exposures of Paleozoic rocks and the lack of high-quality U-Pb geochronology. We have described the Devonian plutons in the core of the Koolen dome and the Devonian tuffs in the Tanatap unit. In the Cape Kiber area (KC in Figure 7), biotite granites intrude clastic rocks that are similar to the rocks bearing Middle Devonian fossils in the central and eastern parts of the uplift. Clasts of the same granites appear in the Lower Carboniferous conglomerate exposed nearby [*Cecile et al.*, 1991a]. A Rb-Sr whole rock age of the granites has been determined as 439 Ma (Early Silurian) with an initial Sr ratio of 0.7042 [*Tibilov et al.*, 1986]. Subsequent studies of the Cape Kiber granite [*Cecile et al.*, 1991a] questioned the Silurian age and recently a U-Pb zircon age has been determined at 360 Ma [L. Lane, personal communication, 1998]. Composition of the granite including REE data indicates that the granite is subduction-related. Small fault-bounded blocks of tuffs and lavas ranging in composition from basalt to dacite containing lenses of limestone with Lower Carboniferous (Visean) corals are exposed at the northern margin of the South Anyui suture (TP in Figure 7) [*Natal'in*, 1984].

We agree with the many authors [e.g., *Dusel-Bacon and Aleinikoff*, 1985; *Rubin et al.*, 1990; *Plafker and Berg*, 1994] who proposed that a Devonian, or in places Devonian to Early Carboniferous, active continental margin existed along the Proterozoic craton of North America and Alaska, and we suggest that this arc system can be extended into northeastern Russia. Some geologists believe that in Alaska the magmatic arc was active only during the Early to Middle Devonian and that it was succeeded in the Middle to Late Devonian by extension that led to the formation of the passive continental margin [*Moore et al.*, 1994, 1997b]. However, the ages of the subduction- and extension-related igneous rocks in the Hammond and Coldfoot subterranes overlap. If euhedral zircons of 370-360 Ma did have granitic sources [*Moore et al.*, 1997a], granitic intrusions and eruption of enriched MORB-type basalts in the same tectonic zone (rift/passive continental margin tectonic setting according to *Moore et al.* [1997a]) seems unlikely. Thus we infer that extension in northern Alaska could be a result of the back arc basin formation related to the Devonian arc. In Chukotka the magmatic arc stretches along the southern margin of the Bennett-Barrovia block. In Alaska the Coldfoot subterrane, in which the majority of the Devonian granites are exposed, is to the south of the Hammond subterrane, and one possible restoration of Mesozoic thrusting places it in the same position [*Moore et al.*, 1997b].

5.3.2. Back arc basin. In the Novosibirsk Islands the rocks of the Novosibirsk carbonate platform are bounded in the south by the Belkovskyi-Nerpalakh Trough (BN in Figure 7). The trough is filled with thick (8900 m) Upper Devonian to Lower Carboniferous limestone, shale, sandstone, and conglomerate that in the Devonian part of the sequence contain dikes and sills of low-potassium gabbro [*Tkachenko and Egiazarov*, 1970; *Vinogradov et al.*, 1974; *Volnov*, 1975]. The mafic intrusions are here interpreted as evidence for an extensional origin of the Belkovskyi-Nerpalakh Trough. The subsidence of the southern margin of the Novosibirsk platform began in the Silurian as evidenced from facies changes of shallow marine Lower Silurian carbonate rocks in the central and northern part of Kotel'nyi Island to the deep-water shales and limestones in the southwestern part of the island [*Kos'ko*, 1977]. Underlying Ordovician rocks do not reveal such changes. The Middle Devonian rocks include debris flow deposits and limestone conglomerate and breccia with local unconformities at the base of these rocks [*Kos'ko et al.*, 1990] that may also indicate tectonic activity related to the formation of the Belkovskyi-Nerpalakh Trough. In spite of the large distance from the Novosibirsk Islands, the Chegitun and the Tanatap units on the Chukotka Peninsula reveal similar ages, composition of rocks, and timing of events.

In the Alyarmaut uplift (AM in Figure 7), metaclastic rocks of amphibolite to greenschist facies are presumably of Devonian age, because they are conformably overlain by Lower Carboniferous metalimestones and black phyllites [*Tilman*, 1973]. These rocks contain actinolite schists [*Markov et al.*, 1980] formed from volcanic(?) rocks. In the Kuyul Uplift (KU in Figure 7), Lower to Middle Devonian rocks up to 1300 m thick are represented by siltstone and shale with minor limestone. Upper Devonian rocks (1200 m) consist of arkose and quartz sandstone [*Rogozov and Vasilyeva*, 1968]. Unconformably overlying these rocks are Lower Carboniferous (2500 m) arkose sandstone, black shale with abundant sulfides, siliceous and calcareous shale, dolomite, limestone, and conglomerate [*Markov et al.*, 1980]. These rocks are twice as thick as coeval rocks on Wrangel Island [*Kos'ko et al.*, 1993]. Exposures of Devonian to Lower Carboniferous rocks in the Alyarmaut and Kuyul uplifts in central and western Chukotka [*Drabkin*, 1970a; *Krasny and Putintsev*, 1984] are in an intermediate position between the Novosibirsk Island and Chukotka Peninsula and argue for former continuity between the Devonian Belkovskyi-Nerpalakh Trough and Tanatap basins.

In Alaska the tectonic equivalent of these basins may be an extensional basin filled with the Givetian(?) (late Middle Devonian) to Early Frasnian (early Upper Devonian) Beaucoup Formation and associated metasedimentary and metavolcanic rocks within the Hammond subterrane (Deitrich River phyllite in the eastern part of the subterrane) [*Moore et al.*, 1994, 1997b]. These rocks are intruded by sills, dikes, and stocks of metadiabase and gabbro. Composition and elemental abundance patterns of igneous rocks are similar to mafic magmatism in an extensional environment through lithosphere with a previous history of subduction magmatism [*Moore et al.*, 1997b]. Detailed studies in the eastern part of the Hammond subterrane have shown that the extension-related rocks occur as a series of thrust-bounded sheets emplaced from the south during the Brookian orogeny [*Moore et al.*, 1997a].

5.3.3. Fore arc region. It is not easy to discern a forearc region for the reconstructed middle Paleozoic magmatic arc in Chukotka and Alaska. All structures to the south of the arc were strongly reworked by Triassic rifting in Chukotka and by Jurassic-Early Cretaceous thrusting and mid-Cretaceous extensional deformation both in Chukotka and in Alaska. Amphibolite and ultramafic rocks have been reported in metamorphic rocks of the Senyavin Uplift of the Chukotka Peninsula (SE in Figure 7) [*Akinin*, 1995; *Calvert and Gans*, 1996]. The Rb-Sr isochron age of these rocks is 365 Ma [*Akinin*, 1995], but it is unclear whether this age reflects the protolith age or a subsequent metamorphic event. Devonian fossils have been found in the weakly metamorphosed limestone and shale of the Senyavin uplift [*Egiazarov and Dundo*, 1985], but their relationship with the ultramafic rocks occurring within the Senyavin metamorphic complex is uncertain. Ultramafic rocks also exist in the lower part of the Lavrentiya Series in the Koolen Lake region. From these data we infer that middle Paleozoic accretionary prism material is present in the metamorphic complexes of the Chukotka Peninsula [*Şengör and Natal'in*, 1996]. Lenticular bodies of Devonian or older mafic and ultramafic rocks of oceanic origin (metavolcanic rocks of NMORB and EMORB type) and a melange in the Coldfoot subterrane in northern Alaska [*Moore et al.*, 1997b] suggest that a part or all of the Coldfoot subterrane may have once composed a middle Paleozoic accretionary prism which was in front of the Devonian arc.

5.4. Chukotka Fold Belt

The Chukotka fold belt (Figures 1 and 7) is a zone of Triassic to Lower Jurassic passive continental margin deposits (Middle Triassic rocks are not confirmed paleontologically) deformed before the mid-Cretaceous during closure of the South Anyui suture [*Natal'in*, 1981, 1984; *Parfenov and Natal'in*, 1977, 1985; *Zonenshain et al.*, 1990]. Thick (5.5 km) Triassic to Lower Jurassic turbidites unconformably overlie the Devonian to Middle Carboniferous rocks exposed in the Kuyul and Alyarmaut uplifts [*Sadovsky*, 1965; *Tilman*, 1973; *Drabkin*, 1970a]. Upper Carboniferous and Permian rocks are almost completely absent. Numerous sills and dikes of gabbro and diabase and sparse lava flows occur among Lower to Middle(?) Triassic rocks. These magmatic rocks indicate a rifting event that can also be recognized along the northern boundary of the Siberian craton, within the Siberian craton itself, in Franz Josef Land, and in the Severnaya Zemlya Archipelago in the Arctic Ocean [*Gramberg and Pogrebitzkiy*, 1984; *Milanovsky*, 1987; *Zonenshain et al.*, 1990]. In the east the Chukotka fold belt terminates at the Kolyuchin-Mechigmen zone of the Chukotka Peninsula (Figures 2 and 7). In the west it narrows toward the Novosibirsk Islands (Figure 7) where Triassic argillite, sandstone, limestone, and basalt (in Lower Triassic part of the section) and Lower Jurassic mudstone, siltstone, and sandstone have been reported [*Tkachenko and Egiazarov;* 1970, *Kos'ko et al.*, 1990]. The Nutesyn zone (Figure 7), consisting of the Middle Jurassic to Neocomian basalt to dacite of island arc affinity, tuff, volcanoclastic sandstone, conglomerate, and shale, rests unconformably atop of the Triassic rocks at the southern margin of the central part of the Chukotka belt but does not continue to the west [*Natal'in*, 1981, 1984]. Similar volcanic rocks exist in the Late Jurassic to Early Cretaceous Rauchua Basin (Figure 7) and in small basins along the southern margin of the eastern part of the Chukotka belt. All these data allow the reconstruction of a Late Jurassic-Early Cretaceous magmatic arc along the southern margin of the eastern part of the Chukotka belt [*Natal'in*, 1981, 1984].

To our knowledge, an equivalent of this early Mesozoic turbidite (plus gabbro) succession of the Chukotka belt does not exist in northern Alaska. There the Carboniferous to Lower Cretaceous Ellesmerian sequence is continuous, and the thickness of Triassic rocks does not exceed 200 m [*Moore et al.*, 1994].

In Chukotka, Triassic rifting led to the formation of a passive continental margin along the southern side of the Bennett-Barrovia block and the opening of the South Anyui ocean. From the location of the middle Paleozoic arc-related rocks at the very boundary of the South-Anyui suture zone (TP in Figure 7) and the location where there is an apparent absence of arc/forearc tectonic zones in the Novosibirsk Islands sector (a back arc extensional basin exists there), we suggest that this rifting was oblique to the Paleozoic structures of the Bennett-Barrovia block and the middle Paleozoic arc-trench system and thus fragments of the arc-trench system could have been rifted away. In the present-day structure they may be presented on the opposite side of the South Anyui suture. Indeed, to the south of the suture within the Oloy zone (Figure 7), numerous fault-bounded fragments of Devonian to Middle Carboniferous arc-related magmatic rocks, Paleozoic ophiolite, and flysch occur among Mesozoic volcanic rocks [*Natal'in*, 1984; *Zonenshain et al.*, 1990]. Their Paleozoic fauna assemblages are similar to Siberian and Chukotkan fauna assemblages [*Krasny and Putintsev*, 1984] which fits a hypothesis of a local origin of these blocks. To the north of the Omulevka terrane, in the basement of the Primorsk Cenozoic basin (PR in Figure 7), continental blocks, island arc complexes, and ophiolites are inferred from geophysical data [*Litinsky and Raevsky*, 1977; *Spector et al.*, 1981]. The Chukotka passive continental margin collided with Siberia at the end of Neocomian time along the South Anyui suture [*Parfenov and Natal'in*, 1977; *Natal'in*, 1981, 1984; *Seslavinsky*, 1980].

6. Summary of the Paleozoic Tectonic History of Northeastern Russia and Northern Alaska

The Paleozoic tectonic evolution of the Late Proterozoic Bennett-Barrovia block in some respects resembles the tectonic evolution of the Arctida microcontinent outlined by *Zonenshain et al.* [1990]. They proposed that in the early Paleozoic, Arctida was separated from the Siberian craton. This is supported by the existence of a pre-Ordovician unconformity and Ordovician felsic volcanic rocks in the Severnaya Zemlya Archipelago [*Milanovsky*, 1987]. Alternatively, *Şengör and Natal'in* [1996] infer a Vendian (latest Precambrian) age of separation by linking it to the main rifting event between the Russian and Angara cratons.

Figure 10 shows the Late Ordovician position of the Bennett-Barrovia block with respect to the Angara craton, the North American craton, and the tectonic units of northeastern Russia. The shape of the Bennett-Barrovia block is corrected by restoration of Mesozoic left-lateral strike-slip faults in the Chukotka belt [*Sutygin and Tibilov*, 1969; *Parfenov and Natal'in*, 1985] and by unbending the Bering Strait orocline [*Patton and Tailleur*, 1977].

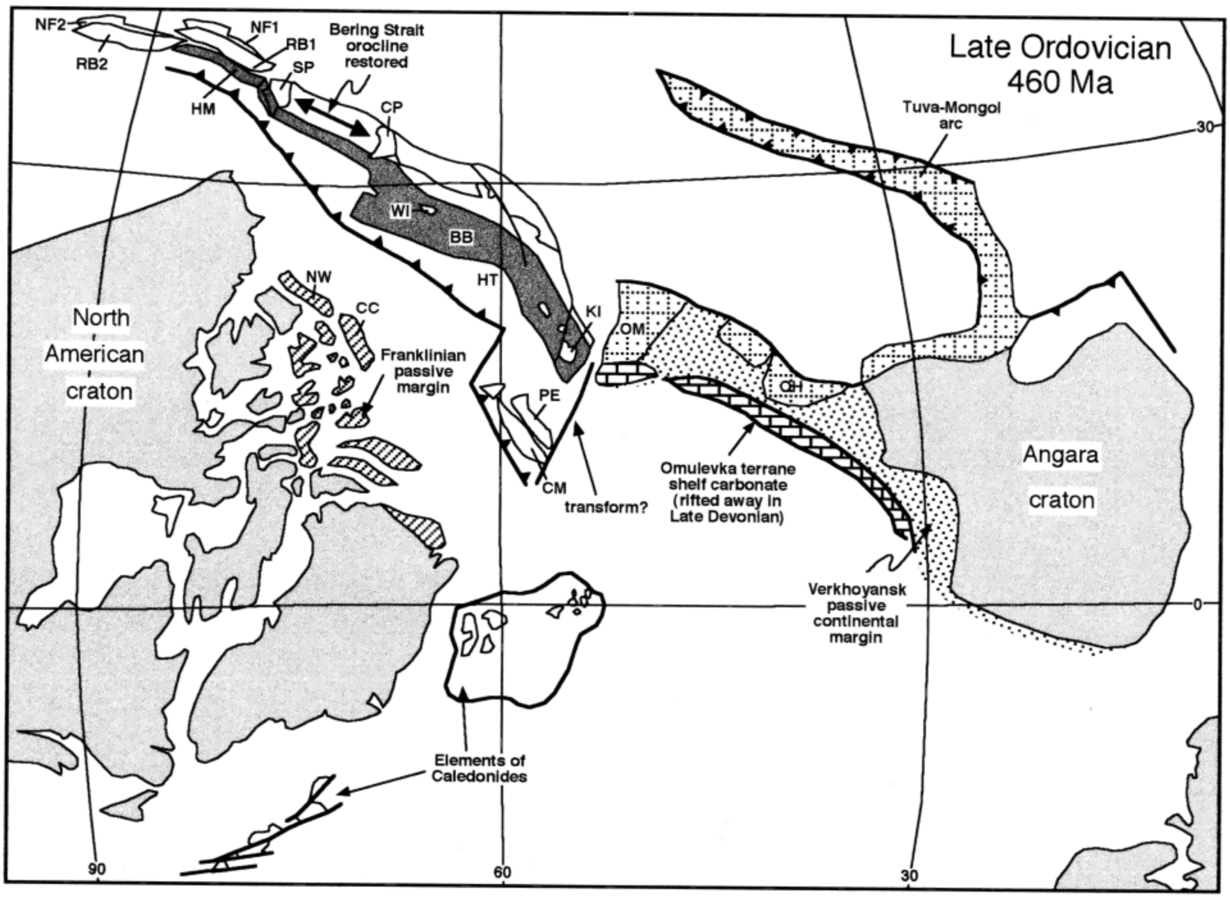

Figure 10. Late Ordovician paleotectonic reconstruction of the Bennett-Barrovia block. The positions of major continents are after *Lawver et al.* [1990]. The reconstruction of the Tuva-Mongol arc, Okhotsk, Omolon, and Omulevka terrane is after *Şengör and Natal'in* [1996]. Abbreviations are the same as those in Figure 9. Positions of the Chukchi Cap and Northwind Ridge are after *Grantz et al.* [1998]. BB - Bennett-Barrovia; CP - Chukotka Peninsula; WI -Wrangel Island.

There are no paleomagnetic data to constrain the position of the Bennett-Barrovia block. Our inference about its location is based on the following reasons.

1. Facies indicate that lower Paleozoic rocks of the block accumulated in a warm climate, and fossil assemblages are similar with the Omulevka terrane, Siberia, and North America.

2. The Omulevka terrane is characterized by Ordovician to Lower Carboniferous reefal limestone, shale, sandstone, and minor gypsum [*Zonenshain et al.*, 1990]. Thus it is reasonable to place the Bennett-Barrovia block either in front of the Omulevka terrane or as a continuation along strike. We have chosen the latter because it makes a simpler subsequent tectonic evolution (see below).

3. The Omulevka terrane was rifted away from the Verkhoyansk passive margin in the Late Devonian [*Parfenov and Natal'in*, 1985; *Zonenshain et al.*, 1990]. If we infer that the Bennett-Barrovia and Omulevka blocks were close to each other during the early Paleozoic and the beginning of the middle Paleozoic, the line of the rifting of the Omulevka terrane would be on the continuation of the Devonian extensional basin of the Bennett-Barrovia block.

4. The lower Paleozoic carbonate rocks of the Bennett-Barrovia block are similar to platformal carbonate successions within the Central Composite terrane, including the Ruby and Nixon Fork terranes [*Plafker and Berg*, 1994; *Moore et al.*, 1997a], which contains both Siberian and North American fossils [*Dumoulin et al.*, 1998]. Therefore we keep the western part (Ordovician paleocoordinates) of the Bennett-Barrovia block closer to North America.

The Ruby and Nixon Fork terranes could have two possible positions: (1) to the north of the Hammond and Coldfoot subterranes (NF1 and RB1 in Figure 10), from which these subterranes could be rifted away during the opening of the Angayucham ocean [*Patton et al.*, 1994, and references therein] or (2) on the continuation of the Hammond and Coldfoot terranes (NF2 and RB2 in Figure 10); from which these terranes could be strike-slipped along the dextral Proto-Tintina fault [*Grantz et al.*, 1991].

In the Late Silurian to Early Devonian the Bennett-Barrovia block collided with North America (Figures 11a and 11b). This collision led to the Ellesmerian orogeny of northern Alaska and the Canadian Arctic Islands. In Arctic Canada, episodes of compressional deformation related to the collision have been recorded until the Early Carboniferous [*Trettin*, 1991]. In northern Alaska, compressional deformation terminated by the Middle Devonian, and then it was followed by extensional deformation and the accumulation of clastic rocks [*Anderson et al.*, 1994; *Moore at al.*, 1994, 1997b]. However, in places (western Baird Mountains), shelf carbonate deposits persist from Silurian until Middle Devonian [*Dumoulin and Harris*, 1994]. Thus a part of the Bennett-Barrovia block in northern Alaska was not affected by the extensional deformation. Traces of the Ellesmerian orogeny may be detected on Wrangel Island by an unconformity at the base of the Middle to Upper Devonian unit and the drastic change in the composition of clasts in sandstones and conglomerates [*Kos'ko et al.*, 1993]. On Kotel'nyi Island, stable shelf sedimentation was succeeded, in places unconformably, by coarse-grained clastic rocks in the Middle Devonian [*Kos'ko et al.*, 1990]. No unconformities have been reported for Devonian sections of Chukotka [*Rogozov and Vasilyeva*, 1968; *Drabkin*, 1970a; *Markov et al.*, 1980; *Nedomolkin*, 1977]. All of this may be interpreted as evidence that the effect of the Ellesmerian orogeny in the Chukotkan part of the Bennett-Barrovia block diminished away from the zone of Ellesmerian collision.

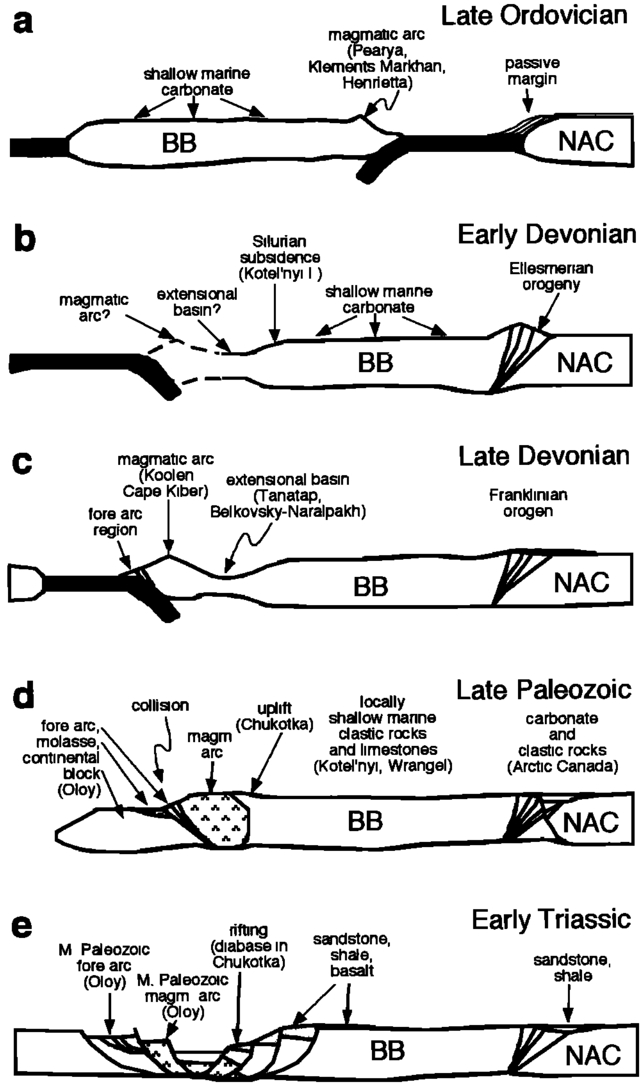

Figure 11. Tectonic evolution of Chukotkan sector of the Bennett-Barrovia block: (a) The Bennett-Barrovia block is separated by an ocean from North America. The early Paleozoic subduction beneath the Bennett-Barrovia block created magmatic arcs (Canadian Arctic Islands, Henrietta belt, northern Alaska). (b) The collision of the Bennett-Barrovia block and North America led to the Elesmerian orogeny in Alaska and the Canadian Arctic Islands. The arc-trench system originated along the southern (present-day coordinates) margin of the Bennett-Barrovia block. (c) The Devonian to Early Carboniferous evolution of the arc-trench system. (d) The collision of an uknown continental object and the Bennett-Barrovia block. (e) The Early Triassic rifting and the origination of the South-Anyui ocean. Slivers of the middle Paleozoic arc-trench system and the continental object were rifted away. See text for discussion. BB, Bennett-Barrovia; NAC, North American craton.

After collision of the Bennett-Barrovia block with North America, the middle Paleozoic arc-trench system and the exten-

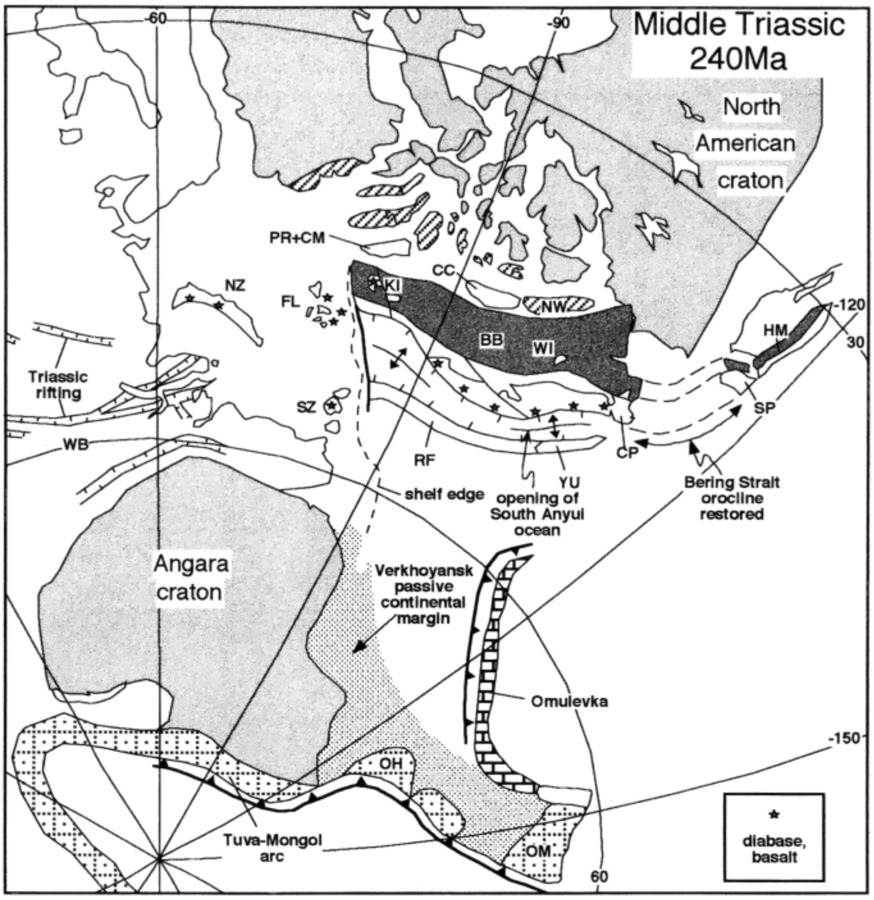

Figure 12. Early Triassic paleotectonic reconstruction of the Bennett-Barrovia block. The positions of major continents after *Lawver et al.* [1990]. The reconstruction of the Tuva-Mongol arc, Okhotsk, Omolon, and Omulevka terrane is after *Şengör and Natal'in* [1996]. Triassic rift zones in the Western Siberian basin (WB) are after *Zonenshain et al.* [1990]. HM, Hammond and Coldfoot subterranes; KI, Kotel'nyi Island; RF, rifted fragments of the fore-arc region of the middle Paleozoic arc-trench system of the Bennett-Barrovia block and unknown continental block collided with it; SP, Seward Peninsula. See Figures 9 and 10 for other abbreviations.

sional basin were established along the opposite side the Bennett-Barrovia block (Figure 11c). The overlap of ages of the magmatic arc and the extensional basin allow the inference that the extensional basin formed as a back arc basin.

In Alaska, arc magmatism started in the Early Devonian. In Chukotka, dated granitic plutons are Late Devonian and Early Carboniferous, but the extensional (back arc) basin is Eifelian (Middle Devonian) or older. In the Kuyul Uplift the stratigraphic succession of the extensional basin includes the Lower Devonian clastic rocks. The Belkovskyi-Nerpalakh Trough (Figure 11c) formed in the early Late Devonian (Frasnian). Visean andesites near the contact of the Chukotka fold belt and South Anyui suture (TP in Figure 7) and Lower Carboniferous clastic rocks and turbidites in the Belkovskyi-Nerpalakh Trough and Tanatap basin suggest that the arc-trench system was still active during the Early Carboniferous.

In Arctic Alaska, Devonian magmatism and extensional basin formation ended with the establishment of a passive margin which lasted from the Late Devonian to the Early Cretaceous. In turn, this passive margin sedimentation ended with the closure of the Angayucham ocean and the onset of the Brookian orogeny. However, the sudden appearance of the enigmatic Nuka Land [*Moore et al.*, 1994] during the Early/Middle Carboniferous in the very southern part of the margin does not fit a model of the stable development of the passive margin facing the Angayucham ocean. In contrast, in the Chukotka segment of the southern margin of the Bennett-Barrovia block, an unknown continental object collided with the magmatic arc in the Middle to Late Carboniferous (Figure 11d).

The following lines of evidence can be used to show that the evolution of the active continental margin at the southern boundary of the Bennett-Barrovia block in Chukotka ended in the Middle to Late Carboniferous time: (1) There are no Middle Carboniferous to Permian rocks in the Chukotka fold belt except presumably Permian shale, coaly shale, and sandstone [*Drabkin*, 1970a] which indicate the existence there of an uplifted area for ~70 Ma. (2) There is an unconformity at the base of the Middle Carboniferous clastic rocks, including conglomerate and limestone breccia and sparse felsic lavas, on Kotel'nyi Island [*Vinogradov et al.*, 1974; *Kos'ko et al.*, 1990]. (3) There is an unconformity at the base of the 200 m thick Permian marine shale predominant section on Kotel'nyi Island and ~150 km to the south on the Bolshoy Lyakhovsky Island (Figure 7); Permian rocks are 1200 m thick and represented by sandstones with coal seams and phyllite [*Kos'ko et al.*, 1990; *Fujita and Cook*, 1990]. Thus the late Paleozoic uplift and formation of continental basins followed the middle Paleozoic active margin development along the southern edge of the Bennett-Barrovia block. The process that was responsible for these events is not well understood, but the collision of a continental mass is a viable hypothesis.

The object which deformed the Devonian arc is inferred to have been removed, together with slivers of the forearc region, during Early-Middle Triassic rifting (Figures 11e and 12). This rifting could have transferred both the continental mass in question and the forearc region of the Devonian active continental margin to the Asian side of the South Anyui suture. Immediately to the south of the suture within the Yarakvaam Uplift (YU, Figure 7), Devonian and Lower Carboniferous andesites and rhyolites are intruded by granite and diorite and unconformably overlain by Upper Carboniferous shallow marine and terrestrial tuffaceous sandstone and conglomerate [*Markov et al.*, 1980; *Natal'in*, 1984]. The first unit may be considered as a rifted fragment of the middle Paleozoic active margin of the Bennett-Barrovia. We interpret the late Paleozoic granites and molasse deposits of the second unit as evidence for the collision. Farther to the south, there are fragments of Paleozoic oceanic rocks, island arc volcanic rocks, and ophiolites which may belong to the aforementioned continental mass and its margin.

Triassic rifting led to the formation of the South Anyui ocean and the Triassic to Early Jurassic passive continental margin of the Bennett-Barrovia block (Figure 12). Note that this zone of rifting lies on the continuation of rifts in the basement of the Western Siberia Basin [e.g., *Zonenshain et al.*, 1990]. Triassic diabase and gabbro in Severnaya Zemlya, Franz Josef Land, and Novaya Zemlya show a link between these two regions. During the Late Jurassic, fragments rifted from the margin of the Bennett-Barrovia block (RF in Figure 12) collided with the Omulevka terrane, leading to the oroclinal bending of the Omulevka terrane [*Şengör and Natal'in*, 1996].

7. Conclusions

The Paleozoic Chegitun and Tanatap units from the study area formed in different tectonic settings. Both units were strongly deformed in the Mesozoic, and their relations with the larger tectonic units and history were reconstructed on the basis of sedimentological and stratigraphic data and regional correlation. The Ordovician to Lower Devonian shallow marine carbonates of the Chegitun unit belong to the Novosibirsk carbonate platform that covers the Precambrian basement of the Bennett-Barrovia block [*Şengör and Natal'in*, 1996]. This unit underlies the Chukchi shelf and the East Siberian Sea and continues into northern Alaska as the Hammond subterrane. The Devonian to Lower Carboniferous deep-water sedimentary rocks of the Tanatap unit formed in an extensional basin most likely behind a Devonian magmatic arc. After being separated from Siberia in the Vendian or in the early Paleozoic, the Bennett-Barrovia block collided with North America during Late Silurian to Early Devonian time and caused the Ellesmerian orogeny. Devonian granites in northeastern Brooks Range and near the Barrow Arch may be related to this collision. In the late Paleozoic an unknown continental object collided with the southern side of the Chukotkan Bennett-Barrovia block. Triassic rifting truncated the southern portion of the Bennett-Barrovia block. In the Mesozoic this block evolved as a part of the Chukotka-Arctic Alaska microplate.

Similarity of Paleozoic stratigraphy and timing of events in the vast area between the Novosibirsk Islands and the Hammond subterrane in Alaska defines the unity of this tectonic province and imposes constraints on the geometry and shape of the Chukotka-Arctic Alaska block. Several models for the opening of the Canada Basin have been proposed [see *Lawver and Scotese*, 1990]. *Fujita and Newberry* [1982] were the first to notice that the Chukotka-Arctic Alaska block is too long to fit against the margin of the Canadian Arctic Islands as is assumed in the rotational model. To solve this space problem, they diminished the size of the Chukotkan sector of the block, placing the western boundary of the Chukotka-Arctic Alaska block across the Chukotka fold belt. The same solution of the problem is typical for all rotational models of the Chukotka-Arctic Alaska block [*Tailleur and Brosge*, 1970; *Newman et al.*, 1977; *Rowley and Lottes*, 1988; *Grantz et al.*, 1990]. The basis of such a solution lies either in the lack of adequate knowledge of the geology of northeastern Russia or in the inference that the South Anyui suture abruptly changes in strike to N-S beyond its last exposure in western Chukotka [e.g., *Rowley and Lottes*, 1988]. Magnetic anomalies which mark the suture and the continuation of the Jurassic to Early Cretaceous magmatic arc which is paired with the suture and stretches to the Svaytoy Nos Cape area (SN in Figure 1), do not allow this last solution [*Natal'in*, 1981, 1984; *Parfenov and Natal'in*, 1985; *Zonenshain et al.*, 1990]. Our correlation of the Paleozoic structures corroborates the real dimensions of the Chukotka-Arctic Alaska block and shows that the rotational model still has a significant space problem.

Acknowledgments. The work was funded by the Continental Dynamics Division of the National Science Foundation, International Division of the National Science Foundation, as part of award EAR-93170087-005 to E. Miller and S. Klemperer, and EAR-9316573 to J. E. Wright, as well as TÜBİTAK-İTÜ joint research unit GloTec. Amato acknowledges the support of the Albert and Alice Weeks Foundation at the U. of Wisconsin and C. Johnson for the use of his laboratory. We are grateful to E. Miller, S. Akinin, A. Calvert, L. Gahagan, K. Fujita, M. Gelman, A. Grantz, A. Kaplan, L. Lane, L. Lawver, and L. Popeko for discussions of different aspects of the geology of Alaska and Chukotka. E. Miller and C. Şengör read the first version of the paper and their constructive remarks improved the final version. The paper was considerably improved owing to comments and suggestions of A. B. Till, T. E. Moore, and W. K. Wallace. We are also grateful to many people from the towns of Lavrentiya and Provideniya who helped us during the fieldwork.

References

Akinin, V. V., Metaultramafites of the crystalline basement of the Chukchi Peninsula, in *1994 Proceedings: International Conference on Arctic Margins*, edited by K.V. Simakov and D. K. Thurston, pp. 214-219, N. East. Inst. of Sci. Res., Magadan, 1995.

Amato, J. M., and J. E. Wright, Geochronologic investigations of magmatism and metamorphism within the Kigluaik Mountains gneiss dome, Seward Peninsula, Alaska, in *Short Notes on Alaskan Geology 1997*, edited by J. G. Clough and F. Larson, Alaska Div. Geol. Geophys. Surv., Prof. Rep. *118*, 1-21, 1998.

Amato, J. M., J. E. Wright, P. B. Gans, and E. L. Miller, Magmatically induced metamorphism and deformation in the Kigluaik gneiss dome, Seward Peninsula, Alaska, *Tectonics*, *13*, 515-527, 1994.

Anderson, A. V., W. K. Wallace, and C. G Mull, Depositional record of a major tectonic transition in northern Alaska: Middle Devonian to Mississippian rift-basin margin deposits, upper Kongakut River region, eastern Brooks Range, Alaska, in *International Conference on Arctic Margins Proccedings,* edited by D. K. Thurston, and K. Fujita, pp. 71-76, Miner. Manag. Serv., Anchorage, Alaska, 1994.

Anders, E., and M. Ebihara, Solar-system abundances of the elements, *Geochim. et Cosmochim. Acta, 46,* 2363-2380, 1982.

Barron, E. J., Ancient climates: investigation with climate models, *Rep. Prog. Phys., 47,* 1563-1599, 1984.

Belyi, V. F., K voprosy o zhestkoy strukture Vostochnoy Chukotki i Alyaski (On a problem of the rigid structure in eastern Chukotka and Alaska), in *Materialy po Geologii i Poleznym Iskopaemym Severo-Vostoka SSSR, 17,* pp. 40-48, Magadan, 1964.

Bering Strait Geological Field Party (BSGFP), Koolen metamorphic complex, NE Russia: Implications for the tectonic evolution of the Bering Strait region, *Tectonics, 16,* 713-729, 1997.

Bjørnerud, M. G., and D. C. Bradley, Silurian foredeep and accretionary prism in Northern Ellesmere Island: Implication for the nature of the Ellesmerian orogeny, in *International Conference on Arctic Margins Proccedings,* edited by D. K. Thurston, and K. Fujita, pp. 129-134, Miner. Manag. Serv., Anchorage, Alaska, 1994.

Bunker, C. M., C. E. Hedge, and C. L. Sainsbury, Radioelement concentrations and preliminary radiometric ages of rocks of the Kigluaik Mountains, Seward Peninsula, Alaska, *U.S. Geol. Surv. Prof. Pap., 1129-C,* 11 pp., 1979.

Calvert, A. T., and P. B. Gans, Jurassic(?) kyanite-grade metamorphism and earliest Cretaceous exhumation of the Senyavin complex, Chukchi Peninsula, NE Russia, *EoS Trans. AGU, 77,* (46), Fall Meet. Suppl., F767, 1996.

Cecile, M. P., Y. M. Buchkov, O. N. Vinogradova, M. E. Gorodinsky, M. K. Kos'ko, and L. S. Lane, Rezultaty polevykh rabot Sovetsko-Kanadskoy gruppy na Severo-Vostoke SSSR letom 1989 goda (Results of field works of the Soviet-Canadian group in northeastern USSR in summer 1989), in *Geologiya Skladchatogo Obramleniya Ameraziyskogo Subbasseyna,* pp. 15-21, NPO Sevmorgeologiya, VNIIOkeangeologiya, St. Petersburg, 1991a.

Cecile, M. P., J. C. Harrison, M. K. Kos'ko, and R. Parrish, Precambrian U-Pb ages of igneous rocks, Wrangel Island Complex, Wrangel Island, U.S.S.R., *Can. J. Earth Sci., 28,* 1340-1348, 1991b.

Cumming, G. L., and J. R. Richards, Ore lead isotope ratios in a continuously changing Earth, *Earth Planet.Sci. Lett., 28,* 155-171, 1975.

Dilles, J. H., and J. E. Wright, The chronology of early Mesozoic arc magmatism in the Yerington District of western Nevada and its regional implications, *Geol. Soc. Am. Bull., 100,* 644-652, 1988.

Dillon, J. T., G. R. Tilton, J., Decker, and M. J. Kelly, Resource implications of magmatic and metamorphic ages for Devonian igneous rocks in the Brooks Range: in *Alaskan North Slope Geology, Field Trip Guideb.* vol. 50, edited by I. L. Tailleur, and P. Weimer, pp. 713-723, Pac. Sec., Soc. of Econ. Paleontol. and Mineral., Bakersfield, Calif., 1987.

Drabkin, I. E. (Ed), Geologiya SSSR (Geology of the USSR. Vol. XXX) Severovostok SSSR: Geologicheskoe opisanie (Northeastern USSR: Geological Description.), book 1, 548 pp., Nedra, Moscow, 1970a.

Drabkin, I. E. (Ed), Geologiya SSSR (Geology of the USSR. Vol. XXX) Severovostok SSSR: Geologicheskoe opisanie (Northeastern USSR: Geological Description.), book 2, 548 pp., Nedra, Moscow, 1970b.

Dumoulin, J. S., and A. G. Harris, Depositional framework and regional correlation of Pre-Carboniferous metacarbonate rocks of the Snowden Mountain area, central Brooks Range, northern Alaska, *U.S. Geol. Surv. Prof. Pap., 1545,* 73 pp., 1994.

Dumoulin, J. S., D. C. Bradley, A. G. Harris, and J. E.Repetski, Sedimentology, conodont biostratigraphy, and subsidence history of the Nixon Fork terrane, Medfra quadrangle, Alaska, paper presented at III International Conference on Arctic Margins, Deutsche Forschungsgemeinschaft (DFG), Celle, Germany, 12-16, Oct. 1998.

Dusel-Bacon, C., and J. N. Aleinikoff, Petrology and tectonic significance of augen gneiss from a belt of Mississippian granitoids in the Yukon-Tanana terrane, east-central Alaska, *Geol. Soc. Am. Bull., 96,* 411-425, 1985.

Dutro, J. T., Jr., A. R. Palmer, J. E. Repetski, and W. P. Brosgé, Middle Cambrian fossils from the Doonerak anticlinorium. central Brooks Range, Alaska, *J. Paleontol., 58,* 1364-1371, 1984.

Eardley, A. J., Ancient Arctica, *J. Geol., 56,* 409-436, 1948.

Egiazarov, B. K., and O. P. Dundo, (Eds.), *Geologiya Beringova Morya i Prilegayuschikh Kontinentalnykh Okrain (Geology of the Bering Sea and Adjacent Continent Margins),* 127 pp., Nedra, Leningrad, 1985.

Ewart, A., The mineralogy and petrology of Tertiary-Recent orogenic volcanic rocks: With special reference to the andesitic-basaltic compositional range, in *Andesites: Orogenic Andesites and Related Rocks,* edited by R. S. Thorpe, pp. 26-87, John Wiley, New York, 1982.

Fujita, K., and D.B. Cook, The Arctic continental margin of eastern Siberia, in *Geology of North America,* v. L, *The Arctic Ocean Region,* edited by A. Grantz, L. Johnson, and J. F. Sweeney, pp. 289-304, Geol. Soc. of Am., Boulder, Colo., 1990.

Fujita, K., and J.T. Newberry, Tectonic evolution of northeastern Siberia and adjacent regions, *Tectonophysics, 89* , 337-357, 1982.

Gelman, M. L., Osnovnye osobennosti posleproterozoyskogo metamorphizma na severo-vostoke SSSR (Main feature of the post-Proterozoic metamorphism in northeastern USSR), in *Metamorficheskie Kompleksy Vostoka SSSR,* pp. 161-180, DVNT, Vladivostok, 1973.

Gill, J. B., *Orogenic Andesites and Plate Tectonics,* Springer-Verlag, New York, 1981.

Gnibidenko, G. S., *Metamorphicheskie Kompleksy v Strukturakh Severo-Zapadnogo Sektora Tikhookeanskogo Poyasa (Metamorphic Complexes in Structures of the Northwestern Sector of the Circum-Pacific Belt),* 135 pp., Nauka, Moscow, 1969.

Gorodinsky, M. E. (Ed.), Geologicheskaya karta severo-vostoka SSSR (Geological map of northeastern USSR), scale 1:1,500,000, 9 Sheets, Minist. Geol. SSSR, Leningrad, Russia, 1980.

Gramberg, I. S., and Y. E. Pogrebitzkiy, (Eds), *Morya sovetskoy Arktiki (Seas of the Soviet Arctic),* v. 9, 280 pp., Nedra, Leningrad, Russia, 1984.

Grantz, A., S. D. May, and P. E. Hart , Geology of Arctic continental margin of Alaska, in *Geology of North America,* v. L, *The Arctic Ocean Region,* edited by A. Grantz, L. Johnson, and J. F. Sweeney, pp. 257-288, Geol. Soc. of Am., Boulder, Colo., 1990.

Grantz, A., T. E. Moore, and S. M. Roeske, Continent-ocean transect A-3: Gulf of Alaska to Arctic Ocean, *Geol. Soc. Am. Centen Continent/Ocean Transect, 15,* 72 pp., 1991.

Grantz, A., D. L. Clark, R. L. Phillips, and S. P. Srivastava, Phanerozoic stratigraphy of Northwind Ridge, magnetic anomalies in the Canada basin, and geometry and timing of rifting in the Amerasia basin, Arctic Ocean, *Geol. Soc. Am. Bull., 100* , 801-820, 1998.

Ivanov, O. N., and Y. V. Kryukov, Dokembriy vostochnogo sektora Sovietskoy Arktiki, *Geol. Geofiz. 9* , 50-59, 1973.

Klaper, E. M., The Paleozoic tectonic evolution of the northern edge of North America: A structural study of northern Ellesmere Island, Canadian Arctic Archipelago, *Tectonics, 11,* 854-870, 1992.

Kos'ko, M. K., Struktumo-formatsionnaya zonalnost ordovik-srednedevonskogo karbonatnogo kompleksa ovov Anzhu (Structural and formation zonation of the Ordovician to Middle Devonian carbonate complex of the Anzhu islands), in *Tektonika Arktiki: Skladchatyy Fundament Shelfovykh Sedimentatsionnykh Basseynov,* edited by Y. E. Pogrebitskiy and M. K. Kos'ko, pp. 55-85, Nauchno-Issled. Inst. Geol. Arktiki, Leningrad, Russia, 1977.

Kos'ko, M. L., Major tectonic interpretation and constraints for the East Siberian Seas, Northeastern Russia, in *International Conference on Arctic Margins Proccedings,* edited by D. K. Thurston, and K. Fujita, pp. 195-200, Miner. Manag. Serv., Anchorage, Alaska, 1994.

Kos'ko, M. K., B. G. Lopatin, and V. G. Ganelin, Major geological features of the islands of the East Siberian and Chukchi seas and northern cost of Chukotka, *Mari. Geol., 93,* 349-367, 1990.

Kos'ko, M. K., M. P. Cecile, J. C. Harrison, V. G. Ganelin, N. V. Khandoshko, and B. G. Lopatin, Geology of Wrangel Island, between Chukchi and East Siberian seas, northeastern Russia, *Bull. Geol. Surv. Can., 461,* 101 pp., 1993.

Krasny, L. I., and V. K. Putintsev (Eds.), *Vostok SSSR. Tom 8 (Eastern part of the USSR, vol.8),* 560 pp., Nedra, Leningrad, Russia, 1984.

Krough, T. E., A low-contamination method for hydrothermal decomposition of zircon and extraction of U and Pb for isotopic age determinations, *Geochim. Cosmochim. Acta, 37,* 485-494, 1973.

Lawver, L. A., C. R. Scotese, A review of tectonic models for the evolution of the Canada Basin, in *Geology of North America,* v. L, *The Arctic Ocean Region,* edited by A. Grantz, L. Johnson, and J. F. Sweeney, pp. 593-618, Geol. Soc. of Am., Boulder, Colo., 1990.

Lawver, L. A., R. D. Müller, S. P. Srivastava, and W. Roest, The opening of the Arctic Ocean, in *Geologic History of the Polar Oceans: Arctic Versus Antarctic,* edited by U. Bleil and J. Thiede, pp. 29-62, Kluwer Academic Publishers, Netherlands., 1990.

Litinsky, V. A., and S. S. Raevsky, Struktura fundamenta Primorskoy nizmennosti i prilegayuschey territorii i akvatorii po geofizicheskim dannym (Geophysical data on structure of the basement of the Primrosk lowland id neighboring areas), in *Tektonika Arktiki: Skladchatyi Fundament Sedimentatzionnykh Bassejnov,* edited by Y. E. Pogrebitzkiy and M. K. Kos'ko, pp. 98-121, Nauchno-Issled. Inst. Geol. Arktiki, Leningrad, Russia, 1977.

Markov, M. S., Y. M. Pushcharovsky, S. M. Tilman, V. S. Fedorovsky, and N. A. Shilo, *Tektonika Kontinentalnykh Okrain Severo-Zapada Tikhogo Okeana (Tectonics of the Continental Margins of the North-West Pacific),* 285 pp., Nauka, Moscow, 1980.

Mattinson, J. M., U-Pb ages of zircon: A basic examination of error propagation, *Chem. Geol., 66,* 151-162, 1987.

Milanovsky, E. E., *Geologiya SSSR, chast 1, Vvedenie: Drevnie Platformy i Meetaplatformennye Oblasti (Geology of the USSR, Part 1, Introduction: Ancient Platforms and Metaplatform Regions),* 415 pp, Izdatelstvo Moskovskogo Univ., Moscow, 1987.

Miller, T. P., Pre-Cenozoic plutonic rocks in mainland Alaska, in *The Geology of North America,* vol. G1, *The Geology of Alaska,* edited by G. Plafker and H. C. Berg, pp. 535-554, Geol. Soc. of Am., Boulder, Colo., 1994.

Moore, T. E., W. K. Wallace, K. J. Bird, S. M. Karl, C. G. Mull, and J. T. Dillon, Geology of northern Alaska, in *The Geology of North America,* vol. G1, *The Geology of Alaska,* edited by G. Plafker and H. C. Berg, pp. 535-554, Geol. Soc. of Am., Boulder, Colo., 1994.

Moore, T. E., J. N. Aleinikoff, and A. G. Harris, Stratigraphic and structural implications of conodont and detrital zircon U-Pb ages from the metamorphic rocks of the Coldfoot terrane, Brooks Range, Alaska, *J. Geophys. Res., 102,* 20,797-20,820, 1997a.

Moore, T. E., W. K. Wallace, C. G. Mull, K. E. Adams, G. Plafker, and W. J. Nokleberg, Crustal implications of bedrock geology along the Trans-Alaska Crustal Transect in the Brooks Range, northern Alaska, *J. Geophys. Res., 102,* 20,645-20,684, 1997b.

Muir, R. J., T.R. Ireland, S. D. Weaver, and J. D. Bradshaw, Ion microprobe dating of Paleozoic granitoids: Devonian magmatism in New Zealand and correlations with Australia and Antarctica, *Chem. Geol., 127,* 191-210, 1996.

Natal'in, B. A., Tektonicheskaya priroda metamorphicheskogo kompleksa Chukotskogo poluostrova (Tectonic nature of the metamorphic complex in Chukotka Peninsula). *Geol. Geof., 6,* 31-38, 1979.

Natal'in, B. A., Mezozoyskie aktivnye kontinentalnye okrainy v Yuzhno-Anyuiskoy skladchatoy sisteme (Mesozoic active continental margins in the South Anyui fold belt), in *Drevnie zony Benioffa,* edited by G. M. Vlasov, pp. 78-109, Dalnevostochnyi Nauchnyi Tsentr Akademii Nauk SSSR, Vladivostok, Russia, 1981.

Natal'in, B. A., *Rannemezozoiskie Skladchatye Sistemy Severnoy Chasti Tikhookeanskogo Obramleniya (Early Mesozoic Folded Belts in the North Part of the Pacific Rim),* Nauka, Moscow, 135 pp., 1984.

Natal'in, B. A., J. Toro, and J. Amato, Paleozoic rocks of northern Chukotka Peninsula, their structural history and relevance to the Mesozoic tectonic evolution of the Arctic, *EoS Trans. AGU, 78(46)*, Fall Meet. Suppl., F665, 1997.

Nedomolkin, V. F., Chegitun, in Gosudarstvennaya Geologicheskaya Karta SSSR (The state geological map of the USSR), scale 1:200,000, sheet Q-2-VII,VII,IX), Minist. Geol., Leningrad, Russia, 1969.

Nedomolkin, V. F., Geologiya Eskimosskogo sredinnogo massiva (Geology of the Eskimos median massif). avtorferat kandidatskoy dissertatsii, 16 pp., Far East Sci. Center Acad. Sci. USSR, Vladivostok, 1977.

Nelson, B. K., S. W. Nelson, and A. B. Till, Nd- and Sr-isotope evidence for Proterozoic and Paleozoic crustal evolution in the Brooks Range, northern Alaska, *J. Geol., 101,* 435-450, 1993.

Newman, G. W., C. G. Mull, and N. D. Watkins, Northern Alaska paleomagnetism, plate rotation, and tectonics, in *The Relationship of Plate Tectonics to Alaskan Geology and Resources: Proceedings of the Sixth Alaska Geological Society Symposium,* edited by A. Sisson, pp. C1-C7, Alaska Geol. Soc., Anchorage, 1977.

Oradovskaya, M. M., and A. M. Obut, Stratigrafiya, korrelyatsiya i paleogeografiya ordovikskikh i siluriyskikh otlozheniy na Chukotskom poluostrove (Stratigraphy, correlation, and paleogeography of the Ordovician and Silurian strata in Chukotka Peninsula), in *Stratigrafiya i Fauna Ordovika i Silura Chukotskogo Poluostrova,* edited by A. M. Obut, pp. 4-42, Nauka, Novosibirsk, Russia, 1977.

Parfenov, L.M., and B.A. Natal'in, Tektonicheskaya evolyutsiya Dalnego Vostoka v mezozoe i kainozoe (Tectonic evolution of north-eastern Asia in the Mesozoic and Cenozoic). *Dok. Acad. Nauk SSSR, 235,* (5), 1132-1135, 1977.

Parfenov, L. M., and B. A. Natal'in, Mesozoic accretion and collision tectonics of northeastern Asia, in *Tectonostratigraphic Terranes of the Circum-Pacific Region,* vol. 1, edited by D. G. Howell, pp. 363-373, Circum-Pac. Counc. for Energy and Miner. Resour., Houston, Tex., 1985.

Patton, W. W., Jr., and I. L. Tailleur, Evidence in the Bering Strait region for differential movement between North America and Eurasia, *Geol. Soc. Am. Bull ., 88,* 1298-1304, 1977.

Patton, W. W., Jr., S. E. Box, E. J. Moll-Stalcup, and Miller, T. P., Geology of west-central Alaska, in *The Geology of North America,* vol. G1, *The Geology of Alaska,* edited by G. Plafker and H. C. Berg, pp. 153-204, Geol. Soc. of Am., Boulder, Colo., 1994.

Plafker, G., and H. C. Berg, Overview of the geology and tectonic evolution of Alaska, in *The Geology of North America,* vol. G1, *The Geology of Alaska,* edited by G. Plafker and H. C. Berg, pp. 989-1022, Geol. Soc. of Am., Boulder, Colo., 1994.

Rejebian, V. A., A. G. Harris, and J. S. Huebner, Conodont color and textural alteration: An index to regional metamorphism, contact metamorphism, and hydrothermal alteration, *Geol. Soc. Am. Bull., 99* 471-479, 1987.

Rogozov, U. G., and N. M. Vasilyeva, Devonskie otlozheniya poberezhya proliva Longa (Devonian rocks of the De Long Strait coast), *Uch. Zap. Naucho-Issled. Inst. Geol. Arktiki, Leningrad, 13,* 51-157, 1968.

Rowley, D. B., and A. L. Lottes, Plate-kinematic reconstructions of the North Atlantic and Arctic: Late Cretaceous to present, *Tectonophysics, 155,* 73-120, 1988.

Rozman, K. S., *Biostratigrafiya i Zoogeografiya Verkhnego Ordovika Severnoy Azii i Severnoy Ameriki (po brakhiopodam) (Stratigraphy and biogeography of the Upper Ordovician of northern Asia and North America (brachiopods)),* 169 pp., Nauka, Moscow, 1977.

Rubin, C. M., M. M. Miller, and G. M. Smith, Tectonic development of Cordilleran mid-Paleozoic volcano-plutonic complexes: Evidence for convergent margin tectonism, *Spec. Pap.Geol. Soc. Am., 255,* 1-16, 1990.

Sadovsky, A. I., Istoriya geologicheskogo razvitiya i tektonicheskoe stroenie Anyuyskogo megasinkliniriya (Geological history and tectonic structure of the Anyui anticlinorium). *Sov. Geol., 3* , 59-73, 1965.

Şengör, A. M. C., and B. A. Natal'in, Palaeotectonics of Asia: fragments of a synthesis, in *The Tectonic Evolution of Asia,* edited by A. Yin and M. Harrison, pp. 486-640, Cambridge Univ. Press, New York, 1996.

Seslavinsky, K. B., Yuzhno-Anyuyskaya sutura (South-Anyui suture), *Dokl. Akad. Nauk SSSR, 249* (5), 1181-1185, 1980.

Shatsky, N. S., O tektonike Arktiki (On tectonics of Arctic), in *Geologiya i Poleznye Iskopaemye Severa SSSR,* Trudy pervoy geologo-razvedochnoy konferentsii Glavsevmorputi, vol. 1, pp. 3-28, Geologiya, Leningrad, Russia, 1935.

Sherwood, K. W., Stratigraphy, structure, and origin of the Franklinian, Northeast Chukchi Basin, Arctic Alaska plate, in *International Conference on Arctic Margins Proccedings,* edited by D. K. Thurston, and K. Fujita, pp. 245-250, Miner. Manag. Serv., Anchorage, Alaska, 1994.

Shuldiner, V. I., and V. F. Nedomolkin, Kristallicheskiy fundament Eskimosskogo massiva (Crystalline basement of the Eskimos massif), *Sov. Geol., 10,* 38-47, 1976.

Spector, V. B., A. M. Andrusenko, E. A. Dudko, and N. F. Kareva, Prodolzhenie Yuzhno-Anyuiskoy sutury v Primorskoy nizmennosti (Continuation of the South Anyui suture in the Primorsk lowland), *Dokl. Akad. Nauk SSSR, 260* (6), 1447-1450, 1981.

Sutygin, G. N., and I. V. Tibilov, Glubinnye sdvigi Tzentralnoy Chukotki i nekotorye voprosy metallogenii (Deep-seated strike-slip faults in central Chukotka and problems of metallogeny), in *Mezozoyskiy Tektogenez,* pp. 100-101, Sov. Tek. Sibiri i Dal. Vostoka, Magadan, Russia, 1969.

Tailleur, I. L., Probable rift origin of Canada Basin, Arctic Ocean, in *Arctic Geology,* edited by M. G. Pitcher, *AAPG Mem., 19,* 252-258, 1973.

Tailleur I. L., and W. P. Brosge, Tectonic history of Alaska, in *Proceedings of the Geological Seminar on the North Slope of Alaska,* edited by W. L. Adkison and W. P. Brosge, E1-E19, AAPG, Los Angeles, 1970.

Tibilov, I. B., A. P. Milov, and I. A. Davydov, O proyavlenii domezozoyskogo granitoidnogo magmatizma na Chukotke (On the appearance of the pre-Mesozoic granitoid magmatism in Chukotka), *Tikhookean. Geol., 4,* 95-98, 1986.

Till, A. B., and J. A. Dumoulin, Geology of Seward Peninsula and Saint Lawrence Island, in *The Geology of North America,* vol. G1, *The Geology of Alaska,* edited by G. Plafker and H. C. Berg, pp. 141-152, Geol. Soc. of Am., Boulder, Colo., 1994.

Tilman, S. M., *Sravnitelnaya Tektonika Mesozoid Severa Tikhookeanskogo Koltsa (Comparative tectonics of the Mesozoides of the Northern Part of the Pacific Rim),* 326 pp., Nauka, Novosibirsk, Russia, 1973.

Tkachenko, B. V., and Egiazarov, B. X. (Eds), *Geologiya SSSR Ostrova Sovetskoy Arktiki: Geologicheskoe opisanie (Geology of the USSR),* vol. XXVI, *(Islands of the Soviet Arctic: Geological descriptions),* 547 pp., Nedra, Moscow, 1970.

Toro, J., Structure and thermochronology of the metamorphic core of the central Brooks Range, Alaska, Ph.D. thesis, 200 pp., Stanford Univ., Stanford, Calif., 1998.

Trettin, H. P., The Proterozoic to Late Silurian record of Pearya, in *The Geology of North America,* vol. E,*Geology of the Innuitian Orogen and Arctic Platform of Canada and Greenland,* edited by H. P. Trettin, pp. 241-259, Geol. Soc. of Am., Boulder, Colo., 1991.

Vinogradov, V. A., G. I. Gaponenko, I. M. Rusakov, and V. N. Shimarayev, *Tektonika Vostochno-Arkticheskogo Shelfa SSSR (Tectonics of the eastern part of the Arctic shelf of the USSR),* 144 pp., Nedra, Leningrad, Russia, 1974.

Vinogradov, V. A., G. I. Kameneva, and G. P. Yavshits, O Giperboreyskoy platforme v svete novyh dannyh o geologicheskom stroenii o-va Genrietty (On the Hyperborean Platform in light of new data on the geologic structure of Henrietta Island), *Tektoni. Arktiki, 1,* 21-25, 1975.

Volnov, D. A., Istoriya geologicheskogo razvitiya Novosibirskikh ostrovov (History of the geological evolution of the Novosibirsk Islands), in Geologia i Poleznye Iskopaemye Novosibirskikh Ostrovov i Ostrova Vrangeya, edited by D. A.. Volnov and V. L. Ivanov, pp. 61-71, Nauchno-Issled. Inst. Geol. Arktiki, Leningrad, Russia, 1975.

Wright, J. E., and M. R. Fahan, An expanded view of Jurassic orogenesis in the western United States Cordillera: Middle Jurassic (pre-Nevadan) regional metamorphism and thrust faulting within an active arc environment, Klamath Mountains, California, *Geol. Soc. Am. Bull., 100,* 859-876, 1988.

Zonenshain, L. P., M. I. Kuzmin, and L. M. Natapov, *Geology of the USSR: A plate tectonic synthesis,* 242 pp., *AGU Geodynamic Series, 21,* 1990.

J. M. Amato, Department of Geological Sciences/3AB, New Mexico State University, P.O. Box 30001, Las Cruces, NM 88003. (amato@nmsu.edu)

B. A. Natal'in, Istanbul Technical University, İ.T.Ü. Maden Fakültesi, Genel Jeoloji ABD, Ayazaga 80626, Istanbul, Turkey. (natalin@itu.edu.tr)

J. Toro, Department of Geology and Geography, West Virginia University, Morgantown, WV 26506-6300. (toro@geo.wvu.edu)

J. E. Wright, Department of Geology and Geophysics, Rice University, MS-126, Houston, TX 77005. (jwright@owlnet.rice.edu)

(Received March 18, 1999;
revised June 28, 1999;
accepted July 21, 1999)

TECTONICS, VOL. 18, NO. 6, PAGES 929-949 DECEMBER 1999

The tectonic evolution of the Kohistan-Karakoram collision belt along the Karakoram Highway transect, north Pakistan

M.P. Searle, M. Asif Khan,[1] J.E. Fraser, and S.J. Gough

Department of Earth Sciences, Oxford University, Oxford England, United Kingdom

M. Qasim Jan

Center for Excellence in Geology, Peshawar University, Peshawar, North-West Frontier Province, Pakistan

Abstract. The Kohistan arc terrane comprises an intra-oceanic island arc of Cretaceous age separating the Indian plate to the south from the Karakoram (Asian) plate to the north within the Indus suture zone of north Pakistan. The intra-oceanic arc volcanics (Chalt, Dras Group) were built on a foundation of dominantly mid-ocean ridge basalt (MORB)-related amphibolites of the Kamila Group. The subarc magma chamber is represented by multiple intrusions of a huge gabbro-norite complex (Chilas complex), which includes some ultramafic assemblages of residual mantle harzburgite and dunite, layered cumulates, and hornblendites cut by late stage dikes of hornblende + plagioclase pegmatites. The Chilas complex norites intrude the Gilgit metasediments of lower amphibolite and greenschist facies in northern Kohistan, which also form xenolithic roof pendants within the top of the Chilas complex. Along the southern margin of Kohistan, Jijal and Sapat complex ultramafics (dunites, harzburgites and websterites) form remnant suprasubduction zone ophiolitic mantle rocks along the hanging wall of the Main Mantle Thrust, the Cretaceous obduction plane along which Kohistan was emplaced onto Indian plate rocks. Garnet granulites of the Jijal complex, formed at 12-14 kbars, represent original magmatic lower crustal rocks subducted to depths of at least 45 km and metamorphosed during high-pressure and high-temperature subduction of earlier arc-related rocks. Obduction of the Sapat ophiolite and Kohistan arc occurred between ~75 and 55 Ma.

The closure of the Shyok suture zone separating Kohistan from the Karakoram plate must have occurred prior to 75 Ma, the age of the Jutal basic dikes which crosscut the closure-related fabrics, mainly late north directed backthrusting in the lower Hunza valley. Andean-type granitoid (gabbro-diorite-granodiorite-granite) emplacement along the Kohistan-Ladakh batholith ended at the time of India-Asia collision, ~ 60-50 Myr ago. Postcollisional crustal thickening along the Karakoram led to multiple episodes of metamorphism from latest Cretaceous and throughout the Tertiary. Sillimanite grade metamorphism in Hunza was actually pre-India-Asia collision and may have resulted from the earlier Kohistan collision. Localized and sporadic crustal melting episodes across northern Kohistan (Indus confluence and Parri granite sheets) and the southern Karakoram (Hunza dikes and Sumayar and Mango Gusar leucogranites) occurred from 51 to 9 Ma and culminated in the huge Baltoro monzogranite-leucogranite intrusion 25-21 Myr ago. A vast network of leucogranitic and pegmatitite dikes containing gem quality aquamarine + muscovite ± tourmaline ± garnet ± biotite quartz are younger than 5 Ma and form the final phase of intrusion in the Haramosh area and parts of the southern Karakoram area.

1. Introduction

The Kohistan arc terrane in north Pakistan is widely regarded as one of the most complete exposed sections from the deep root to the volcanic edifice of an island arc [*Tahirkheli et al.*, 1979; *Tahirkheli*, 1982; *Bard*, 1983; *Coward et al.*, 1987; *Kazmi and Jan*, 1997]. The Kohistan arc has been trapped within the Tethyan suture zones (Shyok suture to the north and Indus suture to the south) between India and Asia during the Himalayan collision (Figure 1). The Kohistan arc has been deformed, tilted to the north, uplifted, and eroded following collision, providing an informative window into the deeper levels of the arc crust [*Tahirkheli and Jan*, 1979; *Searle and Asif Khan*, 1996]. Not only is the Kohistan arc superbly well exposed from base to top, but it also reveals the magmatic and structural evolution of the arc from an intra-oceanic, Marianas-type arc system to an evolved Andean-type magmatic arc following accretion to the Asian (=Karakoram terrane) plate to the north [*Coward et al.*, 1987; *Khan et al.*, 1989, 1993; *Treloar et al.*, 1996].

The Karakoram terrane in north Pakistan is equivalent to the Lhasa Block of south Tibet, and together they formed the southern margin of the Asian plate prior to the collision of first Kohistan during the Late Cretaceous and then India after the early Eocene. Although the Karakoram and the Tibetan plateau have a similar average elevation of around 5.2 km above mean sea level (Msl), the geological exposures are very different [*Searle*, 1991]. Tibet is a high, relatively flat uplifted plateau which has not been deeply eroded and only reveals upper crustal sediments and volcanics, whereas the

[1]Now at Center for Excellence in Geology, Peshawar University, Peshawar, North-West Frontier Province, Pakistan

Paper number 1999TC900042.
0278-7407/99/1999TC900042$12.00

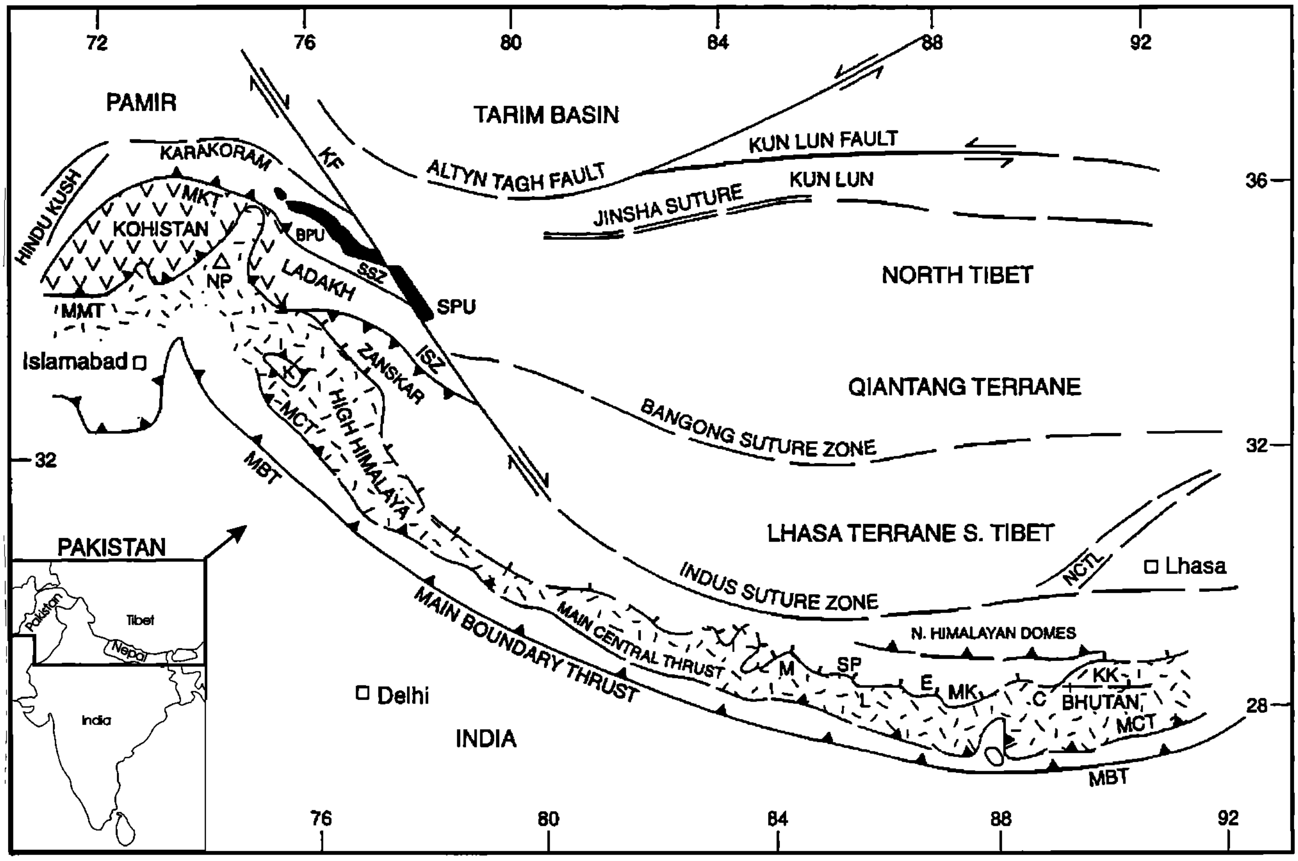

Figure 1. Map of the Himalaya, Karakoram, and Tibet regions, showing major faults, suture zones, and terranes. KF, Karakoram Fault; ISZ, Indus suture zone; MMT, Main Mantle Thrust; MCT, Main Central Thrust; MBT, Main Boundary Thrust. Himalayan sectors are abbreviated as follows: NP, Nanga Parbat; K, Kashmir; A, Annapurna; M, Manaslu; SP, Shisha Pangma; E, Everest; C, Chomolhari; KK, Khula Kangri. SPU is the Siachen plutonic unit offset equivalent of the Baltoro plutonic unit (BPU). SSZ is the Shyok suture zone and MKT is the Main Karakoram Thrust. Inset shows the location of the western Himalaya in south Asia. MKT, Main Karakoram Thrust; NCTL, Nyenchen Tanggla range; ISZ, Indus suture zone.

Karakoram has large topographic differences (7000-8700 m mountain tops to 2500-3000 m valleys) and has suffered enormous amounts of deformation and erosion (up to 35 km of erosion since 35 Myr ago; [*Searle*, 1991; *Searle and Tirrul*, 1991]. Collision processes affecting the deep crust of Asia therefore cannot be studied in the surface geology of Tibet but can be well studied and documented in the Karakoram.

The Karakoram Highway (KKH) from Rawalpindi in Pakistan to Kashgar in Xinjiang is one of only three roads which cross the entire Himalayan belt from the Indian foreland to the Lhasa Block (the others being the Friendship Highway from Kathmandu to Lhasa and the Darjeeling-Sikkim to Tibet road) and the only one which crosses the entire Karakoram mountains. The KKH traverses the western Himalaya, the Kohistan arc terrane, and the Hunza Karakoram and is surely the most spectacular section across the youngest and highest orogenic belt on Earth. The KKH follows the Indus river north to its confluence with the Gilgit river then ascends the Gilgit and Hunza valleys to the Khunjerab pass, the main continental divide (Figure 2).

A large volume of new field structural data combined with geochemistry, isotope chemistry, and geochronology from Kohistan and the Karakoram has emerged in the last 10 years, and we attempt here to compile this new data and use it to propose a tectonic evolutionary model for the Kohistan arc in a strict sense and the collision process, both in the Kohistan arc terrane and in the Karakoram Asian terrane. This paper reviews the geology of the section through Kohistan and the Hunza Karakoram along the KKH route [*Tahirkheli and Jan*, 1979; *Searle and Asif Khan*, 1996] and attempts to correlate the timings of metamorphism, magmatism, and structural history of the India - Kohistan arc - Karakoram collision belt. Figure 3 is a Late Cretaceous - Tertiary time chart which plots all the reliable geochronological data for the Pakistan Himalaya, Kohistan, and Karakoram (both Hunza and Baltoro regions) terranes, as well as our inferred timings of deformation (D1, D2, etc.) and metamorphism (M1, M2, etc.). The Himalayan terrane south of Kohistan is not included in this review, but readers are referred to *Treloar et al.* [1989,a,b,c], *DiPietro* [1991], *DiPietro et al.* [1993] and *Kazmi and Jan* [1997], and references therein, for details of the Pakistani Himalaya.

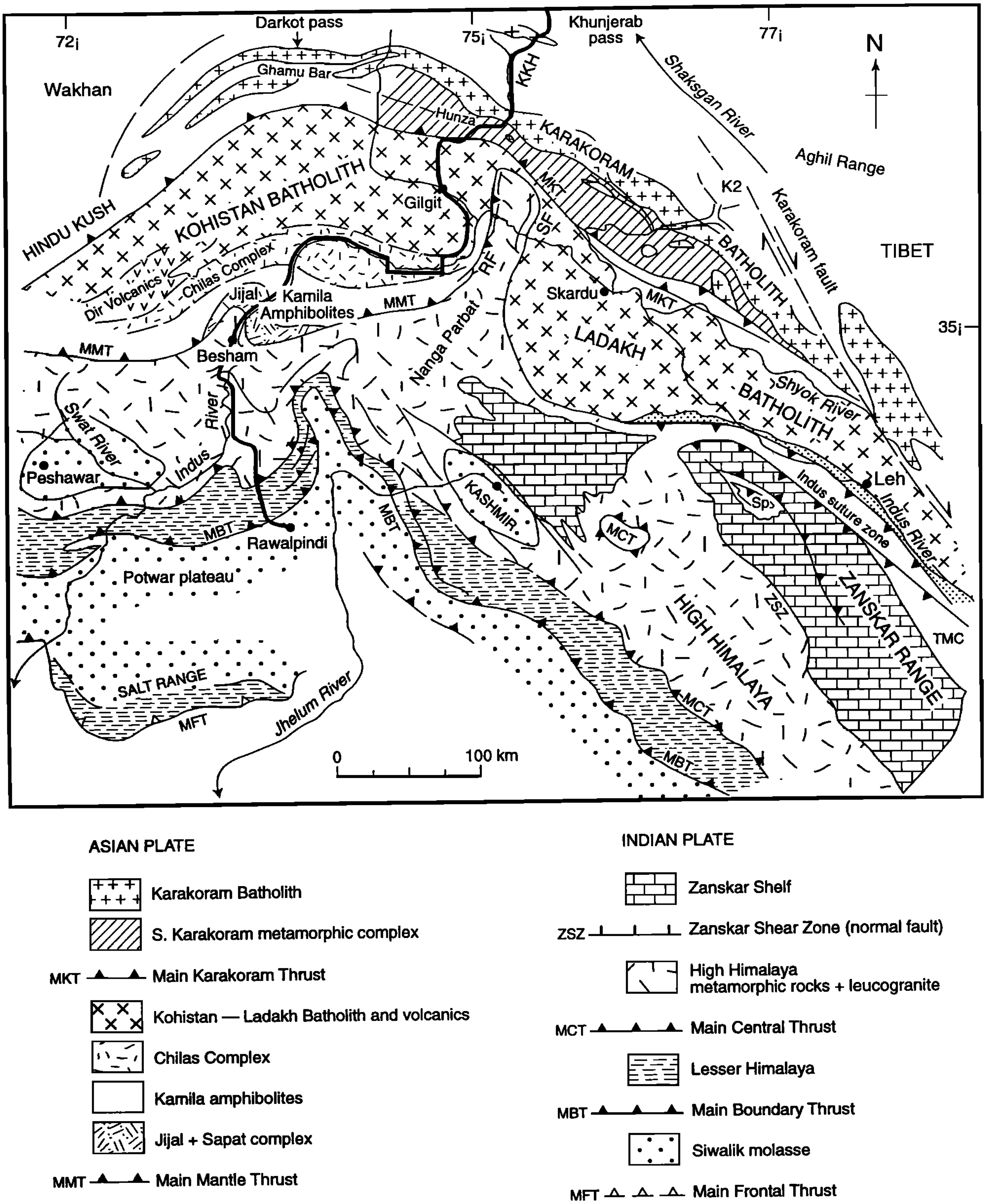

Figure 2. Geological map of the western Himalaya, Kohistan, and Karakoram. SF, Stak Fault; RF, Raikot Fault; Sp, Spontang ophiolite in Ladakh; TMC, Tso Morari complex; ZSZ, Zanskar shear zone; MCT, Main Central Thrust; MBT, Main Boundary Thrust; MFT, Main Frontal Thrust. Thick line shows the route of the Karakoram Highway (KKH).

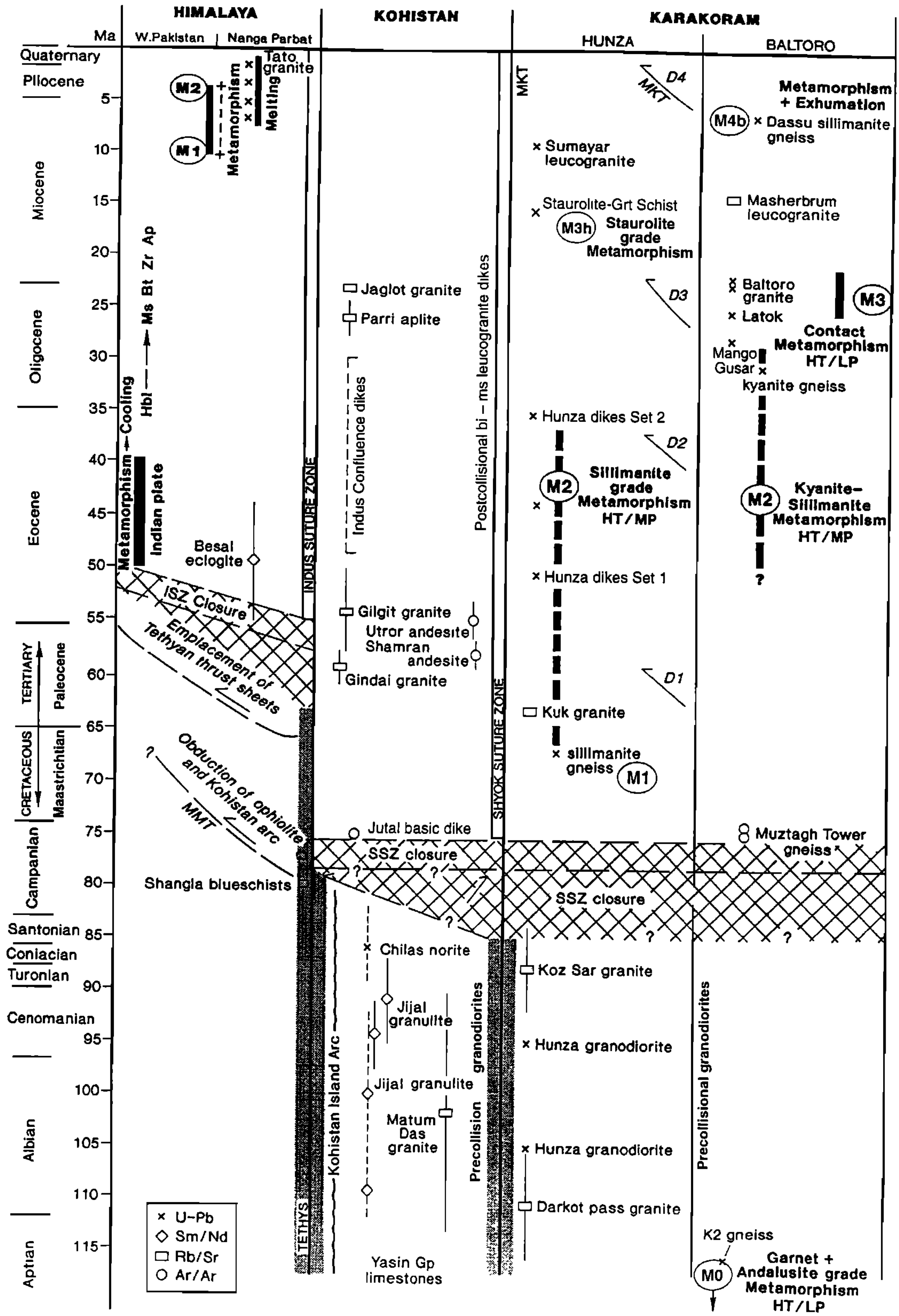

Figure 3. Cretaceous-Tertiary time chart showing all reliable radiometric ages for the Pakistan Himalaya including Nanga Parbat, Kohistan, and the Hunza and Baltoro Karakoram. Sources of data for Nanga Parbat are *Zeitler* [1985], *Zeitler and Chamberlain* [1991], *Zeitler et al.* [1993], *Smith et al.* [1992, 1994], and *Winslow et al.* [1996]; sources of data for the Shangla blueschists within the MMT zone: are *Maluski and Matte* [1984], and *Anczkiewicz et al.* [1998]; Sources of data for the Pakistan Himalaya are *Treloar et al.* [1989a], and *Treloar and Rex* [1990]; Sources of data for Kohistan are *Zeitler and Chamberlain* [1991], *Petterson and Windley* [1985], *Treloar et al.* [1989a], *George et al.* [1995], *Tonarini et al.* [1993], and *Yamamoto and Nakamura* [1996]; sources of data for the Hunza Karakoram are *LeFort et al.* [1983], *Debon* [1995], and *Fraser et al.* [1999]; and sources of data for the Baltoro Karakoram are *Searle et al.* [1989, 1990a], *Parrish and Tirrul* [1989], *Searle and Tirrul* [1991], *Searle* [1991, 1996] and *Fraser et al.* [1999].

2. Tectonic Overview

The India-Asia collision which resulted in the Himalaya and the uplifted plateau of Tibet is complicated in the western part of the orogen by the large Kohistan arc-microplate which has been trapped within the suture zone between India and Asia (Figures 1 and 2). The intra-oceanic Kohistan island arc was a Cretaceous volcanic arc within Tethys which first collided with Asia along the Shyok suture zone (SSZ) during the latest Cretaceous and later collided with India along the Indus suture zone (ISZ), or Main Mantle Thrust (MMT) as it is called in Pakistan, during the early to mid-Eocene [*Searle et al.*, 1987]. The Kohistan arc terrane evolved from an intra-oceanic volcanic arc into an Andean-type magmatic arc, dominated by intrusion of large-scale granodioritic magmas with time following collision with Asia [*Petterson and Windley*, 1985, 1991]. The Kohistan arc is widest and best developed in north Pakistan, but it does continue east into Ladakh (India) where the arc is known as the Dras volcanic arc [*Searle et al.*, 1988; *Reuber*, 1989]. It dies out rapidly to the east and is not present at all to the east of western Ladakh (Figure 1).

The crustal structure of the Asian plate margin is also very different along the strike of the orogen. Prior to collision of Kohistan, the southern margin of Asia included the Karakoram terrane in the west and the Lhasa Block to the east. The precollisional geology of both the Karakoram and Tibet was dominated by subaerial redbed sedimentation, calc-alkaline volcanism and intrusion of long linear calc-alkaline batholiths, similar to the Andes [*Searle et al.*, 1989]. The postcollisional structure, however, is very different. Tibet forms an uplifted plateau where middle and deep crustal rocks are never seen at the surface. The Karakoram is dominantly composed of mid crustal and deep crustal metamorphic rocks, migmatites, and crustal melt leucogranites which show up to 35 km of exhumation since 35 Myr ago [*Searle*, 1991; *Searle et al.*, 1992]. *Searle and Tirrul* [1991] proposed four major phases of metamorphism and deformation in the southern Karakoram, an early (?Jurassic - Early Cretaceous) precollisional M1 associated with widespread granodiorite intrusions, the major postcollision M2 regional Barrovian-type metamorphism, and a younger M3 contact metamorphic aureole around the 25-21 Ma Baltoro granite batholith. Recent geochronology studies in both the Hunza and Baltoro regions of north Pakistan have shed considerable new light on the timings of metamorphism, magmatism, and deformation along the Karakoram plate [*Fraser et al.* 1999]. We now discuss the Kohistan and Karakoram terranes in detail before presenting a tectonic model which accounts for all the data summarized here.

3. Kohistan Terrane

The Kohistan terrane (Figure 4) is sandwiched between the Indian plate (Himalaya) to the south along the ISZ or MMT, and the Asian plate (Karakoram terrane) to the north along the Shyok suture zone SSZ. It is widely regarded as representing a large-scale Cretaceous intra-oceanic island arc complex which has been obducted onto the Indian plate to the south along the MMT and subsequently deformed, partly metamorphosed, and intruded by Andean-type granodioritic plutons of the Transhimalayan batholith. Much of western and central Kohistan remains unmapped, but pioneering mapping, mostly along and around the Karakoram Highway section was carried out by *Tahirkheli* [1982], *Tahirkheli et al.* [1979] and *Bard* [1983]. The most recent reviews were written by *Treloar et al.* [1996], *Kazmi and Jan* [1997] and *Khan et al.* [1997].

3.1. Main Mantle Thrust Zone

The Main Mantle Thrust (MMT) is a zone of southward directed shearing along which the Kohistan arc terrane was emplaced over the Indian plate. The MMT is defined as the Cretaceous subduction zone above which the Kohistan island arc formed, and the Late Cretaceous - earliest Paleocene obduction thrust at the base of Kohistan, during collision with India. The MMT was subsequently folded around small culminations in the underlying Himalayan slab, such as the Besham fold [*Treloar et al.*, 1989b] and much larger ones such as the Nanga Parbat - Haramosh syntaxial anticline (Figure 2). Late stage reactivation along the trace of the MMT has resulted in the development of the Raikot Fault along the west margin and the Stak Fault along the east margin of the Nanga Parbat - Haramosh massif. Both faults result from the rapid phase of uplift of the Nanga Parbat - Haramosh massif (NPH) during the Neogene, when extreme exhumation rates in the NPH massif contrast with the low erosion and exhumation rates in the Kohistan and Ladakh terranes either side of it [*Zeitler*, 1985]. Compression around the NPH syntaxis has resulted in localized westward directed thrusting (Liachar Thrust) [*Butler and Prior*, 1988] along the trace of the earlier MMT in the Raikot bridge area (Figure 4).

The Cretaceous obduction plane along the MMT is marked by a zone of serpentinite melange or ophiolitic melange which includes the Shangla, Mingora, and Charbagh melanges [*Kazmi and Jan*, 1997]. These melanges contain high-presure assemblages such as the Shangla blueschists, which have a crossite, glaucophane + epidote + phengite paragenesis, typical of transitional blueschist - greenschist facies. *Maluski and Matte* [1984] dated the glaucophane schist at 80 Ma using $^{40}Ar/^{39}Ar$ step heating. Recent Rb/Sr dating of amphibole/phengite pairs gave ages of 77 ± 0.4 and 79.7 ± 0.4 Ma [*Anczkiewicz et al.*, 1998]. At Mingora, emeralds occur within talc + magnesite + fuchsite and quartz + carbonate lithologies, resulting probably from infiltration of CO_2 - rich fluids during metasomatism of a serpentinized ultramafic rock [*Arif et al.*, 1996]. Immediately south of the MMT a sequence of greenschist facies, phyllites, psammites, and marbles (Saidu schist) has been interpreted as representing the drowning of the Indian shelf, preceding and during obduction of Kohistan along the MMT [*DiPietro et al.*, 1993]. These low-grade, deep marine sediments may be lateral equivalents of the Lamayuru complex in the Indus suture zone of Ladakh [*Searle et al.*, 1988].

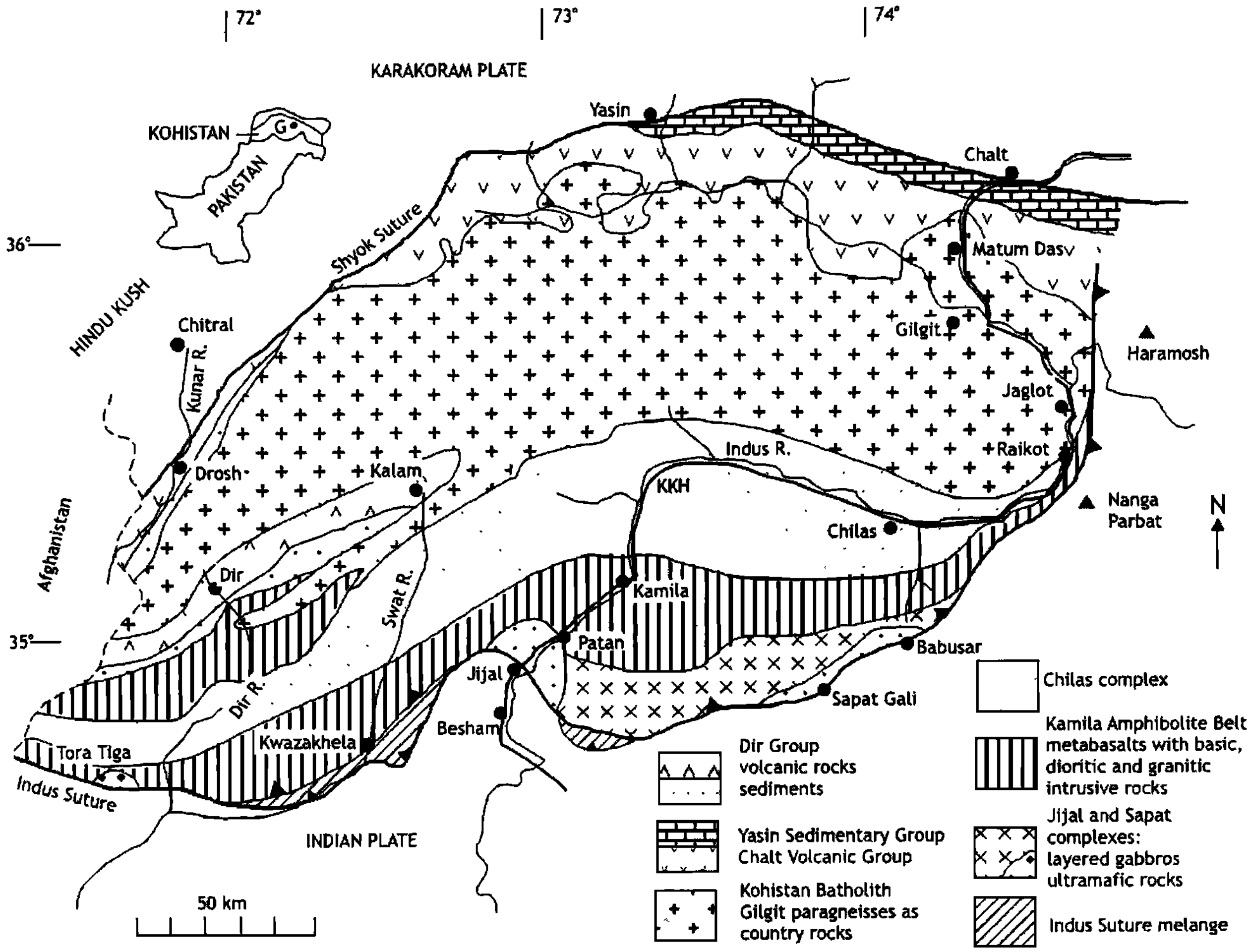

Figure 4. Geological map of Kohistan, [after *Tahirkheli and Jan,* 1979; *Searle and Asif Khan,* 1996; *Khan et al.,* 1997]. KKH is the route of the Karakoram Highway.

3.2. Sapat and Jijal Complexes

The southern margin of Kohistan is marked by a number of ultramafic-gabbroic, probable ophiolitic, assemblages (Figure 4). These include the Tora Tiga, part of the Shangla, lower Jijal, and the Sapat and Babusar complexes [*Jan et al.,* 1993; *Khan et al.,* 1993]. All of these upper mantle and lower oceanic crustal rocks are at the same structural horizon along the hanging wall of the MMT and probably represent remnant Tethyan ophiolites, or part of ophiolites, that were formed in the forearc to the developing Kohistan arc (Figure 5, model A). The ultramafic part of these ophiolites is mainly harzburgite (olivine + orthopyroxene ± chrome spinel) and dunite (olivine ± chrome spinel) which has been partly or wholly replaced by serpentinization. Present assemblages include serpentine minerals such as antigorite and chrysotile, talc, asbestos, and rare rodingite (Ca-metasomatized gabbro). The Sapat complex contains thin-layered pyroxenites, dunites, gabbros, and anorthosites [*Jan et al.,* 1993], which could be interpreted as a cumulate series, overlain by layered gabbros and anorthosites.

The Jijal complex represents the deepest part of the Kohistan arc terrane in southern Kohistan. It is composed of two main units, a lower mainly ultramafic unit of dunites, harzburgites, websterites, and clinopyroxenites and an upper unit consisting predominantly of garnet granulites [*Jan and Howie,* 1980, 1981; *Miller et al.,* 1991]. The Jijal complex appears to be restricted to the area either side of the KKH near Jijal and Patan; however, similar garnet granulites at Kwazakhela in the lower Swat valley are probably lateral equivalents. The granulites are composed of the following main mineral assemblages:

grt + opx + cpx + pl + qtz + ilm + scp + mag
grt + cpx + pl + scp + rt + qtz + ilm + mag; and
grt + cpx + hbl + pl + scp + rt + qtz + ilm + mag

These pyroxene granulite facies rocks have definite metamorphic, granoblastic textures although original igneous textures and layering, with alternating more mafic and more felsic layers, are also recognized, and these rocks sometimes exhibit a cumulus texture. Previous interpretations include a metamorphic origin for the garnet granulites [*Jan*

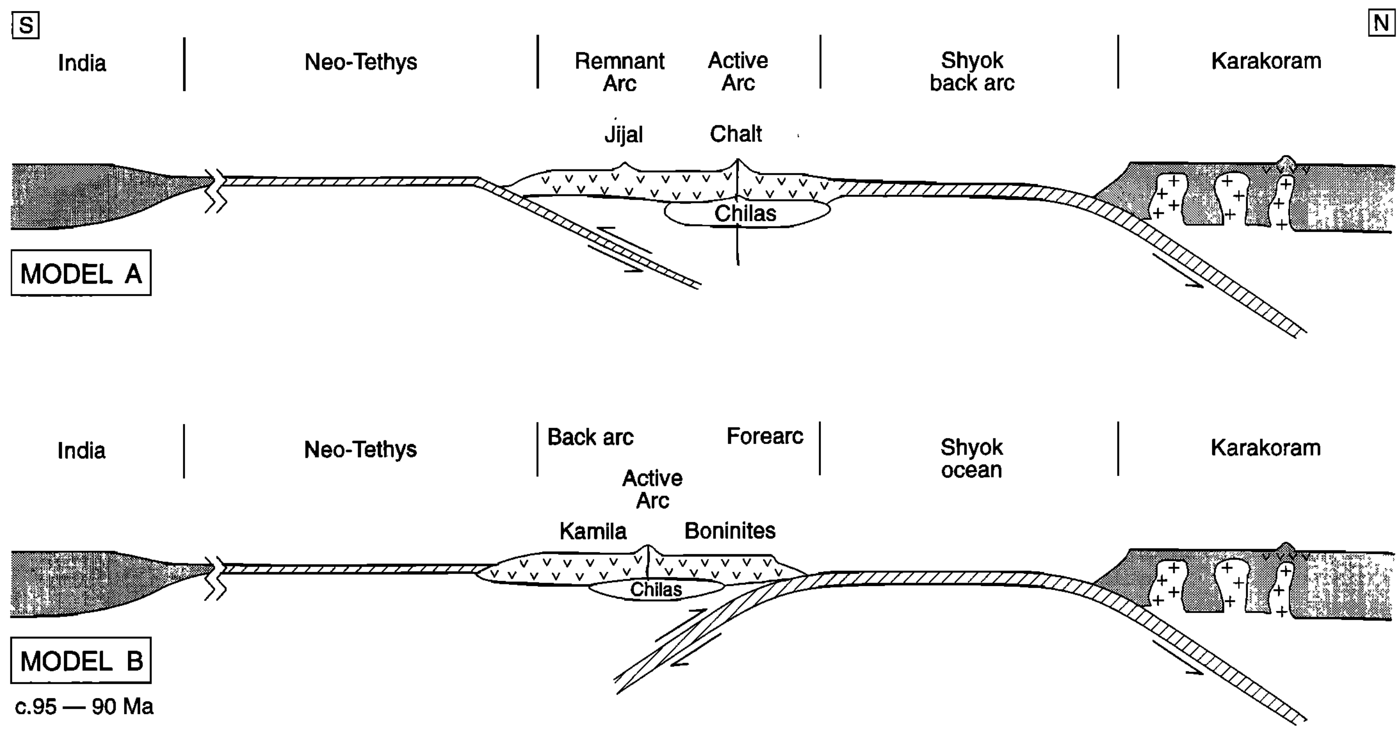

Figure 5. Two contrasting models for the evolution of the Kohistan island arc. Model A shows northward dipping subduction beneath Kohistan, with the Shyok suture as a back arc basin. Model B shows southward dipping subduction from the Shyok ocean to explain the Chalt boninites in the forearc region [after *Khan et al.*, 1997]. HT, high-temperature; HP, high-pressure.

and Howie, 1981] or a magmatic origin [*Ringuette et al.,* 1999]. Experimental data show that if the garnets were magmatic, pressures would have to have been around 20 MPa [*Green,* 1976]. *Ringuette et al.* [1999] showed that most garnets in the Jijal complex are zoned with an increase in grossularite and decrease in almandine and pyrope contents toward the rims, suggesting isobaric cooling. Thermobarometry, based on the grt - cpx exchange reaction and the grt - qtz - cpx - plag net transfer reaction give pressure-temperature (P-T) conditions of 750° - 1150°C and 12 - 19 MPa [*Miller et al.,* 1991; *Ringuette et al.,* 1999]. These P-T conditions suggest postmagmatic metamorphism at very high pressure granulite facies, which we interpret as being the result of the subduction of earlier lower crustal arc-related rocks to depths of at least 45 km along the MMT under conditions of high- temperature as well as high-pressure subduction. Hydration of the dry granulite facies rocks during obduction-related exhumation is evidenced by the development of amphibolite and greenschist facies retrograde metamorphism.

3.3. Kamila Amphibolites

The Kamila amphibolite belt is 10-40 km wide, extending all across southern Kohistan, and is composed of amphibolite facies metavolcanic and metaplutonic oceanic rocks, in which igneous layering is locally preserved. Gabbros, hornblende diorites, norites, and amphibolites (hbl + plag ± grt) have been intruded in places by pegmatite dikes consisting almost entirely of coarse-grained hornblende and feldspar. The Kamila amphibolite belt separates the high-pressure rocks along the hanging wall of the MMT (blueschists and granulites) and ophiolites to the south, from the Chilas complex gabbro - norites to the north (Figure 4). Amphibolites derived from mafic to intermediate volcanic rocks show an E-type mid-ocean ridge basalt (MORB) geochemical signature and are interpreted as representing metamorphosed ocean floor basalts, probably forming the oceanic crust on top of which the Kohistan arc volcanics were subsequently built [*Khan et al.,* 1989, 1993]. Amphibolites derived from plutonic rocks are geochemically very similar to the Chilas complex gabbro –norites, and the two probably have a similar origin [*Khan et al.,* 1989, 1997]. These rocks show a depletion in the high field strength elements and may have a more subduction - related signature.

Structural data [*Coward et al.,* 1987] and $^{40}Ar/^{39}Ar$ hornblende cooling ages of 83-80 Ma [*Treloar et al.,* 1989a] show that much of the deformation and metamorphism occurred prior to the collision of India to the south and suturing along the MMT. The Kamila shear zone [*Treloar et al.,* 1990] is a wide zone characterized by intense ductile shear fabrics, formed at temperatures above 500°C, showing south to SW vergence and thrusting. More detailed work along the KKH section has distinguished the Patan shear zone, a 3 km wide high-strain zone around the village of Patan [*Zeilinger et al.,* 1998; *Arbaret et al.,* 1998]. Numerous anastomosing shear zones show pervasive SW directed thrust shears, some containing leucocratic garnet-bearing veins, interpreted as resulting from partial melting of the mylonites [*Arbaret et al.,* 1998]. Deformation began during the latest phase of igneous activity represented by intrusion of the gabbro-norites and continued during northward subduction and SW thrusting of Kohistan along the proto-MMT. A localized, younger phase of north to NE directed normal shearing along the MMT zone was superimposed on the earlier thrust-related structures and probably relates to uplift and thrusting in the Himalayan rocks to the south of the MMT [*Burg et al.,* 1996; *Vince and Treloar,* 1996]. The Patan fault is still recently active as evidenced by the December 1974 earthquake, the epicenter of which was located at Patan itself [*Jackson and Yielding,* 1998].

3.4 Garnet + Muscovite + Tourmaline Leucogranites

Two intrusions of garnet + muscovite + tourmaline leucogranite pegmatites into the Kamila amphibolites occur along the Karakoram Highway section. One leucogranite sheet, 5 km north of Patan, is a coarse-grained pegmatite consisting of ms + grt + tur + Kfs + qtz + pl + apatite. The sheet is both concordant to the foliation in the amphibolites and locally crosscuting it. Another heterogeneous granitic sheet crops out along the KKH ~ 3 km south of Kamila and consists of ms + grt + Kfs + qtz without tourmaline. Both of these intrusions resemble High Himalayan-type leucogranites or pegmatites and are very unusual in Kohistan. Their origin is probably from melted pelitic metasediments, possibly even from underthrust Himalayan gneisses beneath the MMT.

3.5. Chilas Complex

The Chilas complex is a very large mafic intrusion, dominantly comprised of gabbro-norite with minor intrusive bodies of ultramafic rocks including dunites, harzburgites, troctolites, hornblende gabbros, pyroxenites, and anorthosites [*Khan et al.,* 1989, 1993]. The main gabbro-norites are massive, occasionally layered plutonic rocks consisting of the following assemblage: plag + opx + cpx + mag + ilm ± hbl ± qtz ± Kfs ± bt ± scp. The later intrusive ultramafic rocks include chrome spinel + olivine dunites, which show spectacular gravity-settling layered textures, Mg-rich orthopyroxene and clinopyroxene, and some unusual intrusive rocks composed almost entirely of hornblende. These ultramafic rocks have been emplaced into the base of the main gabbro-norite magma chamber below the main Kohistan island arc. Geochemically, the gabbro-norites define a calc-alkaline trend typical of island arc rocks [*Khan et al.,* 1989, 1993]. P-T conditions of formation have been estimated at 750°-850°C and 5-6.5 kbars [*Jan and Howie,* 1980], conditions compatible with origin in a subarc magma chamber at the base of the crust. Most of the Chilas complex is undeformed, and the margins show intrusive contacts with the surrounding amphibolites of the Kamila complex and the greenschist facies metasediments of the Gilgit complex. Rafters of the latter are enclosed as large xenolithic blocks within the Chilas complex at the structural top of the sequence.

The enormous size of the Chilas complex (~ 300 x 20-40 km in area) suggests that it could never have been one continuous magma chamber molten at the same time. Even mid-ocean ridge magma chambers with high rates of magma supply are thought to have very thin but variable length magma chambers. In suprasubduction zone ophiolite complexes, such as the well-known Oman ophiolite, magma chambers are thought to be narrow and segmented related to batches of magma ponded above the cumulate series and feeding magma upward through the sheeted dikes at different times along the ridge axis [e.g.; *Pearce et al.,* 1981; *Searle and Cox,* 1999]. It is probably likely that the Chilas complex norites had several pulses of magma over time, but detailed mapping of this country would be both difficult and dangerous.

The age of the Chilas complex gabbro-norite is given by a U-Pb zircon age of 84 ± 0.5 Ma from upper Swat [*Zeitler and Chamberlain,* 1991]. *Khan et al.* [1989, 1993] interpret the Chilas gabbro-norites as representing the magma chamber at the base of the Kohistan arc or as an intrusion during intra-arc rifting in a back arc basin. *Treloar et al.* [1996] concluded that the Chilas complex was intruded after suturing of Kohistan with the Karakoram plate to the north. The precise age of closure of the Shyok suture zone (SSZ) can only be bracketed between 95 and 75 Ma. Ninety-Five Ma is the U-Pb monazite age of the pre-collision granodiorites in the Hunza plutonic unit in the Karakoram (see section 5.2), and 75 Ma is the $^{40}Ar/^{39}Ar$ hornblende plateau age of the Jutal basic dikes, a swarm of undeformed dikes which crosscut the SSZ-related fabrics in the Chalt region of the lower Hunza valley [*Petterson and Windley,* 1985].

3.6. Kohistan Arc Volcanics

The volcanic evolution of the Kohistan arc is long and complicated, beginning as an intra-oceanic, suprasubduction zone island arc and evolving after collision with India into an Andean-type volcanic arc with abundant granitic intrusions. The earliest arc volcanics are the Cretaceous Chalt Volcanic Group, including the type locality in the lower Hunza valley along the KKH [*Searle and Asif Khan,* 1996]. In the Hunza valley the Chalt volcanics have a bimodal distribution from basaltic and andesitic to rhyolitic compositions and are strongly deformed, showing stretched pillows [*Pudsey,* 1986, *Petterson et al.,* 1990]. They are continuous westward with the "Western volcanic group" of *Sullivan et al.* [1993] which are also basaltic andesites and rhyolites and probably correlate eastward with the Dras Volcanic Group in western Ladakh [*Searle et al.,* 1988; *Reuber,* 1989]. These arc-related volcanic rocks have previously been thought to have formed above a north dipping subduction zone, related to the early initiation of the Kohistan island arc (Figure 5, model A). However, the presence of boninites or high-Mg andesites with high large-ion lithophile element (LILE) high field strength element (HFSE) ratios and negative Nb anomalies [*Petterson et al.,* 1990], usually typically sited in forearc regions, along the northern side of Kohistan led *Khan et al.* [1997] to suggest that early south directed subduction existed north of Kohistan, with the Chalt boninites along the northern forearc region, and the MORB-related Kamila metavolcanics representing the back arc basin (Figure 5, model B). In their model, later collision of Kohistan with the Karakoram led to the initiation of northward directed subduction along the southern margin of Kohistan leading eventually to the collision with India during the early Eocene.

Paleocene volcanism is represented by the Shamran volcanics along northern Kohistan and the Dir-Utror volcanics along southwestern Kohistan, both groups consisting of basaltic andesites, rhyolites, pyroclastic flows, ignimbrites, and volcanic breccias. An $^{40}Ar/^{39}Ar$ age of 58 ± 1 Ma from a Shamran hornblende-bearing basaltic andesite [*Sullivan et al.,* 1993] shows that the Kohistan arc continued producing large volumes of lavas throughout the Paleocene, after suturing of Kohistan to Asia (Figure 3). This suggests that active oceanic subduction must have occurred along the southern boundary of Kohistan during this time, similar to the situation in model A of Figure 5. Deposition of the late Paleocene Baraul Banda slates has been interpreted as rapid subsidence associated with the collapse of the Kohistan continental margin. Rare interbedded limestones within the Baraul Banda slates, south of Dir in southwestern Kohistan (Figure 4) have yielded late Paleocene (60.2 - 54.9 Ma) marine faunas, the youngest marine faunas in Kohistan [*Sullivan et al.,* 1993]. An $^{40}Ar/^{39}Ar$ age of 55 ± 2 Ma from an Utror basaltic andesite shows that Paleocene volcanism occurred all across the Kohistan arc terrane, which was later intruded by granites of the Kohistan batholith. The Dir-Utror volcanics are largely subaerial with thick silicic lavas and pyroclastic flows. The Kohistan volcanic arc reached its maximum growth during the Paleocene, immediately prior to the collision of India and closure of the Indus suture - MMT [*Searle et al.,* 1987, 1988; *Beck et al.,* 1995].

3.7. Kohistan Batholith

The granitic rocks of the Kohistan batholith intrude the early island arc volcanics (Dras and Chalt Groups) as well as metasediments of the Gilgit complex, which are greenschist facies slates, phyllites, and psammites [*Khan et al.,* 1993; *Searle and Asif Khan,* 1996]. Abundant intercalations of pillow lavas and flows suggest that they formed in an arc-related basin of Cretaceous age and are not related to the metamorphic rocks of the southern Karakoram. These rocks, which show a static, low-pressure thermal metamorphism are the same as the Jaglot schist belt of *Treloar et al.* [1996]. The Kohistan granites are a calc-alkaline suite of gabbro-diorites, granodiorites, and granites with hornblende and biotite as the dominant mafic phases. *Petterson and Windley* [1985] and *Petterson et al.* [1990] defined three main stages of granite emplacement, based on regional mapping, petrology, and Rb/Sr dating. Stage 1 granites are the early bimodal sequence of gabbro-diorites (hbl + bi + pl + qtz) and trondhjemite-tonalites (pl + hbl ± bt ± qtz) which are deformed by a Late Cretaceous deformation episode, such as the Matum Das pluton, north of Gilgit, which has a poorly constrained Rb/Sr isochron age of 102 ± 12 Ma [*Petterson and Windley,* 1985]. Disrupted basic dikes form a minor component of this phase. No U-Pb zircon or monazite ages have been reported from Kohistan granites, although two U-Pb zircon ages of 101 ± 2 and 103 ± 2 Ma have been reported from the western Ladakh sector of the Trans-Himalayan batholith [*Honegger et al.*, 1982; *Schärer et al.*, 1984].

Stage 2 intrusions are more acidic granodiorites and granites, two plutons of which have Rb/Sr ages of 54 ± 4 Ma (Gilgit granite) and 40 ± 6 Ma Shirot granodiorite [*Petterson and Windley*, 1985]. The Shirot pluton has a late-stage grt + ms + qtz + fsp leucogranite phase, which does not appear to be present elsewhere in Kohistan. A suite of undeformed hornblende + plagioclase basic dikes, the Jutal dikes, cuts across earlier deformed granodiorites, such as the Matum Das pluton and the Albian-Aptian Chalt volcanics. The Jutal dikes have a hornblende $^{40}Ar/^{39}Ar$ age of 75 ± 1 Ma [*Treloar et al.*, 1989a] which constrains the youngest timing of closure of the SSZ. Stage 3 intrusions are characterized by swarms of leucogranite dikes, the Indus confluence dikes, which have a poorly defined Rb/Sr age of 34 ± 14 Ma, and layered aplite-pegmatites, such as the Parri aplite sheet, which has a Rb/Sr isochron age of 29 ± 8 Ma [*Petterson and Windley*, 1985] or 26.2 ± 1.2 Ma [*George et al.*, 1993]. These Rb/Sr ages, however, are unreliable intrusion ages of the granites, because Rb and Sr are unlikely to have remained a closed system during subsequent deformation.

The Kohistan batholith records both precollision (Kohistan - Karakoram collision) stage 1 granitoids, intruded during the oceanic island arc phase, and postcollision stage 2 granitoids after Kohistan had become sutured to the Karakoram plate and evolved into an Andean-type continental margin. Stage 3 leucogranite dikes and aplite-pegmatite sheets are probably related more to continental crustal melting as a result of crustal thickening following collision.

4. Tectonic Evolution of Kohistan

4.1. Mid-Cretaceous

The tectonic evolution of Kohistan can best be interpreted with reference to the time chart (Figure 3) and the tectonic reconstructions (Figure 6). Field relations and geochronology show that the oldest component of the Kohistan arc terrane is the Kamila amphibolite group. These high-Ti metabasalts are transitional N-type MORB and E-type MORB and are interpreted as tholeiitic oceanic crustal rocks on which the main arc was built. The Kamila metavolcanic amphibolites were intruded by several gabbro-diorite intrusions which show a subduction component trace element geochemistry [*Khan et al.*, 1993, 1997]. These rocks may indicate the timing of the initiation of subduction along the southern margin of Kohistan some time during the mid-Cretaceous (Figure 6). The high-pressure Jijal complex, consisting of both upper mantle ultramafic rocks and lower crustal granulites, may represent part of the early arc of Kohistan which was later subducted to depths of around 45 km and subjected to high-pressure metamorphism.

The main intra-oceanic phase of arc volcanism during the mid-Cretaceous to Late Cretaceous is represented by the thick calc-alkaline andesites and rhyolites of the Chalt Volcanic Group. The Chalt volcanics occur along the northern margin of Kohistan (Figure 4), and the fact that they contain boninitic volcanic rocks, normally associated with forearc regions, suggests that subduction polarity may have dipped south from the Shyok Ocean north of Kohistan (Figure 5, model B). This is the model suggested by *Khan et al.* [1997] based on geochemical and isotopic constraints. They also demonstrated the involvement of enriched (DUPAL)-type mantle, suggesting that Kohistan formed at or south of the present equator during the mid-Cretaceous to late Cretaceous. Arguments in favor of a northward dipping subduction zone beneath Kohistan (Figure 5, model A) are the presence of Late Cretaceous high-pressure blueschists (Shang-la and western Ladakh) and garnet granulites (Jijal complex) along the southern margin of Kohistan. Limestones of the Yasin Group containing radiolaria and *Orbitolina sp.* foraminifera of Albian-Aptian age are associated with the Chalt volcanics [*Pudsey et al.*, 1985]. These lavas are lateral equivalents of the Western volcanics in northwest Kohistan [*Sullivan et al.*, 1993] and the Dras I volcanics in Ladakh, east of Nanga Parbat [*Searle et al.*, 1988; *Reuber*, 1989]. Early granite plutons of the Kohistan batholith were intruded into the volcanic and metasedimentary ediface of the early island arc.

4.2. Late Cretaceous

Thick calc-alkaline volcanism continued throughout the Late Cretaceous up until the collision of Kohistan with the Karakoram plate and closure of the SSZ around the Santonian-Campanian (Figure 3). The Chilas gabbro-norites were intruded into the base of the island arc sequence, intruding Kamila metavolcanic amphibolites along the south and Gilgit metasediments along the northern contact. Southward thrusting along southern Kohistan during this time is apparent from the ductile shear zones of the Kamila and Patan shear zones. Subduction along the southern margin of Kohistan is evident from high-pressure metamorphism of the Shang-la blueschists and the Jijal garnet granulites along the MMT. Emplacement of the Sapat ultramafic (possibly ophiolitic) rocks east of the KKH section also occurred around this time.

Along northern Kohistan a major phase of deformation occurred around Campanian time associated with the closure of the SSZ (Figure 6). Early gabbro-diorites and trondhjemite-tonalites, such as the Matum Das pluton along the KKH, were deformed, and the Dras I volcanics in Ladakh were also affected by shearing [*Reuber*, 1989]. The undeformed 75 Ma Jutal basic dikes cut across the deformation fabrics in the stage 1 Kohistan plutons and the Chalt volcanics, suggesting that closure of the SSZ was completed before 75 Ma.

4.3. Paleocene

Collision of Kohistan and the Karakoram was completed before the Paleocene, although calc-alkaline volcanism

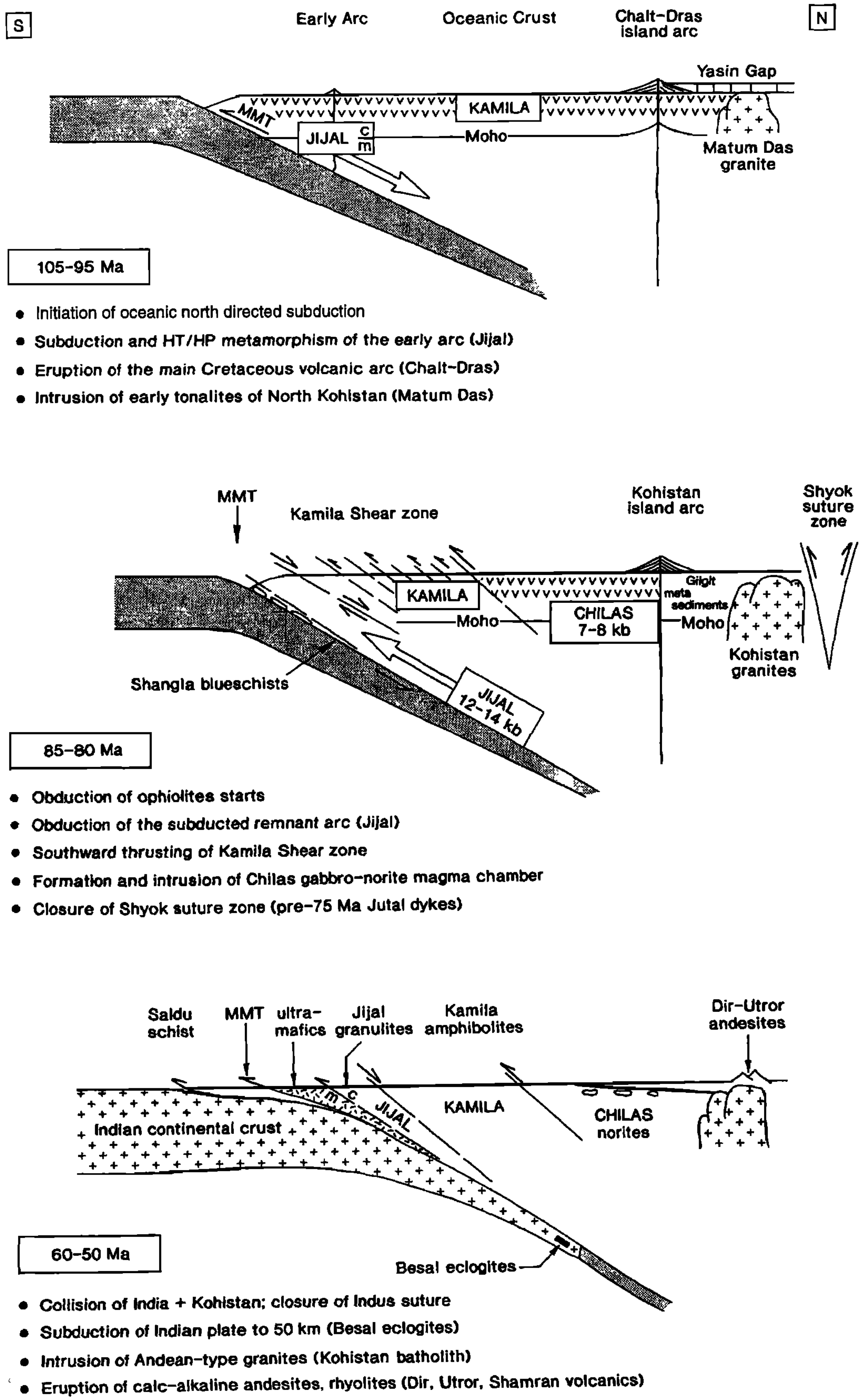

Figure 6. Model for the tectonic evolution of Kohistan (see text for discussion).

continued all across northern Kohistan up to 55 Ma (Figures 3 and 4). The Shamran volcanics along northern Kohistan and the Dir-Utror volcanics along southwestern Kohistan were intruded by later, stage 2 plutons of the Kohistan batholith. This phase of the batholith is the most widespread all along the Kohistan-Ladakh-Gangdese sectors of the Trans-Himalayan batholith and can be compared in size, dimension, and geochemistry to the Andean batholiths in northern Chile and Peru. Paleocene marine sediments, the Baraul Banda slates with rare intercalated limestone beds, are the youngest marine sediments in the Kohistan plate [*Sullivan et al.*, 1993]. Early Eocene foraminiferal limestones are the youngest marine sediments, both within the Indus suture zone and along the north Indian continental margin in Ladakh [*Searle et al.*, 1988]. The collision of India and Kohistan may have been as early as 60 Ma in the far west in Waziristan [*Beck et al.*, 1995]; along the Indian and south Tibet sectors, India-Asia (Lhasa Block) collision is reasonably well constrained at 54 - 50 Ma [*Garzanti and van Haver*, 1988; *Searle et al.*, 1990b].

4.4. Eocene

Figure 6 shows the tectonically restored position of Kohistan during the period of collision of the Indo-Pakistan plate (latest Paleocene - early Eocene 60-50 Ma). Subduction of the leading edge of the Indo-Pakistan plate to depths of ~90 km is known from the recent discovery of coesite inclusions in omphacite in the Besal eclogites [*O'Brien et al.*, 1999]. These eclogites are very fresh and contain garnet, omphacite, and white mica, overgrown by black amphibole crystals. They are metamorphosed mafic lavas and sills within the Permian shelf sequence of the leading edge of the Indian plate, in an identical structural–tectonic position to similar eclogites at the deepest structural level beneath the Oman ophiolite [*Searle et al.*, 1994]. In Oman the eclogites were formed by the subduction of the leading edge of the continental plate beneath a purely ophiolitic, oceanic upper plate and are not related to any continental collision. A similar origin for the Besal eclogites is proposed here, during obduction of the Kohistan arc (Figure 6).

The timing of eclogite facies metamorphism in Pakistan is thought to be 49 ± 6 Ma, the Sm/Nd age of a garnet-clinopyroxene pair [*Tonarini et al.*, 1993]. The Besal eclogites, like the Tso Morari eclogites in northern Ladakh, are metabasaltic sills (tentatively correlated with the Carboniferous-Permian Panjal Trap volcanics) within Permian limestones along the .eading (northern) edge of the Indian plate. U-Pb dating of allanites from an eclogite metapelite and Lu-Hf dating of garnet–omphacite and whole rock from a metabasic eclogite from Tso Morari in Ladakh gave poorly constrained ages of 55 ± 17 and 55 ± 12 Ma [*deSigoyer et al.*, 1999]. These ages are all immediately pre Indian plate collision and support an Oman-type continental subduction model for the leading edge of the Indian plate. Structural, metamorphic, and geochronological data show that the Besal and Tso Morari eclogites record the subduction of Indian plate rocks beneath southern Kohistan during the obduction process and subsequent rapid exhumation along the MMT zone.

Following the India-Kohistan collision after the earliest Eocene (circa 54-50 Ma; [*Garzanti and van Haver*, 1988; *Searle et. al.*, 1990b], crustal thickening and metamorphism occurred in the Indian plate rocks to the south of the MMT and peaked pre-40-Ma [*Treloar et al.*, 1989a]. Deformation in Kohistan was restricted to localized north vergent normal shearing along the MMT zone [*Burg et al.*, 1996; *Vince and Treloar*, 1996]. Post-collisional magmatism is represented by the leucogranite dikes (Indus confluence dikes) and aplite-pegmatite sheets in localized areas of Kohistan. Post-Paleocene deformation in Kohistan is relatively insignificant, whereas large-scale crustal thickening, metamorphism, and magmatism occurred, both along the High Himalayan zone to the south and the Karakoram to the north [*Searle and Tirrul*, 1991]. The youngest phase of metamorphism (10-4 Ma) and magmatism (7.5-1 Ma) occurs in the Nanga Parbat - Haramosh massif (northwestern extent of the High Himalayan zone) and probably parts of the southern Karakoram. U-Pb ages as young as 1 Ma have been reported in tourmaline-bearing leucogranites, sillimanite grade gneisses, and cordierite + quartz + K-feldspar ± plagioclase seams [*Zeitler et al.*, 1993; *Smith et al.*, 1992, 1994].

5. Hunza Karakoram

The Karakoram terrane represents the southern margin of Asian continental crust and is correlated eastward with the Lhasa Block of south Tibet. The KKH runs along the Hunza valley, north of Gilgit, which provides an excellent profile across the Karakoram (Figure 7). Previous work in Hunza has been carried out by *Desio and Martina* [1972], *Debon et al.* [1987], *Rex et al.* [1988], *Searle* [1991] and *Crawford and Searle* [1992, 1993]. The Karakoram terrane has been broadly divided into three main units, a northern sedimentary belt characterized by Ordovician to Early Cretaceous sedimentary rocks [*Gaetani and Garzanti*, 1991] and a southern Karakoram metamorphic complex [*Searle and Tirrul*, 1991] including regional Barrovian facies metamorphic rocks, separated by the Karakoram batholith [*Searle et al.*, 1989, 1992]. The Karakoram batholith includes a number of precollisional hornblende and biotite-bearing granodiorites and tonalites [*Searle et al.*, 1989; *Crawford and Searle*, 1992] as well as the large, early Miocene Baltoro plutonic unit in the central and eastern Karakoram, which includes monzogranites and garnet two-mica leucogranites [*Searle et al.*, 1989, 1992; *Parrish and Tirrul*, 1989; *Searle*, 1991].

5.1. North Karakoram Terrane

Sedimentary rocks crop out along the north Karakoram range, north of the Karakoram batholith [*Gaetani and Garzanti*, 1991]. Widespread Carboniferous black shales were deposited across the Karakoram terrane and crop out along the northern margin of the batholith in the Hunza and Baltoro region. Development of a stable passive continental margin began in the Permian with thick, shallow, marine carbonate sedimentation which continued throughout the

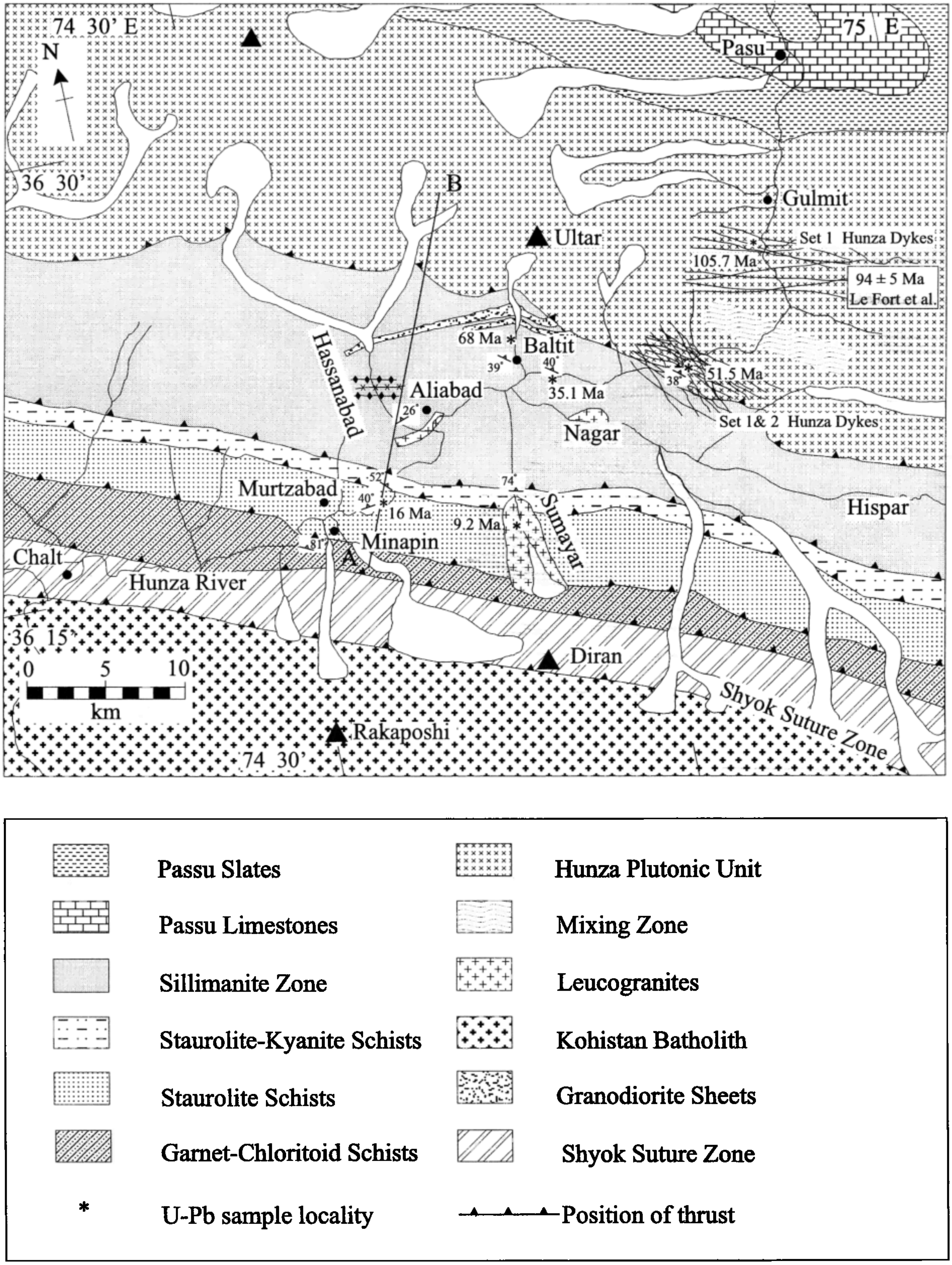

Figure 7. Geological map of the Hunza Karakoram [after *Rex et al.*, 1988; *Searle*, 1991; *Crawford and Searle*, 1992; *Fraser et al.*, 1999].

Triassic and Lower Jurassic (Liassic). The youngest marine sediments in the Karakoram are probably Late Jurassic, after which the southern margin of Asia began uplifting as the Andean-type margin developed. From mid-Jurassic up to the early Eocene the southern margin of Asia has been the site of intrusions of Andean-type gabbro-diorite, granodiorite, granite and tonalite intrusions along long, linear batholiths. These early precollisional granites, such as the K2 gneiss [*Searle et al.*, 1990a]; the Muztagh Tower gneiss, and the Hushe gneiss [*Searle et al.*, 1989; *Searle*, 1991] are often deformed and metamorphosed. Others, such as the Broad Peak porphyry and the Gasherbrum quartz diorites, are essentially undeformed and intrude through the Triassic - Jurassic carbonates. Along the Hunza valley several similar precollisional granitic intrusions, the mid-Cretaceous Khunjerab and Sost plutons, also intrude through the Carboniferous-Permian sediments.

5.2. Hunza and Batura Plutonic Units

The main part of the Hunza plutonic unit (HPU) is a deformed calc-alkaline biotite + hornblende granodiorite, which has a U-Pb age of 95 ± 5 Ma [*LeFort et al.*, 1983] and a more precise U-Pb age given by three concordant zircon analyses of 105.7 ± 0.5 Ma [*Fraser et al.*, 1999]. The Hunza granites are quite complex with a central "mixing zone" composed of quartz diorites, granodiorites, and agmatites (magmatitic migmatites) with both acid and basic gneisses, leucogranitic sweats, and late aplite sheets [*Crawford*, 1988]. Enclaves of both igneous and metasedimentary (calcareous and pelitic) rocks probably represent incompletely assimilated country rock. Most of the Hunza plutonic unit is composed of foliated hornblende and biotite-bearing tonalites and granodiorites, which are probably coeval with similar rocks of the Muztagh Tower unit and K2 gneiss to the north of the batholith [*Searle et al.*, 1990a] and part of the Hushe gneiss to the south of the batholith in the Baltoro Karakoram [*Searle*, 1991].

The northern part of the Karakoram batholith along the Hunza valley consists of the composite Batura plutonic unit comprising early gabbros and diorites and peraluminous leucocratic granodiorites containing biotite [*Debon et al.*; 1987; *Rex et al.*; 1988; *Crawford and Searle*, 1992]. These plutons are undeformed and intrude the older, deformed Hunza granodiorites to the south and Permian slates and marbles to the north. A narrow andalusite-bearing hornfels contact metamorphic aureole lies along the northern margin of the batholith, where a few leucocratic dikes emmanate out from the pluton. Rb-Sr whole rock isochron ages 63.4 ± 2 Ma (Kuk gabbro) and 42.8 ± 5.6 Ma (Sarbzea pluton) have been given by *Debon et al.* [1987] and *Debon* [1995] indicating Paleocene - early Eocene plutonism. These authors have proposed a mantle source with a small crustal contribution for these Paleocene granitoids, similar to the Kohistan plutons, which were associated with Tethyan oceanic subduction northward prior to the Indian plate collision (Figure 5).

The southern part of the Karakoram batholith has a distinct metamorphic foliation overprinting early magmatic fabrics. The strike of the foliation is ~130° NW-SE, and the dip is ~ 60° NE. Postmagmatic metamorphic mineral growth is indicated by the growth of garnet and epidote, the replacement of plagioclase by zoisite and occasionally scapolite, and quartz + hornblende pods [*Crawford and Searle*, 1992]. The southern contact of the HPU is a steep NE dipping thrust emplacing the granites over sillimanite-grade marbles, pelites, and amphibolites. Thermobarometry indicates that recrystallization of the HPU occurred at roughly the same P-T conditions as the sillimanite gneisses to the south [*Debon et al.*, 1987]. At least two sets of leucogranitic dikes, the Hunza dikes, cut the southern and central parts of the HPU.

Although the geology of the KKH section along the Hunza valley is quite well known, it must be emphasized that large tracts of extremely mountainous country to the west and east remain relatively unknown. Boulders of unfoliated tourmaline + muscovite + garnet leucogranites in the moraines of the Hasanabad glacier appear to be derived from a pale-colored leucogranite intrusion making up most of the peak of Shishpare (7611 m) NW of Ultar peak (Figure 7). Together with the Pumari Chhish leucogranite north of the Hispar glacier [*Searle*, 1991], these young undeformed leucogranites may be the westward extension of the Baltoro granites. It is doubtful whether these mountains will ever be properly mapped, however, because they represent the most extreme topography on this planet.

5.3. Hunza Dikes

The Hunza dikes are a cogenetic suite of granodiorites, monzogranites, and leucogranites which intrude the precollisional HPU granodiorites [*Crawford and Searle*, 1993]. There are at least two sets of dikes, which can make up to ~40% of the outcrop. The earliest set, set 1, intrudes the granodiorites but have been rotated into parallelism with the main SSW directed shear fabrics associated with emplacement of the HPU over the metamorphic rocks to the south during simple shear. In the central part of the batholith around the mixing zone along the KKH section, a sub horizontal set of dikes and a sub-vertical set form a criss-cross pattern indicating coaxial extension during intrusion. To the north and south of this zone, non coaxial simple shear has rotated the dikes into parallelogram orientations.

The second set of Hunza dikes cross cuts all lithologies of the HPU, including the set 1 Hunza dikes. These set 2 dikes, which include several localized sub sets of cross-cutting dikes, also intrude across the thrust contact and across the metamorphic fabric in the marbles and pelites below. Both sets of dikes are volatile-depleted non minimum melts with unevolved crustal isotopic ratios similar to the Miocene Baltoro pluton to the east [*Searle et al.*, 1992, *Crawford and Searle*, 1993]. They are interpreted to represent lower Karakoram crustal melts, derived from dehydration melting of metasediments, possibly promoted by limited heat input from the mantle wedge below [*Crawford and Searle*, 1993]. Set 1 dikes have a U-Pb zircon and uraninite age of 51.5 ± 1.5 Ma, and set 2 dikes, which cross cut both southern HPU granites and metamorphic rocks, have been dated using U-Pb methods on zircon, monazite, and uraninite at 35.1 ± 0.6 Ma [*Fraser et al.*, 1999]. This age provides a youngest time constraint on sillimanite grade metamorphism in the southern Karakoram.

5.4. Sillimanite Grade Metamorphism

The southern Karakoram metamorphic complex is a regional high-grade terrane between the Shyok suture zone to the south and the Karakoram batholith to the north. The highest grade rocks lie immediately south of the batholith. In the Baltoro region the isograds have been mapped as right way up but folded and intruded by the 21 Ma Baltoro batholith [*Searle and Tirrul*, 1991]. Along the Hunza valley the metamorphic section is inverted with the Hunza plutonic unit thrust over the sillimanite grade marbles and gneisses, which have then been thrust over the kyanite, staurolite and lower grade rocks to the south. The structures along the KKH section have been interpreted as postmetamorphic thrusting of higher-grade rocks over lower-grade rocks [*Rex et al.*, 1988, *Searle*, 1991, *Crawford and Searle*, 1993]. Most of the rocks immediately south of the HPU are marbles consisting of calcite + phlogopite ± fuchsite ± ruby corundum. Calc silicates may also contain diopside, olivine, tremolite, plagioclase, and garnet. Pelites are relatively uncommon but contain sillimanite, garnet, muscovite, and biotite. Amphibolites are occasionally interbedded with the more massive marble bands and consist of hornblende + plagioclase + garnet ± clinopyroxene. Monazites from two samples of sillimanite grade metapelites from Baltit and Hasanabad (Figure 7) gave U-Pb ages of 64 ± 0.8 and 44 ± 2 Ma, respectively [*Fraser et al.*, 1999]. This could either represent one very long (20 Ma) protracted metamorphism or two events, M1 being related to crustal thickening and metamorphism following the Kohistan-Karakoram collision and M2 being related to crustal thickening and heating following the later India-Asia collision.

5.5 Staurolite Grade Metamorphism

The sillimanite grade marbles and gneisses along the Hunza valley have been thrust over-lower grade metamorphic rocks, probably along a late NE dipping thrust (Figure 7). Kyanite, staurolite, garnet, and chloritoid-chlorite grade rocks mark the zone of apparent inverted metamorphism along the Hunza valley. It was previously assumed that all the metamorphic rocks south of the batholith in the southern Karakoram belonged to one major episode of postcollisional regional metamorphism [*Bertrand et al.*; 1988, *Searle and Tirrul*, 1991]. However, $^{206}Pb/^{238}U$ ages of metamorphic monazites, extracted from staurolite + garnet mica schists from near Nazirabad in the Hunza valley, are 16.0 ± 1.0 Ma [*Fraser et al.*, 1999]. This surprising result shows that there must have been at least two distinct metamorphic episodes, possibly three: a 68 Ma sillimanite grade M1 event, a 44 Ma sillimanite–kyanite grade event, and a 16 Ma staurolite grade M3 Hunza (M3h) event. M3 Baltoro (M3b) is a 21 Ma thermal metamorphic aureole surrounding the Baltoro granite, which at present has no correlative in the Hunza valley, but in the interests of a meaningful correlation along the Karakoram, we retain the numbering. Thus M2 is the main regional metamorphism south of the Karakoram batholith, and M3 is the narrow zone of contact metamorphism around the Baltoro granite intrusion (Figure 3).

An isolated tourmaline + muscovite + biotite ± garnet leucogranite intrusion, the Sumayar leucogranite, intrudes and crosscuts fabrics in the staurolite grade schists south of the Hunza valley. The Sumayar leucogranite has a U-Pb zircon and uraninite age of 9.5 ± 0.2 Ma [*Fraser et al.*, 1999], which is consistent, being younger than the 16 Ma peak staurolite metamorphic rocks into which it has intruded. Several leucogranite-aplite sheets intrude and cut the foliation in the metamorphic rocks. The Bar and Hasanabad sheets are composed of biotite (+ minor muscovite) granodiorites-monzogranites with pegmatite rims rich in garnet, muscovite and secondary tourmaline [*Crawford and Searle*, 1993]. The Hasanabad granodiorite sheet (Figure 7) contains huge xenoliths of metamorphic rocks, one containing a Hunza leucogranite dyke which cuts across the metamorphic fabric in the xenolith. The Hasanabad sheet must therefore be younger than the 35 Ma set 2 Hunza dikes. The southern boundary of the metamorphic series is the Main Karakoram Thrust, a young north to NE dipping breakback thrust which follows the trace of the Shyok suture zone and which was responsible for the uplift and exhumation of the Karakoram during the late Miocene - Pliocene.

Metamorphism in the Baltoro region, east of the KKH section along the Hunza valley is significantly different. Here the initial metamorphic event is a precollision, low-pressure, high-temperature andalusite grade metamorphism, probably related to the pre-collisional Andean-type granites (e.g., Hushe gneiss), [*Searle et al.*, 1989]. M2 is the widespread high-temperature and medium-pressure metamorphism related to crustal thickening of the southern Karakoram. This M2 event represents the timing of major thickening, shortening, burial, heating, and exhumation. The M3 event is the contact thermal aureole surrounding both margins of the 21 Ma Baltoro granite intrusion [*Searle and Tirrul*, 1991]. M4 is the youngest phase of metamorphism dated in the Karakoram and represents a high-temperature sillimanite grade metamorphism affecting Precambrian basement crust exposed in gneiss domes (e.g., Dassu gneiss) along the hanging wall of the Main Karakoram Thrust [*Searle et al.*, 1989; *Fraser et al.*, 1999].

6. Tectonic Evolution of the Hunza Karakoram

6.1. Late Cretaceous - Early Tertiary

The youngest marine sediments in the Karakoram terrane are Late Jurassic [*Gaetani and Garzanti*, 1991], and in the Lhasa Block of south Tibet they are middle Cretaceous [*Murphy et al.*, 1997]. After this, the Karakoram and south Tibet evolved into an uplifted Andean-type continental margin with multiple parallel batholiths or plutons composed of hornblende and biotite-bearing granodiorites and granites. Along the KKH section the Hunza plutonic unit formed the main batholith with minor intrusions to the north, such as the Warbin, Khunjerab, and Sost plutons intruding late Paleozoic and Mesozoic sediments of the northern Karakoram (Figure 8a). The HPU probably had extrusive volcanic rocks at upper crustal levels, but these have been eroded away. The thick marbles in the metamorphic series to the south of the batholith in Hunza probably had a protolith similar to that of the thick carbonates of the Permo-Triassic and Jurassic sediments to the north (Figure 8a). Deformation including folding and thrusting of the northern sedimentary belt occurred during the middle and Late Cretaceous. In common with south Tibet [*England and Searle*, 1986; *Murphy et al.*, 1997], much of the crustal shortening seems to have occurred prior to the India - Asia collision. New U-Pb data of *Fraser et al.* [1999] also shows that at least some of the sillimanite grade metamorphism in Hunza occurred prior to the India-Asia collision but after the Kohistan-Karakoram collision.

The Shyok suture zone closed during this period with the docking of Kohistan to Asia and the switch from subduction north of Kohistan to the main north dipping subduction zone along the southern margin of Kohistan (MMT). Basic dikes of the Jutal swarm intruded at ~75 Ma and crosscut closure-related fabrics along the SSZ [*Petterson and Windley*, 1985, 1991; *Coward et al.*, 1986, 1987].

6.2. Eocene

Postcollisional crustal thickening and metamorphism appears to have initiated along the site of the precollisonal Karakoram batholith and not along the SSZ (Figure 8). The Batura unit granites are more felsic than the HPU, related to lower crustal melting with some possible mantle imput [*Debon*, 1995], and intrude along the northern margin of the batholith (Figure 8b). Field evidence suggests that the site for large-scale melting occurred along the trace of the old batholith, with Hunza dikes forming up to 40% of the batholith in places. Sillimanite grade metamorphism occurred south of the batholith during a high-temperature metamorphic event (M2), possibly associated with a large melt zone hidden at depth in the lower crust. South or SW vergent thrusting emplaced the HPU over the sillimanite grade gneisses to the south. The late, set 2 Hunza dikes crosscut south vergent fabrics in the granite and in the sillimanite grade rocks to the south (Figure 8c). Surprisingly, at this time the southernmost Karakoram rocks, which were the protolith for the staurolite grade metamorphism, were still apparently unaffected by metamorphism or burial.

6.3. Miocene

Large-scale crustal melting occurred along the Baltoro plutonic unit to the east of Hunza during the latest Oligocene - early Miocene (~25 - 21 Ma). In the Hunza valley no major magmatism has been dated at this time (Figure 3), with the Hunza dikes being older (51 and 35 Ma) [*Fraser et al.*, 1999] and the Sumayar pluton being younger (9 Ma) [*Fraser et al.*, 1999]. The southern Karakoram in the Hunza region was finally subjected to crustal thickening, which resulted in the medium-pressure, medium-temperature metamorphism up to staurolite (and in a few places, kyanite) grade (Figure 8d). Postmetamorphic thrusting placed the sillimanite grade rocks southward over the staurolite grade rocks after 14 Ma. South vergent thrusting later propagated to the late Miocene - Pliocene Main Karakoram Thrust, which follows the trace of the SSZ and places the Karakoram metamorphic complex over rocks of the SSZ. Crustal melting continued at depth with crystallization of the Sumayar leucogranite at 9.2 ± 0.1 Ma [*Fraser et al.*, 1999], the youngest event in the Karakoram dated so far.

7. Discussion and Conclusions

A review of the geology of Kohistan and the Hunza Karakoram, coupled with recent data on the timing of metamorphism, magmatism, and deformation events, has resulted in speculative models for the tectonic evolution of Kohistan and the Hunza Karakoram presented here. These models are far from perfect and are based on the geological and geochronological data set up until the present time. They will change as more data become available. However, several important new points can be gleaned from the tectonic models presented here. These are summarized in sections 7.1-7.3.

7.1. Kohistan Arc Evolution

The Kohistan terrane is one of the best exposed and most complete sections through an obducted and uplifted island arc. It is a composite arc terrane composed of multiple episodes of arc magmatism. Early subduction-related arc sequences (Jijal complex remnant arc) were subducted to depths of more than ~45 km and subjected to high-pressure and high-temperature granulite facies metamorphism. Upper mantle peridotites and lower crustal gabbro-norites have been preserved, either as obducted ophiolitic complexes or as intrusive lower crustal magma chambers, along southern Kohistan. The main island arc sequence was constructed on metavolcanic amphibolites with MORB chemistry. The geochemistry of all other rocks in Kohistan shows a subduction component. The Chilas complex gabbro-norites represent a subarc magma chamber of exceedingly large proportions, probably made up of several batches of magma, intruded into the lower crust.

Northern Kohistan was composed of low-grade metasedimentary rocks which form the base of thick sequences of Late Cretaceous and Paleocene basaltic andesites and ignimbrites. Boninites are widespread in the Chalt volcanics along northern Kohistan, which led *Khan et al.* [1997] to propose an early (~100 Ma) southward dipping subduction zone from the Shyok ocean beneath Kohistan (Figure 5, model B). This situation could have a present-day analogue in the Mariana island arc system of the western

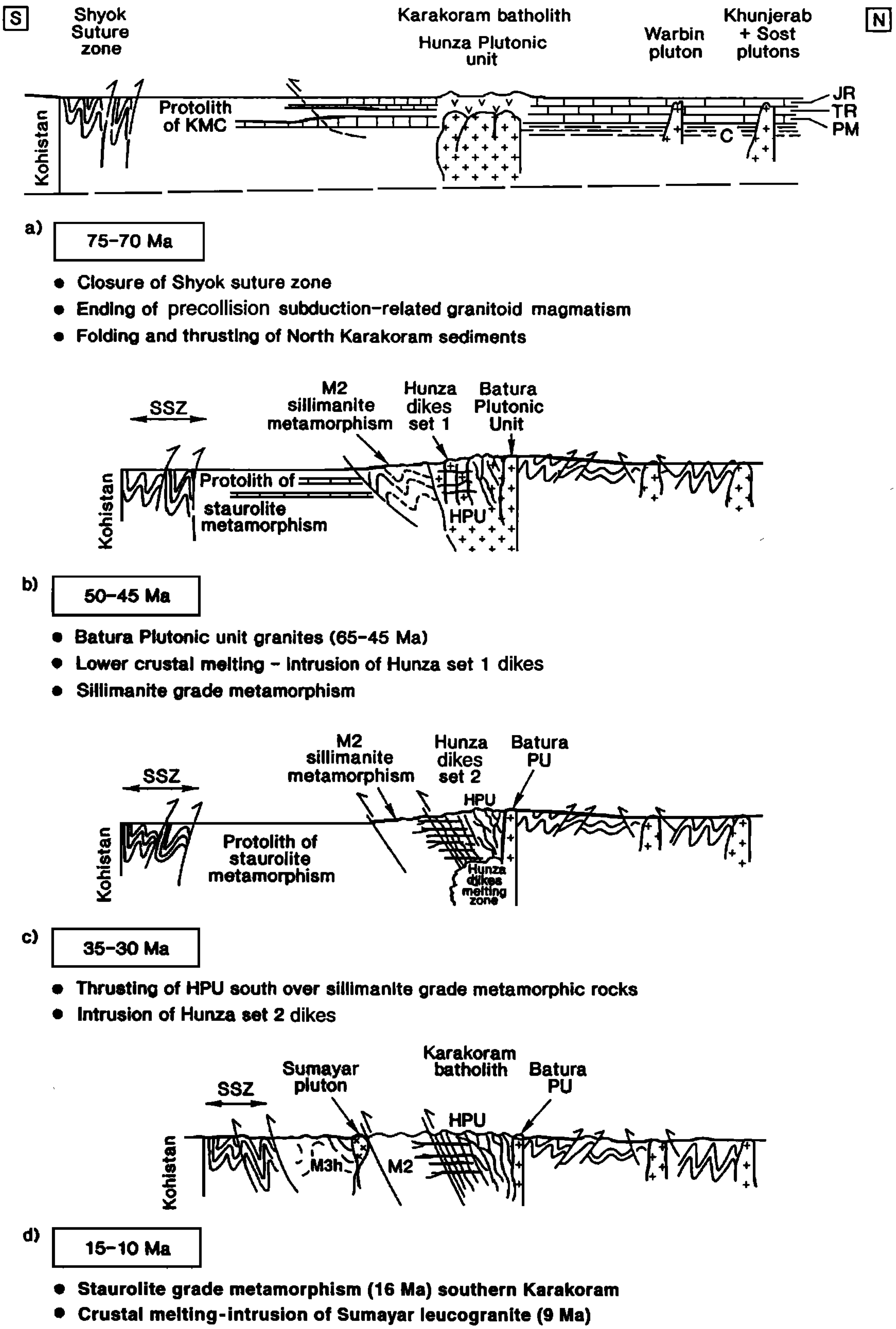

Figure 8. Model for the tectonic evolution of the Hunza Karakoram (see text for discussion): (a) 75-70 Ma, (b) 50-45 Ma, (c) 35-30 Ma, and (d) 15-10 Ma. KMC, Karakoram metamorphic complex; JR, Jurassic; TR, Triassic; PM, Permian; C, Carboniferous; HPU, Hunza plutonic unit; SSZ, Shyok suture zone; M2, M3 refer to metamorphic phases described in text.

Pacific where backarc rifting produced marginal basins such as the west Mariana and Parece Vela basins underlain by MORB-type ocean floor volcanics [*Dietrich et al.*, 1978] leaving older, remnant arcs such as the West Mariana ridge and the Kyushu–Palau ridge some distance away from the subduction front [*Karig*, 1971,a,b, 1972]. In the Kohistan situation the intrusive Chilas magma chamber would have intruded the MORB-related amphibolites of the Kamila Group in an intra-arc setting. The active mid-Cretaceous arc would have occurred to the north (Chalt–Dras arc volcanics) with boninites along the trench forearc region as in the Bonin–Mariana active arc today. However, there is still a big difference in scale. The Kohistan–Dras arc exposed today is around 500 km long from eastern Afghanistan to western Ladakh, whereas the Phillipine arc is some 2000 km long and the Bonin–Mariana arc, in its complete length from Palau to Japan, is some 3000 km long.

In Kohistan the main, later subduction event was, however, from the main Neo-Tethys ocean south of Kohistan, dipping north under the arc. We interpret the subduction zone along the Main Mantle Thrust to have propagated southward with time from an early high-temperature as well as high-pressure subduction, resulting in the subduction of a remnant arc, the metamorphism of the lower arc crust to granulite facies (Jijal complex), and a later medium-temperature and medium-pressure subduction creating the blueschists at Shangla and obduction of the dismembered ophiolite complexes. The entire northern part of the composite Kohistan arc terrane was intruded by early granitoid plutons, which are commonly composed of hornblende-bearing diorites and granodiorites along northern Kohistan, when Kohistan was still a separated, intra-oceanic island arc terrane. These early granitoids were subsequently deformed and intruded by later undeformed plutons during and after the collision with the Asian (Karakoram) plate to the north and the closing of the Shyok suture zone.

7.2. Metamorphic Events in the Karakoram Crust

Following the closure of the Shyok suture zone, crustal thickening, deformation, and metamorphism affected the Karakoram terrane. The earliest metamorphic event along the southern Karakoram was a widespread andalusite + garnet grade static metamorphism spatially associated with precollisional deformed granodiorites [*Searle et al.*, 1989]. The heat source for this HT-LP metamorphism was probably magmatic and may have been associated with some unquantifiable amount of Andean-type crustal thickening and orogenesis along the southern margin of Asia.

Previous interpretations suggested that the postcollisional southern Karakoram metamorphism was one continuous episode from ~50 to 37 Ma [*Searle and Tirrul*, 1991]. However, recent new U-Pb dating of metamorphic monazite and magmatic zircon, monazite and uraninite from crosscutting dikes in Hunza [*Fraser et al.*, 1999] has distinguished two distinct phases of postcollisional metamorphism in the southern Karakoram (Figure 3). The earliest metamorphism (M1) was a widespread sillimanite grade event affecting rocks south of the precollisional Hunza plutonic unit dated at 64.2 ± 0.8 Ma and may have continued until the second sillimanite–kyanite grade event dated at 44 ± 2 Ma [*Fraser et al.*, 1999]. Sillimanite grade metamorphism may have been a long lasting event but must have been over before intrusion of the 35 Ma set 1 Hunza dikes, which crosscut all syn-metamorphic deformation fabrics south of the Karakoram batholith. We speculate that the heat source for this metamorphism was a high heat flow caused by the docking of a recent and still active large island arc complex (Kohistan). The ultimate driving force for all the postcollisional metamorphic events in the Karakoram must have been the collision and continuing northward indentation of first, Kohistan, and later, India into Asia, causing ongoing crustal shortening and thickening.

The third phase (M3) of postcollisional metamorphism in the KKH section along the Hunza valley is characterized by staurolite grade metapelites which have been dated at 16 Ma using U-Pb on metamorphic monazite [*Fraser et al.*, 1999]. This is at least 20 Myr younger (possibly 50 Ma) than the sillimanite grade event. Our model (Figure 8) is consistent with the southward propagation of thrusting from the pre-35 Ma-thrust which places the HPU over the sillimanite gneisses to the Pliocene-Pleistocene Main Karakoram Thrust along the southern boundary of the Karakoram. The puzzling fact to explain is why the protolith rocks of the staurolite grade schists along the southern Karakoram remained unmetamorphosed for so long, when they were adjacent to the highly deformed rocks of the SSZ to the south and the deformed, metamorphosed, and very hot rocks of the sillimanite grade gneisses to the north.

Our conclusion is that regional metamorphic terranes, such as the southern Karakoram, can no longer be assumed to be all related to one event. Structural studies, combined with U-Pb geochronology, have shown that major metamorphic events could be both very long-lasting (up to 20 Ma) and very restrictive, both in time and space, and may also be very different along the strike of the mountain range. It is likely that with more detailed geochronology, combined with thorough field structural relationships, a much more detailed picture of the pressure-temperature-time (P-T-t) evolution will emerge with time, with several "episodes" of metamorphism within the broad spectrum of postcollisional crustal thickening. It is proposed that the major, regional M1-M2 metamorphism in the southern Karakoram could be more related to crustal thickening and heating after the Asia-Kohistan collision during the late Cretaceous rather than to the India-Asia collision during the early Eocene.

7.3. Crustal Melting in the Karakoram

There is also increasing evidence of multiple episodes of postcollisional crustal melting across the Karakoram. Most of the Karakoram batholith in the Hunza section is the precollisional, Andean-type Hunza plutonic unit, related to northward subduction of Tethyan oceanic crust beneath the southern margin of Asia. The granodiorites of the HPU have been intruded by a vast network of postcollisional monzogranite to leucogranite dikes. These Hunza dikes were intruded during several episodes, an early set (51.5 ± 1 Ma) prior to southward thrusting of the HPU and a later set (35.1 ± 0.6 Ma) clearly post-thrusting, with dikes cutting the deformation fabrics. Within each set there are also several crosscutting dikes, but the broad subdivision of set 1 deformed, and set 2 crosscutting dikes remains valid. It is possible that we are only seeing the upper crustal part of an unexposed deep crustal melt zone (Figure 8c), which released crustal melt granites episodically from middle Eocene time up to the late Miocene or Pliocene. Low $^{87}Sr/^{86}Sr$ initial ratios suggest that although the granites are interpreted to be continental crustal melts, there may have been some mantle-related magmatic underplating beneath the southern Karakoram which provided an extra heat source and could account for the Sr and Nd isotopic ratios in the Baltoro granites and the Hunza dikes [*Searle et al.*, 1992; *Crawford and Searle*, 1993].

Localized, postcollisional leucogranites in the northern part of the Kohistan terrane, such as the Parri aplite sheets and Jaglot granite [*George et al.*, 1995], may also be related to this phase. The major Baltoro plutonic unit, which is located east of Hunza, has been dated by U-Pb on zircon and monazite at 25-21 Ma [*Parrish and Tirrul*, 1989; *Schärer et al.*, 1990] and the youngest crustal melting event dated in the Karakoram is the localized 9.2 ± 0.1 Ma Sumayar leucogranite in Hunza [*Fraser et al.*, 1999]. The youngest undated intrusive events are a series of pegmatite and aplite dikes which crosscut all previous structures and occur along the Karakoram and also in the Haramosh massif, the northwestern spur of the High Himalaya (Figure 2). These pegmatites contain gem-quality aquamarine (beryl), tourmaline, muscovite, biotite, and garnet. They are probably temporally related to the Pliocene – Pleistocene (5-1 Ma) high-temperature (sillimanite + cordierite grade) metamorphism and melting in the Nanga Parbat massif to the south [*Smith et al.*, 1992; *Zeitler et al.*, 1993].

Acknowledgments. This work was funded by NERC grant GT5/96/13/E to MPS, NERC D.Phil studentships to JF and SG, and a Commonwealth Scholarship to Asif Khan, which also enabled him to visit Oxford for a year. We are grateful to all these funding agencies and also to Randy Parrish and Steve Noble for extensive and valuable help with U-Pb dating at NIGL Keyworth. We appreciate discussions with Peter Treloar, Jean-Pierre Burg, and Rashid Khan Tahirkheli and constructive reviews from Susan DeBari and an anonymous reviewer.

References

Anczkiewicz, R., F. Oberli, J.P.Burg, M. Meier, H. Dawood, and S. Hussein, Magmatism south of the Indus suture, lower Swat, Pakistan. (abstract) 13th Himalaya-Karakoram-Tibet Workshop, *Geol. Bull. Univ. Peshawar, 31,* 7-9, 1998.

Arbaret, L., J.P. Burg, N Chaudhry, H. Dawood, S Hussain and G. Zeilinger, Different sets of anastomosing shearzones in the Kamila Belt, Kohistan, (abstract) 13th Himalaya-Karakoram-Tibet Workshop, *Geol. Bull. Univ. Peshawar, 31,* 15-17, 1998.

Arif, M., A.E. Fallick and C.J. Moon, The genesis of emeralds and their host rocks from Swat, northwestern Pakistan: A stable-isotope investigation, *Miner. Deposita, 31,* 255-268, 1996.

Bard, J.P., Metamorphism of an obducted island arc: Example of the Kohistan sequence (Pakistan) in the Himalayan collided range, *Earth Planet. Sci. Lett., 65,* 133-144, 1983.

Beck, R.A. et al., Stratigraphic evidence for an early collision between northwest India and Asia, *Nature, 373,* 55-57, 1995.

Bertrand, J.M., J.R. Kienast, and J.L. Pinardon, Structure and metamorphism of the Karakoram gneisses, in the Braldu Baltoro valley (north Pakistan), *Geodyn. Acta, 2,* 135-150, 1988.

Burg, J.P., M.N. Chaudhry, M. Ghazanfar, R. Anczkiewicz, and D. Spencer, Structural evidence for back sliding of the Kohistan arc in the collisional system of northwest Pakistan, *Geology, 24,* 739-742, 1996.

Butler, R., and D.J. Prior, Tectonic controls on the uplift of the Nanga Parbat massif, Pakistan Himalaya, *Nature, 333,* 247-250, 1988.

Coward, M.P., B.F. Windley, R.D. Broughton, I.W. Luff, M.G. Petterson, C.J. Pudsey, D.C. Rex, and M.A. Khan, Collision tectonics in the NW Himalayas, in *Collision Tectonics,* edited by M.P. Coward and A.C. Ries, *Spec. Publ. Geol. Soc. London, 19,* 203-219, 1986.

Coward, M.P., R.W.H. Butler, M. A. Khan, and R.J. Knipe, The tectonic history of Kohistan and its implications for Himalayan structure, *J. Geol. Soc. London, 144,* 377-391, 1987.

Crawford, M.B., Leucogranites of the NW Himalaya: Crust-mantle interaction beneath the Karakoram and the magmatic evolution of collisional belts, Ph.D. thesis, University of Leicester, Leicester, England, 1988.

Crawford, M.B. and Searle, M.P. Field relations and geochemistry of pre-collisional (India - Asia) granitoid magmatism in the central Karakoram, northern Pakistan. *Tectonophysics, 206,* 171-192, 1992.

Crawford, M.B. and M.P. Searle, Collision-related granitoid magmatism and crustal structure of the Hunza Karakoram, north Pakistan, in: Treloar, P.J. and Searle, M.P. *Himalayan Tectonics* edited by P.J. Treloar and M.P. Searle, *Geol. Soc., London, Spec. Publ. 74,* 53-68, 1993.

Debon, F., Incipient India-Eurasia collision and plutonism: The lower Cenozoic Batura granites (Hunza Karakorum, north Pakistan), *J. Geol. Soc., London, 152,* 785-795, 1995.

Debon, F., P. LeFort, D. Dautel, J. Sonet, and J. Zimmerman, Granites of western Karakoram and northern Kohistan (Pakistan): A composite mid-Cretaceous to upper Cenozoic magmatism, *Lithos, 20,* 19-40, 1987.

deSigoyer, J., V. Chavagnac, J. Baldwin, B. Luais, J. Toft, I. Villa, and S. Guillot, Timing of HP-LT Tso Morari evolution: From continental subduction to collision in NW Himalaya., (abstract), *Terra Nostra, 99/2,* 141, 1999.

Desio, A., and E. Martina, Geology of the upper Hunza valley, Karakorum, west Pakistan, *Boll. Soc. Geol. Ital., 91,* 283-314, 1972.

Dietrich, V., R. Emmermann, R. Oberhansli, and H. Puchelt, Geochemistry of basaltic and gabbroic rocks from the West Mariana Basin and Mariana trench. *Earth Planet. Sci. Lett., 39,* 127-144, 1978.

DiPietro, J.A., Metamorphic pressure-temperature conditions of Indian plate rocks south of the Main Mantle thrust, Lower Swat, Pakistan, *Tectonics, 10,* 742-757, 1991.

DiPietro, J.A., K.R. Pogue, R.D. Lawrence, M.S. Baig, A. Hussain, and I. Ahmed, Stratigraphy south of the Main Mantle Thrust, Lower Swat, Pakistan, in *Himalayan Tectonics,* edited by P.J. Treloar and M.P. Searle, *Geol. Soc., London, Spec. Publ. 74,* 207-220, 1993.

England, P.C., and M.P. Searle, The Cretaceous-Tertiary deformation of the Lhasa Block and its implications for the crustal thickening of Tibet, *Tectonics, 5,* 1-14, 1986.

Fraser, J., M.P. Searle, R. Parrish, and S. Noble, U-Pb geochronology on the timing of metamorphism and magmatism in the Hunza Karakoram. (abstract) *Terra Nostra 99/2,* 45-46, 1999.

Gaetani, M., and E. Garzanti, Multicyclic history of the northern India continental margin (Northwestern Himalaya), *AAPG Bull., 75,* 1427-1446, 1991.

Garzanti, E., and T. van Haver, The Indus clastics: Forearc basin sedimentation in the Ladakh Himalaya, *Sediment. Geol., 59,* 237-249, 1988.

George, M.T., N.B.W. Harris, and R.W.H. Butler, The tectonic implications of contrasting post-collisional magmatism between the Kohistan island arc and Nanga Parbat-Haramosh massif, Pakistan Himalaya, in *Himalayan Tectonics,* edited by P.J. Treloar and M.P. Searle, *Geol. Soc. London, Spec. Publ. 74,* 173-191, 1993.

George, M., S. Reddy, and N. Harris, Isotopic constraints on the cooling history of the Nanga Parbat - Haramosh massif and Kohistan arc, western Himalaya, *Tectonics, 14,* 237-252, 1995.

Green, D.H., Experimental testing of equilibrium partial melting of peridotite under water saturated high pressure conditions, *Can. Mineral., 14,* 225-268, 1976.

Honegger, K., V. Dietrich, W. Frank, A. Gansser, M. Thoni, and V. Trommsdorf, Magmatism and metamorphism of the Ladakh Himalayas (the Indus-Tsangpo suture zone), *Earth Planet. Sci. Lett., 60,* 253-292, 1982.

Jackson, J, and G. Yielding, The seismicity of Kohistan, Pakistan: Source studies of the Hamran (1972.9.3), Darel (1981.9.12) and Patan (1974.12.28) earthquakes, *Tectonophysics, 91,* 15-28, 1998.

Jan, M.Q., and R.A. Howie, Ortho- and clinopyroxenes from pyroxene granulites of Swat Kohistan, northern Pakistan, *Mineral. Mag., 43,* 715-728, 1980.

Jan, M.Q., and R.A. Howie, The mineralogy and geochemistry of the metamorphosed basic and

ultrabasic rocks of the Jijal complex, Kohistan, NW Pakistan, *J. Petrol. 22*, 85-126, 1981.
Jan, M.Q., M.A. Khan, and M.S. Qazi, The Sapat mafic-ultramafic complex, Kohistan arc, north Pakistan, in *Himalayan Tectonics*, edited by P.J. Treloar and M.P. Searle, *Spec. Publ. Geol. Soc. London., 74*, 113-121, 1993.
Karig, D.E., Structural history of the Mariana Island Arc System, *Geol. Soc. Am. Bull., 82*, 323-344,. 1971a.
Karig, D.E., Origin and development of marginal basins in the western Pacific, *J. Geophys. Res., 76*, 2542-2561, 1971b.
Karig, D.E., Remnant arcs, *Geol. Soc. Am. Bull., 83*, 1057-1068, 1972.
Kazmi, A.H., and M.Q. Jan, *Geology and Tectonics of Pakistan*, 554 pp., Graphic, Karachi, Pakistan, 1997.
Khan, M.A., M. Qasim Jan, B.F. Windley, J. Tarney, and M.F. Thirlwall, The Chilas mafic - ultramafic igneous complex: The root of the Kohistan island arc in the Himalaya of northern Pakistan, *Spec. Pap. Geol. Soc. Am.,. 232*, 75-94, 1989.
Khan, M.A., M.Q. Jan, and B.L. Weaver, Evolution of the lower arc crust in Kohistan: Temporal arc magmatism through early, mature and intra-arc rift stages, in *Himalayan Tectonics*, edited by P.J. Treloar and M.P. Searle, *J. Geol. Soc. London, Spec. Publ. 74*, 123-138, 1993.
Khan, M.A., R.J. Stern, R.F. Gribble, and B.F. Windley, Geochemical and isotopic constraints on subduction polarity, magma sources and palaeogeography of the Kohistan intra-oceanic arc, northern Pakistan Himalaya, *J. Geol. Soc., London, 154*, 935-946, 1997.
LeFort, P., F. Debon, and J. Sonet, Petrography, geochemistry and geochronology of some samples from the Karakoram batholith (N. Pakistan), in *Granites of Himalayas, Karakoram and Hindu Kush.* edited by F.A. Shams, pp. 377-387, Punjab Univ., Lahore, Pakistan, 1983.
Maluski, H., and P. Matte, Ages of Alpine tectonometamorphic events in the northwestern Himalaya (northern Pakistan) by the $^{39}Ar/^{40}Ar$ method. *Tectonics, 3*, 1-18, 1984.
Miller, D.J., R.R. Loucks, and M. Ashraf, Platinum-group element mineralization in the Jijal layered ultramafic-mafic complex, Pakistani Himalaya, *Econ. Geol. 86*, 1093-1102, 1991.
Murphy, M.A., A. Yin, T.M. Harrison, S.B. Durr, W.S.F. Kidd, Z. Chen, F.J. Ryerson, X. Wang, and X. Zhou, Significant crustal shortening in south-central Tibet prior to the Indo-Asian collision, *Geology, 25*, 719-722, 1997.
O'Brien, P.J., N. Zotov, R. Law, M.A. Khan, and Q. Jan, Coesite in eclogite from the upper Kaghan Valley, Pakistan: A first record and implications. (abstract), *Terra Nostra, 99(2)*, 109, 1999.
Parrish, R.R., and R. Tirrul, U-Pb age of the Baltoro granite, northwest Himalaya, and implications for zircon inheritance and monazite U-Pb systematics, *Geology, 17*, 1076-1079, 1989.
Pearce, J.A., T. Alabaster, A.W. Shelton, and M.P. Searle, The Oman Ophiolite as a Cretaceous arc-basin complex: Evidence and implications, *Philos. Trans. R. Soc., London, Ser. A, 300*, 299-317, 1981.
Petterson, M.G., and B.F. Windley, Rb-Sr dating of the Kohistan arc batholith in the Himalaya of N. Pakistan and tectonic implications, *Earth Planet. Sci. Lett. 74*, 54-75, 1985.
Petterson, M.G., and B.F. Windley, Changing source regions of magmas and crustal growth in the Trans-Himalayas: Evidence from the Chalt volcanics and Kohistan batholith, Kohistan, N. Pakistan, *Earth Planet. Sci. Lett. 102*, 326-346, 1991.
Petterson, M.G., B.F. Windley, and I.W. Luff, The Chalt volcanics, Kohistan, Pakistan: High-Mg tholeiitic and low-Mg calc-alkaline volcanism in a Cretaceous island arc, *Phys. Chem. Earth, 17*, 19-30, 1990.
Pudsey, C.J., The Northern Suture, Pakistan: Margin of a Cretaceous island arc, *Geol. Mag., 123*, 405-423, 1986.
Pudsey, C.J., M.P. Coward, I.W. Luff, R.M. Shackleton, B.F. Windley, and M.Q. Jan, Collision zone between the Kohistan arc and the Asian plate in NW Pakistan, *Trans. R. Soc. Edinburgh Earth Sci., 76*, 463-479, 1985.
Reuber, I, The Dras arc: Two successive volcanic events on eroded oceanic crust, *Tectonophysics, 161*, 93-106, 1989.
Rex, A.J., M.P. Searle, R. Tirrul, M.B. Crawford, D.J. Prior, D.C. Rex, and A. Barnicoat, The geochemical and tectonic evolution of the central Karakoram, north Pakistan, *Philos. Trans. R. Soc., London, Ser. A, 326*, 229-255, 1988.
Ringuette, L., J. Martignole, and B.F. Windley, Magmatic crystallization, isobaric cooling, and decompression of the garnet-bearing assemblages of the Jijal sequence (Kohistan terrane, western Himalayas), *Geology, 27*, 139-142, 1999.
Schärer, U., J. Hamet, and C.J. Allegre, The Trans-himalaya (Gangdese) plutonism in the Ladakh region: A U-Pb and Rb-Sr study, *Earth Planet. Sci. Lett., 67*, 327-339, 1984.
Schärer, U., P. Copeland, T.M. Harrison, and M.P. Searle, Age, cooling history and origin of post-collisional leucogranites in the Karakoram batholith: A multi-system isotope study, N. Pakistan, *J. Geol., 98*, 233-251, 1990.
Searle, M.P., *Geology and Tectonics of the Karakoram Mountains*, 358 pp., John Wiley, Chichester, 1991.
Searle, M.P, Cooling history, erosion, exhumation and kinematics of the Himalaya - Karakoram - Tibet orogenic belt, in *The Tectonic Evolution of Asia*, edited by A. Yin and T.M. Harrison, pp. 110-137, Cambridge Univ. Press, New York, 1996.
Searle, M.P., and M. Asif Khan, *Geological map of north Pakistan and adjacent areas of northern Ladakh and western Tibet*, scale 1:650,000, Oxford Univ., Oxford, England, 1996.
Searle, M.P., and J.S. Cox, Tectonic setting, origin and obduction of the Oman ophiolite, *Geol. Soc. Am. Bull., 111*, 104-122, 1999.
Searle, M.P., and R. Tirrul, Structural and thermal evolution of the Karakoram crust, *J. Geol. Soc., London, 148*, 65-82, 1991.
Searle, M.P., et al., The closing of Tethys and the tectonics of the Himalaya, *Geol. Soc. Am. Bull., 19*, 1-12, 1987.
Searle, M.P., D.J.W. Cooper, and A.J. Rex, Collision tectonics in the Ladakh - Zanskar Himalaya, *Philos. Trans. R. Soc., London, Ser. A, 326*, 117-150, 1988.
Searle, M.P., A.J. Rex, R. Tirrul, D.C. Rex, A. Barnicoat, and B.F. Windley, Metamorphic, magmatic and tectonic evolution of the Central Karakoram in the Biafo-Baltoro-Hushe regions of north Pakistan, *Spec. Pap. Geol. Soc. Am., 232*, 47-73, 1989.
Searle, M.P., R.R. Parrish, R. Tirrul, and D.C. Rex, Age of crystallization and cooling of the K2 gneiss in the Baltoro Karakoram, *J. Geol. Soc. London, 147*, 603-606, 1990a.
Searle, M.P., K. Pickering, and D.J.W. Cooper, Restoration and evolution of the intermontane Indus molasse basin, Ladakh Himalaya, India, *Tectonophysics, 174*, 301-314, 1990b.
Searle, M.P., M.B. Crawford, and A.J. Rex, Field relations, geochemistry, origin and emplacement of the Baltoro granite, Central Karakoram, *Trans. R. Soc. Edinburgh Earth Sci., 83*, 519-538, 1992.
Searle, M.P., D.J. Waters, H.C. Martin, and D.C. Rex, Structure and metamorphism of blueschist – eclogite facies rocks from the northeastern Oman Mountains, *J. Geol. Soc., London, 151*, 555-576, 1994.
Smith, H.A., C.P. Chamberlain, and P.K. Zeitler, Documentation of Neogene regional metamorphism in the Himalayas of Pakistan using U-Pb in monazite, *Earth Planet. Sci. Lett., 113*, 93-105, 1992.
Smith, H.A., P.K. Zeitler, and C.P. Chamberlain, Timing and duration of Himalayan metamorphism within the Indian plate, northwest Himalaya, Pakistan, *J. Geol., 102*, 493-508, 1994.
Sullivan, M.A., B.F. Windley, A.D. Saunders, J.R. Haynes, and D.C. Rex, A palaeogeographic reconstruction of the Dir Group: Evidence for magmatic arc migration within Kohistan, N. Pakistan, in *Himalayan Tectonics*, edited by P.J. Treloar and M.P. Searle, *Geol. Soc. London, Spec. Publ. 74*, 139-160, 1993.
Tahirkheli, R.A.K., Geology of the Himalaya, Karakoram and Hindukush in Pakistan, *Geol. Bull., Univ. Peshawar, 15*, 1-51, 1982.
Tahirkheli, R.A.K., and M.Q. Jan, A preliminary geological map of Kohistan and adjoining areas, N. Pakistan, *Geol. Bull. Univ. Peshawar, 11*, 1979.
Tahirkheli, R.A.K., M. Mattauer, F. Proust, and P. Tapponnier. The India-Eurasia suture zone in northern Pakistan: Synthesis and interpretation of recent data at plate scale, in *Geodynamics of Pakistan*, edited by A. Farah and K.A. Dejong, pp. 125-130, Geol. Surv. of Pakistan, Quetta, Pakistan, 1979.
Tonarini, S., I. Villa, F. Oberli, M. Meier, D.A. Spencer, U. Pognante, and J.G. Ramsay, Eocene age of eclogite metamorphism in Pakistan Himalaya: Implications for India-Eurasia collision, *Terra Nova, 5*, 13-20, 1993.
Treloar, P.J., and D.C. Rex, Cooling and uplift histories of the crystalline thrust stack of the Indian Plate internal zones west of Nanga Parbat, Pakistan Himalaya, *Tectonophysics, 180*, 323-349, 1990.
Treloar, P.J., D.C. Rex, P.G. Guise, M.P. Coward, M.P. Searle, B.F. Windley, M.G. Petterson, M.Q. Jan, and I.W. Luff, K/Ar and Ar/Ar geochronology of the Himalayan collision in NW Pakistan: constraints on the timing of suturing, deformation, metamorphism and uplift. *Tectonics, 8*, 881-909, 1989a.
Treloar, P.J., M.P. Coward, and M.P. Williams, Metamorphism and crustal stacking in the north Indian plate, north Pakistan, *Tectonophysics, 165*, 167-184, 1989b.
Treloar, P.J., R.D. Broughten, M.P. Coward, M.P. Williams, and B.F. Windley, Deformation, metamorphism and imbrication of the Indian plate south of the MMT, north Pakistan, *J. Metamorph. Geol., 7*, 111-127, 1989c.
Treloar, P.J., K.H. Brodie, M.P. Coward, M.Q. Jan, R.J. Knipe, D.C. Rex, and M.P. Williams, The evolution of the Kamila shear zone, Kohistan, Pakistan, in *Exposed Cross-Sections of the Continental Crust*, edited by M.H. Salisbury and D.M. Fountain, pp. 175-214, Kluwer Acad. Norwell, Mass , 1990.
Treloar, P.J., M. G. Petterson, M.Q. Jan, and M.A. Sullivan, A re-evaluation of the stratigraphy and evolution of the Kohistan arc sequence, Pakistan Himalaya: Implications for magmatic and tectonic arc-building processes, *J. Geol. Soc. London, 153*, 681-693, 1996.
Vince, K.J., and P.J. Treloar, Miocene north-vergent extensional displacements along the Main Mantle Thrust, NW Himalaya, Pakistan, *J. Geol. Soc. London, 153*, 677-680, 1996.
Winslow, D.M., P.K. Zeitler, C.P. Chamberlain, and I.S. Williams, Geochronologic constraints on syntaxial development in the Nanga Parbat region, Pakistan, *Tectonics, 15*, 1292-1308, 1996.

Yamamoto, H, and E. Nakamura, Sm-Nd dating of garnet granulites from the Kohistan complex, northern Pakistan, *J. Geol. Soc. London, 153*, 965-969, 1996.

Zeilinger, G., L. Arbaret, J.P. Burg, N. Chaudhry, H. Dawood, and S. Hussain, Structures in the lower units of the Kohistan arc, NW Pakistan: Preliminary results, 13th Himalaya-Karakoram-Tibet Workshop, *Geol. Bull. Univ. Peshawar, 31*, 224-227, 1998.

Zeitler, P.K, Cooling history of the NW Himalaya, Pakistan, *Tectonics, 4*, 127-151, 1985.

Zeitler, P.K., and C.P. Chamberlain, Petrogenetic and tectonic significance of young leucogranites from the northwestern Himalaya, Pakistan, *Tectonics, 10*, 729-741, 1991.

Zeitler, P.K., C.P. Chamberlain, and H.A. Smith, Synchronous anatexis, metamorphism and rapid denudation at Nanga Parbat (Pakistan Himalaya), *J. Geology, 21*, 347-350, 1993.

M. Asif Kahn and M. Qasim Jan, Center for Excellence in Geology, Peshawar University, Peshawar, North-West Frontier Province, Pakistan.

J.E. Fraser, S.J. Gough, and M.P. Searle, Department of Earth Sciences, Oxford University, Parks Road, Oxford OX1 3PR, England, U.K. mike.searle@earth.ox.ac.uk

(Received March 16, 1999;
revised July 13, 1999;
accepted July 23, 1999.)

TECTONICS, VOL. 18, NO. 6, PAGES 1178-1197 DECEMBER 1999

Timing and magnitude of rotations in the frontal thrust systems of southwestern Sicily

F. Speranza,[1] R. Maniscalco,[2] M. Mattei,[1] A. Di Stefano,[2] R. W. H. Butler,[3] and R. Funiciello[1]

Abstract. We report new paleomagnetic and anisotropy of magnetic susceptibility (AMS) results from upper Tortonian to middle Pleistocene sediments which were deposited upon and adjacent to active thrust structures in southwestern Sicily. The data show that the Plio-Pleistocene sediments from the Belice and Menfi basins (covering the Saccense shelf limestones) underwent any internal shortening after the early Pleistocene (Santernian), as well as any net rotation. Sediments around this area (which overlie basinal Meso-Cenozoic successions) record systematic rotations: one upper Tortonian site to the west is ~30° counterclockwise rotated, while to the east, lower Pliocene to middle lower Pleistocene sites within the Gela Nappe domain show 25° to 56° clockwise (CW) rotations. These data show that the ductile basinal sediments were bent and rotated around the rigid Saccense carbonates during the thin-skinned southward propagation of the orogenic front. We document here that the coastal sediments from the southwestern Gela Nappe underwent both a post middle early Pleistocene ~30°CW rotation and a post middle Pleistocene E-W to ESE-WNW flattening (revealed by AMS). Our data then constrain to the late Pleistocene-Holocene the age of the last shortening episode occurring in the southwestern Gela Nappe front. Pleistocene rotations of similar amount also characterize the Sicanian domain, implying that it was incorporated in the Gela Nappe wedge during the recentmost episodes of deformation. This evidence allows us to better understand the very large (up to 114°) post Mesozoic rotations reported by *Channell et al.* [1980, 1990] for the Sicanian limestones, as related to both Miocene (or older?) deformational episodes and the Plio-Pleistocene evolution of the Gela Nappe.

1. Introduction

During the last decades, paleomagnetic data from mountain belts have revealed that orogenic construction is commonly accompanied by significant rotations along vertical axes (for a synthesis, see *Van der Voo* [1993]). These rotations are widespread in those belts, such as the Mediterranean Alpine belt, which describe a large number of bends and arise from the collision of irregular continental margins.

[1]Dipartimento di Scienze Geologiche, Università di Roma Tre, Rome.
[2]Istituto di Geologia e Geofisica, Università di Catania, Catania, Italy.
[3]Department of Earth Sciences, University of Leeds, Leeds, England, United Kingdom.

[1]Now at Istituto Nazionale di Geofisica, Via di Vigna Murata 605, 00143 Roma, Italy.

Paper number 1999TC900029.
0278-7407/99/1999TC900029$12.00

Rotations can be faithfully recorded in preorogenic strata, but in Mediterranean and other orogens these strata may have undergone a long history of segmentation, involving basin formation and transtensive and oblique slip prior to final orogenic construction. Therefore it is desirable to trace paleomagnetic declination data within the synorogenic formations to "backstrip" the rotations. In peninsular Italy, classical paleomagnetic works during the 1970s focused on the pelagic limestones from the Mesozoic successions [*Lowrie and Alvarez*, 1974; *Channell and Tarling*, 1975], but it was later recognized that the observed rotations were due to the more recent Neogene episodes of Apennines building [*Channell*, 1992]. More recent work carried out on the synorogenic late Miocene to Pleistocene deposits [*Sagnotti*, 1992; *Mattei et al.*, 1995; *Speranza et al.*, 1997] revealed more clearly the time-related rotation evolution and emphasized the role played by thrust sheet emplacement and strike-slip fault activity.

In Italy, the largest rotations (over 130°) from preorogenic strata were observed in the Mesozoic-lower Tertiary pelagic limestones from Sicily [*Channell et al.*, 1980, 1990]. These rotations were referred to the late Miocene to Pleistocene major phases of shortening of the Sicilian Maghrebides [*Oldow et al.*, 1990], but data from the synorogenic successions themselves have been lacking, and the temporal evolution of the rotational process still remains largely speculative.

In this study, we report on new magnetic anisotropy and paleomagnetic data from southwestern Sicily, where a wealth of Plio-Pleistocene sediments crop out around the Mesozoic carbonates paleomagnetically studied by *Channell et al.* [1980, 1990]. These data help to better constrain the timing of the rotations observed in Mesozoic sediments, and they highlight the rotational relationships between the Gela Nappe and the western Sicilian belt. It is shown that the paleomagnetism alone does not allow a complete clarification of the tectonic evolution. A multidisciplinary approach combining geological, biostratigraphic, paleomagnetic, and structural data from small-scale structures is needed to unravel the tectonic style and to infer reliable shortening estimates.

2. Geological Setting of Sicily and Previous Paleomagnetic Data

The southern Apennines and the Sicilian Maghrebides form a large-scale arc, whose center is represented by the more advanced Calabro-Peloritan block (Figure 1). Subcrustal seismicity up to 500 km [*Gasparini et al.*, 1982] and mantle tomography [*Selvaggi and Chiarabba*, 1995] show the presence beneath the southern Tyrrhenian Sea of a seismically active Ionian slab. Deep sea drilling studies [*Kastens et al.*, 1986;

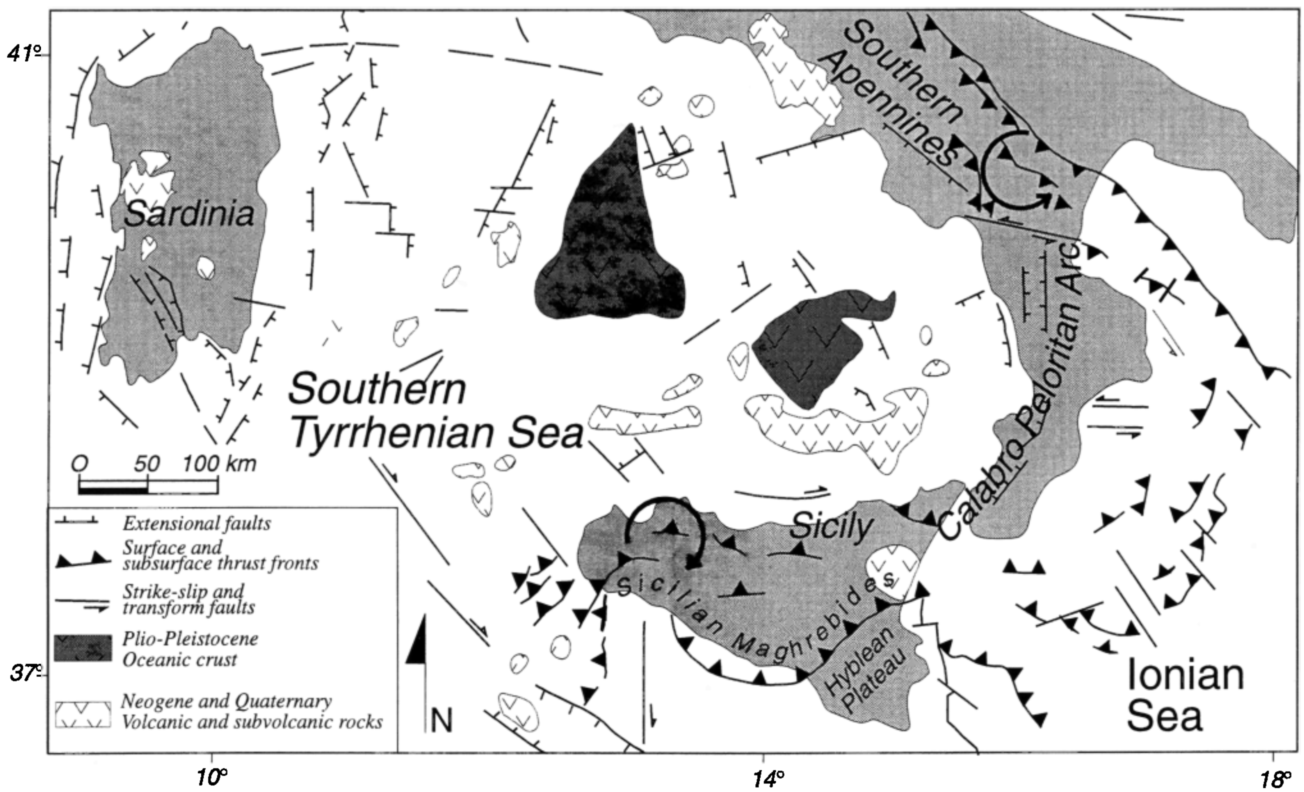

Figure 1. Tectonic scheme of the central Mediterranean. Circular arrows indicate counterclockwise and clockwise rotations observed in the southern Apennines [*Sagnotti*, 1992; *Scheepers et al.*, 1993] and Sicilian Maghrebides [*Channell et al.*, 1980, 1990], respectively.

Mascle et al., 1988] showed that the spreading of the southern Tyrrhenian Sea started during the Tortonian, as a consequence of the passive sinking of the Ionian lithosphere and the induced southestward migration of the Calabro-Peloritan block [*Malinverno and Ryan*, 1986].

In Sicily, three main tectonostratigraphic domains are observed: the southern termination of the Calabro-Peloritan Arc, the Maghrebian thrust belt, and the Hyblean Plateau (Figure 2). The Maghrebian thrust belt trends regionally east-west across Sicily [*Consiglio Nazionale delle Ricerche,* 1991], with the Gela Nappe forming a large arcuate salient along the thrust front. The Hyblean Plateau is the only emergent part of the African foreland [*Grasso et al.*, 1990; *Butler et al.*, 1992; *Lickorish et al.*, 1999].

The Maghrebian thrust front in central west Sicily can be divided, in turn, into three different domains (Figure 2): (1) the Gela Nappe, exposing mainly Oligocene to Pleistocene terrigenous sediments; (2) the area of Sciacca and the Adventure bank on the southwestern end of the belt with imbricated Mesozoic-lower Tertiary platform carbonates; and (3) the central western Sicily belt with east-west thrust sheets alternatively imbricating Mesozoic to lower Tertiary basinal successions (Imerese and Sicanian domains) and platform-seamount carbonates (Panormide, Trapanese, and Monte Genuardo domains). The Mesozoic facies at Sciacca are dominated by platformal limestones (Saccense platform) similar to the Hyblean Plateau [*Catalano et al.*, 1993];

In the Gela Nappe, almost continuous deformation and growing of individual fold-thrust structures occurred since the Tortonian and during the Plio-Pleistocene [*Butler and Lickorish*, 1997]. Offshore drill holes and seismic data in the Sicily Channel document that major southward advancements of the Gela Nappe front occurred during the middle Pliocene, since the basal detachment extensively overlies the lower Pliocene Trubi chalks. Onlap of Pleistocene sediments onto the thrust front suggests that no significant compressive deformation occurred after the lower Pleistocene to mid-Pleistocene [*Butler et al.*, 1992; *Lickorish et al.*, 1999].

In the external western Maghrebides (thrusts derived from the deformation of the Trapanese to Saccense domains), the earliest compressive tectonic episodes are assumed to be Tortonian in age [*Catalano et al.*, 1996] and to continue during the Plio-Pleistocene as well [*Vitale*, 1990]. The large amplitude (and stepwise decreasing toward the external units where no rotation is observed) clockwise (CW) rotations [*Channell et al.*, 1980, 1990] are interpreted as due to contemporaneous thrusting and large-scale rotations. Since the allochthonous units were assumed to undergo coherent and internally semirigid torsional movements, very large displacements were assumed to occur in central Sicily, i. e., in the regions far from the rotation pole [*Oldow et al.*, 1990]. Assuming this deformation style, some authors also interpret the external zones (apart from the Saccense domain) as formed by a stack of tectonic slices detached from their basement and tectonically covering the almost undeformed Saccense succession [*Roure et al.*, 1990; *Vitale*, 1995; *Catalano et al.*, 1996].

Vertical-axis rotations are systematically recorded in the preorogenic and synorogenic deposits from the southern Tyrrhenian realm (Figure 1). Counterclockwise (CCW) rotations

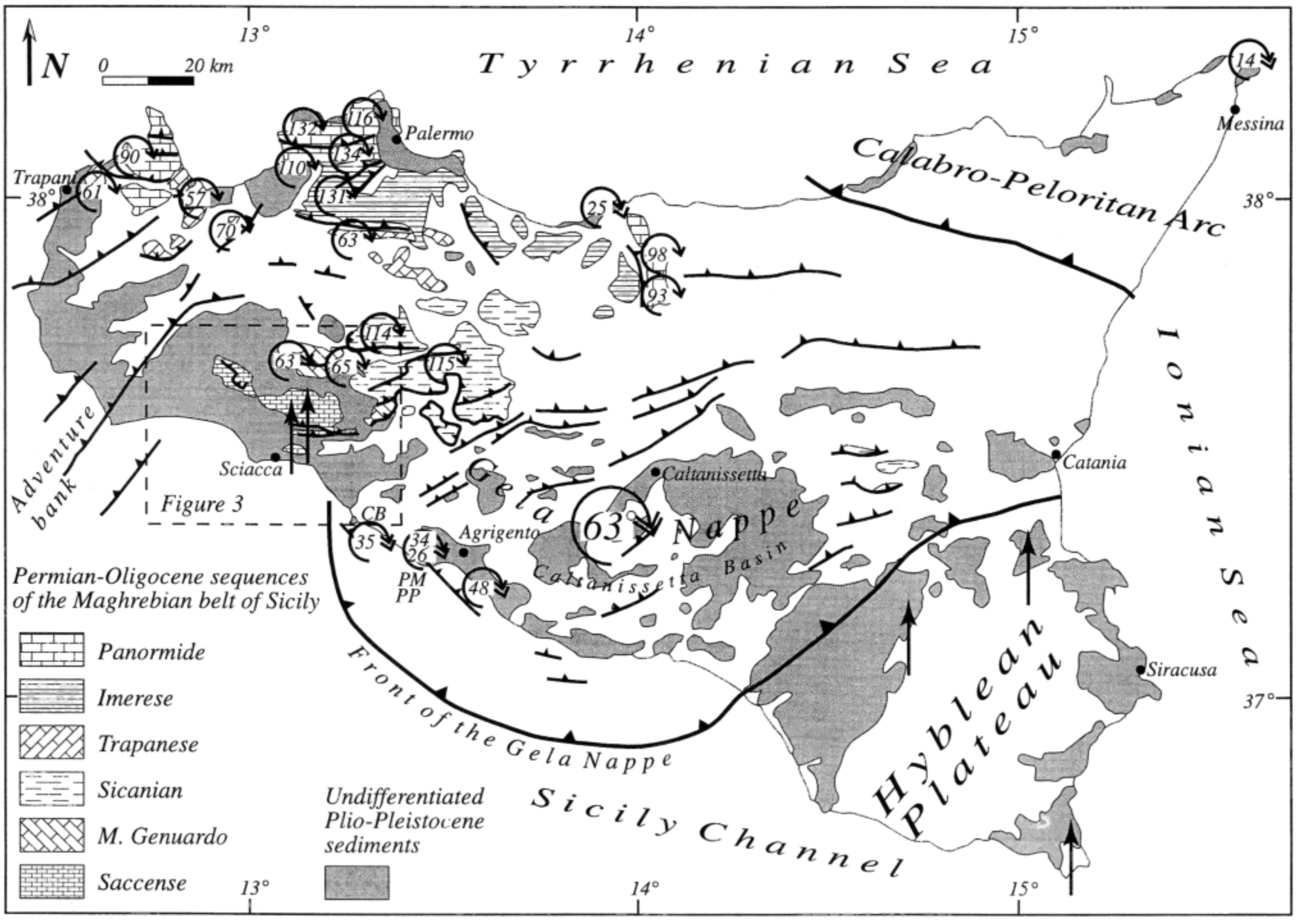

Figure 2. Schematic map of Sicily and synthesis of the previous paleomagnetic results. Vertical arrows indicate nonrotated areas. Circular arrows (and the enclosed angle) indicate the amount of clockwise (CW) rotations calculated for the single sampling localities. The 63° rotation from the Gela Nappe [*Butler et al.*, 1999] is obtained by averaging results from different structures. Circular arrows with simple and double tips indicate results from Mesozoic-Paleogene and Neogene rocks, respectively. Mesozoic-Paleogene and Neogene rotations are calculated by comparing the obtained paleodeclinations to the coeval expected African directions and to the geocentric axial dipole (GAD) field direction, respectively. Paleomagnetic data are from *Channell et al.* [1980, 1990], *Grasso et al.* [1983, 1987], *Besse et al.* [1984], *Aifa et al.* [1988], *Scheepers and Langereis* [1993], and *Butler et al.* [1999]. CB, PM, and PP are the lower-middle Pliocene Capo Bianco, Punta di Maiata, and Punta Piccola sections, respectively, studied by *Scheepers and Langereis* [1993].

of 15°-20° have been documented in Plio-Pleistocene sediments from the southern Apennines [*Sagnotti*, 1992; *Scheepers et al.*, 1993], whereas in Sicily only CW rotations were observed. Here, apart from the Mesozoic to Eocene pelagic limestones yielding very large (up to 134°) CW rotations [*Channell et al.*, 1980, 1990; *Catalano et al.*, 1984; *Nairn et al.*, 1985], also the Neogene deposits from the Gela Nappe were investigated (Figure 2). *Butler et al.* [1999] extensively studied the Messinian "Calcare di base" and "Tripoli" Formations. Data from different folds and thrusts are tightly grouped and coherently indicate a 63° CW rotation for the whole basin. *Grasso et al.* [1987] investigated the lower middle Pliocene "Trubi" chalks from central northern Sicily, which showed a complex magnetic behavior, widespread overprint, and an ill-defined CW rotation of ~25° in northern Sicily. *Scheepers and Langereis* [1993] studied three lower to middle Pliocene sections in the southwestern part of the Gela Nappe, reporting 35°, 34°, and 26° CW rotation for the Capo Bianco, Punta di Maiata, and Punta Piccola sections, respectively (Figure 2). A few kilometers east of these sections, two Pliocene sites yielded a 48° CW rotation [*Besse et al.*, 1984]. Since the Hyblean Plateau, which represents the foreland of the Sicilian belt, has not undergone significant rotations with respect to Africa [*Grasso et al.*, 1983] (Figure 2), the rotations observed within the Sicilian Maghrebides have to be associated with the thin-skinned compressive deformations.

3. The Maghrebian Thrust Front in Southwestern Sicily: Geology of the Study Area

The investigated area is located in southwestern Sicily around Sciacca, where Plio-Pleistocene sediments largely crop out encircling some ridges of Meso-Cenozoic limestones from the Sicanian, Monte Genuardo, and Saccense domains (Figures 2 and 3). The Sicanian sequence is entirely characterized by basinal units [*Mascle*, 1979; *Catalano et al.*, 1978], while the Saccense succession consists of Triassic-lower Lias platform limestones and dolomites followed by younger basinal units intercalated with megabreccias. Since the Monte Genuardo succession is similar to the Saccense succession (and was termed Internal Saccense in the old literature) [*Catalano et al.*, 1978; *Channell et al.*, 1980, 1990] but shows basinal facies from the early Lias, it is considered to represent the Mesozoic slope connecting the Saccense and Sicanian sedimentation domains.

The Mesozoic-lower Tertiary successions are (locally unconformably) overlain by upper Oligocene-middle Miocene clays and sandstones and an upper Tortonian-lower Messinian terrigenuous sequence with clay, sandstone, and conglomerate beds (Terravecchia Formation). The Miocene sequence ends with Messinian evaporitic deposits, widespread in the eastern part of the study area. The Pliocene succession is represented by the Trubi chalks and the following lower-middle Pliocene to Pleistocene clay sequence containing turbiditic sandy levels. The clays are widespread in the western part of the study area, around the Saccense carbonate ridges of Monte Magaggiaro-Monte Arancio-Pizzo Telegrafo (Figure 3). Detailed lithostratigraphic and biostratigraphic studies [*Vitale*, 1997] show that in this area the Trubi chalk to clay transition occurs in the late early Pliocene (~ 4 Ma), ~1 Myr earlier than in other sections from southern central Sicily. North of Monte Magaggiaro (Belice basin), mainly Pliocene clays are exposed, while Pleistocene clays and calcarenites dominate the Menfi basin, located south of Monte Magaggiaro-Monte Arancio. As a result of the persistent tectonic deformation, the Tortonian to Pleistocene formations are commonly separated by unconformities, and the sedimentation appears clearly controlled by the tectonic growth of positive relief structures.

The ridges exposing the Saccense and Monte Genuardo succession limestones appear as broad anticlines surrounded by onlapping Neogene sediments. Field investigations and subsurface exploration well data [*Vitale and Sulli*, 1997] indicate that the carbonates are arranged in complex duplex structures formed by Mesozoic carbonates and Miocene-Pliocene deposits sealed by (virtually undeformed) uppermost Pliocene-Pleistocene sediments. Conversely, *Monaco et al.* [1996] suggested that the upper Pleistocene and Holocene sediments cropping out in the eastern Menfi basin would represent thrust-top basin deposits related to the activity of the Monte San Calogero thrust (Figure 3). These authors also referred the rapid uplift of recent deposits to the activity of the ramp anticlines. They proposed that the 1968 Belice earthquake ($5<M<5.4$) occurred on a blind crustal thrust ramp representing the deep continuation of the surface thrusts, and they inferred that considerable Pleistocene-Holocene N-S compression and thrust activity occurred in the area.

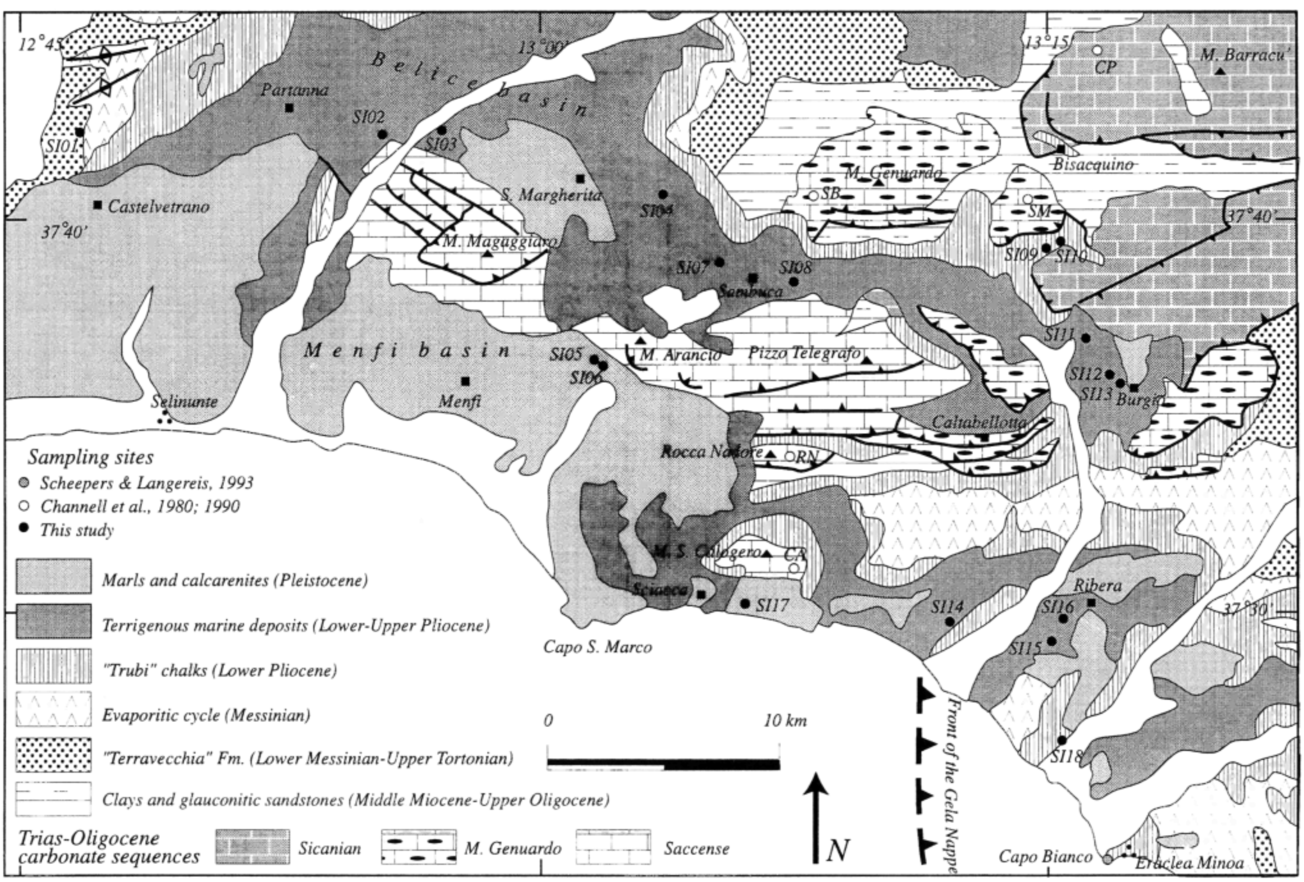

Figure 3. Geological map of the study area and location of the sampling sites. CP, Col Fiorito; SB, Sambuca; SM, Santa Maria; RN, Rocca Nadore; CA, Monte San Calogero.

The Sicanian units, exposed in two ridges in the study area, overthrust the Monte Genuardo sequences and the younger sediments of the Gela Nappe toward the south. On the basis of field studies, the Sicanian successions are considered to be stacked in complex and strongly allochthonous duplex systems overriding the weakly deformed Saccense domain [*Vitale*, 1991; *Catalano et al.*, 1996].

Channell et al. [1980, 1990] sampled several paleomagnetic sites in the Mesozoic pelagic limestones cropping out in the study area (Figure 3). The obtained paleodeclinations, when compared to the coeval expected African ones, yielded large CW rotations in the Sicanian (114°) and Monte Genuardo domains (63-65°), whilst no significant rotation was observed in two sites from the Saccense succession. *Scheepers and Langereis* [1993] studied the lower Pliocene Trubi succession at Capo Bianco, in the southwestern part of the Gela Nappe (Figure 3), reporting a 35° CW rotation (with respect to the geocentric axial dipole (GAD) field direction).

4. Sampling and Biostratigraphy

We sampled 18 new paleomagnetic sites, drilling in each site ~10 cores and orienting them in situ by a magnetic compass. When possible, the cores were located in different beds in order to average out the secular variation of the geomagnetic field. One site (SI01) was sampled in a clay horizon of the Terravecchia Formation, three (SI09, SI10, and SI18) were sampled in the Trubi chalks, and the remaining 14 were sampled in the Plio-Pleistocene clays (Figure 3).

The foraminifera and nannofossils content from 14 sites was carefully determined and referred to the biostratigraphic zones as listed in Table 1 (see appendix for the detailed micropaleontological determinations). The ages of the remaining four sites were inferred considering the results in Table 1. Sites SI06 and SI15, which were sampled from the same clays in the vicinity of sites SI05 and SI16, respectively, were both referred to the middle early Pleistocene (Emilian). Site SI18, sampled in the same Trubi interval studied in a nearby section by *Scheepers and Langereis* [1993], was considered early Pliocene in age. A similar age was inferred also for site SI09, sampled close to site SI10.

Biostratigraphic dates show that the clays sampled north and northeast of the Monte Magaggiaro-Pizzo Telegrafo ridges are early Pliocene to Plio-Pleistocene boundary in age, while south of this area they are early to middle Pleistocene. The Trubi chalk to clay transition in southwestern Sicily is confirmed to be younger in this area than it is in central southern Sicily (as suggested by *Vitale* [1997]).

5. Rock Magnetism

5.1. Thermal Demagnetization of Isothermal Remanent Magnetization

For at least one sample per site, the coercivity and unblocking temperature spectra were investigated. Magnetic remanence measurements were done using a JR5-A spinner magnetometer. After each heating step, the low-field magnetic susceptibility of the samples was measured with a KLY-2 bridge, in order to monitor possible mineralogical transformations. All these measurements were done in the paleomagnetism laboratory of Oxford University.

For some representative clay and chalk samples, the isothermal remanent magnetization (IRM) acquisition curves up

Table 1. Ages and Biostratigraphic Zones of the Sampled Sites

Site	Lit.	Age	Age, Ma	Foraminifera Zone	Nannofossils Zone
SI01	Cl	late Tortonian	7.70-8.16	*G. obliquus extremus*	----------
SI02	Cl	Plio-Pleistocene boundary	1.73-2.13	*G. inflata*	MNN19a
SI03	Cl	Plio-Pleistocene boundary	1.73-1.95	*G. inflata*	MNN19a
SI04	Cl	middle Pliocene	2.82-3.57	*G. crassaformis*	MNN16a
SI05	Cl	early Pleistocene	1.25-1.50	*G. cariacoensis*	MNN19d
SI06	Cl	early Pleistocene	-----------	--------------------------	------------
SI07	Cl	Plio-Pleistocene boundary	1.73-1.95	*G. inflata*	MNN19a
SI08	Cl	Plio-Pleistocene boundary	1.73-1.95	*G. inflata*	MNN19a
SI09	Ch	early Pliocene	-----------	--------------------------	------------
SI10	Ch	early Pliocene	4.52-5.10	*G. margaritae*	MNN12
SI11	Cl	early-middle Pliocene	3.57-3.85	*G. puncticulata*	MNN16a
SI12	Cl	Plio-Pleistocene boundary	1.73-1.95	*G. inflata*	MNN19a
SI13	Cl	early Pliocene	4.11-4.52	*G. margaritae/G. puncticulata*	MNN13
SI14	Cl	early Pleistocene	0.99-1.25	*G. cariacoensis/G. trun. excelsa*	MNN19e
SI15	Cl	early Pleistocene	-----------	--------------------------	------------
SI16	Cl	early Pleistocene	1.25-1.50	*G. cariacoensis*	MNN19d
SI17	Cl	middle Pleistocene	0.58-0.99	*G. truncatulinoides excelsa*	MNN19f
SI18	Ch	early Pliocene	-----------	--------------------------	------------

Lit., lithologies; Cl, clays; Ch, chalks. Ages in mega annum are based on the chronology of biostratigraphic events of *Sprovieri et al.* [1997]. The biostratigraphic zones are from *Iaccarino* [1985], *Spaak* [1983], *Colalongo and Sartoni* [1979], and *Rio et al.* [1990]. The ages of sites SI06, SI09, SI15, and SI18 are inferred (see details in the text). *G. obliquus extremus, Globigerinoides obliquus extremus; G. inflata, Globorotalia inflata; G. crassaformis, Globorotalia crassaformis; G. cariacoensis, Globigerina cariacoensis; G. margaritae, Globorotalia margaritae; G. puncticulata, Globorotalia puncticulata; G. trun. Excelsa, Globigerina truncatulinoides excelsa;* MNN, Mediterranean Neogene nannofossils.

to a maximum applied field of ~ 850 mT were studied. This experiment showed that the clays contain only a soft fraction which is virtually saturated at 300 mT, while both a soft and a hard fraction (which is still not saturated at 800 mT) are observed in the Trubi chalks. After having roughly identified the sample coercivities, a three-component IRM (according to *Lowrie* [1990]) was thermally demagnetized in one sample per site. The IRM values applied to the sample axes were selected so that each of the three axes held comparable amounts of remanence. Maximum and minimum fields applied to the z and x sample axes were of 820 and 50 mT, respectively, for all the samples. The intermediate field applied on the y sample axis was of 100 mT in the clays and of 400 mT in the Trubi chalks.

In the clays, the three components are virtually demagnetized at 300-400°C in 10 sites, the upper Tortonian site (SI01), two Pliocene sites (SI04, SI13), one site from the Plio-Pleistocene boundary (SI07), and all six Pleistocene sites (Figures 4a and 4b). Thus iron sulphides seem to dominate the magnetic mineralogy of these sites. The magnetic susceptibility drops to ~ 50-80% of its initial value between 100-200°C and 300-350°C in three of these sites (SI07, SI14, and SI17; Figure 4a). In that temperature interval, the remanence and susceptibility decrease rates are very similar, implying that the thermal decomposition (of greigite into exagonal pyrrhotite, pyrite, and marcasite according to *Krs et al.* [1992] and *Torii et al.* [1996]) largely prevails over the progressive thermal unblocking of remanence fractions. In 4 out of the 10 clay sites containing iron sulphides, a small amount of remanence (1-15% of the initial value) is still present after 400°C (Figure 4b). In the sites SI05 and SI06, this remanence is eliminated between 400 and 600°C, and thus it is related to titanomagnetite. In the sites SI01 and SI13, the three axes are demagnetized between 650 and ~700°C (Figure 4b). Such high unblocking temperatures are typical for hematite, but hematite is unlikely to represent the soft fraction (with coercivity

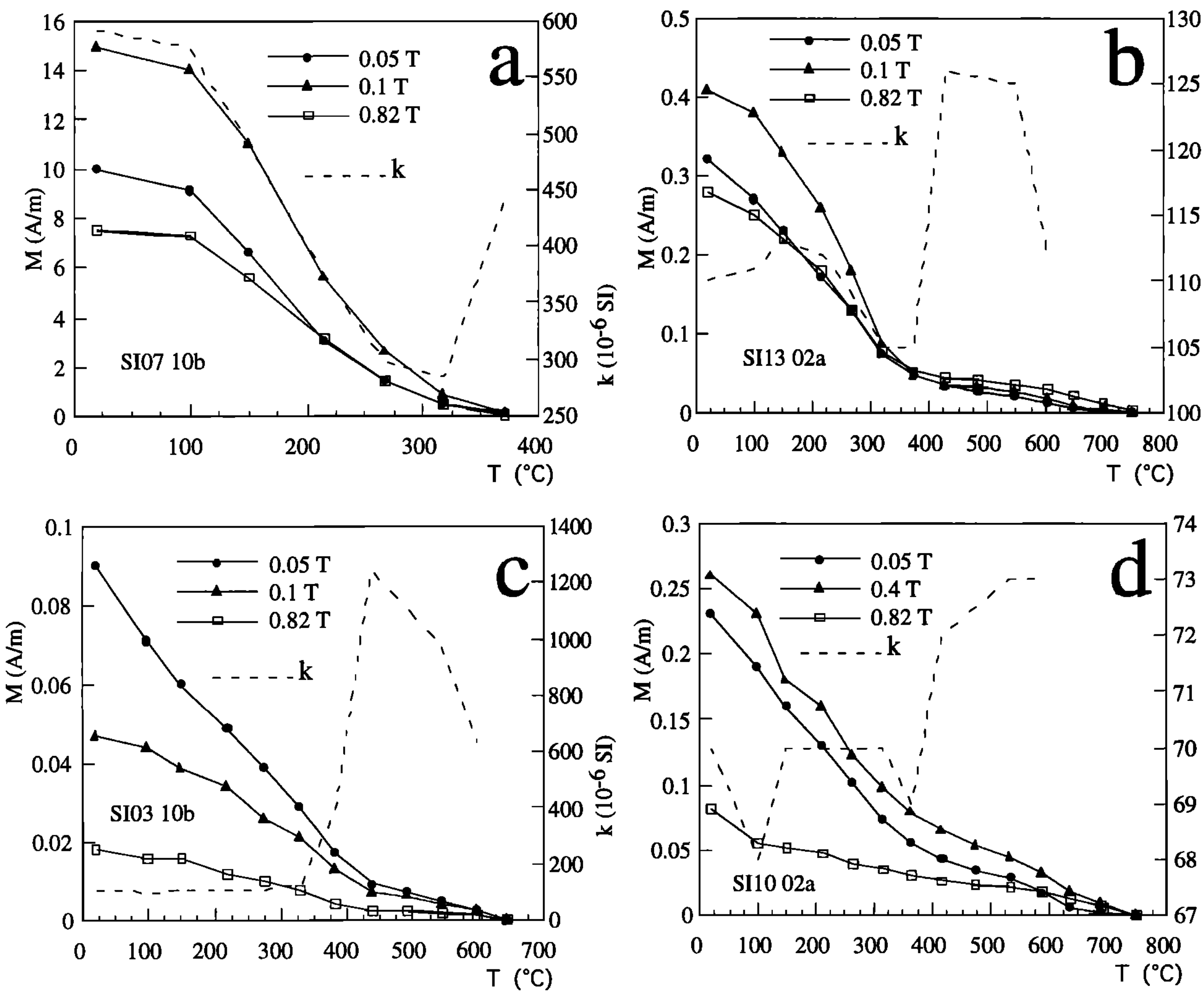

Figure 4. Thermal demagnetization of a three-component isothermal remanent magnetization (IRM) according to the *Lowrie* [1990] method and variation of the low-field magnetic susceptibility after each heating step for four representative samples: (a) clay sample containing greigite, (b) clay sample containing greigite, maghemite and hematite, (c) clay sample containing titanomagnetite and maghemite, (d) Trubi chalk sample containing titanomagnetite, maghemite, goethite and hematite. Double vertical scales are shown for magnetization and susceptibility values.

≤ 50 mT) unblocked after 650°C. Then we speculate that the high-temperature magnetization is carried by both maghemite and hematite.

In the remaining five clay sites (one Pliocene in age (SI11) and four from the Plio-Pleistocene boundary), 70-95% of the remanence is demagnetized between 400 and 500°C, suggesting that titanomagnetite is the main carrier (Figure 4c). The remaining remanences are demagnetized between 550 and 650°C, implying the additional presence of magnetite and possibly maghemite. In all the clays (both those containing iron sulphides and titanomagnetite), a continuous susceptibility increase (up to a factor of ~20) between 320-380°C and 400-600°C is observed (Figures 4a-4c). This susceptibility variation indicates that significant mineralogical changes occurred and that a strongly susceptive fraction was created.

In the Trubi samples, the soft (coercivity ≤ 50 mT) and hard (400 mT < coercivity ≤ 820 mT) fractions represented in the x and z sample axes have significantly different unblocking temperature spectra (Figure 4d). The soft fraction (which carries most of the magnetization) is reduced to 5-20% of its initial value between 400 and 600°C, and then it is completely eliminated between 640 and 690°C. This indicates that titanomagnetites and possibly subordinate maghemite are carriers. The hard fraction abruptly decreases below 100°C and is then completely eliminated at 680-750°C, showing that it is represented by both goethite and hematite.

As a summary, the thermal demagnetization of a three-component IRM shows that (1) the upper Tortonian, two Pliocene, one Plio-Pleistocene, and all six Pleistocene clay sites are dominated by iron sulphides, possibly greigite; (2) the remaining four Plio-Pleistocene clay sites, one Pliocene clay site, and the three Trubi chalk sites are dominated by titanomagnetite; and (3) minor carriers are frequently associated with the main ones.

5.2. Thermal Variation of the Low-Field Susceptibility

The thermal change of the magnetic susceptibility during a heating-cooling cycle from room temperature up to 700°C was investigated in one sample per site using a CS-3 apparatus coupled to a KLY-3 bridge in the paleomagnetism laboratory of the University of Roma Tre. Four samples from four sites (SI01, SI07, SI11, and SI17) were also studied at Oxford University with a CS-2 apparatus coupled to a KLY-2 bridge, using an argon atmosphere to prevent possible mineralogical changes.

In all the thermomagnetic cycles, the susceptibility starts to increase after 250-350°C, confirming that significant mineralogical changes occurred (Figure 5). The newly formed magnetic mineral can be identified as magnetite because of the Curie temperature of ~580-600°C observed both in the heating curves and in the cooling curves. After a complete heating-cooling cycle, the susceptibility has generally increased by a factor of 20-50 with respect to its initial value, except for some clay sites which were shown to contain titanomagnetite and for all the Trubi sites, where the increase was as little as 2-5. This shows that only a minor amount of magnetite is formed in sediments where iron sulphides are absent; that is, oxidation had already occurred during sedimentation and diagenesis. Similar amounts of new magnetite are formed both in the cycles performed in oxygen atmosphere (Figure 5a) and in those performed in argon atmosphere (Figure 5b), implying that the oxygen needed to form magnetite is available from the sample matrix itself.

Because of the strong mineralogical transformations occurring after heating to 250°C, the thermomagnetic curves are virtually useless to constrain the original magnetic mineralogy above 250°C. Important information, however, may be obtained below 250°C, since the part of the thermomagnetic curve below 200-300°C is generally used to separate the paramagnetic and ferrimagnetic contributions to the low-field magnetic susceptibility [e. g., *Hrouda*, 1994]. By fitting a hyperbola (due to paramagnetic minerals) to the susceptibility signal below 200°C according to the method of *Hrouda* [1994], a prevalent contribution of the paramagnetic fraction to the susceptibility is observed in the clays (Figure 5), while similar paramagnetic and ferrimagnetic contributions were inferred in the Trubi chalks. Thermal demagnetization of an IRM showed that for some clays containing iron sulphides, the strong susceptibility decrease

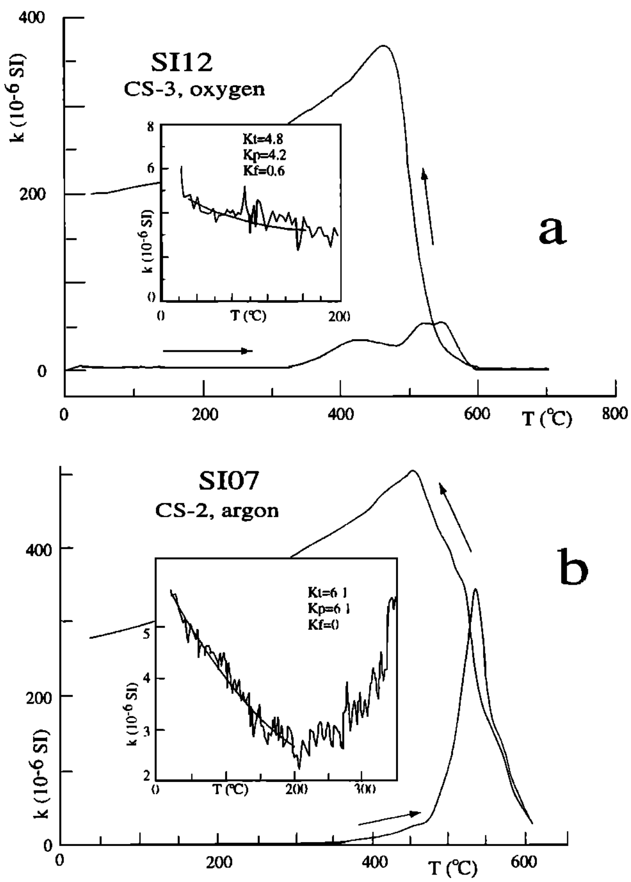

Figure 5. Thermomagnetic curves from a heating-cooling cycle from room temperature to 600-700°C. The boxed inlet shows an enlargement of the first part of the heating curve and the estimates for the total rock susceptibility kt, the paramagnetic susceptibility kp, and the ferrimagnetic susceptibility kf, as computed according to *Hrouda* [1994] (see text for the reliability of these estimates). (a) Curve performed with the CS-3 apparatus in oxygen atmosphere on a sample containing mainly titanomagnetite. (b) Curve performed with the CS-2 apparatus in argon atmosphere on a sample containing mainly iron sulphides, probably greigite.

occurring above 100°C was due to greigite decomposition. In site SI07, the susceptibility is reduced to ~50% of its initial value at 300°C (Figure 4a), implying that the ferrimagnetic susceptibility represents at least 50% of the total room temperature susceptibility. This decrease may be perfectly fitted by an hyperbola to the thermomagnetic curve from the same sample (Figure 5b), giving a (clearly erroneous) 100% paramagnetic contribution to the total susceptibility. This implies that the *Hrouda* technique for inferring paramagnetic and ferrimagnetic susceptibilities must be used with caution in samples containing iron sulphides, since the paramagnetic contribution may be greatly overestimated.

5.3. Magnetic Anisotropy

The low-field magnetic susceptibility of each sample was measured with a KLY-3 bridge in the paleomagnetic laboratory of the University of Roma Tre. The anisotropy of magnetic susceptibility (AMS) at both the specimen level and the site level was evaluated using *Jelinek* [1978] statistics. In each site, the anisotropy degree and the shape of the susceptibility ellipsoids were evaluated by means of the P' and T parameters [*Jelinek*, 1981], respectively. In the clays, the anisotropy degree P' is low (Table 2), with values typical of weakly deformed sediments ($P'<1.04$), and the shape of the AMS ellipsoids is in the field of oblate ($T>0$). In the Trubi chalks, the anisotropy degree is even lower ($P'<1.02$), and the shape of the AMS ellipsoid is triaxial ($T\sim0$).

Despite the low magnetic anisotropy, the magnetic foliation plane is always well defined and parallel to the bedding plane (Figure 6), as is commonly observed in sediments. The magnetic lineation, on the other hand, is well defined only in nine sites (Figure 6a and Table 2), where the e_{12} confidence angle of the Kmax in the Kmax-Kint plane is ≤20°. In three other sites the magnetic lineation is still defined but has a larger confidence angle ($20°<e_{12}<35°$, Figure 6b), while the remaining six sites have a purely oblate fabric with virtually no lineation ($e_{12}\geq35°$, Figure 6c). The tectonic implications of the observed magnetic lineations will be fully discussed in section 7.

As for previous studies performed in clay sediments [e. g., *Scheepers and Langereis,* 1994; *Sagnotti et al.,* 1998], the question arises as to whether the measured fabric reflects the anisotropy of the clay matrix minerals, the ferrimagnetic minerals, or both. The susceptibility thermal variation curves seem to demonstrate that the low-field susceptibility is influenced by both the paramagnetic and ferrimagnetic fractions, but precise estimates of the relative contribution were hampered by the presence of iron sulphides in most of the sites. To try to better understand this problem, we compared in one sample per site the magnetic susceptibility and the saturation isothermal remanent magnetization (SIRM) measured after a 0.82 T field was applied to the samples (Figure 7). While k has moderate variations in most of the samples, those containing iron sulphides have systematically higher SIRMs than the others, regardless of their age. Therefore the SIRM/k values are confirmed here to be diagnostic for identifying iron sulphides ($3.1 \times 10^3 \leq$ SIRM/k $\leq 6.5 \times 10^4$ A/m) among other carriers ($6.5 \times 10^2 \leq$ SIRM/k $\leq 5.1 \times 10^3$ A/m), as also shown elsewhere [*Sagnotti and Winkler*, 1999, and references therein]. In Figure 7, we note that a strongly positive correlation between k and SIRM values exists only for the four samples (from sites SI01, SI07, SI14, and SI17) having $k>200 \times 10^{-6}$ SI. Therefore, in these four sites, the low-field susceptibility (and AMS) is likely to be significantly influenced by the ferrimagnetic (i. e., iron sulphides) susceptibility. The iron sulphides susceptibility adds to the susceptibility "base level" due to the paramagnetic clays, which seems to be dominant in all the other samples having $k<200 \times 10^{-6}$ SI.

Table 2. AMS Results From Southwestern Sicily

Site	Lit.	Age	*Km*	*P'*	*T*	*D*,deg	*I*,deg	e_{12},deg
SI01	Cl	late Tortonian	381 (97)	1.039 (0.017)	0.501 (0.233)	89	11	13
SI02	Cl	Plio-Pleistocene boundary	117 (4)	1.019 (0.009)	0.701 (0.115)	311	13	58
SI03	Cl	Plio-Pleistocene boundary	108 (3)	1.014 (0.002)	0.173 (0.248)	83	3	16
SI04	Cl	middle Pliocene	201 (39)	1.013 (0.003)	0.525 (0.291)	299	7	36
SI05	Cl	early Pleistocene	170 (19)	1.014 (0.002)	0.760 (0.097)	256	4	49
SI06	Cl	early Pleistocene	133 (5)	1.013 (0.002)	0.872 (0.054)	208	8	43
SI07	Cl	Plio-Pleistocene boundary	632 (392)	1.026 (0.025)	0.644 (0.119)	91	1	11
SI08	Cl	Plio-Pleistocene boundary	204 (52)	1.009 (0.004)	0.394 (0.543)	86	3	20
SI09	Ch	early Pliocene	39 (18)	1.009 (0.002)	0.031 (0.451)	334	24	61
SI10	Ch	early Pliocene	58 (14)	1.017 (0.005)	-0.101 (0.304)	278	2	21
SI11	Cl	early-middle Pliocene	102 (12)	1.023 (0.005)	0.414 (0.150)	294	4	17
SI12	Cl	Plio-Pleistocene boundary	182 (29)	1.022 (0.007)	0.609 (0.421)	174	8	63
SI13	Cl	early Pliocene	220 (72)	1.028 (0.008)	0.505 (0.100)	305	5	11
SI14	Cl	early Pleistocene	243 (47)	1.010 (0.002)	0.689 (0.217)	38	5	33
SI15	Cl	early Pleistocene	197 (19)	1.006 (0.002)	0.682 (0.194)	18	10	19
SI16	Cl	early Pleistocene	154 (21)	1.013 (0.002)	0.585 (0.105)	232	3	16
SI17	Cl	middle Pleistocene	1182 (455)	1.038 (0.031)	0.441 (0.297)	7	10	28
SI18	Ch	early Pliocene	54 (27)	1.007 (0.002)	0.247 (0.336)	85	15	15

Lit., lithologies; Cl, clays; Ch, chalks; *Km*, mean susceptibility, in 10^{-6} SI. Standard deviation is in parentheses. P' and T are corrected anisotropy degree and shape factor, respectively, according to *Jelinek* [1981]; standard deviation is in parentheses. D and I are in situ declination and inclination, respectively, of the maximum susceptibility axis. Value e_{12} is the semi-angle of the 95% confidence ellipse around the mean k_{max} axis in the k_{max}-k_{int} plane. AMS, anisotropy of magnetic susceptibility.

5.4. Demagnetization of the Natural Remanent Magnetization

All the natural remanent magnetization (NRM) measurements were done using a 2G cryogenic magnetometer in the shielded room of the paleomagnetic laboratory of the Istituto Nazionale di Geofisica (Rome). A pilot specimen from each site was demagnetized by alternating magnetic field (AF) up to 100 mT. AF cleaning was found to be efficient for all the samples except those from clay sites SI01 and SI07, where little NRM decay was observed and an artificial gyroremanent magnetization [*Stephenson*, 1980] was progressively induced in the samples above 50 mT. Therefore all the samples, except those from these two sites, were AF cleaned in 10-20 steps (13 on average), selecting different field steps depending on the coercivity spectra observed in the pilot samples. The samples from sites SI01 and SI07 (both containing iron sulphides) were thermally demagnetized in 9-13 steps. Demagnetization data were plotted both on orthogonal demagnetization diagrams and on equal-area projections and evaluated using principal component analyses [*Kirschvink*, 1980].

In the Trubi chalks, very different demagnetization paths were observed in each site, and in most of the samples a

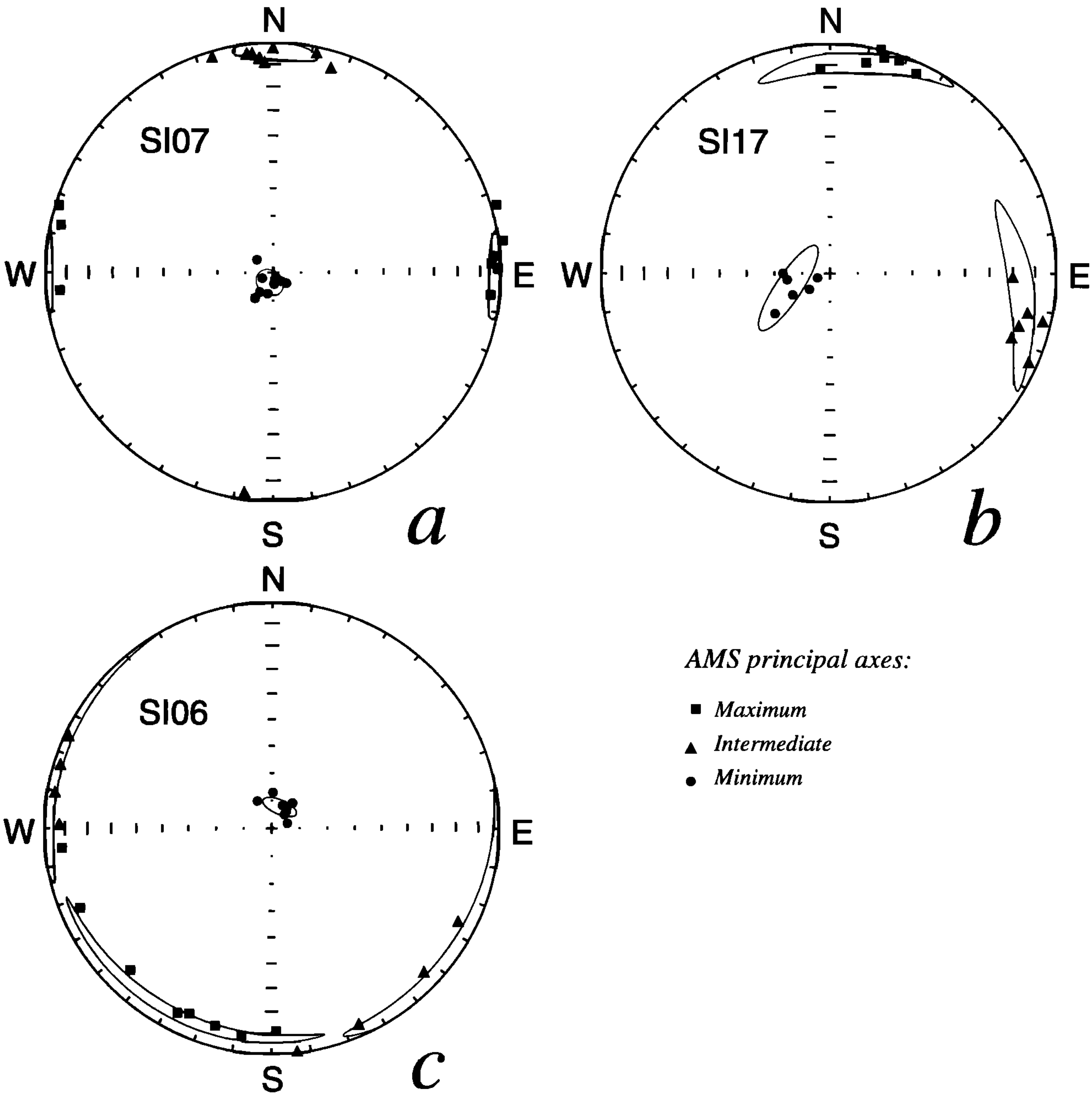

Figure 6. Results of anisotropy of magnetic susceptibility (AMS) analyses for three representative sites, using Schmidt equal-area projection, lower hemisphere geographic coordinates. The ellipses indicate the 95% confidence regions around the principal susceptibility axes. (a) Site with $e_{12} \leq 20°$. (b) Site with $20° < e_{12} < 35°$. (c) Site with $e_{12} \geq 35°$.

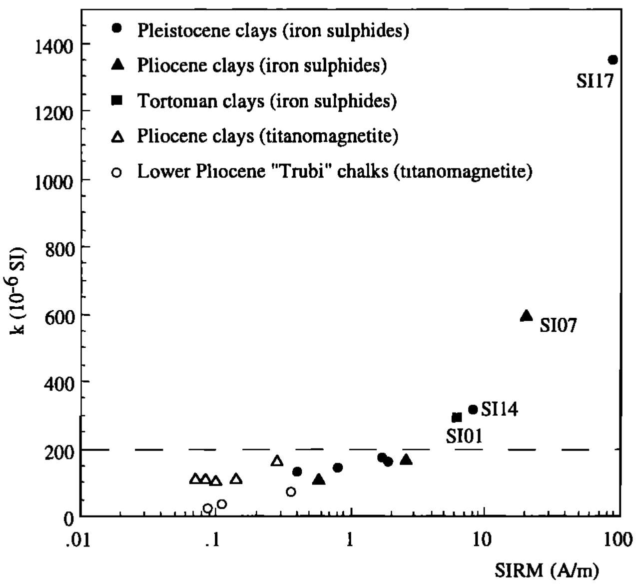

Figure 7. Relation between low-field susceptibility k and saturation isothermal remanent magnetization (SIRM) measured after the application of a 0.82 T field on one sample per site. The SIRM values are plotted on a logarithmic scale. Note that for samples with k<200 x 10^{-6} SI, the k and SIRM values are not correlated (k is dominated by the paramagnetic clay mineral susceptibility). For samples with k>200 x 10^{-6} SI, k and SIRM values are correlated; that is, k is dominated by the ferrimagnetic (iron sulphides) fraction susceptibility.

significant portion of the remanence was shown to be carried by a low-coercivity viscous component parallel to the present-day field (Figure 8). In site SI09, the viscous component was eliminated at 10 mT, then two components of magnetization coexisted up to 50 mT, and finally an ill-defined high-coercivity component was observed in the 50-100 mT interval (Figure 8a). In site SI10, a well-defined component was unblocked in the 15-100 mT interval, but a small amount of remanence was also shown to be carried by an undetermined high-coercivity component (Figure 8b). In site SI18, a viscous component carrying a considerable amount of remanence was eliminated at 20 mT (Figures 8c-8d). Above 20 mT, a well-defined characteristic component (ChRM) was observed only in four samples (Figure 8c). In the remaining six samples (in which the NRM is about one-tenth that in the other four), incoherent changes of the paleomagnetic direction were observed above 20 mT (Figure 8d). The ubiquitous presence of secondary (and often high coercivity) components in the Trubi chalks is considered to arise from the complex magnetic mineralogy and the presence of high-coercivity minerals such as goethite and hematite among the carriers. A similar paleomagnetic behavior for the Trubi chalks from southwestern Sicily was reported by *Scheepers and Langereis* [1993], who found consistent differences between normal and reverse polarity directions, explained by a secondary overprint persisting up to the highest demagnetization steps.

In all the AF cleaned clays (except samples from sites SI04 and SI13), after removal of small viscous components by 10-20 mT, a very well defined ChRM was isolated and demagnetized at 60-80 mT, regardless of the magnetic mineralogy (Figures 9a-9b). In the sample SI04, a random directional scatter of the NRM occurred after each demagnetization step, and the same behavior was observed using thermal treatment. In the site SI13, two components of magnetization coexisted up to 35 mT (Figures 9c-9e). After 35 mT, a ChRM was isolated in nine samples from this site (Figure 9c), while in the remaining one, a gyroremanent magnetization was progressively induced after 40 mT (Figures 9d-9e). Therefore, in this sample (which has low NRM intensity compared to the others), no ChRM could be isolated, and a remagnetization circle was fitted to the low-coercivity part of the demagnetization path.

Two different behaviors were observed in the two thermally demagnetized sites (Figure 10). In site SI01, a ChRM was isolated below 350°C, while incoherent magnetization components appeared at higher temperatures (Figure 10a). The progressive increase of k (measured after each heating step) up to a factor of ~20 in the 350-600°C interval proves that the high-temperature magnetization is laboratory induced and is due to the formation of large amounts of magnetite. Samples from site SI07 were completely demagnetized by 400°C, and a ChRM was isolated between 200 and 400°C (Figure 10b).

6. Paleomagnetic Directions

Site-mean paleomagnetic directions were calculated using *Fisher*'s [1953] statistics on 15 sites where ChRMs were isolated and the *McFadden and McElhinny* [1988] method only on site SI13, where both ChRMs and a remagnetization circle were observed (Table 3). All the site-mean directions from the clays are very well defined, the α_{95} value ranging from 2.1° to 7.3°. In the Trubi chalks, a large within-site directional scatter is observed in sites SI09 and SI18 (α_{95}=19.4° and 14.4°, respectively). Samples were always found to have consistent within-site magnetic polarities except those from site SI15, where three samples from a stratigraphically lower position showed a reverse polarity while the remaining seven were normally magnetized. The mean directions calculated for the normal and reverse intervals of this site are clearly not antipodal (Table 3), suggesting the occurrence of a significant and uncleaned secondary overprint or that they were not acquired during a stable polarity interval. We also thermally demagnetized samples from the site SI15, therefore testing the hypothesis that nonantipodality arose from inefficiency of the AF cleaning, but we obtained ChRMs indistinguishable (within the confidence interval) from those determined by AF demagnetization.

By combining contemporaneously information obtained from biostratigraphy and magnetostratigraphy, the ages of the sampled sites were tightly constrained (Table 3 and Figure 11). As the reference geomagnetic polarity timescale for the Plio-Pleistocene, we adopted the *Ogg* [1995] scale, which is nearly identical to the *Cande and Kent* [1995] scale (both are calibrated with astrochronology). Biostratigraphic and magnetostratigraphic data were found to be inconsistent only in sites SI15 and SI16, located close to each other. The age of these sites was constrained to the early Pleistocene (Emilian, *Globigerina cariacoensis*/ MNN19d zone), implying sedimentation during the C1r.2r polarity subchron (Figure11), but a normal polarity was observed in all the samples from the site SI16 and in seven samples from the site SI15. Given this inconsistency, the normal polarity samples observed in these two sites were considered to be recent overprints, and only the three reverse polarity samples from site SI15 were considered reliable for tectonic interpretation (Table 3).

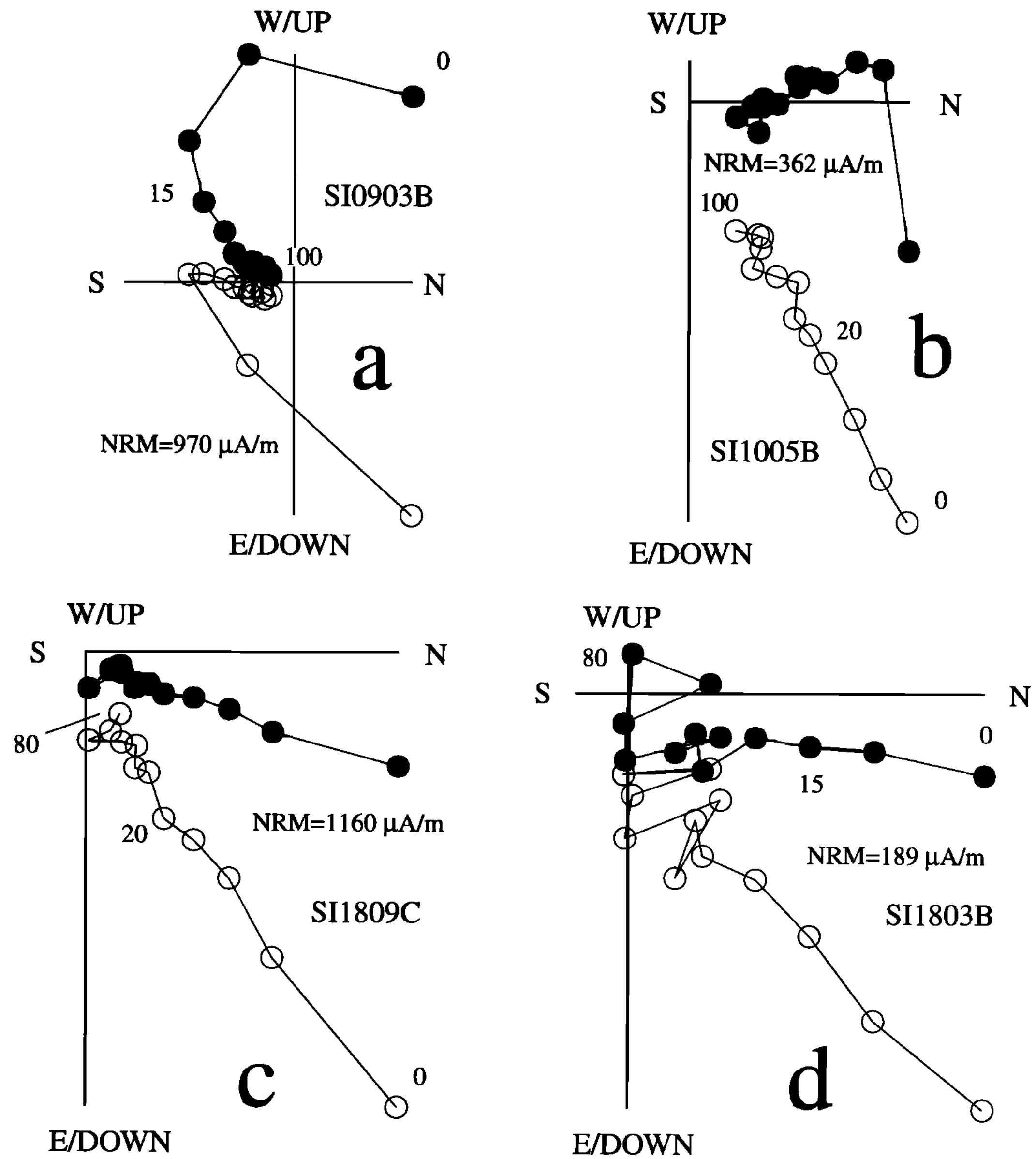

Figure 8. Vector diagrams of typical alternating magnetic field (AF) demagnetization data from the lower Pliocene Trubi chalks, geographic coordinates: (a) sample showing two low-coercivity components of magnetization and an ill-defined high-coercivity component, (b) sample showing a well-defined low-coercivity component and an undetermined high-coercivity component, (c) sample showing a characteristic component of magnetization, (d) sample showing incoherent changes of the paleomagnetic direction after the elimination of the viscous component. Demagnetization step values are in millitesla. Open and solid symbols represent projections on the vertical and horizontal planes, respectively. NRM, natural remanent magnetization.

After tilt correction, paleodeclinations of variable sign and amplitude are observed (Figure 12). A northwestward declination of ~30° (when considered in the normal polarity state) is found only in the upper Tortonian site (SI01), located in the northwestern corner of the study area (Figure 3). Seven reliable Plio-Pleistocene boundary to middle Pleistocene sites from the Belice and Menfi basins and close to Sciacca show consistently northward paleodeclinations, and finally seven lower Pliocene to middle lower Pleistocene sites from the eastern part of the study area give variable northeastward declinations. The data pass the *McFadden* [1990] fold test at the 99% confidence level ($\xi_{in\ situ}$=5.68, $\xi_{unfolded}$=0.94, and $\xi_{99\%}$=5.62; minimum ξ was observed at 85% of complete unfolding). Because of the large scatter of the paleodeclinations, the normal and reverse polarity site-mean directions are not antipodal (negative reversal test according to *McFadden and McElhinny* [1990]).

7. Discussion

The Hyblean Plateau, which represents the foreland to the Sicilian Maghrebides, did not undergo any significant rotations since the Neogene [*Grasso et al.,* 1983]. Therefore the observed

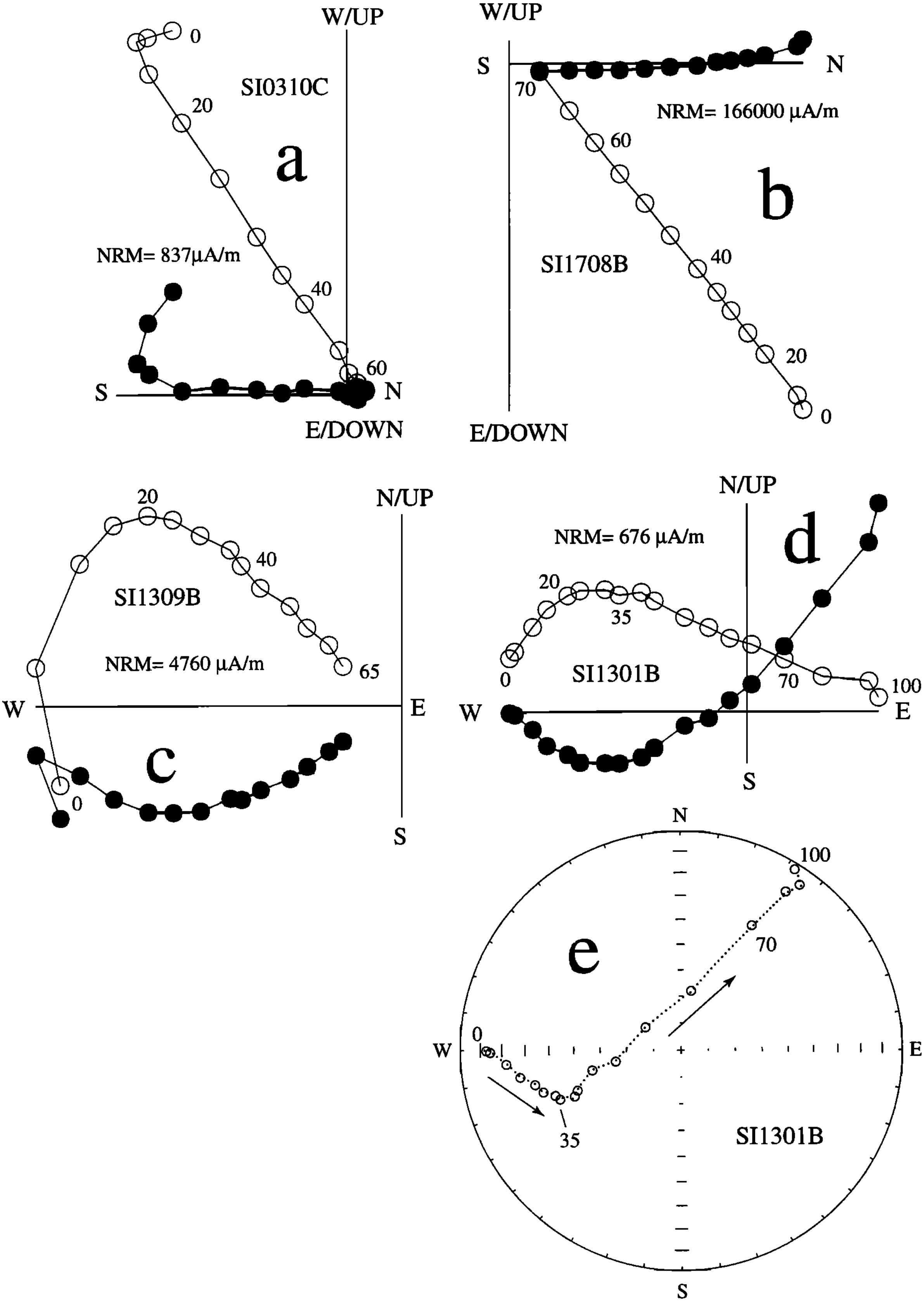

Figure 9. Vector diagrams of typical AF demagnetization data from clays, geographic coordinates. (a) Sample containing titanomagnetite. (b) Sample containing iron sulphides. (c) Data from site SI13, showing two components with overlapping coercivity spectra up to 35 mT. (d) Sample SI1301, showing two components with overlapping coercivity spectra and a gyroremanent magnetization induced after 40 mT. Open and solid symbols represent projections on the vertical and horizontal planes, respectively. (e) Same data as those in Figure 9d but represented in an equal-area projection, with upper hemisphere geographic coordinates. All the demagnetization step values are in millitesla.

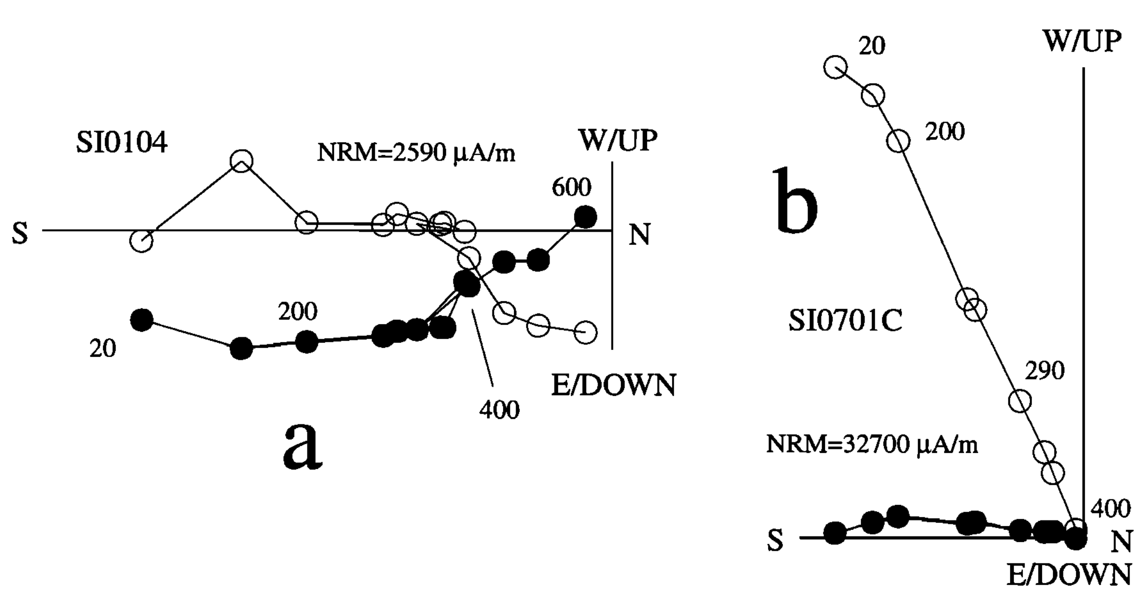

Figure 10. Vector diagrams of typical thermal demagnetization data, geographic coordinates, from (a) the upper Tortonian SI01 site and (b) the Plio-Pleistocene boundary SI07 site. Demagnetization step values are in degrees Celsius. Open and solid symbols represent projections on the vertical and horizontal planes, respectively.

paleodeclinations can be compared to the GAD field direction to infer the vertical-axis rotations. The structures around the Saccense platform carbonates are invariably rotated (Figure 13), and the rotations are coherent with those of a "syntaxial bend" (in the sense of Marshak [1988]). We note that the upper Oligocene-lower Miocene Numidian Flysch, widespread on the Sicilian Maghrebides, did not cover the Saccense successions (nor the Hyblean Plateau). This shows that the Saccense domain was paleogeographically uplifted with respect to the surrounding deeper water successions from the Mesozoic to the Neogene. During the compressional pulses, the basinal sediments from the western Gela Nappe underwent ductile deformation and were bent around the obstacle represented by the rigid Saccense carbonates. A similar mechanism was also proposed for the bending and differential displacements in the eastern margin of the Gela Nappe around the platform carbonates of the Hyblean

Table 3. Paleomagnetic Directions From Southwestern Sicily

Site	Age, Ma	*n/N**	*D*b,deg	*I*b,deg	*D*a,deg	*I*a,deg	*k*	α_{95},deg
SI01	8.02-8.16	8/10	157.1	7.3	149.9	-47.3	61	7.1
SI02	1.73-2.13							
SI03	1.73-1.79	10/10	170.9	-58.7	170.9	-58.7	513	2.1
SI04	2.82-3.57							
SI05	1.25-1.50	10/10	185.2	-59.3	166.2	-62.9	249	3.1
SI06	1.25-1.50	8/8	181.8	-55.5	177.1	-63.0	140	4.7
SI07	1.73-1.79	8/10	195.4	-60.7	195.8	-56.7	235	3.6
SI08	1.73-1.79	10/10	175.2	-63.5	179.7	-60.3	56	6.5
SI09	4.29-4.98	10/10	219.6	-16.2	205.0	-32.2	7.1	19.4
SI10	4.52-5.10	10/10	355.4	57.9	42.6	51.7	51	6.8
SI11	3.57-3.58	9/10	25.4	67.3	27.9	46.4	50	7.3
SI12	1.79-1.95	10/10	28.4	16.4	27.7	30.3	65	6.0
SI13	4.11-4.48	9/10	237.9	-45.5	235.8	-53.3	217	3.5
SI14	1.07-1.25	10/10	173.5	-67.8	178.3	-62.2	300	2.8
SI15n†	1.25-1.50	7/10	358.7	38.8	350.0	26.9	78	6.9
SI15r	1.25-1.50	3/10	221.9	-64.3	208.0	-55.3	484	5.6
SI16†	1.25-1.50	9/10	352.9	49.7	346.9	45.4	71	6.2
SI17	0.58-0.78	10/10	353.6	50.8	5.0	41.9	299	2.8
SI18	4.80-5.23	4/10	21.0	54.6	39.4	38.8	41	14.4

The value *n/N* is the number of samples giving reliable results/ number of studied samples at a site. *D* and *I* are site mean declinations and inclinations calculated before (*D*b and *I*b) and after (*D*a and *I*a) tectonic correction. Value *k* and α_{95} are statistical parameters after *Fisher* [1953]. SI15n and SI15r are normal and reverse polarity samples from site SI15, respectively. *Sites SI02 and SI04 are unstable. † Site was discarded (see text). The ages were inferred considering both the magnetic polarity (chron boundary ages from *Ogg* [1995]) and biostratigraphic data.

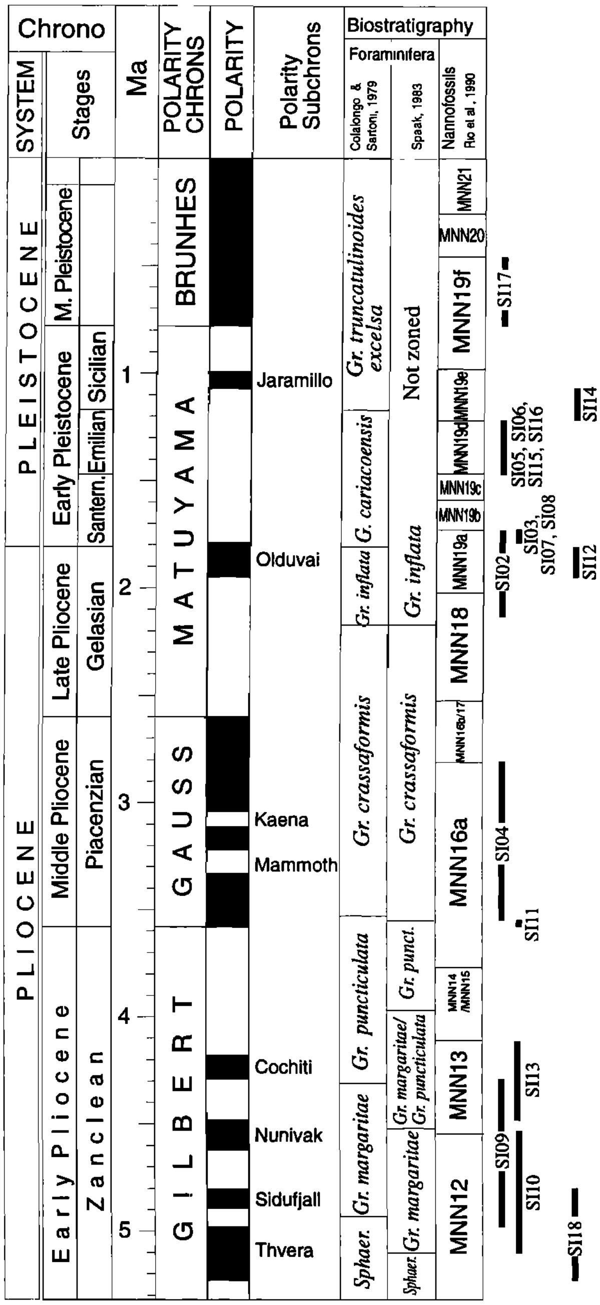

Figure 11. Magnetic polarity and biostratigraphic scales for the Plio-Pleistocene and inferred site ages, taking into account both biostratigraphic and magnetostratigraphic data. The corresponding numerical site ages are reported in Table 3. The chronostratigraphical subdivision of the Plio-Pleistocene is from the work of *Rio et al.* [1994] and *Cita et al.* [1999], the magnetic polarity scale is from the work of *Ogg* [1995]. For simplicity, the Brunhes excursions as well as the Cobb Mountain and Reunion events were omitted.

Plateau [*Grasso et al.*, 1990]. Therefore the arcuate shape of the Gela Nappe front probably arises from oroclinal bending of an originally rectilinear front progressively deflected by two lateral obstacles made up of rigid shelf carbonates.

7.1 The Area West of the Belice Basin

The 30° CCW rotation for the upper Tortonian site (Table 3, and Figures 12 and 13) is the first documented rotation of this sign from Sicily. This rotation could imply that the thrusts from the southwestern border of Sicily, which turn to a NE-SW trend (Figure 2) and keep this orientation through the Sicily Channel up to the Tunisian Maghrebides [*Argnani*, 1993], have undergone a different tectonic evolution than the rest of the belt. More results from southwestern Sicily are needed to examine this hypothesis in further detail.

7.2 Saccense Shelf Carbonates and the Overlying Belice and Menfi Basins

Those unrotated Plio-Pleistocene boundary to middle Pleistocene sites which we infer to have experienced no net rotation lie within the central part of the study area. They yield a regional mean paleomagnetic direction defined by n=7, D=359.8°, I=58.3°, k=70, and α_{95}=6.7°, which is nearly identical to the GAD field direction expected in southwestern Sicily (D=0°, and I=57°). This absence of rotation observed in the Belice and Menfi basins is in agreement with the Mesozoic data from the Monte San Calogero and Rocca Nadore ridges (belonging to the Saccense succession), which did not show any significant rotation with respect to Africa [*Channell et al.*, 1980, 1990] (Figure 13). The null rotation shown by paleomagnetism is in agreement with geological-structural data from this area, showing that the rigid shelf carbonates are ramp-dominated and underwent negligible horizontal translation [*Di Stefano and Vitale*, 1993; *Lickorish et al.*, 1999].

Here the AMS data obtained by us help to solve the controversy of whether there is [*Monaco et al.*, 1996] or is not [*Vitale and Sulli*, 1997] significant Pleistocene-Holocene N-S shortening in the area. The magnetic lineation direction has been widely used in many Tortonian to Pleistocene clay deposits from the external Apennines [*Sagnotti and Speranza*, 1993; *Scheepers and Langereis*, 1994; *Mattei et al.*, 1997; *Sagnotti et al.*, 1998], where it has been shown to form after compression and faithfully represent the local fold axis directions. The clays from the Plio-Pleistocene boundary from the Belice basin (sites SI03, SI07, and SI08) coherently show an E-W oriented magnetic lineation (Figure 13), whereas two middle lower Pleistocene (Emilian) sites (SI05 and SI06) from the Menfi basin have a purely oblate fabric. Then the magnetic fabric documents a N-S compressional episode occurring in the time span comprised between the Plio-Pleistocene boundary and the Emilian (Figure 11). Therefore the recent uplift of the area must be ascribed to regional factors instead of considerable Pleistocene-Holocene N-S compression generating thrust activity and uplift of thrust-top deposits, as proposed by *Monaco et al.* [1996].

Finally, we note that our unrotated Plio-Pleistocene boundary sites SI07 and SI08 are located a few kilometers to the southwest of the carbonate ridge of Monte Genuardo, where five upper Cretaceous sites yielded a 63° CW rotation [*Channell et al.* 1980, 1990] (Figure 13). The Plio-Pleistocene clays, which we sampled, conformably follow all the remaining Pliocene succession, starting with the lower Pliocene Trubi deposition, and all of this sequence discordantly overlies the Meso-Cenozoic succession of Monte Genuardo [*Vitale*, 1990]. Therefore we infer that the deformation and the associated rotation of the Monte

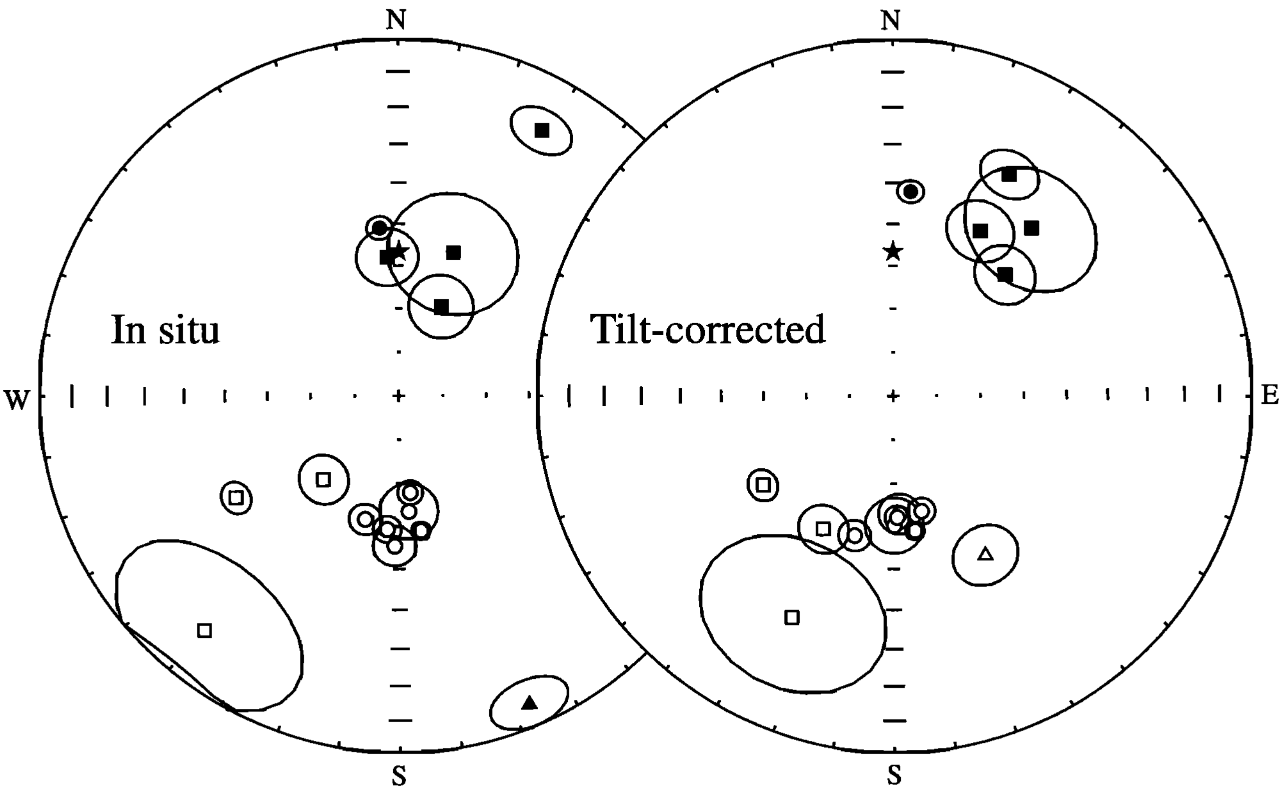

Figure 12. Equal-area projection of the site-mean directions from southwestern Sicily. Open (solid) symbols represent projection onto upper (lower) hemisphere. Triangle represents the late Tortonian direction from site SI01. Circles represent early to middle Pleistocene directions from the central part of the study area (sites SI03-SI08, SI14, and SI17). Squares represent early Pliocene to middle early Pleistocene directions from the eastern part of the study area (sites SI09-SI13, SI15, and SI18; see Figure 3 for precise site location). The star represents the normal polarity GAD field direction for the study area (latitude 37.5°N, longitude 13°E). Open ellipses are the projections of the α_{95} cones about the mean directions.

Genuardo structure must have occurred during Miocene (or older?) times. Although some unconformities are observed at various levels within the Miocene sequence [*Di Stefano and Vitale*, 1993], the timing of this major deformational and rotational event cannot be further constrained at present.

7.3. The Gela Nappe: Magnitude and Timing of Rotations and Constraints for the Tectonic Style

All the lower Pliocene-lower Pleistocene sites from the eastern part of the study area show a variable amount of CW rotations (Figure 13). These sites clearly define the lateral ramp of the recently rotated Gela Nappe with respect to the unrotated area covering the Saccense carbonates. This lateral ramp is actually characterized by negligible N-S strike-slip displacements, as the Messinian to Pleistocene sequences are almost undeformed close to the coast, while to the north they form gentle E-W folds. An analysis of the strain pattern (to compare it to the one expected in the thrust zone lateral tips) [e. g., Coward and Potts, 1983] is lacking, but at a first glance it seems that the Gela Nappe here dies out along strike into folds. Therefore, at least for such an area, the large (~30°) Pleistocene rotation did not produce large rigid displacement.

The CW rotation of the Gela Nappe is associated with southward displacement of the nappe front and internal accretion. The basal detachment of the Gela Nappe is well imaged by seismic stratigraphy and has been reached by several boreholes close to the southern Sicilian coast [*Grasso et al.*, 1995; *Lickorish et al.*, 1999], where it runs along Miocene basinal clays. This datum and the absence of a clear positive magnetic anomaly related to the uplift of the magnetic basement show that the Gela Nappe underwent a thin-skinned shortening and rotation.

The tight biostratigraphic control on our site ages allows us to evaluate the time dependence of the observed rotations. Adjacent to the Sicanian limestones, the clays yield a ~30° rotation in the two middle to upper Pliocene sites SI11 and SI12 and a 56± 6° rotation in the early Pliocene site SI13 (Figure 14). We regard these data as more significant than those obtained from the Trubi chalks in sites SI09-SI10, which show ill-constrained 25°-43° rotations which are affected by unresolved secondary overprints. The data from the clays document a ~25° rotation for the Sicanian domain during the latest early Pliocene. Since the Sicanian and Monte Genuardo limestones overthust the Miocene succession and the Trubi chalks south of the rotated sites (Figure 13), we relate the rotation to the early Pliocene

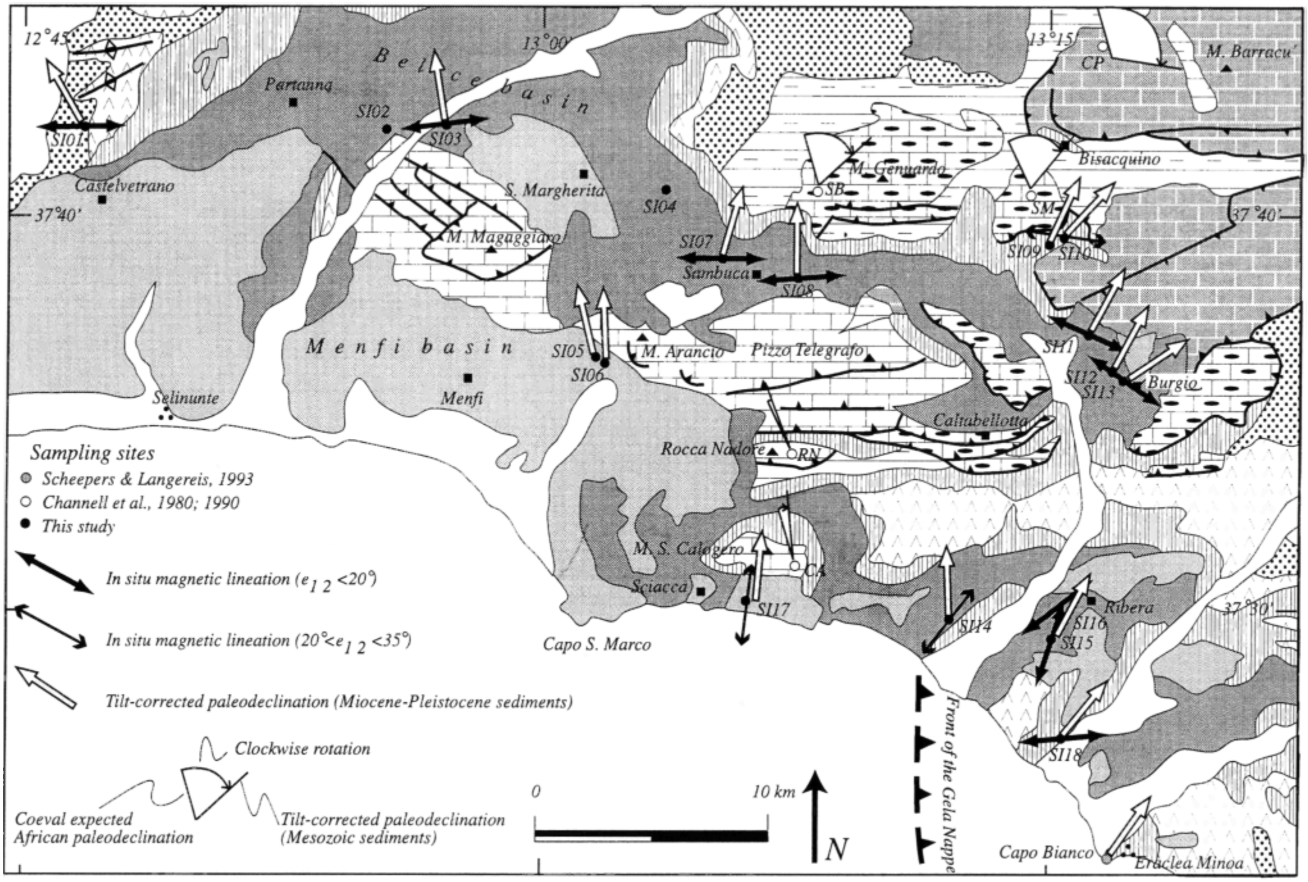

Figure 13. Geological map of the study area and results from paleomagnetism and magnetic anisotropy. Geological formations are as in Figure 3. Paleodeclinations are referred to the normal polarity state.

thrusting of the Sicanian carbonates over the Neogene sediments of the Gela Nappe.

The ~30° rotation documented by us in the middle-upper Pliocene sediments adjacent to the Sicanian structures is not significantly different from the one observed by us (at sites SI15 and SI18) and by *Scheepers and Langereis* [1993] in lower Pliocene-lower Pleistocene sediments from the southwestern Gela Nappe (Figure 14). Therefore it seems that both the Sicanian domain and the front of the Gela Nappe rotated by ~30° during the Pleistocene, owing to tectonic activity along the basal detachment of the Gela Nappe. The age of site SI15 (Emilian, early Pleistocene) would imply that the 30° rotation occurred roughly during the last 1 Myr (Figure 11). More data are needed, however, to strengthen this conclusion, because the paleomagnetic mean of this site was obtained from only three nonremagnetized samples.

Channell et al. [1980, 1990] document ~115° CW rotation of post Cretaceous age from the Sicanian succession, within the same study area as that where we found Plio-Pleistocene rotations. We show here that ~55° of this rotation is post early Pliocene in age, and the older ~70° rotation is similar to the rotation (~65°) characterizing the Monte Genuardo succession, which we constrained to be Miocene (or older?) in age. Therefore it seems likely that the Monte Genuardo and Sicanian domains underwent a similar tectonic evolution and rotation during the Miocene, while the Sicanian ridges underwent additional large rotations during the Plio-Pleistocene, partly in conjunction with the Gela Nappe.

The new paleomagnetic data from the Gela Nappe and adjacent areas can be used to test the compatibility with possible tectonic evolution models. A rigid CW rotation (as assumed by Oldow et al. [1990]) pivoting around a pole located in the western border of the rotated area would imply a progressive eastward increase of the southward displacement. By taking into account the 65° Miocene rotation of the Monte Genuardo-Sicanian domains, a ~60 km displacement can be calculated for the easternmost Sicanian rocks from central Sicily. The ~25° late early Pliocene rotation documented by us for the Sicanian structures would give (if also considered as rigid) an additional ~15 km displacement, for a total ~75 km displacement of the eastern Sicanian succession with respect to the adjacent Gela Nappe sediments. This displacement value seems clearly incompatible with the tectonic framework observed in Sicily [*Butler and Lickorish*, 1997] and implies that the deformation within the Monte Genuardo and Sicanian domains is far from being rigid. Detailed structural data from the Monte Genuardo and Sicanian carbonates would be needed to better understand the deformation style and thus allow determination of the displacements with respect to the rotations. Similarly, it is clear that the Pleistocene ~30° rotation of the Gela Nappe cannot be

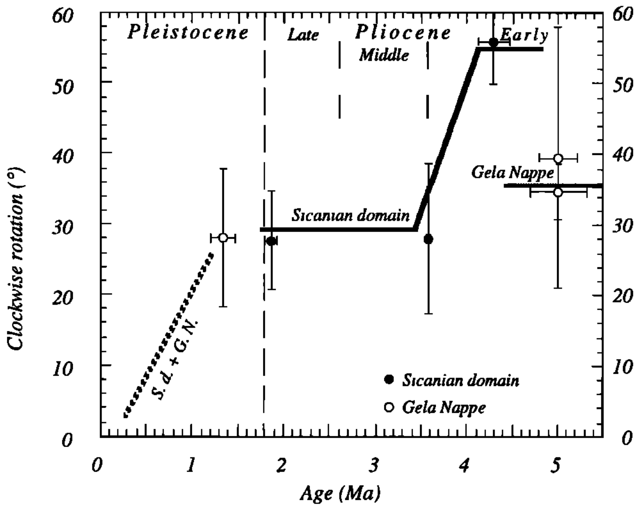

Figure 14. Site-mean CW rotation versus age in the eastern part of the study area and inferred rotational evolutions of the Sicanian domain and Gela Nappe (thick lines). Data from the lower Pliocene Trubi chalks in the Sicanian domain (sites SI09-SI10) were omitted owing to large in situ scatter and secondary overprint. Error bars for rotation are the $\alpha_{95}/\cos I$ site values. Error bars for site age were obtained considering both magnetic polarity and biostratigraphic constraints (see Figure 11 and Table 3). Early Pliocene data of the Gela Nappe are from site SI18 and the work of *Scheepers and Langereis* [1993].

considered as rigid, since it would imply ~60 km of Pleistocene shortening (i. e., more than 30 m/kyr) for the eastern Gela Nappe front.

The Pleistocene ~30° rotation documented in the southwestern part of the Gela Nappe brings new elements to constrain the age of shortening in the frontal thrust system of southern Sicily. Offshore drill hole and seismic data from the southeastern front of the nappe showed significant displacement during the middle Pliocene and continued internal shortening of the nappe during the Pleistocene [*Grasso et al.*, 1995], but no significant deformation is recorded during the Pleistocene along the front of the nappe adjacent to the Gela Basin [*Lickorish et al.*, 1999]. This inconsistency with respect to paleomagnetic data may imply either that (1) the Pleistocene advancement of the nappe front was previously underestimated, (2) a diachronicity of the shortening exists between different parts of the Gela Nappe (drill hole and seismic data were obtained in the eastern part of the nappe), or (3) although the front is locked since the early Pleistocene, Pleistocene internal shortening (and rotations) in the nappe extends southward very close to the front itself.

The hypothesis of significant Pleistocene tectonic activity at the southwestern Gela Nappe front is also corroborated by our AMS data, showing that all the studied Pleistocene sites from the coastal area between Sciacca and Capo Bianco have N-S to NNE-SSW trending magnetic lineations (Figure 13). Since this fabric is observed in sediments as young as the middle Pleistocene, it arises from a post middle Pleistocene compression, E-W to ESE-WNW directed. We propose that this flattening direction is the result of the strain partitioning related to the lateral motion in the southwestern border of the Gela Nappe, as observed in some nappe culminations [*Butler*, 1982; *Frizon de Lamotte et al.*, 1995]. This activity must be late Pleistocene-Holocene in time, in agreement with the Pleistocene rotations shown by paleomagnetism.

8. Conclusions

Paleomagnetic and magnetic anisotropy data from southwestern Sicily provide useful data to further constrain the rotational and tectonic evolution of the external Maghrebide belt. We show that the boundary between rotated and unrotated areas closely mirrors the salients and reentrants formed by the external Sicilian nappes.

CCW and CW rotations (in the western and eastern parts of the study area, respectively) are consistent with a "syntaxial bend" (in the sense of *Marshak* [1988]) formation of the ductile basinal sediments around the backbone of the Saccense carbonates, covered by unrotated Plio-Pleistocene successions. Significant Pleistocene deformation in the southwestern Gela Nappe very close to its front is inferred both by post middle early Pleistocene ~30° CW rotation and by post middle Pleistocene approximately E-W flattening in the coastal sediments. Our data demonstrate that the large CW rotations observed by *Channell et al.* [1980, 1990] in the Mesozoic carbonates of the Monte Genuardo and Sicanian domains are due to the sum of Miocene (or older?) and Plio-Pleistocene rotations. Both the Monte Genuardo unit and the Sicanian unit rotated ~65° during (or before?) the Miocene; then the Sicanian unit further rotated ~55° during the Plio-Pleistocene, as they beame part of the Gela Nappe lateral ramp.

This paper shows that large local variations of the strain trajectories and rotations are observed within small volumes of the belts. Therefore caution is needed when local paleomagnetic data from the chains are used to construct regional models or outline large rotating blocks. It is clear that the tectonic histories of the local structures can be unraveled only by tightly constraining strains and displacements, i. e., integrating paleomagnetic, geological, and structural data. The results of such integrated studies would greatly contribute to the ongoing debate of whether the continental crust behaves as a fluid [*Davies et al.*, 1997] or its deformation occurs through the interaction of discrete and internally semi-rigid plates [*Le Pichon et al.*, 1995].

Appendix

Several biostratigraphic schemes have been proposed for the Neogene and Quaternary of the Mediterranean [*Colalongo and Sartoni*, 1979; *Spaak*, 1983; *Cita*, 1975; *Iaccarino and Salvatorini*, 1982; *Iaccarino*, 1985]; we used the biostratigraphic foraminifera zonations of *Iaccarino* [1985] for the Miocene and those of *Spaak* [1983] and *Colalongo and Sartoni* [1979] for the Plio-Pleistocene. We adopted the calcareous nannofossils biostratigraphy of *Rio et al.* [1990] for the Plio-Pleistocene of the Mediterranean region. In addition, we used the chronology of Pliocene-Pleistocene biostratigraphic events proposed by *Sprovieri* [1993] and *Sprovieri et al.* [1997], and we followed the threefold subdivision of the Pliocene recently proposed by *Rio et al.* [1994] and *Cita et al.* [1999]. The age of the samples ranges within a time interval limited by the absolute ages of two biostratigraphic events (the chronology of datum events follows Sprovieri et al.).

The samples for foraminifera analyses have been washed through a stack of sieves and dried in an oven at about 60°C. The samples for the nannofossils analyses have been prepared following the standard method of the smear slides and have been studied using a light microscope (transmitted light and crossed nicols) at x1250 magnification. The age of each sampled site (indicated by a black bar in Figures 11 and 14) has been constrained between the two closest (nannofossil or foraminifera) adjacent events recorded within the sample (i. e., presence or absence of marker species) and considering the magnetic polarity.

Site SI01 yields *Globigerinoides obliquus extremus* and does not contain *Globorotalia suterae*; consequently, it can be ascribed to the late Tortonian *Globigerinoides obliquus extremus* zone, *Globigerinoides obliquus extremus /Globigerinoides bulloideus* subzone [*Iaccarino and Salvatorini*, 1982; *Iaccarino*, 1985], which ranges from 8.16 to 7.70 Ma [*Sprovieri et al.*, 1997]. The nannofossil content is characterized by the presence of *Helicosphaera stalis, Calcidiscus macintyrei, Discoaster variabilis*; this assemblage does not allow the precise assignment to a nannofossil biozone.

Site SI02 contains *Globorotalia inflata*, *Globorotalia crassaformis crassaformis* and *Helicosphaera sellii, Pseudohemiliania lacunosa, Dictyococcites productus*, found in the *Globorotalia inflata* and MNN19a (*D. productus*) biozones, respectively. It also contains reworked species such as *Globorotalia margaritae, Globorotalia puncticulata* and *Discoaster broweri, Reticulofenestra pseudoumbilicus, Discoaster asymmetricus* and *Discoaster surculus*. The age of the sample is Gelasian (late Pliocene) and is limited by the first occurrence (FO) of *Globorotalia inflata* (2.13 Ma) and the FO of medium size *Gephyrocapsa* sp. (1.73 Ma).

Site SI03 contains *Globorotalia inflata* and rare *Globorotalia crassaformis*, whereas sites SI07 and SI08 only contain *Globorotalia inflata*. The same samples yield *Helicosphaera sellii, Pseudoemiliania lacunosa, Dictyococcites productus* . The nannofossil and foraminifera association is found in the *Globorotalia inflata* /MNN19a biozones (late Pliocene). The age interval is nicely constrained between the last occurrence (LO) of *D. brouweri-D. triradiatus* (1.95 Ma) and the FO of medium size *Gephyrocapsa* sp. (1.73 Ma).

Site SI04 yields *Globorotalia crassaformis crassaformis* but does not contain *Globorotalia crassaformis aemiliana*; consequently, we assign it to the *Globorotalia crassaformis* zone following *Colalongo and Sartoni* [1979]. Among the nannofossils, we find *Helicosphaera sellii, D. brouweri* and *D. tamalis*, and we can refer the sample to the MNN16a (*D. tamalis*) zone. Since *Globorotalia bononiensis* is not present in the sample and there is no general agreement on the range of *Globorotalia crassaformis crassaformis*, the age of the sample (Piacenzian, middle Pliocene) can be limited by the LO of *Globorotalia puncticulata* (3.57 Ma) and the last common occurrence (LCO) of *D. tamalis* (2.82 Ma).

Site SI05 contains *Globorotalia inflata* and *Globigerina calida praecalida. Globigerina cariacoensis* is absent, but the sample, bearing *Gephyrocapsa* spp. >5.5 _ m, is Emilian in age and belongs to the nannofossil zone MNN19d ("large" *Gephyrocapsa*, 1.50-1.25 Ma).

Site SI10 bears *Globorotalia margaritae* without *Globorotalia puncticulata* and *Amaurolithus delicatus, Reticulofenestra pseudoumbilicus, Helicosphaera carteri* found in the early Pliocene (Zanclean) *Globorotalia margaritae* and MNN12 (*A. tricorniculatus*) biozones, respectively. The age of the sample is defined by the FCO of *Globorotalia margaritae* (5.10 Ma) and the FO of *Globorotalia puncticulata* (4.52 Ma).

Site SI11 belongs to the *Globorotalia puncticulata* zone because of the presence of the zonal marker *Globorotalia puncticulata*, and to the MNN16a zone (it contains the same nannofossil association as that of Site SI04). The sample is therefore early Pliocene in age, limited by the following events: the LO of *Reticulofenestra pseudoumbilicus* (3.85 Ma) and the LO of *Globorotalia puncticulata* (3.57 Ma).

The micropaleontological content of site SI12 is characterized by the presence of *Globorotalia crassaformis, Globorotalia inflata* and *Helicosphaera sellii, Pseudoemiliania lacunosa, Dictyococcites productus*. The sample is from the late Pliocene (Gelasian) *Globorotalia inflata*/MNN19a biozones. The age is between 1.95 Ma (LO of *D. broweri-D. triradiatus*) and 1.73 Ma (FO of medium size *Gephyrocapsa*).

Site SI13 bears *Globorotalia margaritae, Globorotalia puncticulata* and *Helicosphaera sellii, Sphenolithu* spp., *Reticulofenestra pseudoumbilicus* and belongs to the *Globorotalia margaritae/ Globorotalia puncticulata* [*Spaak*, 1983] and MNN13 (*C. rugosus*) zones. The age of the site is early Pliocene (Zanclean) between the FO of *Globorotalia puncticulata* (4.52 Ma) and the FCO of *Discoaster asymmetricus* (4.11 Ma).

Site SI14 yields *Hyalinea balthica, Pseudoemiliania lacunosa* and "small" *Gephyrocapsa* and can therefore be assigned to the (early Pleistocene) MNN19e ("small" *Gephyrocapsa*) zone between the LO of *Gephyrocapsa* > 5.5 _m (1.25 Ma) and the FO of *Gephyrocapsa* sp.3 (0.99 Ma).

Site SI16 contains *Globorotalia inflata, Hyalinea balthica*, and large *Gephyrocapsa* and falls, therefore, within the range between 1.50 and 1.25 Ma (Emilian). Site SI17 contains *Globorotalia inflata, Globigerina calida*, fragments of *Hyalinea balthica*, and *Gephyrocapsa* sp. 3. It can be attributed to the MNN19f zone (middle Pleistocene), within the range of *Gephyrocapsa* sp. 3 (0.99-0.58 Ma).

Acknowledgments. FS is indebted to Angelone Di Ponzio for the generous help given in the field as well as to Buffy McClelland and all the Oxford paleomagnetism laboratory staff for the warm welcome given in Oxford. We are also grateful to E. Boschi and A. Meloni for allowing us to measure the remanent magnetization of the samples at the paleomagnetic laboratory of the Istituto Nazionale di Geofisica. Comments by G. Muttoni, G. K. Taylor, and the Associate Editor helped to improve the quality of the paper. ADS was supported by a MURST ex 60% fund (responsible: F. Lentini), FS acknowledges an Accademia dei Lincei / Royal Society exchange scheme grant.

References

Aifa, T., H. Feinberg, and J. P. Pozzi, Pliocene-Pleistocene evolution of the Tyrrhenian arc: Paleomagnetic determination of uplift and rotational deformation, *Earth Planet. Sci. Lett.*, *87*, 438-452, 1988.

Argnani, A., Neogene tectonics of the Strait of Sicily, in Geological Development of the Sicilian-Tunisian Platform, edited by M. D. Max and P. Colantoni, *UNESCO Rep. Mar. Sci.*, *58*, 55-60, 1993.

Besse, J., J.-P. Pozzi, G. Mascle, and H. Feinberg, Paleomagnetic study of Sicily: Consequences for the deformation of Italian and African margins over the last 100 million years, *Earth Planet. Sci. Lett.*, *67*, 377-390, 1984.

Butler, R. W. H., Hangingwall strain: A function of duplex shape and footwall topography, *Tectonophysics*, *88*, 235-246, 1982.

Butler, R. W. H., and W. H. Lickorish, Using high-resolution stratigraphy to date fold and thrust activity: Examples from the Neogene of south-central Sicily, *J. Geol. Soc. London*, *154*, 633-643, 1997.

Butler, R. W. H., M. Grasso, and F. La Manna, Origin and deformation of the Neogene-Recent Maghrebian foredeep at the Gela Nappe, SE Sicily, *J. Geol. Soc. London*, *149*, 547-556, 1992.

Butler, R. W. H, E. McClelland, and R. E. Jones, Calibrating the duration and timing of the Messinian salinity crisis in the Mediterranean: Linked tectono-climatic signals in the thrust-top basins of Sicily, *J. Geol. Soc. London*, in press, 1999.

Cande, S. C., and D. V. Kent, Revised calibration of the geomagnetic polarity timescale for the Late Cretaceous and Cenozoic, *J. Geophys. Res.*, *100*, 6093-6095, 1995.

Catalano, R., et al., Contributi alla conoscenza della struttura della Sicilia occidentale: il profilo Palermo-Sciacca, *Mem. Soc. Geol. Ital.*, *19*, 485-493, 1978.

Catalano, R., B. D'Argenio, C. B Gregor, A. E. M. Nairn, G. Nardi, and P. Renda, The Mesozoic volcanics of western Sicily, *Geol. Rundsch.*, *73*, 577-598, 1984.

Catalano, R., S. Infuso, and A. Sulli, The Pelagian foreland and its northward foredeep: Plio-Pleistocene structural evolution, in Geological Development of the Sicilian-Tunisian Platform, edited by M. D. Max and P. Colantoni, *UNESCO Rep. Mar. Sci.*, *58*, 37-42, 1993.

Catalano, R., P Di Stefano, A. Sulli, and F. P. Vitale, Paleogeography and structure of the central Mediterranean: Sicily and its offshore area, *Tectonophysics*, *260*, 291-323, 1996.

Channell, J. E. T., Paleomagnetic data from Umbria (Italy): Implication for the rotation of Adria and Mesozoic apparent polar wander paths, *Tectonophysics*, *216*, 365-378, 1992.

Channell, J. E. T, and D. H. Tarling, Paleomagnetism and the rotation of Italy, *Earth Planet. Sci. Lett*, *25*, 177-188, 1975

Channell, J. E. T., R. Catalano, and B. D'Argenio, Paleomagnetism and deformation of the Mesozoic continental margin in Sicily, *Tectonophysics*, *61*, 391-407, 1980.

Channell, J. E. T., J. S. Oldow, R. Catalano, and B. D'Argenio, Paleomagnetically determined rotations in the western Sicilian fold and thrust belt, *Tectonics*, *9*(4), 641-660, 1990.

Cita, M. B., Planktonic foraminiferal biozonation of the Mediterranean Pliocene deep sea record: A revision, *Riv. Ital. di Paleontol. e Stratigr.*, *81*, 527-544, 1975.

Cita, M. B., D. Rio, and R. Sprovieri, The Pliocene series: Chronology of the type Mediterranean record and standard chronostratigraphy, *AASP Special Volume*, edited by *P. Wrenn et al.*, Baton Rouge, La., in press, 1999.

Colalongo, M.L., and S. Sartoni, Schema biostratigrafico per il Pliocene e il basso Pleistocene in Italia, in *Contributo Preliminare Carta Neotettonica d'Italia*, pp. 645-654, Consiglio Nazionale delle Ricerche, Rome, 1979.

Consiglio Nazionale delle Ricerche, Progetto finalizzato geodinamica, Structural model of Italy map, edited by G. Bigi et al., scale 1:500,000, Rome, 1991.

Coward, M. P., and G. J. Potts, Complex strain patterns developed at the frontal and lateral tips to shear zones and thrust zones, *J. Struct. Geol.*, *5*, 383-399, 1983.

Davies, R., P. England, B. Parsons, H. Billiris, D. Paradissis, and G. Veis, Geodetic strain of Greece in the interval 1892-1992, *J. Geophys. Res.*, *102*, 24,571-24,588, 1997.

Di Stefano, P., and F. P. Vitale, Carta geologica dei Monti Sicani occidentali, scale 1:50,000, Dip Geol. Geod. Palermo, Palermo, Italy, 1993.

Fisher, R. A., Dispersion on a sphere, *Proc R. Soc. London*, *217*, 195-305, 1953.

Frizon de Lamotte, D., J.-C. Guezou, and O. Averbuch, Distinguishing lateral folds in thrust-systems: Examples from Corbieres (SW France) and Betic Cordilleras (SE Spain), *J. Struct. Geol.*, *17*, 233-244, 1995.

Gasparini, C., G. Iannaccone, P. Scandone, and R Scarpa, Seismotectonics of the Calabrian Arc, *Tectonophysics*, *84*, 267-286, 1982.

Grasso, M., F. Lentini, A. E. M. Nairn, and L Vigliotti, A geological and paleomagnetic study of the Hyblean volcanic rocks, Sicily, *Tectonophysics*, *98*, 271-295, 1983.

Grasso, M., M. Manzoni, and A. Quintili, Misure magnetiche sui Trubi infrapliocenici della Sicilia orientale: possibili implicazioni stratigrafiche e strutturali, *Mem. Soc. Geol. Ital.*, *38*, 459-474, 1987.

Grasso, M., A. De Dominicis, and G. Mazzoldi, Structures and tectonic setting of the western margin of the Hyblean-Malta shelf, central Mediterranean, *Ann Tectonicae*, *4*, 140-154, 1990.

Grasso, M., G. Miuccio, R. Maniscalco, P. Garofalo, F. La Manna, and R. Stamilla, Plio-Pleistocene structural evolution of the western margin of the Hyblean Plateau and the Maghrebian foredeep, SE Sicily. Implications for the deformational history of the Gela Nappe, *Ann. Tecton.*, *9*(1/2), 7-21, 1995.

Hrouda, F., A technique for the measurement of thermal changes of magnetic susceptibility of weakly magnetic rocks by the CS-2 apparatus and KLY-2 kappabridge, *Geophys. J. Int.*, *118*, 604-612, 1994.

Iaccarino, S., Mediterranean Miocene and Pliocene planktic foraminifera, edited by H.M. Bolli, J B. Saunders, and K. Perch-Nielsen, *Plankton Stratigraphy*, vol 1, pp. 283-314, Cambridge Univ Press, New York, 1985

Iaccarino, S., and G Salvatorini, A framework of planktonic foraminiferal biostratigraphy for early Miocene to late Pliocene Mediterranean area, *Paleontol. Stratigr. Evol*, *2*, 115-125, 1982.

Jelinek, V., Statistical processing of anisotropy of magnetic susceptibility measured on a group of specimens and its applications, *Stud. Geophys. Geod.*, *22*, 50-62, 1978.

Jelinek, V., Characterization of the magnetic fabrics of rocks, *Tectonophysics*, *79*, 63-67, 1981.

Kastens, K, J. Mascle, C. Auroux, and ODP Leg 107 party, A microcosm of ocean basin evolution in the Mediterranean, *Nature*, *321*, 383-384, 1986.

Kirschvink, J. L., The least-square line and plane and the analysis of paleomagnetic data, *Geophys. J. R. Astron. Soc.*, *62*, 699-718, 1980

Krs, M., F. Novak, M. Krsova, P Pruner, L. Koukilkova, and J. Jansa, Magnetic properties and metastability of greigite-smythite mineralization in brown-coal basins of the Krusné hory Piedmont, Bohemia, *Phys. Earth Planet. Inter.*, *70*, 273-287, 1992.

Le Pichon, X., N. Chamot-Rooke, S. Lallemant, R. Noomen, and G. Veis, Geodetic determination of the kinematics of central Greece with respect to Europe: Implications for eastern Mediterranean tectonics, *J. Geophys Res.*, *100*, 12,675-12,690, 1995.

Lickorish, W. H., M. Grasso, R. W. H. Butler, A. Argnani, and R. Maniscalco, Structural styles and regional tectonic setting of the "Gela Nappe" and frontal part of the Maghrebian thrust belt in Sicily, *Tectonics*, in press, 1999.

Lowrie, W., Identification of ferromagnetic minerals in a rock by coercivity and unblocking temperature properties, *Geophys. Res. Lett*, *17*, 159-162, 1990.

Lowrie, W., and W. Alvarez, Rotation of the Italian peninsula, *Nature*, *251*, 285-288, 1974.

Malinverno, A., and W. B. F. Ryan, Extension in the Tyrrhenian Sea and shortening in the Apennines as result of arc migration driven by sinking of the lithosphere, *Tectonics*, *5*(2), 227-245, 1986.

Marshak, S., Kinematics of orocline and arc formation in thin-skinned orogens, *Tectonics*, *7*(1), 73-86, 1988.

Mascle, G., Etude geologique des Monts Sicani, *Riv. Ital. Paleontol. Stratigr.*, *16*, 1-431, 1979

Mascle, J., et al, A land-locked back-arc basin: Preliminary results from ODP Leg 107 in the Tyrrhenian Sea, *Tectonophysics*, *146*, 149-162, 1988

Mattei, M., R. Funiciello, and C. Kissel, Paleomagnetic and structural evidence for Neogene block rotations in the central Apennines, Italy, *J. Geophys. Res.*, *100*, 17,863-17,883, 1995.

Mattei, M., L. Sagnotti, C. Faccenna, and R. Funiciello, Magnetic fabric of weakly deformed clayey sediments in the Italian peninsula: Relationships with compressional and extensional tectonics, *Tectonophysics*, *271*, 107-122, 1997.

McFadden, P. L, A new fold test for paleomagnetic studies, *Geophys. J. Int.*, *103*, 163-169, 1990.

McFadden, P. L, and M. W. McElhinny, The combined analysis of remagnetization circles and direct observations in paleomagnetism, *Earth Planet. Sci. Lett.*, *87*, 161-172, 1988.

McFadden, P. L., and M. W. McElhinny, Classification of reversal test in paleomagnetism, *Geophys. J. Int.*, *103*, 725-729, 1990.

Monaco, C., S. Mazzoli, and L. Tortorici, Active thrust tectonics in western Sicily (southern Italy): The 1968 Belice earthquake sequence, *Terra Nova*, *8*, 372-381, 1996.

Nairn, A. E. M., G. Nardi, C. B. Gregor, and A. Incoronato, Coherence of the Trapanese units during tectonic emplacement in western Sicily, *Boll. Soc. Geol. Ital.*, *104*, 267-272, 1985.

Ogg, J. G, Magnetic polarity time scale of the Phanerozoic, in *Global Earth Physics: A Handbook of Physical Constants, AGU Ref. Shelf Ser Vol.* 1, edited by T. J. Ahrens, pp. 240-270, AGU, Washington, D.C., 1995.

Oldow, J. S., J. E T. Channell, R Catalano, and B. D'Argenio, Contemporaneous thrusting and large-scale rotations in the western Sicilian fold and thrust belt, *Tectonics*, *9*(4), 661-681, 1990.

Rio, D., I. Raffi, and G. Villa, Pliocene-Pleistocene calcareous nanofossil distribution patterns in the western Mediterranean, *Proc. Ocean Drill. Program Sci. Results*, *107*, 513-533, 1990.

Rio, D., R. Sprovieri, and E. Di Stefano, The Gelasian Stage: A proposal of a new chronostratigraphic unit of the Pliocene Series, *Riv. Ital. Paleontol. Strat.*, *100*, 103-124, 1994.

Roure, F., D. G. Howell, C. Muller, and I. Moretti, Late Cenozoic subduction complex of Sicily, *J. Struct. Geol.*, *12*, 259-266, 1990.

Sagnotti, L., Paleomagnetic evidence for a Pleistocene counterclockwise rotation of the Sant'Arcangelo basin, southern Italy, *Geophys. Res. Lett*, *19*, 135-138, 1992.

Sagnotti, L., and F. Speranza, Magnetic fabric analysis of the Plio-Pleistocene clay units of the Sant'Arcangelo basin, southern Italy, *Phys. Earth Planet. Inter.*, *77*, 165-176, 1993.

Sagnotti, L., and A. Winkler, Rock magnetism and palaeomagnetism of gregite-bearing mudstones in the Italian peninsula, *Earth Planet. Sci Lett.*, *165*, 67-80, 1999.

Sagnotti, L., F. Speranza, A Winkler, M. Mattei, and R. Funiciello, Magnetic fabric of clay sediments from the external northern Apennines (Italy), *Phys Earth Planet. Inter.*, *105*, 73-93, 1998

Scheepers, P.J.J., and C. G. Langereis, Analysis of NRM directions from Rossello composite: Implications for tectonic rotations of the Caltanisetta basin, Sicily, *Earth Planet. Sci. Lett.*, *119*, 243-258, 1993.

Scheepers, P.J.J., and C.G. Langereis, Magnetic fabric of Pleistocene clays from the Tyrrhenian arc: A magnetic lineation induced in the final stage of the middle Pleistocene compressive event, *Tectonics*, *13(5)*, 1190-1200, 1994.

Scheepers, P.J.J., C.G Langereis, and F. Hilgen, Counterclockwise rotations in the southern Appennines during the Pleistocene: Paleomagnetic evidence from the Matera area, *Tectonophysics*, *225*, 379-410, 1993.

Selvaggi, G., and C. Chiarabba, Seismicity and P-wave velocity image of the southern Tyrrhenian subduction zone, *Geophys J. Int.*, *121*, 818-826, 1995.

Spaak, P., Accuracy in correlation and ecologically aspects of the planktonic foraminiferal zonation of the Mediterranean Pliocene, *Utrecht Micropaleontol. Bull.*, *28*, 1-159, 1983.

Speranza, F., L. Sagnotti, and M. Mattei, Tectonics of the Umbria-Marche-Romagna Arc (central northern Apennines, Italy): New paleomagnetic constraints, *J. Geophys. Res.*, *102*, 3153-3166, 1997.

Sprovieri, R., Pliocene-early Pleistocene astronomically forced planktonic foraminifera abundance fluctuations and chronology of the Mediterranean calcareous plankton events, *Riv Ital. Paleontol. Stratigr*, *99*, 371-414, 1993

Sprovieri, R., E. Di Stefano, and M. Sprovieri, Late Neogene and Pleistocene Calcareous plankton biostratigraphy and chronology in the Mediterranean, paper presented at Eurobasin Euroconference, 8th Workshop of the ILP Task Force "Origin of Sedimentary Basins", Dept. of Geology and Geodesy, Univ. of Palermo, Palermo, Sicily, June 7-13, 1997.

Stephenson, A., A gyroremanent magnetization in anisotropic magnetic minerals, *Nature*, *84*, 49-51, 1980

Torii, M., K Fukuma, C.-S Horng, and T.-Q. Lee, Magnetic discrimination of pyrrhotite- and greigite- bearing sediment samples, *Geophys. Res. Lett.*, *23*, 1813-1816, 1996.

Van der Voo, R., *Paleomagnetism of the Atlantic, Tethys and Iapetus Oceans*, 411 pp., Cambridge Univ. Press, New York, 1993

Vitale, F. P., Studi sulla Valle del medio Belice (Sicilia centro occidentale): L'avanfossa plio-pleistocenica nel quadro dell'evoluzione paleotettonica dell'area, Ph.D. thesis, 201 pp., Univ. of Palermo, Palermo, Italy, 1990

Vitale, F. P., Duplex-type deformative style in the Sicani range, central western Sicily: Examples and tectonic implications, paper presented at Giornate in memoria di Leo Ogniben, Consiglio Nazionale delle Ricerche, Naxos, Italy, June 6-8, 1991.

Vitale, F P., Sezioni geologiche attraverso il segmento Sicano della catena sudtirrenica: bacini neogenici e deformazione attiva, in Geodinamica e tettonica attiva del sistema Tirreno-Appennino, pp. 230-232, Univ. of Camerino, Camerino, Italy, 1995.

Vitale, F. P., The Belice and the Menfi basins: Sequence stratigraphy and evolution during the Pliocene and the early Pleistocene, paper presented at Eurobasin Euroconference, 8th Workshop of the ILP Task Force "Origin of Sedimentary Basins", Dept. of Geology and Geodesy, Univ. of Palermo, Palermo, Sicily, June 7-13, 1997.

Vitale, F. P., and A. Sulli, The regional pattern of the Belice and Menfi basins. A deep geologic profile, paper presented at Eurobasin Euroconference, 8th Workshop of the ILP Task Force "Origin of Sedimentary Basins", Dept. of Geology and Geodesy, Univ. of Palermo, Palermo, Sicily, June 7-13, 1997.

R. W. H Butler, Department of Earth Sciences, University of Leeds, Leeds LS2 9JT, England, U.K.

A. Di Stefano and R. Maniscalco, Istituto di Geologia e Geofisica, Università di Catania, Corso Italia 55, 95129 Catania, Italy.

R. Funiciello, M. Mattei, and F. Speranza[1], Dipartimento di Scienze Geologiche, Università di Roma Tre, Largo S. L. Murialdo 1, 00146 Roma, Italy. (speranza@marte.ingrm.it)

(Received December 7, 1998;
revised April 9, 1999;
accepted April 19, 1999.)

TECTONICS, VOL. 18, NO. 6, PAGES 1084-1098 DECEMBER 1999

Plate deformation at depth under northern California: Slab gap or stretched slab?

Uri S. ten Brink
U.S. Geological Survey, Woods Hole, Massachusetts

Nobumichi Shimizu
Woods Hole Oceanographic Institution, Woods Hole, Massachusetts

Philipp C. Molzer
U.S. Geological Survey, Woods Hole, Massachusetts

Abstract. Plate kinematic interpretations for northern California predict a gap in the underlying subducted slab caused by the northward migration of the Pacific-North America-Juan de Fuca triple junction. However, large-scale decompression melting and asthenospheric upwelling to the base of the overlying plate within the postulated gap are not supported by geophysical and geochemical observations. We suggest a model for the interaction between the three plates which is compatible with the observations. In this "slab stretch" model the Juan de Fuca plate under coastal northern California deforms by stretching and thinning to fill the geometrical gap formed in the wake of the northward migrating Mendocino triple junction. The stretching is in response to boundary forces acting on the plate. The thinning results in an elevated geothermal gradient, which may be roughly equivalent to a 4 Ma oceanic lithosphere, still much cooler than that inferred by the slab gap model. We show that reequilibration of this geothermal gradient under 20-30 km thick overlying plate can explain the minor Neogene volcanic activity, its chemical composition, and the heat flow. In contrast to northern California, geochemical and geophysical consequences of a "true" slab gap can be observed in the California Inner Continental Borderland offshore Los Angeles, where local asthenospheric upwelling probably took place during the Miocene as a result of horizontal extension and rotation of the overlying plate. The elevated heat flow in central California can be explained by thermal reequilibration of the stalled Monterey microplate under the Coast Ranges, rather than by a slab gap or viscous shear heating in the mantle.

1. Introduction

Plate kinematic reconstructions commonly assume plate boundaries that have zero width throughout their thickness. This is reasonable for oceanic plate boundaries where the deformation zone is usually only a few kilometers wide. However, the deformation zone at a continental plate boundary can be hundreds of kilometers wide. In California, reconstructions based on the above assumption predict asthenospheric upwelling into a gap in the underlying subducted slab ("slab gap") as a result of the northward migration of the unstable Pacific-North America-Juan de Fuca triple junction (Figure 1). As the triple junction migrates north, the subducting Juan de Fuca (JdF) plate slides out from beneath the North American plate, leaving a single-plate thickness where previously there was a double-plate thickness (Figure 1). Because the kinematic arguments in California are well established [*Atwater*, 1989], their consequences for geological interpretation have been accepted even when other interpretations of geological, geochemical, and geophysical data can be found. Here we suggest that perhaps a more realistic view of the plate boundary as a continuum with distributed deformation can reconcile the regional plate kinematics with the local geological, geochemical, and geophysical observations. We limit our model to the Coast Ranges, which are underlain by a relatively thin accretionary prism, because surface manifestation of asthenospheric upwelling should be readily recognizable in that region. We do not address a possible slab gap under the Great Valley or the Sierra Nevada, which are underlain by a thicker, more complex ophiolitic and Sierran arc crust and upper mantle [*Godfrey et al.*, 1997; *Godfrey and Klemperer*, 1998].

2. The Slab Gap Model

The geology of the west coast of North America during the last 150 Myr has largely been shaped by the subduction of the Farallon plate. Starting ~ 28-30 Myr ago, however, subduction brought the Pacific plate in contact with North America [*Atwater*, 1989](Figure 1a). Shortly thereafter, the Mendocino triple junction (MTJ) formed between the northern remnant of the Farallon plate (the Juan de Fuca plate), the North American (NOAM) plate, and the Pacific plate (Figure 1a). The triple junction has migrated northward relative to North America during the last ~20 Myr and subduction of the Juan de Fuca (JdF) plate was replaced by a right-lateral strike-slip (or transform) plate boundary (Figures 1 and 2). Upon cessation of subduction the weight of the already subducted plate continued to pull the slab downward, opening a gap into which sub-lithospheric material (asthenosphere) upwelled [*Dickinson*, 1997; *Dickinson and Snyder*, 1979a]. It is easy to visualize

Paper number 1999TC900050.
0278-7407/99/1999TC900050$12.00

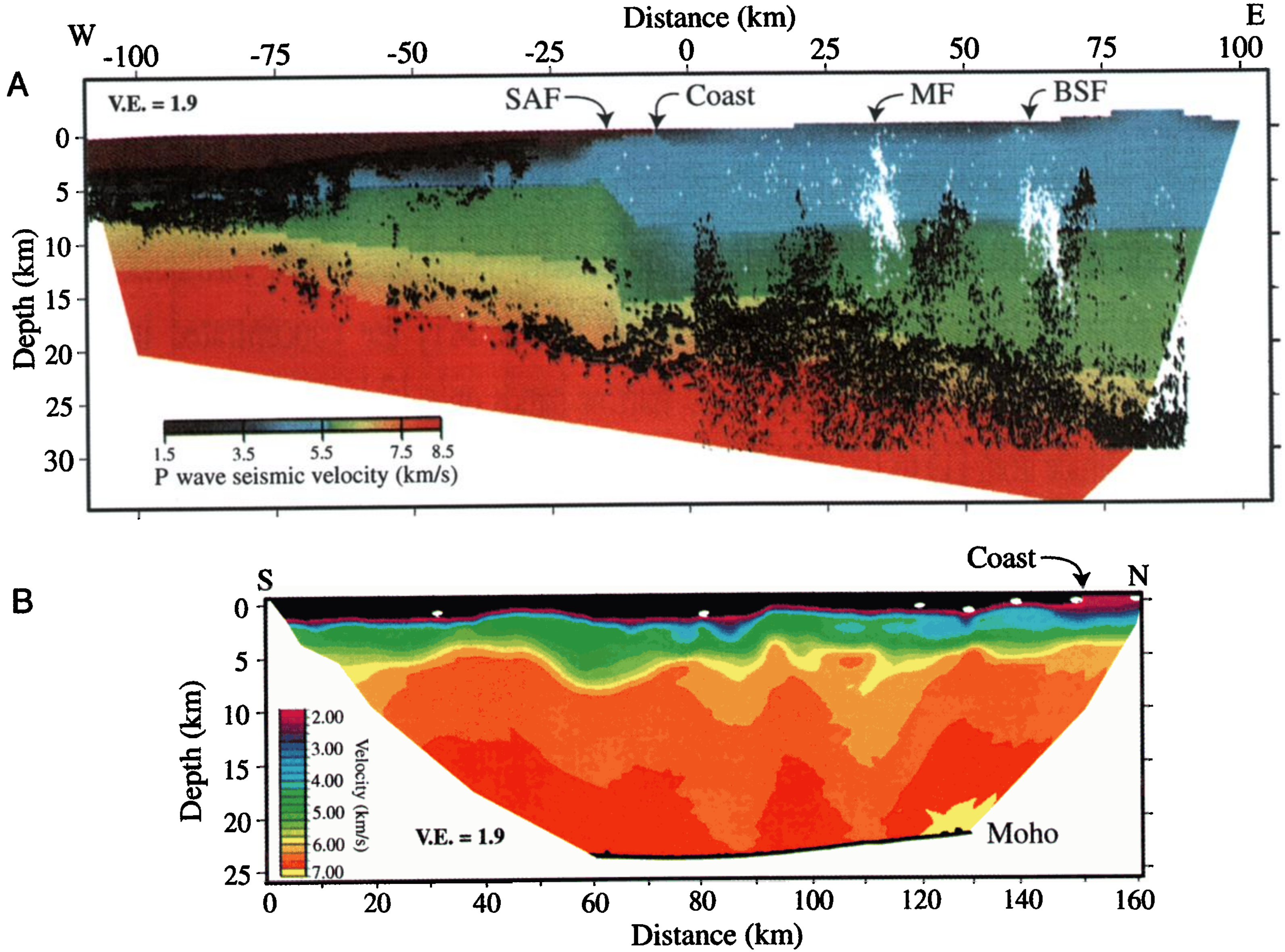

Plate 1. Comparison of crustal *P* wave velocity models from (a) northern California [*Henstock et al.*, 1997] and (b) the Inner Continental Borderland [*ten Brink et al.*, 1999]. See Figure 2 for location. Black regions in Plate 1a are bright reflections and white dots are earthquake epicenters. SAF, San Andreas Fault; MF, Maacama Fault; BSF, Bartlett Fault. White dots in Plate 1b) show the locations of recording stations. Air guns shots produced by the R/V Maurice Ewing at 50 m intervals along the line served as a seismic source. Note the different velocity color scale between Plates 1a and 1b.

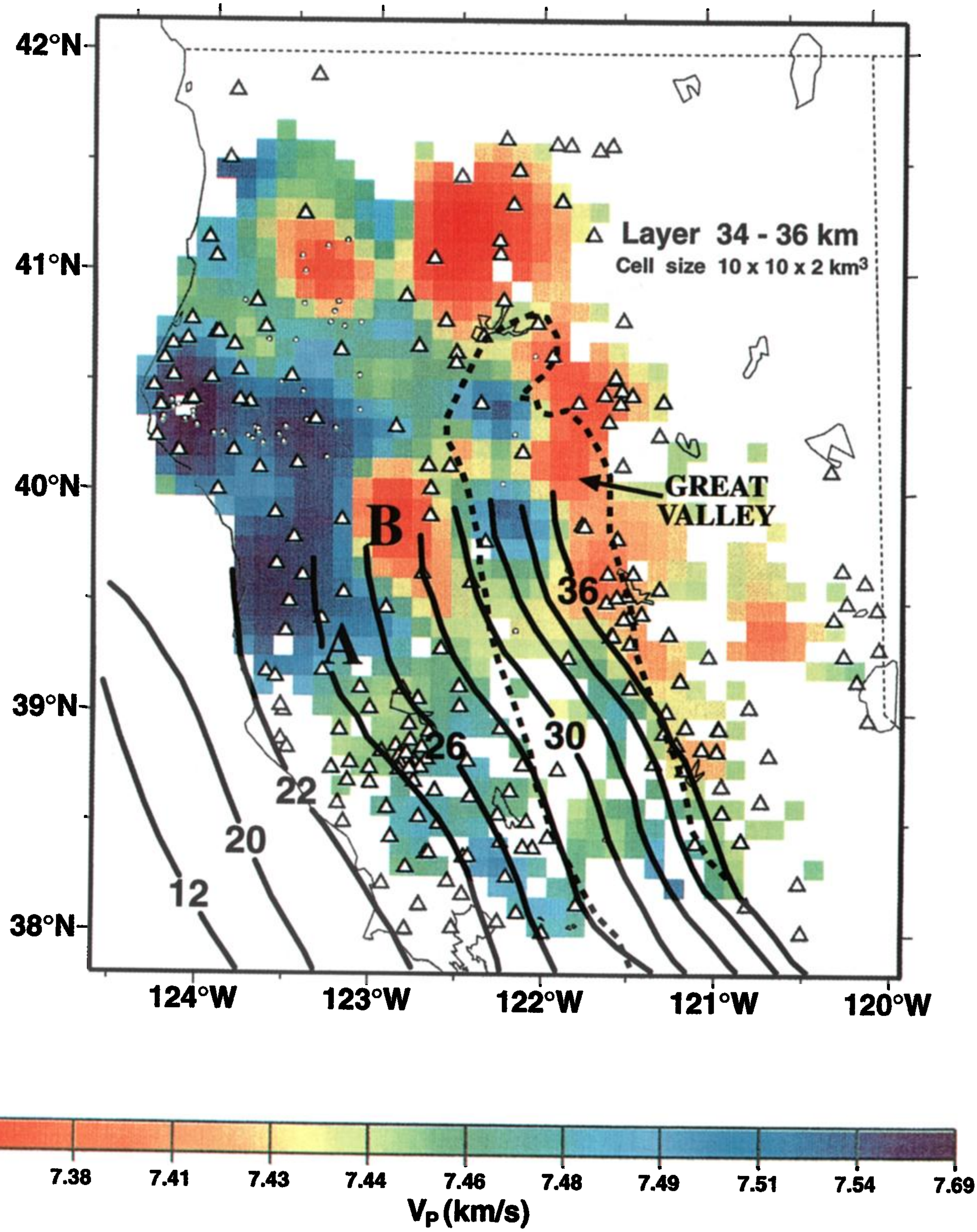

Plate 2. *P* wave velocity variations in a layer 34-36 km deep from travel time tomographic inversion of local earthquakes (H. Benz, written communication, 1998). Dashed line shows the location of the Great Valley. Contours of depth to Moho, based on the synthesis of seismic refraction profiles collected during the 1980s and 1990s between the Sierra Nevada and offshore California [*Brocher et al.*, 1999], show that west of the Great Valley this layer lies below the Moho. Note the lack of a regional low-velocity anomaly under the Coast Ranges, which would correspond to asthenospheric upwelling. Two local low-velocity anomalies were identified from this and other depth slices through the model, one anomaly (A) is between 22 and 30 km (therefore no anomaly is seen at the depth of this slice) and the other anomaly (B) is between 28 and 36 km. For details of the technique see the work of *Benz et al.* [1996]. Small circles show the epicentral locations. Triangles show the recording station locations.

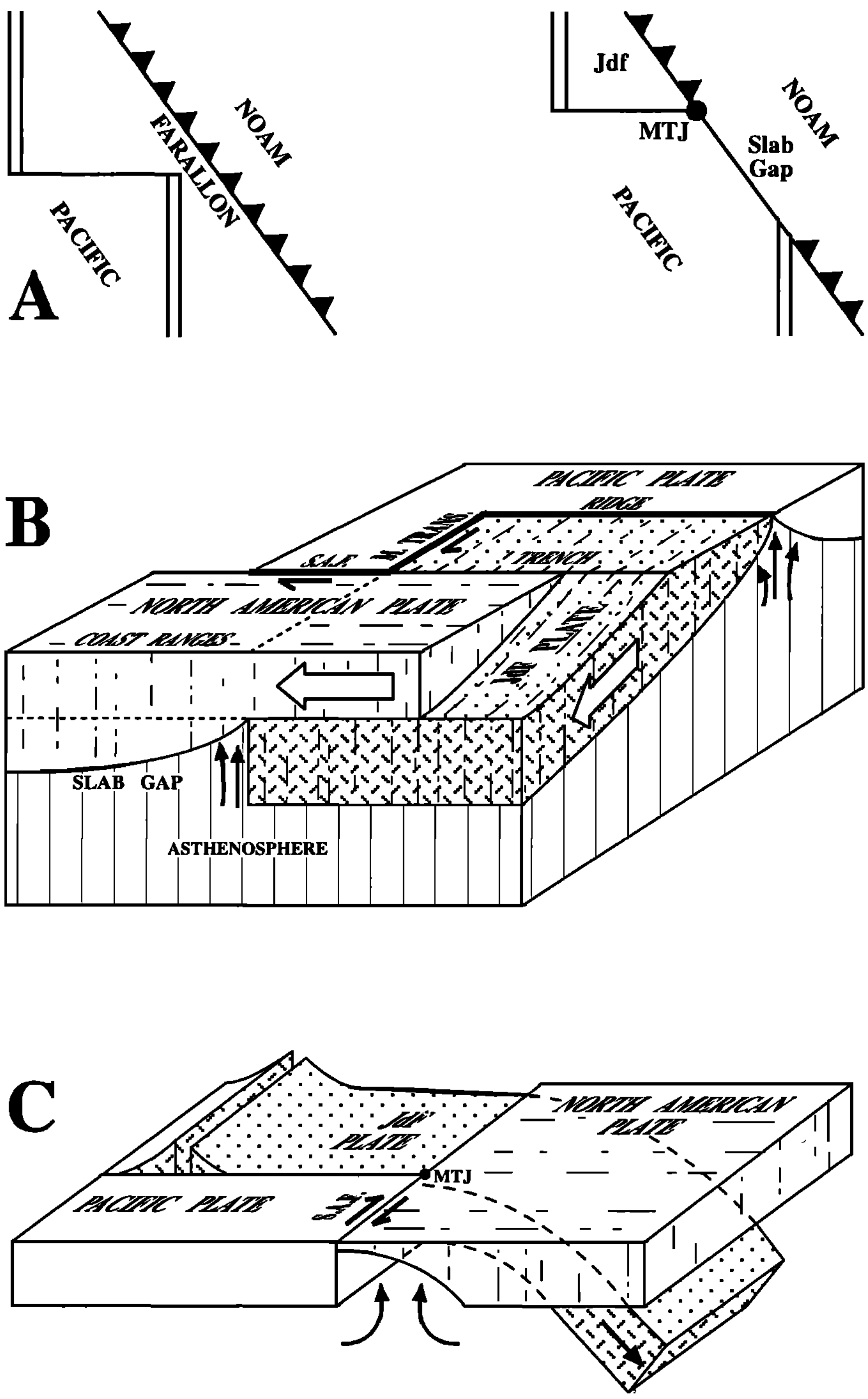

Figure 1. (a) Simplified plate motion prior to and after the collision of the Pacific-Farallon ridge with North America (NOAM). JdF, Juan de Fuca; MTJ, Mendocino triple junction. (b) Motion of Juan de Fuca and North American plates relative to a fixed Pacific plate near the Mendocino triple junction [after *Lachenbruch and Sass*, 1980]. A gap develops in the mantle lithosphere beneath NOAM as it slides off the JdF plate. SAF, San Andreas fault; M. trans - Mendocino fracture zone. (c) Side view of the slab gap assuming a vertical Pacific plate boundary along the San Andreas fault [after *Liu and Furlong*, 1992].

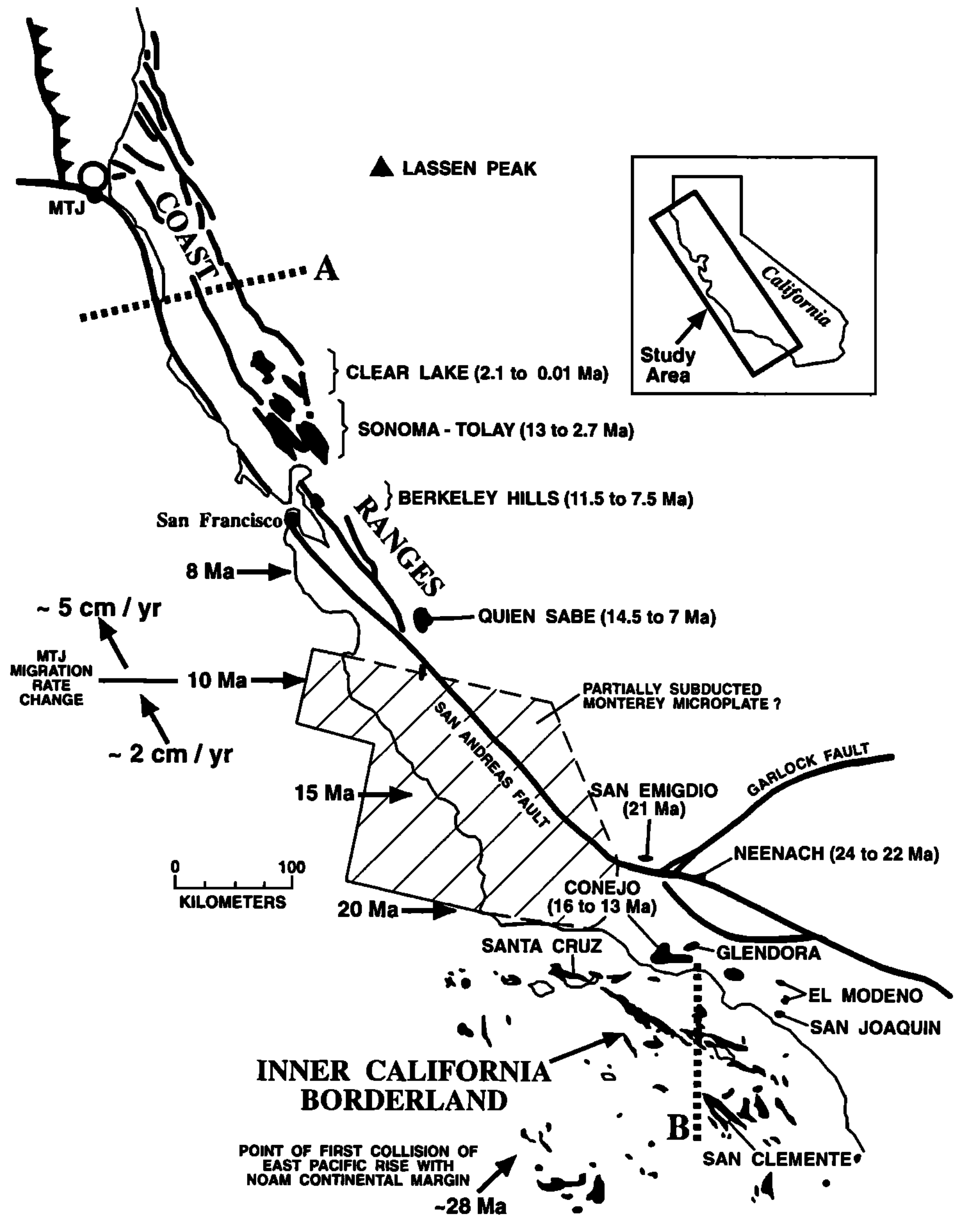

Figure 2. Generalized geologic map of coastal California showing the locations and ages of Neogene volcanic centers (solid regions [after *Johnson and O'Neil*, 1984] and the position of the Mendocino triple junction (MTJ) at various times throughout the Neogene [*Atwater and Stock*, 1998]. The rate of this migration makes it possible to equate the distance from the present location of the MTJ at Cape Mendocino to any point farther south in California with the time since the MTJ swept through this point. Also shown are mid-Miocene volcanic outcrops in southern California [*Vedder*, 1987], which are related to the extension of the California Borderland, not to MTJ migration. Heavy dashed lines show the location of seismic velocity models in Plate 1. Heavy lines show the faults. Faults in northern California are after *Kelsey and Carver* [1988]. Open circle shows the location of the two strongest aftershocks of the 1992 Cape Mendocino earthquake [*Oppenheimer et al.*, 1993].

the formation of the slab gap in a fixed Pacific plate reference frame, as a sideways (southward) slide of NOAM plate along the San Andreas fault (SAF) from an area underlain by subducted Farallon plate to an area where such a plate no longer existed (Figure 1b;)[*Lachenbruch and Sass*, 1980]. Various predictions have been made based on the slab gap hypothesis. The slab gap was envisioned to be the locus of decompression melting in the asthenosphere resulting in the accretion of a several kilometers thick layer of mafic material to the base of the California crust [*Liu and Furlong*, 1992]. Estimates of hydrocarbon maturation were made based on the thermal regime of a slab gap with asthenoshperic upwelling [*Heasler and*

Surdam, 1985]. The Pacific-NOAM plate boundary was envisioned to be subhorizontal at depth (e.g., under the San Francisco Bay Area) and to migrate inland over time as the slab gap annealed [*Furlong et al.*, 1989; *Zandt and Furlong*, 1982].

3. Testing The Slab Gap Model

Several recent publications have questioned some aspects of the slab gap model [e.g., *Hole et al.*, 1998]. The geometry and timing of faults in the San Francisco Bay Area were shown not to fit the slab gap prediction of a subhorizontal plate boundary. Using rheological considerations, *Bohannon and Parsons* [1995] argued that a tear in the downgoing slab should occur at depths of ~ 100 km, which would place it considerably eastward of coastal California. Noting a continuous high basal velocity layer under the continental margin of central California, *Page and Brocher* [1993] suggested that Pacific plate lithosphere underlies the North American plate margin because a change in plate motions 3.5 Myr ago caused transpression between the two plates. *Henstock et al.* [1997] interpreted a continuous high-velocity basal layer that dipped eastward from the former trench out to 200 km farther east in northern California as a possible underplated JdF plate crust.

The size of the assumed gap may also be smaller than was previously assumed. Offshore magnetic anomalies and seismic evidence suggest that the central California margin and Coast Ranges may be underlain by the partially subducted Monterey microplate [*Miller et al.*, 1992, *Howie et al.*, 1993], which has been fully coupled to the Pacific plate since 18 Myr ago [*Nicholson et al.*, 1994](Figure 2). Therefore, only a ~430 km long section of the California Coast Ranges should be considered a candidate for a slab gap [*Atwater and Stock*, 1998]. This section, which extends from the MTJ to Monterey Bay, was swept by the migrating MTJ during the last 9 Myr.

The plate kinematic configuration itself may be more complicated than previously assumed. The slab-gap model is based on the configuration of three independently-moving rigid and competent plates, Pacific, NOAM, and JdF plates, but, in fact, the Pacific plate is the only rigid and competent plate. Nonrigid deformation of the JdF plate, known as the Gorda Deformation Zone, is manifested by curved magnetic anomalies and pervasive faulting [*Wilson*, 1986]. Deformation is pervasive despite the fact that the Gorda Deformation Zone is an oceanic plate whose top surface is at 0°C and has not yet even subducted under NOAM.

Neither does the NOAM plate in California behave as a single rigid plate. Several authors [e.g., *Walcott*, 1993; *Atwater and Stock*, 1998] have suggested that the Sierra Nevada/Great Valley block has been moving together with the Klamath Mountains (Figure 3). This block moved ~200 km northwestward relative to stable North America since 16 Ma and 130 km since 8 Ma, which represents ~30% of the total Pacific-NOAM motion during these time intervals [*Atwater and Stock*, 1998]. In a fixed Pacific plate reference frame the Klamath Mountains have then been moving southward faster than the California Coast Ranges have. The thickened NOAM crust in the Coast Ranges landward of the MTJ and south of the Klamath Mountains [*Beaudoin et al.*, 1998] may be the result of this relative motion. At any rate, NOAM is not a single block in the vicinity of the MTJ. It consists of two blocks, the Sierra Nevada - Great Valley - Klamath Mountains block and the Coast Ranges. The latter is essentially a deformation zone between two more competent blocks, the Pacific plate and the sierra Nevada - Great Valley block [Walcott, 1993] as geodetic measurements suggest [*Prescott and Yu*, 1986].

The slab gap model also assumes that the three plates are moving independently. This has not been the case for the JdF plate after the fragmentation of the Farallon plate. Starting 18 Myr ago, the JdF plate started rotating clockwise and seafloor spreading slowed [*Atwater*, 1989]. The clockwise rotation and the slowing of spreading aligned the JdF plate motion with respect to the Pacific closer to that of NOAM. This phenomenon has been most pronounced at the southern end of the plate, the Gorda Deformation Zone (Figure 3). The 1992 thrust earthquake beneath Cape Mendocino was followed by two M_s 6.6 aftershock within the JdF plate (see Figure 2 for location). The mechanism of these aftershocks indicates right-lateral, strike-slip motion on planes striking NW-SE at epicentral depths, which are within the JdF plate [*Oppenheimer et al.*, 1993]. Onshore, dextral strike-slip faults extend to the NNE across the MTJ, suggesting that some dextral motion of NOAM affects the area north of the MTJ [*Kelsey and Carver*, 1988](Figure 2).

4. Slab-Stretch Model

We propose an alternative model based on kinematics of non rigid plate boundaries with a lithospheric thermal history, which explains the geochemical and geophysical observations. In this model, continuous deformation, rotation, and stretching of the JdF plate fill the geometrical gap without large-scale holes and tears (Figures 3 and 4).

The large and rigid Pacific plate is moving northwestward in a hot spot frame of reference [*Atwater and Stock*, 1998](Figure 3) pushing at the Juan de Fuca plate across the Mendocino Fracture Zone and causing it to move northward. Although the fracture zone may be weak in shear, north-south oriented normal compressive stresses can be transmitted to the southern part of the plate [*Wang et al.*, 1997]. Landward of the MTJ, however, the subducting Juan de Fuca plate is not pushed by the Pacific plate and, in fact, is not confined. This allows the plate to spread into the unconfined region. The spreading may be analogous to the "westward spreading" of western North America, i.e., the extensional and rotational deformation, attributed by some to the northwestward retreat of the Pacific plate away from North America [*Walcott*, 1993; *Atwater and Stock*, 1998].

A more quantitative analysis for the forces acting on the Juan de Fuca plate [*Wang et al.*, 1997] further illuminates how the slab stretch may occur. The main forces acting on the Juan de Fuca plate are the northward transform push across the Mendocino Fracture Zone and the strike-parallel subduction resistance force which balances it [*Wang et al.*, 1997](Figure 5a). Subduction resistance is the viscous drag on both the upper surface and the lower surface of the slab. The absolute motion of the Juan de Fuca plate and its motion relative to North America are roughly parallel to each other (northeastward) and can thus be treated as the combined resistance. The subduction resistance force can be separated into directions orthogonal and parallel to the subduction zone. The orthogonal compo-

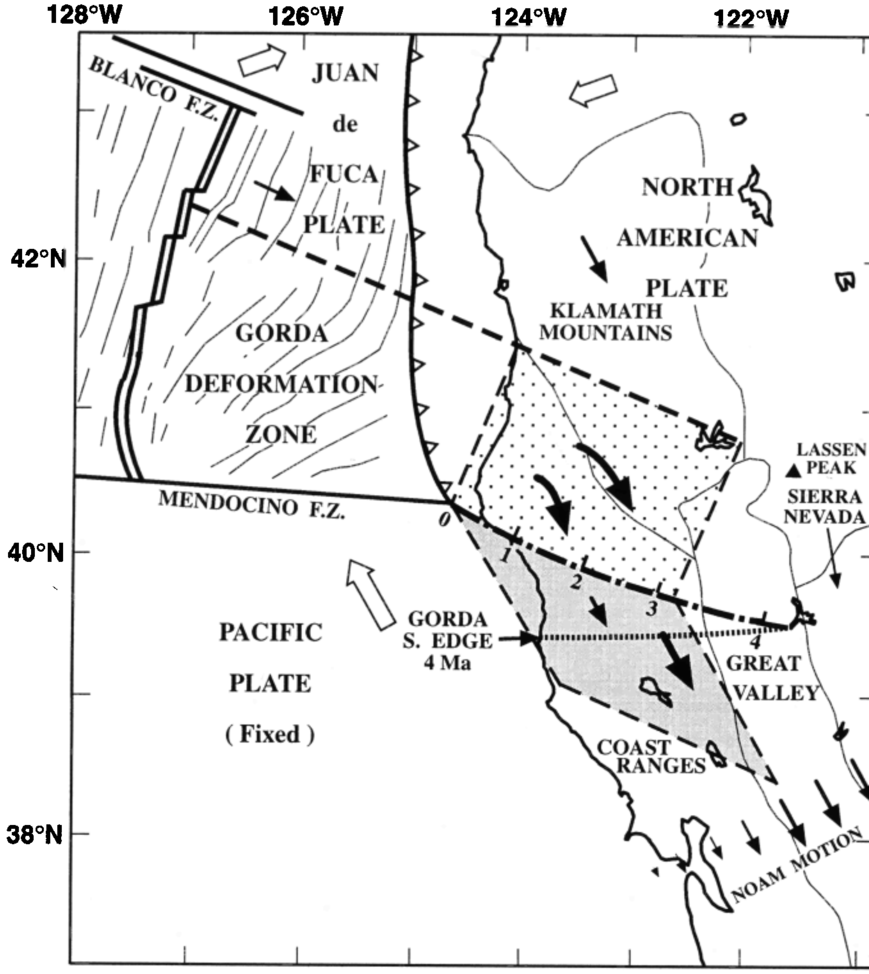

Figure 3. Simplified map of the Mendocino triple junction area and the extent of the subducted Juan de Fuca (JdF) plate. Dotted area is the estimated subducted JdF area during the last 3.2 Myr, determined by the southern edge of the subducted plate (dash-dotted line with numbers corresponding to age in megayears)[*Wilson,* 1986] and the trajectory of the northern edge of the Gorda Deformation Zone (GDZ) parallel to the Blanco Fracture Zone (heavy dashed line). This trajectory extends to the northern edge of the Great Valley and is also the northern limit of strike-slip faults in northern California (Figure 2). Shaded area is the estimated slab gap area under the Coast Ranges assuming a constant North American plate relative motion of 5 cm yr^{-1} during the past 3.2 Myr. However, the actual gap area to be filled by the stretching of the JdF slab is only approximately one-half of the shaded area, because North America motion tapers off from the Great Valley toward the San Andreas fault [*Prescott and Yu,* 1986]. Another estimate for the gap area during the last 4 Myr is given by the area bounded by the southern edge of the Gorda Deformation Zone at 4 Ma [from *Atwater and Stock,* 1998] and the estimated present southern edge of the JdF plate (dashed-dotted line)[*Wilson,* 1986). Heavy arrows represent rotation and stretching of the subducted JdF slab to fill the geometrical gap. Small arrows represent plate motion in a fixed Pacific reference. Open arrows represent Pacific, North American, and JdF plate motion in an "absolute" (hot spot) frame of reference [*Wang et al.,* 1997].

nent (east-west in the southern JdF plate) balances the slab pull force, which is orthogonal to and directly downdip of the subduction zone [*Wang et al.,* 1997]. The parallel component is oriented south and balances the transform push force seaward of the MTJ. However, there is no force to balance the strike-parallel force landward of the MTJ; hence rotation and stretching can occur in this area as shown by the finite element model of Wang et al. [1997](Figure 5b).

We propose that the geometrical gap predicted by a rigid plate model is filled by continuous deformation without large holes and tears due to rotation and stretching of the JdF plate (Figures 3 and 4). The size of the gap can be estimated from the length of the area predicted by rigid plate kinematics to have opened during the last 3.2 Myr (shaded area in Figure 3), calculated assuming an average migration rate of 5 cm y^{-1}. However, NOAM motion relative to the Pacific plate decreases from the Great Valley to zero offshore [*Prescott and Yu,* 1986], implying that the Coast Ranges are increasingly dragged by the Pacific plate. For simplicity, therefore, we consider that only one-half of the shaded area (Figure 3) constitutes the gap. One-

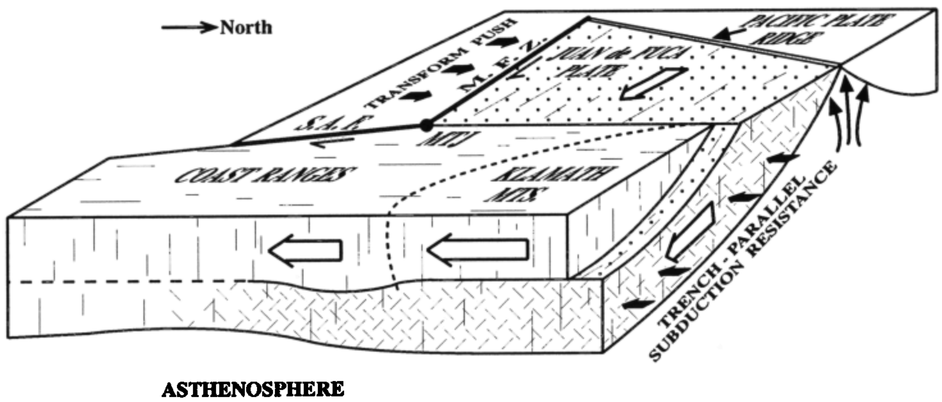

Figure 4. Alternative cartoon to Figure 1b showing continuous plate deformation filling the geometrical slab gap (slab stretch model), the forces acting on the southern end of the Juan de Fuca plate, and the transient thickening of the overlying North American plate due to faster motion of the Klamath Mountains -Sierra Nevada block relative to the Coast Ranges. See text for details.

half of the shaded area is only 37% of the JdF plate area subducted during this time [*Wilson*, 1986](Figure 3). If the JdF slab stretches to fill this gap, it will have to thin by a factor of only 1.37. An alternative estimate of the predicted gap from rigid plate kinematics is the difference between the placements of the southern edge of the JdF plate 4 Myr ago and at present [*Atwater and Stock*, 1998](Figure 3). The triangular area between these two placements is only 27% of the JdF plate area subducted during the past 4 Myr [*Wilson*, 1986](Figure 3).

The age of the subducted plate is 6-10 Ma [*Wilson*, 1986]; hence the thickness of the thermal lithosphere (to a temperature of 1300°C) is 25-30 km. Thinning by a factor of 1.37 reduces the slab's thermal thickness to 18.1-21.7 km, which is equivalent to the thickness of a 4 Ma slab. (Thinning of the subducted slab by a factor of 1.27 reduces the thermal thickness of the lithosphere to 19.7-23.6 km, which is equivalent to the thickness of a 4-5 Ma slab.) Thinning of the mantle at these shallow depths (40-50 km) and by this factor is expected to generate only negligible decompression melting of the upper mantle [*McKenzie and Bickle*, 1988]. Strain may not be uniform, so larger amounts of thinning may take place locally as the tomographic images, discussed in section 6, may suggest.

The depth and expected temperature range (Figure 6) for the JdF plate underlying the Coast Ranges indicate that its rheology under tension at the strain rates corresponding to the above factors of stretching (2-3 x 10^{-15} s^{-1}) may be in the brittle-ductile transition regime [*Brace and Kohlstedt*, 1980]. It is possible, especially under the thinner western part of the

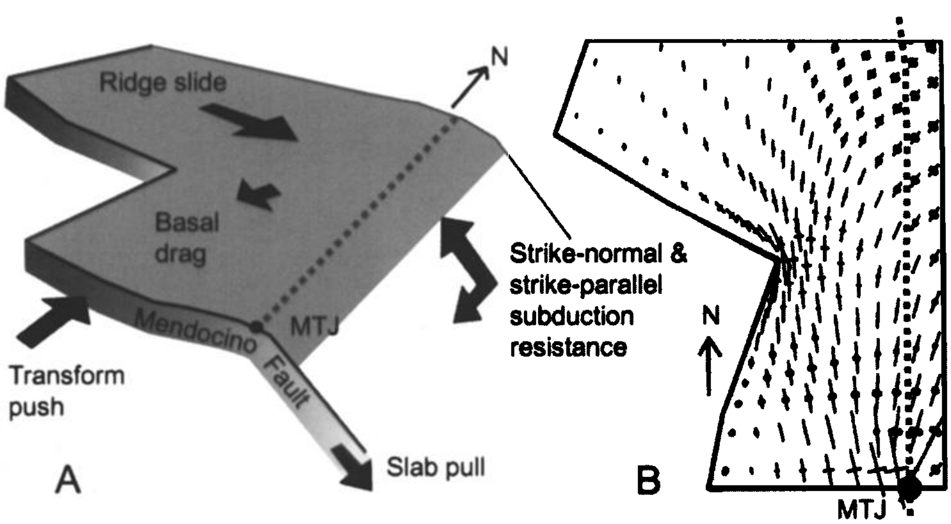

Figure 5. (a) Forces acting on the southern part of the Juan de Fuca (JdF) plate [from *Wang et al.*, 1997]. (b) Stress field in the southern JdF plate calculated by a plane stress finite element method for an elastic lithospheric plate (modified from Model V2 of *Wang et al.*)[1997]. This model includes a 50 km wide zone of the subducted slab landward of the trench (dashed line). Thin bars show the compressive stresses. Thick bars show the tensile stresses. Note the rotation and stretching landward of the Mendocino triple junction, because transform push is absent there.

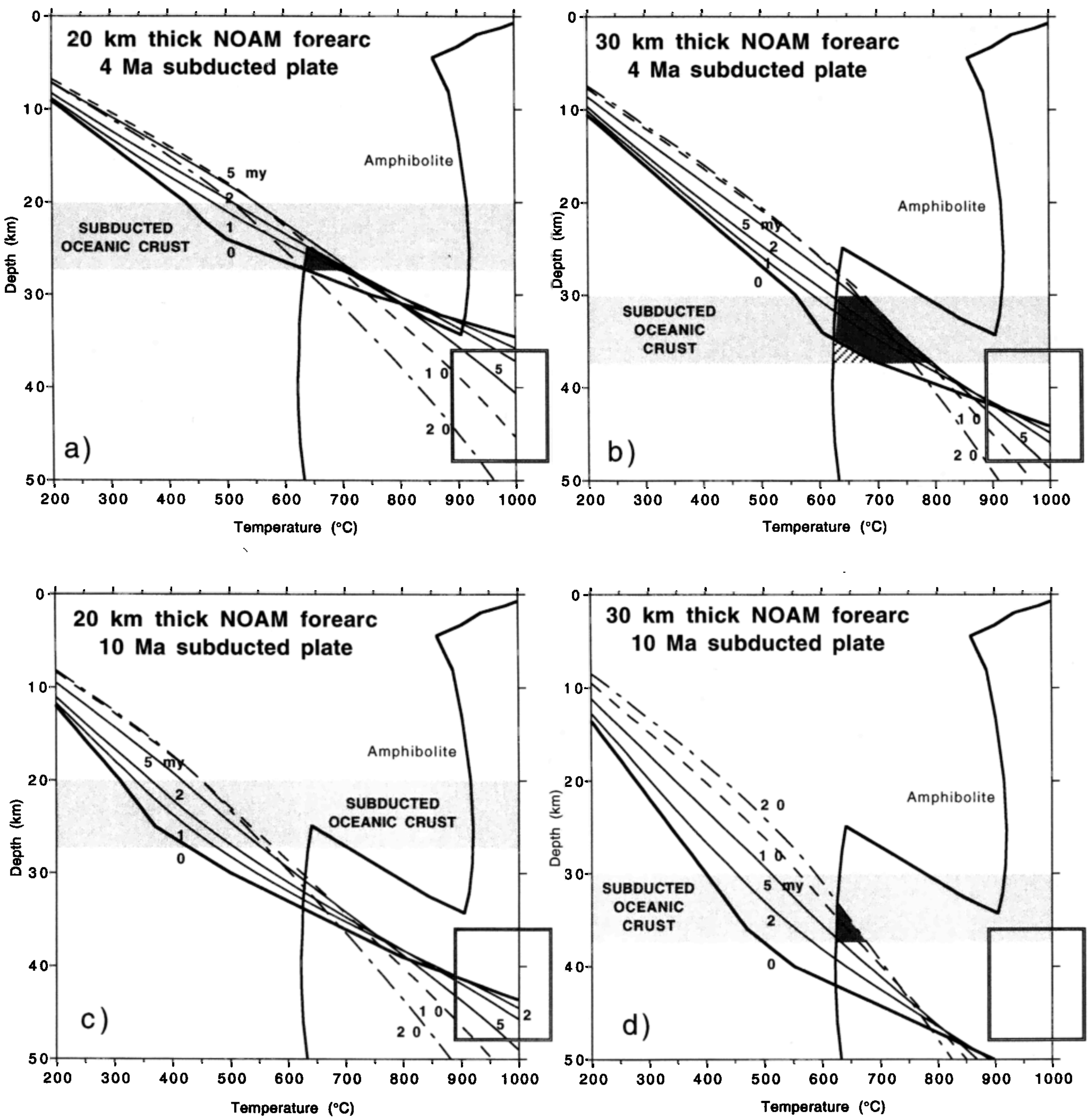

Figure 6. (a-d) Calculated geothermal gradients as a function of time after cessation of subduction (time 0) for subducted slabs with a thermal age of 4 and 10 Ma overlain by 20 and 30 km thick North American plate. (e) Simplified geothermal gradients as a function of time for a partial slab gap (no mantle lithosphere), shown for comparison with Figures 6a - 6d. In the initial geothermal gradient, which is equivalent to a 0.6 Myr old subducted slab, a temperature of 1300°C is placed at the base of the subducted slab 7 km beneath a 20 km thick North American plate. Also shown are solidi for amphibolite (solid line in Figures 6a - 6e) [*Wyllie and Wolf*, 1993] and for red clay, dry basalt, and peridotite solidi (solid lines in Figure 6e; [*Nichols et al.*, 1996; *Peacock*, 1996]. Partial melt of the oceanic crust is expected only at depths where temperatures are higher than the amphibolite solidus (dotted regions), but more voluminous melting at the base of the former forearc, the subducted oceanic crust, and the subducted mantle lithosphere is expected in a slab gap model (Figure 6e). Some melting may occur even before cessation of subduction (cross-hatched regions). Boxes show the thermobarometric estimate based on spinel lherzolites in xenoliths of Pliocene (2.5-3.6 Ma) basalt along the Calaveras fault north of Quien Sabe [*Jove and Coleman*, 1998]. Calculated geothermal gradients for a 4 Ma slab (Figure 6a) 5-10 Myr after cessation of subduction and stretching fall within this temperature-depth estimate, but those for a slab gap (Figure 6e) predict much higher temperatures at this depth range.

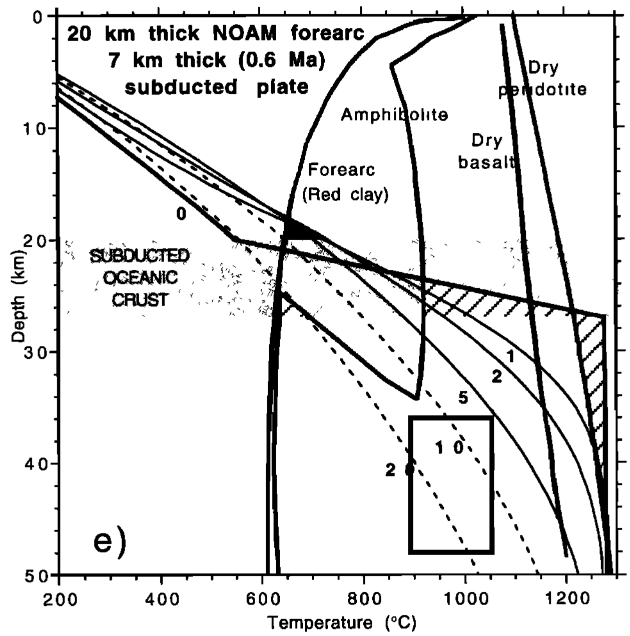

Figure 6. (continued)

Coast Ranges, that temperatures in the underplated JdF oceanic crust are low enough to allow brittle deformation. The vertical offsets in the subducted slab of northern California [*Henstock et al.*, 1997; Plate 1a) may be manifestations of this brittle regime. Under the eastern part of the Coast Ranges and at a deeper level of the JdF lithosphere, ductile deformation probably takes place [*Molnar*, 1992]. Strain rate is governed by temperature; hence the lower part of the slab is expected to thin faster than the upper part of the slab. On the other hand, the oceanic crust is more felsic than the mantle lithosphere and therefore it may deform faster [*Brace and Kohlstedt*, 1980]. Uncertainties in the activation energy for olivine and diabase yield an uncertainty in creep strength of at least a factor 10 at the temperature range of the subducted oceanic crust (Figure 6), making more accurate analysis futile [Molnar, 1992].

5. Thermal and Magmatic Consequences of the Slab Stretch Model

With the slab stretch model in mind, we envision the thermal evolution of the lithosphere to be the result of thermal reequilibration following cessation of subduction and some stretching of the slab. The overlying plate is the forearc region of the subduction zone. This region cools during subduction [e.g., *van der Beukel and Wortel*, 1988], because the cold surface of the subducting plate is underthrusted beneath the forearc. This cooling effect is generally manifested by the low surface heat flow in forearc regions (<45 mW m^{-2}). The geothermal gradient in the forearc depends on the rate of subduction and the age of the subducting plate [*Dumitru*, 1991]. When subduction and stretching stop, thermal reequilibration begins, and the temperature at the base of the forearc rises.

We approximate this process by calculating the geothermal gradients as a function of time after cessation of subduction (time 0) for subducted slabs with a thermal age of 10 and 4 Ma overlain by 20 and 30 km thick forearc. Initial temperature gradients in our calculations are *Dumitru*'s [1991] thermal gradients for 10 and 4 Ma subducted lithosphere and overlying North American plate thicknesses of 20 and 30 km. His calculations use a two-dimensional finite difference grid assuming steady state (~50 Myr) subduction, a subduction rate of ~40 km my^{-1}, a subducting slab ≤ 10 Ma, and a subduction angle of ~15° [*Dumitru*, 1991, and references therein). Our finite-difference numerical calculations used a vertical grid of 1 km to a depth of 125 km, time step of 8000 years, bottom and surface temperatures of 1300°C and 0°C, respectively, specific heat of 1 J kg^{-1} °C^{-1}, forearc and slab thermal conductivities of 2.5 and 3.3 W m^{-1o} C^{-1}, and an exponential radiogenic heat production within the overlying forearc with a "skin depth" of 10 km and a surface production rate of 1.2 μW m^{-3}. Horizontal conduction across the former forearc was neglected following *James et al.* [1989]. Lateral conduction due to localized areas of high strain was ignored for the sake of simplicity and clarity. Initial heat flow is higher than that calculated (Figure 7), because the forearc region was cooler at the end of subduction than that determined from the steady-state calculations (i.e., assuming a constant age of subducting plate)[*Dumitru*, 1991]. Much older slab entered the trench during much of the time prior to cessation and stretching. However, the amount of later transient heating during initial reequilibration is also larger, and the overall effect on the results is small.

There are two important consequences of thermal reequilibration: (1) melting of the subducted crust and (2) elevated heat flow in the overlying plate. Minor volcanic activity occurred in the wake of the northward passage of the MTJ, reflected in the northward younging of volcanic outcrops (Figure 2)[*Dickinson*, 1997; *Dickinson and Snyder*, 1979a]. Present-day activity (< 2 Ma) is located at Clear Lake. It has been suggested that the volcanism resulted from a slab gap under the forearc [*Dickinson and Snyder*, 1979b; *Johnson and O'Neil*, 1984]. Quantitative estimates of asthenospheric upwelling into the gap, however, predict voluminous magmatic production [*Liu and Furlong*, 1992], far more voluminous than the geologic data suggest. In the slab stretch model we explain the volcanism as mainly arising from crustal anatexis. Figure 6 illustrates the magnitude of temperature rise at the subducted oceanic crust and base of the overlying forearc as a function of thermal age of the subducted slab and of forearc thickness. Pressure-temperature conditions of the amphibolite solidus (temperatures ≥ 630°C at depths ≥ 25 km)[*Wyllie and Wolf*, 1993] can be attained during the first 5 Myr after the cessation of subduction of a young (~4 Ma) oceanic crust overlain by 20-30 km thick crust (dotted region in Figure 6). In fact, subduction of very young oceanic slab can lead to slab melting even before subduction ceases (cross-hatched regions in Figures 6b and e)[*Defant and Drummond*, 1990; *Peacock*, 1996]. For older subducted oceanic crust (e.g., 10 Ma, Figures 6c and 6d) or thinner overlying forearc, these conditions are either not met or are met more than 5 Myr after subduction has ceased (Figure 6d). Dehydration melting of amphibolite would cease immediately after small volumes of melt are produced, because water released by dehydration is immediately dissolved into melt, thereby "drying-up" the system; in other words, the vapor present solidus (Figure 6) no longer applies. Magma-

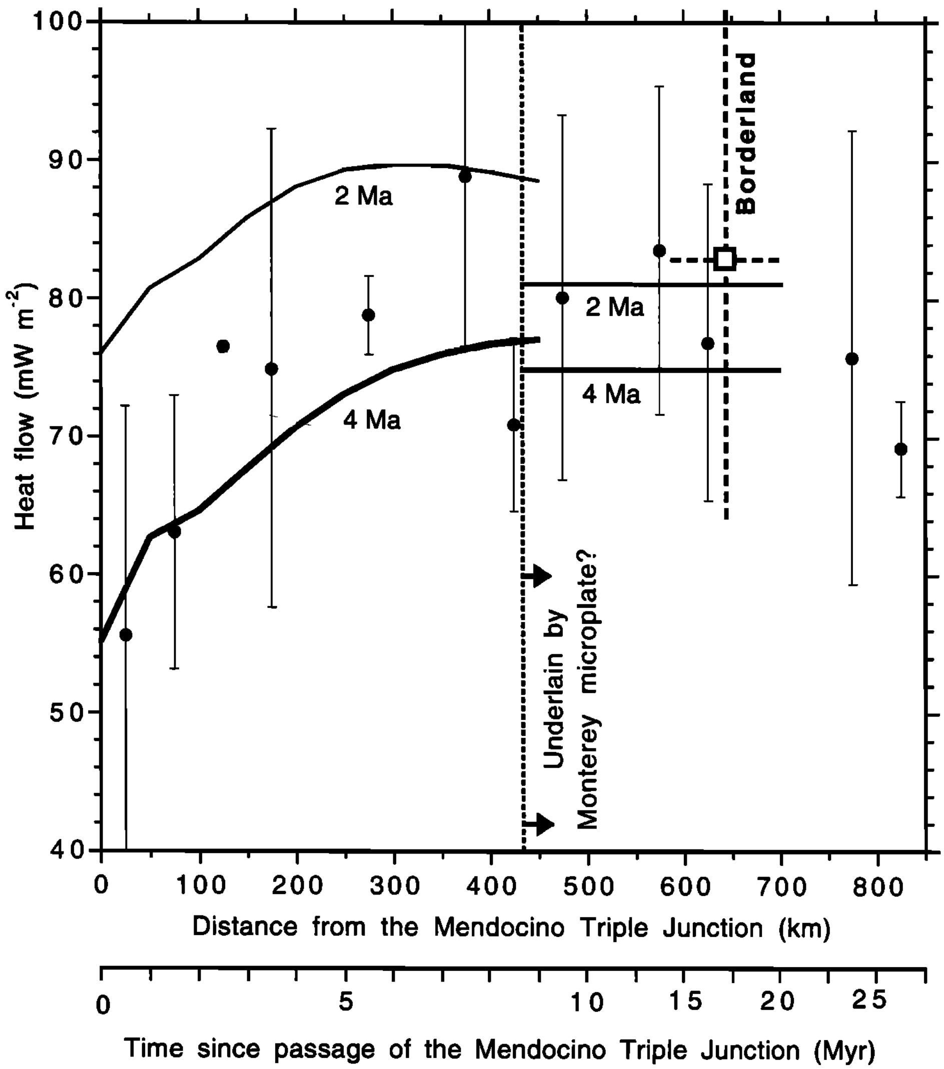

Figure 7. Surface heat flow in western California as a function of distance from the Mendocino triple junction (MTJ) and time since the MTJ passed through the measurement location [*Lachenbruch and Sass*, 1980; *Sass et al.*, 1997]. Heat flow was averaged over 50 km bins with error bars showing one standard deviation. Also marked for comparison is the mean heat flow for the California Inner Continental Borderland [*Lee and Henyey*, 1975] with a range showing one standard deviation (dashed line). It is plotted at an age range of 14-20 Myr, the age range for extension and volcanism in the Inner California Borderland. Curves represent calculated heat flow values from geothermal gradients in Figure 6 for a forearc thickness of 20 km and thermal age of subducted slab of 4 and 2 Ma. The data are best fit by a curve representing a setting with an overlying forearc thickness of 20 km and a subducting slab thermal age of 4 Ma or slightly younger without a slab gap. Heat flow beyond 430 km from the MTJ (vertical gray dashed line) may simply be due to reequilibration of the geothermal gradient after the young Monterey microplate stalled under central California 18 Myr ago [*Nicholson et al.*, 1994; *Atwater and Stock*, 1998]. Horizontal lines represent the calculated heat flow 18 Myr after cessation of 2 and 4 Myr old subducted lithosphere. Lines are horizontal because simultaneous cessation of subduction is assumed along the microplate's boundary with North America. Note that neither a slab gap nor shear heating of the upper mantle is needed to explain the heat flow in central California.

tism in California is typically short lived and produces small volumes of magma. It occurs mainly in the eastern part of the Coast Ranges [*Johnson and O'Neil*, 1984] where the overlying crustal thickness reaches 20-25 km [*Henstock et al.*, 1997]. A seismic profile across northern California where the MTJ was located < 2 Myr ago shows "bright spots" which cluster throughout the fossil oceanic crust (Plate 1a). These have been interpreted to represent melt lenses [*Levander et al.*, 1998]. These observations are consistent with the suggestion that the mid-Cenozoic and younger volcanism that occurs in the wake of the northward migration of the MTJ results dominantly from anatexis of oceanic crust and not from decompression melting of the asthenosphere.

The composition of volcanic rocks along the California

Coast Ranges also supports our model. The volcanic rocks are dominantly intermediate to silicic, have relatively high $^{87}Sr/^{86}Sr$ ratios (0.704-0.706; few samples with ratios of 0.7025-0.704 have Th-Ta-Hf ratios similar to the other rocks), relatively high $\delta^{18}O$ values (7.5-11.5), and relatively high Th contents, suggesting that crustal anatexis played a dominant role in their generation. It was proposed that slab gap induced asthenospheric upwelling triggered melting of the overlying forearc [*Johnson and O'Neil*, 1984], but it does not explain why only small volumes of short-lived volcanism are produced and why asthenospheric-derived melts are rare. Trace element abundance of the Clear Lake Volcanics [*Hearn et al.*, 1981], the youngest surface manifestation of the process, are characterized by strong light rare earth element (REE) enrichment and are consistent with crustal anatexis origin. In contrast, asthenospheric-derived melts (e.g., mid-ocean ridge basalts) are predominantly light REE depleted [*Hofmann*, 1988].

Surface heat flow in western California increases rapidly immediately south of the MTJ, reaching maximum several hundreds of kilometers to the south and then decreasing slightly. Our calculations best fit the data with an overlying crustal thickness of 20 km and an underlying stretched oceanic slab with an equivalent thermal age of 4-2 Ma (Figure 7). The pattern of increasing heat flow south of the MTJ was previously cited as evidence for a slab gap [*Lachenbruch and Sass*, 1980]. Interestingly, however, these authors pointed out that the heat flow variations are best fit with cooler than astheonospheric temperatures (1000°C) emplaced instantaneously at the base of a 20-km-thick crust.

Heat flow beyond a distance of 430 km from the MTJ is neither due to a slab gap nor due to a slab stretch (Figure 7). It may simply be the result of reequilibration of the forearc temperatures following the cessation of subduction when the Monterey microplate stalled and was captured by the Pacific plate (Figure 2) ~18 Myr ago [*Nicholson et al.*, 1994; *Atwater and Stock*, 1998]. This point is further elaborated on in section 8.

Our proposed geothermal gradient (Figure 6a) also matches thermobarometric estimates from spinel lhezorlites [*Jove and Coleman*, 1998] from Coyote Reservoir (east of the San Francisco Bay area and 30 km north of Quien Sabe, Figure 2). These upper mantle xenoliths erupted with small quantities of alkali-olivine basalt along the Calaveras fault during the Pliocene (2.5-3.6 Ma), possibly due to fault-stepping interaction [*Jove and Coleman*, 1998]. The overlying forearc thickness in this region is 20 km [*Brocher et al.*, 1999]. The MTJ passed by this latitude 8 Myr ago, although Coyote Reservoir itself may have been originally farther south and migrated later by strike-slip deformation [e.g., *Johnson and O'Neil*, 1984]. We therefore estimate that these xenoliths erupted 5-10 Myr after the MTJ passed by this outcrop. Our proposed geothermal gradients 5 and 10 Myr after the cessation of subduction and stretching are centered on the estimated range of temperatures and depths from these samples (box in Figure 6a). The fit is less satisfactory for a 20 km thick forearc and a 10 Ma thermal age or for a 30 km thick forearc and a 4 Ma thermal age. The fit to the estimated temperatures and depths is poor for calculated geothermal gradients 5 and 10 Myr after the introduction of asthenospheric temperatures in a slab gap model (Figure 6e).

6. Other Observations

In this section we review different geophysical and geological observations which we believe are consistent with a slab stretch model and the thermal structure that it predicts. Seismic refraction data [*Brocher et al.*, 1999, and references therein) beneath the Coast Ranges show a high-velocity basal layer which is compatible with a fossil subducted oceanic crust. Particularly noteworthy is the existence of a continuous high-velocity basal layer (yellow colors in Plate 1a) that dips eastward from the trench out to 200 km farther east in an area where the MTJ passed only < 2 Myr ago (Plate 1a). This observation directly contradicts the slab gap hypothesis, although a suggestion was made that decompression melting of asthenospheric mantle within the gap was followed by underplating of a 4-5 km thick layer of basalt to the base of the crust [*Liu and Furlong*, 1992]. The *P* wave velocity directly below the Moho in northern California, however, is ≥ 8 km s^{-1} [*Henstock et al.*, 1997], a value too high for a partially molten upper mantle. Additionally, the surface heat flow resulting from underplating a 4-5 km thick layer of basalt is expected to be much higher than that observed unless the top of the layer resides deeper than 30 km depth [*Liu and Furlong*, 1992]. Seismic refraction data in northern California, however, indicate that the layer is substantially shallower than 30 km throughout the Coast Ranges [*Beaudoin et al.*, 1996; *Brocher et al.*, 1999; *Godfrey et al.*, 1997; *Henstock et al.*, 1997](Plate 1).

A regional low-velocity zone in tomographic images of the upper mantle beneath northern California was previously cited in support of the existence of asthenospheric upwelling on a regional scale [*Benz et al.*, 1992; *Zandt and Furlong*, 1982]. The tomographic studies on which the images were based ignored crustal velocity and crustal thickness variations which contribute to the travel time delay (H. Benz, personal communication, 1998). Recent tomographic images of the crust and shallow mantle beneath northern California using local earthquake sources and the permanent northern California seismic stations (H. Benz, written communication, 1998) show no evidence for a regional low-velocity zone within the shallow upper mantle (e.g., Plate 2). Only two local (50x50 km) pockets of low-velocity material in the upper mantle are observed in the tomographic images (anomalies marked A and B in Plate 2) which may indicate localized zones of higher strain.

7. Continental Borderland - A Slab Gap in Coastal California?

The purpose of this section is to illustrate the expected thermal and magmatic consequences from a slab gap under a forearc region of the former subduction zone. We discuss observations from the Inner Continental borderland (ICB) offshore southern California where a local slab gap may have formed [*ten Brink et al.*, 1999]. We compare these observations with similar ones in northern California, where the slab gap model was promoted. The probable slab gap in the ICB was formed by extension, uplift, and translation of the margin 20-18 Ma [*Nicholson et al.*, 1994](Figure 8).

The volume and composition of volcanic rocks in southern California differ from those in central and northern California (Figure 2). There are thick sections (>500 m) of 18-14 Myr old volcanic rocks [*Crouch and Suppe*, 1993; *Cole and Basu*,

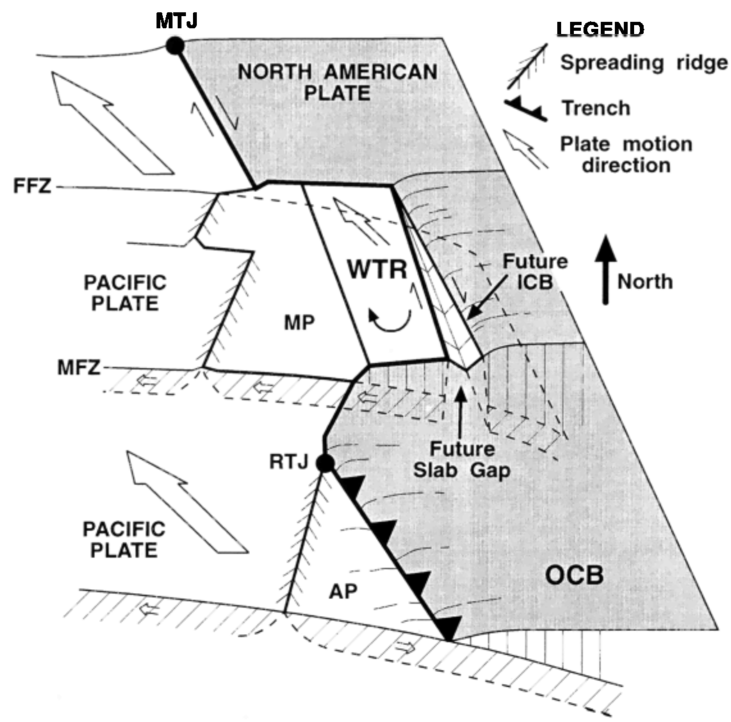

Figure 8. Model for the development of the Inner Continental Borderland (ICB) 20-18 Myr ago in the wake of the rotation and translation of the Western Transverse Ranges (WTR) (after *Nicholson et al.*, 1994). The rotation and translation of the WTR followed the capture of the subducted Monterey microplate (MP) by the Pacific plate and resulted in a high extension rate and a gap in the fossil subducted Farallon plate. OCB, Outer Continental Borderland; FFZ, Farallon Fracture Zone; MFZ, Morro Fracture Zone; RTJ, Rivera Triple Junction; AP, Arguello Microplate.

1995; *Dickinson,* 1997], often with mafic to intermediate composition. Petrogenesis of these volcanic rocks and trace element composition indicate that they were derived by an interaction of a very young, depleted oceanic lithosphere with the continental margin [*Cole and Basu,* 1995]. The rocks have $^{87}Sr/^{1886}Sr$ ratios (0.7025-0.7038) and $\delta^{18}O$ values (5-7.5) close to mid-ocean ridge basalt (MORB) ratios, suggesting that they were derived mainly from a mantle source [*Johnson and O'Neil,* 1984]. With asthenospheric temperatures at the base of the fossil subducted oceanic crust, melting of amphibolite is expected during and for the first few million years following extension, when basal crustal temperatures at the base of the crust are above 920°C (Figure 6e). Some melting of the base of the overlying crust is also expected, and temperatures in much of the middle and lower crust allow for ductile flow. Finally, adiabatically rising asthenospheric mantle with a normal potential temperature will undergo decompression melting when it ascends to depths less than 60 km [*McKenzie and Bickle,* 1988].

Heat flow in southern California is unusually high, particularly in the ICB where values reach between 83±18 mW m^{-2} (Figure 7)[*Lee and Henyey,* 1975]. These values are generally higher than would be expected from cooling and reequilibration of a 4 Ma slab which stopped subducting 20-28 Myr ago (Figure 7). However, if we assume that extension brought asthenospheric temperatures to 27 km depth some 18-20 Myr ago (Figure 6e), then the calculated present heat flow (83-86 mW m^{-2}) falls within the observed range [*ten Brink et al.,* 1999]. The Pacific-NOAM plate boundary was centered on the ICB until 12 Ma, and some tectonic activity probably continued in the ICB until 5 Ma [*Nicholson et al.,* 1994]. Even with a possible contribution to the increased heat flow from this later activity, the ICB heat flow is still higher than the heat flow from most of the Coast Ranges. Although the crust of the ICB was replaced by Catalina Schist 20-18 Myr ago with additional magmatic input lasting until 14 Myr ago [*ten Brink et al.,* 1999], the advective heat from these processes has long dissipated. Advective heat was ignored in the calculations of Figure 6e.

Unlike northern California (Plate 1a), seismic *P* wave velocity models of the ICB do not show high basal velocities associated with a fossil subducted oceanic crust (Plate 1b). The velocity models show relatively low velocities to the Moho, interpreted as Catalina Schist [*ten Brink et al.,* 1999]. The seismic refraction data consist only of upper crustal refractions (*Pg*) and Moho wide-angle reflections (*PmP*). Upper mantle refractions (*Pn*) with an apparent velocity of 7.7-7.9 km s^{-1} were observed only on a single unreversed seismic record [*ten Brink et al.,* 1999].

In summary, high heat flow, voluminous volcanism, a rather primitive isotopic composition of the magmas, and the absence of a high *P* wave velocity basal layer are observed in the Inner

Continental Borderland (ICB) offshore southern California. We would expect similar observations in northern California, if a regional slab gap existed there.

8. Discussion: Is There a Stress-Heat Flow Paradox in California?

Although the difference between the slab stretch and slab gap models can be perceived as simply a difference in the degree of reheating the North American plate, we believe that the implications to the understanding of upper mantle deformation are significant. We have already discussed the fact that a slab stretch model implies spreading of the mantle lithosphere to fill gaps. Here we discuss another implication of our model: the so-called "stress-heat flow paradox" [e.g., *Molnar,* 1992]. There is no measurable increase of heat flow near the San Andreas fault in central California, but there is a broad zone of high heat flow across the entire Coast Ranges averaging 30 mW m^{-2} higher than that typical for continental regions. We focus our discussion on the regional heat flow. The regional high heat flow was explained as a result of shear heating on horizontal planes due to viscous drag of the upper part of the lithosphere over its substratum [*Lachenbruch and Sass,* 1973], shear heating on vertical planes in the lithospheric upper mantle along the Pacific-North American diffuse plate boundary [*Molnar,* 1992], and the effect of the slab gap [*Lachenbruch and Sass,* 1980]. The shear heating argument was used to estimate the magnitude of shear stresses in the mantle lithosphere and to argue about the necessary rheology to support them [*Molnar,* 1992].

As was discussed in section 3, central California is probably underlain by the stalled Monterey microplate (Figure 2)[*Nicholson et al.,* 1994], and therefore a slab gap never existed in central California [*Atwater and Stock,* 1998]. We argue here that shear heating is also not required to explain the elevated heat flow of the Coast Ranges there. The higher heat flow is simply the consequence of reequilibration of the geothermal gradient following the cessation of subduction of the Monterey microplate. This microplate rotated clockwise, and subduction rate slowed, similar to the more recent history of the JdF plate. Subduction finally stopped at Chron 5E (18 Ma) as the northern end of the mid-oceanic ridge was subducted [*Nicholson et al.,* 1994]. The stalled Monterey slab underlying the Coast Ranges was probably less than 4 Myr old, assuming a convergence rate of 30-40 km Myr^{-1}. We can use the thermal model of Figures 6a and 7 to calculate the heat flow as a function of time after the cessation of subduction. As discussed in section 5, the forearc region of the subduction zone is relatively cold during subduction even when it is underlain by a young oceanic litthosphere. However, when subduction stops, thermal reequilibration between the forearc and the underlying hot slab begins and the temperature gradient of the forearc rises. The predicted heat flows for a 2 and 4 Myr old subducted slabs 18 Myr after subduction ceased are 75 and 81 mW m^{-2}, respectively. Mean heat flow of 39 measurements in the central Coast Ranges is 83±3 mW m^{-2}, and the mean heat flow of 17 newer measurements in boreholes in the Parkfield-Cholame area is 74±4 mW m^{-2} [*Sass et al.,* 1997]. We therefore argue that the heat flow regime in central California cannot be used to argue for or against viscous shear heating in the upper mantle. It is simply the consequence of its geological history as a subduction plate boundary.

9. Conclusions

We propose a "slab stretch model" to explain the interaction of plates at depth near the triple junction. In this model the geometrical gap formed owing to the northward migration of the triple junction is filled by stretched and thinned subducted Juan de Fuca plate. The stretching is in response to boundary forces acting on the plate, in particular, the northward push across the Mendocino Fracture Zone, and the southward (trench-parallel) component of subduction resistance. The thinning, estimated from simple geometrical considerations to be, on average, 27-37%, results in an elevated geothermal gradient. Locally, however, the amount of thinning may vary, resulting in higher or lower extension rates. The elevated geothermal gradient is equivalent to a 4 Ma oceanic lithosphere, still much cooler than that inferred by the slab gap model. In this thermal regime the composition and small volumes of Coast Ranges Neogene volcanic rocks are thought to be mainly due to dehydration melting of the fossil subducted oceanic crust. This model is consistent with heat flow measurements, thermobarometry, normal, shallow upper mantle velocities from tomographic inversion of earthquake travel times, and the existence of bright reflections in the high-velocity layer at the base of the crust. To study the effect of asthenospheric upwelling to shallow levels beneath the crust, we draw attention to the Inner Continental Borderland in southern California, which underwent local extension, possibly in a core complex mode, 18-20 Myr ago. The opening in the former forearc of the subduction zone probably extended to the fossil subducted plate, creating a slab gap. High heat flow, voluminous volcanism, a rather primitive isotopic composition of the magmas, and the absence of a high *P* wave velocity basal layer are observed in the Inner Continental Borderland in contrast to northern California. We also argue that the broad zone of high heat flow in central California, averaging 30 mW m^{-2} higher than that typical for continental regions, is neither due to a slab gap nor due to viscous shear heating in the upper mantle, as was previously suggested. It is simply the consequence of cessation of subduction of the Monterey microplate and the thermal reequilibration of the stalled microplate with the overlying Coast Ranges.

Acknowledgments. We thank Harley Benz for permission to publish Plate 2, Craig Nicholson and Stan Hart for illuminating discussions, Dave Scholl for his encouragement, David Okaya for use of his computer code, Chris Anton and Jeff Zwinakis for drafting several figures, and Peter Kelemen and Tom Brocher for reviewing earlier versions of this manuscript. Reviews by Nikky Godfrey, John Hole, and Craig Nicholson greatly improved the manuscript.

References

Atwater, T., Plate tectonic history of the northeast Pacific and western North America, in *The Eastern Pacific Ocean and Hawaii,* edited by E. L. Winterer, D. M. Hussong, and R. W. Decker, pp. 29-72, Geol. Soc. Am., Boulder, Colo., 1989.

Atwater, T., and J. Stock, Pacific-North America plate tectonics of the Neogene southwestern United States: An update, *Int. Geol. Rev., 40,* 375-402, 1998.

Beaudoin, B.C., et al., Transition from slab to slabless: Results from the 1993 Mendocino triple junction seismic experiment, *Geology, 24,* 195-199, 1996.

Beaudoin, B.C., J.A. Hole, S.L. Klemperer, and A.M. Trehu, Location of the southern edge of the Gorda slab and evidence for an adjacent asthenospheric window: Results from seismic profiling and gravity, *J. Geophys. Res., 103,* 30,101-30,115, 1998.

Benz, H.M., G. Zandt, and D.H. Oppenheimer, Lithospheric structure of northern California from teleseismic images of the upper mantle, *J. Geophys. Res., 97,* 4791-4807, 1992.

Benz, H.M., B. Chouet, P.B. Dawson, J.C. Lahr, R.A. Page, and J.A. Hole, Three-dimensional *P* and *S* wave velocity structure of Redoubt volcano, *J. Geophys. Res., 101,* 8118-8128, 1996.

Bohannon, R.G., and T. Parsons, Tectonic implications of post-30 Ma Pacific and North American relative plate motion, *Geol. Soc. Am. Bull., 107,* 937-959, 1995.

Brace, W.F., and D.L. Kohlstedt, Limits on lithospheric stress imposed by laboratory experiments, *J Geophys. Res, 85,* 6248-6252, 1980.

Brocher, T.M., U.S. ten Brink, and T. Abramovitz, Synthesis of crustal seismic structure argues against a slab gap beneath coastal Califronia, *Int. Geol. Rev., 41,* 263-274, 1999.

Cole, R.B., and A.R Basu, Nd-Sr isotopic geochemistry and tectonics of ridge subduction and middle Cenozoic volcanism in western California, *Geol Soc. Am Bull, 107,* 167-179, 1995.

Crouch, J.K., and J. Suppe, Late Cenozoic tectonic evolution of the Los Angeles Basin and Inner California Borderland: A model for core complex-like crustal extension, *Geol. Soc. Am. Bull., 105,* 1415-1434, 1993.

Defant, M.J., and M.S. Drummond, Subducted lithosphere-derived andesitic and dacitic rocks in young volcanic arc setting, *Nature, 347,* 662-665, 1990.

Dickinson, W.R., Tectonic implications of Cenozoic volcanism in coastal California, *Geol. Soc. Am bull., 109,* 936-954, 1997.

Dickinson, W.R., and W.S. Snyder, Geometry of subducted plates related to San Andreas Transform, *J. Geol., 87,* 609-627, 1979a.

Dickinson, W.R., and W.S. Snyder, Geometry of triple junctions related to San Andreas Transform, *J. Geophys. Res., 84,* 561-572, 1979.

Dumitru, T.A., Effects of subduction parameters on geothermal gradients in forearcs, with an application to Franciscan subduction in California, *J. Geophys. Res., 96,* 621-641, 1991.

Furlong, K.P., W.D. Hugo, and G. Zandt, Geometry and evolution of the San Andreas fault zone in northern California, *J. Geophys. Res., 94,* 3100-3110, 1989.

Godfrey, N.J., and S.L. Klemperer, Ophiolitic basement to a fôrearc basin and implications for continental growth: The Coast Range/Great Valley ophiolite, California, *Tectonics, 17,* 558-570, 1998.

Godfrey, N., B.C. Beaudoin, S.L. Klemprerer, and the Mendocino Working Group, Ophiolitic basement to the Great Valley forearc basin, California, from seismic and gravity data: Implications for crustal growth of the North American continental margin, *Geol Soc. Am. bull., 109,* 1536-1562, 1997.

Hearn, B.C., J.M. Donnely-Nolan, and F.E. Goff, The Clear Lake Volcanics: Tectonic setting and magma sources, *U.S. Geol. Surv. Prof. Pap., 1141,* 25-45, 1981.

Heasler, H.P., and R.C. Surdam, Thermal evolution of coastal California with application to hydrocarbon maturation, *AAPG Bull., 69,* 1386-1400, 1985.

Henstock, T.J., A. Levander, and J.A. Hole, Deformation in the lower crust of the San Andreas fault system in northern California, *Science, 278,* 650-653, 1997.

Hofmann, A.W., Chemical differentiation of the Earth: The relationship between mantle, continental crust, and oceanic crust, *Earth Planet. Sci. Lett., 90,* 297-314, 1988.

Hole, J.A., B.C. Beaudoin, and T.J. Henstock, Wide-angle seismic constraints on the evolution of the deep San Andreas plate boundary by Mendocino triple junction migration, *Tectonics, 17,* 802-818, 1998.

Howie, J.M., K.C. Miller, and W.U. Savage, Integrated crustal structure across the south central California margin: Santa Lucia Escarpment to the San Andreas Fault, *J. Geophys. Res., 98,* 8173-8196, 1993.

James, T.S., L.S. Hollister, and W.J. Morgan, Thermal modeling of the Chugach metamorphic complex, *J. Geophys. Res., 94,* 4411-4423, 1989.

Johnson, C.M., and J.R. O'Neil, Triple junction magmatism: A geochemical study of Neogene volcanic rocks in western California, *Earth Planet. Sci. Lett., 71,* 241-262, 1984.

Jove, C.F., and R.G. Coleman, Extension and mantle upwelling within the San Andreas fault zone, San Francisco Bay area, California, *Tectonics, 17,* 883-890, 1998.

Kelsey, H.M., and G.A. Carver, Late Neogene and Quaternary tectonics associated with northward growth of the San Andreas transform fault, northern California, *J. Geophys. Res., 93,* 4797-4819, 1988.

Lachenbruch, A.H., and J.H. Sass, Thermomechanical aspects of the San Andreas fault system, in *Tectonic Problems of the San Andreas Fault System*, edited by R.L. Kovach, and A. Nur, pp. 192-205, Stanford University Press, Stanford, Calif., 1973.

Lachenbruch, A.H. and J.H. Sass, Heat flow and energetics of the San Andreas fault zone, *J. Geophys Res., 85,* 6977-6989, 1980.

Lee, T.-C, and T.L. Henyey, Heat flow through the southern California Borderland, *J. Geophys. Res., 80,* 3733-3743, 1975.

Levander, A., T.J. Henstock, A.S. Meltzer, B.C. Beaudoin, A.M. Trehu, and S.L. Klemperer, Fluids in the lower crust following Mendocino triple junction migration: Active basaltic intrusion?, *Geology, 26,* 171-174, 1998.

Liu, M., and K.P. Furlong, Cenozoic volcanism in the California Coast Ranges: Numerical solutions, *J. Geophys. Res, 97,* 4941-4951, 1992.

McKenzie, D., and M.J. Bickle, The volume and composition of melt generated by extension of the lithosphere, *J. Petrol., 29,* 625-679, 1988.

McLaughlin, R.J., W.V. Sliter, D.H. Sorg, P.C. Russel, and A.M. Sarna-Wojcicki, Large-scale right-slip displacement on the East San Francisco Bay Region fault system, California: Implications for location of late Miocene to Pliocene Pacific plate boundary, *Tectonics, 15,* 1-18, 1996.

Miller, K.C., J.M. Howie, and S.D. Ruppert, Shortening within underplated oceanic crust beneath the central California margin, *J. Geophys. Res., 97,* 19,961-19,980, 1992.

Molnar, P., Brace-Goetze Strength profiles, the partitioning of strike-slip and thrust faulting at zones of oblique convergence, and the stress-heat flow paradox of the San Andreas fault, in *Fault Mechanics and Transport Properties of Rocks,* edited by T.F. Wong and B. Evans, pp. 435-459, Academic, San Diego, Calif., 1992.

Nichols, G.T., P.J. Wyllie, and C.R. Stern, Experimental melting of pelagic sediment, constraints relevant to subduction, in *Subduction: Top to Bottom, Geophys. Monog. Ser.,* vol. 96, edited by G. E. Bebout et al., pp. 293-298, AGU, Washington, D.C., 1996.

Nicholson, C., C.C. Sorlien, T. Atwater, J.C. Crowell, and B.P. Luyendyk, Microplate capture, rotation of the western Transverse Ranges, and initiation of the San Andreas transform as a low-angle fault system, *Geology, 22,* 491-495, 1994.

Oppenheimer, D., et al., The Cape Mendocino, California, earthquakes of April 1992: Subduction at the triple junction, *Science, 261,* 433-438, 1993.

Page, B.M., and T.M. Brocher, Thrusting of the central California margin over the edge of the Pacific plate during the transform regime, *Geology, 21,* 635-638, 1993.

Parsons, T., and P.E. Hart, Dipping San Andreas and Hayward faults revealed beneath San Francisco Bay, California, *Geology,* 27, 839-842, 1999.

Peacock, S., Thermal and petrologic structure of subduction zones, in *Subduction: Top to Bottom, Geophys. Monog. Ser.,* vol. 96, edited by G. E. Bebout et al., pp. 119-133, AGU, Washington, D.C., 1996.

Prescott, W.H., and S.-B. Yu, Geodetic measurement of horizontal deformation in the northern San Francisco Bay region, California, *J. Geophys Res, 91,* 7475-7484, 1986.

Sass, J.H., C.F. Williams, A.H. Lachenbruch, S.P. Galanis, and F.V. Grubb, Thermal regime of the San Andreas fault near Parkfield, California, *J. Geophys. Res., 102,* 27575-27,585, 1997.

ten Brink, U.S., J. Zhang, T.M. Brocher, D.A. Okaya, K.D., Klitgord, and G.S. Fuis, Geophysical evidence for the evolution of the California Inner Continental Borderland as a metamorphic core complex, *J. Geophys., Res.,* in press, 1999.

van der Beukel, J., and R. Wortel, Thermo-mechanical modelling of arc-trench regions, *Tectonophysics, 154,* 177-193, 1988.

Vedder, J.G., Regional geology and petroleum potential of the southern California Borderland, in *Geology and Resource Potential of the Continental Margin of Western North America and Adjacent Ocean Basins· Beaufort Sea to Baja California*, edited by D. W. Scholl, A. Grantz and J. G. Vedder, pp. 403-447, Circum-Pac. Counc for Energy and Miner. Resour., Houston, TX, 1987.

Walcott, D., Neogene tectonics and kinematics of western North America, *Tectonics, 12,* 326-333, 1993.

Wang, K., J. He, and E.E. Davis, Transform push, oblique subduction resistance, and intraplate stress of the Juan de Fuca plate, *J. Geophys. Res., 102,* 661-674, 1997.

Wilson, D.S., A kinematic model for the Gorda deformation zone as a diffuse southern boundary of the Juan de Fuca plate, *J. Geophys. Res., 91,* 10,259-10,269, 1986.

Wyllie, P.J., and M.B. Wolf, Amphibolite dehydration-melting: Sorting out the solidus, in *Magmatic Processes and Plate Tectonics*, edited by H. M. Prichard et al., pp. 405-416, Geol. Soc. of London, London, 1993.

Zandt, G., and K.P. Furlong, Evolution and thickness of the lithosphere beneath coastal California, *Geology, 10,* 376-381, 1982.

P.C. Molzer and U.S. ten Brink, U.S. Geological Survey, 384 Woods Hole Rd., Woods Hole, MA 02543. (utenbrink@nobska.er.usgs.gov)

N. Shimizu, Woods Hole Oceanographic Institution, Woods Hole, MA 02543.

(Received February 10, 1999;
revised June 30, 1999;
accepted July 27, 1999.)

TECTONICS, VOL. 18, NO. 6, PAGES 1245-1274 DECEMBER 1999

Distribution of displacement on and evolution of a young transform fault system: The northern San Andreas fault system, California

John Wakabayashi

Hayward, California

Abstract. This paper presents a working model for the spatial and temporal distribution of dextral slip on the northern San Andreas fault system of coastal California, based primarily on field relations in the San Francisco Bay area, and offers insight into the evolution of a young transform fault system. A fundamental difference between this and previous models of slip distribution is that this model assigns negligible slip to the Pilarcitos fault, which has been suggested to have 120 to 250 +km of post early-Miocene dextral slip, in previous models. Because separation on the San Francisco Peninsula reach of the San Andreas fault is about 25 km, and displacement on the San Andreas fault in central California is 310 to 320 km, more than 250 km of late Cenozoic dextral slip must be accommodated east of the San Francisco Peninsula. The distribution of this dextral slip is constrained by offset late Cenozoic and basement units. Slip distribution, combined with ages of offset features and plate boundary kinematic constraints, show that the distribution of slip rates on groups of faults along the transform boundary has changed in an irregular fashion through time, in contrast to existing models that propose progressive eastward migration of active faulting in the San Andreas system. In addition to the shifting patterns of displacement, a migrating transition zone connecting the eastern faults of the strike-slip system to the Mendocino triple junction may have resulted in distributed dextral faulting and shortening in the northernmost and youngest part of the transform fault system.

1. Introduction

The dextral San Andreas fault system of coastal California is one of the best known transform fault systems in the world. It is part of the broad boundary between the Pacific and North American plates (Figure 1), and is one of the two major zones of deformation that make up this plate boundary, the other zone being the Basin and Range province [e.g., *Argus and Gordon*, 1991]. The San Andreas fault system accommodates approximately 80% of the present-day dextral transform motion between the Pacific and North American plates [*Argus and Gordon*, 1991] and about 70% of the total dextral displacement along the plate boundary that has accumulated over the last 18 Ma [*Atwater and Stock*, 1998].

Paper number 1999TC900049.
0278-7407/99/1999TC900049$12.00

Although the distribution and timing of slip on the faults of the southern part of the San Andreas fault system has been constrained in some detail [e.g., *Powell*, 1993, and references therein], the slip distribution on the rapidly evolving northern part of the fault system is poorly known. Much of the uncertainty in slip distribution is due to of a lack of identified piercing points, which has led to divergent views on the distribution of 310 to 320 km of slip on and splaying from the San Andreas fault at the latitude of the San Francisco Bay area (Bay area) (Figure 1). The 310 to 320 km of slip is more than half of the total slip on the fault system [*Atwater and Stock*, 1998].

The San Andreas fault in central California (Central San Andreas) has accommodated 310 to 320 km of post-18 Ma slip, based on the correlation and offset of the Pinnacles and Neenach volcanic fields [*Matthews*, 1976] and paleogeographic reconstructions of Tertiary sedimentary strata [e.g., *Graham et al.*, 1989] (fault initiation timing from *Atwater and Stock* [1998]). The 310 to 320 km offset along the Central San Andreas and strands that splay from it, such as the Calaveras and Hayward faults, is accommodated at least as far north as the Santa Cruz Mountains [e.g., *Graham et al.*, 1989] (Figure 1). That is, slip does not diverge westward from the San Andreas fault south of the Santa Cruz Mountains.

The San Francisco Peninsula segment of the San Andreas fault (Peninsula San Andreas) (Figures 1 and 2) has only 22 to 27 km of offset based on (1) 27 km of right separation of the structurally highest limestone-bearing thrust nappe in the Franciscan Permanente terrane [*Wakabayashi and Hengesh*, 1995], (2) 25 km of right separation of the Corte Madera facies of the Plio-Pleistocene Santa Clara Formation from a distinctive source terrane of limited extent [*Cummings*, 1968], and (3) 22 km offset of correlated magnetic anomalies [*Jachens et al.*, 1996].

With minor displacement on the Peninsula San Andreas, 283 to 298 km of displacement, referred to herein as the "residual" slip, must be accommodated by other faults at the latitude of the San Francisco Bay area (Bay area). This paper will (1) present field evidence indicating minimal late Cenozoic dextral slip on the Pilarcitos fault, a fault assigned 120 to 250+ km of slip in previous models, and showing that nearly all residual slip must be accommodated east of the Peninsula San Andreas, (2) propose a preliminary model for distribution of residual slip based on multiple piercing points of both late Cenozoic and basement rocks; this includes a discussion of the relationship between volcanic rocks and the evolving transform system, and (3) use the slip distribution and other information on kinematics of the Pacific-North American plate boundary to evaluate the temporal distribution of dextral slip rates associated with the developing transform plate margin.

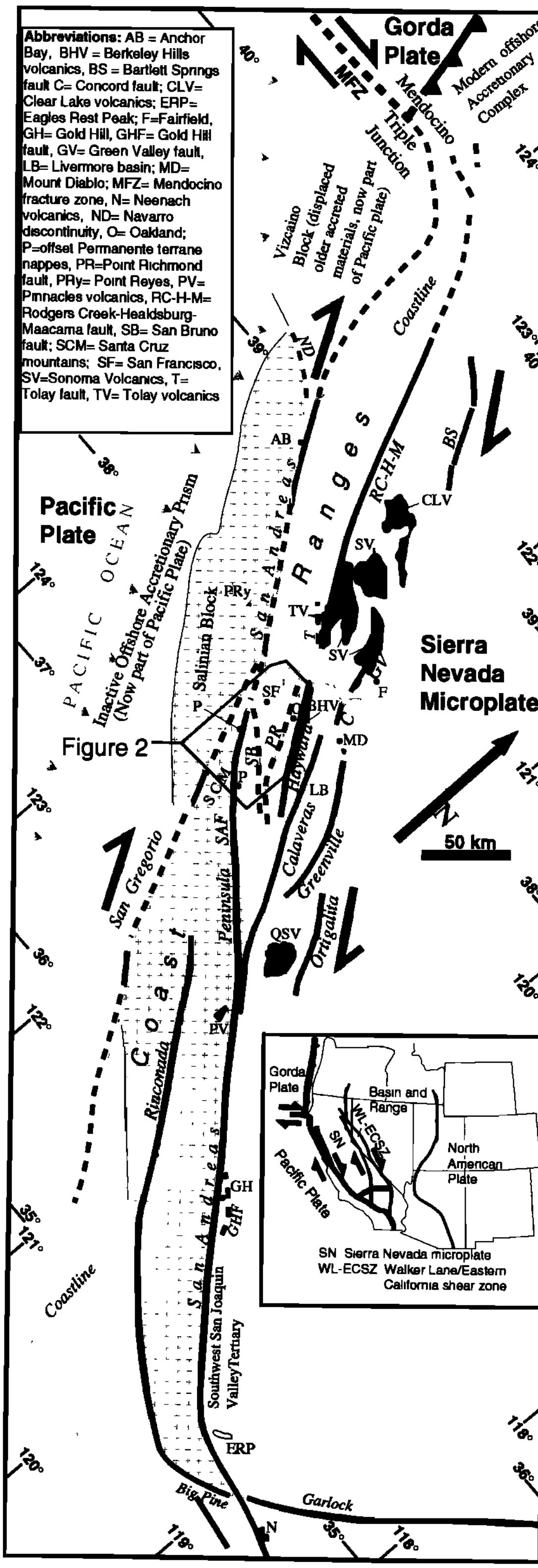

Figure 1. Map showing the main dextral faults of the northern San Andreas fault system of the California Coast Ranges. Granitic Salinian block is shown with pattern. Unshaded onshore rocks consist of Jurassic and Cretaceous accretionary wedge materials (Franciscan Complex), ophiolite (Coast Range ophiolite), and forearc basin strata (Great Valley Group), and their Tertiary cover. Inset shows the San Andreas fault system in the context of major plate boundaries. Onshore modified from *Wakabayashi and Hengesh* [1995]; offshore generalized from *McCulloch* [1987]. Inset based on *Argus and Gordon* [1991] and *Dickinson and Wernicke* [1997].

2. Evidence Precluding Significant San Andreas Slip West of the Peninsula San Andreas Fault: The Case Against Large Post-Eocene Offset on the Pilarcitos Fault

In this section, evidence is presented to show that all or nearly all of the residual slip is partitioned east of the Peninsula San Andreas. Additional supporting data are presented in the Appendix.

2.1. Geologic Relations in the Montara Mountain Area: Evidence for Minimal Post-Eocene Dextral Offset

Several previous models have assigned 250 km or more of late Cenozoic slip to the Pilarcitos fault [*Champion et al.*, 1984; *Page*, 1990; *Powell*, 1993], whereas others [*Griscom and Jachens*, 1990] have assigned about 155 km of slip to the Pilarcitos fault. Two recently proposed models [*McLaughlin et al.*, 1996a and *Dickinson*, 1997] (the latter is derived largely from the former) assign less slip to the Pilarcitos fault, but the amount still exceeds 120 km. Researchers assigned large amounts of slip to the Pilarcitos fault primarily because the structure has been mapped as the contact between the granitic and high-grade metamorphic basement of Salinian Block and the Franciscan subduction complex, and the Central San Andreas forms the faulted contact of these two geologic units in central California (Figures 1, 2, and 3). None of the papers cited above presented geologic evidence directly constraining either the amount or timing of offset on the Pilarcitos fault. As described below, field relationships in the Montara Mountain area (Figure 3) preclude more than 7 km late Cenozoic dextral displacement on the Pilarcitos fault.

2.1.1. Geologic Relations in the Montara Mountain Area. In the Montara Mountain area, the granitic rocks of the Salinian block are overlain by Paleocene turbidites of Point San Pedro [e.g., *Darrow*, 1963; *Morgan*, 1981]. This contact is faulted along much of its length (San Pedro Mountain. fault of *Pampeyan* [1994]; Montara fault of *Darrow* [1963]), but an unfaulted depositional contact locally is preserved on San Pedro Mountain (Appendix) and at Devil's Slide (the sea cliff [*Morgan*, 1981]). At Devil's Slide and on

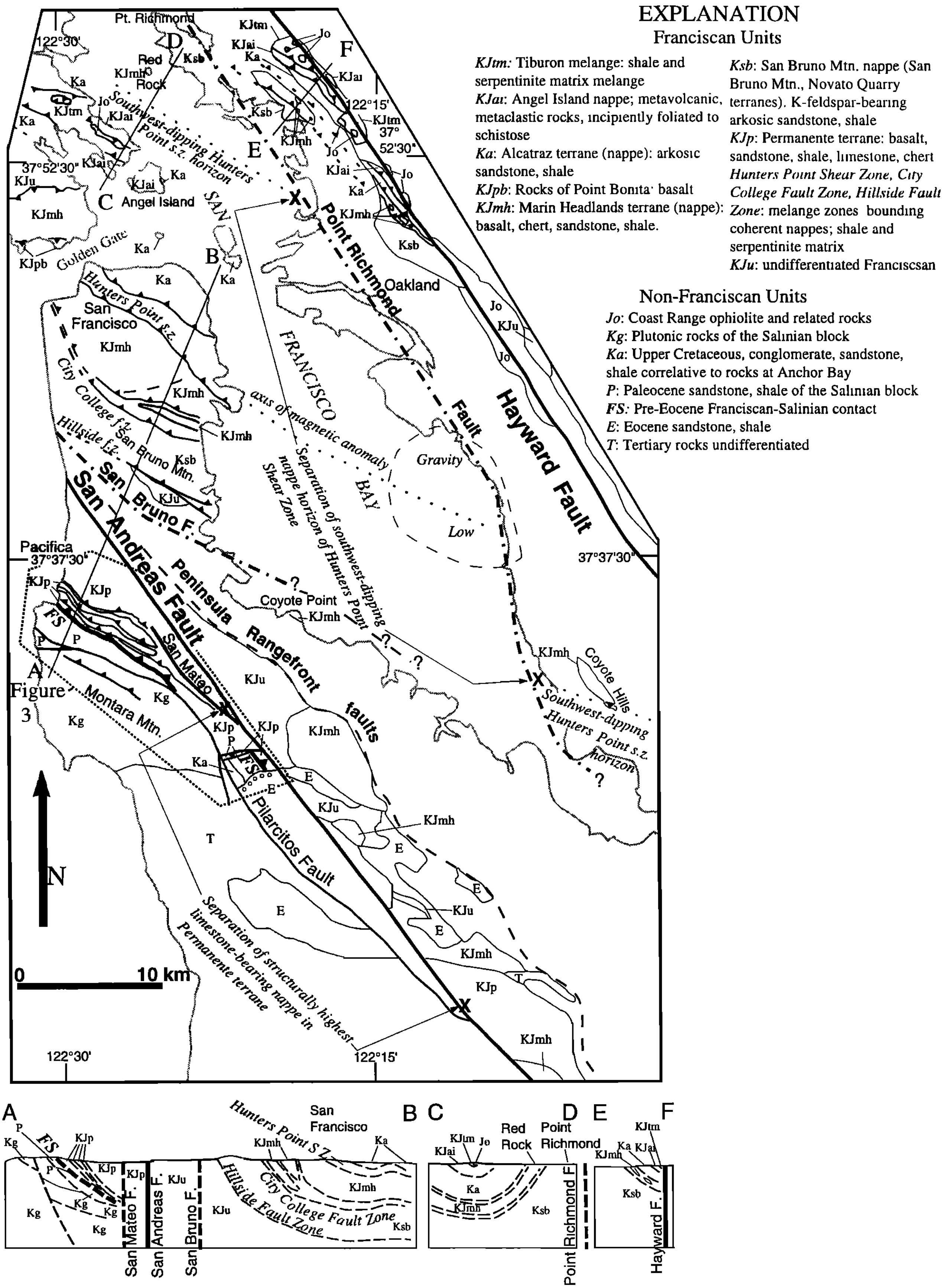

Figure 2. Franciscan Complex and related rocks, San Francisco Bay area and geologic relations constraining offsets on some faults of the San Andreas system; lines A-B, C-D, and E-F denote lines of composite cross section that is shown with no vertical exaggeration. Modified from *Wakabayashi and Hengesh* [1995]

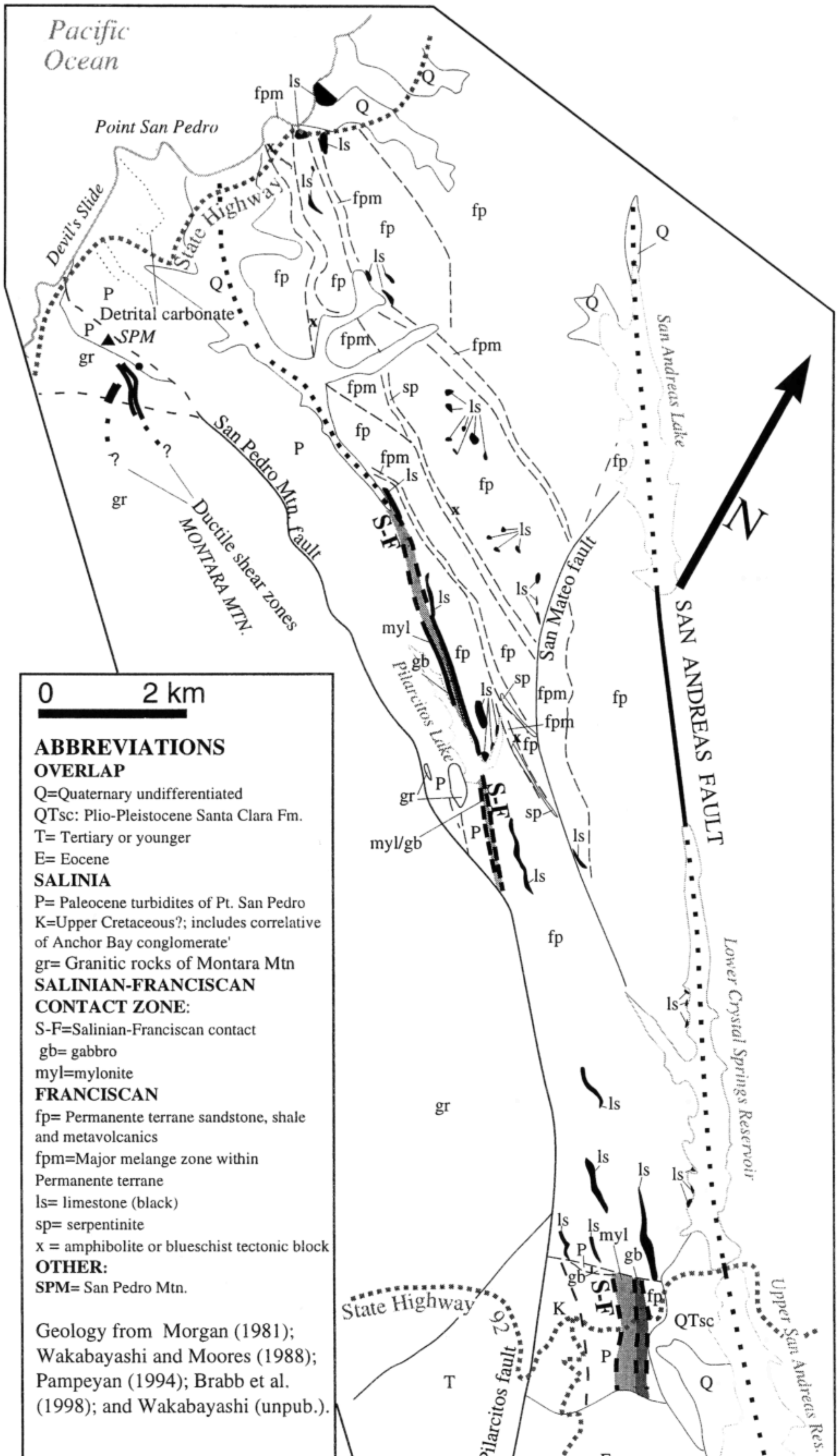

Figure 3. Geologic relations in the Montara Mountain area.

San Pedro Mountain a basal conglomerate containing granitic boulders directly overlies the granitic rocks. Although consisting primarily of detritus derived from the Salinian block, the turbidites also contain Franciscan detritus [*Morgan* 1981], including blue-amphibole-bearing metacherts (this study). Based on the local depositional contact of the turbidites on the granitic rocks, they are considered part of the Salinian block [e.g., *Darrow*, 1963; *Morgan*, 1981].

The Paleocene turbidites are faulted against the Permanente terrane of the Franciscan Complex in the Montara Mountain area (Figure 3). The Permanente terrane is composed of thrust nappes of basaltic volcanics, sandstone, shale, limestone, and minor chert, with melange zones of variable thickness separating the coherent nappe sheets [*Blake et al.*, 1984; *Wakabayashi and Moores*, 1988]. Depositional ages of Permanente terrane cherts and limestones range from Valanginian to early Coniacian (~135 to 88 Ma) [*Murchey and Jones*, 1984; *Sliter*, 1984]. Incorporation of the Permanente terrane into the Franciscan subduction complex must have postdated the deposition of the youngest depositional ages from the terrane and may be as young as 65 Ma [*Tarduno* et al., 1985].

The contact between the Permanente terrane and the Paleocene turbidites in much of the Montara Mountain area is a mylonite zone that strikes northwest and dips at moderate angles to the northeast, based on surface exposures [*Wakabayashi and Moores*, 1988] (Figure 3); the contact may have a steep or vertical dip at depth based on three-dimensional seismic velocity structure of the area [*Parsons and Zoback*, 1997]. This mylonite zone is up to 200 m thick and is composed mostly of mylonitized Paleocene sandstone and shales but includes some sheared Franciscan rocks along the eastern margin of the zone [*Wakabayashi and Moores*, 1988]. A narrow belt of gabbro, up to 20 m in outcrop width, borders the mylonite zone on its eastern margin along much of its exposed length. The gabbro and mylonite are unlike any other rocks present in either the Salinian block or the Franciscan Complex in this area. The gabbro, mylonite, and Paleocene sandstones, well exposed near Pilarcitos Lake, also are exposed along State Highway 92 (Highway 92) (Figure 3) [*Wakabayashi and Moores*, 1988], although the Paleocene rocks along Highway 92 have been mapped by others as Franciscan [*Brabb and Pampeyan*, 1983; *Pampeyan*, 1994] or Eocene [*Brabb et al.*, 1998]. Sandstone that crops out along Highway 92 (P on Figure 3) directly west of the mylonite is identical to sandstone exposed within the undisputed parts of the Paleocene section near Point San Pedro. Sandstone along Highway 92 contains abundant potassium feldspar, as does sandstone near Point San Pedro, whereas Franciscan Permanente terrane sandstone lacks potassium feldspar (Appendix photomicrographs). In addition, the Paleocene sandstone along Highway 92 and near Point San Pedro both contain fossil fragments and detrital carbonate, whereas Franciscan sandstone of the Permanente terrane does not. The Paleocene sandstones along Highway 92 and Point San Pedro also are much more deformed and recrystallized than Eocene rocks south of Highway 92. The correlation of sandstone along Highway 92 with Paleocene rocks at Point San Pedro, as well as the recognition of the gabbro and mylonite along Highway 92, are key observations for the subsequent interpretation.

The Salinian-Franciscan mylonite zone is truncated by younger faulting along the eastern margin of the granitic rocks (San Pedro Mountain fault; Figure 3). The Pilarcitos fault has previously been regarded as the Franciscan-Salinian contact [e.g., *Brabb and Pampeyan*, 1983]; however, based on the field relations presented herein [also *Wakabayashi and Moores*, 1988], the fault follows the Salinian-Franciscan contact north of Pilarcitos Lake but splays west from the main tectonic contact in the vicinity of Highway 92; it is a younger fault that locally truncates the Salinian-Franciscan contact (Figure 3). Most or all of the Miocene and younger displacement on the Pilarcitos fault south of Highway 92 may curve northward into the San Pedro Mountain fault (Figure 3).

2.1.2. Constraints on late Cenozoic dextral displacement in the Montara Mountain area. The Salinian-Franciscan contact mylonite is depositionally overlapped by Eocene clastic rocks (the Whiskey Hill Formation of *Pampeyan* [1994]) south of Highway 92 [*Wakabayashi and Moores*, 1988] (Figure 3). The pre-Eocene juxtaposition of the Franciscan Permanente terrane and Salinia places limits on the amount of post-Eocene displacement on faults between and within these two units, including the Pilarcitos fault. South of Highway 92, post-Eocene dextral offset west of the Peninsula San Andreas fault must be accommodated on the Pilarcitos fault or faults west of it, otherwise the Eocene unit to its east would be dissected (Figure 3). North of Highway 92, such dextral offset is constrained to either (1) splay eastward into the Permanente terrane south of the Pilarcitos Lake or (2) follow the granitic-Paleocene contact (San Pedro Mountain fault) that curves to the west-northwest. Significant dextral faulting in other areas is unlikely, because restoration of such displacement would sliver or duplicate the Paleocene unit, granitic basement or Permanente terrane.

Dextral offset splaying eastward into the Permanente terrane is limited to less than 6 km by the outcrop pattern of the Franciscan-Salinian mylonite contact; restoration of 6 km or more of dextral slip in this area results in doubling of the mylonitic contact (Figure 4a). Offset along the Paleocene-granitic (San Pedro Mountain fault) contact is restricted by the local presence of an unfaulted depositional Paleocene-granitic contact. Some slip may splay westward into the granitic rocks from the southern, faulted part of this contact. No such faults have been mapped, but it may be possible for up to a kilometer of undetected slip to pass through the granitic rocks. Based on these relations, the total allowable amount of post-Eocene dextral slip between the Salinian block and Franciscan Complex in the Montara Mountain area probably is less than 7 km.

2.1.3. Correlation of conglomerate in Montara Mountain area with conglomerate in Anchor Bay area: supporting constraint on displacement. Geologic correlations made between the Montara Mountain area and the Anchor Bay area, near Gualala (AB on Figures 1 and 5), are consistent with a lack of post-Eocene slip along the Pilarcitos fault and related structures. Along State Highway 92, west of the Salinian-Franciscan mylonite contact, but east of the Pilarcitos fault is a conglomerate (Figure 3) that has been correlated to Upper Cretaceous conglomerates at Anchor Bay on the basis of identical clast lithology and presence of rudistid fossils [*Burnham*, 1998] (preliminary correlation by *Seiders and Cox* [1992]). Not only are the conglomerates

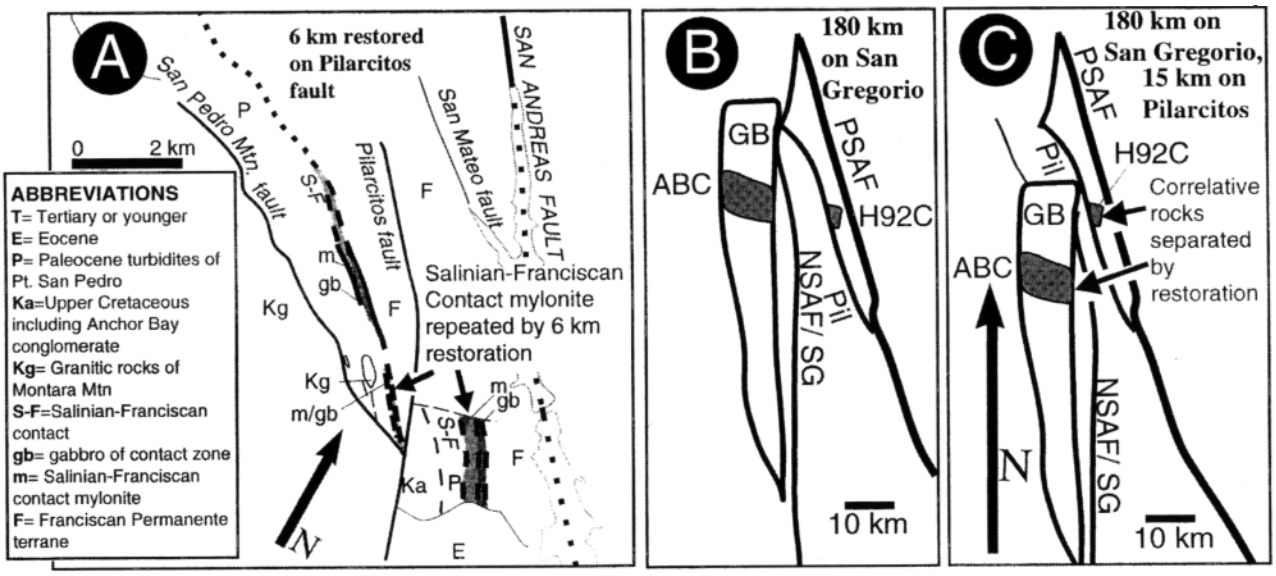

Figure 4. Simplified fault restorations showing that only small amounts of late Cenozoic slip on the Pilarcitos fault are permitted by field relations. (a) Restoration of 6 km of slip repeats the Salinian contact mylonite (present-day relations in Fig. 3). (b) Restored position of the Upper Cretaceous conglomerate of Anchor Bay opposite conglomerate along State Highway 92 according to *Burnham* [1998]. (c) Restoration of 15 km of slip separates the two conglomerate exposures. Abbreviations are ABC, Anchor Bay conglomerate; GB, Gualala block; H92C, Highway 92 conglomerate; NSAF/SG, Northern San Andreas and San Gregorio faults; Pil, Pilarcitos fault; PSAF, Peninsula San Andreas fault.

lithologically identical, but they differ from any other conglomerates of Franciscan complex, Salinian block, or other units of the Coast Ranges [*Seiders and Cox*, 1992]. In addition, a distinctive mottled Eocene red mudstone is present in the Gualala area [*Wentworth et al.*, 1998] and within several hundred meters of the conglomerate locality along Highway 92 [*Brabb et al.*, 1998]. The conglomerates near Gualala and along Highway 92 are separated by 175 to 185 km across the San Gregorio fault (this includes slip on the Rinconada fault, which may merge with the San Gregorio fault south of the Montara Mountain area), and at least seven other tie points indicate a similar offset [*Burnham*, 1998]. Thus Cenozoic slip on the San Gregorio and Rinconada faults accounts for all of the separation of the conglomerate. Post-Late Cretaceous dextral displacement along the Pilarcitos fault of >15 km is not permitted by the location of the conglomerate outcrops, because such displacement would restore the Gualala conglomerate a considerable distance south of the Highway 92 conglomerate [*Burnham*, 1998] (Figures 4b and 4c). The correlation of the conglomerate outcrops not only places limits on late Cenozoic Pilarcitos fault slip, but it also limits the total amount of slip of that age that can splay westward from the Central San Andreas fault. Possible provenance ties between Paleocene carbonate turbidite beds near Point San Pedro and the Permanente terrane also suggest minimal post-Paleocene dextral slip passing through the Montara Mountain area (see Appendix).

2.2. Lack of Residual Slip West of the Peninsula San Andreas

As discussed above, the Montara Mountain area accommodates little or no late Cenozoic dextral slip. In addition, local field relations [*Graham et al.*, 1989] preclude more than 10 km of post-early Miocene dextral slip diverging westward through the Santa Cruz Mountains from the San Andreas fault south of the Montara Mountain area. Most, if not all, of the faults displacing Tertiary strata west of the Peninsula San Andreas in the Santa Cruz Mountains are thrust faults rather than dextral strike-slip faults [*Jayko*, 1996]. As noted above, the regional correlations of *Burnham* [1998] limit the total amount of slip splaying westward from the San Andreas fault (Santa Cruz Mountains and Montara Mountains area sum) to less than 15 km. If these interpretations are correct, nearly all of the residual slip must be distributed east of the Peninsula San Andreas.

2.3. Other Field Relations Consistent With the Hypothesis of Minimal Residual Slip West of the Peninsula San Andreas

Reconstruction of the Permanente terrane is consistent with the hypothesis that all or nearly all residual slip must be distributed east of the Peninsula San Andreas fault. This and other

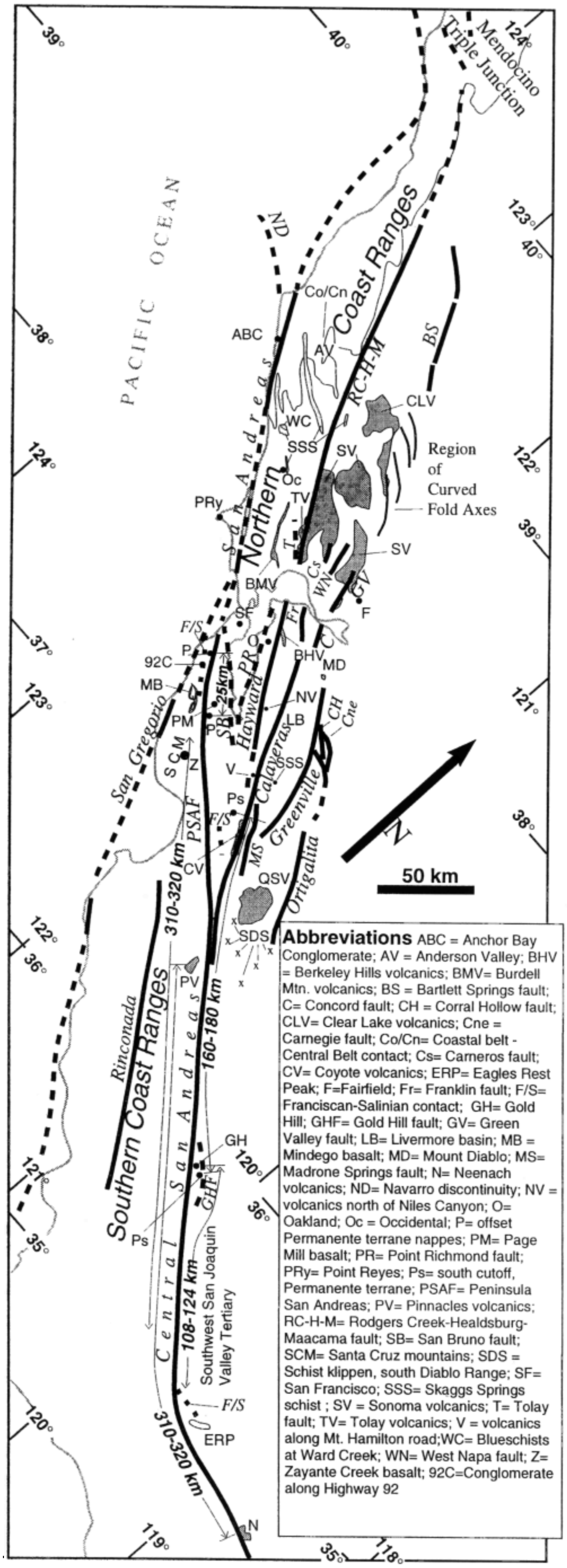

correlations of Franciscan Complex rocks relevant to determinations of slip distribution are discussed in the following section on basement correlations.

Correlated gravity and magnetic anomalies of *Griscom and Jachens* [1990] were interpreted as evidence for 155 km of slip on the Pilarcitos fault. However, 180 km of displacement on the San Gregorio and Rinconada faults, and much smaller amounts of displacement on the Peninsula San Andreas faults and other faults of eastern San Francisco Peninsula can account for the offset geophysical anomalies without slip on the Pilarcitos fault (see subsequent discussion of slip distribution and Appendix).

The position of the 12.6 Ma Burdell Mountain volcanics (Figure 1) at a relatively northerly location within the Coast Ranges is also consistent with the hypothesis that all or nearly all residual slip is accommodated east of the Peninsula San Andreas, although the uncertainties in constrained slip distribution are large (see Appendix).

3. Offset of Franciscan Rock Units: Can Distinctive Franciscan Units Be Used for Late Cenozoic Displacement Estimates?

Although most of the units of the Franciscan Complex displaced by strands of the San Andreas system were incorporated into the subduction complex at least 65 m.y. ago [e.g., *Blake et al.*, 1984; *Wakabayashi*, 1992], over 45 m.y. prior to initiation of faulting on the San Andreas system, reconstruction of the Franciscan Permanente terrane and associated Salinian-(Permanente) Franciscan contact, discussed below, indicates that displacement of Franciscan terranes across strands of the San Andreas system is the same as the late Cenozoic displacement on the same strands. Thus distinctive Franciscan units such as the Permanente terrane can be used to estimate late Cenozoic displacements in addition to late Cenozoic piercing points.

3.1. Reconstruction of the Permanente Terrane

The Franciscan Permanente terrane is unique among Franciscan rock units because of the association of limestone, perhaps the rarest of all Franciscan lithologies, with nappes of basaltic flows and tuffs, in addition to sandstones and shales that are the most common constituents of most of the other Franciscan tectonostratigraphic units or terranes [*Blake et al.*, 1984].

A useful structural marker within the Permanente terrane is the structurally highest nappe in which limestone occurs. This nappe is displaced 22 to 27 km by the Peninsula San Andreas, and possibly up to 9 km (0 to 9 km) more by San Mateo fault (Figure3). The Permanente terrane (but not a specific structural horizon within the unit) east of the Peninsula San Andreas is displaced 160 to 180 km across the Calaveras and other faults from the vicinity of Morgan Hill (northern Ps on Figure 5),

Figure 5. Faults of the northern San Andreas fault system and some key offsets.

from limestone-bearing exposures east of the San Andreas fault, near Parkfield [*McLaughlin et al.*, 1996a] (southern Ps on Figure 5). The 20 km uncertainty results because specific structural horizons in this terrane cannot be identified in the exposures near Parkfield.

The exposures of Permanente terrane near Parkfield are west of the Gold Hill fault, considered a major late Cenozoic dextral fault, based on the offset of the gabbro at Gold Hill (GH on Figure 5) to correlative rocks at Eagle's Rest Peak ('ERP' on Fig. 5) and constraints on timing of this displacement from Tertiary strata [*Sims*, 1993]. Although *Sims* [1993] assigned nearly all of the Gold Hill to Eagle's Rest Peak offset to the Jack Ranch fault, the fault between the Permanente exposures and the gabbro of Gold Hill, large slip on the Gold Hill fault with subordinate slip on the Jack Ranch fault can accommodate the offset equally well, and fit contact relationships better. The lack of post-Paleocene offset across the Salinian-Franciscan contact, noted in the Bay area, suggests that the Permanente terrane and the northeast margin of the Salinian block restore southward together. Eagles' Rest Peak is interpreted as the northern margin of the plutonic rocks correlative to the Salinian block on the eastern side of the San Andreas system [e.g., *Ross*, 1984]. Thus a buried Salinian-Franciscan contact should restore directly north of the Eagle's Rest Peak area. The cutoff of northern limit of granitic/gabbroic rocks in the Eagle's Rest Peak area, the inferred buried Salinian-Franciscan contact, by the San Andreas can be estimated using the gravity and magnetic data of *Griscom and Jachens* [1990]. The offset of this cutoff to gabbroic rocks at Gold Hill is 128 to 134 km. Of the Gold Hill-Eagle's Rest Peak offset, 10 to 20 km must be partitioned onto the Jack Ranch fault so that a Permanente terrane sliver does not intervene between the gabbro of Gold Hill and Eagle's Rest Peak. This leaves 108 to 124 km on the Gold Hill fault. For a reasonable geometry of the restored Salinian-Franciscan contact, the Morgan Hill-Parkfield and Gold Hill fault offsets total 270 to 290 km. The total offset of the Permanente terrane thus is 22 to 36 km (Peninsula San Andreas and San Mateo fault), plus 270 to 290 km (Morgan Hill area to Parkfield area, plus Gold Hill fault), a total of 292 to 326 km. This total is the maximum possible dextral displacement of Franciscan nappes west of the Salinian block that postdates their accretion (post ~65 Ma). The total post-nappe assembly offset, within uncertainty, is comparable to the 310 to 320 km late Cenozoic displacement along the Central San Andreas estimated by *Graham et al.* [1989].

3.2. Correlation of Distinctive Franciscan Blueschist Unit

A distinctive unit of intact Franciscan blueschist (i.e., not tectonic blocks in melange) is present as klippen around the southern margin of the Diablo Range Franciscan core (J. Wakabayashi and T. Dumitru, unpublished data, 1996) (labeled SDS on Figure 5). One of the distinctive features of the schist is that it is much coarser-grained (metamorphic grain sizes commonly reach 1 mm) than other intact schists of the Franciscan (for which the average metamorphic grain size seldom exceeds 0.3 mm). The schist is quartz rich, with growth of glaucophane, lawsonite, white mica, and some jadeite. Based on some of the least recrystallized outcrops, the schist may be a metagreywacke or metashale. In the exposures labeled SDS, the schist is associated with and structurally below small (from 100s of meters to 1.5 km in long dimension) thrust sheets of intact blueschist-greenschist facies and higher grade metabasaltic rocks (J. Wakabayashi and T. Dumitru, unpublished data, 1996). The northern and westernmost of the small klippe of this unit in the Diablo Range crops out west of the margin of the Quien Sabe volcanic field. This schist crops out in the northern Coast Ranges (labeled SSS on Figure 5), the largest exposure being a 70 km long belt near Healdsburg that has been informally called the Skaggs Springs schist (Wakabayashi, 1992). The southernmost exposure of this schist in the northern Coast Ranges is near Occidental (Fig. 5). Depending on the geometry of faults between these schists and their equivalents in the Diablo Range, the amount of separation between the various outcrops of schist is 230 to 250 km. Note that the distribution of this schist does not constrain all of the faulting east of the Peninsula San Andreas, however, because slip may occur west of the westernmost outcrop of this schist and east of the San Andreas fault.

4. Distribution of Residual Slip in the San Francisco Bay Area: A Working Model

4.1. General Problems

Geologic evidence summarized above indicates that little residual slip is accommodated west of the San Andreas fault. The sum of permissible slip splaying west from the San Andreas is 0 to 15 km, based on both local and regional constraints. The Peninsula San Andreas and San Mateo faults have a combined permissible slip range of 22 to 36 km. Thus the total permissible slip on the Peninsula San Andreas and faulting splaying to the west of it is 22 to 51 km. The permissible amount of displacement east of the Peninsula San Andreas is 259 to 298 km, based on a total for the system of 310 to 320 km.

Following a general discussion of uncertainties, displacement estimates for individual faults and groups of faults east of the Peninsula San Andreas are presented. The displacement estimates are summarized in Figure 7, and the San Andreas fault system is restored at 10 Ma and 18 Ma according to these displacements in Figure 8.

4.2. Uncertainties in Displacements on Specific Faults

Slip estimates are subject to uncertainty in the configuration of restored separated units, such as the shape of a volcanic field, sedimentary channel, basin margin or other paleogeographic feature. Because true piercing "points" (truncated linear features such as fold hinges, unconformity/stratigraphic contact intersections, dike/stratigraphic contact intersections, etc.) have not been identified along the San Andreas fault system, there is uncertainty resulting from uncertainty in reconstructed outcrop patterns. In many cases, any value within the full uncertainty range is equally plausible, so the displacement will be given as a range, rather than as a median value and plus or minus that may erroneously suggest (to some) that the extremes of the range are less likely than the median.

4.3. Uncertainties Associated With the Geochronology of Late Cenozoic Volcanism in the Coast Ranges

Late Cenozoic volcanic rocks of the Coast Ranges offer critical constraints on displacements on the San Andreas system, because they are the easiest rocks to obtain accurate ages for, and the extent of many of the volcanic fields is limited enough that correlative volcanic fields constrain fault offsets between them. A persistent problem in correlating volcanic rocks and constraining slip histories of faults, however, is the uncertainty in the ages of volcanic rocks of the Coast Ranges. Isotopic ages for most major late Cenozoic volcanic fields of the California Coast Ranges span several million years (Table 1). Those volcanic fields lacking large age ranges are those with only one or two dates (the Mindego basalt, for example; Table 1). It is not clear how much of the age range for each volcanic field is a consequence of eruption of lava over an extended period of time, or analytical uncertainty related to the isotopic systematics of the samples. Nearly all of the published dates on Cenozoic volcanic rocks are conventional K/Ar ages. $^{40}Ar/^{39}Ar$ step heating analyses have proved superior to conventional K/Ar in dating Cenozoic volcanic rocks, because problems of Ar loss and excess Ar can be evaluated, and, in many cases, corrected for [e.g., *Sharp et al.*, 1996]. Recent redating of the Berkeley Hills volcanics illustrates the problems associated with the existing geochronologic data set. The full range of published K/Ar dates for the Berkeley Hills volcanics is 7.9 to 12 Ma [*Lindquist and Morganthaler*, 1991], whereas $^{40}Ar/^{39}Ar$ step heating analyses, supported by paleomagnetic reversal data, indicate that the top and bottom of the volcanic section is 9.2 and 10 Ma, respectively [*Grimsich et al.*, 1996]. Thus the conventional K/Ar age spread from the Berkeley Hills volcanics is largely a consequence of a combination of Ar loss (for the younger ages) and excess Ar (for the older ages) and not a reflection of a 4 Ma duration of eruption. New Ar/Ar dates are presented along with older K/Ar ages for volcanic rocks in Table 1.

4.4. Interpretation of Late Cenozoic Volcanic Rocks in the California Coast Ranges: How Do They Relate to the Development of the San Andreas Fault System and Can Models of Their Evolution Be Used for Specific Slip Estimates?

The age distribution of late Cenozoic volcanism in the Coast Ranges has been used to support models of northward

Table 1. Age Ranges of Cenozoic Volcanic Rocks Along Central and Northern San Andreas Fault System Strands

Volcanic Field	Age, Ma	Dating Method	Comments	Reference
Clear Lake	0.01 to 2.06±0.02	K/Ar		1
Coyote Reservoir	2.5±0.1 to 3.6±0.1	K/Ar		2
Sonoma (east of Rodgers Creek fault)	1.4±0.8 to 8.9±4.5	K/Ar		3
Sonoma	2.6±0.3 to 8.0±0.1	K/Ar	age range excluding samples with high relative uncertainty	3
Sonoma, eastern part	3.4±0.2 to 5.4±0.4	K/Ar		3
Sonoma, northern part	2.6±0.3 to 3.7±0.5	K/Ar		3
Sonoma, western part	3.80±0.01 to 8.0±0.1	K/Ar		3
San Luis Reservoir	7.4±0.2 to 9.0±0.1	K/Ar		2
Tolay (between Rodgers Creek and Tolay faults)	8.5±0.2 to 10.6±0.3	K/Ar		3
Berkeley Hills	9.20±0.03 to 9.99±0.02	Ar/Ar step heating	dates consistent with paleomagnetic data and relative stratigraphic position	4
Berkeley Hills	7.9 to 12.0	K/Ar	no uncertainties given	5
Berkeley Hills	8.7±1.5 to 10.2±0.3	K/Ar	range of dates published with uncertainties	5
Quien Sabe	10.02±0.02 to 10.30±0.03	Ar/Ar step heating	from intrusions cutting volcanic field; four dates from two samples	6
Quien Sabe	11.57±0.06 (p) 11.1±0.1 (i)	Ar/Ar step heating	from stratigraphically low position	6
Quien Sabe	9.3±0.1 to 11.6±0.1	K/Ar		2
Burdell Mountain	12.9±0.1 (p) 12.6±0.1 (i)	Ar/Ar step heating	date from single sample	6
Burdell Mountain	11.8±0.4 to 13.6±2.4	K/Ar		3
Page Mill	15.61±0.04 (p)	Ar/Ar step heating	date from single sample, volcanic field of limited extent	6
Page Mill	12.2±6.5 and 14.8±2.4	K/Ar		5
Mindego	20.2±1.2	K/Ar	single date	5
Zayante	23.7±0.7	K/Ar	single date	5
Pinnacles	22.8±0.2 (p)	Ar/Ar step heating	single date	7
Pinnacles	22.1±3.2 to 24.5±0.2	K/Ar		8
Neenach	21.3±0.2 and 23.6±0.3 (p)	Ar/Ar step heating	two dates	7
Neenach	22.5 to 24.1	K/Ar	no uncertainties given	8

For $^{40}Ar/^{39}Ar$ dates (i) denotes isochron age and (p) denotes plateau age; both isochron and plateau ages given because $^{40}Ar/^{36}Ar$ intercept indicates presence of excess argon. Data sources are 1, *Donnelly-Nolan et al.* [1981]; 2, *Nakata et al.* [1993]; 3, *Fox et al.* [1985b]; 4, *Grimsich et al.* [1996]; 5, *Lindquist and Morganthaler* [1991] (a compilation of data from several sources); 6, C. Swisher (unpublished data, 1999); 7, P. Weigand and C. Swisher (unpublished data, 1991); 8, *Turner* [1968], recalculated by *Sims* [1993].

younging volcanism following passage of the Mendocino triple junction [*Johnson and O'Neil*, 1984; *Fox et al.*, 1985a; *Dickinson*, 1997], but these volcanic rocks may represent several different types of environments: One group of volcanic rocks apparently erupted in the wake of the northward migrating Mendocino triple junction, whereas a different suite of volcanic rocks resulted from spreading ridge-trench collisions, based on petrologic and geochemical characteristics [*Johnson and O'Neil*, 1984; *Cole and Basu*, 1995]. Depending on the distribution of displacement, the former group of volcanic rocks may restore to a northward younging trend (or two distinct northward younging trends) ranging in age from about 24 to 0.01 Ma, and cropping out east of the San Andreas fault, with the exception of the Pinnacles volcanics. Volcanic rocks associated with ridge-trench interactions mostly range between about 20 and 25 Ma and occur west of the San Andreas fault [*Cole and Basu*, 1995]. Of the volcanic fields shown in Figures 5 and 6, and tabulated in Table 1, only the Mindego and Zayante basalts are considered to be part of the ridge-trench suite, but smaller volcanic fields of this type locally are present in northern California.

A third, smaller, group of volcanic rocks occurs east of the San Andreas fault and does not fit a northward younging trend, no matter what type of slip distribution scheme is used. The best examples of this type of volcanic rock are the 2.5 to 3.6 Ma basalts that crop out at Anderson and Coyote Reservoirs [*Nakata et al.*, 1993] (referred to as "Coyote volcanics" herein; CV on Figures 5 and 6). Any possible combination of fault displacements will leave older volcanic rocks north of the Coyote volcanics at the time of their eruption.

Because of the different types of occurrences of late Cenozoic volcanic rocks in the Coast Ranges and the uncertainties of their ages, a northward younging model of volcanism will not be assumed herein for quantitative slip estimates across faults; only correlation of rocks of similar age and lithology will be used. The northward younging model of volcanism will be used for one qualitative assessment of slip in the region of the Sonoma volcanics, and this qualitative assessment is independently supported by other geologic data. All of the volcanic fields discussed in the following sections on slip distribution belong to either the northward younging or Coyote volcanics-type suites. Although a northward younging trend is not assumed in the text for these volcanic rocks, they are considered to have erupted south of the migrating Mendocino triple junction by virtue of the fact that they are not the product of ridge-trench interactions.

4.5. Displacement Estimates From Correlated Late Cenozoic Units and Franciscan Rocks

Clasts of fine-grained, epidote blueschist are found in conglomerates of the Miocene Contra Costa Group that underlie the Berkeley Hills volcanics [*Dickerman*, 1998] (CC on Figure 6). These clasts are similar to Franciscan rocks found in the Ward Creek area (WC on Figure 6). Such coherent epidote

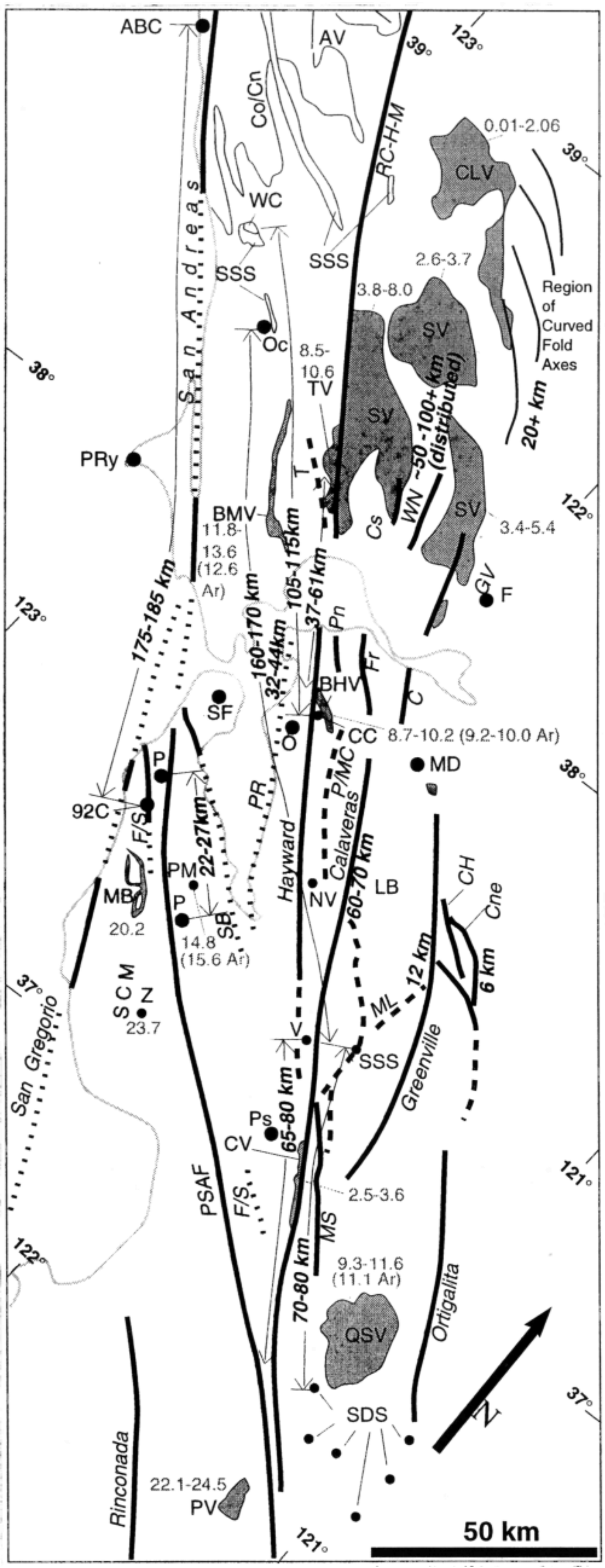

Figure 6. Detail of faults and offsets, San Andreas system, greater San Francisco Bay area. Abbreviations same as Figure 5 except CC, Contra Costa Group conglomerate beneath Berkeley Hills volcanics; ML, Mt. Lewis fault trend; and Pn, Pinole fault. Screened numbers are K/Ar dates of volcanic rocks in Ma (Ar-Ar step heating dates in parentheses).

blueschists are rare in the Franciscan (and absent in other units of the Coast Ranges), other than along the eastern margin of the northern Coast Ranges [*Blake et al.*, 1988]. South of Ward Creek, the only known occurrences of similar rocks, here associated with the Skaggs Springs schist, are in small klippe (SDS in Figures 5 and 6) in the southern Diablo Range (J.Wakabayashi and T. Dumitru, unpublished data, 1996). The estimated offset of the epidote-blueschist-bearing Contra Costa Group conglomerates from their Franciscan source is 105 to 115 km, depending on the geometry of the faults carrying the slip. This slip must be accommodated on the Hayward fault, and parallel structures west of the Hayward fault that pass east of WC on Figure 6.

Correlation of the Tolay and Berkeley Hills volcanics (Figure 6) has been suggested on the basis of somewhat similar K/Ar age ranges and lithologies, and similar underlying strata [*Youngman*, 1989; *Curtis*, 1989; *Liniecki-Laporte and Andersen*, 1988]. Using a permissible range of reconstructions of the volcanic rocks and enveloping strata, the offset between these two areas is estimated as 37 to 61 km, which would be accommodated on the Hayward and Rodgers Creek faults. Note that the term "Tolay volcanics," as applied herein, denotes Cenozoic volcanic rocks that occur between the Rodgers Creek and Tolay faults. Older late Cenozoic volcanic rocks west of the Tolay volcanics are referred herein to as the "Burdell Mountain volcanics," and younger volcanic rocks east of the Rodgers Creek fault are referred to as "Sonoma volcanics." Subtracting the 37 to 61 km estimate for the Hayward fault from the 105 to 115 km total, 44 to 78 km of slip must be accommodated on the Tolay fault and other unnamed structures that must continue northward and pass east of the Ward Creek schists. In the Bay area, some of the 44 to 78 km of slip may be accommodated on the Point Richmond fault discussed below, as well as faulting between the Hayward and Point Richmond faults.

Much of the displacement on the Hayward fault transfers north to the Rodgers Creek fault, but some may step right to the Carneros and West Napa faults (Figure 6), as suggested by the presence of what may be a late Cenozoic pull-apart basin (no longer actively extending) that is bordered on the east by the West Napa and Carneros faults [*Wright and Smith*, 1992]. Field relations in the North Berkeley Hills (area along Hayward fault near 37°52'30" on Figure 2), indicate that the main stratigraphic offset along the Hayward fault in this area is the faulted contact between Franciscan and Tertiary rocks, situated 200 to 1000 m east of the present active trace; additional offsets may be present west of the active trace as well (J. Wakabayashi, unpublished mapping, 1989). Apparently, the active trace of the Hayward fault has shifted across a zone several kilometers wide over the past 10 Ma [see *Graymer et al.*, 1995b]. A similar history appears to apply to the Central San Andreas [*Sims*, 1993], parts of the Calaveras fault, and may characterize the development of all of the major dextral faults of the San Andreas system. Such broad zones of displacement may be the result of progressive migration of step overs or bends along the faults; the development of strike-slip duplexes [*Wakabayashi and Hengesh*, 1998].

Correlation of the Quien Sabe volcanics and Berkeley Hills volcanics has been suggested, indicating 160 to 190 km of displacement between the two fields [*Curtis*, 1989; *Youngman*, 1989], but the Quien Sabe volcanics differ in lithology and age. Most of the Quien Sabe volcanics consist of felsic and volcaniclastic rocks [*Drinkwater et al.*, 1992] that are not present in the Berkeley Hills volcanic deposits. In addition to lithologic dissimilarities between the Quien Sabe and Berkeley Hills volcanics, C. Swisher (unpublished data, 1999) has obtained an Ar-Ar step heating age of 11.1 Ma from the only part of the Quien Sabe volcanics that bears any lithologic similarity to the (9.2 to 10 Ma) Berkeley Hills volcanics. Thus the correlation between the Berkeley Hills and Quien Sabe volcanics appears to be invalid.

Fault slices of volcanic rocks, located north of the Quien Sabe volcanics but south of the Berkeley Hills volcanics [*Graymer et al.*, 1995a; J. Grimsich, unpublished data, 1996] (v and NV on Figure 6), resemble the Quien Sabe volcanics. The Quien Sabe volcanics and the above-mentioned fault slices originally may have been contiguous or nearly so, but new age dates and more detailed field data are needed to verify this correlation. In addition to the lithologic similarity of these small volcanic remnants to the Quien Sabe rocks, the occurrence of a remnant of Skaggs Springs schist north of the Mount Hamilton area (SSS between the Calaveras and Greenville faults on Figure 6) is consistent with the offset of these volcanic remnants from the Quien Sabe field. About 70 to 80 km of offset is necessary to displace this schist remnant north from the northwesternmost of the correlative SDS schist bodies, and 65 to 80 km is necessary to offset the volcanic fault slice v of Figure 5 (the southernmost of the two remnants) from the Quien Sabe volcanics (Figure 6). Offset between v and Quien Sabe would be accommodated on the Calaveras, Greenville, Mount Lewis, and related faults; offset between SSS and SDS would be accommodated on the same faults, except it would exclude slip on the Calaveras south of where unnamed faults intersect the Calaveras fault, south of the Livermore Basin (LB on Figure 6). Fifteen to 35 km of additional offset may be necessary to bring volcanic NV adjacent to volcanic remnant v, if these two volcanic remnants restore adjacent to each other.

Of the displacement east of the Hayward fault, 12 km occurs on the combined Greenville and Mount Lewis faults (based on correlations of offset ultramafic basement nappes), 60 to 70 km on the Calaveras fault and any faulting between the Calaveras and Greenville fault trends (based on both correlations of volcanic rocks in fault slices to the Quien Sabe volcanics and the correlation of the Skaggs Springs schist, less the slip for the Greenville and Mount Lewis trends).

The position of Skaggs Springs schist constrains most of the slip that splays northward onto the Calaveras and Greenville fault trends, and faulting between these trends, to be accommodated on the now-dormant Madrone Springs fault trend and related faults at the latitude of the Quien Sabe volcanic field. The 60 to 70 km of displacement on the Calaveras and related faults may be accommodated as follows: (1) on the Calaveras fault itself; (2) most of the slip is carried on faults east of the Calaveras, such as the Madrone Springs fault and unnamed faults splaying from the north end of the Madrone Springs fault (Figure 5) that merge westward back onto the Calaveras fault (constrained by position of SSS and SDS on Figure 6); (3) some displacement may step eastward from the Calaveras fault near the south border of the Livermore Basin; (4) some slip may splay westward from the Calaveras fault onto faults between the Hayward and Calaveras faults, including the Palomares-Miller Creek fault trend; (5) some of the slip may have been accommodated by pull-apart development of the late Cenozoic Livermore basin in the past (the Livermore basin is currently not in a pull-apart setting). Displacements in categories 2 through 5 may pass east of the eastern piercing point used by *Page* [1984] to estimate 16 to 24 km of displacement on this part of the Calaveras fault zone. Much of the displacement in the region between the Hayward and Calaveras faults may be accommodated on the Palomares and Miller Creek faults, which are considered to bound contrasting Tertiary stratigraphic packages by *Graymer et al.* [1994] and *Jones et al.* [1994], and pass east of the Berkeley Hills volcanic field. In the northern part of the eastern Bay area, slip east of the Hayward fault may be accommodated on the Concord fault and also distributed on several faults that splay northwestward from the northern end of the Calaveras fault, including the Franklin fault.

Displacement may be accommodated on faults between the Hayward and Calaveras faults that is independent of the displacement amounts on assigned to the bounding faults. The possible correlation of volcanic remnants v and NV may record some of this offset (15 to 35 km if they correlate), but the correlation of these remnants as well as the fault geometry between them is uncertain. The total displacement of the Skaggs Springs schist (230 to 250 km), less the total slip amounts estimated for various faults or groups of faults accounting for these offsets, leaves about 30 to 50 km of slip that may occur on structures between the Hayward and Calaveras faults. Such structures may include faults that connect northward to the Miller Creek-Palomares fault trend. Displacement along this trend may link northward with the Pinole and/or Franklin and related faults (Figure 6). Displacement on the Pinole fault probably merges northward onto the Rodgers Creek fault but would not be recorded in the Tolay-Berkeley Hills volcanic offset, because the Pinole fault passes east of the Berkeley Hills volcanics (Figure 6).

The Ortigalita fault (Figure 6) is a late Cenozoic dextral fault that passes east of the Quien Sabe volcanics and may have several kilometers of displacement on it (Anderson et al., 1982). No piercing points have been identified across it, possibly because the fault had significant dip-slip displacement prior to its recent history as a dextral fault [*Raymond*, 1973a]. Slip appears to transfer northward from the Ortigalita fault onto several structures, such as the northern Peg Leg fault of *Raymond* [1973b], and connect or transfer slip to faults such as the Tesla, Corral Hollow, Carnegie and, possibly, the Black Butte faults. *Throckmorton* [1988] determined an aggregate right-lateral displacement of about 6 km on the Carnegie and Corral Hollow faults, based on an offset syncline in late Cenozoic rocks. Displacement on the Tesla fault cannot be determined because of the lack of identified piercing points, but displacement may be significant based on contrasting units across the fault (much of the contrast, however, may be related to an earlier dip-slip history). Based on the above, the Ortigalita and related faults are estimated to have a late Cenozoic dextral displacement of 6 to 10 km.

4.6. Other Estimates of Displacement From Offset Franciscan Features

Franciscan nappes observed on land in the Bay area can be partly extrapolated into the Bay because some of the melange horizons between coherent nappes contain serpentinite that is associated with prominent magnetic anomalies [*Jachens and Roberts*, 1993a]. One such melange, the Hunters Point shear zone, is associated with one of the most prominent magnetic anomalies in the Bay area, and this anomaly allows this horizon to be traced southeastward into the Bay (Figure 2). In San Francisco, the Hunter's Point shear zone structurally overlies the Marin Headlands nappe (terrane) and the nappe stack dips northeastward. The same melange zone and underlying coherent nappe are present at Coyote Hills, along the eastern margin of the San Francisco Bay, but the stack dips southwest at Coyote Hills [*Snetsinger*, 1976]. Thus the rocks in San Francisco and Coyote Hills are part of different fold limbs of the folded nappe stack. A truncation of the magnetic anomaly associated with the southeast continuation of the Hunters Point shear zone is present a few km northwest of Coyote Hills [*Jachens and Roberts*, 1993a] and probably coincides with a break in the folded nappe stack. A southwest dipping fold limb of the nappe stack, which may match the southwest dipping limb at Coyote Hills, is present north of Tiburon Peninsula (Figure 2). In this area, the structural horizon equivalent to the Hunters Point shear zone is submerged, but its location is estimated based on its structural position relative to the adjacent coherent nappes. A major break in the folded nappe sequence is present east of Point Richmond. If this break in the nappe sequence connects with the discontinuity west of the Coyote Hills, then the right separation of the southwest dipping fold limb is about 32 to 44 km. This fault may accommodate some of the estimated 44 to 78 km of slip west of the Hayward fault that passes east of the Ward Creek area. *Wakabayashi and Hengesh* (1995) have inferred the presence of a structure called Point Richmond fault to account for this discontinuity. A major basin filled with Quaternary and possibly older sediments (deepest boreholes bottom in Quaternary sediments but basement is not reached [*Rogers and Figuers*, 1992]) is present along the Point Richmond fault and is marked by a prominent gravity low [*Jachens and Roberts*, 1993b]. This basin cannot be easily explained in the context of present-day tectonics, but it could have formed as a pull-apart basin when significant dextral movement was taking place along the now-dormant Point Richmond fault.

The magnetic anomaly associated with the Hunters Point shear zone indicates that the relatively coherent Franciscan section exposed in San Francisco extends southeastward into San Francisco Bay. This magnetic anomaly and the coherent nature of the Franciscan nappe stack in San Francisco suggests that late Cenozoic dextral faulting between the San Andreas and Hayward faults must pass east of this anomaly and the San Francisco area, or west of San Bruno Mountain (Figure 2). The eastern "permissible" zone includes the Point Richmond fault and also any faulting east of the Coyote Hills and west of the Hayward fault. The western zone includes the San Bruno fault and faulting along the San Francisco Peninsula (Peninsula) eastern rangefront.

A major break in the Franciscan nappe stack is present southwest of San Bruno Mountain (Figure 2). The nappe stacks on either side of this discontinuity are substantially different. Although the Marin Headlands terrane is present in the nappe stacks in both areas, the coherent blueschist facies rocks of the Angel Island nappe are not present west of the discontinuity, and the limestone-bearing Permanente terrane is not present east of the discontinuity [*Wakabayashi*, 1992]. This discontinuity is nearly parallel to the Franciscan structural grain, and no surface piercing points have been identified. Interpretation of matching gravity and magnetic anomalies by *Griscom and Jachens* [1990] suggests that 14 to 66 km displacement may pass through this area (Appendix). This zone of displacement includes the San Bruno fault of *Bonilla* [1964]. Temporal distribution of slip on the San Andreas system suggests an amount of slip on the San Bruno and related faults that is similar to the estimate derived above from correlated gravity and magnetic anomalies. Displacement occurred on the Central San Andreas between 18 Ma (the initiation of slip on the fault [*Atwater and Stock*, 1998]) and 15 Ma [*Sims*, 1993], and any displacement on the Central San Andreas must be accommodated on the Peninsula San Andreas and faults east of it at the latitude of the Bay area. The Point Richmond and faults to the east of it probably could not have been active prior to 15 Ma, because of the position the Mendocino triple junction restores south of their northern extension at that date. Additionally, the Peninsula San Andreas may have only accommodated slip since 2 Ma (discussed in the following section on temporal distribution of slip). Thus the San Bruno and related faults are the most likely faults in this area to have accommodated slip derived from the Central San Andreas during the 18 to 15 Ma period. The amount of displacement on the Central San Andreas during this period may be about 40 km based on an 18 Ma initiation of slip and an average 13mm/yr slip rate during this period (*Sims* [1993] adjusted for 18 Ma initiation of faulting from *Atwater and Stock* [1998]). Given the uncertainty in the slip rate along the Central San Andreas from 18 to 15 Ma, the permissible displacement range for the San Bruno and related faults is about 30 to 50 km.

Displacement passing through the Peninsula along the San Bruno fault may continue southward as shown in Figure 2 or some displacement may be accommodated along the eastern rangefront of the Peninsula (approximately following the trend of the Peninsula rangefront faults labeled on Figure 2). The faults along the present-day Peninsula rangefront are reverse or right-oblique reverse faults [*McLaughlin et al.*, 1996b; *Angell and Hall*, 1995; *Hengesh et al.*, 1996]. During the main period of inferred activity on the San Bruno and related faults (15 to 18 Ma), the movement on the rangefront faults may have been more purely strike slip [*McLaughlin et al.*, 1996b], as there was a major change in the azimuth of Pacific-North America motion at about 8 Ma, with a small component of contraction developed since then [*Atwater and Stock*, 1998]. Major gravity lows, interpreted to represent buried Cenozoic deposits south of the Bay [*Jachens and Roberts*, 1993b; *McLaughlin et al.*, 1997], are difficult to explain on the basis on position of presently active faults; they may have formed as pull-apart basins along now-(largely) dormant dextral faults along what is now the eastern rangefront of the Peninsula or the San Bruno fault.

4.7. Sum of Estimates of Displacement

If the 30 to 50 km displacement for the San Bruno and related faults (western permissible zone) is added to the 230 to 250 km displacement for the Skaggs Springs schist, and the 6 to 10 km displacement for the Ortigalita and related faults (that pass east of all Skaggs Springs schist exposures), the total displacement for faulting east of the Peninsula San Andreas is 266 to 310 km. This total is essentially identical to the 259 to 298 km total of permissible residual slip.

4.8. Approximate Locations of Some Qualitative Displacements North of the Eastern San Francisco Bay Area (Not Additive to Totals of Estimates Above)

Geologic evidence indicates that tens of kilometers of displacement may be accommodated on faulting through the Sonoma volcanics and along the eastern margin of the northern Coast Ranges (Figure 6). Faulting through these regions is the northward continuation of dextral faulting east of the Hayward fault.

Based on published K/Ar dates, the Sonoma volcanics are older on the western part of the field (3.8 to 8.0 Ma) than the east (3.4 to 5.4 Ma) [*Fox et al.*, 1985a] (Table 1 and Figure 6). If these volcanic rocks are the product of volcanism progressively erupted in the wake of the migrating triple junction [e.g., *Fox et al.*, 1985a], then the difference in age between the eastern and western parts of the Sonoma volcanics suggests a large magnitude of dextral slip between these rocks. Depending on the true age range of the rocks in the eastern and western parts of the volcanic field (see earlier geochronology discussion) and the rate of migration of volcanism, the age difference may reflect a negligible offset to one of over 100 km. The distribution of displacement south of the Sonoma volcanic field, discussed in earlier sections, suggests that tens of kilometers of displacement through the Sonoma volcanics is likely. Displacement through this area may be accommodated on faults such as the West Napa and Carneros faults (Figure 6). *Fox* [1983] suggested an offset of as much as 35 km on the Carneros fault. Other offsets in this region remain to be evaluated by detailed correlations. *Dickinson* [1997] assigned 100 km of slip to pass entirely east of the Sonoma volcanics on the basis of the model of progressive northward migration of volcanic centers and *McLaughlin et al.*'s [1996a] assignment of 100 km of slip to the Calaveras and related faults. Displacement of 100 km on the Calaveras fault system that continues northward east of the Sonoma volcanics is difficult to reconcile with paleogeographic relationships of San Pablo Group and related Miocene strata [*Buising and Walker*, 1995]; distributing this (or a smaller amount of) displacement both through and east of the Sonoma volcanic field is more consistent with these relationships. Indeed, faulting through as well as east of the Sonoma volcanics would fit the general premise of the *Dickinson* [1997] model better than placing 100 km of displacement entirely east of these rocks.

Cenozoic fold axes typically are convex toward the NE and curve asymptotically toward the eastern margin of the northern Coast Ranges north of the Carquinez strait [*Jennings*, 1977] (Figure 6). If this pattern is associated with dextral faulting, the drag-fold-like geometry of the traces of the fold axes, reminiscent of the trace of s surfaces in a c-s mylonite, suggests that tens of kilometers of late Cenozoic right lateral shear may have passed through this region. Most of this slip would pass east of the Sonoma volcanics (excluding the sliver of Sonoma volcanics east of the Green Valley fault; Figure 6).

5. Displacement on Faults Independent of the Central San Andreas and the Total Slip for the Northern San Andreas Fault System and Pacific-North American Plate Boundary

In order to evaluate the total slip on the northern San Andreas system, and the evolution of the system in the larger context of the plate boundary, faulting exclusive of the Central San Andreas must be addressed. This faulting occurs west of the Central San Andreas and is accommodated on the Rinconada, San Gregorio, and faults west of the San Gregorio [e.g., *Sedlock and Hamilton*, 1991]. The estimated for total slip for the combined San Gregorio and Rinconada faults is 175 to 185 km [*Burnham*, 1998].

Faulting west of the San Gregorio fault is referred to herein as "offshore" faults, because such faulting is entirely offshore in the northern San Andreas system. Although slip on some offshore strands may be estimated by offset submarine canyons [*Greene et al.*, 1991], the total slip for all such strands is not directly constrained by identified piercing points. *Dickinson and Wernicke* [1997] have estimated the amount of "transrotational" (combination of measured dextral displacements on faults and dextral displacement accommodated by rotation) slip in the Transverse Ranges since 16 Ma as 208 ± 22 km. This total is partitioned northwest of the Transverse Ranges on the Rinconada, San Gregorio, and offshore faults. If the slip for the San Gregorio and Rinconada faults (175 to 185 km) is subtracted from the transrotational amount, then the slip remaining for offshore faults is 1 to 55 km. *Atwater and Stock* [1998] estimated 250 km of slip for the sum of displacements for the San Gregorio, Rinconada and offshore faults. The *Atwater and Stock* [1998] slip estimate for this group of faults also is consistent with their total estimated slip for the plate boundary and the other components of the plate boundary (Central San Andreas, Basin and Range), and accounts for slip that may not be recorded by transrotation. No uncertainty is given for this estimate. If a ±20 km uncertainty is given for the estimate (comparable to uncertainty estimated by *Dickinson and Wernicke* [1997]), then subtraction of Rinconada and San Gregorio slip, from 250 ± 20 km yields 45 to 95 km of slip for the offshore faults. Following the discussion above, a 230 to 270 km total will be adopted as the estimate of the sum of northern San Andreas system displacement exclusive of the Central San Andreas. The estimated slip for the northern San Andreas fault system is thus 310 to 320 km (Central San Andreas) plus 230 to 270 km (west of Central San Andreas), for a total of 540 to 590 km. The N40°W dextral component of deformation east of the Sierra Nevada (Basin and Range) is about 200 to 240 km [*Dickinson and Wernicke*, 1997; *Wernicke and Snow*, 1998], and the total N40°W dextral slip across the Pacific-North American plate boundary since the inception of the transform margin is about 800 km [*Atwater and Stock*, 1998].

6. Temporal Distribution of Displacement: Northern San Andreas Fault System

Timing of displacement on individual faults and groups of faults can be constrained both by offset Cenozoic units along each strand, and offset history for the system as a whole. Constraints on the timing of displacement allow assessment of how the distribution of slip rates across the plate boundary has changed as it has evolved. For the plate boundary the migration rate and past positions of the Mendocino triple junction [*Atwater and Stock*, 1998] can be used to estimate the dextral slip rate and total displacement; displacements for various components of the plate boundary are shown in Figure 7. The total N40°W slip rate for the plate boundary was about 35 mm/yr from the inception of the San Andreas system at 18 to 12 Ma, 45 mm/yr from 12 to 11 Ma, 58 mm/yr from 11 to 8 Ma, 41 mm/yr from 8 to 5 Ma, and 55 mm/yr since 5 Ma. For the faults that splay off the Central San Andreas, the aggregate slip rate was about 13 mm/yr from about 18 to 6 Ma and about 25 to 35 mm/yr thereafter [*Crowell*, 1962; *Powell*, 1993; *Sims*, 1993] (modified for 18 Ma initiation of faulting from *Atwater and Stock* [1998]). Some of the age constraints for individual faults are discussed below and shown diagramatically on Figure 7, and approximate slip rates for groups of faults during various time periods are shown on Figure 9.

6.1. Peninsula San Andreas

Peninsula San Andreas may only have been active for the last 2 million years or so, whereas other parts of the San Andreas fault have been active for much longer. This estimate is calculated by dividing the total offset (22 to 36 km) by the estimate of latest Quaternary slip rate (~17 mm/yr [*Clahan et al.*, 1995]). This age also is coincident with the beginning of the deposition of the Merced Formation, which is interpreted to have formed in a pull-apart basin along the San Andreas fault that has now migrated offshore (west) of San Francisco [*Hengesh and Wakabayashi*, 1995]. North of the intersection between the San Andreas fault and the San Bruno and related faults, the San Andreas fault has been active since about 18 Ma, based on the slip history of the Central San Andreas and the slip distribution presented here.

6.2. Eastern Faults: Hayward, Calaveras, Greenville, Ortigalita, Point Richmond, and Related Faults

The Hayward, Calaveras, Greenville and Ortigalita faults presently are active, slipping at an estimated 9±1 mm/yr , 5±1 mm/yr, 2±1 mm/yr, and a few tenths of a mm/yr, respectively [*Anderson et al.*, 1982; *Lienkaemper et al.*, 1991; *Kelson et al.*, 1996; J. R. Unruh and T. L. Sawyer, oral communication, 1995]; the Calaveras fault slip rate is the rate north of the Hayward-Calaveras fault bifurcation. Faulting between the Hayward and Calaveras faults is presently taking place at low slip rates (tenths of mm/yr [*Wakabayashi and Sawyer*, 1998]).

The Point Richmond fault is not presently active (or it ac-

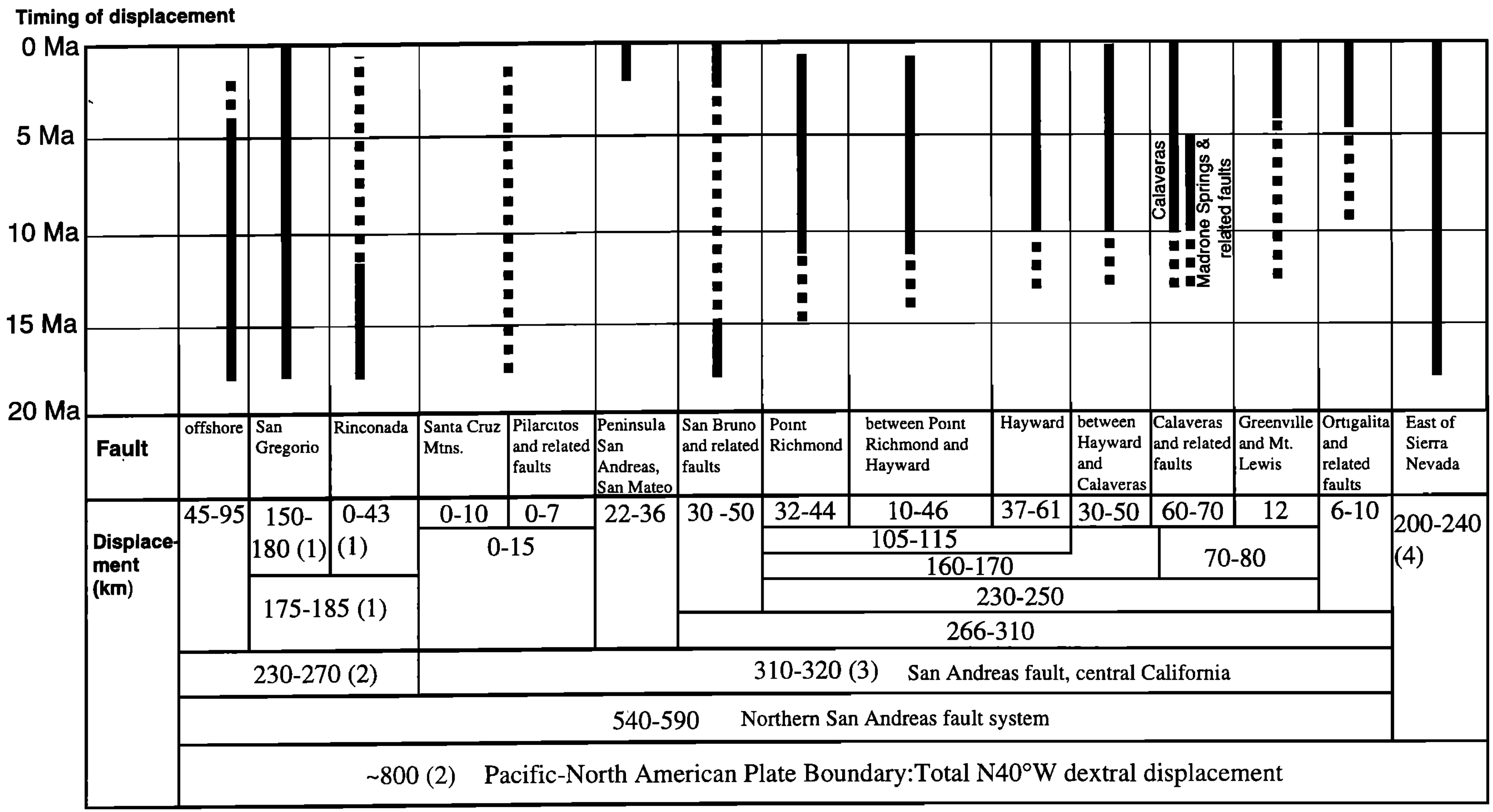

Figure 7. Dextral slip distribution and timing of displacement, northern Pacific-North American transform plate boundary, including northern San Andreas fault system. Sources are 1, highest part of range for San Gregorio, lowest part of range for Rinconada, and San Gregorio-Rinconada sum from *Burnham* [1998], lowest part of range for San Gregorio from *Clark et al.* [1984], highest part of range for Rinconada from *Graham* [1978], 2, *Atwater and Stock* [1998], 3, *Graham et al.* [1989], 4, *Dickinson and Wernicke* [1997]. Other slip estimates derived from this study and discussed in text.

commodates an extremely low slip rate of 0.1 mm/yr or so), because there is no evidence for Holocene faulting in the San Francisco Bay [*Marlow et al.*, 1994]. The Point Richmond fault was probably active into the Quaternary because of the thick Quaternary deposits that occur in the basin along it. Flat-lying sediments, estimated to be 200 ka or older, unconformably overlie folded, older Quaternary sediments in this basin [*Marlow et al.*, 1999], suggesting that activity along the Point Richmond fault may have largely ceased by 200 ka.

Movement on the Hayward and Calaveras faults and faulting between them may have initiated as early as 12 to 13 Ma, based on the age of strata from transform-related basins [*Buising and Walker*, 1995]. This estimate for initiation of movement is consistent with the delay of eruption of volcanics in the wake of the migrating triple junction (the oldest volcanic rocks offset by the Calaveras and Hayward faults are about 11 Ma), shown by present-day spatial relations (the 2 Ma to 0.01 Ma Clear Lake volcanics are 150 km or more south of the Mendocino triple junction) that are probably representative of relationships of older volcanic rocks, based on the estimated position of the southern edge of the subducted slab and thermal considerations [*Atwater and Stock*, 1998; *Furlong*, 1984]. Movement on the Point Richmond fault and faults between the Point Richmond and Hayward fault began after about 15 Ma. Movement on these faults could not have initiated much earlier otherwise the Mendocino triple junction would restore south of the northern extension of these faults at that time. These faults probably started slipping prior to 12 or 13 Ma, in order to accommodate slip from the Central San Andreas during the 12 to 15 Ma period.

If present-day rates are extended back to 2 Ma, when slip on the Peninsula San Andreas initiated, and the slip rate and displacement budgets for the Central San Andreas are adhered to, the average total slip rate for these "eastern" faults for the 6 to 2 Ma time interval is about 31 mm/yr. This rate is significantly higher than the present-day rate and would constitute the fastest slipping part of the plate boundary at the time. Several faults among these "eastern" faults that are presently either inactive or moving at slip rates of tenths of mm/yr or less must have accommodated slip rates of several mm/yr in the past because they have large cumulative displacement. These faults include the Point Richmond, Madrone Springs, East Chabot, and Palomares-Miller Creek faults, and faulting between the Point Richmond and Hayward faults. *McLaughlin et al.* [1996a] suggested an aggregate slip rate of up to 50 mm/yr for the eastern faults of the San Andreas system between 8 Ma and 6 Ma, but such slip rates may be difficult to reconcile with the 13 mm/yr, pre-6 Ma slip rates on the Central San Andreas.

6.3. San Bruno Fault and Other Faults

The San Bruno fault does not display evidence of Holocene activity [*Marlow et al.*, 1994; *Hengesh and Wakabayashi*, 1995]. The northern part of the San Bruno fault may have bounded the basin in which the Merced Formation was deposited, in which case it may have been active until 100 ka to 200 ka, on its northern end with the shut-off of activity getting progressively older to the south [*Hengesh and Wakabayashi*, 1995]. Rangefront faults along the eastern front of the Peninsula (Peninsula rangefront faults in Figure 2) are still active and oblique slip rates are in the range of tenths of mm/yr [*McLaughlin et al.*, 1996b; *Hengesh et al.*, 1996; *Angell and Hall*, 1995]. As discussed previously, it is possible that most of the slip on these faults occurred between 18 and 15 Ma at a rate of about 13 mm/yr.

6.4. San Gregorio Fault

The present-day slip rate of the San Gregorio fault is estimated to be 3 to 10 mm/yr, based on offset marine terraces [*Weber and Lajoie*, 1980], differences in slip rate estimates along the San Andreas fault north and south of the merging of the San Gregorio [*Simpson et al.*, 1997], and slip rate estimates on a strand of the Seal Cove fault (part, but not all, of the San Gregorio fault zone) [*Simpson et al.*, 1998]. A slip rate of about 5 mm/yr averaged over the last 2 Ma is consistent with post-2 Ma estimates of displacement of the Merced Formation by the San Gregorio and Peninsula San Andreas faults [*Hengesh and Wakabayashi*, 1995]. Pre-Quaternary slip rates on the San Gregorio fault are poorly constrained and the fault may have been active from the inception of the transform system at 18 Ma. If much of the slip on the San Gregorio fault occurred prior to the establishment of the transform system, as suggested by *Sedlock and Hamilton* [1991], then post-18 Ma average slip rates will be lower (and estimated offshore displacement will be higher).

6.5. Rinconada Fault

The Rinconada fault does not appear to have a significant present-day slip rate, based on lack of evidence for Holocene activity [*Jennings*, 1994]. *Sedlock and Hamilton* [1991] proposed that most of an estimated 43 km slip on the Rinconada fault [*Graham*, 1978] was accumulated between 18 and 12 Ma. Alternatively, *Burnham* [1998] suggests that similarity of displacement along the length of the San Gregorio fault indicates negligible dextral displacement on the Rinconada fault. For general slip rate partitioning in Figure 9, the Rinconada will be considered in sum with the San Gregorio and offshore faults.

6.6. Offshore Faults

Presently, these faults are either inactive or moving at low slip rates (<1 mm/yr), because there is no direct evidence for major activity on these structures [e.g., *Sedlock and Hamilton*, 1991] and the combined slip rate estimates of the on-land faults of the San Andreas system essentially equal the slip rate budget for the San Andreas system based on space geodesy [*Argus and Gordon*, 1991]. These faults may have been active fairly recently, however, based on offset submarine canyons along them [*Greene et al.*, 1991].

6.7. Proto San Andreas Fault

Restoration of 315 and 180 km of displacement on the San Andreas, and combined San Gregorio-Rinconada faults, re-

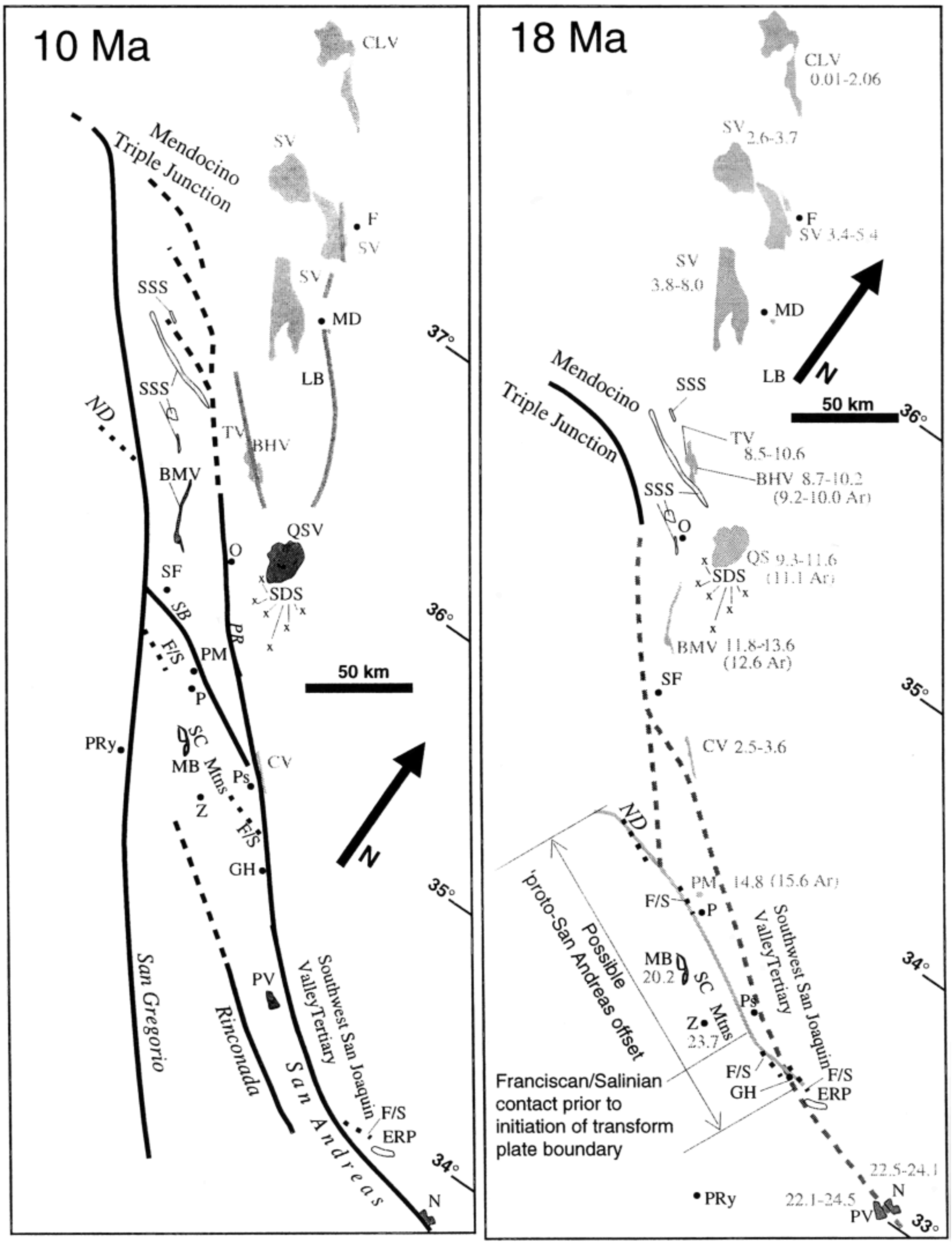

Figure 8. Reconstruction of the northern San Andreas fault system at 10 and 18 Ma. Abbreviations on Figure 5. Screened letters for volcanic units and corresponding lightly shaded fields shown without outlines indicates that specific volcanic units were not present at that time; this is the future position of those volcanics for reference purposes. Screened numbers are K/Ar dates of volcanic rocks in Ma (Ar-Ar step heating dates in parentheses). Screened faults correspond to faults that may not have come into existence at the time of the reconstruction. The exception to this is the pre-San Andreas, Franciscan-Salinian contact.

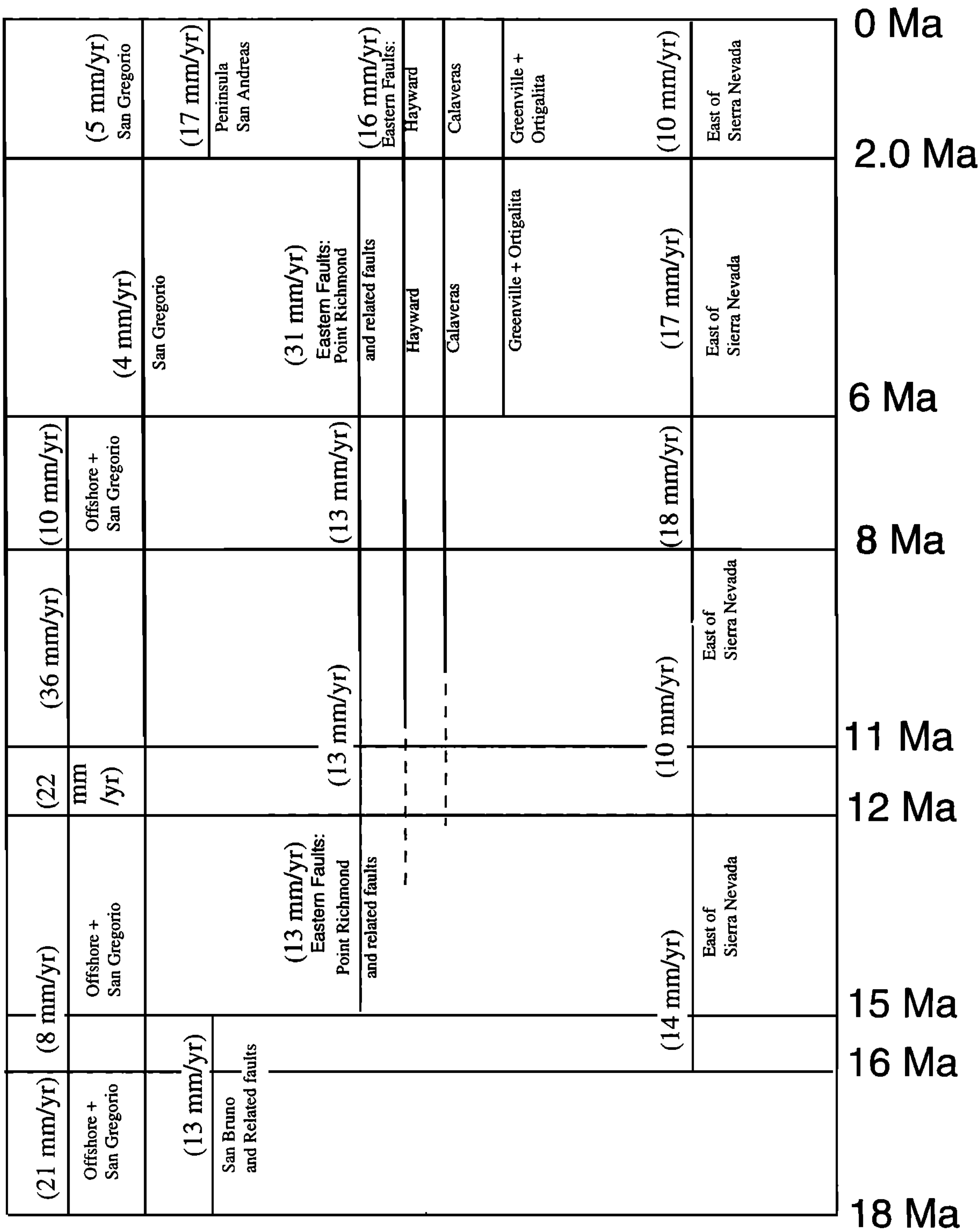

Figure 9. Approximate partitioning of N40°W dextral slip rate with time on the Pacific-North American transform system at the latitude of the central San Francisco Bay Area (37.5°N). Vertical lines schematically represent relative E-W position of active faults for a given time period. Sources discussed in text. The initiation and ending times of periods of activities of various faults have been generalized to illustrate the regional-scale slip rate distribution.

spectively [*Graham et al*, 1989; *Burnham*, 1998] restores the older Salinian-Franciscan contact (this includes the Navarro discontinuity, the Salinian-Franciscan contact in the Montara Mountain area and the buried equivalent of this contact to the south) (Figures 5 and 8). This restoration leaves the northern end of the granitic Salinian block ~150 to 200 km north of the probable source region in the southern Sierra Nevada or Mojave, juxtaposed against Franciscan to the east [*Page*, 1981] (Figure 8). Most of this apparent dextral offset is constrained to be pre-Paleocene based on provenance links between the detrital carbonate turbidites at Point San Pedro and the limestones of the Permanente terrane (see Appendix), and post-late Cretaceous (105 to 120 Ma) based on the age of the offset plutons of the Salinian block (*Mattinson and James*, 1985).

6.8. Temporal Distribution of Slip Rates Across the Evolving Plate Boundary

General partitioning of slip rates for given time periods can be estimated for groups of faults to examine how distribution of slip rate across the transform plate boundary varied through time (Figure 9). This analysis will focus on a transect across the plate boundary at the present latitude of the central San Francisco Bay area (37.5°N). The present-day general distribution of slip rates may have persisted since about 2 Ma, when the Peninsula San Andreas fault began activity. Some adjustment in slip rates during the Quaternary may have occurred when major activity ceased on the Point Richmond fault, which may have been active well into the Quaternary. Between 6 and 2 Ma, the eastern faults of the San Andreas system may have accommodated the largest component of slip rate on the transform boundary, and all of the slip from Central San Andreas, about 31 mm/yr. Between 15 Ma and 6 Ma, the eastern faults of the San Andreas fault system are constrained to have slipped at about 13 mm/yr, because they branch from the Central San Andreas that is constrained to have had this slip rate [e.g., *Sims*, 1993]. From 8 to 2 Ma faulting east of the Sierra Nevada took place at 17 to 18 mm/yr, with slower rates of 10 to 14 mm/yr from 16 to 8 Ma [*Wernicke and Snow*, 1998] (adjusted for lower slip rates during the last 2 m.y. to reflect current slip rate estimates). For the total slip rate to be compatible with the total transform margin slip rate estimated from *Atwater and Stock* [1998], the "western faults," the Rinconada, San Gregorio, and offshore faults slipped at an aggregate rate of 8 mm/yr from 16 to 12 Ma, 22 mm/yr from 12 to 11 Ma, 36 mm/yr from 11 to 8 Ma, 10 mm/yr from 8 to 6 Ma, and 4 mm/yr from 6 to 2 Ma. From 18 to 16 Ma, 13 mm/yr was accommodated on the San Bruno and related faults (all faults branching from the Central San Andreas). This leaves a 21 mm/yr aggregate rate for the western faults for the 18 to 16 Ma period.

Although there are relatively large uncertainties in temporal distribution of slip rates for individual faults, the constraints on groups of faults are somewhat better. The grouping of faults in Figure 9 allows evaluation of the pattern of shifting slip rates through time on the developing northern San Andreas fault system. The fastest slipping group of faults along the transform fault system has shifted several times during the history of the transform margin. From 18 to 16 Ma the western faults were the fastest slipping group, but during the 16 to 12 Ma period, the same faults were slipping at considerably lower rates than either the central part of the system branching off the central San Andreas fault or the deformation east of the Sierra Nevada. From 12 to 8 Ma, the western faults were dominant, and from 6 Ma to the present, faults branching off of the Central San Andreas were dominant, although there was a major westward shift within this group of faults at 2 Ma, when the Peninsula San Andreas began slipping. The pattern of temporal partitioning of slip rates across the transform boundary conflicts with models of progressive eastward migration of the most active part of the San Andreas system [e.g., *Furlong et al.*, 1989].

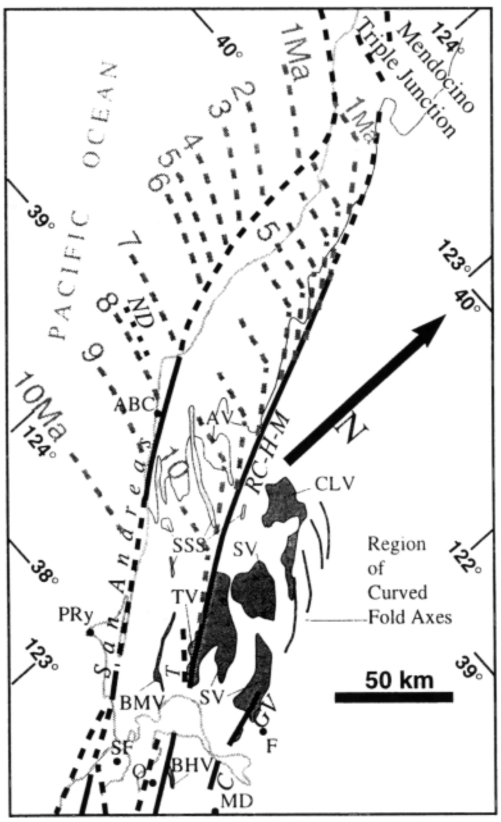

Figure 10. The northern San Andreas fault system showing past positions of the Mendocino Triple Junction relative to the San Andreas fault system. The western set of dashed and screened lines and numbers are the triple junction position with respect to the present trace of the San Andreas fault at given time in the past: these are the positions of the triple junction as it migrated along the northern San Andreas fault with respect to the eastern parts of the fault system. The eastern set of lines and numbers shows the past position of the transition zone linkage faults (see text for explanation). The relative triple junction position is based on slip assignments in the text for San Andreas system faults (including offshore) and faults east of the Sierra Nevada. Relationship betwen longititude, latitude, and geologic and geographic elements are valid for the present day only; these would shift for earlier times. Abbreviations same as in Figure 5.

7. Transitional Tectonics in the Wake of the Migrating Triple Junction: How Is Displacement Accommodated in the Youngest Part of the Transform System?

The position of the migrating Mendocino triple junction may have contributed to distributed faulting and deformation within the northernmost San Andreas fault system. This is primarily because major dextral faulting in the eastern part of the fault system (east of the San Andreas fault) does not continue north of the triple junction [*Kelsey and Carver*, 1988]; such slip must connect to the triple junction in some fashion. At present, the eastern faults of the San Andreas fault system (eastern faults), principally the Hayward-Rodgers Creek-Maacama and the Calaveras-Concord-Green Valley fault systems, accommodate approximately 16 mm/yr of dextral motion [*Kelson et al.*, 1992]. In the northern Coast Ranges, many tens of kilometers to over 100 km south of the Mendocino Triple Junction, these faults, particularly the easternmost of them (Calaveras-Concord-Green Valley trend) lose their geomorphic continuity and seismic expression [*Wakabayashi and Hengesh*, 1995]. The slip on these eastern faults may curve, or progressively step over (left) westward to intersect the triple junction.

The Mendocino Triple Junction moves northward at approximately 25 mm/yr relative to the eastern faults, based on the latest Quaternary slip rate of the northern San Andreas fault [*Niemi and Hall*, 1992; *Prentice*, 1989]. Thus, the point at which movement along the eastern faults "transfers" westward to the triple junction moves northward with time. The eastern faults in the northern Coast Ranges may lack continuity and coherent expression, because the location of this deformation is constantly changing through time [*Wakabayashi and Hengesh*, 1995]. The transfer of slip to the triple junction may require a small change in average strike of the eastern faults, or a left or "restraining" bend or step, so a component of shortening may be associated with this transfer region in addition to distributed strike-slip faulting.

This kinematic interpretation of the slip transfer is consistent with the observation that uplift rates are much higher in the triple junction region than to the north (in the pure subduction setting) or south (in the transform environment) [e.g., *Merritts and Bull*, 1989]. A zone of transitional tectonics occurs tens of kilometers north and south of the on-land projection of the Mendocino fracture zone. In this region contractional faulting can be traced southward to where it is overprinted by strike-slip faulting [*Kelsey and Carver*, 1988]. This transitional zone in part accommodates the transfer of slip from the eastern faults of the San Andreas system to the triple junction area and illustrates the early structural development of the eastern part of the strike-slip system. As the triple junction migrated northward, this transition zone would have passed through the Coast Ranges. Although much of the transfer of slip to the triple junction from the eastern faults may occur near the triple junction, some transfer of slip westward within the northern part of the San Andreas system may occur much further south. An example of such a westward transfer of slip may be associated with a concentration of seismicity in the Anderson Valley area [*Goter et al.*, 1994].

The progressive migration of the triple junction with respect to the eastern faults of the northern San Andreas fault and the migration of slip transfer structures in the vicinity of the triple junction is shown in Figure 10. The estimated position of the southern limit of major deformation traversed by the transition zone shown on Figure 10 is consistent with the relatively gently folded Franciscan nappe sequence of the Bay area between the Hayward and San Andreas faults (south of the southern limit of area traversed by the transition zone) and the comparatively large amount of postaccretionary imbrication and tight folding of the Franciscan nappe stack observed in the Healdsburg area (within the southern part of the area traversed by the transition zone) [*Wakabayashi and Hengesh*, 1995].

The concept of a migrating "transition zone" has implications for the spatial distribution of strike-slip displacement in the northern Coast Ranges. Because of this relative movement, the cumulative slip on the eastern faults may be distributed over a wide area in the northern Coast Ranges in the region where the displacement on the eastern faults transferred westward to the triple junction. No discrete fault cutting across the northern Coast Ranges to the former location(s) of the triple junction would be expected to have a significant displacement, because such a fault should not be expected to be active at a given location for any great length of time. The 230 to 250 km of right slip on the eastern faults of the San Andreas system may be distributed over many faults cutting across the northern Coast Ranges over a broad zone extending from the location of the present triple junction southward to the inferred position of the triple junction at the time of initiation of the slip on those faults. The inferred distribution of slip in the transition zone is consistent with the lack of evidence for large displacements (20 km or so) on any single fault cutting the Franciscan Coastal belt-Central belt boundary in the northern Coast Ranges [*Jennings*, 1977].

8. Conclusions

The distribution of slip rate on faults of the San Andreas system has changed in an irregular fashion during the evolution of the transform system in northern and central California, and a progressively migrating zone of slip transfer from the eastern faults of the strike-slip system to the Mendocino triple junction may have produced an area of distributed deformation in the northern Coast Ranges. The evolution of the transform system in northern California is certainly complex, and the model presented here is merely a preliminary attempt to document and explain this complexity. Much additional work is necessary to fully understand the evolution of this transform system. All aspects of this model can be tested with detailed field based studies of late Cenozoic deposits, particularly in the eastern Bay area and Santa Cruz Mountains.

Appendix: Additional Evidence Supporting Proposed Dextral Slip Distribution

A1. Additional Documentation of Field Geology in the Montara Mountain Area

Shown here are photographs illustrating some of the details of field relations in the Montara Mountain area. Figure A1 is

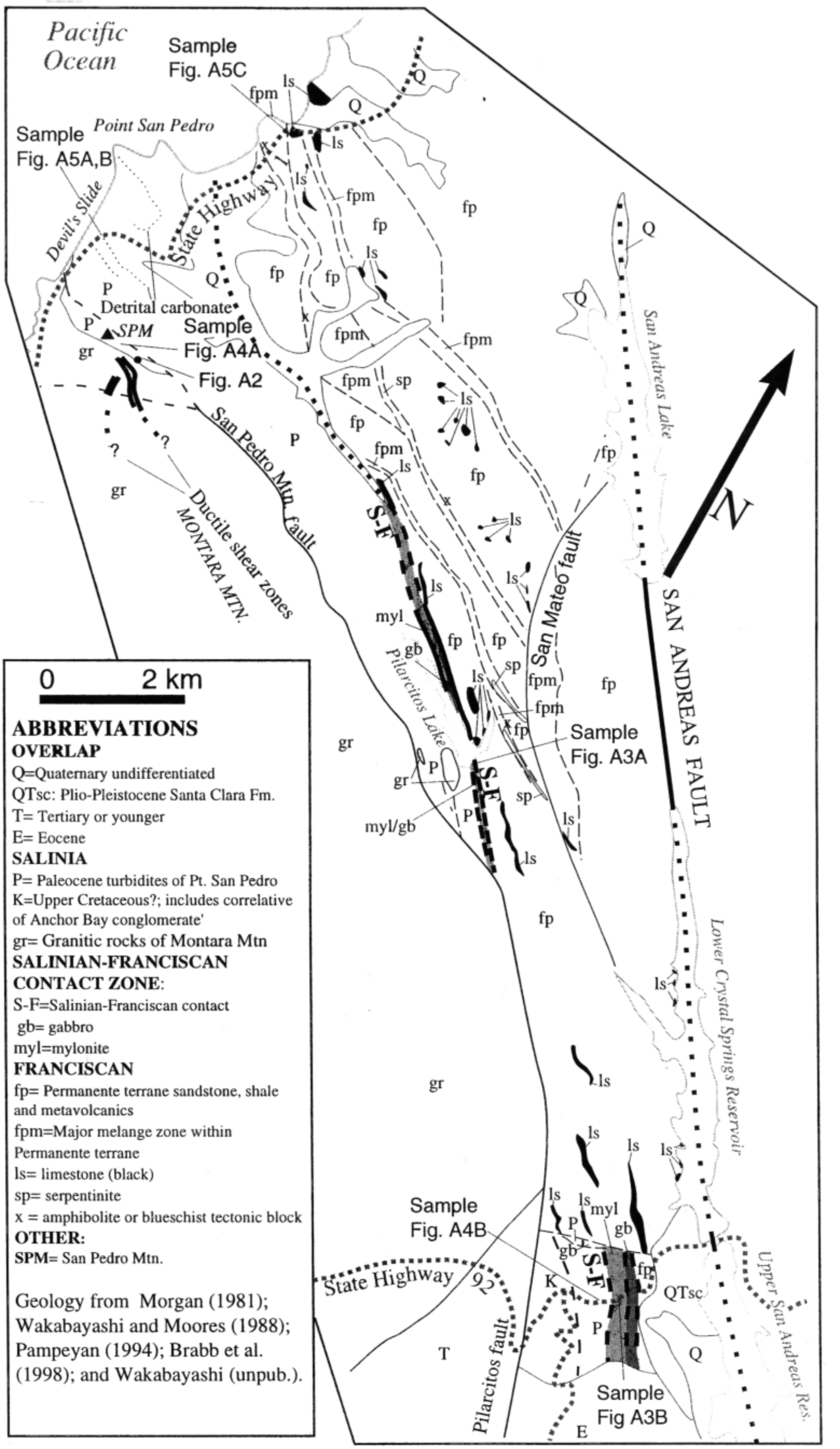

Figure A1. Geologic relations in the Montara Mountain area showing location of photos or samples taken for photomicrographs.

Figure A2. Photo of depositional contact of the Paleocene turbidite unit on granitic rocks on the ridgetop of San Pedro Mountain. Conglomerate overlies granitic rocks. Hammer handle points in stratigraphic up direction. Total length of the hammer is 38 cm, and the contact passes about 5 cm below the hammer head and slants slightly down to the right. Most of the large clasts in the conglomerate are granitic and sandstone. One granitic clast, about 35 cm across, is present to the left of the end of the hammer handle.

the Montara Mountain area geologic map (Figure 3 in main paper) with added localities of photos included in this appendix. Figure A2 shows the depositional contact of Paleocene turbidites on granitic rocks on San Pedro Mountain. Figure A3 shows that the identical nature of mylonitic rocks at Pilarcitos Lake and along Highway 92. Figure A4 shows that the Paleocene sandstones at Point San Pedro and along Highway 92 are identical and different from Franciscan sandstones of the Permanente terrane.

A2. Detrital carbonate in Paleocene turbidites: sourced from the Franciscan Permanente terrane

Pre-Eocene juxtaposition of the Salinian Block and the Permanente terrane of the Franciscan, and minimal subsequent strike-slip faulting between these units, is consistent with the occurrence of abundant detrital carbonate in beds in the upper stratigraphic levels of the Paleocene turbidite unit [*Nilsen and Yount*, 1981]. The detrital carbonate makes up 30 to 85% of the framework grains of the beds. The beds must have had a proximal source because carbonate is extremely rare in coastal California [*Nilsen and Yount*, 1981]; greater than 5 km or so between the source and the depocenter would probably swamp the carbonate detritus with other grains. Marble roof pendant rocks occur in the Salinian block, but they are not abundant, particularly in the part of the Salinian block near the Point San Pedro turbidites [*Pampeyan*, 1994]. These marbles and the much more abundant limestones of the Permanente terrane (that are still but a small fraction of the terrane) are the only possible proximal sources of detrital carbonate of pre-Paleocene age. The scarcity of marble roof pendants in the Salinian block in the vicinity of the Point San Pedro turbidites makes these marbles an unlikely source for the detrital carbonate [*Nilsen and Yount*, 1981], although post-Paleocene erosion may have reduced the amount of preserved marble roof pendant rock. Petrographic examination of the carbonate-bearing turbidites shows that the grain size of the original carbonate source was much finer than the Salinian marbles and resembles the grain size of the limestones of the Permanente terrane (Figure A5). Thus it is likely that the Franciscan

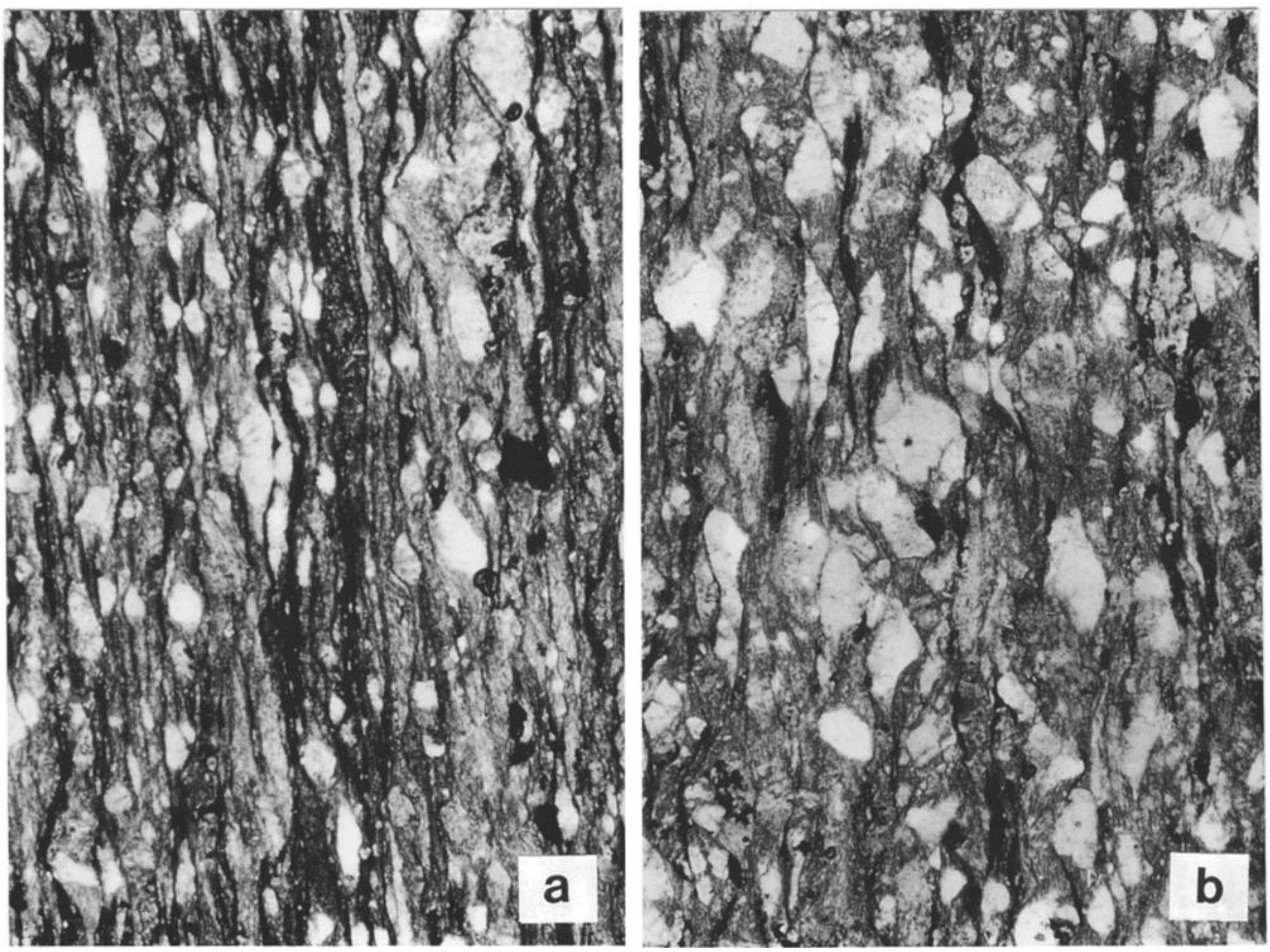

Figure A3. Photomicrographs of mylonite (a) at Pilarcitos Lake and (b) along State Highway 92, showing their similarity. There are no other comparable rocks in this region. Plane polarized light. Field of view is 2.5 mm.

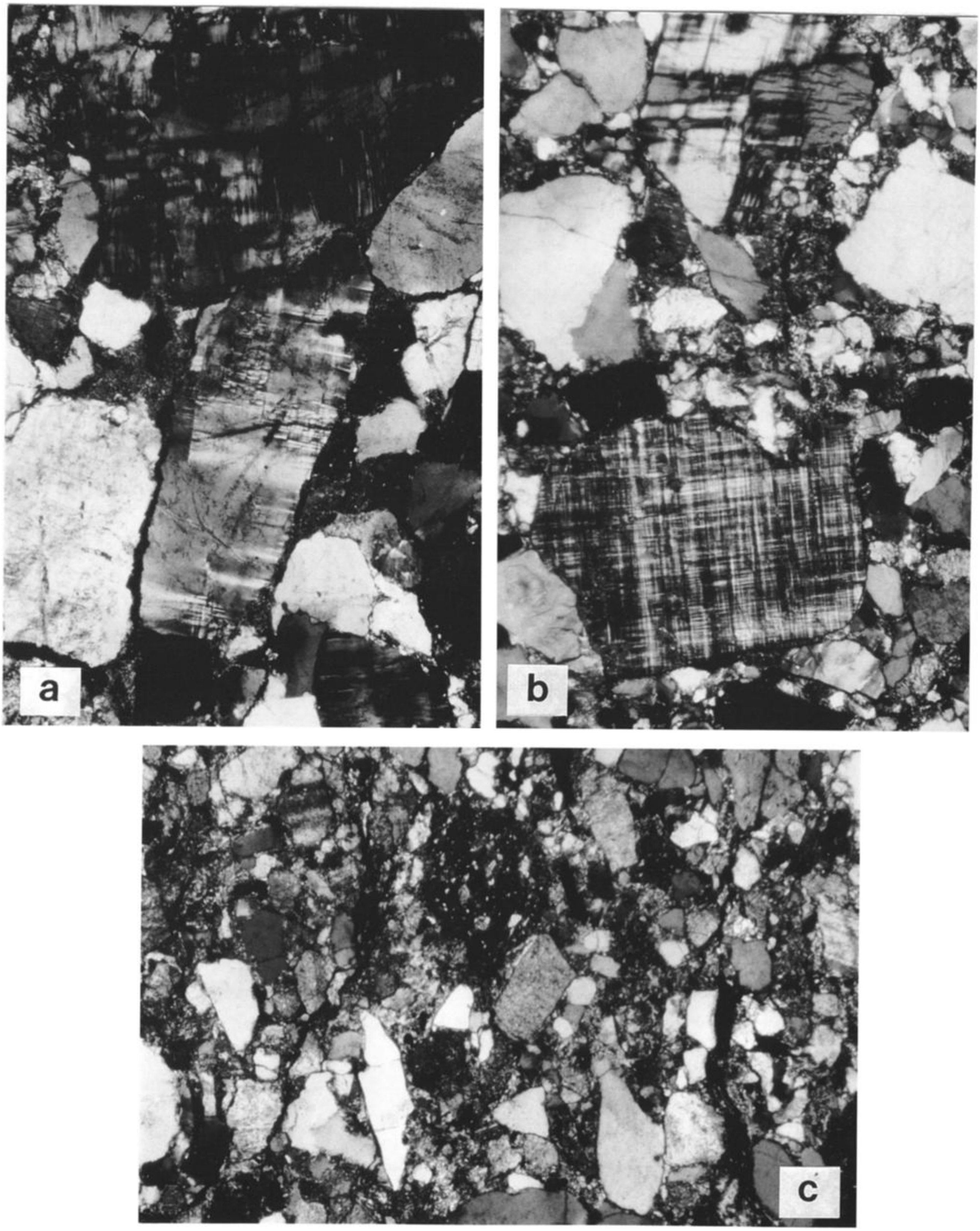

Figure A4. Photomicrographs of Paleocene sandstone from (a) San Pedro Mtn. and (b) State Highway 92, showing the abundance of potassium feldspar (tartan-twinned grains). (c) Typical sandstone of the Permanente terrane from Linda Mar that lacks potassium feldspar. Cross-polarized light. Field of view is 2.5 mm.

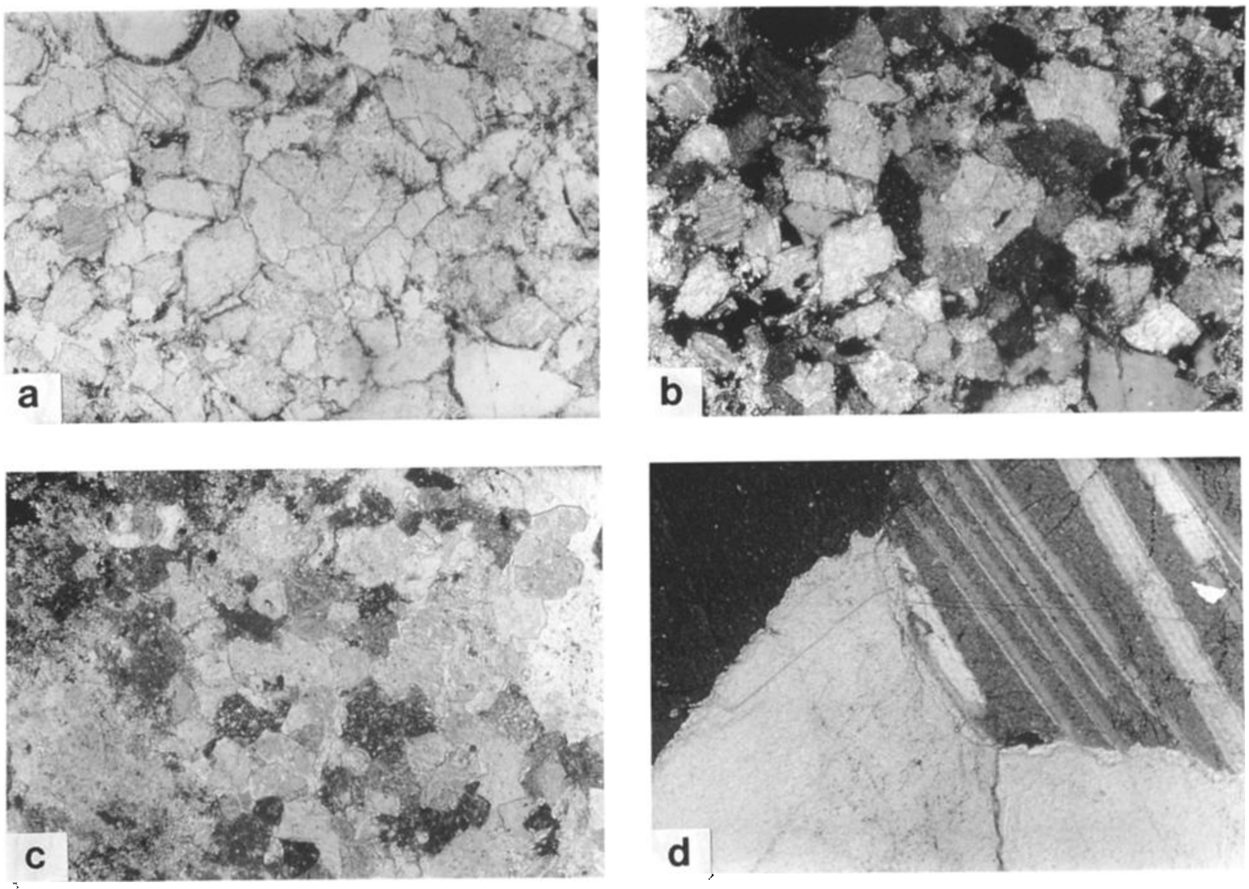

Figure A5. Photomicrographs of Paleocene Point San Pedro carbonate bearing turbidites and possible sedimentary source rocks. For all photos field of view is 1 mm. (a) Detrital carbonate grains in Paleocene turbidite, plane polarized light; note crystal grain boundaries in detrital grains, particularly the one polycrystalline grain near center of photo; grain boundaries of polycrystalline grains show the grain size of the carbonate source. (b) Detrital carbonate, cross-polarized light; crystal grain boundaries are better highlighted in this view, although detrital grain boundaries are somewhat obscured. (c) Permanente terrane limestone from the Linda Mar area, 3 km from the detrital carbonate locality; cross-polarized light; note similarity in grain size between this rock and the crystal grain size in the detrital grains in Figures A5a and A5b. (d) Marble from Salinian block metamorphic rocks, Santa Cruz mountains, cross-polarized light; notice very coarse grain size compared to both the detrital carbonate crystal grain size and Permanente terrane limestone grain size.

Permanente terrane was very close to the basin in which the Paleocene Point San Pedro turbidites were deposited and was the source of the detrital carbonate found in those turbidites. The turbidites, the underlying Salinian basement, and the Franciscan Permanente terrane apparently were faulted against each other soon after the deposition of the turbidites, and this contact was overlapped by sandstones in Eocene time. If this interpretation is correct, the existing relationship allows little post-Eocene dextral faulting between the Paleocene unit and the Permanente terrane: restoration of more than 18 km dextral slip places intervening geologic units between the Permanente terrane and the carbonate-bearing turbidites (Figure 3 of main manuscript present-day configuration; Figure A6 restoration).

A3. Supporting Field Evidence for Large Late Cenozoic Dextral Displacements East of the Peninsula San Andreas Fault

A3.1. Offset of gravity and magnetic anomalies. *Griscom and Jachens* [1990] interpreted gravity and magnetic anomaly patterns to estimate offset on the San Andreas system. Several of the anomalies do not strictly constrain late Cenozoic offset in the San Francisco Peninsula region, as they constrain either total offset for all faults splaying from the Central San Andreas or they may reflect both late Cenozoic and earlier strike-slip movement.

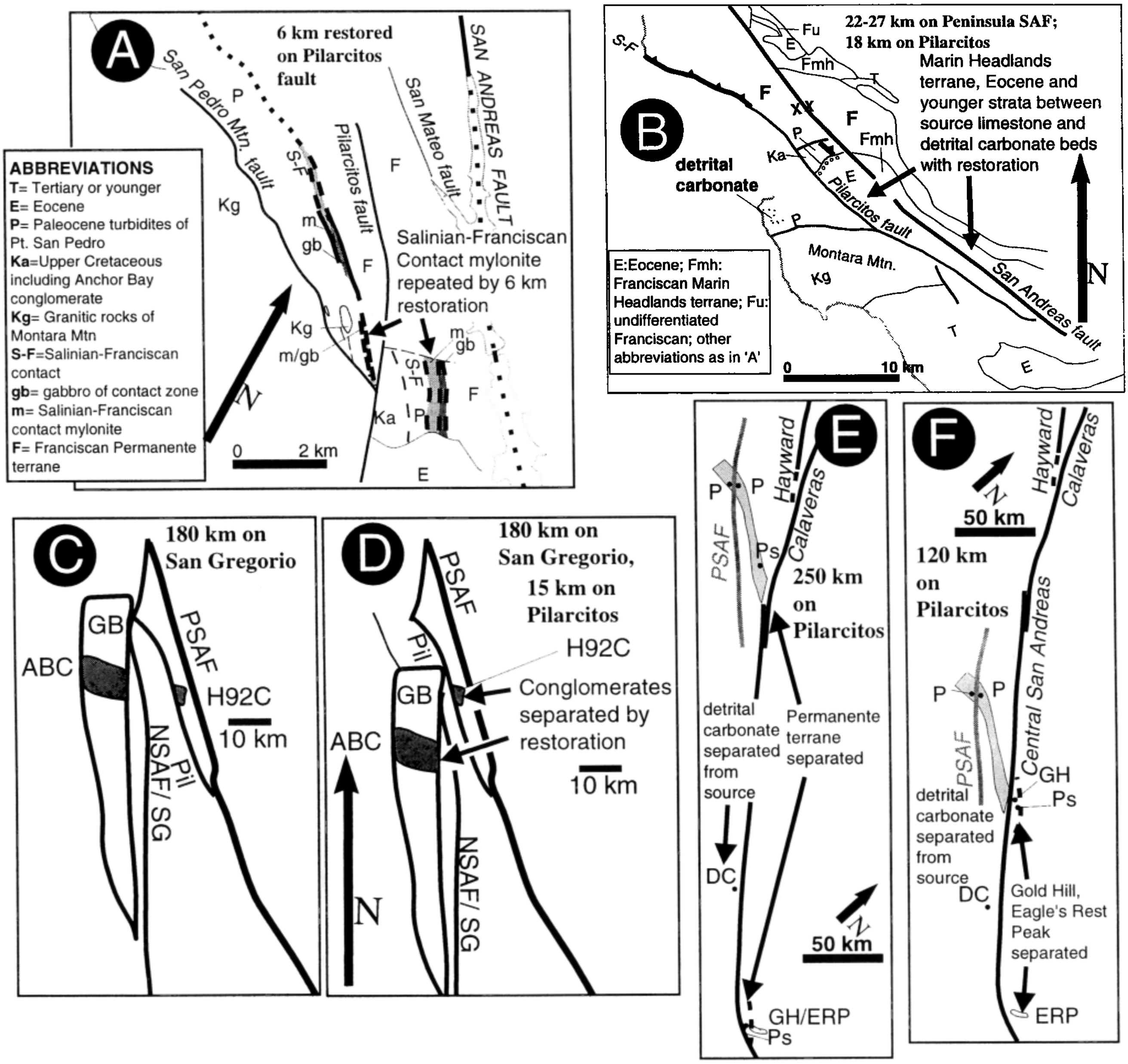

Figure A6. Simplified fault restorations showing that only small amounts of late Cenozoic slip on the Pilarcitos fault are permitted by field relations. (a) Restoration of 6 km of slip repeats the Salinian contact mylonite (present-day relations in Figure 3). (b) Restoration of >18 km of slip (as well as restoration of 22 to 27 km on the Peninsula San Andreas) places Eocene and other non-Permanente terrane units between the detrital carbonate-rich turbidites at Point San Pedro and their probable Permanente limestone source (present day relations in Figure 2). (c) Restored position of the Upper Cretaceous conglomerate of Anchor Bay opposite conglomerate along State Highway 92 according to *Burnham* [1998]. (d) Restoration of 15 km of slip separates the two conglomerate exposures. Abbreviations for Figures A6c and A6d are ABC, Anchor Bay conglomerate; GB, Gualala block; H92C, Highway 92 conglomerate; NSAF/SG, Northern San Andreas and San Gregorio faults; Pil, Pilarcitos fault; PSAF, Peninsula San Andreas fault. (e) Regional view with 120 km of slip restored on the Pilarcitos fault [*McLaughlin et al.* 1996a]. (f) Restoration of 250 km of slip on the Pilarcitos fault [*Powell*, 1993]. Figures A6e and A6f also violate the relations in Figures A6a to A6d as well as those shown in Figures A6e and A6f. Abbreviations for Figures A6e and A6f same as Figure 5, except DC denotes detrital carbonate beds at Point San Pedro.

However, their piercing points F1-F2 and G1-G2 (Figure 9.4 and text pp. 251-252 of *Griscom and Jachens* [1990]) can be used to constrain faulting in the Peninsula region. These pairs of anomalies are displaced 250 and 263 km, respectively, from the east side of the San Andreas fault in the Bay area to points west of the San Andreas fault north of Point Arena (Point Arena is near AB on Figure 1). The total offset of these points and published estimates of slip for the San Gregorio fault were used by *Griscom and Jachens* [1990] to infer 155 km of slip on the Pilarcitos fault. The required amount of slip on the Pilarcitos fault can be drastically reduced, however, by considering the most recent estimates of separation across the San Gregorio fault and combined Rinconada and San Gregorio fault [*Clark et al.*, 1984; *Burnham*, 1998], and considering the possibility of slip in other regions that can contribute to offset of the piercing points.

The combined San Gregorio-Rinconada offset of 180 ± 5 km [*Burnham*, 1998], added to the Peninsula San Andreas offset of 22 to 27 km, totals 197 to 212 km. The offset along the Peninsula San Andreas may be slightly higher if 0 to 9 km of slip on the San Mateo fault (discussed in following section on Franciscan Complex offsets) is added to the Peninsula San Andreas total. The modified Peninsula San Andreas displacement (22 to 36 km) added to the San Gregorio-Rinconada offset totals 197 to 221 km. This total, subtracted from the total offset of the geophysical anomalies, leaves a residual of 29 to 66 km, that can be permissibly distributed on (1) faults splaying west of the San Andreas, including, but not limited to, the Pilarcitos fault, and (2) faults that merge from the east onto the Peninsula San Andreas fault south of Griscom and Jachens' point F1 which is located directly west of San Francisco. Category 2 includes the San Bruno (Figures 2 and 6) and related faults discussed in the section on slip distribution in the San Francisco Bay area. The location of the correlated anomalies does not constrain partitioning of the 29 to 66 km of slip between any of the faults in either of the two categories above. The correlations of *Burnham* [1998], as discussed above, place more stringent constraints on faults in category (1) (0 to 15 km), leaving a permissible total of 14 to 66 km for faults in category 2.

A3.2. Qualitative constraint: position and age of Burdell Mtn. volcanics. The position of the Mendocino triple junction relative to faults and volcanic units in the northern Coast Ranges also places general constraints on the distribution of slip in the San Andreas system, because the late Cenozoic volcanic rocks of the Coast Ranges apparently have erupted in the wake of the northward migrating Mendocino triple junction and are associated with the transform regime [e.g., *Johnson and O'Neil*, 1984; *Fox et al.*, 1985a; *Dickinson*, 1997]; no analogous rocks are found north of the triple junction. In the present-day Coast Ranges, volcanism at Clear Lake (as young as 10 ka [*Donelly-Nolan et al.*, 1981]), trails over 150 km to south of the triple junction; this is the northernmost transform-related volcanism in the Coast Ranges (Figure 1). If the older ages for the Clear Lake volcanics are adopted (~2 Ma, but see discussion of geochronology), then these volcanics trailed the triple junction by about 95 km in north-south distance at the time of eruption, based on the position of the triple junction and southern edge of the subducted slab according to *Atwater and Stock* [1998], and restoration of deformation east of the Sierra Nevada [*Wernicke and Snow*, 1998]. Such a lag between the passage of the triple junction and eruption of volcanics also is predicted based on thermal models [e.g., *Furlong*, 1984]. Similarly, the 9.2 to 10 Ma Berkeley Hills volcanics erupted several million years after underlying sediments that are interpreted to have formed in strike-slip controlled basins [*Buising and Walker*, 1995].

One volcanic field that places broad constraints on the amount of dextral slip in the eastern part of the San Andreas system is the 12.6 Ma (Ar/Ar date (C. Swisher unpublished data, 1999)) Burdell Mountain volcanics (BMV on Figure 6). At the time of the eruption of the Burdell Mtn. volcanics, migration of the trailing edge of the Gorda plate slab was as fast or faster than it was for the 2 m.y. prior to and following the eruption of the Clear Lake volcanics, because the southern edge of the Gorda plate has "stalled" since 4 Ma [*Atwater and Stock*, 1998]. Thus the Burdell Mtn. volcanics may have lagged further behind the triple junction than the Clear Lake volcanics did at the time of their eruption. If the transform-parallel component of deformation east of the Sierra Nevada [*Wernicke and Snow*, 1998] is restored to the time of eruption of the Burdell Mountain volcanics, then about 245 ± 50 km of San Andreas fault system slip is required east of the 12.6 Ma Burdell Mountain volcanics (Figure 6) to maintain a 100 km lag distance south of the triple junction position according to *Atwater and Stock* [1998]. This constraint is broad because of the uncertainty of the lag distance of eruption south of the triple junction and uncertainties in the triple junction position and the magnitude of the N40°W cumulative deformation east of the Sierra Nevada. However, the position and age of the Burdell Mountain volcanics at least provide a qualitative indication that large magnitudes of slip are partitioned onto the eastern part of the San Andreas system.

A3.3. Correlation of Franciscan conglomerates. The offset of the Permanente terrane is consistent with correlations of a Franciscan conglomerate near Cazadero (near WC on Figure 5 and 6) by *Seiders* [1992]. *Seiders* [1992] interprets 275 to 375 km of dextral displacement to pass east of the Cazadero locality. His lower slip estimate, added to the Peninsula San Andreas offset (22 to 36 km) is similarly comparable to 310 to 320 km late Cenozoic displacement on the central part of the San Andreas fault.

Acknowledgments. Initial stages of this research were supported by the U.S. Geological Survey (USGS), Department of the Interior, under USGS award number 1434-94-G-2426. The views and conclusions in this document are those of the author and should not be interpreted as necessarily representing the official policies, either expressed or implied, of the U.S. Government. The paper benefited from reviews by R. Sedlock, A. Buising, D. Andersen, R. Bohannon, R. Graymer, R. Bürgmann, and J. Unruh, and, particularly, reviews and editorial advice of D. Scholl. I thank Peter Weigand and Carl Swisher for permission to present their unpublished geochronologic data.

References

Anderson, L.W., M.H Anders, and D.A. Ostenaa, Late Quaternary faulting and seismic hazard potential, eastern Diablo Range, in *Proceedings of the Conference on Earthquake Hazards in the Eastern San Francisco Bay Area*, edited by E.W. Hart, S.E. Hirschfeld, and S.S. Schulz, *Spec. Publ. Calif. Div Mines Geol 62*, 197-206, 1982

Angell, M., and N.T. Hall, Compressive structures along the San Andreas fault in northern California: A relationship between Miocene and Quaternary tectonics and implications for seismic hazard (abstract), *AAPG Bull*, *79*, 578, 1995.

Argus, D.F, and R G. Gordon, Current Sierra Nevada-North America motion from very long baseline interferometry Implications for the kinematics of the western United States, *Geology*, *19*, 1085-1088, 1991.

Atwater, T., and J. Stock, Pacific-North America plate tectonics of the Neogene southwestern United States. An update, *Int. Geol. Rev.*, *40*, 375-402, 1998

Blake, M.C., Jr., D G. Howell, and A.S Jayko, Tectonostratigraphic terranes of the San Francisco Bay Region, in *Franciscan Geology of Northern California*, vol. 43, edited by M C. Blake Jr., pp 5-22, Soc Econ. Paleontol. Mineral. Pac. Sect., Los Angeles, Calif, 1984.

Blake, M.C, Jr., A.S Jayko, R.J McLaughlin, and M.B. Underwood, Metamorphic and tectonic evolution of the Franciscan Complex, northern California, in *Metamorphism and Crustal Evolution of the Western United States*, *Rubey Vol. VII*, edited by W.G. Ernst, pp. 1035-1060, Prentice-Hall, Englewood Cliffs, N. J., 1988

Bonilla, M G., Bedrock-surface map of the San Francisco South quadrangle, California, *U.S. Geol. Surv.*, *Basic Data Contribution 26*, scale 1· 31,680, San Francisco Bay Reg. Environ. and Resourc. Plann. Study, San Francisco, Calif., 1964.

Brabb, E.E, and E.H. Pampeyan, Geologic map of San Mateo County, California, *U.S. Geol. Surv. Misc. Invest. Ser. Map I-1257*, 1983.

Brabb, E E., R.W. Graymer, and D.L. Jones, Geology of the Palo Alto 30 x 60 minute quadrangle, California Derived from the digital database· *U.S Geol Surv Open File Rep. 98-348*, 1998.

Buising, A.V, and J P Walker, Preliminary palinspastic paleogeographic reconstructions for the greater San Francisco Bay area, 15 Ma-5 Ma, in *Recent Geologic Studies in the San Francisco Bay Area*, vol 76, edited by E.M. Sangines, D W. Andersen, and A V Buising, pp. 141-159, Soc Econ. Paleontol Mineral. Pac. Sect, Los Angeles, Calif., 1995.

Burnham, K., Preliminary comparison and correlation of two Cretaceous conglomerates, the strata of Anchor Bay and an unnamed unit in the Pilarcitos block, across the San Gregorio and San Andreas faults, in *Geology and Tectonics of the Gualala Block, Northern California*, vol. 84, edited by W.P. Elder, pp. 95-120, Soc. Econ Paleontol. Mineral. Pac. Sect, Los Angeles, Calif, 1998

Champion, D E., D G. Howell, and C S. Gromme, Paleomagnetic and geologic data indicating 2500 km of northward displacement for the Salinian and related terranes, California, *J Geophys. Res*, *89*, 7736-7752, 1984

Clahan, K B., R.H Wright, and N.T. Hall, Paleoseismic investigation of the San Andreas fault on the San Francisco Peninsula, CA, *Final Technical Report, Award No. 14-08-001-G2081*, National Earthquake Hazards Reduction Program, U S Geol Surv., Reston, Virg.,1995

Clark, J C., E.E Brabb, H.G Greene, and D C. Ross, Geology of Point Reyes Peninsula and implications for San Gregorio fault history, in *Tectonics and Sedimentation Along the California Margin*, vol. 38, edited by J.K. Crouch and S.B. Bachman, pp. 67-86, Soc Econ Paleontol Mineral. Pac. Sec, Los Angeles, Calif., 1984.

Cole, R.B., and A. Basu, Nd-Sr isotopic geochemistry and tectonics of ridge subduction and middle Cenozoic volcanism in western California, *Geol. Soc. Am Bull*, *107*, 167-179, 1995

Crowell, J.C., Displacement along the San Andreas fault, California: *Spec Pap. Geol. Soc. Am*, *71*, 1-61, 1962.

Cummings, J C., The Santa Clara Formation and possible post-Pliocene slip on the San Andreas fault in central California, in *Proceedings of Conference on Geologic Problems of the San Andreas Fault System* edited by W.R Dickinson and A. Grantz, *Stanford Univ. Publ. Geol. Sci.*, *11*, 191-207, 1968.

Curtis, G.H, Late Cenozoic volcanic rocks of the central Coast Ranges, in *Geology of San Francisco and Vicinity*, *International Geological Congress Field Trip Guidebook T105*, edited by C. Wahrhaftig and D. Sloan, pp. 33-35, AGU, Washington, D.C., 1989.

Darrow, R.L., Age and structural relationships of the Franciscan Formation in the Montara Mountain quadrangle, San Mateo County, California, *Spec Rep Calif. Div. Mines Geol.*, *78*, 23 pp., 1963

Dickerman, S., Paleogeographic significance of granitic, high temperature metamorphic, and blueschist clasts in conglomerates of the Upper Miocene Contra Costa Group, Alameda and Contra Costa Counties, California (abstract), *Eos Trans. AGU*, *79* (46), Fall Meet. Suppl., F807, 1998.

Dickinson, W.R, Overview: Tectonic implictions of Cenozoic volcanism in coastal California, *Geol. Soc Am. Bull*, *109*, 936-954, 1997.

Dickinson, W.R, and B P. Wernicke, Reconciliation of San Andreas slip discrepancy by a combination of interior Basin and Range extension and transrotation near the coast, *Geology*, *25*, 663-665, 1997

Donelly-Nolan, J.M., B C Hearn Jr, G H Curtis, and R.E. Drake, Geochronology and evolution of the Clear Lake volcanics, *U.S. Geol. Surv. Prof. Pap.*, *1141*, 47-60, 1981

Drinkwater, J.L., D.H. Sorg, and P.C. Russell, Geologic map showing ages and mineralization of the Quien Sabe Volcanics, Mariposa Peak Quadrangle, west-central California, scale 1:24,000, *U.S. Geol. Survey Misc. Field Stud. Map*, *MF-2200*, 1992

Fox, K F, Tectonic setting of Miocene, Pliocene, and Pleistocene rocks in part of the Coast Ranges north of San Francisco, California, *U.S. Geol Surv. Prof Pap.*, *1239*, 33 pp., 1983

Fox, K.F., R.J. Fleck, G.H Curtis, and C E. Meyer, Implications of the northwestardly younger age of volcanic rocks in west-central California, *Geol Soc. Am Bull.*, *96*, 647-652, 1985a.

Fox, K.F., R.J Fleck, G H Curtis, and C.E Meyer, Potassium-argon and fission-track ages of the Sonoma volcanics in an area north of the San Pablo Bay, California *U S Geol. Surv Misc. Field Stud. Map*, *MF-1753*, scale 1:250,000, 1985b.

Furlong, K.P. , Lithospheric behavior with triple junction migration: An example based on the Mendocino triple junction, *Phys. Earth Planet. Inter.*, *36*, 213-223, 1984.

Furlong, K P., W.D. Hugo, and G. Zandt, Geometry and evolution of the San Andreas Fault zone in northern California, *J Geophys Res.*, *94*, 3100-3110, 1989

Goter, S K, D H Oppenheimer, J.J. Mori, M K Savage, and R.P. Masse, Earthquakes in California and Nevada, *U S. Geol. Surv Open File Rep.*, *94-647*, 1994

Graham, S A., Role of the Salinian block in the evolution of the San Andreas fault system, *AAPG Bull.*, *62*, 2214-2231, 1978.

Graham, S.A., R G. Stanley, J V. Bent, and J B Carter, Oligocene and Miocene paleogeography of central California and displacement along the San Andreas fault, *Geol. Soc. Am. Bull.*, *101*, 711-730, 1989.

Graymer, R.W, D.L Jones, and E.E. Brabb, Preliminary geologic map emphasizing bedrock formations in Contra Costa County, California: A digital database, *U.S. Geol. Surv. Open File Rep. 94-622*, 1994.

Graymer, R.W., D.L. Jones, and E.E Brabb, Geologic map of the Hayward fault zone, Contra Costa, Alameda, and Santa Clara, California. A digital database, *U.S. Geol Surv. Open File Rep. 95-597*, 1995a.

Graymer, R.W., D.L. Jones, and E.E. Brabb, Is there more Quaternary displacement on the Chabot fault than on the Hayward fault? (abstract), *AAPG Bull*, *79*, 585, 1995b

Greene, H.G., S.H. Clarke, and M.P. Kennedy, Tectonic evolution of submarine canyons along the California continental margin: *Spec. Publ. Soc. Econ. Paleontol Mineral.*, *46*, 231-248, 1991.

Grimsich, J.L., G.R Scott, C.C. Swisher III, and G.H. Curtis, Paleomagnetism and 40Ar/39Ar dating of the Miocene Contra Costa Group, Berkeley Hills, California (abstract), *Eos Trans. AGU*, *77* (46) Fall Meet. Suppl., F165, 1996.

Griscom, A., and R.C Jachens, Crustal and lithospheric structure from gravity and magnetic studies, in *The San Andreas Fault System, California*, edited by R.E Wallace, *U S. Geol. Surv. Prof. Pap 1515*, 239-259, 1990.

Hengesh, J.V., and J. Wakabayashi, Dextral translation and progressive emergence of the Pleistocene Merced basin and implications for timing of initiation of the San Francisco Peninsula segment of the San Andreas fault, in *Recent Geologic Studies in the San Francisco Bay Area*, vol 76, edited by E.M. Sangines, D.W. Andersen, and A V. Buising, pp. 47-54, Soc. Econ. Paleontol. Mineral. Pac Sect, Los Angeles, Calif., 1995

Hengesh, J.V., J.M. Nolan, and J. Wakabayashi, Holocene displacement along the Serra fault, San Francisco Peninsula, California (abstract), *Eos Trans AGU*, *77*(46), Fall Meet. Suppl., F744, 1996

Jachens, R C., and C W Roberts, Aeromagnetic map of the San Francisco Bay Area, scale 1: 286,500, *U.S Geol Surv*, *Geophys. Invest.*, *Map GP-1007*, 1993a

Jachens, R. C, and C W Roberts, Residual isostatic gravity map of the San Francisco Bay Area, scale 1: 286,500, *U.S Geol. Surv., Geophys Invest., Map GP-1008*, 1993b.

Jachens, R.C, C.W. Roberts, and M.L. Zoback, Total offset and right-stepping geometry of the San Francisco Peninsula segment of the San Andreas fault, California, defined by aeromagnetic anomalies (abstract), *Eos Trans. AGU*, *77*(46), Fall Meet Suppl., F742, 1996.

Jayko, A.S., Late Cenozoic strain rates across the La Honda basin, in Toward Assessing the Seismic Risk Associated With Blind Faults, edited by A.S.Jayko and S.D Lewis, *U.S. Geol. Surv. Open File Rep.*, *96-267*, 74-80, 1996

Jennings, C W, Geologic map of California, scale 1.750,000, California Division of Mines and Geology, Sacramento, Calif, 1977

Jennings, C W., Fault activity map of California and adjacent areas, scale 1·750,000, California Division of Mines and Geology, Sacramento, Calif., 1994

Johnson, C.M, and J.R O'Neil, Triple junction magmatism: A geochemical study of Neogene volcanic rocks in western California, *Earth Planet. Sci. Lett*, *71*, 241-262, 1984.

Jones, D.L., R Graymer, C. Wang, T.V. McEvilly, and A. Lomax, Neogene transpressive evolution of the California Coast Ranges, *Tectonics 13*, 561-574, 1994.

Kelsey, H.M., and G A. Carver, Late Neogene and Quaternary tectonics associated with northward growth of the San Andreas transform fault, northern California, *J Geophys Res*, *93*, *4797-4819*, 1988

Kelson, K.I., W.R. Lettis, and M. Lisowski, Distribution of geologic slip and creep along faults in the San Francisco Bay region: in Proceedings of the Second Conference on Earthquake Hazards in the Eastern San Francisco Bay Area, edited by G. Borchardt et al., *Spec*

Publ. Calif. Div. Mines Geol., 113, 31-38, 1992.

Kelson, K.I., G.D. Simpson, W.R. Lettis, and C. Haradan, Holocene slip rate and recurrence of the northern Calaveras fault at Leyden Creek, northern California, *J. Geophys. Res., 101*, 5961-5975, 1996.

Lienkaemper, J.J., G. Borchardt, and M. Lisowski, Historic creep rate and potential for seismic slip along the Hayward fault, California, *J. Geophys. Res., 96*, 18261-18283, 1991.

Lindquist, T.A., and J.D. Morganthaler, Radiometric ages of rocks in the San Francisco-San Jose quadrangle, California, accompanies *Calif. Div. Mines Geol. Region. Geol. Map Ser., Map 5A* (see Wagner et al., 1990), Sacramento, Calif., 1991.

Liniecki-Laporte, M., and D.W. Andersen, Possible new constraints on late Miocene depositional patterns in west-central California, *Geology, 16*, 216-220, 1988.

Marlow, M.S., P.E. Hart, P.R. Carlson, J.R. Childs, D.M. Mann, R.J. Anima, and R.E. Kayen, High-resolution seismic-reflection profiles and interpretation pitfalls created by acoustic anomalies from Holocene muds beneath south San Francisco Bay, *U.S. Geol. Surv. Open File Rep., OFR 94-639*, 1994

Marlow, M.S, R.C. Jachens, P.E. Hart, P.R. Carlson, R.J. Anima, and J.R. Childs, Development of San Leandro synform and neotectonics of the San Francisco Bay block, California, *Mar. Petrol. Geol., 16*, 431-442, 1999.

Matthews, V., Correlation of the Pinnacles and Neenach volcanic formations and their bearing on the San Andreas fault problem, *AAPG Bull., 60*, 2128-2141, 1976

Mattinson, J.M., and E.W. James, Salinian block U/Pb age and isotopic variations: Implications for origin and emplacement of the Salinian terrain, in *Tectonostratigraphic Terranes of the Circum-Pacific Region*, vol. 1, *Earth Sci. Ser.*, edited by D.G. Howell, pp. 215-226 Circum-Pacific Counc. for Energy and Miner. Resour., Houston, Tex., 1985.

McCulloch, D.S., Regional geology and hydrocarbon potential of offshore central California, in *Geology and Resources of the Continental Margin of Western North America and Adjacent Basins, Beaufort Sea to Baja California*, vol. 6, *Earth Sci. Ser.*, edited by D.W. Scholl, A. Grantz and J.G. Vedder, pp. 353-401, Circum Pacific Counc. for Energy and Miner. Resourc., Houston, Tex., 1987.

McLaughlin, R.J., W.V. Sliter, D.H. Sorg, P.C. Russell, and A.M. Sarna-Wojcicki, Large-scale right-slip displacement on the East San Francisco Bay region fault system, California: Implications for location of late Miocene to Pliocene Pacific plate boundary, *Tectonics, 15*, 1-18, 1996a

McLaughlin, R.J., D.H. Sorg, and E.J. Helley, Constraints on slip histories of thrust faults of the southwestern San Francisco Bay area from geologic mapping investigations: in Toward Assessing the Seismic Risk Associated With Blind Faults, edited by A.S.Jayko and S.D. Lewis, *U.S. Geol. Surv. Open File Rep., 96-267*, 65-70, 1996b.

McLaughlin, R.J., R.C. Jachens, R.G. Stanley, A.S. Jayko, V.E. Langenheim, C.M. Wentworth, and K.A. McDougall, Neogene compressional and extensional tectonism northeast of the San Andreas fault, southwestern Santa Clara Valley, California (abstract), *Geol. Soc. Am. Abstr Programs, 29*(5), 28, 1997

Merritts, D., and W.B Bull, Interpreting Quaternary uplift rates at the Mendocino triple junction, northern California, from uplifted marine terraces, *Geology, 17*, 1020-1024, 1989.

Morgan, S.R., General geology of the strata at Point San Pedro, San Mateo County, California, in *Upper Cretaceous and Paleocene Turbidites, Central California Coast (Annual Meeting Pacific Section SEPM Field Trip 6)*, vol. 20, edited by V. Frizzell, pp. 13-19, Soc Econ. Paleontol. Mineral. Pac Sect., Los Angeles, Calif., 1981

Murchey, B.M., and D.L. Jones, D.L., Age and significance of chert in the Franciscan Complex, San Francisco Bay region, in *Franciscan Geology of Northern California*, vol. 43, edited by M.C. Blake Jr., pp. 51-70, Soc Econ Paleontol. Mineral. Pac Sect., Los Angeles, Calif., 1984

Nakata, J.K., D.H. Sorg, P.C. Russell, C.E Meyer, J Wooden, M A Lanphere, R J. McLaughlin, A.M Sarna-Wojcicki, J.Y. Saburomaru, M S Pringle, and J. Drinkwater, New radiometric ages and tephra correlations from the San Jose and northeastern part of the Monterey 1:100,000 map quadrangles, California, *Isochron/West, 60*, p.19-32, 1993.

Niemi, T.M., and N.T. Hall, Late Holocene slip rate and recurrence of great earthquakes on the San Andreas fault in northern California, *Geology, 20*, 195-198, 1992

Nilsen, T.H., and J.C Yount, Sedimentology of the Paleocene strata of Point San Pedro, California: in *Upper Cretaceous and Paleocene Turbidites, Central California Coast (Annual Meeting Pacific Section SEPM Field Trip 6)*, vol 20, edited by V Frizzell, pp. 21-29, Soc. Econ. Paleontol Mineral. Pac Sect., Los Angeles, Calif., 1981

Page, B.M., The southern Coast Ranges, in *Geotectonic Development of California, Rubey Vol. I*, edited by W.G Ernst, pp 329-417, Prentice-Hall, Englewood Cliffs, N J., 1981.

Page, B.M., The Calaveras fault zone of California: An active plate boundary element, in *The 1984 Morgan Hill, California, Earthquake*, edited by J H. Burnett and R.W. Sherburne, *Spec. Publ. Calif. Div. Mines Geol., 68*, 109-122, 1984.

Page, B.M., Evolution and complexities of the transform system in California, U.S.A., *Ann. Tecton., 4*, 53-69, 1990.

Pampeyan, E.H., Geologic map of the Montara Mountain and San Mateo 7-1/2' quadrangles, San Mateo County, California, *U. S. Geol. Surv Misc Invest. Ser., Map I-2390*, 1994.

Parsons, T., and M L Zoback, Three-dimensional upper crustal velocity structure beneath San Francisco Peninsula, California, *J. Geophys. Res, 102*, 5473-5490, 1997.

Powell, R.E., Balanced palinspastic reconstruction of pre-late Cenozoic paleogeography, southern California: Geologic and kinematic constraints on evolution of the San Andreas fault system, in *The San Andreas Fault System: Displacement, Palinspastic Reconstruction and Geologic Evolution*, edited by R.E. Powell, R.J. Weldon II, and J.C. Matti, *Mem Geol. Soc. Am., 178*, 1-106, 1993.

Prentice, C.S., Earthquake geology of the northern San Andreas fault near Point Arena, California, Ph.D. dissertation, 252 pp., Calif. Inst. of Technol., Pasadena, 1989

Raymond, L.A., Tesla-Ortigalita fault, Coast Range thrust fault, and Franciscan metamorphism, northeastern Diablo Range, California, *Geol Soc. Am. Bull., 84*, 3547-3562, 1973a.

Raymond, L.A., Franciscan geology of the Mount Oso area, California: Ph.D. dissertation, 180 pp., Univ. of Calif., Davis, 1973b.

Rogers, J.D., and S.H. Figuers, Late Quaternary stratigraphy of the East Bay plain, in Proceedings of the Second Conference on Earthquake Hazards in the Eastern San Francisco Bay Area, edited by G. Borchardt et al., *Spec. Publ. Calif. Div. Mines Geol., 113*, 19-28, 1992.

Ross, D.C., Possible correlations of basement rocks across the San Andreas, San Gregorio-Hosgri, and Rinconada-Reliz-King City faults, California, *U. S. Geol. Surv. Prof. Pap., 1317*, 37 pp., 1984.

Sedlock, R.L., and D.H. Hamilton, Late Cenozoic tectonic evolution of southwestern California, *J Geophys. Res., 96*, 2325-2351, 1991

Seiders, V. M., Tectonic implications of Franciscan conglomerate at Cazadero, Sonoma County, northern California (abstract), *Geol. Soc. Am. Abstr. Programs, 24*(5), 80, 1992.

Seiders, V.M., and B F Cox, Place of origin of the Salinian block, California, as based on clast compositions of Upper Cretaceous and Lower Tertiary conglomerates, *U.S. Geol. Surv. Prof. Pap., 1526*, 80 pp., 1992.

Sharp, W.D., B.D. Turrin, P.R. Renne, and M A. Lanphere, The $^{40}Ar/^{39}Ar$ and K/Ar dating of lavas from the Hilo 1-km core hole, Hawaii Scientific Drilling Project, *J. Geophys. Res., 101*, 11,607-11,616, 1996.

Simpson, G.D., S.C. Thompson, J.S. Noller, and W.R. Lettis, The northern San Gregorio fault zone: Evidence for timing of late Holocene earthquakes near Seal Cove, California, *Bull. Seismol. Soc. Am., 87*, 1158-1170, 1997

Simpson, G.D., W.R. Lettis and C.E. Randolph, Slip rate of the northern San Gregorio fault near Seal Cove, California (abstract), *Eos Trans. AGU, 79*(45), Fall Meet. Suppl., F611, 1998

Sims, J D., Chronology of displacement on the San Andreas fault in central California: evidence of reversed positions of exotic rock bodies near Parkfield, California, in *The San Andreas Fault System: Displacement, Palinspastic Reconstruction and Geologic Evolution*, edited by R.E. Powell, R.J. Weldon II, and J.C. Matti, *Mem. Geol. Soc. Am., 178*, 231-256, 1993.

Sliter, R.V., Foraminifers from Cretaceous limestone of the Franciscan Complex, northern California, in *Franciscan Geology of Northern California*, vol. 43, edited by M.C. Blake Jr., pp. 149-162, Soc. Econ. Paleontol. Mineral. Pac. Sect., Los Angeles, Calif., 1984.

Snetsinger, K.G., Rock types of the Franciscan Formation, Coyote Hills, Alameda County, California, *Calif. Geol., 30*, 174-177, 1976.

Tarduno, J.A.; M.O. McWilliams, M.G. Debiche, W.V. Sliter, and M.C. Blake Jr., Franciscan Complex Calera limestones: Accreted remnants of Farallon Plate oceanic plateaus, *Nature, 317*, 345-347, 1985.

Throckmorton, G.K., Geology and paleontology of the Tesla formation, Alameda and San Joaquin counties, central California, *U.S. Geol. Surv. Open File Rep., OFR 88-59*, 104 pp., 1988.

Turner, D.L., Potassium-argon dates concerning the Tertiary foraminiferal time scale and the San Andreas fault displacement, Ph.D. dissertation, 99pp., Univ. of Calif., Berkeley, 1968.

Wagner, D.L., E.J. Bortugno, and R.D. McJunkin, Geologic map of the San Francisco-San Jose quadrangle, scale: 1:250,000, *Calif. Div. Mines Geol. Region. Geol. Map Ser., Map 5A*, Sacramento, Calif., 1990.

Wakabayashi, J., Nappes, tectonics of oblique plate convergence, and metamorphic evolution related to 140 million years of continuous subduction, Franciscan Complex, California, *J. Geol., 100*, 19-40, 1992.

Wakabayashi, J., and J.V. Hengesh, Distribution of late Cenozoic displacement on the San Andreas fault system, northern California, in *Recent Geologic Studies in the San Francisco Bay Area*, vol. 76, edited by E.M. Sangines, D.W. Andersen, and A.V. Buising, pp. 19-30, Soc. Econ. Paleontol. Mineral. Pac. Sect, Los Angeles, Calif, 1995.

Wakabayashi, J, and J.V. Hengesh, 4-D processes in transform fault systems: progressive development of step-overs and bends (abstract), *Geol. Soc. Am. Abstr. Programs, 30*(7), A74-A75, 1998.

Wakabayashi, J., and E. M. Moores, Evidence for the collision of the Salinian Block with the Franciscan subduction zone, *J. Geol., 96*, 245-253, 1988.

Wakabayashi, J., and T.L. Sawyer, Holocene (?) oblique slip on the Miller Creek fault, eastern San Francisco Bay area, California (abstract), *Eos Trans. AGU, 79*(45), Fall Meet. Suppl., F613, 1998.

Weber, G.E., and K.R. Lajoie, Map of Quaternary faulting along the San Gregorio fault zone, San Mateo and Santa Cruz counties, California, scale: 1:24,000, sheet 1 of 3, *U.S. Geol. Surv Open-File Rep., 80-907*, 1980.

Wentworth, C.M., D.L. Jones, and E.E. Brabb, Geology and regional correlation of the Cretaceous and Paleogene rocks of the Gualala block, California, in *Geology and Tectonics of the Gualala Block, Northern California*, vol 84, edited by W.P Elder, pp. 3-26, Soc. Econ. Paleontol. Mineral. Pac. Sect, Los Angeles, Calif., 1998.

Wernicke, B., and J.K. Snow, Cenozoic tectonism in the central Basin and Range: motion of the Sierran-Great Valley block, *Int. Geol. Rev., 40*, 403-410, 1998.

Wright, T.L., and N. Smith, Right step from the Hayward fault to the Rodgers Creek fault beneath San Pablo Bay, in Proceedings of the Second Conference on Earthquake Hazards in the Eastern San Francisco Bay Area, edited by G. Borchardt et al., *Spec. Publ. Calif. Div. Mines .Geol., 113*, 407-417, 1992.

Youngman, M.R , K-Ar and $^{40}Ar/^{39}Ar$ geochronology, geochemistry, and structural reinterpretation of the southern Sonoma volcanic field, Sonoma County, California, M.S. thesis, 92pp., Univ. of Calif., Berkeley, 1989.

J. Wakabayashi, 1329 Sheridan Lane, Hayward, CA 94544 (wako@tdl.com)

(Received February 16, 1999;
revised June 28, 1999;
accepted July 27, 1999.)

TECTONICS, VOL. 18, NO. 6, PAGES 967-976 DECEMBER 1999

Uplift and convergence along the Himalayan Frontal Thrust of India

Steven G. Wesnousky

Center for Neotectonic Studies and Department of Geological Sciences, University of Nevada, Reno

Senthil Kumar, R. Mohindra, and V. C. Thakur

Wadia Institute of Himalayan Geology, Dehra Dun, India

Abstract. Along the Himalayan thrust front in northwestern India, terrace deposits exposed 20 to 30 m above modern stream level are interpreted to have been uplifted by displacement on the underlying Himalayan Frontal Thrust. A radiocarbon age limits the age of the terrace to ≤ 1665 ± 215 calendar BC (≤ 3663 ± 215 radiocarbon years before present), yielding a vertical uplift rate of ≥ 6.9 ± 1.8 mm/yr. In combination with published studies constraining the dip of the Himalayan Frontal Thrust fault to about 30° in the study area, the observed uplift rate equates to horizontal shortening across the Himalayan Frontal Thrust of ≥ 11.9 ± 3.1 mm/yr and the slip rate of the Himalayan Frontal Thrust of ≥ 13.8 ± 3.6 mm/yr. This is similar to previously reported rate estimates along the Himalayan arc based on displacement of older Plio-Miocene age rocks, or the much shorter records of geodesy and historical seismicity. The similarity is consistent with the idea that convergence across the Himalayan front has occurred at a relatively steady rate through time. The seismic expression of this deformation includes several great (M~8) historical earthquakes which, due to lack of surface rupture during those events, have been attributed to their occurrence on blind thrusts. Yet, the occurrence of a possible fault scarp in the field area indicates that past earthquakes have been sufficiently large to rupture to the surface and produce coseismic scarps. These observations suggest a potential for earthquakes along the Himalayan Frontal Thrust larger than those observed historically.

1. Introduction

The topography, geologic structure, and earthquakes of the Himalaya and surrounding regions are a consequence of the northward progression and collision of India into Eurasia (Figure 1), a process that has accommodated an estimated 2000-3000 km of convergence since the Late Cretaceous [*Molnar and Tapponnier,* 1977] and continues today at a rate of about 55 to 60 mm/yr [*Demets et al.*, 1994; *Bilham et al.*, 1997, 1998]. Understanding the manner in which the convergence is accommodated by active faults is required to understand the mechanics of Himalayan mountain building and the hazard imposed by earthquakes accompanying that process (Figure 1).

Prior studies indicate that of the total convergence across the Himalayan orogen, only a fraction (~20±10 mm/yr) is accommodated by shortening at the front of the Himalaya [e.g., *Baker et al.*, 1988; *Armijo et al.*, 1989]. However, quantitative constraints on the amount of convergence taken up by thrusting along the Himalayan front have been limited primarily to the analysis of older Plio-Miocene age rocks [*Lyon-Caen and Molnar,* 1985; *Baker et al.*, 1988; *Powers et al.*, 1998; *DeCelles et al.*, 1998], or the much shorter 90-year record of historical earthquakes [*Molnar and Deng*, 1984; *Molnar*, 1990] and less than decadal-length Global Positioning System (GPS) surveys [*Freymueller et al.*, 1996; *Bilham et al.*, 1997, 1998].

To date, the only limit placed on late Pleistocene convergence across the Himalayan front arises from the recent work of *Avouac et al.* [1998] that reports 21.5 ± 1.5 mm/yr of convergence in eastern Nepal based on the distribution of Holocene river terraces situated above the Himalayan Frontal Thrust. Toward understanding the Holocene rate of uplift and shortening across the front of the Indian Himalaya, we mapped and surveyed, during the fall of 1997, fluvial terrace deposits along a 40 km stretch of the Himalayan Frontal Thrust near Dehra Dun (Figures 1 and 2).

2. Geologic Framework

The major geologic structures of the Himalaya mark relatively continuous bands along the Himalayan arc, a distance of about 2500 km (Figure 1). The Paleozoic to lower Tertiary sedimentary rocks of the Tethyan Himalaya and Precambrian metamorphic rocks of the Greater Himalaya sit north of the Main Central Thrust (MCT), which has not been observed to cut Quaternary deposits [*Nakata,* 1989]. The Lesser Himalaya, composed largely of pre-Tertiary clastic sedimentary rocks subjected to low-grade metamorphism, is bounded to the south by the Main Boundary Thrust (MBT), which is clearly expressed as a fault in bedrock along its length and, which locally, displaces Quaternary deposits [*Nakata*, 1972, 1989; *Valdiya*, 1992]. The Subhimalaya are the lowest foothills of the Himalaya and expose Tertiary-Quaternary sediments of the Siwalik Group. The southern limit of the Subhimalaya corresponds to the active Himalayan Frontal Thrust (HFT), which transports sediments of the Siwalik Group southward over the Indo-Gangetic plain.

Paper number 1999TC900026.
0278-7407/99/1999TC900026$12.00

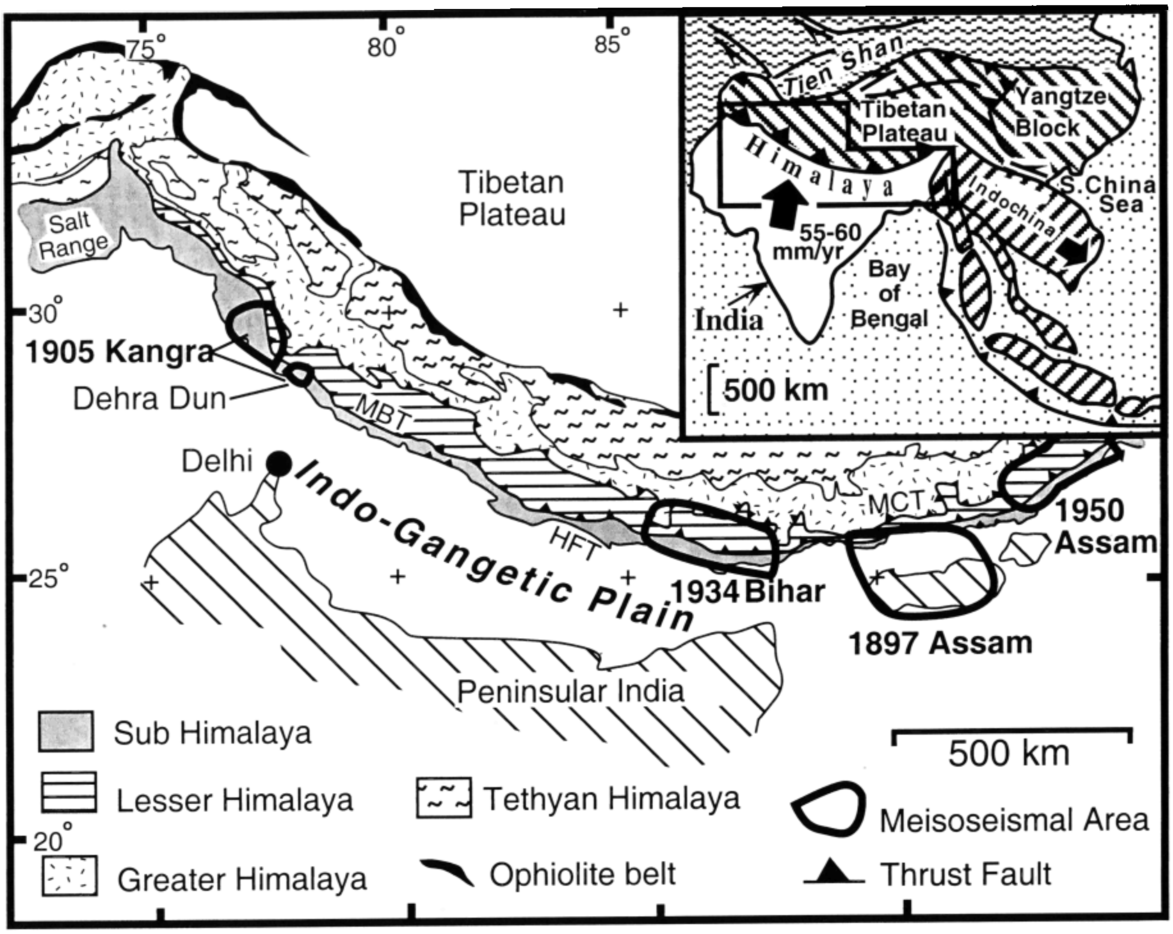

Figure 1. Location of Dehra Dun, major structural elements, and meisoseismal zones of great (M>8) historical earthquakes along the Himalayan arc. The sections of the Himalayan arc between about 75°E and 80°E and 80°E and 88°E are located in India and Nepal, respectively. Major thrust faults are the Main Central Thrust (MCT), the Main Boundary Thrust (MBT), and the Himalayan Frontal Thrust (HFT). The date and name of great historical earthquakes are annotated adjacent to the outlined meisoseismal zones. Structural data taken from *Gansser* [1981] and earthquake data from *Seeber and Armbruster* [1981] and *Molnar and Pandey* [1989].

Sediments of the Indo-Gangetic plain fill a flexural basin related to the subduction of the Indian continent beneath Eurasia [*Lyon-Caen and Molnar*, 1985].

Between the MBT and HFT, there occur a number of structurally controlled valleys along the length of the Himalayan arc [*Nakata,* 1972], locally referred to as Doon or Dun valleys. The town of Dehra Dun shares the name of the valley in which it sits (Figures 1 and 2). Displacement along the north dipping MBT has produced a sharp escarpment and raised the Lesser Himalaya to elevations of 2000 to 4000 m. Broad synclinal folding of the Siwalik Group as a result of displacement along the HFT and MBT is responsible for presence of the Doon Valley.

The Siwalik Group of the Subhimalaya consists of fluvial sediments deposited outboard of the rising Himalaya. Ranging in age from 0.5 to 18 Ma, the sequence coarsens upwards from the predominantly mudstone and siltstone of the lower facies through the predominantly sandstones and conglomerates of the middle and upper facies, respectively [*Kumar et al.*, 1991; *N. Johnson et al.*, 1982; *G. Johnson et al.*, 1982, 1983].

Displacement along the Himalayan Frontal Thrust has raised the Siwalik Hills to elevations of about 1000 m, 500 to 600 m above the adjacent Indo-Gangetic plain near Dehra Dun (Figure 2). The Siwalik Hills to the northeast of the Mohand Thrust, a segment of the Himalayan Frontal Thrust (HFT), comprise mainly homoclinal strata with northerly dips generally ranging between 20° and 30°. Along a relatively narrow zone adjacent to the HFT, a dip reversal defines the Mohand Anticline [*Rao et al.*, 1974], with dips of 50° and greater on its southern flank. The anticline is well defined to the west of the Yamuna River but, to the east between the town of Mohand and the Yamuna River, the anticlinal structure merges closer to the HFT and is characterized by numerous closely spaced and laterally discontinuous folds [*Rao et al.*, 1974; *Raiverman et al.*, 1993].

Within the area of mapping (Figure 2), the HFT is not

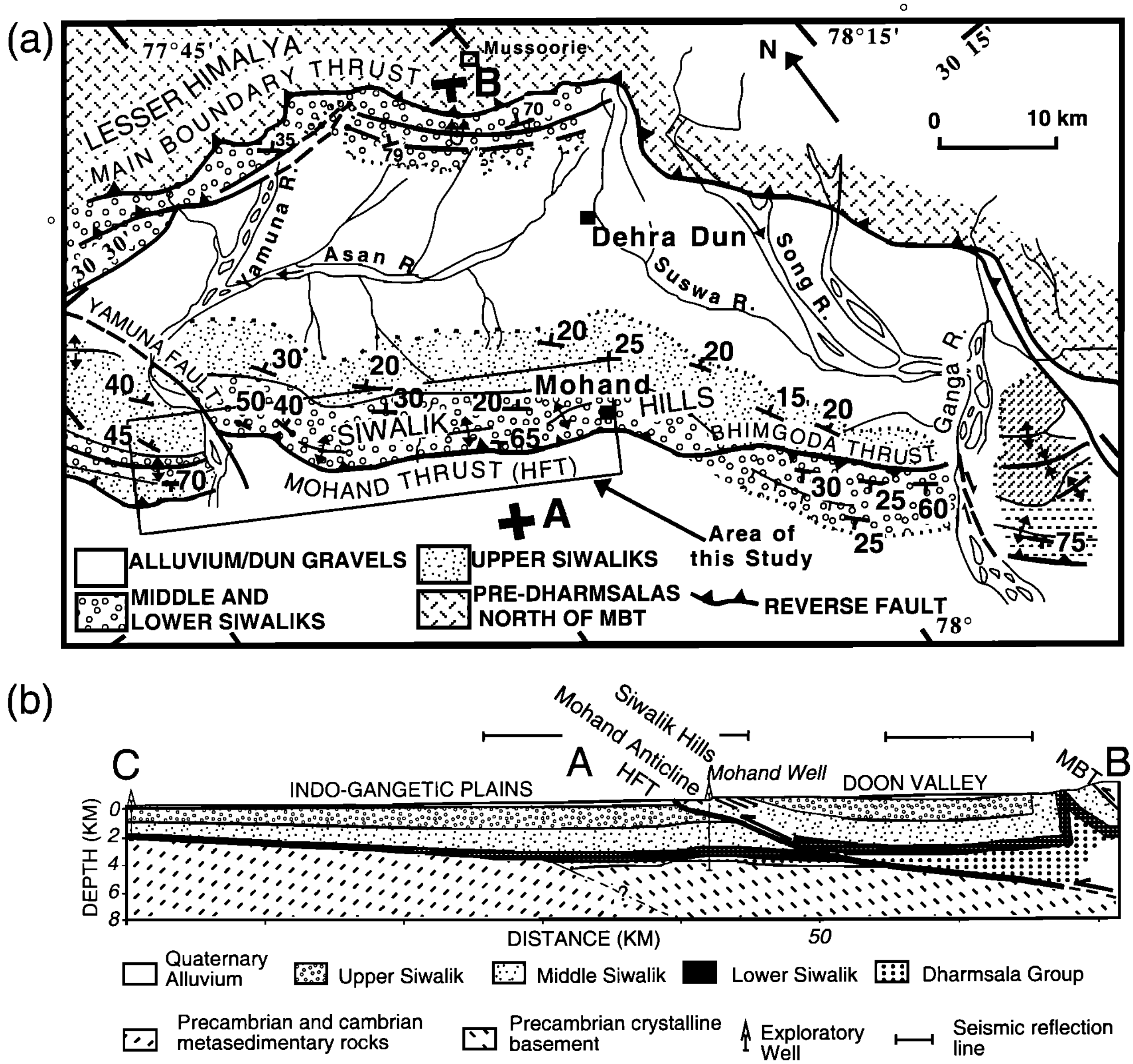

Figure 2. (a) Geology of Dehra Dun (valley) (modified from *Thakur* [1995]). Box outlines portion of Himalayan Frontal Thrust (locally referred to as Mohand Thrust) examined during the course of this study. (b) Structural section across Dehra Dun adapted from *Powers et al.* [1998] , based on seismic reflection and borehole data. Location of section between A and B is located on map. Dharmsala Group is upper Eocene to Miocene in age and sits conformably beneath sediments of Siwalik Group.

clearly exposed at the surface; however, observations from (1) a deep borehole near the town of Mohand (Figure 2), (2) another nearby shallow exploratory well at the southern fringe of the Siwalik Hills (Figure 3), and (3) seismic reflection lines about 10 km northwest of Mohand provide geometrical constraint (Figure 2) that the HFT dips northerly at about 30° and extends to or very close to the surface at the foot of the Siwalik Hills [*Rao et al.*, 1974; *Lyon-Caen and Molnar*, 1985; *Raiverman et al.*, 1993 ; *Powers et al.*, 1998].

3. Fluvial Terrace Deposits

The distribution of fluvial terrace deposits is depicted by the map in Figure 3. The perennial Yamuna River crosses the Siwalik Range. Additionally, there are numerous ephemeral raos (streams) that originate in the Subhimalayan foothills and issue onto the Gangetic Plain. The region receives about 1600 mm/yr of rainfall of which about 80-85% falls during the months of July through September [*Mohindra et al.*, 1992;

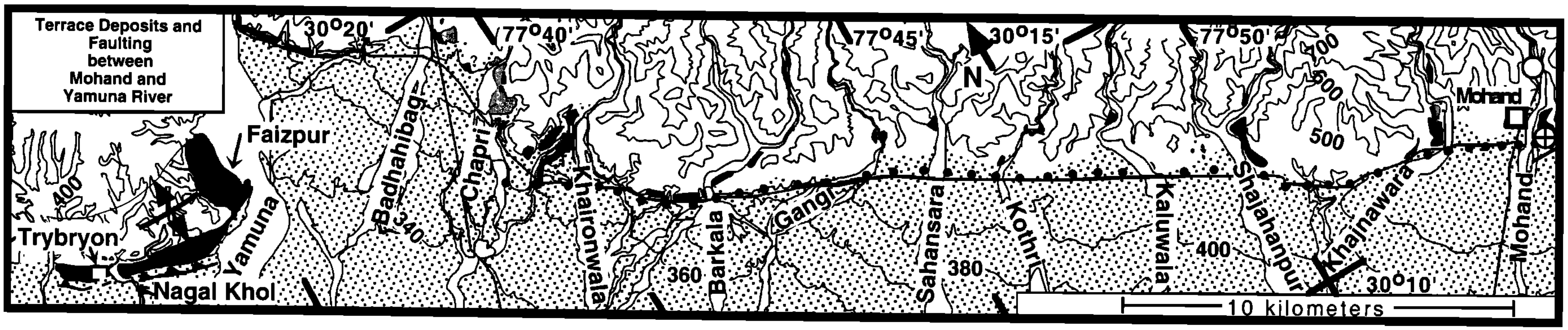

Figure 3. Fluvial terrace deposits and range front faulting along the Siwalik range front from near the Yamuna River to the town of Mohand. Bedrock in the Siwalik Hills and active streambeds are left unshaded. Fan deposits are stippled. Highest terraces along each stream are interpreted to be correlative in time and shaded black. Terraces at lesser intermediate levels are also observed along Chapri, Badhahibag, and Khajnawara raos and shaded gray. Dotted line is inferred trace of Himalayan Frontal Thrust. Scarp at Trybryon in Quaternary deposits probably reflects surface displacement along Himalayan Frontal Thrust (teeth on hanging wall). Offset of fault trace from terrace deposits near Nagal Khol is for clarity of illustration. Circle and circle with cross are locations of Mohand deep well and nearby shallow exploratory well, respectively. Contours are at 100 m intervals within the Siwalik Hills and at 20 m intervals on the fans.

National Atlas Association of India, 1977]. Most of the wash and fan deposits in the map area may be attributed to the ephemeral streams. Stream gradients at the range front are generally between 1 and 2 percent. Although the lengths (~5-8 km) and catchment basins (~20-40 km^2) of the lesser streams are relatively small, competency of the streams is large during the summer months, resulting in braided stream channels which commonly reach several hundred meters or more in width at their mouths. Streambeds are composed of rounded pebble and cobble gravels in a sand matrix and, locally within gravel bars, beds of well-sorted fine-grained sands. Bar and swale topography is generally limited to about 1 m. Both clast size and bar and swale topography are greater along the Yamuna River.

The raos have produced an apron of coalescing fan deposits of similarly low gradient. Fan-head incision of streams is generally shallow, of the order of 1 – 2 m, though locally, along the Mohand fan and smaller tributaries issuing onto it, incision reaches 4 – 6 m close to the range front. Fan remnants located significantly above current floodplain are not observed immediately outboard of the range front. It appears that the streams are currently at equilibrium or aggrading, and fan surfaces in the region are active and potentially subject to flooding. Fan deposits are typically capped by a layer of loamy sand, generally of the order of 0.5 m, and locally up to 3 m thick. This sand layer is interpreted to be deposited at time of floods and perhaps reworked and added to by aeolian processes. The fan gravel shares the same fabric and clast size distribution as the gravel observed in the active washes.

Older fluvial strath terrace deposits now situated well above the beds of the active stream channels occur along all of the drainages. The strath terrace deposits consist of rounded pebble-cobble gravels that are generally capped by a 1- to 3-m-thick layer of loamy sand, identical to the capping deposits observed on modern fan deposits immediately outboard of the Siwaliks (Figure 4). Broad remnants of the original geomorphic surfaces are locally preserved, particularly along the Khajnawara and Shajahanpur raos.

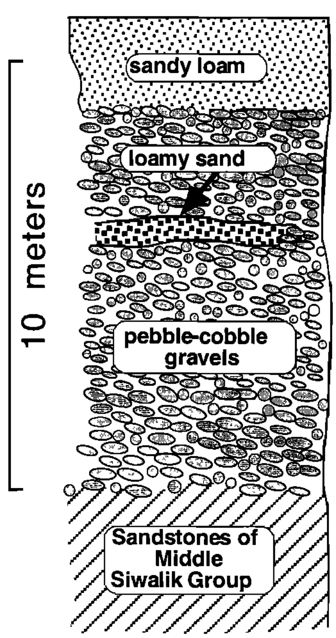

Figure 4. Schematic illustration of fabric and composition of fluvial strath terrace deposits. Base of strath terrace deposits typically rest unconformably upon sandstones of the Middle Siwalik Group about 20 m above active stream grade.

To document the extent, elevation, and relationship of the terrace deposits to the underlying structure of the Siwalik Hills, we constructed larger scale maps and elevational surveys of the slopes of the Khajnawara and Shajahanpur rao surfaces (Figure 5). Along the margins of Khajnawara rao, two distinct terraces are preserved: the higher and middle terraces. Along Shajahanpur rao, only the higher is preserved. The surfaces of the southernmost remnants of the high terrace are broad and flat along both raos. The strath terrace deposits are about 10 m thick, with the surfaces and bases at about 30 and 20 m above the current stream grade, respectively. The variation in terrace deposit thickness and disparity between the slope of the surface and base of the terrace deposit along Shajahanpur rao is probably not real because the northernmost survey point on the surface is taken on a smaller degraded remnant of the surface. For both raos, the grades of the active stream and the base of the uplifted fluvial deposits are indistinguishable, ranging between 1 and 2%. The Khajnawara terrace sits upon a tight and overturned fold within the underlying Siwalik Group (Figure 5). The structure is inferred to be a subsidiary drag fold on the southern limb of a broader Mohand Anticline. The elevational profiles of the overlying terrace deposits show no signature of folding or tilting.

The Yamuna terrace deposit is the broadest in extent (Figure 3). The relief of the currently cultivated Yamuna terrace is greater than that observed along the Shajahanpur and Khajnawara raos and is characterized by broad hills and swales ranging from several meters to 10 m in height. The larger size of geomorphic features in comparison to those observed on similar surfaces along the ephemeral raos reflects in part the greater size and energy of the Yamuna River along which the terrace is formed. Visual inspection of cliff exposures near Faizpur shows the deposits are coarser (containing boulders) than the lesser raos, that they reach about 25 m above current grade and, in turn, rest upon a 9-m-high exposure of upper Siwalik strata which dip steeply to the south. The Yamuna terrace surface thus appears correlative to those along Khajnawara and Shajahanpur raos farther to the east. The higher fluvial terrace deposits observed along the other raos of the map area are generally limited to erosional remnants with basal contacts of the terrace deposits resting on Siwaliks at elevations like those observed at Khajnawara and Shajahanpur raos.

4. Age of Terrace Deposits

We excavated numerous pits on the Khajnawara and Shajahanpur rao terraces to examine soil development and to search for dateable material (Figure 5). The pits were all placed in the fine-grained deposits capping the strath terraces (Figure 4) and all exhibited similar characteristics. We describe in detail two pits, 10 m apart, on the Shajahanpur terrace surface (SHA1 and SHA2, Figure 5). Horizon thicknesses, colors,

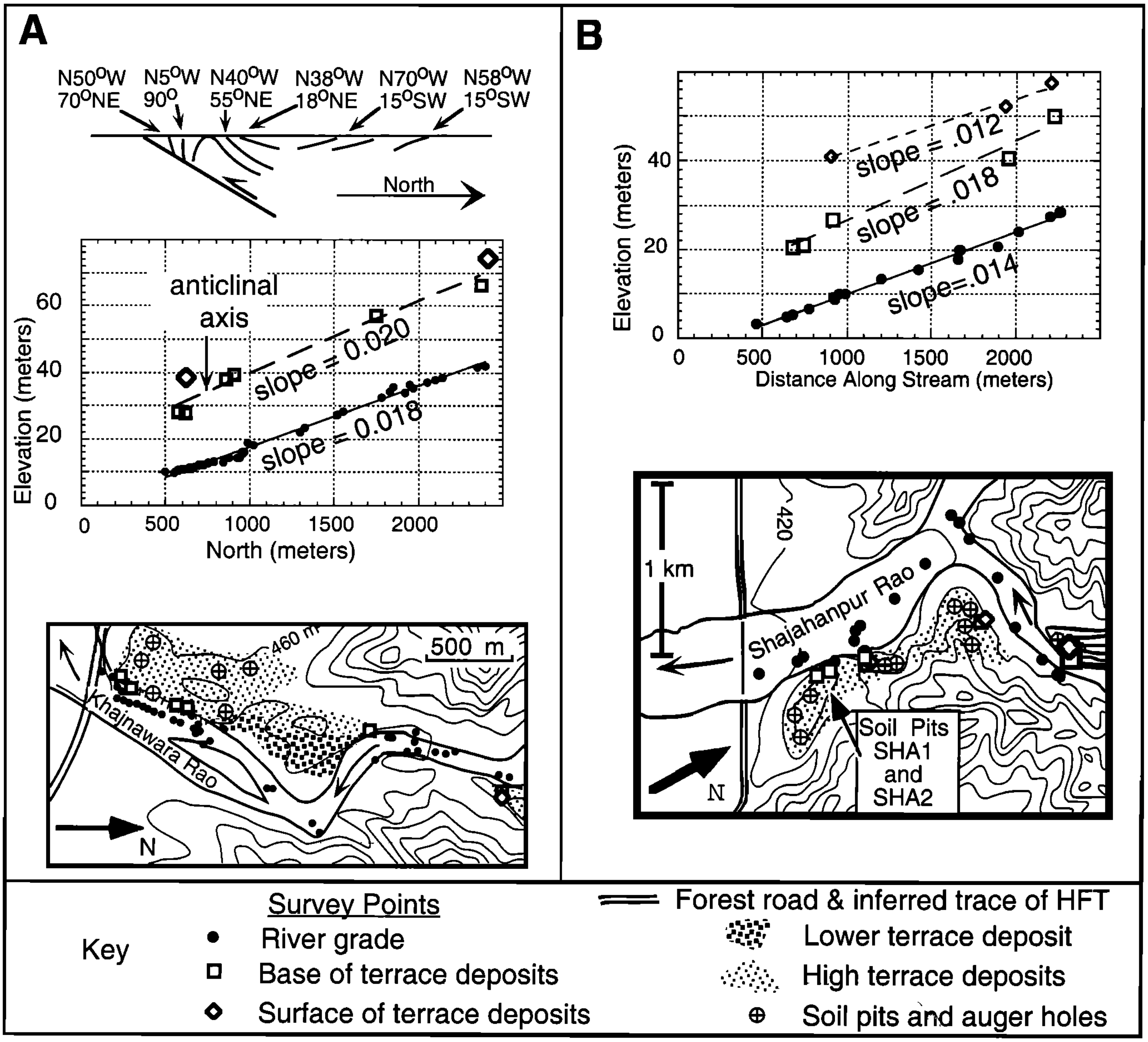

Figure 5. Map distribution and elevational surveys of abandoned fluvial terrace deposits along (a) Khajnawara rao and (b) Shajahanpur rao. Highest and intermediate strath terrace deposits are shaded dark and light gray, respectively. Strike and dip measurements show the Khajnawara terrace deposits are underlain by a tight and overturned fold of Siwalik sediments. The cross section and strike and dip measurements of the Siwalik beds along Khajnawara rao are aligned with and plotted at same horizontal scale as the elevational survey below. Elevation and distance measurements taken with respect to arbitrary datum near mouth of raos using electronic total station (Sokkia Set2b). Note extreme vertical exaggeration of profile plots. Contour intervals are 20 m. Inferred trace of HFT follows the forest road (see Figure 3 also). Thick vegetation precluded systematic survey of terrace surfaces. Surveys conducted from river beds by sighting on local cliff exposures. Arrow points to site of soil Pits SHA1 and SHA2 described in text.

structure, consistency, and reaction with acid were described in the field (Table 1) and weight percentages of sand, silt, and clay for each horizon were determined in the lab (Figure 6).

In soil pits SHA1 and SHA2, fragments of red clay pottery are disseminated through the B horizon to depths of 120 and 85 cm, respectively (Figure 6). In SHA1, disseminated charcoal between 80 and 120 cm depth was observed, collected, and dated at 1665 ± 215 calendar years B.C. (3663 ± 215 radiocarbon years before present) (sample BETA-114197). The presence of pottery raises the concern that the terrace deposits have been disturbed, which motivated us to excavate about two dozen test pits and auger holes on the Shajahanpur and Khajnawara terraces (Figure 5) as well as farther to the west on Kaluwala and Sahansara terraces (Figure 3). Many of

Table 1. Soil Characteristics

Soil Horizon	Depth, cm	Munsell Color[a] (moist)	Boundaries[b]	Texture[c]	Structure[d]	Consistence (wet)[e]	Comments
					Pit SHA1		
A1	0-12	10YR3/2 vdgb	ci	sl	1msbk	wso wss	
A2	12-43	10YR3/1 vdg	gs	sl	1msbk	wss	
Bw	43-200	10YR4/4 dyb	aw	sl	1msbk	wss	Thickness attributed to cumulate origin, pottery fragments and charcoal disseminated in Bw horizon to depth of 100 cm. Charcoal sampled for radiocarbon dating at 80 to 100 cm depth
2Bw	200- >220	7.5YR4/4 b	-	sl	1msbk	wss?	Change in parent material from sl to pebble-cobble gravels of fluvial origin
					Pit SHA2		
A1	0-17	10YR4/2.5 dgb & b	gs	ls	1mcsbk	wso wpo	
A2	17-47	10YR4/2.5 dgb & b	dw	ls	1fmsbk	wso wpo	
Bw	47-283	10YR5/5 to 10YR4/5 yb to dyb	ds	ls to sl	12fmsbk	wps	Thickness attributed to cumulate origin, gradational from ls to sl at about 150cm depth. Gradation in color occurs at about 120 cm. Small patches of original lamination? observed between 83-118 cm. weak to moderate reaction with HCL below 325 cm. no reaction with HCL observed in any other horizons.
C	283- >360	10YR4.5/5 dyb	-	ls	0	wss	

a, abbreviations are v very; d dark; g gray(ish); b brown; y yellowish.
b, abbreviations are ds diffuse smooth; aw abrupt wavy; gs gradual smooth; ci clear irregular; ds diffuse wavy.
c, abbreviations are sl sandy loam; ls loamy sand.
d, abbreviations are 0 structureless; 1 weak; 2 moderate; f fine; m=medium; sbk subangular blocky.
e, abbreviations are wss slightly sticky; wso nonsticky; wpo nonplastic; wps slightly plastic.

the pits were purposely located at sites least suitable for habitation or disturbance by humans, such as small rounded erosional remnants, along cliff edges, and sites where only a thin cap of overbank deposits covered underlying fluvial gravels. All the test pits and auger holes contained bits of brick pottery in the upper meter of the profiles. This suggests that the brick pottery fragments and charcoal were disseminated and incorporated into the deposits while the surface was still an active floodplain. The lack of any disturbed fabric within the SHA1 and SHA2 soil pits and the apparently undisturbed nature of the surface and deposit are consistent with this interpretation. The radiocarbon age obtained on the charcoal collected from soil pit SHA1 thus places a maximum bound on the age of the uplifted terrace surface.

The radiocarbon age for the terrace is supported by a study of Holocene soil development along the Gandak River, a tributary to the Ganga. The Gandak River sits approximately 800 km east of Dehra Dun and shares the same climatic factors as the Siwalik range front near Dehra Dun [*National Atlas Association of India*, 1977]. *Mohindra et al.* [1992] and *Mohindra* [1995] documented the degree of soil development on Holocene surfaces of the Gandak fluvial megafan within the middle Gangetic Plain of India and determined the ages of those surfaces based on archaeological considerations and radiocarbon dates on correlative surfaces. There, on surfaces of parent material like that observed on the terraces considered in this study, moderate to strong argillic horizons reaching 55 cm in thickness typify soils developed on surfaces older than 2500 years. In comparison, clay illuviation on the Shajahanpur surface is weak to absent and the weak Bw horizonation extends to thicknesses of 150 to 200 cm (Table 1 and Figure 6). We interpret the weak structural grade yet significantly thicker Bw horizons on the Shajahanpur and Khajnawara rao terraces to represent cumulative soil profiles, whereby soil development was accompanied by continued deposition. In comparison to soil development on the Gandak megafan [*Mohindra et al.*, 1992; *Mohindra,* 1995], the minimal to absent clay illuviation observed in the Shajahanpur and Khajnawara profiles would indicate no more than about 2500 years of soil development.

5. Fault Slip Rate

The presence of fluvial terraces above modern streams may generally be attributed to climatically induced changes in fluvial regime from one of aggradation to one of incision, geomorphic evolution of the source drainage basins resulting in variations in discharge and sediment, or stream incision resulting from tectonic uplift. In this area, a number of observations point to tectonic uplift due to displacement on an underlying fault as the likely cause of the strath terrace deposits (Figure 3). The raos issuing from the Siwalik Hills are currently producing an apron of coalescing fan deposits.

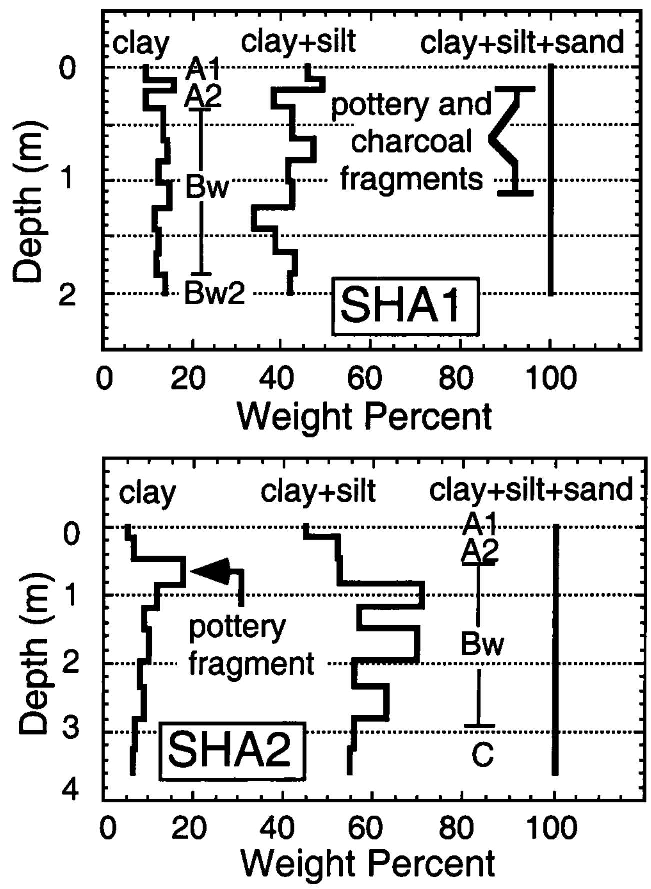

Figure 6. Cumulative weight percent clay, silt and sand as a function of depth for Shajahanpur soil pits SHA1 and SHA2. Soil horizons identified in field are labeled.

Fan-head incision along the major streams is generally small, of the order of 1-2 m and less than water levels at flood stage, which is consistent with the streams being in a stage of dynamic equilibrium or aggradation. Older fan remnants directly adjacent to the range front that might be correlated with the mapped strath terrace deposits preserved upstream are not observed in the study area. Rather, the distribution of strath terrace deposits ends at the Siwalik range front. The truncation of the terraces at the range front and the 20 m of incision into Siwalik bedrock beneath the strath terrace deposits are most simply explained by displacement on an underlying Mohand thrust fault that projects to or very close to the surface at the Siwalik range front. Additionally, the apparent lack of any significant degree of warping or folding of the terraces is consistent with displacement on an underlying fault that lacks any significant curvature beneath the terraces.

The strath terraces are consistently 30 m above modern stream grade. Only the lower 20 m of the elevation difference is represented by incision of Siwalik bedrock. Because incision of the upper 10 m of gravel deposits may reflect a climatic signal, and assuming that the incision of bedrock is best explained by tectonic uplift, the amount of uplift postdating terrace formation is estimated at 20 to 30 m. In conjunction with the single radiocarbon age, this yields a vertical uplift rate of $\geq 6.9 \pm 1.8$ mm/yr. The rate is expressed as a minimum with the recognition that the radiocarbon age is a maximum for the displaced surfaces. Assuming the 30° dip indicated by previously discussed drillhole and seismic reflection data is representative of the HFT beneath the terrace deposits, the uplift rate equates to horizontal shortening and fault slip rates across the Himalayan Frontal Thrust of $\geq 11.9 \pm 3.1$ mm/yr and $\geq 13.8 \pm 3.6$ mm/yr, respectively.

6. Scarps in Alluvium

Raiverman et al. [1993] noted that the Himalayan Frontal Thrust is "concealed" by Quaternary deposits or eroded within the map area, and our observations largely support their conclusion. However, a short segment of the range front near Chapri rao and west of the Yamuna River displays a morphology suggestive of surface faulting in late Pleistocene or younger deposits. West of the Yamuna River near the village of Trybryon (Figure 3) a scarp cuts through alluvial gravels and strikes westward and parallel to the range front (Figure 7). The scarp ranges in height from about 9 m west of Trybryon to about twice that toward the Yamuna River. In contrast to results of survey measurements east of the Yamuna River, back-tilting of the hanging wall is suggested by the capture and deflection of Nagal Khol (stream) before it crosses the scarp (Figure 3). Because of such stream capture and deflection, the gravels east of Trybryon and between the fault and the Siwaliks now form a long rounded ridge striking parallel to the scarp. The morphology resembles a small-scale Doon Valley, where in a similar manner the uplifted and tilted Siwaliks capture, deflect, and then allow the southward escape of the Yamuna River (Figure 2).

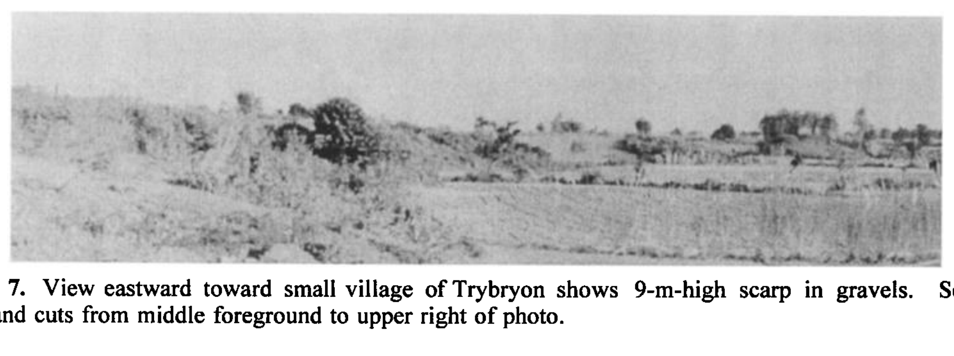

Figure 7. View eastward toward small village of Trybryon shows 9-m-high scarp in gravels. Scarp faces south and cuts from middle foreground to upper right of photo.

7. Discussion and Conclusions

The only other direct estimate of convergence rate along the HFT based on offset of late Pleistocene and Holocene deposits arises from recent work of *Avouac et al.* [1998]. About 800 km southeast of Dehra Dun in Nepal, they interpret a suite of abandoned fluvial terrace deposits to indicate that the HFT is taking up 21+/-1 mm/yr of convergence. If both the Dehra Dun rate ($\geq 11.9 \pm 3.1$ mm/yr) and Nepal rate estimates closely reflect the actual rates, convergence across the Himalayan Frontal Thrust decreases systematically from east to west. Utilizing a finite modeling technique and information bearing on the Quaternary slip rate of faults to the north of the Himalayan arc, *Peltzer and Saucier* [1996] recently examined the residual amount of convergence expected along the Himalayan front. Their preferred model predicts a similar westward decrease in convergence along the HFT from 18 mm/yr in Nepal to 10 mm/yr northwest of Dehra Dun.

Baker et al. [1988] utilized retrodeformable cross section analysis in the Salt Range of Pakistan to place a minimum bound of 9 - 14 mm/yr of convergence across the Himalayan front averaged over the last 2.1 to 1.6 Ma. Similar analysis of similar age rocks by *Powers et al.* [1998] determined shortening rates of 11±5 mm/yr and 14±2 mm/yr across the HFT in Dehra Dun and northwest of Dehra Dun in the meisoseismal area of the 1905 Kangra earthquake, respectively. Using deep well data to document the age of basal sediments in the Indo-Gangetic Plain as a function of distance from the Himalayan arc, *Lyon-Caen and Molnar* [1985] estimated convergence across the front of the Indian Himalaya to average 15±5 mm/yr over the last 15 to 20 Ma. Temporally bracketed restorations of regional cross sections across the Lesser Himalaya have yielded similar rates of crustal shortening since early Tertiary at 13±5 mm/yr and ~21 mm/yr in eastern and western Nepal, respectively [*Srivastava and Mitra*, 1994; *DeCelles et al.*, 1998]. The similarity of the Holocene rate at Dehra Dun to these previous estimates is most simply interpreted to indicate that, within the uncertainties of the measurements, thrust motion and shortening along the Himalayan arc has been relatively steady through the Neogene.

Based on estimates of the seismic moments of the largest Himalayan thrust earthquakes during the last 90 years and assumption of the dimensions of the Himalayan thrust, *Molnar and Deng* [1984] and *Molnar* [1990] calculated to within a factor of 2 uncertainty that thrust earthquakes accommodate about 17 mm/yr of convergence along the Himalayan arc, a result similar to the rate we have determined from the displaced terrace deposits at Dehra Dun. On an even shorter timescale, *Bilham et al.* [1998] analyzed 4 years of Global Positioning System (GPS) data in Nepal. Their results showed elastic contraction which they attribute to convergence of 21±3 mm/yr, which is essentially the same as convergence rates across the HFT based on late Pleistocene deposits in Nepal [*Avouac et al.*, 1998]. The general agreement between the Holocene fault slip rates and those interpreted from historical and geodetic records can be interpreted to indicate that Holocene rates of deformation are a good indicator for rates of elastic strain accumulation and long-term rates of seismicity, although the agreement could be fortuitous because secular variation in elastic strain and rates of seismicity may be greater than the respective recording periods.

Somewhat unexpectedly, the measurements of *Bilham et al.* [1997] show that the geodetic strain is focused above the MCT, whereas the work of *Avouac et al.* [1998] indicates that the permanent accommodation of that strain is recorded well to the south along the HFT. The observations suggest a process whereby elastic strain accumulation occurs beneath the MCT and is periodically released by a slip pulse that propagates southward on an underlying decollement and registered as permanent displacement along the HFT [*Bilham et al.*, 1998; *Brune*, 1996]. Thus the patterns of interseismic strain accumulation and permanent strain release appear not to be symmetric. The observation that historical earthquake meisoseismal regions are concentrated to the south of the MCT (Figure 1) and the rate of late Holocene uplift recorded along the HFT in this study are consistent with such a process, although geodetic measurements in India are currently insufficient to test the idea.

Dehra Dun sits at the eastern edge of the great 1905 Kangra earthquake meisoseismal areas (Figure 1). It is assumed that the event was the result of thrust motion on the HFT based on the isoseismal distribution, the tectonic framework, and the observation that nearby instrumentally recorded earthquakes show shallow northward dipping nodal planes [*Seeber and Armbruster*, 1981; *Molnar and Pandey*, 1989]. It is not certain whether the rupture actually extended to Dehra Dun [*Molnar*, 1990]. On the basis of intensity, *Molnar* [1990] estimated the seismic moment of the 1905 event to be about 2 x 10^{21} N/m^2, with coseismic slip of 5-10 m. Dividing the coseismic slip by the slip rate at Dehra Dun ($\geq 13.8 \pm 3.6$ mm/yr) yields a maximum bound of 290 to 980 years for 1905-type events. Primary surface rupture was not observed during 1905 or the other great thrust events (Figure 1) of Assam (1897 and 1950) and Bihar (1934) along the arc [*e.g.*, *Molnar*, 1990; *Yeats and Thakur*, 1998]. The lack of surface rupture during these events has been attributed to their occurrence on blind thrusts [*Yeats et al.*, 1992; *Yeats and Thakur*, 1998]. Yet the occurrence of the possible fault scarp at Trybryon suggests the occurrence of earthquake ruptures of size sufficient to rupture to the surface and produce coseismic scarps. The scalloped, embayed, and fluvially incised morphology of the scarp at Trybryon implies the scarp predates the 1905 earthquake. These latter observations and the lack of primary surface rupture during great historical earthquakes suggest a potential for earthquakes along the Himalayan Frontal Thrust larger than those observed historically.

Acknowledgments. A special thanks to Firoze and Sucheta Dotiwala for their help and kindness. The work was conducted while S.G.W. was a Fulbright Fellow and guest of the Wadia Insitute of Himalayan Geology in Dehra Dun, India. The manuscript was prepared while S.G.W. was a Visiting Fellow of CIRES, University of Colorado at Boulder. R. Bilham, T. Rockwell, and K. Mueller, and P. Molnar provided useful comments on an early draft of the paper. The final manuscript benefited significantly from the constructive reviews of P. DeCelles, D. Scholl, R. Schweickert, and two anonymous reviewers. Center for Neotectonics contribution 30.

References

Armijo, A., P. Tapponnier, and H. Tonglin, Late Cenozoic right-lateral strike-slip faulting in southern Tibet, *J. of Geophys Res*, *94*, 2787-2838, 1989.

Avouac, J P., J Lave, R. Cattin, M.R. Pandey, and R.P Tandukar, Active mountain building in the Himalaya of Nepal, *Eos Trans AGU, 79*, (US), Fall Meet Suppl., F204, 1998.

Baker, D.M., R.J. Lillie, R S Yeats, G.D. Johnson, M. Yousuf, and A.S.H. Zamin, Development of the Himalayan frontal thrust zone, Salt Range, Pakistan, *Geology, 16*, 3-7, 1988.

Bilham, R., K Larson, J. Freymueller, and Project Idylhim members, GPS measurements of present-day convergence across the Nepal Himalaya, *Nature, 386*, 61-64, 1997.

Bilham, R., F. Blume, R Bendick, and V.K. Gaur, Geodetic constraints on the translation and deformation of India, implications for future great Himalayan earthquakes, *Curr Sci*, *74*, 213-229, 1998.

Brune, J N, Particle motions in a physical model of shallow angle thrust faulting, Proc. Indian Acad. Sci., *Earth and Planetary Sciences, 105*, L197-L206, 1996.

DeCelles, P G., G.E Gehrels, J. Quade, T.P Ojha, P.A. Kapp, and B N. Upreti, Neogene foreland basin deposits, erosional unroofing, and the kinematic history of the Himalayan fold-thrust belt, western Nepal, *Geol Soc Am Bull*, *110*, 2-21, 1998.

Demets, C., R. Gordon, D. Argus, and S. Stein, Effect of recent revisions to the geomagnetic reversal time scale on estimates of current plate motions, *Geophys Res Lett.*, *21*, 2191-2194, 1994.

Freymueller, J., R. Bilham, R. Burgmann, K.M. Larson, J Paul, S Jade, and V.K. Gaur, Global positioning system measurements of Indian plate motion and convergence across the Lesser Himalaya, *Geophys Res Lett*, *23*, 3107-3110, 1996.

Gansser, A, The geodynamic history of the Himalaya, in *Zagros•Hindu Kush•Himalaya•Geodynamic Evolution, Geodyn Ser vol 3*, edited by H K. Gupta and F.M Delany, AGU, Washington D. C., pp.111-121, 1981.

Johnson, G D., P Zeitler, C.W. Naeser, N.M. Johnson, D.M Summers, C.D. Frost, N. D. Opdyke, and R.A.K. Tahirkheli, The occurrence and fission-track ages of Late Neogene and Quaternary volcanic sediments, Siwalik Group, Northern Pakistan, *Paleogeogr*, *Palaeoclimatol., Palaeoecol, 37*, 63-93, 1982.

Johnson, G.D., N.D Opdyke, S.K. Tandon, and A.C Nanda, The magnetic polarity stratigraphy of the Siwalik Group at Haritalyangar (India) and a new last appearance datum for Ramapithecus and Sivapithecus in Asia, *Paleogeogr*, *Palaeoclimatol*, *Palaeoecol.*, *44*, 223-249, 1983.

Johnson, N. M., N. D Opdyke, G. D. Johnson, E. H. Lindsay, . and R. A. K. Tahirkheli, Magnetic polarity stratigraphy and ages of Siwalik group rocks of the Potwar Plateau, Pakistan, *Paleogeogr*, *Palaeoclimatol*, *Palaeoecol*, *37*, 17-42, 1982.

Kumar, R., S K Ghosh, N.S. Virdi, and N R Phadtare, The Siwalik foreland basin, *Spec. Pub. 1*, p 61, Wadia Inst. of Himalayan Geol, Dehra Dun, India, 1991

Lyon-Caen, H., and P. Molnar, Gravity anomalies, flexure of the Indian Plate, and the structure, support and evolution of the Himalaya and Ganga basin, *Tectonics, 4*, 513-538, 1985.

Mohindra, R., Holocene soil chronoassociation in part of the Middle Gangetic Plain, morphological and micromorphological characteristics, *Terra Nova, 7*, 305-314, 1995.

Mohindra, R., B. Parkash, and J. Prasad, Historical geomorphology and pedology of the Gandak Megafan, Middle Gangetic Plains, India, *Earth Surf. Processes Landforms, 17*, 643-662, 1992.

Molnar, P., A review of the seismicity and the rates of active underthrusting and deformation at the Himalaya, *J of Himalayan Geol*, *1*, 131-154, 1990.

Molnar, P., and D. Deng, Faulting associated with large earthquakes and the average rate of deformation in central and eastern Asia, *J Geophys Res*, *89*, 6203-6227, 1984.

Molnar, P, and M.R. Pandey, Rupture zones of great earthquakes in the Himalaya region, Proc. Indian Acad. of Sci., *Earth Planet Sci*, *98*, 61-70, 1989.

Molnar, P., and P. Tapponnier, The collision between India and Eurasia, *Sci. Amer.*, *236*, 30-41, 1977.

Nakata, T, Geomorphic history and crustal movements of the foothills of the Himalayas, Sci. Rep. *Tohoku Univ*, *Ser. 7th Ser*, *22*, 39-177, 1972.

Nakata, T, Active faults of the Himlaya of India and Nepal, *Geological Society of America Special Paper, 232*, 243-264, 1989.

National Atlas Association of India, National Atlas of India, plate 68, New Dehli, 1977.

Peltzer, G., and F. Saucier, Present-day kinematics of Asia derived from geologic fault rates, *J Geophys Res*, *101*, 27,943-27,956, 1996.

Powers, P M., R.J Lillie, and R.S. Yeats, Structure and shortening of the Kangra and Dehra Dun Reentrants, Sub-Himalaya, India, *Geol Soc Am Bull., 110*, 1010-1027, 1998.

Raiverman, V., A.K. Srivastava, and D.N. Prasad, On the Foothill Thrust of northwestern Himalaya, *J of Himalayan Geol., 4*, 237-256, 1993.

Rao, Y.S N., A A. Rahman, and D.P. Rao, On the structure of the Siwalik range between rivers Yamuna and Ganga, *Himalayan Geol*, *4*, 137-150, 1974.

Seeber, L., and J.G. Armbruster, Great detachment earthquakes along the Himalayan arc and long-term forecasting, *Earthquake Prediction An International Review*, *Maurice Ewing Series* vol. 4, edited by D W. Simpson and P.G. Richards, AGU, pp. 259-277, Washington, D.C, 1981.

Srivastava, P., and G. Mitra, Thrust geometries and deep structure of the outer and lesser Himalaya, Kumaon and Garhwal (India): Implications for evolution of the Himalayan fold-and-thrust belt, *Tectonics, 13*, 89-109, 1994.

Thakur, V. C., Geology of Dun Valley, Garhwal Himalaya, neotectonics and coeval deposition with fault-propagation folds, *J. of Himalayan Geol*, *6*, 1-8, 1995.

Valdiya, K.S., The Main Boundary Thrust zone of the Himalaya, India, *Ann Tectonicae, 6* suppl, 54-84, 1992.

Yeats, R.S, and V C Thakur, Reassessment of earthquake hazard based on a fault-bend fold model of the Himalayan plate-boundary fault, *Curr Sci*, *74*, 230-233 1998.

Yeats, R.S., T. Nakata, A. Farah, M. Fort, M. A. Mirza, M. R. Pandey, and R S. Stein, The Himalayan frontal fault system, *Ann Tectonicae*, *6* suppl., 85-98, 1992.

S. Kumar, R. Mohindra, and V.C. Thakur, Wadia Institute of Himalayan Geology, 33 General Mahadeo Singh Road, Dehra Dun 248 001 (U.P.) India.

S. G. Wesnousky, Center for Neotectonic Studies and Department of Geological Sciences, University of Nevada, M.S. 169, Mackay School of Mines, Reno, NV 89557-0135 (stevew@seismo unr edu)

(Received July 17, 1998;
revised May 18, 1999,
accepted May 26, 1999.)